Edited by C. L. Hussey, J. S. Wilkes,
S. N. Flengas, and Y. Ito
SEVENTH INTERNATIONAL SYMPOSIUM

MOLTEN SALTS

PV 90-17

PROCEEDINGS OF THE SEVENTH INTERNATIONAL SYMPOSIUM ON

MOLTEN SALTS

Edited by

Charles L. Hussey
Department of Chemistry
University of Mississippi
University, Mississippi

S. N. Flengas
Department of Metallurgy and Materials Science
University of Toronto
Toronto, Ontario, Canada

John S. Wilkes
F. J. Seiler Research Laboratory
U.S. Air Force Academy
Colorado Springs, Colorado

Yasuhiko Ito
Department of Nuclear Engineering
Kyoto University
Kyoto, Japan

PHYSICAL ELECTROCHEMISTRY AND HIGH TEMPERATURE MATERIALS DIVISIONS

Proceedings Volume 90-17

THE ELECTROCHEMICAL SOCIETY, INC., 10 South Main St., Pennington, NJ 08534-2896

PROCEEDINGS OF THE SEVENTH INTERNATIONAL SYMPOSIUM ON

MOLTEN SALTS

Edited by

Charles L. Hussey
Department of Chemistry
University of Mississippi
University, Mississippi

S. N. Flengas
Department of Metallurgy and Materials Science
University of Toronto
Toronto, Ontario, Canada

John S. Wilkes
F. J. Seiler Research Laboratory
U.S. Air Force Academy
Colorado Springs, Colorado

Yasuhiko Ito
Department of Nuclear Engineering
Kyoto University
Kyoto, Japan

PHYSICAL ELECTROCHEMISTRY AND HIGH TEMPERATURE MATERIALS DIVISIONS

Proceedings Volume 90-17

THE ELECTROCHEMICAL SOCIETY, INC., 10 South Main St., Pennington, NJ 08534-2896

Copyright 1990
by
The Electrochemical Society, Incorporated

Papers contained herein may not be reprinted and may not be digested by publications other than those of The Electrochemical Society in excess of 1/6 of the material presented.

Library of Congress Catalog Number: 90-84376
Printed in the United States of America

PREFACE

The Seventh International Symposium on Molten Salts was held May 6-11, 1990, at the Queen Elizabeth Hotel in Montreal, Quebec, Canada in conjunction with the 177th Meeting of the Electrochemical Society. Financial support for the symposium was provided by the Physical Electrochemistry and High Temperature Materials Divisions of the Society and by the U. S. Air Force Office of Scientific Research. The co-organizers of this symposium were Prof. Charles L. Hussey, University of Mississippi; Dr. John S. Wilkes, United States Air Force Academy; Prof. Spiro N. Flengas, University of Toronto; and Prof. Yasuhiko Ito, Kyoto University. These same individuals also serve as the co-editors of this volume.

One of the highlights of the meeting was the presentation of the Max Bredig Award to Dr. G. Pedro Smith, who received the award for his many important contributions to field of molten salt chemistry. A short biographical sketch of Dr. Smith is provided on the next two pages by Prof. Gleb Mamantov of the University of Tennessee and is followed by a text of Dr. Smith's award address.

The Seventh International Symposium on Molten Salts was truly international in that symposium participants originated from Belgium, Canada, China, Czechoslovakia, Denmark, England, France, Germany, Greece, Italy, Japan, the Netherlands, Norway, and the U.S. Sixty-nine of the seventy papers presented at this symposium are included in this volume. These papers cover a diverse range of topics, including batteries and fuel cells, electrochemistry, structure, theory, thermodynamics, transport properties, and both inorganic and organic synthesis.

I wish to extend my appreciation to Dr. Wilkes, Prof. Flengas, and Prof. Ito for their help with the planning and administration of the symposium and for their editorial assistance during the preparation of this volume. I also wish to acknowledge the assistance of Ms. Harriet D. Hearn.

Charles L. Hussey
University of Mississippi

FACTS ABOUT THE ELECTROCHEMICAL SOCIETY, INC.

The Electrochemical Society, Inc., is a nonprofit, scientific, educational, international organization founded for the advancement of the theory and practice of electrochemistry, electrothermics, electronics, and allied subjects. The Society was founded in Philadelphia in 1902 and incorporated in 1930. There are currently over 5000 scientists and engineers from more than 40 countries who hold individual membership; the Society is also supported by more than 100 corporations through Patron and Sustaining Memberships.

The technical activities of the Society are carried on by Divisions and Groups. Local Sections of the Society have been organized in a number of cities and regions.

Major international meetings of the Society are held in the Spring and Fall of each year. At these meetings, the Divisions and Groups hold general sessions and sponsor symposia on specialized subjects.

The Society has an active publications program which includes the following.

JOURNAL OF THE ELECTROCHEMICAL SOCIETY - The JOURNAL is a monthly publication containing technical papers covering basic research and technology of interest in the areas of concern to the Society. Papers submitted for publication are subjected to careful evaluation and review by authorities in the field before acceptance, and high standards are maintained for the technical content of the JOURNAL.

EXTENDED ABSTRACTS - Extended abstracts of all technical papers presented at the Spring and Fall Meetings of the Society are published in serialized softbound volumes.

PROCEEDINGS VOLUMES - Papers presented in symposia at Society and Topical Meetings are published from time to time as serialized softbound Proceedings Volumes. These provide up-to-date views of specialized topics and frequently offer comprehensive treatment of rapidly developing areas.

MONOGRAPH VOLUMES - The Society has, for a number of years, sponsored the publication of hardbound Monograph Volumes, which provide authoritative accounts of specific topics in electrochemistry, solid state science and related disciplines.

G. Pedro Smith - 1990 Recipient of the Max Bredig Award

The Max Bredig Award was established in 1984 by the Physical Electrochemistry Division of the Electrochemical Society. This award is granted to a scientist working in the area of molten salt chemistry to recognize important scientific contributions to molten salt chemistry. The first such award was given to Milton Blander in 1987 at the time of the 6th International Molten Salt Symposium in Honolulu. This award is financed from the income of the Max Bredig Award Fund established for this purpose by contributions from ARCO Metals Co. and the Aluminum Co. of America.

The award is named in honor of Max Bredig, a member of the Chemistry Division, Oak Ridge National Laboratory, during 1946-77. Max Bredig is best remembered for his pioneering studies on phase equilibria, electrical conductivity and thermodynamic properties of alkali metal-alkali metal halide systems. As a student in Haber's Institute in Berlin and as a research associate in Gottingen in the 1920's, he had contact with Nernst, Planck and other scientific giants of that era. He was probably influenced by his father, Professor Georg Bredig of Karlsruhe, who is the originator of the Bredig arc method for preparing colloidal suspensions of metals. I remember Max as a key contributor to a number of Gordon Conferences, including the one he chaired in 1965, and as a lecturer in a course on molten salt chemistry that I organized in 1965. Another lecturer in that course was this year's award winner, G. Pedro Smith.

Pedro was born in Norfolk, VA in 1923; he received his BS, MS, Ph.D. (1950) from the University of Virginia. His graduate research dealt with the chemistry of single metal crystals. In 1950 he joined ORNL where he first headed a group studying corrosion at high temperatures.

In mid - 1950's he organized a group to investigate optical spectra of molten salts; this pioneering research was continued until 1970. At that time Pedro started exploring possibilities for using molten salts as catalysts in the manufacture of synthetic fuels from coal.

In 1972-73 he was a Visiting Professor, Technical University of Denmark. He also served as a visiting lecturer at the Norwegian Institute of Technology in 1970 and 1978. In 1975 he and his colleagues began mechanistic studies of the reactions of aromatic compounds in molten metal halides. In addition to his work at ORNL, Dr. Smith has had an active teaching career at the University of Tennessee, as a lecturer in Metallurgy (1951-63), UT-ORNL Professor of Chemistry (1963-76), and Adjunct Professor of Chemistry (1982 - present). He has supervised the research of several UT graduate students.

He has served as the chairman of the 1971 Gordon Research Conference on Molten Salts, program chairman, SE ACS Regional Meeting, 1976, coeditor of the first 3 volumes of Advances in Molten Salt Chemistry, and as a lecturer at the NATO Advanced Study Institute on Molten Salt Chemistry (1986).

Dr. Smith has made key contributions to several areas of molten salt chemistry. A central theme of his work has been the discovery and spectroscopic characterization of unusual chemical species that can be stabilized in molten salts, including halide coordination complexes of transition metal ions, subvalent ions and clusters of Group V elements, and conjugate acids and cation radicals of aromatic hydrocarbons.

Dr. Smith retired from ORNL at the end of 1988. His involvement in molten salt chemistry is profoundly missed by all of us.

Gleb Mamantov
University of Tennessee,
Knoxville

TABLE OF CONTENTS

DOI: 10.1149/199017.0001PV

THE SEARCH FOR UNUSUAL REACTIONS AND SPECIES IN MOLTEN METAL HALIDES

G. Pedro Smith
7925 Chesterfield Drive
Knoxville, Tennessee 37909, USA

Thank you Professor Mamantov for your introduction. I also wish to thank the Organizing Committee of the Seventh International Symposium on Molten Salts for having so thoughtfully arranged tonight's award banquet - good food and drink, old friendships renewed - it is an evening to savor and remember.

For me it is especially meaningful that this banquet is being held here in the city of Montreal. A generation ago, in 1961, Montreal was host to a symposium on molten salts held in conjunction with the International Congress of Pure and Applied Chemistry. At that time molten salt research was in the midst of a renaissance that had been gathering momentum for over a decade. I had only recently begun work in this field and for me that meeting was an exhilarating experience.

A leader in that renaissance and a prominent personality at that meeting was the late Max Bredig in whose honor the award in molten salt chemistry was established. Max was the foremost experimentalist of his time and a gem of a person. I had the good fortune to know him well. His encouragement and advice did much to shape my career.

This week, here in Montreal, we are once more attending an outstanding symposium on molten salts at a time when this field is in the midst of a new period of growth and accomplishment under the leadership of a new generation. I like to think of tonight's banquet as a time to remember the old while we celebrate the new.

In that context it is now incumbent upon me to deliver an "award address", a response to the honor bestowed on me for research that was in fact the result of collaboration with many scientists over the years. To them I say, Thank you; without your scientific insight and hard work I would not be here tonight. To the rest of you gathered here there is little about our research that I haven't recounted many times in the past. Perhaps one last retelling of a bit of it will do no harm.

Much of the research that my colleagues and I did had the character of a treasure hunt. It was a search for unusual solute species and reactions in molten salts. Such a search could not be planned in any detail. Usually we set forth with only a sketchy notion of where we were going and what it was we were looking for. Although a risky venture, it was not a frivolous one. On the contrary, the occurrence of unusual solute species in stable or persistent states tells us important things about the chemical environments that favor their presence. And when one happens upon a species that is new to science, one is blessed with a unique opportunity to characterize it and learn something new about chemical structure and behavior.

Much of our research was done with anhydrous, molten metal halides and their mixtures. These liquids encompass a diverse array of chemical types, most of them quite different from the solvents familiar to chemists, many remain liquid at very high temperatures where few chemists venture. What more likely place to look for uncommon chemistry?

Tonight I shall tell of two treasure hunts that took place at different times and that began with completely different objectives but that in the end proved far more closely related than we could ever have guessed.

Once upon a time a very hot topic in molten salt research was the solubility of metals in their molten halides. Max Bredig, Sam Yosim and their colleagues were the leading investigators. By the time of the 1961 Montreal meeting the very difficult task of determining the phase diagrams of metal/metal halide systems was in an advanced state and research was increasingly being directed toward describing these melts on an atomic scale. In many cases, especially in the case of metal-rich melts, an appropriate description was best formulated in terms of concepts drawn from solid state physics. However, some dilute solutions of metals seemed to be something a chemist might sink his teeth in (figuratively, that is). Solutions of bismuth in its molten trihalides became the objects of a particularly intense debate. Bismuth in its 3+ state is very stable and no state inbetween this and the metal had been identified. Perhaps the solute was in the zero oxidation state. Among solute species proposed were Bi atoms and their dimers, Bi_2. However, phase diagrams of the bismuth/bismuth trihalide systems showed the presence of compounds with the approximate composition "BiX" (X = Cl, Br, I). Although these compounds decomposed on melting and nothing was known about their structures, they provided a basis for supposing that the 1+ oxidation state of bismuth might be stable in the right environment. Thus the Bi^+ ion and some of its polymers, $(Bi^+)_2$ and $(Bi^+)_4$, were suggested as possible solute species.

While this was going on, my colleagues and I were using UV-VIS spectroscopy for other purposes but we decided to have a look at solutions of Bi in $BiCl_3$. We found, not one but two solute species. However, we were unable to identify them. There were several problems. One was interference from a very broad intervalence bond due to the presence of Bi^{3+} in high concentration. Well, half a loaf is better than none, so we presented this result at the 1961 Montreal meeting.

Very soon after that Leo Topol and Bob Osteryoung presented electrochemical evidence that convincingly supported the identification of these two solute species as Bi^+ and $(Bi^+)_4$ in equilibrium, thus

$$4Bi^+ \rightleftarrows (Bi^+)_4$$

Now, the presence of Bi^{3+} at a high and virtually constant concentration precluded an experimental determination of its role. For example, the equilibrium

$$4Bi \rightleftharpoons (Bi_3)^+ + Bi^{3+}$$

also fitted the data, at least in a formal way. But one could reject this reaction as implausible because metal ions with fractional oxidation states were unknown to chemistry.

Then John Corbett determined the correct formula and crystal structure of "BiCl". Its formula was Bi_6Cl_7 and it contained an extraordinary ion, Bi_9^{5+}, a homopolyatomic cluster ion with a fractional oxidation state. Although this ion did not appear to survive in the melt, its existence completely changed our assumptions about the solution chemistry of Bi and sent us off on a treasure hunt.

Any further research in Bi-$BiCl_3$ melts seemed pointless. We needed solvents that mimicked the ability of bismuth trihalides to provide hospitable environments for lower oxidation states but in which Bi^{3+} need be present only at a low and controllable concentration. Working on the surmise that Lewis acidity was the controlling factor, we found that molten halozincates and haloaluminates served our purpose well.

Using these melts we found three solute species in low oxidation states: Bi^+, Bi_5^{3+} and Bi_8^{2+}. All had distinctive spectra. The formulas of these solutes were determined by changing the solvent composition and temperature in such a way as to change their relative stabilities and, thereby, shift their chemical equilibria. Subsequently, other investigators confirmed our identifications by preparing compounds containing these ions and determining their crystal structures.

The Bi^+ ion might have seemed quite ordinary by comparison with the exotic cluster ions, but, in fact, it was quite extraordinary. Its optical spectrum showed that its electron configuration was $\ldots 6p^2$, that is, it had an incomplete p shell in exactly the same sense that many transition metal ions are said to have incomplete d shells. Although ions with incomplete p shells are quite plentiful in stellar atmospheres and lightning bolts, they are most unusual as stable species in condensed matter.

During the last decade of my career as a molten salt chemist, my colleagues and I investigated organic reactions in molten metal halides. We often used molten $SbCl_3$ as a solvent. This substance is a chemical relative of $BiCl_3$ and, as you will see later, this relationship will tie my two stories together. But don't jump to conclusions, Sb metal is virtually unsoluble in molten $SbCl_3$, a fact that was established during the hay day of metal/metal halide chemistry.

Molten $SbCl_3$ is also a weak Lewis acid and a leveling solvent for strong Lewis acids and bases so that the acidity of the melt can be controlled over a moderate range by additions of acidic or basic chlorides. We made much use of this fact because many organic reactions are sensitive to melt acidity.

In our first experiments we simply dissolved polycyclic aromatic hydrocarbons (PAHs) in $SbCl_3$ under very clean conditions and watched what happened by using various in situ techniques as well as conventional quench-and-separation. Many of the PAHs underwent a well-known type of reaction, called a Scholl condensation, in which two PAH molecules condense to form a higher molecular weight PAH with the loss of two atoms of hydrogen for each carbon-carbon bond formed. Figure 1 shows some Scholl reactions for anthracene.

Scholl reactions are usually carried out in molten metal chlorides with a high Lewis acidity, typically $AlCl_3$. Thus, the ease with which they occurred in mildly acidic $SbCl_3$ was somewhat surprising but not nearly so surprising as what happened to the hydrogen that was released. No one had ever bothered to find out where this hydrogen went. The usual assumption was that it was liberated in elemental form and that may be true in $AlCl_3$ melts but in $SbCl_3$ we found it had a quite different fate; it quantitatively hydrogenated unreacted substrate PAH. An example of this reaction is shown in Fig. 2 where anthracene is again used as the substrate.

Since $SbCl_3$ is not usually thought of as a hydrogenation catalyst, this reaction posed a mechanistic puzzle. But an even more unexpected reaction took place when we increased the acidity with a small addition of $AlCl_3$. The reaction is illustrated in Fig. 3 with anthracene as the substrate. The hydrogen liberated by Scholl reactions quantitatively protonated the substrate with the release of an electron. The protonated PAHs (i.e., arenium ions) formed in this reaction are usually very unstable as solutes except in the presence of very strong protic acids. However, in these melts under essentially aprotic conditions they were formed in massive amounts and were quite stable. How they got there and why they were stable proved to be questions with important answers, but tonight I wish to focus attention on the fate of the electrons released by this reaction.

At first we thought the reduced product was Sb metal. Following quench we recovered the metal in the amount required by the reaction stoichiometry. However, there were some strange things about this reduction process. For one we could not recover any Sb metal by filtering the hot melt. For another, the metal recovered following quench was amorphous but quickly crystallized when heated.

Given our experience with Bi, it was tempting to suppose that the reduced form in the melt was an Sb species in a low oxidation state. In iodide melts Sb is known to form a catenated species, $I_2Sb\text{-}SbI_2$, in the formal oxidation state 2+ but nothing of that sort had been found in chloride melts and it was not likely to be stable in an acidic melt. Furthermore, in pure $SbCl_3$ the metal was virtually insoluble, as had been demonstrated long ago.

Then a happy accident occurred. While preparing an Sb electrode in $SbCl_3$ containing CsCl, we found the metal to be moderately soluble in such melts although the solubility rapidly diminished as the CsCl concentration was decreased. In this case the solute species clearly required a basic environment and was possibly related to $I_2Sb\text{-}SbI_2$. Since we were old-fashioned chemists, we were familiar with the phenomenon of amphoteric behavior and so we tried $SbCl_3$ acidified with $AlCl_3$. The metal was very soluble. We had stumbled upon a class of low oxidation state species that had been overlooked by prior investigators. When the melt was frozen, these species did not survive as stable entities and they have not been observed in other media. Their presence as solutes in molten $SbCl_3$ provides the basis for some quite unusual homogeneous reactions. Subsequently, we found similar organic reactions in molten Ga_2Cl_6 where the soluble reduced form was Ga^+, a species with a very limited stability range except in molten metal halides.

This research also had a frustrating side: We never pinpointed the identity of the low oxidation states of Sb. But time catches up with us all; in 1988 I retired from the Oak Ridge National Laboratory and from research on molten salt chemistry.

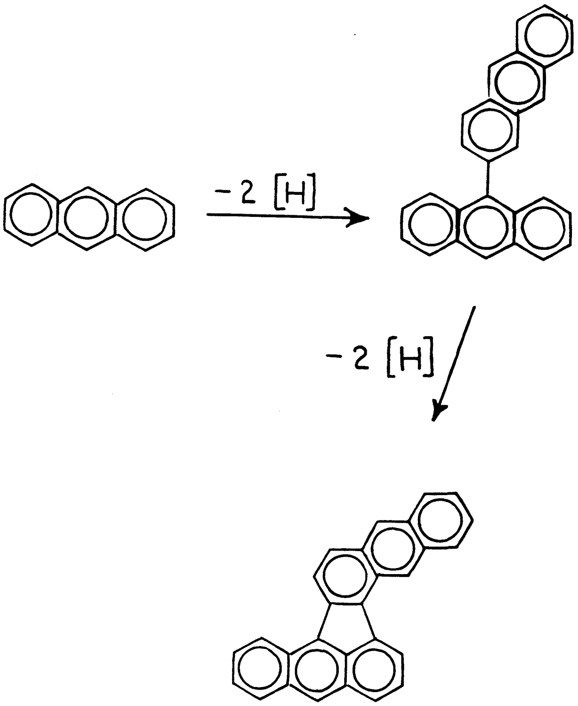

Fig. 1. Examples of Scholl condensation reactions in acidic melts.

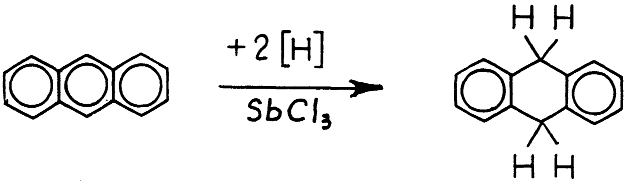

Fig. 2. Hydrogenation in molten $SbCl_3$.

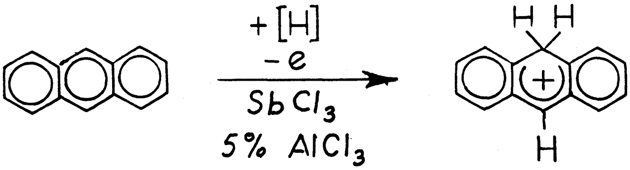

Fig. 3. Protonation/oxidation in $SbCl_3$ containing 5 mol % $AlCl_3$.

10.1149/199017.0008PV

STRUCTURE OF MOLTEN SALTS

Marie-Louise Saboungi, M. A. Howe,* and D. L. Price

Argonne National Laboratory
Argonne, Illinois 60439

ABSTRACT

A brief review of the structure of molten salts is given with special emphasis on structural features in reciprocal space. Selected diffraction results on halide salts containing monovalent and divalent cations are presented, along with recent results on salts containing trivalent cations. Different models and computational techniques, such as random packing of structural units, the reference interaction site model, and reverse Monte Carlo are used to derive structural information at the partial level.

INTRODUCTION

Improvements in pulsed neutron sources, reactors, and x-ray sources have resulted in an increased accuracy in the determination of structure factors, especially at small wave vectors. New facets in the structure of liquids have been revealed, especially in molten salts and their solutions. The present paper highlights progress achieved in the determination of the structure of some halide molten salts containing a trivalent cation. In the first section, we briefly review diffraction results on monovalent and divalent molten salt (1-3). In the second section, we present recent diffraction results obtained on molten salts containing trivalent cations, which can be classified into two classes, the low-melting and high-melting salts. Several models available in the literature have been used to further our understanding of the structure. For liquids containing complex structural entities, two models were used, random packing of structural units (4) (RPSU) and the reference interaction side model (5) (RISM), which have been found to adequately represent the main features of the structure; in the case of salts where an ionic character is observed, the reverse Monte Carlo (RMC) method was used to extract structural information at a partial level (6).

The most fundamental information about the structure on an atomic scale is obtained from diffraction measurements, with either neutrons or x-rays. The wave

---

*Present address: Clarendon Laboratory, Parks Road, Oxford OX1 3PU, England.

nature of a beam of particles is used to measure the interference pattern of the intensity I(Q) of the waves coherently scattered from the ions in the liquid:

$$I(Q) = \sum_{i,j} \overline{b}_i^* \overline{b}_j \exp\ i\mathbf{Q} \cdot (\mathbf{r}_j - \mathbf{r}_i) \tag{1}$$

where the scattering vector Q is the difference between the wave vectors of the incident and scattered beams and $\bar{b}_i$ is the coherent scattering length. For neutron diffraction, the $\bar{b}_i$ are generally constant, while for x-ray diffraction they are a function of Q through the form factor of the target atom. A single diffraction experiment yields the total structure factor S(Q), which is related to I(Q) by:

$$I(Q) = N\left[\langle\bar{b}\rangle^2\,[S(Q) - 1] + \langle\bar{b}^2\rangle\right]. \tag{2}$$

For a salt containing a cation M and an anion X, the total structure factor is a linear combination of three partial structure factors, S_{XX}, S_{MM}, and S_{MX}. In terms of these, the measured intensity reads:

$$I(Q) = N\left[\sum_{\alpha\beta} x_\alpha x_\beta \overline{b^*}_\alpha \overline{b}_\beta S_{\alpha\beta}(Q) - \langle\overline{b}\rangle^2 + \langle\overline{b}^2\rangle\right] \tag{3}$$

where α, β = M or X and x_α and x_β are the atomic fractions of the ions α and β. The pair correlation functions $g_{\alpha\beta}(r)$ are related to $S_{\alpha\beta}$ through the relation:

$$S_{\alpha\beta}(Q) = 1 + \frac{4\pi\rho}{Q}\int \left[g_{\alpha\beta}(r) - 1\right] r \sin Qr\, dr. \tag{4}$$

The most crucial information about the structure is contained in the partial structure factors, which are still difficult to measure directly with as good an accuracy as the total structure factor. In order to experimentally determine the partials, several independent measurements of I(Q) must be done. For neutron diffraction, this can be achieved by using different isotopes when applicable, and for x-ray diffraction, by using differential anomalous scattering, or a combination of x-ray and neutron diffraction can be made if the scattering lengths are favorable (1). Most of the problems associated with the isotopically substituted samples stem from the high amount of impurities present in the isotopes, impurities that are difficult to remove, such as hydroxides, and from the limited contrast in the scattering. Differential anomalous scattering is a promising technique, but is limited to those compounds where the K edges do not overlap; in practice, results obtained for liquids, such as $GeBr_4$ (7), have not been as accurate as those obtained from neutron diffraction. Thus, a theoretical approach to the structure is still essential if one is to extract detailed information.

MOLTEN SALTS WITH MONOVALENT AND DIVALENT CATIONS

An excellent review of the structure of molten alkali halides and salts containing divalent cations was published by Enderby and Biggin in 1983 (1). Careful work done by the British groups of Enderby (1) and Mitchell (8) have shown that alkali halides have similar radial distribution functions for the cation-cation and the anion-anion pairs. A characteristic peak in the partial structure factors S_{MM} and S_{XX} and a corresponding dip in S_{MX} is present; the peak and dip are due to the coulomb interactions and usually located in the vicinity of 2 $Å^{-1}$. Finally, Enderby and Biggin (1) pointed out that a small amount of penetration of the cation-cation and anion-anion pairs into the first coordination shell is observed in all of the monovalent salts. Interestingly, the measurements confirm findings obtained by molecular dynamics simulations based on rigid ions (9). A notable exception is molten CuCl where the radial distribution functions of Cu-Cu and Cl-Cl are remarkably dissimilar (10). CuCl remains an exceptional salt whose properties are not fully understood.

In the molten salt containing divalent cations, the three radial distribution functions are quite different, especially the anion-anion and cation-cation. Biggin and Enderby have shown that the anion-anion peak position and coordination number change little with cation, but the height decreases significantly for larger cations. An increased penetration of like ions into the first coordination shell is also observed as the cation size increases. In most cases, the coordination number of the unlike ions changes very little from that in the solid; a remarkable exception is $MgCl_2$ where Biggin *et al.*(11) found a decrease in the coordination number from six to four upon melting, implying a rearrangement of the ions from octahedral to tetrahedral sites.

In some of the divalent salts, e.g., $ZnCl_2$ (12), NiX_2 (3), an interesting feature is observed in the total structure factor, the appearance of a peak at a small wavelength, Q ~1 $Å^{-1}$. This first diffraction peak is present in either the three partial structure factors or in the like partial structure factors. The signature of this first peak in the radial distribution functions is not significant. However, its presence in reciprocal space implies that ordering in these salts is rather of intermediate range and could have a different origin than the coulomb alternation of charges. The formation of complex species in most of the melts, such as $MgCl_4^{2-}$, which are usually inferred to from Raman spectroscopy measurements might be responsible for the manifestation of the low-Q diffraction peak. Using isotopically substituted samples, the partial structure factors thus obtained show this peak only in the cation-cation structure factor for $CaCl_2$, but in the cation-cation and cation-anion structure factor for $ZnCl_2$ and the nickel halide salts.

MOLTEN SALTS WITH TRIVALENT CATIONS

There have been very few studies of molten trivalent salts, particularly at the partial structure level. We have initiated a systematic experimental study of the total structure factor of these salts including those with high melting points, e.g., NdX_3, LaX_3, YCl_3, and those with low melting points, e.g., AlX_3 and GaX_3, where X = Cl, Br, I. The purpose of this study is to establish trends, derive information related to the atomic distribution, and deduce radial distribution functions by combining experimental results with models and/or molecular dynamics simulation. Finally, the availability of Nd and Cl isotopes makes it possible to obtain partial structure factor information for salts containing one of these ions.

In what follows, we compare the results obtained for $NdCl_3$ and $AlBr_3$, contrasting the behavior of a high-melting salt with that of a low-melting salt. In Table I, we have compiled some properties of trivalent molten salts. Note the relatively small values of ΔS_m for the low-melting salts with the exception of $AlCl_3$ where the entropy is quite large, implying a major change in structure upon melting. For the high-melting salts, the entropy takes normal values reflecting the increased degree of disorder.

Experimental

The samples were contained in thin walled SiO_2 ampoules. The chemicals were prepared by APL Engineered Materials, Inc., Urbana, Illinois, and were analyzed for H_2O contamination; typically less than a few ppm of H_2O were detected using Carl-Fisher titration methods. No evidence of any etching or attack of the silica tubes was detected. The samples were maintained in the liquid state for less than five hours, sufficient to collect diffraction data. The experiments on the low-melting salts were carried out on the Special Environment Powder Diffractometer at the Intense Pulsed Neutron Source, Argonne National Laboratory, using time-of-flight diffraction. The experiments on the neodymium and lanthanum halides were carried out using the D20 diffractometer of the Institute Laue-Langevin, Grenoble, France, with monochromatic neutrons of wavelength 0.94 Å. On both machines, spectra were obtained for the liquid sample, an empty silica ampoule, room background, and a vanadium rod. The measurement of the scattering from the vanadium was used to calibrate the instrument and put the scattering on an absolute scale.

Data reduction is discussed elsewhere (13). In the case of the neodymium salts, a correction for the magnetic scattering from the neodymium ion was applied using the magnetic form factor of the free Nd^{3+} ion.

Structure of a Low-Melting Trihalide Salt, $AlBr_3$

The total structure factor of $AlBr_3$ at T = 413 K is shown in Figure 1. The main features of S(Q) are the presence of a first sharp diffraction peak at low wave vector, $Q \approx 1$ Å^{-1}, and the long range of oscillations at high Q. In real space, the pair correlation function g(r) obtained from S(Q) via Fourier transformation shows a prominent sharp peak at $r \approx 2.3$ Å, which can be ascribed to M–X correlations within the molecules. The cation coordination numbers are 4.0 for $AlBr_3$, 3.8 for $GaBr_3$, and 3.7 for GaI_3. The coordination number of four, which is expected for the M_2X_6 molecules, contrasts with three, which is expected of MX_3 and so indicates that the $AlBr_3$ consists of Al_2Br_6 molecules in the melt, and that the gallium salts are dimerized only up to ≈70–80%, in agreement with earlier Raman scattering studies (14). We have used the Reference Interaction Site Model (RISM) to calculate S(Q) under the assumption that the melt consists entirely of M_2X_6 interacting via site-site hard sphere potentials. The parameters needed are the molecular geometry, the density of the liquid, and the hard sphere diameters of the atoms in the molecule. The good agreement obtained between measurements and calculations (the dashed line in Figure 3) can be considered as further proof of the dimerization of $AlBr_3$. The RISM calculations might be improved by considering different potentials.

Structure of a High-Melting Trihalide Salt, $NdCl_3$

Figure 2 shows the total structure factor, S(Q), corrected for the magnetic scattering of the Nd^{3+} ions. Here there is less structure at high momentum transfer, but the first diffraction peak at $Q \approx 1$ Å^{-1} is still present and is a common feature to all the trivalent molten salts that we have examined. In the case of $NdCl_3$, x-ray data were made available to us (15) and were used in conjunction with the neutron results to obtain a model structure using the Reverse Monte Carlo method (6). This method enables one to obtain a three-dimensional structure that reproduces the measurements; from the ionic distributions, one can further probe the ionic arrangements in a system and compute partial structure factors and the radial pair distribution functions. Such calculations were carried out for $NdCl_3$ and the correspondence between measurements and calculations are illustrated in Figure 2. The computations carried out on a system containing 1024 ions inside a box of length 31.52 Å yielded the three partial functions in real and reciprocal space. Furthermore, triplet correlation functions were calculated. In the solid state, $NdCl_3$ crystallizes in the $Y(OH)_3$ (UCl_3) structure, a hexagonal lattice composed of chains of MX_3 trigonal pyramids. Figure 3 shows six triplet correlation functions for both liquid and crystalline states, the former calculated using RMC, the latter from a distorted lattice.

The remarkable similarity between the crystalline and liquid triplet correlations suggests that the local structure in the melt, although considerably more disordered than in the solid, still retains some characteristics of the solid phase.

CONCLUDING REMARKS

In conclusion, the structures of trivalent molten salts show interesting differences. In high-melting salts such $NdCl_3$, the short-range order of the crystal structure is present in the melting process where the long-range order is destroyed. In low-melting salts such as $AlBr_3$, the melt is characterized by M_2X_6 dimers. In all the salts studied, the presence of first diffraction peaks at $Q \sim 1$ Å^{-1} indicates a substantial degree of intermediate-range order.

ACKNOWLEDGMENTS

We acknowledge technical assistance of the staff at IPNS (ANL) and ILL (Grenoble) and especially K. J. Volin (ANL) and P. Convert (ILL). We thank Prof. Kazuo Igarashi for kindly providing us with his x-ray diffraction results prior to publication, and Dr. R. L. McGreevy for the use of the RMC program.

This work was performed under the auspices of the U.S. Department of Energy, Office of Basic Energy Sciences, Division of Materials Sciences, under Contract W-31-109-ENG-38.

REFERENCES

1. J. E. Enderby and S. Biggin in *Advances in Molten Salt Chemistry*, Vol. 5, ed. G. Mamantov, Elsevier (1983) p. 1.
2. J. E. Enderby, D. M. North, and P. A. Egelstaff, Phil. Mag. **14**, 961 (1966).
3. N. D. Wood and R. A. Howe, J. Phys. C: Solid State Physics **21**, 3177 (1988); N. D. Wood, R. A. Howe, R. J. Newport, and J. Faber, Jr., J. Phys. C: Solid State Physics **21**, 669 (1988).
4. S. C. Moss and D. L. Price in *Physics of Disordered Materials*, Eds. D. Adler, H. Fritzche, and S. R. Ovshinsky, Plenum, New York (1985) p. 77.
5. H. C. Anderson and D. Chandler, J. Chem. Phys. **57**, 1918 (1972); D. Chandler and H. C. Anderson, J. Chem. Phys. **57**, 1930 (1972).
6. R. L. McGreevy and L. Pusztai, Mol. Simul. **1**, 359 (1988).
7. K. F. Ludwig, Jr., W. K. Warburton, L. Wilson, and A. Bienenstock, J. Chem. Phys. **87**, 604 (1987); **87**, 613 (1987).
8. E. W. J. Mitchell, P.F.J. Poncet, and R. J. Stewart, Phil. Mag. B **34**, 721 (1976); R. L. McGreevy and E. W. J. Mitchell, J. Phys. C: Solid State Phys. **15**, 5537 (1982).
9. J. R. D. Copley and A. Rahman, Phys. Rev. **A 13**(6), 2276 (1976).

10. S. Eisenberg, J.-F. Jal, J. Dupuy, P. Chieux, and W. Knoll, Phil. Mag. **46A**, 195 (1982).

11. S. Biggin, M. Gay, and J. E. Enderby, J. Phys. C: Solid State Phys. **17**, 978 (1984).

12. S. Biggin and J. E. Enderby, J. Phys. C: Solid State Phys. **14**, 3129 (1981).

13. H. T. J. Reijers, M.-L. Saboungi, D. L. Price, J. W. Richardson, K. J. Volin, and W. van der Lugt, Phys. Rev. **B 40**, 6018 (1989).

14. A. Balls, A. J. Downs, N. N. Greenwood, and B. P. Straughan, Trans. Farady Soc.. **62**, 521 (1968).

15. K. Igarashi and I. Mochinaga, private communication (1989).

Table I. Properties of Selected Trivalent Molten Salts

Compound	T_m (°K)	ΔH_m (kcal mol^{-1})	ΔS_m (e.u. mol^{-1})	ΔV(%)	Structure Type at 25°C
$AlCl_3$ ††	465.7	8.45	18.15	84	$AlCl_3$ (layers of MX_3 units)
$AlBr_3$ ††	370.6	2.69	7.26		$AlBr_3$ (M_2X_6 dimers)
AlI_3 ††	464.15	3.8	8.19		
$GaCl_3$ **	351	2.75	7.84		$GaCl_3$ (M_2X_6 dimers)
$GaBr_3$ **	396	2.8	7.07		
GaI_3 **	486	5.3	10.91		
$LaCl_3$ †	1131	13.0	11.5	19.1	$Y(OH_3)$ (chains of MX_3 units)
$LaBr_3$ †	1061	13.0	12.3		$Y(OH)_3$
LaI_3 †	1051	13.4	12.7		$PuBr_3$ (chains of MX_3 units
$NdCl_3$ †	1032	12.0	11.6	21.8	$Y(OH_3)$
$NdBr_3$ †	955	10.9	11.4		$PuBr_3$
NdI_3 †	1060	9.9	9.4		$PuBr_3$
	(847)*	(3.3)*	(3.9)*		
$ScCl_3$ †	1240	16.1	13.0		$ScCl_3$ (M_2X_6 dimers)
ScI_3 *†	1225	19.0	15.51		–
YCl_3 †	994	7.5	7.6	0.5	$AlCl_3$

* Transition in solid state.

† A. S. Dworkin and M. A. Bredig, High Temp. Sci. **8**, 81-90 (1971).

**I. Barin, Thermochemical Data of Pure Substances (1989).

††JANAF.

*†P. A. G. O'Hare, G. K. Johnson, I. R. Tasker, H. E. Flotow, and C. W. Struck, J. Chem. Thermodyn. **19**, 77 (1987).

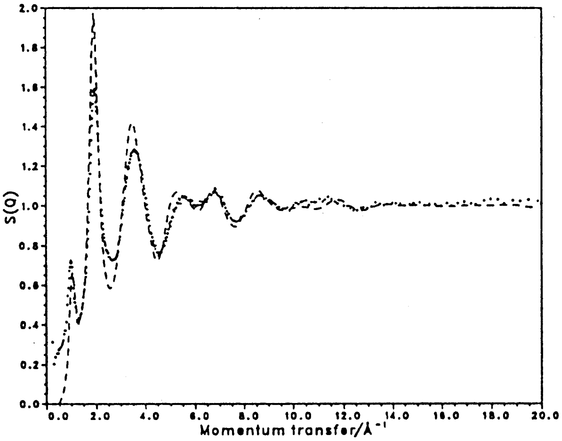

Figure 1. The structure factor for molten aluminium bromide. The points are the experimental data and the dashed line is the result of the RISM calculations.

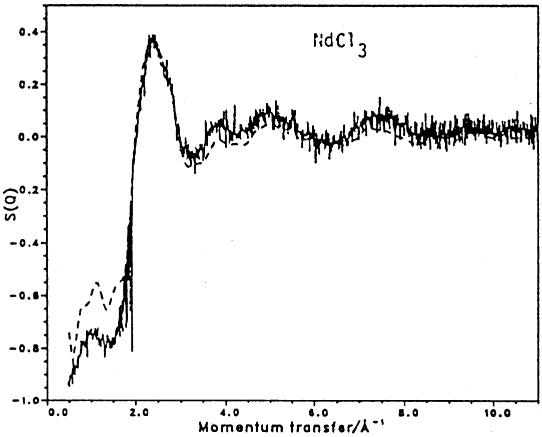

Figure 2. The total structure factor obtained by RMC (dashes) compared with the experimental neutron diffraction data.

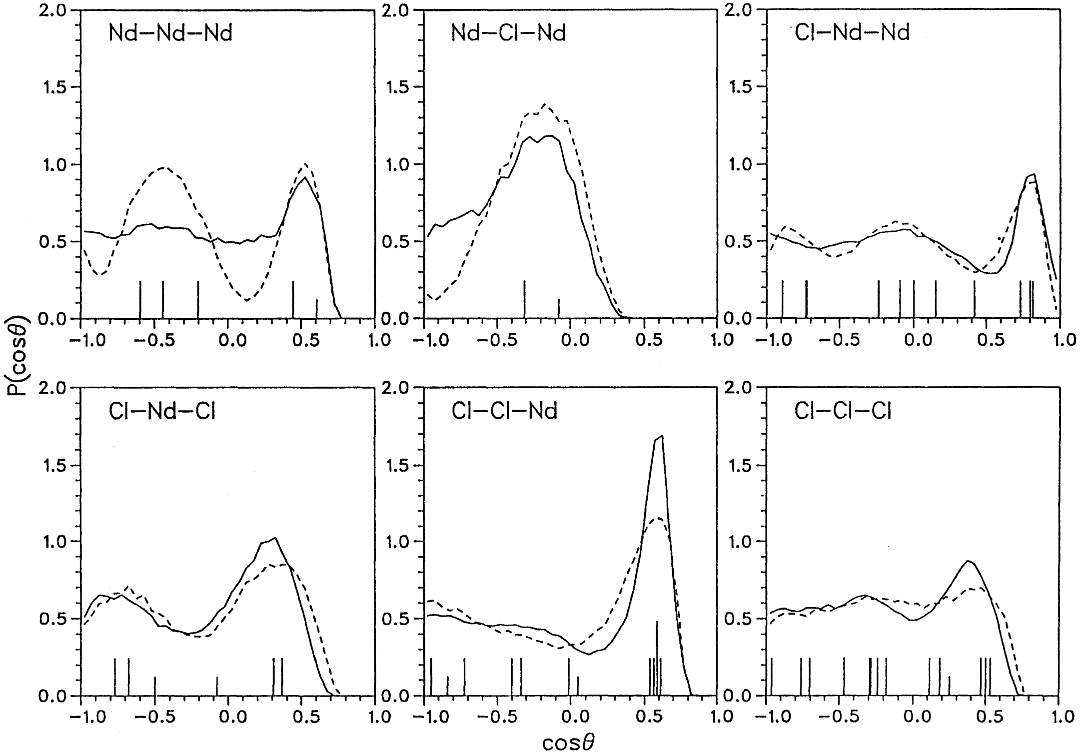

Figure 3. The triplet correlation functions for molten $NdCl_3$ (solid lines) compared with those obtained from a model of the crystal (dashed lines). The vertical lines show, on an arbitrary scale, the distribution of the triplet angles in a perfect crystal.

DOI: 10.1149/199017.0018PV

CALCULATION OF THE SOLUBILITIES OF OXIDES IN MOLTEN CARBONATES*

Milton Blander and Arthur Pelton†

Argonne National Laboratory
9700 South Cass Avenue
Argonne, Illinois 60439

†Ecole Polytechnique
P.O. Box 6079, Station'A'
Montreal, Quebec, Canada H3C 3A7

ABSTRACT

Analyses of data on the solubilities of NiO in molten alkali carbonates, M_2CO_3, provides values of thermodynamic parameters of the solution constituents $NiCO_3$, NiO, and M_2NiO_2 in an alkali carbonate solution. These data and data on the free energies of mixing of alkali carbonate mixtures permit one to calculate solubilities of NiO in the mixtures using molten salt solution theories. This procedure avoids the inconsistencies inherent in correlating oxide solubilities with intuitive acid-base concepts and is general enough to be used with other solvents (e.g., alkali sulfates and halides) and solutes (other oxides).

INTRODUCTION

An understanding of the dissolution (i.e., the fluxing) of oxides by molten salts is important in understanding hot corrosion phenomena,[1-9] and the degradation of oxide cathodes in carbonate fuel cells.[10-15] One aspect of hot corrosion is a mode of corrosion in which molten sulfates formed from combustion effluents dissolve protective oxide coatings of structural alloys and accelerate degradation of the alloys. Although most experimental studies have focused on Na_2SO_4, calculations have shown that sulfates from e.g., coal combustion are composed of variable compositions of Na_2SO_4, $CaSO_4$, and $MgSO_4$ (and K_2SO_4 as well if potassium is present in the coal).[16] In fuel cells, the solubility of NiO cathodes in molten carbonates is a major factor limiting the lifetime of the cells.

It is the purpose of this paper to deduce a fundamental formalism for the thermodynamics of the dissolution of oxides that would permit one to more readily understand the chemistry and to make useful predictions at temperatures and compositions outside the range of measurements. Such predictions can be important in minimizing hot corrosion and in optimizing the performance of molten carbonate fuel cells. In addition, as will be shown, even a simple qualitative understanding of the chemistry in the range of compositions and temperatures of operation of fuel cells defines the particular parameter that will most likely control the solubility of NiO. In this paper, we focus on the solubilities of NiO in molten carbonates because of the availability of a broad range of data.[14,15] Insights gained in this study should apply to the analogous phenomenon in sulfates relevant to hot corrosion.

Of particular significance is the framework for our discussion, which is based on thermodynamic and statistical mechanical concepts and theories that have been developed for molten salts. Acid-base concepts have been applied to molten sulfates and carbonates.[14,15] There are fundamental inconsistencies in such concepts* that make it difficult to deduce clear interrelationships among thermodynamic properties in different solvents. As we will show, our methods clarify the chemistry and suggest methods for improving performance of NiO cathodes. Our analyses will be based on a particularly complete set of measurements by Orfield and Shores[14,15] of NiO solubilities in four alkali carbonate melts and in binary mixtures of Li_2CO_3-K_2CO_3 and Na_2CO_3-K_2CO_3 at 910°C. Their results provide clear insights into the total chemistry and help to define an approach for decreasing the solubility of NiO in fuel cell electrolytes.

MEASUREMENTS AND THEIR ANALYSIS

The measurements of Orfield and Shores for the NiO solubilities are given in Figure 1 plotted as log $[(X_{Ni} \times 10^6)$ mol ppm$]$ (where X_{Ni} is a mole fraction) versus the negative of the logarithm of the activity of M_2O in the melt at 910°C, which varies with the partial pressure of CO_2 according to the relation

$$a_{M_2O} = K_{DISS}^{SOL}/p_{CO_2} \qquad (1)$$

K_{DISS}^{SOL} is the equilibrium constant for the reaction

$$M_2CO_3(s) \rightleftarrows M_2O(s) + CO_2 \qquad M = Li, Na, K, Rb$$

and the standard states for the activities of the oxides are the solids. Orfield and Shores defined a basicity scale for the pure carbonates as log a_{M_2O}. The values of log K_{DISS}^{SOL} for the four alkali carbonates are 2.503 for Li_2CO_3, 6.776 for Na_2CO_3, 9.865 for K_2CO_3, and 10.578 for Rb_2CO_3.[14] One does not see any particular regularity of the solubilities as a function of basicity in the plot in Figure 1.

Orfield and Shores followed a procedure of Rapp and coworkers in analyzing these data. In the relatively acid melts (higher p_{CO_2}) for a given carbonate, the

---

*In carbonates, for example, there exist compositions in the Li_2CO_3-Li_2O system in which both the acidity and basicity are higher than compositions in Na_2CO_3-Na_2O melts when acidity is defined as p_{CO_2} and basicity is the activity of the alkali oxide.

solubility should rise linearly with a slope of +1 due to the formation of $NiCO_3$ (the Ni^{2+} ionic species with carbonate being the only anionic nearest neighbors) by the reaction

$$NiO(s) + CO_2 \rightleftarrows NiCO_3(soln) \tag{2}$$

For a fixed CO_2 pressure, reaction (2) leads to a constant activity of $NiCO_3$. We can gain insight into some of the results by shifting from the negative of the basicity scale as the abscissa in Figure 1 to log p_{CO_2}. This can be accomplished by adding the appropriate values of log K_{DISS}^{SOL} to all the values of -log a_{M_2O}. This brings the curves very close to each other. There is a significant observation on the high p_{CO_2} side of the "V"-shaped curves. The solubility of NiO at a fixed p_{CO_2} on this part of the curve decreases in going from Rb_2CO_3 to Na_2CO_3, and from the data given for Li_2CO_3, it can be deduced that the solubility of NiO caused by its dissolution as $NiCO_3$ in Li_2CO_3 must be the lowest of the four salts. Obviously, the activity coefficient of $NiCO_3$ is lowest in Rb_2CO_3 and increases as one goes through the series to Li_2CO_3. This result is consistent with expectations from the known relationships between solvent alkali cation radii and the activity coefficients of divalent transition metal solute salts with the same anion as the alkali salt.[17] Since fuel cells operate near 650°C at partial pressures of CO_2 where the most important solute species is Ni^{2+}, this result suggests a method for improving the performance of the NiO cathode by the use of additives to the electrolyte that raise the activity coefficient of $NiCO_3$

Orfield and Shores[14,15] ascribed, with reservations, the parts of the plots in Figure 1 that have a negative slope (at higher log a_{M_2O} and lower p_{CO_2}) to the formation of NiO_2^{2-} species by the reaction

$$NiO(s) + O_2^{2-} \rightleftarrows NiO_2^{2-} \tag{3a}$$

In order to define this reaction thermodynamically in a self-consistent manner that will apply to binary and higher order carbonate solvents, one must do so in terms of components in the melts since it is not possible to define single (an)ion (O_2^{2-}, NiO_2^{2-}) activities in any melts, or even the ratios of single (an)ion activities in reciprocal systems with at least two cations and two anions.[18] In a one-component alkali carbonate melt, one can write

$$NiO(s) + M_2O(soln) \rightleftarrows M_2NiO_2(soln) \tag{3b}$$

If one uses the fact that binary mixtures of two molten salts with the same cation, but different anions, generally deviate little from ideal behavior,[19] one can deduce details of the chemistry of formation of nickelate species. For example, if molten M_2O-M_2CO_3 solutions are ideal mixtures, the calculated activity of M_2O is then the mole fraction. Recalculating K_{DISS} with liquid oxides as the standard state using known data,[20] one obtains values of log K_{DISS}^{LIQ} at 910°C of −3.410 for Li_2CO_3 and −7.130 for Na_2CO_3. We estimate that the free energy of fusion of K_2O at 910°C is −117 cal mol^{-1} (i.e, pure K_2O melts somewhat below 910°C), and we deduce a value of −9.843 for log K_{DISS}^{LIQ} with molten K_2O as standard state. It seems likely that this quantity for Rb_2CO_3 will be somewhat higher than −10.578. Values of a_{M_2O} calculated from these values of K_{DISS} make it clear that the concentration of oxide at any fixed partial pressure of CO_2 is highest in Li_2CO_3 and decreases considerably with an increase in the radius of the alkali cation.

Before analyzing the data, we will have to understand anomalies in the data that are inconsistent with the presence of only the two nickel species Ni^{2+} and NiO_2^{2-}.

The reaction in Eq. (3) should lead to a contribution to the total solubility, which should have a slope of −1 when plotted in Figure 1. Examination of the data indicates that the apparent slope is essentially unity for Li_2CO_3 as solvent. The slope is somewhat less than unity for Na_2CO_3 and becomes progressively smaller for K_2CO_3 and Rb_2CO_3. Orfield and Shores[14] have shown that a nickel species with a different valence could not account for this oddity. These anomalous slopes can be understood when one considers the possibility of a solution species, NiO. The contribution of this species to the total concentration of nickel in an NiO(s) saturated melt is a constant. Thus, based on the apparent slopes discussed above, one expects very little of the NiO species in Li_2CO_3 and progressively higher concentrations of this species as one goes from Na_2CO_3 to Rb_2CO_3. Therefore, the formation constants for the nickel containing solution species are for the reactions (4) and (5)

$$Ni^{2+} + O^{2-} \rightleftarrows NiO \qquad K_{11} \tag{4}$$

$$NiO + O^{2-} \rightleftarrows NiO_2^{2-} \qquad K_{12} \tag{5}$$

Analysis of the data of Orfield and Shores was performed by fitting the data to the equation

$$X_{Ni}(\text{mol ppm}) = Aa_{M_2O} + Ba_{M_2O}^{-1} + C \tag{6}$$

where a_{M_2O} is the activity of the appropriate alkali oxide based on the solid as the standard state. The abscissa in Figures 1 and 2 are the logarithms of this activity. Values of A, B, and C and the dissociation constant used by Orfield and Shores, K_{DISS}^{SOL}, are given in Table I. Of the terms in Eq. (6), Aa_{M_2O} is the concentration of NiO_2^{2-}, $Ba_{M_2O}^{-1}$ is the concentration of Ni^{2+}, and C is the concentration of the NiO species. From the values of A, B, C, and log K_{DISS}^{LIQ}, we can calculate values of the concentrations of all the species in solution at any fixed CO_2 concentration, as well as of K_{11}, K_{12}, and the solubility product, $K_{SP} \equiv X_{Ni^{2+}}X_{O^{2-}}$, where $X_{Ni^{2+}}$ is a cation fraction and $X_{O^{2-}}$ is an anion fraction. As can be seen in Table II, the values of K_{11} and the ratios of K_{11}/K_{12} increase with an increase in alkali cation radius. This general trend was also observed for the associations of silver and halide ions in molten alkali nitrates.[17] Of particular note are the extremely large values of K_{11} and K_{12} deduced for the Na_2CO_3, K_2CO_3, and Rb_2CO_3 solvents. Values for both K_{11} and K_{12} are uncertain for the Li_2CO_3 solvent and K_{12} is uncertain for the Rb_2CO_3 solvent because the data were inadequate in the range of log p_{CO_2} or log a_{M_2O} where the NiO_2^{2-} species is most evident. Because of a lack of data on the free energy of fusion of Rb_2CO_3, there is also a small independent uncertainty in K_{SP}, K_{11}, and K_{12} in Rb_2CO_3. This uncertainty is noted by the parentheses about these three quantities in Table II. We exhibit a comparison of our calculated values of the NiO solubility with the measured data in Figure 2. The correspondence of the solid curve to the measured points is very good. There are significant deviations from our calculated values due to the scatter in the data or to the possible precipitation of a solid nickelate species. For example, at the highest values of log a_{M_2O} (lowest values of -log a_{M_2O}) for M = Na and K in Figure 1, there are three points that were left out of our fit, which may be related to the precipitation of a solid alkali nickelate (Na_2NiO_2, K_2NiO_2). The value of A for Rb_2CO_3 is very uncertain because of too few points at low p_{CO_2}. One of the points lies far from our fit and might be related to a solid precipitate; there are not enough data to fully define the constant A in this solvent. At and near the minimum in the measured solubility, some of the measured solubility points lie below our calculations. This is not related to our model and must be related to scatter in the data since such deviations would occur even when the NiO species is not considered; with no NiO species, the measured solubility is log ($X_{Ni^{2+}} + X_{NiO_2^{2-}}$) where log $X_{Ni^{2+}}$ is proportional to $a_{M_2O}^{-1}$ and log $X_{NiO_2^{2-}}$ to a_{M_2O}. Thus, the minimum in the curve for this case must lie 0.3 units above the point of the V formed by the individual plots of log $X_{Ni^{2+}}$ and log $X_{NiO_2^{2-}}$ and the bottom of the solubility curve must be rounded off. The points that lie below our calculated plots would define a "V" shape, which is too sharp even in this case, which is limited to two species. It should be emphasized that the lines in Figure 1, which were taken from Orfield and Shores,[14] are drawn to represent the data and were not calculated.

BINARY ALKALI CARBONATE SOLVENTS

Modern theories of molten salts permit one to calculate the properties of solutions containing Ni^{2+}, NiO, and NiO_2^{2-} solution species from the properties of lower order systems, often with more than one method being possible. In this section, we will very briefly discuss some of the theories that could be used. As has been pointed out, some of the data concerning Ni^{2+} and NiO in molten Li_2CO_3 and NiO_2^{2-} in molten Rb_2CO_3 could not be deduced adequately from the measurements. Let us consider a binary carbonate mixture A_2CO_3-B_2CO_3 and the dissolution reaction (2) for the formation of $NiCO_3$ in solution. One can deduce an expression for these solubilities based on the Conformal Ionic Solution Theory[21] or the Coordination Cluster Theory.[22]

From the Conformal Ionic Solution Theory up to third order terms,[21] one deduces the equation for the activity coefficient of $NiCO_3$ in the A_2CO_3-B_2CO_3 mixture:

$$\begin{aligned} \ln \gamma_{NiCO_3} = {} & X_A \ln \gamma^{(A)}_{NiCO_3} + X_B \ln \gamma^{(B)}_{NiCO_3} - a_{AB} X_A X_B + b_{NiA}(1 - X_A^2) \\ & + b_{NiB}(1 - X_B^2) + 2b_{AB} X_A X_B (X_B - X_A) + A X_A X_B \end{aligned} \tag{7}$$

where the X's are mole fractions, $a_{jj'}$ is the second order interaction parameter in the binary carbonate of the cations j' and j and $b_{jj'}$ is the analogous third order coefficient of the term $X_j X_{j'}(X_{j'} - X_j)$. The activity coefficients γ_{NiCO_3} in Eq. (6) can be substituted by the reciprocals of the solubility of $NiCO_3$, X_{NiCO_3}. A is a ternary interaction parameter defined in terms of the $b_{jj'}$ parameter for the three binary systems. An analogous expression can be deduced from the Coordination Cluster Theory

$$X_{NiCO_3} = \sum_{i=0}^{Z} \frac{Z!}{(Z-i)!i!} \left(X_A \left(X^{(A)}_{NiCO_3} \gamma_A \right)^{1/Z} \right)^{Z-i} \left(X_B \left(X^{(B)}_{NiCO_3} \gamma_B \right)^{1/z} \right)^{i} \exp\left(\frac{-g_i^E}{RT} \right) \tag{8}$$

where X_j, γ_j are the mole (ion) fraction and activity coefficient of the component j, Z is a next nearest neighbor coordination number, taken as 6, $X^{(j)}_{NiCO_3}$ is the concentration of Ni^{2+} in equilibrium with solid NiO at a given pressure of CO_2 in the pure component j and g_i^E is a parameter (which is likely to be negligible for this case) that represents the excess free energy of mixing of A^+ and B^+ cations in the next nearest neighbor coordination shell of the Ni^{2+} cations.

For the NiO_2^{2-} species in the A_2CO_3-B_2CO_3 binary solvent, we can utilize the Conformal Ionic Solution Theory applied to the reaction

$$M_2CO_3(\ell) + NiO(S) \rightleftarrows M_2NiO_2(soln) + CO_2 \tag{9}$$

with an equilibrium constant K_{NiO_2} related to the standard free energy change for the reaction (9), $\Delta G^o_{NiO_2} = -RT \ln K_{NiO_2}$. In the binary solvent, M can be either A or B, and the difference between the free energy for reaction (9) with B_2CO_3 and A_2CO_3 as solvents is the standard free energy change for the metathetical reaction, ΔG^o_{AB}

$$B_2CO_3 + A_2NiO_2 \rightleftarrows A_2CO_3 + B_2NiO_2 \tag{10}$$

From the Conformal Ionic Solution Theory for reciprocal systems,[23,24] one can deduce the ratio of the activity coefficients of A_2NiO_2 to those of A_2CO_3 in dilute solutions of A_2NiO_2, which allows one to calculate the $X_{NiO_2^{2-}}/X_{CO_3^{2-}}$ ratio that in dilute solution is equal to $X_{NiO_2^{2-}}$, the anion fraction of NiO_2^{2-}

$$\ln \frac{\gamma_{A_2NiO_2}}{\gamma_{A_2CO_3}} = \frac{X_B \Delta G^o_{AB}}{RT} + X_A \frac{a_A}{RT} + X_B \frac{a_B}{RT} + X_A X_B \left(\frac{a_{NiO_2} - a_{CO_3}}{RT} \right) - X_A X_B \frac{\left(\Delta G^o_{AB}\right)^2}{4ZRT} \tag{11}$$

where a_k is the molar regular solution interaction parameter for the binary mixture containing two salts with k as the common ion. Quantities, such as a_A and a_B, which are for mixtures of A_2NiO_2 with A_2CO_3 and B_2NiO_2 with B_2CO_3, are generally small and can be assumed to be negligible; of all these parameters,the only unknown is a_{NiO_2}, which is likely to have the same sign (negative) as a_{CO_3}.

One could also use an equation that applies to reciprocal systems deduced from the Coordination Cluster theory.[25] Similar calculations could be carried out for the activity coefficients of alkali oxides in binary carbonate melts, as well as for the concentrations of oxide ions in solution.

The most difficult species on which to perform calculations is NiO. An extension of the coordination cluster theory[25] could be applied to deducing the concentration dependence of K_{11} and K_{12} in binary mixtures. In general, the concentration dependence of ln K_{11} and ln K_{12} in binary nitrate solvents has been approximately linear and the concentration dependence of K_{11} in the binary carbonate mixtures is not likely to deviate much from linearity.

In essence, the theoretical framework exists for the calculation of the total solubilities of NiO in binary carbonate melts, such as Li_2CO_3-K_2CO_3. There are some necessary data that are unavailable and some for which the precision is not adequate. One method that should be useful would be to utilize the equations outlined above to perform a global analysis of all the available data on a given binary solvent (including measurements in the pure carbonate end members). In such a calculation, the small number of unknown data could be used as parameters to be determined by the global analysis. The advantage of such an analysis is that the results should permit one to extrapolate and interpolate reliably to make predictions outside the range of measurements.

CONCLUSIONS

Our analyses indicate that the experimental data of Orfield and Shores on the solubility of solid NiO in pure alkali carbonates can be represented by a model that postulates the formation of Ni^{2+}, NiO, and NiO_2^{2-} species. About three measured points in the Na_2CO_3 and K_2CO_3 systems are consistent with the precipitation of a solid nickelate compound. In the Rb_2CO_3 system, the deduced values of the solubility of nickel as NiO_2^{2-} ions have a large uncertainty because there are too few data to determine the coefficient A in Eq. (6) or to judge whether the measurement at the highest value of a_{M_2O} could be due to the precipitation of a solid phase. In any case, the possible presence of the NiO solution species in other solvents, such as the sulfates, should be considered.

Fuel cells operate on the high p_{CO_2} side of the type of "V" shaped curves we are discussing where $NiCO_3$ is the major solution species.[26] In order to decrease the solubility of NiO, we have to alter the solvent to increase the activity coefficient of $NiCO_3$. There are several approaches one could take to change the solubility based on this idea.

Perhaps the most important point is that our approach has provided fundamental insights into the chemistry of NiO(s) solubilization. In addition, analyses of the data based on fundamental solution theories provides a means for ultimately predicting relevant thermodynamic properties of multicomponent solvents. By contrast, acid-base concepts are fundamentally flawed and cannot lead to a self-consistent description nor can they be used to make reliable predictions in such systems.

ACKNOWLEDGMENTS

This work was supported by the U.S. Department of Energy, Division of Materials Sciences, Office of Basic Energy Sciences, under Contract W-31-109-ENG-38.

REFERENCES

1. D. K. Gupta and R. A. Rapp, J. Electrochem. Soc., **127**, 2194 and 2656 (1980).
2. M. L. Deanhardt and K. H. Stern, J. Electrochem. Soc., **128**, 2577 (1981).
3. A. K. Misra, D. P. Whittle, and W. L. Worrell, J. Electrochem. Soc., **129**, 1840 (1982).
4. M. L. Deanhardt and K. H. Stern, J. Electrochem. Soc., **129**, 2228 (1982).
5. Y. S. Zhang and R. A. Rapp, J. Electrochem. Soc., **132**, 734 (1985).
6. P. D. Jose, D. K. Gupta, and R. A. Rapp, J. Electrochem. Soc., **132**, 735 (1985).
7. Y. S. Zhang, J. Electrochem. Soc., **133**, 655 (1986).
8. D. Z. Shi and R. A. Rapp, J. Electrochem. Soc., **133**, 849 (1986).
9. R. A. Rapp, Corrosion, **42**, 568 (1986).

10. T. D. Kaun, in "Fourth International symposium on Molten Salts," M. Blander, D. S. Newman, G. Mamantov, M.-L. Saboungi, and K. Johnson, Editors, p. 489, The Electrochemical Society Softbound Proceedings Series PV 84-2, Pennington, NJ (1984).

11. C. E. Baumgartner, J. Electrochem. Soc., **131**, 1850 (1984).

12. C. E. Baumgartner, J. Am. Ceram. Soc., **69**, 162 (1986).

13. M. L. Orfield and D. A. Shores, "High Temperature Materials Chemistry–III," Z. A. Munir and D. Cubiciotti, Editors, p. 246, The Electrochemical Society Softbound Proceedings Series, PV 86-2, Pennington, NJ (1986).

14. M. L. Orfield and D. A. shores, J. Electrochem. Soc., **135**, 1662 (1988).

15. M. L. Orfield and D. A. Shores, J. Electrochem. Soc., **136**, 2862 (1989).

16. M. Blander, S. Sinha, A. Pelton, and G. Eriksson, "Calculations of the Chemistry of Coal combustion Effluents" in Proc. of the American Flame Research Committee Int. Symp. on Coal: Fuel for Today and for the Future, Pittsburgh PA, October 14-6, 1988, Paper No. 25 (1988).

17. M. Blander, "Thermodynamic Properties of Molten Salt Solutions" in Molten Salt Chemistry, ed. M. Blander, Interscience, New York (1964) pp. 127-237.

18. M. Blander, Metall. Trans., **8B**, 529 (1977).

19. O. J. Kleppa, "Thermodynamics of Molten Salt Mixtures" in Molten Salt Chemistry: An Introduction and Selected Applications, eds. G. Mamantov and R. Marassi, NATO ASI Ser. C., D. Reidel, Dordrecht, Holland (1987) pps. 79-122.

20. M. W. Chase et al., JANAF Thermochemical Tables, third Edition, Am. Chem. Soc. and Am. Phys. Soc. (1986).

21. M.-L. Saboungi and M. Blander, J. Chem. Phys., **63**, 212 (1975).

22. M. Blander, M.-L. Saboungi, and P. Cerisier, Metall. Trans., **10B**, 613-22 (1979).

23. M. Blander and S. J. Yosim, J. Chem. Phys., **39**, 2610 (1963).

24. M.-L. Saboungi and M. Blander, J. Am. Ceram. Soc., **58**, 1 (1975).

25. M. Blander and M.-L. Saboungi, Acta Chem. Scand., **A34**, 671 (1980).

26. J. D. Doyon, T. Gilbert, G. Davies, and L. Paetsch, J. Electrochem. Soc., **134**, 3035 (1987).

Table I. Dissociation Constants of Alkali Carbonates and Parameters Deduced from Measured Oxide Solubilities in Alkali Carbonates[14] by Fits to the Equation $X_{Ni} = Aa_{M_2O} + Ba_{M_2O}^{-1} + C$ (mol ppm)

Solvent	A	B	C	log K_{DISS}^{SOL} *	log K_{DISS}^{LIQ} *
Li_2CO_3	3.33×10^3	--	--	−2.503	−3.410
Na_2CO_3	1.61×10^7	2.57×10^{-6}	1.8	−6.776	−7.7130
K_2CO_3	2.95×10^8	4.00×10^{-7}	30.0	−9.865	−9.843
Rb_2CO_3	5.55×10^{10}	5.16×10^{-8}	109.0	−10.578	(−10.578)

*Log K_{DISS}^{SOL} and log K_{DISS}^{LIQ} are the dissociation constants for the reaction $M_2CO_3 \rightleftarrows M_2O + CO_2$ with solid or liquid M_2O as standard states, respectively. The fits to the equation above were made with a_{M_2O} defined with solids as standard state.[14]

Table II. Values of the Solubility Product for NiO (Solid), K_{SP}, and the Formation Constants for the NiO and NiO_2^{2-} Solution Species, K_{11} and K_{12}

Solvent	K_{SP}	K_{11}	K_{12}
Na_2CO_3	3.0×10^{-13}	6.1×10^6	7.7×10^7
K_2CO_3	4.2×10^{-13}	7.1×10^7	9.4×10^6
Rb_2CO_3	(5.2×10^{-14})	(2.1×10^9)	(5.1×10^8)

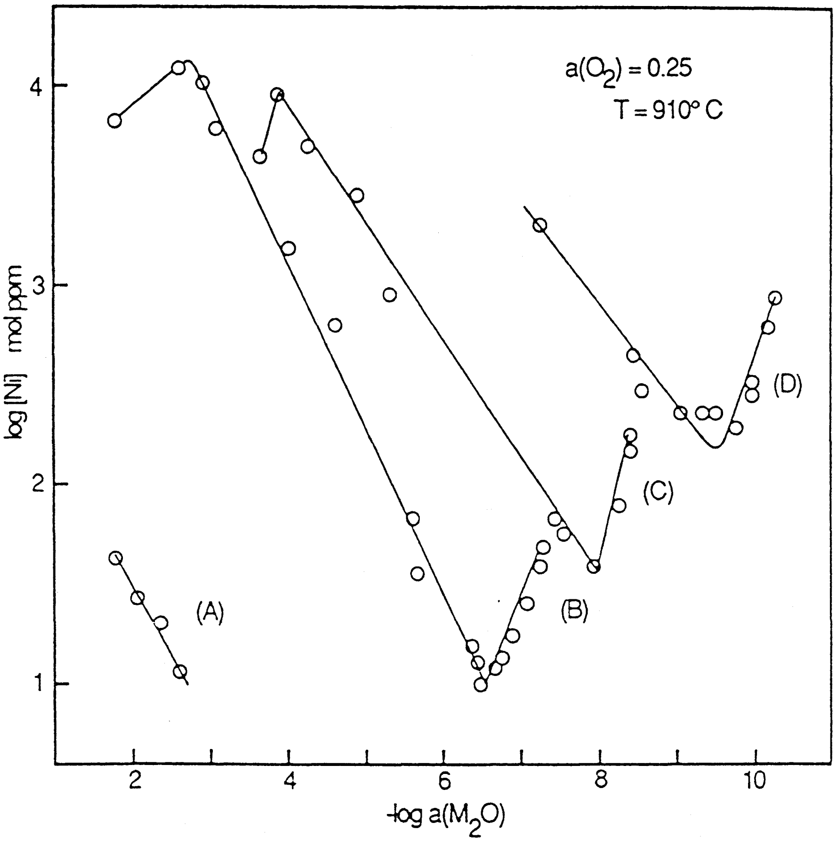

Figure 1. Solubilities of NiO at 910°C in Li_2CO_3, Na_2CO_3, K_2CO_3, and Rb_2CO_3 as a function of basicity, at a(O_2) = p(O_2) = 0.25, where basicity is defined as -log a(M_2O) with M being, Li, Na, K, or Rb.

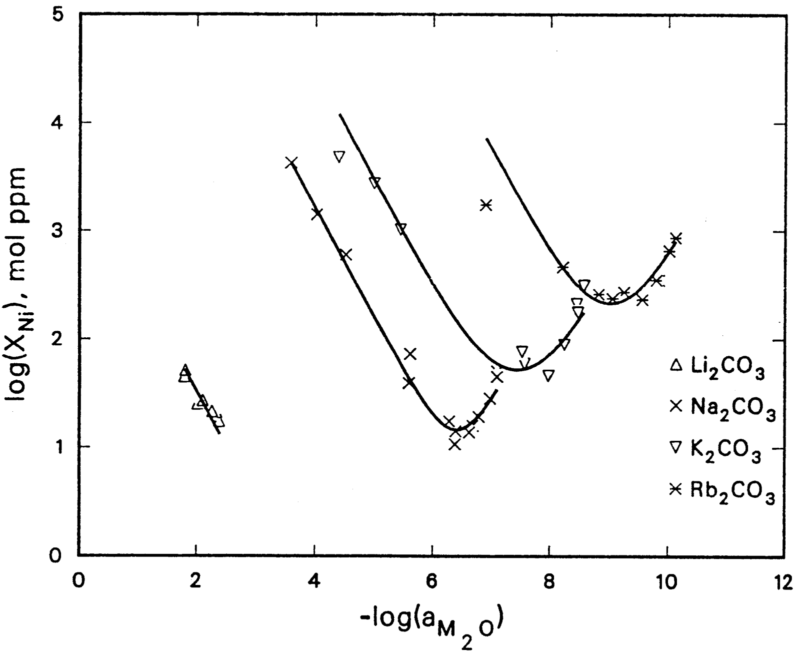

Figure 2. The logarithm of the solubility of NiO versus the logarithm of the activity of the alkali oxide. The lines were calculated from Eq. (6) using the parameters in Table I. The points are from Orfield and Shores. Those points that are likely to be related to the formation of a solid phase were not used in the fit of the data.

DOI: 10.1149/199017.0030PV

ORDERED IONIC LIQUIDS: CHLOROALUMINATES AND SILICATES

Milton Blander, Peter Tumidajski,[1]
Ira Bloom, and David Newman[2]

Argonne National Laboratory
Argonne, Illinois 60439-4837

ABSTRACT

Ordering in NaCl-$AlCl_3$ melts leads to sharp minima in the solubility of divalent chlorides MCl_2 (e.g., $CoCl_2$, $FeCl_2$, and $NiCl_2$) near the 50-50 mole % composition. The composition dependence of these solubilities in acid melts can be described by using either the coordination cluster theory or the solubility product principle. The magnitudes of the solubility products are largely related to the fact that the standard free energy of formation of $2NaAlCl_4$ from 2NaCl and $2AlCl_3$ is considerably more negative than the corresponding free energy for $M(AlCl_4)_2$. In basic melts, solubilities are largely related to the formation of the associated species MCl^+, MCl_2, MCl_3^-, and MCl_4^{2-}, which appear to have very large formation constants.

INTRODUCTION

Molten chloroaluminates and silicates belong to a class of ordered ionic solutions that have striking physicochemical properties. In this paper, we will examine the influence of ordering on solubilities in molten chloroaluminates to explain the very steep minima that have been observed near the most ordered composition. These minima in solubilities (and maxima in activity coefficients in dilute solution) are predicted by physical solution theories[1-4] and concepts. Solubilities in very highly ordered solutions can also be described in chemical terms[5] that provide clarifying insights into these phenomena.

The properties of molten chloroaluminates parallel those of silicates. For example, addition of $AlCl_3$ to NaCl produces the tetrahedral $AlCl_4^-$ anion in the melt. Beyond the 50-50 (neutral) composition, the addition of $AlCl_3$ produces $Al_2Cl_7^-$ and

---

[1] Present address: University of Western Ontario, Department of Materials Engineering, London, Ontario, Canada N6A-5B9.

[2] Present address: Bowling Green State University, Department of Chemistry, Bowling Green, OH 43403-0213.

$Al_3Cl_{10}^-$ ions in which the aluminum pairs are connected by a bridging chloride ion to form a bent Al-Cl-Al triplet. Similar molecular ions (SiO_4^{4-}, $Si_2O_7^{6-}$, $Si_3O_{10}^{8-}$) are formed in silicates at silica mole fractions less than 0.43. The last two ions have bridging oxygens with Si-O-Si bridging angles analogous to those for the corresponding chloroaluminate ions. Because of the low temperatures of the liquids, there is a considerable body of very accurate data for the chloroaluminates. On the other hand, because of generally high liquidus temperatures, data for silicate melts are not as accurate. Thus, one can perform much more precise and detailed analyses of chloroaluminates than one can for the silicates, and studies of chloroaluminates, in addition to being significant in their own right, also can provide insights into the properties of silicates.

ORDERING

Because there are different types of ordering phenomena in different liquids, one needs to examine the particular liquids under study. In this section, we discuss ordering in $NaCl-AlCl_3$ mixtures to illustrate the phenomenon and its thermodynamic consequences. The most ordered composition in this binary melt is at 50-50 mole % where NaCl and $AlCl_3$ combine to form a low melting liquid, which largely contains Na^+ cations and $AlCl_4^-$ anions. Except for the structural complexity of the polyatomic anion, this liquid is a simple molten salt analogous to alkali halides exhibiting coulomb ordering represented in one dimension as $\cdots + - + - + - \cdots$. Since the tetrahedral $AlCl_4^-$ ions, which are the nearest neighbors of Na^+ cations, have their four chlorides on their periphery, the coulomb order leads to topological order of the next nearest neighbor sodiums and aluminums, which can be written in one dimension as ···Na-Al-Na-Al-Na-Al···, where the order is defined in terms of repetitive Na-Al pairs in sequence. In addition, there is a chemical order related to the definitiveness of the structures of the molecular ions ($AlCl_4^-$ here and $Al_2Cl_7^-$ and/or $Al_3Cl_{10}^-$ at higher concentrations of $AlCl_3$). Addition of NaCl or $AlCl_3$ to the 50-50 mixture decreases the topological order by decreasing the range of repetition of the Na-Al pairs by the substitution of Cl^- or $Al_2Cl_7^-$ ions for $AlCl_4^-$ ions in the ordered array.

Such solutions cannot be perfectly ordered and one must consider the degree of disorder. One measure of disorder is the extent of disproportionation of the $AlCl_4^-$ anions according to the reaction

$$2AlCl_4^- \rightleftarrows Cl^- + Al_2Cl_7^- \tag{1}$$

with a disproportionation constant, K_D, of 1.06×10^{-7} at 175°C.[6] When one considers that a number of Na^+ cations are next nearest neighbors to any one Al in $AlCl_4^-$ or $Al_2Cl_7^-$ and are nearest neighbors to Cl^-, disproportionation can be re-expressed in terms of the disordering reaction

$$2Na - Al \rightleftarrows Na - Na + Al - Al \tag{2}$$

The very small value of K_D indicates very little disorder (i.e., the melt is highly ordered). By this measure, the organic chloroaluminates (e.g., methylethylimidazolium tetrachloroaluminate) are considerably more ordered than $NaAlCl_4$. This order is dramatically reflected in the thermodynamic properties of the binary NaCl-$AlCl_3$ solutions shown in Figure 1, in which are plotted FE/RT, ln a_{NaCl}, and ln a_{AlCl_3} versus the mole fraction of $AlCl_3$. The activities of the two components, a_{NaCl} and a_{AlCl_3}, were deduced[7] from the electromotive force measurements of Boxall and Osteryoung[6] (plotted as FE/RT) for the concentration cell Al|NaCl-$AlCl_3$||NaCl(saturated) - $AlCl_3$|Al. The activities are plotted for the solids as the standard states. The salient feature of this plot is the extremely steep change in the activities at the 50-50 composition. This steepness is related to the disproportionation constant (K_D) and to the Darken excess stability function[8]

$$ES = \frac{RT}{1 - X_{NaCl}} \left(\frac{d \ ln \ \gamma_{NaCl}}{d \ X_{NaCl}} \right) \tag{3}$$

which has been correlated with the degree of order. A plot of this function, directly calculated from the data by numerical differentiation, is shown in Figure 2 and shows an exceptionally high narrow peak. Because of the narrowness of the peak, the error in the peak height is relatively large. One can determine the peak height more accurately by calculation from the value of K_D, which, in effect, uses all the data near the 50-50 composition for the calculation; this leads to a value for the peak height of 1.1×10^6 cal mol^{-1} (4.7×10^6 joules mol^{-1}). This solution is indeed highly ordered.

SOLUBILITIES OF SOLUTES

How does ordering manifest itself in the thermodynamic properties of solutes? The coordination cluster theory[1,2] for the activity coefficients of a solute C dissolved in the solvent A-B can be used to illustrate these properties. The theory leads to the expression for the activity coefficient of C, γ_C, in terms of the coordination number Z (for additive molten salt systems, this is for the coordination of next nearest neighbors), the mole fractions and activity coefficients of the solvent components, $X_A, X_B, \gamma_A, \gamma_B$, the activity coefficients of the solute in pure A and pure B, $\gamma_{C(A)}, \gamma_{C(B)}$, a parameter g_i^E, which represents the excess free energy of mixing of A and B in the next nearest neighbor shell of solute ions (cations in the case we cite) containing (Z-i)A^+ cations and iB^+ cations, and a parameter t, which is 1/Z for this case

$$\frac{1}{\gamma_C} = \sum_{i=O}^{Z} \frac{Z!}{(Z-i)!i!} \left(\frac{X_A \gamma_A^t}{\gamma_{C(A)}^{1/Z}}\right)^{Z-i} \left(\frac{X_B \gamma_B^t}{\gamma_{C(B)}^{1/Z}}\right)^{i} exp\left(-g_i^E/RT\right) \tag{4}$$

Examination of the ratios of the activity coefficients of NaCl(A) and $AlCl_3$(B) (essentially the same as the activity ratios near $X_{AlCl_3} = 0.5$) in Figure 1 provides insights into the solute properties. At concentrations below $X_{AlCl_3} = 0.5$, $\gamma_{NaCl}/\gamma_{AlCl_3}$ is very large and, with a small change of concentration to $X_{AlCl_3} > 0.5$, this ratio becomes very small. As a consequence, only two of the Z terms in the summation on the r.h.s. of Eq. (4) are important, with the term for i = 0 being predominant in basic solutions ($X_{AlCl_3} < 0.5$) and that for i = Z being predominant in acidic solutions ($X_{AlCl_3} > 0.5$). For both these terms, the value of $g_i^E = 0$. Calculations of the activity coefficients in the NaCl-$AlCl_3$ solvent at 175°C for a hypothetical solute C, for which $\gamma_{C(A)}$ and $\gamma_{C(B)}$ are both unity, and for Z = 4 are illustrated in Figure 3. There is a steep maximum in the activity coefficients at about $X_{AlCl_3} = 0.5$. For a relatively insoluble material, a sharp maximum in the activity coefficient denotes a sharp minimum in the solubility. This property should be common with strongly ordered solvents for a solute that interacts much more weakly with the two solvent components than the solvent components interact with each other. Recent measurements at 175°C of the solubilities of solid $CoCl_2$ in NaCl-$AlCl_3$ solutions at $X_{AlCl_3} > 0.5$ have been well fitted by Eq. (4) for a value of the activity coefficient of solid $CoCl_2$ in molten $AlCl_3$ of 0.35.[5] This derived value indicates that $CoCl_2$ interacts relatively weakly with $AlCl_3$.

Because ordering in this melt is very strong, one can also describe this solubility in chemical terms. In basic melts, the solvent can be considered to be primarily a binary mixture of NaCl with $NaAlCl_4$ with very small concentrations of $NaAl_2Cl_7$. On the acid side, not very far from the 50-50 composition, the melt can be considered to be an essentially binary mixture of $NaAlCl_4$ with $NaAl_2Cl_7$ with very small concentrations of Cl^-. The solubility of $CoCl_2$ in acidic melts can be described in terms of the solubility product, K_{SP}

$$K_{SP} = X_{Co^{2+}} X_{Cl^-}^2 = X_{Co^{2+}} \left(K_D^2 / X_{Al_2Cl_7^-}^2\right) \tag{5}$$

where $X_{Co^{2+}}$ and $X_{Al_2Cl_7^-}$ are cation and anion fractions, respectively, in the reciprocal system $Na^+, Co^{2+}/AlCl_4^-, Al_2Cl_7^-, Cl^-$. At 175°C, the solubility product was found to be 4.66×10^{-15}.[5] The values of the standard free energy of solution of $CoCl_2$ at infinite dilution is given by -RT ln K_{SP} (29.39 kcal mol^{-1}) and is exactly given by the sum of the standard free energies for the following reactions[9,10]

$$CoCl_2(s) + NaAlCl_4(\ell) \rightleftarrows 2NaCl(\ell) + Co(AlCl_4)_2(\ell) \tag{6a}$$

$$2NaCl(\ell) \rightleftarrows 2NaCl \text{ (infinite dilution)} \tag{6b}$$

$$Co(AlCl_4)_2(\ell) \rightleftarrows Co(AlCl_4) \text{ (infinite dilution)} \tag{6c}$$

A value of -5.2 kcal mol^{-1} has been deduced for the free energy of formation of $Co(AlCl_4)_2(\ell)$ from $CoCl_2(\ell)$ and $AlCl_3(\ell)$.[5] This small value again reflects the weak interactions of $CoCl_2$ with $AlCl_3$. In fact, the insolubility of solid $CoCl_2$ in acid melts is directly related to the fact that the standard free energy of formation of $Co(AlCl_4)_2(\ell)$ from solid $CoCl_2$ and liquid $AlCl_3$ (-5.2 kcal mol^{-1}) is much larger than the free energy of formation of 2 $NaAlCl_4(\ell)$ from 2 $NaCl(\ell)$ + 2 $AlCl_3(\ell)$. An analogous conclusion is deduced from the coordination cluster theory where RT ln $\gamma_{CoCl_2(AlCl_3)}$ (0.35) is considerably larger than the very small values of the activity coefficients of 2 NaCl (based on liquid as the standard state) in the acid melts.

Both the coordination cluster theory and the chemical concept of K_{SP} lead to the conclusion that other insoluble divalent salts (such as solid $FeCl_2$ and $NiCl_2$, which are reactants in the "Zebra" batteries under development for automobile propulsion) will, in all likelihood, have the same dependence of their solubilities on concentration, but with a different magnitude. Thus, the general behavior of solubilities of divalent salts in somewhat acidic haloaluminate melts of any one basic halide is universal and requires knowledge of but a single constant for each salt at a given temperature. Differences between the solubility products for different divalent salts in any one solvent are largely related to differences in the standard free energies of formation of the tetrachloroaluminate from the pure divalent chloride and $AlCl_3$.

Solubilities in basic compositions are not this simple unless one considers compositions where there is only one species, e.g., for Co^{++}, the $CoCl_4^{2-}$ species, which was spectroscopically observed by Øye and Gruen in KCl-$AlCl_3$ solutions.[11]

These authors observed another species at low chloride ion concentrations. At somewhat higher concentrations where the very large majority of cobalt ions are present as $CoCl_4^{2-}$, one can represent the solubilities of $CoCl_2(s)$ and their dependence on the solvent composition with but a single parameter. Using the coordination cluster theory, this parameter is the activity coefficient of $CoCl_2$ at infinite dilution in molten NaCl. For the chemical description, this is the formation constant of $CoCl_4^{2-}$ from Co^{2+} and four Cl^- ions. However, at smaller concentrations of chloride one must consider all four of the constants for the reactions to form $CoCl_n^{2-n}$, $n = 1-4$.

$$Co^{2+} + Cl^- \rightleftarrows CoCl^+ \qquad K_{11} \tag{7a}$$

$$CoCl^+ + Cl^- \rightleftarrows CoCl_2 \qquad K_{12} \tag{7b}$$

$$CoCl_2 + Cl^- \rightleftarrows CoCl_3^- \qquad K_{13} \tag{7c}$$

$$CoCl_3^- + Cl^- \rightleftarrows CoCl_4^{2-} \qquad K_{14} \tag{7d}$$

where the formation constants are related to bond free energies, ΔA_{1n}, through the statistical mechanical relations[12]

$$K_{11} = Z(\beta_{11} - 1) \tag{8a}$$

$$K_{11}K_{12} = \frac{Z(Z-1)}{2!}(\beta_{11}\beta_{12} - 2\beta_{1} + 1) \tag{8b}$$

$$K_{11}K_{12}K_{13} = \frac{Z(Z-1)(Z-2)}{3!}(\beta_{11}\beta_{12}\beta_{13} - 3\beta_{11}\beta_{12} + 3\beta_{11} - 1) \tag{8c}$$

$$K_{11}K_{12}K_{13}K_{14} = \frac{Z(Z-1)(Z-2)(Z-3)}{4!}(\beta_{11}\beta_{12}\beta_{13}\beta_{14} - 4\beta_{11}\beta_{12}\beta_{13} + 6\beta_{11}\beta_{12} - 4\beta_{11} + 1) \tag{8d}$$

where $\beta_{1n} = \exp(-\Delta A_{1n}/RT)$ and Z is a coordination number for Co^{2+}.[12] Values of the bond free energies for each of the four successive chloride additions to the coordination shell of Co^{2+} can all be different. In the coordination cluster theory, the analogous differences are contained in the term g_i^E in Eq. 4. When we use the simple approximation for g_i^E

$$g_i^E = (Z - i)(i)h \tag{9}$$

then values of the analogue to ΔA_{1n} differ by Z^2h according to the relation $\Delta A'_{1n} = \Delta A'_{11} - (n-1)Z^2h$. An approximation for values of ΔA_{1n} can be made crudely from the expression[13] $\Delta A_{1n} \sim \frac{\Delta G^O}{Z}$ where ΔG^O is the standard free energy change for reaction (6a) and Z is a coordination number. For a value of Z of 4, we estimate a value of K_{11} of the order of 50,000. Thus, even at the neutral composition (50-50 mole % NaCl-$AlCl_3$), where the concentration of chloride in the solvent is 3.3×10^{-4} at 175°C, one expects that a large fraction of the cobalt ions in solution would be present as $CoCl^+$ and some of the other species. In fact, examination of the natural logarithm of the apparent solubility products at 175°C in Table II of Ref. 5 indicates a value that is 0.2–0.3 larger than those at higher acidity at $X_{AlCl_3} = 0.513$ and 3.0–3.1 larger at $X_{AlCl_3} = 0.502$. If K_{11} is of the order of 5×10^4, the magnitude of the difference at 0.513 is correct for the presence of $CoCl^+$ and at $X_{AlCl_3} = 0.502$, there would have to be more than one species. Thus, at $X_{AlCl_3} = 0.502$, about 95% of the solubilization of $CoCl_2$ is caused by the formation of chlorocobalt species, which are present at a much higher total concentration than Co^{2+} ions with no Cl^- as a near neighbor. Measurements are underway to investigate this point, and preliminary data confirm this phenomenon at 255°C.

CONCLUSIONS

Both a physical theory (coordination cluster theory) and chemical concepts (solubility product principle and the formation of associated species) lead to useful descriptions of the concentration dependence of the solubilities of divalent chlorides in chloroaluminates. Both points of view provide insights into the strikingly sharp minima in the solubility of solutes in the highly ordered molten $NaCl$-$AlCl_3$ solutions. Further work is underway to investigate the formation constants for chlorocobalt species in basic melts in this system.

In addition, these results provide valuable insights into the properties of other ordered liquids, such as silicates. Largely because of the much higher temperatures of stabilities of molten silicates, the thermodynamic properties of silicates[14,15] indicate that the relatively more ordered binary silicate systems, such as Na_2O-SiO_2 and CaO-SiO_2 are considerably less ordered than the $NaCl$-$AlCl_3$ system. This implies that the chemical description of the thermodynamic properties of silicates will not be as well defined and as simple as those in the $NaCl$-$AlCl_3$ system discussed here. Despite this, there is a clear maximum near 33 mole % SiO_2 in the activity coefficients of a solute, such as FeO, in either the Na_2O-SiO_2 or CaO-SiO_2 system and, for example, the phase diagram of the ternary FeO-CaO-SiO_2 system exhibits minima in the concentration of FeO for different FeO liquidus isotherms near a line connecting the FeO composition corner with the composition at the 33.3 mole % SiO_2 in the CaO-SiO_2 binary line. The thermodynamic data for, e.g., CaO-SiO_2, are consistent with a larger degree of disproportionation of the SiO_4^{4-} anion that are likely to be present at 33 mole % SiO_2, and there is probably a broader distribution of different species at all compositions where the nominal average composition of the species parallels those of chloroaluminates. For one of the least ordered binary silicate systems, FeO-SiO_2, the degree of disproportionation of SiO_4^{4-} is undoubtedly considerable.

ACKNOWLEDGMENTS

This work was supported by the U.S. Department of Energy, Division of Materials Sciences, Office of Basic Energy Sciences, under Contract W-31-109-ENG-38.

REFERENCES

1. M. Blander, M.-L. Saboungi, P. Cerisier, Metall. Trans. **10B**, 613 (1979).
2. M. Blander, M.-L. Saboungi, The Coordination Cluster Theory of Solutions in *Chemical Metallurgy–A Tribute to Carl Wagner*, ed., N. A. Gockcen, Metallurgical Society of AIME, Warrendale, PA, 1981, pp. 223-31.
3. M.-L. Saboungi, P. Cerisier, M. Blander, Metall. Trans. **13B**, 429 (1982).
4. M.-L. Saboungi and M. Blander, J. Chem. Phys. **63**, 212 (1975).
5. C. Wai, I. Bloom, D. Caveny, and M. Blander, J. Phys. Chem. **94**, 1666 (1990).

6. L. G. Boxall, H. L. Jones, and R. A. Osteryoung, J. Electrochem. Soc. **120**, 223 (1973).

7. M. Blander and M.-L. Saboungi in *Proceedings of the Third International Symposium on Molten Salts*, eds., G. Mamantov, M. Blander, and G. P. Smith, The Electrochemical Society, Pennington, NJ, 1981, pp. 212-20.

8. L. S. Darken, Trans. AIME **239**, 80 (1967).

9. M. Blander and E. B. Luchsinger, J. Am. Chem. Soc. **86**, 319 (1964).

10. M. Blander, Thermodynamic Properties of Molten Salt Solutions, in *Molten Salt Chemistry: An Introduction and Selected Applications*, NATO ASI Ser. C., eds., G. Mamantov and R. Marassi, D. Reidel, Dordrecht, Holland, 1987, pp. 17-62.

11. H. A. Øye and D. M. Gruen, Inorg. Chem. **4**, 1173 (1965).

12. M. Blander, J. Chem. Phys. **34**, 432 (1961).

13. M. Blander and M.-L. Saboungi, Acta Chimica Scand. **A34**(9), 671 (1980).

14. A. D. Pelton and M. Blander, Metall. Trans. **17B**(4), 805 (1986).

15. M. Blander and A. D. Pelton, Geochim. Cosmochim. Acta **51**, 85 (1987).

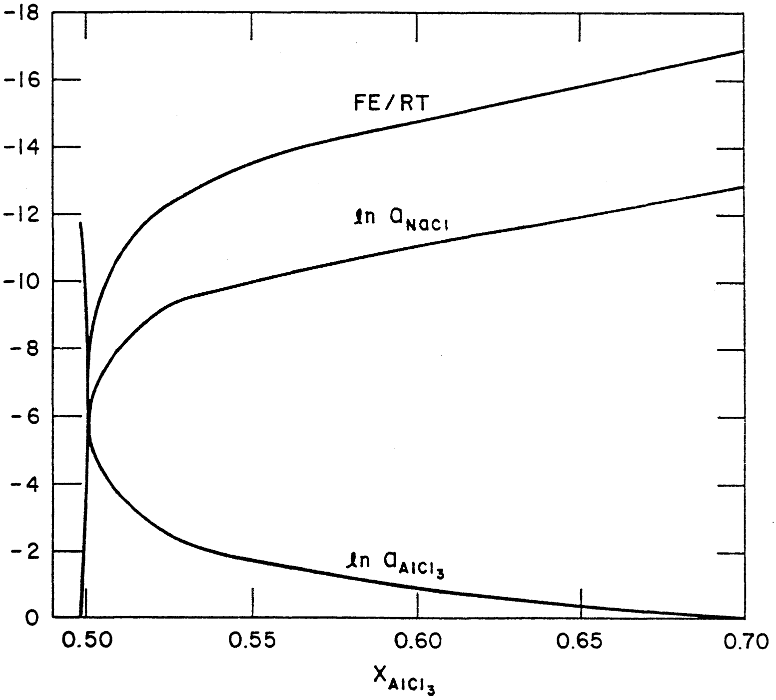

Figure 1. Plots of the EMF (as FE/RT) of the measurements of Boxall *et al.*[5] and of values of ln a_{NaCl} and ln a_{AlCl_3} deduced from these measurements. a_{NaCl} and a_{AlCl_3} are the activities based on solid as the standard state.

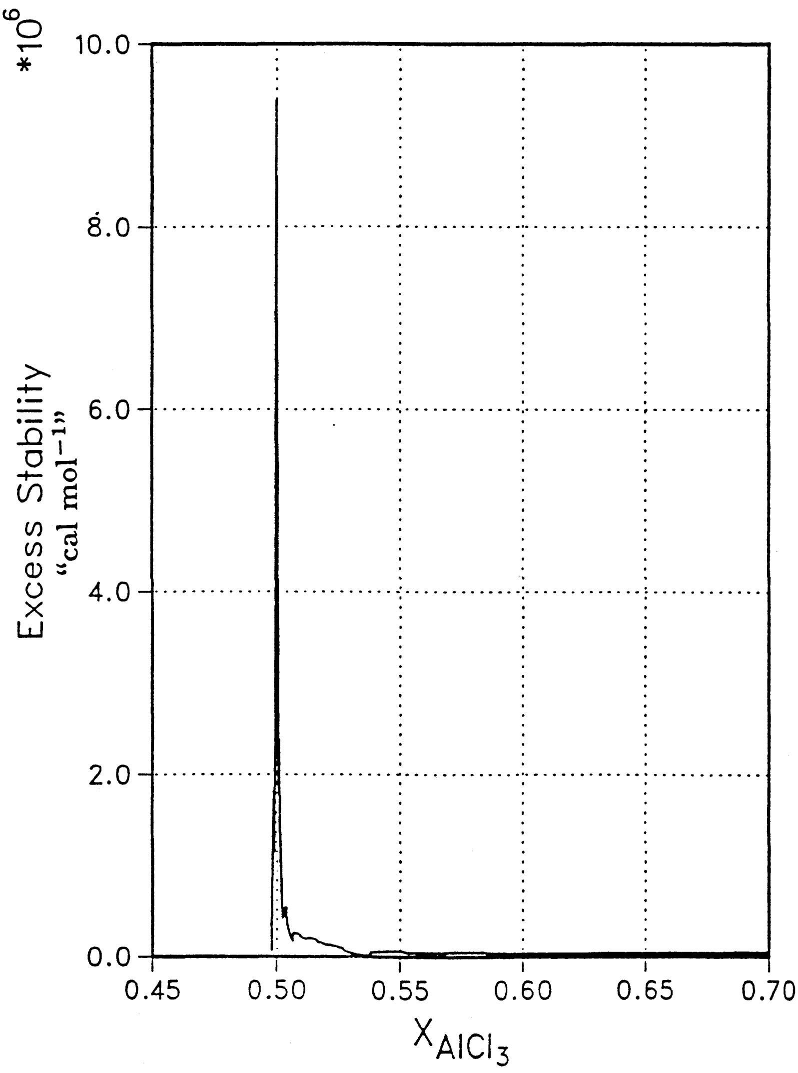

Figure 2. The Darken excess stability function[8] calculated directly from the data of Boxall *et al.*[5] The actual peak height calculated from the disproportionation constant is 1.1 × 10^6 cal mol^{-1}.

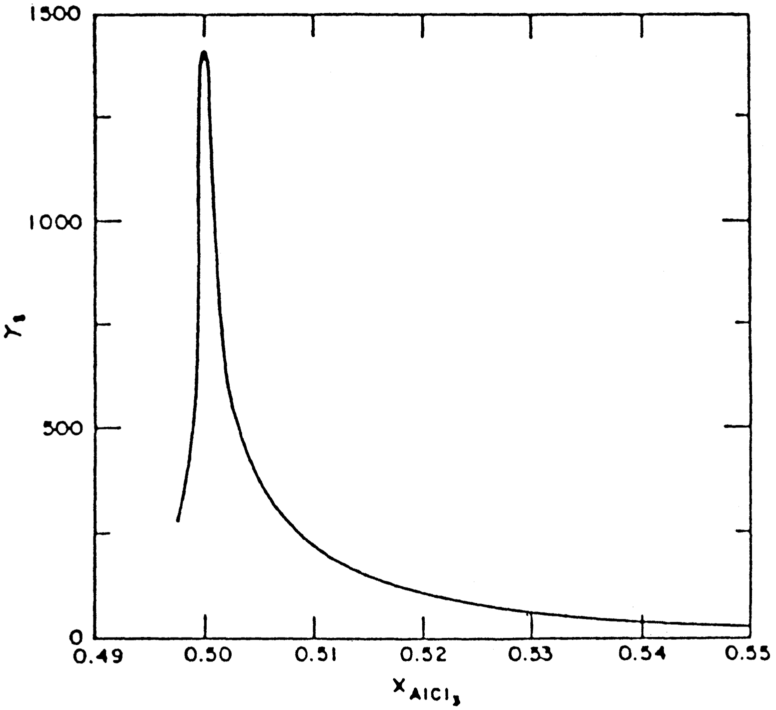

Figure 3. Activity coefficients of a hypothetical solute C in a binary NaCl-$AlCl_3$ solvent calculated from the Coordination Cluster Theory, where the activity coefficient of C is unity in NaCl and $AlCl_3$.

DOI: 10.1149/199017.0041PV

EMPIRICAL RULES FOR SOLUTE-SOLVENT INTERACTIONS IN FUSED SALTS AND CONCENTRATED AQUEOUS SOLUTIONS

Reiko Notoya and Akiya Matsuda

Catalysis Research Center
Hokkaido University
Sapporo, 060, Japan

ABSTRACT

It was found that the same empirical rules concerning the relative standard free energies for solvation of monoatomic ions referred to a definite ion as recently found for solvation in usual solvents, also hold for that in fused salts. Using these rules, we could found the absolute values of solvation energies, the absolute acidities and basicities of fused salts, and some linear relationships also in concentrated aqueous solutions concerning the activity coefficients of ions and water. On the basis of these facts, the solute -solvent interactions in fused salts and the concentrated aqueous solutions of salts were also found to be elucidative by the electron donor-acceptor concept.

INTRODUCTION

The aim of this paper is to provide an empirical method for estimating the standard chemical free energy of solvation $\Delta G^o_{i(x),g\leftarrow s}$ of a cation i(anion x) in a fused salt solvent s and to elucidate the electron donor-acceptor interaction between ions and species in fused salts or in concentrated aqueous solutions, where g means the gas phase. In different fused salts, there is a difficulty in comparing the electrode potential due to the absence of a common standard reference electrode, comparable to the hydrogen electrode in aqueous solutions. This problem had remained unsolved till recently even for usual non-aqueous solvents. Resently, we found two empirical rules concerning the standard chemical free energy of solvation of ions in aqueous and non-aqueous solvents; namely $\Delta G^o_{i,g\leftarrow s}/z_i=\beta_s(\Delta G^o_{i,g\leftarrow w_a}/z_i)=\varepsilon_i\cdot\rho^a_s$ for an individual cation, where z_i, ε_i, β_s and ρ^a_s, denote respectively, valence, a constant characteristic of the cation i, constants characteristic of solvent s, w means water (1). On the other hand, $\Delta G^{o}_{x,g\leftarrow s}=\beta_{s}\Delta G^{o}_{x,g\leftarrow w} = \varepsilon_{s}\ (\rho^{a}_{x} - 0.8)$ were found to hold for the solvation of an individual anion. On the basis of these rules we can estimate the absolute values of chemical free energies of solvation of ions. Also we have successfully obtained the absolute standard EMF $\Phi^{o}_{i,s}$ of the following electrode reaction in solvent s, if the surface potential of solvent χ_{s} is known;

$$M_{i}^{z_{i}} + z_{i}\ e^{-} = M_{i} \qquad [1]$$

By this method, we have determined the $\Delta G^{o}_{i(x),g\leftarrow s}$ and $\Phi^{o}_{i(x),s}$ for more than 70 species of monoatomic ions in 15 solvents, such as organic solvents, and liquid hydrazine and ammonia. Furthermore, this method has been applied to fused salt systems with two or three components. In 10 systems, $\Delta G^{o}_{i(x),g\leftarrow s}$ and $\Phi^{o}_{i(x),s}$ of monoatomic ions from 5 to 45 species have been determined (2).

These empirical rules have been established on the basis of the electron donor-acceptor concept. This paper is concerned with the electron donating and accepting properties, that is, the absolute basicity ρ^{a}_{s} and absolute acidities ε_{i} and ε_{s} which affect the interactions between monoatomic ions and surrounding species in fused salts and in concentrated aqueous solutions.

BASIC CONSIDERATION

Recently, we have found a empirical method for estimating the standard chemical free energy of solvation $\Delta G^{o}_{i,g\leftarrow s}$ of an ion in any solvent, by use of the relative standard free energy of solvation, $i\Delta j(\Delta G^{o}_{g\leftarrow s}/z)$ of an ion i referred to that of a definite ion j in the same solvent s and an extrathermodynamic assumption as described in the latter. The relative quantity $i\Delta j(\Delta G^{o}_{g\leftarrow s}/z)$ can be defined by the following equation;

$$i\Delta j(\Delta G^{o}_{g\leftarrow s}/z)\equiv(\Delta \bar{G}^{o}_{i,g\leftarrow s}/z_{i})-(\Delta \bar{G}^{o}_{j,g\leftarrow s}/z_{j}) \qquad [2]$$

where $\Delta \bar{G}^{o}_{i,g\leftarrow s}/z_{i}$ and $\Delta \bar{G}^{o}_{j,g\leftarrow s}/z_{j}$ denote the standard electrochemical free energy of solvation of ions i and j. The electrochemical one $\Delta \bar{G}^{o}_{i,g\leftarrow s}/z_{i}$ may be given by the chemical part of the solvation energy $\Delta G^{o}_{i,g\leftarrow s}/z_{i}$ and the surface potential χ_{s} of the solvent;

$$\Delta \bar{G}^{o}_{i,g\leftarrow s}/z_{i} = (\Delta G^{o}_{i,g\leftarrow s}/z_{i}) - F\chi_{s}. \qquad [3]$$

The last term in eq.[3] for an ion i equals that in a similar equation for j. Therefore, eq.[2] can be rewritten by the chemical ones;

$$i\Delta j(\Delta G^o_{g\leftarrow s}/z) = (\Delta G^o_{i,g\leftarrow s}/z_i) - (\Delta G^o_{j,g\leftarrow s}/z_j) \qquad [4]$$

As seen from the thermodynamical cycle shown in Fig.1, the standard electrochemical free energy of solvation $\Delta\bar{G}^o_{i,g\leftarrow s}$ of an ion i can be expressed in terms of the standard electrochemical free energy of formation of an ion i $M_i^{z_i}$ and the electrons $z_i e^-$, $\Delta\bar{G}^o_i$, and the absolute standard electromotive force, $\Phi^o_{i,s}$ of the ion/pure substance electrode in solvent s;

$$\Delta\bar{G}^o_{i,g\leftarrow s} = \Delta\bar{G}^o_i - z_i F\Phi^o_s \qquad [5]$$

where $\Phi^o_{i,s}$ is given by the difference in the standard electrochemical potentials $\bar{\mu}^o_{e,g}$ and $\bar{\mu}^o_{e,m}$ of the electron e^- in the gas phase and in the electrode m;

$$F\Phi^o_{i,s} = \bar{\mu}^o_{e,g} - \bar{\mu}^o_{e,m}. \qquad [6]$$

The value of $\Delta\bar{G}^o_i$ is also given by the standard free energies of atomization A_i of M_i and the ionization I_i of $M_{i,g}$ in the gas phase;

$$\Delta\bar{G}^o_i = A_i + I_i \qquad [7]$$

Using the eqs.[2] and [5] for ions i and j, we obtain;

$$i\Delta j(\Delta G^o_{g\leftarrow s}/z) = (\Delta\bar{G}^o_i/z_i) - (\Delta\bar{G}^o_j/z_j) - FE^o_{ij,s} \qquad [8]$$

where $\Delta\bar{G}^o_j$ denotes the standard free energy of formation of an ion j $M_j^{z_j}$ and electrons $z_j e^-$ in the gas phase from its pure substance M_j, and $E^o_{ij,s} = \Phi^o_{i,s} - \Phi^o_{j,s}$ and its numerical value can be known as the standard potential of the electrode reaction expressed by eq.[1] of i species referred to that of a similar reaction of j species in the same solvent. In this way $i\Delta j(\Delta G^o_{g\leftarrow s}/z)$ can be expressed in terms of the well-defined measurable thermodynamic quantities $\Delta\bar{G}^o_i$, $\Delta\bar{G}^o_j$ and $E^o_{ij,s}$.

Using the values in thermodynamic tables in the literature, we could obtained the quantities $i\Delta j(\Delta G^o_{g\leftarrow s}/z)$ for many species of monoatomic ions in 15 solvents, as described above. We have found three linear relationships between the relative quantities $i\Delta j(\Delta G^o_{g\leftarrow s}/z)$ and the ionization energy of cations divided by z_i, I_i/z_i. Monoatomic cations are divided into three groups (a, b and c) and the cations in each group are classified by the electronic configuration. In these relationships, the absolute value $\Delta G^o{}_{j,g\leftarrow s}/z_j$ could be obtained on the extrathermodynamic assumption that the electronic configuration of the ideal ion is a rare gas type, its ionization energy I_i equals zero and such an ion has no chemical interaction with any solvent. In this way, we could know the absolute value of $\Delta G^o{}_{i,g\leftarrow s}/z_i$ for all ions available here and it could be expressed as the function of I_i/z_i. In this way, we have found two empirical rules named the first(I) and second(II) ones, and further have found to be applicable to the bond energy of gaseous di- and tri-atomic metal halides D'_{MXn}, if we consider the bond strength of the molecule as defined by the energy required to separate the constituent atoms into the cation M^{n+} and the anion X^-. These empirical rules and the related correlations are summarized in Table I.

Table I. Summary of Empirical Rules and Related Correlations for Solvation of Ions and Bond of MX_n.

Solvation(cation i)	Bond of MX_n	Solvation(anion x)
Rule I		
$\Delta G^o{}_{i,g\leftarrow s}=\beta_s\Delta G^o{}_{i,g\leftarrow w}$	$D'_{MXn}=\beta_x D'_{MCl}$	$\Delta G^o{}_{x,g\leftarrow s}=\beta_s\Delta G^o{}_{x,g\leftarrow w}$
Rule II		
$\Delta G^o{}_{i,g\leftarrow s}/z_i=\varepsilon_i\,\rho^a{}_s$	$D'_{MXn}/n=\varepsilon_i\rho^a{}_x$	$\Delta G^o{}_{x,g\leftarrow s}=\varepsilon_s(\rho^a{}_x-0.08)$
$\beta_s=\rho^a{}_s/\rho^a{}_w=\rho^b{}_s/\rho^b{}_w=\rho^c{}_s/\rho^c{}_w$	$\beta_x=\rho_x/\rho_{Cl}$	$\beta_s=\varepsilon_s/\varepsilon_w$
$\rho^a{}_s=0.099(DN+8.83)$,eV		$\varepsilon_s=0.30(AN+211.2)$

$\varepsilon_i=I_i/z_i$ (electronic configuration of i; rare gas type)
$=0.936[(I_i/z_i)-0.93\}$ ($d^{3\sim10}$ in outer shell)
$=0.862[(I_i/z_i)-1.42]$ ($5d^{10}+4f^{14}$).

In Table I, the parameters $\rho^a{}_s$ or ε_s and $\rho^a{}_x$ or ε_i mean the absolute basicity or acidity of a solvent and that of an anion or a cation. $\rho^a{}_s$ and ε_s were found to be regarded as the absolute values of Gutmann's and Mayer's electron donor and acceptor numbers, DN and AN (3), respectively. It is obvious from Table I that the solvations is due to the electron donor-acceptor interaction.

RESULTS

Applying the donor-acceptor concept to fused salt systems on the basis of the following equation at $T^{o}K$ where the temperature effect was taken into account, instead of eq.[8], we have found the same two empirical rules in 10 fused salt systems with two or three components as obtained in the non-aqueous solvents;

$$i\Delta j(\Delta G^{o}_{g\leftarrow s}/z)(T)=(\Delta\bar{G}^{o}_{i}/z_{i})(T)-(\Delta\bar{G}^{o}_{j}/z_{j})(T)-FE^{o}_{ij,s}(T) \quad [9]$$

The relative quantities for various ions were estimated by use of the quantities of $\Delta\bar{G}^{o}_{i}(T)$ and $E^{o}_{ij,s}(T)$ mainly quoted the data in (4) and (5). The empirical rule I was found to hold for fused salt systems as exemplified in Fig.2. The value of $-\Delta G^{o}_{j,g\leftarrow s}/z_{i}(T)$in fused salt was given by the intersection of this line with the vertical one in Fig.2 on the basis of the empirical rule I and eq.[4]. The empirical rule II was also found to hold for fused salt systems as shown in Fig.3. In this way, $\Delta G^{o}_{i,g\leftarrow s}/z_{i}(T)$, β_{s} and ρ^{a}_{s} for 10 systems were determined which are summarized in Table II with the standard deviation $\pm\delta$ from the rule I.

Table II. Values of $\Delta G^{o}_{j,g\leftarrow s}/z_{j}(T)$ and $\Phi^{o}_{j,s}(T)$ of j=Ag^{+} and Zn^{2+} in Fused Salts, β_{s}, ρ^{a}_{s}.

Fused Salt	**Temp.** ^{o}**K**	**j**	$\Delta G^{o}_{j,g\leftarrow s}$ **eV**	$\Phi^{o}_{j,s}$ **V**	β_{s}	ρ^{a}_{s}	$\pm\delta$ **eV**
LiCl-KCl	723	Ag^{+}	5.50	4.43	0.970	0.919	0.23
$MgCl_2$-NaCl-KCl	748	Ag^{+}	5.11	4.69	0.937	0.887	0.23
$AlCl_3$-NaCl-KCl	423	Ag^{+}	5.53	4.62	0.957	0.906	0.30
$LiNO_3$-KNO_3	450	Ag^{+}	4:86	5.30	0.997	0.944	0.11
$NaNO_3$-KNO_3	523	Ag^{+}	5.18	4.95	0.968	0.917	0.13
Li_2SO_4-K_2SO_4	898	Ag^{+}	5.45	3.50	1.035	0.980	0.30
NaSCN-KSCN	435	Ag^{+}	4.80	5.14	0.911	0.863	0.33
CH_3COOLi-CH_3COONa-CH_3COOK	495	Zn^{2+}	11.28	3.23	1.013	0.950	0.05
$NaPO_3$-KPO_3	973	Ag^{+}	4.51	4.12	0.923	0.874	0.03
Li_2CO_3-Na_2CO_3	823	Ag^{+}	4.82	4.29	0.972	0.920	0.02

It is surprizing that β_{s} is quite close to unity in any fused salt available. The absolute standard EMFs $\Phi^{o}_{i,s}(T)$ are also summarized in Table II. The value of $\Phi^{o}_{i,s}(T)$ were determined by use of $\Delta G^{o}_{i,g\leftarrow s}/z_{i}(T)$on the basis of eq.[3] and the assumption of $\chi_{s}=0$, due to a random distribution for the surface dipoles of fused salts at higher temperatures as compared with the aqueous solution (2). This assumption seems to be permissible, because an experimental result has shown that the surface potential at mercury-aqueous solution interface decreases with an increase of temperature and vanished at 85°C (6).

In order to reveal the effect of the components of fused salts on the absolute basicities ρ^a_s obtained thus, we determined the values of ρ^a_s or ε_s of single component fused salts by use of the standard potentials $E^o_{ij,s}$ of the following electrode reactions [10 and 11];

$$Ti^{2+} + 2e^- = Ti, \qquad [10]$$

$$2Cl^- = Cl_2 + 2e^-, \qquad [11]$$

in various molten alkali metals and alkaline earths chlorides at 1300°K. Fig.4 showed the linear dependence of the absolute basicity ρ^a_s of fused salt upon the absolute acidity $\varepsilon_{M^{n+}}$ of the component cation of fused salt. The value of ρ^a_s became smaller in the greater value of $\varepsilon_{M^{n+}}$ of the component cation of fused salt. On the other hand, it was shown in Fig.5 that the absolute acidity ε_s of fused salt also became smaller in the greater value of the absolute acidity $\varepsilon_{M^{n+}}$ of the component cation of fused salt. Consequently, the interaction between solute ion and fused salt became less in the greater value of the absolute acidity $\varepsilon_{M^{n+}}$ of the component cation of fused salt, in any case that the solute is a cation or an anion. At the point of view of the micro structure of such a system, it seems that the interactions are very complicated. But, it was found that the thermodynamical consideration on the basis of the electron donor-acceptor concept may be a useful method to obtain the knowledge concerning even multiple interactions among ions and molecules as shown above.

It was found that the solute-solvent interactions in concentrated aqueous solution are also related to the electron donor-acceptor nature. The Sechenov factor $K_\gamma = \partial \log \gamma_\pm / \partial m$ and the activity coefficient γ_w of water quoted from (8) and (9) showed linear relations with the absolute acidity $\varepsilon_{M^{n+}}$ of the component cation of various solute salts, as shown in Figs.6 and 7, respectively.

SUMMARY

The standard chemical free energy of solvation of a cation in fused salt is given by the product of the absolute acidity of the cation and the absolute basicity of fused salt.

The empirically obtained linear relationships between the absolute basicity(and acidity) of single component fused salt and the absolute acidity of the component cation of fused salt are useful to estimate the absolute basicity(and acidity) of any kind of single component fused salt and furthermore the standard free energy of the solvation of ion, whose experimental data of $E^{o}_{ij,s}$ are absent in the literature.

It was found that the solute-solvent multiple interactions in concentrated aqueous solution affecting the activity coefficients of ions and water, are due to the electron donor-acceptor interaction.

REFERENCES

1. R. Notoya and A. Matsuda, J. Phys. Chem., 89, 3922(1985).

2. R. Notoya and A. Matsuda, Nippon Kagaku Kaishi, 990 (1982).

3. V. Gutmann, in The Donor-Acceptor Approach to Molecular Interaction, Plenum Press, 1978.

4. in Natl. Bur. St. US., Selec. V of Chem. and Therm. Pro., 1952.

5. J. A. Plammbeck, in Ency. Elec. Chem., A.J.Bard, ed., Marcell Dekker, 1975.

6. S.Trasatti, in Modern Aspects of Electrochem., B. E. Conway and J. O'M. Bockris, eds. Plenum Press, 13, 81(1979).

7. M. V. Smirnov, in Electrode Potential in Molten Metal Halides, Nauka, 1973.

8. V. I. Ionov and Yu. A. Zolotov, DAN, 223, 907(1975).

9. K. Tajiri, T. Asahina, M. Kosaka, Pro. 2nd Japan-China Bilateral Conference on Molten Salt, 161(1988).

$$\begin{tikzcd}
M_{i,g} \arrow[r, "I_i"] & z_i e^-_g & + & M^{z_i}_{i,g} \\
M_i \arrow[u, "A_i"] \arrow[r, shift left] & z_i e^-_m \arrow[u, "z_i F\phi^0_{i,s}"'] \arrow[l, shift left] & + & M^{z_i}_{i,s} \arrow[u, "\Delta\overline{G}^0_{i,g\leftarrow s}"']
\end{tikzcd}$$

Figure 1. The Thermodynamic Cycle for the Formation of a Gaseous Ion from Its Pure Element.

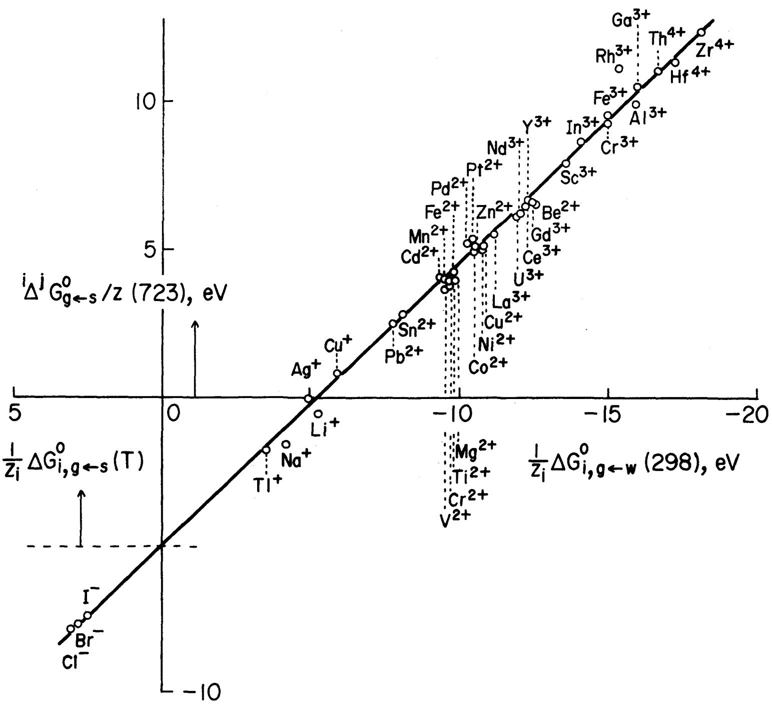

Figure 2. Relation between $^i\Delta^j(\Delta G^0_{g\leftarrow s}/z)(T)$ for LiCl-KCl (mol% 59:41) at 723 ^oK and $\Delta G^0_{i,g\leftarrow w}/z_i$ at 298^{o}K, Ag^+ being Taken as j.

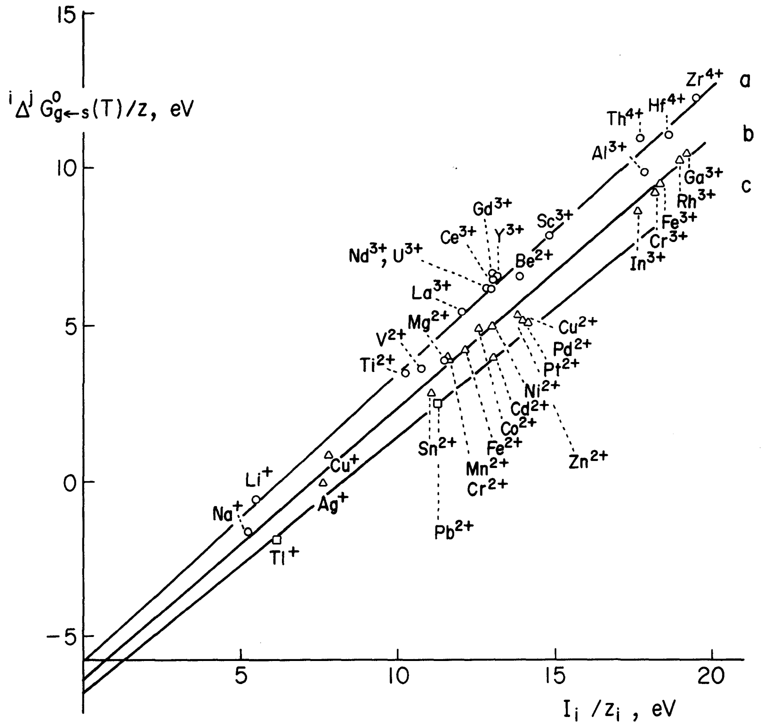

Figure 3. Relation between $\Delta G^o_{i,g\leftarrow s}/z_i(T)$ for the Same System as Exemplified in Figure 2 and I_i/z_i.

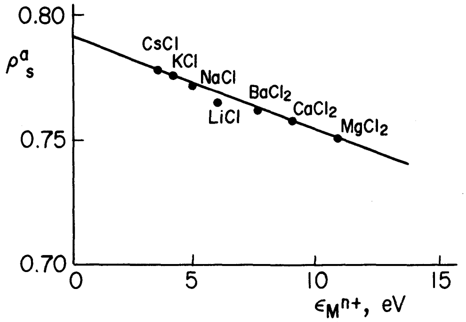

Figure 4. Relation between ρ^a_s at 1300°K and $\varepsilon_{M^{n+}}$ at 0°K of the Component Cation of Fused Salt.

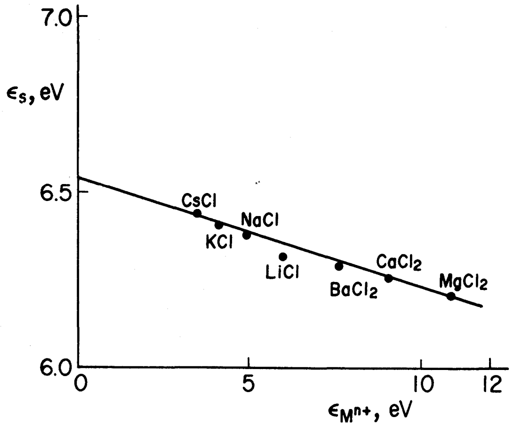

Figure 5. Relation between ε_s at 1300°K and $\varepsilon_{M^{n+}}$ at 0°K of the Component Cation of Fused Salt.

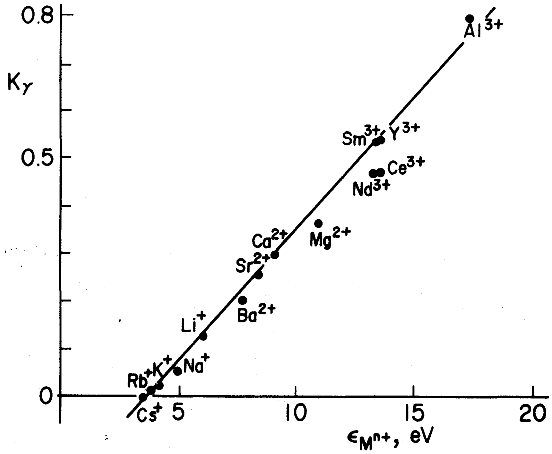

Figure 6. Relation between the Sechenov Factor K_γ of M_iCl_n and $\varepsilon_{M^{n+}}$ of the Cation, in Concentrated Aqueous Solution.

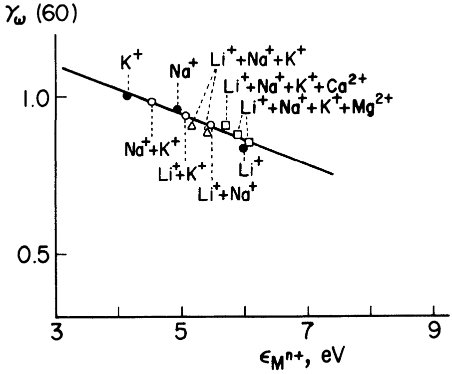

Figure 7. Relation bewteen Activity Coefficient γ_w of Water and $\varepsilon_{M^{n+}}$ of the Cation, in Aqueous Solutions of $M_i(NO_3)_n$ (●) or $\varepsilon_{M^{n+}}$ Estimated as the Mean Value of the Component Cations on the Basis of the Component Ratio in Mixed Solutions of Two(○), Three(△) or Four(□) Species of $M_i(NO_3)_n$, at the Total Mole Fraction=0.1, T=60°C.

DOI: 10.1149/199017.0052PV

MULTICOMPONENT PHASE EQUILIBRIUM CALCULATIONS IN MOLTEN SALT SYSTEMS

Yves Dessureault and Arthur D. Pelton

Centre de Recherche en Calcul Thermochimique
Ecole Polytechnique
P.O. Box 6079, Station "A",
Montreal, Quebec, Canada H3C 3A7

ABSTRACT

Thermodynamic and phase diagram data for a large number of binary molten salt systems have been fully optimized and the resulting parameters stored in a computer database.

Thermodynamic properties and phase diagrams of multicomponent salt solutions can be calculated from the binary parameters by means of solution models. To this end, the sublattice model of reciprocal salt systems has been modified to account more correctly for non-random distribution when the exchange Gibbs energy is large.

INTRODUCTION

A thermodynamic database for multicomponent molten salt solutions is being developed for use with the F*A*C*T (Facility for the Analysis of Chemical Thermodynamics) on-line computer system(1). Over 200 binary and ternary salt systems have already been fully optimized to yield binary and ternary parameters for the database. Much of this work has been supported by the American Ceramic Society as part of the "Phase Diagrams for Ceramists" project(2).

In order to use the optimized binary and ternary parameters to calculate activities in multicomponent salt solutions, we have employed a sublattice model (3,4). Interactive Gibbs energy minimization programs, which form part of the F*A*C*T system, and which have automatic access to the database, can be used to calculate ternary and higher-order phase diagrams and to calculate complex multiphase equilibria involving multicomponent molten salt solutions with other phases (gases, oxides, metals, etc.) for which evaluated databases have also been prepared.

In the case of reciprocal ternary salt systems, it was found that the standard sublattice model (5-7) gives unsatisfactory results in systems with strong ionic interactions. An extended quasichemical model has thus been developed which takes into account the non-randomness inherent in such systems.

The present article outlines our activities in developing the molten salt database and describes the essential features of the model for reciprocal salt solutions.

It is assumed that in a molten salt solution, the cations A,B,C, ... reside on a cation sub-lattice while the anions X,Y,Z ... reside on an anion sub-lattice. The cationic and anionic site fractions are denoted by X_i . For example:

$$X_A = n_A/(n_A+n_B+n_C+ \ldots) \qquad [1]$$

$$X_X = n_X/(n_X+n_Y+n_Z+ \ldots) \qquad [2]$$

where n_i is the number of moles of ion i in solution.

BINARY COMMON-ION SYSTEMS

In a common-anion binary system AX-BX, the molar Gibbs energy of the liquid phase can be written as:

$$g = (X_A g^o_{AX} + X_B g^o_{BX}) + RT(X_A \ln X_A + X_B \ln X_B) + g^E \qquad [3]$$

where g^o_{AX} and g^o_{BX} are the standard molar Gibbs energies of the pure salts and the cationic fractions, X_A and X_B , are equal, in this common-ion system, to the component mole fractions, X_{AX} and X_{BX} . The second term in Eq [3] represents the ideal mixing of cations on the cation sublattice. The excess Gibbs energy, g^E , may be expanded as a polynomial:

$$g^E = X_A X_B w_{A,B/X}(X_B) \qquad [4]$$

where: $w_{A,B/X}(X_B) = (h_o + h_1 X_B + h_2 X_B^2 + \ldots)$

$$-T(s_o + s_1 X_B + s_2 X_B^2 + \ldots) \qquad [5]$$

where h_i and s_i are, respectively, coefficients for the excess enthalpy and entropy. Alternatively, $w_{A,B/X}$ could be expanded as a Redlich-Kister or Legendre polynomial(8). For common-cation systems, AX-AY, expressions analogous to Eqs [3-5] can be written. For charge-asymmetric systems (containing cations and anions of different charges, e.g. $NaF-Na_2CO_3$), equivalent ionic fractions are used in place of the ionic fractions for the excess terms. This is discussed in (3,4).

In a quasichemical approach, $w_{A,B/X}$ can be considered to be the energy of formation of second-nearest-neighbor A-B pairs according to:

$$A\text{-}X\text{-}A + B\text{-}X\text{-}B = 2\ A\text{-}X\text{-}B \qquad [6]$$

where A-X-A, B-X-B and A-X-B represent second-nearest-neighbor cation pairs in a solution in which the only anions are X^- anions.

The coefficients of Eq [5] can be determined by optimization of thermodynamic and phase equilibrium data. As an example, consider the KF-LiF system. Experimental liquidus points(9) are shown in Fig.1. Several other investigations, summarized by(10), indicate a eutectic in the range 487° to 493°C at $X_{LiF} = 0.50 \pm 0.01$. Gibbs energies of fusion of KF and LiF were taken from(11). In addition, the excess enthalpy of the liquid has been measured calorimetrically(12). These data were optimized simultaneously (10) in one least-squares analysis to obtain the following expression for g^E:

$$g^E = X_K X_{Li}\ [(-15724-8259X_{Li}+4732X_{Li}^2) - T(-1.375 -3.146X_{Li})] \quad \text{J/mol} \qquad [7]$$

The phase diagram in Fig.1. was calculated from Eq.[7]. The liquidus points(9) are reproduced within 5° and at the same time the excess enthalpy data are reproduced within experimental error limits. The coupled thermodynamic/phase diagram optimization method is discussed in (13), and the relationships between phase diagrams and thermodynamics are treated in (14).

As a further illustration, the calculated optimized (15) phase diagram for the K_2SO_4-Li_2SO_4 system is compared with some experimental data points (16,17) in Fig.2. Full details of the analysis are given in (15). The excess Gibbs energy of the liquid was expressed with two excess enthalpy and two excess entropy coefficients in Eq.[5]. The experimental excess liquid enthalpy (18) was simultaneously optimized. Solid phases were treated as Henrian solutions.

A list of some of the systems which have been optimized in a systematic manner is given in Table 1. All these have been published in *Phase Diagrams for Ceramists*, vol. 7(2) and elsewhere (10,15,19,20). We have also optimized many other binary salt systems.

The technique of coupled thermodynamic/phase diagram optimization provides a set of self-consistent thermodynamic equations which simultaneously reproduce the thermodynamic properties and the phase diagram of a system. The technique yields a thermodynamically correct "smoothing" of the experimental data. Discrepancies among various sets of data can often be resolved in this way, and error limits can more easily be assigned. Furthermore, such a thermodynamic analysis is the first step in estimating ternary and higher-order phase diagrams from binary data as discussed in the following sections.

TERNARY COMMON-ION SYSTEMS

For a common-anion ternary system, AX-BX-CX, the molar Gibbs energy of the liquid may be written as:

$$g = (X_A g^o_{AX} + X_B g^o_{BX} + X_C g^o_{CX}) + RT(X_A \ln X_A + X_B \ln X_B + X_C \ln X_C) + g^E \qquad [8]$$

An analogous expression can be written for common-cation systems.

For a large number of ternary common-ion molten salt systems, we have had much success in expressing g^E by the following expression first proposed by Kohler (21):

$$g^E = X_A X_B w_{A,B/X}(X_B/(X_A+X_B)) + X_B X_C w_{B,C/X}(X_C/(X_B+X_C)) + X_C X_A w_{C,A/X}(X_C/(X_C+X_A)) + \text{(Ternary terms)} \qquad [9]$$

where $w_{A,B/X}(X_B/(X_A+X_B))$ is the value of $w_{A,B/X}$ from the AX-BX binary sytem at the same ratio $X_B/(X_A+X_B)$ as in the tenary system. For a more complete discussion, see (3,4).

As an example, the liquidus surface of the KF-LiF-NaF system, calculated solely from optimized binary parameters by means of Eq.[9] with no "ternary terms", is shown in Fig.3. The calculated ternary eutectic at 463°C agrees with the measured (22) eutectic point to within 6° and 2 mol %.

If accurate ternary data are available, then small optimized "ternary terms", such as $aX_A X_B X_C$ where a is an adjustable parameter, can be added to Eq.[9] in order to bring the calculated and reported ternary phase diagrams into coincidence.

As shown in Table 1, all possible common-ion ternary alkali-halide phase diagrams have been calculated and published(2). For 47 of these, phase diagrams have been reported. In only 5 systems was a ternary term required in order to reproduce the measured diagram within experimental error limits.

We have similarly analyzed many other ternary common-ion systems. For charge-asymmetric systems, equivalent ionic fractions are used in the excess terms (3,4). Models other than Eq.[9] can also be used to estimate g^E of the ternary solution from binary parameters. These include other models based on regular solution theory such as the "Toop" and "Muggianu" techniques and the Conformal Ionic Solution Theory(23). All these techniques can be generalized for quaternary and higher-order systems (3,4).

RECIPROCAL TERNARY SYSTEMS

A reciprocal ternary system A,B/X,Y is one involving two cations, A and B, and two anions, X and Y. Compositions are usually plotted on a square as in Figs. 4, 5, with cationic fractions along one axis and anionic fractions along the other.

The molar Gibbs energy of the liquid is commonly expressed by the following equation:

$$\begin{aligned} g = {} & (X_A X_X g^o_{AX} + X_B X_X g^o_{BX} + X_A X_Y g^o_{AY} + X_B X_Y g^o_{BY}) \\ & + RT(X_A \ln X_A + X_B \ln X_B + X_X \ln X_X + X_Y \ln X_Y) \\ & + X_A X_B X_X w_{A,B/X} + X_A X_B X_Y w_{A,B/Y} + X_A X_X X_Y w_{A/X,Y} \\ & + X_B X_X X_Y w_{B/X,Y}) - X_A X_B X_X X_Y \Lambda \end{aligned} \tag{10}$$

where the first term contains the standard molar Gibbs energies of the pure salts; the second term is equal to the Gibbs energy of an ideal mixture of A and B cations on the cation sub-lattice and of X and Y anions on the anion sub-lattice; the third term involves the excess terms from the four limiting binary systems; and the final term is a non-ideal mixing term. For charge-asymmetrical systems, equivalent ionic fractions may be used, and the equation can be extended to reciprocal quaternary and higher-order systems (3,4).

It was shown by Blander and Yosim (5) that an equation of the form of Eq.[10] results from Conformal Ionic Solution Theory. The equation can also be derived from quasichemical theory (24,25) as will be discussed below.

The standard molar Gibbs energies g^o_{AX}, g^o_{BX}, g^o_{AY} and g^o_{BY} in Eq.[10] are related by the Gibbs energy change, Δg^{EX}, of the exchange reaction among the pure salts:

$$BX + AY = AX + BY \quad \Delta g^{EX} = (g^o_{AX} + g^o_{BY} - g^o_{BX} - g^o_{AY}) \qquad [11]$$

If $\Delta g^{EX}<0$, then AX and BY are called stable pair. By differentiation of Eq.[10], expressions for the activities of the neutral salts AX, AY, BX and BY can be obtained (3,4). For the stable pair, positive deviations result, while negative deviations are calculated for the salts which form the unstable pair. The magnitude of these deviations varies as the magnitude of Δg^{EX}.

In the Na,K/F,Cl system, Fig.4, NaF and KCl form the stable pair. The resultant positive deviations in their activities is manifested by flat liquidus surfaces with widely-spaced isotherms, while the negative deviations in the case of KF and NaCl are manifested by steep liquidus surfaces.

In the Li,K/F,Br system, Fig.5, Δg^{EX} is so large that a liquid miscibility gap is formed along the "stable diagonal" joining the stable pair, LiF and KBr.

In quasichemical terms, if $\Delta g^{EX}<0$, then a configuration with A^+-X^- and B^+-Y^- nearest-neighbors is energetically favorable to one with A^+-Y^- and B^+-X^- nearest neighbors. When the pure salts AX and BY which form the stable pair are mixed, some energetically unfavorable B^+-X^- and A^+-Y^- pairs are formed at the expense of the more favorable A^+-X^- and B^+-Y^- pairs. Hence, this process is energetically unfavorable and positive deviations occur along the stable diagonal. On the other hand, mixing of the pure salts AY and BX, which form the unstable pair, results in the formation of energetically favorable A^+-X^- and B^+-Y^- pairs in solution, and so negative deviations are observed along the unstable diagonal.

From these considerations it can also be seen that there will be a tendency to non-random mixing with A^+-X^- and B^+-Y^- pairs tending to predominate. The degree to which such clustering occurs will vary as Δg^{EX}.

The final term in Eq.[10] arises because of this non-random mixing. From a first-order quasichemical approximation, it may be shown (24) that:

$$\Lambda = (\Delta g^{EX})^2/2ZRT \qquad [12]$$

where Z is a coordination number usually taken as 6.

In quasichemical terms, the third term in Eq.[10], which involves the binary excess terms, states that the energy of formation of second-nearest neighbor A-B cation pairs varies linearly with the anionic fractions X_X and X_Y between the value $w_{A,B/X}$ for the formation of A-X-B groupings in the AX-BX binary system and the value $w_{A,B/Y}$ for the formation of A-Y-B groupings in the AY-BY system. Also, the energy of formation of second-nearest neighbor X-Y anion pairs varies linearly with the cationic fractions X_A and X_B between the values $w_{A/X,Y}$ and $w_{B/X,Y}$ for X-A-Y and X-B-Y groupings respectively in the AX-AY and BX-BY binary systems.

The liquidus surface of the Na,K/F,Cl system was calculated from Eq.[10] with Δg^{EX} and the Gibbs energies of fusion of the pure salts taken from thermodynamic tables (11), with the values of $w_{Na,K/F}$, $w_{Na,K/Cl}$, $w_{Na/F,Cl}$ and $w_{K/F,Cl}$ taken from our optimizations of the binary systems (2,10), and with Λ given by Eq.[12] with Z=6. The calulated diagram, shown in Fig.4b, agrees very well with the measured diagram (26) in Fig.4a.

However, when the same calculation was performed for the Li,K/F,Br system, the diagram of Fig.5b resulted. Agreement with the experimental diagram (27) in Fig.5a is poor. The calculated miscibility gap is split in two.

Calculations were performed for several other reciprocal systems. It was found that whenever Δg^{EX} is large enough to give rise to a miscibility gap and, at the same time, $w_{A,B/X}$ and $w_{A,B/Y}$ are quite negative, similarly poor results are obtained from the calculations, with the miscibility gap tending to split in the middle.

Clearly, the model is predicting a Gibbs energy, g, of the liquid which is too negative in the centre of the composition square. This appears to be related to the terms $X_A X_B X_X w_{A,B/X}$ and $X_A X_B X_Y w_{A,B/Y}$ in Eq.[10] providing two negative a contribution to g since, when $w_{A,B/X}$ and $w_{A,B/Y}$ are small, the problem does not arise. (It may be noted that in the majority of simple common-anion molten salts, $w_{A,B/X}$ is negative, while in the majority of simple common-cation molten salts, $w_{A/X,Y}$ is very small.)

This same observation was made by Saboungi and Blander (6,7) who attempted to correct the model by calculating Λ as:

$$\Lambda = (|\Delta g^{EX}|+(w_{A,B/X}+w_{A,B/Y}+w_{A/X,Y}+w_{B/X,Y})/2)^2/2ZRT \qquad [13]$$

The phase diagram of the Li,K/F,Br system, recalculated with Eq.[13], is shown in Fig.5c. Results are improved.

Although the modified value of Λ in Eq.[13], usually gives better results than the unmodified expression in Eq.[12], this is not the case for all systems. Furthermore, the correction is not based upon a clearly defined theoretical model.

AN EXTENDED QUASICHEMICAL MODEL FOR RECIPROCAL TERNARY SYSTEMS

In order to understand why the model fails, the following explanation is proposed.

$w_{A,B/X}$ and $w_{A,B/Y}$ are the energies of formation of A-X-B and A-Y-B second-nearest-neighbor pairs. In Eq.[10] a random distribution of cations and anions on their respective sites is assumed such that the probability of A-X-B and A-Y-B groupings are $X_A X_B X_X$ and $X_A X_B X_Y$ respectively. However, when Δg^{EX} is large, there is a tendency to form A-X and B-Y clusters. This reduces the number of A-X-B and A-Y-B groupings and increases the number of A-X-A and B-Y-B groupings. This effect is greatest near the middle of the composition square. The terms $X_A X_B X_X w_{A,B/X}$ and $X_A X_B X_Y w_{A,B/Y}$ in Eq.[10] are thus too negative in this composition region and so Eq.[10] overestimates the stability of the liquid.

In the case of a random distribution of cations and anions on their respective sublattices, the probability that a given nearest-neighbor cation-anion pair is an A^+-X^- pair is equal to $X_A X_X$. In the non-random mixture, following the notation of Forland (25), this probability is increased to $(X_A X_X + y)$ where y is a positive number. Similarly, the probabilities of B-Y, A-Y and B-X pairs are $(X_B X_Y + y)$, $(X_A X_Y - y)$ and $(X_B X_X - y)$.

The molar Gibbs energy of the solution is written as follows:

$$
\begin{aligned}
g = {} & [(X_A X_X + y) g^o_{AX} + (X_B X_Y + y) g^o_{BY} + (X_A X_Y - y) g^o_{AY} + (X_B X_X - y) g^o_{BX}] \\
& - T\Delta S^{config} \\
& + [X_X (X_A + y/X_X)(X_B - y/X_X) w_{A,B/X} + X_Y (X_A - y/X_Y)(X_B + y/X_Y) w_{A,B/Y} \\
& + X_A (X_X + y/X_A)(X_Y - y/X_A) w_{A/X,Y} + X_B (X_X - y/X_B)(X_Y + y/X_B) w_{B/X,Y}]
\end{aligned}
\qquad [14]
$$

The term involving, for example, g^o_{AX} is now written as $(X_A X_X + y) g^o_{AX}$ in order to take account of the increased frequency, in the non-random case, of A^+-X^- nearest-neighbor pairs.

For the second-nearest-neighbor interactions, the energy of forming an A-B-X grouping, $w_{A,B/X}$, is now multiplied by the probability, P(AXB), of finding such a grouping.

This probability is given by:

$$P(AXB)=P(X)\ P(A|X)\ P(B|X) = X_X\ \left(\frac{X_A X_X + y}{X_X}\right)\ \left(\frac{X_B X_X - y}{X_X}\right) \qquad [15]$$

where P(X) is the probability that an anion site is occupied by an X^- ion, P(A|X) is the conditional probability that a cation site is occupied by an A^+ cation given that the neighboring anion site is occupied by an X^- ion, and P(B|X) is defined similarly.

ΔS^{config} is the molar configurational entropy. This is given by the following approximate expression (exact for a one-dimensional lattice) for the distribution of the A-X, A-Y, B-X and B-Y "bonds" over the Z bond positions in one mole of solution:

$$\Delta S^{config} = -R(X_A \ln X_A + X_B \ln X_B + X_X \ln X_X + X_Y \ln X_Y)$$

$$-RZ\ \left[(X_A X_X + y)\ln\frac{X_A X_X + y}{X_A X_X} + (X_B X_Y + y)\ln\frac{X_B X_Y + y}{X_B X_Y}\right.$$

$$\left. + (X_A X_Y - y)\ln\frac{X_A X_Y - y}{X_A X_Y} + (X_B X_X - y)\ln\frac{X_B X_X - y}{X_B X_X}\right] \qquad [16]$$

Note that for random mixing, when y=0, Eq.[16] reduces to the ideal entropy expression in Eq.[10].

In order to solve Eq.[14], we must calculate y. The value of y adopted by the system will be that which minimizes the Gibbs energy. Setting dg/dy=0 we obtain the following expression:

$$\frac{(X_A X_X + y)(X_B X_Y + y)}{(X_B X_X - y)(X_A X_Y - y)} + e^{-(\Delta g^{EX} + Q)/ZRT} \qquad [17]$$

where:

$$Q = (X_B - X_A - 2y/X_X)w_{A,B/X} + (X_A - X_B - 2y/X_Y)w_{A,B/Y}$$

$$+ (X_Y - X_X - 2y/X_A)w_{A/X,Y} + (X_X - X_Y - 2y/X_B)w_{B/X,Y} \qquad [18]$$

Equations [17,18] can be solved for y by an iterative technique. On the first pass, Q is assumed equal to zero and Eq.[17], which is now quadratic, is solved for y. This value is then substituted into Eq.[18] to obtain a second estimate for Q, and so on.

Although the equations of the extended model are lengthy, their solution with a computer is straightforward. It must be stressed that the model introduces no new adjustable parameters. As was the case with Eq.[10], only values of Δg^{EX} and of the binary excess terms, $w_{A,B/X}$, etc. are required.

When Δg^{EX} is small Eq.[14] reduces Eq.[10]. The phase diagram of the Na,K/F,Cl system, calculated with the extended model, is virtually identical to Fig.4b.

For the Li,K/F,Br system, in which Δg^{EX} as well as $w_{Li,K/F}$ and $w_{Li,K/Br}$ are negative and large, the phase diagram calculated with the extended model is shown in Fig.5d. Agreement with the measured diagram is better than that obtained with Eq.[10] and the modified expression of Eq.[13] for Λ, and is much better than that obtained with Eq.[12] for Λ.

Equally good results have been obtained for several other ternary reciprocal molten salt systems.

DISCUSSION

The extended quasichemical model for reciprocal molten salt solutions will be developed and discussed in more detail in a forthcoming article. The inclusion of charge-asymmetry through the use of equivalent ionic fractions and the extension to quaternary and higher-order systems will be treated.

With the extended model, ternary and higher-order reciprocal salt phase diagrams can be calculated with satisfactory precision from the thermodynamic properties of the pure salts and from optimized parameters for the binary sub-systems. Thus it is now possible to set up databases of such parameters for purposes of calculating the thermodynamic properties and phase diagrams of multicomponent salt systems.

ACKNOWLEDGEMENTS

Financial assistance from the Natural Sciences and Engineering Research Council of Canada and from the American Ceramic Society are gratefully acknowledged.

REFERENCES

1. W.T. Thompson, C.W. Bale and A.D.Pelton, "F*A*C*T (Facility for the Analysis of Chemical Thermodynamics) Users' Instruction Manual", 500 pages, 2nd edition (1985).

2. "Phase Diagrams for Ceramists", edited by E.M. Levin, C.R. Robbins, H.F. McMurdie, R.S. Roth, T. Negas, and L.P. Cook, American Ceramic Society, Columbus, OH, vol. 7 (1990).

3. A.D. Pelton, Calphad J., 12, 127-142 (1988).

4. A.D. Pelton, Proc. Symp. on Molten Salts, Honolulu, Electrochem. Soc., Warrendale, PA (1988).

5. M. Blander and S.J. Yosim, J. Chem. Phys., 39, 2610 (1963).

6. M.L. Saboungi and M. Blander, High Temperature Science, 6, 37 (1974).

7. M.L. Saboungi, H. Schnyders, M.S. Foster and M. Blander, J. Phys. Chem., 78, 1091 (1974).

8. A.D. Pelton and C.W. Bale, Met. Trans., 17A, 1057-63 (1986).

9. E. Aukrust, B. Bjorge, H. Flood and T. Forland, Ann. N.Y. Acad. Sci., 79, 830 (1960).

10. J. Sangster and A.D. Pelton, J. Phys. Chem. Ref. Data, 16, 509-61 (1987).

11. I. Barin, O. Knacke, and O. Kubaschewski, "Thermochemical Properties of Inorganic Substances", Springer, Berlin (1977).

12. K.C. Hong and O.J. Kleppa, J. Chem. Thermodyn., 8, 31 (1976).

13. C.W. Bale and A.D. Pelton, Met. Trans., 14B, 77-84 (1983).

14. A.D. Pelton, chapter entitled "Phase Diagrams", in "Physical Metallurgy, 3rd edition", ed. R.W. Cahn and P. Haasen, pp 328-81, North-Holland, N.Y. (1983).

15. Y. Dessureault, J. Sangster and A.D. Pelton, J. Electrochem. Soc., accepted.

16. K. Schroeder, Ph.D. Thesis, Goteborg University, (1975).

17. E.K. Akopov, Sov. Prog. Chem., 33(5), 23 (1967).

18. T. Ostvold and O.J. Kleppa, Acta Chem. Scand., 25, 919 (1971).

19. Y. Dessureault, J. Sangster et A.D. Pelton, J. Chim. Phys., accepted.

20. Y. Dessureault, J. Sangster and A.D. Pelton, J. Phys. Chem. Ref. Data, accepted.

21. F. Kohler, Mh. Chem., 91, 738 (1960).

22. H.W. Hoffman, Report ORNL-CF-58-2-40, p. 32, Oak Ridge National Laboratory, Oak Ridge, Tenn. (1958).

23. H. Reiss and O.J. Kleppa, J. Phys. Chem., 36, 144 (1962); M. Blander and S.J. Yosim, J. Chem. Phys., 39, 2610 (1963); M.-L. Saboungi and P. Cerisier, J. Electrochem. Soc., 121, 1258 (1974); M.-L. Saboungi and M. Blander, J. Chem. Phys., 63, 212 (1975); M. Blander and M.-L. Saboungi, "Molten Salts", pp. 93-106, The Electrochemical Society, Inc. (1976).

24. M. Blander and J. Braunstein, Ann. N.Y. Acad. Sci., 79, 838 (1960).

25. T. Forland, Ch. 2 in "Fused Salts", B.R. Sundheim ed., McGraw Hill, N.Y. (1964).

26. V.D. Polyakov, Izv. Sektora Fiz.-Khim. Analiza Inst. Obshch. Neorgan. Khim. Akad. Nauk SSSR, 13, 308 (1940).

27. C. Margheritis, G. Flor and C. Sinistri, Z. Naturforsch., A34, 836 (1979).

Table 1 LIST OF EVALUATED SYSTEMS(2)

LiF-NaF
LiF-KF
LiF-RbF
LiF-CsF
NaF-KF
NaF-RbF
NaF-CsF
KF-RbF
KF-CsF
RbF-CsF
LiCl-NaCl
LiCl-KCl
LiCl-RbCl
LiCl-CsCl

NaCl-KCl
NaCl-RbCl
NaCl-CsCl
KCl-RbCl
KCl-CsCl
RbCl-CsCl
LiBr-NaBr
LiBr-KBr
LiBr-RbBr
LiBr-CsBr
NaBr-KBr
NaBr-RbBr
NaBr-CsBr
KBr-RbBr

KBr-CsBr
RbBr-CsBr
LiI-NaI
LiI-KI
LiI-RbI
LiI-CsI
NaI-KI
NaI-RbI
NaI-CsI
KI-RbI
KI-CsI
$LiNO_3$-$NaNO_3$
$LiNO_3$-KNO_3
$NaNO_3$-KNO_3

LiOH-NaOH
LiOH-KOH
NaOH-KOH
Li_2CO_3-Na_2CO_3
Li_2CO_3-K_2CO_3
Na_2CO_3-K_2CO_3
Li_2SO_4-Na_2SO_4
Li_2SO_4-K_2SO_4
Na_2SO_4-K_2SO_4

LiF-LiCl
LiF-LiBr
LiF-LiI
LiF-$LiNO_3$
LiF-LiOH
LiF-Li_2CO_3
LiF-Li_2SO_4
LiCl-LiBr
LiCl-LiI
LiCl-$LiNO_3$
LiCl-LiOH
LiCl-Li_2CO_3

LiCl-Li_2SO_4
LiBr-LiI
NaF-NaCl
NaF-NaBr
NaF-NaI
NaF-$NaNO_3$
NaF-NaOH
NaF-Na_2CO_3
NaF-Na_2SO_4
NaCl-NaBr
NaCl-NaI
NaCl-$NaNO_3$

NaCl-NaOH
NaCl-Na_2CO_3
NaCl-Na_2SO_4
NaBr-NaI
KF-KCl
KF-KBr
KF-KI
KF-KNO_3
KF-KOH
KF-K_2CO_3
KF-K_2SO_4
KCl-KBr

KCl-KI
KCl-KNO_3
KCl-KOH
KCl-K_2CO_3
KCl-K_2SO_4
KBr-KI

LiF-NaF-KF
LiF-NaF-RbF
LiF-NaF-CsF
LiF-KF-RbF
LiF-KF-CsF
LiF-RbF-CsF
NaF-KF-RbF
NaF-KF-CsF
NaF-RbF-CsF
KF-RbF-CsF

LiCl-NaCl
LiCl-NaCl-RbCl
LiCl-NaCl-CsCl
LiCl-KCl-RbCl
LiCl-KCl-CsCl
LiCl-RbCl-CsCl
NaCl-KCl-RbCl
NaCl-KCl-CsCl
NaCl-RbCl-CsCl
KCl-RbCl-CsCl

LiBr-NaBr-KBr
LiBr-NaBr-RbBr
LiBr-NaBr-CsBr
LiBr-KBr-RbBr
LiBr-KBr-CsBr
LiBr-RbBr-CsBr
NaBr-KBr-RbBr
NaBr-KBr-CsBr
NaBr-RbBr-CsBr
KBr-RbBr-CsBr

LiI-NaI-KI
LiI-NaI-RbI
LiI-NaI-CsI
LiI-KI-RbI
LiI-KI-CsI
LiI-KI-CsI
NaI-KI-RbI
NaI-KI-CsI
NaI-RbI-CsI
KI-RbI-CsI

LiF-LiCl-LiBr
LiF-LiCl-LiI
LiF-LiBr-LiI
LiCl-LiBr-LiI

NaF-NaCl-NaBr
NaF-NaCl-NaI
NaF-NaBr-NaI
NaCl-NaBr-NaI

KF-KCl-KBr
KF-KCl-KI
KF-KBr-KI
KCl-KBr-KI

RbF-RbCl-RbBr
RbF-RbCl-RbI
RbF-RbBr-RbI
RbCl-RbBr-RbI

CsF-CsCl-CsBr
CsF-CsCl-CsI
CsF-CsBr-CsI
CsCl-CsBr-CsI

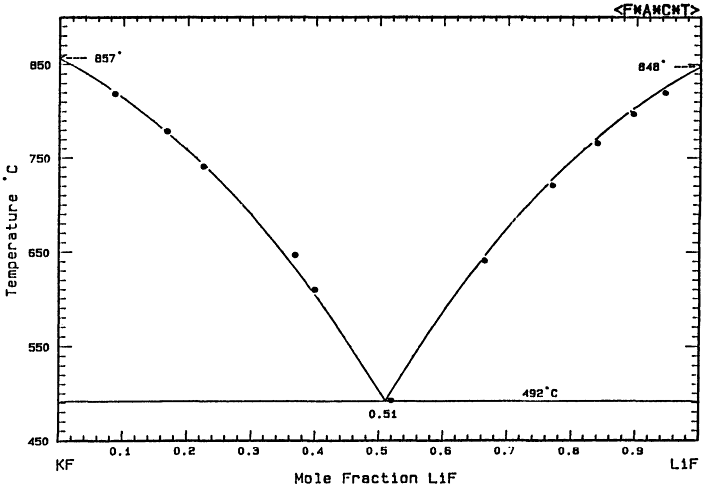

Fig. 1: Optimized KF–LiF phase diagram. Experimental points from (9)

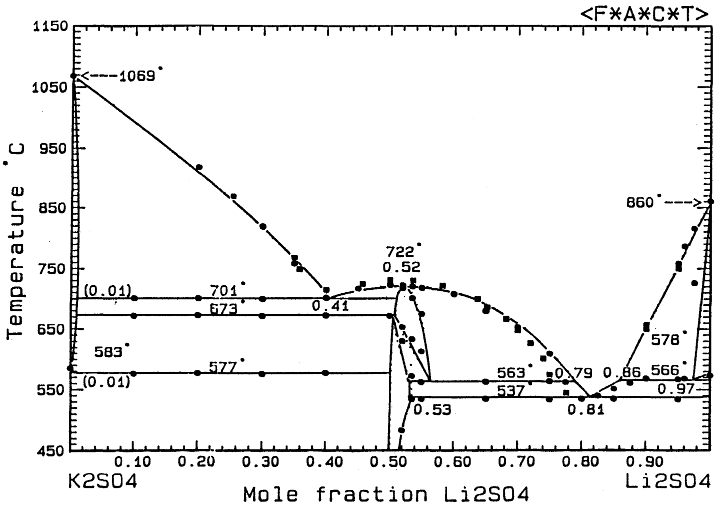

Fig. 2: Optimized K_2SO_4–Li_2SO_4 phase diagram. Experimental points from (16,17)

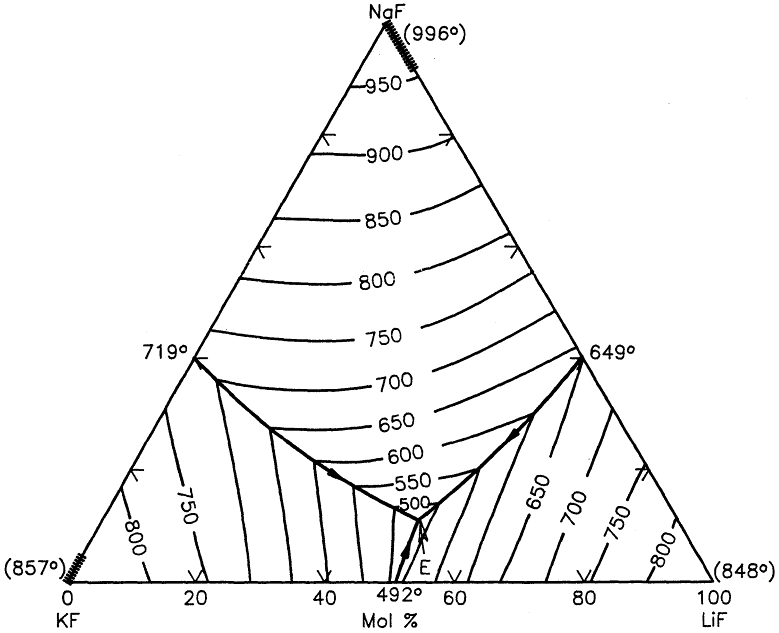

Fig. 3: KF-NaF-LiF phase diagram calculated solely from binary parameters

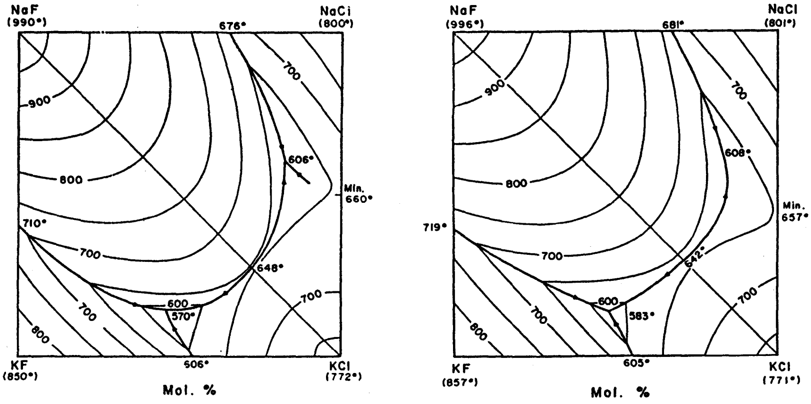

Fig. 4: Liquidus of the Na,K/F,Cl System
(a) As reported by (26)
(b) Calculated

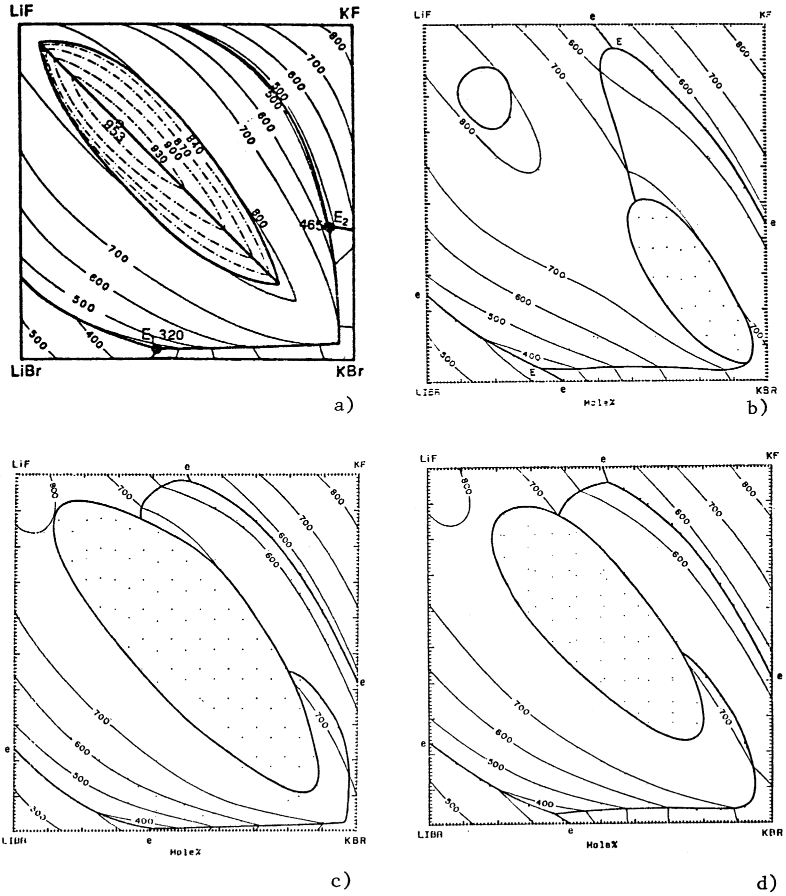

Fig. 5: The Li,K/F,Br phase diagram.
(a) As reported by (27)
(b) Calculated from Eqs. (10) and (12)
(c) Calculated from Eqs. (10) and (13)
(d) Calculated from the extended quasichemical model

DOI: 10.1149/199017.0068PV

THERMODYNAMIC TREATMENT OF MULTICOMPONENT FUSED SALT SOLUTIONS: COMMON ANION REACTIVE SYSTEMS APPROXIMATION

S.N. Flengas

Department of Metallurgy and Materials Science
University of Toronto
Toronto, Ontario
Canada M5S 1A4

Abstract

From a modified F.F.G.$^{(1)}$ thermodynamic cycle, equations have been developed from which the molar and partial molar excess thermodynamic properties of j-component molten salt solutions may be predicted from binary data.

The theory is applicable to reactive molten salt systems and particularly to charge asymmetric fused salt solutions with common anions.

It is shown that for a system having j+1 components, such as, MX_q-AX-BX••• ••• JX, any molar or partial molar property of mixing for MX_q, may be calculated from available data on corresponding j-binary systems, such as MX_q-AX, MX_q-BX and ••• MX_q-JX.

The equations are of the general form,

$$\underset{\left(\text{in } j+1 \text{ component system at } X_{MX_q}\right)}{\Delta Z_{MX_q}} = \frac{X_2}{1-X_1}(\Delta Z_{MX_q})_{MX_q-AX} + \frac{X_3}{1-X_1}(\Delta Z_{MX_q})_{MX_q-BX} \cdots + \frac{X_j}{1-X_1}(\Delta Z_{MX_q})_{MX_q-JX}$$

The latter is applicable only when the multicomponent and the binary solutions have the same MX_q content, and same temperature.

The theoretical expressions have been found to predict quite well available data on ternary and quarternary systems.

New composition parameters for expressing the compositions in quarternary and quinary systems have been established.

INTRODUCTION

The thermodynamic properties of binary fused salt solutions have been the object of several systematic investigations and extensive compilations of thermodynamic data are available.

However, similar information for ternary solutions is very limited and for quarternary systems there is hardly any information at all. Yet systems of industrial and of metallurgical importance are usually multicomponent, and the application of thermodynamics to the calculation of equilibria and to the efficiency of chemical reactions is usually restricted by the lack of the appropriate experimental data.

Regarding binary systems, an activity isotherm is usually obtained from about five experimental measurements. In a ternary system, the Gibbs isothermal surface may be covered with about 25 separate experiments on activities, and, for a quarternary system a minimum of about 200 experiments are needed in order to cover adequately the entire composition range. It is evident that the large number of experiments required have discouraged researchers from undertaking the systematic investigation of multicomponent systems.

Because of the shortage of experimental data, there is considerable theoretical and practical interest in the establishment of expressions from which the thermodynamic properties of ternary and quarternary molten salt systems may be predicted from available data on the corresponding binary solutions.

For ternary metallic solutions several such equations have been proposed. These include the analytical expressions by Kohler,(2) Bonnier and Caboz,(3) and by Muggianu et al.,(4) and those derived by Alcock and Richardson,(5) and by Toop.(6)

The relative merits of each of these expressions have been compared by Spencer et al.(7) and by Ansara(8) and by Hillert.(9)

In general, these expressions include terms representing the thermodynamic properties of the three binary component systems and differ mainly in the kind of composition parameters used and in the composition path to be followed within the ternary isothermal composition surface.

Saboungi and Blander(10) have extended the Conformal Ionic Solution theory to additive ternary molten salt solutions. However, the derived expressions were rather complex, and, even for mixtures of monovalent salts, they required fourth order terms. Their applicability to a large number of ternary charge asymmetric systems has not been demonstrated.

The thermodynamic properties of charge asymmetric molten salt solutions are of considerable theoretical and practical interest, as they are characterized by very low activity values and by highly exothermic enthalpies of mixing. This behaviour is usually interpreted as indicating strong interactions between the ionic specie in solution, and to the formation of complex species. To interpret such systems Pelton and Thompson(11) have proposed a Discrete Complex Anion Model which has been applied to systems such as binary $MgCl_2$-containing systems and to the system $MgCl_2NaCl$-$CaCl_2$. (12)

In previous publications from this laboratory(13-17) a "hybrid" regular solution model representing the combination of a reaction mechanism followed by the regular mixing of the products of reaction, has been applied to the derivation of equations which allow the calculation of the thermodynamic properties of ternary and quarternary charge asymmetric fused salt solutions from the properties of the component binary systems. However, this model was based on the assumption that all complex forming reactions proceeded to completion and the thermodynamic requirement of equilibrium between specie in solution was not considered.

In the present publication, equations relating thermodynamic properties of multicomponent, common anion charge asymmetric fused salt solutions to the properties of the component binary system, are derived in a rigorous manner. To this and a modified form of the F.F.G. thermodynamic cycle(1) which is ideally suited to mixed equilibria, has been developed. The theoretical treatment makes use of well established thermodynamic relationships and should not be described as a "model".

For the treatment it is necessary to consider solutions that contain at least one charge asymmetric component, MX_q, as in the system, MX_q - AX - BX - ••• JX in which the components AX and BX etc. are acting as ligand donors for reactions like,

$$MX_q \;+\; rAX \;\rightarrow\; A_rMX_{q+r} \tag{1}$$

An exact knowledge of the type or the stoichiometry of the complex specie formed is not required for the derivation of the thermodynamic relationships.

Thermodynamic Treatment of Multicomponent Molten Salt Solutions

For the thermodynamic treatment of a j + 1 component, common anion and charge asymmetric molten salt system, like the solution of MX_q-AX-BX ••• jX, will be considered.

The derivation is based on a modified form of a thermodynamic cycle for successive reactions first proposed by Flood, Förland and Grojtheim(1). The steps considered are given in Table 1.

The cycle consists of chemical reactions a, b ••• j and of two mixing reactions 1 and 2. Standard states are chosen as the pure molten salts at all temperatures. Mole numbers are taken as,

$$n_2 \;+\; n_3 \;+\; \cdots \;+\; n_j \;=\; 1$$

and the summation,

TABLE I

EQUILIBRIA IN MIXED SYSTEMS

CHEMICAL REACTIONS	GIBBS FREE ENERGY
a− $n_2MX_{q(l)} + n_2rAX_{(l)} = n_2A_rMX_{q+r(l)}$	$n_2\Delta G_1^\circ$
b− $n_3MX_{q(l)} + n_3rBX_{(l)} = n_3B_rMX_{q+r(l)}$	$n_3\Delta G_2^\circ$
$\vdots$	$\vdots$
j− $n_jMX_{q(l)} + n_jrJX_{(l)} = n_jJ_rMX_{q+r(l)}$	$n_j\Delta G_j^\circ$

MIXING REACTIONS

1− $n_2rAX_{(l)} + n_3rBX_{(l)} + \cdots\cdots n_jrJX_{(l)} = r\left[(AX)_{n_2}\cdot(BX)_{n_3}\cdots(JX)_{n_j}\right]_{solution}$ $\quad r\Delta G_M(1$

2− $n_2A_rMX_{q+r(l)} + n_3B_rMX_{q+r(l)} + \cdots\cdots n_jJ_rMX_{q+r(l)} =$

$=\left[(A_rMX_{q+r})_{n_2}\cdot(B_rMX_{q+r})_{n_3}\cdots\cdots(J_rMX_{q+r})_{n_j}\right]_{solution}$ $\quad \Delta G_M\,(2)$

Where : $n_2 + n_3 + \cdots\cdots n_j = 1$

From Equations : $a + b + \cdots\cdots n_j - 1 + 2$,

$$\boxed{\begin{array}{l} MX_{q(l)} + r\left[(AX)_{n_2}\cdot(BX)_{n_3}\cdots\cdots(JX)_{n_j}\right]_{solution} = \\ = \left[(A_rMX_{q+r})_{n_2}\cdot(B_rMX_{q+r})_{n_3}\cdots\cdots(J_rMX_{q+r})_{n_j}\right]_{solution} \\ \text{(Standard State Reaction)} \end{array}} \qquad (3)$$

$$\Delta G^\circ_{R,M} = n_2\Delta G^\circ_a + n_b\Delta G^\circ_2 + \cdots\cdots n_j\Delta G^\circ_j - r\Delta G_{M(1)} + \Delta G_{M(2)}$$
$$= RT\ln K_M \qquad (4)$$

$$\boxed{K_M = \frac{a^{n_2}_{A_rMX_{q+r}}\cdot a^{n_3}_{B_rMX_{q+r}}\cdots\cdots a^{n_j}_{J_rMX_{q+r}}}{a^{n_2r}_{AX}\cdot a^{n_3r}_{BX}\cdots\cdots a^{n_jr}_{JX}\cdot a_{MX_q}}} \qquad (5)$$

Standard States

For, MX_q, The Standard State is The Pure Molten MX_q

For, $A_rMX_{q+r}, B_rMX_{q+r}, \cdots\cdots J_rMX_{q+r}$, The Standard State is The Solution $\left[(A_rMX_{q+r})_{n_2}\cdot(B_rMX_{q+r})_{n_3}\cdots\cdots(J_rMX_{q+r})_{n_j}\right]$

For, $AX, BX, \cdots\cdots JX$, The Standard State is The Solution $\left[(AX)_{n_2}, (BX)_{n_3}, \cdots\cdots(JX)_{n_j}\right]$

From : $\overline{\Delta G}_i = RT \ln a_i$ (5a)

$$\boxed{\begin{array}{c}\overline{\Delta G}_{MX_q} = \Delta G^{\circ}_{R(M)} + \sum_{n_2}^{n_j} n_j \overline{\Delta G}_{J_r MX_{q+r}} - \sum_{n_2}^{n_j} n_j \overline{\Delta G}_{JX} \\ (J = A, B \cdots\cdots J \text{ and } j = a, b, \cdots\cdots j)\end{array}} \qquad (6)$$

For The Mixed System At A Given Composition (Solutions As Standard States)	In Mixed System With Respect To Pure Molten JX Or $J_r MX_{q+r}$ As Standard States	In Solutions Having Compositions, * a) $(AX)_{n_2} \cdot (BX)_{n_3} \cdots (JX)_{n_j}$ And b) $(A_r MX_{q+r})_{n_2} \cdot (B_r MX_{q+r})_{n_3} \cdots\cdots (J_r MX_{q+r})_{n_j}$

$$\overline{\Delta G}_{JX} = \overline{\Delta G}''_{JX} - \overline{\Delta G}'_{AX} \quad (\text{in a}) \qquad (7)$$

$$\overline{\Delta G}_{J_r MX_{q+r}} = \overline{\Delta G}''_{J_r MX_{q+r}} - \overline{\Delta G}'_{J_r MX_{q+r}} \quad (\text{in b}) \qquad (8)$$

* Pure Molten JX And $J_r MX_{q+r}$ As Standard States

From : 3, 4, 6, 7, 8

(In $n_j + 1$ Component System)

$$\begin{aligned}\overline{\Delta G}_{MX_q} = {} & n_2 \left[\Delta G^{\circ}_{R(a)} - r\overline{\Delta G}''_{AX} + \overline{\Delta G}''_{A_r MX_{q+r}}\right] + \\ & + n_3 \left[\Delta G^{\circ}_{R(b)} - r\overline{\Delta G}''_{BX} + \overline{\Delta G}''_{B_r MX_{q+r}}\right] + \cdots\cdots \\ & + n_j \left[\Delta G^{\circ}_{R(j)} - r\overline{\Delta G}''_{JX} + \overline{\Delta G}''_{J_r MX_{q+r}}\right]\end{aligned} \qquad (9)$$

For Binary Solutions Having The Same X_{MX_q}, from eq. 9

(In $n_j + 1$ Component System)

$$\overline{\Delta G}_{MX_{q(y)}} = n_2 \left(\overline{\Delta G}''_{MX_q}\right)_{MX_q - AX(y)} + n_3 \left(\overline{\Delta G}''_{MX_q}\right)_{MX_q - BX(y)} + \cdots\cdots n_j \left(\overline{\Delta G}''_{MX_q}\right)_{MX_q - JX(y)} \qquad (10)$$

Also:

$$n_j = \frac{n_j / \Sigma n}{n_2 + n_3 + \cdots\cdots n_j / \Sigma n} = \frac{X_j}{X_2 + X_3 + \cdots\cdots X_j} \qquad (11)$$

where X's are mole fractions

(In $n_j + 1$ Component System)

$$\boxed{\begin{aligned}\overline{\Delta G}_{MX_{q(y)}} = {} & \frac{X_2}{X_2 + X_3 + \cdots\cdots X_j} \left(\overline{\Delta G}''_{MX_q}\right)_{MX_q - AX(y)} + \frac{X_3}{X_2 + X_3 + \cdots\cdots X_j} \left(\overline{\Delta G}''_{MX_q}\right)_{MX_q - BX(y)} + \cdots\cdots \\ & \frac{X_j}{X_2 + X_3 + \cdots\cdots X_j} \left(\overline{\Delta G}''_{MX_q}\right)_{MX_q - JX(y)}\end{aligned}} \qquad (12)$$

$MX_q - JX$ are <u>binary</u> systems

$$n_2 MX_q \; + \; n_3 MX_q \; + \; \cdots \; + \; n_j MX_q$$

represent 1 g.mole of pure molten MX_q. Through addition of reactions in the sequence a + b + ••• + j - 1 + 2, the overall reaction of MX_q with a mixed melt is obtained as reaction 3. Reaction 3 may be taken as "standard" if the two solutions

$$[(AX)_{n_2} \cdot (BX)_{n_3} \cdots (JX)_{n_j}], \quad \text{and} \quad \left[(A_r MX_{q+r})_{n_2} \cdot (B_r MX_{q+r})_{n_3} \cdots (J_r MX_{q+r})_{n_j}\right],$$

are chosen as the "standard states" for the mixed system containing all species at their equilibrium compositions.

In Table 1 the "Standard free energy" for reaction 3 is given by equation 4 and it defines the mixed equilibrium constant K_m, as in equation 5. The "standard state" for MX_q is still the state of pure molten MX_q at all temperatures. For the other compounds JX and $J_r MX_{q+r}$ etc, their standard states, respectively, are the above mentioned "mixed" solutions (Appendix 1).

From the well known relationships, 4 and 5a in Table 1, equation 5 may be written in terms of the partial molar free energies of mixing, $\overline{\Delta G_i}$, and is given as equation 6. The latter may be simplified through conversion of the standard states using equations 7 and 8, which are derived in Appendix 1.

From equations, 3,4,6,7,8 and appendix 1, equation 9 is readily derived. In the latter the quantities $\overline{\Delta G''_{JX}}$ and $\overline{\Delta G''_{J_r MX_{q+r}}}$ represent partial molar Gibbs free energies of mixing; expressed with respect to pure molten JX and pure molten $J_r MX_{q+r}$ as standard states, respectively, where J stands for A, B ••• J.

Considering reactions a, b, c ••• j in Table 1, the equilibrium constant for a j-type reaction may be written in terms of activities as,

$$k_j \;=\; \frac{a_{J_r MX_{q+r}}}{a_{MX_q} \cdot a_{JX}^{n_j}} \qquad (j-1)$$

Following the same general method, as for the derivation of equation 9 in Table 1, it is readily shown that for a binary system,

$$\underset{(MX_q - JX)}{\overline{\Delta G}_{MX_q}} \;=\; \Delta G_j^o - r\overline{\Delta G''_{JX}} + \overline{\Delta G''_{JrMX_{q+r}}} \qquad (j-2)$$

In this equation $\overline{\Delta G''_{JX}}$ and $\overline{\Delta G''_{JrMX_{q+r}}}$ refer to the binary solution $JX - MX_q$ at equilibrium. Standard states of reference are the pure molten salts.

From Table 1 equations similar to j-2 may be derived for all the other complex forming reactions in binary solutions and are designated, respectively, as a-2, b-2, etc.

Considering solutions representing the same mole fraction for MX_q, it will be assumed that the partial molar Gibbs free energies of mixing for pairs like AX - A_rMX_{q+r}, BX - B_rMX_{q+r}, --- J_rMX_{q+r}, in the multicomponent system, have approximately the same values as in the corresponding binary solutions.

The combination of equation 9 with equations like a-2, b-2 ••• J-2, yields equation 10. Also, by introducing equation 11, the final expression 12 relating Gibbs free energies of mixing of multicomponent to binary systems is obtained.

This expression allows the calculation of the activities of MX_q in a multicomponent system, from their values in the component binary systems, when the mole fraction of MX_q is the same throughout.

From the well known van't Hoff expression

$$\left[\frac{d(\overline{\Delta G_i})}{d\left(\frac{1}{T}\right)}\right]_{P,X_i} = \left[\frac{\overline{\Delta H_i}}{R}\right]_{\text{at same } X_i} \qquad (13)$$

it is readily seen that partial molar enthalpies of mixing are also expressed by equations similar to eq. 12 in Table 1.

In general it may be shown that any molar or partial molar solution property for MX_q in a multicomponent system, may be written as:

$$\Delta Z_{\underset{(1,2\cdots J+1)}{MX_q}} = \frac{X_2}{1-X_1}(\Delta Z_{MX_q})_{1,2} + \frac{X_3}{1-X_1}(\Delta Z_{MX_q})_{1,3} + \cdots \frac{X_j}{1-X_1}(\Delta Z_{MX_q})_{1,j} \qquad (14)$$

where X_{MX_q} and temperature are the same for the multicomponent as for the binary mixtures.

The assumptions that the Gibbs partial molar free energies of mixing for components like JX and J_rMX_{q+r}, are "frozen" at their levels in the binary solutions for compositions representing the same MX_q content, have important structural and theoretical implications. They can only be valid if the cations A^T, B^T -- and J^+ are randomly distributed when short range interactions of the next neighbour type, like in a sequence $A^+ X^- M^{q+}$, are significant.

Ternary Charge Asymmetric Fused Salt Solutions

The composition of a ternary system is usually represented by points within a Gibbs equilateral triangle. Pure components are situated at the corners, as shown in Fig. 1.

Any composition point P is found by drawing through P lines parallel to each of the three sides. The complement of the distance from each corner to the respective line through P gives the amount of the particular component. If the composition variable is the mole fraction, then the values thus calculated must satisfy the relationship

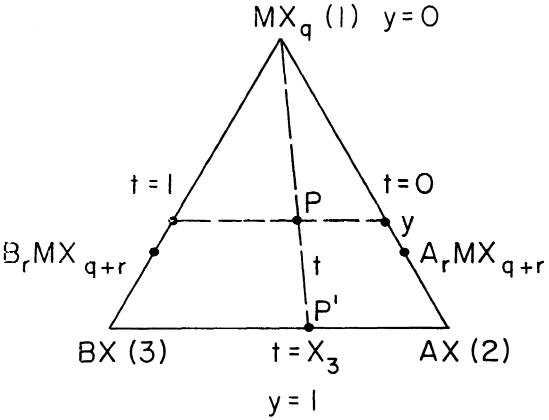

Figure 1. Composition paths in a ternary system $t = \frac{X_3}{X_2+X}$ and $y = 1 - X$.

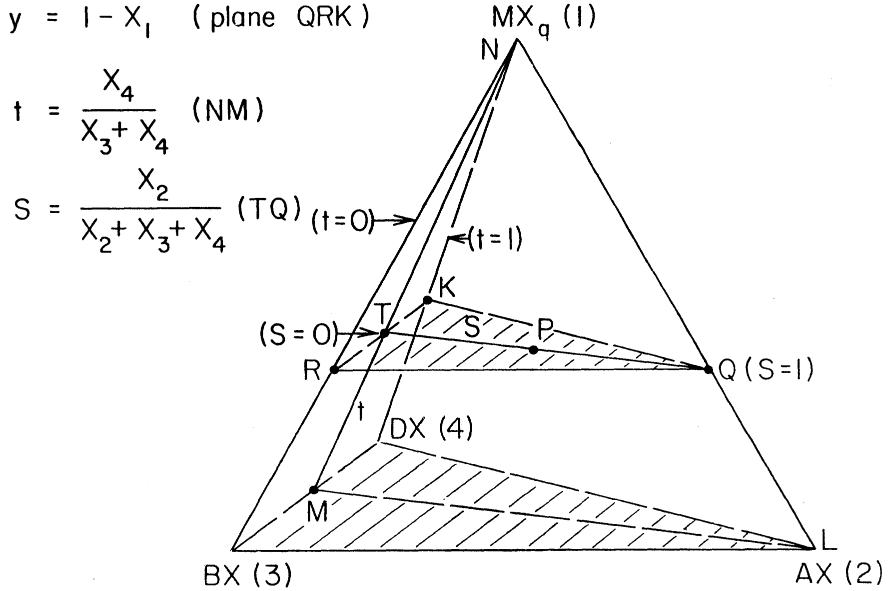

Figure 2. Isothermal composition diagram in a quarternary system represented by an equilateral tetrahedron. t, y, S are composition parameters. Equilateral triangle QRK represents a section of the quarternary having the same MCl_q content.

$$X_1 + X_2 + X_3 = 1 \qquad (15)$$

where 1, 2 and 3 are components MX_q, AX and BX respectively.

A tie-line from 1 to the 2, 3 binary represents compositions for which,

$$t' = \frac{X_3}{X_2} = \text{constant} \qquad (16)$$

but since t' goes to infinity as X_2 goes to zero, it is more convenient to define

$$t = \frac{X_3}{X_2 + X_3} \qquad (17)$$

which varies from 0 and 1.

At constant X_i, the parameter y is defined as $y = I - X_1$. In the binary 1-2, $t = 0$, and in the binary 1-3, $t = 1$. For pure component 1, $y = 0$, and for all values of t in the 2-3 binary $y = 1$.

It is also readily calculated that

$$X_1 = 1 - y \qquad (19)$$

$$X_2 = y(1-t) \qquad (20)$$

$$X_3 = ty \qquad (21)$$

from equation 12 in Table 1, and equations 19, 20, 21, the corresponding expressions for the activities and for the other molar and partial molar properties in ternary solutions are derived, respectively, as,

$$a_{MX_{q(1,2,3)_y}} = a^{(1-t)}_{MX_{q(1,2)_y}} \cdot a^{t}_{MX_{q(1,3)_y}} \qquad (22)$$

and as,

$$\Delta Z_{MX_{q(1,2,3)_y}} = (1-t)\Delta Z_{MX_{q(1,2)_y}} + t\Delta Z_{MX_{q(1,3)_y}} \qquad (23)$$

where, 1,2 and 1,3 refer to the binary systems, AX-MX_q and BX-MX_q, respectively. ΔZ could represent, molar volumes, enthalpies or Gibbs free energies of mixing.

Quarternary Charge Asymmetric Fused Salt Solutions

Compositions in a quarternary system are represented(18) by points within the volume of an equilateral tetrahedron, as shown in Fig. 2. The four vertices correspond to the pure components MX_q, AX, BX and DX, and the edges represent the six binary systems MX_q-AX, MX_q-BX, MX_q-DX, AX-BX, BX-DX and DX-AX.

The triangular faces represent the four ternary systems MX_q-AX-BX, MX_q-AX-DX, MX_q-BX-DX and AX-BX-DX.

It is a property of all equilateral tetrahedra that lines originating from any internal point P, drawn parallel to the four different faces, have a total length equal to one edge, and each of these segments may be taken to define the mole fraction of a particular component occupying an apex.

In view of the complexity of such three-dimensional plots, useful composition paths have been defined mathematically, and the composition parameters, y, t, and S have been defined in terms of mole fractions by the following expressions:(17)

$$y = 1 - X_1 \tag{24}$$

where $1.0 > y > 0$

$$t = \frac{X_4}{X_3 + X_4} \tag{25}$$

where $1.0 > t > 0$, $t = 1$ along the MX_q-DX binary, and $t = 0$ along the MX_q-BX binary.

$$S = \frac{X_2}{X_2 + X_3 + X_4} \tag{26}$$

where, $0 > S > 1$, $S = 1$ along the MX_q-AX binary and $S = 0$ for all compositions in the ternary MX_q-BX-DX.

Considering Fig. 2, in which MX_q is placed at the apex of the tetrahedron, constant "t" represents the pseudo-quarternary composition surface LMN. All compositions along that surface have in common the constant ratio of $X_4/X_3 + X_4$.

Also, constant "y" represents compositions along a pseudoternary surface parallel to the base of the equilateral tetrahedron having a constant X_{MX_q} content.

The intersection of the planes, t and y, defines the line "S".

The relationship between primary mole fractions and the composition parameters y, t, and S, is readily found as,

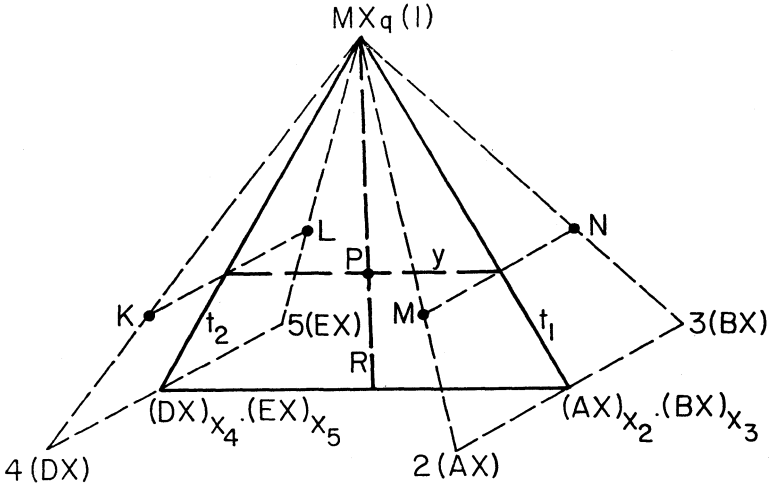

$$y = 1 - X_1 \qquad t_1 = \frac{X_2}{X_2+X_3} \qquad R = \frac{X_4+X_5}{X_2+X_3+X_4+X_5}$$

$$t_2 = \frac{X_5}{X_4+X_5}$$

$$X_1 + X_2 + X_3 + X_4 + X_5 = 1$$

Figure 3. Representation of compositions in a quinary system. y, t_1, t_2, R are composition parameters.

$$X_1 = X_{MX_q} = 1-y \tag{27}$$

$$X_3 = y(1-t)(1-S) \tag{28}$$

$$X_2 = ys \tag{29}$$

$$X_4 = ty(1-S) \tag{30}$$

Considering the S path QT, within the quarternary tetrahedron shown in Fig. 2, all compositions along QT have the same X_{MX_q} content and the same ratio of DX to BX. However, as S changes from 0 (point T) to 1 (point Q), the amount of AX in the quarternary changes in proportion to S (eq. 26) and the value of any thermodynamic property measured along the S-composition path should reflect the reactivity of AX towards MX_q. In this melt, the ratio of DX/BX remains constant, but the absolute amounts of these two components decrease as they are replaced by AX.

It follows that the y, S, and t parameters, proposed in this paper, define quarternary composition paths along which it is possible to follow the relative contributions of the various salt components to the magnitude of the thermodynamic properties of the solutions.

When expressions 27-30 are applied to the general expressions 12 and 16, the corresponding equations for a quarternary system are derived as,

$$a_{MX_{q(1,2,3,4)_y}} = a^{S}_{MX_{q(1,2)_y}} \cdot a^{(1-S)(1-t)}_{MX_{q(1,3)_y}} \cdot a^{t(1-S)}_{MX_{q(1,4)_y}} \tag{31}$$

and

$$\Delta Z_{MX_{q(1,2,3,4)_y}} = S\Delta Z_{MX_{q(1,2)_y}} + (1-S)\left[t\Delta Z_{MX_{q(1,4)_y}} + (1-t)\Delta Z_{MX_{q(1,3)_y}}\right] \tag{32}$$

Extension of the Theory to Quinary Molten Salt Solutions

For a five component system there is no simple geometric method for the graphic representation of the composition. In general, a j+1 component system requires plots in J dimensions(18,19).

For the purpose of this treatment the composition of a five component system is represented on the surface of a Gibbs equilateral triangle in which the apex is occupied by the reactive molten MCl_q component and the other two vertices are occupied by solutions having fixed ratios of ligand donors,[5] as in Figure 3.

For the system MX_q-AX-BX-DX-EX having the mole fraction composition defined by x_1, x_2, x_3, x_4, and x_5, respectively, the composition parameters are defined as,

$$y = 1-x_1 \qquad (33)$$

$$t_1 = \frac{x_3}{x_2+x_3} \qquad (34)$$

$$t_2 = \frac{x_5}{x_4+x_5} \qquad (35)$$

$$R = \frac{x_2+x_3}{x_2+x_3+x_4+x_5} \qquad (36)$$

The relationship between conventional mole fractions and the above composition parameters are readily derived as,

$$x_1 = 1-y \qquad (37)$$

$$x_2 = yR(1-t_1) \qquad (38)$$

$$x_3 = yRt_1 \qquad (39)$$

$$x_4 = (1-t_2)(1-R)y \qquad (40)$$

$$x_5 = t_2(1-R)y \qquad (41)$$

Through introduction of equations 37-41, into equations 12 and 16, the quinary system expressions are derived as,

$$a_{MX_{q\,(\text{In quinary})_y}} = a_{MX_{q(1,2)_y}}^{t_1(1-R)} \cdot a_{MX_{q(1,3)_y}}^{(1-t_1)\cdot(1-R)} \cdot a_{MX_{q(1,4)_y}}^{R(1-t_2)} \cdot a_{MX_{q(1,5)_y}}^{Rt_2} \qquad (42)$$

Similarly,

$$\Delta Z_{MX_{q(\text{quinary})_y}} = (1-R)\left[t_2\Delta Z_{MX_{q(1,5)_y}} + (1-t_2)\Delta Z_{MX_{q(1,4)_y}}\right] + R\left[t_1\Delta Z_{MX_{q(1,3)_y}} + (1-t_1)\Delta Z_{MX_{q(1,2)_y}}\right] \qquad (43)$$

Limiting values for the y, t_1, t_2 and R terms are,

$y = 1$ for pure MX_q

$y = 0$, in the quarternary AX-BX-DX-EX.

$t_1 = 1$, in pure AX	$R = 0$, in AX-BX binary, and
$t_1 = 0$, in pure BX	$R = 1$, in DX-EX binary.
$t_2 = 1$, in pure EX	
$t_2 = 0$, in pure DX	

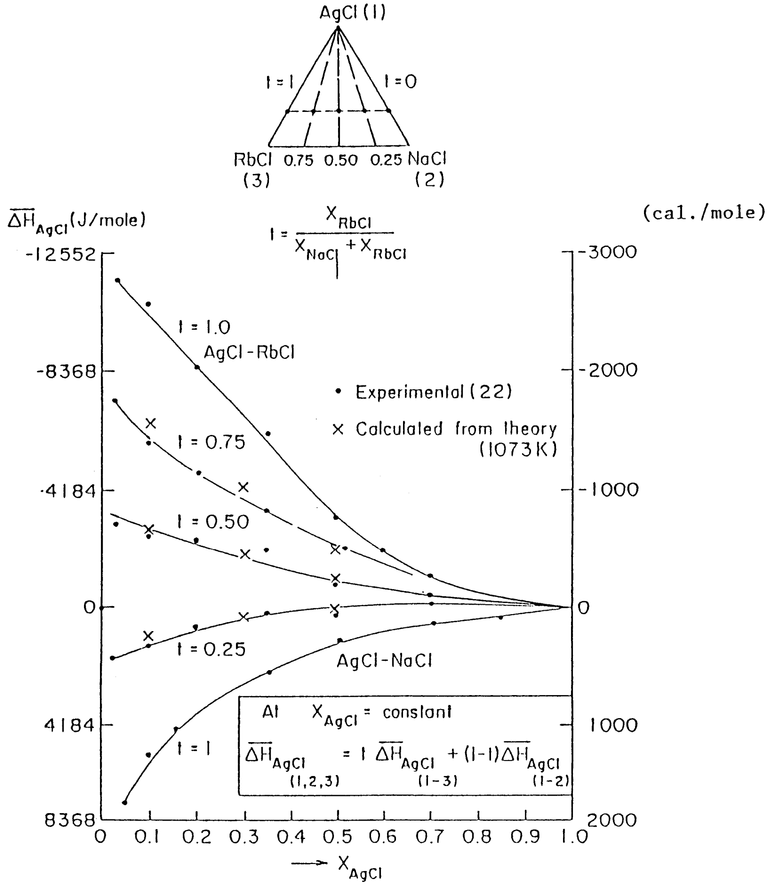

Figure 4. Comparison between calorimetric and electrochemical data in the system NaCl-RbCl-AgCl.

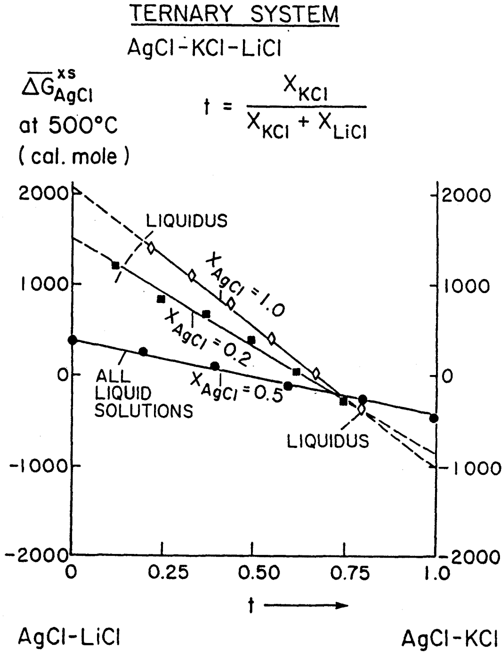

Figure 5. Plots of $\overline{\Delta G}^{XS}_{AgCl}$ versus t for the ternary system AgCl-KCl-LiCl.(26) Points are experimental. Straight lines have been calculated from equation 23.

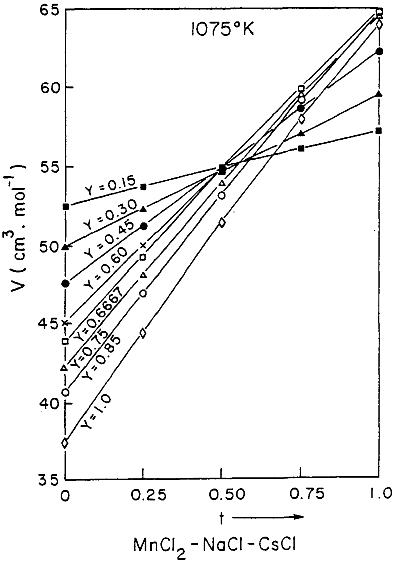

Figure 6. Plots of the molar volumes V versus t for various y values in the ternary system $MnCl_2$-NaCl-CsCl[(23)] calculated from equation 23.

Figure 7. Plots of the molar volumes versus t for various ẏ values in the ternary system $PbCl_2$-LiCl-KCl.[(27)] Points are experimental. Straight lines have been calculated from equation 23.

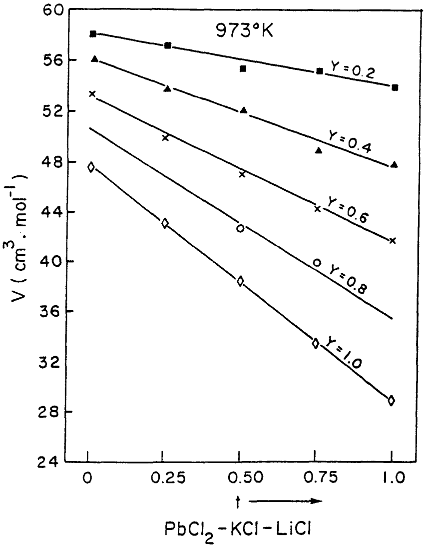

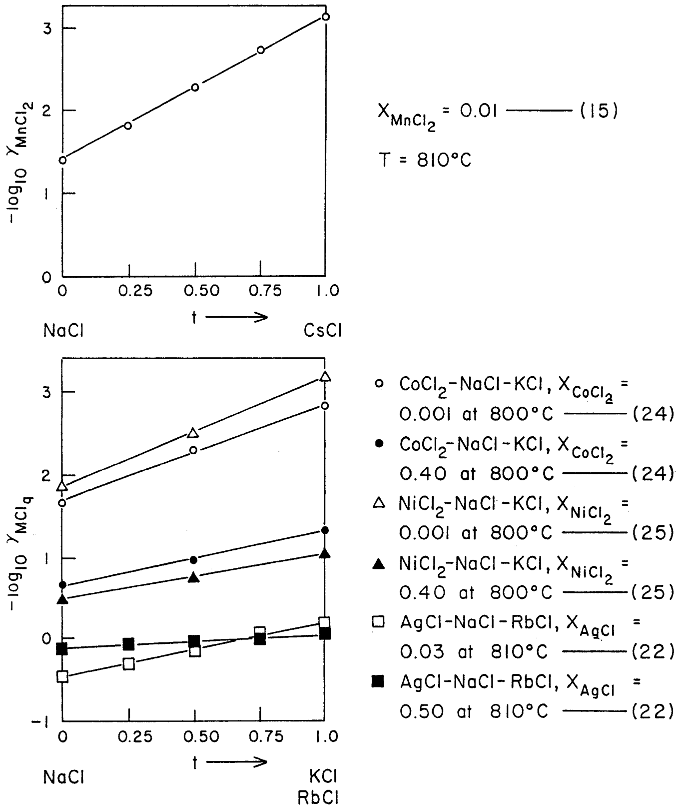

Figure 8. log γ_{MCl_q} plotted as function of t, for various systems. Points are experimental while straight lines have been calculated from equation 22 expressed in terms of activity coefficients.

Equation 43 implies that the partial molar free energies of mixing for the reactive M_q component are linear functions of R, when y has a common value for the binary and the quinary solutions and t_1 and t_2, are fixed to represent given ratios.

Agreement with Experimental Evidence

There is overwhelming evidence for the validity of the expressions 22-23, for "reactive" or charge asymmetric ternary systems, for which there is reliable information on the corresponding binaries.

Table 2, lists some of the ternary systems for which agreement between theory and experimental values is excellent.

For example, the binary systems AgCl-NaCl and AgCl-CsCl have been investigated by the emf method(31) and by calorimetry.(32,33) Enthalpy of mixing information on the binary NaCl-CsCl is also available(34) and the electrochemical and the calorimetric data are in very good agreement. The ternary system AgCl-NaCl-CsCl has been investigated by the emf method(21) and the comparison between experimental and calculated excess free energies of mixing is excellent.

The binary systems AgCl-NaCl and AgCl-RbCl have been investigated in this laboratory(31) and by Kleppa and associates(32,33) calorimetrically.

These data indicate that the NaCl-AgCl system exhibits exothermic enthalpies of mixing, while the RbCl-AgCl system mixes endothermically and should be described as a "reactive system". The ternary system AgCl-NaCl-RbCl has also been investigated by the emf method in this laboratory(22) and, as shown in Fig. 4, there is excellent agreement between experimental and calculated molar enthalpies of mixing, over the entire composition range.

Plots of $\overline{\Delta G}^{xs}_{AgCl}$ versus t, for the system AgCl-KCl-LiCl investigated by Gruner and Thompson(26) shown in Fig. 5, are also linear, indicating the compliance of this system with equation 22.

The $MnCl_2$-alkali chloride systems are of interest as they demonstrate negative deviations from ideality, which increase dramatically from the $MnCl_2$-NaCl to the $MnCl_2$-CsCl binary.

For these systems the agreement between the calorimetric(34) and the electrochemical(35) enthalpies of mixing is very good. For the ternary $MnCl_2$-NaCl-CsCl(23) molar volumes calculated from the corresponding expression

$$V_{\substack{\text{ternary}\\1,2,3}} = (1-t)V_{(1,2)_y} + tV_{(1,3)_y} \qquad (44)$$

are shown in Fig. 6, and indicate excellent agreement with the experimental data.

Molar volumes for the system $PbCl_2$-LiCl-KCl, measured by Gutierrez and Toguri(27) and shown in Fig. 7 are in excellent agreement with calculated values from binary data using equation 23.

Figure 8 demonstrates the validity of equation 22 to a number of ternary systems.

Agreement between experimental and calculated partial molar free energies of mixing is also found for the systems $MgCl_2$-NaCl-KCl and $PbCl_2$-LiCl-KCl, as shown in Fig. 19.

The recently reported NaCl-$CaCl_2$-$MnCl_2$ system is of interest as it represents a ternary containing two ligand acceptors, e.g. $CaCl_2$ and $MgCl_2$, and NaCl as the single ligand donor.

If $t = \frac{x_{MgCl_2}}{x_{CaCl_2}+x_{MgCl_2}}$ and NaCl is placed at the apex of the Gibbs triangle, the calculated and experimental enthalpies of mixing shown in Table 3 are in good agreement with theory, considering that the ternary Gibbs-Duhem had been used for the calculation of the activities for the three components.(12)

Similar agreement between experimental data and theory is demonstrated by all the systems given in Table 2.

Regarding quarternary systems, the only system which has been systematically investigated by the emf method is the system $MnCl_2$-NaCl-KCl-CsCl.(17)

From available data on binary systems(35), the theoretical plot of $\overline{\Delta G}_{MnCl_2}$ as a function of S, for a number of t values which cover entire y-planes within the quarternary, has been calculated from equation 31.

Figures 10a, 10b, 10c, and 10d show the actual comparison between experimental(17) and calculated values of $\overline{\Delta G}_{MnCl_2}$ for four different y compositions.

It is seen that all compositions along a constant y-plane, which are obtained when t is changed from 0 to 1, are represented by a family of curves which are terminated in the three component binary systems, as shown on the graph.

Equations 31 and 32 are applicable only if the ligand acceptor component $MnCl_2$ is placed at the apex of the tetrahedron, while the three ligand donors, namely the NaCl, KCl and CsCl, are located at the three remaining vertices.

In a recent publication(38) from this laboratory "formal" formation potentials in the dilute solutions of the binary systems $CaCl_2$-ACl, $NiCl_2$-ACl, $FeCl_2$-ACl, $FeCl_3$-ACl, $CrCl_2$-ACl, $CrCl_3$-ACl, CaCl-ACl, $CaCl_2$-ACl and $ThCl_4$-ACl where, A, was respectively

TABLE 2

List of ternary and quarternary fused salt solutions which are in agreement with the present thermodynamic treatment of the "Reactive Systems Approximation"

Ternary System	Method/Property	Temp. (°C)	Authors
AgCl-NaCl-KCl	EMF/γ_{AgCl}	650-850	Flengas and Ingraham(20)
AgCl-NaCl-KCl	EMF/$\overline{\Delta G}_{AgCl}$	650-850	Guion, Blander, Hugstenberg and Hagemark(21)
AgCl-NaCl-CsCl	EMF/$\overline{\Delta G}_{ACl}$	700-850	Guion, Blander and Hagemark(21)
AgCl-NaCl-RbCl	EMF/γ_{AgCl} $\overline{\Delta H}_{AgCl}$	500-900	Pelton and Flengas(22)
$MnCl_2$-NaCl-CsCl	EMF/activities	700-900	Sadoway and Flengas(15)
$MnCl_2$-NaCl-CsCl	Molar Volumes (V_m) (Density)	550-1050	Carmichael and Flengas(23)
$MnCl_2$-NaCl-CsCl	Electrical Conductivities	510-1054	Carmichael and Flengas(23)
$NiCl_2$-NaCl-KCl $\left(\frac{1}{1}\right)$	EMF/γ_{NiCl_2}	700-900	Hamby and Scott(24)
$CoCl_2$-NaCl-KCl $\left(\frac{1}{1}\right)$	EMF/γ_{CoCl_2}	650-900	Hamby and Scott(25)
AgCl-KCl-LiCl	EMF/$\overline{\Delta G}^{XS}_{AgCl}$	500	Gruner and Thompson(26)
NaCl-$CaCl_2$-$MgCl_2$	EMF/ΔH_M	700-850	Karakaya and Thompson(12)
$PbCl_2$-LiCl-KCl	Molar Volumes (V_M) (Density)	700	Gutierrez and Toguri(27)
$PbCl_2$-LiCl-KCl $\left(\frac{1}{1}\right)$	EMF/$\overline{\Delta G}_{PbCl_2}$	750	Takahashi(28)
$MgCl_2$-NaCl-KCl $\left(\frac{1}{1}\right)$	EMF/$\overline{\Delta G}_{MgCl_2}$	800	Neil, Clark and Wiswall(29)
$AlCl_3$-NaCl-CsCl	EMF/$\gamma^{H}_{AlCl_3}$	850	Tumidajski and Flengas(30)

$AlCl_3$-KCl-CsCl	EMF/$\gamma^{H}_{AlCl_3}$	850	Tumidajski and Flengas(30)
Quarternary System			
$MnCl_2$-NaCl-KCl-CsCl	EMF/$E-E^{\circ}$	650-850	Flengas and Pickles(17)

TABLE 3

Integral Enthalpies of Mixing in the System NaCl-$MgCl_2$-$CaCl_2$(26)

for, $t = \frac{X_{CaCl_2}}{X_{CaCl_2}+X_{MgCl_2}}$ and $y = 1-X_{NaCl}$

		ΔH_M (J/mole)	
y	t	Experimental*	Theoretical**
0.40	0.50	-5,820	-5,820
0.60	0.67	-4.064	-4,574
0.62	0.20	-5,864	-6,032
0.75	0.33	-3,448	(-4,034)
0.77	0.10	-4,397	-4,290
0.80	0.75	-1,700	(-2,515)
0.85	0.18	-2.509	-2,748

* From ternary Gibbs-Duhem integration.(12) Only the a_{MgCl_2} in the ternary was measured electrochemically.

** From calorimetric data on the binary systems NaCl-$MgCl_2$ and NaCl-$CaCl_2$.

$$\Delta H_{M(1,2,3)} = (1-t)\ \underset{(NaCl-MgCl_2)}{\Delta H_M} + t\ \underset{(NaCl-CaCl_2)}{\Delta H_M} \qquad (32-a)$$

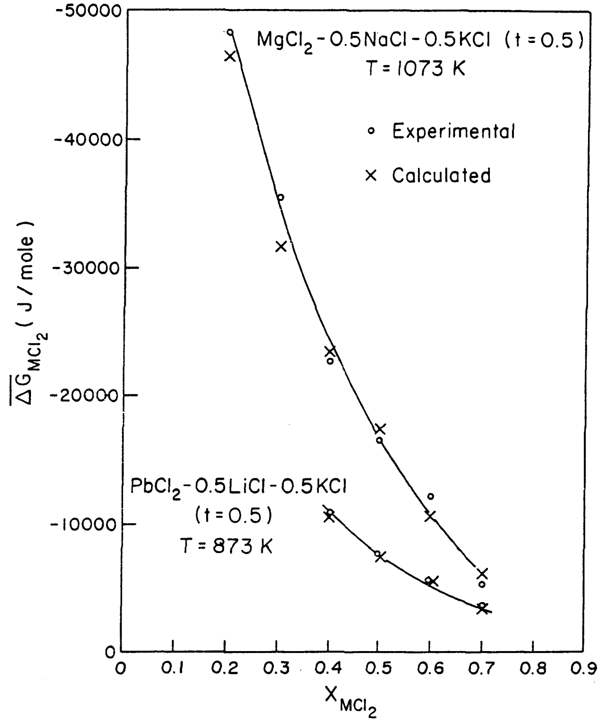

Figure 9. Plots of $\overline{\Delta G}_{MCl_2}$ versus X_{MCl_2} for t = 0.5, for the systems $PbCl_2$-LiCl-KCl(28) and $MgCl_2$-NaCl-KCl.(29)

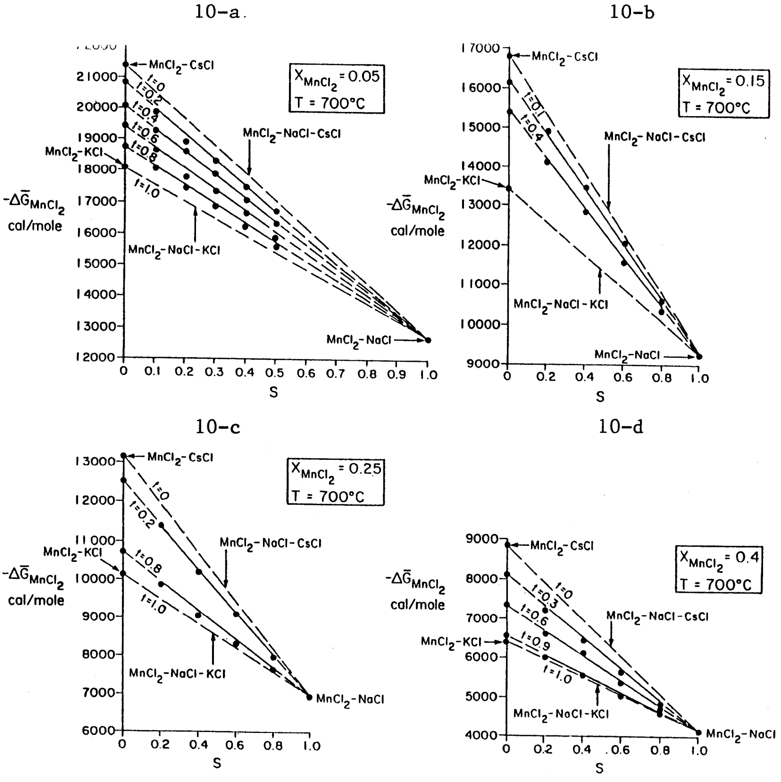

Figures 10a to 10d Excess partial molar free energies of mixing for the quarternary system $MnCl_2$-NaCl-KCl-CsCl[(17)] as functions of s and for various t-values. Points are experimental. Straight lines are theoretical.

NaCl, KCl or CsCl, were investigated by e.m.f. measurements. Also, "formal" potentials were measured in the corresponding ternary systems in which the solvents were respectively the equimolar mixtures NaCl-KCl, NaCl-CsCl and KCl-CsCl.

In all cases it was shown that the "formal" formation potentials of the ternary systems were in good agreement to within 2 to 5 per cent with values calculated from the theoretical expression,

$$E^0_{f(1,2,3)} = (1-t)E^0_{f(1,2)_y} - tE^0_{f(1,3)_y} \qquad (45)$$

which, is equivalent to equation 32 written for an excess partial molar free energy.

Standard "formal" potentials, E^0_f, are related to the usual "standard" potentials, E^0_s, by the well known relationship

$$E^0_f = E^0_s - \frac{RT}{ZF}\ln\gamma_n \qquad (46)$$

which, γ_n is the Henrian activity coefficient for a salt in solution. In such dilute solutions the formation of a complex specie and its coordination, is expected to have reached a limiting value and a complex should remain unchanged over the entire "Henrian" concentration range.

Therefore, dilute solutions ought to be ideally suited for investigating relationships between multicomponent and their component binary systems.

Conclusions

It has been shown that the thermodynamic properties of non-ideal and non-regular charge asymmetric fused salt systems may be predicted from data on the component binary systems, along isothermal composition paths representing a constant content of the charge asymmetric or reactive component MX_q.

Although the derivation of equations 22 and 23 for ternary systems, 31 and 32 for quarternary systems and of equations 42 and 43 for quinary systems, have been based on assumptions that complexes are formed, such assumptions are not really necessary. Any kind of internal reactivity should satisfy the theoretical treatment and the derived expressions should be applicable.

Regarding quarternary systems, the introduction of the composition parameters y, t, and S serves in the planning of experiments and in reducing the large number of compositions to be studied in order to adequately characterize a quarternary system. The use of these composition parameters makes it possible to plot thermodynamic data along well-defined composition paths and to identify the effects of competing interactions on a charge asymmetric cation. For example, the different complexing effects of CsCl or KCl on $MnCl_2$ become evident as the quarternary solutions become richer in CsCl, or in KCl, respectively.

The successful application of eqns. 22, 23, 31 and 32 to nonideal charge asymmetric fused-salt solutions indicates that in ternary, quarternary, and possibly even in higher order systems, reactions within the binary solutions account for most of the internal reactivity which is responsible for deviations from ideality.

In quarternary systems which may deviate from equation 31 or 32, plots such as Figures 10a, 10b, 10c and 10d are useful in that they display the thermodynamic data in a systematic way. For example, isoactivity paths are readily obtained, and activity plots covering an entire S-composition surface are readily constructed.

Regarding five component systems, an experimental verification of the derived expressions could not be made, at this time, because of the lack of the appropriate experimental data. However, in systems for which the ternary and the quarternary approximations have been found to be applicable, it is reasonable to expect that the corresponding five component systems should also obey approximately to equations 42 and 43.

The present treatment takes into account that reacting systems reach equilibrium and it should not be described as a "model". The formulation of specific complex species is not required except in a most general way.

The assumptions that the partial molar properties for the alkali chlorides and for the complex compounds are "frozen" at their levels in the corresponding binary solutions at same MCl_q content, are expected to be valid only if short range coulombic interactions are truly significant and if the cations A, B, ••• J are randomly distributed in the multicomponent mixed melt.

Although an exact knowledge of the structure of complexes is not necessary for the thermodynamic treatment, there are certain indirect indications regarding their probable configuration. For example, structural evidence(39) as well as measurements of electrical conductivities and of molar volumes,(23) suggest that solutions of $MnCl_2$ in alkali chloride melts appear to contain tetrahedrally coordinated complexes of the type $MnCl_4^{2-}$. Similarly, thermodynamic evidence indicates that the solutions of $ZrCl_4$, $HfCl_4$, $NbCl_5$ and $TaCl_5$(36,37) in alkali chlorides contain octahedrally coordinated complexes of the type MCl_6^{2-} or MCl_6^{-}. In all these systems, the negative deviations from ideality increase as the size of the alkali metal cation increases as in the sequence, LiCl-NaCl-KCl-RbCl-CsCl.(36,37)

These trends reflect the effects of competing interactions between the M^{q+} and alkali metal cations for the same Cl^- anions, in which the alkali chloride acts as a ligand donor and the reactive metal chloride MCl_q is the ligand acceptor. Alkali metal cations like Li^+, because of their small ionic radius are strongly attracted to their chloride anions and effectively the LiCl salt is less "dissociated" than other alkali metal chlorides containing larger cations like K^+, Rb^+ or Cs^+. The difference in the strength of the complexes which are formed when a reactive metal chloride MCl_q is mixed with either of the alkali chlorides ACl or BCl should be reflected by the difference in the bond distances in configurations of the type M-Cl-A or M-Cl-B.

References

1. H. Flood, T. Forland and K. Grojtheim, The Correlation Between Activity and Composition in Mixtures of Fused Salts, in The Physical Chemistry of Melts, Institution of Mining and Metallurgy, London (1953).
2. F. Kohler, Monatsch, Chemie, 91, 738 (1960).
3. E. Bonnier and R. Caboz, C.R. Acad. Sc. 250, 527 (1960).
4. Y.M. Muggianu, M. Gambino and J.P. Bros, J. Chimie Physique, 72, 83 (1975).
5. C.B. Alcock, F.D. Richardson, Acta Met. 6, 305 (1958).
6. G.W. Toop, Trans. TMS-AIME, 233, 850 (1965).
7. P.J. Spencer, F.H. Hayes and O. Kubaschewski, Rev. Chim. Miner. 9, 13 (1972).
8. I. Ansara, Metallurgical Chemistry, Proc. Sympos. Brunel Univ. and NPL, (1971), HMSO, p. 403 (1972).
9. M. Hillert, Calphad, 4, 1 (1980).
10. Sabounigi and Blander, J. Chem. Phys. 63, 1, 212 (1975).
11. A.D. Pelton and W.T. Thompson, Can. J. Chem. 48, 1585 (1970).
12. I. Karakaya and W.T. Thompson, Can. Met. Quarterly 25, 4, 307 (1986).
13. S.N. Flengas and A.S. Kucharski, Can. J. Chem. 49, 24, 3971 (1971).
14. S.N. Flengas and J.M. Skeaff, Can. J. Chem. 50, 9, 1345 (1972).
15. D.R. Sadoway and S.N. Flengas, J. Electrochem. Soc. 122, 4, 515 (1975).
16. S.N. Flengas and D.R. Sadoway, Proc. of the 3rd International Symposium on Molten Salts, Ed. G. Manantov, M. Blander and G.P. Smith, pp. 68-94 (1981).
17. C.A. Pickles and S.N. Flengas, J. Electroch. Soc. 131, 9, 2, 069 (1984).
18. A. Prince, "Alloy Phase Equilibria", Elsevier, New York (1966).
19. L. S. Palatnik and A.I. Landa, "Phase Equilibria in Multicomponent Systems", Holt, Rinehart and Winston, New York-London, 1961. Translated by Scripta Technical.
20. S.N. Flengas and T.R. Ingraham, J., J. Electroch. Soc. 106, 8, 714 (1959).
21. J. Guion, M. Blander, D. Hugstenberg and K. Hagemark, J. Phys. Chem. 72, 6, 2086 (1968).
22. D.D. Pelton and S.N. Flengas, J. Electroch. Soc. 118, 8, 1307 (1971).

23. N.R. Carmichael and S.N. Flengas, J. Electroch. Soc. 128, 2098, 1979, 126, 2104 (1979).

24. D.C. Hamby and A. Scott, J. Electroch. Soc. 115, 7, 704 (1968).

25. D.C. Hamby and A. Scott, J. Electroch. Soc. 117, 3, 319 (1970).

26. A.C. Gruner and W.T. Thompson, Can. J. Chem. 53, 1084 (1975).

27. A. Gutierrez and J.M. Toguri, J. Chem. Eng. 27, 109 (1982).

28. M. Takahshi, J. Electroch. Soc. Jap. 25, N8, 432 (1957).

29. D.E. Neil, H.M. Clark, and R.H. Wiswall, J. Chem. and Eng. Data, 10, 1,2 (1965).

30. P.J. Tumidajski and S.N. Flengas, Can. J. Chem. 63, 5, 1080 (1985).

31. A.D. Pelton and S.N. Flengas, J. Electroch. Soc. 117, 9, 1130 (1970).

32. P. Dantzer and O.J. Kleppa, J. Chem. Phys. 2, 71, 216 (1974).

33. L.S. Hersh, O.J. Kleppa, J. Chem. Phys. 42, 4, 1309 (1965).

34. G.N. Papatheodorou and O.J. Kleppa, J. Inorg. and Nucl. Chem. 5, 33, 1249 (1971).

35. A.S. Kucharski and S.N. Flengas, J. Electroch. Soc. 119, 9, 1170 (1972).

36. R.L. Lister and S.N. Flengas, Can. J. Chem. 43, 2947 (1965).

37. D.R. Sadoway and S.N. Flengas, Can. J. Chem. 56, 2538 (1978).

38. P.J. Tumidajski and S.N. Flengas, Potential Measurements of Reactive Metal Chlorides in Alkali Halide Solutions, in Proceedings 7th International Symposium on Molten Salts, Montreal, May 1990.

39. K. Tanemoto and T. Nakamura, Chem. Lett. 351, 356 (1975).

SUMMARY

For A Multicomponent System : $MX_q - M_2AX - n_3BX \cdots\cdots n_jJX$

where : $n_2 + n_3 + \cdots\cdots n_j = 1$

$X_2 + X_3 + \quad X_j = 1 - X_1$

$$\Delta Z_{MX_q} = \frac{X_2}{1-X_1}\left(\Delta Z_{MX_q}\right)_{AX-MX_q} + \frac{X_3}{1-X_1}\left(\Delta Z_{MX_q}\right)_{BX-MX_q} + \cdots\cdots \frac{X_j}{1-X_1}\left(\Delta Z_{MX_q}\right)_{JX-MX_q} \qquad \text{(S-1)}$$

for X_{MX_q} values which are the same in the binary and in the multicomponent systems.

ΔZ is Any Partial Or Molar Solution Property.

For A Ternary System: $MX_q - n_2AX - n_3BX$

$y = 1 - X_{MX_q} = 1 - X_1$

$t = \dfrac{X_3}{X_2 + X_3}$

or

$X_1 = 1 - y$

$X_2 = y(1-t)$

$X_3 = ty$

$$\underset{(1,2,3)}{\overline{\Delta H}_{MX_{q(y)}}} = (1-t)\,\overline{\Delta H}_{MX_{q(1,2)(y)}} + t\,\overline{\Delta H}_{MX_{q(1,3)(y)}} \qquad \text{(S-2)}$$

$$a_{MX_{q(1,2,3)(y)}} = \left(a_{MX_q}^{1-t}\right)_{1,2(y)} \cdot \left(a_{MX_q}\right)^{t}_{1,3(y)} \qquad \text{(S-3)}$$

For A Quarternary System: $MX_q - n_2AX - n_3BX - n_4CX$

$y = 1 - X_1$

$t = \dfrac{X_4}{X_3 + X_4}$

$S = \dfrac{X_2}{X_2 + X_3 + X_4}$

or

$X_1 = 1 - y$

$X_2 = yS$

$X_3 = y(1-t)(1-S)$

$X_4 = yt(1-S)$

$$\underset{(1,2,3,4)}{\overline{\Delta H}_{MX_{q(y)}}} = S\left(\overline{\Delta H}_{MX_q}\right)_{1,2(y)} + (1-S)\left[t\left(\overline{\Delta H}_{MX_q}\right)_{1,4(y)} + (1-t)\left(\overline{\Delta H}_{MX_q}\right)_{1,3(y)}\right] \qquad \text{(S-4)}$$

$$\underset{(1,2,3,4)}{a_{MX_{q(y)}}} = a^{S}_{MX_{q(1,2)(y)}} \cdot a^{(1-S)(1-t)}_{MX_{q(1,3)(y)}} \cdot a^{t(1-S)}_{MX_{q(1,4)(y)}} \qquad \text{(S-5)}$$

For A Quinary System : $MX_q - n_2AX - n_3BX - n_4CX - n_5DX$

$y = 1 - X_1$

$t_1 = \dfrac{X_3}{X_2 + X_3}$

$t_2 = \dfrac{X_5}{X_4 + X_5}$

$R = \dfrac{X_2 + X_3}{X_2 + X_3 + X_4 + X_5}$

or

$X_1 = 1 - y$

$X_2 = y(1-t_1)R$

$X_3 = yRt_1$

$X_4 = y(1-t_2)(1-R)$

$X_5 = yt_2(1-R)$

$$\underset{(1,2,3,4,5)}{\overline{\Delta H}_{MX_{q(y)}}} = (1-R)\left[t_2\left(\overline{\Delta H}_{MX_q}\right)_{1,5(y)} + (1-t_2)\left(\overline{\Delta H}_{MX_q}\right)_{1,4(y)}\right] + R\left[t_1\left(\overline{\Delta H}_{MX_q}\right)_{1,3(y)} + (1-t_1)\left(\overline{\Delta H}_{MX_q}\right)_{1,2(y)}\right] \qquad \text{(S-6)}$$

$$a_{MX_{q(y)}} = a^{R(1-t)}_{MX_{q(1,2)(y)}} \cdot a^{Rt_1}_{MX_{q(1,3)(y)}} \cdot a^{(1-R)(1-t_2)}_{MX_{q(1,4)(y)}} \cdot a^{(1-R)t_2}_{MX_{q(1,5)(y)}} \qquad \text{(S-7)}$$

X_{MX_q} = Common

APPENDIX 1

Standard state conversion.

Considering reaction 3 at equilibrium, the "overall" mixed system contains species such as MX_q, AX, ••• JX and A_rMX_{q+r}, ••• J_rMX_{q+r}, at their equilibrium concentrations which are determined by the condition that $\Delta G_R = 0$.

Reaction 3 could also be taken as "standard", if the solutions

$$[(AX)_{n_2} \cdot (BX)_{n_3} \cdots (JX)_{n_j}],$$

and,

$$\left[(A_rMX_{q+r})_{n_2} \cdot (B_rMX_{q+r})_{n_3} \cdots (J_rMX_{q+r})_{n_j}\right]$$

where,

$$n_2 + n_3 + \cdots + n_j = 1$$

are taken as the "standard states" in the "overall mixed" system which contains all of the above species.

For components AX, BX ••• JX in this "overall mixed" melt, the standard state is the solution of fixed composition given as $[(AX)_{n_2} \cdot (BX)_{n_3} \cdots (JX)_{n_j}]$, at all temperatures.

Similarly, the standard state for either A_rMX_{q+r}, B_rMX_{q+r} ••• and J_rMX_{q+r}, is the solution containing n_2 moles, A_rMX_{q+r}, n_3 moles B_rMX_{q+r} and ••• n_j moles J_rMX_{q+r}. The terms $r\Delta G_{m(1)}$ and $\Delta G_{M(2)}$ in equation 4 of Table 2 are readily eliminated during the conversion of the standard states to those representing the pure liquids at same temperatures. $\overline{\Delta G}_{MX_q}$, represents the partial molar Gibbs free energy of mixing for pure molten MX_q, as before.

Activities are defined by relationships like

$$\underset{\text{(in "mixed" melt)}}{(a_{JX})} = \frac{(P_A)\text{over "mixed" melt}}{(P_A^1)\text{over "standard" solution } [(AX)_{n_2} \cdot (BX)_{n_3} \cdots (JX)_{n_j}]} \qquad (A-1)$$

and,

$$\underset{\text{(in mixed melt)}}{a_{J_rMX_{q+r}}} = \frac{(P_{J_rMX_{q+r}})\text{over "mixed" melt}}{\left(P^1_{J_rMX_{q+r}}\right)\text{over "standard" solution } [(A_rMX_{q+r})\cdots(J_rMX_{q+r})]} \qquad (A-2)$$

For conversion purposes Gibbs free energies will be defined as follows:

$\overline{G}_{JX}$, for JX in the "overall" mixed system at the equilibrium composition (reaction 3 at equilibrium).

G^0_{JX}, for pure molten JX.

and,

$\overline{G}'_{JX}$, for JX in the "standard" solution $[(AX)_{n_2} \cdot (BX)_{n_3} \cdots (JX)_{n_j}]$

Gibbs free energies of mixing may be expressed in terms of the two different standard states given. These are:

$$\underset{\text{(in mixed system)}}{\overline{\Delta G}''_{JX}} = \overline{G}_{JX} - G^0_{JX} \qquad A-3$$

$$\underset{\text{(in "standard" solution)}}{\overline{\Delta G}'_{JX}} = \overline{G}'_{JX} - G^0_{JX} \qquad A-4$$

and,

$$\underset{\text{(in mixed system)}}{\overline{\Delta G}_{JX}} = \overline{G}_{JX} - \overline{G}'_{JX} \qquad A-5$$

From equations A-3, A-4 and A-5,

$$\overline{\Delta G}_{JX} = \overline{\Delta G}''_{JX} - \overline{\Delta G}'_{JX} \qquad A-6$$

Similarly, considering the standard states for pure molten J_rMX_{q+r}, as $G^0_{J_rMX_{q+r}}$ and of J_rMX_{q+r} in the standard solution

$$(A_rMX_{q+r})_{n_2} \cdot (B_rMX_{q+r})n_3 \cdots (J_rMX_{q+r})n_j$$

as, $\overline{G}'_{J_rMX_{q+r}}$, it is possible to relate the partial molar Gibbs free energy of mixing for J_rMX_{q+r}, by the expression

$$\overline{\Delta G}_{J_rMX_{q+r}} = \underset{(A-5)}{\overline{\Delta G}''_{J_rMX_{q+r}}} - \Delta G'_{J_rMX_{q+r}} \qquad A-5$$

where $\overline{\Delta G}''_{J_rMX_{q+r}}$, is the Gibbs free energy of mixing for J_rMX_{q+r} with respect to the state of J_rMX_{q+r} in the "standard" solution.

Equations A-4 and A-5 in this appendix are also listed as equations 7 and 8 in Table 1.

DOI: 10.1149/199017.0098PV

EVIDENCE FOR HYDROGEN-BONDING IN SOLUTIONS OF 1-METHYL-3-ETHYLIMIDAZOLIUM HALIDES, AS DETERMINED BY ^{1}H, ^{35}Cl AND ^{127}I NMR SPECTROSCOPY, AND ITS IMPLICATIONS FOR ROOM-TEMPERATURE HALOGENOALUMINATE(III) IONIC LIQUIDS

Anthony G. Avent, Penelope A. Chaloner, Martin P. Day, Kenneth R. Seddon and Thomas Welton

School of Chemistry and Molecular Sciences, University of Sussex,
Falmer, Brighton BN1 9QJ, UK.

ABSTRACT

Over the past five years, the perception of the ability of the 1-methyl-3-ethylimidazolium cation, [MeEtim]$^+$, to enter into hydrogen-bonds with halide ions has developed from not possible, through controversial, to widely accepted. However, the strongest evidence for these claims has always rested upon X-ray crystallographic determinations of the structure of [MeEtim]$^+$ salts. Although many first class studies have been reported, no incontrovertible evidence has yet been presented that the [MeEtim]$^+$ cation is capable of forming hydrogen bonds in solution. Here, we demonstrate, using multinuclear NMR spectroscopy and conductivity measurements, that [MeEtim]$^+$ not only forms strong hydrogen bonds (using <u>all</u> three ring protons; H^2, H^4 and H^5) with halide ions in polar molecular solvents (*e.g.* ethanenitrile, MeCN) and ionic liquids, but that it exists in a *quasi*-molecular state, [(MeEtim)X], in non-polar solvents (*e.g.* trichloromethane and dichloromethane), showing a conventional aromatic stacking phenomenon.

INTRODUCTION

Over the past five years, the perception of the ability of the 1-methyl-3-ethylimidazolium cation, [MeEtim]$^+$ (1,2), to enter into hydrogen-bonds with halide ions has developed from not possible (3), through controversial (4), to widely accepted (5,6). However, the strongest evidence for these claims has always rested upon solid state X-ray crystallographic determinations of the structures of both [MeEtim]$^+$ (4,7) and [Me$_2$Etim]$^+$ ([Me$_2$Etim]$^+$ = the 1,2-dimethyl-3-ethylimidazolium cation) salts (8). Although many first class solution studies have been reported (5,6,9), no incontrovertible evidence has yet been presented that the [MeEtim]$^+$ cation is capable of forming hydrogen bonds in solution. We demonstrate here, using principally the techniques of multinuclear NMR spectroscopy and conductivity measurements, that [MeEtim]$^+$ not only forms strong hydrogen bonds (using <u>all</u> three ring protons; H^2, H^4 and H^5; see Figure 1) with halide ions in polar molecular solvents (*e.g.* ethanenitrile, MeCN) and ionic liquids, but that it exists in a *quasi*-molecular state, [(MeEtim)X], in non-polar solvents (*e.g.* $CHCl_3$ and CH_2Cl_2), showing a conventional aromatic stacking phenomenon.

EXPERIMENTAL

NMR STUDIES

A series of [MeEtim]Cl–$AlCl_3$ ionic liquids of differing composition were prepared, and treated with phosgene as described elsewhere (10). ^1H and ^{13}C NMR spectra were recorded at 303 K, on a Bruker WM360 spectrometer.

Deuterium oxide (99 %) was distilled *in vacuo* before use. CD_3CN and CD_2Cl_2 were distilled from calcium hydride under dry dinitrogen. Samples of [MeEtim]X (X = Cl, Br or I) were weighed and solutions in CD_3CN and CD_2Cl_2 were prepared in a glove box through which dry dinitrogen was passed.

^1H and ^{13}C NMR spectra were recorded using tetramethylsilane (TMS) as the reference, at 360.13 and 90.55 MHz, respectively. ^{35}Cl NMR spectra were recorded using 2 *M* aqueous KCl as a reference, at 35.29 MHz. ^{127}I NMR spectra were recorded using 2 *M* aqueous KI as the reference, at 72.08 MHz. All NMR spectra were recorded at 303 K.

CONDUCTANCE MEASUREMENTS

Solution Preparation

Conductivity water was obtained from the Centre for Medical Research (University of Sussex); it had been purified by reverse osmosis in a Millipore Milli RO 60 system followed by passage through a Millipore Milli Q Super C system (consisting of two ion exchange cartridges and an Organex–Q cartridge). It was used without further purification.

Aqueous solutions were prepared by weighing samples of [MeEtim]Cl into volumetric flasks in a Faircrest glove box with an atmosphere of dry dinitrogen, removing the sample from the box, and adding water. Only 'A'–grade volumetric flasks were used.

Ethanenitrile and dichloromethane were twice distilled from calcium hydride under an atmosphere of dry dinitrogen. The distillate was transferred to a Faircrest glove box, through which dry dinitrogen was passed. Solutions were prepared inside this glove box.

Calibration and Background Conductivities of Solvents

All conductivity measurements were made at 25 °C, with continuous stirring of the solution, using a Phillips PW9506 digital conductivity meter. The cell, fitted with platinum electrodes, was calibrated using aqueous 10^{-3} *M* KCl solutions. Background conductivities were measured for all solvents (H_2O, 1.8; CH_3CN, 2.0; CH_2Cl_2, 1.4 $\mu S\ cm^{-1}$).

SYNTHESIS OF 1–METHYL–3–ETHYLIMIDAZOLIUM HALIDES

1–Methyl–3–ethylimidazolium Chloride

1–Methylimidazole (20 cm^3, 0.36 mol) was distilled *in vacuo* from potassium hydroxide (1 g) directly into a dry pressure vessel fitted with a Rotaflo greaseless tap and a B19 Quickfit ground glass socket. Chloroethane (70 cm^3, 0.43 mol) was added by distillation *in vacuo* from phosphorus(V) oxide (1 g) while the pressure vessel was maintained at −78 °C. The pressure vessel was then sealed, transferred to a vacuum line and further evacuated whilst being maintained at −196 °C for 1 h. The pressure vessel was then sealed, placed inside a steel bomb, and heated in an electric furnace at 76 °C for 72 h. After this time, two immiscible layers had formed; when cooled to −13 °C, a white precipitate formed. The pressure vessel was opened in a fume cupboard, and the excess chloroethane allowed to evaporate through a drying tube containing calcium chloride. When the evaporation was nearly complete, the solid was dissolved in dry, hot ethanenitrile (50 cm^3) and the mixture filtered using standard Schlenk techniques. Dry ethyl ethanoate (100 cm^3) was added to the filtrate. The mixture was left overnight at −13 °C and the resulting precipitate was isolated by Schlenk filtration. The solid was redissolved in a minimum of ethanenitrile (20 cm^3) and the mixture filtered. The filtrate was cooled at −13 °C for 48 h. The resulting precipitate was isolated by Schlenk filtration, dried *in vacuo* for 36 h and transferred to the dry box. The yield was 36.5 g (69.2 %). Calculated for $C_6H_{11}ClN_2$: C, 49.15; H, 7.56; N, 19.10 %. Found: C, 48.68; H, 7.43; N, 18.69 %.

1-Methyl-3-ethylimidazolium Bromide

1-Methylimidazole (35 cm^3, 0.63 mol) was distilled *in vacuo* from potassium hydroxide (1.5 g) into a round bottomed flask (250 cm^3) fitted with a side arm. Bromoethane (90 cm^3, 0.69 mol) was added by distillation *in vacuo* from phosphorus(V) oxide (1 g). The mixture was heated under reflux under dry dinitrogen for two hours and left to cool overnight. The resulting white solid was dissolved in hot ethanenitrile (50 cm^3) and the solutions was filtered under dry dinitrogen. Dry ethyl ethanoate (100 cm^3) was added to the filtrate and the mixture cooled to −13 °C. The resulting precipitate was isolated by Schlenk filtration and recrystallized from a minimum of ethanenitrile (20 cm^3). The resulting white precipitate was isolated by Schlenk filtration, dried *in vacuo* for 36 h, and transferred to the dry box. Yield: 69.3 g (57.6 %). Calculated for $C_6H_{11}BrN_2$: C, 37.71; H, 5.80; N, 14.66 %. Found: C, 38.91; H, 5.70; N, 13.79 %.

1-Methyl-3-ethylimidazolium Iodide

1-Methylimidazole (25 cm^3, 0.45 mol) was distilled *in vacuo* from potassium hydroxide (1 g) directly into a round bottomed flask (250 cm^3) fitted with a side arm. Iodoethane (60 cm^3, 0.49 mol) was added by distillation *in vacuo* from phosphorus(V) oxide. Heat was evolved and the solution became pale yellow. The solution was heated under reflux, under dry dinitrogen, for two hours. After this time, two immiscible layers had formed, the upper of which became a yellow solid on cooling to room temperature. The lower layer was removed by Schlenk filtration and the solid was dissolved in dry ethanenitrile (40 cm^3) and then recrystallised by addition of dry ethyl ethanoate (80 cm^3). This recrystallisation procedure was repeated twice before the white precipitate was finally recrystallized from a minimum of hot, dry ethanenitrile (20 cm^3) whilst protecting the product from light. The solid was dried *in vacuo* for 36 h and transferred to the dry box. Yield: 63.0 g (79.7 %). Calculated for $C_6H_{11}IN_2$: C, 30.27; H, 4.65; N, 11.76 %. Found: C, 30.06; H, 4.68; N, 11.22 %.

RESULTS

^{1}H NMR Spectra of [MeEtim]Cl–AlCl$_3$ Ionic Liquids

The ^{1}H NMR spectra are presented for one series of eight [MeEtim]Cl–AlCl$_3$ ionic liquids (Table 1, Figure 2). These spectra clearly demonstrate the dependence of the chemical shifts of the protons H^4, H^5, H^2, CH_2CH$_3$ and NCH$_3$ on the composition of the ionic liquid. The implications of this behaviour for inter-ionic interactions in the ionic liquids will be discussed later.

Table 1. The ^{1}H NMR Spectra (360.13 MHz; 303 K) of a Series of [MeEtim]Cl–AlCl$_3$ Ionic Liquids.

Parameters	X(AlCl$_3$)							
	0.30	0.35	0.40	0.45	0.50	0.55	0.60	0.65
δ(CH$_2$CH_3)/p.p.m.	0.92	0.92	0.91	0.91	0.90	0.90	0.89	0.89
δ(NCH$_3$)/p.p.m.	3.43	3.42	3.38	3.33	3.30	3.29	3.26	3.26
δ(CH_2CH$_3$)/p.p.m.	3.75	3.74	3.70	3.66	3.62	3.61	3.58	3.58
δ(H^5)/p.p.m.	7.32	7.21	7.02	6.81	6.73	6.71	6.66	6.65
δ(H^4)/p.p.m.	7.43	7.31	7.09	6.86	6.78	6.76	6.70	6.69
δ(H^2)/p.p.m.	9.31	9.12	8.68	8.00	7.77	7.73	7.64	7.61
^3J(CH$_2$CH_3)/Hz	7.3	7.3	7.3	7.3	7.3	7.3	7.3	7.3
^3J(CH_2CH$_3$)/Hz	7.3	7.3	7.3	7.3	7.3	7.3	7.4	7.4
^4J(H^{4,5},H^2)/Hz	--	--	--	--	1.6	--	1.7	--
^3J(H^4,H^5)/Hz	--	--	--	--	1.7	--	1.8	--

The ^{1}H NMR signals of the protons H^4, H^5 and H^2 are broadened under the influence of the ring nitrogens; hence, the H^2 signal is unresolved in all of the spectra and resolution of the H^4 and H^5 signals has only been achieved in two of the spectra recorded. An expanded spectrum of the [MeEtim]Cl–AlCl$_3$ ionic liquid {X(AlCl$_3$) = 0.60} shows the H^4 and H^5 signals resolved into two asymmetric triplets (Figure 3), which result from a doublet of doublets in which the innermost lines coalesce. Close examination of the H^2 signal reveals that it is broad and non-Lorentzian in shape, suggesting that the H^2 proton is coupled with the other ring protons. Upon irradiation of the H^2 proton of [MeEtim]I (11), the H^4 and H^5 signals become doublets, confirming that the H^2 proton is indeed coupled with the other ring protons.

Irradiation of the protons of the N-methyl group of an ionic liquid

{$X(\mathrm{AlCl_3})$ = 0.60, Figure 4} leads to an enhancement of the most downfield signal (H^2) of 3%. Of the signals attributed to the other ring protons (H^4 and H^5), the upfield signal is enhanced by 2% whilst the downfield signal shows only very slight enhancement (<1%). The nuclear Overhauser effect (NOE) is such that the decoupling of a signal leads to enhancement of signal intensities with those nuclei which are closest (through space) showing the greatest effect (12). Therefore, the assignments of H^5 to the upfield signal and H^4 to the downfield signal is confirmed.

^{13}C *NMR Spectra of [MeEtim]Cl–AlCl₃ Ionic Liquids*

Proton coupled ^{13}C NMR spectra are presented for a series of [MeEtim]Cl–$\mathrm{AlCl_3}$ ionic liquids (Table 2, Figure 5). As with the ^{1}H NMR chemical shifts, the ^{13}C NMR spectra show a dependence on the composition of the ionic liquid, although it is much less pronounced for ^{13}C chemical shifts. The carbon–proton coupling constants show little change with the composition of the ionic liquid.

Table 2. The ^{13}C NMR Spectra (90.55 MHz; 303 K) of a Series of [MeEtim]Cl–$\mathrm{AlCl_3}$ Ionic Liquids.

Parameters	$X(\mathrm{AlCl_3})$							
	0.30	0.35	0.40	0.45	0.50	0.55	0.60	0.65
$\delta(\mathrm{CH_2}\mathit{C}\mathrm{H_3})$/p.p.m.	15.64	15.59	15.49	15.39	15.36	15.32	15.27	15.23
$\delta(\mathrm{NCH_3})$/p.p.m.	36.58	36.63	36.77	36.98	37.01	37.00	36.97	36.98
$\delta(\mathit{C}\mathrm{H_2CH_3})$/p.p.m.	45.08	45.16	45.33	45.53	45.58	45.61	45.64	45.70
$\delta(C^5)$/p.p.m.	122.07	122.02	122.02	122.05	122.03	122.10	122.14	122.25
$\delta(C^4)$/p.p.m.	124.31	124.26	124.26	124.28	124.23	124.31	124.38	124.48
$\delta(C^2)$/p.p.m.	136.84	136.61	136.10	135.29	134.91	134.70	134.38	134.30
$^1J(\mathrm{CH_2}\mathit{C}\mathrm{H_3})$/Hz	128.7	129.0	128.9	128.7	129.1	129.2	129.2	128.9
$^1J(\mathrm{NCH_3})$/Hz	143.6	143.6	143.8	144.1	144.1	144.2	144.2	144.4
$^1J(\mathit{C}\mathrm{H_2CH_3})$/Hz	144.1	144.1	144.2	144.0	144.4	144.3	144.4	144.5
$^1J(C^5H)$/Hz	132.7	138.4	140.8	150.7	154.1	155.9	153.2	148.9
$^1J(C^4H)$/Hz	132.5	136.9	141.7	151.7	154.5	153.9	154.3	148.0
$^1J(C^2H)$/Hz	220.4	220.1	220.0	220.0	219.3	219.4	219.1	218.7

^1H *and* ^{13}C *NMR Spectra of [MeEtim]X (X = Cl, Br or I) in 2 M Solution*

The ^{1}H and ^{13}C NMR spectra of the [MeEtim]X (X = Cl, Br or I) salts were recorded in $\mathrm{CDCl_3}$; these spectra show a distinct concentration dependence which will be discussed later. The spectra reported in this section were recorded using 2 *M* solutions of the salts. The ^1H and ^{13}C NMR spectra are presented in Figures 6 and 7, and Tables 3 and 4, respectively. Assignments of these spectra follow those found in the [MeEtim]Cl–$AlCl_3$ ionic liquids, and are in accord with those found in the literature (3,11,13).

The imidazolium ring proton H^2 is shifted downfield under the influence of the two nitrogen atoms of the ring. The protons H^4 and H^5 are shifted less under the influence of only one neighbouring nitrogen atom. The spectrum of [MeEtim]I in D_2O (11) shows a broad singlet for the H^2 signal and a multiplet integrating to two protons, attributed to the H^4 and H^5 protons. In addition, irradiation of the H^2 signal results in a simplified multiplet for the $H^{4,5}$ signal, showing that H^2 is coupled to H^4 and H^5, and that the H^4 and H^5 are not equivalent. The irradiation of the NCH_3 signal (*vide supra*) of a [MeEtim]Cl–$AlCl_3$ ionic liquid shows that the H^5 signal is upfield of the H^4 signal.

Table 3. The ^1H NMR Spectra (360.13 MHz; 2 *M*, $CDCl_3$; 303 K) of [MeEtim]X (X = Cl, Br or I).

	X					
Parameters	Cl	Br	$\Delta\delta^{Cl}$ a	I	$\Delta\delta^{Cl}$ a	
$\delta(CH_2CH_3)$/p.p.m.	1.39	1.34	0.05	1.30	0.09	triplet
$\delta(NCH_3)$/p.p.m.	3.93	3.88	0.05	3.82	0.09	singlet
$\delta(CH_2CH_3)$/p.p.m.	4.24	4.20	0.04	4.13	0.09	quartet
$\delta(H^5)$/p.p.m.	7.69	7.61	0.08	7.46	0.23	singlet
$\delta(H^4)$/p.p.m.	7.72	7.67	0.05	7.51	0.21	singlet
$\delta(H^2)$/p.p.m.	10.20	9.86	0.34	9.56	0.64	singlet
$^3J(CH_2CH_3)$/Hz	7.29	7.22		7.30		
$^3J(CH_2CH_3)$/Hz	7.31	7.20		7.28		

a $\Delta\delta^{Cl} = \delta(Cl) - \delta(X)$.

The different values of the chemical shifts for the analogous protons in each of the three salts suggest (as shown by $\Delta\delta^{Cl}$) that there is significant cation–anion interaction in solution in $CDCl_3$. This is most pronounced at the proton H^2, but detectable at H^4 and H^5.

The ^{13}C NMR spectra of the salts (Table 4) show qualitatively similar behaviour to the ^1H NMR spectra, although changes are much less pronounced. Chemical shifts particularly indicate the acidity of the C^2 site.

Table 4. The $^{13}C\{^1H\}$ NMR Spectra (90.55 MHz; 2 *M*, $CDCl_3$; 303 K) of [MeEtim]X (X = Cl, Br or I).

	X				
Parameters	Cl	Br	$\Delta\delta^{Cl}$ [a]	I	$\Delta\delta^{Cl}$ [a]
$\delta(CH_2CH_3)$/p.p.m.	15.37	14.76	0.61	14.32	1.05
$\delta(NCH_3)$/p.p.m.	36.26	35.73	0.53	35.72	1.15
$\delta(CH_2CH_3)$/p.p.m.	44.93	44.25	0.68	43.92	1.01
$\delta(C^5)$/p.p.m.	121.74	121.30	0.44	120.90	0.84
$\delta(C^4)$/p.p.m.	123.51	122.90	0.61	122.41	1.10
$\delta(C^2)$/p.p.m.	137.38	135.69	1.69	134.56	2.82

[a] $\Delta\delta^{Cl} = \delta(Cl) - \delta(X)$.

^1H NMR Spectra of [MeEtim]Cl in D_2O

The ^1H NMR chemical shift data of 2.0 *M* and 0.005 *M* solutions of [MeEtim]Cl in D_2O are presented in Table 5. The change in chemical shift of the proton signals is negligible, indicating that there is little interaction between the cation and anion in aqueous solutions. The proton integrals for a 2.0 *M* solution of [MeEtim]Cl are compared to those of the same solution with added Na[OD] (Table 6). All ring protons exchange with deuterium in both solutions, but the

Table 5. ^1H NMR Chemical Shift Data for Solutions of [MeEtim]Cl in D_2O (360.13 MHz, 303 K).

Concentration/*M*	δ/p.p.m.				
	H^2	$H^{4,5}$	CH_2CH_3	NCH_3	CH_2CH_3
2.0	8.63	7.35	4.09	3.76	1.35
0.005	8.65	7.38	4.16	3.82	1.43

Table 6. ^1H NMR Integrals for Solutions of [MeEtim]Cl in D_2O and CD_3CN.

Solution	H^2	$H^{4,5}$	CH_2CH_3	NCH_3	CH_2CH_3
D_2O	0.89	1.92	2.0	3.0	3.0
D_2O + NaOD	0.05	0.13	2.0	3.0	3.0
CD_3CN	1.0	2.0	2.0	3.0	3.0

degree of exchange is significantly greater when the solution is made basic. Deuterium exchange is faster for the proton H^2 than for the protons H^4 and H^5. Hence, it may be concluded that all protons of the imidazolium ring are acidic, and that the proton H^2 is more acidic than the protons H^4 and H^5.

Table 7. ^1H NMR (360.13 MHz; 303 K) Chemical Shift Data for Solutions of [MeEtim]Cl in CD_3CN.

Conc/M	δ/p.p.m.					
	H^2	H^4	H^5	CH_2CH_3	NCH_3	CH_2CH_3
3.5596	10.54	8.49	8.35	4.61	4.26	1.68
1.7798	10.67	8.50	8.39	4.78	4.43	1.89
0.8899	10.76	8.47	8.37	4.89	4.54	2.04
0.4450	10.73	8.40	8.31	4.94	4.60	2.13
0.2225	10.63	8.33	8.26	4.97	4.62	2.17
0.1112	10.52	8.28	8.21	4.98	4.62	2.19
5.561×10^{-2}	10.37	8.24	8.18	4.97	4.62	2.20
2.781×10^{-2}	10.19	8.20	8.14	4.97	4.61	2.21
1.391×10^{-2}	10.01	8.18	8.12	4.95	4.60	2.21
6.952×10^{-3}	9.81	8.16	8.10	4.94	4.59	2.20
3.476×10^{-3}	9.67	8.15	8.09	4.93	4.58	2.20
1.738×10^{-3}	9.51	8.14	8.08	4.92	4.58	2.20
8.690×10^{-4}	9.38	8.13	8.07	4.90	4.57	2.20
4.345×10^{-4}	9.28	8.12	8.07	4.90	4.56	2.20
2.173×10^{-4}	9.22	8.12	8.06	4.90	4.56	2.20

^1H *NMR Spectra of Solutions of [MeEtim]X (X = Cl, Br or I) in* CD_3CN

The ^1H NMR chemical shift data for solutions of [MeEtim]X (X = Cl, Br or I) in CD_3CN are presented in Tables 7–9, and Figures 8–14.

Table 8. **^1H NMR (360.13 MHz; 303 K) Chemical Shift Data for Solutions of [MeEtim]Br in CD_3CN.**

Conc/*M*	δ/p.p.m.					
	H^2	H^4	H^5	CH_2CH_3 (*H* of CH_2)	NCH_3	CH_2CH_3 (*H* of CH_3)
1.7598	10.23	8.33	8.32	4.75	4.40	1.87
0.8799	10.28	8.34	8.25	4.88	4.52	2.04
0.4400	10.23	8.31	8.24	4.93	4.58	2.12
0.2200	10.14	8.27	8.20	4.95	4.60	2.16
0.1100	10.01	8.24	8.17	4.96	4.61	2.19
5.499×10^{-2}	9.88	8.21	8.15	4.96	4.60	2.20
2.750×10^{-2}	9.72	8.18	8.12	4.95	4.60	2.20
1.375×10^{-2}	9.58	8.16	8.11	4.95	4.59	2.20
6.874×10^{-3}	9.46	8.15	8.09	4.93	4.58	2.20
3.437×10^{-3}	9.34	8.13	8.08	4.92	4.57	2.20
1.719×10^{-3}	9.27	8.13	8.07	4.91	4.56	2.20
8.593×10^{-4}	9.21	8.12	8.07	4.90	4.56	2.19
4.296×10^{-4}	9.18	8.12	8.07	4.85	4.55	2.19
2.148×10^{-4}	9.16	8.11	8.06	4.84	4.55	2.19
1.074×10^{-4}	9.13	8.11	8.06	4.82	4.56	2.18

The NMR spectra of [MeEtim]X (X = Cl, Br or I) show qualitatively similar behaviour. It can be seen (Figures 8–10) that, when compared to the ring protons, there is negligible change in the chemical shifts of the methyl and ethyl protons of the cation. The H^2 signal (Figure 11) shows a marked change in chemical shift to higher field as the solution is made more dilute (after a smaller change to lower field at high concentrations). The H^5 (Figure 12) and H^4 signals show a similar but less pronounced behaviour. This is also true, but to a very much lesser extent, for the $C\mathit{H}_2CH_3$ and NCH_3 signals (Figure 13). The signal for the $CH_2C\mathit{H}_3$ protons (Figure 14), which are the most remote from the imidazolium ring, at higher concentrations moves to lower field as the solutions are made more dilute, then changes very little at low concentrations.

Table 9. ^1H NMR (360.13 MHz; 303 K) Chemical Shift Data for Solutions of [MeEtim]I in CD_3CN.

Conc/M	δ/p.p.m.					
	H^2	H^4	H^5	$C\textit{H}_2CH_3$	NCH_3	$CH_2C\textit{H}_3$
1.9575	9.67	8.08	7.99	4.62	4.27	1.78
0.9788	9.75	8.18	8.10	4.81	4.45	2.00
0.4894	9.73	8.20	8.13	4.88	4.52	2.09
0.2446	9.66	8.20	8.13	4.91	4.56	2.14
0.1223	9.57	8.18	8.12	4.93	4.58	2.17
6.117×10^{-2}	9.51	8.17	8.11	4.93	4.58	2.19
3.059×10^{-2}	9.41	8.16	8.10	4.92	4.58	2.20
1.529×10^{-2}	9.33	8.14	8.09	4.92	4.57	2.20
7.646×10^{-3}	9.27	8.13	8.08	4.91	4.56	2.20
3.823×10^{-3}	9.20	8.12	8.07	4.90	4.56	2.19
1.912×10^{-3}	9.17	8.12	8.06	4.90	4.55	2.19

The ^1H NMR data show that cation–anion interactions occur at the H^4 and H^5 ring protons, but are strongest for the proton H^2. The change in chemical shift with concentration is indicative of the formation of a hydrogen bond (14).

It is well known that the formation of a hydrogen bond will cause a proton chemical shift to move to lower field (12). The solution species present may be described by the equation (1).

$$(AH^+...X^-)_{solvent} \rightleftharpoons (AH^+)_{solvent} + (X^-)_{solvent} \qquad (1)$$

Although, at low temperatures, the hydrogen–bonded and non–hydrogen–bonded protons may show separate signals (15), more usually only one signal is seen. The chemical shift of the signal is the population–weighted mean of the chemical shifts of the hydrogen–bonded and the non–hydrogen–bonded protons (14). When the cation–anion interaction is weak, as the conductivity data (*vide infra*) demonstrates is the case for [MeEtim]Cl in ethanenitrile, the equilibrium (1) is very sensitive to changes in solute concentration. As the solution becomes more dilute, the right–hand side of equilibrium (1) is more favoured, the population of the more shielded proton increases and the signal moves upfield. This is the behaviour observed for the H^2 and, to a lesser extent, for the H^4 and H^5 signals of [MeEtim]X (X = Cl, Br or I) in CD_3CN. The behaviour of the CH_2CH_3 and NCH_3 signals is best attributed to changes in electronic distribution in the cation.

^{1}*H NMR of Solutions of a Fixed Concentration of [MeEtim]Cl in* CD_3CN*, with added* $[NEt_4]Cl$

The ^{1}H NMR chemical shift data for solutions of a fixed concentration of [MeEtim]Cl in CD_3CN with added $[NEt_4]Cl$ are presented in Table 10 and Figure 15, and show qualitatively similar behaviour to that of increasing the concentration of [MeEtim]X (X = Cl, Br or I). It has been shown that when a base {X^-, in the case of [MeEtim]X (X = Cl, Br or I)} is in excess, this behaviour is indicative of hydrogen bond formation (16). As the concentration of the Cl^- ion is increased, the population of the more deshielded proton is increased, and the signal moves downfield. It is also noted that the range of chemical shifts found is similar to that found for the [MeEtim]Cl–$AlCl_3$ ionic liquids (see Figure 2, Table 1, and ref. 3).

Table 10. ^{1}H NMR (360.13 MHz; 303 K) Chemical Shift Data for Solutions of a Fixed Concentration of [MeEtim]Cl [a] in CD_3CN, with added $[NEt_4]Cl$.

Conc of Cl^- /M	δ/p.p.m.					
	H^2	H^4	H^5	CH_2CH_3	NCH_3	CH_2CH_3
1.0307	10.58	8.40	8.33	4.90	4.54	2.05
0.5254	10.62	8.36	8.29	4.96	4.60	2.13
0.2727	10.58	8.31	8.24	4.98	4.62	2.17
0.1464	10.50	8.27	8.21	4.98	4.63	2.19
0.0833	10.37	8.23	8.17	4.98	4.62	2.20
0.0517	10.23	8.21	8.15	4.97	4.62	2.21
0.0359	10.13	8.19	8.14	4.96	4.61	2.21
0.0280	10.04	8.18	8.13	4.96	4.61	2.21
0.0201	9.87	8.16	8.11	4.95	4.60	2.20

[a] 0.0201 M

^{35}*Cl NMR Studies of Solutions of* $[NEt_4]Cl$ *in* CD_3CN

It has been reported that at low concentrations (<1 M), the value of ^{35}Cl NMR chemical shifts of solutions of $[NEt_4]Cl$ in water and ethanenitrile show little dependence on the concentration of the salt (17,18). In order to reaffirm this under our experimental conditions, the ^{35}Cl NMR spectra of solutions of $[NEt_4]Cl$ in CD_3CN have been recorded (Table 11, Figures 16 and 17). This demonstrates that the effect of concentration, in a given solvent, on the chemical shift of a fully solvated unassociated chloride ion is negligible. The line width changes show that the nuclear relaxation becomes slower as the solution becomes more dilute, as expected.

Table 11. ^{35}Cl NMR (35.29 MHz; 303 K) Spectral Data for Solutions of [NEt$_4$]Cl in CD$_3$CN.

Conc/*M*	δ/p.p.m.	$\Delta\nu_{\frac{1}{2}}$/Hz
1.6945	40.0	90
0.4236	39.5	55
0.1059	39.5	47
0.0265	39.7	30
0.0066	39.2	30

^{35}Cl NMR Spectra of Solutions of [MeEtim]Cl in CD$_3$CN

The ^{35}Cl NMR chemical shift data for solutions of [MeEtim]Cl are presented in Table 12 and Figures 16 and 17. The dissociation of [MeEtim]Cl in CD$_3$CN is described by the equilibrium (1), and dilution of the solution is accompanied by a change in ^{35}Cl chemical shift to higher field, indicating that hydrogen bonds are being broken. Examination of Figure 16 also suggests that the chemical shift at infinite dilution will be close to that of [NEt$_4$]Cl.

Table 12. ^{35}Cl NMR (35.29 MHz; 303 K) Spectral Data for Solutions of [MeEtim]Cl in CD$_3$CN.

Conc/*M*	δ/p.p.m.	$\Delta\nu_{\frac{1}{2}}$/Hz
3.2127	58.5	136.0
1.6063	55.9	73.1
0.8032	54.0	52.8
0.4016	52.3	44.8
0.2008	50.6	38.2
0.1004	49.0	30.7
0.0502	47.7	31.1
0.0251	46.0	36.5
0.0125	44.7	36.8

It is well known (19) that the breaking of a hydrogen bond causes ^{35}Cl NMR chemical shifts to move upfield. As the hydrogen bond is broken, the electron density of the chloride ion becomes more located around the ion itself, and so its nucleus becomes more shielded.

The changes in the line width of the ^{35}Cl NMR signals of solutions of [MeEtim]Cl in CD_3CN shadow those of [NEt_4]Cl in CD_3CN; hence it may be deduced that the same mechanisms are involved (*i.e.* viscosity/mobility) (19).

^{35}Cl NMR Spectra of Solutions of a Fixed Concentration of [MeEtim]Cl in CD_3CN, with added [NEt_4]Cl

The ^{35}Cl NMR chemical shift data for solutions of a fixed concentration of [MeEtim]Cl in CD_3CN, with added [NEt_4]Cl, are presented in Table 13 and Figure 18, and demonstrate a marked downfield change in chemical shift as the concentration of chloride ion is reduced.

Table 13. ^{35}Cl NMR (35.29 MHz; 303 K) Data for Solutions of a Fixed Concentration of [MeEtim]Cl [a] in CD_3CN, with added [NEt_4]Cl.

Conc of Cl^-/*M*	δ/p.p.m.	$\Delta\nu_{\frac{1}{2}}$/Hz
1.0307	32.5	60.8
0.5254	33.7	39.0
0.2727	34.9	27.8
0.1464	36.6	21.6
0.0833	38.6	18.0
0.0517	40.6	17.8
0.0359	41.8	18.5
0.0280	42.6	16.0
0.0201	43.7	21.1

[a] 0.0201 *M*

As chloride ion is added to the solution, the equilibrium (1) moves to the left, as indicated by the ^{1}H NMR results (see Table 10 and Figure 15), increasing the population of the deshielded ^{35}Cl nuclei. However, there is a concomitant increase in the concentration of chloride ion, and so the increase in the population of the more shielded unassociated solvated ion is greater than that of the ion-paired $^{35}Cl^-$ ion. Hence, the ^{35}Cl NMR signal of the solution moves upfield as [NEt_4]Cl is added. The change in the line width of the ^{35}Cl signal (Table 5.12) is again indicative of changes in physical, rather than chemical, phenomena.

^{127}I NMR Spectra of Solutions of [MeEtim]I in CD_3CN

To ensure that the effect of changing concentration on halogen chemical shifts is not restricted to ^{35}Cl NMR measurements, and to establish that the weaker hydrogen bond acceptor, I^-, behaves in the same way as Cl^-, the ^{127}I NMR spectra of solutions of [MeEtim]I in CD_3CN were recorded, and are presented in Table 14 and Figures 19 and 20.

Table 14. ^{127}I NMR (72.08 MHz; 303 K) Spectral Data for Solutions of [MeEtim]I in CD_3CN.

Conc/*M*	δ/p.p.m.	$\Delta\nu_{\frac{1}{2}}$/Hz
0.9788	137.1	5250
0.4894	128.8	3609
0.2446	120.5	3107
0.1223	112.7	2681
0.0612	109.9	2544
0.0306	104.7	1787
0.0153	101.7	2930
7.65×10^{-3}	100.6	1125
3.82×10^{-3}	96.5	1059
1.91×10^{-3}	95.6	689

As with ^{35}Cl NMR chemical shifts, the ^{127}I chemical shifts move to higher field with dilution of the solutions. This behaviour indicates, again, that the equilibrium between a hydrogen-bonded ion-pair and unassociated solvated ions is the dominant factor in the dissolution of [MeEtim]X (X = Cl, Br or I) in ethanenitrile (*cf*. Ref. 18).

^{1}H NMR Spectra of Solutions of [MeEtim]X (X = Cl, Br or I) in CD_2Cl_2

The ^{1}H NMR chemical shift data for solutions of [MeEtim]X (X =Cl, Br or I) in CD_2Cl_2 are presented in Tables 15–17 and Figures 21–23.

The ^{1}H NMR spectra of all three salts show qualitatively similar behaviour, although quantitative differences are seen. The ^{1}H chemical shifts of the methyl and ethyl protons of the cation show little dependence on the concentration of the solution in CD_2Cl_2. In contrast to the behaviour in CD_3CN, the H^2 proton signal moves downfield and the $H^{4,5}$ proton signal moves upfield as the solution is diluted (Figure 24). The reasons for this will be considered in the Discussion section.

Table 15. ^{1}H NMR Spectral Data for Solutions of [MeEtim]Cl in CD_2Cl_2.

Conc/*M*	δ/p.p.m.				
	H^2	$H^{4,5}$	CH_2CH_3	NCH_3	CH_2CH_3
2.0722	10.31	7.87	4.19	3.87	1.29
1.0361	10.45	7.73	4.23	3.91	1.36
0.5181	10.54	7.63	4.25	3.93	1.41
0.2590	10.62	7.53	4.25	3.93	1.43
0.1295	10.70	7.44	4.27	3.96	1.45
0.0648	10.76	7.35	4.26	3.95	1.46
0.0324	10.87	7.27	4.27	3.96	1.47
0.0162	10.88	7.19	4.26	3.95	1.47
0.0081	10.95	7.13	4.26	3.95	1.47

Table 16. ^{1}H NMR Spectral Data for Solutions of [MeEtim]Br in CD_2Cl_2.

Conc/*M*	δ/p.p.m.				
	H^2	$H^{4,5}$	CH_2CH_3	NCH_3	CH_2CH_3
2.0217	9.96	7.81	4.15	3.74	1.24
1.0109	10.09	7.69	4.19	3.87	1.32
0.5054	10.23	7.63	4.25	3.93	1.40
0.2527	10.32	7.55	4.26	3.94	1.44
0.1264	10.41	7.47	4.29	3.98	1.47
0.0632	10.46	7.41	4.28	3.97	1.48
0.0316	10.51	7.35	4.28	3.98	1.49
0.0158	10.71	7.19	4.27	3.97	1.50
0.0079	10.65	7.14	4.26	3.96	1.49

Table 17. ^{1}H NMR Spectral Data for Solutions of [MeEtim]I in CD_2Cl_2.

Conc/*M*	δ/p.p.m.				
	H^2	$H^{4,5}$	CH_2CH_3	NCH_3	CH_2CH_3
1.3442	9.47	7.49	4.09	3.77	1.23
0.6721	9.59	7.48	4.15	3.83	1.32
0.3361	9.74	7.45	4.22	3.91	1.41
0.1680	9.77	7.42	4.23	3.92	1.42
0.0840	9.85	7.37	4.24	3.93	1.45
0.0420	9.90	7.32	4.25	3.94	1.47
0.0210	9.96	7.26	4.25	3.94	1.48
0.0105	10.02	7.20	4.24	3.94	1.49
5.251×10^{-3}	10.07	7.16	4.24	3.94	1.49
2.625×10^{-3}	10.09	7.15	4.24	3.94	1.49
1.313×10^{-3}	10.13	7.12	4.23	3.94	1.49
6.563×10^{-4}	10.66	7.10	4.23	3.94	1.50

Table 18. ^{35}Cl NMR (35.29 MHz; 303 K) Spectral Data for Solutions of [MeEtim]Cl in CD_2Cl_2.

Conc/*M*	δ/p.p.m.	$\Delta\nu_{\frac{1}{2}}$/Hz
2.0722	47.1	189
1.0361	43.8	134
0.5181	41.8	99
0.2590	40.3	91
0.1295	38.8	77
0.0648	37.6	68
0.0324	35.8	85
0.0162	35.0	58
0.0081	34.5	61

^{35}Cl NMR Spectra of Solutions of [MeEtim]Cl in CD_2Cl_2

The ^{35}Cl NMR data for [MeEtim]Cl in CD_2Cl_2 are presented in Table 18 and Figures 25 and 26. The ^{35}Cl NMR chemical shifts of [MeEtim]Cl solutions in CD_2Cl_2 show a marked change in chemical shift as the solution is diluted. The reasons for this will be considered in the Discussion section.

^{127}I NMR Spectra of Solutions of [MeEtim]I in CD_2Cl_2

The ^{127}I NMR data for solutions of [MeEtim]I in CD_2Cl_2 are presented in Table 19 and Figures 27 and 28. The effect of dilution on the ^{127}I NMR chemical shifts is qualitatively similar to the behaviour of ^{35}Cl NMR chemical shifts of solutions of [MeEtim]Cl in CD_2Cl_2.

Table 19. **^{127}I NMR (72.08 MHz; 303 K) Spectral Data for Solutions of [MeEtim]I in CD_2Cl_2.**

Conc/*M*	δ/p.p.m.	$\Delta\nu_{\frac{1}{2}}$/Hz
1.3442	139.3	6660
0.6721	128.1	5580
0.3361	122.2	4900
0.1680	118.4	4490
0.0840	110.5	3790
0.0420	106.5	3740
0.0210	104.4	3250

Conductivity of Solutions of [MeEtim]Cl

The conductivities, K, of solutions of [MeEtim]Cl in water, ethanenitrile and dichloromethane were measured at 25 °C. Their molar conductivities, Λ_m, were calculated from equation (2), were *c* is the molar concentration (20).

$$\Lambda_m = K/c \tag{2}$$

$$\Lambda_m = (\Lambda_m)_0 - \alpha c^{\frac{1}{2}} \tag{3}$$

Equation (3) gives a common form of the Onsager limiting law, where $(\Lambda_m)_0$ is the limiting molar conductivity, and α is the Onsager coefficient, and this equation was used to fit the experimental data by a conventional least-squares linear regression procedure, as shown in Figure 29. The limiting conductance of the solutions at infinite dilution and the molar conductance at a concentration of 10^{-3} *M* are presented in Table 20.

Table 20. **The limiting and molar conductances of solutions of [MeEtim]Cl.**

Solvent	$(\Lambda_m)_0$/S cm^2 mol^{-1}	Λ_m/S cm^2 mol^{-1} [a]
H_2O	111 ± 4	109 ± 4
CH_3CN	168 ± 4	164 ± 4
CH_2Cl_2	2.4 ± 0.3	1.6 ± 0.3

[a] At 10^{-3} *M*.

The values of $(\Lambda_m)_0$ for solutions of [MeEtim]Cl in H_2O lie within the range found for tetraalkylammonium salts (95–122 S cm^2 mol^{-1}) (20), unambiguously and unsurprisingly identifying the solution species as a 1:1 electrolyte. The value of $(\Lambda_m)_0$ for solutions of [MeEtim]Cl in ethanenitrile also lie within the range found for tetraalkylammonium salts (162–196 S cm^2 mol^{-1}) (21,22), again identifying the solution species as a 1:1 electrolyte. The difference in the slope of the plots of the conductance of [MeEtim]Cl in water and ethanenitrile {gradient(H_2O)/gradient(CH_3CN) = 0.39} indicates that cation–anion association is greater in solutions in ethanenitrile than in aqueous solutions. Hence, the solvation of [MeEtim]Cl in ethanenitrile can be described by the equilibrium between the solvated ion pair and the solvated unassociated ions, equation (4).

$$([\text{MeEtim}]^{+}\ldots\text{Cl}^{-})_{\text{MeCN}} \rightleftharpoons ([\text{MeEtim}]^{+})_{\text{MeCN}} + (\text{Cl}^{-})_{\text{MeCN}} \qquad (4)$$

The value of $(\Lambda_m)_0$ for tetraalkylammonium salts in dichloromethane could not be found in the literature, and so $(\Lambda_m)_0$ for tetraethylammonium chloride was measured {$(\Lambda_m)_0$ = 28 ± 2 S cm^2 mol^{-1}; Λ_m (10^{-3} *M*) = 26 ± 2 S cm^2 mol^{-1}}. The value of $(\Lambda_m)_0$ for solutions of [MeEtim]Cl in dichloromethane is significantly lower than that for tetraethylammonium chloride, indicating that the solution species is not a 1:1 electrolyte, but probably contains non–conducting *quasi*–molecular ion–pairs.

DISCUSSION

SYNTHESIS OF 1-METHYL-3-ETHYLIMIDAZOLIUM HALIDES

The 1–methyl–3–ethylimidazolium halides ([MeEtim]X; X = Cl, Br, or I) are white, crystalline solids at room temperature. [MeEtim]I was first prepared by the addition of iodoethane to a solution of 1–methylimidazole in dry ethanenitrile (11). Preparation of the salts by the addition of the appropriate haloethane to a solution of 1–methylimidazole in dry benzene has been reported (23). However, although the bromide and iodide salts were successfully isolated as solids, [MeEtim]Cl was originally reported as a liquid (23).

[MeEtim]Cl was successfully prepared as a solid by the reaction of 1-methylimidazole with chloroethane in a pressure vessel at 70 °C (2). Subsequently, both [MeEtim]Br (24) and [MeEtim]I (4) have been prepared by direct combination of the haloethane and 1-methylimidazole. The crude products from these preparations were recrystallised from solution in ethanenitrile by the addition of ethyl ethanoate.

The principal difference between the previous successful preparations (2,23) of the [MeEtim]X (X = Cl, Br or I) salts and those reported here is the method of recrystallisation. Ethyl ethanoate was used as a co-solvent in the recrystallisation to ensure that all of the unreacted 1-methylimidazole was removed from the product. However, removal of ethyl ethanoate from the product proved to be difficult. Therefore, the final recrystallization was from ethanenitrile alone. [MeEtim]I is photosensitive, turning yellow on exposure to light. Hence, the preparation was protected from light at all times.

NMR SPECTRA OF [MeEtim]Cl-AlCl$_3$ IONIC LIQUIDS

^{1}H NMR spectra of room temperature [MeEtim]Cl-AlCl$_3$ ionic liquids are known to be very composition dependent, particularly in the basic régime (3,25). In particular, the H^2 proton is very sensitive, moving significantly upfield with increasing acidity. This has been widely interpreted in terms of a stacked oligomeric model (3,5) in which anions and cations alternate, the anions being associated with the imidazolium ring both directly above and below its plane. The presence of hydrogen-bonds was dismissed, "since no hydrogen bonding is possible (*sic*)" (3). Nevertheless, a ^{1}H NMR study (26) of several imidazole and imidazolium derivatives in CD$_2$Cl$_2$ has shown that the chemical shift of the H^2 proton was sensitive to the nature of the anion present, and hydrogen-bonding between discrete ion pairs was postulated to explain this result (26). We thus decided to undertake a definitive study of the NMR characteristics of [MeEtim]X (X = Cl, Br or I) in molecular solvents, free of the aporia associated with ionic liquids.

As a preliminary to this study, we reexamined the ^{1}H and ^{13}C NMR spectra (at high field) of the ionic liquids themselves. We find ourselves in total accord with the published data (allowing for differences in referencing technique), and have used this study to definitively assign the spectra (for the first time), using the nuclear Overhauser effect.

NMR SPECTRA OF [MeEtim]Cl IN D$_2$O

The strong hydrogen-bonding ability of water ensures that the cations and anions of [MeEtim]Cl remain solvent-separated, irrespective of concentration. Thus, the ^{1}H NMR chemical shift data are essentially concentration independent (see Table 5). However, evidence of H/D exchange at H^2, H^4, and H^5 was obtained, and this effect was markedly enhanced by the addition of Na[OD] (see Table 6).

[MeEtim]X IN ETHANENITRILE

Conductivity measurements (20) show that [MeEtim]Cl behaves as a classical 1:1 electrolyte in MeCN (and in water); see Fig. 29. Concentration dependent ^{1}H NMR spectra were recorded for [MeEtim]X (X = Cl, Br or I) in CD$_3$CN, and the NCH_3,

$-CH_2CH_3$ (Fig. 13) and $-CH_2CH_3$ (Fig. 14) signals show the expected insensitivity towards concentration; the H^2 proton shift moves to lower field as the concentration of the solution increases (Fig. 11), and the H^4/H^5 signals behave in a similar manner, though with a smaller overall effect (Fig. 12). This is the change in chemical shift with concentration which has long been recognized as being indicative of hydrogen bond formation (27). The effect decreases in the order Cl > Br > I, again consistent with their relative hydrogen-bonding abilities. The simplest equilibrium which can be written to describe this situation is that given in equation (1). Thus, at high solution concentrations, the halide ion is very effectively hydrogen-bonded to the cation, and this is nicely illustrated by the concentration dependence of the ^{35}Cl (Fig. 16) and ^{127}I (Fig. 19) NMR spectra of [MeEtim]Cl and [MeEtim]I in CD_3CN, respectively. The contrast between the behaviour of [MeEtim]Cl and $[NEt_4]Cl$ (Fig. 16) is particularly important in illustrating the effectiveness of the hydrogen bonds formed between $[MeEtim]^+$ and Cl^-.

There can be no doubt that the combined evidence of conductivity measurements and multinuclear NMR spectroscopy overwhelmingly argues that all three of the ring protons are involved in hydrogen bonding with halide anions. The position that "no hydrogen bonding is possible" is no longer tenable.

The implications of these observations for the structure of basic ionic liquids is clear. They must now be considered not as statistical aggregates of anions and cations, but as a three-dimensional network of anions and cations, linked by a network of fragile hydrogen bonds; each cation will be hydrogen bonded to three anions, *via* H^2, H^4 and H^5, and their affinity for Cl^- will be much greater than that for $[AlCl_4]^-$.

[MeEtim]X IN DICHLOROMETHANE

In contrast to the situation found in ethanenitrile, with increasing concentration in dichloromethane, the H^2 proton signal of [MeEtim]X moves to higher field, whilst the H^4/H^5 signal moves to lower field (Fig. 24). Moreover, the solution is essentially non-conducting (Fig. 29). This suggests a system in which the imidazolium rings are so strongly hydrogen-bonded to the halide ions that they form a *quasi*-molecular species, [(MeEtim)X]. These then stack parallel to each other (in the manner of conventional neutral aromatic systems in a low dielectric constant medium) with the H^2 proton inside, and the H^4/H^5 protons outside, the shielding cone of the neighbouring ring (Fig. 30). The existence of such a stacking phenomenon has recently been confirmed in the solid state, as it was observed in the X-ray crystal structure of $[Me_2Etim]Cl.H_2O$ (28).

The evidence for stacking will now be considered in more detail. The effects of magnetic anisotropy of conjugated systems in NMR spectroscopy are well known (29): the ^1H NMR signal of benzene is significantly downfield of that of ethane. This behaviour has been attributed, classically, to the formation of an electronic ring current in the π-orbitals, which produces a secondary magnetic field which opposes the applied magnetic field, so increasing the field outside the ring and deshielding the benzene protons (30). This is a general effect, and is demonstrated in heterocyclic compounds such as pyridine, although the electronegativity of the ring nitrogen and its lone pairs reduce the symmetry of the induced magnetic field so that the 2,6-protons are more deshielded than the 4-protons, which in turn are more deshielded than the

3,5-protons (31).

The ring current effect also operates within a conjugated ring, decreasing the magnetic field which gives rise to the high field chemical shifts of internal protons such as is seen in the ^1H NMR spectra of some porphyrins (32). The ^1H NMR spectra of 1,4-polymethylene benzenes demonstrate that this behaviour extends beyond the plane of the ring, since the methylene protons which lie close to the benzene ring and above it experience a strong upfield shift (33). This effect may also be intermolecular, as is demonstrated by the effect of adding benzene to NMR samples in non-aromatic solvents to produce shifts to high field (34). The effects of ring currents may be visualised as shielding cones above and below the plane of the ring (35).

The crystal structure of [MeEtim]I (4) reveals that the imidazolium ring is conventionally aromatic and, therefore, capable of sustaining a ring current. It is the effects of this ring current which are observed in the NMR chemical shift data of solutions of [MeEtim]X (X = Cl, Br or I) in CD_2Cl_2. At high concentration, the discrete [MeEtim]X (X = Cl, Br or I) ion-pairs are in close proximity to each other, and protons which lie inside the shielding cone of the imidazolium ring of neighbouring ion-pairs experience an upfield chemical shift whilst protons which lie outside the shielding cone (but close to the ring) experience a downfield chemical shift. As the solution is diluted, the separation of neighbouring ion-pairs becomes greater, and the intermolecular ring current effects diminish. Therefore, the chemical shifts of protons lying inside the shielding cone of neighbouring ion-pairs move downfield with dilution of the solution and protons lying outside the shielding cone (but close to the ring move) upfield with dilution. This identifies the H^2 proton as lying inside, and the H^4 and H^5 protons as lying outside, the shielding cone of neighbouring ion-pairs. All other protons are sufficiently distant from the ring that the ring current effects are negligible.

This suggests a model for the structure of [MeEtim]X (X = Cl, Br or I) in CD_2Cl_2 in which the imidazolium rings arrange in a stack with the rings parallel and staggered (Fig. 30). This type of stacking behaviour is seen in the crystal structure of imidazolium dihydrogenphosphate (36), in which columns of stacked imidazolium rings, with any two adjacent rings related by a centre of symmetry (staggered), are seen.

It should be noted that the stacking of [MeEtim]X (X = Cl, Br or I) ion-pairs in CD_2Cl_2 is not the same as the oligomeric stacks of alternating cations and anions in the model of the [MeEtim]Cl-$AlCl_3$ ionic liquids proposed by Wilkes and coworkers (3). Firstly, the ion-pairs in CD_2Cl_2 have no nett charge, and so may approach each other without large coulombic repulsion; secondly, the large anion sandwiched between two rings would prevent the rings from coming close enough for intermolecular ring current effects to be seen.

The ^{35}Cl NMR data for [MeEtim]Cl solutions in CD_2Cl_2 show a marked change in chemical shift as the solution is diluted. This was somewhat surprising since, although some evidence for ring current effects in ^{13}C NMR spectroscopy has been reported (37-39), these are rarely unambiguous (40,41), and discussion of ring currents has been almost entirely in terms of their effect on proton NMR chemical shifts.

The change in ^{35}Cl chemical shifts of solutions of [MeEtim]Cl from lower to higher field with decreasing concentration (Fig. 25) indicates that the Cl^- ion of the ion–pair lies outside the shielding cone of neighbouring imidazolium rings. Clearly, then, the Cl^- ion cannot lie directly above the imidazolium ring, but must be positioned closer to the plane of the ring, as suggested in Fig. 30.

Analogous results (Fig. 27) for [MeEtim]I in CD_2Cl_2 indicate that the I^- ion lies outside the shielding cone of neighbouring imidazolium rings, and close to the plane of the imidazolium ring in the $[MeEtim]^+ \ldots I^-$ ion–pair. This is in agreement with the X–ray crystal structure of [MeEtim]I (4).

ACKNOWLEDGMENTS

We are indebted to the BP Venture Research Unit for their generous funding of this research, and to Dr. J.S. Wilkes for a copy of ref. 7 prior to its publication

REFERENCES

1. C.L. Hussey, *Adv. Molten Salt Chem.*, 5, 185 (1983).

2. J.S. Wilkes, J.A. Levisky, R.A. Wilson and C.L. Hussey, *Inorg. Chem.*, **21**, 1263 (1982).

3. A.A. Fannin, Jr., L.A. King, J.A. Levisky and J.S. Wilkes, *J. Phys. Chem.*, **88**, 2609 (1984).

4. A.K. Abdul–Sada, A.M. Greenway, P.B. Hitchcock, T.J. Mohammed, K.R. Seddon and J.A. Zora, *J. Chem. Soc., Chem. Commun.*, 1753 (1986).

5. K.M. Dieter, C.J. Dymek, Jr., N.E. Heimer, J.W. Rovang and J.S. Wilkes, *J. Am. Chem. Soc.*, 110, 2722 (1988).

6. C.J. Dymek, Jr. and J.J.P. Stewart, *Inorg. Chem.*, **28**, 1472 (1989).

7. C.J. Dymek, Jr., D.A. Grossie, A.V. Fratini and W.W. Adams, *J. Mol. Struct.*, 213, 25 (1989).

8. A.K. Abdul–Sada, S. Al–Juaid, A.M. Greenway, P.B. Hitchcock, M.J. Howells, K.R. Seddon and T. Welton, *Struct. Chem.*, in press.

9. S. Tait and R.A. Osteryoung, *Inorg. Chem.*, **23**, 4352 (1984).

10. A.K. Abdul–Sada, A.G. Avent, M.J. Parkington, T.A. Ryan, K.R. Seddon and T. Welton, *J. Chem. Soc., Chem. Commun.*, 1643 (1987).

11. R.F. Borne, H.Y. Aboul–Enein and J.K. Baker, *Spectrochim. Acta, Part A*, **28**, 393 (1972).

12. J.W. Akitt, "N.M.R. and Chemistry: An Introduction to the Fourier Transform – Multinuclear Era", 2nd Edition, Chapman and Hall, London, 1983.

13. J.S. Wilkes, J.S. Frye and G.F. Reynolds, *Inorg. Chem.*, **22**, 3870 (1983).

14. M. Nakano, N.I. Nakano and T. Higuchi, *J. Phys. Chem.*, **71**, 3954 (1967).

15. H. Shanan–Atidi and K.H. Bar–Eli, *J. Phys. Chem.*, **74**, 961 (1970).

16. R. Mathur, E.D. Becker, R.B. Bradley and N.C. Li, *J. Phys. Chem.*, **67**, 2190 (1963).

17. C.H. Langford and T.R. Stengle, *J. Am. Chem. Soc.*, **91**, 4014 (1969).

18. T.R. Stengle, Y.–C.E. Pan and C.H. Langford, *J. Am. Chem. Soc.*, **94**, 9037 (1972).

19. C. Hall, G.L. Haller and R.E. Richards, *Mol. Phys.*, **16**, 377 (1969).

20. W.J. Geary, *Coord. Chem. Rev.*, **7**, 81 (1971).

21. J.F. Coetzee and G.P. Cunningham, *J. Am. Chem. Soc.*, **87**, 2529 (1965).

22. A.C. Harkness and H.M. Daggett, *Canad. J. Chem.*, **43**, 1215 (1965).

23. B.K.M. Chan, N.–H. Chang and M.R. Grimmel, *Aust. J. Chem.*, **30**, 2005 (1977).

24. J.R. Sanders, E.H. Ward and C.L. Hussey, *J. Electrochem. Soc.*, **133**, 325 (1986); **133**, 1526 (1986).

25. J.S. Wilkes, C.L. Hussey and J.R. Sanders, *Polyhedron*, **5**, 1567 (1986).

26. S.A. Lapshin, A.Yu. Chervinskii, L.M. Litvinenko, V.A. Dadali, L.M. Kapkan and A.N. Vdovichenko, *Zh. Org. Khim.*, **21**, 357 (1985).

27. M. Nakano, N.I. Nakano and T. Higuchi, *J. Phys. Chem.*, **71**, 3954 (1967).

28. A. Elaiwi, P.B. Hitchcock, K.R. Seddon and T. Welton, unpublished observations (1989).

29. C.W. Haig and R.B. Mallion, *Prog. Nucl. Magn. Reson. Spectrosc*, **13**, 303 (1980).

30. L. Pauling, *J. Chem. Phys.*, **4**, 673 (1936).

31. W.G. Schneider, H.J. Bernstein and J.A. Pople, *Canad. J. Chem.*, **35**, 1487 (1957).

32. E.D. Becker and R.B. Bradley, *J. Chem. Phys.*, **31**, 1413 (1959).

33. J.S. Waugh and R.W. Fessenden, *J. Am. Chem. Soc.*, **79**, 846 (1957).

34 A.D. Buckingham, T. Schaefer and W.G. Schneider, *J. Chem. Phys.*, **32**, 1227 (1960).

35. C.E. Johnson, Jr. and F.A. Bovey, *J. Chem. Phys.*, **29**, 1012 (1958).

36. R.H. Blessing and E.L. McGaudy, *J. Am. Chem. Soc.*, **94**, 4034 (1972).

37. T.D. Alger, D.M. Grant and E.G. Paul, *J. Am. Chem. Soc.*, **88**, 5397 (1966).

38. A.J. Jones, P.J. Garratt and K.P.C. Vollhart, *Angew. Chem., Int. Edit. Engl.*, **12**, 241 (1973).

39. B.M. Trost and W.B. Herdle, *J. Am. Chem. Soc.*, **98**, 4080 (1976).

40. R.H. Levin and J.D. Roberts, *Tetrahedron Lett.*, **2**, 135 (1976).

41. H. Günther, H. Schmickler, H. Königshofen, K. Recker and E. Vogel, *Angew. Chem., Int. Edit. Engl.*, **12**, 243 (1973).

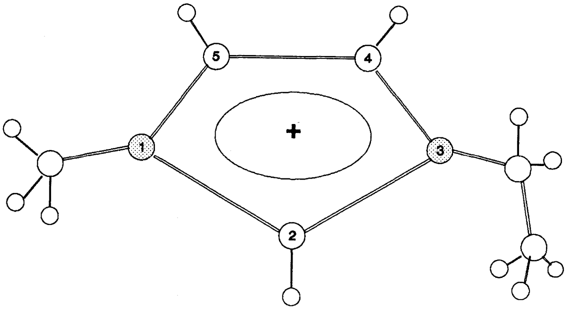

Figure 1. The 1-Methyl-3-ethylimidazolium Cation.

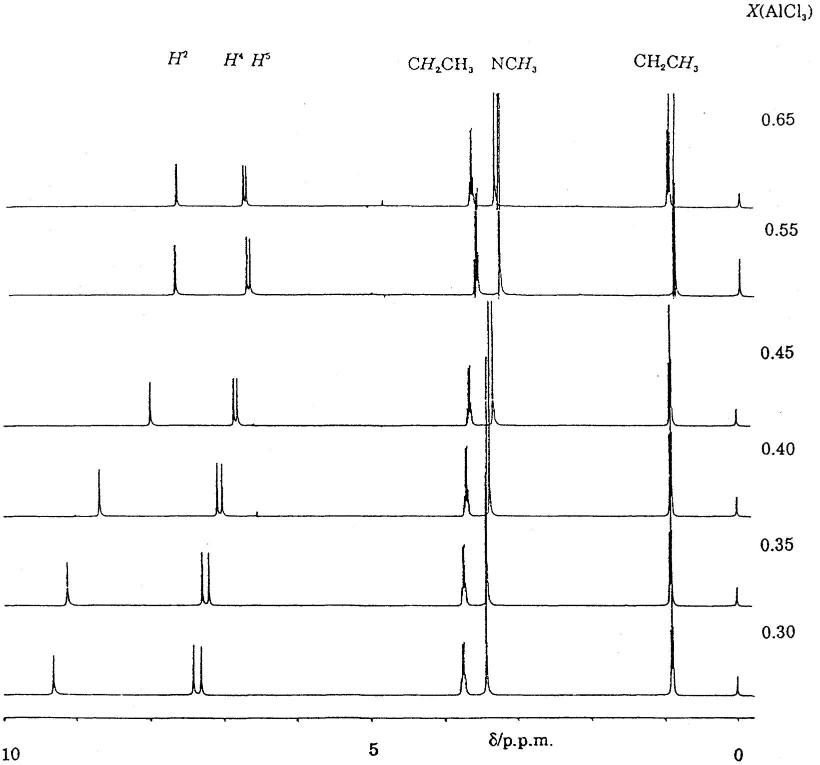

Figure 2. The ^{1}H NMR (360.13 MHz; 303 K) Spectra of a Series of [MeEtim]Cl–AlCl$_3$ Ionic Liquids.

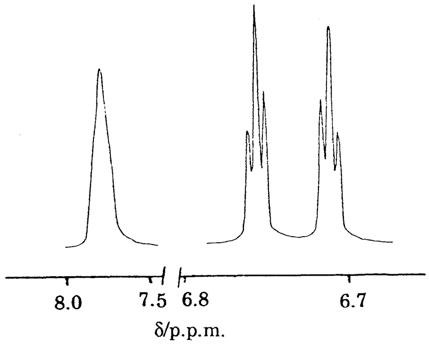

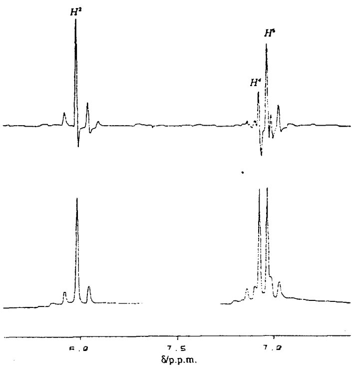

Figure 3. Partial ^1H NMR Spectrum (360.13 MHz; 303 K) of an Acidic (X = 0.60) Ionic Liquid (*Above Left*).

Figure 4. Partial ^1H NMR Spectra (360.13 MHz; 303 K) of (lower) Acidic (X = 0.60) Ionic Liquid and (upper) the NOE Spectrum of the Same Liquid with the NCH_3 Protons Irradiated (*Above Right*).

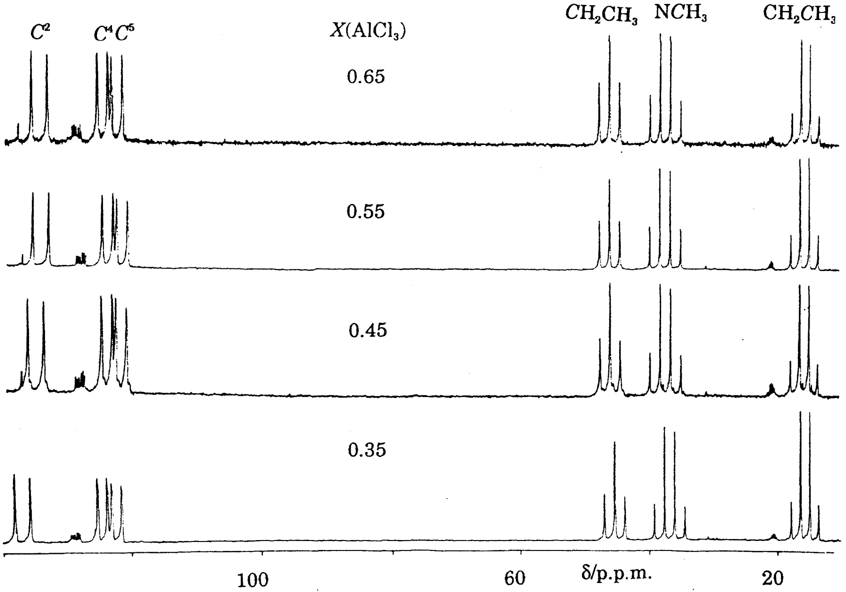

Figure 5. The ^{13}C NMR Spectra (90.55 MHz; 303 K) of a Series of [MeEtim]Cl–$AlCl_3$ Ionic Liquids.

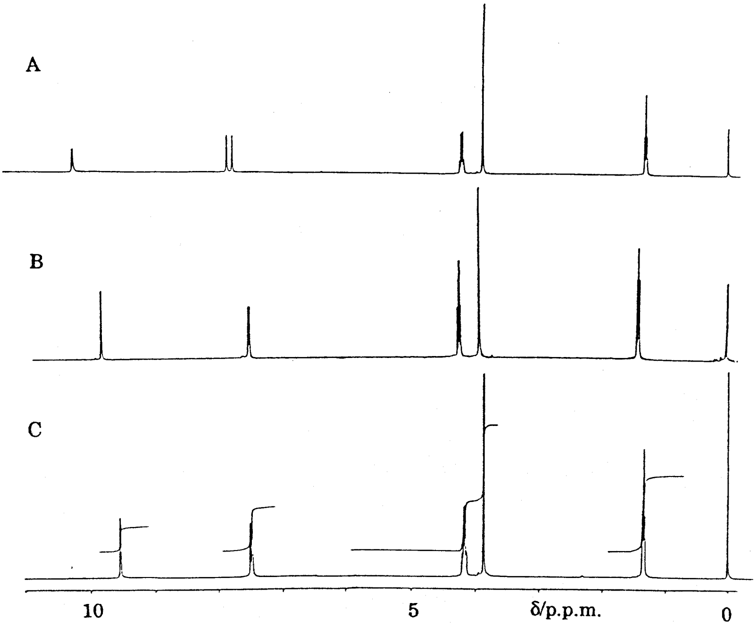

Figure 6. The ^{1}H NMR Spectra of (A) [MeEtim]Cl, (B) [MeEtim]Br and (C) [MeEtim]I (360.13 MHz; 2 M, $CDCl_3$; 303 K).

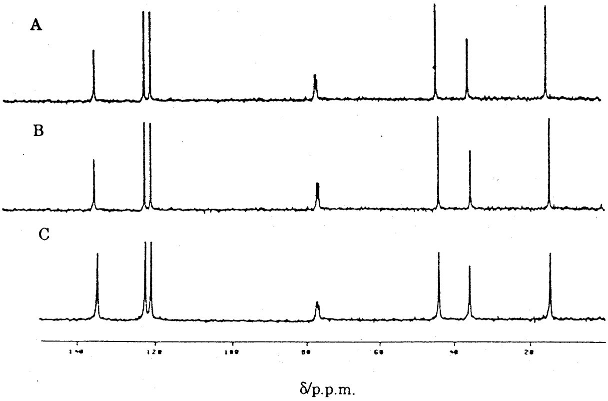

Figure 7. The ^{13}C NMR Spectra of (A) [MeEtim]Cl, (B) [MeEtim]Br and (C) [MeEtim]I (90.55 MHz; 2 M, $CDCl_3$; 303 K).

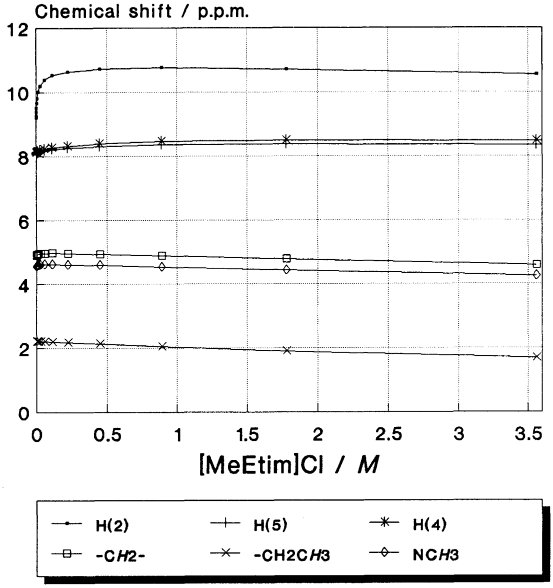

Figure 8. The ^1H NMR (360.13 MHz; 303 K) Chemical Shifts of Solutions of [MeEtim]Cl in CD_3CN as a Function of Concentration.

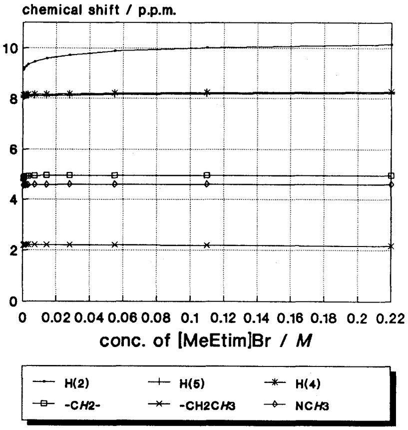

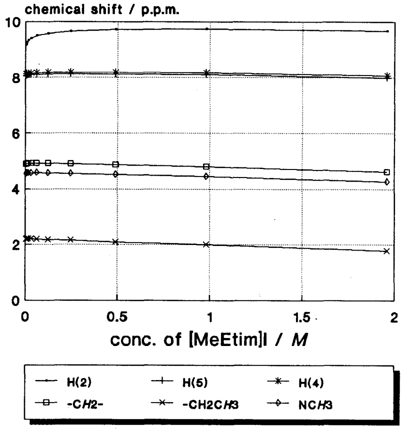

Figure 9. The ^1H NMR (360.13 MHz; 303 K) Chemical Shifts of Solutions of [MeEtim]Br in CD_3CN as a Function of Concentration (*Above Left*).

Figure 10. The ^1H NMR (360.13 MHz; 303 K) Chemical Shifts of Solutions of [MeEtim]I in CD_3CN as a Function of Concentration (*Above Right*).

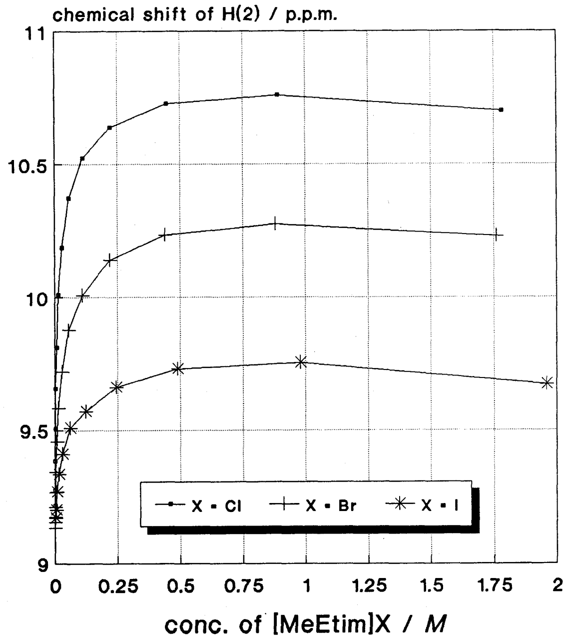

Figure 11. The Effect of Concentration upon the H^2 Chemical Shift for [MeEtim]X (X = Cl, Br or I) in CD_3CN.

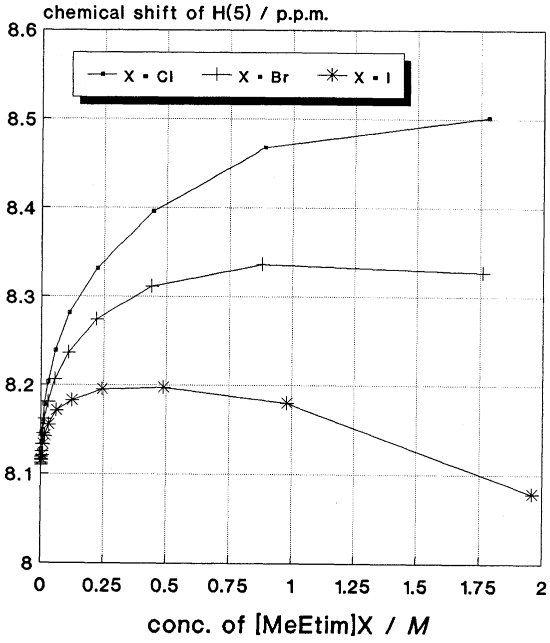

Figure 12. The Effect of Concentration upon the H^5 Chemical Shift for [MeEtim]X (X = Cl, Br or I) in CD_3CN.

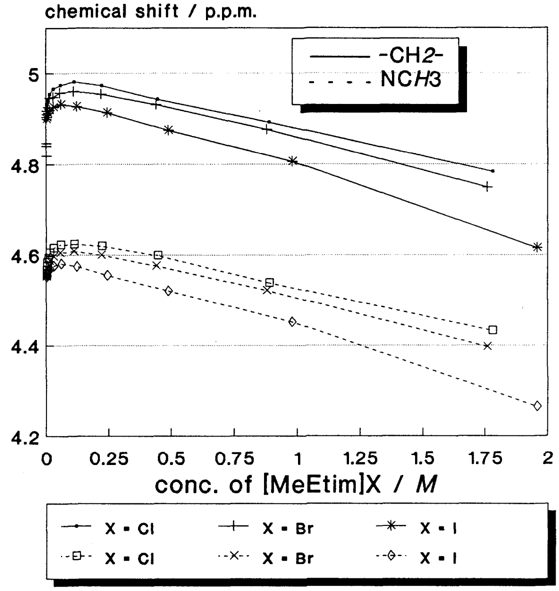

Figure 13. The Effect of Concentration upon the CH_2CH_3 and NCH_3 Chemical Shifts for [MeEtim]X (X = Cl, Br or I) in CD_3CN.

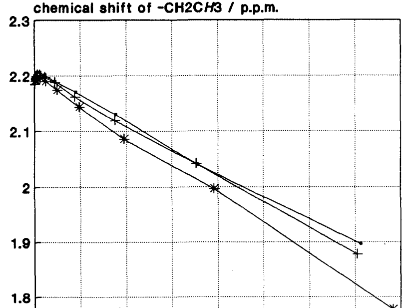

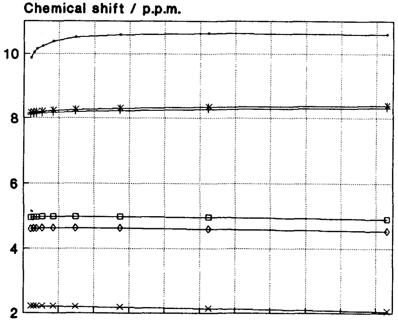

Figure 14. The Effect of Concentration upon the CH_2CH_3 Chemical Shift for [MeEtim]X (X = Cl, Br or I) in CD_3CN (*Above Left*).

Figure 15. ^1H NMR (360.13 MHz; 303 K) Chemical Shifts of Solutions of a Fixed Concentration of [MeEtim]Cl in CD_3CN, with Added $[NEt_4]Cl$, as a Function of the Chloride Ion Concentration (*Above Right*).

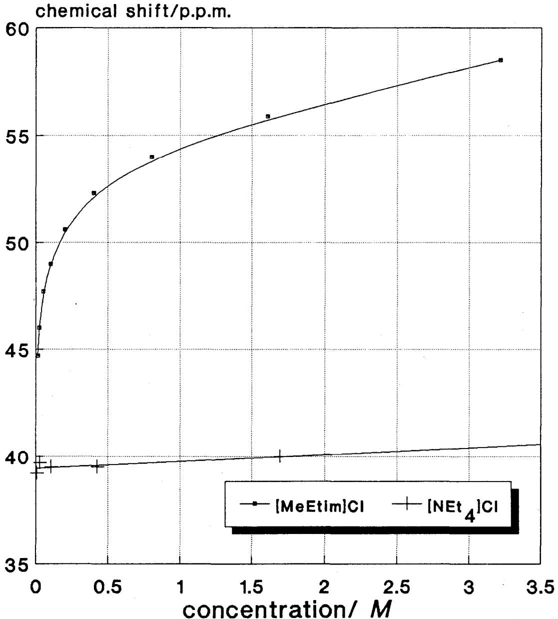

Figure 16. The Effect of Concentration on the ^{35}Cl Chemical Shift for [MeEtim]Cl or [NEt$_4$]Cl in CD_3CN.

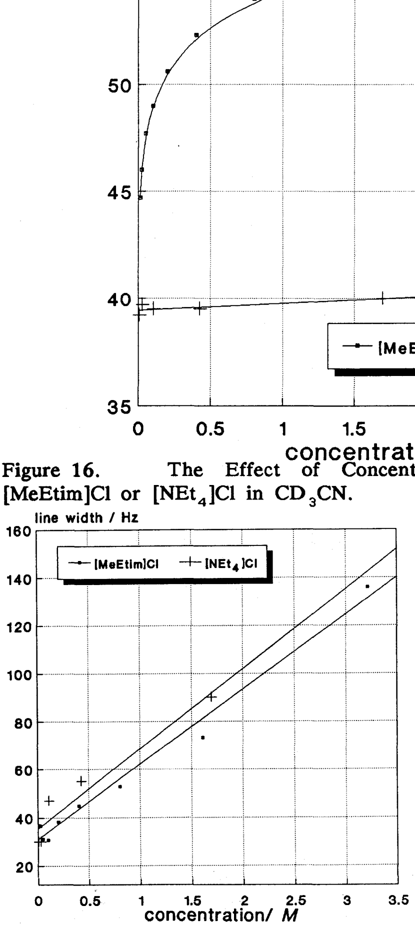

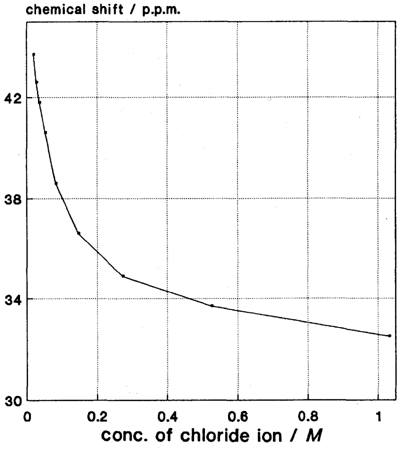

Figure 17. The Effect of Concentration on the Line Width of the ^{35}Cl NMR Signal of [MeEtim]Cl or [NEt$_4$]Cl in CD_3CN (*Above Left*).

Figure 18. ^{35}Cl NMR (35.29 MHz; 303 K) Chemical Shifts of Solutions of a Fixed Concentration of [MeEtim]Cl in CD_3CN, with Added [NEt$_4$]Cl, as a Function of the Chloride Ion Concentration (*Above Right*).

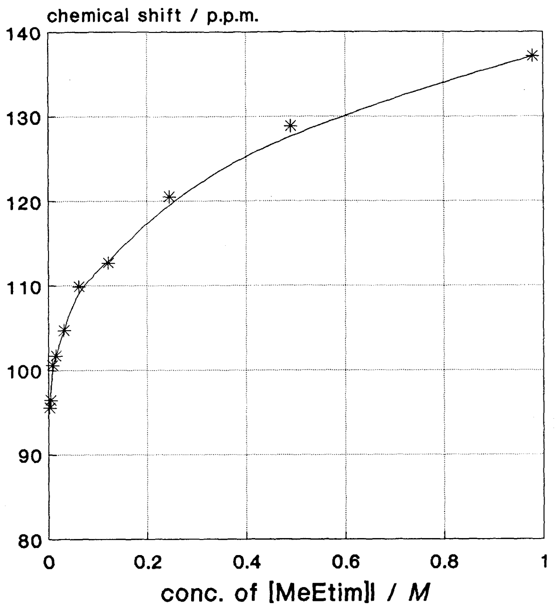

Figure 19. The Effect of Concentration upon the ^{127}I Chemical Shift of [MeEtim]I in CD_3CN.

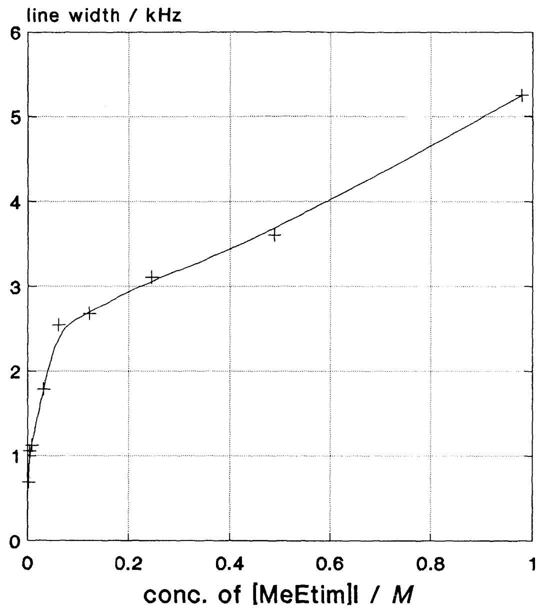

Figure 20. The Effect of Concentration upon the Line Width of the ^{127}I NMR Signal of [MeEtim]I in CD_3CN.

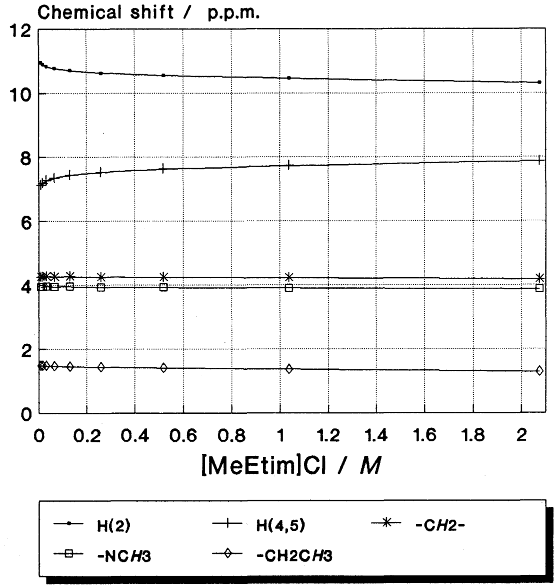

Figure 21. The ^{1}H NMR (360.13 MHz; 303 K) Chemical Shifts of Solutions of [MeEtim]Cl in CD_2Cl_2 as a Function of Concentration.

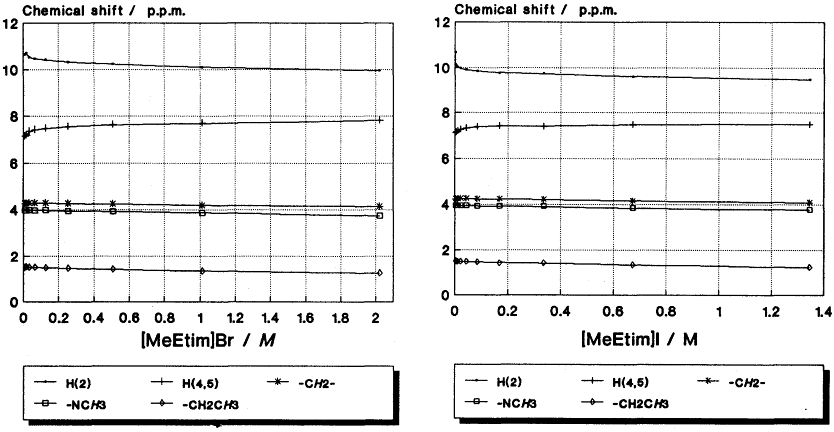

Figure 22. The ^{1}H NMR (360.13 MHz; 303 K) Chemical Shifts of Solutions of [MeEtim]Br in CD_2Cl_2 as a Function of Concentration (*Above Left*).
Figure 23. The ^{1}H NMR (360.13 MHz; 303 K) Chemical Shifts of Solutions of [MeEtim]I in CD_2Cl_2 as a Function of Concentration (*Above Right*).

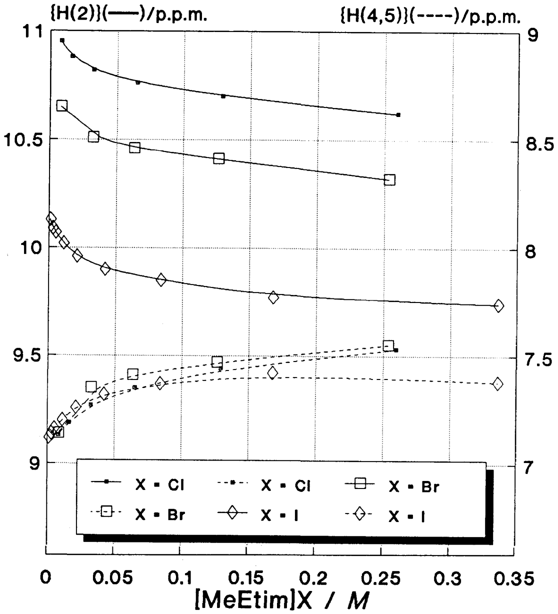

Figure 24. The Effect of Concentration upon the H^2 and $H^{4,5}$ Chemical Shifts for [MeEtim]X (X = Cl, Br or I) in CD_2Cl_2.

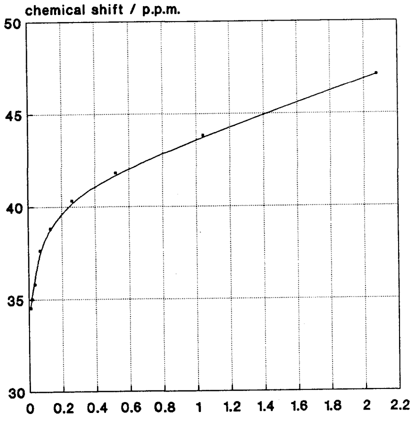

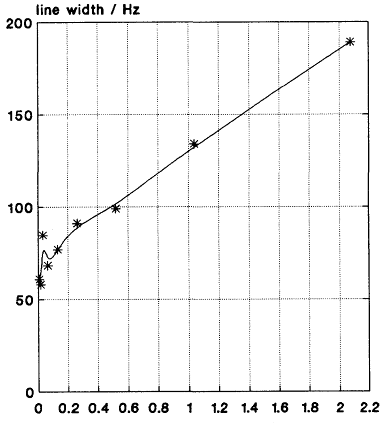

Figure 25. The Effect of Concentration upon the ^{35}Cl Chemical Shift of [MeEtim]Cl in CD_2Cl_2 *(Above Left)*.

Figure 26. The Effect of Concentration upon the Line Width of the ^{35}Cl NMR Signal of [MeEtim]Cl in CD_2Cl_2 *(Above Right)*.

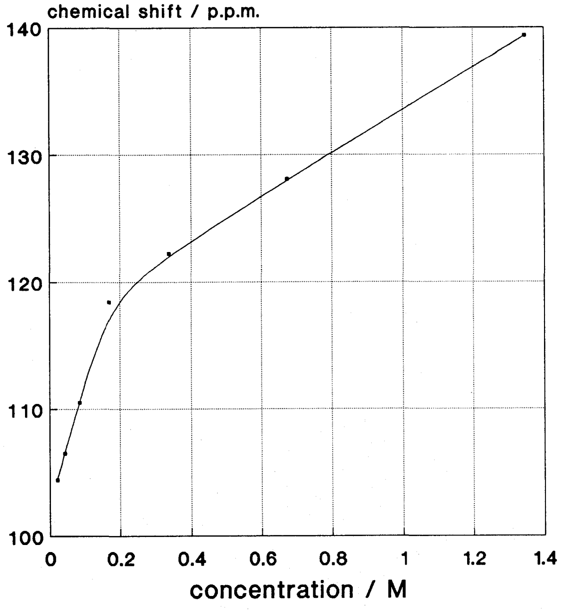

Figure 27. The Effect of Concentration upon the ^{127}I Chemical Shift of [MeEtim]I in CD_2Cl_2.

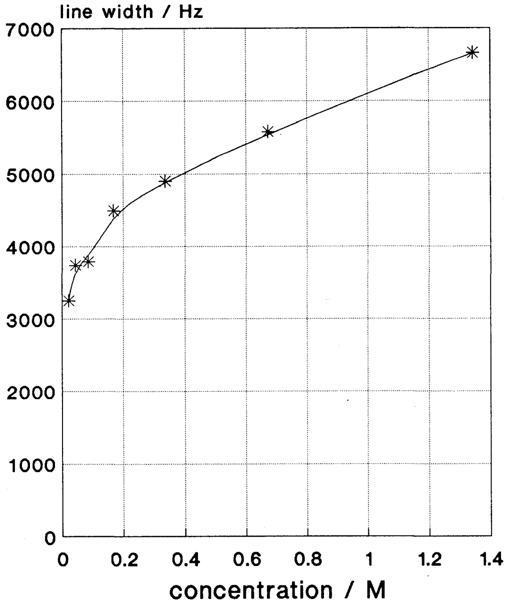

Figure 28. The Effect of Concentration upon the Line Width of the ^{127}I NMR Signal of [MeEtim]I in CD_2Cl_2.

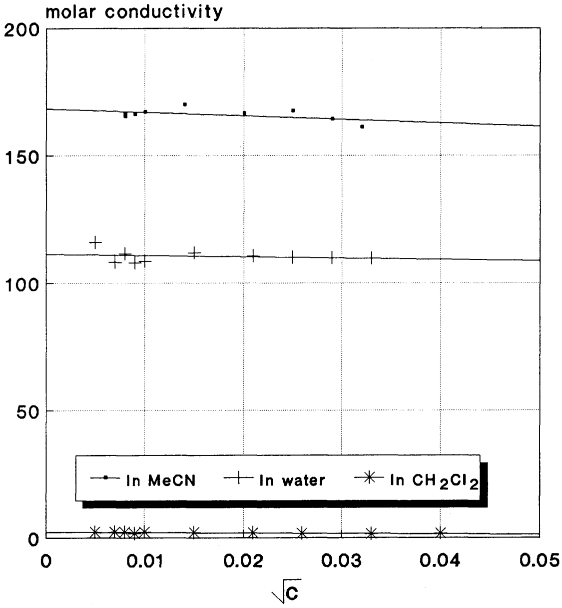

Figure 29. The Molar Conductivity (units of S cm^2 mol^{-1}) of [MeEtim]Cl as a Function of $c^{\frac{1}{2}}$ (units of $mol^{\frac{1}{2}}$ $l^{-\frac{1}{2}}$).

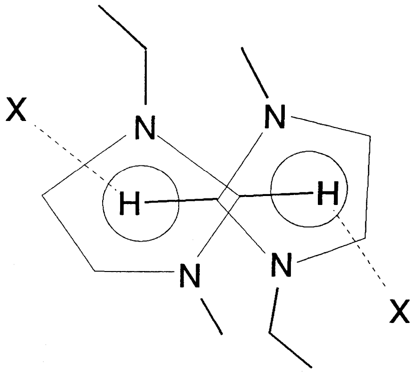

Figure 30. The Proposed Structure for the Stacks of *Quasi*–molecules of [(MeEtim)X] in Solution in Dichloromethane.

DOI: 10.1149/199017.0134PV

STRUCTURAL ANALYSIS OF AN AMBIENT TEMPERATURE MOLTEN SALT

Donald M. MacArthur, Gholam-Abbas Nazri, and Ricardo Aroca*

Physical Chemistry Department
General Motors Research Laboratories
Warren, MI 48090-9055

*University of Windsor
Windsor, Ontario, Canada

ABSTRACT

Ambient temperature ionic melts with high ionic conductivity are very attractive electrolytes for batteries and for electroplating of technologically important alloys. We studied the ion-ion interactions in a melt containing 1-methyl, 3-ethylimidazolium chloride (MEICl) and $AlCl_3$ using vibrational spectroscopy. In basic melts ($AlCl_3 <$ MEICl) there appears to be ion pair formation involving strong interaction of Cl^- with MEI^+. The Cl^- interacts with the methyl and ethyl C-H bonds presumably through hydrogen-type bonding. The vibrational spectra of the acidic melt ($AlCl_3 >$ MEICl) can be interpreted as a stacked model of type $AlCl_4^-/MEI^+/Al_2Cl_7^-/MEI^+$. We also obtained some previously unpublished NMR data for a strongly basic composition. The FTIR data can be shown to be in agreement with the NMR data regarding the chemical shifts of the different C-H bonds, assuming that chemical shifts result from loss of aromaticity of the imidazole.

INTRODUCTION

Imidazolium chloride/$AlCl_3$ mixtures form ionic melts which are liquid at ambient temperature over a wide composition range. The ionic conductivities of these melts are comparable to high temperature molten salts (1). They are promising electrolytes for batteries and for the electrodeposition of metals, semiconductors and alloys. In this work, we investigate the molecular structure of the 1-methyl, 3-ethylimidazolium chloride (MEICl) melt. An understanding of the structure will be useful to further application of the melts.

Aluminum chloride reacts with MEICl to provide an ionic melt which is liquid at ambient temperatures in the range of 30 to 70 mole% $AlCl_3$. The ionic melt of $AlCl_3$/MEICl has acid - base character depending upon the ratio of the $AlCl_3$ to MEICl. At $AlCl_3$/MEICl < 50 mole% the melt contains the Lewis base, Cl^-, and for $AlCl_3$/MEICl > 50 mole% the melt contains the Lewis acid, $Al_2Cl_7^-$. The melt is neutral when equal moles of $AlCl_3$ and MEICl are mixed. The ionic species in the basic, neutral and acidic melts are postulated as the following;

$$xAlCl_3 + yMEICl \xrightarrow[\text{Basic}]{x < y} xAlCl_4^- + yMEI^+ + (y-x)Cl^-$$

$$AlCl_3 + MEICl \xrightarrow[\text{Neutral}]{AlCl_3/MEICl = 1} AlCl_4^- + MEI^+$$

$$xAlCl_3 + yMEICl \xrightarrow[\text{Acidic}]{x > y} (2y-x)AlCl_4^- + (x-y)Al_2Cl_7^- + yMEI^+$$

The relative concentrations of each anion species has been summarized in the literature (2).

The Cl^- fraction decreases smoothly from unity in the most basic condition to essentially zero at the neutral point and remains at this value through the acid range. The tetrachloroaluminate fraction reaches essentially unity at the neutral point and the sum of the tetrachloroaluminate and heptachloroaluminate fractions remains essentially unity through the acid range.

The molecular structure of MEI^+, $AlCl_4^-$ and $Al_2Cl_7^-$ are shown below. We will refer to the subscripts shown for the atoms of the imidazole ring. Note that the methyl groups may rotate freely in the MEI molecule.

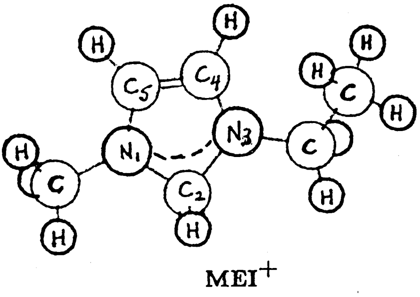

MEI^+

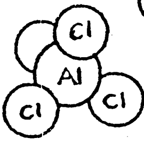

$AlCl_4^-$

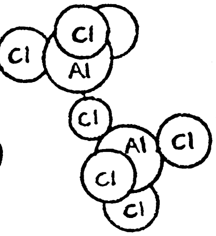

$Al_2Cl_7^-$

The molecular structure of the basic $MEICl/AlCl_3$ has been treated theoretically by Dieter et al. (3) using AMI and MNDO calculations. According to them, the optimized configuration of the $AlCl_4^-$-MEI^+-Cl^- system tends to be a sandwich type, with Cl^- located between two parallel MEI^+ and with two $AlCl_4^-$; one located above and one below the two MEI^+. This stack model can be shown as $AlCl_4^-/MEI^+/Cl^-/MEI^+/AlCl_4^-$. However, NMR studies show that the nature of the interaction of Cl^- and $AlCl_4^-$ with the MEI^+ ring is more complex (4). A crystal structure analysis of the iodine analog suggests hydrogen bond type interaction of iodine with the C_2 hydrogen (5). IR studies of the melt also suggest the interaction of the Cl^- anion with the C_2-H through a hydrogen bonding interaction (6). We have studied the ionic interaction of the negatively charged species with the MEI^+ ring and with the substituted aliphatic branches (methyl and ethyl groups) over the entire composition range.

EXPERIMENTAL

Materials

The 1-methyl, 3-ethylimidazolium chloride was prepared from methyl imidazole (Aldrich Chemicals) following the procedure described by Wilkes et al. (7). The salt was precipitated twice from ethyl acetate under a nitrogen atmosphere, dried and stored in an argon atmosphere dry box. The molten salt mixtures were prepared from this MEICl by careful addition of Alfa puratonics $AlCl_3$ in the required amount. (The strongly exothermic reaction can increase temperatures to where decomposition or polymerization reactions can occur.) Compositions are provided as the mole ratio of MEICl to $AlCl_3$.

IR Spectroscopy

A diffuse reflectance (DRIFT) accessory from Spectra Technology, Inc. (model 30103) was used. The throughput of the IR spectrometer was reduced by a factor of 20 when this accessory was used. The sample preparation was done inside a dry box filled with argon. A drop of the liquid was placed on a polished, mirror surface of a platinum disk and spread to form a uniform film. The platinum disk was sealed in the DRIFT accessory before transfer to the IR spectrometer. This procedure prevented any exposure of the sample to air and allowed purging and evacuation of the spectrometer during data collection. The spectra were obtained on an IBM - 98 spectrometer with the sample chamber under vacuum. A glowbar IR source and a liquid nitrogen cooled mercury-cadmium-teluride (MCT) detector were used. The DRIFT accessory with a platinum disk without the sample was used as a reference. Spectra were collected at room temperature and at 500 scans.

NMR Spectroscopy

^1H NMR spectra of the 1-methyl,3-ethylimidazolium chloride - $AlCl_3$ mixtures were recorded with a Bruker FT-NMR spectrometer. The NMR measurements were carried out for a composition of 30 mole% $AlCl_3$ between 27°C and 75°C using a Bruker BVT-1000 temperature controller. The sample was in a sealed NMR tube under He atmosphere. The chemical shifts were referenced to an external dimethyl sulfoxide solution. The resonance frequency of ^1H NMR was 270 MHz.

RESULTS AND DISCUSSIONS

The IR spectra are shown in Figures 1, 2 and 3 which encompass the range 400-1200, 1100-2200, and 2500-3300 cm^{-1}, respectively. The band assignments are shown in Table 1. These assignments were made using Tait and Osteryoung (6) as the primary source and empirical structure assignments (8) as a secondary source. Notable differences from Tait and Osteryoung are: the assignment of 705 cm^{-1} to a bending mode and not an impurity and the 1550-1840 cm^{-1} region to aromatic modes. The peak at 3049 cm^{-1} discussed by Dieter et al. (3) was not readily observed. It may be seen in the figures that the intensity ratios of the IR bands are changed markedly as a function of $AlCl_3$ salt concentration. We will first discuss the characteristics of the $AlCl_4^-$ symmetric vibrational mode, then the C-H bending and stretching modes of the aliphatic carbons and the ring carbons, and finally the bending and stretching modes of the aromatic ring.

The IR band at 680 cm^{-1} is assigned to the symmetric vibration of the $AlCl_4^-$ anion. The intensity of this band increased to a maximum at the neutral composition of $AlCl_3$/MEICl = 1. Further addition of $AlCl_3$ into the neutral melt resulted in a sharp decrease in the intensity of the band. This observation is in agreement with the postulated equilibrium conditions which exist between $AlCl_3$ and MEICl salts. At $AlCl_3$ concentrations less than MEICl concentration--basic melts--all the $AlCl_3$ interacts with the Cl^- anion to form $AlCl_4^-$. The concentration of $AlCl_4^-$ anion reaches a maximum at the neutral point. According to the well-established equilibrium described in the molten salt literature (9), $AlCl_3$ in excess of MEICl--acid melts--interacts with the $AlCl_4^-$ anion to form a dimer anion, $Al_2Cl_7^-$. The 680 cm^{-1} symmetric vibrational mode is not present in the dimer and the intensity of this band is very low in acid compositions.

The frequency of the C-H out-of-plane bending mode of the methyl and ethyl groups is located around 705 cm^{-1} and 830 cm^{-1}. The intensity of these bands was very low in the basic melts and increased in the acidic melts. The methyl and ethyl C-H rocking modes are observed in the 1100 to 1200 cm^{-1} region. These rocking modes are relatively stronger in the acidic melt compared to those in the basic melts. The methyl and ethyl C-H in-plane bending modes (around 1400 cm^{-1}) are weak in the basic melt and the intensity of this band increased significantly in the acidic melts. These observations suggest that, in the basic melt, with Cl^- present, the methyl and ethyl hydrogens are interacting strongly with Cl^-. This can be due to hydrogen type bonding between C-H and Cl^- in the basic melt.

An effect opposite to that for the aliphatic part of the molecule was observed for the C-H ring in-plane bending mode at 790 cm^{-1}. A strong IR band was observed in basic melts and a very weak IR band in the acidic melts.

The aliphatic C-H stretching vibrations are observed in the 2800 - 3200 cm^{-1}. These bands are stronger in the acidic melts compared to those in the basic melts and are consistent with the observations of the aliphatic C-H bending modes.

The aromatic and ring C-H stretching modes are observed in the range 3200 - 3400 cm^{-1}. These bands are stronger in the basic melts, also in contrast to the aliphatic modes.

The ring breathing mode was observed at 1470 cm^{-1}. This IR band is relatively strong in both basic and acidic melts and suggests that the ring breathing mode is not affected by the various anions. The C=C stretching mode appeared at 1520 cm^{-1}. This band is strong in basic melts but weak in acidic melt. The aromatic C-C stretching vibration is usually in the 1700 - 1850 cm^{-1} range. The IR bands at these frequencies are weaker in the acidic melt compared to in the basic melts. This result, along with the ring C-H bending and stretching modes suggests loss of ring aromaticity in acid. This conclusion was also reached by Tait and Osteryoung (6). This can be interpreted as the interaction of the chloroaluminate anions in the acidic melts with the π electrons of the imidazole.

The changes in the intensity of the methyl and ethyl C-H bending and stretching modes clearly show that in the basic melt there is a strong interaction between methyl and ethyl C-H with the anion. This interaction is much less in the acidic melts. The Cl^- apparently interacts more effectively with the C-H of the methyl and ethyl groups and the C_2-H of the ring than $AlCl_4^-$. There is also indication of slight changes in the intensity and frequency of the C_4-H and C_5-H vibrational modes in the basic melts. These observations indicate that the Cl^- is not in the plane of the MEI^+ ring. This slight out-of-plane geometry of Cl^- may also cause charge delocalization on one of the nitrogens which may provide a resonance stabilization in the basic melts. A striking observation is the lack of aromaticity in the acidic melts compared to the aromaticity in the basic melts. We interpret this as an indication that the chloroaluminate anions are stacking above and below the plane of the imidazole cation and interacting with the π electrons to destroy the aromatic character of the ring.

The NMR spectrum of a strongly basic melt (30 mole% $AlCl_3$) at ambient temperature, and at 50°C is shown in Figure 4. The hydrogens of the ethyl group form a triplet centered (downfield) at 1.5 ppm for the CH_3 and a quartet at 4.5 ppm for the CH_2 attached to the nitrogen atom of the imidazole ring. The hydrogens of the CH_3 group attached to the nitrogen of the imidazole form a singlet at 4.2 ppm. The C_4 and C_5 hydrogens of the imidazole ring are located at 8.1 ppm and the C_2 hydrogen at 10.1 ppm. We note that the resonances are broad for this composition at ambient temperatures because of the high viscosity. A temperature of 50°C is required for the resonances to be as narrow as observed for more acid compositions at room temperature. The ^1H NMR of these melts has been extensively studied by Fannin et al. (4), but they did not include a melt as basic as the one shown. These authors pointed out the strong shift of the ring hydrogens as a function of the basic nature of the melt. The spectrum shown here is consistent with the observed shifts which they observed. It was observed that the NMR resonance of these hydrogens shift upfield as the basic melt approaches the neutral composition, and that there is almost no further shift of the resonances in the acid region. This result is consistent with the loss in aromaticity of the ring on going from basic to acidic compositions. However, it was interpreted by the authors (4) as an interaction of Cl^- with the hydrogens on the ring. In our view a preferred explanation is that the Cl^- is interacting only to a small extent with the ring and that the $AlCl_4^-$ has a dominant effect on the ring aromaticity. However, the IR changes in the aliphatic part of the molecule do not agree with the NMR data. Only small shifts in the hydrogen on the aliphatic carbons are observed in the NMR whereas large effects are observed in the IR. We must postulate that shielding of the Cl^- does not affect the spin relaxation of the NMR but does affect the vibrational modes observed in the IR.

ACKNOWLEDGEMENTS

We thank John O'Gara, of General Motors Research Laboratories, for many helpful discussions.

REFERENCES

1. A. A. Fannin, Jr., D. A. Floreani, L. A. King, J. S. Landers. B. J. Piersma, D. J. Stech, R. L. Vaughn, J. S. Wilkes and J. L. Williams, Inorg. Chem. 88, 2614 (1984).

2. C. J. Dymek Jr., G. F. Reynolds and J. S. Wilkes, J. Electrochem. Soc., 134, 1658 (1987).

3. K. M. Dieter, C. J. Dymek, Jr., N. E. Heimer, J. W. Rovang and J. S. Wilkes, J. Am. Chem. Soc., 110, 2722 (1988).

4. A. A. Fannin, Jr., L. A. King, J. A. Levisky, and J. S. Wilkes, Inorg. Chem. 88, 2609, (1984).

5. A. K. Abdul-Sada, A. M. Greenway, P. B. Hitchcock, T. J. Mohammed, K. R. Seddon and J. A. Zora, J. Chem. Soc., Chem. Commun. 17753, (1986).

6. S. Tait and R. A. Osteryoung, Inorg. Chem., 23, 4352 (1984).

7. J. S. Wilkes, J. A. Levinsky, R. A. Wilson and C. L. Hussey, Inorg. Chem., 21, 1263 (1982).

8. H. M. Randall, R. G. Fowler, N. Fuson and J. R. Dangl, Infrared Determination of Organic Structures, D. Van Nostrand, 1949.

9. G. Torsi, G. Mamantov and G. M. Gegun, Inorg. Nucl. Chem. Lett. 6, 553 (1970); E. Rytter, H. A. Oye, S. J. Cyvin, B. N. Cyvin and P. Klaeboe, J. Inorg. Nucl. Chem., 35, 1185 (1973); J. E. D. Davies and D. A. Long, J. Chem. Soc., A, 1273 (1971).

Table 1. IR Frequencies and (cm-1) Band Assignments for AlCl3/MEICl Mixtures

Assignments	Composition			
	40/60	50/50	55/45	60/40
Al-Cl		480 m		480 m
ring def.	520 s	510 m	520 s	520 s
ring def.	580 s	580 w		580 m
			660 w	630 m
$AlCl_4^-$	680 m	680 s		
CH_3, CH_2 o/p bend			705 m	705 s
ring o/p bend			750 m	745 m
C-H ring i/p bend	790 s	790 s		
C-H, CH_3, CH_2 o/p bend.		830 m	835 m	835 s
Meth. C-N	870 sh	870 s-sh		
C-H i/p bend			970 m	970 m
CH_3-N rock	1040 w-sh	1040 m	1035 w	1040 w
CH_3CH_2-N rock	1100 sh	1100 sh	1100 w	1110 m
CH rock + comb.	1190 m	1190 m	1180 m	1170 s
**				
CH_3-N def-bend				1350 s
methyl C-H bend	1420 w	1420 w	1420 w	1400 s
ring sym. str.	1470 s	1470 s	1470 s	1460 s
C=C str.	1520 s	1510 s	1510 s	
ring sym. str.	1530 s	1540 s		
C-C=N,			1560 s	1580 s
				1600 s
combination	1640 s	1650 s	1650 s	
C=N ring	1680 s	1695 s	1700 s	1700 m
C=C aromatic	1720 w	1740 s	1735 m	
C=C aromatic	1840 w	1840 w	1840 w	
**				
C-H, CH_2 str.				2830 w
C-H, CH_3 str.				2890 m
C-H, CH_2 str.	2930 w		2940 w	
C-H, CH_3 str.		2960 m		2960 s
				2995 s
		3030 m	3020 w	
C_2-H str				3115 s
C-H ring str.	3190 w		3170 w	3160 s
ring C-H str.	3260 w	3260 w	3260 w	
combination	3300 w	3300 w		3390 s
?	3420 m			

Note: s- strong, m- medium, w weak, sh- shoulder, i/p b- in plane bending, o/p b- out of plane bending, str.- stretching vibration, def.- deformation mode, comb. combination modes.

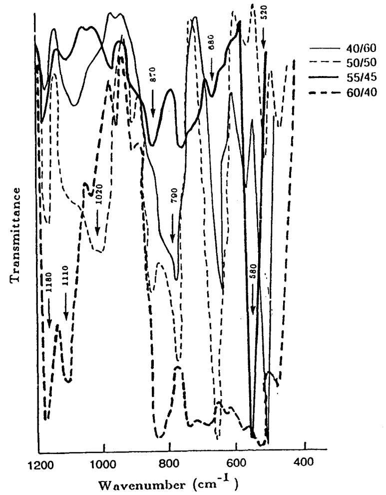

Figure 1. IR transmittance spectra of the low frequency range.

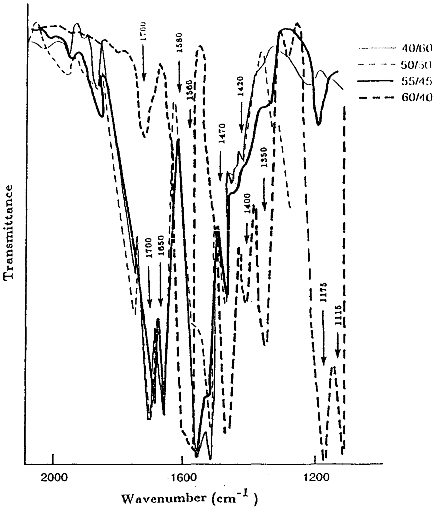

Figure 2. IR transmittance spectra of the mid frequency

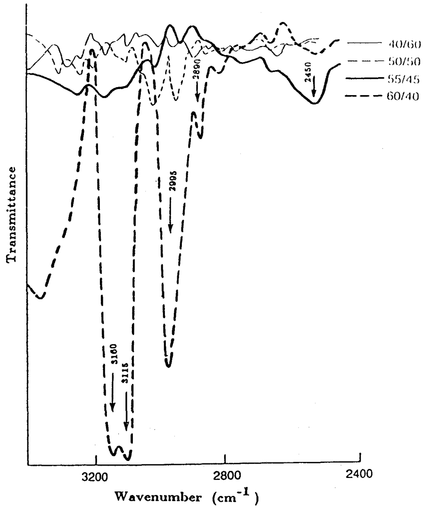

Figure 3. IR transmittance spectra of the high frequency range.

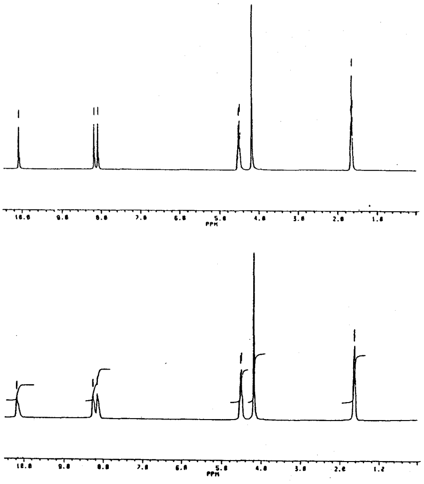

Figure 4. Proton NMR spectra of a 30 mole% $AlCl_3$ melt showing the broad peaks obtained at room temperature (lower curve) and the sharp peaks obtained at 50°C (upper curve).

DOI: 10.1149/199017.0143PV

REFRACTIVE INDICES AND ELECTRONIC POLARIZABILITIES OF ALKALI HALIDE SINGLE AND BINARY MELTS

Mamoru Endo, Masayuki Ishizuka, Toshiaki Hayasaka,
Yuzuru Sato, Tsutomu Yamamura, Tatsuhiko Ejima

Department of metallurgy, Tohoku University, Sendai 980 JAPAN

ABSTRACT

The refractive indices of alkali halide single and LiCl-CsCl, LiBr-CsBr, NaCl-CsCl, NaCl-NaI, KCl-KI and CsCl-CsI binary melts have been measured with high accuracy at the wave length of 470 to 670nm. The electronic polarizabilities of the melts have been determined from the measured refractive indices by the Lorentz-Lorenz equation. The relation between the electronic polarizability and the structure of the salts has been examined. The electronic polarizabilities of the melts have the positive temperature dependence and those of the binary melts deviate slightly from the additive rule. Factors which affect the electronic polarizabilities of the melts have been investigated.

NOMENCLATURE

A	apex angle of prism
δ_{min}	minimum deviation angle
n	refractive index
α	electronic polarizability
V	molar volume
N	Avogadro's number
r_s	first neighboring distance of the crystal at m.p.
r_l	first neighboring distance of the melt
V_s	molar volume of the crystal at m.p.
V_l	molar volume of the melt
CN_s	coordination number of the crystal at m.p.
CN_l	coordination number of the melt

INTRODUCTION

The refractive index is indispensable for the optical measurements such as the Brillouin scattering. Furthermore, the electronic polarizability derived from the wave length dependence of the refractive index gives us the information about the extent of the electronic polarization of ions under applied electric field.

The alkali halide melts are comprised completely spherically symmetric halide anions and alkali cations. Therefore, the alkali halide melt has been considered as a simple ionic liquid. But, it should be noted that electronic polarization of the ions exists even in such a typically ionic melt as alkali halide melts, and may influence the transport and thermodynamic properties of the ionic melts. Therefore, it is interesting to determine the electronic polarizability of the melts and to clarify the effect of the electronic polarization on physicochemical properties.

This paper reports the results of the measurements of the refractive index at the wave length of 470 to 670 nm for the single melts and the binary LiCl-CsCl, LiBr-CsBr, NaCl-CsCl, NaCl-NaI, KCl-KI and CsCl-CsI systems. The electronic polarizabilities of the melts have been derived from the refractive indices observed, and the relative importance of the factors which control the electronic polarization has been investigated.

EXPERIMENTAL

The refractive index was measured at the wave length of 470 to 670nm and at the temperatures ranging from the m.p. up to 1200K. The schematic diagram of the experimental apparatus is shown in Fig.1. It consists of a halogen lamp, a monochromator, an oven, a collimator, a prism cell and a telescope. The prism cell was constructed of the optical parallel plates of transparent quartz. The purified salts were sealed under vacuum into the cell.

The refractive index was determined by the minimum deviation angle method. The deviation angle takes minimum value when the incident beam and the refracted beam are symmetrical about the axis of the prism cell. The refracted beam was observed by the telescope. The prism cell was turned so as to minimize the deviation angle. The refractive index is calculated by eq.1 from the minimum deviation angle, δ_{min}, observed.

$$n = \frac{\sin\left(\frac{A+\delta_{min}}{2}\right)}{\sin\left(\frac{A}{2}\right)} \qquad (1)$$

The apex angle, A was measured by means of an auto-collimation method. Therefore, this measurement is an absolute method without a calibration process.

RESULT AND DISCUSSION

I. Error Sources of The Measurement

The factors of the error involved in the measurement of the refractive index and their contribution to the results have been evaluated. Three factors being important as the error sources are as follows:

1. The error involved in the measurement of the apex angle and the minimum deviation angle.
2. Deviation of the incident angle from right angle.
3. Parallel of the out side and inside of the windows of the optical cell.

Taking account of the error sources discussed above, the total error involved in the determination of the refractive index is estimated to be less than 0.08%.

II. Refractive Index

The refractive indices of CsCl-CsI binary melts decrease linearly with increasing temperature. The same temperature dependence has been observed for all the melts measured. According to the Lorentz-Lorenz eq.2, refractive index depends on the number density and the electronic polarizability of the constituent ions of the melts.

$$\frac{n^2-1}{n^2+3} = \frac{4\pi N\alpha}{3V} \qquad (2)$$

We consider that the negative temperature dependence of the refractive index of the melts is mainly due to the decrease in the number density of the melts with an increase in temperature.

The isotherm curves of the refractive indices for the binary melts are shown in Fig.3. There are curve-linear relations between the refractive index and composition. As mentioned above, refractive index is a function of electronic polarizability and number density. Assuming the additive rule for electronic polarizability of salts, refractive index of the mixture can be reproduced within a few percent.

The dispersion curves of the refractive index for CsCl-CsI binary melts are shown in Fig.4. The refractive indices of the melts decrease monotonically with increasing wave length at the wave length range of 470 to 670nm. These dispersion curves are typical of normal dispersion. The same normal dispersion curves have been observed for the other melts. The dispersion observed is considered to be due to the electronic polarization of the constituent ions of the melts.

III. Electronic Polarizability

The electronic polarizabilities of the melts have been determined from the refractive index and the molar volume by the Lorentz-Lorenz eq.2. The molar volumes of the single melts and the binary melts except LiBr-CsBr system are quoted from Janz (1). The molar volume of LiBr-CsBr binary melts is quoted from Smirnov et al (2).

Temperature Dependence of Electronic Polarizability

The temperature dependence of the electronic polarizabilities of CsCl-CsI binary melts is shown in Fig.5. The electronic polarizabilities of the melts increase slightly but more than the limits of the experimental errors with increasing temperature. The same positive temperature dependence of the electronic polarizability has been observed for the other melts investigated. The electronic polarizability is a parameter expressing the extent of the polarization of ions under the applied electric field, and is proportional to the ionic volume if the electronic structure is the same. According to the quantum mechanical calculations and the calculations of the atomic scattering factor for X-ray of crystalline alkali halides (3-6), the electronic polarizability of the anion decreases, on the contrary, that of the cation increases somewhat in passing from the free ionic state into the condensed state (7). The extent of the variation accompanying the change in state is larger for the anion than the cation (3-8). Wilson (8)pointed out the correlation between the electronic polarizability of ions and the inter-ionic distance of crystalline alkali halide. On the other hand, in molten state, the volume expansion induced by the temperature increase is mainly due to the decrease in coordination number, and the first neighboring ionic-distance is almost kept constant upon an increase in temperature. Therefore, the positive temperature dependence of the electronic polarizability observed in the present investigation are considered to be due to the decrease in coordination number upon temperature increase. The contribution of the coordination number to the electronic polarizability has not yet been examined for the case of crystalline state. So, the relative importances of the inter-ionic distance and coordination number in molten and solid station have been investigated taking the cesium halide as a sample substance, because cesium halides show a structural transformation from CsCl type, whose coordination number is 8, to NaCl type, whose coordination number is 6.

The electronic polarizabilities of the cesium halides are plotted against inter-ionic distance and shown in Fig.6. The electronic polarizabilities of the CsCl type and NaCl type crystals are quoted from Tessman et al. (9) and Jaswal et al. (10), respectively. The coordination numbers are cited in parentheses for the reference. As shown in Fig.6, the correlation between the electronic polarizability and the inter-ionic distance of each salt at constant coordination number can be examined only for the case of coordination number, 8. In this case, the electronic polarizability increases with increasing inter-ionic distance. However, if the electronic polarizabilities of different coordination number of each salt are compared, there is no systematic correlation between the electronic polarizability and the inter-ionic distance. The electronic polarizabilities of cesium halide melts and crystals are plotted against coordination number and shown in Fig.7. The coordination number of the melts are determined by the Furukawa's eq.3 (11).

$$CN_l = CN_s \frac{V_s}{V_l}\left(\frac{r_l}{r_s}\right)^3 \qquad (3)$$

As shown in Fig.7, the electronic polarizability of each salt decreases with increasing coordination number. Two plots of each salt at the coordination number 8 represent the values measured at different temperatures. The same coordination number dependence of the electronic polarizabilities are observed for the other salts investigated.

Composition Dependence of Electronic Polarizability

The electronic polarizabilities of the binary melts observed are plotted against composition and shown in Fig.8. The electronic polarizabilities of the binary melts, except LiBr-CsBr binary melts, agree well with the additive values. But the electronic polarizability of LiBr-CsBr binary melts deviates from the additive values by 1% at 50 mol% CsBr exceeding the limits of experimental error. As discussed above, the coordination number and the inter-ionic distance are the important factors for the electronic polarizability of the melts. In case of the binary melts of LiBr-CsBr, the molar volume deviates significantly from additive rule by maximally 3% at 10~40 mol% CsBr. This may be because of the difference of the ionic sizes of LiBr-CsBr binary melts, Li^+, Cs^+ or Br^-, is the largest of the binary melts investigated. Composition dependence of electronic polarizability will be discussed in detail in the following. It seems that the volume expansion is due to the decrease in the mean coordination number or the increase in the inter ionic distance. So it is considered that the positive deviation of the electronic polarizability of LiBr-CsBr binary melts is due to the decrease in the mean coordination number, because the electronic polarizabilities of the salts are mainly influenced by the change in the coordination number.

CONCLUSION

The refractive index of the single and the LiCl-CsCl, LiBr-CsBr, NaCl-CsCl, NaCl-NaI, KCl-KI and CsCl-CsI binary melts have been measured with high accuracy at the wave length range of 470 to 670 nm. The electronic polarizabilities of the melts have been determined from the measured refractive indices by the Lorentz-Lorenz equation. The factors which affect the electronic polarizabilities of the salts have been investigated. The conclusion to be drawn from these results is as follows:

1. The electronic polarizability varies with the change in coordination number and inter-ionic distance.
2. The coordination number is the most important factor of the electronic polarizabilities of the salts.

ACKNOWLEDGEMENT

The authors acknowledge the financial support of a Grant-in-Aid for Scientific Research (62303029) from the Ministry of Education, Japan.

REFERENCE

(1) G.J.Janz, J.Phys.Chem.Ref.Data, 17(1988), Supplement No.2
(2) M.V.Smirnov and V.P.Stepanov, Electrochim.Acta, 27(1982),1551.
(3) J.E.Mayer and M.G.Mayer,Phys.Rev.,43(1933),605.
(4) E.Paschalis and A.Weiss, Theoret.Chim.Acta, 13(1969),381.
(5) P.C.Schmidt and A.Weiss, Z.Naturforsch., 34a(1979),1471.
(6) G.D.Mahan, Phys.Rev.A, 22(1980),1780.
(7) D.R.Yorder and R.Colella, Phys.Rev.B, 25(1982),2545.
(8) J.N.Wilson and R.M.Curtis, J.Phys.Chem., 74(1970),187.
(9) J.R.Tessman, A.H.Kahn and W.Shockley, Phys.Rev., 92(1953),890.
(10) S.S.Jaswal and T.P.Sharma, J.Phys.Chem.Solids, 34(1973),509.
(11) K.Furukawa, Discuss.Faraday Soc.,32,(1961),53.

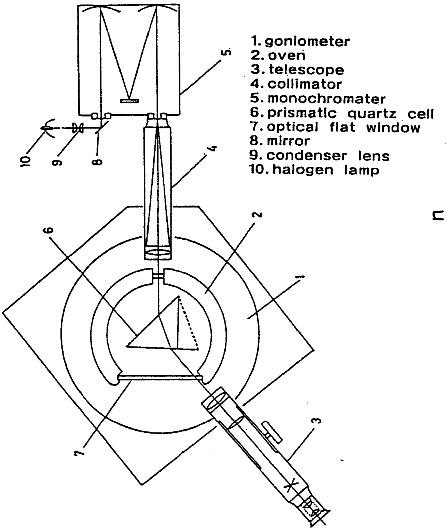

Figure 1. Schematic Diagram of Apparatus.

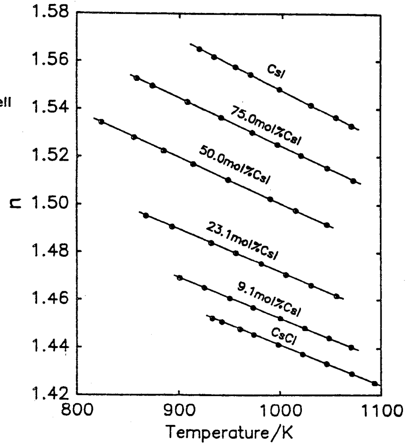

Figure 2. Temperature Dependence of Refractive Index at 589.35 nm for CsCl-CsI binary Melts.

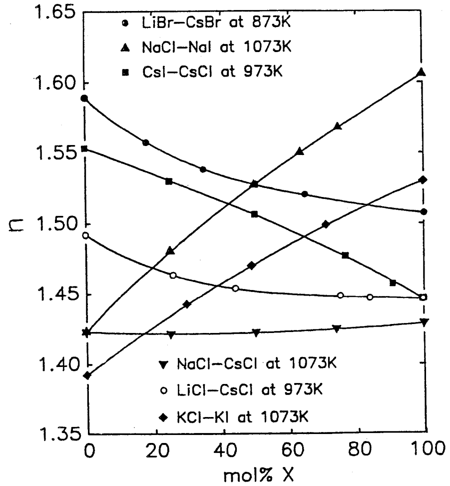

Figure 3. Isotherms of Refractive Index for Alkali Halide Binary Melts.

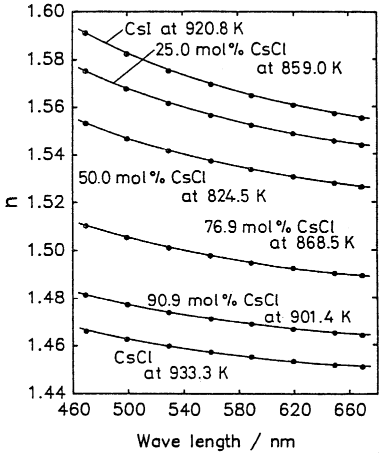

Figure 4. Dispersion in Refractive Index for CsCl-CsI Binary Melts.

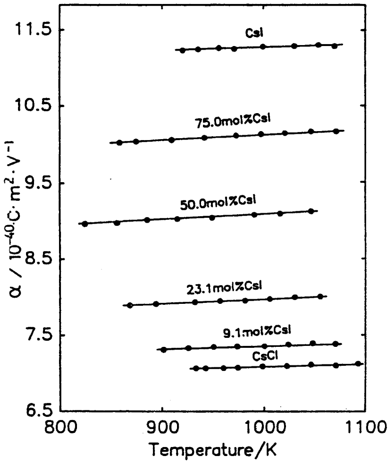

Figure 5. Temperature Dependence of Electronic Polarizability for CsCl-CsI Binary Melts.

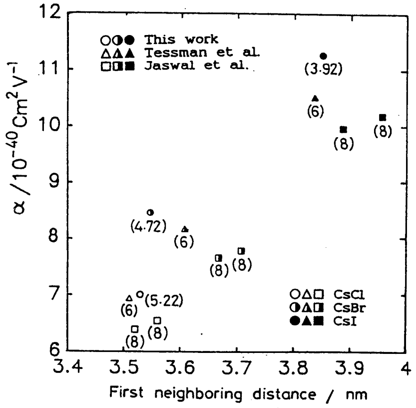

Figure 6. Correlation Between Electronic Polarizability and Inter-ionic Distance for Cesium Halides.

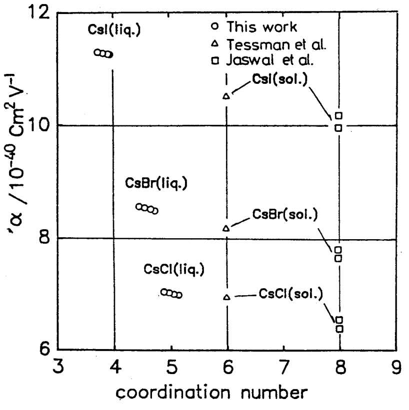

Figure 7. Correlation Between Electronic Polarizability and Coordination Number for Cesium Halides.

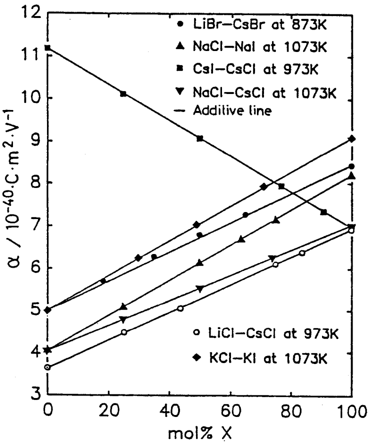

Figure 8. Isotherms of Electronic Polarizability for Alkali Halide Binary Melts.

DOI: 10.1149/199017.0152PV

SONIC SPECTROSCOPY IN $ZnCl_2$ AND ALKALI METAL CHLORIDE BINARY MELTS

Hong-Min Zhu, Yoshiyuki Sato, Yuzuru Sato
Tsutomu Yamamura and Tatsuhiko Ejima

Department of Metallurgy, Tohoku University
Sendai 980, Japan

ABSTRACT

The ultrasonic velocity and absorption coefficient in molten alkali chlorides and zinc chloride have been measured by a pulse transmission method. The hypersonic velocity in $ZnCl_2$, $ZnCl_2$-NaCl and $ZnCl_2$-KCl melts have been measured by means of a Brillouin scattering method. A dispersion of sound wave propagation occurs in $ZnCl_2$ single melt, $ZnCl_2$-NaCl and $ZnCl_2$-KCl binary melts. The effects of the increases of temperature and the addition of an alkali chloride on the relaxation phenomenon in the melt have been clarified.

INTRODUCTION

Among the molten salts, zinc chloride has unusually high viscosity. This is due to the presence of the network structure in the melt. But as temperature increases the network structure breaks, and polymeric species becomes to a low degree's one, finally to $ZnCl_4^{=}$. So, the structure of $ZnCl_2$ melt varies with temperature. On the other hand, molten alkali chlorides are typical ionic melts, they are almost completely ionized with the species M^+ and Cl^-. They act as a Cl^- donor when added to $ZnCl_2$ melt, and causes the variation in the structure of the melt. The sonic spectroscopy is one of the most effective method for the detection of the change in the structure. From the sonic spectroscopy the relaxation phenomenon which is connected with structure change can be also elucidated.

In the present study, $ZnCl_2$ single melt, $ZnCl_2$-NaCl and $ZnCl_2$-KCl binary melts have been studied by the sonic spectroscopy. The sound velocity and absorption coefficient in pure $ZnCl_2$ and alkali chloride melts have been measured by pulse transmission method in the frequency range of 5～55MHz. By means of a Brillouin scattering method, the sound velocity in pure $ZnCl_2$ and $ZnCl_2$-NaCl, $ZnCl_2$-KCl binary melts have been measured over the frequency range of 3 to 9GHz. The relaxation phenomenon in the melts has been clarified. The structure variation of $ZnCl_2$ melt with increasing temperature and with the addition of alkali chlorides has been investigated.

EXPERIMENTAL

Pulse Transmission Method

The ultrasonic velocity and absorption coefficient were measured by a pulse transmission method. The experimental arrangement was described elsewhere(1). The sound pulses piezoelectrically generated by a X cut quartz crystal are introduced into the melt through a conduction rod made of fused quartz. The sound pulses propagated through the melt are received by an upper conduction rod, and are transduced into electrical signals by a quartz crystal attached to the conduction rod. The sound velocity and absorption coefficient are determined from the measured delay time and the amplitude change accompanying the displacement of the spacing between the upper and lower conduction rod. The sound velocity and absorption coefficient in alkali chlorides and $ZnCl_2$ were determined over the temperatures ranging from the melting point of the salts to about 150K above it. The measurement was carried out over a frequency range of 5 to 55MHz.

Brillouin Scattering Method

The hypersonic velocity of pure $ZnCl_2$ melt, and $ZnCl_2$-NaCl and $ZnCl_2$-KCl binary melts were measured by a Brillouin scattering method. Details of the Brillouin scattering method was described in the previous paper(2). The light source was a He-Ne gas laser operated in single mode at a wave length of 632.8nm. The laser beam was modulated into 225Hz and focused at the center of a scattering cell placed inside a furnace. The scattering cell was made of fused quartz. The light scattered into the angle θ was focused on a pin hole with a collecting lens, was collimated with a collimating lens and was analyzed by a Fabry-Perot interferometer. The light scattered by a homogeneous liquid consists of the central Rayleigh line with the same frequency as that of the incident beam, and a doublet whose components are shifted symmetrically from the frequency of the incident beam. The latter is induced by the collision of a photon in the liquid under thermal equilibrium. The frequency shift, $\Delta\nu$ between the Brillouin peaks and the Rayleigh peak is expressed as follows(3):

$$\Delta\nu = 2\nu_i n (V/C)\sin\theta \qquad (1)$$

where ν_i is the frequency of the exciting light, n is the refractive index of the liquid, V and C are the velocities of sound wave and light, respectively, and θ is the scattering angle. The frequency shift is also equal to the frequency of the sound wave which induces the light scattering. The sound velocity can be obtained from the frequency shift and scattering angle.

Sample

The moisture absorbed by $ZnCl_2$ would affect the viscositic property of the melts by modifying the melt structure as well as by forming hydroxides or oxychlorides. Therefore, the reagent grade $ZnCl_2$ was pretreated to remove the moisture and inclusions which would cause the spikes in the spectrum obtained by the Brillouin scattering experiment. The dried salt was loaded into a reaction tube made of quartz, and was melted. Then dried HCl was bubbled into the melt for 20ks to remove the residual trace amount of moisture, and melt was filtered to remove the inclusions. For the Brillouin scattering measurement, the purified $ZnCl_2$ was distilled further. Alkali chlorides were also purified by the bubbling of HCl.

RESULTS AND DISCUSSION

Sonic Spectroscopy in Pure Alkali Chloride and $ZnCl_2$ Melts

The ultrasonic velocity and absorption coefficient in pure alkali chloride melts were measured by the pulse transmission method. Fig.1 shows the temperature dependence of ultrasonic velocity in alkali chlorides. The ultrasonic velocity decreases linearly with increasing temperature over the temperature range measured. The ultrasonic velocity is not dependent on frequency in the frequency range investigated (5~55MHz) for alkali chloride melts.

The absorption coefficient was measured as a function of frequency at each temperature. The value of α/f^2 (α : absorption coefficient, f: frequency) did not exhibit frequency dependence . The value of α/f^2 is plotted against temperature and is shown in Fig.2. The absorption coefficient decreases with increasing temperature. In the series of alkali chloride, absorption coefficient increases as the cationic size increases with the exception of LiCl.

The fact that the ultrasonic velocity and the value of α/f^2 don't exhibit frequency dependence indicates there is no dispersion in the frequency range investigated. In Fig.1, the hypersonic velocities determined by the Brillouin scattering method are represented by dotted lines for NaCl, KCl and CsCl. The hypersonic velocities were reported by Torell et al.(4) and Qiu et al.(5). As shown in the figure, ultrasonic and hypersonic velocities agree well within the limits of the experimental error, accordingly no dispersion was found at the frequencies lower than the frequencies covered by Brillouin scattering method (several GHz).

The absorption coefficient of ultrasound in $ZnCl_2$ was determined over the frequency range of 5~55MHz. The value of α/f^2 is plotted against temperature and frequency, and shown in Fig.3. At the temperatures near the melting point (591K), the value of absorption coefficient is very high , and the value of α/f^2 depends on frequency obviously in the low temperature region. This fact indicates the presence of a sound wave disperssion in the melt. On the basis of the single relaxation theory, the value of α/f^2 at a constant temperature may be represented as a function of frequency as follows(6):

$$\alpha/f^2 = \frac{A}{1+(f/f_r)^2} + B \qquad (2)$$

where A and B are frequency-independent quantities, f_r is the relaxation frequency. The value of α/f^2 at different temperatures, are plotted against log$f$ in Fig.4. One can see that the plots agree well with the single-relaxation curves. The relaxation frequencies where the values of α/f^2 decreases steeply, are a few ten's maga Hertz (10^7Hz) at 590, 600 and 610K. It is clear in Fig.4, that the relaxation frequency increases with increasing temperature, and go beyond the range of the pulse method at temperatures higher than 650K.

The Brillouin scattering measurement of $ZnCl_2$ was done at the temperature range of 570 to 980K. The hypersonic velocities were determined from the observed Brillouin shifts by Eq.(1), and are plotted against temperature in Fig.5. The Brillouin scattering studies on molten $ZnCl_2$ have been also done by Soltwisch et al.(7) and Knape(8), their results are also shown in Fig.5 for comparison. The temperature dependence of hypersonic velocity can be classified into three temperature regions: the hypersonic velocities determined at three different angles agree within experimental error both in the low temperature region ($570K< T< 620K$) and high temperature region ($880K< T$). In these temperature regions, the hypersonic velocity decreases linearly with increasing temperature. On the other hand, the hypersonic velocity in the intermediate temperature region depends on the scattering angle, the velocities measured at a scattering angle of 140° being the highest, and those measured at 70° being the lowest. The scattering angles of 70° , 90° and 140° correspond to the sound frequency ranges of 4.5~5.7, 5.6~7.1 and 6.9~9.5GHz, respectively. That is to say the hypersonic velocity in the intermediate temperature region depends on the frequency of the sound, accordingly a dispersion of sound wave propagation occurs in the frequencies around 5GHz.

According to the single relaxation theory, the sonic velocity, V is given by Eq.(3) as a function of the frequency, f,

$$V^2 = V_0{}^2 + \frac{(V_\infty{}^2 - V_0{}^2)}{1+(f_r/f)^2} \qquad (3)$$

where V_∞ and V_0 are the velocities of limiting high and limiting low frequency, respectively. We consider that the hypersonic velocities determined at temperatures lower than 620K can be regarded as V_∞ , on the other hand , the hypersonic velocities determined at the temperatures higher than 880K can be regarded as V_0, because there are linear relations between velocity and temperature at the respective temperature ranges. On the basis of the single relaxation theory, the relaxation frequency can be given as follows:

$$f_r = (V_\infty{}^2 - V_0{}^2)/A V_0 V_\infty{}^2 \qquad (4)$$

where A is given by Eq.(2). Assuming that the values of V_∞ and V_0 can be extrapolated from the hypersonic velocities obtained in the low and high temperature regions, respectively, the relaxation frequency were calculated by Eq.(4) from the ultrasonic absorption coefficient. The dispersion curves determined are shown in Fig.6. It is clear that the relaxation frequency increases with increasing temperature. At the temperatures near 600K the relaxation frequency is the order of 10MHz (10^7Hz), and 10GHz (10^{10}Hz) at 700K. This agrees well with the results of ultrasonic and hypersonic velocity in the present study, as shown in Figs.4 and 5.

The structural study of molten $ZnCl_2$ have been done by several researchers(9),(10),(11). It has been considered that molten $ZnCl_2$ consists of polymeric $(ZnCl_2)_n$ species of various sizes. These species are made up of $ZnCl_4$ tetrahedra joined at the corners to give a three dimensional network. With increasing temperature the degree of polymerization lowers.

The sound absorption is due to the delay of the response of the internal variables to the sound wave, and the relaxation frequency can be taken as a measure of the speed of the response. In the low temperature $ZnCl_2$ melt, the response to the sound wave is very slow because of the presence of large sized polymeric species. This is the reason of low relaxation frequency. The response speed increases with increasing temperature because the depolymerization in the melt. Therefore the relaxation frequency increases with increasing temperature.

Sound Spectroscopy in $ZnCl_2$-NaCl and $ZnCl_2$-KCl Binary Melts

The Brillouin scattering measurement was also carried out for $ZnCl_2$-NaCl and $ZnCl_2$-KCl binary melts. Figs.7 and 8 show the temperature dependence of hypersonic velocity in these binary melts. Filled circles represent the data on 12.5mol% NaCl(KCl). The hypersonic velocity of 12.5mol% NaCl decreases steeply upto 650K, then reduces its slope gradually until 780K, and decreases linearly from 800K with increasing temperature. As we have discussed on the relaxation behavior of pure $ZnCl_2$, the curve linear dependence of the velocity on temperature is associated with the sound wave dispersion. In this temperature region the relaxation frequency is around the frequency of hypersound (several GHz). At temperatures higher than the transition region, the relaxation frequency is higher than the frequency range of present measurements. So the hypersonic velocities in high temperature region which have a linear temperature dependence, can be considered as the velocities of limiting low frequency.

As proposed by Moyer et al.(9), the addition of alkali chloride to $ZnCl_2$ induces the depolymerization reaction.

$$(ZnCl_2)_n + Cl^- = (ZnCl_2)_{n-m} + (ZnCl_2)_mCl^- \quad (m< n)$$

and further addition of the Cl^- donor will cause a second process,

$$(ZnCl_2)_mCl^- + Cl^- = ZnCl_4^{=} + (ZnCl_2)_{m-1}$$

Therefore, it is reasonable to consider that the addition of NaCl or KCl causes the breaking of network structure in $ZnCl_2$ and results in the increase of the relaxation frequency of the binary melts. On the other hand, the breaking of network structure occurs due to a temperature rise, too. So, the addition of chloride ion donor has the similar effect as the increase of temperature for the relaxation frequency of $ZnCl_2$ melt. As shown in Figs.7 and 8, the temperature region where a transition from the steep curve linear to the linear occurs decreases with increasing the composition of NaCl (or KCl). That is to say, the relaxation frequency increases with the addition of NaCl (or KCl) at a constant temperature.

CONCLUSION

The ultrasonic velocity and absorption coefficient in molten alkali chlorides and zinc chloride have been determined by means of a pulse transmission method. The hypersonic velocity in $ZnCl_2$, $ZnCl_2$-NaCl and $ZnCl_2$-KCl melts has been determined by a Brillouin scattering method. The absorption coefficient of molten $ZnCl_2$ takes high values at the temperatures near the melting point because of the presence of large sized polymeric species. A dispersion of sound wave propagation has been observed in $ZnCl_2$, $ZnCl_2$-NaCl and $ZnCl_2$-KCl melts. The relaxation frequency increases sharply with increasing temperature and an addition of NaCl or KCl due to the breaking of the network structure in $ZnCl_2$.

ACKNOWLEDGMENT

The work described in this paper was financially supported by the Ministry of Education under Grant-in Aids for Scientific Research (No62302029 and No01470057).

REFERENCES

1. T. Ejima and T. Mitsuhashi, J. Japan Inst. Metals, **39**, 687(1975).
2. T. Ejima and T. Yamamura, J. Thermophys.,. **5**, 131(1984).
3. L. Brillouin, Compt. Rend., **156**, 1331(1914).
4. L. M. Torell and E. G. Knape, Z. Naturforsch., **34a**, 899(1979).
5. S. L. Qiu, R. A. J. Bunten, M.Dutta, E. W. J. Mitchell and H. Z. Cummins, Phys. Rev. B, **31**, 2456(1985).
6. G. J. Gruber and T. A. Litovitz, J. Chem. Phys., **40**, 13(1964).
7. J. Soltwisch, J. Sukmanowski and D. Quitman, J. Chem. Phys., **86**, 3207(1987).
8. H. E. G. Knape, J. Chem. Phys., **8**, 4788(1984).
9. J. R. Moyer, J. C. Evans and G. Y-S. Lo, J. Electrochem. Soc., **113**, 158 (1966).
10. M. Itoh, K. Sakai and T. Nakamura, Inorg. Chem., **21**, 3552(1982).
11. D. E. Irish and T. F. Young, J. Chem. Phys., **43**, 1765 (1965).

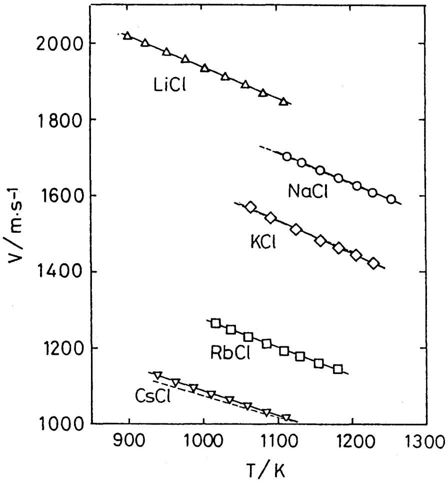

Figure 1 Temperature dependence of sound velocity in molten alkali chloride.

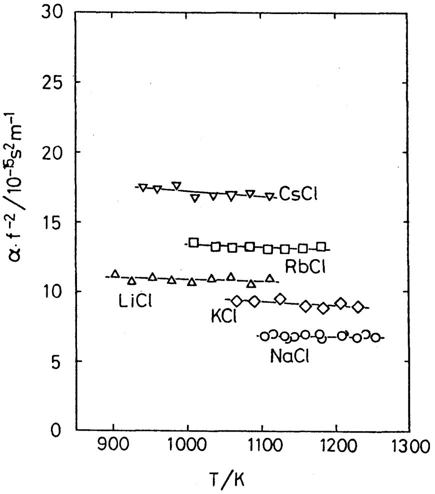

Figure 2 Temperature dependence of sound absorption coefficient in molten alkali chlorides.

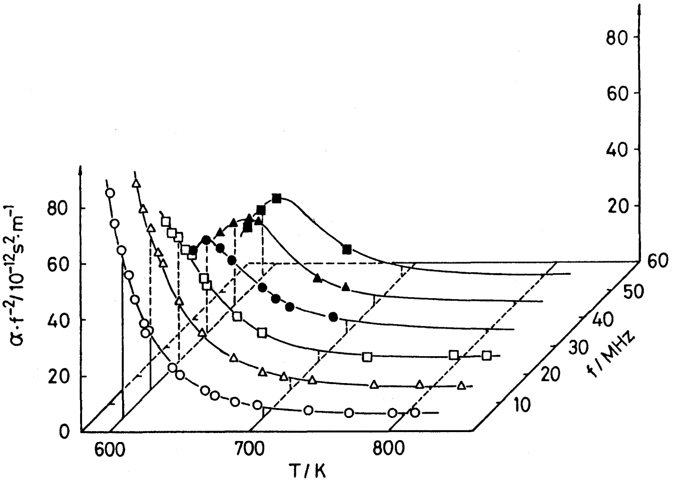

Figure 3 Temperature and frequency dependence of α/f^2 in molten $ZnCl_2$.

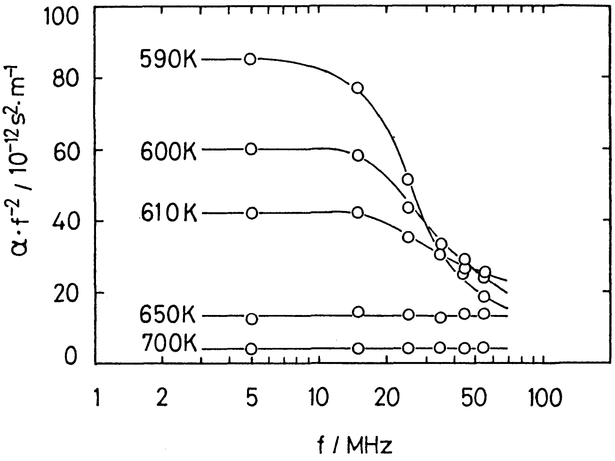

Figure 4 Frequency dependence of α / f^2 in molten $ZnCl_2$.

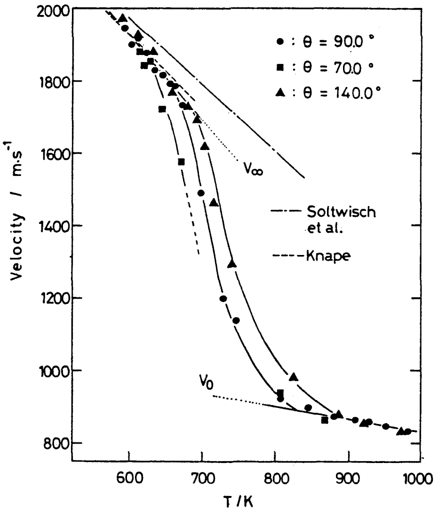

Figure 5 Temperature dependence of hypersonic velocity in molten $ZnCl_2$ determined at various scattering angles.

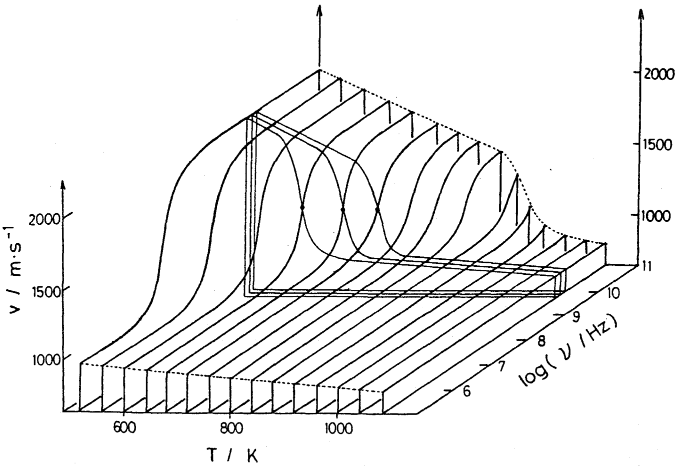

Figure 6 Temperature and frequency dependence of sound velocity in molten $ZnCl_2$.

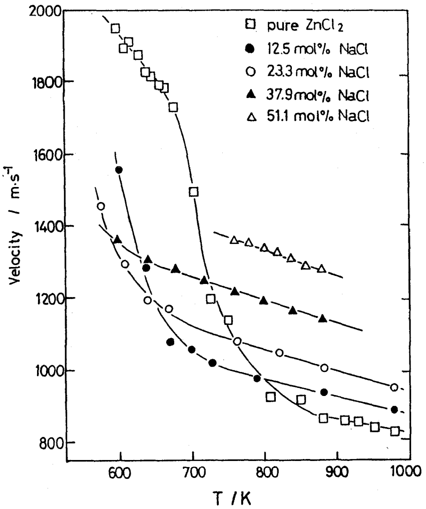

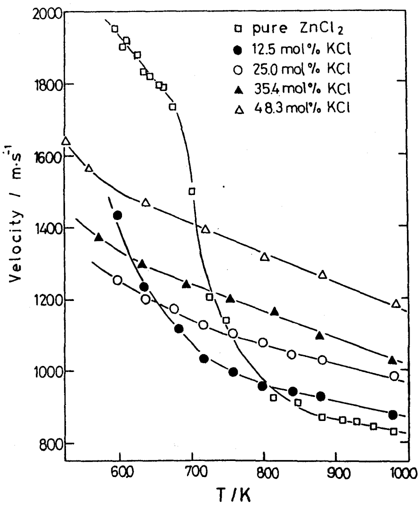

Figure 7 Temperature dependence of hypersonic velocity in molten $ZnCl_2$-NaCl binary system.

Figure 8 Temperature dependenc of hypersonic velocity in molten $ZnCl_2$-KCl binary system.

DOI: 10.1149/199017.0161PV

RAMAN SPECTRA AND STRUCTURE OF METAL-METAL HALIDE MELTS: THE Hg-HgX_2, Cd-CdX_2 and Cd-$Cd(AlX_4)_2$ (X=F,Cl,Br,I) SYSTEMS

G.A. Voyiatzis and G.N. Papatheodorou

Institute of Chemical Engineering and High Temperature
Chemical Processes, and Department of Chemical Engineering
University of Patras
P.O. Box 1239, GR 26110 Patras, GREECE

ABSTRACT

Raman spectra of liquid mixtures of Hg-HgX_2 (X=F, Cl, Br, I) and of Cd-CdX_2 and Cd-Cd $(AlX_4)_2$ (X=Cl, Br, I) with metal mole fractions up to 0.30 for the mercury systems and excess of metal for the cadmium systems have been measured at ~500-900K. Experimental difficulties arising from the darked colored mixtures were overcome by backscattering techniques and the use of the red Kr^+ laser lines. The dissolution of Hg in HgX_2 and in mixed HgXX' (X,X=F, Cl, Br, I) melts gave rise to new Raman bands which were assigned to metal-metal vibrations. The frequencies of these bands exhibit a red shift as the fluoride is substituted by chloride, bromide and iodide.The data indicate that the dissolution of Hg in "molecular" like HgX_2 melts forms linear tetratomic molecular subhalides Hg_2X_2 and Hg_2XX'. Raman spectra of the Cd-CdX_2melts show the presence of broad but well defined bands which were blue shifted as chloride was substituted by bromide and/or iodide. Diatomic subvalent cations are argued to exist in these "ionic" CdX_2 melts mixed with Cd metal. In contrary the Raman bands observed in the Cd-$Cd(AlX_4)_2$ mixtures indicate the presence of subvalent cadmium forming $Cd_2(AlX_4)_2$ type molecules.

INTRODUCTION

The electronic and thermodynamic properties of metal- metal halide melt mixtures have been extensively studied and comprehensive reviews are available (1-5). Spectroscopic studies related to the structure of the "metal species" formed as well as the overall structure of the mixture are limited. Neutron scattering experiments have been carried out in certain alkalimetal-alkalihalide systems (6) and Raman measurements have been reported for the In-InX_3 and Ga-GaX_3 (X=Cl, Br, I) systems (7). In the latter systems the formation of In^+, InX_4^- and Ga^+, GaX_4^- ions has been established.

The purpose of the present work is to investigate by means of Raman spectroscopy the structural properties of the mercury and cadmium metals dissolved in the

corresponding metal halides and haloaluminate melts. The solubility of Hg in the "molecular" HgX_2 melts (8) is high, leading finally to the formation of the solid Hg_2X_2 compounds which have been investigated by X-ray diffraction (9) and vibrational (10) spectroscopy. Cadmium metal is dissolved in the "ionic" CdX_2 melts (11) forming saturated solutions at metal mole fractions less than 0.1. Similar appears to be the behavior of the solution of Cd in $Cd(AlX_4)_2$ melts (12). The main reasons for choosing these sets of systems were: (1) the high solubility of the metal in the solvent melt which is expected to give appreciable concentration of species to be detected by Raman spectroscopy and (2) the structural differences of the solvents which are either molecular [(HgX_2, Hg_2XX", $Cd(AlX_4)_2$] or ionic (CdX_2).
The results reported in this paper indicate a dual behavior for these metal-molten salt systems. It appears that the dissolution of metal (Hg or Cd) in a "molecular" melt leads to the formation of subvalent molecular species having metal-to-metal bonds (i.e X-Hg-Hg-X' or $Cd_2(AlX_4)_2$) while the dissolution of Cd in the "ionic" CdX_2 melts leads to the formation of subvalent ionic species Cd_2^{+2}.

EXPERIMENTAL

The chemicals HgX_2, CdX_2, AlX_3, I_2, Al, Hg and Cd were purchased from commercial sources (Merk, Riedel-de Haen and /or Cerac Pure). The metals, I_2, and anhydrous HgF_2 were used without further purification. The iodides were prepared by reacting I_2 with the metal in evacuated and sealed "quartz" (fused silica) tubes. Aluminum chloride and bromide and the HgX_2 and CdX_2 (X=Cl, Br) salts were purified by slow vacuum sublimation in sealed "quartz" tubes. The haloaluminate salts of cadmium, $Cd(AlX_4)_2$, were prepared by melting together equimolar quantities of the component salts. The anhydrous materials were handled in sealed pyrex or "quartz" tubes or in a N_2-atmosphere glove box with a water content of less than 1 ppm.

The Raman spectroscopy system, the optical furnace and the techniques for preparing the Raman cells were the same as before (7,13). A total amount of ~180 mg of salts were contained in round "quartz" Raman cells (3 mm ID, 4 mm OD). Pure HgF_2 melt reacts with the silica container and the Raman spectra could not be obtained directly. It was possible however to measure indirectly the spectra of the mercuric fluoride solutions by mixing HgF_2 with HgX_2 (X=Cl, Br, or I) salts at ratios ~ 2:3 and then dissolving the metal in the mixed halide melt. These mixtures attacked slowly (1-2h) the container thus permitting "fast" (~15 -30 min) Raman spectral measurements.

As described in the following sections most metal-molten salt mixtures are deeply colored, from red to black-red to black, and thus all the Ar^+ and many of the Kr^+ laser lines are absorbed by these melts. Exemptions were the red (647.1 and 676.4 nm) lines of the Kr^+ laser which for dilute mixtures could be used for measuring the spectra in a 90° configuration. For the strongly absorbing concentrations the same red lines and back scattering Raman techniques were used.

THE MERCURY SYSTEMS: Hg-HgX_2 (X=F, Cl, Br, I) , Hg-$HgCl_2$-$AlCl_3$

Pure $HgCl_2$ is a colorless transparent melt. Progressive additions of Hg metal causes a light coloration of the melt without any loss of its transparency. At about mole fraction of Hg, X_{Hg}~0.04, the melt is tint green and with further metal additions becomes yellow (X_{Hg} ~ 0.07), yellow-orange (X_{Hg} ~ 0.15), black-red (X_{Hg} ~ 0.20) and black (X_{Hg} ~ 0.29). The addition of Hg in $HgBr_2$ melts gives color changes similar to those observed in the chloride system. Pure HgI_2 is a transparent deep red melt which turns to black-red at compositions $X_{Hg} > 0.03$. Opaque deep black-red to black melts were observed at mercury mole fractions from ~0.07 to ~0.29 . The colors of the HgF_2-HgX_2-Hg melts as well as the colors of a variety of HgX_2-HgX_2'-Hg (X,X'=Cl, Br, I) mixtures investigated were combinations of the colors described above for the HgX_2-Hg systems.

Figures 1-3 show the Raman spectra of the HgX_2-Hg (X=Cl, Br, I) melt mixtures at metal mole fractions up to 0.30. The spectra of pure HgX_2 melts have been also measured (the lowest spectrum in Figures 1-3) and the observed vibrational frequencies and a tentative assignment is given in Table I. The assignment is based on a molecular type melts containing X-Hg-X linear molecules as it has been suggested by electrochemical (14) and Raman spectroscopic studies (15). Further evidence for this assignment is given by temperature dependence measurements of solid and melt $HgCl_2$ (Fig 4). The Cl-Hg-Cl vibrations in the <u>molecular</u> solid (16) appear to be preserved in the melt. The Raman inactive $\nu_2(\Pi u\text{-})$ and $\nu_3(\Sigma_u^-)$ modes of the linear gaseous molecule (17) presumably become active in the solid (and in the melt) from a breakdown of the selection rules due to environmental perturbations.

The addition of Hg into the HgX_2 melts gives rise mainly to a strong and well defined polarized band at frequency below the Hg-X stretching of the pure melt. The frequency of the new band measured for each halide system is similar to that reported for solid Hg_2X_2 (10) and is assigned to the symmetric stretching of the Hg-Hg bond in the linear tetratomic X-Hg-Hg-X molecule. The red shift observed from chloride to iodide (Table I) arises from the increase of the halide mass which increases the reduced mass of the Hg-X side and thus diminishes the Hg-Hg stretching frequency.

The existence of linear Hg_2X_2 molecules is further verified by the Raman spectra of mixed HgX_2-HgX_2' -Hg melts. A series of bands is observed (see Figs. 5 and 6) with frequencies in a sequence expected for mixed linear X-Hg-Hg-X' molecules. Table II lists the vibrational frequencies of the Hg-Hg stretching for all these tetratomic molecules.

Mercury is easily soluble in HgX_2-AlX_3 melts with composition 1:2. Figure 7 shows the spectra of the $HgCl_2$:$2AlCl_3$ melt with or without addition of Hg. The spectrum of the pure solvent is complicated and can be regarded as a superposition of the Raman bands of different species, such as $HgCl_2$, $Hg(AlCl_4)_2$, present in the melt. The dissolution of Hg metal is followed by the appearance of a strong polarized band at ~ 157 cm^{-1} superimposed on the pure solvent bands. The proximity of the frequency of this band to that measured for the Hg-$HgCl_2$ melts indicate the presence of Cl-Hg-Hg-Cl molecules in the chloroaluminate melts. By adding Hg at ratios 2Hg:$HgCl_2$:2$AlCl_3$ the compound $Hg_3(AlCl_4)_2$ is formed which is known (18) to contain linear Hg_3 units bound $AlCl_4$ tetrahedra. The Raman spectra of the $Hg_3(AlCl_4)_2$ melt are dominated (see insert in Fig. 7) by a band at ~ 90 cm^{-1} which is assigned to the stretching of the Hg_3 unit.

Raman band having their origin from species containing Hg_3 have been also seen in the Hg-HgX_2 systems with metal mole fractions above 0.15. Figures 1 and 2 show the presence of these bands at 100 and 87 cm^{-1} for the chloride and bromide melts respectively. For the iodide melts (Fig. 3) a weak shoulder band at ~ 80 cm^{-1} appears in the X_{Hg} ~ 0.29 melts. As in the case of the Hg_2X_2 molecules the symmetric stretching frequency of the X-Hg-Hg-Hg-X molecules shifts to lower energies by increasing the mass of the end atoms.

THE CADMIUM SYSTEMS: Cd-CdX_2, Cd-$Cd(AlX_4)_2$ (X=Cl, Br, I)

At temperature 50-100° above the melting points of the cadmium halides the solubility of cadmium metal reaches a maximum mole fraction of 0.1-0.15. Increasing amounts of metal change the color of the mixture from red to dark -red. Due to these deep colors the Raman measurements were limited to X_{Cd} ~ 0.02 contents.

Figure 8 shows the spectra of the Cd-CdX_2 mixtures and of the pure solvents CdX_2. The 676.4 nm Kr^+ laser line and backscattering Raman techniques were used. For each system the dissolution of the Cd metal gives rise to a new polarized Raman band superimposed on the solvent spectra . The position of the new band is at 158 and 183 cm^{-1} for the chloride and iodide melts respectively, while for the bromide melt the band is not easily recognized since it overlaps with the 142 cm^{-1} broad band of $CdBr_2$. In contrast to the corresponding mercury melts a "blue" shift is observed on going from chloride to iodide. The strong and broad polarized band (Table III) of each of the pure CdX_2 melts has been attributed (19) to a Cd-X vibrations of a variety of halide geometries distributed around the Cd^{+2} ion. In other words the covalent forces between cadmium - halogen are rather weak, no definite geometry is formed and the melts prevails an ionic character. In such melts the dissolution of Cd is more likely to yield Cd_2^{+2} ions having a "diatomic ion" frequency in the range where the new bands are measured in our spectra (158-183 cm^{-1}). The nearest neighbours to Cd_2^{+2} are the halide anions which by their ionic strenght $(\frac{1}{r_{ion}})$ influence the Cd-Cd bonding and vibrational frequency. By substituting Cl^- by Br^- and / or by I^- the Cd-Cd covalent bonding is increasing and thus a blue shift is expected for the vibrational frequency. The experimental data are in accordance with this view and give a further support for the presence of Cd_2^{+2} ions in these melts.

The Cd-$Cd(AlX_4)_2$ melts are slightly colored and Raman spectra could be obtained rather easily in a 90° scattering configuration. The main features of the $Cd(AlX_4)_2$ solvent (Fig. 9-11) are four bands - two polarized and two depolarized - which are attributed to

AlX_4 distorted tetrahedra bound by an edge to the Cd atom (20). The same bands prevail in the spectra of the Cd-Cd(AlX_4)$_2$ melts (Fig. 9-11) plus new bands at 168, 123 and 91 cm^{-1} for the chloride, bromide and iodide salts respectively. A predominant band at 168 cm^{-1} overcomes the solvent bands of the Cd-Cd($AlCl_4$)$_2$ spectra (Fig. 9). The 123 cm^{-1} band of the bromide mixture (Fig. 10) is weak but its relative intensity increases as the laser excitation line changes to higher frequencies (preresonance enhancement). Two bands at 91 and 186 cm^{-1} are observed (Fig. 11) for the Cd-Cd(AlI_4)$_2$ melts. One of these bands at 91 cm^{-1} as well as the 168 and 123 cm^{-1} bands measured in the chloride and bromide melts respectively , are assigned (Table III) to the Cd-Cd vibration in the $Cd_2(AlX_4)_2$ molecule. The chloride to iodide red shift is similar to that seen for the Hg-HgX$_2$ melts and is a consequence of the Hg_2X_2 like structure i.e.:

$$(AlX_4) - Cd - Cd - (AlX_4)$$

Finally the additional band at 186 cm^{-1} of the Cd-Cd(AlI_4)$_2$ spectra is very close to the 183 cm^{-1} band of the Cd-CdI$_2$ system and is assigned to Cd_2^{+2}. Presumably an equilibrium of the type:

$$Cd_2^{+2} + 2AlI_4^- = Cd_2(AlI_4)_2$$

is established which depends on the acid-basis properties of the solvent.

CONCLUSIONS

Raman spectroscopic measurements of metal-molten salt systems involving mercury and cadmium have shown that :

1. New bands due to metal - metal vibrations are present in the spectra.
2. For the molecular melts HgX_2 and $Cd(AlX_4)_2$ (X= halide) the dissolution of metal leads to the formation of linear type Y-M-M-Y molecules (M=Cd, Hg; Y=X, AlX_4) .
3. At high metal contents in the Hg-HgCl$_2$ melts trinuclear in mercury Hg_3Cl_2 molecules are formed.
4. For the CdX_2(X=Cl, Br, I) ionic like melts the dissolution of cadmium metal yields ionic Cd_2^{+2} subvalent species.

Acknowledgements : This work has been supported by the GSRT of the Greek Ministry of Industry Energy and Technology.

REFERENCES

1. M.A. Bredig, in Molten Salt Chemistry ,M. Blander, ed., p. 367, Interscience, (1964).
2. J. D. Corbett, in Fused Salts ,B. Sundheim, ed., Chap. 6, McGraw-Hill (1964).
3. J.D. Corbett in Chemistry ,Lippard, ed., Vol. 21, p. 129, Wiley, (1976).

4. W.W. Warren,Jr, in Advances in Molten Salt Chemistry, (G. Mamantov and J. Braunstein, eds., Vol. 4, p.1, Plenum Press, (1979).
5. W.W. Warren, Jr., in Molten Salt Chemistry, G. Mamantov and R. Marassi, eds., p. 237, D. Reidel Publishine Company (1987).
6. a) J.F. Jal, J. Dupuy, and P. Chieux, J. Phys. C. Solid State Phys., 18, 1347 (1985) , b) G. Chabrier, J. F. Jal, P. Chieux and J. Dupuy, Phys. Lett., 93A, 47 (1982).
7. a) P.L. Radloff and G.N. Papatheodorou, J. Chem. Phys., 72, 992 (1980), b) M.H. Brooker and G.N. Papatheodorou, in Advances in Molten Salt Chemistry, G. Mamantov and C.B. Mamantov, eds., Vol. 5, p. 104, Elsevier, (1983).
8. G.J. Janz and J.D.E. McIntyre, J. Electrochem. Soc., 109, 842 (1962).
9. a) D. Grdenic and J. Djordjevic, J. Chem. Soc.,1316 (1956), b) R.J. Havighurst, J. Am. Chem. Soc., 48, 2113 (1926), c) E. Dorm, Chem. Commun.,466 (1971).
10. a) H. Stammreich and T.T. Sans, J. Mol. Struct., 1, 55 (1967), b) J. R. Durig, K.K. Lau, G. Nagarajan, M.Walker, and J. Bragin, J. Chem. Phys., 50, 2130 (1969).
11. J.OM. Bockris, E.H. Cook, H. Bloom and N.E. Richards, Proc. Roy. Soc., A 255, 558 (1960).
12. J.D. Corbett, W.J. Burkhard and L.F. Druding, J. Am. Chem. Soc., 83, 76, (1961).
13. S. Boghosian and G.N. Papatheodorou, J. Phys. Chem., 93, 415 (1989).
14. a) L. Grantham and S.J. Yosim, J. Chem. Phys., 45, 1192 (1966), b) B. Cleaver and P. Zani,Z. Naturforsch., 38a, 120 (1983).
15. a) G.J. Janz and D.W. James, J. Chem. Phys., 38, 902 (1963), b)A.J. Melveger, R.K. Khanna, B.R. Guscott and E.R. Lippincott, Inorg. Chem., 7, 1630 (1968).
16. a) Y. Subramanian and Karl Seff, Acta Cryst., B36, 2132 (1980) b) H. Poulet and J. P. Mathieu, J. Chim. Phys., 60, 442 (1963), c) Y. Mikawa, R.J. Jakobson and J.W. Brasch, J. Chem. Phys., 45(12), 4528 (1966).
17. R.J. H. Clark and D.M. Rippon, J. Chem. Soc. Faraday Trans, 69, 1496 (1973).
18. a) G.Torsi, K.W. Fung, G.M. Begun and G. Mamantov, Inorg. Chem., 10, 2285 (1971),b) R.D. Ellison, H.A. Lery and K.W. Fung, Inorg. Chem., 11, 838 (1972).
19. a) V.A. Maroni and F.J. Hathaway, Electrochim. Acta ,15, 1837 (1970), b) J.H.R. Clarke, P.J. Hartley and Y. Kuroda, J. Phys. Chem., 76, 1831, (1972)
20. M.A. Einarsrud, Thesis, Institutt for uorganisk Kjemi, NTH, Norway, (1987)

TABLE I: Observed Raman Frequencies (in cm^{-1}) for the Hg-HgX_2 melts

Hg-$HgCl_2$	Hg-$HgBr_2$	Hg-HgI_2	Assignement
375 dp	260 dp	205 dp	HgX_2 antisym. stretch.
322 (dp)	200 (dp)	(145) (dp)	HgX_2
310 p	194 p	138 p	HgX_2 sym. stretch.
(100) dp	(70) dp		HgX_2
(50) dp	(35) dp	(25) dp	HgX_2 or Rayleigh wing
154 p	124 p	100 p	Hg-Hg stretch
100 p	87 p	(80) p	Hg-Hg-Hg stretch

TABLE II: Symmetric Stretching Frequency (in cm^{-1}) of the linear X-Hg-Hg-X' Molecules

Molecule	$\bar{\nu}_{Hg-Hg}$	Molecule	$\bar{\nu}_{Hg-Hg}$
F-Hg-Hg-F	180	F-Hg-Hg-I	128
F-Hg-Hg-Cl	170	Br-Hg-Hg-Br	124
Cl-Hg-Hg-Cl	154	Cl-Hg-Hg-I	118
F-Hg-Hg-Br	142	Br-Hg-Hg-I	112
Cl-Hg-Hg-Br	137	I-Hg-Hg-I	100

TABLE III: Observed Raman Frequencies (in cm^{-1}) for the Cd-CdX_2 (X=Cl, Br, I) Melts

Cd-$CdCl_2$	Cd-$CdBr_2$	Cd-CdI_2	Assignement
		50 dp	CdX_2 or Rayleigh wing
210 p	142 p	107 p	Cd-X stretch. of CdX_2
158 p	(170)	183 p	Cd_2^{2+} sym. stretch.

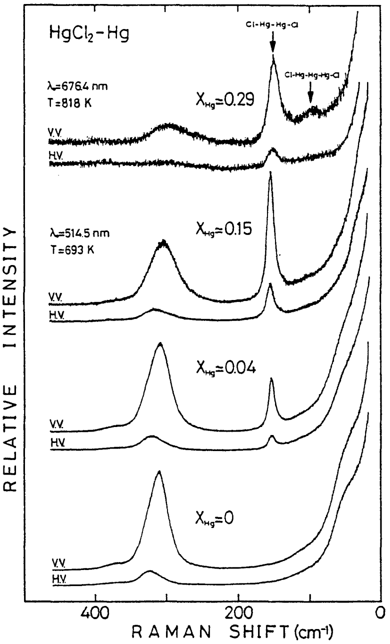

Figure 1. Raman spectra of HgCl$_2$ -Hg molten system. $0 \le X_{Hg} < 0.15$: P=40 mW; SSW~1.5. $X_{Hg} \sim 0.29$: P=50 mW; SSW ~ 3.5.

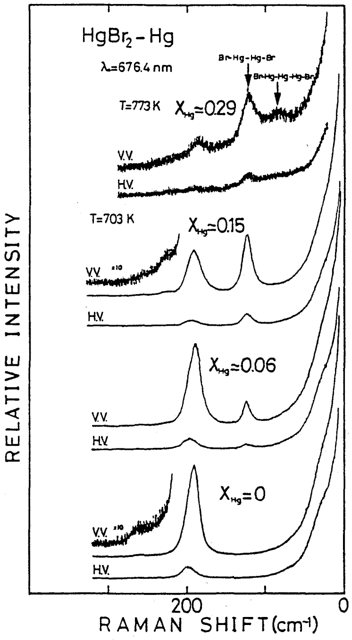

Figure 2. Raman spectra of HgBr$_2$-Hg molten system. P=50 mW (X_{Hg}=0; $X_{Hg} \sim$ 0.06); P=100 mW ($X_{Hg} \sim$ 0.15; $X_{Hg} \sim$ 0.29); SSW ~ 2 (SSW~3.5 for X_{Hg} ~ 0.29).

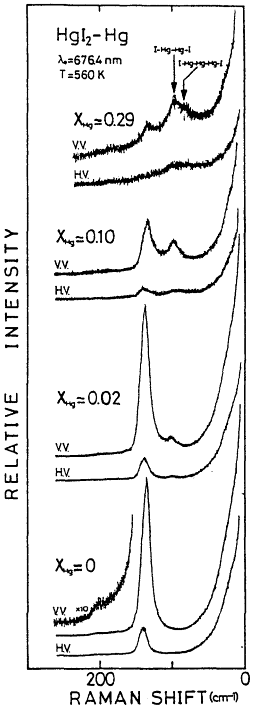

Figure 3. Raman spectra of HgI_2-Hg molten system. X_{Hg}=0: P=30 mW; SSW~2. X_{Hg} ~ 0.02: P=75 mW; SSW ~ 2. X_{Hg} ~ 0.10: P=75 mW; SSW ~ 2.5. X_{Hg} ~ 0.29: P=100 mW; SSW ~ 3.5.

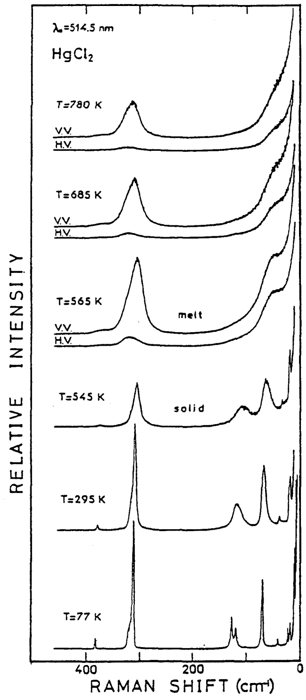

Figure 4. Temperature dependence of the Raman spectra of polycrystalline and liquid $HgCl_2$. P=60 mW; SSW ~ 2. T=77K: P=200 mW;SSW~1.

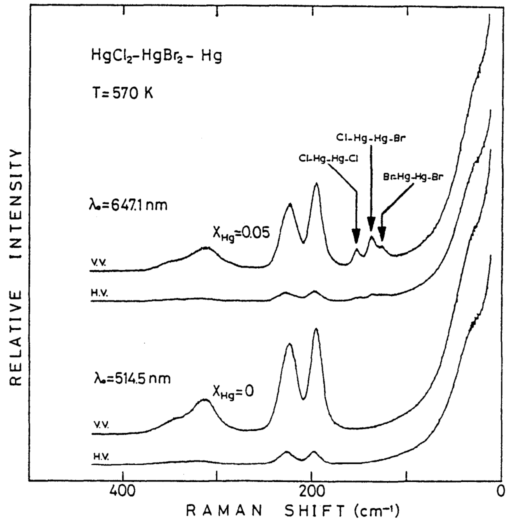

Figure 5. Raman spectra of the mixted $HgCl_2$-$HgBr_2$-Hg molten system. P=60 mW (X_{Hg}=0); P=160 mW (X_{Hg} ~ 0.05); SSW ~1.5.

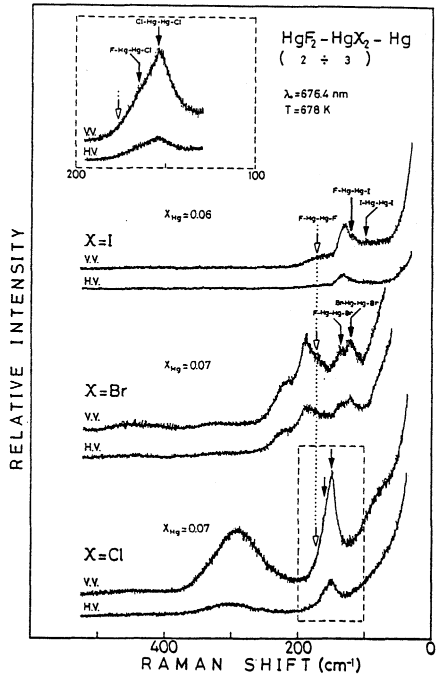

Figure 6. Raman spectra of the mixted HgF_2-HgX_2-Hg (X=Cl, Br, I) molten systems. X=Cl: P=90 mW; SSW ~ 1. X=Br: P=120 mW; SSW ~ 2.5. X=I: P=140 mW; SSW ~ 3.5. Insert X=Cl: P=140 mW; SSW ~ 0.5.

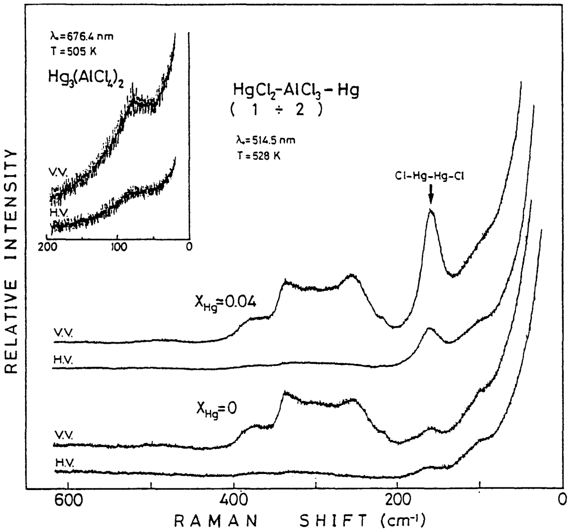

Figure 7. Raman spectra of liquid $Hg_3(AlCl_4)_2$ and of $HgCl_2$-$AlCl_3$ (1:2) - Hg molten system . P=80mW; SSW ~ 2 [SSW~3 for insert $Hg_3(AlCl_4)_2$]

Figure 8. Raman spectra of CdX_2-Cd (X=Cl, Br, I) molten systems. $X_{Cd}=0$: λ_0=647.1 nm (X=Cl, Br) ; λ_0 = 676.4 nm (X=I); T=888 K (X=Cl, Br); T=719 K (X=I); P= 350 mW (X=Cl); P=200 mW (X=Br); P=180 mW (X=I); SSR~ 2 (X=Cl, Br); SSR ~2.5 (X=I). X_{Cd}~ 0.02 : λ_0 = 676.4 nm; T=878 K (X=Cl, Br); T=686 K (X=I); P=180 mW; SSW ~3.5.

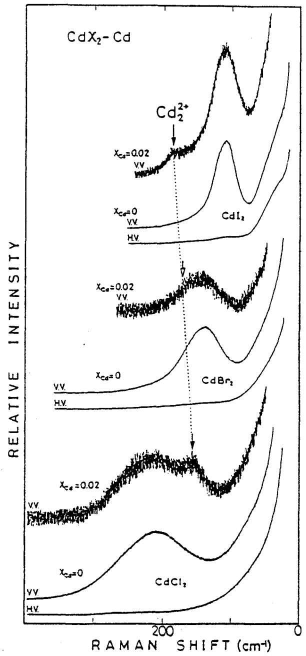

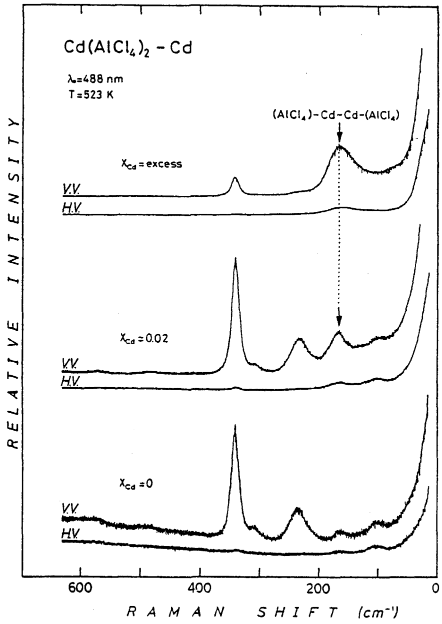

Figure 9. Raman spectra of Cd(AlCl$_4$)$_2$ - Cd molten system. P=60 mW (P=140 mW for X_{Cd} = 0); SSW ~ 2.

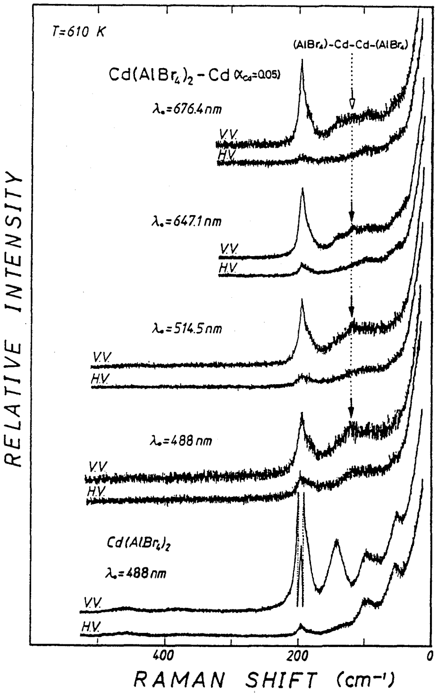

Figure 10.Raman spectra of Cd(AlBr$_4$)$_2$ - Cd molten systems obtained with different laser line frequencies. SSW ~ 2. λ_0= 488.0 nm : P=100 mW. λ_0=514.5 nm: P=40 mW. λ_0 = 647.1 nn : P=60 mW. λ_0=676.4 nm : P=70 mW.

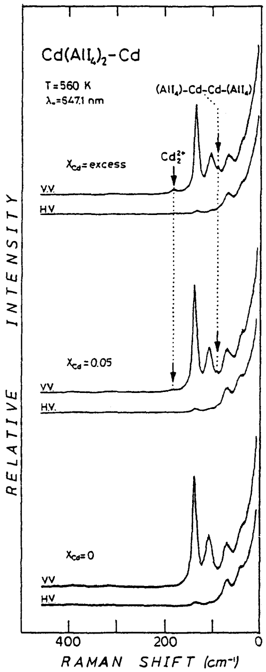

Figure 11.Raman spectra of $Cd(AlI_4)_2$-Cd molten systems. P=50 mW (P=110 mW for X_{Cd}=0); SSW ~2.

DOI: 10.1149/199017.0174PV

ELECTRICAL CONDUCTIVITY MEASUREMENTS OF MOLTEN ALKALINE-EARTH FLUORIDES

Kwangbum Kim and Donald R. Sadoway

Department of Materials Science and Engineering
Massachusetts Institute of Technology
Cambridge, Massachusetts 02139

ABSTRACT

The electrical conductivities of molten CaF_2 and SrF_2 were measured in a double capillary cell by complex impedance spectroscopy.

INTRODUCTION

As part of an investigation of the physical properties of fluxes for use in electroslag welding of titanium, the electrical conductivities of binary solutions containing CaF_2 and other alkaline earth fluorides are being measured. This paper describes results for pure one-component melts of CaF_2 and SrF_2.

LITERATURE

The database for electrical properties of molten fluorides is poor. Not only are there wide gaps in information, but there are serious discrepancies in much of what has been reported. Previous measurements of the electrical conductivity of CaF_2 have been reviewed by Mills and Keene (1). Missing from that review was a study by Voronin, Prisyazhnyi, Khizhnyak, and Kompan (2). As for SrF_2, it appears that the only report in the literature is the article by Voronin et al. (2), cited previously in connection with CaF_2.

EXPERIMENTAL

Electrical conductivity was measured by complex impedance spectroscopy. The instrumentation consists of a potentiostat[1] driven by a

---

[1] 1286 Electrochemical Interface, Schlumberger Instruments, Burlington, Massachusetts

frequency spectrum analyzer.[2] The heart of the apparatus is the conductance cell comprising twin capillaries, 5 mm I.D. × 10 cm long, made of pyrolytic boron nitride tubing,[3] electrodes of spectroscopic grade graphite, and a molybdenum crucible. Prior to deployment the electrodes were chlorinated for 4 hours at 800°C with thionyl chloride in helium carrier gas. The conductivity apparatus is heated by a carbon block resistance furnace. Temperature is measured by a thermocouple, ASTM Type B, protected by a closed-one-end molybdenum tube immersed in the melt. The melt is protected by an atmosphere of argon. Measurements are made over the frequency interval spanning 1 kHz to 100 kHz. The amplitude of the excitation signal is 5 mV peak to peak. The entire data acquisition process is controlled by computer using code written in house expressly for this investigation. Solution resistance is taken as the value of complex impedance at which the imaginary component is zero. This occurs at a frequency of 10 to 20 kHz, typically, the exact value varying with temperature, of course, as well as with the actual dimensions of the electrodes employed. In addition, measurements are made at different values of electrode separation. Linearity in resistance with respect to electrode separation validates the data. The measurements showed no evidence of induced emf caused by the ac power to the furnace. The cell constant is determined by measuring the electrical conductivity of pure molten NaCl and further checked by measuring that of pure molten KCl. Salts[4] are of the highest commercially available purity and are treated prior to experiment by vacuum drying at 300°C for 12 hours.

RESULTS AND DISCUSSION

The measured values of specific electrical conductivity have been fit by least-squares regression to an Arrhenius-type equation and can be represented as follows:

$$\ell n\ \kappa_{CaF_2} = -\ 1548\ /\ T\ +\ 2.750$$

$$\ell n\ \kappa_{SrF_2} = -\ 1155\ /\ T\ +\ 2.391$$

where κ is in $\Omega^{-1}cm^{-1}$ and T is in Kelvins.

---

[2] 1255 Frequency Spectrum Analyser, Schlumberger Instruments, Burlington, Massachusetts

[3] Union Carbide Corp., Cleveland, Ohio

[4] Cerac, Inc., Milwaukee, Wisconsin

The measured values of the specific electrical conductivity of CaF_2 along with selected data from the literature are plotted in Figure 1. There is excellent agreement with the results of Voronin et al. (2). For example, at 1500°C the values differ only by 3%. As well, the present results are in good agreement with those of Mitchell and Cameron (3), Ogino, Hashimoto and Hara (4), and Sveshkov, Kalmykov, Kamenetskii and Nasrednikov (5). The data from these five studies lie within a bandwidth of 10%. The other data in the literature differ by substantially more than this and are not compared with the present results. The last three studies (3,4,5) all employed a crucible-type conductance cell. In contrast, Voronin et al. and the present authors employed a capillary-type conductance cell and obtained values of κ greater than those measured in crucible-type cells. One of the attributes of a capillary-type conductance cell is its relatively high cell constant compared to that of a crucible-type conductance cell. As for possible impurity effects, it is known that oxides, carbides, and other halides all decrease the specific electrical conductivity of molten CaF_2. Accordingly, the fact that the CaF_2 results of this study are the highest values of κ cannot be explained by contamination of the melt.

The measured values of the specific electrical conductivity of SrF_2 along with data reported by Voronin et al. (2) are plotted in Figure 2. The agreement is excellent. At 1500°C the values differ by less than 0.7%.

ACKNOWLEDGEMENT

The financial support for this work from the U.S. Office of Naval Research (ONR), Contract No. N00014-82-K-0564, is gratefully acknowledged. Also, the authors wish to recognize the technical assistance of Mr. Guenther Arndt in the construction of the apparatus.

REFERENCES

1. K.C. Mills and B.J. Keene, Internat. Metals Rev., (1) (1981), 21-68.

2. B.M. Voronin, V.D. Prisyazhnyi, K.K. Khizhnyak and Ya.Yu. Kompan, Ukr. Khim. Zh., 46 (3) (1980), 229-233.

3. A. Mitchell and J. Cameron, Metall. Trans., 2 (1971), 3361-3366.

4. K. Ogino, H. Hashimoto and H. Hara, Tetsu to Hagane, 64 (2) (1978), 225-231.

5. Yu.V. Sveshkov, V.A. Kalmykov, M.V. Kamenetskii and V.Kh. Nasrednikov, Izv. Akad. Nauk SSSR, Neorg. Mater., 13 (6) (1977), 1045-1047.

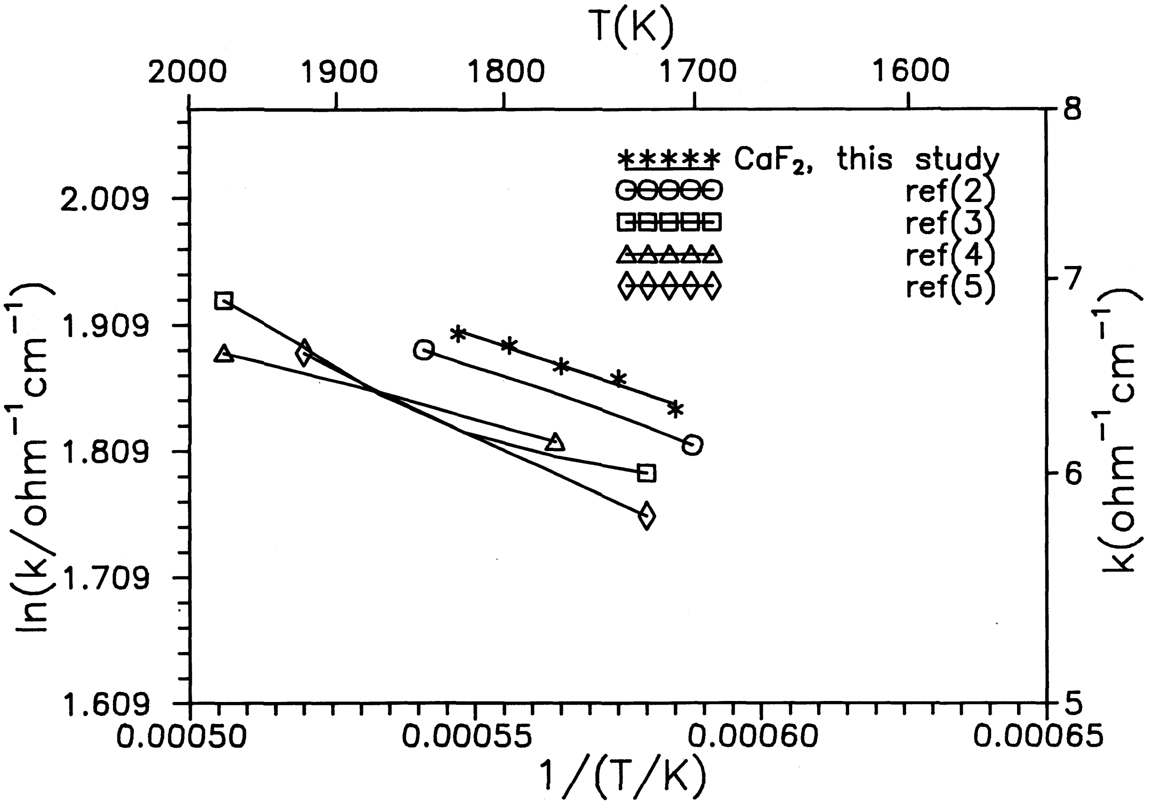

Figure 1. Specific electrical conductivity of CaF$_2$

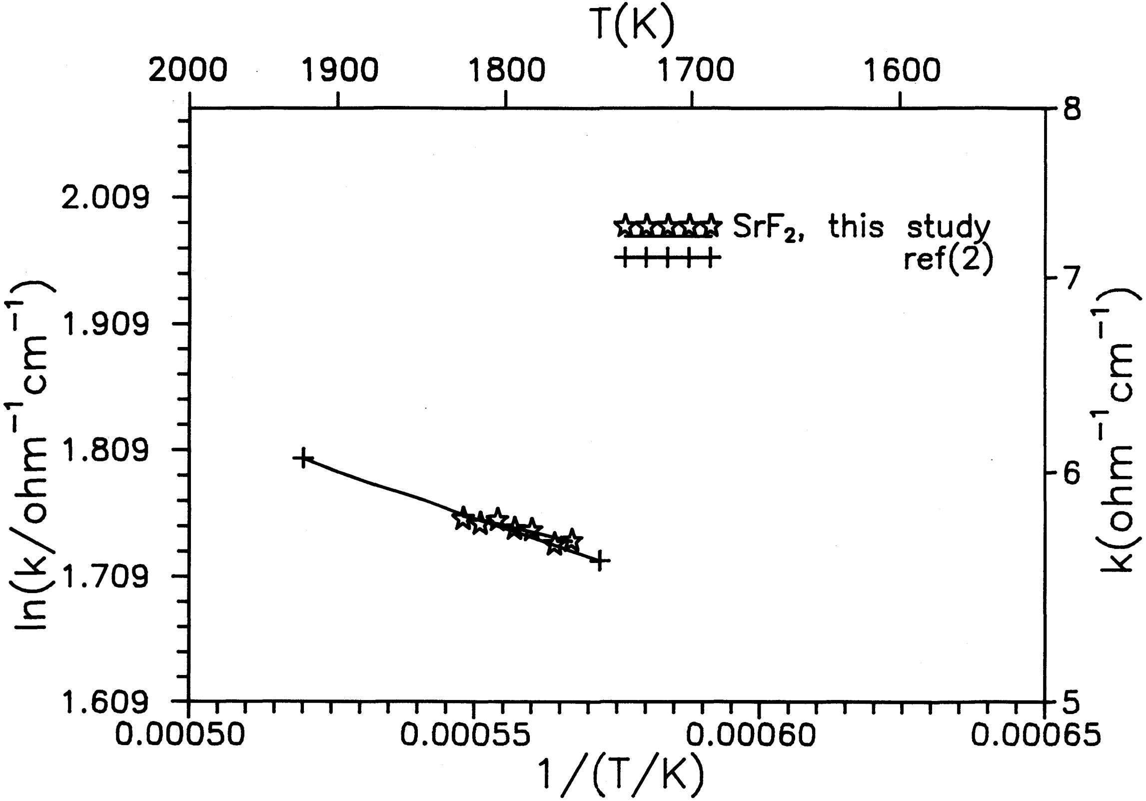

Figure 2. Specific electrical conductivity of SrF$_2$

DOI: 10.1149/199017.0179PV

STUDY OF PHASE DIAGRAMS OF SOME BaB2O4 BASED SYSTEMS*

QIAO Zhiyu (Z.Y.Qiao)
University of Science & Technology Beijing
Beijing 100083, China

G.H.Rao, J.K.Liang
Institute of Physics, Academia Sinica
Beijing 100080, China

ABSTRACT

The binary phase diagrams of BaB2O4-BaF2, BaB2O4-Na2B2O4, BaB2O4-K2B2O4 and K2B2O4-Na2B2O4 have been constructed by combining limited DTA and XRD experimental measurements and computer calculation. Based on the phase diagrams and thermodynamic data of three subsystems, the ternary phase diagram of the BaB2O4(A)-Na2B2O4(B)-K2B2O4(C) system has been calculated and partly measured. The agreement between them is good.

INTRODUCTION

The singal crystal of the low temperature phase of barium metaborate, β-BaB2O4 is an excellent ultraviolet SHG(Second Harmonic Generator) crystal and it was firstly developed in China. As a systematic search for appropriate flux that could lower the growth temperature of β-BaB2O4 single crystal, the phase diagrams of some BaB2O4 based binary and ternary systems have been constructed.

EXPERIMENTAL

1. Sample specimens

All used materials were laboratory agents. The pure components BaB2O4,Na2B2O4 and K2B2O4 were synthesized by mixing BaCO3,Na2CO3 and K2CO3 with H3BO3, respectively;sintering at 1000°C for 3-4 h, then cooling to 700°C and maintaining at this temperature for 10 h for crystallization, afterwards cooling to room temperature slowly. The synthesized products were confirmed to the congruent melting compounds by DTA and to be pure phase of BaB2O4, Na2B2O4 and K2B2O4 by X-ray diffraction analysis respectively.

The specimens for phase diagram determination were prepared by the same heat treatment procedure.In order to

---

* The Project Supported by National Natural Science Fundation of China

confirm the specimens to be well in equilibrium, the powders of the prepared specimens were annealed at 400°C for 10 days.

2. Experimental methods

The thermal analysis was carried out with home-made CR-G type DTA apparatus. The accuracy of the measured temperature was ±3 °C. Because the specimen was hydrated even at room temperature, the phase analysis was made by high temperature Gunier-Lenne monochromatic focusing camera, CuK radiation. The powder of specimen was wrapped by Al foil, which was also used as inner standard, and heated at expected temperature for 24h to reach equilibrium, then subjected to X-ray irradiation.

CALCULATION

1. Optimization and calculation of binary phase diagrams

As pointed out in Ref.[1], for molten salt system the ionic and equivalent fractions were introduced to represent ideal mixing entropy and excess Gibbs free energy. For binary system, using the notation DmQp=A and EnQr=B, Gm is expressed as:

$$Gm = X_A{}^{\circ}G_A + X_B{}^{\circ}G_B + RT[mX_A \ln Y_A + nX_B \ln Y_B] + (pX_A + rX_B)\sum_{\alpha}\sum_{\beta}(h_{\alpha\beta} - TS_{\alpha\beta})Z_A^{\alpha}Z_B^{\beta}$$

where, X_A and X_B are mole fractions of A and B, repectively;
and are positive integral powers;
$h_{\alpha\beta}$ and $S_{\alpha\beta}$ are coefficients which are assumed to be independent of T and related to enthalpy of mixing and excess entropy of mixing:

$$H\overset{M}{m} = (pX_A + rX_B)\sum_{\alpha}\sum_{\beta} h_{\alpha\beta} Z_A^{\alpha} Z_B^{\beta}$$

$${}^{E}Sm = (pX_A + rX_B)\sum_{\alpha}\sum_{\beta} S_{\alpha\beta} Z_A^{\alpha} Z_B^{\beta}$$

The experimental liquidus was fitted in the form of $T = b_0 + b_1 X_B + b_2 X_B + \ldots\ldots$ by least square method at first, a set of liquidus data calculated after the fitted liquidus equation were used to compute ${}^{E}G_m$ and G_m, then to obtain $h_{\alpha\beta}$ and $S_{\alpha\beta}$.

2. Calculation of ternary phase diagram

Based on the phase diagrams and the thermodynamic properties of three sub-binary systems, the ternary phase diagram of the BaB2O4(A)- Na2B2O4(B)- K2B2O4(C) system has been calculated by Toop[2] model and Li-Qiao model[3]. Then, the ternary phase diagram of A-B-C system can be calculated by CALTER program.

RESULTS AND DISCUSSION

1. BaB2O4-BaF2 system

As shown in Fig.1, there existed a congruent compound, BaBO2F, in this system. The eutectic temperature for L ⇌ β-BaB2O4+BaBO2F and L ⇌BaBO2F + BaF2 reactions are 749.1°C and 875.4°C,respectively. The agreement between measured and calculated results is good enough.

2. BaB2O4-Na2B2O4 and BaB2O4-K2B2O4 systems

Using the same experimental method metioned above, the phase diagrams of these two systems have been measured by Huang et al.(4.5), as shown in Fig.2 and Fig.3. The measured phase diagrams agreed well with calculated ones.

3. Na2B2O4-K2B2O4 system

The phase diagram of Na2B2O4-K2B2O4 binary system was determined by means of DTA and X-ray diffraction methods to be complete solid solution system with minimum melting point:T_{min}=836°C,X_{min}=0.375molK2B2O4. The solidus was calculated from measured liquidus by generalized Kohler and Pelton method (6). The miscibility gap of solid solution was predicted thermodynamically and confirmed by high temperature X-ray diffraction experiments.

4.The BaB2O4-Na2B2O4-K2B2O4 system

As shown in figure 5,it is a simple eutectic system with a eutcetic point at T =788°C and $X_B^{S_1}=0.769$,$X_C^{S_1}=0.231$,$X_B^{S_2}=0.681$, $X_C^{S_2}=0.319$, $X_B^L=0.436$, $X_C^L=0.245$, where S1 and S2 denote Na2B2O4 and K2B2O4 rich solid solution(Na,K)2B2O4,respectively. In the liquidus surface for saturation with the (Na,K)2B2O4 solid solution a univariant line starts from a point $X_A^L=0.534$,$X_B^L=0.260$,$X_C^L=0.206$ at 795.2°C. In order to check the calculated results,the liquidus of the vertical section through A and $X_B/X_C=1$ have been measured. The experimental liquidus data well agreed with calculated ones.

The results showed that the BaF2,BaBO2F,Na2B2O4, K2B2O4 could be possible flux condidates for getting β-BaB2O4 single crystal.

REFERENCE

(1)G.H.Rao, Z.Y.Qiao and J.K.Liang,CALPHAD,2,177(1989)
(2)G.W.Toop, Trans.AIME, 233,850(1965)
(3)R.Q.Li and Z.Y.Qiao, Rare Metals, 1,16(1990)
(4)Q.Z.Huang and J.K.Liang, Acta Physica Sinica, 30, 559(1981)
(5)G.F.Wang and Q.Z.Huang, Acta Physica Sinica, 34, 562(1985)
(6)H.Kohler and A.D.Pelton,CALPHAD, 6,39(1982)

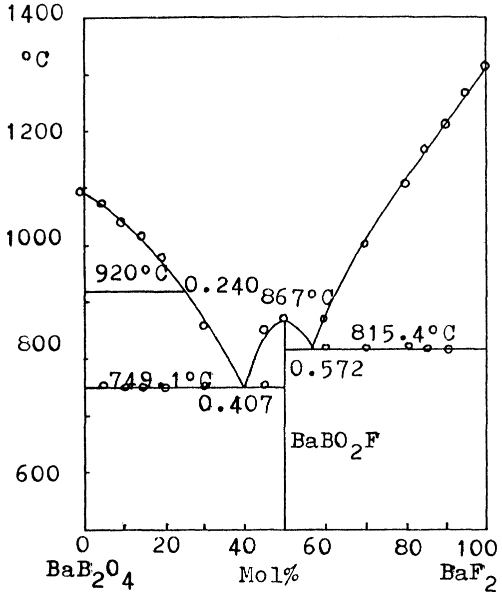

Fig.1.
BaB_2O_4-BaF_2
Phase Diagram

—— Calculated
○ Measured

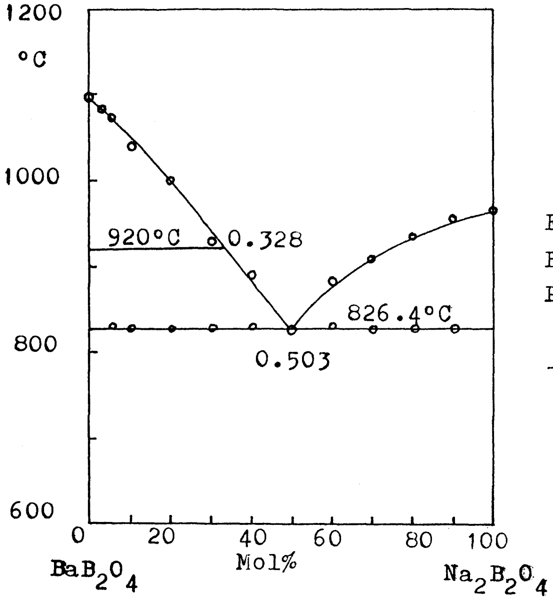

Fig.2.
BaB_2O_4-$Na_2B_2O_4$
Phase Diagram

—— Calculated
○ Measured

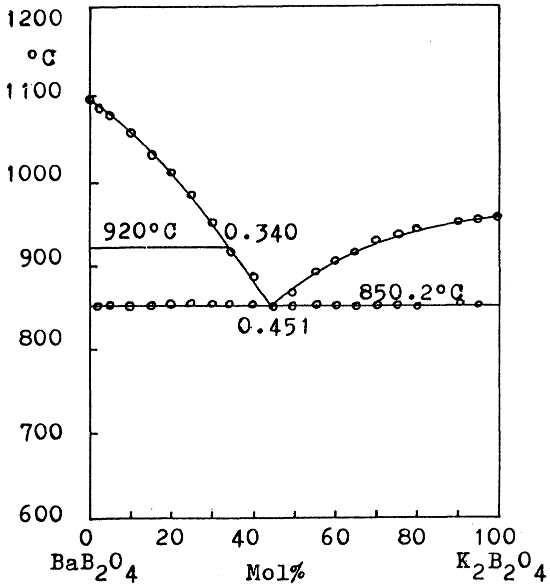

Fig.3.
BaB_2O_4-$K_2B_2O_4$
Phase Diagram

—— Calculated
o Measured

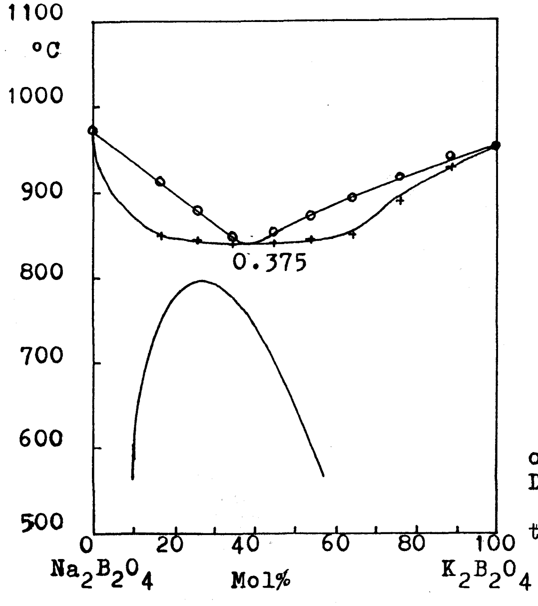

Fig.4.
$Na_2B_2O_4$-$K_2B_2O_4$
Phase Diagram

—— Calculated

Measured:

o top temperature of melting peak in DTA curve;

+ extrapolated onset temperature of melting peak

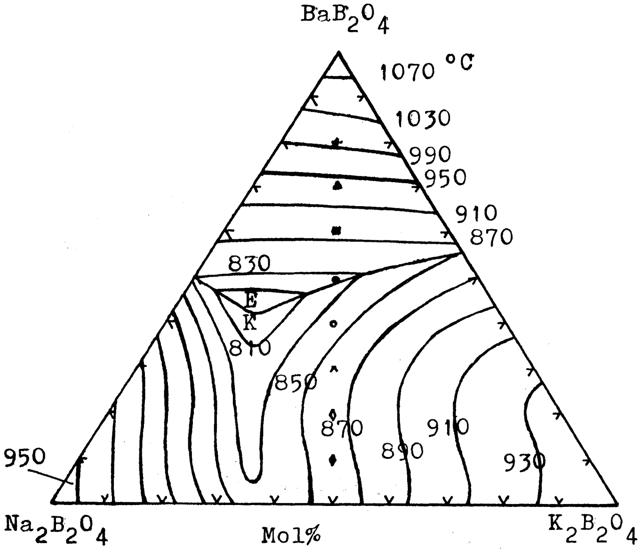

Fig.5. BaB_2O_4-$Na_2B_2O_4$-$K_2B_2O_4$ Phase Diagram

Calculated:

Experimental: °C

+1001, ▲934, ■ 894, • 829,
∘ 844, ^ 859, ◊ 851, ♦ 860

DOI: 10.1149/199017.0185PV

Electronic Conduction In Molten Cryolite Saturated With Alumina

Geir M. Haarberg, Karen S. Osen, Jomar Thonstad
University of Trondheim
Laboratories of Industrial Electrochemistry
N-7034 Trondheim, Norway

Raymond J. Heus, and James J. Egan
Brookhaven National Lab
Department of Applied Science
Upton, NY 11973

Abstract

The Wagner polarization technique was used to study the electronic conduction in the melt $Na_3AlF_6 + Al_2O_3$ at 1000^0C. Cells of the following type were employed

$$TaC(s) \mid Na_3AlF_6 + Al_2O_3(sat.)(l) \mid Na - Bi(l)_{x_{Na}=0.05} \qquad (I)$$

Currents were measured at applied potentials lower than those which would decompose the melt. In this way ionic currents are suppressed and only electronic currents flow. The electronic conductivity is determined from the current versus potential relation. Transient measurements taken on cell (I) yield the diffusion coefficient of electrons in the melt.

INTRODUCTION AND THEORY

The Wagner polarization technique is usually used to study electronic conduction in solids with both ionic and electronic conductivity, especially in systems where the electronic part is low. The theory has been treated in the literature by Wagner (1) and Kroeger (2). The method has also been employed to determine electronic conductivity of molten salts equilibrated with metal (3,4). In this work the method is applied to molten Na_3AlF_6 saturated with Al_2O_3. This melt is close in composition to that used for the production of aluminum metal in the Hall-Heroult process, so the results have application to the study of the current efficiency in this process. In the cryolite-alumina-aluminum system, it is believed that any electronic component of the total conductivity is caused by the presence of sodium due to the following equilibrium

$$Al + 3NaF = 3Na + AlF_3 \tag{1}$$

Polarization measurements were applied on cells of the following type

$$TaC(s) \mid Na_3AlF_6 + Al_2O_3(sat.)(l) \mid Na - Bi(l)_{x_{Na}=0.05} \qquad (I)$$

where the Na-Bi alloy serves as a reference electrode with known activity of sodium and the tantalum carbide serves as an inert electron conductor electrode. The TaC electrode is made negative by applying potentials across the cell. The current through the cell is entirely electronic provided that the potentials are lower than the decomposition potential of the electrolyte and no impurities are present. There is no gradient of electrical potential within the bulk of the electrolyte since ions do not move. The concentration of electrons will build up at the negative electrode, and the current through the cell is caused by the concentration gradient of electrons. Under these conditions the electronic conductivity can be calculated from the steady state current versus the potential using the following equation

$$\kappa_e = G\frac{d|I|}{dE} \tag{2}$$

where G is the cell constant. Since the measured potential corresponds to a certain activity of Na at the negative electrode, the electronic conductivity can be determined as a function of the activity of Na in the salt using the following equation

$$a_{Na} = exp\left[\frac{(E - E^0)F}{RT}\right] \tag{3}$$

where E^0 is the potential of the Na-Bi electrode versus pure sodium taken from thermodynamic data for Na-Bi alloys (5,6,7). The diffusion coefficient of electrons in the melt may be measured during transient experiments using the same cell. When a potential is imposed on the TaC electrode, a chemical potential of Na is produced in the salt at this point corresponding to a certain concentration of electrons. These electrons will diffuse toward the reference electrode according to Fick's second law. By solving the necessary equations [see Crank(8) or ref.(4)] the following equation is obtained

$$D = \frac{Il^2}{3(Q - It)} \tag{4}$$

where l is the length of the cell. By measuring the total number of coulombs Q passed through the cell until steady state the diffusion coefficient of electrons D can be determined. The mobility of electrons can be calculated from the Nernst-Einstein equation

$$u_e = (DF)/(RT) \tag{5}$$

EXPERIMENTAL

The experimental cell is shown in Figure 1. The cell consists of an alumina tube containing the Na-Bi alloy (5 mole % Na) and the cryolite-alumina electrolyte. A sapphire capillary (4.2 cm long, 3 mm bore) with a TaC electrode is dipped into the melt forming a cell of known geometry. The TaC electrode and the sapphire form a vacuum tight seal which is necessary to prevent sodium evaporation from this electrode. A constant potential is impressed across the cell making the Na-Bi electrode positive and the TaC electrode negative. A tantalum rod coated with TaC and protected by an alumina tube serves as the current lead to the alloy. The current through the cell is measured as a function of time, and the steady state value recorded. A series of corresponding current versus potential data is measured so that the electronic conductivity can be calculated as a function of potential according to equation (2). The cell constant is determined by the geometry of the sapphire capillary. The value of the cell constant is also controlled by AC resistance measurements between the two electrodes.

A transient technique is applied to the same cell in order to measure the diffusion coefficient of electrons. The current time relation is measured until steady state is attained. The number of coulombs passed is recorded and the diffusion coefficient is obtained from equation (4).

RESULTS AND DISCUSSION

The steady state currents measured at various applied potentials are shown in Figure 2 for $Na_3AlF_6 - Al_2O_3$ at 1000^0C. The experimental points were fit to an exponential equation using a least squares program. The fit of the data was good at potentials above 0.3 V, so the derivative of the I-E curve was used to obtain the electronic conductivity as a function of Na activity using equations (2) and (3). Results are shown in Figure 3. Results from transient measurements are given in Table 1.

Measurements were not extended to high potentials because aluminum starts to deposit. The activity of Na in liquid aluminum in contact with molten cryolite-alumina at 1000^0C was determined by separate emf measurements (to be published), yielding $a_{Na} = 0.06$. The transport number of electrons can be calculated from the obtained results, giving 0.2 at $a_{Na} = 0.06$. This indicates that electronic conduction may cause a significant reduction of the current efficiency during Al production. Industrial electrolysis is usually performed at lower temperatures (950^0C) with excess AlF_3 and CaF_2, causing a decrease of the activity of Na. A gradient of dissolved metal near the cathode also reduces the electronic conduction.

Initial attempts to apply the polarization technique in pure fluoride melts (NaF and Na_3AlF_6) failed due to the lack of inert materials. It was found that sapphire was not attacked significantly in $NaF - AlF_3$ melts saturated with alumina. Tantalum carbide was found to be the only satisfactory electrode material. Iron and tantalum, which have been used sucessfully in other alkali halide systems (3,4), formed alloys when polarized in cryolite melts.

Preliminary experiments indicate that the electronic conductivity versus the Na activity is not sifnificantly affected by addition of excess AlF_3 corresponding to a NaF to AlF_3 molar ratio of 2.5.

ACKNOWLEDGEMENT

This work was supported by the Division of Chemical Sciences, US Department of Energy under Contract No. DE-AC02-76CH00016 and the Royal Norwegian Council for Scientific and Industrial Research.

REFERENCES

1. C. Wagner, *Proc. CITCE* 7, 361 (1957).
2. F.A. Kroeger, *The Chemistry of Imperfect Crystals*, Vol. 2, 2nd ed., North Holland, American Elsevier, 1974.
3. G.M. Haarberg, K.S. Osen, J.J. Egan, H. Heyer, and W. Freyland, *Ber. Bunsenges. Phys. Chem.* 92, 139 (1988).
4. G.M. Haarberg, K.S. Osen, R.J. Heus and J.J. Egan, *J. Electrochem. Soc.*, in press.
5. T-S. Yih and J.C. Thompson, *J. Phys. F: Met. Phys.* 12, 1625 (1982).
6. M-L. Saboungi and T.P. Corbin, *J. Phys. F: Met. Phys.* 14, 13 (1984).
7. J.J. Egan, *High Temperature Science* 19, 111 (1985).
8. J. Crank, *The Mathematics of Diffusion*, 2nd ed., Oxford University Press, Ely House, London, 1975.

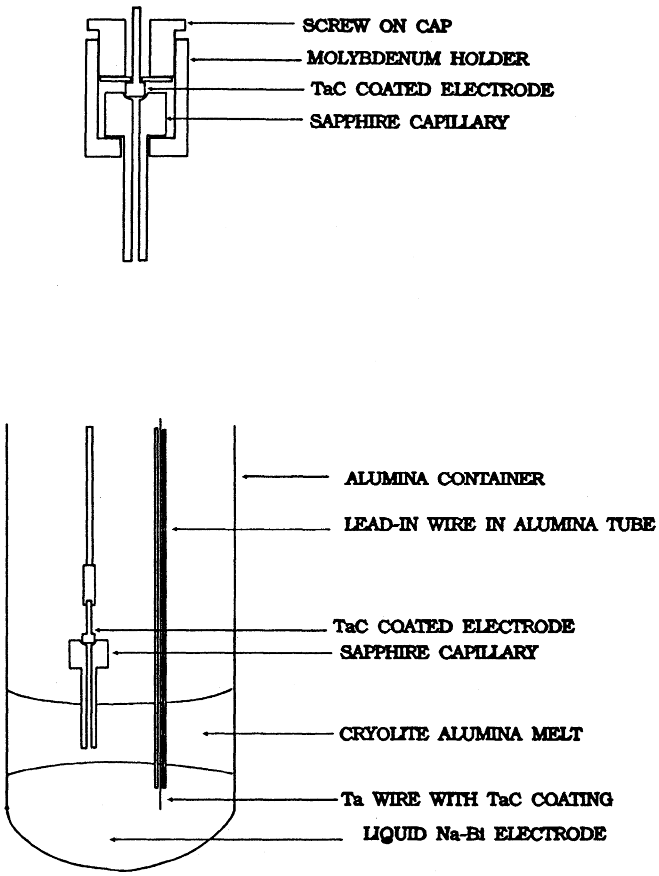

Figure 1. Experimental Arrangement and Details of the Sapphire Capillary.

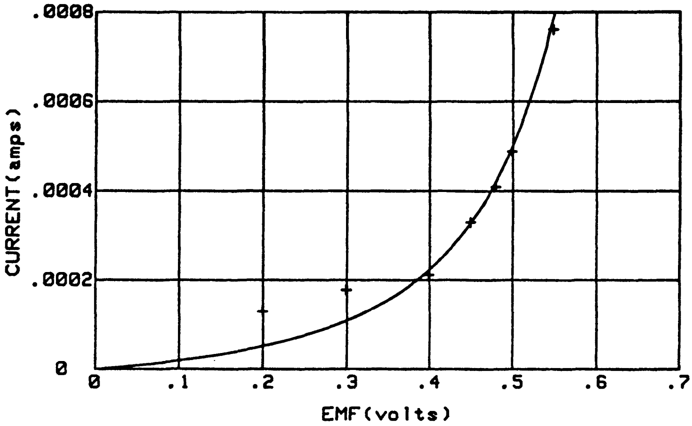

Figure 2. Current Versus Potential at 1000^0C for Cell (I). Experimental Data and Calculated Curve.

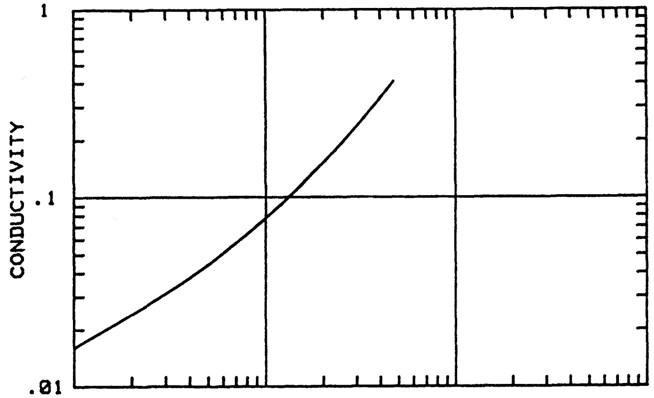

Figure 3. Electronic Conductivity in $Ohm^{-1}cm^{-1}$ as a Function of Na Activity in $Na_3AlF_6 - Al_2O_3$ (sat.) at 1000^0C.

Table 1. Results of Transient Measurements on Cell (I).

$T = 1000^0C$ $E^0 = 0.875$			
E[volts]	D[cm^2sec^{-1}]	$I_{steady}[\mu amps]$	$u_e[cm^2volt^{-1}sec^{-1}]$
0.400	0.037	210	.337
0.450	0.039	328	.356
0.480	0.036	408	.328
0.500	0.038	487	.347
0.550	0.029	752	.265?

DOI: 10.1149/199017.0193PV

Electrical Conductivity of Powder - Hydrated Melt Coexisting System

Shigehito Deki, Minoru Mizuhata, Shinya Nakamura,
Akihiko Kajinami and Yukio Kanaji

Department of Industrial Chemistry,
Faculty of Engineering, Kobe University
Rokko-dai, Nada-ku, Kobe 657 Japan

ABSTRACT

The electrical conductivity and its temperature dependency was measured for the coexisting systems of Al_2O_3 powder and a hydrated melt of $CaCl_2$, and on the basis of those results, the extent of vicinal liquid phase which was influenced by the surface of solid phase was discussed. The measurements were made on the systems ranging in liquid content from 17.1 to 42.9 vol%. Plots of the apparent activation energy versus the apparent average thickness, [volume of liquid phase]/[surface area of solid phase], indicate that the apparent activation energy decreased with increasing average thickness, until 30-40 nm, and it became constant for higher values. This behavior indicates the existence of a finite liquid layer of 30-40 nm thickness.

INTRODUCTION

In the solid-liquid coexisting system in which the solid phase is a fine powder, the chemical and physical properties depend on the content of solid phase. If the solid content is very low, the system is called a suspension and considered to be a kind of liquid. On the other hand, if the solid content is much higher, the system is called a slurry or a paste and considered a kind of solid. In the latter system, the restricted liquid layer near the solid phases relatively increases and influences remarkably the physical and chemical properties. The powder-liquid coexisting system with a high solid content is of great technical interest and an very important system for the industrial inorganic chemistry. Especially, with respect to the industries of batteries, ceramics, metal refining and so on, the heterogeneous system takes an important role in their chemical reaction mechanism.

We have been studying the physico-chemical properties of the liquid phase in the powder and electrolyte aqueous solution coexisting systems.(1)

On this paper, the electrical conductivity and its temperature dependence was measured and discussed as a function of solid content for the coexisting systems of aluminum oxide powder and hydrated melts of calcium chloride.

EXPERIMENTAL

As a solid phase in this study, α -Al_2O_3 powder which had various particle size from 0.4 to 100 μ m and specific surface area from 0.6 to 25.3 m^2/g. A hydrated melt of $CaCl_2$, in which $[H_2O]/[CaCl_2]$ ratio was in the range from 6.00 to 7.35, were used as a liquid phase. For the measurement of conductivity, aluminum oxide powder was mixed with the hydrated melt and pressed into a tablet. The measurements were made on the systems ranging in liquid content from 17.1 to 42.9 vol%. The electrical conductivity was measured at various temperatures by the AC impedance method with an impedance analyser. The range of frequency was from 5 Hz to 13 MHz.

A constant temperature Teflon cell with Pt electrodes, shown in Fig.1, was designed and used to investigate the temperature dependence of the electric conductivity. The complex plane plot of the variation of impedance with frequency showed semi-circles and/or a spike. The conductivity was determined from the intercept of the semi-circle or the spike to the real axis.

RESULTS AND DISCUSSION

A typical complex impedance plots is shown in Fig.2. Different types of plots were obtained with the variation of measuring temperature.

The observed electrical conductivity can be regarded as that of liquid phase, which is called the effective medium of conductivity (2), because α -Al_2O_3 is a typical electric insulator and its own conductivity is negligibly small. As shown in Fig.3 and Fig.4, the conductivity varied with the content of the liquid phase and remarkably increased with the liquid content at ca. 30 vol.% in which it is considered that alumina powders of the solid phase are randomly packed. This variation of conductivity with the liquid content could be explained by a percolation model(3).

The temperature dependence of conductivity for the system Al_2O_3 - $CaCl_2 \cdot 6.00H_2O$ and $CaCl_2 \cdot 7.35H_2O$ are shown as the plots of $\ln \sigma$ vs. $1/T$, shown in Fig.5 and Fig.6. Linear relationships were observed between the logarithmical conductivity and the reciprocal temperature in the temperature region above ca. 30 °C. Below the temperature, the conductivity rapidly decreased with lowering temperature and deviated from the linear relationship. Those plots frequently showed temperature hysteresis during heating-cooling arising from supercooling, as shown in Fig.8. It indicates that the deflection point, T_t, is attributed to the phase transition of liquid phase which is caused by a solidification of the liquid phase.

The temperature of the deflection point was lowered with a decrease in the liquid phase content and with an increase in $[H_2O]/[CaCl_2]$ ratio of the liquid phase, [Fig. 9]. In the system containing less liquid phase, T_t was lowered and was not observed in our measuring temperature range, though the liquid phase gave a certain melting point, at 29.8 °C for $CaCl_2 \cdot 6H_2O$, in a state of bulk liquid, as shown in Fig.6. The melting point depression may be larger than that estimated by the capillary condensation theory (4), which was derived only from the change in the radius of curvature of capillary liquid.

The apparent activation energy for the conductivity was determined from the temperature dependence by using the Arrhenius equation. It varied from 32 to 50 kJ/mol with the decrease of the liquid content and also with increase of the surface area of solid phase, [Fig. 10, 11]. The apparent average thickness of the liquid phase layer was calculated by dividing the total volume of the liquid phase with the surface area of powder in the system. It has a linear dimension and indicates the average distance from the surface of solid phase. Plots of the apparent activation energy versus the apparent average thickness, which could be varied with the variations of either the surface area or the volume, showed to be related in Fig.12 and Fig.13. With increasing the average thickness, the activation energy decreased rapidly at ca. 30-40 nm, and it gave a constant value beyond that thickness. These results suggest the existence of the restricted liquid zone, as proposed by Drost-Hansen (5), having a certain thickness in the powder - hydrated melt coexisting systems. It is considered that this surface zone is created by structural changes in water as reported by Perscell, Israelachvili and Etzler et.al.(6),(7),(8).

REFERENCES

(1) S. Deki, M. Mizuhata, A. Kajinam and Y. Kanaji, Ext. Abs. of 40th ISE Meeting (1989), Vol.2 p.1026

(2) J. R. Macdonald, Ed.; Impedance Spectroscopy,(1987) p.198, John Wiley & Sons, N.Y.

(3) K. Onizuka, J. Phys. Soc. Japan, **39**, 527 (1975)

(4) Y.Morioka, J. Kobayashi and I. Higuchi, J. Colloid Interface Sci., **42**, 156 (1973)

(5) W. Drost-Hansen, Ind. Eng. Chem. **61**, 10 (1969)

(6) G. Perschell and K. H. Adlfinger, J. Colloid Interface Sci., **34**, 505 (1970)

(7) J. N. Israelachvili and G. E. Adams, J. Chem. Soc., Faraday Trans. I, **74**, 975 (1978)

(8) F. M. Etzler and D. M. Fagundus, J. Colloid Interface Sci., **115**, 513 (1987)

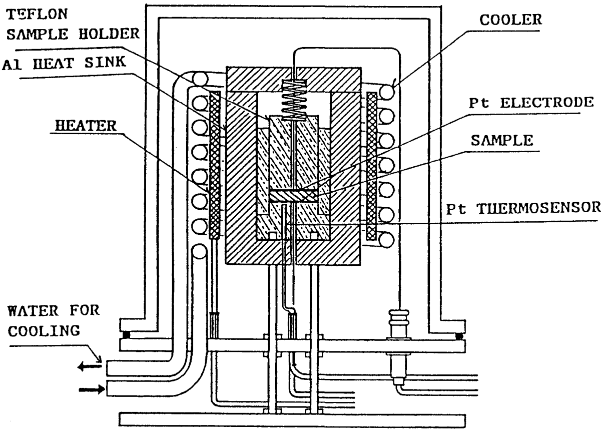

Fig. 1 Apparatus for impedance measurement.

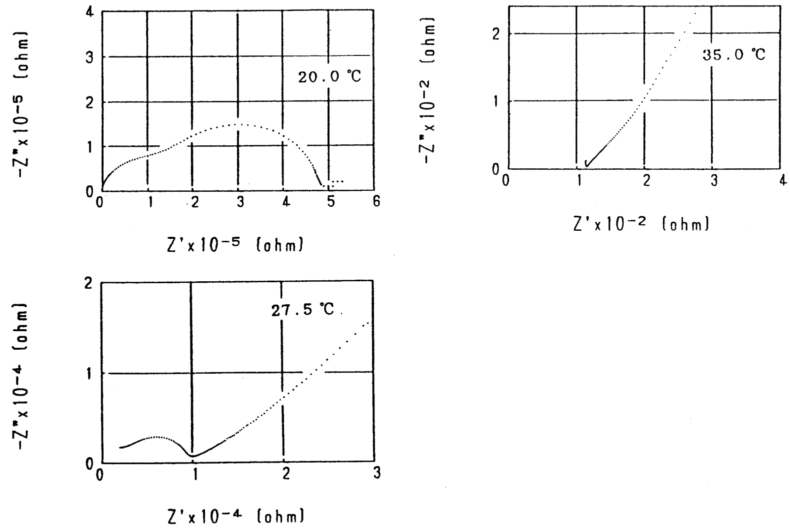

Fig.2 Complex impedance plots for α -Al_2O_3 (surface area:0.6m^2/g)- $CaCl_2 \cdot 6H_2O$ system with liquid content of 42.9vol%.

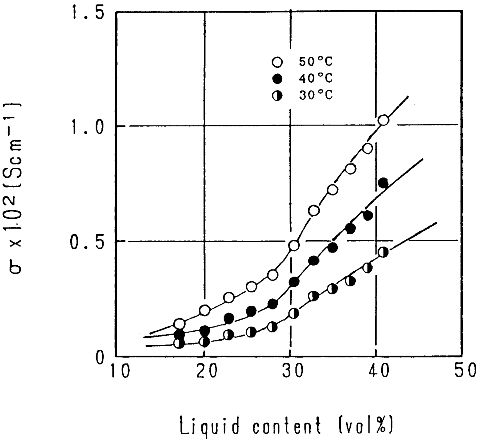

Fig. 3 Variations of electrical conductivity with liquid content for α - Al_2O_3 (surface area:0.6m^2/g) - $CaCl_2 \cdot 6H_2O$ system.

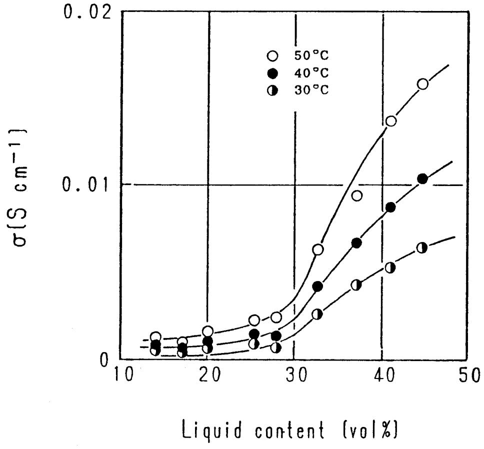

Fig. 4 Variations of electrical conductivity with liquid content for α - Al_2O_3 (surface area:0.6m^2/g) - $CaCl_2 \cdot 6.18H_2O$ system.

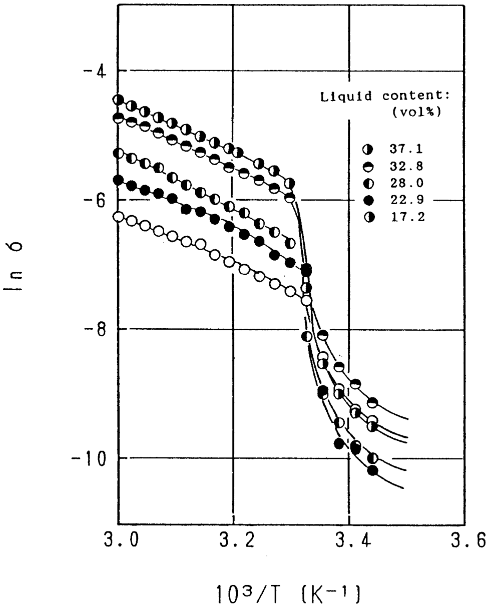

Fig. 5 Temperature dependency of electrical conductivity for α-Al_2O_3 (surface area: $0.6m^2/g$)- $CaCl_2 \cdot 6.00H_2O$ system.

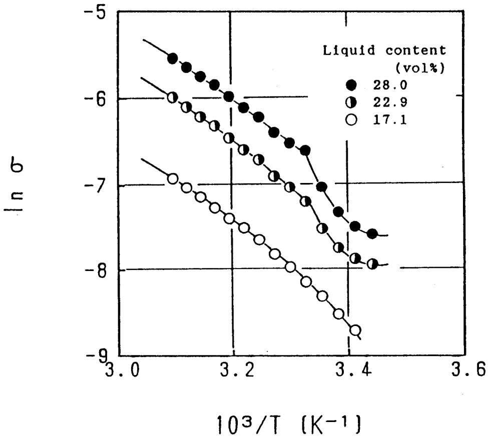

Fig. 6 Temperature dependency of electrical conductivity for α-Al_2O_3 (surface area: $25.3m^2/g$)- $CaCl_2 \cdot 6.00H_2O$ system.

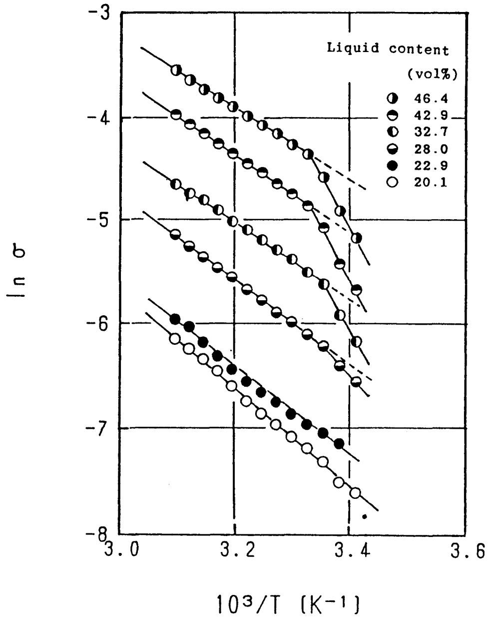

Fig. 7 Temperature dependency of electrical conductivity for α -Al_2O_3 (surface area: $0.6m^2/g$)- $CaCl_2 \cdot 7.35H_2O$ system.

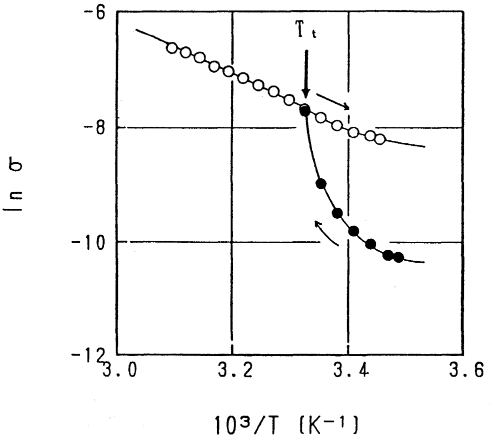

Fig. 8 Typical temperature hysteresis of electrical conductivity for α -Al_2O_3 (surface area: $0.6m^2/g$) - $CaCl_2 \cdot 6.18H_2O$ system.

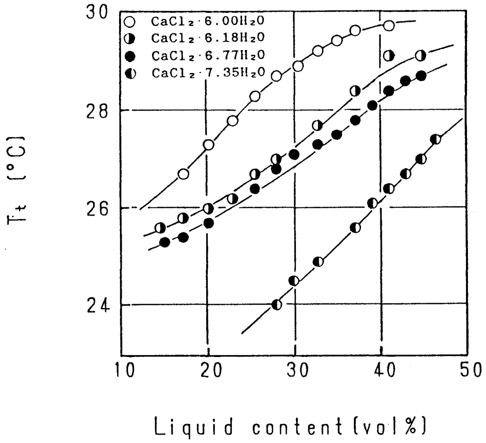

Fig. 9 Variations of transition temperature with liquid content for α-Al_2O_3 (surface area: 0.6m^2/g)-$CaCl_2\cdot nH_2O$ system.

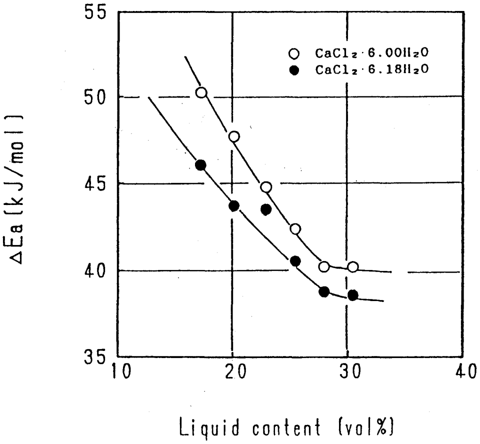

Fig.10 Variations of activation energy of electrical conductivity with liquid content for α-Al_2O_3 (surface area: 0.6m^2/g)-$CaCl_2\cdot nH_2O$ system.

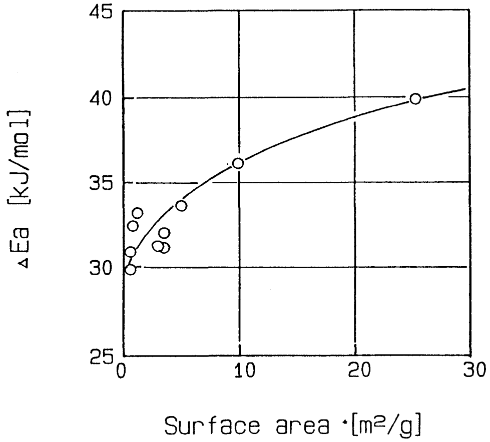

Fig.11 Variations of activation energy electrical conductivity with surface area for α -Al_2O_3 - $CaCl_2 \cdot 7.35H_2O$ system.

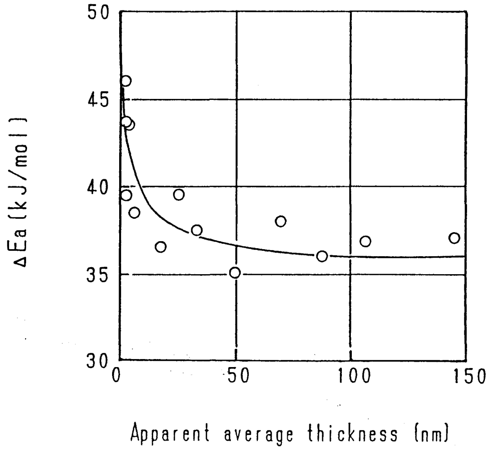

Fig.12 Relationship between activation energy of electrical conductivity and apparent average thickness of liquid phase in α -Al_2O_3 - $CaCl_2 \cdot 6.18H_2O$ system.

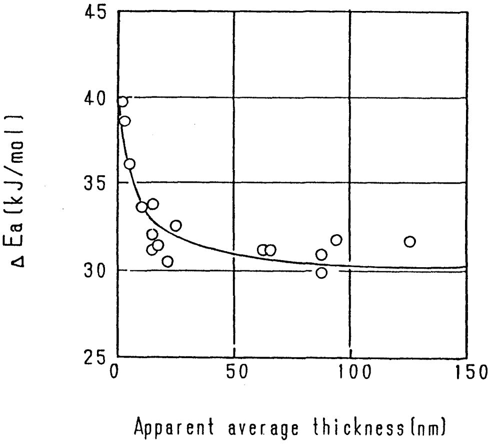

Fig.13 Variation of activation energy with apparent average thickness α-Al_2O_3 - $CaCl_2 \cdot 7.35H_2O$ system.

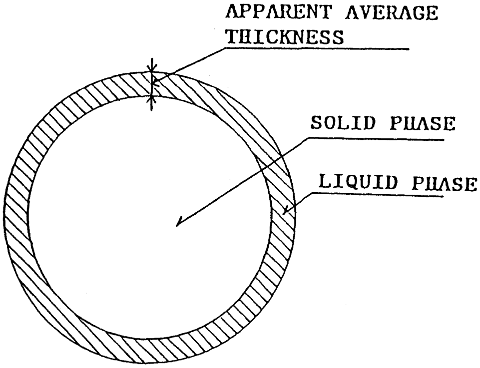

$$\text{Apparent average thickness} = \frac{\text{volume of liquid phase}}{\text{surface area of solid}}$$

DOI: 10.1149/199017.0203PV

ELECTRICAL CONDUCTIVITY OF MELTS IN THE SYSTEM Fe_2O_3-FeO-CaO

Jaroslav Fedor and Ľudovít Bobok

Research Institute of Metallic Materials
Technical University Košice

ABSTRACT

The paper discusses the mechanism of the electrical conductivity of the slags consisting of Fe_2O_3, FeO and CaO. From the experimental results the contributions of individual ionic species and of electrons to the overall transfer of charge were determined. The ionic component of the conductivity has been considered and discussed in terms of the assumed structure of the melt. The discussion of the electronic conductivity is carried out from the point of view of the mechanism of exchange of electrons between Fe^{2+} and Fe^{3+} cations.

INTRODUCTION

As a result of an increasing interest in the possibility of the application of the calcium-ferrite slags in pyrometallurgical extraction processes it has become necessary to know their physical properties and to better understand the structure of this unconventionl type of slag. The electrical conductivity of the conventional electrolytic melts is very sensitive to their structure. The conductivity depends on the amount of the charge carriers present in the melt and on their mobilities. It is well known that in the melts of oxides the transfer of charge is carried out exclusively by simple cations (e.g. Na^+, K^+, Ca^{2+} atc.) Other cations (e.g. Si^{4+}, P^{5+}, B^{3+}) create long structural units that have extremely low mobility. Oxides of amphoteric metals (e.g. Al^{3+}, Fe^{3+}) may behave either as network formers or as network modifiers. Their participation in the transfer of charge in the melt depends on the type of their behaviour. Slag systems containing polyvalent metals in two different valency states (e.g. Fe^{2+} and Fe^{3+} or Bi^+ and Bi^{3+}) exhibit also an electronic conductance. This is the reason why it is virtually impossible to arrive at any definite conclusion concerning their structure in the molten state simply on the basic of experimentally determined electrical conductivities.

In an attempt to describe the mechanism of the electronic conductivity two different approaches have been used. The first is based on the band theory of electronic structure. Due the disturbances in the stoichiometry of a chemical compound free electrons appear in a conductive band or vacancies are being created in a valency band. In the case of the slag system investigated in this work this theory has only limited validity as it can describe the behaviour of the slag at the extremely high or extremely low oxygen potentials. Moreover, the band theory is based on the periodicity of a lattice potential which implies the existence of a longe-range order in a solid. When the solid melts, band boundaries become distorted and broadened and new energy levels may appear in the so far forbidden zones šhich is why it is virtually impossible to find an analytical expression for the description of the electrical conductivity (1).

The melts investigated in this paper behave in accordance with the polaron theory according to which electrons and electron holes are localized on the ions. Electronic conductivity of the melts is direct consequence of the jump of an electron from a cation in its lower valency state to the one in the higher one. The exchange of electrons may occur between cations with different valencies and the electrons can be exchanged at appreciably high frequencies even in the case that the distance between the pair of ions between which the electron is being exchanged is several times longer than the atomic radius, particularly when the bridging groups are present in the melt (2).

The objective of this investigation was to assess the contribution of individual ions and electrons to the transfer of charge in the melt, to find a correlation between the structure of the melt and its ionic conductivity and, last but not least, to verify the applicability of the jumping electron model of the electronic conductivity to the melts of the Fe_2O_2-FeO-CaO system.

EXPERIMENTAL

As the calcium ferritic slags are highly corrosive with respect to the refractory oxides and alloys of the metals of platinum group and also because the composition of the melt was strongly dependent on temperature and oxygen potential, the electric conductivity measurements were rather elaborate. The final version of the experimental assembly and the range of temperatures that have been finally adopted should therefore be considered as a compromise between what was available in terms of equipment and what was necessary from the point of view of what we intended to achieve.

A bridge circuit method was used for measurements. The simplified schematic diagram of the circuit is depicted in Fig 1. The most important unit of the circuit was the RCL radio-frequency Wayne-Kerr bridge. Two platinum electrodes 2 mm in diameter situated 12 mm apart were used. The melt was held in platinum or magnesia under purified nitrogen at temperatures between 1550-1600 K. The composition ot the furnace gas was monitored by using gas chromatography. Samples of melts were quenched and chemically analysed for Fe^{2+} and Fe^{3+} contents, other constituents of the slag were analysed by Atomic absorption spectrometer.

RESULTS

The chemical composition of the melts and the corresponding results of their electrical conductivities are summarized in Tab.1.

Table 1: Chemical analysis and specific conductivity in the Fe_2O_3-FeO-CaO system at 1573 K

Chemical analysis (mol.%)			specific conductivity ($S.m^{-1}$)		
FeO	Fe_2O_3	CaO	$\mathcal{H}^{total}$	$\mathcal{H}_1^{reg}$	$\mathcal{H}_2^{tun}$
52.12	18.43	27.8	2440	2250	1927
54.47	21.52	22.21	2505	2326	2689
26.31	22.96	50.71	1591	1436	1475
25.82	28.04	46.12	1651	1512	1267
20.36	29.39	50.24	1479	1347	834
18.72	33.81	47.46	1442	1324	659
11.92	40.30	47.77	1022	923	330
49.01	16.19	33.63	2194	1997	2068
49.88	15.82	33.15	2252	2053	1972
52.21	15.07	31.42	2425	2221	1889
6.85	43.72	45.3	686	602	143
6.74	49.33	43.91	680	604	145
56.45	19.08	24.45	2537	2346	2482
23.35	33.89	42.75	1727	1606	972
7.96	45.09	46.93	812	726	183
30.74	24.78	44.46	1777	1625	1724
26.11	29.83	44.04	1648	1515	1404

The variation of the conductivity of the melt with the composition can be fitted to the following equation:

$$\mathcal{H} = \sum_{i=1} z_i \cdot F \cdot u_i \cdot c_i \tag{1}$$

where c_i is the concentration of the conductive particles having the charge z_i, u_i is the mobility and F Faraday's constant.

Concentrations of individual ionic species were determined from the results of the density measurements and calculated as the ratio of molar fraction and molar volume. The number of electrons that participated in the transfer of charge in the melt was estimated on the basis of assumption that and electron may jump from Fe^{2+} ion as long as the Fe^{3+} ion is present (3). The concentration of cations in the melt can be calculated from the relation:

$$C(e^-) = 2\ X_{Fe_2O_3} \cdot X_{FeO} / V_m \tag{2}$$

We used multiple regression method for the determination of the coefficients of the following equation:

$$\mathcal{H} = -A + B_1 \cdot C\,(Ca^{2+}) + B_2 \cdot C\,(Fe^{2+}) + B_3 \cdot C\,(Fe^{3+}) + B_4 \cdot C\,(O^{2-}) + B_5 \cdot C\,(e^-) \tag{3}$$

Best correlations were obtiained on the assumption that Ca^{2+}, Fe^{2+} and e^- were the only species that participated in the transfer of charge. The mobilities of the charge transfering species were calculated from the coefficients B_i ($u = B_i / z_i F$) and the diffusion coefficents calculated from the Nernst/Einstein's equation. The results are summarized in Tab.2.

Table 2: Regression coefficients, mobilities and difusion coefficients of the particles Ca^{2+}, Fe^{2+} and e^- in the the Fe_2O_3-FeO-CaO system at 1573 K

Parameter	Ca^{2+}	Fe^{2+}	e^-
$\frac{B}{S.m^2.mol^{-1}}$	$3.6369.10^{-3}$	$5.8252.10^{-3}$	0,2739
$\frac{u.10^8}{m^2.s^{-1}.V^{-1}}$	1,88	3,02	283.9
$\frac{D.10^9}{m^2.s^{-1}}$	1,3	2,1	384,8

DISCUSSION

The magnitudes of the calculated coefficients of the equation (3)allow us to assume that Ca^{2+}, Fe^{2+} ions and electrons have the highest contributions to the transfer of charge. The size of O^{2-} ion is relatively large hence it exhibits low mobility. Statistical insignificance of the coefficients B_3 of equation (3) stems from tendency of Fe^{2+} cation to create larger structural units which can be represented by the general formula $Fe_xO_y^{z-}$. This property depends on the magnitude of the ratio Fe^{3+}/O^{2-}. Any increase in the concentration of O^{2-} anion in the melt brings about a gradual change in the coordination number of the Fe^{3+} ion which can be represented in a following manner:

$$Fe^{3+}\ (6) \rightarrow FeO^{+} \rightarrow FeO_2^{-} \rightarrow Fe_2O_5^{4-} \rightarrow FeO_4^{5-}\ (4) \qquad (4)$$

This assumption has been inderectly confirmed at our laboratory by the result obtained from the density viscosity and surface tension measurements. Mobilities of large ferrite anions are small and the contribution of Fe^{3+} ion to the overall conductivity is insignificant.
Mobilities of Ca^{2+} and Fe^{2+} cations are very similar and their diffusion coefficients are higher than in the silicate melts. These conclusions are in a good agreement with low viscosities that were measured in calcium ferrite slags. To our surprise, both the mobility and the diffusion coefficient of Fe^{2+} cation exceed those of Ca^{2+} cation.

The mobility of electrons is by two orders of magnitudes higher than the mobility of any other charge transferring specie. For this reason the electronic conductivity may greatly exceed the contribution of ions to the overall conductivity. The magnitude of the electronic component of conductivity depends however on the concentration of Fe^{2+}, Fe^{3+} ion in the melt. According to the electron jumping model (1), the frequency of an electron jump may be expressed in the following manner:

$$\nu_r = u_e \cdot 6 \cdot kT /(.e.r^2) \qquad (5)$$

where e is the charge of an electron, u_e the mobility of electron, r-the distance between Fe^{2+} and Fe^{3+} cations, k-the Boltzmann constant, T-temperature.
The applicability of this model has been tested by calculating the frequency of electron jump from the experimentally determined conductivities and by comparison with the results calculated from the theory. The frequencies determined from the experiments were expressed as the ratio $\varkappa_e/F\ C(e^-)$ whe-

re as the electronic conductivities were determined after subtracting ionic portion of conductivity from the overal conductivity and applying the regression coefficients from equation (3).
The fact that the plot $\log \nu_r$ vs r is linear (Fig.2) is in accord with the electron jump model. The slope of the line corresponds to the effective potential energy barrier of the exchange of one electron between the ions.
If $\alpha = 0{,}2510^{10}\ m^{-1}$ is substituted to the equation (7) which assumes the transfer of an electron by its tunneling through the effective energy barrier

$$\alpha = (2\ m_e\ .\ H)^{1/2}\ /\ \hbar \qquad (7)$$

where m_e is the mass of an electron
H is the height of the energy barrier
$\hbar = h/2\pi$ and h is the Planck's constant
The calculated value of H is equal to 0,3 eV and its magnitude is similar to 0.375 eV found in wustite on the basis of quantum theory approach (4).
Mott (5) expressed the electronic conductivity in the melts that consisted of transition metals in the following manner:

$$\varkappa_e = \nu\ X(1-x)\ .\ F^2/(R.T.N.r)\exp\ (-2\ \ r).\exp\ (-W/RT) \qquad (8)$$

where ν is the phonon frequency, X, (1-X) are the mole fractions of the two valency states of a metal and W is the activation energy. The electronic conductivities calculated from the Mott's model were then compared with the electronic conductivities calculated as a product:

$$\varkappa_e = B_5\ .\ c\ (e^-) \qquad (9)$$

Satisfactory agreement has been found between the results calculated by two methods. The existing disciepancies may have been caused by the fact that the term exp (-W/RT) in equation (8) was approximate. Nevertheless one can assume that the activation energy of the electronic conductivity is small in system rich in Fe_2O_3.(Fig.3)

CONCLUSION

In oxidic melts comprising Fe_2O_3, FeO and CaO, Fe^{2+}, Ca^{2+} and free electrons have been found to be the main carriers of the charge. Fe^{3+} cations may create the ferrite anions that do not participate in the transfer of charge. Mobilities of electrons are by two orders of magnitudes higher than those of cations. Electronic conductivity occurs through the exchange of electrons between Fe^{2+} and Fe^{3+} ions. According to quantum theory tunneling phenomenon, the height of an effective potential energy barrier is lower than 0.5 eV. We have found satisfactory agreement between the electronic conductivity calculated on the basis of the electron jump model and the one determined from the regression analysis.

REFERENCES

1. D.O. Raleigh, J.Chem.Phys., 38, 1677, (1963)
2. J.Halpern and L.E.Orgel, Discus.Faraday Soc., 29, 32, (1960)
3. V.Daněk, T.Ličko and Z. Pánek, Research report Inst. Inorg.Chem. Slovak Ac.Sc., Bratislava, 1984
4. G.G. Michajlov and V.A. Kožeurov, Zhurnal fiz.chim, 39, 775, (1965)
5. N.F. Molt, Adv.Physics, 16, 49, (1967)

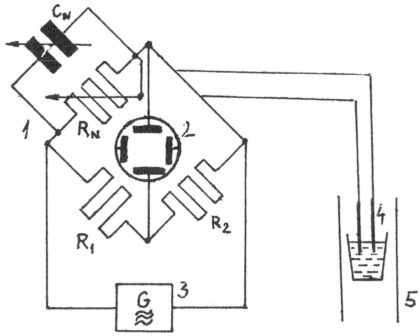

Figure 1. Schematic diagram of the measuring circuit
1- RCL bridge 2- oscilloscope 3- high-frequency generator 4- electrode
5- electrical furnace

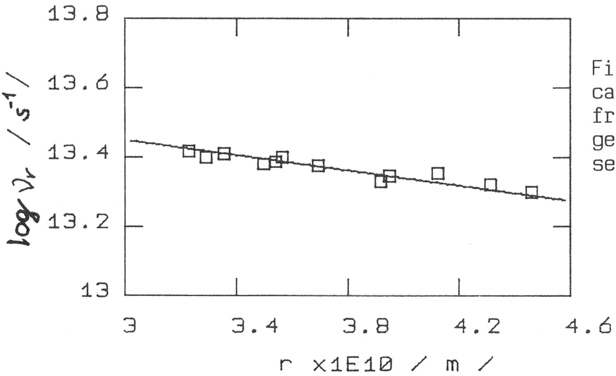

Figure 2. Log calculated jump ^{r} frequency vs average exchange pair separation

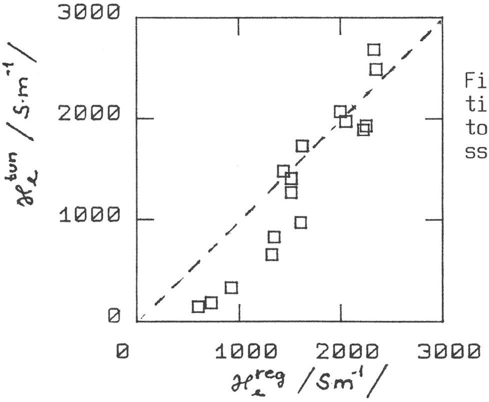

Figure 3. Electronic conductivity calculated according to Mott's model and regression analysis

DOI: 10.1149/199017.0211PV

CONDUCTIVITY, VISCOSITY, HNMR SPECTRA AND DENSITY OF MIXTURES OF 2-METHYLPYRIDINIUM CHLORIDE AND μ-HYDROGENBIS(2-METHYLPYRIDINIUM) IODIDE.

David S. Newman and Yong Zhang

Department of Chemistry
Bowling Green State University
Bowling Green, OH 43403

ABSTRACT

The viscosity, electrical conductivity, and density of binary solutions of 2-methylpyridinium chloride and μ-hydrogenbis(2-methylpyridinium) iodide were measured as a function of composition and as a function of temperature. It was found that the transport properties showed an Arrhenius temperature dependence and that the densities were linear in temperature. However, the isothermal variation of density with composition showed a fairly sharp maximum at $X_I = 0.9$ which is accounted for by a model in which the u-hydrogen bond breaks as the Cl^- ion concentration increases.

INTRODUCTION

Correlating transport properties of binary molten organic salt solutions with thermodynamic properties and molecular structure allow inferences to be drawn regarding the interionic forces extant in the liquid and the microscopic changes in melt structure that cause these transport and thermodynamic phenomena (1). A particularly interesting system in this respect is the binary solution of 2-methylpyridinium chloride (2-MPCl) and μ-hydrogenbis(2-methylpyridinium) iodide (μ-H-I). μ-H-I is shown in Fig. 1.

In an earlier study, it was found that the reaction between 2-methylpyridine and HI(g) produced μ-H-I rather than the expected 2-methylpyridinium iodide (2-MPI) (2). The μ-H-I melt has unusual transport properties as well as an exceptionally low liquid density compared to the other methylpyridinium iodides. This low density is attributed to the μ compound's inability to pack tightly in the liquid state so that if the μ-hydrogen bond were to break, the liquid structure might "collapse", causing a precipitous increase in melt density accompanied by changes in transport properties. This bond might be cleaved by adding 2-MPCl to the µ-H-I because the Cl^- ion would compete with the ring nitrogen for the hydrogen and is also capable of forming strong hydrogen bonds. Therefore, it was decided to vary the composition of a binary mixture of 2-MPCl and µ-H-I and observe the changes in density and transport properties that resulted. In addition, the low liquidus temperatures of these binary solutions make them easily accessible to NMR measurements so that structural properties might be correlated with transport properties.

EXPERIMENTAL DETAILS

2-MPCl was synthesized by passing HCl(g) through 2-methylpyridine that had been dried over CaO and distilled at 128-129 °C. The reaction is

$$HCl(g) \quad + \quad 2\text{-}CH_3C_5H_5N(l) \quad \text{--->} \quad 2\text{-}CH_3C_5H_6NCl(s) \qquad [1]$$

The melting point of 2-MPCl was 88-89°C which is in exact agreement with literature values (1,3). The µ-H-I was synthesized by a reaction similar to Eq. [1] except that gaseous HI was bubbled through 2-methyl pyridine and the reaction vessel was covered with aluminum foil so as to prevent light from reaching the µ-H-I. The final recrystallized product had a melting point of 93-94°C. which is in agreement with our earlier result (2).

A capillary cell with cylindrical platinum electrodes and a Jones bridge were used to measure the ac conductivity at 1000 Hz. The variable temperature probe of a Varian XL-200 NMR machine was used to obtain the NMR spectra. DMSO was used as an external standard. A Lipkin bicapillary arm pycnometer was used to measure melt densities and a Cannon-Fenske viscometer was used to measure viscosity. All transfer operations were done in a controlled atmosphere dry box in which the "boil off" from liquid nitrogen was circulated.

RESULTS

Figure 2 shows a plot of the natural log of the equivalent conductance (Λ) vs. 1000/T for various compositions, and Fig. 3 shows a graph of the natural log of the melt viscosity (η) vs. 1000/T for the same compositions. Figure 4 shows a graph of density vs T for the different melt compositions. It is clear that, within experimental error, these curves are all linear. It is also obvious from Fig. 4 that the pure μ-H-I is *not* the most dense melt. Figure 5 is a plot of density vs composition at three different temperatures; 373 K, 393 K, and 408 K. The dashed curve is the "measured" density vs composition behavior at 408 K if our proposed model were correct (*vide infra*). Figure 6 is a plot of the specific conductance vs mole fraction at three different temperatures and it is clear there are two maxima in each of the curves. Figure 7 shows the equivalent conductance vs composition at the same three temperatures and, at least at the two lower temperatures, there seems to be an inflection point. To calculate the Λ values in Fig. 7, the equivalent weight of the u-H-I was used. Figure 8 is the HNMR spectrum of pure 2-MPCl at 102°C. The HNMR spectrum for the pure μ-H-I is given elsewhere (2). Figure 9 is a graph of the nitrogenic and u-proton chemical shifts as a function of composition at 102°C. The lower curve in this figure shows the chemical shifts of the gamma proton as a function of composition. At 200 MHz, the machine could not resolve the two gamma peaks. Figure 10 shows the isothermal changes in viscosity as a function of composition.

DISCUSSION

The conductivity and viscosity at each melt composition shows strict Arrhenius behavior over the relatively narrow temperature range investigated. However, isothermal measurements of Λ and η show a negative deviation from ideality as a function of composition, the deviation decreasing with increasing temperature. Moreover, the negative deviation is considerably more pronounced for viscosity than it is for conductivity. Although the density at each composition is a linear function of temperature, the isothermal changes in density as a function of composition go through a sharp maximum at around X_I = 0.9. This maximum becomes less pronounced as the temperature increases.

The model we propose to account for these results is one in which the μ-H-I dissociates into 2-MPI and 2-methylpyridine as X_I varies from 1 to 0. In other words, at all concentrations other than X_I = 1 and X_I = 0 there is some 2-methylpyridine in the solution, and there are four constituents in the mixture: 2-MPCl, 2-MPI, μ-H-I and 2-methylpyridine. Therefore, the densities of the 2-MPI and 2-methylpyridine have to be considered when calculating the density of the mixture at all intermediate compositions between $X_I = 1$ and $X_I = 0$. The density of 2-MPI is not known, but the density of 3-MPI is known (2), and it is expected to be within +/- 1% of the density of 2-MPI because this is the case with 2-MPCl and 3-MPCl as well as with 2-MPBr and 3-MPBr (1). The density of 2-methylpyridine is easily measured as a function of temperature. Using these data and the additional assumption that $\Delta V_{mix} = 0$, the dashed curve in Fig. 5 was calculated. It is obvious that the measured density vs mole fraction curves exhibit a sharper and more complex maximum than the model density vs mole fraction curve does. But, considering that the actual ΔV_{mix} is almost certainly not zero and that hydrogen bonded species like $[>N\text{-}H..Cl..HN<]^+$ form between two 2-methylpyridinium ions and a Cl^- ion (3), the fact that the calculated maximum is near the measured maximum and the calculated curve has the same general shape as the measured curve is very reassuring.

This simple model also predicts one broad maximum in the specific conductance vs composition curves. Since the total number of charges is constant, as the density increases the number of charge carriers per unit volume must increase. In addition, the mobility of these charge carriers would be expected to increase at first because the 2-methylpyridine molecules formed by the dissociation of the μ-H-I acts as a sort of lubricant and reduces the viscosity. The combination of these two phenomena increases the specific conductance. As the melt becomes richer in Cl^-, hydrogen bonding between Cl^- and $2\text{-}MP^+$ ions begins to control the transport mechanism (that is why the pure 2-MPCl is a poorer conductor than the pure μ-H-I) and the specific conductance would be expected to decrease monotonically until the pure 2-MPCl conductance is reached. Although the measured specific conductance vs composition roughly approximates this behavior, the observed shallow minimum or second maximum cannot be explained by this simple model alone. In a future study we will offer a more detailed explanation for the "second maximum" in these curves.

A further indication that this model is essentially correct arises from the equivalent conductance vs. composition curves. In Fig. 7, if the equivalent weight of μ-H-I (314 amu) is used to compute the equivalent conductances from the specific conductances (which is correct way to proceed if the μ-H-I did not dissociate) an inflection point arises in the Λ vs composition curve (Fig.6). If, on the other hand, the equivalent weight of 2-MPI (221 amu) is used with the appropriate mole fractions of 2-MPCl and μ-H-I, e.g., at a nominal $X_I = 0.5$ only the equivalent weight of 2-MPI and 2-MPCl were used to compute the equivalent conductance from the specific conductance because there is no longer any μ-H-I present, the typical smooth Λ vs composition curves shown in Fig. 11 are obtained and the inflection point vanishes.

Our preliminary HNMR curves indicate that some μ-H-I persists at $X_I = 0.4$ whereas our model predicts it should all be gone at $X_I = 0.5$. This small discrepancy is almost certainly due to the fact that some of the Cl^- ions are hydrogen bonded to the $2\text{-}MP^+$ ions and are not free to compete for the μ-hydrogen.

CONCLUSION

The binary mixture of 2-MPCl and μ-H-I exhibited unusual density vs. mole fraction behavior at each of three different temperatures. This unusual behavior is explained to a first approximation by a model in which the μ-H-I dissociates into 2-MPI and 2-picoline as the system becomes richer in 2-MPCl. In a future study, this model will be refined to include nonideal mixing and hydrogen bonding between the Cl^- ions and the $2\text{-}MP^+$ ions.

REFERENCES

1. D. S. Newman, R. R. Rhinebarger, D. Siconolfi, O. A. Banjoko, J. Electrochem. Soc., *128*, 2331 (1981).

2. D. S. Newman and R.M. Stevens, J. Electrochem. Soc., *131*, 1275 (1984).

3. J.W. Shuppert and C.A. Angell, J.Chem. Phys, *67*, 3050 (1977).

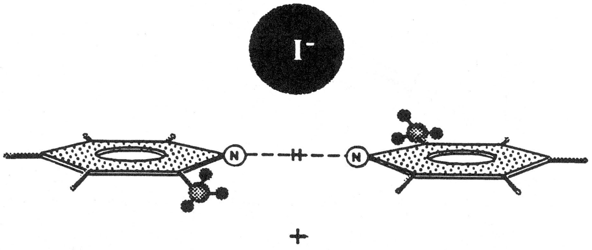

Figure 1. Structure of U- hydrogenbis (2 - methylpyridinium) iodide

Figure 2.
ln Λ vs. 1/T

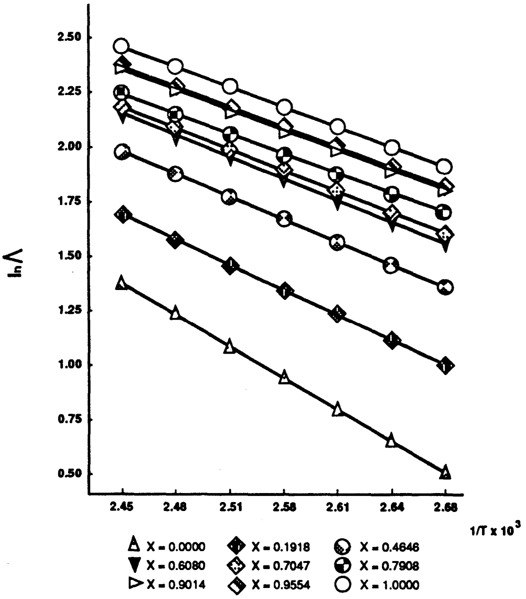

Figure 3.
ln η vs. 1/T

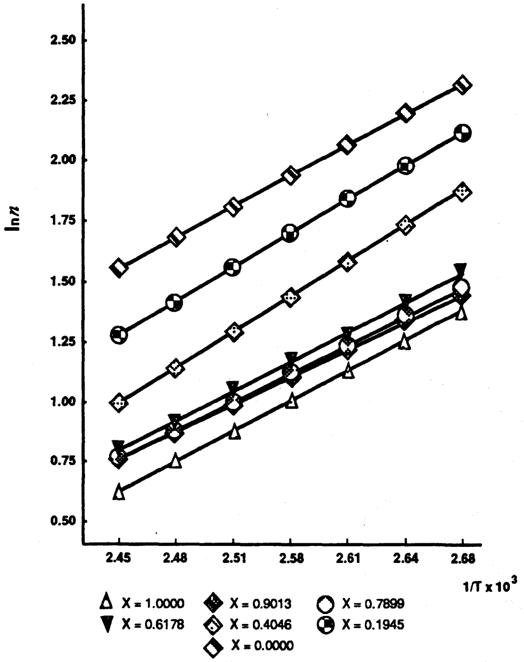

Figure 4.

Densities as a function of temperature

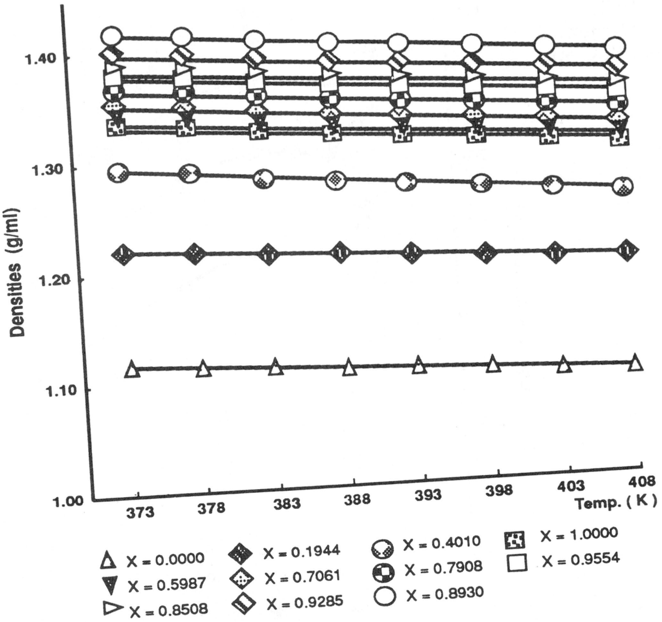

Figure 5.

Densities as a function of mole fraction

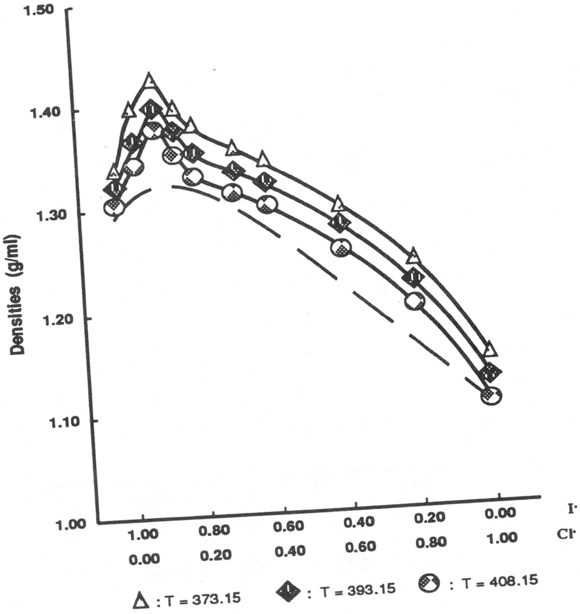

Figure 6.

Specific conductances as a function of mole fraction

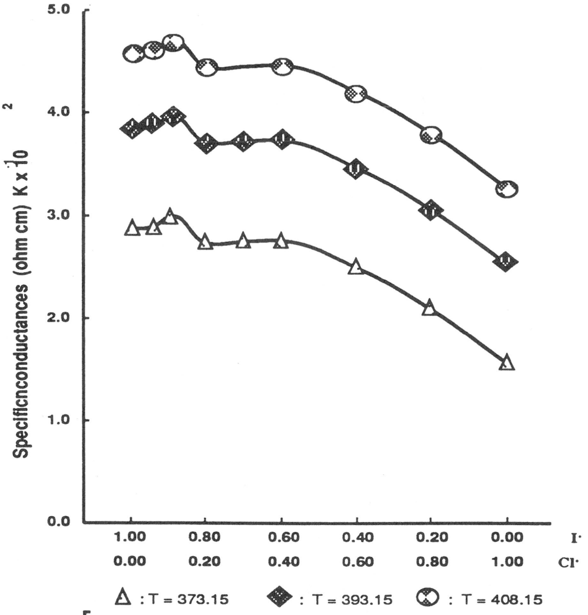

Figure 7.

Equivalent conductances as a function of a mole fraction

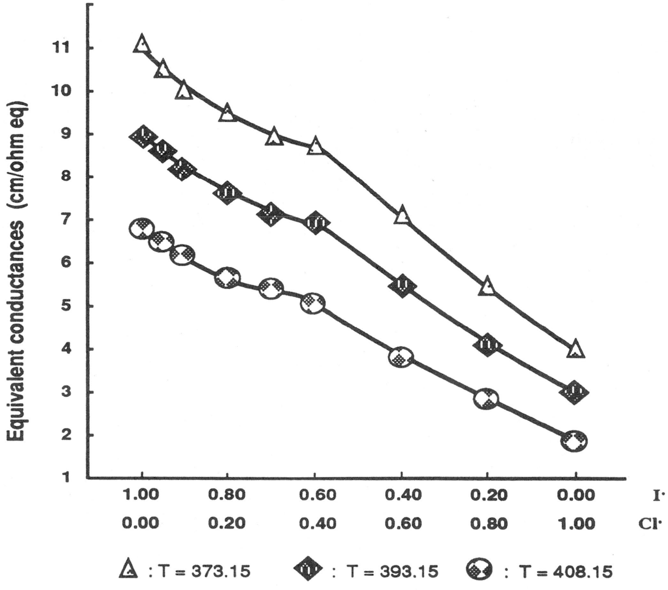

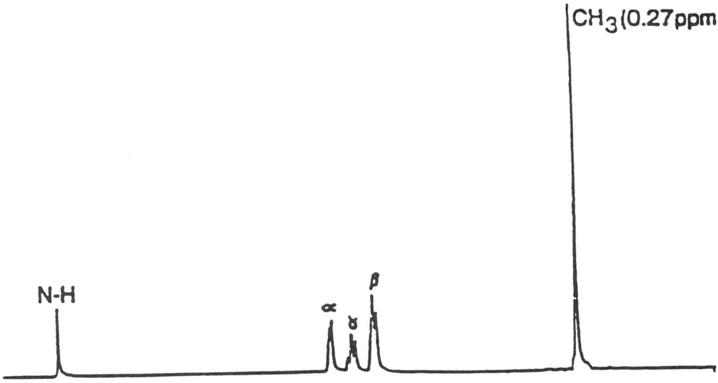

Fig. 8. ^{1}HNMR spectrum of μ-hydrogenbis(2-methylpyridinium) iodide. 102°C

Figure 9.

Chemical shift δ

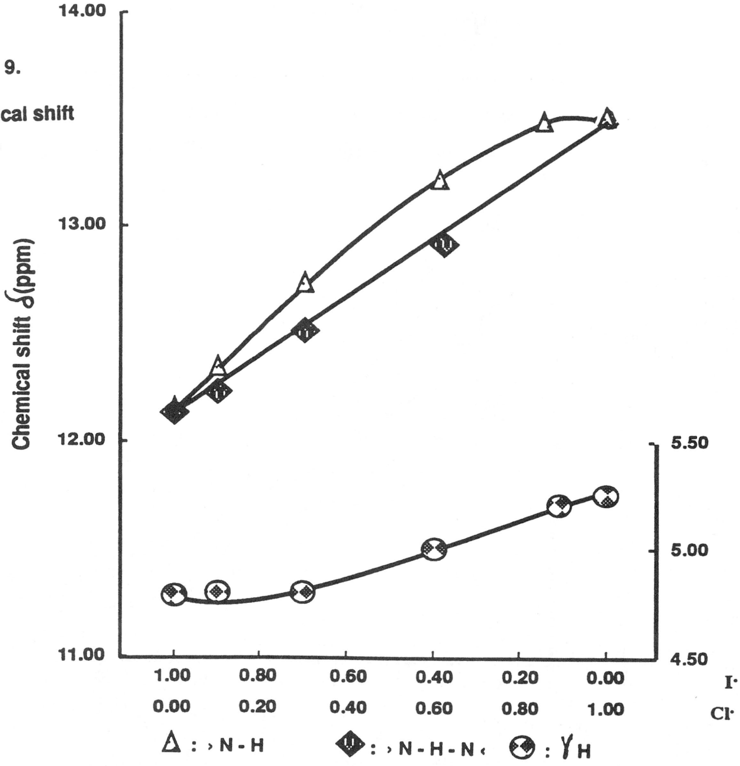

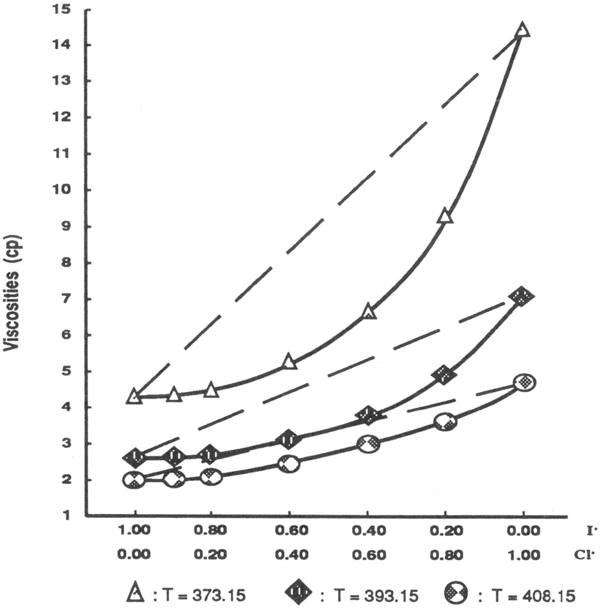

Figure 10.

Viscosities as a function of mole fraction

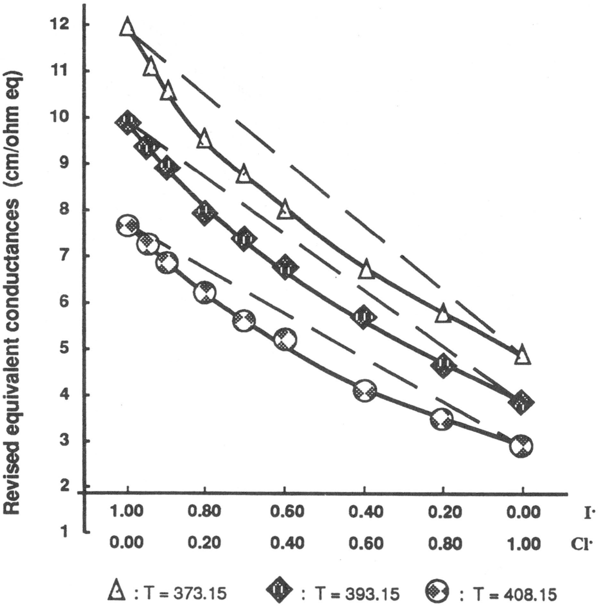

Figure 11.

Revised equivalent conductances as a function of mole fraction

DOI: 10.1149/199017.0221PV

THERMOPHYSICAL PROPERTIES OF HIGH TEMPERATURE MELTS - ACTIVITIES OF A JAPANESE RESEARCH GROUP

Akira Nagashima [1] , Nobuyuki Araki[2] , Tatsuhiko Ejima[3] , Shoichiro Fukusako[4] , Mamoru Harada [5] , Kiyosi Kobayasi[6] , Toshiro Makino[5] , Yuji Nagasaka , Hiroyuki Ozoe [8] and Tsutomu Yamamura [3]

[1] Keio University, Hiyoshi, Yokohama, 223, Japan.
[2] Shizuoka University, [3] Tohoku University, [4] Hokkaido University, [5] Kyoto University, [6] Toyota Technological Institute, [7] Kyushu University.

ABSTRACT

Molten salt is one of the so-called high temperature melts which include molten semiconductor materials, liquid metals, molten glasses and so on. Reliable Informations on their thermophysical properties are extremely limited due to experimental difficulties common to these materials. Purposes of the present project were to develop new measurement techniques for high temperature melts, to study such effects as thermal radiation and convection in fluid layer, and to produce new data sets.

INTRODUCTION

High temperature melts are materials which are solid at room temperature and turn to liquid only at high temperatures. Molten semiconductor materials, liquid metals , molten salts, molten glasses and volcanic lava are typical examples. Many of them have common characteristics and therefore common treatise is possible. They are chemically and electrically active. Thermophysical properties of high temperature melts are information strongly needed for such advanced technologies as single crystal production for semiconductor industry, high-temperature fuel cell development, high temperature heat storage technology, and so on. Although there exist increasingly strong demands for reliable informations on thermophysical properties of these materials, such difficulties as corrosiveness to container wall, rapid degradation of the sample and electrical conductivity prevent accurate experimental measurement and even establishment of measurement method. As pointed out by one of the present authors[1,2], the present status of these information is far from satisfactory.

Among various high temperature melts, molten salts are most systematically studied as seen in comprehensive reviews by Janz and collaborators[3]. However, even after these devoting efforts, informations on such properties as the thermal conductivity and the thermal diffusivity is quite limited. Discrepancies among available data are often chaotic and no standard reference data are available. In the case of other properties, substances and temperature range are not fully covered by available references.

ACTIVITY OF THE PRESENT RESEARCH GROUP

In 1987, a research project was started with the three-years grant from the Ministry of Education in order to develop measurement techniques suitable for high temperature melts and to produce reliable data sets. The research team was consisted of nine researchers (A. Nagashima as the chairman) from eight universities in Japan. Their names with principal coworkers are listed in the Table 1.

Table 1 Researchers and subjects of the project

A. Nagashima(Keio University)	chairman
K. Kobayasi(Toyota Technological Institute) Y. Takano	specific heat & heat of fusion
N. Araki(Shizuoka University)	thermal diffusivity, spacific heat & density
T. Makino(Kyoto University)	radiation properties
T. Ejima(Tohoku University) T. Yamamura Y. Sato	viscosity, surface tension & sound velosity
S. Fukusako(Hokkaido University) M. Tago	melting temoerature & supercooling
M. Harada(Kyoto University)	thermal conductivity & theoretical prediction
H. Ozoe(Kyushu University)	convection control
Y. Nagasaka(Keio University) A. Nagashima	thermal conductivity & surface tension

The subjects covered were the thermal conductivity, the specific heat, the density, the viscosity, the surface tension, the melting point, the heat of fusion, the radiation properties, and also such effects as convection in fluid layer and supercooling behaviors. The group met three to four times every year and had discussions on measurement techniques and critical evaluations on measured as well as collected data. Outline of the accomplishments on molten salts are summarized in the present report.

RESULTS ON TRANSPORT PROPERTIES

The viscosity of alkali carbonates were experimentally studied by Ejima, Yamamura and Sato at Tohoku University using an oscillating cup viscometer. The cup was made of gold-plated nickel for corrosive carbonates. By blowing argon gas in the sample, the viscometer was improved for mixtures and measurement of carbonates mixtures were performed. They have done determination of also the bulk viscosity of nitrates and carbonates by measuring the ultrasonic absorption coefficient in the temperature range up to 1300 K [4,5].

The thermal conductivity and the thermal diffusivity of molten salts were studied at three institutions using different experimental methods. The forced Rayleigh scattering method for the thermal diffusivity and the transient hot-wire method for the thermal conductivity were used Nagasaka, Nagashima and coworkers at Keio University. The thermal conductivity of nitrates in the temperature range 584-712 K were measured by the transient hot-wire method using a ceramic-coated probe[6]. In the much higher temperature range up to 1441 K, the forced Rayleigh scattering method, a new high-speed optical method, was used to measure the thermal diffusivity of alkali halides[7]. These transient methods have significant advantages at high temperatures since they can get rid of errors due to convection, temperature variation and, in many cases, radiation. The most striking thing about the present results is that the temperature dependences of all the salts measured were negative on contrary to most of previous studies. A typical results are shown in Figure 1. Previously available data showed scatter as large as 400 %. In addition, most of previous studies gave strong positive dependence against temperature. Two different methods by Nagasaka and Nagashima gave quite similar negative dependences for all of salts measured.

Araki and coworkers at Shizuoka University studied the effect of radiation in the fluid layer and applied their method to estimate the magnitude of correction to measured thermal conductivity by the stepwise heating method[8]. The radiation data for molten salts were obtained from the results by Makino and coworkers in the present project. The thermal conductivity of nitrates by stepwise heating method by Araki and coworkers showed negative temperature dependence. One example of results is shown in Figure 2 which indicates the magnitude of radiation correction for molten nitrates.

At Kyoto University, Harada and coworkers have done researches on measurement method of the thermal conductivity of molten salts and also on the corresponding states correlation of transport properties. The thermal diffusivity of nitrates and alkali halide were measured by the modified laser flash method[9]. A metal disk on the fluid layer was heated by a ruby laser as a flash source. In the corresponding states correlation, Harada and coworkers showed that the electrical conductivity, the viscosity and the self diffusion coefficient of a wide variety of molten salts can be correlated in a generalized equation based on the characteristic mass. In the case of the viscosity, all the experimental data of 17 salts were expressed by their correlation within the root-mean-square error of 11 %.

RESULTS ON THERMODYNAMIC PROPERTIES

The specific heat and the heat of fusion were studied by Kobayasi, Takano and coworkers at Toyota Technological Institute using a differential calorimeter[11]. Their interest is on salts proposed for thermal energy storage. Measurements were carried out on carbonates, sulfates, chlorides and their binary and ternary mixtures. An example of specific heat of Na_2CO_3 - Li_2CO_3 system is shown in Figure 3.

Density of alkali carbonates were measured by Araki and coworkers with the instrument based on Archimedes principle[12,13]. Although density data are normally available for most of substances even at high temperatures, only few are available for cabonates mixtures. For Li_2CO_3 -K_2CO_3 - Na_2CO_3 system, the linear dependence of density on the mole fraction was confirmed. They also measured the specific heat of alkali carbonates and their mixtures using an adiabatic scanning calorimeter[12, 14].

The melting temperature was measured by Fukusako and coworkers at Hokkaido University[15]. Fourteen samples were newly measured. Various affecting factors such as cooling rate and sample quantity were studied. They also observed supercool behavior of molten salts which were serious problems in such applications as thermal energy storage unit.

RADIATION AND OTHER PROPERTIES

Thermal radiation properties were investigated by Makino and coworkers at Kyoto University [16, 17]. Reflectance spectra of the salt layer was measured in the wavelength range 0.5 - 13.0 μm. The results were then analyzed to evaluate the spectra of refractive index and absorption coefficient. Measurements were performed for nitrates, chlorides and carbonates. An example of absorption coefficient as well as refractive index for chlorides is shown in Figure 4.

The refractive index was measured for mixtures also at Tohoku University. The minimum deviation angle method with a triangle cell made of quartz was used for ZnCl-NaCl binary melts and some other melts[18, 19].

Studies of the surface tension of molten salts were done at Tohoku University and Keio University. Ejima and coworkers at Tohoku University used the capillary method for measurement of chlorides and carbonates[20, 21]. The final aim of the study by Nagashima and coworkers at Keio University was measurement of molten semiconductor materials which were very sensitive to material or gas in contact. So they selected the surface wave method and some check measurements were made using molten salts.

The ultrasonic velocity and the absorption coefficient of molten salts were measured by means of the pulse method and the hypersonic velocity was measured by means of Brillouin scattering spectroscopy by Ejima and coworkers [4, 5]. In addition to the bulk viscosity described earlier, other thermodynamic properties such as the compressibility and the internal pressure were derived.

STUDY OF CONVECTION CONTROL

Convection in the fluid layer is one of the most serious error sources in measurement of transport properties of fluids, namely convection heat loss in thermal conductivity measurement and secondary flow effect in viscosity measurement. They are more significant at higher temperatures. Furthermore, in the case of single crystal formation, convection in the melt affects the quality of the product. In the present research project, a study of convection control for high temperature melts was included. Ozoe and coworkers at Kyushu University studied the effect of magnetic field on convection [22-24]. Numerical calculations were performed on liquid metals and they gave informations also for molten salts. One of the results are given as Figure 5 which shows change of flow pattern in a vertical fluid layer due to change of magnetic field.

CONCLUDING REMARKS

In the past, high temperature melts meant metal slugs and liquid metals for metallurgy and steel production, or molten salts for aluminum production. However, now much more interest is on molten semiconductor materials, heat storage materials and so on. There are only few reliable informations on thermophysical properties of these substances. As shown for the thermal conductivity, many of experimental data published in 1960-1970 are not reliable and new measurements are strongly needed. As previously done for molten salts by Janz and coworkers, international efforts by experts are needed, especially for creation of internationally agreeable databases.

REFERENCES

1. A. Nagashima, Appl. Mech. Rev., 41, 113(1988).
2. A. Nagashima, Int. J. Thermophys., 11, 417(1990).
3. G. J. Janz, Thermodynamic and Transport Properties of Molten Salts., Amer.Chem.Soc. & Amer.Inst.Phys., (1988). Also earlier reviews by his group appeared in J.Phys.Chem.Ref.Data.
4. H. M. Zhu, K. Tan, Y.Sato, T.Yamamura and T.Ejima, Proc.9th Japan Symp.Thermophys.Prop., Nagaoka, 124 (1988).

5. H. M. Zhu, T. Saito, Y. Sato, T. Yamamura and T. Ejima, Proc.2nd Asian Thermophys.Prop.Conf., Sapporo, 555(1989).
6. S. Kitade, Y. Kobayashi, Y. Nagasaka and A. Nagashima, High Temp.-High Pres., 21,219(1989).
7. Y. Nagasaka and A. Nagashima, Int.J.Thermophys., 9, 923(1988).
8. N. Araki and Y. Takano, Annual Meeting on Thermal Engineering, JSME, Kobe, No.890-63(1989),p.13.
9. M. Harada, A. Shioi, S. Okumi and Y. Uchiyama, Proc.9th Japan Symp.Thermophys.Prop., 135(1988).
10. Y. Tada, S. Hiraoka, T. Uemura and M. Harada, I&EC Research, 27,1042(1988).
11. K. Kobayasi, N. Inoue and T. Takano, (to be published.)
12. N. Araki, M. Matsuura, A. Makino, T. Hirata and Y. Kato, Int.J.Thermophys., 9,1071(1988).
13. N. Araki, M. Matsuura and A. Makino, Proc.9th Japan Symp.Thermophys.Prop.,Nagaoka,115(1988).
14. N. Araki, M. Matsuura, A. Makino and Y.Kato, Proc. 10th Japan Sump.Thermophys.Prop.,Sapporo,43(1989).
15. S. Fukusako and M. Tago, Proc.9th Japan Symp.Thermophys.Prop., Nagaoka,131(1988).
16. T. Makino, T. Maeda, M. Edamura and A. Yoshida, (to be published).
17. T. Makino, T. maeda, T. Yasuo and A. Yshida, (to be published).
18. M. Endo, T. Nito, T. Yamura and T. Ejima, Proc. 9th Japan Symp.Thermophys.Prop., Nagaoka,127(1988).
19. T. Ejima, T. Yamamura, Y. Sato, H.M. Zhu, Y. Sato and M. Kasuga, Proc.2nd Asian Symp.Thermophys. Prop., Sapporo,381(1989).
20. T. Ejima, Y. Sato, T. Yamamura and M. Fukasawa, paper presented at 40th Int.Soc.Electrochem. Kyoto, (1989).
21. K. Tan, S. Fujii, M. Hoshi, T. Yamamura and T. Ejima, paper presented at Japan Inst.Metals, Narashino, (1988).

22. H. Ozoe and H. Matsuo, Proc.9th Japan Symp.Thermophys.Prop.,Nagaoka,139(1988).
23. K. Okada and H. Ozoe, Proc.10h Japan Symp.Thermophys.Prop.,Sapporo, 171(1989).
24. H. Ozoe, H. Matsuo and K. Okada, Annual Meeting on Thermal Eng., JSME, Kobe,No.890-63,7(1989).

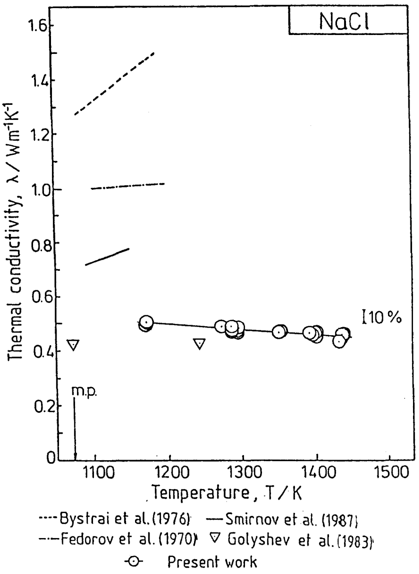

Figure 1 Comparison of measured thermal conductivity of molten NaCl

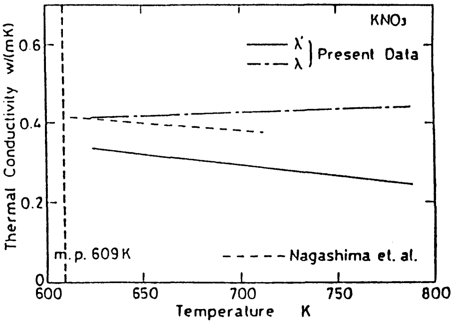

Figure 2 Thermal conductivity of KNO_3 by the stepwise heating method: λ uncorrected data, λ 'corrected data

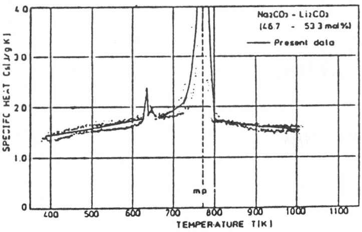

Figure 3 Specific heat of eutectic mixture of carbonate salts

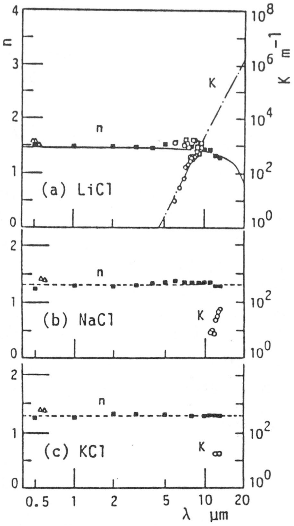

Figure 4 Spectra of refractive index n and absorption coefficient K for molten chlorides

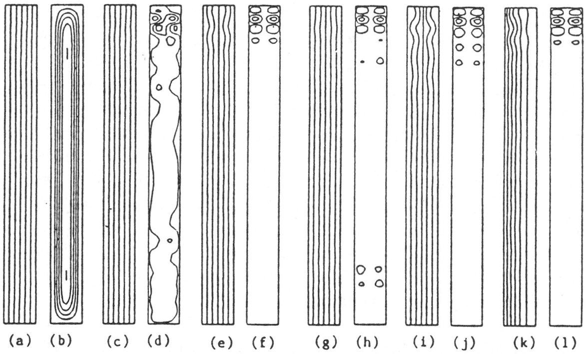

(a) Isotherms (b) The stream function at Ra=10^2 Ha=10
(c) (d) 10^2 Ha=100
(e) (f) 10^2 Ha=1000
(g) (H) 10^3 Ha=500
(i) (j) 10^4 Ha=1000
(k) (l) 10^5 Ha=10000

Figure 5 Computed contour maps

DOI: 10.1149/199017.0230PV

THE TEMPERATURE DEPENDENCE OF THE THERMAL CONDUCTIVITY OF MOLTEN SALTS

Yuji Nagasaka and Akira Nagashima

Department of Mechanical Engineering
Keio University, Hiyoshi, Yokohama 223 JAPAN

ABSTRACT

By using newly developed transient methods, namely transient hot-wire method with ceramic-coated probe and forced Rayleigh scattering method, the thermal conductivities of two molten nitrates ($NaNO_3$ and KNO_3 up to about 440 °C) and five molten alkali metal chlorides (LiCl, NaCl, KCl, RbCl and CsCl up to about 1200 °C) have been determined. The present thermal conductivity results show a weak negative temperature dependence and one of the smallest values among other previous data obtained by steady-state methods; the difference is a factor of four at most.

INTRODUCTION

Reliable data for the thermal conductivity of molten salts are required for the thermal design of latent-heat thermal storage system, molten salt fuel cell and so on. However, there have been a very limited number of experimental studies, with discrepancies often far beyond their claimed accuracy. It seems quite difficult to judge which data are reliable from the experimental results scattering by a factor of two to four. We even do not know the temperature dependence of the thermal conductivity of molten salts. This is mainly due to the fact that the thermal conductivity measurement of molten salts is very intricate, owing to their corrosiveness and high melting temperatures. Moreover, by using conventional methods such as the steady-state concentric-cylinder and the parallel plate, it is extremely difficult to avoid the effects of natural convection and radiation which considerably increase the apparent measured thermal conductivity under high temperature conditions.

In order to overcome above-mentioned problems on the measuring techniques for the thermal conductivity of molten salts, we recently have developed two new methods: the transient hot-wire method with ceramic-coated probes and the forced Rayleigh scattering method. Employing these methods, we have obtained the results for two molten nitrates ($NaNO_3$ and KNO_3) and five molten alkali metal chlorides (LiCl, NaCl, KCl, RbCl and CsCl). All these thermal conductivity results do not exhibit a positive temperature dependence as previously believed but a weak negative dependence like other common liquids.

EXPERIMENTAL

Transient hot-wire method with ceramic-coated probe:
The most valuable feature of the transient hot-wire method when applied to fluids is its capability to experimentally eliminate the convective error ; this is a great advantage, especially for high-temperature conditions. In order to apply this method to molten salts, however, a bare metallic wire has to be insulated. We have developed ceramic-coated probes which can be appropriate up to about 440 °C (1,2). It has to be noted that the most essential element of the present apparatus is an insulated probe which possesses enough electrical resistivity in corrosive atmosphere at high temperature. It is therefore very important what kind of insulation materials are used and also which insulation techniques are applied both on thin metallic wire and thick struts which are electrical leads at the same time.

Figure 1 illustrates the present ceramic-coated probe and the cross-sectional view of the insulated strut which has been developed through many trials and errors. The construction of the probe is as follows. Titanium rods (ϕ 3 mm) (6) coated with plasma sprayed Al_2O_3 of thickness 0.2 to 0.4 mm (7) and with protective layer (8) are fastened to the ceramic disc (3) by means of titanium screw (1). The reason for using titanium as a strut material is that the thermal expansion coefficient of titanium is very close to that of platinum (which is a material for wire) thus we can avoid slacking or tightening of the wire during the course of temperature cycles. The electrical resistivity of the insulated struts is high enough by employing high purity (99.9 %) small particles (16 μm) of Al_2O_3 for plasma spray. The thickness of the plasma-sprayed layer is chosen so as not to make any cracks at high temperatures. Furthermore, in order to fill small pores in the sprayed layer, Si-Ti-C-O ceramic paint (Ube : Tyranno coat) is used as extra protective layer (thickness is 0.2 to 0.3 mm). These insulating materials and insulating techniques were chosen by examining their heat-resisting properties and insulating resistance in molten salts at high temperatures. The thin platinum hot-wire (ϕ 30 μm) (5) is insulated also by Al_2O_3 produced with the aid of ion plating. The covering ability of ion plating is excellent with fine structure and the layer thus produced sticks tightly enough on the wire. After assembling the probe with insulated struts, a bare platinum wire is spot welded to the struts whose insulation layer at the ends are removed with diamond-cutter. Then the entire probe is brought into the ion plating chamber. It took six hours to produce ion plating coating layer of about 4 μm thickness.

The experimental apparatus is shown in Fig. 2. The main part of this apparatus was previously developed (3). All data acquisition and instrument control can be performed using a computer (HP-9000 model 310) communicating via the IEEE-488 interface. In order to apply this apparatus to molten salts, the sampling period of a digital voltmeter (Advantest : TR-6861) was improved to be much shorter (25 ms). The temperature of the electric furnace is controlled by three separate heaters. Upper and lower heaters are used to keep a temperature gradient preventing initial natural convection in the sample. Also a sheathed heater (1) is attached above the probe to reduce the heat loss through the leads. A sample container (4) is made of high purity alumina (SSA-S) in order to avoid unexpected electrical combinations with the molten salts. The temperature of the sample is measured with the aid of a sheathed thermocouple (3)(ϕ 1.6 Type K) inserted into a alumina tube. The thermocouple was calibrated with a standard resistance thermometer on IPTS-68 from about 100 °C - 200 °C and with three fixed points, namely, tin (231.968°C), zinc (419.58°C) and aluminum (660.40°C).

Forced Rayleigh scattering method:

The forced Rayleigh scattering method is a contact-free optical technique for the thermal diffusivity measurement. The distinguishing features of this method are summarized as follows. (1) The method has an advantage in the case when it is difficult to insert sensors in a sample such as high-temperature corrosive melts because of its basic feature of contact-free measurement. (2) The influence of natural convection is negligible, since the measuring time is very short (typically within 1 ms). (3) The temperature rise during measurement is very small (less than 0.1 K), thus the error due to radiation may not be significant even at high temperatures. (4) A sample volume of only a few cubic millimeters is required, which is also advantageous at high temperatures. The detailed theory and apparatus have been described elsewhere (4-8).

Figure 3 displays the present experimental apparatus. The heating laser is a single-mode argon-ion laser (wavelength : 514.5 nm, 1.8 W) and its continuous light is chopped by a rotating mechanical chopper into a short pulse. The heating pulse duration time can be changed from 40 to 1200 μs. The heating lasers, divided into two beams of equal intensity by means of a beam splitter, intersect in the sample to produce interference pattern. A He-Ne laser (wavelength : 632.8 nm, 5 mW) is employed for probing the relaxation of the temperature distribution. The first order diffracted beam is detected by a photomultiplier through a pinhole of 500 μm diameter and an interference filter. The output from photomultiplier is recorded by a digital memory (12 bits, sampling time : 5 μs) and is transferred to a computer.

A sample cell is made of two quartz glasses (15 mm x 18 mm thickness 1 mm) with spacers. The thickness of the sample layer is fixed about 1 mm by employing quartz glass spacers which are welded onto cell walls with the aid of a micro-torch. The amount of sample needed for this cell is only 0.2 - 0.3 grams. An infrared furnace is utilized for the measurement at high temperatures because it readily heats up small amount sample and also ensures the optical path of the laser beams. It is to be noted that the surface of cell wall is painted by a high emissivity coating excluding the laser spot area in order to secure enough absorption of infrared light from the furnace. The temperature is measured by a thermo-couple (Type K) enclosed in a cell holder, since it is difficult to insert the thermo-couple directly into the sample Thus the accuracy of the temperature is estimated to be ±15°C, which is not so inferior taking into account the weak temperature dependence of the thermal diffusivity of molten salts.

Finally, the grating period is determined by means of a CCD image sensor which has been written in Ref. 6.

RESULTS

Molten nitrates:
The results for molten $NaNO_3$ and KNO_3 are compared with earlier works in Figs. 4 and 5, respectively. The measurements have been performed with the aid of the transient hot-wire method with ceramic-coated probes (1,2). The results have an estimated accuracy of ±3%. In these figures, the references of earlier works are omitted for the sake of space. In the case of $NaNO_3$, the present results agree with the data of Omotani *et al.* obtained by the liquid-metal-probe transient hot-wire method near melting point. The results of Bloom *et al.*, White and Davis, and McDonald and Davis, measured by the steady-state concentric cylinder method, are about 5% to 10% higher at the melting point and show a positive temperature dependence of the thermal conductivity. However, the results of Tufeu *et al.*, obtained by the same method with a thin fluid layer (0.2 mm) to minimize the error due to the heat transfer by convection and radiation, have a weak negative temperature dependence, and their results agree well with the present results within the estimated accuracy. From a comparison of the present results with other data, it may be concluded that the past experimental data for molten $NaNO_3$ and KNO_3, mainly measured by steady-state methods, contain systematic errors owing to radiation and convection.

Molten alkali metal chlorides:
Figure 6 shows the present thermal conductivity for molten NaCl derived from the measured thermal diffusivity by the forced Rayleigh scattering method and the density with the heat capacity (8). The accuracy of the thermal conductivity is estimated to be ±8%. It should be particularly noted that the previous thermal conductivity values of molten NaCl scatter from about 0.4 to 1.5 W/(m·K) and their temperature coefficients are considerably large positive values. In contrast, the present results are the one of the smallest of all and agree with the data of Golyshev *et al.* obtained by the concentric-cylinder method with careful radiation correction. Moreover, the temperature dependence of the thermal conductivity exhibits a weak negative. We may conclude these significant differences attribute to the systematic error caused by radiation and convection which become more serious as the temperature goes higher.

Figure 7 displays the thermal conductivity of molten alkali metal chlorides measured by the forced Rayleigh scattering method. Again, all of them exhibit weak negative temperature dependence and their absolute values are smaller than the ones obtained by the steady-state method.

ACKNOWLEDGMENT

The work described in this paper was financially supported in part by the Ministry of Education under a Grant-in-Aid for Scientific Research.

REFERENCES

1. S. Kitade, Y. Kobayashi, Y. Nagasaka and A. Nagashima, *High Temperatures-High Pressures*, 21, 219 (1989).

2. S. Kitade, Y. Kobayashi, Y. Nagasaka and A. Nagashima, *Trans. JSME*, 55, 2411, (1989) (in Japanese).

3. N. Kawaguchi, Y. Nagasaka and A. Nagashima, *Rev. Sci. Instrum.*, 56, 1788 (1985).

4. T. Hatakeyama, Y. Nagasaka and A. Nagashima, *Proc. ASME-JSME Thermal Engineering Joint Conf.*, Vol.2, 311 (1987).

5. T. Hatakeyama, Y. Miyahashi, M. Okuda, Y. Nagasaka and A. Nagashima, *Trans. JSME*, 54, 1131 (1988) (in Japanese).

6. Y. Nagasaka, T. Hatakeyama, M. Okuda and A. Nagashima, *Rev. Sci. Instrum.*, 59, 1156 (1988).

7. Y. Nagasaka and A. Nagashima, *Int. J. Thermophys.*, 9, 923 (1988).

8. N. Nakazawa, M. Akabori, Y. Nagasaka and A. Nagashima, *Trans. JSME*, (1990) (in press).

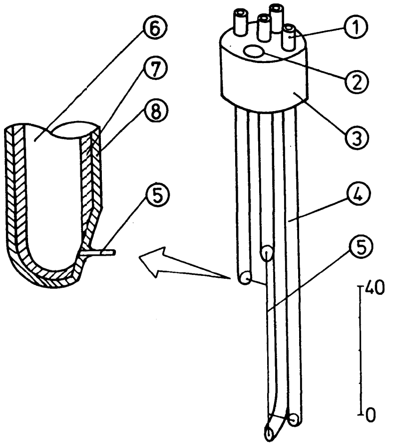

Figure 1. Ceramic-coated probe for the transient hot-wire method: 1, titanium screw; 2, drilled hole for thermocouple; 3, ceramic disc; 4, insulated strut; 5, insulated platinum wire ($\phi 30$ µm); 6, titanium rod ($\phi 3$); 7, plasma-sprayed Al_2O_3; 8, protective layer of painted Si-Ti-C-O ceramic.

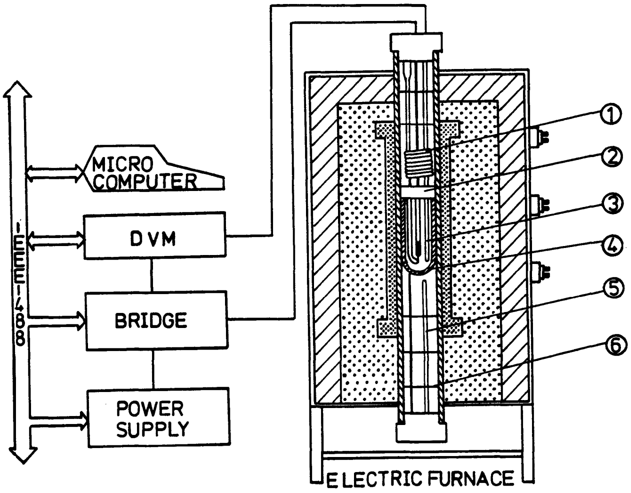

Figure 2. Experimental apparatus for the transient hot-wire method: 1, sheathed heater; 2, probe; 3, thermocouple; 4, alumina sample container; 5, thermocouple for temperature control; 6, radiation shields.

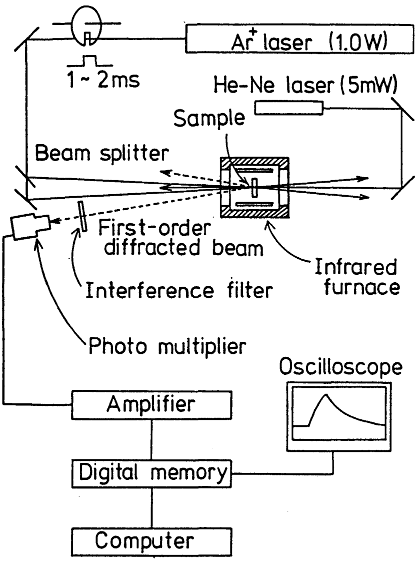

Figure 3. Experimental apparatus for the forced Rayleigh scattering method.

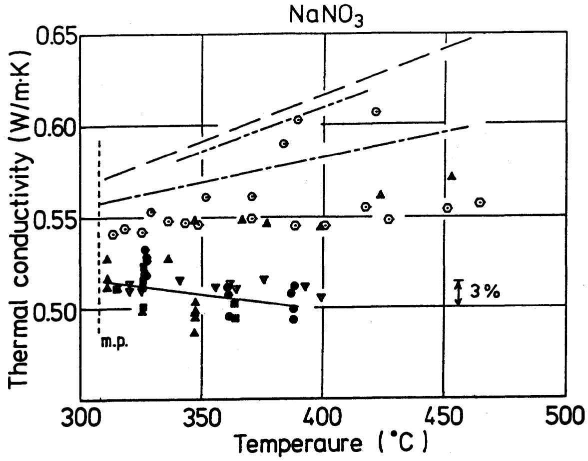

Figure 4. Thermal conductivity of molten $NaNO_3$;— — —White and Davis (1967), —·—McDonald and Davis (1970),—— Santini *et al.* (1984), ⊙ McLaughlin (1964), ○ Bloom *et al.* (1965), △Gustafsson *et al.* (1967), ⊡ Omotani *et al.* (1982), ▽ Tufeu *et al.* (1985), Present work ; ● probe 1, ▲probe 2, ■ probe 3.

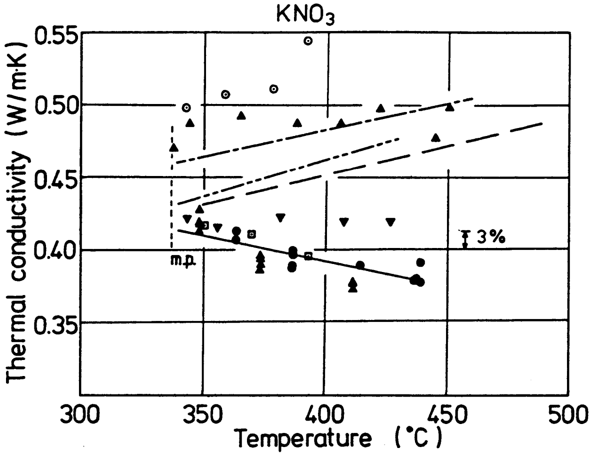

Figure 5. Thermal conductivity of molten KNO$_3$;-·-·-White and Davis (1967), —·—McDonald and Davis (1970),— — Santini *et al.* (1984), ⊙ Bloom *et al.* (1965), △ Gustafsson *et al.* (1967), ▽ Tufeu *et al.* (1985), ⊡ Karasawa *et al.* (1986), Present work ; ● probe 4, ▲ probe 5.

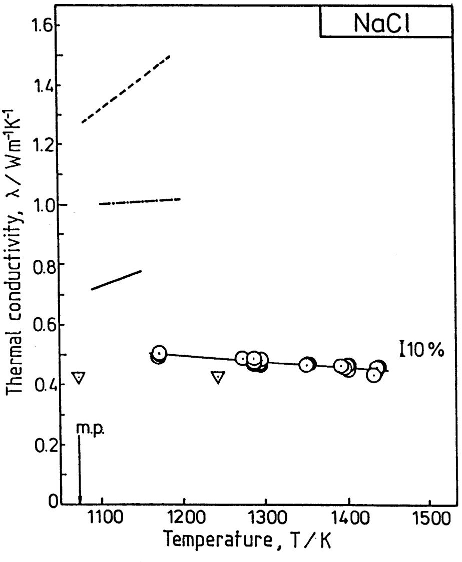

Figure 6. Thermal conductivity of molten NaCl;---- Bystrai *et al.* (1976), ——Smirnov *et al.* (1987),—·—Fedorov *et al.* (1970), ▽ Golyshev *et al.* (1983), ⊙ Present work.

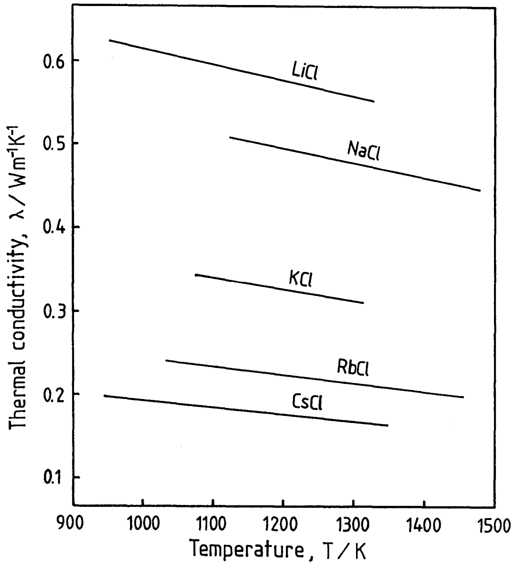

Figure 7. Temperature dependence of the thermal conductivity of five molten alkali metal chlorides.

DOI: 10.1149/199017.0239PV

A NEW METHOD FOR DETERMINING SORET COEFFICIENTS IN MOLTEN SALTS,EMPLOYING FIBRE-OPTIC SPECTROSCOPY

Trevor R. Griffiths and Nicolas J. Phillips

School of Chemistry, The University of Leeds,
Leeds, LS2 9JT England

ABSTRACT

Soret coefficients are conventionally determined electrochemically from concentration measurements at two positions in a column of liquid exhibiting a thermal gradient. These concentration changes with temperature have not previously been recorded using absorption spectroscopy measurements and Beer's Law. Such measurements can be achieved with a fibre optic spectrophotometer and an accurately calibrated thermal gradient furnace, and many readings were taken, yielding statistically significant Soret coefficient values for Fe(III), Cr(III), and Ni(II) in molten LiCl-KCl eutectic and for Ni(II) in molten Li_2SO_4-Na_2SO_4-K_2SO_4 eutectic. The results were comparable to those obtained in aqueous systems. The necessary precautions are assessed and described. The high temperature systems chosen are probably the most severe test possible for this new technique for determining Soret coefficients.

INTRODUCTION

The Soret effect, the coupling of heat and material transport, is observed as diffusion. The presence of a temperature gradient within a solution gives rise to thermal diffusion processes such that the concentration becomes non-uniform with temperature, with usually the cooler regions becoming the more concentrated. This separation develops until it is exactly balanced by the thermal diffusion process and the system reaches a steady state, referred to as Soret Steady State: thermal diffusion is thus exactly balanced by ordinary diffusion. The Soret coefficient, σ, may be defined as

$$\sigma = \frac{1}{m}\frac{dm}{dT} \qquad (1)$$

where m is the molality of the ionic complex, to overcome the effect of concentration change with increase in volume, and T is the temperature (K). Upon integrating we have

$$\sigma T = - \ln m \quad (2)$$

Thus a plot of ln m against temperature will give a straight line of gradient σ, the Soret coefficient.

The Soret coefficient of a species in solution can be determined, in principle, by analysis of the concentration of the species in regions of known temperature. Sampling may disturb the system, and so the change in concentration is often monitored by following some physical property until the Soret Steady State is reached. Such properties include change in thermoelectric power, refraction indices or, most commonly, electrochemical measurements. Also, because the temperature must be known accurately the general practice is to have two containers, carefully thermostatted, with the two solutions therein directly linked. The Soret coefficient is therefore usually determined from repetitive measurements, but only between two fixed temperatures.

Since concentration is directly related to absorbance by the well-known Beer-Lambert Law it occured to us that a vertical column of liquid, under an applied thermal gradient, could be sampled at many temperatures, using a spectrophotometer, to give more statistically significant Soret coefficients. Moreover, the measurements would be simple and applicable to a wide range of ionic species.

We were interested in obtaining the Soret coefficients of transition metal ions in sulphate and chloride melts as part of a study on the hot corrosion of stainless steels, and therefore our choice of conditions for developing and establishing a new technique for measuring Soret coefficients is probably the most testing and severe possible.

An extensive literature survey revealed that Soret coefficients had not previously been determined by spectrochemical techniques and the application of the Beer-Lambert law. Also almost all previous determinations were made between ambient temperatures and 100°C at most, the majority employing electrochemical measurements. There were no determinations using temperatures below ambient and only two at elevated temperatures. Backlund *et al* (1), using a conventional electrochemical cell, measured thermal diffusion in molten binary mixtures of silver nitrate with alkali nitrates, obtaining Soret coefficient values ranging from 2×10^{-3} to 5.5×10^{-3} K^{-1}. More recently Williams and Philbrook (2) used a vertical column held at a known linear temperature gradient until a steady state for the distribution had been achieved. The melt was then rapidly quenched, and chemically sampled at intervals along its length. Using this approach Soret coefficients at three silver concentrations were found to range from a minimum of 0.08 $\times 10^{-3}$ to 1.03×10^{-3} K^{-1}, but with an estimated error of up to 50% and were obtained for Ag-Te solutions previously held molten in the range

899 to 1239 K. The only comprehensive survey of methods employed for the determination of Soret coefficients is still that of Tyrell, published in 1961 (3).

THEORETICAL AND PRACTICAL CONSIDERATIONS

There are some features of our approach which are inherent and others which appertain to spectroscopic measurements at temparatures of around 1000 K.

(a) The Soret coefficient is defined in terms of molality but the Beer-Lambert law employs molarity units: specifically the law states that $A = \varepsilon c l$, where A is the measured absorbance, ε the molar absorbance, at the wavelength of interest, in $dm^3 mol^{-1} cm^{-1}$, c the concentration in mol dm^{-3}, and l is the path length in cm. In principle a correction factor could be applied to absorbance measurements, but if a small temperature range is employed, and we have used around 25^0C, then the correction factor is negligible.

(b) Absorbance spectral profiles can change with temperature change, some more than others. Charge transfer to solvent spectra shift and broaden, some quite dramatically over a 25^0C range, with a consequent progressive decrease in peak height with temperature increase (4,5): anions such as iodide which exhibit such spectral changes cannot therefore be investigated by our technique. Charge transfer bands arising from intra-electronic transitions between transition metal ions and ligands are much less temperature sensitive, with *d-d* transitions even less sensitive, and *f-f* transitions probably almost temperature insensitive: we have examined *d-d* transitions, recording changes at peak maxima to minimise any broadening contiributions, and the charge transfer edge of Fe(III). Since this last is a d^5 species, and since its *d-d* transitions are now all Laporte and spin-forbidden, they are thus of low intensity and scarcely discernable on the charge transfer absorption edge.

(c) Normally electronic absorption spectra are recorded through cross-sectional areas around 8 x 10 mm. If solutions are to be held in standard 1 cm silica cells, themselves in a temperature gradient, then a mask must be placed in the light beam in front of the cell. With our instrumentation the light beam could be reduced from 10 mm to 1mm high and still allow sufficient light throughput so that the spectrophotometer could perform within an acceptable response range.

(d) The temperature profile within the solution must be accurately known. A common problem for spectrophotometric measurements, particularly at high temperatures, is the need for two relatively large opposing light ports in the hot zone of a furnace, and hence problems with uniform temperature control. Using thermal gradient furnaces, with separate heating elements above and below the molten salt sample, does not produce a linear (with distance) temperature gradient in the sample. The sample must first have its temperature profile accurately mapped with a calibrated and preferably miniature, thermocouple.

Other problems and precautions were more specific to the apparatus used and the systems examined and will be included in the next section, but it may be here concluded that absorbance can replace molality in the Soret coefficient eqn. (2) and we can investigate the relationship

$$\ln A = -\sigma T \qquad (3)$$

EXPERIMENTAL

Preparation and handling of materials. Chemicals were stored, weighed and handled in a drybox maintained at ca. 2 ppm moisture. The eutectic LiCl-KCl, mole cation %, Li, 58.5; K, 41.5, (Unichem Ltd) was used directly from ampoules. The Li_2SO_4-Na_2SO_4-K_2SO_4 eutectic (78, 13.5, 8.5 mole cation % respectively) was prepared by weighing the pre-dried sulphates. The chlorides of iron(III), chromium(III) and nickel(II), and $NiSO_4$, were prepared and dried by standard methods.

Aliquots of these eutectic mixtures, corresponding to a final melt volume of 4.5 cm^3 were weighed into a standard 1 cm silica optical cell to which a neck had been attached (so that it would protrude outside the furnace). The cell was sealed before removal from the drybox, and subsequently connected to the dried gas supply. The iron, chromium and nickel salts were either weighed out into sealed vials for later transfer into the molten eutectics, or added with the eutectic mixture in the optical cell.

The gas supply. The ingress of atmospheric moisture to the molten eutectics was prevented by the slow passage of a dried gas over the melt: the velocity of the gas was insufficient to cool or otherwise affect the melt. For the chloride melts argon was used, which had been dried over self-indicating silica gel and 4Å molecular sieve columns, and a synthetic flue gas mixture was used for the sulphate melt. This gas was similarly dried and its compostion was, by volume, 16% CO_2, 3% O_2, 4000 ppm SO_2, balance N_2. Some of the SO_2 was oxidised to SO_3 by passage over a platinised Kaowool catalyst at 400°C, and an average concentration of 50 ppm SO_3 was obtained. The SO_3 was required to prevent the decomposition of the sulphate melt, which otherwise occurs above 600°C.

Furnaces. Two types of furnaces were used, one was an isothermal furnace and the other a thermal gradient furnace, with separately controlled heating elements above and below the optical ports, to create the desired temperature gradient in the melts. The former was used in the conventional way to record the spectra of the iron, chromium and nickel complexes as a function of temperature, to determine the temperature range over which any band broadening was insignificant. Both types of furnace have been described elsewhere (6,7).

Temperature profile. Our approach demands an accurate knowledge of the temperature at all points over which spectra are to be measured. The thermal gradient furnace was therefore carefully calibrated. A cell containing molten salt was secured in place in the furnace, and the furnace in the light beam of the spectrophotometer. A mask with an 8 x 1 mm aperture was located in the middle of the beam and close to the front surface of the cell. The furnace could be raised and lowered precisely, via a 1 mm pitch screw thread. A thermocouple was fixed so that its tip was in line with the aperture and in contact with the side of the cell. A second thermocouple, which had previously been accurately calibrated, was placed in a thin silica protective sheath and then in the melt so that its tip was in the centre of the light beam. The dried gas was also passed slowly over the melt to replicate as far as possible the experimental conditions. When thermal equilibrium had been attained, and the temperature readings had been constant for at least one hour the readings of both thermocouples were recorded, and the furnace position raised 3 mm and the process repeated. It was established that raising and lowering the furnace to a previous position reproduced the previous readings. A calibration plot is shown in Fig. 1.

The calibrated thermocouple was also located at both ends of the aperture and nearer and further from the mask and the above procedure repeated: there was no lateral thermal gradient within experimental error. Spectral determinations of concentration changes could now be made. No change in the temperature profile occured during these measurements and this was confirmed since the reading from the thermo- couple adjacent to the cell was still the same as that at the same furnace positions during the calibration.

Spectroscopic measurements. A key-board controlled fibre optic spectophotometer was employed (Guided Wave Analyser, Model 200). The fibre optic probes were set up either side of the furnace and on an optical bench. The single fibres, 0.5 mm diameter, terminated in stainless steel sheaths and against a collimating lens, which produced an only slightly diverging beam. The masked beam therefore entered the cell 1.13 mm high and was 1.30 mm high on exiting. The probes were placed as close to the hot sample as possible without allowing the tip to be overheated, (and thus degrade the fibre coating). The optimum alignment was achieved using a supplied computer program which indicated the light level received by the detector.

Spectra take around 30 sec to collect, and when thermal equilibrium had been attained five spectra were taken and averaged. Reference spectra were first recorded at selected positions in the thermal gradient, before addition of the transition metal salt. A total of eight baseline spectra were always taken, at 3 mm vertical intervals, and from 400 to 1200 nm at 0.5 nm sampling intervals. Normally this attention to detail is not generally required but it does eliminate any unforseen errors, including possible minor imperfections in the optical faces of the cell.

Addition of solute. Normally in molten salt spectroscopy, after the baseline spectra have been recorded, the transition metal solute is tipped carefully into the cell and the cell contents stirred or rocked gently until the solute has dissolved. In this work the cell could not be moved as the same thermal gradient would not be obtained again, since some of the melt would be withdrawn on the stirring rod or left higher up on the walls of the cell. Two methods of adding the solute were investigated.

First, the solute was dropped, in the form of a lightly compressed pellet, directly on to the surface of the melt. Second, the cell containing eutectic only, after the baseline spectra had been taken, was removed from the furnace, the melt tipped out, and after cleaning and drying, was refilled in the drybox. The anhydrous transition metal salt was first weighed into the cell and the same weight of eutectic used for the baseline spectra was added. The cell was then sealed and transferred to the furnace as before.

The first method is in principle the better but in practice the rate of dissolution was too slow, in excess of 48 h, and by the end of the experiment the cell windows would be etched, due to the temperatures involved. The second method was therefore used. It also has the advantage that because the transition metal salt is largely at the bottom of the cell initially it diffuses upwards upon dissolving in the eutectic melt, and therefore it was possible to monitor this diffusion process spectroscopically. For this study it enabled the time when equilibrium had been reached to be determined. The method was to record spectra at a fixed position some distance above the base of the cell. The upward diffusion was seen as a continual increase in the recorded absorbance spectra: when the spectra did not increase further in absorbance the system was considered at equilibrium. The time taken to attain equilibrium was now 10 - 15 h, and thus spectra could be recorded for Soret coefficient determinations before any detrimental effects on the silica windows occured.

Problems encountered. When salts melt they often contain initially small gas bubbles, from the air trapped between the powder particles. These generally rise very slowly to the surface, but may need encouraging by applying a little vibration to the cell. Thus before finally locating the cell (containing molten salt) precisely in the thermal gradient it was inspected for absence of bubbles.

When chromium(III) chloride was added to the LiCl-KCl eutectic under dried argon the spectrum at first was not stable, and after 20 minutes had changed from that of the octahedral $CrCl_6^{-3}$ species to that of the tetrahedral species $CrCl_4^{2-}$. Further, a comparison of published Cr(III) spectra in molten chlorides showed considerable variation (and the investigation this engendered will be published elsewhere). This reduction is well known in aqueous and alcoholic solutions when a catalytic amount of Cr(II) is present. The source of the reductant here must be water in $CrCl_3$ or in the argon gas. The $CrCl_3$ was analysed and found to contain 11 ppm moisture, which would produce sufficient HCl to bring about complete reduction of the Cr(III). A fresh, dried sample of $CrCl_3$ gave a stable spectrum, with no evidence of $CrCl_4^{2-}$ formation after two hours.

However, the bands then began to decrease in height, and after ten hours the spectrum of Cr(III) had disappeared: a green precipitate was observed at the bottom of the cell, and this was later confirmed by X-ray diffraction as Cr_2O_3. Oxide ions arising from decomposition of the silica cell is not feasible thermodynamically, even at the temperatures of 870-1070 K involved.

Attention was therefore focussed on the oxygen content of the argon, reported as 4-10 vpm by the supplier, but calculations showed this insufficient to precipitate all the chromium, over a ten hour period, at the flow-rate employed. However it is now considered that oxygen had permeated through the plastic tubing used.

The problem was finally eliminated by connecting a vacuum pump to this cell, and pumping continually during the melting of the eutectic: this also rapidly and effectively removed gas bubbles in the melt. After two hours the cell was sealed, and a constant check performed during the experimental run to ensure that the vacuum was constant. Melts so prepared were completely stable for one week and more.

RESULTS

Effect of temperature on spectral profiles. An isothermal furnace was employed to record the spectra of Fe(III), Cr(III) and Ni(II) in the LiCl-KCl eutectic, and Ni(II) in the Li_2SO_4-Na_2SO_4-K_2SO_4 eutectic as a function of temperature. Spectra were recorded at regular temperature intervals and compared with one another by superimposition and by difference. Small variations could be seen between spectra taken around 100°C apart, generally some slight band broadening with temperature increase, as expected. Careful examination showed that the minimum absorbance decrease was around peak maxima, and that over a 25°C range the absorbance change is negligible. This range was therefore chosen as the maximum for the Soret coefficient determinations. However, for the Fe(III) containing solutions, as indicated earlier, the spectral profile consists essentially of a charge transfer absorption edge containing very weak spin-forbidden bands. This edge was slightly temperature dependent over a 25°C range, and therefore Soret coefficient determinations were made at two wavelengths. The wavelengths chosen were ones at which spin-forbidden peak maxima had been previously identified by fourth derivative analysis (8).

Spectral changes across the thermal gradient. Figs 2-5 show the spectra recorded for the four systems under investigation in the thermal gradient furnace, at 3 mm vertical intervals, after the systems have reached the Soret steady state condition. The spectra were recorded first upon progressively lowering the furnace in the light beam and then raising it, and each pair of spectra were identical within experimental error, confirming no disturbance to the thermal equilibrium.

Soret coefficient determinations. Figs 6-9 show plots of ln(absorbance) against temperature (eqn. 3) for each of the four systems, and a good linear relationship is seen, as now expected. The value of the Soret coefficient is obtained from the slope of these plots, and the results, and their standard derivations are collected in the Table, together with some selected published values. Also as expected the results for the band edge studies of Fe(III) have more scatter than those for Cr(III) and Ni(II), obtained around peak maxima.

DISCUSSION

An examination of the Table shows that the results obtained here are comparable with those found at elevated temperatures, as well as those reported for transition metal ions in aqueous solutions. We have therefore shown that, with due care and attention to detail, Soret coefficients can be obtained from absorption spectra for species around 900 K. This new technique is therefore viable and has great potential. There are however several observations which should be made concerning this study and concerning future applications.

(a) Although each Soret coefficient has been determined from eight data points, instead of the normal two, much more data are in principle available for use. With each spectrum digitised at 0.5 nm intervals there are several hundred data points, and hence wavelengths at which Soret coefficients may be determined, and with greater precision. Computer programs could be written to extract progressively absorbance data from a set of spectra at one wavelength; calculate a least squares fit to ln(absorbance) against temperature; and prepare a plot like Figs. 6-9. A plot of Soret coefficient, with its standard deviation, against wavelength would then be expected to be linear and independent of wavelength, but to have the largest, and probably unacceptable standard deviations either side of peak maxima. Soret coefficients determined this way would thus be definitive, compared with the more common approach of making concentration measurements at only two temperatures. It was not considered appropriate to extend our high temperature data in this way but, having established this new method for determining Soret coefficients, that it should next be applied to aqueous systems.

(b) The fibre optic spectrophotometer system has certain advantages over more conventional spectrophotometers. Normally samples have to be enclosed in a light-tight housing, but the optical arrangement of a fibre optic spectrophotometer, together with the light collecting properties of optical fibres, means that the absorption spectra of samples can be recorded in daylight, and hence of hot glowing samples. Molten salt spectroscopists have generally used a reversed beam optical system which eliminates unwanted light (this is only commercially available on the Cary 14H spectrophotometer). We initially used this instrument in an attempt to determine Soret coefficients, but the optical system required too high an aperture in the mask for adequate spectra, and hence the temperature of the section examined contained too large a temperature gradient for acceptable Soret coefficients. The investigation did however define the problems to be overcome, and indicated that Soret coefficients were potentially available from absorbance measurements and the Beer-Lambert law.

This present study therefore made use of furnaces with large optical ports, designed to admit a light beam of standard cross-sectional area for use with 1 cm cells. As indicated earlier this necessitated detailed assessment and calibration of the temperature profile in the melt. In future, furnaces with much smaller optical parts could be used, since optical fibre probes fitted with collimating lenses are only a few millimeters in diameter. Thus better thermal gradients will be available, and if taller cells were used, the maximum usable temperature difference could be employed over an extended vertical distance, and larger mask apertures (or possible no masks) could be used, all features that would make Soret determinations easier and more accurate. In addition, the fibre optic spectrophotometer manufactured by Guided Wave now has a photo multiplier detector which records absorbance values to the seventh decimal place. We have conducted tests which have shown that data are reliable to the fifth and probably to the sixth decimal place. Conventional spectrophotometers normally are restricted to the fourth decimal place. Thus absorbance changes and differences can now be resolved to an accuracy more than an order of magnitude better than previously.

For making measurements at high temperatures the necessary separation between the fibre optic probes (to prevent decomposition of the organic coating on the silica fibres, which is required for total internal reflection within the fibre walls) means that a photomultiplier detector must be used; a silicon detector is not sufficiently sensitive under these conditions. However, developments are expected in fibre optic technology and that in future alternative heat-resisting coatings may become available, and the probes could be located closer to the molten salt solution, and silicon detectors employed.

(c) There are fibre optic spectrophotometers commercially available which use photodiode array detectors. These instruments could also be used for Soret coefficient determinations. They have the advantage that spectral scans are more rapid, generally less than one per second, compared with around 30 seconds which the Guided Wave Analyser needs to record a spectrum. However, speed is not essential when measuring a system at equilibrium. Currently photodiode arrays do not cover the same spectral range as photomultiplier, silicon and germanium detectors, but again developments are expected. Photodiode arrays have inherently less resolution than can be obtained with grating instruments, though this does not significantly reduce the number of wavelengths at which absorbance measurements may be made.

(d) When our results in Table 1 are compared with other published data some interesting conclusions may be drawn. Our extensive literature survey also revealed that Soret coefficients have been determined for atoms, molecules and electrolytes, but not for specific ions. This is largely because of the techniques used which, unlike absorption spectroscopy, do not specifically focus on only one ionic species, for example the emf technique for the thermoelectric power of an electrolytic thermocouple (8). However there are points in common.

Soret coefficients are by definition temperature independent, and our results are certainly not atypical. Our results were not obtained at the highest temperatures employed, which is around 1200 K for molten Ag-Te solutions by Williams and Philbrook (2), but they are for concentration measurements of the system while hot. Soret coefficients are also often reported as appertaining to a particular temperature, but this is the mean of the high and low temperatures employed. Thus our results could be described as applying to around 878 K.

Soret coefficients, according to the standard definition, eqn. 2, are negative, but can be obtained as positive if calculated by other ways. Of course, when electrolytes are not considered but, say, two organic solvents, then one will have a negative Soret coefficient and the other a positive.

We would draw attention to a possible correlation, not remarked upon previously. When a series of electrolytes is studied, sometimes a trend may be seen. For example, in Table 1 we include the data for a series of chlorides in water, reported by Ikeda and Miyoski (9). These results are for concentrations of 1×10^{-2} mol^{-1} dm^{-3} and a mean temperature of 25°C. The datum for LiCl is in brackets because it was used as a reference. The data for the other electrolytes appear to increase with increasing cation size. The quaternary ammonium ions are hydrophobic and hence are not solvated whereas the proton in HCl in these dilute solutions will be solvated and thus effectively much larger than its crystallographic radius. When we look at our data for the transition metal complexes we can detect a similar trend. For example, the octahedral $[Ni(SO_4)_3]^{4-}$ complex ion is larger than the tetrahedral ion $[NiCl_4]^{2-}$, which has a more negative Soret coefficient, and the tetrahedral ion $[FeCl_4]^-$, with the central ion at a higher oxidation state, will therefore be smaller still, and this ion has an even more negative Soret coefficient.

When we examine the molten nitrate data of Backlund *et al.* (1) reproduced in Table 1 we would point out that these are selected data, and that the proposals for the identity of the species present are ours. The concentration of the alkali ion is the 10 mole per cent value, except for caesium, where the lowest concentration given was 17.5 mole per cent. It is reasonable to suppose that these cations, except lithium, have an approximately octahedral arrangement of six oxygen atoms surrounding them, supplied by three planar nitrate ions in approximately the locations expected if they were acting as bidentate ligands: such an arrangement is well known for transition metal ions in nitrate melts (10). Further, the Soret coefficients are essentially the same at all concentrations of alkali metal ion, around $1.3 \pm 0.3 \times 10^{-3}$ K^{-1}, including lithium, except at the 5 and 10 mole per concentrations where they are around 5.5×10^{-3} K^{-1}. This leads us to speculate that under these conditions the smaller lithium ion has four essentially monodentate nitrate ions about itself, and is therefore larger, and thus has a higher Soret coefficient. At the higher lithium concentrations there is a greater competition for the nitrate ions, the species becomes smaller as the cation is less 'solvated' and so its Soret coefficient in these mixture drops to around 2.2×10^{-3} K^{-1}.

We finally note that the only transition metal salt for which a Soret coefficient has been determined is $NiCl_2$ in water at 5×10^{-3} mol^{-1} dm^{-3} at 25°C, with values reported of 2.67×10^{-3} K^{-1} (11) and 3.20×10^{-3} K^{-1} (12). These values apply to octahedral $[Ni(H_2O)_6]^{2+}$ and are numerically very close to our values for $NiCl_4^{2-}$ in molten chloride around 600°C. This gives us further confidence in the validity of our data, and demonstrates further that Soret coefficients for the other transition metal ions can conveniently and accurately be determined in aqueous and other room temperature media by our approach.

CONCLUSION

At this time we content ourselves with pointing out a possible trend with the size of the diffusing ion, and which might not be unexpected.

The majority of the data available was recorded in the 60's and little has been published recently. If Soret coefficients can be determined with greater precision then the validity or otherwise of this and other trends can be established, and their implications examined. We believe that this new approach, of measuring Soret coefficients from absorbance data, has been shown to work under extreme conditions and now should be applied systematically to, in particular, transition metal ions in aqueous and other room temperature systems. The improved accuracy thereby anticipated to result will permit genuine correlations to emerge.

ACKNOWLEDGEMENTS

NJP thanks the Science and Engineering Research Council and the Central Electricity Generating Board, N.E. Region, for a CASE Award. We also thank Dr H.V. St. Aubyn Hubbard for valued discussions. T.R.G. thanks the Royal Society and the University of Leeds for contributions towards travel expenses.

Table. A List of Soret Coefficients σ

Species	Solvent	Temperature Range/K	Wavelength /nm	Soret Coefficient /$10^{-3}K^{-1}$	Correlation Coefficient	Reference
$[FeCl_4]^-$	(Li,K)Cl	867-892	532	-5.45	0.988	(a)
			548	-4.80	0.965	(a)
$[CrCl_6]^{3-}$	(Li,K)Cl	866-890	555	-5.08	0.995	(a)
			800	-4.70	0.994	(a)
$[NiCl_4]^{2-}$	(Li,K)Cl	866-891	627	-3.15	0.999	(a)
			703	-3.91	0.989	(a)
$[Ni(SO_4)_3]^{4-}$	$(Li,Na,K)SO_4$	865-890	456	-2.83	0.996	(a)
			980	-3.35	0.999	(a)
		Low High				
$[Li(NO_3)_4]^{3-}$	$(Li,Ag)NO_3$	496 521		5.5±0.7		1
$[K(NO_3)_3]^{2-}$	$(K,Ag)NO_3$	537 612		1.4±0.2		1
$[Rb(NO_3)_3]^{2-}$	$(Rb,Ag)NO_3$	531 605		1.2±0.1		1
$[Cs(NO_3)_3]^{2-}$	$(Cs_2Ag)NO_3$	464 564		1.3±0.2		1
Solute						
HCl	H_2O	290 305		8.95		9
LiCl	H_2O	290 305		(-0.01)		9
KCl	H_2O	290 305		1.58		9
Me_4NCl	H_2O	290 305		5.17		9
Et_4NCl	H_2O	290 305		8.61		9
$h-Pr_4NCl$	H_2O	290 305		10.91		9
$n-Bu_4NCl$	H_2O	290 305		13.27		9
$NiCl_2$	H_2O(b)	290 305		2.67		11
$NiCl_2$	H_2O(b)	(c)		3.20		12

(a), This work. (b), Concentration of $NiCl_2$ was 5 x 10^{-3} mol^{-1} dm^{-3}. (c) No temperature range given but Soret coefficient reported at 25°C (298 K). The selected molten nitrate data, ref. (1), is for alkali ion concentrations of 10 mole per cent, except for caesium where it is for 17.5 mole per cent.

REFERENCES

1. V. Backlund, J. Dupuy, S. Gustafsson and A. Lundén, *Z. Naturforsch.*, *A22*, 471 (1967).
2. R.K. Williams and W.O. Philbrook, *J. Electrochem. Soc.*, 138m 1034 (1981).
3. H.J.V. Tyrell, *Diffusion and Heat Flux in Liquids*, Butterworths, 1961.
4. T.R. Griffiths and R.H. Wijayanayake, *Trans. Faraday Soc.*, 66, 1563 (1970).
5. M.J. Blandamer and M. Fox, *Chem. Rev.*, 70, 59 (1970).
6. T.R. Griffiths and P.J. Potts, *Inorg. Chem.*, 14, 1039 (1975).
7. T.R. Griffiths, K. King and d. Mortimer, *Power Ind. Res.*, 2, 79 (1982).
8. T. Ikeda and H. Kimura, *J. Phys. Chem.*, 69, 41 (1965).
9. T. Ikeda and H. Miyoshi, *J. Phys. Chem.*, 70, 3361 (1966).
10. C.H. Liu, J. Hasson and G.P. Smith, *Inorg. Chem.*, 7, 2244 (1968).
11. T. Ikeda, H. Ohe and S. Kawamura, *Bull. Chem. Soc. Jap.*, 41, 2858 (1968).
12. C.J. Petit, M. -H. Hwang and J. -L. Lin, *Int. J. Thermophys.*, 7, 687 (1986).

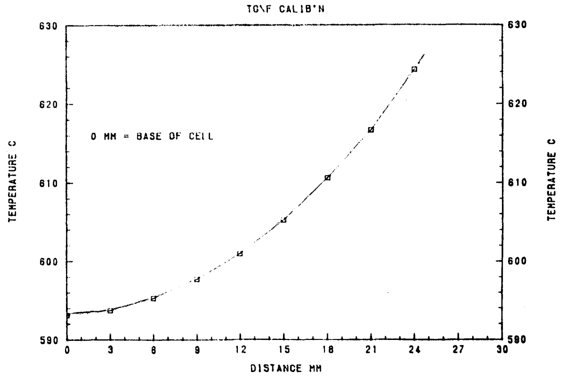

Figure 1. Plot of temperature against distance in an optical silica cell containing molten salt in the thermal gradient furnace, showing the thermal profile obtaining therein.

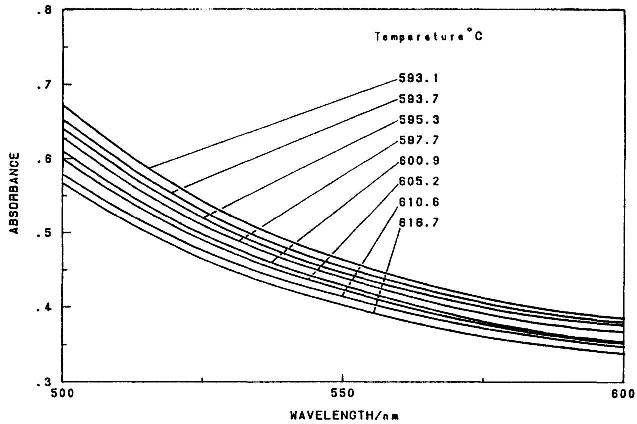

Figure 2. Charge transfer absorption edge for Fe(III) in molten LiCl-KCl eutectic recorded at different positions within the thermal gradient when the system was at the Soret Steady State.

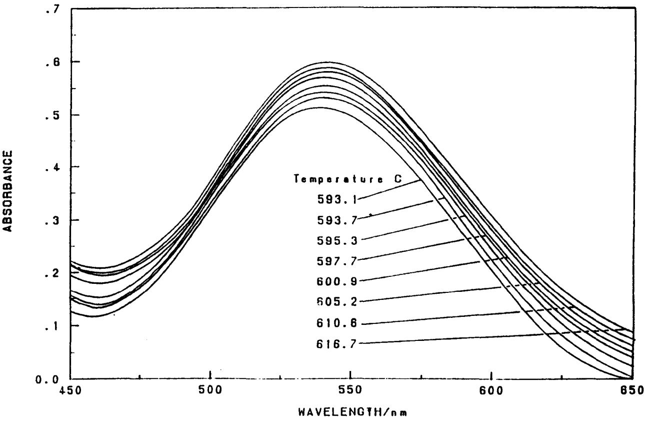

Figure 3. Ligand field spectrum of Cr(III) in molten LiCl-KCl eutectic recorded at different positions within the thermal gradient when the system was at the Soret Steady State.

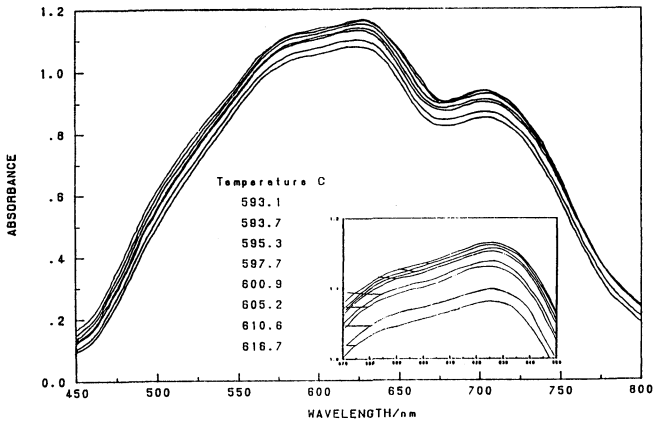

Figure 4. Ligand field spectrum of Ni(II) in molten LiCl-Kcl eutectic recorded at different positions within the thermal gradient when the system was at the Soret Steady State.

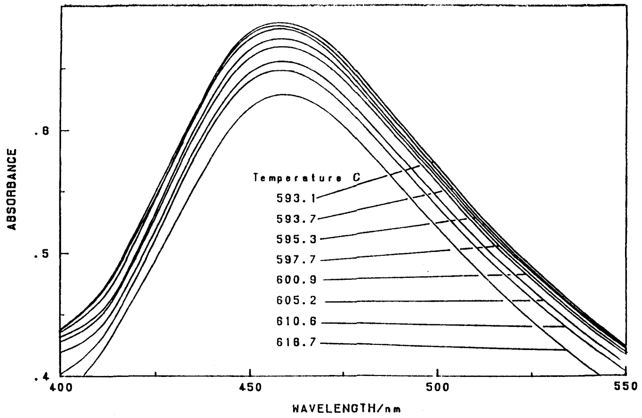

Figure 5. Ligand field spectrum of Ni(II) in molten Li_2SO_4-Na_2SO_4-K_2SO_4 eutectic recorded at different positions within the thermal gradient when the system was at the Soret Steady State.

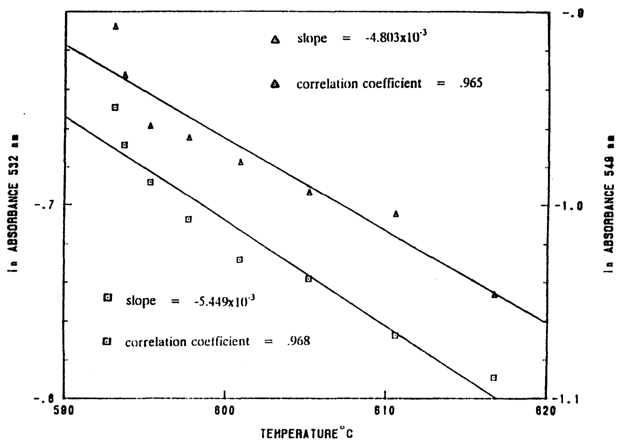

Figure 6. Plot of ln(absorbance) at 539 and 549 nm against temperature from the spectra in Figure 2. Slope of the least square linear fit to the data is the Soret coefficient. The goodness of fit is indicated by the correlation coefficient.

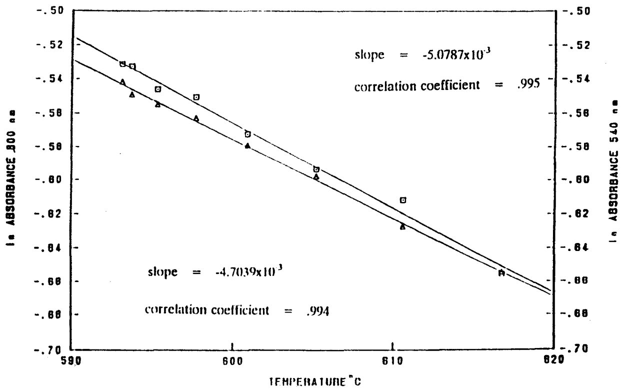

Figure 7. Plot of ln(absorbance) at 555 and 800 nm against temperature from the spectra in Figure 3. Slope of the least squares linear fit to the data is the Soret coefficient. The goodness of fit is indicated by the correlation coefficient.

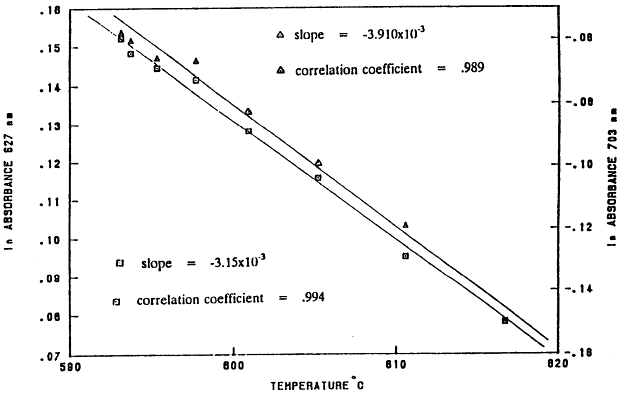

Figure 8. Plot of ln(absorbance) at 627 and 703 nm against temperature from the spectra in Figure 4. Slope of the least squares linear fit to the data is the Soret coefficient. The goodness of fit is indicated by the correlation coefficient.

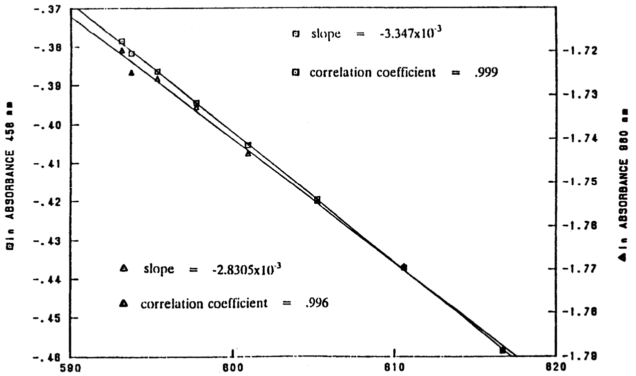

Figure 9. Plot of ln(absorbance) at 456 and 980 nm against temperature from the spectra in Figure 5. Slope of the least square linear fit to the data in the Soret coefficient. The goodness of fit is indicated by the correlation coefficient.

DOI: 10.1149/199017.0257PV

THE FREE ENERGY OF FORMATION OF CeF_3, AND ITS ACTIVITY COEFFICIENT IN CRYOLITE.

Ernest W. Dewing and Paul Desclaux

Alcan International Laboratory,
P.O. Box 8400, Kingston, Ont., Canada, K7L 5L9.
Alcan International Laboratory,
P.O. Box 1250, Jonquière, Qué., Canada, G7S 4K8.

ABSTRACT

Measurements were made of the equilibrium:

$$Al(l) + CeF_3(s) = AlF_3(s) + Ce\ (Al)$$

from which $\Delta_f H°_{298}$ of CeF_3 = -1701 kJ mol^{-1}. Values of the partition coefficient of Ce between Al and molten cryolite then give activity coefficients of CeF_3 in solution. These activity coefficients decrease as the NaF/AlF_3 ratio is raised, showing acid behaviour of CeF_3. It appears to dissolve mainly in the form of Na_2CeF_5.

INTRODUCTION

A recent paper by Walker, Kinoph, and Saha(1) has given some details of the chemistry of the deposition of solid CeO_2 on oxygen-evolving anodes in cryolite melts containing dissolved cerium compounds. The phenomenon was first observed by workers at ELTECH Electrosearch(2), and has led to a patent(3), since the coatings of cerium oxide may have applications in dimensionally-stable anode technology. The present work arose from a joint program between ELTECH and ALCAN, and is intended to develop some of the thermodynamic quantities involved.

Measurements have been made of the equilibrium

$$Al(l) + CeF_3(s) = AlF_3(s) + Ce(Al) \qquad (1)$$

with the two fluorides and the aluminum present at essentially unit activity; with literature data on the activity coefficient of Ce in Al (γ_{Ce}) the standard free energy of formation of CeF_3 is established. Data on the partition coefficient of Ce between Al and cryolite melts then yields values for the activity coefficient of CeF_3 in the molten salt.

THE ACTIVITY COEFFICIENT OF Ce IN Al

The data from which the activity coefficient of Ce in Al is derived were obtained by Kober et al.(4). An analysis, differing in some details from theirs, is being published elsewhere(5), and leads to

$$\log_{10} \gamma_{Ce} = -11\,356/T + 4.261 \qquad (2)$$

THE FREE ENERGY OF FORMATION OF CeF_3

To measure equilibrium (1), 5 g samples of super-pure Al were put in closed graphite crucibles with 5 g of a cryolite - AlF_3 - CeF_3 mixture of overall composition $NaF.2AlF_3.CeF_3$. At the temperatures used, this mixture forms a liquid phase, which facilitates mass-transfer, but remains saturated with solid AlF_3 and solid CeF_3. After holding at temperature for about 1 h, the crucibles were lifted from the furnace and chilled by standing on a cold surface.

XRD analysis of the salt phase showed, as expected, chiolite ($5NaF.3AlF_3$), AlF_3, and CeF_3. The metal was cleaned of adhering salt, and analyzed for Ce with an Inductively-Coupled Plasma atomic-absorption apparatus.

The results are shown in Table 1. It can be seen that the agreement of duplicates is excellent. With the values of γ_{Ce} from equation (2) the activity of Ce is calculated, and, since Al, CeF_3, and AlF_3, are all present at essentially unit activity, values of ΔG follow.

By means of a third-law calculation, each value of ΔG can be converted to a value of $\Delta_f H^\circ_{298}$ CeF_3. The thermodynamic functions for Al and AlF_3 are taken from the JANAF Tables(6), for Ce from Hultgren et al.(7) and the standard entropy and high-temperature enthalpy capacity of CeF_3 from King and Christensen(8). The mean value of $\Delta_f H^\circ_{298}$ CeF_3 is -1701.4 kJ mol^{-1}, with a standard deviation of ±4.6 kJ mol^{-1}.

In itself, this mean value of $\Delta_f H^\circ_{298}$ CeF_3 is very satisfactory. Johnson et al.(9) have determined, by fluorine-bomb calorimetry, values of -1699.5 ± 2.0 kJ mol^{-1} for LaF_3 and -1689.1 ± 2.6 kJ mol^{-1} for PrF_3; CeF_3 lies between them in the periodic table, and should be very similar. Moreover, Kholokhonova and Rezukhina(10) have measured essentially zero emf for the cell

$$La + LaF_3 | CaF_2 | CeF_3 + Ce$$

at 850 - 960 K, so that the supposition that CeF_3 should be very close in properties to LaF_3 seems verified. (Earlier work on the enthalpy of formation of the rare-earth trifluorides has been reviewed by Johnson et al.(9).) The only disconcerting circumstance is the obvious trend with measurement temperature of the values of $\Delta_f H^o_{298}$ CeF_3 shown in Table 1. If it were caused simply by a wrong entropy, then the mean value would also be wrong. No explanation can be offered.

With the mean value of ΔH^o from Table 1, the free energy for reaction (1) can be written

$$\Delta G^o = 183\,360 + 19.456\,T\ J \qquad (3)$$

THE ACTIVITY COEFFICIENT OF CeF_3 IN CRYOLITE

When cerium is added to a system consisting of a molten NaF - AlF_3 mixture and molten Al, it partitions itself between the two phases. The equilibrium constant for reaction (1), when the AlF_3 and CeF_3 are no longer at unit activity, is

$$K = a_{AlF_3}\left(\frac{a_{Ce}}{a_{CeF_3}}\right)$$

$$= a_{AlF_3}\left(\frac{N_{Ce}}{N_{CeF_3}}\right)\left(\frac{\gamma_{Ce}}{\gamma_{CeF_3}}\right) \qquad (4)$$

(The Al is essentially at unit activity, and is omitted.) K is determined from equation (3), the activity of AlF_3 is taken from a recent review of the thermodynamics of the binary NaF - AlF_3 system(11), together with a correction for the effect of dissolved Al_2O_3((12), and see Discussion below), γ_{Ce} comes from equation (2), and the weight partition coefficient yields (N_{Ce} /N_{CeF_3}). The only quantity not known is γ_{CeF_3}, and it can be calculated with respect to either a solid or a liquid standard state, since the free energy of fusion is available(8). In the following discussion the liquid standard state is taken.

Figures 1 and 2 show, respectively, the partition coefficients and the activity coefficients calculated from them. Some values are taken from Walker, Kinoph, and Saha(1). All the data came from tests in which CeO_2 was deposited anodically on an inert substrate from a cryolite bath; the bath and cathode metal pool were sampled and analyzed for Ce. Walker et al., report values at the end of a 10 h run; only values beyond 48 h have been used from our work. Our cathode pool was larger, and took longer to come to equilibrium. Nominal temperature was 1250 K (977C), although it was not closely controlled in any of the work. The partition coefficients are weight ratios (Ce in Al)/(Ce in cryolite). Concentration of CeF_3 in cryolite is calculated as mol fraction, based on NaF, AlF_3, 1/3 Al_2O_3, and CeF_3 as constituents. The small quantity of CaF_2 present in some melts is ignored.

DISCUSSION

The symbols in Figure 1 distinguish between melts with a low (2-5 wt%) and a high (5-8 wt%) alumina content. (Melts for which the Al_2O_3 content was determined to be >8% were considered to be saturated, and the level was taken as 8%.) Within the scatter of the data, alumina content does not seem to influence the partition coefficient, and neither does ratio, contrary to the expectation of Walker et al. The reason will be discussed below. The mean coefficient is 7.7 ± 1.5 (standard deviation).

Figure 2 shows that, unlike the partition coefficient, the activity coefficient is a very strong function of ratio. This arises because the activity of AlF_3, which enters the calculation, is itself a function of ratio. Although a correction for the effect of the Al_2O_3 concentration on a_{AlF_3} was applied, there is again no statistically significant effect of alumina concentration on γ_{CeF_3} (It should be noted that the correction applied is strictly applicable only at a weight ratio of 1.5 (molar ratio 3), and in this work weight ratios as low as 0.86 were encountered. The magnitude, and even the direction, of the error thereby introduced is unknown.)

It is quite apparent from Figure 2 that CeF_3 is, in this system, behaving as an acid, and combining with NaF rather than with AlF_3. As NaF is added to the melt, γ_{CeF_3} drops. The invariance of the partition coefficient arises because the activity coefficients of CeF_3 and AlF_3 respond in the same manner to varying NaF concentrations in the melts. CeF_3 is, however, a much weaker acid than AlF_3. At a weight ratio of 1.4, for example, its activity coefficient is around 4, while that of AlF_3 is about 3×10^{-3}.

One can take speculation further. If CeF_3 is forming a complex $nNaF.CeF_3$, and if that complex is dissolving ideally (i.e. its activity coefficient is constant), then a plot of log γ_{CeF_3} against log a_{NaF} should have a slope of -n. Figure 3 shows the plot, and it can be represented by:

$$\log \gamma_{CeF_3} = -(2.27 \pm 0.12) \log a_{NaF} - (0.66 \pm 0.09) \qquad (5)$$

with a standard deviation of ± 0.10. The uncertainties given are standard errors.

The value of n of 2.27 ± 0.12 strongly suggests that the predominant complex species in the melts is Na_2CeF_5. This is not surprising, since there is spectroscopic evidence that Na_2AlF_5 is a major species in the NaF - AlF_3 binary system(13). The constant in equation (5) suggests that γ_{CeF_3} in dilute solution in NaF at 1250 K should be about 0.2. The liquidi in the binary diagram(14) certainly show negative deviations from ideality, but it is not possible to make any reliable estimate of γ_{CeF_3} in dilute solution and as a function of temperature. All that can be said is that it is probably between 0.01 and 0.1 at 1250 K. Agreement is thus qualitative, but not quantitative.

Figure 4 shows a comparison of the activity coefficients in cryolite melts of the relatively few substances for which data are available. It is interesting that, at an NaF/AlF$_3$ ratio of 3, the four solutes investigated have coefficients close to unity.

ACKNOWLEDGEMENT

The measurements reported in Table 1 were made by Mr. G. Stratford. The measurements of the partition coefficient were made by Mr. J.-M. Tchernoff and Dr. C. Gilbert.

REFERENCES

(1) J.K. Walker, J. Kinoph and C.K. Saha: J. App. Electrochem., 1989, vol. 19, pp. 225-30.

(2) J.J. Duruz and V. DeNora: Paper presented at the Fall Meeting of the Electrochemical Society, San Diego, Cal., 1986.

(3) J.J. Duruz, J.P. Derivaz, P. Debely and J. Adorian: U.S. Patent 4,614,569.

(4) V.I. Kober, V.A. Lebedev, I.F. Nichkov, S.P. Raspopin and L.F. Yamshchikov: Russian Metallurgy, 1973 (2), pp. 163-66.

(5) E.W. Dewing and P. Desclaux: Paper accepted by Metall. Trans. B.

(6) M.W. Chase, Jr., C.A. Davies, J.R. Downey, Jr., D.J. Frurip, R.A. McDonald and A.N. Syverud: JANAF Thermochemical Tables, 3rd, ed., J. of Phys. & Chem. Reference Data, 1985, vol. 14, Supplement No. 1.

(7) R. Hultgren, P.D. Desai, D.T. Hawkins, M. Gleiser and K.K. Kelley: Selected Values of the Thermodynamic Properties of the Elements, American Society For Metals, Metals Park, Ohio 44073, 1973, p. 118.

(8) E.G. King and A.U. Christensen: U.S. Bureau of Mines, Report of Investigations 5510, U.S. Dept. of the Interior, 1959.

(9) G.K. Johnson, R.G. Pennell, K-Y. Kim and W.N. Hubbard: J. Chem. Thermodynamics, 1980, vol. 12, pp. 125-36.

(10) L.I. Kholokhonova and T.N. Rezukhina: Russ. J. Phys. Chem., 1976, vol. 50 (3), pp. 451-2.

(11) E.W. Dewing: Metall. Trans. B, 1990, vol. 21B, pp. 285-94.

(12) E.W. Dewing: Metall. Trans. B, 1989, vol. 20B, pp. 675-77.

(13) B. Gilbert and T. Materne: App. Spectroscopy, 1990, vol. 44 (2), pp. 299-305.

(14) C.J. Barton, J.D. Redman and R.A. Strehlow: J. Inorg. Nucl. Chem., 1961, vol. 20, pp. 45-54.

(15) E.W. Dewing: Metall. Trans. B, 1980, vol. 11B, pp. 245-49.

(16) E.W. Dewing and E. Th. van der Kouwe: Metall. Trans. B, 1989, vol. 20B, pp. 671-77.

(17) H.G. Johansen, Å. Sterten, and J. Thonstad: Acta Chem. Scand., 1989, vol. 43, pp. 417-20.

TABLE 1

The Equilibrium $Al(l) + CeF_3(s) = Ce(l) + AlF_3(s)$

$\frac{T}{K}$	Ce in Al wt%	Mean	$10^4 N_{Ce}$	γ_{Ce}	$\frac{\Delta G^o}{J}$	$\frac{\Delta H^o}{J}$	$\frac{\Delta_f H^o_{298} CeF_3}{J}$
977	0.093 0.093	0.093	1.79	4.34×10^{-8}	207 790	188 780	-1 706 770
1098	0.100 0.099	0.099	1.92	8.29×10^{-7}	205 960	184 600	-1 702 590
1196	0.093 0.096	0.095	1.82	5.83×10^{-6}	205 470	182 204	-1 700 200
1288	0.110 0.110	0.110	2.12	2.78×10^{-5}	202 920	177 862	-1 695 860

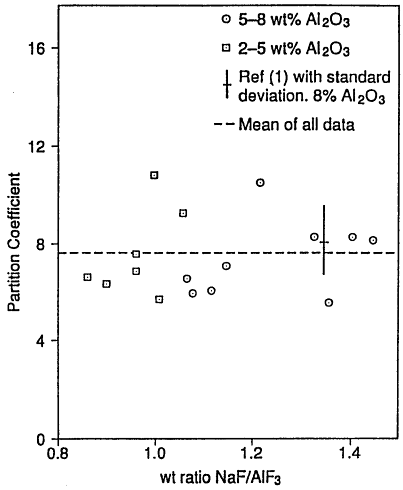

1.Partition coefficient of Ce between Al and cryolite melts.

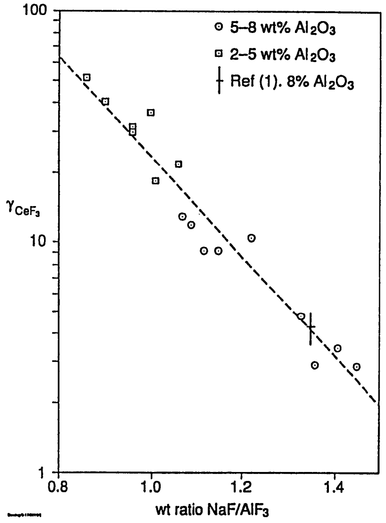

2.Activity coefficient of CeF_3 in cryolite melts. (Liquid standard state.)

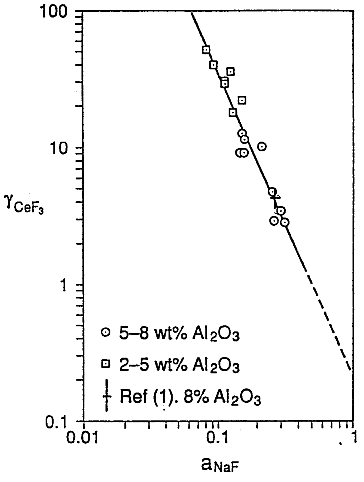

3.Activity coefficient of CeF_3 as a function of activity of NaF.

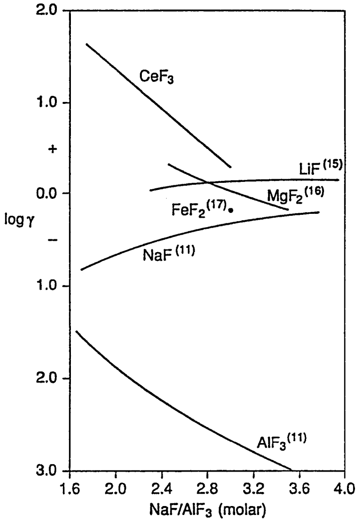

4.Activity coefficients in cryolite melts.

DOI: 10.1149/199017.0264PV

CORRELATIONS BETWEEN STRUCTURE, SPECTRA, AND THERMODYNAMICS IN SOLUTIONS OF COBALT CHLORIDE IN SODIUM TETRACHLOROALUMINATES.

David S. Newman, Peter J. Tumidajski, and M. Blander.

Chemical Technology Division
Argonne National Laboratory
Argonne, Il 60439

ABSTRACT

An EMF technique using the cell $Co/CoCl_2\text{-}NaAlCl_4$ // $(AgCl)_x\text{-}NaAlCl_4$ (x fixed)/Ag was used to measure the solubility of $CoCl_2$ in $NaCl.AlCl_3$ melts. The changes in EMF as a function of changes in melt composition were correlated with changes in the UV-Vis spectra of the dissolved cobalt species. From these data the microscopic structural contributions to the macroscopic thermodynamic properties of the solutions were estimated.

INTRODUCTION

In recent years organic and inorganic tetrachloroaluminates have become the focal points of a considerable amount of research.(1,2,3,4) The solution chemistry of the chloroaluminates is theoretically interesting because the thermodynamic properties are highly dependent on composition. In addition there is the potential to generate practical applications in the areas of energy storage batteries,(5,6) coal liquefaction, and coal desulfuriztion.(7)

Sodium tetrachloroaluminate ($NaCl\text{-}AlCl_3$) may be viewed as the prototype for these melts; the 50% - 50% mixture is best described as a highly ordered liquid,(8) consisting of Na^+ and $AlCl_4^-$ ions. It is well known that the tetrachloroaluminate system disproportionates only slightly.(9) Values for the disproportionation constant:

$$2AlCl_4^- = Cl^- + Al_2Cl_7^- \qquad [1]$$

vary from 1.06×10^{-7} at 175°C to 5.83×10^{-6} at 355°C.(10)

An acid - base chemistry for these melts arises by considering the 50% - 50% mixture as neutral, a solution with more than 50% $AlCl_3$ as acidic and a solution with less than 50% $AlCl_3$ as basic. In the acidic melts, up to 66.6% $AlCl_3$, the dominant anionic species are $AlCl_4^-$ and $Al_2Cl_7^-$ while in the basic melts they are Cl^- and $AlCl_4^-$. In addition, the liquid's topological order decreases as the composition varies in either the acidic or basic direction from the neutral point.

Topological order may be defined as follows. Designating Na^+ as A, Al^{+3} as B, and Cl^- as C, a pure $NaAlCl_4$ melt can be described topologically in one dimension as ...A - C - B - C - A - C - B - C ... and coulombically as ... + - + - + - ...., where Na^+ = + and $AlCl_4^-$ = -. When some excess NaCl is added, for example, we have an excess of A and C so that the coulombic order (...+ - + - ..) is preserved, but not the topological order. A particular sample of the liquid might be ...A - C - A - C - B - C - A -C ... which is of lower topological order than ... A - C- B- C -A- C- B- C where the A-C-B-C unit is repeated endlessly. From this it can be deduced that the degree of topological order at the 50 - 50 m% composition is larger the smaller the value of the disproportionation constant for Eq. [1]. For $NaAlCl_4$ (and undoubtedly for almost all other ordered liquids), topological ordering decreases with an increase in temperature.

Since the rate of change in order is large at the neutral point (because of the very small disproportionation constant), a striking minimum in the solubility of metal chlorides and maximum in solute activity coefficients occur at, or near, this composition.(8) Both the chemical and spectroscopic properties of an appropriate solute should reflect this change in order as a function of composition. Moreover, since the solubility is a thermodynamic property which to a great extent reflects the magnitude of the disproportionation constant and the ordering, there is the possibility of an unambiguous correlation of topological ordering with spectroscopic and thermodynamic properties.

Cobalt chloride was chosen as the probe molecule in this preliminary study since its spectra in a similar salt, $KCl.AlCl_3$, are well known (12) and its solubility in $NaAlCl_4$ has recently been directly measured by an analytical technique in which aliquots of the saturated melts are removed and Na, Co, and Al contents measured by inductively coupled plasma atomic emission spectroscopy (ICP -AES).(8) These data, in effect, serve to calibrate the simpler EMF measurements.

EXPERIMENTAL DETAILS

Polarographic grade $NaAlCl_4$ and $AlCl_3$ were obtained from Anderson Physics Laboratory (Urbana Il).

The electrochemical cell used in our experiments is a Co - Ag Galvanic cell which can be described schematically as:

$Co/\ CoCl_2 - NaAlCl_4\ //\ (AgCl)_X - NaAlCl_4$ (X fixed) /Ag
asbestos
diaphragm

The anodic and cathodic cell compartments were separated by an asbestos diaphragm sealed into pyrex glass as described previously.(11) The fibers allow electrical contact, but minimal mass diffusion. Junction potentials were minimized by using dilute solutions of $CoCl_2$ and AgCl on either side of the diaphragm. The reference electrode composition was fixed at $X = 1.252 \times 10^{-4}$. Fig. 1 represents data for the reference electrode. It should be noted that at 175°C the solution of AgCl in $NaAlCl_4$ is Nernstian up to approximately $X = 1.0 \times 10^{-2}$. In addition, the solubility of AgCl in $NaAlCl_4$ is relatively high with X approximately equal to 1.87×10^{-2}.

Temperatures were measured with a sheathed K-type thermocouple directly immersed into the melt and the solutions were continuously stirred. All experiments were conducted in a controlled atmosphere glove box filled with anhydrous He and with a moisture content around 1 ppm. EMF measurements were made with a high impedance electrometer. Compositions were changed by adding $CoCl_2$, NaCl, or $AlCl_3$ to the electrode compartment. Cell voltages were stable to within + 2 mv approximately 30 minutes after each addition. The measured cell potential is related to the activities of the solutes by the Nernst equation in the form:

$$/\backslash E = (RT/2F)\ln\{a_{CoCl_2}/a^2_{AgCl}\} \qquad [2]$$

$$= E - E^o_{Co} + E^o_{Ag} \qquad [3]$$

The UV-Vis spectra of the $CoCl_2$-NaCl-$AlCl_3$ solutions were obtained with a Carey 17 H spectrophotometer using a 1 mm quartz cell. A Carey 17 H has the optics reversed so that black body radiation does not interfere with the spectrum.(12) Solutions of known $CoCl_2$ composition were made by dissolving carefully weighed amounts of the compound in $NaCl.AlCl_3$ in a furnace inside of the glovebox and filling the cell inside of the box.

RESULTS AND DISCUSSION

The UV-Vis spectra of six $CoCl_2$ - $NaAlCl_3$ - $AlCl_3$ solutions are shown in Figures 2 - 5. Two salient features of these spectra are immediately obvious. The first is that on the basic composition side of the melt,(Fig. 2), the spectra of saturated solutions of crystalline $CoCl_2$ are indicative of a tetrahedral structure,(12) and the second is that the height of the three peaks (absorption) increases with increasing temperature. This is consistent with the fact that NaCl's solubility increases with increasing temperature. The greater the Cl^- concentration, the more tetrahedral $CoCl_4^-$ species and the more intense the spectrum.

In the 50.17 m% $AlCl_3$ melt (just barely acidic) the cobalt's spectrum (Fig.3) is distinctly different than it is in the basic melts and is probably due to octahedrally coordinated Co^{++} ions having $AlCl_4^-$ and/or $Al_2Cl_7^-$ nearest neighbors.(12,5,14) At the 50.00% composition (Fig. 4,5) the spectra seem to derive from a mixture containing some octahedral and some tetrahedral character, but with reduced intensity and with the tetrahedral species favored. However, since the extinction coefficient of a species with tetrahedral symmetry is generally much greater than the extinction coefficient of the same species with octahedral symmetry, the fact that the spectrum looks more tetrahedral than octahedral does not necessarily mean that the tetrahedrally coordinated species has a higher concentration than the octahedrally coordinated species. In fact, these spectra may represent neither symmetry, but represent species coordinated by different combinations of Cl^- and $AlCl_4^-$.

Table I lists the EMFs for the 50.00 m% mixture as $CoCl_2$ is added and also lists the EMF for the saturated solution after enough $AlCl_3$ is added to change the composition of the solvent to 50.17 m%. The temperature was 175 °C.

These data indicate that saturation occurs somewhere around $X_{CoCl_2} = 3 \times 10^{-4}$, which is consistent with the value of 2×10^{-4} obtained by Wai et.al.(8), but the striking feature is the sign reversal and magnitude of the EMF that results from the addition of $AlCl_3$ to the neutral melt. The explanation for this unusual behavior is the following. Cobalt chloride solubilities reach a very low minimum near the 50%-50% NaCl-$AlCl_3$ composition and increase rapidly with increase in the concentration of either $AlCl_3$ or NaCl.(8) Such steeply rising solubilities are predicted by the coordination cluster theory (13) which has been shown to represent the concentration dependence of the solubilities of $CoCl_2$ at concentrations of $AlCl_3$ above 50 m%. However, these changes can be described more clearly with a chemical description. On the acid side, the solubilities have been described in terms of the solubility product of $CoCl_2$ in $NaAlCl_4$:

$$K_{sp} = X_{Co^{++}} X^2_{Cl^-} \qquad [4]$$

where $\ln K_{sp}$ was found to be -33 at 175 °C, and where $X_{Co^{++}}$ and X_{Cl^-} are the cation and anion fractions in the reciprocal system $Na^+, Co^{++}/AlCl_4^-, Al_2Cl_7^-, Cl^-$. With an increase in the concentration of $AlCl_3$, the anion fraction of $Al_2Cl_7^-$ increases (according to Eq.[1]), that of Cl^- decreases and $X_{Co^{++}}$ increases rapidly according to Eq.[4].

Adding NaCl to a 50%-50% solution increases the solubility of $CoCl_2$ for a very different reason. At the 50%-50% composition, with the dissolution of $CoCl_2$ and just enough $AlCl_3$ to form $Co(AlCl_4)_2$, a pseudobinary solution of $Co(AlCl_4)_2$ in $NaAlCl_4$ is formed. Additional NaCl will lead to association reactions of the Co^{++} and the Cl^- ions to form a series of species

$$Co^{++} + Cl^- = CoCl^+ \qquad [5]$$

$$CoCl^+ + Cl^- = CoCl_2 \qquad [6]$$

$$CoCl_2 + Cl^- = CoCl_3^- \qquad [7]$$

$$CoCl_3^- + Cl^- = CoCl_4^= \qquad [8]$$

where the coordination of Co^{++} ions with tetrachloroaluminate anions is not specified. The appropriate values for the formation constants of these species can be estimated. For example, the average bond free energy for forming a Co - Cl "bond" can be estimated from the negative of the standard free energy of the metathetical reaction

$$CoCl_2 + 2NaAlCl_4 = Co(AlCl_4)_2 + 2NaCl \qquad [9]$$

This free energy is - 141.7 +/- (10.5) kj/mol (8) which, when divided by 4, the assumed coordination number, gives a value of - 35.4 kj/mol, the negative of which is the average "bond energy", ΔE_1. Knowing this bond energy allows the corresponding formation constant for the $CoCl^+$ species to be calculated from the equation

$$K_1 = Z[\exp(-\Delta E_1/RT) - 1] \qquad [10]$$

where Z is a coordination number of Co^{++} for Cl^- and here presumed to be 4. From this we estimate the value of K_1 to be about 50,000. For silver halides this procedure underestimates values of K_1. With a value this high, or higher, there should be a significant amount of $CoCl^+$ even at the neutral composition; the disproportionation reaction of $AlCl_4^-$ leads to a Cl^- ion concentration (anion fraction) of about 3.3×10^{-4}. With K_1 = 50,000, the ratio of the concentration of $CoCl^+$ to that of Co^{++} is about 17. With the addition of modest amounts of $CoCl_2$, a major fraction of the cobalt is tied up in the four complex species and the apparent solubilities will be considerably higher than that predicted from the solubility product. If the bond energies of $CoCl_3^-$ and $CoCl_4^=$ are large enough, the solubility will increase with increasing Cl^- concentration. Moreover, the unusual reversal in sign of the EMF shown in Table I is accounted for. As $CoCl_2$ is added to the neutral melt, the activity of the $Co(AlCl_4)_2$ (free Co^{++} no complexing Cl^- as nearest neighbors) *decreases* because of complex formation, e.g.,

$$Co^{++} + 2CoCl_2 = 2CoCl^+ \qquad [11]$$

and the EMF increases as long as the average complex formed by the addition of $CoCl_2$ has less than two chlorides. Upon addition of $AlCl_3$, the reaction:

$$CoCl^+ + Al_2Cl_7^- = Co^{++} + 2AlCl_4^- \qquad [12]$$

causes the Co^{++} concentration and the activity of $Co(AlCl_4)_2$ (sensed by the cobalt electrode) to rise sharply, thus reversing the sign of the EMF. We plan to do more detailed measurements of EMF and solubilities in order to deduce the individual formation constants of the different chlorocobalt species present in the melt.

CONCLUSION

In very basic $NaCl$-$AlCl_3$ melts, Co^{++} ions are tetrahedrally coordinated by Cl^- ions with large UV-Vis absorption. In the 50.00% -50.00% melt, the spectra are indicative of a mixture of species which cannot be uniquely defined without independent information. In the slightly acidic 50.17% $AlCl_3$ melt the Co^{++} environment is apparently octahedral. At this composition the Cl^- ion concentration is so low that the species whose formation is described by Eq[5] - Eq[8] which have relatively small extinction coefficients are not present at a high enough concentration to be readily detected and distinguished from the octahedral species.

ACKNOWLEDGMENT

This work was performed under the auspices of the U.S. Department of Energy, Division of Basic Energy Sciences, Division of Material Sciences, under contract No. W-31-109-ENG-38. We also wish to thank Argonne National Laboratory, Division of Educational Programs for their support.

LIST OF REFERENCES

1. R.J. Gale, R.A. Osteryoung; "Haloaluminates" in Molten Salt Technology, edited by D.G. Lovering and R.J. Gale, pp 55 - 78, Plenum Press, New York, 1983

2. J. S. Wilkes, J.A. Levisky, R.A. Wilson, C.L. Hussey, Inorg.Chem., *21*, 1263 (1982)

3. R.R. Rhinebarger, J.W. Rovang, A.I. Popov; Inorg.Chem., *23*, 2557 (1984)

4. M-L. Saboungi, A. Rahman, M. Blander; J.Chem.Phys., *80*, 2141 (1984)

5. S.W. Orchard, G. Mamantov; J.Electrochem.Soc., *136* 3565 (1990)

6. D.S. Newman, R.E. Winans, R.L. McBeth; J.Electrochem.Soc., *131*, 1079 (1984)

7. D.S. Newman, E.M. Kurt, D.Chen; Preprints of Papers Presented at the 196th ACS National Meeting, Los Angeles, CA, *33*, 113 (1988)

8. C. Wai, I. Bloom, D. Caveny, M. Blander; J.Phys. Chem., *94*, 1669 (1990)

9. G. Torsi, G. Mamantov; *Inorg.Chem.,10*, 1900 (1971)

10. L.G. Boxall, H.L. Jones, R.A. Osteryoung; J. Electrochem. Soc., *120* 233 (1973)

11. S.N. Flengas, E.K. Rideal; Proc.Roy.Soc.(London),*A233*, 443 (1956)

12. H.A. Oye, D.M. Gruen; Inorg.Chem., *4*, 1173 (1965)

13. M. Blander, M-L. Saboungi, P. Cerisier; Met.Trans. *B10*, 613 (1979)

14. C.L. Hussey, T.M. Laher; Inorg.Chem. *20*, 4201 (1981)

Table 1. EMF as a Function of $CoCl_2$ Mole Fraction

X_{CoCl_2}	X_{CoCl_2}/X^2_{AgCl}	EMF(mv)
50.00 m%		
8.17×10^{-5}	5205	122.5
2.46×10^{-4}	15703	138.1
3.65×10^{-4}	23291	148.6
4.21×10^{-4}	26810	149.9
50.17 m%		
4.1×10^{-4}	2500	- 44.7

Figure 1. Reference Calibration $X_{AgCl} = 1.252 \times 10^{-4}$

T = 175°C

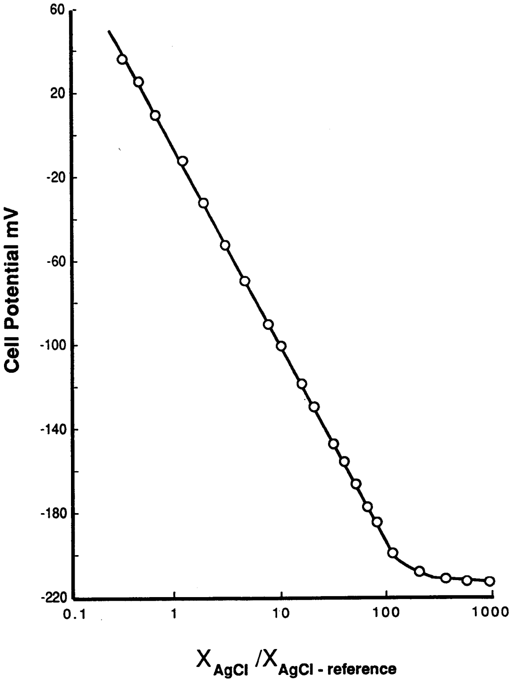

Figure 2. — $CoCl_2$ in basic melt $X_{CoCl_2} \cong 4.21 \times 10^{-4}$
T = 190° C Saturated with NaCl

▨ $CoCl_2$ in basic melt $X_{CoCl_2} \cong 4.21 \times 10^{-4}$
T = 230° C Saturated with NaCl

tetrahedral geometry

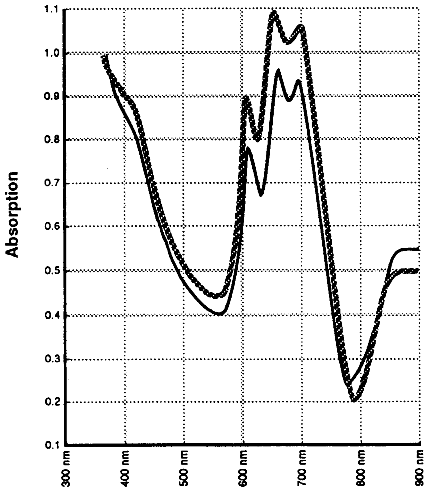

Figure 3. $CoCl_2$ in $NaAlCl_3$ 50.17 m% $AlCl_3$ (slightly acid)
T = 180° C Saturated with NaCl

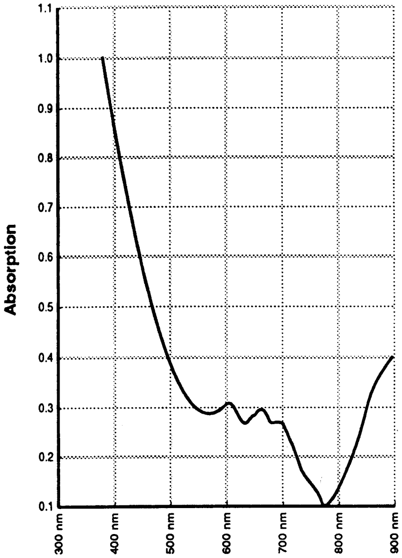

Figure 4. $CoCl_2$ in neutral melt $X_{CoCl_2} \cong 4.21 \times 10^{-4}$
T = 177° C Saturated with NaCl

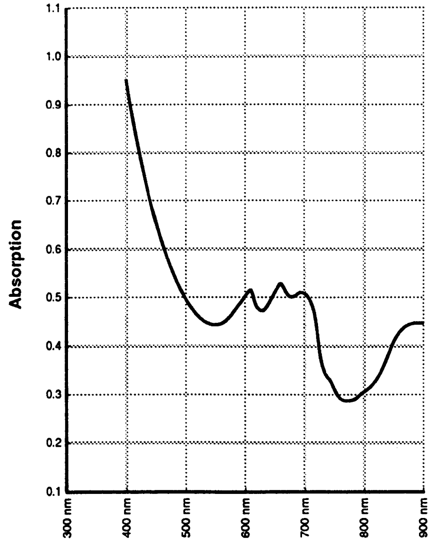

Figure 5. $CoCl_2$ in neutral melt $X_{CoCl_2} \cong 1.33 \times 10^{-4}$
T = 173° C Saturated with NaCl

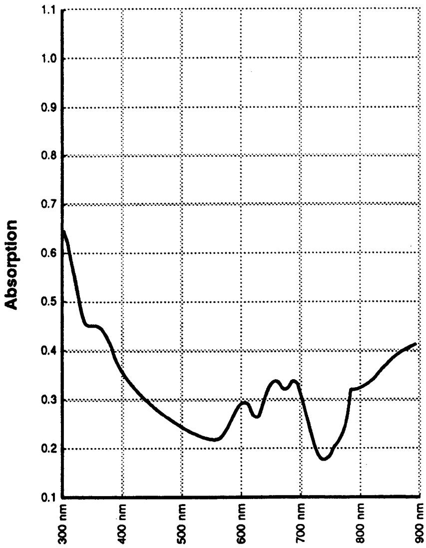

DOI: 10.1149/199017.0273PV

Low Temperature Molten Salt Electrolytes Containing Ternary Alkyl Sulfonium Salts

S.D. Jones and G.E. Blomgren

Eveready Battery Company, Inc.
Technology Laboratory
25225 Detroit Road
Westlake, Ohio 44145

Abstract

A new family of low temperature molten salts has been found. These electrolytes are based on the ternary alkyl sulfonium salts in mixtures with inorganic metal halides. A typical composition is the mixture of trimethylsulfonium chloride (TMSC) and $AlCl_3$ in a 1:2 mole ratio. This melt has a conductivity of 5.5 mS/cm, remains fluid until somewhat below -50 °C, and can plate and strip aluminum. TMSC has the same electrochemically stable window as 1-methyl-3-ethylimidazolium chloride.

Introduction

In recent years, considerable attention has been given to low temperature molten salt electrolytes, particularly those that are liquid at room temperature and below. Room temperature melts made from mixtures of inorganic salts such as aluminum chloride with certain organic salts such as N-(n-butyl) pyridinium chloride (BPC), 1-methyl-3-ethylimidazolium chloride (MEIC), or trimethylphenylammonium chloride (TMPAC) have been disclosed (1-3).

Unfortunately, the above melts all have inherent problems associated with them. Melts containing BPC have a foreshortened electrochemically stable window due to reduction of the pyridinium cation. Melts containing MEIC have a significantly larger electrochemically stable window than those containing BPC, however, MEIC is not commercially available and must be specially synthesized. Also, melts containing MEIC are somewhat difficult to prepare due to the rapid and highly exothermic reaction between the MEIC and $AlCl_3$ that will decompose the MEIC unless special precautions are taken to control the reaction rate. Melts containing TMPAC have the same electrochemically stable window as those made with MEIC and TMPAC is commercially available, however, the conductivity of this melt is considerably lower than the other melts.

Because of the shortcomings of the known melts, an investigation of new compounds capable of forming a low temperature melt with $AlCl_3$ was undertaken. The family of sulfonium salts was chosen for study. One of these salts, trimethylsulfonium chloride (TMSC), may prove to be a useful battery electrolyte (4).

Experimental

The chemicals were dried under vacuum at low heat except for the $AlCl_3$ (Fluka) which was used as received. The TMSC was synthesized from dimethyl sulfide and methyl chloroformate by the method of Byrne et al. (5). The synthesized TMSC was characterized using a Digilab FTS-80 Infrared Spectrometer with CsI pellets, a Finnigan Model 4021 Automated GC/MS using a glass column packed with 0.2% Carbowax 1500 on 80/100 Carbopack C with the injection port temperature set at 175°C, and a Varian Nuclear Magnetic Spectrometer. A sample of TMSC dissolved in water was obtained from the Stauffer Chemical Company. Trimethylsufonium iodide (TMSI-Aldrich), which sublimes at 213°C, was dried at 70-80°C under vacuum. The melts were prepared and tested in a Vacuum/Atmospheres stainless steel dri-lab. An MO-40 dri-train kept the moisture content of the dri-lab below 1 ppm and the oxygen content below 20 ppm.

Conductivities of the melts were measured using an ESI 253 Impedance Meter with YSI 3403 Conductivity Cells. Cannon-Fenske viscometers were used for the kinematic viscosity determinations while the densities were determined by the weighing of 5 ml graduated cylinders. All of the above physical properties were measured in the dry box without thermostating. The temperature of the dry box was approximately 27°C.

Cyclic voltammetry measurements were made on a PAR 173 potentiostat equipped with a 276 interface and controlled by an H-P 9816 computer. The working and counter electrodes were glassy carbon. The reference electrode for use with molten salts was an aluminum wire in MEIC:$AlCl_3$ (0.60 mole fraction $AlCl_3$) that was separated from the melt by a fine glass frit. The reference electrode for use with acetonitrile solutions was a silver wire in 0.1M tetramethylammonium perchlorate in acetonitrile solution separated from the sample by a fine glass frit.

Results and Discussion

The analytical characterizations of the synthesized TMSC show that it is indeed TMSC. The infrared spectra is shown in Figure 1 with the major peaks assigned. If the methyl groups are assumed to be freely rotating, the cation assumes a C_{3v} symmetry for the molecular vibrations. In this case, and considering the large disparity in mass between the proton and carbon, a separation into skeletal S-C modes (in the C_{3v} point group) and vibrations characteristic of the methyl group can be reasonably expected. With this assumption, we would expect four allowed $S-C_3$ vibrations in the infrared. Because of the cationic nature of the ion, the degenerate v_3 C-S stretching vibration would be expected to be at a higher frequency than the C-S stretching frequency in dimethyl sulfide, assigned at around 700 cm^{-1} by Trotter and Thompson (5) and by Sheppard (6). Therefore, we assigned this vibration to the peak at 930 cm^{-1}. We assign the two lower frequency peaks at 710 and 640 cm^{-1} to the symmetric stretching vibration, v_1, and the degenerate bending vibration, v_4. The symmetric bend, v_2, probably occurs at lower frequencies than our observations. The rest of the assignments, due to the methyl group vibrations, are as shown in Figure 1. Several additional small peaks were identified in the as-prepared sample as due to the dimethyl sulfide starting material and were easily removed with a water wash.

The proton NMR exhibits a single peak as would be expected from the symmetrical shape of TMSC, again assuming free rotation of the methyl groups. A literature reference (7) indicated that the single peak would be at 2.88 ppm in D_2O but we found that the peak occurred at 3.12 ppm in either D_2O or trifluoroacetic acid. The TMSC appears to thermally degrade into methyl chloride and dimethyl sulfide when subjected to either solid probe/mass spectroscopy or gas chromatography/mass spectroscopy. However, these would be the expected decomposition products and the technique shows no difference in the TMSC that was synthesized in-house and that obtained from Stauffer.

The newly discovered melts are made up of a mixture of an inorganic metal halide such as $AlCl_3$ and a ternary alkyl sulfonium salt such as trimethylsulfonium chloride or iodide. We believe that the relatively large sulfur atom with its hybridized 3p electrons can be easily polarized and acts similarly to an aryl group with its pi electrons (8). This increases the interaction between the cation and the easily polarizable chloroaluminate anions and lowers the melting point of the mixture. Other factors which contribute to melting point lowering are the delocalized nature of the interaction (induced dipole-induced dipole) and the low lattice energy of the crystalline salts (8). The striking fact in this work is that small methyl rather than large aryl substituents can accomplish the melting point lowering if the central atom is large and polarizable.

DSC measurements failed to show a freezing point or melting point for the TMSC:$AlCl_3$ (1:2) melt. Visual observations of the melt showed that solidification occured somewhat below -50°C. On warming, the mixture stayed solid until about -5°C where it became a thick, viscous liquid. This indicates that on cooling, the melt becomes a supercooled liquid that probably has a glass transition point rather than a freezing point. The TMSI:$AlCl_3$ (1:2) mixture required gentle heating to become molten, but then remained a light yellow liquid at ambient temperature. It is assumed that the light yellow color comes from a small amount of iodine or triiodide ion present in the solution.

The TMSC:$AlCl_3$ melt shows a conductivity of 5.5 mS/cm at the temperature of the dry box, while the TMSI:$AlCl_3$ melt conductivity was 4.5 mS/cm. These values are intermediate between TMPAC (or BPC)/aluminum chloride melts, and the cyclic MEIC/aluminum chloride melt, and they are much higher than the large aromatic sulfonium ions discussed previously (see (8) for data comparisons and discussion). The measured viscosity for the TMSC melt was 39.3 cP and the density 1.40 g/cm^3, both at dry box temperature. The viscosity is higher than MEIC, BPC or TMPAC in combination with aluminum chloride, while the density is comparable with MEIC and slightly larger than TMPAC or BPC. Clearly, there is an interaction of effects since the TMSC has the lowest molecular weight of the four salts and might therefore be expected to have the most mobile cation of the four, giving rise to higher conductivity and lower viscosity. Although only one of the atoms on the aluminate anion is iodide in the TMSI case, one might expect a larger effect compared to TMSC if the anion mobility were controlling. Therefore, we conclude that the cation mobility is more important.

The cyclic voltammogram of the TMSC:$AlCl_3$ (0.67) melt is shown in Figure 2. It can be seen that aluminum will plate and strip from this acid melt in a manner very similar to acid melts made with MEIC or TMPAC (8). The plating and stripping of aluminum has also been done by cycling two aluminum electrodes at 0.5 mA/cm^2, but shape change due to electrolyte stratification was a problem as seen before (8). Figure 3 shows the cyclic voltammetry results for 20 mM solutions of TMSC and MEIC in acetonitrile. It can be seen that the inherent electrochemical stability of TMSC is nearly identical to that of MEIC and TMPAC on both anodic and cathodic sides and considerably better than BPC. Figure 4 shows a cyclic voltammogram for the TMSI:$AlCl_3$ (0.67) melt. The aluminum deposition and stripping look similar to the other solutions, but the anodic sweep shows high currents at much lower potentials. Subsequent sweeps show interference with aluminum deposition unless the region of anodic current (higher than 1400 mV) is avoided, in which case the peaks are normal. Figure 5 shows the voltammetry of TMSI in AN which indicates that the low voltage oxidation is inherent in the TMSI. Figure 6 shows voltammograms for successive sweeps with this solution where cycling limits are +500 and +1500 mV. We attribute the two anodic peaks at 800 and 1100 mV to the reactions:

$$3I^- \dashrightarrow I_3^- + 2e \qquad [1]$$

$$2I_3^- \dashrightarrow 3I_2 + 2e \qquad [2]$$

respectively. The cathodic peak at about 900 mV is the reverse of [2]. It is smaller in size than the anodic peak because the following reaction occurs in solution:

$$I_2 + I^- \dashrightarrow I_3- \qquad [3]$$

[3] accounts for the decrease in the anodic peak at 800 mV and the growth of the anodic peak at 1100 mV with subsequent scans. The reverse of [1] is not observed in the region which was scanned. Similar voltammetry effects have been observed on platinum electrodes in iodide solutions of organic solvents with a supporting electrolyte (9). In the cited work, however, a side reaction with tetrahydrofuran complicated the results. One of the surprising results from our work on TMSI is that, although the iodide ion is undoubtedly complexed to aluminum in the melt, the solution behaves very much like the simple iodide, iodine, triiodide system seen with the uncomplexed salt in organic solvents. The narrower voltage range of the TMSI solutions and the effects on aluminum deposition and stripping limit the usefulness of this salt compared to TMPAC and MEIC, but the work illustrates the usefulness of these media for studying electrochemical reactions.

Acknowledgements

The authors would like to thank Susan Humphrey for her assistance in conducting the experimental portion of this work. We would also like to thank Zorica Bubnick for

carrying out the synthesis of TMSC, and our analytical group for infrared, DSC and mass spectrometric measurements.

References

1. J.C. Nardi, C.L. Hussey and L.A. King, U.S. Patent 4,122,245, October 24, 197$_8$.
2. P.R. Gifford, L.W. Shacklette, J.E. Toth and J.F. Wolf, U.S. Patent 4,463,071, July 31, 1984.
3. S.D. Jones and G.E. Blomgren, U.S. Patent 4,764,440, August 16 1988.
4. S.D. Jones and G.E. Blomgren, U.S. Patent 4,839,249, June 13, 1989.
5. B. Byrne and L.M.L. Lawter, Tetrahedron Letters, 27, 1233 (1986).
6. I. F. Trotter and H. W. Thompson, J. Chem. Soc. 1948, 481.
7. N. Sheppard, Trans. Faraday Soc. 46, 429 (1950)
8. S.D. Jones and G.E. Blomgren, J. Electrochem. Soc. 136, 424 (1989).
9. W. K. Behl and D. Chin, J. Electrochem. Soc. 135, 16 (1988)

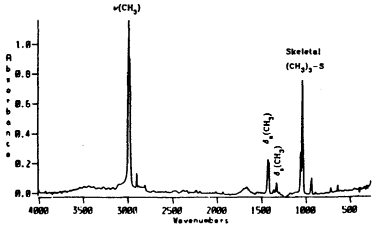

Figure 1

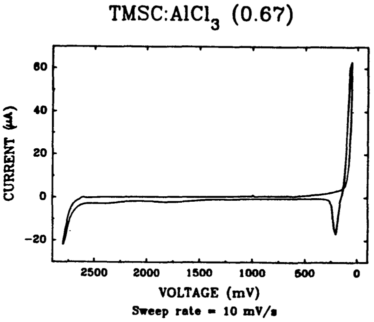

Figure 2

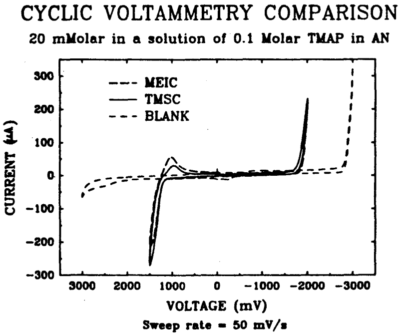

Figure 3

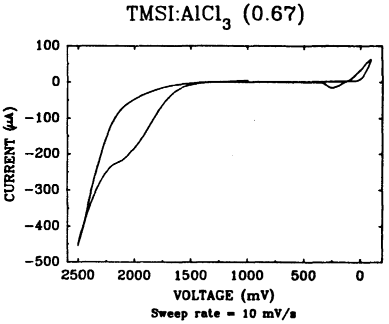

Figure 4

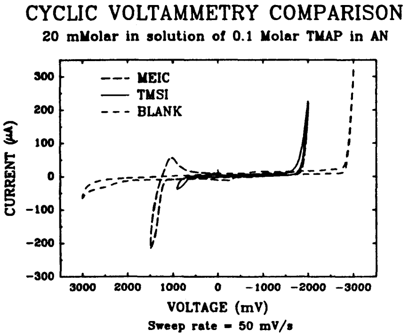

Figure 5

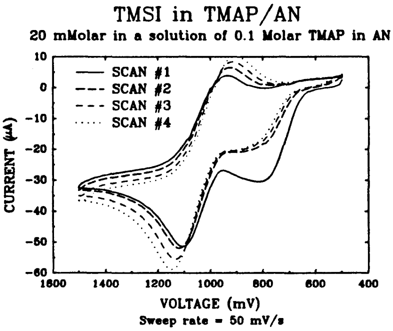

Figure 6

DOI: 10.1149/199017.0281PV

Novel Ambient Temperature Ionic Liquids Formulated from 1-Methyl-3-ethylimidazolium Chloride and Anhydrous Metal Chloride Salts other than Aluminum Chloride

Towner B. Scheffler and M. Stacey Thomson

Department of Chemistry
The University of South Florida
Tampa, Florida 33620

ABSTRACT

The reactions of several anhydrous metal chlorides with 1-methyl-3-ethylimidazolium chloride were studied. In most cases, low temperature (≤ 90 ^{0}C) molten salts were formed according to: $MCl_n + mCl^- \rightleftharpoons MCl_{n+m}{}^{m-}$. Generally, the metal chloro complexes formed were of lowest stoichiometry. Ionic interactions occurring in chlorolithate molten salts were studied by multinuclear NMR techniques.

Introduction - True ionic liquids that are molten at or below room temperature were first reported nearly forty years ago (1). Since then, a large number of reports appeared, detailing these unique materials (2). The chloroaluminates are the most widely studied and best understood example. These are typically a mixture of a quaternary ammonium salt, such as 1-methyl-3-ethylimidazolium chloride, and an anhydrous metal chloride salt, such as aluminum chloride (2). However, there are a number of closely related melts that are much less studied, but no less interesting or potentially useful. Recently, reports appeared detailing the use of other metal chlorides in place of aluminum chloride (3,4). The present study details some of our investigations of ionic liquids formulated from AgCl, CuCl, LiCl, $CdCl_2$, $CuCl_2$, $SnCl_2$, $ZnCl_2$, $LaCl_3$, YCl_3, $SnCl_4$, and $TiCl_4$, used with 1-methyl-3-ethylimidazolium chloride (MEIC). Nearly all of these mixtures produced ionic liquids at or near room temperature, at least at some compositions.

Experimental - All experimental manipulations were performed inside a Kawaunee Scientific Equipment Corp. dry box, which recirculated a dry nitrogen atmosphere containing < 5 ppm H_2O and O_2. The metal salts used were of at least reagent grade purity, and dried at 110 ^{0}C for several days. Some were obtained as hydrated salts; these were dried by refluxing in thionyl chloride. All NMR spectra were obtained on a JEOL

FX90Q spectrometer equipped with a multinuclear, variable temperature probe. Spectra were recorded at 30 and 90 ^{0}C, as indicated. The NMR reference materials were hexamethyldisiloxane for all proton studies, and aqueous lithium chloride at 0.5 or 2.0 mol/dm^3. In all cases, external references were used. Melting points were obtained with a Meltemp apparatus that was modified to allow cooling with LN_2-cooled dry nitrogen. Melting points were spot verified with a DuPont model 910 differential scanning calorimeter.

Results and Discussion - Figures 1 and 2 are compilations of ^{1}H NMR data obtained for a variety of melts at 30 ($AlCl_3$, CuCl, $CdCl_2$, and $ZnCl_2$-based mixtures) or 90 ^{0}C (all others). From these figures, several different behaviors were indicated: 1) melts which saturated or underwent compound formation at the 1:1 mole fraction (AgCl and LiCl); 2) melts which appeared to saturate at the 2:1 RCl/MCl_n composition ($CdCl_2$ and $ZnCl_2$); and the familiar Lewis acid-base melts based on CuCl and $AlCl_3$ (2). Of special note is the behavior of $SnCl_2$/MEIC mixtures. This formulation appeared to undergo compound formation at *both* the 2:1 and 1:1 RCl/MCl_n compositions.

Chlorocuprates

Chlorocuprate melts were first obtained during studies of the reactions of copper(I) and copper(II) chlorides with triethylamine (5). An equimolar mixture of CuCl and triethylammonium chloride results in triethylammonium dichlorocuprate:

$$(C_2H_5)_3NHCl + CuCl \rightleftharpoons [(C_2H_5)_3NH^+][CuCl_2^-] \qquad (1)$$

which is liquid at room temperature. Recently, studies were made of the CuCl/MEIC system, with similar results (6). Figures 1 and 2 contain comparisons of the C-2 proton chemical shift of the imidazolium ring observed in chloroaluminate and chlorocuprate melts. The chlorocuprates, also display Lewis acid base behavior similar to the chloroaluminates, however, the appropriate autosolvolysis is not as large. Qualitatively, the systems are quite similar, although comparison of the dependencies of their respective physical properties on composition reveal marked differences (6,7). Unlike the chloroaluminates, the exact anionic nature of the chlorocuprates is unknown. Due to the extremely broad NMR resonances observed for ^{63}Cu complex ions, multinuclear magnetic resonance studies of this system were not performed.

Chloroargentates

Mixtures of silver(I) chloride and MEIC also formed room temperature melts. Figure 1 shows proton chemical shift data over the 0.0 to 0.45 AgCl mole fraction composition range. Of particular interest in both the chlorocuprate and chloroargentate system is the discrepancy of behavior of these salts as one half of a binary system and as a solute in the chloroaluminate system. Laher and Hussey reported that very stable chloro complexes are formed by these salts in the $AlCl_3$/MEIC system, *i.e.*, $CuCl_4^{3-}$ and $AgCl_4^{3-}$ (8,9). Formation of these ions would result in compound formation at the 3:1 or 0.25 mol% composition. Clearly, this was not the case and these formulations require further study.

Chlorocadmiates and chlorozincates

Anhydrous $CdCl_2$and $ZnCl_2$ each formed binary ambient temperature fused salts when mixed with 1-methyl-3-ethylimidazolium chloride. Figure 1, again contains ^1H chemical shift data for these systems. These melts were clear, colorless liquids, with relatively low viscosities, comparable to the chloroaluminates. Little physical data has been tabulated for these systems, however, these melts appeared to saturate at *ca.* 0.333 mol% metal chloride composition indicating that the principal anionic species in these melts were $CdCl_4^{2-}$ and $ZnCl_4^{2-}$. Of particular note is the fact that these data were obtained at room temperature over a limited (0.2 - 0.3 MCl_n mole fraction) composition range.

Chlorostannates and chlorotitanates

Anhydrous tin(IV) chloride and titanium(IV) chloride, which are liquids at room temperature, *did not* make ambient temperature fused salts until at or just beyond the 0.50 mole fraction composition. We have only preliminary data on these systems, having synthesized melts from *ca.* 0.0 to *ca.* 100 mol% metal chloride. Their melting points appeared to go through a maximum near the 0.333 mol% point to another maximum just before the 0.5 mol% composition, indicating two distinct regions of differing behavior, giving rise to the speculation of two melts systems comprised of $SnCl_6^{2-}$ or $TiCl_6^{2-}$ before the 0.333 mole fraction composition and $SnCl_5^-$ or $TiCl_5^-$ between mole fractions 0.333 and 0.50. Most surprisingly, these systems saturated at or just beyond the 0.50 mol% point, forming ambient temperature melts at that point, with very low liquidus temperature ($< 0\ ^0C$). Beyond the 0.50 composition, a bi-phasic system was formed, with the lighter, undissolved metal chloride salt above the saturated melt. These saturated melts had low viscosities, comparable to the pure anhydrous metal salt. Both of these melts required careful synthesis, as they were the only other examples, other than the chlorocuprates and chloroaluminates, wherein the reaction between the quaternary ammonium salt and the metal chloride was exothermic. Charring of these melts occured very easily. Additionally, the titanate melts were a deep, pure orange, while the stannate melts had little or no native color.

Chlorolithates

As the behavior of lithium salts as solutes in the chloride ion-rich chloroaluminate fused salt was well studied via NMR and other means (10), LiCl/MEIC mixtures were chosen for detetailed study. Figure 3 is a phase diagram obtained in this melt over the 0.0 to 0.55 mol% composition range. Compositions between *ca.* 0.28 and 0.45 mol% LiCl were liquid below room temperature. Also of note is the fact that these compositions did not crystallize on cooling, they underwent glass transitions (as shown by the open circles in the figure.) In fact, at any composition beyond *ca.* 0.30 mole-%, the melts could be caused to form glasses, if cooled slowly enough.

Figure 4 is the composition dependent chemical shift (at 90 ^{0}C) of the C-2 proton of the imidazolium ring. The solid line is a calculated fit using the stacked trimer ion association model proposed by Wilkes (11). Though this model has caused some controversy, it appears to be an adequate representation of these melts. The dashed line is a linear least squares fit, included for comparison.

Figures 5, 6, and 7 are the results of ^{7}Li NMR studies performed using aqueous Li^+ as an external reference. Figure 5 shows a typical response obtained for a mole fraction = 0.250 melt. Of note here are the large positive chemical shift and the relatively broad resonance. These observations indicated the presence of a large amount of negative character associated with the lithium nucleus, as well as suggested that the lithium center was in fast exchange.

Figure 6 is the composition dependent chemical shift of the lithium resonance. This dependence was obviously linear, which was in contrast to other reports (10) of lithium ion in similar melts, wherein the lithium resonance showed a marked curvature with composition, which was interperated in terms of a dinuclear lithium species. We found no evidence to support dinuclear lithium complexes or higher chloride coordination of the lithium nucleus (*vide infra*).

Figure 7 is a plot of the observed relaxation time (T_1) of the lithium center as a function of melt composition. For a system in fast exchange, the relaxation time of the exchanging nucleus was shown to be inversely proportional to the maximum probability of encounter of the exchanging moieties (12). For a melt which displays compound formation at the equimolar composition, such as $AlCl_3$/MEIC or LiCl/MEIC, the maximum probability of encounter occurs at the 0.333 mole fraction, that is, when the anion fractions of the metal chloro complex and free chloride ion are equal, as indicated with the solid and dashed lines in the figure, which are proposed anion distribution curves for Cl^- and a lithium chloro complex, such as the dichlorolithate ion, $LiCl_2^-$, respectively.

Taken together, these data indicated that LiCl reacted with MEIC according to:

$$LiCl + MEIC \rightleftharpoons LiCl_2^- + MEI^+, \; K_f > 1 \qquad (2)$$

However, K_f in the chlorolithate system was apparently smaller that that observed for the aluminum chloride-based melts. Therefore, it was most likely that the ionic species present in chlorolithate melts at less than the 1:1 composition were the imidazolium cation, free chloride ion, and a lithium chloro complex, such as $LiCl_2^-$. The minimum in relaxation time near the 0.333 mole fraction composition is strong evidence for the preponderence of a lithium chloro complex, such as $LiCl_2^-$. We are presently performing electrochemical and vibrational spectroscopic studies to confirm the presence of the dichlorolithate ion $LiCl_2^-$ in these melts, and are attempting to extract information on the magnitude of K_f from the chemical shift and relaxation time data.

Other systems

Several other systems were given cursory examination. Barium chloride, copper(II) chloride, lanthanum chloride, and yttrium chloride did not readily form low melting fused salts over an appreciable composition range, either because the melts did not form or because their liquidus temperatures are above room temperature. However, all of these salts did form melts at elevated temperature (60 - 100 ^{0}C), though the barium, ytterium, and lanthanum systems formed fused salts over a very restricted composition range (< 0.20 mol% metal chloride). Of these systems, the barium chloride melts are the most interesting, as barium is known to form complex ions only with some difficulty, and the nature of the ionic species present in these melts may be interesting.

Summary

Many anhydrous metal chlorides react with 1-methyl-3-ethylimidazolium chloride to form fused salts, some of which were liquid at room temperature. The probable formation reaction was:

$$MCl_n + mCl^- \rightleftharpoons MCl_{n+m}^{m-} \qquad (3)$$

The exact nature of the metal chloride complexes in such melts is unknown, however available evidence indicated that complex ion of the lowest coordiantion was commonly formed.

We wish to acknowledge the University of South Florida

Research Council's President's Award in support of this study.

REFERENCES

1. Hurley, F. H.; Weir, T. P. *J. Electrochem. Soc.* **1951**, *98*, 203.

2. For a comprehensive review, see Hussey, C. L. *Advances in Molten Salt Chemistry*; Mamantov, G.; Mamantov, C., Eds; Elsevier: New York, 1983; Vol. 5, p 185.

3. Reynolds, G. F.; Scheffler, T. B.; Wilkes, J. S. Technical Report FJSRL-TR-85-0002, Frank J. Seiler Res. Labs. USAF Academy, CO 80840 **1985**.

4. Koura, N.; Takami, N. Japanesse Patent Application 87/250794 **1987**; see *Chem. Abs.* **1989**, CA111(8): 61048d.

5. Ford, W. T.; Hauri, R. J.; and Hart, D. J.; *J. Org. Chem.*, **1973**, *38*, 3916.

6. Bolkan, S. A.; Yoke, J. T.; *J. Chem. Eng. Data* **1986** , *31*, 194.

7. Fannin, A. A.; Floreani, D. A.; King, L. A.; Landers, J. S.; Piersma, B. J.; Stech, D. J.; Vaughn, R. L.; Wilkes, J. S.; Williams, J. L. *J. Phys. Chem.* **1984**, *21*, 2614.

8. Laher, T. M. and Hussey, C. L., *Inorg. Chem.*, **1983**, *22*, 3247

9. Laher, T. M. and Hussey, C. L., *ibid.*, **1983**, *22*, 1279.

10. Rhinebarger, R. R.; Rovang, J. W.; Popov, A. I. *Inorg. Chem.* **1986**, *25*, 4430.

11. Wilkes, J. S.; Frye, J. S.; Reynolds, G. F. *Inorg. Chem.* **1983**, *22*, 3870

12. Melendres, C. A.; Hertz, H. G. *J. Chem. Phys.* **1974**, *61*, 1974.

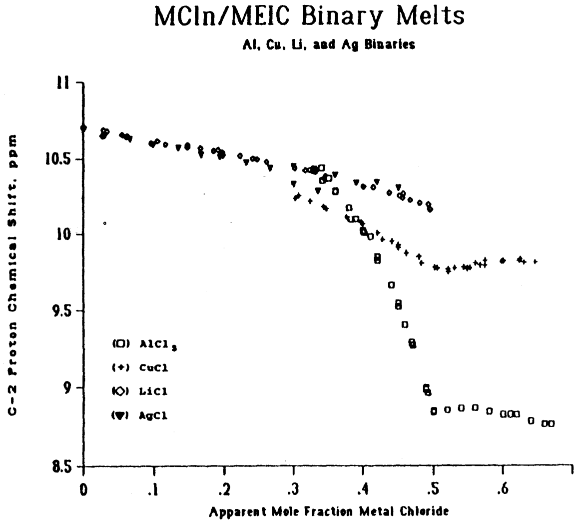

Figure 1 - ^1H chemical shift of the C-2 proton of the imidazolium ring (hexamethyldisiloxane external reference) for a variety of melts of the type MCl_n/MEIC. MCl_n = (□), $AlCl_3$, 30 °C; (+), CuCl, 30 °C; (◇), LiCl, 90 °C; (▼) AgCl, 90 °C.

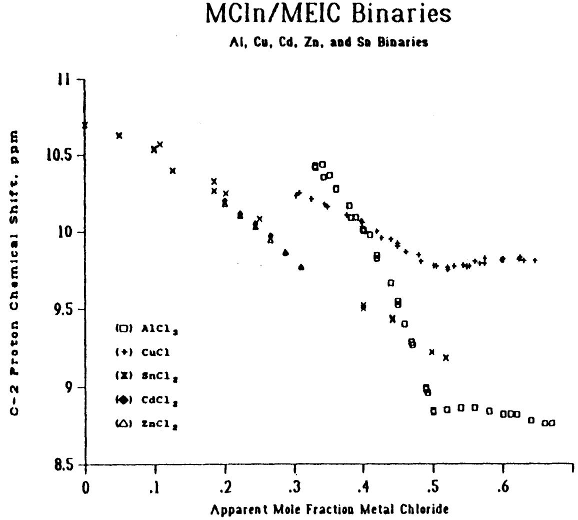

Figure 2 - ^1H chemical shift of the C-2 proton of the imidazolium ring (hexamethyldisiloxane external reference) for a variety of melts of the type MCl_n/MEIC. MCl_n = (□), $AlCl_3$, 30 °C; (+), CuCl, 30 °C; (X), $SnCl_2$, 90 °C; (◆) $CdCl_2$, 90 °C; (△), $ZnCl_2$, 90 °C.

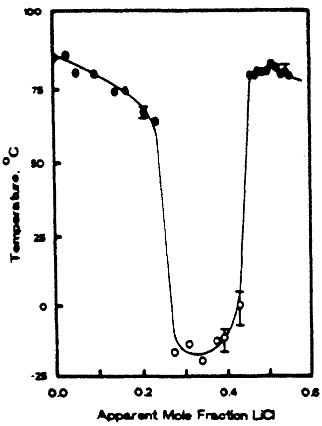

Figure 3 - Phase diagram for LiCl/MEIC melts. The open circles are glass transitions. For data points without error bars, the observed varience for replicate measurements was smaller than the symbol size.

Figure 4 - Chemical shift of C-2 proton as a function of the apparent mole fraction LiCl. The solid line is a fit to the ion-trimer associative model of Wilkes. The dashed line is a linear fit, included for comparison.

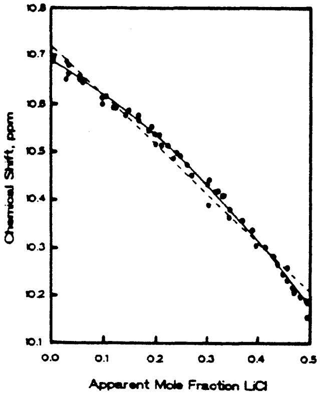

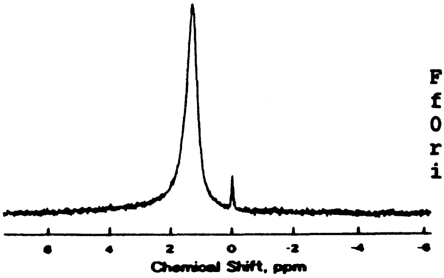

Figure 5 - ^{7}Li resonance line for a melt of mole fraction 0.2503 obtained at 90 ^{0}C. The reference was LiCl, 0.5 mol/dm^3 in D_2O.

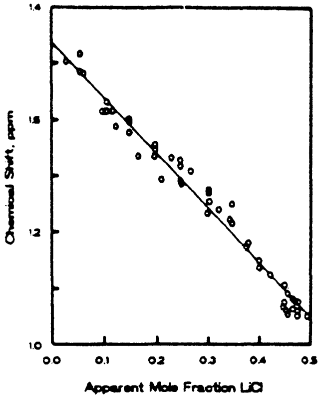

Figure 6 - ^{7}Li chemical shifts as a function of the apparent mole fraction LiCl at 90 ^{0}C, using an aqueous Li$^+$ external reference. The straight line is a linear least squares fit to this data.

Figure 7 ^{7}Li relaxation time (T_1) as a function of the apparent mole fraction LiCl at 90 ^{0}C, compared with the proposed anion fraction of chloride ion (———) and dichlorolithate ion (– – –), based on eqn. (2).

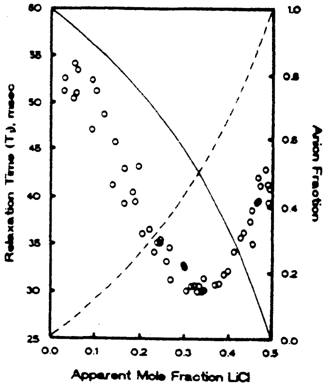

DOI: 10.1149/199017.0290PV

PROTONS IN AMBIENT TEMPERATURE CHLOROALUMINATE MOLTEN SALTS: ELECTROCHEMICAL AND NMR STUDIES OF THEIR INTERACTION WITH DIMETHYLANILINE

Soo-Gil Park, Paul Trulove, Richard T. Carlin and
Robert A. Osteryoung

Department of Chemistry
State University of New York
Buffalo, NY 14214

ABSTRACT

The Brønsted acidity of protons in the ambient temperature molten salt, $AlCl_3$:1-ethyl-3-methylimidazolium chloride (ImCl), can be varied by changing the underlying acidity of the molten salt. We have examined the electrochemistry and NMR spectroscopy of dimethylaniline, DMA, in a basic melt, where the mole ratio of $AlCl_3$:ImCl is less than 1, and in an acidic melt, where the mole ratio of $AlCl_3$:ImCl is greater than 1, with and without the addition of protons. The oxidation of DMA in the acidic melt is ca 1.5 V more positive than in the basic melt, indicating $AlCl_3$ adduct formation. On addition of proton to either melt, the DMA oxidation wave is shifted outside of the melt electrochemical window, indicating formation of protonated adducts in both acidic and basic melts. ^{13}C and ^{1}H NMR spectra show the presence of both the protonated and unprotonated species and, in the acidic melt, the presence of both an $AlCl_3$ adduct and a protonated adduct.

INTRODUCTION

In prior work in ambient temperature molten salts, consisting of aluminum chloride mixed with an organic chloride, either N-butylpyridinium chloride or 1-ethyl-3-methylimidazolium chloride, ImCl, we noted that very large shifts in the potential for proton reduction, of the order of +1.5 V, were observed as the melt composition was varied from acidic (excess $AlCl_3$), to basic (excess organic chloride) (1). These shifts in potential could be correlated by donor-acceptor theory to imply large changes in the donicity of the underlying solvent (2,3). Recent work by Smith and co-workers determined the value of the Hammett acidity function, H_o, for protons, added as HCl(g), in the ImCl-$AlCl_3$ melt. In slightly acidic ImCl-$AlCl_3$ melts, an H_o value of -12.6 was found, while in a melt saturated with $AlCl_3$, -67 mol % $AlCl_3$, the H_o value was -18 (4,5). Thus, protons in these melts are more acidic than 100% H_2SO_4, where H_o = -12, which is arbitrarily assigned as the lower limit for superacidity. Therefore, protons in the ambient temperature melts may be considered Brønsted superacids.

Prior work in our laboratory on the electrochemistry of a variety of amines in these molten salts had indicated the possible formation of $AlCl_3$ adducts, particularly in acidic melts (6). We concluded, at that time, that dimethylaniline formed an aluminum chloride adduct in the acidic melt. A similar conclusion regarding the formation of $AlCl_3$ adducts was arrived at from studies of quinones in the molten salts (7,8).

Here we report on the effect of quantitative proton addition on the chemistry and electrochemistry of dimethylaniline.

EXPERIMENTAL

All experiments were carried out in a Vacuum Atmosphere dry-box under a Helium atmosphere. 1-ethyl-3-methylimidazolium chloride was synthesized following reported procedures (9); aluminum chloride (Fluka, iron free) was purified by sublimation.

The molten salt $ImHCl_2$ was prepared from direct reaction of ImCl and HCl(g) (10). Methylaluminum sesquichloride (MAC), $Me_3Al_2Cl_3$, was obtained from Aldrich and used without further purification.

Cyclic voltammetric studies were performed with an EG&G PARC Model 175 Universal Programmer with a Model 173 Potentiostat/Galvanostat. Voltammograms were plotted on a Houston Instruments Model 2000 X-Y recorder. All other electrochemical studies were carried out using an EG&G Model 273 Potentiostat/Galvanostat controlled by a DEC PDP-8/e computer (11). An LNO3 Plus laser printer was used to obtain plots from the computer experiments.

For cyclic and pulse voltammetric studies, Pt disc (radius 0.08 cm) or glassy carbon, GC, electrodes, (radius 0.15 cm) were used. The electrodes were obtained from Bioanalytical Systems. For all melt electrochemical measurements the reference electrode was an Al wire (5N Alfa Inorganics) immersed in a 1.5:1 $AlCl_3$:ImCl melt in a separate fritted glass compartment. The counter electrode was a coiled wire of Al.

Rotating disc voltammetric experiments were carried out with a three electrode system consisting of a Pine Instruments Pt-Pt ring-disk electrode (r_1 = 0.09 in, r_2 = 0.097 in, r_3 = 0.101 in), a Pine Instrument's RDE-4 potentiostat, and an Al wire counter and reference electrode.

^1H NMR experiments were performed using either a Varian Gemini-300 or a Varian VXR-400 S spectrometer operating at 300.075 or 399.952 MHz, respectively. ^{13}C NMR experiments were performed using broad-band proton decoupling on the instruments indicated above operating at 75.462 and 100.57 MHz, respectively. ^1H and ^{13}C samples were prepared in the dry-box and pipetted into 5-mm tubes fitted with precision coaxial inserts (Wilmad Glass Co.). All NMR samples were capped and sealed with

Parafilm prior to removal from the dry-box. ^1H and ^{13}C chemical shifts are reported relative to 0.1% TMS in $CDCl_3$ in the coaxial insert.

RESULTS AND DISCUSSION

I. Electrochemistry and NMR of DMA and protonated DMA in 0.8:1.0 $AlCl_3$:ImCl.

Staircase cyclic voltammetry was performed to obtain an overview of the DMA electrochemical behavior in the presence and absence of deliberately added protons. Figure 1 shows a staircase cyclic voltammogram of DMA at a Pt electrode in a basic melt. An oxidation wave at 0.75 V is observed which is near the melt's anodic limit. No reduction waves associated with products of DMA oxidation are observed upon scan reversal. Based on previous work, we assume that the DMA oxidation is a 2-electron process (6).

Normal pulse, NP, voltammograms were obtained as a function of pulse width and DMA concentration. In these NP experiments the initial surface boundary conditions were reestablished after each pulse by holding the electrode at the open-circuit potential and stirring the solution for 2 s, followed by a waiting period of 5.9 s, prior to each new pulse application. The relevant parameters obtained from these experiments for a solution 53 mM in DMA are summarized in Table I for Pt and GC electrodes. As t_p is decreased, $E_{1/2}$ is observed to shift anodically. Plots of i_{lim} vs [DMA], for 50 and 100 ms pulse widths, are linear but have a non-zero intercept; this is the result of the presence of an initial protonic impurity, most likely arising from water, which protonates DMA, forming $DMAH^+$ (1). This species (see below) cannot be oxidized in the melt window. The level of protonic impurities in the basic melt can be estimated from the intercepts of such plots, and experiments to be described below, and is of the order of 4 mM.

A diffusion coefficient for DMA can be calculated from the limiting current (Cottrell equation) for the NP voltammograms,

$$i_{lim} = nFAC(D/\pi t_p)^{1/2} \qquad [1]$$

where n is the number of electrons involved in the process, F is the Faraday constant, A the area of the electrode, C the concentration of the diffusing species, and t_p is the pulse width. A plot of log i_{lim} vs log t_p is linear with slopes of 0.49 and 0.52 for the Pt and GC electrodes, respectively, indicating a diffusion controlled reaction. Because the exact concentration of DMA undergoing oxidation in these experiments is somewhat less than that added, as discussed above, plots of i_{lim} vs C, which have slopes independent of C, should provide more accurate values for the determination of the diffusion coefficient of DMA than plots of i_{lim} vs $t_p^{-1/2}$. Diffusion coefficients, using the plot of the [DMA] vs i_{lim}, at Pt were found to be 1.92 x 10^{-7} and 1.60 x 10^{-7} cm^2 s^{-1} for pulse widths of 100 and 50 ms, respectively, assuming an n value of 2.

A ^{13}C NMR spectrum for the methyl carbons is shown in Figure 2 for neat DMA, 2-a, and DMA in the basic melt, 2-b; the chemical shifts are identical and show that DMA does not form an $AlCl_3$ adduct in the basic melt.

Staircase cyclic voltammograms at a Pt electrode for a melt containing no DMA, added DMA, then proton, added as $ImHCl_2$, are shown in Figure 3. $ImHCl_2$ is a quantitative source of protons (10). Figure 3-a shows voltammograms of the melt with no added DMA; a cathodic wave at ca -0.4V is seen, and is due to the presence of protonic impurities (1). Upon addition of DMA, Figure 3-b, the wave at -0.4V disappears, a new cathodic wave, at -0.7V, appears, and the anodic DMA oxidation wave can be seen. The wave at -0.7V appears to be due to the reduction of proton from the protonated DMA (see below). On addition of $ImHCl_2$ in excess of the amount of DMA present, Figure 3-c, the DMA oxidation wave disappears, and, on a cathodic going scan, reduction waves for "free" proton and an increase in the protonated DMA wave is seen. In a basic melt, "free" protons exist largely as HCl_2^- (10).

Although DMA oxidation is found at a GC electrode, no cathodic waves are seen. Protons cannot be reduced in the melt at the GC surface, and apparently the $DMAH^+$ is also not reducible on this surface (1).

To further investigate the reaction between DMA and proton, an amperometric titration was carried out. The change of the NP limiting current for the DMA oxidation wave was examined as a function of added $ImHCl_2$. $ImHCl_2$ was added to a solution initially 53 mM in DMA. The results are shown in Figure 4. The DMA oxidation limiting current is seen to decrease linearly with added HCl_2^-, indicating a quantitative reaction with the DMA. The current goes to zero after the solution is ca 55 mM in HCl_2^-.

Staircase cyclic voltammetric reduction waves following the addition of trimethylaluminum sesquichloride, MAC, to the DMA solution containing excess proton, result in marked changes. MAC, like ethylaluminum chloride, is an effective reagent for proton removal (12). The staircase voltammograms initially show only one reduction wave at a potential characteristic of the free proton; as more MAC is added, two reduction waves, corresponding to the free proton reduction and the proton on the $DMAH^+$, appear. As still more MAC is added, the free proton reduction wave disappears, leaving only the $DMAH^+$ reduction wave. The $DMAH^+$ wave decreases slowly with time, indicating a sluggish reaction of the $DMAH^+$ with MAC.

To further examine the $DMAH^+$ reduction, reverse pulse, RP, voltammetry was carried out at a Pt electrode (13). In this experiment, the potential of the Pt electrode was stepped from an initial value, E_i, of +0.2, to -1.1 V for a generation time, τ. It was then stepped in 20 mV increments to increasingly positive potentials for a time, t_p, the analysis pulse, to examine the oxidation of products generated during the $DMAH^+$ reduction. After each generation and analysis pulse, the solution was stirred for 2.1 s, and then maintained in a quiet state for 5.9 s to renew the surface concentrations to their initial state. An NP oxidation wave for a DMA containing solution, and an RP wave for the same solution, as shown in Figure 5. As should be the case if t_p values for the NP and RP experiments are the same, the two oxidation waves coincide. Also shown is the RP voltammogram resulting when the mole ratio of DMA to $ImHCl_2$ was 1:1. At the -1.1V generating potential, the $DMAH^+$ is reduced, as discussed above. A slight "dc" cathodic current is seen on the reverse pulse voltammogram. We assign the first oxidation wave at ca 0.2 V to the oxidation of H_2 generated during the reduction, while the second oxidation wave is at the same potential as that for the DMA oxidation. Since no excess HCl_2^- is present, the H_2 arises from the $DMAH^+$ reduction; the DMA is liberated from the proton-adduct at the same time, and its oxidation is seen as well. The reaction taking place during the $DMAH^+$ reduction, therefore, may be written as:

$$DMAH^+ + e == DMA + 1/2\ H_2 \qquad [2]$$

It was not possible to quantitative the reverse pulse voltammetry due to the absence of theory and the lack of quantitatively reproducible voltammograms. Qualitatively, however, similar behavior was always observed.

Some rotating ring-disc voltammetry was carried out to confirm the above observations. A series of ring disc voltammograms at a Pt-Pt electrode are shown in Figure 6 for an experiment in the basic 0.8:1.0 melt. Comparison is made between a ring scan, with the disc being open-circuited, and with the disc held at various cathodic potentials to reduce the protonated $DMAH^+$. The melt contains an excess of DMA over proton added as $ImHCl_2$. Two features are noted. First, as the potential of the disc is made increasingly negative, an increase in the DMA oxidation current is clearly noted. The increase in current also becomes approximately constant for disc potentials more negative than -0.9 V. Secondly, a slight anodic current is noted in the vicinity of zero volts, which we attribute to the oxidation of H_2 formed during the $DMAH^+$ reduction. These results are in reasonable agreement with the results of the RP experiment, indicating the regeneration of the DMA and the presence of hydrogen.

The ^{13}C spectrum for the methyl carbons on addition of proton to DMA in a basic melt is shown in Figure 7. Under conditions where an excess of proton is in solution, i.e., only $DMAH^+$ is in solution, the line is at 46 ppm (vs TMS), compared to 41 ppm for DMA in the basic melt. The ^1H spectrum shows a line for HCl_2^-, at 13.55 ppm, and a line at 13.4 ppm which we attribute to proton on the amine nitrogen; this indicates exchange between the two species is slow on the NMR time scale. However, only a single line, at 3.01 ppm, is observed for the methyl protons, although a doublet is expected, and is seen in the acidic melt (see below); this single line indicates some exchange and an approach to the slow exchange limit. In basic melts containing both DMA and the protonated $DMAH^+$, a single ^{13}C line is found, the position of which is proportional to the population weighed average of the species present. This indicates that the exchange between the protonated and unprotonated DMA is fast on the NMR time scale.

II. Electrochemistry and NMR of DMA and protonated DMA in acidic $AlCl_3$:ImCl.

A staircase cyclic voltammogram for the oxidation of DMA at GC is shown in Figure 8-a. The peak current occurs at 2.5 V, near the acidic melt anodic limit at a GC electrode. The overpotential for the oxidation of Cl^- from $AlCl_4^-$, the limiting reaction in an acidic melt, is much larger on GC than on Pt, by ca 0.5V, thus forcing these studies, at least in the examination of the DMA oxidation, to be carried out at GC electrodes.

The oxidation potential of DMA in the 1.2:1.0 $AlCl_3$:ImCl melt is ca 1.75 V more positive than in the basic melt. This effect was attributed, in our previous study on this system, to the formation of a DMA:$AlCl_3$ adduct in the acidic melt, and this has also been verified by NMR spectroscopy, which show marked changes in the ^{13}C NMR chemical shift in going from basic to acidic melts (see below). Thus, in the acidic melt, the reaction:

$$Al_2Cl_7^- + DMA === DMA{:}AlCl_3 + AlCl_4^- \qquad [3]$$

takes place. No such complexation is observed in the basic melt. The Lewis acid, $AlCl_3$, removes electron density from the DMA molecule, making it more difficult to oxidize.

Addition of $ImHCl_2$ to the acidic melt containing DMA results in a marked decrease in the DMA oxidation wave at +2.5 V; we assume this is due to the replacement of the $AlCl_3$ by a proton on the DMA. Cyclic staircase voltammograms for this are shown in Figure 8-b through 8-e. However, in the acidic melt the DMA oxidation wave does not disappear upon addition of an amount of $ImHCl_2$ equivalent to the DMA.

The DMA limiting current was monitored as a function of DMA concentration, and, as in the basic melts, plots of i_{lim} vs [DMA] had non-zero intercepts. From the x-intercept, the concentration of an impurity, proton, was estimated as ca 7.4 mM. The higher impurity level in the acidic melt may result from a difference in the quality of the reagents or from the greater scavenging ability of the acid melt for advantitious water in the dry box. From the slope of i_{lim} vs [DMA] the diffusion coefficient of DMA in the acidic melt is calculated to be 8.4 and 9.1 x 10^{-7} cm^2 s^{-1} for 50 and 100 ms pulse widths, respectively. From the slope of i_{lim} vs $t_p^{-1/2}$ plots, the diffusion coefficient is calculated to be 5.5 and 6.9 x 10^{-7} cm^2 s^{-1}, for 30.3 and 50.5 mM DMA, respectively. If these were corrected for the 7.4 mM DMA initially tied up with proton, the values of 9.7 and 9.5 x 10^{-7} cm^2 s^{-1} for the 30 and 50 mM solutions, respectively, were obtained. The values are about five times greater than those in the basic melt. Based solely on viscosity effects, we would anticipate that the diffusion coefficient of the DMA would be two to three times larger in the acidic melt than in the basic melt (14). However, in view of the formation of the $AlCl_3$ adduct, we also might anticipate a larger diffusing entity in the acidic melts.

Normal pulse parameters in the 1.2:1 melt for a 30 and 51 mM DMA are summarized in Table II. Values of $it_p^{1/2}/C_{DMA}$ are tabulated for the [DMA] corrected for the protonic impurity and are quite constant. The value of the ratio of the limiting currents for the two concentrations of DMA are also in good agreement with the ratio of the concentrations of DMA if these concentrations are corrected for the ca 7 mM protonic impurity which effectively removes the DMA from the melt as discussed above.

A plot of the i_{lim} for a normal pulse voltammogram of DMA oxidation vs [$ImHCl_2$] added is shown in Figure 9. The DMA oxidation current initially shows a linear decrease, but then shows marked curvature, and an extrapolation to the [$ImHCl_2$] axis yields an intersection well in excess of the amount (51 mM) of DMA present in solution. This indicates the presence of an equilibrium between a DMA:$AlCl_3$ adduct and a protonated DMA adduct, $DMAH^+$. In more acidic melts the extent of the curvature seen during such a titration increases.

The ^{13}C spectrum of the methyl carbons in the acidic melt are shown in Figure 2-c. A shift to 47 ppm is seen, compared to 41 ppm in the basic melt. We take this to show the presence of an $AlCl_3$ adduct. In melts containing mixtures of free DMA and the $AlCl_3$ adduct a single ^{13}C peak for the methyl carbons is found. The position of this line is proportional to the population weighted average of the species present. This indicates that the exchange between the free DMA and the $AlCl_3$ adduct is fast on the NMR time scale.

If excess proton is added to an acidic melt containing DMA, i.e., to the DMA:$AlCl_3$ species, the methyl ^{13}C peak shifts down-field by 1.5 ppm, to 48.5 ppm, and a new ^1H line at 7.8 ppm, vs TMS, is seen. A split in the methyl protons, indicative of coupling, is also seen. (Irradiation of the 7.8 ppm line results in a collapse of the doublet, clearly indicating coupling of the two peaks.) These results are shown in Figure 10. A comparison of the chemical shift for the ^1H peak for $DMAH^+$ in the basic and acidic melt indicates it is at 13 ppm (vs TMS) and 7.8 ppm, respectively. We believe the large difference is the result of the interaction of the proton on the DMA with chloride ion in the basic melt.

NMR spectra for a melt containing both $DMAH^+$ and the DMA:$AlCl_3$ adduct are shown in Figure 11. Lines for both the protonated and $AlCl_3$ species are clearly evident. This indicates that the exchange between the protonated DMA and the DMA-$AlCl_3$ adduct is slow on the NMR time scale. To our knowledge this is the first NMR observation of a mixture of both a Brønsted and Lewis acid adduct of an organic base.

Of concern in this work is the relative acidity of protons and $Al_2Cl_7^-$ in the melts. To compare relative acidities, it is necessary to remember that the concentration of the $Al_2Cl_7^-$ is ca 0.86 M in the 1.2:1 melt. Since DMA is complexed by $AlCl_3$ in the acidic melt, the proton versus $Al_2Cl_7^-$ competition reaction is represented by:

$$DMA{:}AlCl_3 + HCl == DMAH^+ + AlCl_4^- \qquad [4]$$

Since only small additions of $ImHCl_2$ are required to produce significant decreases in the DMA concentration, the proton competes very effectively for DMA despite the high concentration of $Al_2Cl_7^-$. While the DMA-proton reaction may not be quantitative, it appears that the equilibrium constant for Equation 4 is large.

SUMMARY

The results presented indicate that DMA is not complexed in the basic melt, but forms an $AlCl_3$ adduct in the acidic melt. The formation of protonated DMA takes place in both basic and acidic melts; the reaction of DMA with proton in the basic melt appears quantitative, while in the acidic melt, where a $DMA{:}AlCl_3$ adduct is formed, an equilibrium between the protonated species and $AlCl_3$ adduct exists. Both electrochemistry and NMR support these conclusions.

ACKNOWLEDGEMENTS

This work was supported by the Air Force Office of Scientific Research.

REFERENCES

1. S. Sahami and R. A. Osteryoung, Anal. Chem., 55, 1970 (1983).

2. V. Gutmann, "The Donor-Acceptor Approach to Molecular Interactions", Plenum, New York (1978).

3. T. A. Zawodzinski, Jr. and R. A. Osteryoung, Inorg. Chem., 28, 1710 (1989).

4. G. P. Smith, A. S. Dworkin, R. M. Pagni, and S. P. Zingg, J. Am. Chem. Soc., 111, 5075 (1989).

5. G. P. Smith, A. S. Dworkin, R. M. Pagni, and S. P. Zingg, J. Am. Chem. Soc., 111, 525 (1989).

6. J. Robinson and R. A. Osteryoung, J. Am. Chem. Soc., 102, 4415 (1980).

7. G. T. Cheek and R. A. Osteryoung, J. Electrochem. Soc., 1293, 2488 (1982).

8. F. A. Uribe and R. A. Osteryoung, J. Electrochem. Soc., 135, 378 (1988).

9. J. S. Wilkes, J. A. Levisky, R. A. Wilson, and C. L. Hussey, Inorg. Chem., 21, 1263 (1982).

10. T. A. Zawodzinski, Jr. and R. A. Osteryoung, Inorg. Chem., 27, 4383 (1989).

11. T. R. Brumleve, J. J. O'Dea, R. A. Osteryoung and J. Osteryoung, Anal. Chem., 53, 702 (1981).

12. T. A. Zawodzinski, Jr., R. T. Carlin, and R. A. Osteryoung, Anal. Chem., 59, 2639 (1987).

13. J. Osteryoung and E. Kirowa-Eisner, Anal. Chem., 52, 62 (1980).

14. A. A. Fannin, Jr., D. A. Floreani, L. A. King, J. S. Sanders, B. Piersma, D. J. Stech, R. L. Vaughn, J. S. Wilkes, and J. L. Williams, J. Phys. Chem., 88, 2614 (1984).

Table 1

$E_{1/2}$ and Limiting Current Variation with Pulse Width for 52.8 mM DMA in 0.8:1.0 $AlCl_3$:ImCl melt at Pt and GC Electrodes

	Pt		GC	
t_p	$-i_{lim}$[1]	$E_{1/2}$	$-i_{lim}$[2]	$E_{1/2}$
(ms)	(uA)	(V)	(uA)	(V)
1000	45.1	0.74	140	0.76
750	51.3	0.77	162	0.76
500	65.7	0.78	209	0.77
250	91.5	0.79	297	0.79
100	140	0.81	472	0.81
75	164	0.83	527	0.82
50	233	0.84	--	--

1. $it_p^{1/2} = 46.1 \pm 2.7$

2. $it_p^{1/2} = 145 \pm 4$

Table 2

$E_{1/2}$ and Limiting Current Variation with Pulse Width for 30.3 and 50.5 mM DMA in 1.2:1.0 $AlCl_3$:ImCl melt at GC Electrode

t	$-i_{lim}$[1]	$E_{1/2}$	$-i_{lim}$[2]	$E_{1/2}$	$i_{lim}(50.5)/i_{lim}(30.3)$*
(ms)	(uA)	(V)	(uA)	(V)	
1000	162	2.27	309	2.29	1.90
750	187	2.28	361	2.30	1.93
500	224	2.29	449	2.31	2.00
250	346	2.31	664	2.34	1.92
100	520	2.34	993	2.37	1.91
75	621	2.36			
50	751	2.37			
25	993	2.40			

* Ratio of concentrations added (50.5/30.3) = 1.66; ratio of concentrations corrected for loss of initial DMA due to ca 7.4 mM proton impurity (see text) ((50.5 - 7.4)/30.4 - 7.4)) = 1.88.

1. $it_p^{1/2}/C_{corr} = 7.18 \pm 0.24$

2. $it_p^{1/2}/C_{corr} = 7.35 \pm 0.20$

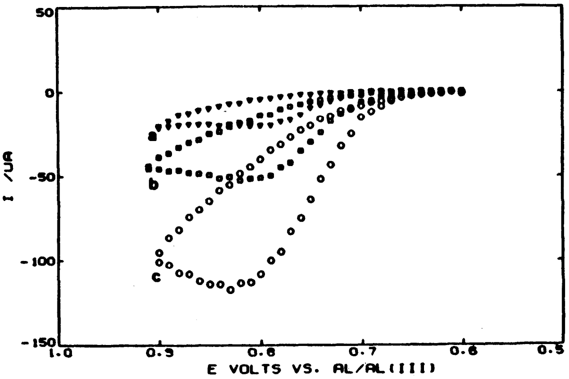

Figure 1. Staircase cyclic voltammogram for DMA in 0.8:1 melt at a Pt electrode, A = 0.02 cm^2. Scan rate 250 mV s^{-1} (step height 10 mV, step width 40 ms). [DMA], mM: a) 10.4; b) 29.7; c) 52.8.

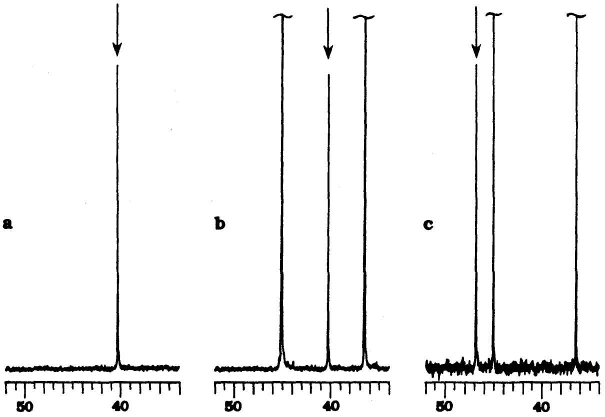

Figure 2. ^{13}C spectrum of methyl carbons in a) neat DMA; b) basic melt and c) acidic melt.

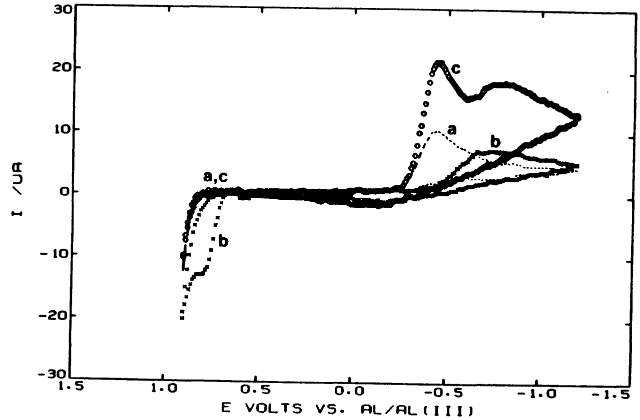

Figure 3. Staircase cyclic voltammograms for DMA in 0.8:1 melt; conditions as in Figure 1. Pt electrode. Sweep rate 100 mV s^{-1} : (step height 10 mV, step width 100 ms). a) Melt background; b) 17 mM DMA added; c) as b, but 30 mM $ImHCl_2$ added.

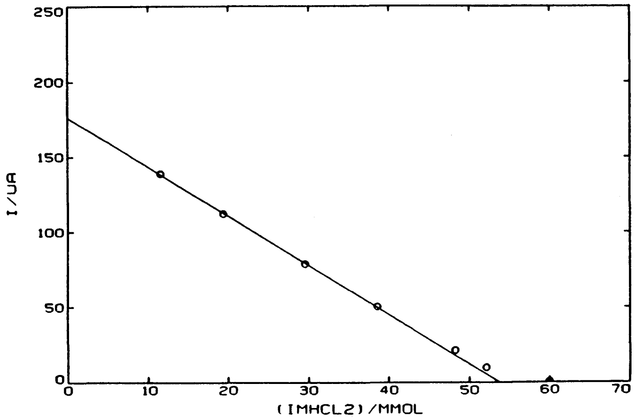

Figure 4. Normal pulse voltammetric limiting current for oxidation of DMA vs $[ImHCl_2]$ added to a 0.8:1 melt. t_p, 100 ms. $[DMA]_{initial} = 53$ mM. Pt electrode.

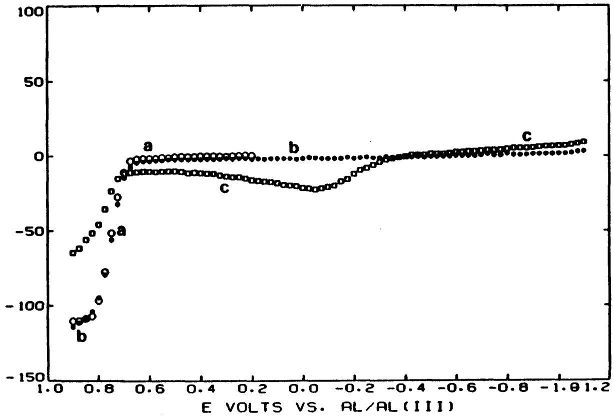

Figure 5. Normal and reverse pulse voltammograms for 0.8:1 melt containing DMA and DMA + $ImHCl_2$. Pt electrode. Pulse width 50 ms; delay time between pulses 8s (2.1 s stirred, 5.9 s quiescent); a) NP - 37 mM DMA; b) RP on same solution from -1.1 V, τ = 5s; c) RP from -1.1V on same solution but after 37 mM $ImHCl_2$ added; τ = 5s.

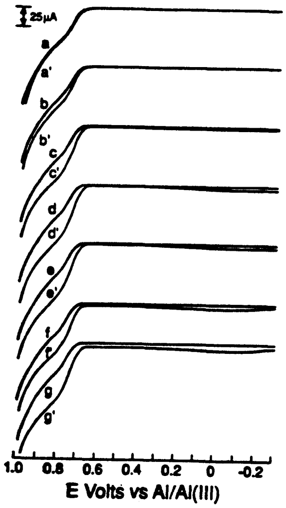

Figure 6. Rotating disc ring voltammograms for DMA in basic melt; [DMA] = 54 mM; [$ImHCl_2$] = 31 mM. Ring scan rate 10 mV s^{-1}. a, b, etc are ring voltammograms with disc at open circuit. Ring voltammograms with disc at: a') -0.5V; b') -0.7V; c') -0.9V; d') -1.1V; e') -1.3V; f') -1.5V; g') -1.7V.

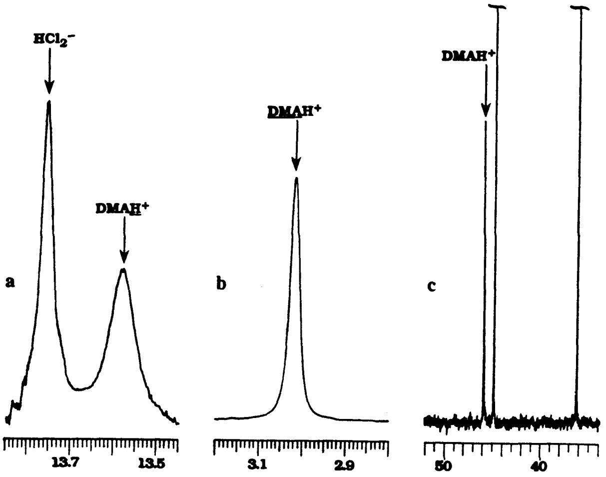

Figure 7. ^{13}C and ^1H NMR of DMA in basic melt following addition of $ImHCl_2$ to basic melt.

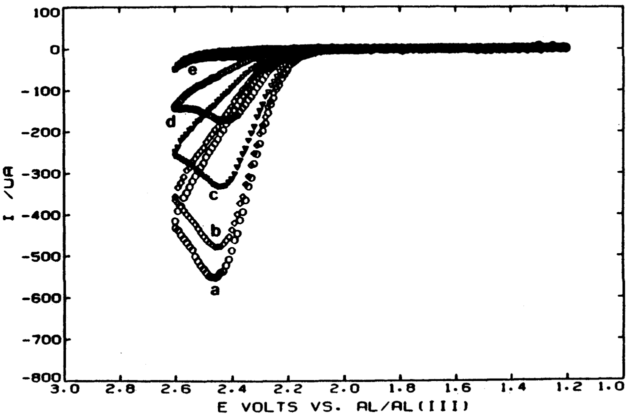

Figure 8. Staircase cyclic voltammogram for DMA in acidic, 1.2:1, melt. GC electrode, $A = 7.07 \times 10^{-2}\ cm^2$. Scan rate 250 mV s^{-1}, (step height 10 mV, step width 40 ms). With and without addition of $ImHCl_2$. [DMA] = 51 mM. [$ImHCl_2$], mM: a) 0; b) 8; c) 29; d) 52; e) 81.

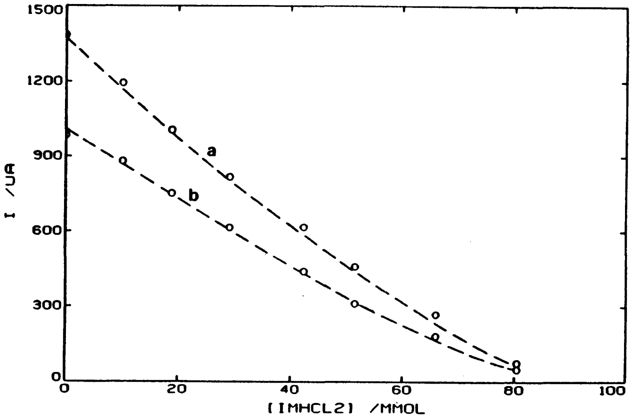

Figure 9. Normal pulse limiting currents for DMA oxidation versus $[ImHCl_2]$ added. GC electrode. Initial [DMA], 51 mM. t_p, ms: a) 50; b) 100.

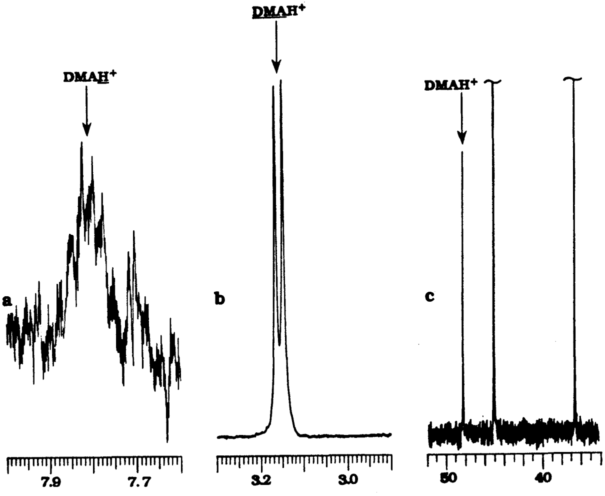

Figure 10. ^1H NMR(a,b) and ^{13}C(c) spectra for DMA in acidic melt containing proton well in excess of DMA present.

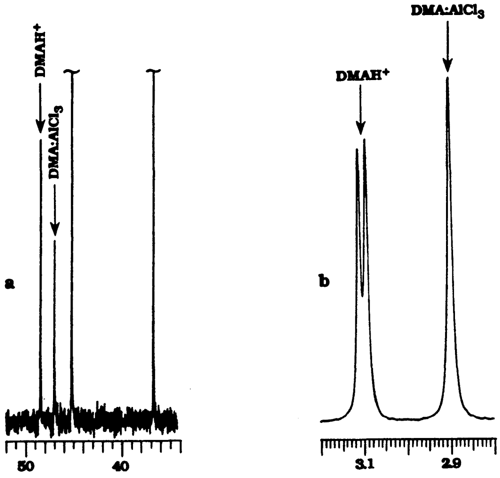

Figure 11. ^{13}C(a) and ^{1}H(b) NMR spectra for DMA in acidic melt containing DMA in excess of proton.

DOI: 10.1149/199017.0306PV

INTERACTION OF PROTONS WITH SOLUTES IN AMBIENT TEMPERATURE CHLOROALUMINATE MOLTEN SALTS: ELECTROCHEMISTRY AND NMR SPECTROSCOPY OF PROTONATED AND UNPROTONATED ANTHRACENE

Paul C. Trulove, Richard T. Carlin* and Robert A. Osteryoung

Department of Chemistry
State University of New York at Buffalo
Buffalo, NY 14214

ABSTRACT

The Brønsted acidity of protons in an ambient temperature molten salt, $AlCl_3$:1-ethyl-3-methylimidazolium chloride (ImCl), can be varied by changing the underlying acidity of the molten salt. In a basic melt, where the mole ratio of $AlCl_3$:ImCl is less than 1, the proton is a relatively weak acid, whereas in an acidic melt, where the mole ratio of $AlCl_3$:ImCl is greater than 1, its acidity increases enormously. Electrochemistry has been employed to study the interactions of protons with anthracene in the acidic melt. It was found that anthracene is protonated to give the anthracenium ion, which cannot be oxidized within the melt electrochemical window; however, it can be reduced to yield H_2 and free anthracene. NMR spectra show anthracene to be unprotonated in the basic melt, whereas in the acidic melt it forms a proton adduct.

INTRODUCTION

Ambient temperature organic chloroaluminate molten salts, $AlCl_3$:MCl, where MCl is either 1-ethyl-3-methylimidazolium chloride (ImCl) or n-butylpyridinium chloride (BuPyCl), are excellent solvents for studying the electrochemistry of organic compounds. These molten salts are liquids at room temperature over a wide range of $AlCl_3$:MCl ratios. Melts are acidic, neutral, or basic when the

---

* Present Address: Department of Chemistry, University of Alabama, Tuscaloosa, Alabama.

$AlCl_3$:MCl molar ratio is greater than, less than, or equal to unity, respectively (1). The acidic melts contain heptachlorodialuminate ion, $Al_2Cl_7^-$, which is a strong Lewis acid, while the basic melts contain chloride ion, a Lewis base.

Recent work by Smith and co-workers (2,3) has shown that the value of the Hammett acidity function for protons in acidic $AlCl_3$:ImCl melts is in the range of a Brønsted superacid. Furthermore, their work demonstrated that the relative superacidity of protons in acid melts can be varied by changing the underlying melt Lewis acidity.

Anthracene has been shown to be protonated to the anthracenium ion in acidic $AlCl_3$:ImCl melts containing proton (3). We had demonstrated much earlier that the electrochemically generated cation radical of anthracene is somewhat stable in an acidic $AlCl_3$:BuPyCl melt, but did not study this quantitatively (4).

Here we report on the investigation of the electrochemistry and NMR spectroscopy of anthracene in this mixed Lewis–Brønsted acid system.

EXPERIMENTAL

The preparation and purification of the $AlCl_3$:ImCl melts was performed as previously described (5). The source of protons for all experiments, 1–ethyl–3–methylimidazolium hydrogen dichloride ($ImHCl_2$), was prepared by reaction of ImCl with $HCl_{(g)}$ (6). 1–ethyl–3–methylimidazolium deuterium dichloride ($ImDCl_2$) was obtained by substituting $DCl_{(g)}$ for $HCl_{(g)}$. Anthracene–h_{10} (99.9%, Aldrich), anthracene–d_{10} (98% D, Cambridge Isotope), and 9,10–dihydro-anthracene (97%, Aldrich) were used as received. Methylaluminum sesquichloride (MAC), $Me_3Al_2Cl_3$ (Aldrich), was used as appropriate to remove protonic impurities from the melts.

All electrochemical experiments were performed under a purified helium atmosphere in a Vacuum Atmospheres dry–box. Electrochemical experiments were performed using an EG&G PARC Model 273 Potentiostat/Galvanostat controlled by a DEC PDP–8/e computer (7). Working electrodes, obtained from Bioanalytical Systems, were either Pt disc (area = 0.02 cm^2) or glassy carbon, GC, (area = 0.071 cm^2). The reference electrode consisted of an Al wire (5N Alfa Inorganics) immersed in a 1.5:1 $AlCl_3$:ImCl melt in a separate fritted tube. The counter electrode was a coiled Al wire.

^2H NMR experiments were performed on a Varian VXR–400 S spectrometer operating at 61.395 MHz with broad–band proton decoupling. Samples were prepared in the dry–box and pipetted into 10–mm tubes (Wilmad Glass Co.). The tubes were then capped and sealed with Parafilm prior to removal from the dry–box. The ^2H NMR experiments were performed with the spectrometer unlocked. Natural abundance D_2O in water was used as the reference and assigned a value of 0 ppm. Referencing was performed by substitution.

RESULTS AND DISCUSSION

I. Anthracene in proton free acidic $AlCl_3$:ImCl melts.

Anthracene in acidic $AlCl_3$:ImCl melts is oxidized in two one–electron oxidation steps as shown by the cyclic staircase voltammogram (CSV) in Figure 1a for a scan positive from 1 V at GC. A CSV for a negative scan from 1 V (Figure 1b) reveals a small wave at ca 0.3 V corresponding to the reduction of anthracenium ion produced from the protonation of anthracene by adventitious protonic impurities (*vide infra*). The first one–electron oxidation produces a cation radical which is sufficiently stable for the corresponding reduction wave to be observed, even at relatively slow scan rates. The second oxidation wave is due to the formation of a dication for which there is no associated reduction wave.

Normal pulse voltammograms were obtained as a function of pulse width for anthracene oxidation in a 1.2:1.0 melt with a small excess of MAC. Table I summarizes the normal pulse parameters pulse width (t_p), half–wave potential ($E_{1/2}$), diffusion–limited current (i_l), and the slope of E vs. $\log[i/(i_l - i)]$ which has a theoretical value of 59 mV for a one–electron process at 25 °C. The values for the slope in Table I for the first oxidation vary; however, they are consistent with a one–electron process. The $E_{1/2}$ values for the first oxidation are essentially constant and independent of t_p. The second anthracene oxidation wave appears much more complex than the first. The $E_{1/2}$ values for the second wave remain relatively constant at shorter pulse widths but shift to less positive potentials at longer pulse widths. The limiting currents for the second oxidation are approximately the same as those for the first oxidation indicating that the second oxidation wave is also a one–electron process. This is in contrast to previous work on anthracene oxidation in more conventional solvents, such as acetonitrile, where the first wave, except at very high scan rates at microelectrodes, is a two-electron process (8,9).

The diffusion coefficient for anthracene was calculated from the normal pulse limiting currents using the Cottrell equation

$$i_l = nFAC(D/\pi t_p)^{1/2} \tag{1}$$

where n is the number of electrons, F is the Faraday constant, A is the area of the electrode, C is the concentration of the diffusing species, and t_p is the pulse width. A plot of i_l vs $t_p^{-1/2}$ for the first oxidation is linear (R = 0.999) with a slope of 39.2 μA $s^{-1/2}$. From this slope a diffusion coefficient of 1.1 x 10^{-6} cm^2 s^{-1} was calculated for anthracene in a 1.2:1.0 melt at 27 °C.

The ^{2}H NMR spectra of anthracene-d_{10} in benzene and in a 1.2:1.0 melt are shown in Figure 2. The observed spectra in both solvents are essentially identical to that previously reported for fully deuterated anthracene (10). The spectrum for the 1.2:1.0 melt indicates that anthracene does not form an $AlCl_3$ adduct in acidic melts. This contradicts conclusions made in previous work in the acidic $AlCl_3$:BuPyCl melts (4), but it is in agreement with more recent work in the acidic $AlCl_3$:ImCl melts (3). To obtain the spectrum in Figure 2b great care was taken to remove all protonic impurities.

Kinetics of Anthracene Radical Cation Decomposition. The first oxidation wave was examined in more detail using cyclic staircase voltammetry. Theoretical curves were fit to voltammograms assuming an initial reversible one-electron transfer followed by an irreversible homogeneous reaction, i.e. a classic E_rC_i case (10,12). The $E_{1/2}$ value for the electron transfer and the first order rate constant, k, were obtained using a non-linear least squares program developed in this laboratory (13). The fitted voltammograms were collected for several melt compositions. These melts were made by starting with 20 mM anthracene in a 2.0:1.0 melt and adding ImCl to produce the less acidic melt compositions; consequently, the anthracene concentration decreased to ca. 15 mM for the least acidic melt.

Representative values for $E_{1/2}$ and k for various melt compositions and scan rates are shown in Table II. Characteristic voltammograms at various scan rates and two different melt acidities are shown in Figure 3. The dots are the experimental data, and the solid line is the fit of the data. In general the E_rC_i model fits the data quite well. Apparent in Table II, however, is the decrease in the homogeneous rate constant with increasing melt acidity. This would seem to indicate the stability of the cation radical is enhanced in melts of greater Lewis acidity. Also apparent in Table II is an increase in the rate constant and a slight shift of $E_{1/2}$ towards positive potentials with increasing scan rate. Ideally, the same k and $E_{1/2}$ values should be obtained for all scan rates for a particular melt. There is no obvious reason for these shifts with scan rate, and we can offer no explanation for this trend at this time.

When rate constants for anthracene concentrations of 7, 20, and 35 mM in a 1.5:1.0 melt were determine for a scan rate of 100 mV s^{-1} values of 0.17, 0.22, and 0.27 s^{-1}, respectively, were obtained. The increase in pseudo first-order rate constant with increasing anthracene concentration may indicate a higher-order process such as coupling of radical cations to form bianthracenes (14). The relatively small change in the rate constant with concentration does not alter the discussion of the rate constant as a function of melt composition since the concentration of anthracene varied only from 20 to 15 mM for the experiments summarized in Table II.

In the acidic melts the anthracene radical cation is much more stable than in conventional organic solvents (8,15). In rigorously dried acetonitrile, for example, a value for the first-order rate constant of 125 s^{-1} has been determined (8). Although no rate constant was determined, the radical cation in dichloromethane over alumina was found to be quite stable, judging from the fact that a reverse peak for the reduction of the radical cation was seen at a scan rate of ca. 100 mV s^{-1} (16).

II. Anthracene in acidic $AlCl_3$:ImCl melts containing proton.

It has been shown recently that proton in acidic $AlCl_3$:ImCl is a Brønsted-superacid which readily protonates anthracene forming the anthracenium cation (3). Figure 4 shows both anodic and cathodic scans at GC starting from 1 V in a 1.5:1.0 melt containing 18 mM anthracene and 28 mM of the proton source, $ImHCl_2$. The anthracenium ion is not oxidized in the melt window. On the other hand, the anthracenium ion reduction at ca. 0.3 V is the major electrochemical process in this solution. The oxidation waves for unprotonated anthracene are also seen, albeit at much lower currents, indicating that anthracene is not quantitatively protonated even in the presence of an excess of protons. No proton reduction is observed because protons are not electroactive at GC within the melt window (17). However, when a cathodic scan from 1 V is performed on Pt, reduction waves for both proton and anthracenium ion are seen. Normal pulse voltammograms for anthracenium ion reduction in this solution were performed at various pulse widths. Table III summarizes the relevant parameters. Although anthracene is not quantitatively protonated at 28 mM $ImHCl_2$, it is more than 90% protonated. Thus, the anthracenium ion concentration can be approximated as 18 mM. From the slope of a plot of i_l vs. $t_p^{-1/2}$ ($R = 0.997$) an estimate for the anthracenium ion diffusion coefficient of 4×10^{-7} cm^2 s^{-1} was obtained assuming an n value of 1. Unfortunately, at high proton concentrations the mechanism of anthracenium ion reduction changes (*vide infra*), and n approaches two. Consequently, it was not possible to add a large excess of protons to quantitatively protonate the anthracene without changing the reduction process.

The ^2H NMR spectrum of 15 mM anthracene-d_{10} with 30 mM $ImDCl_2$ in a 1.2:1.0 melt is shown in Figure 5a. The observed spectrum is consistent with a fully deuterated anthracenium ion (18), confirming the conclusions made from the electrochemical experiments. Unfortunately, due to the inherent broad nature of ^2H peaks it was not possible to determine the completeness of deuteration. Interestingly, the ^2H spectrum of 15 mM anthracene-h_{10} with 30 mM $ImDCl_2$ in a 1.2:1.0 $AlCl_3$:ImCl melt (Figure 5b) is essentially identical, except for peak intensities, to that for the fully deuterated anthracenium ion (Figure 5a). The presence of a deuterium spectrum indicates that H–D exchange occurs at all positions on the anthracene ring. This is not entirely surprising when considering the highly acidic nature of proton in acidic melts and the fact that Lewis acids have been shown to catalyze H–D exchange on anthracene (10).

A cyclic staircase voltammogram of anthracene oxidation at Pt in the presence of excess $ImHCl_2$ is shown in Figure 6a. A significant increase in the anthracene oxidation wave was observed when the potential was held at 0.7 V before scanning through the wave (Figure 6b). At 0.7 V "free" protons are reduced but anthracenium ion is not. These results strongly suggest that, at the electrode surface, the equilibrium

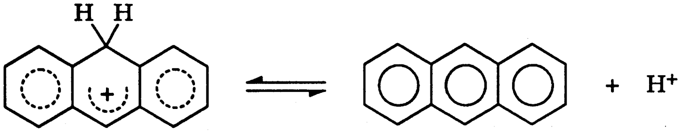

(2)

is followed by

$$H^{+} + e^{-} \rightarrow \frac{1}{2}H_2 \qquad (3)$$

As the proton concentration at the electrode surface is reduced by the reduction of "free" proton, the anthracenium ion dissociates (Eq. 2) producing anthracene.

An attempt was made to determine the equilibrium constant for Eq. 2. Aliquots of $ImHCl_2$ were added to an acidic melt containing anthracene and the decrease in the first anthracene oxidation wave and the concomitant increase in the anthracenium ion reduction wave were monitored at GC by normal pulse voltammetry. Unfortunately, evaluation of the equilibrium constant proved difficult due to the slow decomposition of the anthracene/anthracenium solution. Consequently, an equilibrium constant was obtained for only one melt composition. For a 1.2:1.0 melt with 31 mM anthracene a value of 0.02 mol L^{-1} was obtained for the equilibrium constant. The observed trend for other melt acidities was toward greater protonation with increasing melt acidity.

The reduction of the anthracenium cation was examined at GC and Pt electrodes. Figures 7b and 8b show cyclic staircase voltammograms at GC and Pt, respectively, for anodic scans recorded in a 1.5:1.0 melt containing 18 mM anthracene and 28 mM $ImHCl_2$ after holding the potential at 0.1 V (reducing the anthracenium ion) for 5 s. These are compared to anodic scans starting at 1 V where small amounts of unprotonated anthracene are observed (Figures 7a and 8a respectively). At GC, where the H^+/H_2 couple is inactive, reduction of anthracenium takes place and produces unprotonated anthracene as indicated by the large increase in the anthracene oxidation wave at 1.3 V. At Pt, reduction of anthracenium ion and free proton takes place and produces both H_2 (oxidation wave at ca. 0.9 V) and unprotonated anthracene.

Cyclic staircase voltammograms of anthracenium ion reduction showed a shift of the reduction wave to more negative potentials and and an increase in the peak current with increasing proton concentrations. With a large excess of protons the peak current reached a relatively constant value approximately twice that of the anthracenium cathodic current at lower proton levels. At high proton concentrations the anthracene oxidation wave at 1.3 V disappears, and on the reverse anodic scan, a new oxidation wave at 1.9 V is observed. Figure 9 compares the oxidation wave following an anodic scan from a potential hold at 0.1 V with the oxidation wave observed upon addition of 9,10-dihydroanthracene to a 1.5:1 melt. It appears that at high concentrations of proton, the anthracenium ion is reduced to form 9,10-dihydroanthracene.

The reduction scheme we see in the molten salt for the anthracenium ion is shown in Scheme I. We do not understand the details of the process; however, in view of the fact that we see the anthracenium reduction at both GC and Pt, and at about the same potentials, whereas on GC we do not see reduction of "free" proton (nor H_2 oxidation), it is reasonable to conclude that the electron interacts initially with the ring system and ultimately ends up reducing the proton.

III. Anthracene in basic $AlCl_3$:ImCl.

Anthracene oxidation is not observed in the basic $AlCl_3$:ImCl melts because the anodic window is limited to ca. 1 V by chloride oxidation. Furthermore, in basic melts containing anthracene and a large excess of $ImHCl_2$, there was no evidence of a reduction wave for anthracenium ion. Figure 10a shows a ^2H NMR spectrum of 15 mM anthracene-d_{10} in a 0.7:1.0 melt. The spectrum is essentially identical to that found in benzene and in a 1.2:1.0 melt (Figure 2). When 30 mM of $ImDCl_2$ was added to this melt the spectrum in Figure 10b was obtained. The only observable change is the appearance of a new peak at δ 6.1, which is due to the DCl_2^- ion. This indicates that anthracene does not protonate in basic melts. Finally, unlike the acidic melt, the ^2H NMR spectrum for 15 mM anthracene-h_{10} and 30 mM $ImDCl_2$ in a 0.7:1.0 melt (Figure 10c) shows no evidence of H-D exchange.

SUMMARY

In acidic, proton free, melts anthracene is oxidized in two one-electron steps. The first oxidation forms a cation radical that is relatively stable, and the second oxidation produces a dication which is unstable. In acidic melts containing proton, anthracene is protonated in an equilibrium process to form the anthracenium cation. The reduction of the anthracenium ion produces anthracene and H_2. In basic melts anthracene exhibits no electrochemistry. However, NMR experiments show that anthracene does not form a proton adduct in basic melts.

ACKNOWLEDGEMENTS

This work was supported by the Air Force Office of Scientific Research.

REFERENCES

1. (a) R. A. Osteryoung, in *Molten Salt Chemistry*, G. Mamantov and R. Marassi, Eds., NATO ASI Series C, Vol 202, pp. 329–364, Ridiel, Dordrecht, The Netherlands (1987). (b) C. L. Hussey, in *Adv. in Molten Salt Chemistry*, **5**, 185 (1983).

2. G. P. Smith, A. S. Dworkin, R. M. Pagni, and S. P. Zingg, *J. Am. Chem. Soc.*, **111**, 5075 (1989).

3. G. P. Smith, A. S. Dworkin, R. M. Pagni, and S. P. Zingg, *J. Am. Chem. Soc.*, **111**, 525 (1989).

4. J. Robinson and R. A. Osteryoung, *J. Am. Chem. Soc.*, **101**, 323 (1979).

5. J. S. Wilkes, J. A. Levisky, R. A. Wilson and C. L. Hussey, *Inorg. Chem.*, **21**, 1263 (1982).

6. T. A. Zawodzinski, Jr. and R. A. Osteryoung, *Inorg. Chem.*, **27**, 4383 (1989).

7. T. R. Brumleve, J. J. O'Dea, R. A. Osteryoung and J. Osteryoung, *Anal. Chem.*, **53**, 702 (1981).

8. O. Hammerich and V. D. Parker, *J. Chem. Soc., Chem. Comm.*, 245 (1974).

9. J. O. Howell and R. M. Wightman, *J. Phys. Chem.*, **88**, 3915 (1984).

10. T. Yokono, T. Kohno and Y. Sanada, *Bull. Chem. Soc. Jpn.*, **58**, 401 (1980).

11. A. J. Bard and L. Faulkner, "Electrochemical Methods," pg. 451, John Wiley & Sons, Inc., New York (1980).

12. M. M. Murphy, J. J. O'Dea, D. Arn and J. Osteryoung, *Anal. Chem.*, **62**, 903 (1990).

13. J. O'Dea, J. Osteryoung and T. Lane, *J. Phys. Chem.*, **90**, 2761 (1986).

14. S. P. Zingg, A. S. Dworkin, M. Sørlie, D. M. Chapman, A. C. Buchanan and G. P. Smith, *J. Electrochem. Soc.*, **131**, 1602 (1984).

15. L. Eberson and J. Utley, in "Organic Electrochemistry," M. Bazier and H. Lund, Eds., pg. 413, Dekker, New York (1983).

16. O. Hammerich and V. D. Parker, *J. Am. Chem. Soc.*, **96**, 4289 (1974).

17. S. Sahami and R. A. Osteryoung, *Anal. Chem.*, **55**, 1970 (1983).

18. V. A. Koptyug, I. S. Isaev and A. I. Rezvukhin, *Tetrahedron Lett.*, **9**, 823 (1967).

Scheme I:

Small Excess of Proton

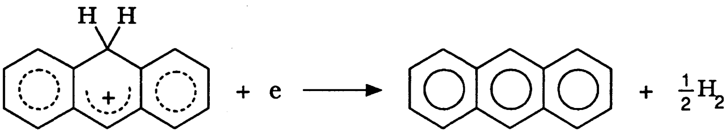

Large Excess of Proton

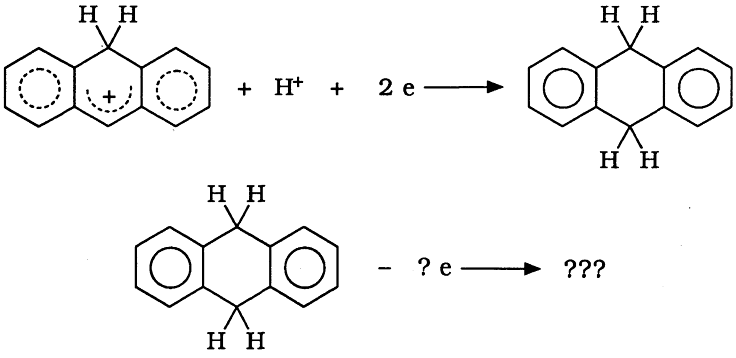

Table I. Normal Pulse Parameters for Oxidation of 9.6 mM Anthracene in 1.2:1.0 $AlCl_3$:ImCl; GC Electrode at 24 °C.

	First Oxidation Wave		
t_p, ms	$E_{1/2}$, V	i_l, μA	Slope,[b] mV
25	1.304	-233	55.7
50	1.306	-168	62.5
100	1.303	-144	68.8
250	1.306	-68.9	51.8
500	1.296	-39.4	46.8

	Second Oxidation Wave		
t_p, ms	$E_{1/2}$, V	i_l, μA[a]	Slope,[b] mV
25	1.934	-210	86.5
50	1.942	-136	73.9
100	1.937	-89.8	52.6
250	1.921	-56.9	60.0
500	1.898	-27.4	34.8

[a]Measured from plateau of first oxidation. [b]Reciprocal slope of E vs. $\log\{(i_d - i)/i\}$.

Table II. Kinetic Parameters from Staircase Cyclic Voltammetry for Anthracene Oxidation in various melt compositions: GC electrode at 26 °C.

Scan Rate, mV/s	$E_{1/2}$, V	k, s^{-1}
	2.0:1.0 Melt (0.8 → 1.7 V)[a]	
50	1.310 (0.002)	0.10 (0.01)
100	1.313 (0.002)	0.12 (0.01)
250	1.317 (0.002)	0.14 (0.03)
	1.78:1.0 Melt (0.8 → 1.7 V)[a]	
50	1.306 (0.002)	0.12 (0.01)
100	1.309 (0.002)	0.17 (0.02)
250	1.312 (0.002)	0.23 (0.03)
	1.46:1.0 Melt (0.8 → 1.6 V)[a]	
50	1.304 (0.002)	0.18 (0.02)
100	1.305 (0.002)	0.25 (0.03)
250	1.308 (0.002)	0.35 (0.04)
	1.21:1.0 Melt (0.8 → 1.6 V)[a]	
50	1.300 (0.003)	0.19 (0.03)
100	1.302 (0.003)	0.29 (0.04)
250	1.304 (0.002)	0.41 (0.06)
	1.0:1.0 Melt (0.8 → 1.5 V)[a]	
50	1.318 (0.004)	0.16 (0.04)
100	1.316 (0.003)	0.52 (0.10)
250	1.316 (0.005)	0.74 (0.14)

[a] Potential range scanned.

Table III. Normal Pulse Parameters for Reduction of ca. 18 mM Anthracenium in 1.5:1.0 $AlCl_3$:ImCl at GC.

t_p, ms	$E_{1/2}$, V	i_l, μA	$i_l t_p^{1/2}$, μA $ms^{1/2}$
25	0.353	269	1345
50	0.379	177	1251
100	0.385	124	1240
250	0.400	78.5	1241
500	0.423	51.6	1153

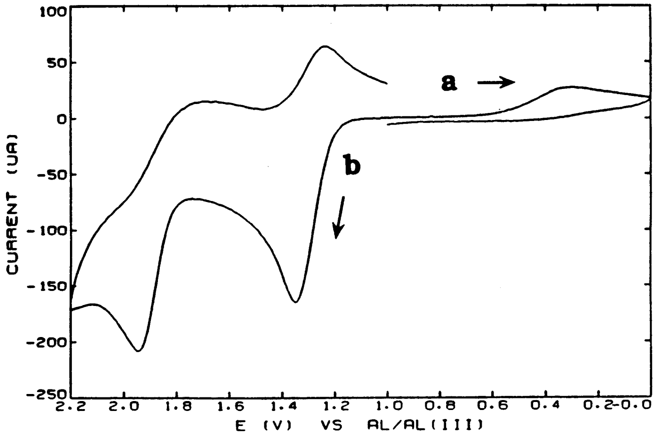

Figure 1. Cyclic staircase voltammograms for 18 mM anthracene in 1.5:1.0 $AlCl_3$:ImCl at GC electrode. a) cathodic scan from 1 V, 500 mV s^{-1}; b) anodic scan from 1 V, 500 mV s^{-1}. On addition of MAC wave at 0.4 V was eliminated.

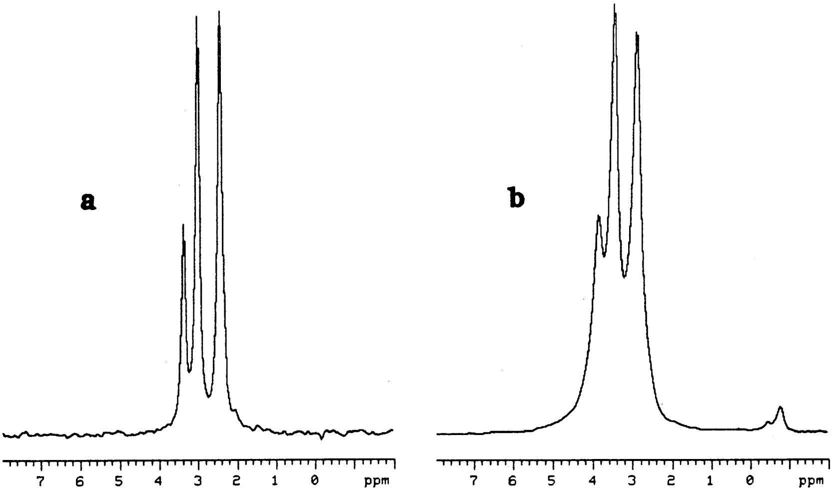

Figure 2. ^2H NMR spectra of 15 mM anthracene-d_{10} in a) benzene; b) 1.2:1.0 $AlCl_3$:ImCl.

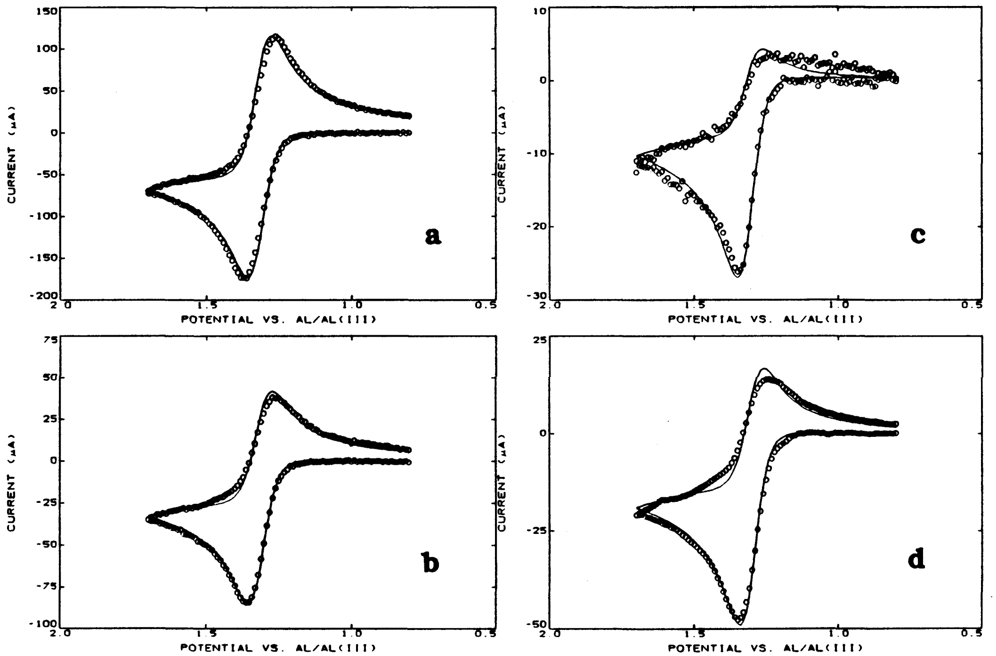

Figrue 3. Cyclic staircase voltammograms, GC electrode, for a–c) 8.5 mM anthracene in 1.2:1.0 melt at a) 2,000 b) 500 c) 50 mV s^{-1} and d) 15 mM anthracene in 2.0:1.0 melt at 50 mV s^{-1}.

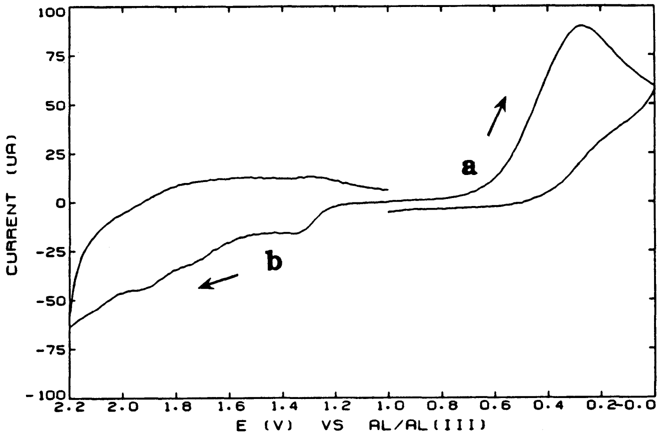

Figure 4. Cyclic staircase voltammogram for 18 mM anthracene and 28 mM $ImHCl_2$ in 1.5:1.0 $AlCl_3$:ImCl at GC electrode. a) cathodic scan from 1 V; b) anodic scan from 1 V. Scan rate 500 mV s^{-1}. No MAC was added so actual proton concentration is greater due to protonic impurities.

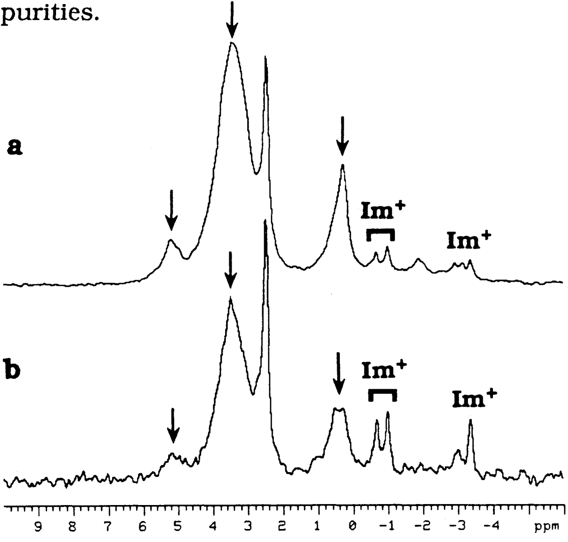

Figure 5. ^2H NMR of 1.2:1.0 $AlCl_3$:ImCl 30 mM $ImDCl_2$ a) 15 mM anthracene-d_{10} b) 15 mM anthracene-h_{10}. Peak at δ 2.5 is the acidic form of proton.

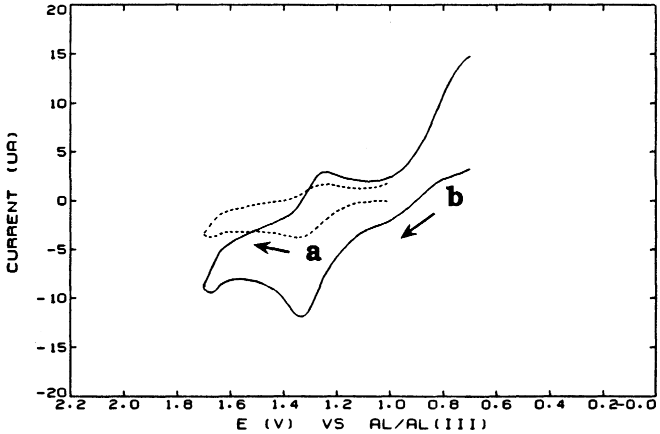

Figure 6. Cyclic staircase voltammograms for 18 mM anthracene and 28 mM $ImHCl_2$ in 1.5:1.0 $AlCl_3$:ImCl melt at a Pt electrode. a) anodic scan from 1 V; b) anodic scan after a 5 s hold at 0.7 V. Scan rate 500 mV s^{-1}.

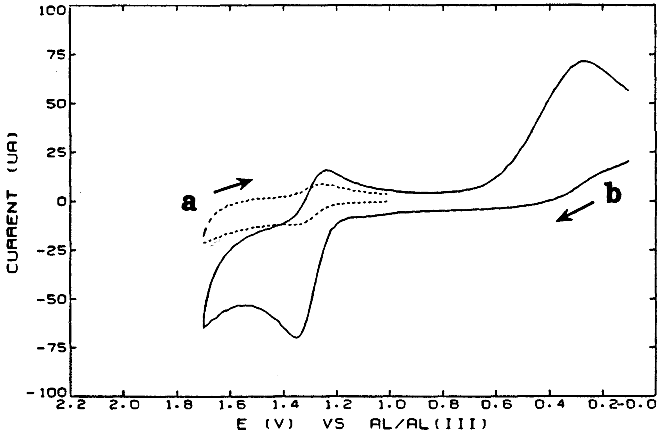

Figure 7. Cyclic staircase voltammogram for 18 mM anthracene and 28 mM $ImHCl_2$ in 1.5:1.0 $AlCl_3$:ImCl melt at a GC electrode. a) anodic scan from 1 V; b) anodic scan after a 5 s hold at 0.1 V. Scan rate 500 mV s^{-1}

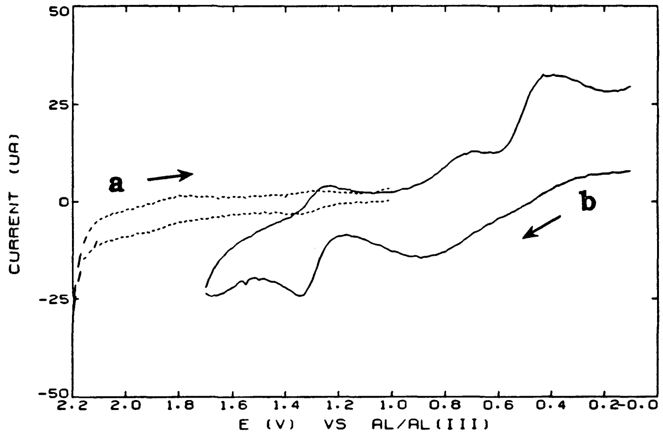

Figure 8. Cyclic staircase voltammogram for 18 mM anthracene and 28 mM $ImHCl_2$ in 1.5:1.0 $AlCl_3$:ImCl melt at a Pt electrode. a) anodic scan from 1 V; b) anodic scan after a 5 s hold at 0.1 V. Scan rate 500 mV s^{-1}.

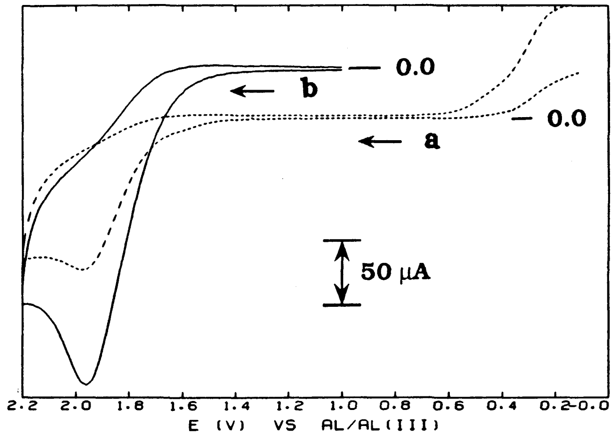

Figure 9. a) Cyclic staircase voltammogram for 18 mM anthracene and 177 mM $ImHCl_2$ in a 1.5:1.0 $AlCl_3$:ImCl melt at a GC electrode. Anodic scan from a 5 s hold at 0.1 V, 500 mV s^{-1}. E_{pa} = 1.95 V. b) cyclic staircase voltammogram for 11 mM 9,10-dihydroanthracene in same melt. E_{pa} = 1.96 V.

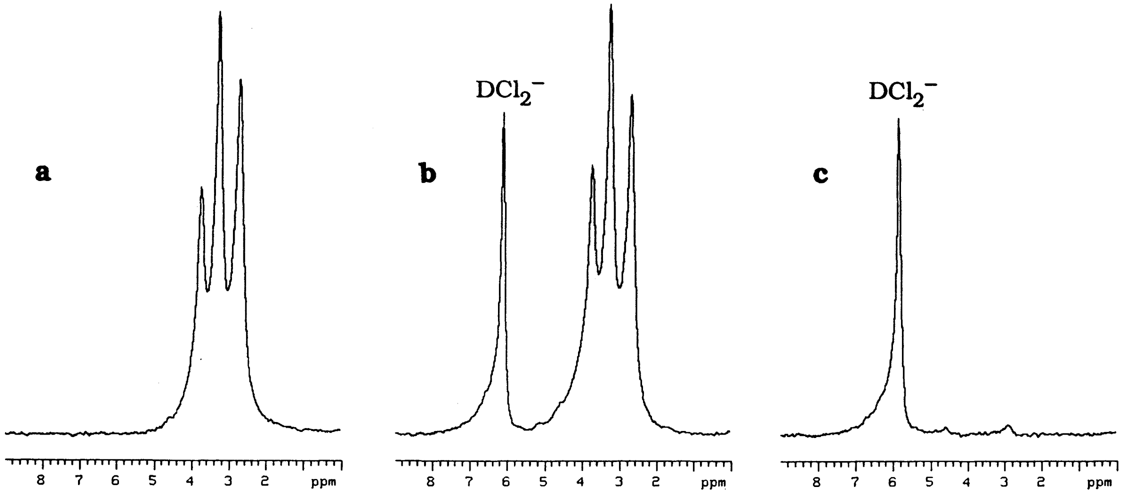

Figure 10. ^{2}H NMR spectra of 0.7:1.0 $AlCl_3$:ImCl melt a) 15 mM anthracene-d_{10} b) solution in a) with 30 mM $ImDCl_2$, and c) 15 mM anthracene-h_{10} and 30 mM $ImDCl_2$.

DOI: 10.1149/199017.0325PV

ELECTROCHEMICAL REDUCTION OF FLUORENONE IN A ROOM-TEMPERATURE MOLTEN SALT

Graham T. Cheek
Chemistry Department, Stop 9b
United States Naval Academy
Annapolis, Maryland 21402

ABSTRACT

The electrochemical reduction of fluorenone in the aluminum chloride : 1-methyl-3-ethylimidazolium chloride molten salt system has been studied. As with other carbonyl compounds, fluorenone undergoes complexation by aluminum chloride in the acidic melt. In addition to changing the usual yellow color of fluorenone to red, this complexation shifts the reduction potential by +1.1 V. Comparative studies have been carried out in acetonitrile solutions by adding small amounts of sulfuric acid, resulting in similar shifts in reduction potential caused by protonation of the fluorenone. In both acidic and basic melts, a one-electron reduction is involved, giving rise to an anion radical which is rapidly complexed by the chloroaluminate species in the melt. Subsequent coupling of these radicals produces the pinacol in both acidic and basic melts. The coupling rate of the anion radicals in the melt has been found to be 500 times faster in the basic melt than in the acidic melt. This difference in coupling rates is attributed to the higher degree of complexation of the anion radicals in the acidic melt compared to the basic melt.

INTRODUCTION

Chloroaluminate molten salt systems have been employed as useful media for the electrochemical investigation of organic compounds, beginning with the sodium tetrachloroaluminate system (1). With the discovery of lower-temperature systems based on the butylpyridinium cation (2), a more convenient solvent system for this work became available, leading to studies of such compound types as aromatic amines (3), quinones (4,5), and ketones (6). Further investigations into the effect of cation structure on melt properties led to the aluminum chloride : 1-methyl-3-ethylimidazolium chloride (MEIC) system (7), which is particularly attractive because work can be carried out at room-temperature while maintaining the acid/base characteristics of earlier systems.

One of the most intriguing properties of the low-temperature systems is the wide range of acidity available in the melt. The solvent system is characterized by the equilibrium (7):

$$2\ \mathrm{AlCl_4^-} \rightleftharpoons \mathrm{Al_2Cl_7^-} + \mathrm{Cl^-}.$$

Melt acidity is usually reported as the ratio of aluminum chloride to MEIC, with acidic melts having ratios greater than one and basic melts having ratios less than one. The acidic species ($Al_2Cl_7^-$) is capable of forming aluminum chloride complexes with electron-donating species such as amines (3) and quinones (4,5) by displacement of tetrachloroaluminate. Such interactions have an enormous effect on the electrochemical behavior of such compounds (4-6). Recent studies have further defined the "superacid" characteristics of the acidic melt (8,9).

The reduction of ketones has been studied in a wide variety of solvent systems (10). Considering that the solvent acidity can profoundly change the course of reduction (11,12), the product distribution for electrochemical reduction of ketones can give valuable information about the solvent characterisitics of the medium. With these considerations in mind, the present study of fluorenone reduction was begun.

EXPERIMENTAL

1-Methyl-3-ethylimidazolium chloride (MEIC) was prepared according to the procedure of Smith (8), except that all operations were carried out in a Vacuum Atmospheres glovebox. A different Vacuum Atmospheres glovebox was used for electrochemical studies. Aluminum chloride (Fluka puris.) was purified by sublimation. Melt purification involved small additions of ethyl aluminum dichloride where necessary to remove traces of protonic impurities from the melt (13). Voltammograms were obtained using a PAR 174A Polarographic Analyzer with a Bioanalytical Systems CV-27 instrument for potential scanning.

A PAR Model 170 Electrochemistry System was used for fast-scan cyclic voltammetry (>500 mV/s). Preparative electrolysis/coulometry was carried out using a PARC Model 273 Electrochemistry System. Glassy carbon (3 mm rod, Tokai GC-30 sealed in Pyrex) was used as electrode material for recording voltammograms unless otherwise indicated. Potentials are given with respect to an aluminum wire immersed in 2:1 aluminum chloride : MEIC melt.

RESULTS AND DISCUSSION

Initial investigations of fluorenone electrochemistry were carried out by cyclic voltammetry, the results of which are shown in Figure 1. The effect of melt acidity on fluorenone reduction is evident, considering that the peak potential for the reduction process shifts from -1.00 V in the basic melt to +0.10 V in the acidic melt. This shift in electrochemical characteristics is accompanied by a color change from yellow, the usual color for fluorenone, in the basic melt to red in the acidic melt. Studies of anthraquinone (4) and chloranil (5) in chloroaluminate molten salt systems have shown that these changes are brought about by the complexation of the carbonyl oxygen by aluminum chloride, thereby substantially altering the electron energy levels of this part of the molecule. Fluorenone is stable in the acidic melt (1.2 : 1.0) for at least several days, indicating that the interaction is not strong enough to actually remove oxygen from the molecule.

The complexation of fluorenone in the molten salt system was compared with protonation in a nonaqueous solvent by adding increasing amounts of sulfuric acid to a fluorenone solution in acetonitrile. As seen in Figure 2, fluorenone reduction in acetonitrile itself involves two one-electron processes, the first of which occurs at a potential approximately the same as that for fluorenone reduction in the basic melt. Reduction in dimethylformamide solution gives a similar value for the potential of the first reduction step (14). Addition of acid results in the appearance of a peak due to the protonated ketone at -0.45 V, giving a shift of 0.85 V. The voltammograms in Figure 1 indicate a shift of 1.1 V for complexation of fluorenone with aluminum chloride. These shifts indicate a somewhat higher degree of interaction of fluorenone with the acidic melt than that which occurs upon protonation. To further explore the role of chloroaluminate species in fluorenone electrochemistry, an interesting study was carried out in which fluorenone was added to a melt consisting of pure MEIC (no added aluminum chloride). Even at 95°C, required because the melting point of MEIC is 87-88°C (8), the first reduction process is reversible (Figure 3), with the second electron transfer clearly showing as a separate peak. Due to the absence of chloroaluminate species in the melt, the anion radical remains uncomplexed upon formation and the voltammogram greatly resembles those obtained in nonaqueous solvents such as dimethylformamide (14) or acetonitrile (Figure 2).

Coulometric studies of fluorenone reduction in the 0.8 : 1.0 basic melt show that a one-electron process is involved. In the acidic melt, the situation appears to be somewhat more complicated, there being two reduction processes and at least two subsequent oxidation processes. Coulometric reduction at 0.00 V (first process) reveals that this step is also a one-electron process. Coulometric results for the second reduction step were invalidated by the eventual deposition of aluminum at -0.25 V, but this step apparently is a one-electron process as well, as suggested by the similar peak heights of the reduction steps. The anodic processes, not seen in the basic melt, give valuable clues concerning the reduction mechanism and will be discussed in some detail.

For convenience in discussing the fluorenone electrochemistry occurring in the acidic melt, the various redox processes are labelled in Figure 4. Upon scanning past the first reduction process (Ic), two anodic peaks (Ia and IIa) are evident (solid curve). Following coulometric reduction at 0.00 V, cyclic voltammetry showed that only IIa was present at a peak height approximately 45% of the initial Ic peak height. The negative-going sweep showed that fluorenone is regenerated from the IIa process, confirmed by the coulometric oxidation of the IIa process to give Ic and IIc with peak heights at 45-50% of the original values. These results indicate that the pinacol (dimeric coupling product) is formed during the reduction of fluorenone in the acidic melt, with IIa corresponding to pinacol oxidation (Figure 5). Variation of the scan rate shows that the species corresponding to Ia is also involved in the reduction pathway. At 1 V/s, only Ia is present, while lower scan rates give increasing amounts of IIa at the expense of Ia. Pinacol formation is, then, rather slow in the acidic melt. According to the scheme given in Figure 5, Ia is due to the oxidation of the fluorenone anion radical which undergoes subsequent coupling to give the pinacol. The significant peak separation between Ic and Ia indicates that the anion radical undergoes very rapid complexation by the melt during reduction, causing the shift of the corresponding oxidation to Ia instead of appearing as the oxidative component of a true reversible system involving Ic. No such oxidation process was observed at scan rates up to 200 V/s.

The second reduction step in the acidic melt, IIc, evidently involves the further reduction of the complexed anion radical to give the alcohol (dianion). At scan rates of 100 mV/s and higher, the peak heights for Ic and IIc are nearly the same; however, at lower scan rates it is expected that coupling of the anion radical produced in Ic to form the pinacol should result in less of the anion radical for further reduction in IIc. This is indeed found to be the case; for instance, at 10 mV/s the peak height of IIc is only half that of Ic.

Reduction of fluorenone in the basic melt is also a one-electron process, although no product responses are visible after exhaustive electrolysis. Scanning 0.1 V into anodic background, however, results in the appearance of the fluorenone reduction process at approximately 5% of the original value. This observation suggests that the pinacol is formed in the reduction but is not oxidizable in the potential range normally employed. Pinacol formation is also indicated by the isolation of fluorenone from a hydrolyzed melt (aqueous solution). Air oxidation during the workup procedure, carried out in air, is apparently responsible for formation of fluorenone from the pinacol.

From the absence of a process corresponding to Ia in the acidic melt at 100 mV/s (Figure 1), it would appear that the coupling process leading to pinacol formation is much faster than it is in the acidic melt. This was confirmed by voltammetric experiments at high scan rates (up to 1000 V/s) at a small-diameter (0.25 mm) platinum electrode. At scan rates above 200 V/s, a peak corresponding to Ia in the acidic melt appeared, and above 500 V/s the peak current ratio of this peak to the initial reduction peak was approximately the same as the limiting value in the acidic melt. Considering that the latter value is reached at 1 V/s, this indicates that pinacol formation occurs 500 times faster in the basic melt than it does in the acidic melt. One interesting consequence of this rapid coupling is that the anion radical does not exist long enough in solution for significant further reduction to take place, as is observed in the acidic melt as process IIc. Only a very small indication of such a process is seen in the basic melt at -1.15 V. Finally, the complexation of the anion radical in the basic melt, depicted in Figure 6, occurs quite rapidly, as inferred again from the potential separation of the redox processes even at 1000 V/s. Similar behavior has been observed for benzoquinone reduction in the basic melt (15).

The rather remarkable difference in coupling rates in pinacol formation between the acidic and basic melts evidently involves the degree of complexation of the anion radical, since both species have the same overall charge (-1) and electron configuration (radical). Two possible explanations of this rate difference are simple steric hindrance around the oxygen atoms and alteration of electron density at the coupling site. In the acidic melt, the more highly complexed anion radical would be more crowded around the vicinity of the coupling carbon atom than it would be in the basic melt, and the electron density at this atom would also be less due to the electron-withdrawing effect of the complexation. Both effects would be expected to lower the rate of coupling in the acidic melt compared to the basic melt.

CONCLUSIONS

Fluorenone reduction occurs as a one-electron process in both acidic and basic 1-methyl-3-ethylimidazolium chloride chloroaluminate melts. The anion radical formed in the initial reduction is rapidly complexed by the melt and then couples to form the pinacol in both cases, although the rate of coupling in the basic melt is 500 times faster than it is in the acidic melt. This rate difference is apparently due to the greater extent of complexation of the anion radical in the acidic melt.

ACKNOWLEDGEMENT

The support of this work by the United States Naval Academy Chemistry Department is gratefully acknowledged.

REFERENCES

1. H.L. Jones and R.A. Osteryoung, Adv. Molten Salt Chem., 3, 121 (1975).

2. H.L. Chum, V.R. Koch, L.L. Miller, and R.A. Osteryoung, J. Am. Chem. Soc., 97, 3264 (1975).

3. J. Robinson and R.A. Osteryoung, J. Am. Chem. Soc., 102, 4415 (1980).

4. G.T. Cheek and R.A. Osteryoung, J. Electrochem. Soc., 129, 2488 (1982).

5. G.T. Cheek and R.A. Osteryoung, J. Electrochem. Soc., 129, 2739 (1982).

6. G.T. Cheek and R.B. Herzog, in Proceedings of the Fourth International Symposium on Molten Salts; M. Blander, D.S. Newman, G. Mamantov, M.-L. Saboungi, and K. Johnson, eds., The Electrochemical Society Inc., Princeton, NJ, 1984, p. 163.

7. J.S. Wilkes, J.A. Levisky, R.A. Wilson, and C.L. Hussey, Inorg. Chem., 21, 1263 (1982).

8. G.P. Smith, A.S. Dworkin, R.M. Pagni, and S.P. Zingg, J. Am. Chem. Soc., 111, 525 (1989).

9. G.P. Smith, A.S. Dworkin, R.M. Pagni, and S.P. Zingg, J. Am. Chem. Soc., 111, 5075 (1989).

10. L.G. Feoktistov and H. Lund, "Saturated Carbonyl Compounds and Derviatives," Chapter 9 in **Organic Electrochemistry**, M.M. Baizer

and H. Lund, Eds., Marcel Dekker, New York, 1983.

11. M.E. Peover, in "Electroanalytical Chemistry," Vol. 2, A.J. Bard, Editor, Chap. 1, Marcel Dekker, New York, 1967.

12. L. Nadjo and J.M. Saveant, J. Electroanal. Chem. Interfacial Electrochem., 33, 419 (1971).

13. T.A. Zawodzinski, R.T. Carlin, and R.A. Osteryoung, Anal. Chem., 59, 2639 (1987).

14. J.M. Fritsch, T.P. Layloff, and R.N. Adams, J. Am. Chem. Soc., 87, 1724 (1965).

15. F.A. Uribe and R.A. Osteryoung, J. Electrochem. Soc., 135, 378 (1988).

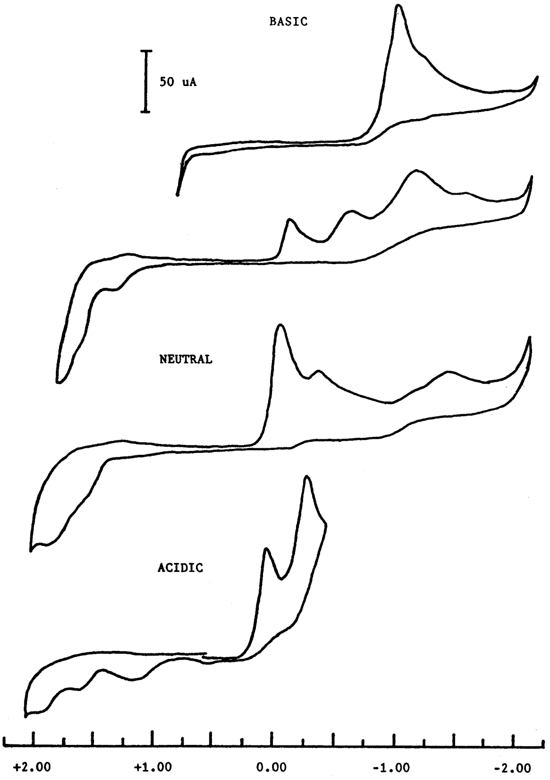

E, V vs 2 : 1 acidic melt

Figure 1. Cyclic voltammograms of fluorenone in aluminum chloride : 1-methyl-3-ethylimidazolium chloride molten salt. Composition ratios are 1.2 : 1.0 for acidic melt, 0.8 : 1.0 for basic melt.
Scan rate: 100 mV/s Temperature: 40°C
Concentrations: Acidic melt, 27 mM
Neutral melt, 24 mM
Basic melt, 29 mM

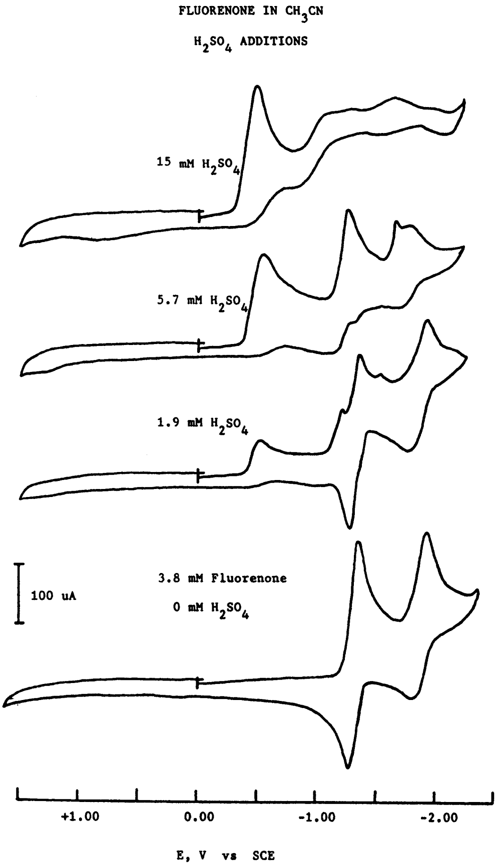

Figure 2. Cyclic voltammograms of fluorenone in acetonitrile/0.1 M tetraethylammonium perchlorate, with additions of sulfuric acid as indicated.
Scan rate: 100 mV/s Temperature: 25°C

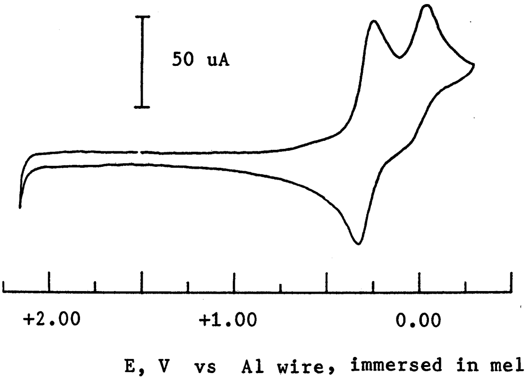

Figure 3. Cyclic voltammogram of fluorenone (21 mM) in molten MEIC.
Scan rate: 100 mV/s Temperature: 95°C

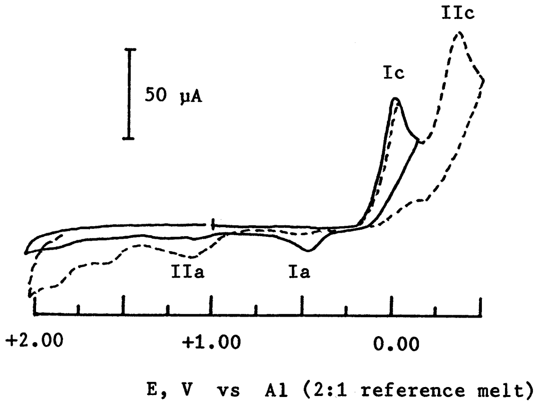

Figure 4. Cyclic voltammogram of fluorenone (23 mM) in 1.2 : 1.0 acidic melt. Dashed curve represents scan beyond second reduction process.
Scan rate: 100 mV/s Temperature: 40°C

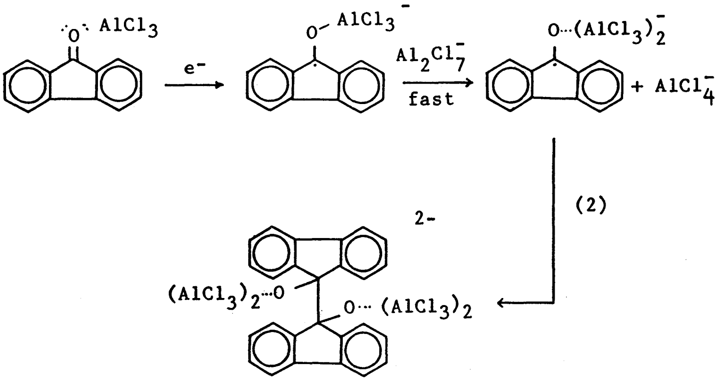

Figure 5. Reaction pathway for fluorenone reduction in acidic melt.

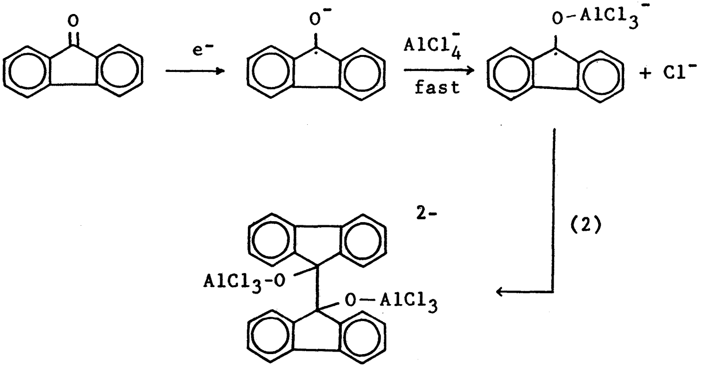

Figure 6. Reaction pathway for fluorenone reduction in basic melt.

DOI: 10.1149/199017.0336PV

REDUCTION OF AROMATIC COMPOUNDS IN BASIC CHLOROALUMINATE MELTS

J. E. Coffield, G. Mamantov

Department of Chemistry
University of Tennessee
Knoxville, TN 37996

S. P. Zingg, G. P. Smith

Chemistry Division
Oak Ridge National Laboratory
Mail Stop 6100, Bldg. 4500S
Oak Ridge, TN 37831-6100

ABSTRACT

The electroreduction of perylene and phenazine in basic mixtures of $AlCl_3$ and 1-ethyl-3-methyl-1H-imidazolium chloride (EMIC) (44.4 mol % $AlCl_3$) has been investigated by electrochemical and spectroelectrochemical (SE) techniques using a fiber optics based rapid scanning spectrometer for SE experimentation inside of a dry box. Although initial results indicated that the reduction of perylene and phenazine proceeds through a two-electron process coupled with two protonations to form a dihydro-species of the parent, further investigation, using authentic dihydrophenazine, indicated that these reduction products may not be the result of proton exchange reactions but rather the $AlCl_4^-$ ion may be acting as the acidic species in these melts.

INTRODUCTION

The use of molten salts as solvents for organic chemistry is an interesting and largely unexplored area. An excellent review of the current state of this field was reported by Pagni in 1987 (1). One class of molten salts which is particularly attractive for organic chemistry is the room temperature molten salts (2). Their low liquidus temperatures allow for easier handling and milder reaction conditions. In order to further develop this field, investigation into the interactions between organic species and the room temperature melts is essential.

Several classes of ambient temperature ionic liquids have been reported in the literature (2). Among these are the chloroaluminates. These consist of mixtures of $AlCl_3$ and an organic halide, usually N-butylpyridinium chloride (BPC) (3,4) or 1-ethyl-3-methyl-(1H)-imidazolium chloride (EMIC) (5). The EMIC-containing basic (EMIC/$AlCl_3$ mole ratio > 1) mixtures have a significantly larger electrochemical window and all compositions have a lower UV cut-off than BPC-based melts. They are also less viscous than the BPC-based melts.

The properties of room temperature chloroaluminate melts have been discussed in a number of articles (6-8). One of the more common interactions between the melt and solute species is Lewis acid complexation involving $AlCl_3$ (9). While this is particularly prevalent in the acidic melts where the acidic species $Al_2Cl_7^-$ is present, there have also been reports of Lewis acid complexation involving the $AlCl_4^-$ species in basic melts (9). Identification of these complexes often relies on their similarity to protonated species; however, since the danger of proton contamination is always present in these very hygroscopic melts, additional proof is warranted. The following work describes the investigation of the reduction chemistry of phenazine and perylene in basic room temperature chloroaluminate melts. Attempts at eliminating possible sources of protons, and comparison of the phenazine reduction product with authentic dihydrophenazine are also reported.

EXPERIMENTAL

Due to their hygroscopic nature, $AlCl_3$, EMIC and 1,2-dimethyl-3-propylimidazolium chloride (DMPIC) were handled in an argon atmosphere dry box in which the levels of water vapor and oxygen were maintained below 2 ppm. Melts were prepared by slowly adding weighed amounts of $AlCl_3$ to weighed amounts of EMIC or DMPIC while stirring.

Organic reactions involving hygroscopic or air sensitive materials were performed using a dual manifold vacuum line and Schlenk-type glassware.

Cyclic voltammetry (CV) was performed in the dry box using cells which have been previously described (10). The working electrodes used for CV were made of tungsten (area=0.126 cm^2). In all experiments, the reference electrode was an aluminum wire (Alfa, puratronic, 4N8) immersed in a 2:1 $AlCl_3$-EMIC (or $AlCl_3$-DMPIC) melt saturated with solid $AlCl_3$ and separated from the bulk solution by a fine quartz frit.

The instrumentation used for the CV and bulk coulometry consisted of a Princeton Applied Research Model 175 Waveform Generator and a Model 173 Potentiostat/Galvanostat with a Model 179 Digital Coulometer.

UV/visible absorption spectroscopy of stable solutions was performed using a Cary 14 spectrophotometer. The cells used have been described previously (11).

Spectroelectrochemical (SE) experiments were performed using a Princeton Applied Research Model 273 Potentiostat/Galvanostat. The spectroscopy for the spectroelectrochemical experiments was performed with a diode array based multichannel spectrograph. This consisted of a EG&G Princeton Applied Research Model 1460 OMA-III multichannel analyzer which used a Model 1461 remote interface to operate a Model 1463 detector controller. The detector used was a Reticon (EG&G Model 1412) 1024-channel, unintensified linear diode array detector, thermoelectrically cooled to -20 °C to reduce thermal noise. The light sources used were a 10-watt halogen/tungsten lamp (Oriel Model 6323) for visible spectroscopy, and either a 35-watt deuterium lamp (Oriel Model 6312) or a 75-watt xenon arc lamp for ultraviolet work.

For most SE experiments (12-15) the spectrometer was interfaced to a dry box using fiber optics to minimize the possibility of atmospheric contamination and to provide additional flexibility. Silica clad silica fibers with a core diameter of 600 microns were employed. Fused silica lenses were used to direct the light into and out of the fibers. A detailed description of this setup and of a short pathlength SE cell needed for solutes with high molar absorptivities may be found in reference 16. Due to light losses at the various coupling points in the fiber optic setup along with the increased absorbance of the fibers in the ultraviolet, it was necessary to use a 75-watt xenon arc lamp powered by an Oriel Model 8510-1 power supply. In the transmission UV/visible SE performed in this work, an optically transparent electrode (OTE), usually constructed from a platinum screen, was employed. The SE cell was constructed using a 1-mm quartz cuvette (17). The reference electrode was the same as that used for CV.

ESR spectrometry was performed using a Varian Model E-109 spectrometer. NMR spectroscopy was performed using a Nicolet Model NT200, 200 MHz, ^{1}H spectrometer.

Aluminum chloride (Fluka puriss. grade) was purified in a manner similar to that previously described (11). Ethyl chloride (Matheson) was used as received. Acetonitrile (Burdick and Jackson) and 1-methylimidazole (Chemical Dynamics Corp.) were purified as previously described (10). 1-Chloropropane (Aldrich, 99%) was first washed with sulfuric acid, water, saturated sodium carbonate and finally water (18). It was then dried over magnesium sulfate. After filtering, the 1-chloropropane was refluxed over calcium hydride (under an argon atmosphere), and distilled onto 4-Å molecular sieves. 1,2-Dimethylimidazole (Aldrich, 98%) was purified in the same manner as the 1-methylimidazole. Perylene (Aldrich Gold Label, 99+%) was recrystallized from ethanol. Phenazine (Aldrich, 98%) was used as received.

EMIC was prepared as previously described (10). DMPIC was prepared by combining 250 g of a dimethylimidazole-acetonitrile mixture (25 wt% acetonitrile) with 390 g of 1-chloropropane in a three neck reaction flask (all procedures were done under an argon atmosphere). This mixture was then refluxed under argon at approximately 50°C. This is a modification of the procedure described by Gifford and Palmisano (18). During the refluxing, crystals formed in the reaction mixture. These crystals and the solution were slightly yellow. After refluxing for one week, the excess propyl chloride was removed by applying a vacuum to the reaction flask. The product was then worked up in the manner described for the EMIC (10). The identity of the product was confirmed using ^{1}H-NMR spectroscopy.

Dihydrophenazine (H_2PN) was synthesized using a modification of the methods of Scholl (19) and Wheaton, et al. (20).

The level of protic impurities in melts composed of mixtures of $AlCl_3$ and EMIC was determined spectrophotometrically using the 9H-anthracenium ion (10). When anthracene was added to an acidic melt it reacted with the protic impurities to form the anthracenium ion. The concentration of this ion was determined spectroscopically using the molar absorptivity obtained from anthracene in an HCl-saturated melt. In all cases, the level of protic impurities was found to be between 0.3 and 0.5 m$\underline{M}$.

RESULTS AND DISCUSSION

A. Phenazine in $AlCl_3$-EMIC (0.8/1)

Phenazine (PN) was dissolved in the basic $AlCl_3$-EMIC melt at a concentration of 10 m$\underline{M}$ to give a light yellow solution. The UV/visible spectrum was similar to that reported in the literature for PN in methanol (see Table I) (20) which indicates that there is no detectable interaction between the PN and the melt (i.e. $AlCl_3$ does not appear to form a Lewis acid adduct with the lone electron pair of one of the nitrogens). Cyclic voltammetry at a tungsten electrode (Figure 1) exhibited one reduction wave at -1.3 V (all potentials are vs Al in $AlCl_3$(sat) $AlCl_3$-EMIC). This wave was totally irreversible even at scan rates of 10 V/s. After sweeping through this reduction wave, several oxidation waves appeared with the first (and most prominent) being at -0.16 V. This large oxidation wave was irreversible at all scan rates (up to 10 V/s). If this region of the CV was cycled several times without sweeping through the original reduction wave of PN, the predominant irreversible oxidation wave disappeared, and two small "reversible" waves with oxidation peak potentials of -0.18 and 0.17 V appeared. As stated above, the large oxidation wave at -0.16 V only occurs after sweeping through the reduction wave of the PN, indicating that it is the result of a product formed during that reduction. If the reduction wave of the PN is cycled without sweeping through this oxidation wave, the height of the reduction wave decreases with each cycle. If the scan is then allowed to sweep through the oxidation wave, the height of the reduction wave increases. This indicates that the oxidation occurring at -0.16 V is regenerating the original PN.

Bulk coulometry was performed on a 11.11 m$\underline{M}$ solution of PN in $AlCl_3$-EMIC (0.8/1) at -1.60 V using a glassy carbon crucible as the working electrode. After the passage of 1.63 equivalents of charge the electrolysis was stopped and a UV/visible spectrum of the nearly colorless solution was obtained. The resulting spectrum was similar to that reported in the literature for dihydrophenazine (H_2PN) which is produced by a 2-electron reduction of PN in the presence of an acid (20-22). If an n-value of two is therefore used to determine the contribution of unreduced PN to the spectrum and subtracted, the resulting spectrum is close to that reported in the literature for H_2PN (see Table I).

Superficial examination of the results above would lead to the conclusion that PN is reduced in a 2-electron process involving chemical reactions with some proton source to produce H_2PN. The concentration of protic impurities in these melts, however, was below 0.5 m$\underline{M}$ which is too low to account for the amount of H_2PN formed. Another possible source of protons in the melt is the imidazolium cation. The hydrogen in the 2-position of this cation has been shown to be acidic under certain conditions (23). In order to test this theory, another imidazolium chloride was used in which the hydrogen on the 2-carbon is replaced by a methyl group. Gifford and Palmisano reported that the methyl substituted imidazolium chloride (DMPIC) produces an ambient temperature molten salt with $AlCl_3$ (18). DMPIC was therefore synthesized and used to study the reduction of PN.

B. Phenazine in $AlCl_3$-DMPIC (0.9/1)

Cyclic voltammetry and bulk coulometry of PN in the basic DMPIC melt produced results which were identical to those obtained in the EMIC experiments. Apparently the acidic species reacting with the reduced PN does not arise from the EMIC cation.

C. Dihydrophenazine (H_2PN) in $AlCl_3$-EMIC (0.8/1)

In order to determine if the product of the reduction of PN in the basic melt is H_2PN, authentic H_2PN was synthesized and added to the melt. This produced a solution with UV/visible spectrum qualitatively similar to that of the reduction product of PN, but with the maximum shifted toward longer wavelengths by 18 nm (Table I). A CV of a 7.03 m$\underline{M}$ solution of H_2PN in an $AlCl_3$-EMIC (0.8/1) melt at 100 mV/s is shown in Fig. 2. This CV is quite different from that of the PN reduction product and consists of two oxidation waves of approximately equal height at -0.18 and 0.12 V. A single reduction wave occurs at -0.25 V; it corresponds to the first oxidation wave. No reduction wave was observed at -1.3 V, indicating that PN was not produced during the oxidation of H_2PN. The peak separation of the first oxidation wave is close to that of a one-electron process (59 mV at 25°C) at scan rates from 5 to 500 mV/s, and the anodic to cathodic peak ratios are close to one even at 5 mV/s indicating that the product of the one-electron oxidation is stable on the time scale of the CV's. A plot of i_p vs $v^{1/2}$ was linear with an intercept near zero indicating a diffusion controlled oxidation (24).

Bulk coulometry was performed at -0.15 V on the H_2PN solution described above. After passing 0.75 equivalents of charge, the coulometry was stopped; the resulting solution was green. The spectrum of this solution was identical to that reported for the radical cation of H_2PN (25) (Table I) which would be the result of the one-electron oxidation of H_2PN. This solution was stable for a minimum of several days.

In order to confirm the identity of the product from the coulometry at -0.15 V, ESR spectroscopy was performed on the solution. The spectrum contained only the seven major bands of the radical cation. The number of bands along with the spectral width is in agreement with that reported in the literature (26-28). In an attempt to increase the resolution, the temperature of the cell was raised to 100 °C in order to increase the molecular tumbling of the PN (29). This resulted in a much more highly resolved spectrum in which the hyperfine splitting was observable. Table II lists the coupling constants and spectral widths from the above experiments along with those reported in the literature.

The results obtained for the oxidation of H_2PN in the basic $AlCl_3$-EMIC melt clearly indicate that the species produced during the reduction of PN in this melt is not H_2PN. The similarity in the UV/visible spectra of the reduction product and H_2PN does, however, support the hypothesis that the reduction product of PN is a Lewis acid adduct involving the dianion of PN and two Lewis acid species. The most obvious Lewis acid present in these melts is $AlCl_3$ (9).

In Figure 1 two small "reversible" oxidation waves were observed under certain conditions (see above) for the reduction product of PN in the basic $AlCl_3$-EMIC melt. The peak potentials of these waves were -0.18 and 0.17 V. These values are very close to those observed for the oxidation of H_2PN in the basic melt. It is very likely that these two waves were caused by the oxidation of H_2PN produced by the reaction of the reduced PN with trace protic impurities.

D. Perylene (PE) in $AlCl_3$-EMIC (mole ratio 0.8/1)

In order to further investigate interactions between the melt and reduced species, the reduction of PE was investigated. CV was performed on solutions of PE in basic $AlCl_3$-EMIC with PE concentrations of 4 to 5 m$\underline{M}$. The PE dissolved slowly (usually overnight) to give a yellow solution with blue fluorescence. This solution had a UV/visible absorption spectrum similar to that reported for PE in other solvents (Table III) (30), and was stable for a minimum of several weeks. As shown in Fig. 3, the reduction of PE in this melt occurs in two steps. The first reduction step has a peak potential of -1.83 V and the second -2.17 V (all potentials are vs. Al in $AlCl_3$(sat) $AlCl_3$-EMIC). Upon reversing the scan, the second wave shows no anodic wave even at very high scan rates, while the first wave exhibits a reverse wave at all scan rates studied (5-500 mV/s). The potential of the first cathodic wave is consistent with that reported for the one electron reduction of PE to the radical anion (31,32). The potential of the second wave is considerably less negative than that reported for the reduction of the radical anion to the dianion (32). This type of shift has been reported for the reduction of aromatic compounds when there was a source of protons present (i.e. decreased stability of the anion and dianion) (33,34). Due to the close proximity of the melt limit to the second reduction wave, only the first cathodic wave was studied in detail.

A study of the first wave on a tungsten electrode at various scan rates revealed that the ratio of the anodic to cathodic peak currents was approximately unity at scan rates of 20 mV/s and greater, and less than one at scan rates below 20 mV/s. This indicates that the product is unstable and that the decay is slow enough to be observed at the lower scan rates (24). At scan rates above 20 mV/s the peak separation is 75 mV which is somewhat higher than the value reported for a one electron process, namely 59 mV (24). The value of $i_p/v^{\frac{1}{2}}$ increases at low scan rates. This is consistent with the presence of a catalytic follow-up reaction (EC′) (24). The large peak separation at slow scan rates is also expected for an EC′ process. In a catalytic EC′ process, the species being reduced is regenerated by a following chemical reaction. At slower scan rates, more of the reduced species is converted back to the parent causing the current function ($i_p/v^{\frac{1}{2}}$) to increase (24). The decrease in $i_{p,a}/i_{p,c}$ with decreasing scan rate is, however, not expected for a catalytic follow-up reaction (24). This inconsistency will be discussed below.

Bulk coulometry at -1.85 V was performed on 14.34 grams of a 4.632 m$\underline{M}$ solution of PE in the basic melt using a glassy carbon crucible as the working electrode. After the passage of 4.843 coulombs, a spectrum was taken of an aliquot of the solution. Four of the new bands observed (352, 334, 319 and 305 nm) were similar to those reported for dihydroperylene (H_2PE) (see Table III) (32). Based on the decrease in the concentration of the PE during the coulometry (determined from the absorption spectra of PE taken before and after the coulometry) and the number of coulombs passed, the number of electrons per PE molecule was calculated to be 2.01. This result is consistent with the ECEC process producing an H_2PE analog. The mechanism for this process will be discussed below.

During the coulometry, the solution turned blue. An attempt was made to obtain the absorption spectrum of this solution; however, the blue color disappeared before the optical cell could be removed from the dry box. It was thought that this color was due to the radical anion which is reported to be blue (35). It was, therefore, decided to obtain SE data for the PE reduction to observe this intermediate.

SE (1-mm cell) was performed on a 0.2304 m$\underline{M}$ solution of PE in the basic melt. Due to the fact that the PE has a molar absorptivity of 3.22×10^4 $\underline{M}^{-1}$ cm^{-1} at 440 nm, and the pathlength of the SE cell is 1 mm, it was necessary to use such a low concentration to produce a UV/visible spectrum of the parent with maxima below 1.0 absorbance units. This solution was made by diluting the 4.588 m$\underline{M}$ solution with neat melt of the same composition. The light source used for this experiment was a tungsten lamp in order to observe any bands in the visible and therefore the species absorbing below 400 nm (i.e. the final product) could not be observed. The potential of the working electrode (40-mesh platinum screen) was stepped from -1.5 V to -1.85 V and spectra were taken every 15 seconds.

During the electrolysis, the PE bands decreased with time and a small band grew in at 580 nm reaching approximately 0.05 absorbance units at its maximum. When the circuit to the cell was opened, this band disappeared. The wavelength of this band was very close to that of the main band of the radical anion of PE (30,35).

In order to better observe this intermediate, the experiment was performed using the undiluted solution (4.588 m$\underline{M}$). Due to the high concentration, the bands from PE were off-scale. Fig. 4 shows the result of this experiment. The positions and relative heights of the new bands (Table III) correspond very well with those reported in the literature for the radical anion of PE (30,35). When the circuit to the cell was opened, these bands decayed back to the original base line. A plot of the log of the absorbance (A) (open circuit) of the main band at 580 nm vs time was nearly linear indicating that the decay of the radical anion is first order in PE (36). From the slope of the first order plot, the half-life of the radical anion was calculated to be 1.7 minutes.

In order to observe the final product, a deuterium lamp was used for SE of the dilute PE solution. Fig. 5 shows the results for this experiment. As can be seen, there is a well-defined isosbestic point at approx. 367 nm indicating an uncomplicated conversion of PE to the dihydro-like product.

As mentioned above, very low concentrations of PE were necessary to keep the bands of the parent and final product on scale. This low concentration was below that determined for the protic impurities, and therefore makes interpretation of the data uncertain. The thin layer SE cell (0.05 mm) was therefore used in order to work at a PE concentration greater than 4 m$\underline{M}$. Fig. 6 shows the results of this experiment. Due to the more rapid electrolysis of the starting material, a higher concentration of the radical anion was generated. This allowed all three PE species (neutral, radical anion and dihydro) to be observed simultaneously.

In order to positively confirm the identity of the intermediate formed during the reduction of PE, ESR spectroscopy was performed. The radical was generated in the ESR cavity using a modified SE cell. A constant potential of -1.85 V (vs. Al in an $AlCl_3$(sat) $AlCl_3$-EMIC melt) was applied to the working electrode. The slow electrolysis time of the cell (approx. 1 hr) allowed ample time for the optimization of the ESR parameters and the collection of the spectrum. Fig. 7 shows the ESR spectrum obtained from this experiment. Table IV lists the coupling constants, spectral width and g-value determined from the data; all parameters agree well with those reported in the literature (37,38).

From the information obtained above, it was assumed that the final product formed during the reduction of PE in the basic EMIC melt was the dihydro-like species (H_2PE) (32) formed by two successive reduction/complexation steps (ECEC) with the radical anion being the product of the first reduction and responsible for the single electron reduction wave observed at -1.8 V in the cyclic voltammograms. Once complexed, the radical has a reduction potential less negative than PE and will, therefore, be reduced to the dianion at potentials negative enough to reduce the neutral PE (32). The reduction of this radical is the second reduction process in the ECEC mechanism and accounts for the n-value of 2 observed during the bulk coulometry. Fig. 8 shows this reaction scheme along with a possible disproportionation reaction which would give the same final product along with the same total charge transfer (39). Since the only intermediate observed is the radical anion, and it is the initial product in both pathways, it is not possible to determine which of the pathways is responsible for the production of the dihydro species. The lack of an ESR signal from the neutral radical even when the radical anion is allowed to decay with no potential applied to the cell supports pathway 2; however, it is possible that both pathways are occurring simultaneously during the electrolysis.

The above conclusion is supported by the CV data. The reduction of the neutral radical at the same potential as the unreduced PE should give results similar to that for a catalytic follow-up reaction (increasing $i_{p,c}/v^{\frac{1}{2}}$ with decreasing scan rate), while the fact that the final product (H_2PE) is not electroactive should cause $i_{p,a}/i_{p,c}$ to decrease with decreasing scan rate (24), as was observed.

CONCLUDING REMARKS

The acidic properties of $AlCl_4^-$ in basic room temperature melts are of interest and should be investigated further. These investigations could include use of neat EMIC (or DMPIC) as the solvent (the radical anion of PN has been observed to be stable in neat EMIC) along with millimolar additions of $AlCl_3$ in order to study the reaction kinetics of the PN complexation. Another area of future interest is the stability of the radical cation of H_2PN in the basic melt as this is the first time it has been shown to be stable in something other than a highly acidic solvent.

ACKNOWLEDGMENTS

We are grateful to Dr. A. C. Buchanan and Dr. L. L. Brown for obtaining the ESR spectra and to Dr. R. M. Pagni for obtaining the NMR spectra. This research was sponsored by the Division of Chemical Sciences, Office of Basic Energy Sciences, U.S. Department of Energy, under Contract DE-AC05-840R21400 with Martin Marietta Systems, Inc.

REFERENCES

1. R. M. Pagni, in "Advances in Molten Salt Chemistry"; G. Mamantov, C. B. Mamantov, and J. Braunstein, Eds.; Elsevier Science Publishing Co.: New York, 1987; Vol. 6, pp. 211-346.

2. C. L. Hussey, in "Advances in Molten Salt Chemistry"; G. Mamantov, Ed.; Plenum Press: New York, 1983; Vol. 5, p. 185.

3. J. Robinson and R. A. Osteryoung, J. Am. Chem. Soc., 101, 323 (1979).

4. R. J. Gale, B. Gilbert, and R. A. Osteryoung, Inorg. Chem., 17, 2728 (1978).

5. J. S. Wilkes, J. A. Levisky, R. A. Wilson, and C. L. Hussey, Inorg. Chem., 21, 1263 (1982).

6. R. J. Gale and R. A. Osteryoung, Inorg. Chem., 18, 1603 (1979).

7. J. P. Schoebrechts and B. P. Gilbert, J. Electrochem. Soc., 128, 2679 (1981).

8. A. A. Fannin, Jr., D. A. Floreani, L. A. King, J. S. Landers, B. J. Piersma, D. J. Stech, R. L. Vaughn, J. S. Wilkes, and J. L. Williams, J. Phys. Chem., 88, 2614 (1984).

9. G. T. Cheek and R. A. Osteryoung, J. Electrochem. Soc., 129, 2488 (1982).

10. G. P. Smith, A. S. Dworkin, R. M. Pagni, and S. P. Zingg, J. Am. Chem. Soc., 111, 525 (1989).

11. S. P. Zingg, A. S. Dworkin, M. Sorlie, D. M. Chapman, A. C. Buchanan, III, and G. P. Smith, J. Electrochem. Soc., 131, 1602 (1984).

12. V. E. Norvell and G. Mamantov, in "Molten Salt Techniques"; D. G. Lovering and R. G. Gale, Eds.; Plenum Press: New York, 1983; Vol 1, Chapter 7.

13. W. R. Heineman and P. T. Kissinger, Anal. Chem., 50, 166R (1978).

14. T. Kuwana and N. Winograd, in "Electroanalytical Chemistry"; A. J. Bard, Ed.; Marcel Dekker: New York, 1974; Vol. 7, Chapter 1.

15. W. H. Heineman, F. M. Hawkridge, and H. N. Blount, in "Electroanalytical Chemistry"; A. J. Bard, Ed.; Marcel Dekker: New York, 1984; Vol. 13, Chapter 1.

16. J. E. Coffield, Ph. D. Dissertation, University of Tennessee, 1989.

17. M. Sorlie, G. P. Smith, V. E. Norvell, G. Mamantov, and L. N. Klatt, J. Electrochem. Soc., 128, 333 (1981).

18. P. R. Gifford and J. B. Palmisano, J. Electrochem. Soc., 134, 610 (1987).

19. R. Scholl, Monatsh. Chem., 39, 231 (1918).

20. G. A. Wheaton, L. J. Stoel, N. B. Stevens, and C. W. Frank, Appl. Spectrosc., 24, 339 (1970).

21. D. N. Bailey, D. K. Roe, and D. M. Hercules, Appl. Spectrosc., 22, 785 (1968).

22. T. Iwaoka, S. Niizuma, and M. Koizumi, Bull. Chem. Soc. Jpn., 43, 2786 (1970).

23. M. R. Grimmett, in "Comprehensive Heterocyclic Chemistry"; A. R. Katritzky, and C. W. Rees, Eds.; Pergamon Press: Oxford, 1984; Vol. 5, pp. 375,417.

24. R. S. Nicholson and I. Shain, Anal. Chem., 36, 706 (1964).

25. R. E. Hester and K. P. J. Williams, J. Raman Spectrosc., 13, 91 (1982).

26. Y. Matsunaga and C. A. McDowell, Proc. Chem. Soc., 80, 175 (1960).

27. B. L. Barton and G. K. Fraenkel, J. Chem. Phys., 41, 1455 (1964).

28. D. W. Schieser and P. Zvirblis, J. Chem. Phys., 35, 2237 (1962).

29. F. Gerson, "High Resolution E.S.R. Spectroscopy"; John Wiley and Sons, Ltd.: Weinheim, 1970; pp. 22-23.

30. G. J. Hoijtink, N. H. Velthorst, and P. J. Zandstra, Mol. Phys., 3, 533 (1960).

31. G. J. Hoijtink, J. Van Schooten, E. DeBoer, and W. I. J. Aalbersberg, Rec. Trav. Chim., 73, 355 (1954).

32. L. Rampazzo and A. Zeppa, J. Electroanal. Chem., 105, 221 (1979).

33. B. S. Jenson and V. D. Parker, J. Amer. Chem. Soc., 97, 5211 (1975).

34. B. S. Jenson and V. D. Parker, Acta Chem. Scand. B, 30, 749 (1976).

35. P. Balk, G. J. Hoijtink, and J. W. H. Schreurs, Rec. Trav. Chim., 76, 813 (1957).

36. J. H. Espenson, "Chemical Kinetics and Reaction Mechanisms"; McGraw-Hill, Inc: New York, 1981, pp. 12-30.

37. B. G. Segal, M. Kaplan, and G. K. Fraenkel, J. Chem. Phys., 43, 4191 (1965).

38. A. Carrington, F. Dravnieks, and M. C. R. Symons, J. Chem. Soc., 947 (1959).

39. L. Nadjo and J. M. Saveant, J. Electroanal. Chem., 33, 419 (1971).

TABLE I

ABSORPTION MAXIMA OF PHENAZINE AND ITS DERIVATIVES IN VARIOUS SOLVENTS

species	solvent	λ, nm (log ϵ($\underline{M}^{-1}$ cm^{-1}))			
PN	AlCl$_3$-EMIC (0.8/1)[a]		364(4.13)		
	MeOH[b]		362.5(4.12)		
	AlCl$_3$-EMIC (0.8/1)[a,c]		335(3.81)		
H$_2$PN	AlCl$_3$-EMIC (0.8/1)[a]		353(3.84)		
	MeOH[b]		350(3.87)		
	MeOH[d]		325(3.8)		
H$_2$PN$^{\cdot+}$	AlCl$_3$-EMIC (0.8/1)[a]	314(3.20)	379(3.76)	436$_{sh}$	444(3.90)
	EtOH+0.1$\underline{M}$ HCl[e]		370	434$_{sh}$	444

a. This work.

b. Ref. 20.

c. Product from reduction of PN at -1.60 V.

d. Ref. 21.

e. Ref. 25.

TABLE II

ESR PARAMETERS FOR $H_2PN^{+\cdot}$ IN VARIOUS SOLVENTS

solvent	μ^a	$a_{H\mu}{}^c$	$a_{N\mu}$	g	spectral width[c]
$AlCl_3$-EMIC[b]	1	--		2.00297	56.97
(0.8/1)	2	--			
25 °C	9(N)	6.6	6.6		
$AlCl_3$-EMIC[b]	1	0.6		2.00311	--
(0.8/1)	2	1.1			
102 °C	9(N)	6.2	6.2		
DMF+$HClO_4$[d]	1	0.66		--	47.02
	2	1.71			
	9(N)	6.49	6.14		
Aqueous acid[e]	1	0.6		--	46.8
	2	1.2			
	9(N)	6.6	6.6		

a. μ is the position of the magnetic nuclei in the compound.

b. 7.033 m<u>M</u> solution of H_2PN in $AlCl_3$-EMIC (0.8/1) at 25°C, electrolyzed at -0.15 V.

c. In gauss.

d. Ref. 27.

e. Ref. 28.

TABLE III

ABSORPTION MAXIMA OF PERYLENE AND ITS DERIVATIVES IN VARIOUS SOLVENTS

species	solvent	λ, nm (log ϵ(M^{-1} cm^{-1}))				
PE	$AlCl_3$-EMIC[a] (0.8/1)	254	373 (3.64)	392 (4.05)	413 (4.39)	440 (4.51)
	DMF/24mM HA[b]		366	385	405	428
	THF[c]	253 (4.56)	363 (3.58)	387 (4.01)	406 (4.33)	431 (4.38)
	$AlCl_3$-EMIC[a,d] (0.8/1)		305 (3.93)	319 (4.04)	334 (4.11)	352 (4.06)
H_2PE	DMF/24mM HA[b]	287	297	310	328	343
$PE^{\cdot -}$	$AlCl_3$-EMIC[a] (0.8/1)	580 (1.00)[e]	682 (0.16)[e]	737	771	809
	THF[f]	581 (4.63)	675 (3.77)	725	758	800

a. This work.

b. Ref. 32.

c. Ref. 30.

d. Product from reduction at -1.85 V.

e. Relative peak heights.

f. Ref. 35.

TABLE IV

ESR PARAMETERS FOR $PE^{-\cdot}$ IN VARIOUS SOLVENTS

Solvent	a_{H3}[b]	a_{H1}[b]	a_{H2}[b]	g	spectral width[b]
$AlCl_3$-EMIC[a] (0.8/1)	3.52	3.07	0.47	2.00270	28.28
$AlCl_3$-DMPIC[c] (0.9/1)	3.52	3.07	0.47	2.00262	28.24
THF[d]	3.53	3.09	0.46	--	28.32
DME[e,f]	--	--	--	2.00267	--

a. 4.488 m*M* solution of PE in $AlCl_3$-EMIC (0.8/1) at 25° C, electrolyzed in the ESR cavity at -1.85 V.

b. In gauss.

c. Ref. 16

d. Ref. 38.

e. Ref. 37.

f. DME is 1,2-dimethoxyethane.

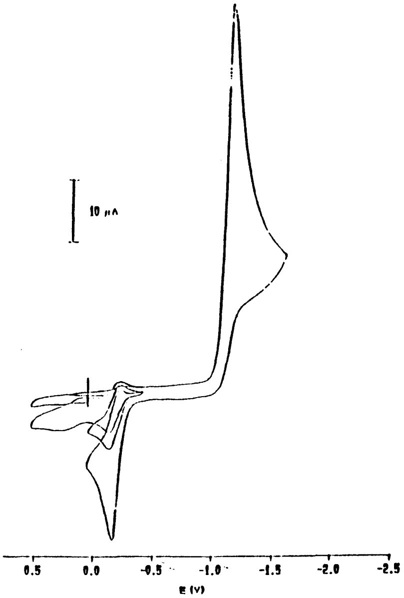

Figure 1. CV of 11.11 mM phenazine in $AlCl_3$-EMIC (0.8/1). Tungsten working electrode, area = 0.126 cm^2, t = 25°C. Reference electrode - Al in $AlCl_3$(sat) $AlCl_3$-EMIC. Sweep rate = 0.020 V/s.

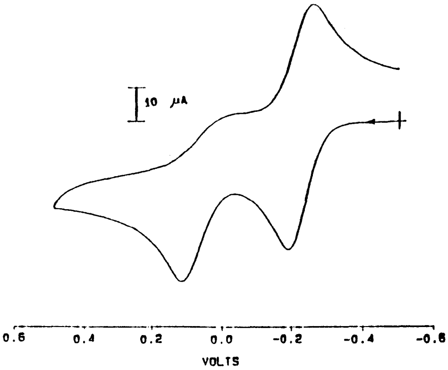

Figure 2. CV of 7.033 mM H_2PN in $AlCl_3$-EMIC (0.8/1). Tungsten working electrode, area = 0.126 cm^2, t = 25°C. Reference electrode - Al in $AlCl_3$(sat) $AlCl_3$-EMIC. Sweep rate = 0.100 V/s.

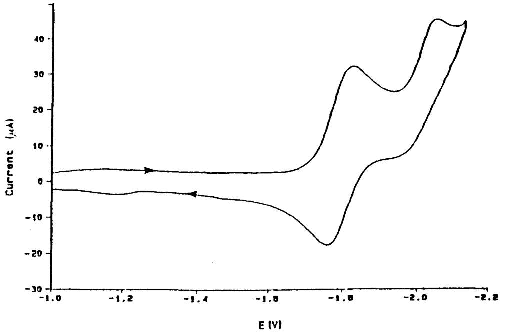

Figure 3. CV of 4.488 mM perylene in AlCl$_3$-EMIC (0.8/1). Tungsten working electrode, area = 0.126 cm^2, t = 25°C. Reference electrode - Al in AlCl$_3$(sat) AlCl$_3$-EMIC. Sweep rate = 0.100 V/s. Initial potential = -0.5 V.

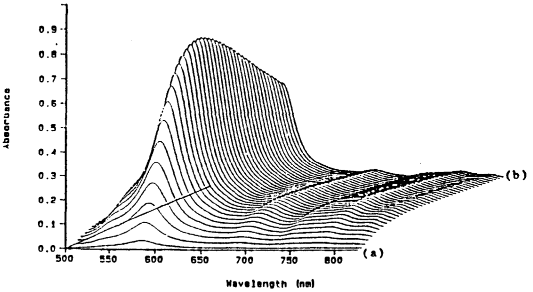

Figure 4. Absorption spectra measured every 90 s during a 60-min electrolysis at -1.85 V of 4.588 mM perylene in AlCl$_3$-EMIC (0.8/1). 40-mesh platinum screen electrode, pathlength = 0.10 cm. (a) Initial spectrum, electrolysis time = 0 min. (b) Final spectrum, electrolysis time = 60 min.

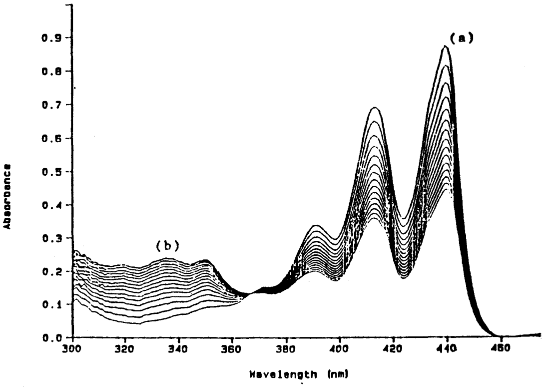

Figure 5. Absorption spectra measured every 2 min during a 30-min electrolysis at -1.85 V of 0.230 m$\underline{M}$ perylene in $AlCl_3$-EMIC (0.8/1). 40-mesh platinum screen electrode, pathlength = 0.10 cm. (a) Initial spectrum, electrolysis time = 0 min. (b) Final spectrum, electrolysis time = 28 min.

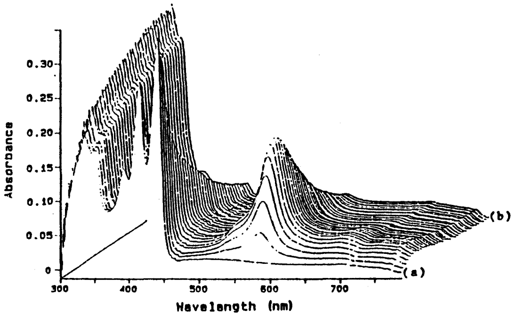

Figure 6. Absorption spectra measured every 4 s during a 140-s electrolysis at -1.85 V of 4.632 m$\underline{M}$ perylene in $AlCl_3$-EMIC (0.8/1). 200-mesh gold minigrid electrode, pathlength = 0.005 cm. (a) Initial spectrum, electrolysis time = 0 s. (b) Final spectrum, electrolysis time = 140 s.

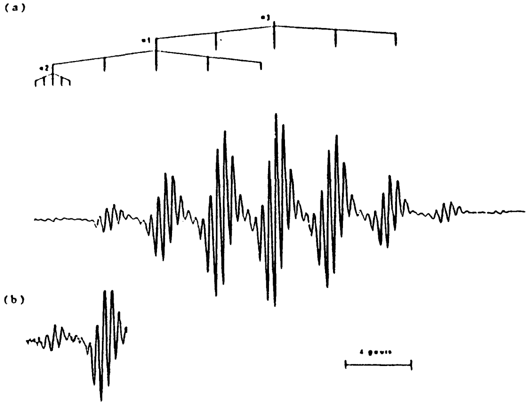

Figure 7. ESR spectrum of $PE^{\cdot -}$ in $AlCl_3$-EMIC (0.8/1). Applied potential = -1.85 V. (a) Mod. amp. = 44 mG, field = 3249.0 G, freq. = 9.474 GHz, microwave power = 0.5mW, scan rate = 1 G/min. (b) Improved signal level, mod. amp. = 184 mG, microwave power = 1 mW.

$$Pe + e^- \longrightarrow Pe^{\cdot -}$$

$$Pe^{\cdot -} + AlCl_4^- \longrightarrow Pe(AlCl_3)^{\cdot -} + Cl^-$$

$$Pe(AlCl_3)^{\cdot -} + e^- \longrightarrow Pe(AlCl_3)^{2-}$$

$$Pe(AlCl_3)^{2-} + AlCl_4^- \longrightarrow Pe(AlCl_3)_2^{2-} + Cl^-$$

OR

$$Pe^{\cdot -} + Pe(AlCl_3)^{\cdot -} \longrightarrow Pe + Pe(AlCl_3)^{2-}$$

$$Pe(AlCl_3)^{2-} + AlCl_4^- \longrightarrow Pe(AlCl_3)_2^{2-} + Cl^-$$

Figure 8. Proposed reaction mechanism for perylene reduction at -1.85 V in $AlCl_3$-EMIC (0.8/1).

DOI: 10.1149/199017.0356PV

ELECTROCHEMISTRY AND SPECTROSCOPY OF BISMUTH CLUSTERS IN ACIDIC ROOM–TEMPERATURE CHLOROALUMINATES

Luc Heerman and W. D'Olieslager

Laboratorium Radiochemie, K.U.Leuven
Celestijnenlaan 200G, B–3030 Heverlee, Belgium

ABSTRACT

In 2:1 mole ratio $AlCl_3$–BuPyCl melts, the electrochemical reduction of $[Bi_5]^{3+}$ ion to the metal is the sum of two processes : 1) the reversible two–electron reduction of the closo–trigonal bipyramid with the formation of a closed shell nido–square pyramid and 2) the further reduction of this instable intermediate to the metal. On glassy carbon electrodes both processes give raise to separate waves because the deposition of the metal is retarded by nucleation phenomena. Anodisation of the metal or reaction of the metal with $BiCl_3$ produces $[Bi_5]^{3+}$ ion (or its solid salt $Bi_5(AlCl_4)_3$) and minor traces of another low–valent species, probably "$BiAlCl_4$".

INTRODUCTION

Bismuth possesses a number of unusual low oxidation states, i.e. lower than that of the familiar Bi(III), which include Bi^+ and a series of homopolyatomic ions ; in fact, bismuth has become the classical exemple of an element forming "naked" metallic polycations (1,2).

Early investigations were concerned mainly with solutions of bismuth metal in $BiCl_3$–melts. The results of emf studies and spectroscopic measurements are consistent with the presence of Bi^+ and $[Bi_3]^+$ (3–6). The solid phase $Bi_{24}Cl_{28}$ (originall formulated as "BiCl" (7)) which can be separated from these melts has been shown by X–ray diffraction studies to be $([Bi_9]^{5+})_2([BiCl_5]^{2-})_4([Bi_2Cl_8]^{2-})$ (8,9) (more recent work however suggests that the anionic part is better described as polymeric instead of the idealized $([BiCl_5]^{2-})([Bi_2Cl_8]^{2-})$ structure (10)).

Several workers investigated the reaction between bismuth metal and dilute solutions of $BiCl_3$ in acidic ($AlCl_3$–rich) chloroaluminate melts which are particularly good solvents for the stabilisation of low oxidation states (11). Bjerrum et al. (12–15) characterized the products of this reaction in molten $AlCl_3$–NaCl eutectic (63 mole % $AlCl_3$ – 37 mole % NaCl) by UV–visible spectroscopy. These workers studied quantitatively the equilibria

$$2\,Bi_{liq} + Bi^{3+}_{sol} \rightleftharpoons 3\,Bi^{+}_{sol} \quad (1)$$

$$4\,Bi_{liq} + Bi^{3+}_{sol} \rightleftharpoons [Bi_5]^{3+}_{sol} \quad (2)$$

$$6\,Bi^{+}_{sol} \rightleftharpoons Bi^{3+}_{sol} + [Bi_5]^{3+}_{sol} \quad (3)$$

DOI: 10.1149/199017.0356PV

In addition to Bi^+ and $[Bi_5]^{3+}$, the polycation $[Bi_8]^{2+}$ was characterized in the presence of excess liquid metal (no information was obtained on the number of ligands, chloride or chloroaluminate ions, attached to these entities). Corbett (16,17) subsequently isolated the solid phases $Bi_5(AlCl_4)_3$ and $Bi_8(AlCl_4)_2$ from the pseudo–binary system Bi–($BiCl_3$–3 $AlCl_3$). In view of the absence of a salt of the $[Bi_9]^{5+}$ cation in the chloroaluminate system, Corbett (18) also investigated the system Bi–(2 $BiCl_3$ + 3 $HfCl_4$) to explore the effect of a large cation of relatively high stability and obtained a product with composition $Bi_{10}Hf_3Cl_{18}$. An X–ray diffraction study showed that actual the composition of this compound is $([Bi_9]^{5+})(Bi^+)([HfCl_6]^{2-})_3$ and not $([Bi_5]^{3+})_2([HfCl_6]^{2-})_3$. The structure of the $[Bi_5]^{3+}$ ion was investigated by infrared and Raman spectroscopy (19). More recently, the preparation of single crystals and the full structural analysis of $Bi_5(AlCl_4)_3$ (10) and $Bi_8(AlCl_4)_2$ (20) was reported.

Torsi and Mamantov (21) investigated the reduction of Bi^{3+} at solid electrodes in molten $AlCl_3$–NaCl eutectic at 175°C and reported a reversible reduction of Bi^{3+} to Bi^+ (spectroelectrochemical experiments with a rather high concentration of $BiCl_3$, ~ 0.3 M $BiCl_3$, also indicated the formation of $[Bi_5]^{3+}$) ; however, the further reduction of Bi^+ is complex and involves an intermediate oxidation state which was not characterized electrochemically. Three reduction waves were observed for the electrochemical reduction of Bi^{3+} on glassy carbon electrodes in 2:1 mole ratio $AlCl_3$–BuPyCl melts (BuPyCl : N–(n–butyl)pyridinium chloride) : the first wave corresponds with the reduction of Bi^{3+} to $[Bi_5]^{3+}$ but again the further reduction of the cluster ion to the metal was not well understood (22). The $AlCl_3$–BuPyCl molten salt system belongs to a class of chloroaluminates, including $AlCl_3$–MEIC melts (MEIC : 1–methyl–3–ethylimidazolium chloride) which exist as ionic liquids at ambient temperatures (23,24). A comparison of available literature data indicates that these ($AlCl_3$–rich) room temperature chloroaluminate melts are by far more acidic solvents than systems such as ($AlCl_3$–rich) $AlCl_3$–NaCl melts (25,26). This probably explains why the reduction of Bi^{3+} in the room temperature molten salt results in the formation of $[Bi_5]^{3+}$ and not Bi^+ as was observed in $AlCl_3$–NaCl melts since acidic conditions and low temperatures generally enhance the stability of homopolyatomic ions. This paper reports some results on the electrochemistry and spectroscopy of bismuth in 2:1 mole ratio $AlCl_3$–BuPyCl melts and specifically on the reduction/oxidation of $[Bi_5]^{3+}$ in these melts.

EXPERIMENTAL

The synthesis and purification of BuPyCl, the sublimation of $AlCl_3$ (Fluka) and the preparation of the melts was described previously (27). Anhydrous $BiCl_3$ (99.999 % ; Alfa Inorganics) was used as received ; a pure bismuth rod (99.999 % ; Goodfellow Metals) was used for anodisation experiments. Solid $Bi_5(AlCl_4)_3$ was prepared by fusing the stoichiometric quantities of bismuth powder, $AlCl_3$ and $BiCl_3$ (19).

All experiments were carried out under a purified nitrogen atmosphere (VAC drybox ; HE–493 Dri Train). The temperature of the melts (25°C, unless indicated otherwise) was controlled by circulating oil, from a thermostat outside the dry box, through the jacket of the conventional Pyrex cell used for the electrochemical measurements.

DOI: 10.1149/199017.0356PV

A rotating disk electrode (Bruker ER–5 ; speed control E–RS–1) with interchangeable tips (glassy carbon/platinum ; geometrical area : 0.282 cm^2) was used for the voltammetric measurements ; for cyclic voltammetry, the electrode was used in the non–rotating mode. A glassy carbon crucible was used as the working electrode for controlled–potential electrolysis experiments. The reference and counter electrodes consisted of 1 mm diam. aluminum wire spirals, immersed in a melt of the same composition and separated from the working electrode compartment by fine porosity glass frits. A bismuth indicator electrode, prepared by electrodeposition of the metal on a gold wire from aqeous perchlorate solution, was used for emf measurements. The electrochemical instrumentation includes a PAR 173/179 potentiostat/digital coulometer, a PAR 175 function generator and a Houston 2000 XY–recorder. Potentials were measured with a Beckman 4500 digital pH meter.

UV–visible absorption spectra were obtained using 1–cm rectangular quartz cells and were recorded on a Beckmann Acta MIV instrument against a reference cell containing solvent. X–ray powder diffraction data were obtained from samples in thin–walled Pyrex capillaries using a Philips Debye–Scherrer camera (diameter : 5.73 cm) with Ni–filtered CuKα radiation.

RESULTS AND DISCUSSION

A cyclic voltammogram of a ~ $1.0 \cdot 10^{-3}$ M $BiCl_3$ solution at glassy carbon electrode (25^{0}C) (fig.1a) exhibits three cathodic peaks at 0.95 V, 0.71 V and 0.2 V for the reduction of Bi^{3+} to the metal *. The cyclic voltammogram also exhibits three anodic peaks : a sharp peak at 0.92 V which evidently corresponds to the stripping of the metal with formation of a solute species and two peaks at 1.45 V and 1.65 V for the oxidation of this species to Bi^{3+} as is shown by the fact that successive scans are identical with the first. Cyclic voltammograms of the same solution but with different cut–off potentials (fig.1b,c) reveal the presence of other anodic peaks at 0.74 V and 1.05 V which are clearly associated with the first two reduction processes. Increase of the temperature (80^{0}C) (fig.2) has no effect on the cyclic voltammograms beside the normal increase of the current exception made on two points : the stripping peak is much more narrow and is shifted slightly to less positive potentials and the small anodic peak at 1.00 V is now observed directly.

The first cathodic peak corresponds to the reduction of Bi^{3+} to $[Bi_5]^{3+}$ as was shown earlier (22) (the peak current of the first reduction process is rather large when compared with the peak currents of the subsequent reduction reactions : this immediately suggests the formation of a low–valent species). Thus, $[Bi_5]^{3+}$ was prepared by exhaustive electrolysis (0.85 V) : the solution, initially colorless, turned red–brown during the experiment and the spectrum of the solution, recorded after

---

* Controlled–potential electrolysis (0.2 V) results in the formation of a finely divided, powdery deposit of bismuth metal. However, the metal reacts slowly with an impurity in the melt with formation of $[Bi_5]^{3+}$ ion. A similar observation was reported by Habboush and Osteryoung (28) who noted a slight oxidation of antimony metal in acidic melts and suggested that the metal reacts with a proton containing species which is present as an "hidden" impurity in these melts (29).

completion of the electrolysis, is in good agreement with the spectrum of $[Bi_5]^{3+}$ reported by Bjerrum et al. (12,13). Furthermore, the spectrum is identical with the spectrum of a solution prepared by dissolving a solid sample of $Bi_5(AlCl_4)_3$ in the melt. However, the actual mechanism of the reduction of Bi^{3+} to $[Bi_5]^{3+}$ no doubt is more complex. This is shown by the presence of the small peak at 1.05 V which does not correspond to the reverse anodic reaction, i.e. oxidation of $[Bi_5]^{3+}$ to Bi^{3+} (vide infra) but which must be attributed to the oxidation of an intermediate species formed in the reduction reaction. Therefore, it seems logical to assume, in concordance with the work of Torsi and Mamantov (21), that Bi^{3+} is reduced in a first step to Bi^+ (or another Bi(I) species) and that the oxidation peak at 1.05 V corresponds to the oxidation of this species : the cluster ion can then be formed by a follow–up chemical disproportionation step (reaction 3). The results obtained in this study did not provide any conclusive evidence for this mechanism : thus, a variation of the scan rate over the range 0.020–0.500 V/s has no effect on the general shape of the cyclic voltammograms, the relative heights of the peak currents or the position of the peak potentials (however, application of a 30–60 second potental hold at 0.85 V before scan reversal results in the disappearance of the small anodic peak). Therefore, the actual mechanism of the reduction of Bi^{3+} to $[Bi_5]^{3+}$ must be left open for further investigation.

The cyclic voltammogram of a $[Bi_5]^{3+}$ solution, started from 1.0 V in the cathodic direction, exhibits cathodic peaks at 0.71 V and 0.2 V and, after scan reversal, the stripping peak at 0.92 V and the anodic peaks at 1.45 V and 1.65 V ; a second scan, after a scan reversal at 1.80 V, exhibits again the large reduction peak at 0.95 V. A cyclic voltammogram started from 1.0 V in the cathodic direction but with the scan reversed at 0.5 V, i.e. after the first reduction peak, shows the corresponding anodic peak at 0.74 V, thus revealing the presence of a reversible oxido–reduction couple (which was shown already in fig.1c).Voltammograms for the reduction/oxidation of $[Bi_5]^{3+}$ at glassy carbon rotating disk electrodes (fig.4) exhibit two reduction and two oxidation waves as is expected on the basis of the results of cyclic voltammetry. The half–wave potential of the first reduction wave, 0.75 V, is in good agreement with the position of the corresponding peaks in the cyclic voltammogram. The deposition of the metal on carbon however requires a rather large nucleation overvoltage as is shown by a reverse scan, started after the deposition of the metal was initiated. The reverse scan shows that deposition of the metal is observed at potentials as positive as 0.83 V, i.e. slightly more positive than the half–wave potential of the first wave (but slightly negative with respect to the position of the first reduction peak in the cyclic voltammogram of $BiCl_3$ solutions). This observation implies that the first wave is observed as a separate reduction step only because the deposition of the metal is retarded by nucleation phenomena (in fact, on platinum rotating disk electrodes both waves strongly overlap so that the reduction of $[Bi_5]^{3+}$ to the metal almost appears as a single wave). As a consequence, the product of the first wave is not a stable species ; this is confirmed by the fact that controlled–potential electrolysis on the limiting current plateau of the first wave (on carbon electrodes) simply results in the deposition of the metal. Therefore, it was impossible to obtain any spectral information on this intermediate species.

The exact measurement of the ratio of the limiting currents of both reduction waves is obscured by the fact that the limiting current plateau for the deposition of the metal is not well–defined. The increase of the current in the limiting current region must be due to the predeposition of aluminum with formation of intermetallic compounds and not to roughening of the electrode surface since the current decreases again during the reverse scan. Therefore, the ratio of the limiting currents was measured at 0.55 V, i.e. the limiting current of the first wave was obtained from the forward scan whereas the limiting current of the second wave was obtained from the reverse scan. The results obtained this way at different rotation rates (fig.5) indicate a 2:1 ratio ** so that the reduction of $[Bi_5]^{3+}$ can be written as :

$$[Bi_5]^{3+} \quad + \quad 2e^- \quad \rightleftharpoons \quad [Bi_5]^{+} \qquad (4)$$

$$[Bi_5]^{+} \quad + \quad e^- \quad \longrightarrow \quad 5\ Bi \qquad (5)$$

The conclusion that the first wave corresponds to a two–electron reduction is also supported by the separation of the cyclic voltammetric peaks, 0.030–0.035 V, in good agreement with the theoretical value (0.030 V). The $[Bi_5]^{3+}$ ion has a trigonal bipyramidal structure with 12 bonding electrons. However, for main group elements there exist no naked trigonal bipyramidal clusters with 12 + 2 bonding electrons : the two–electron reduction of a closo-trigonal bipyramid always results in the formation of a closed shell nido-square pyramid (31). The results of cyclic voltammetry indicate that the couple $[Bi_5]^{3+}/Bi$ is reversible so that the rate of the intramolecular rearrangement must be fast with respect to the time window of the measurements. At the same time, the observed reversibility virtually excludes any complicated stoichiometry of the reaction and thus indirectly supports the proposed mechanism.

Anodisation of a metallic bismuth rod at low current densities (typically < 100 μA, with an exposed electrode surface of 2–3 cm^2) such that the potential of the electrode was less than 0.95 V results in the formation of red–brown solutions of $[Bi_5]^{3+}$ (although there is some other minor component in the solution ; vide infra). In a series of experiments, the equilibrium potential of a bismuth indicator electrode was measured after each charge addition. A plot of E vs. $\log([Bi_5]^{3+})$ has a slope close to 0.020 V/decade, in excellent agreement with the theoretical value for a 3–electron electrode reaction (fig.6). The standard potential of the $[Bi_5]^{3+}/Bi$-couple was estimated as $E^0([Bi_5]^{3+}/Bi) = 0.925 \pm 0.015$ V (this value roughly corresponds with the position of the stripping peak in the voltammetric experiments). Anodic dissolution of bismuth at higher current densities results in a red–brown solution with the concomitant formation of a peach–colored film on the electrode. This film was identified by X–ray diffraction as solid $Bi_5(AlCl_4)_3$ (excess melt adhering to the electrode was removed by repeated washings with dry toluene). The solution is a mixture of $[Bi_5]^{3+}$ (and the minor component) and rather high concentrations of Bi^{3+}–ion : this was evidenced by the presence of a reduction wave at 0.95 V in the rotating disk electrode voltammograms (besides the waves for the reduction of $[Bi_5]^{3+}$). During the anodisation experiments at higher current densities strong potential oscillations were observed although apparently the potential never became more positive than 1.10 V : this seems to indicate that the standard potential of the $Bi^{3+}/[Bi_5]^{3+}$ –redox couple is in the range 1.00–1.10 V and that the oxidation of

---

** The diffusion coefficient of $[Bi_5]^{3+}$ was estimated from the data of fig.5 using Levich's equation (30) as $D \simeq 2.0 \times 10^{-7}\ cm^2/s$.

$[Bi_5]^{3+}$ on carbon (or platinum) electrodes is an irreversible process.

The absorption spectrum of $[Bi_5]^{3+}$ solutions prepared by anodisation of the metal (or by reaction of bismuth metal with $BiCl_3$ solutions) always exhibits an absorption band at 730 nm (fig.7), indicating the presence of another species in the solution. Bi^{3+} –ion does not absorb in the spectral region of interest whereas Bi^+ (in $AlCl_3$–NaCl melts) has its strongest absorption peaks at 585 nm and 663 nm (13). However, a species with a strong absorption band at 723 nm ($\epsilon = 5.4 \times 10^4$ l $mole^{-1}cm^{-1}$) and identified as $BiAlCl_4$ was observed by Lynde and Corbett (32) in the gaseous ternary system Bi–$BiCl_3$–$AlCl_3$ (at temperatures above 400–450°C). Therefore it is suggested that small amounts of Bi(I) exist in these solutions as a chloroaluminate complex, "$BiAlCl_4$" (it is not clear whether the weak absorption in the region 610–660 nm can be attributed to Bi^+–ion). As noted earlier, the occurence of the small anodic peak at 1.05 V in the cyclic voltammograms at higher temperatures (fig.2) provides further, albeit indirect, evidence for the formation of a Bi(I) species during the anodisation of the metal.

Two anodic waves are observed in the voltammograms for the oxidation of $[Bi_5]^{3+}$ to Bi^{3+} at carbon rotating disk electrodes (fig.4) but the actual electrode reactions no doubt are complicated. Thus, the total height of both anodic waves equals four times the sum of both reduction waves, as expected from the stoichiometry of the reactions. However, the ratio of the anodic wave heights varied from one experiment to another, almost at random (the height of the first wave is never less than about one half of the total wave height). A similar observation was made with platinum electrodes but the reason for this behavior is not understood at present. Apparently, the oxidation initially occurs only at preferred sites on the electrode surface : once these sites are saturated (or poissoned), the reaction can occur on the rest of the electrode surface but only at more positive potentials. It is not clear however what species is responsible for this saturation (or poissoning) or what is the reason for the observed non–reproducibility of the relative wave heights.

ACKNOWLEDGEMENT

The authors are indebted to the I.I.K.W. (Interuniversitair Instituut voor Kernwetenschappen, Brussels) for financial support of this work.

REFERENCES

1. R.J. Gillespie and J. Passmore, in Advances in Inorganic Chemistry and Radiochemistry, H.J. Emeléus and A.G. Sharpe, eds., Academic Press, 1975, p.49

2. J.D. Corbett, in Progress in Inorganic Chemistry, S.J. Lippard, ed., John Wiley & Sons, 1976, p.129

3. S.J. Yosim, D.J. Darnell, W.G. Gehman and S.W. Mayer, J. Phys. Chem., 63, 230 (1959)

4. L.E. Topol, S.J. Yosim and R.A. Osteryoung, J. Phys. Chem., 65, 1511 (1961)

5. C.R. Boston, G.P. Smith and L.C. Howick, J. Phys. Chem., 67, 1849 (1963)

6. J.D. Corbett, F.C. Albers and R.A. Sallach, Inorg. Chim. Acta, 2, 22 (1968)

7. J.D. Corbett, J. Am. Chem. Soc., 80, 4757 (1958)

8. A. Hershaft and J.D. Corbett, Inorg. Chem., 2, 979 (1963)

9. R.M. Friedman and J.D. Corbett, Inorg. Chim. Acta, 7, 525 (1973)

10. B. Krebs, M. Mummert and C. Brendel, J. Less–Common Metals, 116, 159 (1986)

11. G. Mamantov and R.A. Osteryoung, in Characterisation of Solutes in Nonaqueous Solvents, G. Mamantov, ed., Plenum Press, 1978, p.223

12. N.J. Bjerrum, C.R. Boston, G.P. Smith and H.L. Davis, Inorg. Nucl. Chem. Letters, 1, 141 (1965)

13. N.J. Bjerrum, C.R. Boston and J.P. Smith, Inorg. Chem., 6, 1162 (1967)

14. N.J. Bjerrum and G.P. Smith, Inorg. Nucl. Chem. Letters, 3, 165 (1967)

15. N.J. Bjerrum and G.P. Smith, Inorg. Chem., 6, 1968 (1967)

16. J.D. Corbett, Inorg. Nucl. Chem. Letters, 3, 173 (1967)

17. J.D. Corbett, Inorg. Chem., 7, 198 (1968)

18. R.M. Friedman and J.D. Corbett, Inorg. Chem., 12, 1134 (1973)

19. R.C. Burns, R.J. Gillespie and Woon–Chung Luk, Inorg. Chem., 17, 3596 (1978)

20. B. Krebs, M. Hucke and C.J. Brendel, Angew. Chem. Int. Ed., 21,445 (1982)

21. G. Torsi and G. Mamantov, J. Electroanal. Chem., 30,193 (1973)

22. L. Heerman and W. D'Olieslager, Proceedings of the First International Symposium on Molten Salt Chemistry and Technology, Kyoto, 1983, p.465

23. H.L. Chum and R.A. Osteryoung, in Ionic Liquids, D. Inman and D. Lovering, eds., Plenum Press, 1981, p.407

24. C.L. Hussey, in Advances in Molten Salt Chemistry, G. Mamantov, ed., Elsevier, 1983, p.185

25. L.G. Boxall, H.L. Jones and R.A. Osteryoung, J. Electrochem. Soc., 120, 223 (1973)

26. M. Lipsztajn and R.A. Osteryoung, Inorg. Chem., 24, 716 (1985)

27. R. De Waele, L. Heerman and W. D'Olieslager, J. Less–Common Metals, 122, 319 (1986)

28. D.A. Habboush and R.A. Osteryoung, Inorg. Chem., 23, 1726 (1985)

29. Saeed Sahami and R.A. Osteryoung, Anal. Chem., 55, 1970 (1983)

30. A.J. Bard and L.R. Faulkner, Electrochemical Methods. Principles and Applications, John Wiley & Sons, 1980, p.288

31. A. Ceulemans, personal communication

32. R.A. Lynde and J.D. Corbett, Inorg. Chem., 10, 1746 (1971)

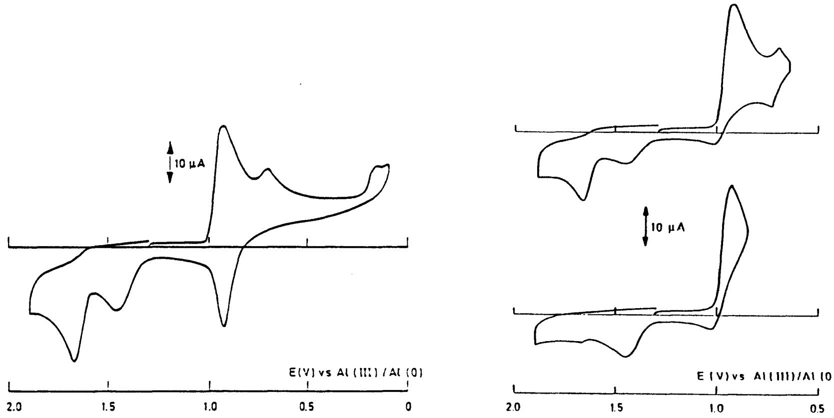

Figure 1. Cyclic voltammogram for the reduction/oxidation on glassy carbon electrode of ~ 1 mM $BiCl_3$ solution in a 2:1 mole ratio $AlCl_3$:BuPyCl melt with different cut-off potentials (scan rate : 0.1 V/s ; 25°C).

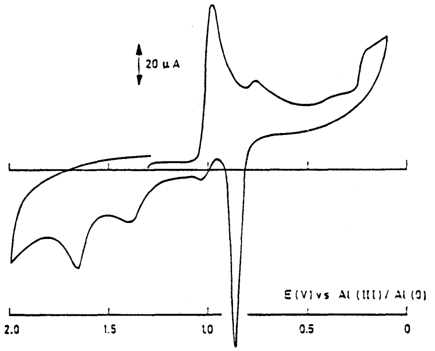

Figure 2. Cyclic voltammogram for the reduction/oxidation on glassy carbon electrode of ~ 1 mM $BiCl_3$ solution in a 2:1 mole ratio $AlCl_3$:BuPyCl melt (scan rate : 0.1 V/s ; 80°C).

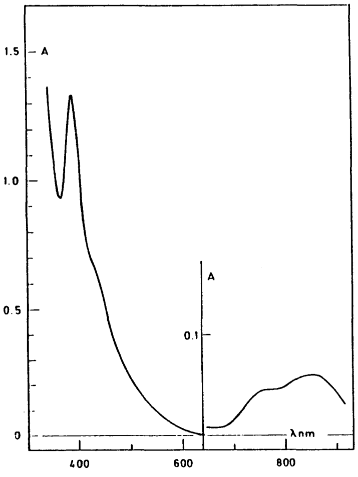

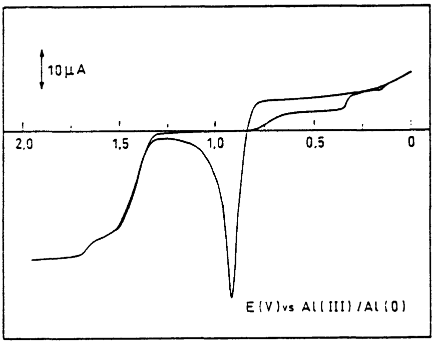

Figure 3. Electronic absorption spectrum of $[Bi_5]^{3+}$ in a 2:1 mole ratio $AlCl_3$:BuPyCl melt.

Figuur 4. Voltammogram for the reduction/oxidation of $[Bi_5]^{3+}$ on glassy carbon rotating disk electrode in a 2:1 mole ratio $AlCl_3$:BuPyCl melt ; also shown is the reverse scan started after the deposition of the metal was initiated.

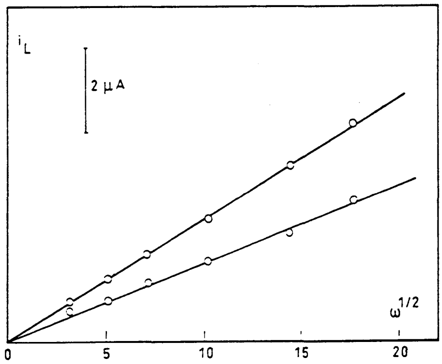

Figure 5. Plot of i_l vs. $\sqrt{\omega}$ for the reduction of $[Bi_5]^{3+}$ on glassy carbon rotating disk electrode in a 2:1 mole ratio $AlCl_3$:BuPyCl melt : 1) first reduction wave 2) sum of first and second reduction waves. Both limiting currents were measured at 0.55 V (see text).

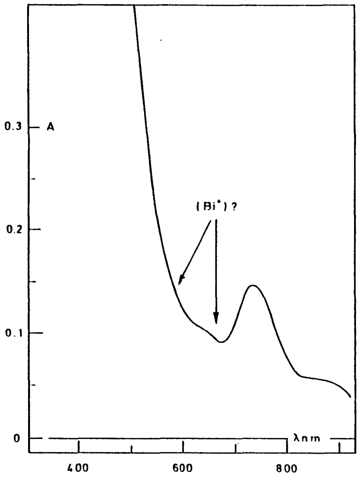

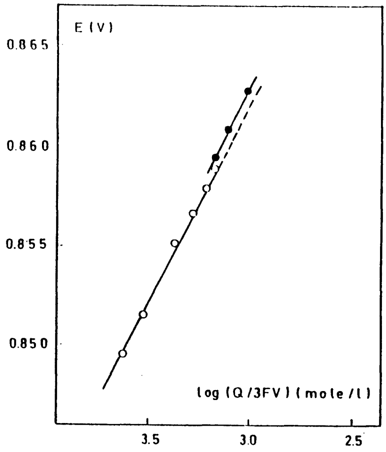

Figure 6. Plot of E ($[Bi_5]^{3+}/Bi$) vs. log ($[Bi_5]^{3+}$). Experimental points were obtained by measuring the potential of a bismuth indicator electrode after each charge addition during the anodisation of bismuth metal (filled circles are values measured when the experiment was continued the next day after standing overnight).

Figure 7. Absorption spectrum (part) of a solution prepared by anodisation of bismuth metal (see text).

DOI: 10.1149/199017.0367PV

"ELECTROCHEMISTRY OF SOME METAL-METAL BONDED TRANSITION METAL CLUSTER COMPLEXES IN A ROOM-TEMPERATURE CHLOROALUMINATE MOLTEN SALT"

S. K. D. Strubinger, P. A. Barnard, I-W. Sun[1], and C. L. Hussey*

Department of Chemistry
University of Mississippi
University, MS 38677

[1]Present address: University of Tennessee, Knoxville, TN 37996-1600

ABSTRACT

The electrochemistry and spectroelectrochemistry of several metal-metal bonded transition metal cluster complexes, including $[(Mo_6Cl_8)Cl_6]^{2-}$, $[(Nb_6Cl_{12})Cl_6]^{2-}$, $[Re_2Cl_8]^{2-}$, and $[Re_3Cl_{12}]^{3-}$, were investigated in the "basic" aluminum chloride-1-methyl-3-ethylimidazolium chloride room-temperature chloroaluminate molten salt. All of these complexes are electroactive in this solvent; however, the oxidation of $[(Mo_6Cl_8)Cl_6]^{2-}$ can be seen only in the neutral-basic melt. The one-electron reduction products of both of the rhenium(III) clusters are stable in basic $AlCl_3$-MeEtimCl in contrast to results found in molecular solvents.

INTRODUCTION

Combinations of aluminum chloride and certain quaternary ammonium chloride salts such as 1-(1-butyl)pyridinium chloride (BupyCl) and 1-methyl-3-ethylimidazolium chloride (MeEtimCl) are molten at room temperature (1, 2). These mixtures have proven themselves to be particularly useful solvents for the characterization of transition metal chloride complexes because processes such as solvolysis and solvation, which can alter the chemistry and electrochemistry observed for these species in conventional solvents, are avoided (3). One of the major advantages in using these ionic liquids is their adjustable Lewis acidity. Melts that contain < 50 mol % $AlCl_3$ are said to be basic due to the presence of unbound chloride ion; those that contain > 50 mol % $AlCl_3$ are acidic due to the presence of $Al_2Cl_7^-$, which is a chloride ion acceptor. When melts are prepared with equal amounts of $AlCl_3$ and organic chloride salt, R^+Cl^-, then the resulting melt is said to be neutral, and it contains small amounts of Cl^- and $Al_2Cl_7^-$ due to the following self-ionization reaction:

$$2R^+AlCl_4^- \rightleftharpoons R^+Al_2Cl_7^- + R^+Cl^- \qquad [1]$$

This equilibrium is analogous to the autosolvolysis of water.

Transition metal halide clusters are distinguished from classical polynuclear Werner complexes by their metal-metal bonding; the latter contain metal atoms that are joined only by ligands. In a true cluster, the metal-metal bonding is of sufficient strength to contribute significantly to the heat of formation of these species. Metal clusters are of great interest due to their unusual structures, reactivities, and the unique properties imposed upon them by the metal-metal bonding as well their potential application as catalysts. Due to its proven ability to stabilize transition metal chloride complexes (4), the basic $AlCl_3$-MeEtimCl molten salt was chosen as a medium in which to study the anionic transition metal chloride clusters $[(Mo_6Cl_8)Cl_6]^{2-}$, $[(Nb_6Cl_{12})Cl_6]^{2-}$, $[Re_2Cl_8]^{2-}$, and $[Re_3Cl_{12}]^{3-}$.

EXPERIMENTAL

Apparatus. The experimental procedures and equipment used to collect electrochemical and spectroscopic data as well as the glovebox system used for those experiments have been described (5, 6). A description of the instrumentation used for spectroelectrochemistry experiments has also been presented (7). All experiments were carried out at 40 °C unless otherwise stated.

Chemicals. The preparation and purification of the components of the $AlCl_3$-MeEtimCl ionic liquid were carried out as previously reported (8). Molybdenum(II) chloride, $(Mo_6Cl_8)Cl_4$, (Cerac, 99.5 %) was used as received. The niobium salt, $[MeEtim]_2[(Nb_6Cl_{12})Cl_6]$, was supplied by Dr. Kenneth R. Seddon of the University of Sussex, U.K. Tetrabutylammonium octachlorodirhenate(III), $[Bu_4N]_2[Re_2Cl_8]$, was prepared according to the method described by Barder and Walton (9). Rhenium(III) chloride, Re_3Cl_9, (Johnson Matthey, 99.9 %) was also used as received.

RESULTS AND DISCUSSION

$[(Mo_6Cl_8)Cl_6]^{2-}$. $(Mo_6Cl_8)Cl_4$ dissolved in the basic $AlCl_3$-MeEtimCl ionic liquid to produce intense yellow solutions of the complex, $[(Mo_6Cl_8)Cl_6]^{2-}$. Temperatures of 90 °C were required for dissolution; however, no precipitate formed upon cooling to 52 °C. The identity of this cluster was confirmed through results obtained from absorption spectroscopy and amperometric titration experiments (10, 11); UV-vis spectral data for this cluster in this ionic liquid are in good agreement with data for the same species in 12 M HCl (10). The use of the titration method developed by Osteryoung and Lipsztajn (11) confirmed the uptake of two chloride ions per cluster unit upon dissolution of $(Mo_6Cl_8)Cl_4$ into neutral-basic melt.

Figure 1 shows cyclic voltammograms of a neutral-basic melt containing $[(Mo_6Cl_8)Cl_6]^{2-}$ at 52 °C. A reduction wave without reverse current is evident at about -1.20 V. Even at very fast scan rates, no reverse current is observed. Controlled potential electrolysis experiments conducted at potentials negative of this wave resulted in the destruction of the cluster. It was necessary to use neutral-basic melt, i.e., melt that is 50 mol % in $AlCl_3$ containing only enough extra chloride ion to convert the added $(Mo_6Cl_8)Cl_4$ to $[(Mo_6Cl_8)Cl_6]^{2-}$, in order to observe the oxidation of $[(Mo_6Cl_8)Cl_6]^{2-}$, which takes place at potentials more positive than the oxidation of chloride ion in the basic melt. A reversible redox couple corresponding to the electrode process

$$[(Mo_6Cl_8)Cl_6]^{2-} \rightleftharpoons [(Mo_6Cl_8)Cl_6]^{-} + e^{-} \qquad [2]$$

with a voltammetric half-wave potential, $E_{1/2}$, of 1.56 V was observed. The product of this oxidation appears to be stable on the voltammetric time scale. The Stokes-Einstein product for $[(Mo_6Cl_8)Cl_6]^{2-}$ is 1.6 X 10^{-10} g cm s^{-2} K^{-1}, and the oxidation product appears to be stable on the voltammetric time scale. Bulk oxidative electrolysis experiments that were carried out at a potential of 1.80 V were not successful in producing solutions of the oxidized species. The current decayed only slightly during the electrolysis, and the color of the solution changed from yellow to orange and finally to a brown color with the appearance of a precipitate. Termination of the bulk oxidative electrolysis experiment for only a short period of time or the addition of a drop or two of basic melt to the electrolyzed solution caused the solution to revert back to its original yellow color, indicating that the electrolysis product probably oxidizes a component of the melt and becomes reduced.

Spectropotentiostatic experiments performed on a solution of the molybdenum cluster yielded the results shown in Figure 2. Because the electrode area to solution volume ratio is quite large in this cell, it is possible to maintain a large steady-state concentration of electrogenerated product for simultaneous spectral analysis. The absorption band appearing at 480 nm along with the shoulder at 420 nm (obtained by subtracting the original spectrum from that for the oxidized product) are indicative of the formation of $[(Mo_6Cl_8)Cl_6]^-$. This species is known to be a powerful oxidant (12).

$[(Nb_6Cl_{12})Cl_6]^{2-}$. $[MeEtim]_2[(Nb_6Cl_{12})Cl_6]$ dissolved in the basic $AlCl_3$-MeEtimCl ionic liquid to produce dark green colored solutions of $[(Nb_6Cl_{12})Cl_6]^{4-}$, i.e., the former species oxidizes a component of the melt and becomes reduced in the process (13). Temperatures of ca. 100 °C were required for dissolution of this salt, and this temperature was maintained during all experiments.

Cyclic voltammograms of a solution of $[(Nb_6Cl_{12})Cl_6]^{4-}$ in the 49.0 mol % melt are shown in Figure 3. These are similar in appearance to cyclic voltammograms obtained in dichloromethane for species containing the $\{Nb_6Cl_{12}\}^{2+}$ cluster unit (13). Two successive one-electron reversible oxidation waves were observed in these basic melts, corresponding to the

$$[(Nb_6Cl_{12})Cl_6]^{4-} \rightleftharpoons [(Nb_6Cl_{12})Cl_6]^{3-} + e^- \qquad [3]$$

and

$$[(Nb_6Cl_{12})Cl_6]^{3-} \rightleftharpoons [(Nb_6Cl_{12})Cl_6]^{2-} + e^- \qquad [4]$$

electrode reactions. The $E_{1/2}$ values for these two oxidation processes are -0.010 and 0.391 V, respectively, in the 49.0 mol % melt. The Stokes-Einstein products for the $[(Nb_6Cl_{12})Cl_6]^{4-}$ and $[(Nb_6Cl_{12})Cl_6]^{3-}$ clusters are 1.12 X 10^{-10} and 1.19 X 10^{-10} g cm s^{-2} K^{-1}, respectively. It was possible to produce stable bulk solutions of the first oxidation product, $[(Nb_6Cl_{12})Cl_6]^{3-}$, but it was not possible to produce solutions of the one-electron oxidation product of this complex due to interference from oxidation of the melt. Transmission spectroelectrochemistry was also used to monitor these two oxidation processes as shown in Figure 4. The applied potential was stepped in small increments and an absorption spectrum was taken at each potential after the current had decayed to the background level. The transition from one oxidation state to another is clearly seen in this figure.

Solutions of $[(Nb_6Cl_{12})Cl_6]^{4-}$ also exhibited a single one-electron reversible electrode process centered near -1.30 V (Figure 3), corresponding to the following reaction:

$$[(Nb_6Cl_{12})Cl_6]^{4-} + e^- \rightleftharpoons [(Nb_6Cl_{12})Cl_6]^{5-} \qquad [5]$$

Efforts to electrolytically produce a bulk solution of the reduced species failed due to reduction of the melt since the reduction of the melt cation occurs much sooner at 100 °C than at room temperature. It was not possible to investigate this reduction process with the spectroelectrochemistry system because a black "sludge" was produced at the working electrode during the reduction process. Similar electrochemical and spectroscopic results were found for this cluster in the 44.4 mol % melt.

$[Re_2Cl_8]^{2-}$. Dissolution of $[Bu_4N]_2[Re_2Cl_8]$ into the basic melt produced blue-green solutions. Comparison of absorption spectroscopic data obtained for these solutions with literature values for this species verified that $[Re_2Cl_8]^{2-}$ was indeed the complex present in the melt (14). The dimer was found to be very stable in the melt, even at high temperatures.

A cyclic voltammogram taken of a solution of $[Re_2Cl_8]^{2-}$ in the 49.0 mol % $AlCl_3$-MeEtimCl ionic liquid, covering the nominal electroactive window of the melt, is shown in Figure 5a. The first redox couple is due to the reversible, one-electron electrode reaction

$$[Re_2Cl_8]^{2-} + e^- \rightleftharpoons [Re_2Cl_8]^{3-} \qquad [6]$$

The $E_{1/2}$ value of this reaction is -0.557 V. The Stokes-Einstein product for $[Re_2Cl_8]^{2-}$ was found to be 1.9 X 10^{-10} g cm s^{-2} K^{-1}. A navy-blue solution of $[Re_2Cl_8]^{3-}$ was produced when controlled potential electrolysis was performed on this solution at -0.71 V. This species is very sensitive to oxidation by oxygen and is very difficult to produce even in the supposedly oxygen-free environment of a nitrogen-filled glovebox. Figure 5b is a cyclic voltammogram of this reduced solution. The $E_{1/2}$ value for the oxidation process is indistinguishable from that for the reduction process. The Stokes-Einstein product for this species is 1.1 X 10^{-10} g cm s^{-2} K^{-1}. Further confirmation of the identity of the reduced species was made possible through spectropotentiostatic experiments like the one shown in Figure 6 and from near infrared spectral data. A Nernst plot that was constructed from the set of spectral data in Figure 6 had slope of 0.066 V, in good agreement with the predicted slope of 0.062 V at 40 °C for a one-electron reversible reaction. A near-infrared spectrum that was recorded for a solution of the reduced dimer contained an absorption band centered around 1460 nm as predicted (15). Similar electrochemical and spectroscopic results were obtained in the 44.4 mol % melt.

$[Re_3Cl_{12}]^{3-}$. The addition of Re_3Cl_9 to the basic ionic liquid produced deep red solutions of $[Re_3Cl_{12}]^{3-}$ as confirmed by UV-vis spectrophotometry experiments (16). This trimeric cluster was stable in the melt at low temperatures, but was converted to $[Re_2Cl_8]^{2-}$ in situ in a 1:1 ratio at temperatures exceeding 175 °C (17).

Figure 7a shows a cyclic voltammogram of a solution of Re_3Cl_9 in the 44.4 mol % melt. This voltammogram exhibits characteristics similar to that of $[Re_2Cl_8]^{2-}$, i.e., it appears to be a one-electron reversible process. The voltammetric half-wave potential of the first redox process is -0.439 V, and it shifts about 0.095 V/pCl unit as the melt composition is changed. For a reduction process in which the reduced species exhibits the same chloride coordination as the oxidized species, the shift in $E_{1/2}$ should be around 0.020 V/pCl unit (18). However, the shift in $E_{1/2}$ with pCl found during the reduction of $[Re_3Cl_{12}]^{3-}$ suggests that this process results in the loss of chloride ion and that x is probably 1:

$$[Re_3Cl_{12}]^{3-} + e^- \rightleftharpoons [Re_3Cl_{12-x}]^{(4-x)-} + xCl^- \qquad [7]$$

The Stokes-Einstein product for $[Re_3Cl_{12}]^{3-}$ is 1.3 X 10^{-10} g cm s^{-2} K^{-1}. Bulk potential electrolysis of a solution of $[Re_3Cl_{12}]^{3-}$ at an applied potential of -0.55 V caused the color of the solution to change from red to purple. A cyclic voltammogram of the reduced solution is shown in Figure 7b. The $E_{1/2}$ value for the first redox couple is the same as that for the unreduced solution, indicating that $[Re_3Cl_{12-x}]^{(4-x)-}$ is indeed the species produced. The Stokes-Einstein product for this species is 1.0 X 10^{-10} g cm s^{-2} K^{-1}. Figure 8 illustrates the results of a spectropotentiostatic experiment performed on a solution of $[Re_3Cl_9]$. A Nernst plot constructed from the spectral data in this figure had a slope of -0.066 V at 40 °C, confirming the reaction shown in Eq. [7].

REFERENCES

1. H. L. Chum and R. A. Osteryoung, in "Ionic Liquids", D. Inman and D. G. Lovering, Editors, pp. 407-423, Plenum Press, New York (1981).
2. C. L. Hussey, in "Advances in Molten Salt Chemistry", Vol. 5, G. Mamantov and C. B. Mamantov, Editors, pp. 185-230, Elsevier, Amsterdam (1983).
3. D. Appleby, C. L. Hussey, K. R. Seddon, and J. E. Turp, Nature, **323**, 614 (1986).
4. C. L. Hussey, Pure Appl. Chem., **60**, 1763 (1988).
5. T. B. Scheffler and C. L. Hussey, Inorg. Chem., **23**, 1926 (1984).
6. I-W. Sun and C. L. Hussey, Inorg. Chem., **28**, 2731 (1989).
7. E. H. Ward and C. L. Hussey, Anal. Chem., **59**, 213 (1987).
8. J. S. Wilkes, J. A. Levisky, R. A. Wilson, and C. L. Hussey, Inorg. Chem., **21**, 1263 (1982).
9. T. J. Barder and R. A. Walton, Inorg. Synth., **23**, 116 (1985).

10. J. C. Sheldon, J. Chem. Soc., 1007 (1960).

11. (a) M. Lipsztajn and R. A. Osteryoung, Inorg. Chem., **23**, 1735 (1984). (b) M. Lipsztajn and R. A. Osteryoung, Inorg. Chem., **24**, 716 (1985).

12. A. W. Maverick, J. S. Najdzionek, D. McKenzie, D. G. Nocera, and H. B. Gray, J. Am. Chem. Soc., **105**, 1878 (1983).

13. D. D. Klendworth and R. A. Walton, Inorg. Chem., **20**, 1151 (1981).

14. F. A. Cotton, N. F. Curtis, B. F. G. Johnson, and W. R. Robinson, Inorg. Chem., **4**, 326 (1965).

15. (a) J. R. Ebner and R. A. Walton, Inorg. Chim. Acta, **14**, L45 (1975). (b) B. E. Bursten, F. A. Cotton, P. E. Fanwick, G. G. Stanley, and R. A. Walton, J. Am. Chem. Soc., **105**, 2606 (1983).

16. R. A. Bailey and J. A. McIntyre, Inorg. Chem., **5**, 1940 (1966).

17. S. K. D. Strubinger, I-W. Sun, W. E. Cleland, and C. L. Hussey, Inorg. Chem., **29**, 993 (1990).

18. I-W. Sun, E. H. Ward, C. L. Hussey, K. R. Seddon, and J. E. Turp, Inorg. Chem., **26**, 2140 (1987).

ACKNOWLEDGEMENTS

This work was supported by National Science Foundation Grant CHE-8715464. S. K. D. S. acknowledges support through the United States Air Force Laboratory Graduate Fellowship Program. The authors acknowledge Dr. W. E. Cleland and Dr. Kenneth R. Seddon for synthesis of the $[Bu_4N]_2[Re_2Cl_8]$ and the $[MeEtim]_2$-$[(Nb_6Cl_{12})Cl_6]$ salts, respectively, and express their appreciation to Mr. B. J. Clark for his assistance in carrying out the spectroelectrochemistry experiments.

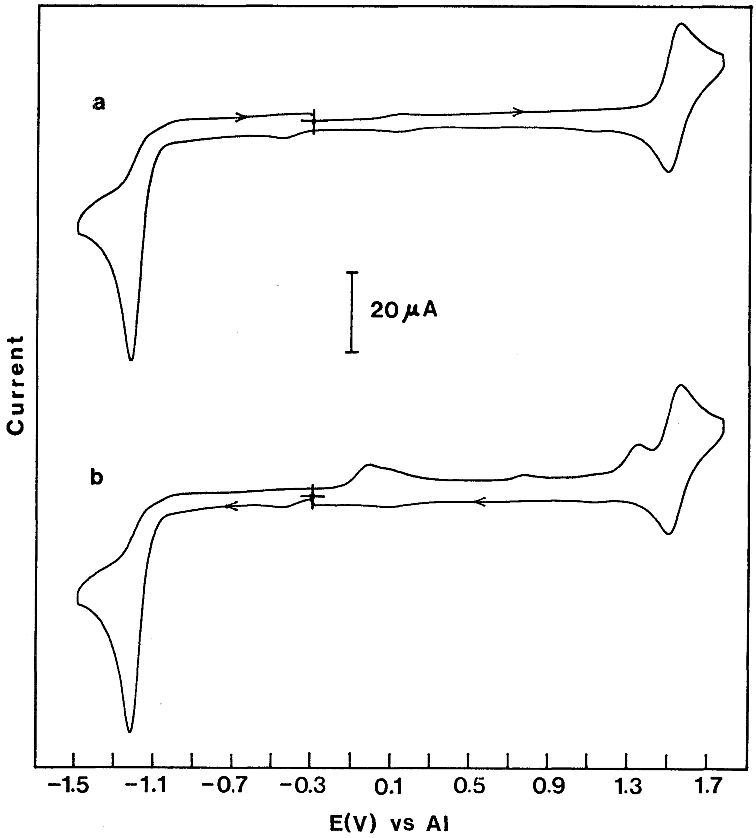

Figure 1. Cyclic voltammograms of a 5.34 x 10^{-3} M solution of molybdenum(II) chloride in 50.0 mol % $AlCl_3$-MeEtimCl at a glassy-carbon electrode at 53 °C: (a) positive-going sweep and (b) negative-going sweep. The scan rates were 100 mV s^{-1}.

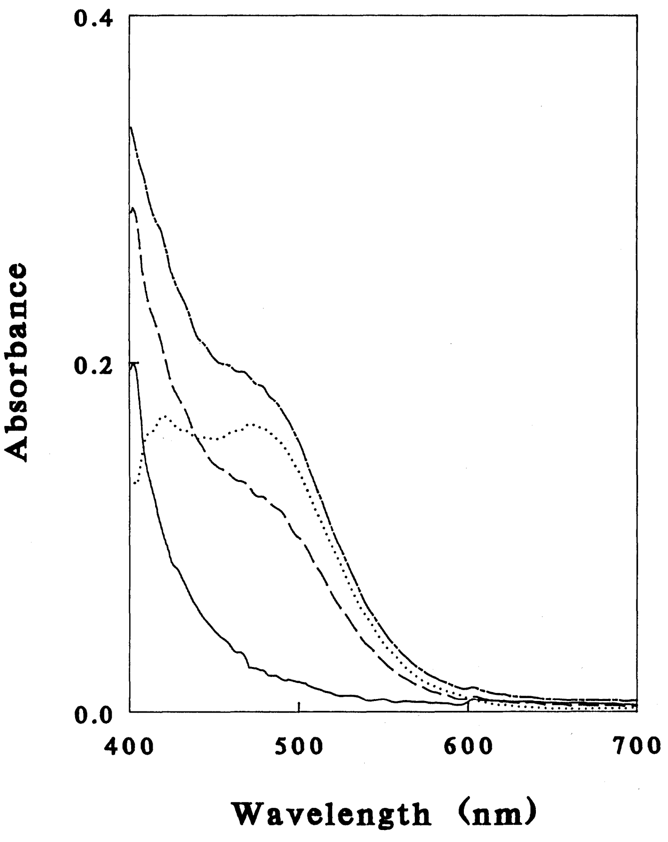

Figure 2. Visible absorption spectra recorded in the RGC-OTE cell at 40 °C during controlled potential oxidation of a 1.97 x 10^{-3} M solution of $[(Mo_6Cl_8)Cl_6]^{2-}$ in 50.0 mol % $AlCl_3$-MeEtimCl at an applied potential of 1.80 V: (——) open circuit, (— —) at some intermediate time during the electrolysis, (—-—) after steady-state conditions were achieved, and (·····) difference between the latter spectrum and the background spectrum.

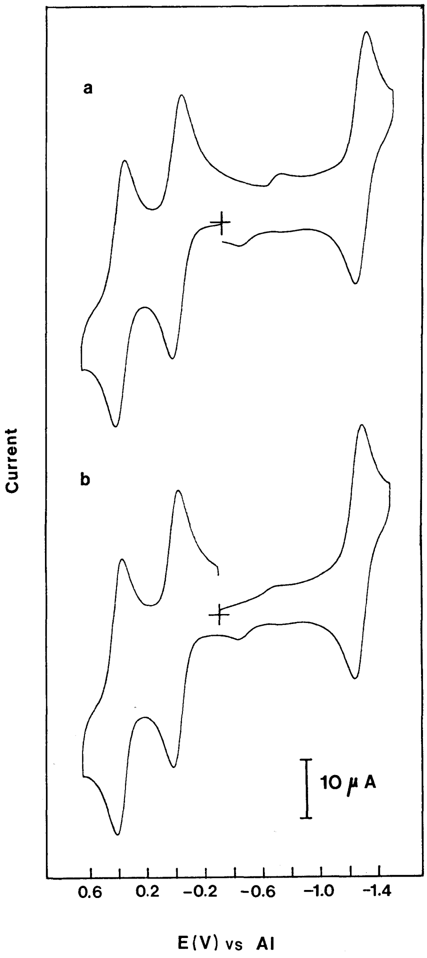

Figure 3. Cyclic voltammograms of a 4.70 x 10^{-3} M solution of $[MeEtimCl]_2$-$[(Nb_6Cl_{12})Cl_6]$ in 49.0 mol % $AlCl_3$-MeEtimCl at a glassy-carbon electrode at 97 °C: (a) positive-going sweep and (b) negative-going sweep. The scan rates were 100 mV s^{-1}.

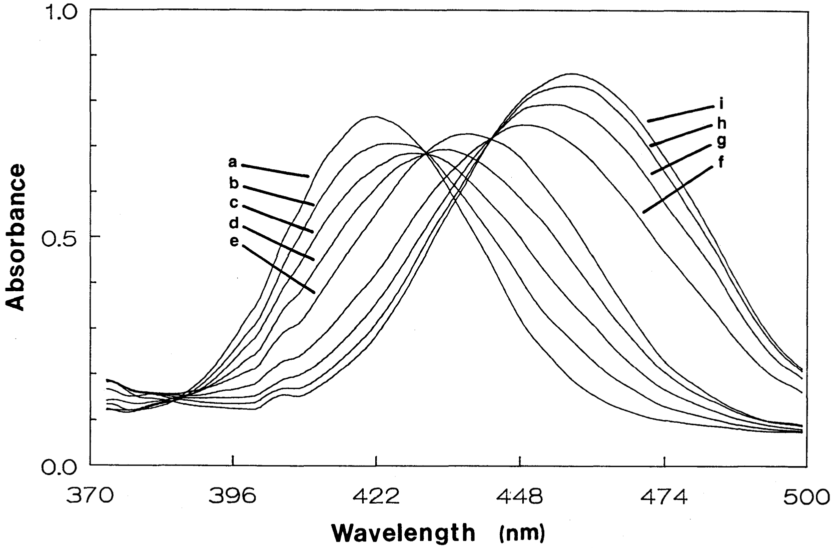

Figure 4. Visible absorption spectra of a 5.4 x 10^{-4} M solution of $[MeEtimCl]_2$-$[(Nb_6Cl_{12})Cl_6]$ in 49.0 mol % $AlCl_3$-MeEtimCl ionic liquid recorded in the RGC-OTE cell at 40 °C at various potentials (V): (a) -0.30, (b) 0.24, (c) 0.27, (d) 0.30, (e) 0.33, (f) 0.51, (g) 0.54, (h) 0.57, and (i) 0.63.

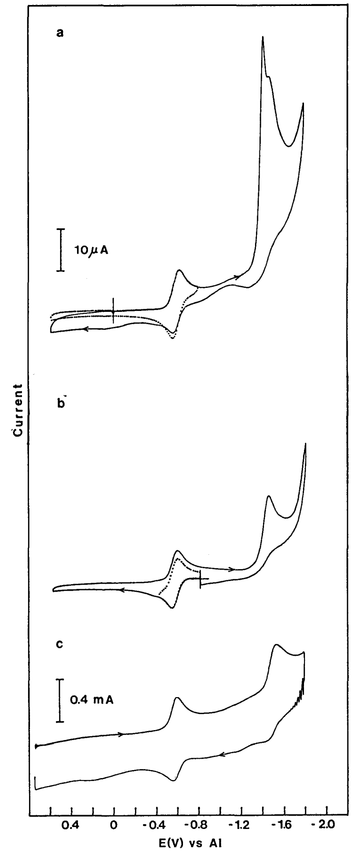

Figure 5. Cyclic voltammograms of dimeric rhenium chloride complexes at a glassy-carbon electrode in 49.0 mol % $AlCl_3$-MeEtimCl at 40 °C: (a) 3.55 x 10^{-3} $[Bu_4N]_2[Re_2Cl_8]$ at a scan rate of 50 mV s^{-1}; (b) solution in (a) after exhaustive reduction at -0.71 V (note: the scan rate was the same as in (a)); and (c) 5.73 x 10^{-3} M $[Bu_4N]_2[Re_2Cl_8]$ at a scan rate of 20 V s^{-1}.

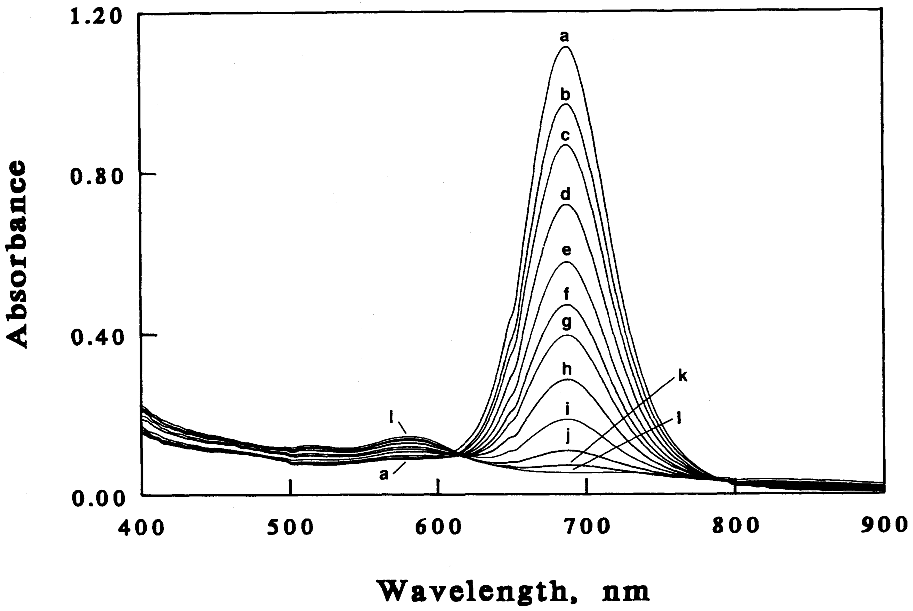

Figure 6. Absorption spectra of a 5.53 x 10^{-3} M solution of $[Bu_4N]_2[Re_2Cl_8]$ in 49.0 mol % $AlCl_3$-MeEtimCl at 40 °C in the RGC-OTE cell at various potentials (V): (a) open circuit, (b) -0.480, (c) -0.506, (d) -0.529, (e) -0.545, (f) -0.556, (g) -0.565, (h) -0.581, (i) -0.600, (j) -0.625, (k) -0.648, and (l) -0.800.

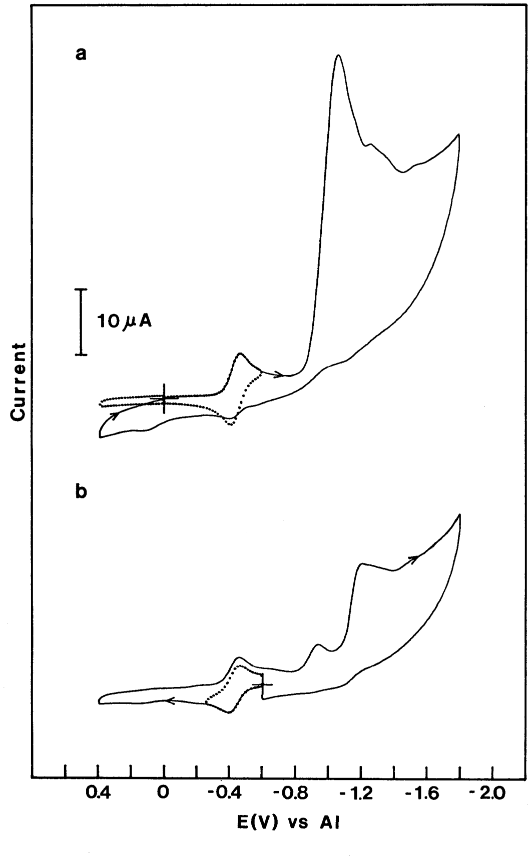

Figure 7. Cyclic voltammograms of trimeric rhenium chloride complexes at a glassy-carbon electrode in 44.4 mol % $AlCl_3$-MeEtimCl at 40 °C: (a) 3.80×10^{-3} M Re_3Cl_9 and (b) solution in (a) after exhaustive reduction at -0.60 V. The scan rates were 50 mV s^{-1}.

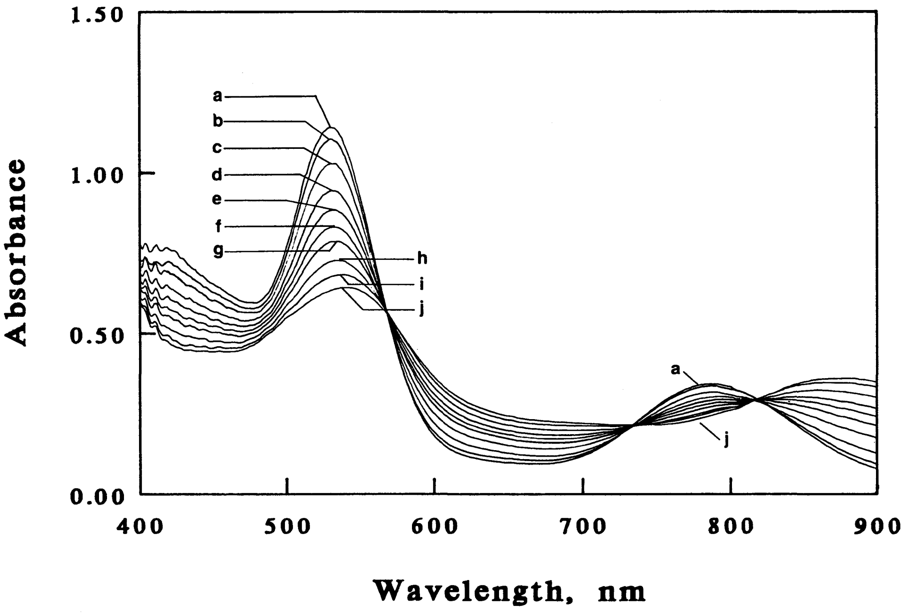

Figure 8. Absorption spectra of a 6.08 x 10^{-3} M solution of Re_3Cl_9 in 49.0 mol % $AlCl_3$-MeEtimCl at 40.0 °C in the RGC-OTE cell at various potentials (V): (a) open circuit, (b) -0.266, (c) -0.303, (d) -0.325, (e) -0.340, (f) -0.352, (g) -0.364, (h) -0.383, (i) -0.405, and (j) -0.550.

DOI: 10.1149/199017.0383PV

MECHANISM OF CADMIUM DEPOSITION FROM AN ACIDIC CHLOROALUMINATE MELT

Rajeeva R. Agarwal

Department of Chemical Engineering
University of Connecticut
Storrs, CT 06269

ABSTRACT

Cyclic voltammetry was applied to study cadmium deposition on nickel from purified $AlCl_3$-NaCl-$BaCl_2$ (Eut., 50°C) containing 2.1 and 4.25 wt.% $CdCl_3$. Both diffusion and adsorption peaks formed between 1-1000 mV/s and 95-175°C. Whereas cadmium deposition gave three peaks, its dissolution involved three to five peaks. Based on the formation of Cd^{2+} and Cd_2^{2+} ions in chloroaluminate melts, a mechanism involving step-wise electrochemical reactions, intermediates, adsorption, disproportionation, and lattice incorporation is deduced for cadmium deposition.

INTRODUCTION

Molten solutions of cadmium chloride in aluminum chloride or chloroaluminates ($AlCl_3$ melts) form the complexes, $Cd(AlCl_4)_2$ and $Cd_2(AlCl_4)_2$ (1-2). Acidic melts (> 50 mole % $AlCl_3$) stabilize the cadmium subhalide as $Cd_2(AlCl_4)_2$ (2). During cadmium deposition from such melts, one expects to note the above and the overall chemical (3) and electrochemical reactions (4-5). In this work (6), (in mole percent) 63.5 $AlCl_3$-34 NaCl-2.5 $BaCl_2$ (mp= 50°C) (7) containing (in weight percent) 2.1 and 4.25 $CdCl_2$ was studied between 95-175°C under a helium atmosphere.

EXPERIMENTAL

Cadmium electrochemistry was studied in the following electrochemical cell:

$$Cd/\ AlCl_3\text{-}NaCl\text{-}BaCl_2\ (Eut.),\ CdCl_2/\ Ni$$

where an excess 8.8 wt.% $AlCl_3$ was added. The melt was purified by constant potential electrolysis between aluminum electrodes, and then $CdCl_2$ (99.995%) was added to the chloroaluminate melt. A cadmium (99.998%) counter electrode was used, and the working electrode consisted of a 5 mm dia. nickel disc electrode in teflon. The working electrode was replaceable between the experiments.

The electrolyte was contained inside a thick-walled pyrolytic coated graphite crucible. A well-fitted teflon cover carried the electrodes and a chromel-alumel thermocouple. The nickel working electrode was typically polished to 0.05 microns. The actual melting point of the melt varied from 66 to 83°C.

Cadmium deposition and dissolution was studied by cyclic voltammetry in 2.1 and 4.25 wt.% $CdCl_2$ solutions. Experiments were carried out at 1-1000 mV/s and at constant temperatures between 95-175°C. Typically, potentials were first scanned between nickel dissolution and aluminum deposition. Then cadmium peaks were individually separated from these and the background peaks. All potential scans were carried out after steady-state rest potentials were achieved.

RESULTS AND DISCUSSION

Figure 1 shows the cyclic voltammetric cadmium peaks soon after the addition of $CdCl_2$ (2.1% by wt.) to the melt, at 100 mV/s and 172°C. Peaks 1-2-3 and 1′-2′-3′ appeared during cadmium deposition and dissolution, respectively. With an increase in the scan rate (1000 mV/s), 3′ decreased, 2′ increased and became symmetrical, and the apparent peak current ratio $ip_{2'}/ip_{3'}$ >1. At lower temperatures, peaks were smaller (lower fluxes) and 3′ appeared at smaller scan rates (20 mV/s). In 4.25% $CdCl_2$, the ratio $ip_{2'}/ip_{3'}$ reduced to <1 as the scan rate was decreased from 1000 to 100 mV/s at 170-119°C. Based on the redox potential range, it was concluded that 1-1′ was the Cd^{2+}/Cd_2^{2+} couple; 2-2′ and 3-3′ were due to the cadmium monolayer and its bulk deposition-dissolution, respectively.

Further, in 4.25% $CdCl_2$ melt the peak currents 3-3′ increased but 1 remained about the same. Moreover, the $E_{equ.}$ became more cathodic, the concentration overpotentials (E_p-$E_{equ.}$) for 1 decreased and for 1′ increased. Thus, the Cd_2^{2+} ions appeared to stabilize when Cd^{2+} ions were added. This was an indication of complexation. Also, 1′ became symmetrical and was composed of a pair of pre and post peaks.

Figure 2 shows the CV in 2.1% $CdCl_2$ melt at 1 and 4 mV/s and 119°C. At low scan rates (1-10 mV/s), resolution of peaks 2-2′ was weak, thus other peaks could be studied. The peak current of 1 was diffusion limited, but "z" based on $E_p-E_{p/2}$ increased from 2 to 2.8 between 172-118°C. Further, peak 3 was diffusion limited with z=1 [8] and only 72-78% of the cadmium was recovered in peak 3′ at 118°C. Finally, the peak current of 3′ varied with scan rate according to the product-adsorbed CV theory (9).

In 4.25% $CdCl_2$ melt, the peak currents and potentials for 3 showed quasi-reversible form between 2-100 mV/s (the effect of convection became appparent at 1 mV/s and at the higher temperature) and 170-120°C. But $ip/v^{1/2}$ decayed with an increase in scan rate (10), which indicated disproportionation at the cadmium surface during slow scan rates. Also, as expected from the disproportionation reaction, there was an excess of dissolved cadmium in the melt.

From the above studies, a mechanism for cadmium deposition from an acidic chloroaluminate melt would be expected to involve step-wise electrochemical reactions, adsorption, disproportionation, and lattice incorporation steps. This is described below:

$$Cd^{2+} + e^- \longrightarrow Cd^+ \text{ (ad)} \qquad [1]$$

$$2Cd^+ \text{ (ad)} \longrightarrow Cd_2^{2+} \qquad [2]$$

$$Cd^+ \text{ (ad)} + e^- \longrightarrow Cd \text{ (ad)} \qquad [3]$$

$$Cd_2^{2+} + e^- \longrightarrow Cd_2^+ \text{ (ad)} \qquad [4]$$

$$Cd_2^+ \longrightarrow Cd \text{ (ad)} + Cd^+ \text{ (ad)} \qquad [5]$$

$$Cd \text{ (ad)} \longrightarrow Cd \text{ (incorp.)} \qquad [6]$$

$$Cd^{2+} + Cd \longrightarrow Cd_2^{2+} \qquad [7]$$

Further, one would expect that the cadmium adsorption, surface diffusion, and lattice incorporation are affected by temperature and substrate.

SUMMARY

The deposition and dissolution of cadmium was studied from a new acidic chloroaluminate melt, $AlCl_3$-NaCl-$BaCl_2$ (Eut., 50°C) containing 2.1 and 4.25 wt.% $CdCl_2$, by cyclic voltammetry on nickel electrode and against the cadmium reference. Multiple diffusion and adsorption peaks formed between 1-1000 mV/s and 95-175°C. Based on the formation of Cd^{2+} and Cd_2^{2+} ions in the chloroaluminates, a step-by-step mechanism is deduced for the cadmium "deposition" onto nickel from the cyclic voltammograms obtained.

ACKNOWLEDGEMENT

The author is thankful to Dr. P. A. Nelson (Argonne National Laboratory), Professors D. T. Wasan and P. Nash (Illinois Institute of Technology) for their support during his work at the Argonne National Laboratory as a PhD Thesis Laboratory Participant.

REFERENCES

1. J. D. Corbett, W. J. Burkhard, and L. F. Druding, J. Am. Chem. Soc., 83, 76, (1961).

2. J. D. Corbett, and R. K. McMullan, J. Am. Chem. Soc., 78, 2906, (1956).

3. K. Grjotheim, F. Gronvold, and J. Krogh-Moe, J. Am. Chem. Soc., 77, 5824, (1955).

4. T. C. F. Munday and J. D. Corbett, Inorg. Chem., 5, 1263, (1966).

5. D. A. Hames and J. A. Plambeck, Can. J. of Chem., 46, 1727, (1968).

6. R. R. Agarwal, "Electrodeposition, Nucleation, and Film Formation of Cadmium from a Low Melting Molten Salt", PhD Preliminary Thesis, Illinois Institute of Technology, Chicago, Illinois, (1988).

7. G. J. Janz, R. P. T. Tomkins, and C. B. Allen, "Physical Properties Data Compilations Relevant to Energy Storage I. Molten Salt: Eutectic Data ". Report NSRDS-NBS 61, Part 1, (1978).

8. G. Mamantov, D. L. Manning, and J. M. Dale, J. Electroanal. Chem., 9, 253, (1965).

9. R. H. Wopschall and I. Shain, Anal. Chem., 39, 1514, (1967).

10. R. S. Nicholson and I. Shain, Anal. Chem., 36, 706, (1964).

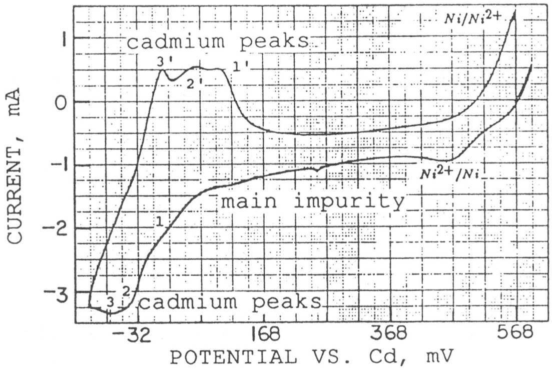

Figure 1. Cyclic voltammogram after the addition of $CdCl_2$ (2.1 Wt.%) to purified $AlCl_3$-NaCl-$BaCl_2$ (Eut., 50°C) melt containing 8.8 Wt.% excess $AlCl_3$, at 100 mV/s and 172°C on nickel (0.306 cm^2), against a cadmium reference. Peaks 1-2-3 and 1′-2′-3′ appeared during cadmium deposition and dissolution respectively.

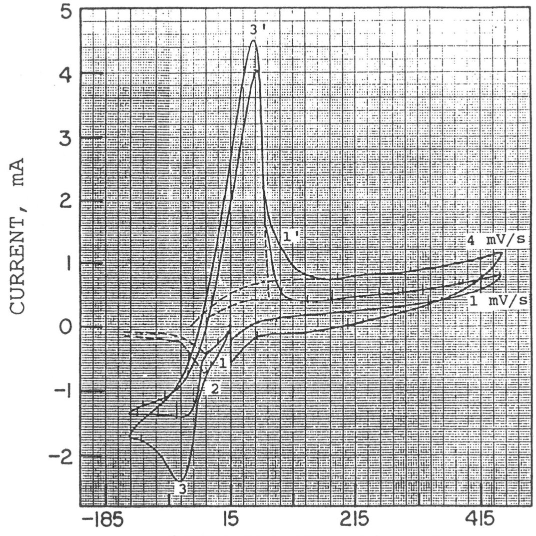

Figure 2. Cyclic voltammogram in purified $AlCl_3$-NaCl-$BaCl_2$ (Eut., 50°C), $CdCl_2$ (2.1 Wt.%) melt containing 8.8 Wt.% excess $AlCl_3$, at 1 mV/s and 4 mV/s, and 119°C on nickel (0.306 cm^2), against a cadmium reference. Peaks 1-2-3 and 1′-3′ formed during cadmium deposition and dissolution respectively.

DOI: 10.1149/199017.0389PV

KINETIC AND TRANSPORT PROCESSES FOR $FeCl_3$ AND $CuCl_2$ POSITIVE ELECTRODES IN LOW TEMPERATURE MOLTEN SALTS

Sarah E. Mancini and Francis M. Donahue

Chemical Engineering Department
The University of Michigan
Ann Arbor, MI 48109-2136

ABSTRACT

The transport and kinetic properties of $FeCl_3$ and $CuCl_2$ in acidic mixtures of 1-methyl-3-ethylimidazolium chloride and aluminum chloride were determined at a rotating glassy carbon disk electrode. These properties are necessary for evaluation of a model of battery positive electrodes which has been developed. Development of a quantitative analytical technique for determination of the metal chloride species in the melt would have been helpful for monitoring the distribution of active material within the electrode. Quantitative analysis for $FeCl_3$, $FeCl_2$, $CuCl_2$, CuCl in acidic melts was attempted using UV-Vis spectroscopy. Quantitative analysis for $FeCl_3$ in acidic melts was also attempted using chronopotentiometry.

INTRODUCTION

Recently secondary Al/$FeCl_3$ and Al/$CuCl_2$ batteries were tested using acidic mixtures of 1-methyl-3-ethlyimidazolium chloride (MEIC) and $AlCl_3$ as the electrolyte (1,2). Reticulated vitreous carbon was used as the positive current collector. The positive reactant ($FeCl_3$ or $CuCl_2$) was introduced into the current collector by an evaporative impregnation process. The overall reactions for these batteries are

$$Al + 3FeCl_3 = AlCl_3 + 3FeCl_2 \qquad 1$$

and

$$Al + 3CuCl_2 = AlCl_3 + 3CuCl \qquad 2.$$

Figure 1 shows the discharge curves for an Al/$FeCl_3$ battery at discharge currents of 20, 50, and 70 mA. One observes that utilization of the positive reactant is dependent upon the discharge current (decreases with increasing current).

The reactions occurring at the positive electrode in these batteries are:

$$FeCl_3 + Al_2Cl_7^- + e^- = FeCl_2 + 2AlCl_4^- \qquad 3$$

and

$$CuCl_2 + Al_2Cl_7^- + e^- = CuCl + 2AlCl_4^- \qquad 4$$

where the iron and copper chlorides are assumed to be present as solids. Improvements in polarization and utilization of the positive electrode materials were observed when the specific area of the positive current collector was increased (2). Further, cycling of the batteries (charging and discharging at constant current) has shown an improvement in cell capacity as the cycling progresses (2). It is believed that there may be redistribution of the active material within the RVC matrix through a dissolution/precipitation mechanism. Cell polarization and utilization are believed to be associated with the coupled effects of kinetics and transport of the active species within the positive current collector. The kinetic processes are enhanced by the available surface area of the collector matrix while the transport processes are facilitated by the open pore structure.

A mathematical model of the steady state electrochemical behavior of metal chlorides in porous electrode matricies has been developed in terms of the kinetic and transport properties of the metal chlorides, the electrolyte, and the physical properties of the porous electrode (3). This model is an extension of one developed by Austin (4). The solution to the mathematical model of the porous electrode will be included here to highlight the important parameters of porous electrode operation. Two forms of the solution exist, the current density distribution in the electrode, i (mA/cm^2):

$$i = nFk^o([A]_b \exp\Phi_c - 2[B]_b \exp\Phi_a)$$

$$(\exp(zP) + \exp(-zP)/(\exp(LP) + \exp(-LP)) \qquad 5$$

where the P is:

$$(k^o A_v / D_{Am} \epsilon)^{1/2} (4\exp\Phi_a + \exp\Phi_c)^{1/2}.$$

and the total current, I (mA), the equation which describes the macroscopic polarization behavior of the electrode:

$$I = (nFk^o A_v A_{xs} / P)([A]_b \exp\Phi_c - 2[B]_b \exp\Phi_a)$$

$$(\exp(LP) - \exp(-LP)/(\exp(LP) + \exp(-LP)) \qquad 6.$$

Definitions of the parameters appearing in these equations are given in Table 4.

The current or electrode potential are the adjustable parameters of the model. The electrode potential appears in equations 5 and 6 in the dimensionless potential terms, Φ_c and Φ_a:

$$\Phi_c = (\varphi^o - \varphi_i)/\beta_c \qquad 7$$

$$\Phi_a = (\varphi^o - \varphi_i)/\beta_a \qquad 8$$

where φ_i is the perturbed potential, φ^o is the standard electrode potential, and β is the anodic or cathodic Tafel slope. Modeling and analysis of the discharge-charge behavior of the metal chloride positive electrodes requires the evaluation of the parameters appearing in equations 5 and 6. The current density distribution equation permits calculation of the reaction distribution in the electrode. Development of a quantitative analytical technique for the determination of metal chloride species in the melt would be useful to evaluate the distribution of $FeCl_3/FeCl_2$ and $CuCl_2/CuCl$ in the porous matrix as a function of the history of the electrode.

The electrochemical and spectrochemical properties of the electrolytes and redox systems under consideration here have been studied by others, e.g. the binary electrolyte (5), iron chloride (6-8), copper chloride (9, 10), and $Al_2Cl_7^-$ reduction (11, 12).

This paper focuses on the estimation of the appropriate chemical and physical properties for evaluation of the model.

EXPERIMENTAL

The synthesis and purification of the MEIC was conducted in a manner similar to that of Wilkes and coworkers (5). Aluminum chloride (Fluka) was purified by vacuum sublimation. Anhydrous $FeCl_3$ (Fisher), $FeCl_2$ (Cerac), $CuCl_2$ (Cerac), and CuCl (Cerac) were not purified further. All experiments were conducted under a helium and nitrogen atmosphere in a Vacuum Atmoshperes Company glove box at ambient temperature. The moisture level was maintained below 1 ppm and the oxygen level was maintained below 10 ppm. The temperature within the dry box was measured daily.

The binary mole fraction of $AlCl_3$ in the test electroyte was 0.58 except for the aluminum transport experiments which were conducted in a 0.505 electrolyte. The iron and copper chlorides were introduced into the test electrolyte as the anhydrous solids. Viscosities of several of the ternary and binary solutions were measured using a Brookfield Model LVTD plate and cone viscometer. These measurements were conducted at 25°C. UV-Vis spectra of the binary and ternary solutions were obtained with a Hewlett Packard 845IA Diode Array Spectrophotometer using a 1 cm path length.

The $FeCl_3$ and $CuCl_2$ transport and kinetic experiments were conducted with a rotating glassy carbon disk electrode, RGCDE (Pine Instruments). The $Al_2Cl_7^-$ transport experiments were conducted using an aluminum disk electrode fabricated in-house consisting of a 6.25 mm aluminum rod (Alfa Products, m5N) which was insulated on the sides by a PTFE sleeve 3.25 mm thick. Rotation of the working electrodes was provided by a Pine Rotator (Model MSR). The reference electrode was an aluminum plated platinum wire immersed in a 0.505 melt and separated from the working electrode compartment by an ultra-fine porosity glass frit (Witeg Scientific, Anaheim, CA.; Catalog # 2.350.P5). The aluminum cylinder counter electrode (Alpha Products, m5N) was also separated from the working electrode compartment by a fine porosity glass frit (Catalog # 2.350.P5). The electrochemical measurements were made using a PARC Model 273 Potentiostat-Galvanostat equipped with a current interrupt IR compensation device. The data were collected and stored on an IBM PC/XT using the PARC Headstart software.

RESULTS

UV-Vis spectroscopy was chosen as the quantitative analytical technique for determination of the metal chloride species in the melt. Absorption data for the metal chloride species ($FeCl_3$, $FeCl_2$, $CuCl_2$, and CuCl) in the melt was obtained by pointwise subtraction of the binary melt spectrum from the ternary melt spectrum for each of the metal chlorides. The resulting absorption peak was attributed to the metal chloride. Table 1 shows the absorbance wavelength regions for each of the metal chloride species and the binary melt. The spectroscopic results indicate that the metal chlorides and the melt absorb in the same wavelength region. While UV-Vis spectroscopy proved unsuccessful as a quantitative analytical technique, chronopotentiometry of $FeCl_3$ ternary solutions indicated that this technique may be useful.

Figures 2 and 3 are linear sweep voltammograms (scan rate = 5mV s^{-1}, 1000 RPM) for $FeCl_3$ reduction and $CuCl_2$ reduction, respectively, at a RGCDE in the test electrolyte. In the case of $FeCl_3$, both kinetic (charge transfer) and mass transport controlled regions are observed. The Tafel slope and exchange current density for this redox reaction were obtained from slow potential sweeps (scan rates 0.5 to 0.25 mV s^{-1}) in the kinetic controlled region (see Table 2). The linear sweep voltammogram for $CuCl_2$ reduction indicates that this reaction is immediately transport controlled. In this case the limiting current provides a lower bound for the exchange current density of this reaction.

Diffusion coefficients for $FeCl_3$ and $CuCl_2$ species and $Al_2Cl_7^-$ were computed from limiting current measurements at RDE. The computed diffusivities and the $D\mu/T$ quantities for the species are presented in Table 3.

DISCUSSION

The exchange current densities cannot be used directly in the model while the Tafel slopes can. The exchange current densities are used to compute the standard specific rate constant used in the model. For example the standard specific rate constant for $FeCl_3$ reduction can be estimated from

$$k^o = i_o/\{nF[FeCl_3]\} \qquad 9.$$

The mean value, based on the data in Table 2, is $8 \cdot 10^{-6}$ cm/s. Other investigators have reported values on the order of 10^{-4} (6) and 10^{-5} (7), at 30 and 40 °C, respectively. These data were obtained by using a technique proposed by Galus and Adams (13).

Since there were no Tafel data for the copper system, i.e. cupric ion reduction was immediately mass transport limited, neither exchange current density nor Tafel slope could be determined. The limiting current density, $49 \cdot 10^{-3}$ mA/cm^2, was used as a lower bound for the exchange current density in the calculation of the standard specific rate constant. The mean value was $3 \cdot 10^{-4}$ cm/s. Nanjundiah and Osteryoung found values on the order of $3 \cdot 10^{-4}$ at 40°C in basic BPC melts (9). Since the Tafel slope obtained for ferric chloride reduction was consistent with a one electron transfer process, this value was used as a basis for the Tafel slope for the cupric/cuprous reaction in the model.

The diffusivity of $Al_2Cl_7^-$ is required for the model (see Eq. 3-6). The value of the $D\mu/T$ quantity computed here is approximately twice that reported by Donahue and Wilkes, $1.3 \cdot 10^{-10}$, in similar melts (11). Robinson and Osteryoung, using multiple techniques and three different electrodes, obtain diffusivities in the range 3.5 - 10 $\cdot 10^{-7}$ cm^2/s (12).

The remaining $D\mu/T$ groups, while not necessary for the model, permit direct comparison with these measurements and those of others. $D\mu/T$ for the $FeCl_3$ species is in agreement with that obtained in n-butyl pyridinium chloride/aluminum chloride ($BPC/AlCl_3$) melts using limiting current measurements (7). The $D\mu/T$ quantities for the iron and copper species are smaller than those reported by others in similar systems (8) and (9, 10), respectively. Nevertheless, these $D\mu/T$ data are consistent with suggestions that the Cu(II) is complexed as $Cu(AlCl_4)_4^{-2}$ (9) while the Fe(III) complex is suggested to be $FeCl_4^-$ (7).

Using the estimated kinetic and transport parameters and the physical properties for 80 ppi RVC, the total current equation can be revised for the specific cases of the $FeCl_3$ and $CuCl_2$ porous electrodes using a 0.58 electrolyte. The evaluated model parameters specific for each reaction are shown in Table 5. The revised equation for the $FeCl_3$ electrodes is:

$$I=(1.95\cdot 10^5/P)(2[B_b]\exp\Phi_a - [A_b]\exp\Phi_c)$$

$$(\exp(LP)-\exp(-LP)/(\exp(LP)+\exp(-LP)) \qquad 10$$

where P is:

$$(26.7)(4\exp\Phi_a+\exp\Phi_c)^{1/2}.$$

The revised equation for the $CuCl_2$ electrodes is:

$$I=(7.30\cdot 10^6/P)(2[B_b]\exp\Phi_a - [A_b]\exp\Phi_c)$$

$$(\exp(LP)-\exp(-LP)/(\exp(LP)+\exp(-LP)) \qquad 11$$

where P is:

$$(163)(4\exp\Phi_a+\exp\Phi_c)^{1/2}.$$

The remaining parameters in the model are the operating parameters - either current or potential.

REFERENCES

1. L. R. Simonsen and F. M. Donahue, Proceedings 33rd International Power Sources Symposium, Electrochemical Society, Inc., Pennington (NJ), pp. 346-350, (1988).

2. F. M. Donahue, S. E. Mancini, and L. R. Simonsen, Department of Defense (Air Force) SBIR Final Report, Contract No. F33615-88-C-2689, (March 1989).

3. S. E. Mancini and F. M. Donahue, unpublished results.

4. L. G. Austin in Handbook of Fuel Cell Technology, C. Berger, ed., Prentice-Hall, Inc., 1968.

5. J. S. Wilkes, J. A. Levisky, R. A. Wilson, and C. L. Hussey, Inorg. Chem., **21**, 1263 (1982).

6. C. L. Hussey, L. A. King, and J. S. Wilkes, J. Electroanal. Chem., **102**, 321, (1979).

7. C. Nanjundiah, K. Shimizu, and R. A. Osteryoung, J. Electrochem., **129**,

2474, (1982).

8. M. Lipsztajn and R. A. Osteryoung, Inorg. Chem., **24**, 716, (1985).

9. C. Nanjundiah and R. A. Osteryoung, J. Electrochem. Soc., **130**, 1312, (1983).

10. C. L. Hussey, L. A. King, and R. A. Carpio, ibid., **126**, 1029, (1979).

11. F. M. Donahue and J. S. Wilkes, International Soc. of Electrochem. Extended Abstracts, Berkeley (CA), pp. 541-543, (1984).

12. J. Robinson and R. A. Osteryoung, J. Electrochem. Soc., **127**, 122, (1980).

13. Z. Galus and R. N. Adams, J. Phys. Chem., **67**, 866, (1963).

Table 1. Spectroscopic Data for Copper Chlorides and Iron Chlorides in 0.58 $AlCl_3$/MEIC.

System	λ_{abs} (nm)
Blank Binary	183-244
$FeCl_3$ Ternary	258,358
$FeCl_2^-$ Ternary	244
$CuCl_2^-$ Ternary	248,334
$CuCl^-$ Ternary	249

Table 2. Tafel Slopes and Exchange Current Densities for $FeCl_3$ in X=0.58 $AlCl_3$/MEIC

10^6 $FeCl_3$ (mole/cm^3)	10^6 i_o (A/cm^2)	b_2 (mV)
4.15	6.2	132
4.70	1.6	133
7.62	3.8	143
AVERAGE		136

Table 3. D and Dμ/T for $FeCl_3$, $CuCl_2$, and $Al_2Cl_7^-$ in $AlCl_3$/MEIC

10^6 $FeCl_3$ (mole/cm^3)	10^7 D (cm^2/s)	10^{10} Dμ/T (gcm/s^{2}K)
3.18	7.4	3.6
11.9	7.6	3.7
18.3	7.3	3.6
32.7	6.0	2.9
AVERAGE	7.1	3.5

10^6 $CuCl_2$ (mole/cm^3)	10^7 D (cm^2/s)	10^{10} Dμ/T (gcm/s^{2}K)
1.51	2.0	1.0
1.53	2.5	1.2
1.54	1.3	0.6
1.57	1.8	0.9
AVERAGE	1.9	0.9

10^5 $Al_2Cl_7^-$ (mole/cm^3)	10^7 D (cm^2/s)	10^{10} Dμ/T (gcm/s^{2}K)
9.26	5.7	3.2
9.26	5.1	2.8
AVERAGE	5.4	3.0

Table 4. Model Parameters

Adjustable Parameters	
Φ_a	Anodic dimensionless potential
Φ_c	Cathodic dimensionless potential
i	Current density (mA/cm^2)
I	Total apparent current (mA)
Constant Parameters	
n	Number of electrons transferred in electrochemical reaction (eq/mole)
F	Faraday's constant, 96,500 (coul/eq)
k^o	Standard specific rate constant (cm/s)
A_b	Bulk concentration $Al_2Cl_7^-$ (mole/cm^3)
B_b	Bulk concentration $AlCl_4^-$ (mole/cm^3)
L	Electrode thickness (cm)
D_{am}	Diffusion coefficient of $Al_2Cl_7^-$ with respect to mixture (cm^2/s)
A_{xs}	Cross-sectional area of electrode perpendicular to current flow (cm^2)
A_v	Specific area of electrode (cm^2/cm^3)
ϵ	Porosity of electrode

Table 5. Model Parameters for $X=0.58$ $AlCl_3$/MEIC and 80 ppi RVC.

Parameters		$FeCl_3$	$CuCl_2$
n	(eq/mole)	1	1
F	(coul/eq)	96,500	96,500
k^o	(cm/s)	$8 \cdot 10^{-6}$	$3 \cdot 10^{-4}$
A_b	(mole/cm^3)	$1.54 \cdot 10^{-3}$	$1.54 \cdot 10^{-3}$
B_b	(mole/cm^3)	$2.51 \cdot 10^{-3}$	$2.51 \cdot 10^{-3}$
L	(cm)	0.48	0.48
D_{am}	(cm^2/s)	$5.96 \cdot 10^{-7}$	$5.96 \cdot 10^{-7}$
A_{xs}	(cm^2)	4.9	4.9
A_v	(cm^2/cm^3)	51.5	51.5
ϵ		0.97	0.97

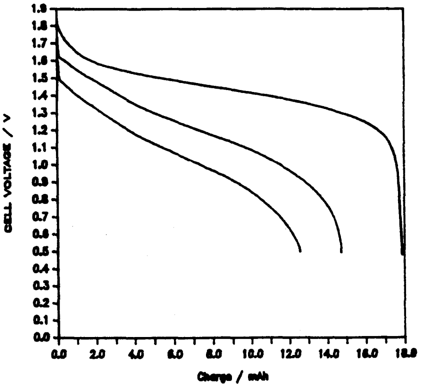

Figure 1. Discharge curves for an Al/$FeCl_3$ battery at discharge currents of 20, 50, and 70 mA.

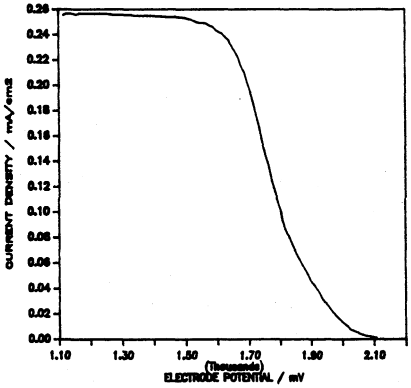

Figure 2. Linear sweep voltammogram for Fe(III) reduction at a RGCDE in 0.58 $AlCl_3$/MEIC (3.0 mM Fe(III) scan rate = 5 mV/s, 1000 RPM).

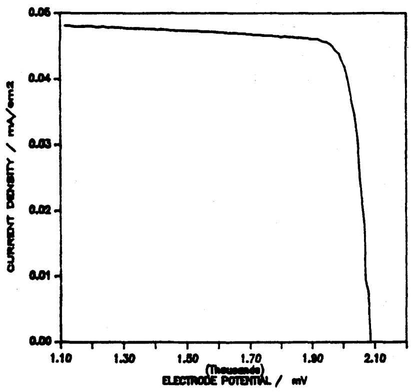

Figure 3. Linear sweep voltammogram for Cu(II) reduction at a RGCDE in 0.58 $AlCl_3$/MEIC (1.5 mM Cu(II) scan rate = 5 mV/s, 1000 RPM).

DOI: 10.1149/199017.0398PV

MEMBRANE POTENTIALS ACROSS MULLITE IN MIXTURES OF MOLTEN BROMIDES

M.L. Orfield
University of Wisconsin-Stout
Menomonie Wisconsin 54751

ABSTRACT .

At high temperatures Mullite functions as an ionic conductor of alkali metal cations. Two mullite membanes, M30 and MV33, were investigated. The membrane potentials of each were measured in mixtures of the alkali metal cations. The selectivity of MV30 for each of the alkali metal cations, Li^+, Na^+, and K^+ and the selectivity of MV33 for Na^+ were evaluated. The range of composition over which the behavior of each mullite may be predicted is discussed.

INTRODUCTION

Glassy membranes, sensitive to a single ion, form the basis for many separators and ion selective electrodes in use in aqeous systems. The success of such electrodes depends upon an understanding of the relationship between the composition of the solution and the potential generated across the membrane. In aqueous systems this relationship has been thoroughly examined and exploited to prepare glasses selective for a variety of ions.

Since glassy membranes are known to conduct ions well in molten salt solutions, it seems likely that they may obey the same kind of mathematical relationships applicable in aqueous systems. A few investigators have explored this area. Doremus measured the potentials across silica and pyrex glasses in molten nitrates. (1,2) Notz and Keenan also measured potentials across pyrex in molten nitrates. (3,4) Reenan et al, and Stern investigated potentials across silica in molten chlorides to a limited extent. (5-7) However potentials across these glasses could not be measured in higher melting salts because all except silica softened below the melting points of the salts or were quickly degraded in the harsh environment.

As a result most separators, and solid electrolytes used today in molten salt cells are ceramics. Mullite, a cation conductor and zirconia an oxide ion conductor are the most common. Mullite is useful in molten salt systems and other corrosive environments because of its high thermal stability and resistance to corrosion. It is believed to conduct alkali metal cations via a glassy phase at the grain boundaries. Its selectivity might be thought to obey the same mathematical relationships as those employed for glassy membranes in aqueous systems. It is the purpose of this work to investigate the relationship between potential developed across a mullite membrane and the activity of the alkali metal ions on either side of it; to determine if mullite does obey the same relationships established for glassy membranes in aqueous systems

THEORETICAL BACKGROUND

When two solutions, each containing a unique activity of cation N+, are separated by a membrane which conducts only cation N+ a potential develops across the membrane. The magnitude of the potential is determined by the gradient in the activity of N+ across the membrane. It is described

$$E_{mem} = RT/nF \ln [a(N^+)_I / a(N^+)_O] \tag{1}$$

where R is the gas constant, T is temperature, n is the absolute value of the charge on the cation, F is Faradays constant, and $a(N^+)_I$ and $a(N^+)_O$ are the activities of cation N+ on side I and side O of the membrane respectively. A membrane described by this equation is said to be perfectly selective for cation N+. It conducts only that cation.

Most glassy solid electrolytes are not exclusive conductors of one cation. In general they conduct the alkali metal cations, Li+, Na+, and K+ and some other small univalent cations such as Ag+. If a membrane separates two solutions, each of which contains two conducting cations, the potential is desribed by the equation. (8)

$$E_{mem} = RT/nF \ln \left(\frac{a(N^+)_I + K_{NM}^{POT} a(M^+)_I}{a(N^+)_O + K_{NM}^{POT} a(M^+)_O.} \right) \tag{2}$$

where the meaning of all terms used in Eq. 1 is the same, M+ is the second ion conducted by the electrolyte, and K_{NM}^{POT} is the potential selectivity coefficient which describes the the relative conductivity of each ion in the electrolyte. K_{NM}^{POT} is a measure of the preference of the membrane for M+ over N+ as a means of moving ionic current. Obviously, if $K_{NM}^{POT}=0$, the membrane is perfectly selective for N+ and will function as an ion selective electrode for that ion. Eq. 2 has been used extensively in characterizing the conductivity of glassy membranes in aqueous solutions, and in formulating those membranes to be highly selective for a single ion. Since mullite is believed to conduct via a glassy phase at the grain boundaries, it seems reasonable to assume that this material may also be characterized by the equation 1 or 2.

EXPERIMENTAL

The experimental apparatus is diagrammed in Fig. 1. A 7.0 cm. diameter mullite tube, 30.48 cm. long, with a stainless steel cap and fittings contained the cell used for membrane potential measurements. A mixture of of alkali metal bromides, M^1Br and M^2Br, with an activity of AgBr which was maintained at the same value as the activity of AgBr in the reference melt, was placed in a silver crucible inside the chamber. All salts were Baker Reagent grade. A silver wire, 99.99%, dipped in the melt formed the indicator electrode. The atmosphere in the chamber was dry Argon of 99.99% purity. The membrane was a mullite tube 0.95 cm. in diameter and 45.7 cm. long composed of mullite crystals with 15% by weight additional SiO_2 found as a glassy phase at the grain boundaries. It was purchased as MV30 from McDanel Refractory. The tube contained a reference melt of alkali metal bromides and the same activity of AgBr as found in the indicator melt. The reference electrode was also silver wire dipped into this melt making the cell:

$Ag|AgBr(N=Y), M^1Br\ (N=X), M^2Br\ (N=1-X-Y)|mullite|M^1Br(ref), M^2Br(ref), AgBr(ref)|Ag$

where M^1Br and M^2Br define one of the combinations, NaBr-KBr, LiBr-KBr, or NaBr-LiBr, and N is the mole fraction of each component in the mixture. The mole fractions of the alkali metal bromide components in the indicator melts were varied from 0.10 to 0.90 for each cation series. The mole fraction of AgBr in the indicator melt was adjusted to maintain equivalent activities of Ag^+ at the electrodes.

The reference melt composition, ref, was constant for each specific series of M^1Br-M^2Br melts. The reference melt compositions were (mol fractions) 0.81LiBr, 0.11KBr, 0.08AgBr for the LiBr-KBr series, 0.085NaBr, 0.835KBr, 0.08AgBr for the NaBr-KBr series, and 0.83NaBr, 0.08LiBr, 0.09AgBr for the NaBr-LiBr series. The reference electrode melt was prepared by premelting the appropriate mixture, grinding it, and storing it in an Ar purged dessicator. A small amount was placed in the membrane tube and then maintained under Argon continuously throughout the time it was used.

The salts were weighed, placed in the silver crucible, and dried in the Lindberg furnace under a flowing Argon atmosphere for 30 minutes at approximately 250°C. The temperature was raised to 755°C and maintained at that temperature ±2°C until the system equilibrated. Equilibration time was usually about 10 minutes. The potential was measured with a Simpson voltmeter and recorded. Individual experiments were repeated with the same mullite membrane and with other tubes. The potentials were reproducible within 5 mv. under all circumstances, and usually within 2 mv.

Some additional experiments were performed using a membrane of stoichiometric mullite. (MV33 from McDanel Refractory). Although this product is sold as non glassy phase mullite, in reality it contains about 2-3% glassy SiO_2 phase at the grain boundaries. (9) A tube, 1.90 cm. OD and 7.62 cm. high, was placed in the molten salt and supported by a gas inlet tube as shown in Fig. 2. The experimental apparatus was similar to that used with the MV30 membranes. The experimental procedure was the same.

CALCULATIONS

Since the membrane potential was to be measured,the Ag|Ag+ indicator and reference electrodes were maintained at the same potential throughout the experiments. The activity coefficient for AgBr in each indicator melt was calculated using the equation for a ternary solution, (10)

$$RT \ln\gamma_x = k_{12}N_1N_2 + (k_{x1}N_xN_1 + k_{x2}N_xN_2)(N_1 + N_2) \qquad (3)$$

for a ternary solution where x indicates AgBr and 1 and 2 the alkali metal bromide components of the mixture, γ_x is the activity coeficient of AgBr, and k is the interaction coefficient of the pair of components indicated by the subscript. Activity coefficients for the alkali metal bromides were calculated with the same equation using appropriate interaction coefficients. (11-15)

The potential selectivity coefficient was calculated from equation 2, using the measured values of the membrane potential and the calculated activities as described above.

RESULTS AND DISCUSSION

A $K^{POT}_{Na\text{-}K}$ has been calculated from each measured potential using equation 2 as written for these experiments

$$E_{mem} = RT/nF \ln\left(\frac{a(Na^+)_l + K^{POT}_{Na\text{-}K}\, a(K^+)_l}{a(Na^+)_{ref} + K^{POT}_{Na\text{-}K}\, a(K^+)_{ref.}}\right) \qquad (4)$$

where l now refers the indicator melt being measured; ref. describes the reference melt and E_{mem} indicates the measured cell potential. The activites of each salt are calculated from Eq. 3.

The average of the K^{POT}_{Na-K} values so calculated was 0.048±0.010, indicating that the mullite behaves reasonably like a glassy membrane which conducts both Na^+ and K^+ ions.

The experimental membrane potentials E(meas) generated across the mullite membrane (MV-30) are plotted in Fig. 3 as a function of the activity of NaBr in the melt. In addition, the average K^{POT}_{Na-K} has been employed in Eq. 4 to plot a curve of E(calc) vs a(NaBr). Agreement between the experimental data and the theoretical curve substantiates the idea that the potentials generated by a membrane in molten salts may be described by equation 2 similarly to membrane potentials in aqueous systems.

The value of the K^{POT}_{Na-K} for this system suggests that, as an ionic conductor, MV30 is highly selective selective for Na^+ over K^+. It suggests further that if the activities of K^+ in a melt, and reference melt, are sufficiently low with respect to the activity of Na^+, the second terms in the numerator and denominator of Eq. 2 will become insignificant; Eq. 2 will approximate Eq. 1 and the mullite may be characterized as membrane perfectly selective for Na^+ with little error. For example, if both salt mixtures were in excess of 0.90 mol fraction Na^+ the difference between Eq. 1 and Eq.2 would be only a few tenths of a millivolt. However, at the compositions used in this experiment significant error would result from using Eq. 1. Fig. 4 shows a comparison of potentials calculated using $K^{POT}_{Na-K} = 0.048$ in Eq. 2 and those calculated assuming the electrode is perfectly selective for Na^+ using Eq. 1.

A further refinement of Eq. 2 has been suggested by Eisenman et. al. They have included a factor, n, used to account for nonideality of the activity of sites of conduction in the glass membrane. (16)

$$E_{mem} = RT/nF \ln\left(\frac{(a(Na^+)_l)^{1/n} + (K^{POT}_{Na-K}\, a(K^+)_l)^{1/n}}{(a(Na^+)_{ref})^{1/n} + (K^{POT}_{Na-K}\, a(K^+)_{ref})^{1/n}}\right) \qquad (5)$$

Equation 5 was used, in conjunction with a least squares iteration program, to calculate simultaneously a K^{POT}_{Na-K} and an n value for the system. The K^{POT}_{Na-K} and the n calculated using this method were 0.066 and 0.77 respectively. The curve calculated from this K^{POT}_{Na-K} and n is plotted in Fig. 5 with the experimental potentials. The agreement between experimental and theoretical is good. Comparison of these two curves with the two curves in Fig. 4 indicates that very little congruence is gained with the use of the more complicated equation. It suggests that any difference between experimental data and a theoretical curve is not due to non ideality of activity of sites in the glass membrane.

The membrane potentials measured at a(NaBr)>0.90 are not as reproducible as the others. At a(NaBr) < 0.90 the error was ±0.002 volts. It was much greater at a(NaBr) > 0.90, as can be seen from the two repeated measurements shown on the plot. These potentials result from very large differences in composition between indicating and reference melts, and seem to suggest that the useful range of MV30 as a predictable conducting membrane does not extend to this differential in composition.

The average K_{Li-K}^{POT} for a series of KBr-LiBr melts was calculated in manner similar to that described for the NaBr-KBr system. The average value was 0.034 ± 0.017. It varied systematically with the composition of the melt, becoming larger with increasing a(LiBr). The variation resulted in a large error for the average value. Again the K_{Li-K}^{POT} indicates that the electrode is highly selective for Li^+ over K^+. Apparently the glassy phase of MV30 is of a composition which conducts Li^+ ions equally as well as Na^+. It could be used as a perfectly selective electrode for Li^+ if the activity of the K^+ were sufficiently low in both melt and reference melt, and no gradient in Na^+ was present.

The potentials generated in the KBr-LiBr system are plotted in Fig. 6 in a manner similar to that described for the NaBr-KBr system. The agreement between the measured potentials and calculated curve is not as satisfactory as in the NaBr-KBr system because of the systematic variance of K_{Li-K}^{POT} with a(LiBr).

A K_{Li-K}^{POT} and n were also calculated using Eq. 5 and found to be 0.0018 and 2.56 respectively. The curve of this equation is plotted in Fig. 7 with the experimental values. The agreement between the experimental and the theroretical is much better with this calculation. Since n is fairly great and this value of K_{Li-K}^{POT} differs greatly from the average value calculated, one might conclude that the activity of sites for conduction of Li^+ is far from ideal where that for Na^+ ions is much closer to ideal as evidenced by the NaBr-KBr plots.

A value of K^{POT}_{Na-Li} , calculated in a manner similar to that described for the NaBr-KBr melts, was found to be 3.20±0.50. The value suggests that mullite conducts both Na^+ and Li^+ but has a slightly greater selectivity for Li^+. Because of the similarity of selectivity between Na^+ and Li^+ no composition of these salts will result in a negligible potential for either ion and Eq. 1 cannot be used for any composition. Unlike K^{POT}_{Li-K} the K^{POT}_{Na-Li} does not vary systematically with composition.

Experimental data and a theoretical curve using K^{POT}_{Na-Li} = 3.20 are plotted in Fig. 8. Agreement between experimental data and theoretical curve is modest. The error in these data appears to be random. When the K^{POT}_{Na-Li} and n are calculated (2.787 and 0.685 respectively) and plotted with the experimental data in Fig. 9 the agreement between the theoretical and the experimental does not improve much over that in Fig. 8.

As previously stated, the conduction of ions by MV30 has been commonly believed to be accomplished via the glassy SiO_2 phase at the grain boundaries of the crystalline mullite. With this fact in mind a second series of experiments, similar to those described, was performed using MV33 as the membrane. This material, while marketed as a stoichiometric mullite, ie. no glassy phase, has approximately 2-3% residual glassy SiO_2, as opposed to 15% in the MV30. It was assumed that the MV33 would behave like an insulator and no meaningful potentials could be measured. However this was not the case.

Potentials were measured across MV33 and an average K^{POT}_{Na-K} = .153 ± 0.02, The measured potentials and a theoretical curve using the average K^{POT}_{Na-K} are plotted in Fig. 10. Not only do these appear consistent with Eq. 2, the aggreement is good. While the variation in K^{POT}_{Na-K} is not large, it is systematic with composition of the melt. A K^{POT}_{Na-K} and n were computed to be 0.170 and 0.787 respectively. The curve calculated using these values and the experimental data are plotted in Fig. 11. With the small correction for nonideality the agreement between experimental and theoretical is excellent. In fact the MV33 behaves in a more predictable manner than the the MV30.

The K^{POT}_{Na-K} is approximately 3 times that of the MV30 membrane indicating that the glassy phase in the MV33 is less selective for Na^+ over K^+

than the MV 30. The difference in selectivity may be due to the differences in composition between the two glassy phases. The bulk composition of impurities in the MV30 differs from that in the stoichiometric mullite. Because of this and processing differences, the final glassy phase composition is likely to differ as well.

The measurements across MV33 are consistent and the percent error small suggesting that the amount of glassy phase necessary to provide good conduction is small. If the grain boundary is very narrow in both mullites and the excess glassy phase is found in the pockets where three or more grains meet then 2 or 3% SiO_2 may be enough to provide a continuous glassy phase for conduction.

Alternatively, one might speculate that an second mode of conduction: directly across the crystalline mullite is active in these membranes . If so each mode of conduction would have a unique $K_{Na\text{-}K}^{POT}$ and the measured $K_{Na\text{-}K}^{POT}$ would be some combination of the two. If one assumes that the much smaller amount of glassy phase in the MV33 means that the grain boundary conduction is negligible, the excellent convergence with theory is explained.

SUMMARY

The behavior of an MV30 membrane may be predicted by equations used for membranes in aqueous solutions. NaBr-KBr mixtures are well described by equation 2 , where n=1. The potential selectivity coefficient suggests that the activity of KBr may be ignored when it is less than 0.10. LiBr-KBr melts may be accurately described by the Eisenman modification of equation 2, where n does not equal 1. Again the membrane may be treated as perfectly selective for Li^+ when the activity of K^+ is less than 0.10 and no other alkali metal cations are present. Melts composed of NaBr-LiBr are not as well described which may be due to the small potentials measured in these melts. The potential selectivity suggests that both ions are conducted well and neither may be ignored in calculating the membrane potetial when both are present.

The MV33 membrane is very well characterized by equation 2 and its modification. The potential selectivity coefficient for this membrane in NaBr-KBr melts differs from that for MV30. The variation may be due to differences in composition between the glassy phases in MV33 and MV30.

ACKNOWLEDGEMENT

The technical assistance of Robert Ulrich, David Zemke and Andrew Joswiak is gratefully acknowledged.

REFERENCES

1. R. H. Doremus, J. Phys. Chem., **72**, 2877 (1968).

2. R. H. Doremus, J. Electrochem. Soc., **115**, 924 (1968).

3. K. Notz and A. G. Keenan, J. Phys. Chem., **70**, 662 (1966).

4. A. G. Keenan, K. Notz, F. L. Wilcox, J. Phys. Chem., **72**, 1085 (1968).

5. T. J. van Reenen, M. van de Niekerk, and W. J. Wet, J. Phys. Chem., **75**, 2815 (1971).

6. K. H. Stern, J. Phys. Chem., **72**, 1963 (1968).

7. K. H. Stern, J. Phys. Chem., **74**, 1323 (1970).

8. G. Eisenman in Glass Electrodes for Hydrogen and Other Cations, G. Eisenman, Ed., Dekker, New York, 1966, Chap. 5.

9. McDanel Refractory, Private Communication.

10. J. Lumsden, Thermodynamics of Molten Salt Mixtures, Academic Press, London, 1966, p. 96.

11. E. Aukrust, B. Bjorge, H. Flood, and T. Forland, Ann. N. Y. Acad. Sci., **79**, 830 (1960).

12. E. J. Salstrom and J. H. Hildebrand, J. Am. Chem. Soc., **52**, 4650 (1930).

13. E. J. Salstrom, J. Am. Chem. Soc., **53**, 1794 (1931).

14. E. J. Salstrom, J. Am. Chem. Soc., **53**, 3385 (1931).

15. L. S. Hersh and O. J. Kleppa, J. Chem. Phys., **42**, 1309 (1965).

16. G. Eisenman, "The Chemistry of Cation-Sensitive Electrodes" in Advances in Analytical Chemistry and Instrumentation, Vol. 4, C. N. Reilly, Ed., Interscience, New York, 1965.

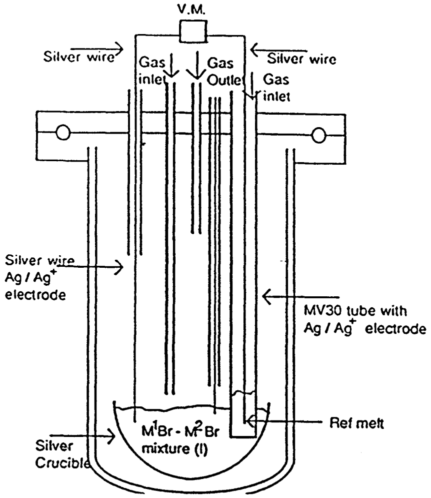

Fig. 1. Diagram of experimental apparatus for measuring membrane potential across MV30; mullite with 15% glassy phase

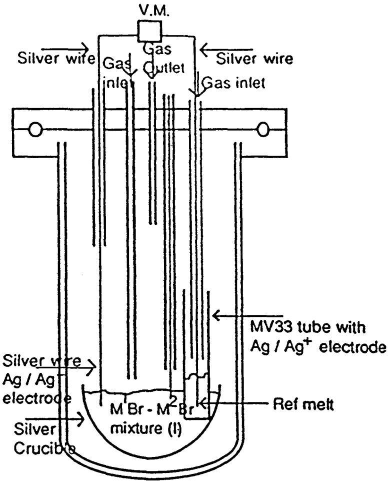

Fig. 2. Diagram of experimental apparatus for measuring membrane potential across MV33; mullite with 2-4% glassy phase

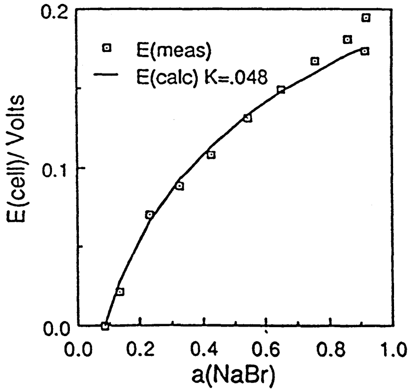

Fig. 3. Measured and calculated membrane potentials across MV30 in KBr-NaBr mixtures.

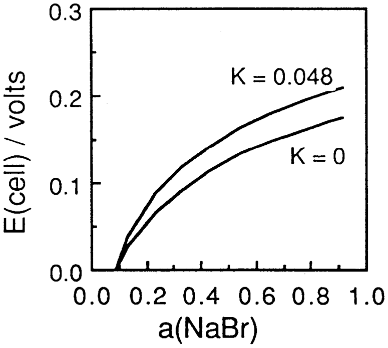

Fig. 4. Calculated potentials using Eq. 2, K=0.048 and Eq. 1, K = 0 for NaBr-KBr melts

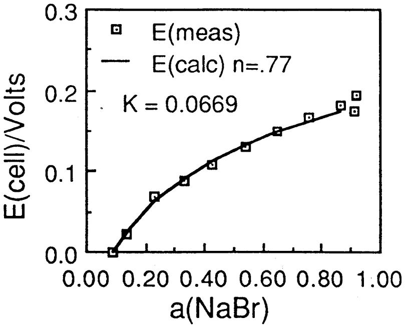

Fig. 5. Cell potentials across MV30 in NaBr-KBr melts. K = 0.0669, n=0.77

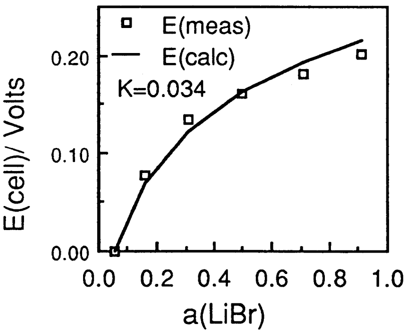

Fig. 6. Cell potentials across MV30 in LiBr-KBr melts. K = 0.034, n=1

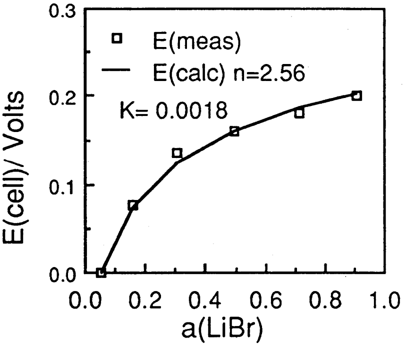

Fig. 7. Cell potentials across MV30 in LiBr-KBr melts. K = 0.0018, n=2.56

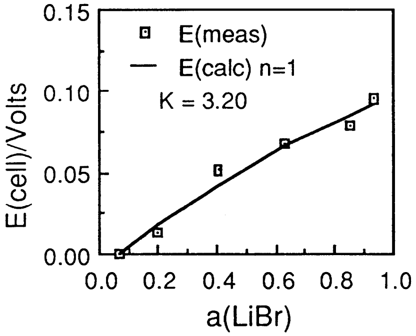

Fig. 8. Cell potential across MV30 in NaBr-LiBr melts. K = 3.20, n = 1.

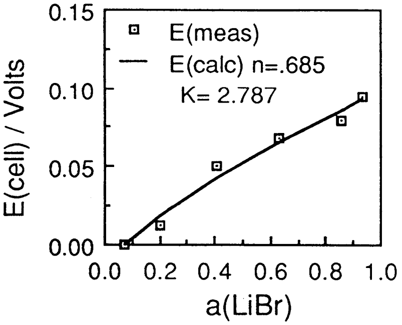

Fig. 9. Cell potential across MV30 in NaBr-LiBr melts. K = 2.79, n = 0.685.

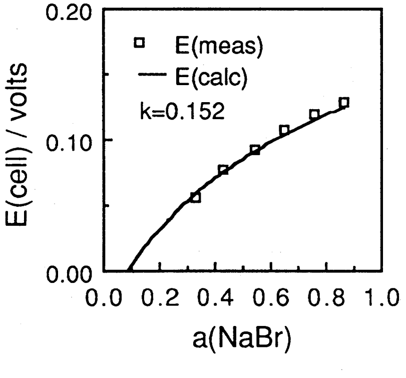

Fig. 10. Cell potential across MV33 in NaBr-KBr melts. K = 0.152, n = 1.

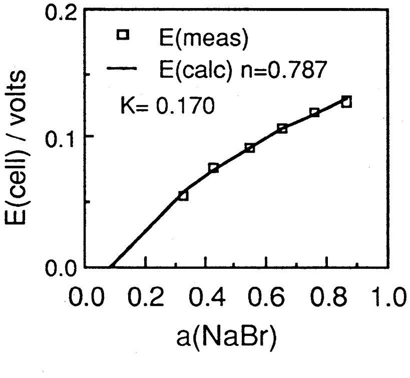

Fig. 11. Cell potential across MV33 in NaBr-KBr melts. K = 0.170, n = 0.787.

DOI: 10.1149/199017.0410PV

POTENTIAL MEASUREMENTS OF REACTIVE METAL CHLORIDES IN ALKALI HALIDE SOLUTIONS

P.J. Tumidajski* and S.N. Flengas
Department of Metallurgy and Materials Science
University of Toronto
Toronto, Ontario
Canada M5S 1A4

*Present Address: Department of Materials Engineering, The University of Western Ontario, London, Ontario, Canada N6A 5B9

ABSTRACT

The thermodynamic behaviour of AgCl, $CoCl_2$, $NiCl_2$, $FeCl_2$, CuCl, $FeCl_3$, $CuCl_2$, $CrCl_2$, $CrCl_3$ and $ThCl_4$ was investigated in NaCl, KCl, CsCl or the equimolar mixtures of these salts between 700-900°C, using galvanic or redox cells. The results indicate solutions are reactive and non-ideal. A thermodynamic model is presented which allows the calculation of thermodynamic properties. The model has only one adjustable parameter.

INTRODUCTION

In previous publications from this laboratory, the thermodynamic properties of solutions of metal chlorides in alkali chloride solvent melts have been investigated by emf measurements (1-9). The data have been used for the calculation of activities and other partial molar properties. The measurements also provide valuable information on emf series in molten salt solutions, on the feasibility of new processes for the recovery of metals by fused salt electrolysis, and on high temperature batteries and energy storage devices. In this publication, the thermodynamic properties of dilute solutions of AgCl, $CoCl_2$, $NiCl_2$, $FeCl_2$, $FeCl_3$, CuCl, $CuCl_2$, $CrCl_2$, $CrCl_3$ and $ThCl_4$ in binary solvent melts like NaCl, KCl, and CsCl, and ternary combinations like NaCl-KCl, NaCl-CsCl, and KCl-CsCl, are reported. In addition, the thermodynamic properties of $ThCl_4$ in the more concentrated $ThCl_4$-CsCl solutions are presented.

EXPERIMENTAL

All the metal chlorides and CsCl were anhydrous. They were received in sealed ampoules packed under argon gas. Consequently, these chemicals were used without further purification. The AgCl, NaCl, and KCl, were reagent grade and were purified and treated in an anhydrous HCl atmosphere at 400°C. The NaCl-CsCl, KCl-CsCl, and NaCl-KCl binary solvent melts were prepared by mixing the component salts, then melting under vacuum for 24 h. The resulting solutions were cooled, crushed, and stored inside a drybox. Before use, metal electrodes were polished with fine emery paper, and then washed several times with a 10 v/o HF solution, distilled water, and finally acetone. Weighing, handling, and the transfer of all chemicals were conducted within a drybox filled with anhydrous argon gas.

The basic design of the emf cell used for the measurements is shown in Figure 1. Details have been reported elsewhere (8-10). The cell consisted of two half cell compartments separated by an asbestos diaphragm made by tightly rolling a small strand of asbestos fibers, firing to a white ash and then collapsing 6 mm quartz tubing around it. As a result, very fine capillaries were formed which allowed for electrical contact, but minimal mass diffusion. In addition, the resistance of such diaphragms was very large and all measured electrode potentials were totally reproducible and remained stable over long periods of time.

Dilute Solutions

Three types of electrochemical cells were employed for the dilute solution experiments. The AgCl formation cell can be described as,

$$(-)\ Ag\ /\ \underset{(X)}{AgCl-ACl}\ //\ asbestos\ diaphragm\ //\ \underset{(X)}{AgCl-ACl}\ /\ C,\ Cl_{2_{(g,\ 1\,atm)}}(+)$$

Cell A

where, ACl represents the salt components NaCl, KCl, CsCl, or the binary equimolar mixtures of these salts. The overall cell reaction is,

$$Ag_{(s)} + \frac{1}{2}Cl_{2_{(g,\ 1\,atm)}} \rightarrow \underline{AgCl}_{(at\ X_{AgCl})} \qquad (1)$$

where, the line under AgCl denotes AgCl in solution with the alkali chloride. The corresponding Nernst equation is,

$$E = E^o_{AgCl} - \frac{2.303RT}{F}\log\gamma_{AgCl} - \frac{2.303RT}{F}\log X_{AgCl} \qquad (2)$$

where, F is Faraday's constant of 96,487 J V^{-1} mol^{-1}, and R is the universal gas constant given as 8.3144 J K^{-1} mol^{-1}. T is the absolute temperature. The standard state in all cases is the pure liquid metal chloride at the temperature of the experiments. E^o_{AgCl} is the "standard formation" potential for the formation of pure liquid AgCl. Values for E^o_{AgCl} were obtained from a previous investigation (5). For dilute solutions obeying Henry's law, γ_{AgCl} is composition independent. Accordingly, a "formal formation" potential can be defined as representing the free energy of formation of unit mole fraction of a salt behaving thermodynamically as if it were infinitely diluted in a given solvent. The "formal formation" potential is defined by the expression,

$$E^o_{f(AgCl)} = E^o_{AgCl} - \frac{2.303RT}{F}\log(\gamma_{AgCl})_{x\rightarrow 0} \qquad (3)$$

where, $E^o_{f(AgCl)}$ represents the "formal formation" potential. Substitution of Eq. (3) into Eq. (2) yields the simplified expression for dilute solutions,

$$E \;=\; E^o_{f(AgCl)} \;-\; \frac{2.303RT}{F}\log X_{AgCl} \qquad (4)$$

The galvanic type cells employed in this investigation may be described by,

$$(-)\,M \;\;/\;\; \underset{(X_2)}{MCl_z - ACl} \;\;//\;\; asbestos\ diaphragm \;\;//\;\; \underset{(X_1)}{AgCl - ACl} \;\;/\;\; Ag\,(+)$$

Cell B

where, M is Co, Ni, Fe, Cu, Cr or Th, respectively. MCl_z is $CoCl_2$, $NiCl_2$, $FeCl_2$, CuCl, $CrCl_2$ or $ThCl_4$ and ACl has the same meaning as for the AgCl formation cell described above. The AgCl concentration (X_1) was fixed at 0.05 mol fraction. The spontaneous cell reaction is,

$$M_{(s)} \;+\; z\underline{AgCl} \;\rightarrow\; \underline{MCl_z} \;+\; zAg_{(s)} \qquad (5)$$

The corresponding Nernst equation is,

$$E \;=\; E^o_{MCl_z} \;-\; E^o_{AgCl} \;-\; \frac{2.303RT}{zF}\log\frac{\gamma_{MCl_z}}{\gamma^z_{AgCl}} \;-\; \frac{2.303RT}{zF}\log\frac{X_{MCl_z}}{X^z_{AgCl}} \qquad (6)$$

where, T, R, and F have been defined earlier. The standard state for all salts was the pure molten metal chloride at the experimental temperature. Following the same development as for the AgCl formation cells, when solutions are dilute and Henry's law is obeyed, then Eq. (6) simplifies to,

$$E \;=\; \left[E^o_{f(MCl_z)} - E^o_{f(AgCl)}\right] \;-\; \frac{2.303RT}{zF}\;\log\frac{X_{MCl_z}}{X^z_{AgCl}} \qquad (7)$$

From Eq. (4) and Eq. (7), $E^o_{f(MCl_z)}$ may be calculated with respect to the standard chlorine electrode as reference. The latter represent reactions of the type,

$$M_{(s)} \;+\; \frac{z}{2}Cl_{2(g,\ 1\,atm)} \;\rightarrow\; (MCl_z)^o \qquad (8)$$

where, the superscript ° indicates an hypothetical solution of unit mole fraction of MCl_z but which has the properties extrapolated from an infinitely diluted MCl_z - ACl solution.

The redox cell employed in this investigation may be described schematically as,

$$(-)\,Ag \;\;/\;\; \underset{(X_1)}{AgCl - ACl} \;\;//\;\; asbestos\ diaphragm \;\;//\;\; \underset{(X_2)}{MCl_z} - \underset{(X_3)}{MCl_{z+1}} - ACl \;\;/\;\; Pt \;\;(+)$$

Cell C

MCl_z was $FeCl_2$ or CuCl, and MCl_{z+1} was $FeCl_3$ or $CuCl_2$. The cell reaction is,

$$Ag_{(s)} \;+\; \underline{MCl_{z+1}} \;\rightarrow\; \underline{MCl_z} \;+\; \underline{AgCl} \qquad (9)$$

The corresponding Nernst expression is,

$$E \;=\; \left[E^o_{MCl_z} + E^o_{AgCl} - E^o_{MCl_{z+1}}\right] - \frac{2.303RT}{F}\log\frac{\gamma_{AgCl}\gamma_{MCl_z}}{\gamma_{MCl_{z+1}}} \;-\; \frac{2.303RT}{F}\log\frac{X_{AgCl}\,X_{MCl_z}}{X_{MCl_{z+1}}} \qquad (10)$$

In dilute solutions where Henry's law is applicable, Eq. (10) simplifies to

$$E = \left[E^o_{f(MCl_z)} + E^o_{f(AgCl)} - E^o_{f(MCl_{z+1})}\right] - \frac{2.303RT}{F}\log\frac{X_{AgCl}\,X_{MCl_z}}{X_{MCl_{z+1}}} \quad (11)$$

where,

$$E^o_r = \left[E^o_{f(MCl_z)} + E^o_{f(AgCl)} - E^o_{f(MCl_{z+1})}\right] \quad (12)$$

E^o_r represents the formal redox potential for reaction (9). The formal redox potential for the reaction,

$$(MCl_z)^o + \frac{1}{2}Cl_{2_{(g,\ 1atm)}} \rightarrow (MCl_{z+1})^o \quad (13)$$

written as, $E^o_{r(MCl_{z+1},MCl_z)}$, is readily calculated from Eq. (12) by subtracting the formal potential for AgCl from measurements on Cell A. Hence, Eq. (12) allows the calculation of $E^o_{f(MCl_{z+1})}$ which is generally not directly measurable because of the extreme reactivity of MCl_{z+1} solutions with metal M. The "formal redox" potential for the reaction of Eq. (13) can also be expressed as,

$$E^o_{r(MCl_{z+1},\ MCl_z)} = (z+1)E^o_{f(MCl_{z+1})} - zE^o_{f(MCl_z)} \quad (14)$$

Concentrated Solutions

The cell design was similar to the chloride formation cells described elsewhere (8-10). The cell consisted of a thorium metal indicator electrode immersed in the $ThCl_4$-CsCl molten solution of known composition, and a graphite chlorine electrode, which also dipped into a molten solution of the same composition. The two cell compartments were separated by an asbestos fiber diaphragm fused into silica glass. The spontaneous cell reaction is,

$$Th_{(s)} + 2Cl_{2(g,\,1\,atm)} = \underline{ThCl_4} \quad (15)$$

The Nernst equation is,

$$E_{cell} = E^0_{ThCl_4} - \frac{2.303RT}{4F}\log(\gamma_{ThCl_4}) \quad (16)$$

RESULTS

The interpretation of the emf results from the galvanic and redox cells, through Eq. (6) and Eq. (10), respectively, and the calculation of solution properties are entirely dependent upon the accuracy of the measured standard formation potentials for the pure liquid metal chlorides and of the formal formation potentials of AgCl in the various solvent melts used in this investigation. The standard formation potentials for pure molten AgCl have been measured previously in this laboratory (5), and are in good agreement with other electrochemical measurements (11-13) and thermochemical data (14). The expression for $E^o_{AgCl(liquid)}$ calculated through the third law method is given as,

$$E^o_{AgCl} = 1227.0 - 1.5973T + 0.182T\ln T - 4.48\times10^{-5}T^2\,(mV) \quad (17)$$

with a standard deviation of 0.57 mV.

Potentials measured for the systems AgCl-NaCl, AgCl-KCl, AgCl-CsCl, AgCl-NaCl-CsCl, and AgCl-KCl-CsCl have been reported previously (9) and the results are summarized in Table 1. Tables 2 to 10 contain the emf results, as functions of temperature, for all the remaining dilute systems investigated, expressed as linear functions of temperature. Table 11 summarizes the results for the $ThCl_4$-Csl formation cell. Also included in Table 2 to 11 are the correlation coefficients for the linear least squares analysis for E versus T. It can be seen that the coefficients are almost one indicating an excellent fit of the experimental data to a straight line. Potentials recorded in Tables 2 to 11, represent spontaneous cell reactions and are given positive signs in order to conform with the thermodynamic requirement of a decrease in reaction free energy. However, if it is desired to tabulate the emf values in the format of a series against a common reference electrode, such as the silver chloride or the chlorine reference electrodes, then it is necessary to conform with the IUPAC sign convention and assign negative values to the more reactive electrode systems.

Nernst plots following Eq. (6) and Eq. (10) for the dilute galvanic and redox cells, respectively, were linear as expected for solutions that obeyed Henrian behaviour. Slopes for a one or two electron transfer reaction were in excellent agreement with theoretical values.

DISCUSSION

Formal potentials corresponding to the reactions of Eq. (8) and Eq. (13) are summarized in Tables 12 and 13, respectively. The potentials have been corrected to correspond to the chlorine gas reference electrode in a manner described previously (8,9). The potentials represents an emf series in various solvent melts. It can be seen that the magnitude of the formal potentials in the binary solutions increase in the order NaCl-KCl-CsCl. The trend shows the pronounced effect of CsCl in creating thermodynamically stable solutions. Furthermore, the magnitude of the formal potentials decreases as the temperature is increased, which indicates a decrease in thermodynamic stability at the higher temperatures. Tables 12 and 13 also includes the formal potentials in the ternary systems calculated from the previously proposed relationship (15),

$$E^o_{f(123)} = (1-t)\,E^o_{f(12)} + tE^o_{f(13)} \tag{18}$$

Ternary solutions are denoted by the subscript (123), while the binaries are denoted by (12) and (13). The t parameter is a composition variable defined as,

$$t = X_{CsCl} \ / \ (X_{CsCl}+X_{NaCl}) \tag{19a}$$

or,

$$t = X_{CsCl} \ / \ (X_{CsCl}+X_{KCl}) \tag{19b}$$

for the CsCl containing solutions, and

$$t = X_{KCl} \ / \ (X_{KCl}+X_{NaCl}) \tag{19c}$$

for the NaCl-KCl solutions. It can be seen from Tables 12 and 13 that Eq. (18) approximates the experimental results to within five percent at the most.

A comparison of the previous experimental results for formal potentials shows that there is good agreement for the $FeCl_2$ (16,17), CuCl (3,18), $NiCl_2$ (2,16,18,19,20), $CoCl_2$ (1,18,21), $CrCl_2$ (3,22) and $ThCl_4$ (23) binary systems, but there are very few data available on ternary and for redox systems.

"Standard" potentials are only known with confidence for the salts AgCl, CuCl, and $FeCl_2$. Table 14 contains a linear least squares fit of $E^o_{MCl_z}$. Table 14 also includes the uncertainty in the standard potential values where available (5,24). It follows that enthalpies of mixing and activity coefficients can only be reported for the solutions of the above mentioned salts. These have been calculated previously (9). The results are given in Table 15. It should be mentioned that for the AgCl solutions there is good agreement between the limiting partial enthalpies of mixing calculated from electrochemical and calorimetric (25) data. The latter were only obtained from solutions containing 10 m/o of AgCl, and therefore are not strictly comparable with the electrochemical work which represents true Henrian conditions, where the partial properties reach truly constant limiting values.

For the binary solutions of AgCl in NaCl, KCl, and CsCl respectively, the partial enthalpies of mixing over the entire composition range are presented in Figures 2, 3, and 4. The figures include data obtained from both electrochemical (5,11,26,27) and calorimetric (25) work. The agreement is generally good particularly for the AgCl-CsCl solutions. In all cases, for compositions containing less than five mole percent AgCl, where solutions became Henrian, partial enthalpies are also taken to having reached a constant limiting value. Limiting enthalpy values indicate that interactions affecting solute species have reached saturation. The strong exothermic enthalpies of mixing found in KCl and CsCl solvents indicate the formation of thermodynamically highly stable complex species. The endothermic mixing reaction in the presence of NaCl could indicate cluster formation due to repulsive interactions.

Complex Ion Formation

Charge asymmetric molten salt solutions are known to exhibit highly exothermic enthalpies of mixing, and the activities indicate pronounced negative deviations from ideality. The behaviour is indicative of strong interactions between the ionic specie in solution leading to the formation of complex species.

The concept of complex formation in molten salts has been described elsewhere (6,30-32). A complex like $(MCl_{z+r})^{r-}$ should be understood as a local configuration represented by a cation M^{z+} surrounded by (z + r) Cl^- anions. Within the complex itself, the M-Cl bond distances and, accordingly the corresponding bond energies, should be different from the M-Cl bond distances in the non-complexed state, which is usually taken to be the pure molten MCl_z salt. However, because of the requirement of overall electrical neutrality, it is also necessary that the anions and cations which form the complex should occupy single anionic and cationic lattice sites within the quasi-lattice structure of the ionic solution. Thus, it would be meaningless to consider the $(MCl_{z+r})^{r-}$ entities as discrete ions occupying single anionic sites and the only evidence of the presence of a complex specie should be a perturbation in the cation to anion bond distance within the continuum of the molten ionic phase.

Considering solutions of MCl_z in ACl, it is possible that the co-ordination within a complex could vary as the composition changes. However, within the concentration range for which Henry's law is applicable, the co-ordination is expected to have reached a limiting value and the structure of the complex should remain unchanged. This structure represents the final form of a complex specie which is realized only in dilute solutions when the few metal cations present are surrounded by a large excess of anionic ligands.

Therefore, dilute solutions of charge asymmetric systems should be ideally suited for investigating the effects of complex formation in molten salts and for understanding the relations between their structure and the corresponding thermodynamic properties.

In previous publications (29), it has been shown that for reactive and non-ideal systems the activity of any component MCl_z may be given as,

$$a_{MCl_z} = \left[N_{M^{2+}} \cdot N^{z}_{Cl^-}\right]_{at\ \ equilibrium} \tag{20}$$

where, $N_{M^{z+}}$ and N_{Cl^-} are respectively the ionic fractions of cations M^{z+} and anions N_{Cl^-}, corresponding to a specific complex ion formation reaction such as,

$$MCl_z \ + \ rACl \ \rightarrow \ [MCl_{2+r}]^{z-} \ + \ rA^+ \tag{21a}$$

or

$$M^{z+} \ + \ (2+r)Cl^- \ \rightarrow \ [MCl_{2+r}]^{z-} \tag{21b}$$

where, the value for r determines whether the complex is branched (r=2), tetrahedrally (r=4) or octahedrally (r=6) co-ordinated. Considering a solution which initially contained n_1 moles of MCl_z and n_2 moles of ACl, and if α represents the degree of reaction (or the amount of MCl_z reacted per mole), then the mass balance at equilibrium is given in Table 16. The activity coefficient for MCl_z, which is readily derived from Eq. (20), is,

$$\gamma_{MCl_z} = \frac{(1-\alpha)}{(1-\alpha)+r}\left[\frac{n_1 z + n_2 r - \alpha n_1(z+r)}{n_1(z(1-\alpha)+\alpha(1-r)+n_2 r)}\right]^z \tag{22}$$

The equilibrium constant for the complex forming reaction is given as,

$$K = \frac{N_{(MCl_{2+r})^{r-}}}{N_{M^{z+}} \cdot N^{(2+r)}_{Cl^-}} \tag{23}$$

Degrees of reaction for various MCl_z mole fractions may be calculated from experimentally measured activity coefficients using Eq. (22). For truly Henrian solutions, the equilibrium constant calculated from Eq. (23) should be constant, at constant temperature, for all concentrations for which the activity coefficient remains constant. The application of the theory is only possible for AgCl-KCl and AgCl-CsCl systems because these systems have exothermic enthalpies of mixing and well established values for their activity coefficients. Both the degree of reaction (α) and equilibrium constant (K) values calculated over a composition range of about 10 m/o AgCl are shown in Table 17. For this calculation z=1 and r=2 for a branched type complex.

CONCLUSIONS

Reversible emf measurements have been used to establish the thermodynamic behaviour of a number of metal chlorides in binary and ternary fused alkali chloride solvents. For dilute solutions, Henrian behaviour is observed. Emf series in a number of solvent melts based on the formal standard state were developed. The magnitude of the formal potentials indicates negative deviations from ideality except for the AgCl-NaCl system. The deviations become increasingly negative as the size of the alkali metal cation in the solvent increases from sodium to cesium. The results support the hypothesis for complex formation particularly for the charge asymmetric solutions of metal chloride in alkali chlorides.

Table 1. **Formal Formation Potentials of the Molten Dilute Solutions of AgCl in Alkali Chlorides.**

System	$E^{\circ}_{f} = A + BT$ (V)*		E°_{f} (V)		±ΔE (V)
	A	$B \times 10^{4}$	1073 K	1173 K	
AgCl-NaCl	1.0445	-2.400	0.785	0.763	0.004
AgCl-KCl	1.1420	-2.450	0.879	0.855	0.002
AgCl-CsCl	1.2230	-2.600	0.944	0.920	0.001
AgCl-NaCl-KCl	1.0883	-2.500	0.820	0.795	0.004
AgCl-NaCl-CsCl	1.2550	-3.700	0.858	0.821	0.002
AgCl-KCl-CsCl	1.2834	-3.500	0.908	0.873	0.001

* Equations are applicable to the temperature range 973 K to 1173 K except for the NaCl solvent.

Table 2. E versus temperature for the $CoCl_2$ galvanic cell.

Solvent	X_{CoCl_2}	E = BT + A (V)		C Coeff.	Range (K)
		B × 10^4	A		
NaCl	2.02×10^{-3}	-0.471	0.343	-0.999	1108-1178
	3.88×10^{-3}	-7.550	0.344	-0.999	1101-1166
	6.56×10^{-3}	-0.984	0.344	-0.999	1111-1186
	8.55×10^{-3}	-1.096	0.344	-0.999	1107-1181
KCl	3.55×10^{-3}	-1.272	0.426	-0.996	1081-1174
	5.63×10^{-3}	-1.504	0.430	-0.999	1091-1174
	7.61×10^{-3}	-1.627	0.429	-0.998	1100-1197
	1.03×10^{-2}	-1.753	0.428	-0.999	1075-1181
CsCl	6.11×10^{-3}	-1.804	0.497	-0.999	961-1118
	1.01×10^{-2}	-2.023	0.498	-0.999	965-1107
	1.31×10^{-2}	-2.137	0.498	-0.999	937-1104
	1.87×10^{-2}	-2.291	0.498	-0.999	941-1096
NaCl-KCl*	1.72×10^{-3}	-1.207	0.453	-0.999	985-1101
	3.04×10^{-3}	-1.454	0.453	-0.999	957-1096
	5.20×10^{-3}	-1.678	0.452	-0.999	957-1109
	7.87×10^{-3}	-1.865	0.453	-0.999	946-1105
NaCl-CsCl*	2.98×10^{-3}	-0.929	0.406	-0.999	966-1103
	7.35×10^{-3}	-1.320	0.406	-0.999	968-1102
	1.02×10^{-2}	-1.453	0.405	-0.999	969-1092
	1.26×10^{-2}	-1.545	0.405	-0.999	961-1105
KCl-CsCl*	4.91×10^{-3}	-2.334	0.538	-0.999	990-1136
	8.11×10^{-3}	-2.550	0.538	-0.999	974-1109
	1.05×10^{-2}	-2.664	0.538	-0.999	960-1109
	1.43×10^{-2}	-2.800	0.539	-0.999	960-1102

*Equimolar.

Table 3. E versus temperature for the $NiCl_2$ galvanic cell.

Solvent	X_{NiCl_2}	E = BT + A (V)		C Coeff.	Range (K)
		$B \times 10^4$	A		
NaCl	1.36×10^{-3}	-0.050	0.120	-0.972	1131-1189
	2.00×10^{-3}	-0.206	0.118	-0.999	1128-1185
	3.94×10^{-3}	-0.495	0.118	-0.999	1123-1186
	4.61×10^{-3}	-0.559	0.117	-0.998	1126-1191
KCl	2.00×10^{-3}	-0.041	0.106	-0.985	1078-1152
	3.43×10^{-3}	-0.256	0.104	-0.998	1068-1110
	5.23×10^{-3}	-0.440	0.104	-0.999	1048-1105
	6.78×10^{-3}	-0.565	0.106	-0.994	1077-1107
CsCl	5.25×10^{-3}	-1.016	0.170	-0.999	968-1100
	8.19×10^{-3}	-1.211	0.171	-0.999	937-1106
	1.19×10^{-2}	-1.374	0.172	-0.999	937-1094
	1.51×10^{-2}	-1.476	0.172	-0.999	940-1094
NaCl-KCl*	1.27×10^{-3}	-1.801	0.335	-0.999	978-1093
	2.92×10^{-3}	-2.209	0.340	-0.997	973-1098
	4.46×10^{-3}	-2.353	0.336	-0.999	976-1101
	6.06×10^{-3}	-2.479	0.335	-0.998	970-1095
NaCl-CsCl*	3.23×10^{-3}	-1.229	0.210	-0.999	953-1087
	6.96×10^{-3}	-1.555	0.209	-0.999	950-1087
	9.52×10^{-3}	-1.699	0.210	-0.999	954-1091
	1.27×10^{-2}	-1.817	0.209	-0.999	916-1091
KCl-CsCl*	3.88×10^{-3}	-0.389	0.134	-0.998	947-1109
	7.60×10^{-3}	-0.680	0.134	-0.998	934-1109
	1.05×10^{-2}	-0.813	0.133	-0.999	934-1100
	1.32×10^{-2}	-0.917	0.134	-0.999	940-1100

*Equimolar.

Table 4. E versus temperature for the $FeCl_2$ galvanic cell.

Solvent	X_{FeCl_2}	E = BT + A (V)		C Coeff.	Range (K)
		$B \times 10^4$	A		
CsCl	3.41×10^{-3}	-1.713	0.683	-0.992	969-1044
	8.46×10^{-3}	-2.105	0.683	-0.999	967-1070
	1.26×10^{-2}	-2.231	0.678	-0.997	958-1053
	1.68×10^{-2}	-2.400	0.683	-0.994	968-1051
NaCl-CsCl*	2.79×10^{-3}	-1.279	0.614	-0.995	966-1029
	6.25×10^{-3}	-1.779	0.629	-0.998	953-1033
	9.18×10^{-3}	-1.849	0.619	-0.998	965-1036
	1.18×10^{-2}	-1.875	0.611	-0.998	957-1035
KCl-CsCl*	3.06×10^{-3}	-1.789	0.679	-0.997	974-1036
	6.25×10^{-3}	-2.119	0.682	-0.998	967-1036
	9.70×10^{-3}	-2.184	0.669	-0.999	962-1036
	1.26×10^{-2}	-2.438	0.684	-0.998	962-1031

*Equimolar.

Table 5. **E versus temperature for the CuCl galvanic cell.**

Solvent	X_{CuCl}	E = BT + A (V)		C Coeff.	Range (K)
		B × 10^4	A		
NaCl	1.01×10^{-3}	2.687	0.335	0.999	1090-1176
	1.93×10^{-3}	2.121	0.335	0.999	1087-1171
	2.84×10^{-3}	1.780	0.336	0.999	1082-1178
	3.68×10^{-3}	1.563	0.335	0.999	1084-1178
KCl	9.58×10^{-4}	2.228	0.432	0.999	1057-1156
	1.91×10^{-3}	1.623	0.433	0.999	1072-1181
	3.34×10^{-3}	1.150	0.432	0.999	1075-1173
	4.68×10^{-3}	0.858	0.432	0.998	1068-1181
CsCl	9.54×10^{-4}	1.642	0.511	0.998	962-1172
	1.91×10^{-3}	1.042	0.511	0.998	965-1175
	3.05×10^{-3}	0.633	0.512	0.997	986-1176
	4.94×10^{-3}	0.186	0.515	0.978	944-1181
NaCl-KCl*	9.00×10^{-4}	1.036	0.548	0.999	983-1181
	1.80×10^{-3}	4.370	0.549	1.000	994-1177
	3.09×10^{-3}	-0.025	0.548	-0.999	954-1173
	4.24×10^{-3}	-0.301	0.549	-0.999	942-1175
NaCl-CsCl*	9.25×10^{-4}	1.659	0.419	0.999	976-1175
	1.70×10^{-3}	1.140	0.418	0.999	966-1173
	2.77×10^{-3}	0.712	0.419	0.999	976-1173
	3.84×10^{-3}	0.432	0.419	0.999	964-1171
KCl-CsCl*	1.02×10^{-3}	1.661	0.497	0.999	979-1174
	2.04×10^{-3}	1.068	0.496	0.999	980-1169
	3.05×10^{-3}	0.714	0.497	0.999	975-1174
	4.40×10^{-3}	0.395	0.497	0.985	976-1180

*Equimolar.

Table 6. **E versus temperature for the $CrCl_2$ galvanic cell.**

Solvent	X_{CrCl_2}	E = BT + A (V)		C Coeff.	Range (K)
		B × 10^4	A		
NaCl	6.90×10^{-4}	1.234	0.660	0.999	1115-1172
	1.24×10^{-3}	1.356	0.619	0.999	1122-1173
	2.16×10^{-3}	1.035	0.630	0.999	1117-1175
	2.80×10^{-3}	1.105	0.609	0.999	1110-1166
KCl	7.01×10^{-4}	-2.695	1.076	-0.999	1082-1173
	1.21×10^{-3}	-1.552	0.925	-1.000	1086-1166
	1.72×10^{-3}	-1.611	0.914	-0.999	1092-1169
	2.29×10^{-3}	-2.234	0.970	-0.999	1084-1172
CsCl	1.65×10^{-3}	-3.459	1.071	-0.999	980-1114
	3.29×10^{-3}	-3.768	1.072	-0.999	980-1109
	5.03×10^{-3}	-3.949	1.072	-0.999	980-1107
	6.99×10^{-3}	-4.088	1.071	-0.999	981-1107
NaCl-KCl*	6.67×10^{-4}	-1.152	0.929	-0.993	984-1122
	1.09×10^{-3}	-1.416	0.935	-0.998	984-1122
	1.76×10^{-3}	-1.691	0.940	-0.998	984-1131
	2.36×10^{-3}	-1.833	0.940	-0.998	978-1131
NaCl-CsCl*	1.48×10^{-3}	-1.951	0.925	-0.998	1010-1132
	2.51×10^{-3}	-2.166	0.924	-0.999	977-1136
	3.38×10^{-3}	-2.269	0.921	-0.984	979-1118
	4.24×10^{-2}	-2.398	0.925	-0.999	978-1118
KCl-CsCl*	9.76×10^{-4}	-2.758	1.016	-0.999	981-1105
	1.76×10^{-3}	-3.007	1.015	-0.999	978-1129
	2.83×10^{-3}	-3.217	1.016	-0.999	981-1118
	3.60×10^{-3}	-3.321	1.016	-0.999	979-1110

*Equimolar.

Table 7. **E versus temperature for the $ThCl_4$ galvanic cell.**

Solvent	X_{ThCl_4}	E = BT + A (V)		C Coeff.	Range (K)
		$B \times 10^4$	A		
KCl	7.75×10^{-4}	-2.230	1.750	-0.999	1100-1179
	1.53×10^{-3}	-2.387	1.752	-0.999	1071-1174
	2.12×10^{-3}	-2.455	1.751	-0.999	1072-1173
	2.70×10^{-3}	-2.510	1.752	-0.999	1067-1173
CsCl	2.64×10^{-3}	-5.981	2.207	-0.999	981-1087
	4.13×10^{-3}	-6.082	2.208	-0.999	972-1085
	5.52×10^{-3}	-6.144	2.208	-0.999	955-1080
	7.74×10^{-3}	-6.207	2.206	-0.999	960-1079
NaCl-KCl*	6.73×10^{-4}	-4.007	1.936	-0.999	1009-1111
	8.22×10^{-4}	-4.064	1.937	-0.999	982-1092
	2.09×10^{-3}	-4.260	1.937	-0.999	982-1101
	2.88×10^{-3}	-4.324	1.936	-0.999	982-1101
	3.87×10^{-3}	-4.392	1.937	-0.999	981-1100
NaCl-CsCl*	1.71×10^{-3}	-0.489	1.590	-0.999	953-1083
	4.18×10^{-3}	-0.663	1.588	-0.999	948-1079
	6.81×10^{-3}	-0.777	1.589	-0.999	950-1085
	8.85×10^{-3}	-0.836	1.589	-0.999	896-1085
KCl-CsCl*	1.84×10^{-3}	-3.614	1.903	-0.999	961-1095
	3.68×10^{-3}	-3.769	1.904	-0.999	963-1092
	5.65×10^{-3}	-3.861	1.904	-0.998	963-1093
	8.35×10^{-3}	-3.944	1.903	-0.996	948-1093

*Equimolar.

Table 8. E versus temperature for the $FeCl_2$ - $FeCl_3$ redox cell.

Solvent	X_{FeCl_2}	X_{FeCl_3}	E = BT + A (V)		C Coeff.	Range (K)
			B × 10^4	A		
CsCl	3.46×10^{-3}	2.58×10^{-3}	1.010	0.666	0.997	955-1024
	3.45×10^{-3}	6.29×10^{-3}	1.897	0.655	0.997	950-1024
	3.44×10^{-3}	9.73×10^{-3}	2.344	0.649	0.999	950-1026
	3.43×10^{-3}	1.21×10^{-2}	2.430	0.659	0.998	960-1026
NaCl-CsCl*	3.17×10^{-3}	4.33×10^{-3}	1.433	0.643	0.998	962-1026
	3.16×10^{-3}	8.73×10^{-3}	2.065	0.641	0.999	953-1031
	3.14×10^{-3}	1.31×10^{-2}	2.452	0.637	0.998	953-1021
	3.13×10^{-3}	1.53×10^{-2}	2.532	0.643	0.998	945-1017
KCl-CsCl*	3.57×10^{-3}	2.79×10^{-3}	0.425	0.714	0.969	953-1024
	3.56×10^{-3}	4.94×10^{-3}	1.208	0.685	0.997	948-1024
	3.55×10^{-3}	7.19×10^{-3}	1.409	0.697	0.996	948-1019
	3.53×10^{-3}	1.20×10^{-2}	1.937	0.689	0.998	950-1019

*Equimolar.

Table 9. E versus temperature for the CuCl - $CuCl_2$ redox cell.

Solvent	X_{CuCl}	X_{CuCl_2}	E = BT + A (V)		C Coeff.	Range (K)
			B × 10^4	A		
NaCl	8.57×10^{-4}	4.86×10^{-4}	1.642	0.633	0.999	1096-1183
	8.56×10^{-4}	9.71×10^{-4}	2.260	0.631	0.999	1101-1174
	8.56×10^{-4}	1.50×10^{-3}	2.625	0.632	0.999	1092-1177
	8.55×10^{-4}	2.23×10^{-3}	2.977	0.631	0.999	1093-1179
KCl	8.84×10^{-4}	9.40×10^{-4}	-0.556	0.986	-0.999	1079-1171
	8.83×10^{-4}	1.73×10^{-3}	-0.031	0.986	-0.995	1071-1169
	8.82×10^{-4}	2.82×10^{-3}	0.394	0.985	0.999	1069-1165
	8.81×10^{-4}	3.68×10^{-3}	0.621	0.986	0.999	1068-1163
CsCl	1.48×10^{-3}	1.72×10^{-3}	-3.866	1.401	-1.000	988-1170
	1.48×10^{-3}	4.04×10^{-3}	-3.121	1.400	-1.000	985-1166
	1.48×10^{-3}	6.36×10^{-3}	-2.727	1.400	-0.999	990-1162
	1.47×10^{-3}	8.98×10^{-3}	-2.435	1.401	-0.998	987-1164
NaCl-KCl*	4.03×10^{-4}	3.46×10^{-4}	4.048	0.440	0.999	985-1171
	4.03×10^{-4}	7.16×10^{-4}	4.678	0.439	0.999	984-1164
	4.02×10^{-4}	1.11×10^{-3}	5.053	0.440	0.999	998-1167
	4.02×10^{-4}	1.51×10^{-3}	5.318	0.439	0.999	989-1172
NaCl-CsCl*	1.13×10^{-3}	1.25×10^{-3}	-0.840	1.014	-0.999	962-1099
	1.13×10^{-3}	2.60×10^{-3}	-0.205	1.014	-0.996	963-1105
	1.12×10^{-3}	4.05×10^{-3}	0.186	1.013	0.992	963-1103
	1.12×10^{-3}	5.49×10^{-3}	0.440	1.014	0.999	962-1103
KCl-CsCl*	1.06×10^{-3}	1.33×10^{-3}	-2.096	1.197	-0.999	953-1095
	1.06×10^{-3}	2.80×10^{-3}	-1.454	1.197	-0.999	948-1102
	1.06×10^{-3}	4.25×10^{-3}	-1.094	1.197	-0.999	961-1099
	1.06×10^{-3}	5.69×10^{-3}	-0.832	1.196	-0.999	961-1100

*Equimolar.

Table 10. **E versus temperature for the $CrCl_2$ - $CrCl_3$ redox cell.**

Solvent	X_{CrCl_2}	X_{CrCl_3}	E = BT + A (V)		C Coeff.	Range (K)
			$B \times 10^4$	A		
NaCl	1.11×10^{-3}	1.72×10^{-3}	10.98	-0.491	0.999	1098-1181
	1.10×10^{-3}	3.51×10^{-3}	11.60	-0.492	0.999	1093-1180
	1.10×10^{-3}	5.13×10^{-3}	11.91	-0.490	0.999	1093-1184
	1.10×10^{-3}	6.95×10^{-3}	12.18	-0.491	0.999	1091-1182
	2.41×10^{-3}	6.94×10^{-3}	11.51	-0.491	0.999	1091-1187
KCl	6.75×10^{-4}	1.31×10^{-3}	6.286	-0.034	0.999	1097-1184
	6.72×10^{-4}	4.54×10^{-3}	7.374	-0.036	0.999	1089-1179
	6.71×10^{-4}	6.82×10^{-3}	7.731	-0.036	0.999	1088-1181
	6.69×10^{-4}	8.93×10^{-3}	7.958	-0.035	0.999	1083-1180
	1.67×10^{-3}	8.92×10^{-3}	7.169	-0.035	0.999	1076-1175
CsCl	2.21×10^{-3}	3.06×10^{-3}	3.618	0.178	0.999	996-1103
	2.20×10^{-3}	6.11×10^{-3}	4.220	0.178	0.999	976-1103
	2.19×10^{-3}	9.85×10^{-3}	4.619	0.180	0.999	983-1109
	2.18×10^{-3}	1.49×10^{-2}	5.000	0.177	0.999	983-1115
	3.74×10^{-3}	1.48×10^{-2}	4.531	0.178	0.999	979-1109
NaCl-KCl*	9.68×10^{-4}	2.39×10^{-3}	10.83	-0.484	0.999	986-1126
	9.66×10^{-4}	4.03×10^{-3}	11.30	-0.485	0.999	985-1126
	9.65×10^{-4}	5.20×10^{-3}	11.52	-0.485	0.999	985-1130
	9.63×10^{-4}	7.80×10^{-3}	11.86	-0.484	0.999	978-1130
	2.40×10^{-3}	7.78×10^{-3}	11.08	-0.485	0.999	978-1135
NaCl-CsCl*	7.80×10^{-4}	3.48×10^{-3}	8.189	-0.145	0.999	902-1098
	7.76×10^{-4}	8.65×10^{-3}	8.978	-0.145	0.999	917-1098
	7.73×10^{-4}	1.18×10^{-2}	9.248	-0.145	0.999	925-1131
	7.70×10^{-4}	1.56×10^{-2}	9.501	-0.146	0.999	923-1127
	3.36×10^{-3}	1.55×10^{-2}	8.223	-0.145	0.999	893-1127
KCl-CsCl*	1.46×10^{-3}	4.22×10^{-3}	5.500	0.055	0.999	924-1118
	1.45×10^{-3}	8.34×10^{-3}	6.082	0.056	0.999	905-1086
	1.44×10^{-3}	1.34×10^{-2}	6.503	0.055	0.999	943-1086
	1.43×10^{-3}	1.70×10^{-2}	6.704	0.058	0.999	943-1120
	3.25×10^{-3}	1.70×10^{-2}	5.995	0.056	0.999	923-1120

*Equimolar.

Table 11. E versus temperature for the $ThCl_4$ - CsCl formation cell.

X_{ThCl_4}	E = A + BT (V)		C Coeff.	Range (K)
	A	$B \times 10^4$		
0.0513	3.583	-8.010	-0.999	940-1097
0.0979	3.527	-7.685	-0.999	916-1092
0.1846	3.487	-7.477	-0.998	963-1083
0.2696	3.435	-7.198	-0.999	886-1034
0.3413	3.370	-6.892	-0.998	908-1025
0.4408	3.307	-6.782	-0.999	898-1029

Table 12. **Formal Formation Potentials of the Molten Dilute Solutions of Metal Chlorides in Alkali Chlorides.**

System	E°_f (V)*				±ΔE(V)
	1073 K		1173 K		
ThCl$_4$-KCl	2.502		2.465		0.002
ThCl$_4$-CsCl	2.649		2.603		0.002
ThCl$_4$-NaCl-KCl	2.434		2.379		0.001
ThCl$_4$-NaCl-CsCl	2.576		2.534		0.001
ThCl$_4$-KCl-CsCl	2.555	(2.576)	2.496	(2.534)	0.001
CrCl$_2$-NaCl	1.519		1.503		0.006
CrCl$_2$-KCl	1.605		1.562		0.004
CrCl$_2$-CsCl	1.624		1.562		0.004
CrCl$_2$-NaCl-KCl	1.563	(1.562)	1.520	(1.533)	0.006
CrCl$_2$-NaCl-CsCl	1.550	(1.572)	1.491	(1.533)	0.006
CrCl$_2$-KCl-CsCl	1.590	(1.615)	1.530	(1.562)	0.005
CrCl$_3$-NaCl	1.151		1.107		0.007
CrCl$_3$-KCl	1.262		1.215		0.005
CrCl$_3$-CsCl	1.311		1.259		0.006
CrCl$_3$-NaCl-KCl	1.209	(1.207)	1.147	(1.161)	0.007
CrCl$_3$-NaCl-CsCl	1.213	(1.231)	1.147	(1.183)	0.007
CrCl$_3$-KCl-CsCl	1.273	(1.287)	1.214	(1.237)	0.007
CoCl$_2$-NaCl	1.070		1.040		0.008
CoCl$_2$-KCl	1.185		1.149		0.006
CoCl$_2$-CsCl	1.289		1.251		0.004
CoCl$_2$-NaCl-KCl	1.126	(1.128)	1.087	(1.095)	0.008
CoCl$_2$-NaCl-CsCl	1.172	(1.180)	1.127	(1.146)	0.006
CoCl$_2$-KCl-CsCl	1.227	(1.237)	1.171	(1.200)	0.006
NiCl$_2$-NaCl	0.870		0.846		0.008
NiCl$_2$-KCl	0.970		0.944		0.006
NiCl$_2$-CsCl	1.040		1.010		0.004
NiCl$_2$-NaCl-KCl	0.930	(0.920)	0.882	(0.895)	0.006
NiCl$_2$-NaCl-CsCl	0.948	(0.955)	0.904	(0.928)	0.006
NiCl$_2$-KCl-CsCl	1.020	(1.005)	0.983	(0.977)	0.006
FeCl$_2$-CsCl	1.456		1.418		0.004
FeCl$_2$-NaCl-CsCl	1.339		1.289		0.006
FeCl$_2$-KCl-CsCl	1.407		1.357		0.006
CuCl-NaCl	1.047		1.018		0.006
CuCl-KCl	1.185		1.148		0.006
CuCl-CsCl	1.267		1.223		0.004
CuCl-NaCl-KCl	1.096	(1.116)	1.059	(1.083)	0.006
CuCl-NaCl-CsCl	1.086	(1.157)	1.031	(1.121)	0.008
CuCl-KCl-CsCl	1.223	(1.226)	1.170	(1.186)	0.006
FeCl$_3$-CsCl	1.110		1.081		0.007
FeCl$_3$-NaCl-CoCl	1.015		0.974		0.007
FeCl$_3$-KCl-CsCl	1.072		1.033		0.009
CuCl$_2$-NaCl	0.624		0.601		0.007
CuCl$_2$-KCl	0.711		0.696		0.007
CuCl$_2$-CsCl	0.758		0.757		0.005
CuCl$_2$-NaCl-KCl	0.653	(0.668)	0.614	(0.649)	0.007
CuCl$_2$-NaCl-CsCl	0.654	(0.691)	0.625	(0.679)	0.009
CuCl$_2$-KCl-CsCl	0.729	(0.735)	0.709	(0.727)	0.007

* Values in brackets refer to values calculated with Eq. (18).

Table 13. **Formal Redox Potentials of the Molten Dilute Solutions of Metal Chlorides in Alkali Chlorides.**

System	E°_f (V)*				
	1073 K		1173 K		± E
$CrCl_2$-$CrCl_3$-NaCl	0.416		0.314		0.001
$CrCl_2$-$CrCl_3$-KCl	0.577		0.522		0.001
$CrCl_2$-$CrCl_3$-CsCl	0.685		0.653		0.002
$CrCl_2$-$CrCl_3$-NaCl-KCl	0.502	(0.497)	0.402	(0.418)	0.001
$CrCl_2$-$CrCl_3$-NaCl-CsCl	0.539	(0.551)	0.459	(0.484)	0.001
$CrCl_2$-$CrCl_3$-KCl-CsCl	0.638	(0.631)	0.583	(0.588)	0.002
$FeCl_2$-$FeCl_3$-CsCl	0.418		0.406		0.003
$FeCl_2$-$FeCl_3$-NaCl-CsCl	0.367		0.344		0.001
$FeCl_2$-$FeCl_3$-KCl-CsCl	0.402		0.384		0.003
CuCl-$CuCl_2$-NaCl	0.200		0.183		0.001
CuCl-$CuCl_2$-KCl	0.236		0.244		0.001
CuCl-$CuCl_2$-CsCl	0.249		0.290		0.001
CuCl-$CuCl_2$-NaCl-KCl	0.209	(0.218)	0.168	(0.214)	0.001
CuCl-$CuCl_2$-NaCl-CsCl	0.221	(0.225)	0.219	(0.237)	0.001
CuCl-$CuCl_2$-KCl-CsCl	0.234	(0.243)	0.247	(0.267)	0.001

* Bracketed values correspond to calculated potentials using Eq. (18).

Table 14. **Standard Potentials for Pure Molten Metal Chlorides as a Function of Temperature.**

System	$E^\circ = A^\circ + B^\circ T$* (Volts)		E° (Volts)		±ΔE (mV)	Melting point (°K)	Reference
	A	$B \times 10^4$	1073 (°K)	1173 (°K)			
AgCl**	1.0828	-2.405	0.8243	0.8005	2.0	728	5
CuCl	1.2400	-3.000	0.918	0.888	-	703	24
$FeCl_2$	1.4500	-3.000	1.128	1.097	21.7	950	24

* Calculated in the temperature range 973°K to 1173°K.

** The expanded expression is given as:
$E^\circ\,(mV) = 1227.0 - 1.5973\,T + 0.182\,T \ln T - 4.48 \times 10^{-5}\,T^2$
which is applicable to the temperature range 728°K to 1173°K. The linear equation given in this table represents only the temperature range 973°K to 1173°K.

Table 15. **Thermodynamic Properties of the Molten Dilute Solutions of Metal Chlorides in Alkali Chlorides.**

System	γ_{MCl_x} at $(X_{MCl_x} \to 0)$		$\overline{\Delta H}_{MCl_x}$ at $(X_{MCl_x} \to 0)$ $(KJmol^{-1})$		
	1073 K	1173 K	This work:	Calorimetric*	Reference
AgCl-NaCl	1.530	1.449	3.70±0.40	(4.77)	25
AgCl-KCl	0.553	0.583	-5.70±0.30	(-6.47)	25
AgCl-CsCl	0.273	0.306	-13.65±0.30	(-16.90)	25
AgCl-NaCl-KCl	1.048	1.056			
AgCl-NaCl-CsCl	0.694	0.816	-16.85±0.40		
AgCl-KCl-CsCl	0.404	0.488	-13.46±0.40		
CuCl-NaCl	0.247	0.276	-13.45		
CuCl-KCl	0.056	0.076	-32.55		
CuCl-CsCl	0.023	0.036	-47.95		
CuCl-NaCl-KCl	0.146	0.118	-38.22		
CuCl-NaCl-CsCl	0.162	0.213	-41.27		
CuCl-KCl-CsCl	0.037	0.061	-54.39		
$FeCl_2$-CsCl	0.00083	0.00174	-88.07	(-83.46)	28
$FeCl_2$-NaCl-CsCl	0.01042	0.02239	-79.58		
$FeCl_2$-KCl-CsCl	0.00239	0.00583	-100.7		

* Calorimetric data are reported uniformly only to a concentration of metal chloride of 10 mole % because solution calorimetry is unable to accurately measure very dilute solutions.

Table 16. **Mass Balance for the MCl_2 - ACl System.**

$MCl_2 + r \cdot ACl \qquad (MCl_{2+r})^{r-} + r \cdot A^+$

or

$M^{2+} + (2+r)Cl^- \qquad (MCl_{z+r})^{r-}$

α = degree of reaction per mol MCl_z

INITIAL COMPOSITION		**IONIC COMPOSITION AFTER REACTION HAS REACHED EQUILIBRIUM**
Compound	mols	(n_1 are ion numbers)
MCl_2	n_1	$n_{M^{z+}} = n_1 \cdot (1-\alpha)$ $n_{A+} = n_2 \cdot r$
ACl	n_2	
		$\Sigma(+ve) = n_1 \cdot (1-\alpha) + n_2 \cdot r$
		$n_{Cl^-} = n_1 \cdot z + n_2 \cdot r - \alpha \cdot n_1 \cdot (2+r)$ $n_{(MCl_{2+r})} r- = \alpha \cdot n_1$
		$\Sigma(-ve) = n_1 \cdot (2(1-\alpha) + \alpha(1-r)) + n_2 \cdot r$

$$K = \frac{N_{(MCl_{2+r})^{r-}}}{N_{M^{2+}} \cdot N_{Cl^-}^{(2+r)}} = f(n_1, n_2, \alpha, r)$$

N_i's = ion fractions = $\frac{n_i}{\Sigma n_i}$

Table 17. Model Calculations for the AgCl systems at 1073 K.

XAgCl	α	$N_{AgCl_2^-}$	N_{Ag^+}	N_{Cl^-}	K
CsCl solvent:					
5.15×10^{-3}	0.7270	3.758×10^{-3}	1.411×10^{-3}	9.962×10^{-1}	2.68
1.02×10^{-2}	0.7270	7.471×10^{-3}	2.806×10^{-3}	9.925×10^{-1}	2.70
4.98×10^{-2}	0.7266	3.754×10^{-2}	1.413×10^{-2}	9.625×10^{-1}	2.86
1.00×10^{-1}	0.7253	7.820×10^{-2}	2.962×10^{-2}	9.218×10^{-1}	3.10
					Avg = 2.84 ± 0.26
KCl solvent:					
1.14×10^{-3}	0.4470	5.098×10^{-4}	6.307×10^{-4}	9.995×10^{-1}	0.809
9.89×10^{-3}	0.4470	4.440×10^{-3}	5.494×10^{-3}	9.956×10^{-1}	0.815
5.00×10^{-2}	0.4467	2.284×10^{-2}	2.829×10^{-2}	9.772×10^{-1}	0.845
1.00×10^{-1}	0.4458	4.666×10^{-2}	5.800×10^{-2}	9.533×10^{-1}	0.885
					Avg = 0.84 ± 0.05

REFERENCES

1. S.N. Flengas and T.R. Ingraham, Can. J. Chem. 35, 1139 (1957).
2. S.N. Flengas and T.R. Ingraham, Can. J. Chem. 35, 1254 (1957).
3. S.N. Flengas and T.R. Ingraham, Can. J. Chem. 36, 1103 (1958).
4. S.N. Flengas and T.R. Ingraham, Can. J. Chem. 36, 1662 (1958).
5. A.D. Pelton and S.N. Flengas, J. Electrochem. Soc. 117, 1130 (1970).
6. A.S. Kucharski and S.N. Flengas, J. Electrochem. Soc. 119, 1170 (1972).
7. C.A. Pickles and S.N. Flengas, J. Electrochem. Soc. 131, 2069 (1984).
8. P.J. Tumidajski and S.N. Flengas, Can. J. Chem. 63, 1080 (1985).
9. P.J. Tumidajski and S.N. Flengas, J. Electrochem. Soc. in press.
10. S.N. Flengas, High Temp. High Pres. 5, 551 (1973).
11. J. Guion, M. Blander, D. Hengstenberg, and K. Hagemark, J. Phys. Chem. 72, 2086 (1968).
12. S. Senderoff and G.W. Mellors, Rev. Sci. Instr. 29, 151 (1958).
13. J. Leonardi and J. Brenet, Compt. Rend. 261, 116 (1965).
14. W.J. Hamer, M.S. Malmberg, and B. Rubin, J. Electrochem. Soc. 103, 8 (1956).
15. D.R. Sadoway and S.N. Flengas, J. Electrochem. Soc. 122, 515 (1975).
16. H. Kuhnl, M. Wittner, and W. Simon, Electrochem. Acta 24, 55 (1979).
17. M.V. Smirnov, A.V. Pokrobskii, and N.A. Loginov, Russ. J. Inorg. Chem. 15, 1644 (1970).
18. R. Combes, J. Vedel, and B. Tremillon, J. Electroanal. Chem. 27, 174 (1970).
19. D.C. Hamby and A.B. Scott, J. Electrochem. Soc. 115, 704 (1968).
20. D.C. Hamby and A.R. Hohimer, J. Electrochem. Soc. 121, 104 (1974).
21. D.C. Hamby and A.B. Scott, J. Electrochem. Soc. 117, 1130 (1970).
22. M.V. Smirnov, A.V. Pokrobskii and N.A. Loginov, Zh. Prikl. Kh. 43, 2334 (1970).
23. R. Srinivasan and S.N. Flengas, Can. J. Chem. 42, 1315 (1964).
24. O. Kubaschewski and C.B. Alcock, "Metallurgical Thermochemistry", 5th ed., Pergamon Press, New York (1979).
25. P. Dantzer and O.J. Kleppa, J. Chem. Phys. 71, 216 (1974).
26. Z. Moser, M. Kucharski, and K. Rzyman, J. Electrochem. Soc., 125, 692 (1978).
27. Z. Moser, W. Gasior, and K. Rzyman, J. Electrochem. Soc. 126, 1467 (1979).
28. G.N. Papatheodorou and O.J. Kleppa, J. Inorg. Nucl. Chem. 33, 889 (1970).

29. A. Hacetoglu and S.N. Flengas, "Proceedings of the Joint International Symposium on Molten Salts", ed. M.L. Saboungi, M. Blander, and D.S. Newman. (The Electrochemical Society, N.J. 1987), pp 28-51.
30. A.S. Kucharski and S.N. Flengas, J. Electrochem. Soc. 121, 1298 (1974).
31. S.N. Flengas and J.M. Skeaff, Can. J. Chem. 50, 1345 (1972).
32. S.N. Flengas and A.S. Kucharski, Can. J. Chem. 49, 3971 (1971).

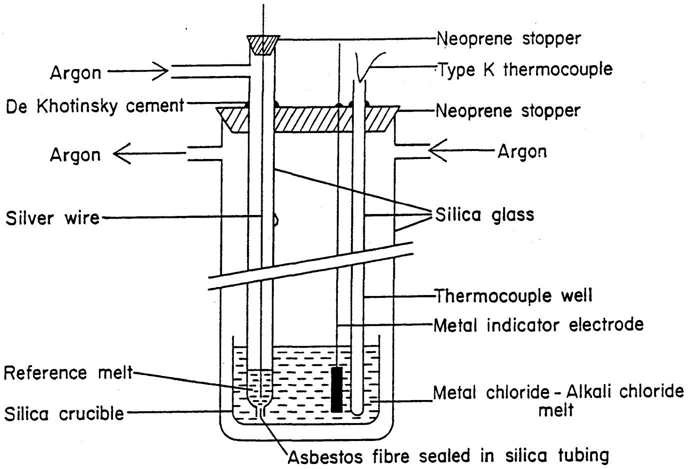

Figure 1. Emf cell design.

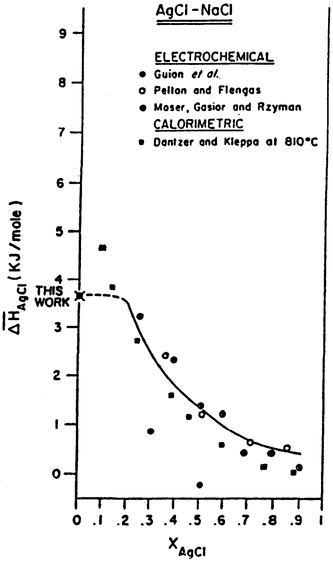

Figure 2. Partial molar enthalpies of mixing in the NaCl-AgCl system. Comparison between calorimetric and electrochemical data.

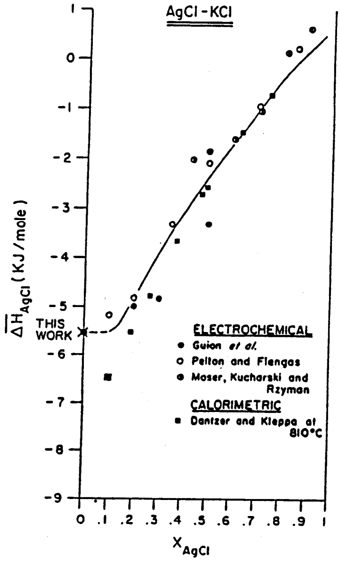

Figure 3. Partial molar enthalpies of mixing in the KCl-AgCl system. Comparison between calorimetric and electrochemical data.

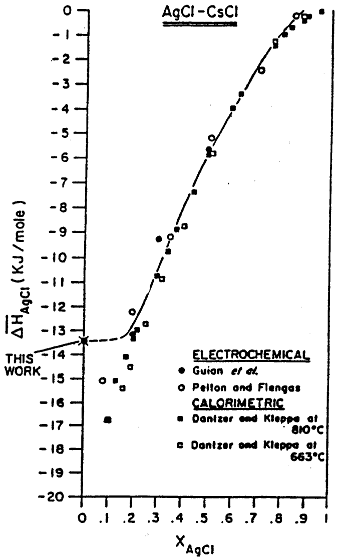

Figure 4. Partial molar enthalpies of mixing in the CsCl-AgCl system. Comparison between calorimetric and electrochemical data.

DOI: 10.1149/199017.0438PV

BEHAVIOR OF THE CHLORINE ELECTRODE IN FUSED ALKALI CHLORIDES

Frédéric Lantelme, Hiraclis Alexopoulos, Marius Chemla and Otto Haas*

Laboratoire d'Electrochimie, U. A. 430 C. N. R. S.,
Université Pierre et Marie Curie, 4 Place Jussieu,
F 75252 Paris cedex 05, France.

*Swiss federal Institute Paul Scherrer (P. S. I)
Villingen-PSI, CH5232 Switzerland.

ABSTRACT

A model is presented to describe the behavior of a gas electrode: the chlorine gas, introduced inside the electrode, flowed through the porous wall of the electrode made of carbon or graphite. The model takes into consideration the main parameters which influence the electrolysis : the properties of carbon and graphite (density, porosity, pores distribution), the wetting properties of the electrode process, the chlorine pressure and the temperature.

INTRODUCTION

Electrochemical couples such as Li-Cl_2 or Al-Cl_2 offer a possibility of obtaining high energy capacity electrochemical generators. Their future depends mainly on the control of the efficiency of the chlorine electrode. The aim of the present work is the study of parameters leading to a high current density chlorine gas electrode.

The reduction of chlorine at the cathode level occurs through a three-phase reaction which involves the liquid electrolyte, the solid electrode and the gaseous reagent. The behavior of such systems is often critical. A model was recently developed (1) to describe the reduction of a gaseous reagent present in bubbles attached at the electrode surface. It was shown that the main part of the reaction is concentrated in the region very close by the triple contact around the bubble. This behavior is similar to that of a static gas electrode-gas electrolyte system. Bockris and Cahan (2) showed that in the region very near the tip of the meniscus the charge transfer is the primary limiting factor; then starts a second region which has a mixed diffusion and activation limitation up to a third zone where the meniscus is so thick that negligible additional currents can be drawn.

To obtain high current densities the active surface had been increased using porous electrodes where the gaseous component is spread through the electrode material. We were led to use an injection electrode (3) constituted by a porous graphite tubing closed at one end; the chlorine gas was sent under pressure in the inner part of the tubing.

The primary objective of the present work was to elucidate the behavior of the chlorine electrode based on the results of transient electrochemical techniques. The fused electrolyte used was an eutectic mixture lithium chloride - potassium chloride with eventual additions of aluminum chloride. Special attention was paid to the influence of the chlorine pressure, of the temperature and of the structure of the electrode material.

EXPERIMENTAL

The electrochemical cell consisted of an outer Pyrex envelope at the bottom of which rested the Pyrex vessel with molten bath. The experiments were carried out at about 450°C under an argon atmosphere. The LiCl-KCl eutectic mixture was purified according to a procedure of high vacuum dessication, chlorine bubbling, argon flushing, electrolysis and filtering (4). The introduction of aluminum chloride was carried out by anodic dissolution of a rod of pure aluminum, the cathode being a chlorine electrode.

In order to observe the formation of gas bubbles a transparent electrical furnace was used. For more details concerning the cell, the electrolyte preparation and the atmosphere purification see ref.(5).

Table I. Technical characteristics of various graphite and carbon samples.

Sample	Density	Porosity	Gas permeability $cm^2\ s^{-1}\ atm^{-1}$	Electrical resistivity $10^{-3}\ \Omega\ cm$
Graphite				
N°208(a)	1.68	0.20	0.15	1.3
Pyrolytic(a)	2.25	0	0	0.4 // ≈50 ⊥
3780(a)	1.6	0.24	0.38	1.3
5501(a)	1.6	0.25	0.60	1.2
PG60(b)	1.05	0.49	250.	—
Carbon				
P2P(c)	1.5	0.15	not measured	4

Manufacturer: (a)Le Carbone Lorraine, (b)Union Carbide, (c)Société des Electrodes et Réfractaires de Savoie.

The counter electrode and the reference electrodes were chlorine electrodes similar to that already described (3). The working electrodes consist in an hollow rod of porous graphite sealed at the end of an Inconel tubing; the chlorine gas was introduced under pressure in the tubing and diffused through the electrode wall. Different graphite or carbon grades were used (Table I): graphite grades N° 208, N° 3780, N° 5501 Le Carbone Lorraine, PG60 Union Carbide, and carbon P2P Société des Electrodes et Réfractaires de Savoie. The chlorine gas was injected through the Inconel tubing at overpressures varying from a few mmHg to one and a half atmosphere.

For the generation of different potential or current programs a Tacussel PRT 20/10 potentiostat and a Tacussel GSTP4 programmer were used. The transient responses were collected on a Sefram X/Y recorder, unless stored in a digital Nicolet 3091 as an intermediate stage.

RESULTS

A sufficient pressure of chlorine inside the hollow electrode is applied to maintain gas bubbles at the electrode surface. For not too large current density which depends on the nature of the electrode and on the sweep rate (generally less than 1 A/cm^2) the observed cyclic voltammograms are straight lines the slope of which corresponds to the ohmic resistance of the electrical circuit. For higher current departures appear from the straight line which show that additional limitations occur. To obtain a better view of the efficiency of the electrode its behavior was examined under galvanostatic conditions. A representative chronopotentiogram is drawn in Fig. 1 . First a rapid change of the potential is observed. Then, for high current densities or when the chlorine flux through the electrode is not high enough to satisfy the reduction reaction, the electrode potential decreases continuously down to the reduction of alkali ions and formation of intercalation compounds alkali metals-graphite. To avoid this disadvantage the current intensity should be reduced or the chlorine pressure increased. A stationary state can then be reached which corresponds to a stable potential of the electrode (Fig. 2). This potential and thus the electrode efficiency depends mainly on four factors : the current density, the electrode material, the chlorine pressure and the temperature.

In Figs. 3 and 4 the curves η vs. i are reported for various electrodes, i is the current density at the steady state. These curves show the decisive influence of the nature of the graphite. The porous graphites such as PG60 or 3780 Carbone Lorraine appear to be the most interesting materials. Moreover the influence of the temperature is detected (Fig. 4); for a given overpotential a temperature changes from 420 to 470°C increases the current density by a factor about 2.5 .

The chlorine pressure plays also an important role; in general the current increases when the pressure increases . However for thin walled electrodes large pressures have a negative effect on the electrode performance (Fig. 3). Probably as revealed by the fundamental studies of Dukovic and Tobias (6) the high gas flux increases the ohmic obstruction within the electrolyte and induces a masking effect which reduces the active area of the electrode.

In addition to these investigations duration tests of aluminum-chloride cellswere performed. It is observed that the carbon electrodes has a short life-time, whereas prototypes using graphite 3780 or PG60 exhibit a stable behavior during several days. One of the best result was obtained using a graphite electrode PG60 (wall thickness : 2 mm, chlorine overpressure 0.54 atm., temperature : 470°C), the stable emf of the Al-Cl_2 battery was 0.58 V and the current 1.93 A cm^{-2}; i.e. a power density of about 1 W cm^{-2}.

DISCUSSION

When a flow of chlorine is maintained through the wall of an hollow electrode, bubbles are continuously present at the electrode surface; the electrolyte remains saturated with chlorine gas. Large current densities can only be maintained with high overpotentials, intense chlorine feed and active triple contact.

The efficiency of the gas electrode depends on the volume distribution of the three phases : solid, liquid and gas. Amongst the most important factors to be considered are the size of the pores, their repartition and their state (filled or not with the electrolyte). Different models were used to take account of these factors. Here, in a simplifying assumption the porous material is represented by a set of cylindrical capillaries perpendicular to the electrode surface. It is considered that the distribution of the diameters of the capillaries is non-uniform. The electrode being used as cathode in the aluminum-chlorine batteries the electrolyte contains always a certain amount of aluminum chloride and, in this case, it has been shown (7) that the electrolyte wetted the graphite. As a consequence the pores of small diameter are completely filled with the electrolyte and, then, are electrochemically inactive. The larger pores are filled with the gas; their wall being wetted by the electrolyte, they promote a strong electrochemical activity since, at their level, exists a triple contact between the active components : the electrode, the gas and the electrolyte. Our aim is to calculate the number of active pores for a given material and to determine the current coming from the whole set of these pores. To perform this calculation we introduce the concept of critical radius r_0 which depends on the surface tension σ, on the contact angle θ, and on the chlorine pressure ΔP .

$$r_0 = 2\sigma \cos \theta / \Delta P \qquad [1]$$

The pores whose radius is lower than r_0 are filled with the electrolyte and are inactive. The current density coming from the contribution of active pores ($r > r_0$) is

$$i = \int_{\infty}^{r_\circ} I(r)\ [d\phi(r)/\pi r^2 dr]dr \qquad [2]$$

where I(r) is the current coming from a capillary of radius r. In the above expression the quantity $d\phi(r)/\pi r^2$ represents the number of capillaries whose radius lies between r and r+dr. $\phi(r)$ is the distribution of the pore size expressed as the porosity due to the pores whose radius is equal or greater than r.

The problem of the wetted capillary was examined by de Levie (8). For a given overpotential $\eta = E-E^*$ ($\eta \leq 0$) and when the thickness of the liquid layer which covers surface of the capillary is small with respect to the radius r of the capillary, the current I(r) obeys the equation

$$I(r) = -2\pi r\{2RTDc^*/\rho\}^{1/2}\{-1 - F\eta + \exp[F\eta]\}^{1/2} \qquad [3]$$

ρ is the electrical resistivity of the electrolyte. Here for a battery working at atmospheric pressure $E=E°$ and $c^* = c_0$; for the reduction process the current I(r) is negative. By introducing [3] in [2] it is obtained

$$i = -2(2RTDc^*/\rho)^{1/2}[f(\eta)]^{1/2}\int_{\infty}^{r_\circ}(1/r)[d\phi(r)/d(r)]dr \qquad [4]$$

with $f(\eta) = -F\eta - 1 + \exp(F\eta)$ and $\eta \leq 0$

From this equation, it is possible to calculate the current density of the chlorine electrode for a given overpotential and chlorine pressure, r_0 being deduced from [1]. The physicochemical parameters required for this calculation are indicated in Table II. Moreover, to achieve this calculation it is necessary to know the function $\phi(r)$. In a general way the porosity measurements indicate that the distribution of pore size $\phi(r)$ can be represented by a sigmoid function (7)

$$\phi(r) = \phi_\circ\{1-[1-u]\exp[u]\} \qquad [5]$$

with $u = \zeta\log(r/\lambda)$. This function exhibits an inflexion point for $u = -1$.

ϕ_0 is the total porosity of the material. λ and ζ are two parameters which define the function ϕ (r); λ is a length which corresponds to the maximum radius of the pores : for $r \geq \lambda$, $\phi=0$. The dimensionless parameter ζ characterizes the shape of the curve

$$\zeta=1/\log(\lambda/r_c) \qquad [6]$$

r_c is the pore radius at the inflexion point where $\phi(r_c)=0.265\ \phi_o$. The values of these parameters used in our calculations are shown in Table II for three graphite samples.

For a given overpotential the current density was deduced from [4] by numerical integration using the Simpson's method. In order to compare these results with experiments the power density of an aluminum-chlorine battery was calculated; it was considered that the overpotential on the aluminum electrode remained negligible (7). In Fig. 5 are represented the dependence of power densities of Al-Cl_2 batteries on the chlorine pressure for different types of graphite cathodes; these values correspond to the discharge through a resistor. The theoretical curves deduced from the model developed above are in agreement with the experimental behavior. These calculations correctly predicts the behavior of the gas electrode; they take into account the crucial influence of the gas overpressure; As deduced from [1] this is attributed to the increasing number of active capillaries at higher pressures.

Table II. Data used in the calculations [1,4 and 5].

-Literature data concerning the physicochemical properties of the electrolyte.

Temperature T	Electrical resistivity (9)	Concentration of dissolved chlorine (p_{Cl_2} =1 atm) (10, 11)	Diffusion coefficient D (9)	surface tension σ (9)
°C	ρ / Ω cm	c_o/mol cm^{-3}	$cm^2\ s^{-1}$	dyn cm^{-1}
420	0.72	1.35 10^{-7}	1.0 10^{-4}	131
470	0.58	1.60 10^{-7}	1.6 10^{-4}	128

-Parameters used in equation [5] to describe the porosity distribution of some graphite samples used for the injection electrodes.

Sample	Porosity ϕ_o	λ µm	ζ
PG60	0.48	50	1.6
3780	0.24	50	1.3
P2P	0.15	200	1.6

Table III. Power density P_w and voltage E of the aluminium-chlorine battery vs.cathodic current density i and chlorine overpressure P_{Cl2}. Experimental results in the steady regime, after at least one hour working; the external electrical circuit is a resistance R; S is the area of the chlorine electrode and R_i the internal resistance of the battery (including the resistance of the carbon material).

Battery N°1 : Graphite sample 3780, $S=4\ cm^2$, $R_i=0.42\ \Omega$, T= 420°C.
Battery N°2 : Graphite sample 3780, $S=2.5\ cm^2$, $R_i=0.42\ \Omega$, T= 470°C.
Battery N°3 : Graphite sample PG60, $S=14\ cm^2$, $R_i=0.214\ \Omega$, T= 420°C.
Battery N°4 : Graphite sample PG60, $S=3\ cm^2$, $R_i=0.2\ \Omega$, T= 470°C.
Battery N°5 : Carbon sample P2P, $S=10\ cm^2$, $R_i=0.472\ \Omega$, T= 425°C.

	R/Ω	$i/A\ cm^{-2}$	$P_{Cl_2}/mmHg$	E/V	$P_w/W\ cm^{-2}$
Battery	0.1	0.300	10	0.12	0.036
N°1	0.1	0.375	14	0.15	0.056
E°=2.17 V	0.1	0.425	16	0.17	0.072
	0.1	0.525	25	0.21	0.110
	1.0	0.137	10	0.55	0.075
	1.0	0.280	25	1.12	0.313
Battery	1.0	0.468	10	1.17	0.547
N°2	1.0	0.540	25	1.36	0.729
E°=2.17 V					
Battery	0.1	0.364	4	0.51	0.185
N°3	1.0	0.107	4	1.51	0.162
E°=2.16 V	10.	0.015	4	2.11	0.032
Battery	0.1	0.666	8	0.20	0.133
N°4	0.1	0.866	12	0.26	0.225
E°=2.12 V	0.1	1.533	17	0.46	0.703
	0.1	1.670	30	0.50	0.833
	0.1	1.933	43	0.58	1.120
Battery	0.1	0.121	15	0.121	0.014
N°5	0.1	0.152	25	0.152	0.023
E°=2.15 V	0.1	0.163	33	0.163	0.027
	1.0	0.070	9	0.70	0.047
	1.0	0.080	15	0.80	0.064
	1.0	0.090	23	0.90	0.081
	1.0	0.095	32	0.95	0.090
	10.	0.018	11	1.77	0.031
	10	0.018	14	1.82	0.033
	10	0.019	19	1.90	0.036
	10	0.020	32	1.96	0.038

It is also observed that the battery works better at high temperatures. This behavior is predicted by the model which shows that the current density is proportional to the square root of the product TDc^*/ρ. From the literature data (Table II) it is calculated that, for a given overpotential, a temperature rise of 50°C should increase the current by about 60% . This deduction is in good agreement with the experimental results (Table III and Fig. 4). Moreover at low temperatures (<400°C) some battery failures may occur as a consequence of the vicinity of the freezing point and of the composition change resulting from transport processes.

Our experiments indicate the decisive influence of the structure of the graphite electrode. For example, as a result of the high current density obtained in our experiments, the resistivity of the graphite electrode itself is an important parameter. The efficiency of the battery is improved when materials having a large porosity and thin pores such as the PG60 are used. This effect is taken into account in the theoretical model through the factors ϕ_o, λ and ζ. Roughly, for a given porosity ϕ_o, the smaller λ (maximal pore radius) and ζ (related to the position of the inflexion point, eq. 6) the thinner are the pores.

In conclusion the theoretical analysis developed above may be useful in contributing to the choice of materials for the gas electrode. This study confirms that the highest power densities are obtained using graphites with large porosities and small pore radii. Moreover as a consequence of the gas flow required by the electrochemical reaction a pressure gradient exists through the capillaries. This pressure drop should be taken into account to calculate the pressure ΔP in [1]. In most of our experiments this pressure drop remains negligible (7). This effect should increase rapidly as the capillaries become thinner than a few μm. The present experiments indicate that the best performances are obtained with graphite having a porosity of 50% and a mean pore size of 50 μm; under a chlorine overpressure of about 40 mmHg, power densities of 1.1 W cm^{-2} can be reached with a current density of about 2 A cm^{-2}. In this laboratory cell the heat loss remains high, about 10 W for a cathode area of 3 cm^2 and a cell volume of about 30 cm^3. The temperature increase at the steady state is about 15°C.

REFERENCES

1 - F. Lantelme, H. Alexopoulos and O. Haas, J. Appl. Electrochem., **19**, 649 (1989).

2 - J'Om Bockris and B. D. Cahan, J. Chem. Phys., **50**, 1370 (1969).

3 - M. Chemla and J. Périé, French Patent N° 1332 518 (1963).

4 - T. Vargas and D. Inman, J. Appl. Electrochem. **17**, 270 (1987).

5 - F. Lantelme, D. Inman and D. G. Lovering, "Electrochemistry" Vol.2 "Molten Salt Techniques" ed. R. J. Galeand D. G. Lovering, Plenum Press (1984).

6 - J. Dukovic and C. W. Tobias, J. Electrochem. Soc., **134**, 331 (1987)

7 - A. Alexopoulos, Thesis, University Pierre et Marie Curie, Paris (1988).

8 - R. de Levie in "Advances in Electrochemistry and Electrochemical Engineering" Vol. 6, p. 329, Ed. P. Delahaye and C. W. Tobias Interscience (1967).

9 - G. J. Janz, "Physical Properties Data Compilations relevant to Energy Storage", NBS 61, Part II (1979).

10 - J. D. Van Norman and R. J. Tivers, J. Electrochem. Soc., **118**, 258 (1971).

11 - T. Nakajima, H. Imoto, K. Nakanishi and N. Watanabe, Denki Kagaku, 42, 85 (1974).

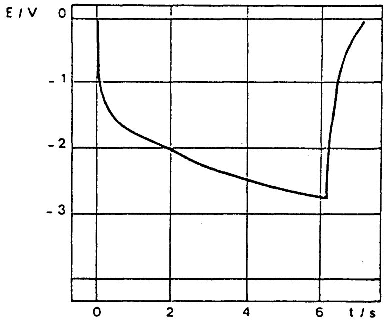

Fig. 1. Potential variation of an injection electrode vs. time. Working electrode: graphite sample N° 5501. Wall thickness: 1.2 mm. T= 420°C. Constant current density: 0.38 A cm^{-2} during 6.3 s, ΔPcl_2= 10 mmHg.

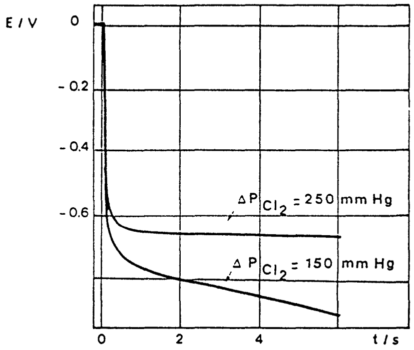

Fig. 2. Potential variation of an injection electrode vs. time for two chlorine overpressures ΔPcl_2. Working electrode: graphite sample N° 5501. Wall thickness: 1.2 mm. T= 420°C. Constant current density: 0.088 A cm^{-2}.

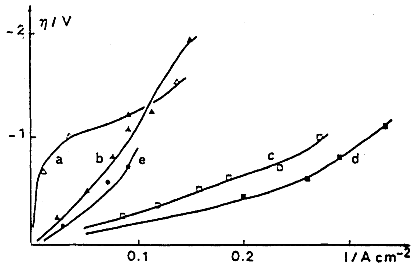

Fig. 3. Polarisation of chlorine electrodes vs. the current density, graphite sample 5501; data after one working hour. Wall thickness δ. Chlorine overpressure: ΔPcl_2. Temperature: T. *Curve a*: δ=0.8 mm, ΔPcl_2=40 mmHg, T=470°C; *curve b* :δ=0.8 mm, ΔPcl_2=5 mmHg, T=470°C; *curve c*: δ= 1.2 mm, ΔPcl_2=40 mmHg; T=470°C; *curve d*: δ=1.2 mm, ΔPcl_2=5 mmHg, T=470°C; *curve e*: δ=2.5 mm,ΔPcl_2=40 mm Hg. T=450°C.

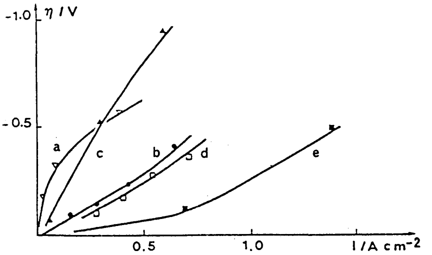

Fig. 4. Polarisation of chlorine electrodes vs. the current density, data after one working hour. Wall thickness δ. Chlorine overpressure: ΔPcl_2. Temperature : T.- Graphite sample PG60 - *Curve a*: δ=2 mm, ΔPcl_2=4 mmHg, T=420°C; *curve b* :δ=2 mm, ΔPcl_2=4 mmHg, T=470°C. - Graphite sample 3780 - *Curve c*: δ= 2.5 mm, ΔPcl_2=10 mmHg, T=420°C; *curve d*: δ=2.5 mm, ΔPcl_2=10 mmHg, T=470°C; *curve e*: δ=2.5 mm, ΔPcl_2=25 mmHg, T=470°C.

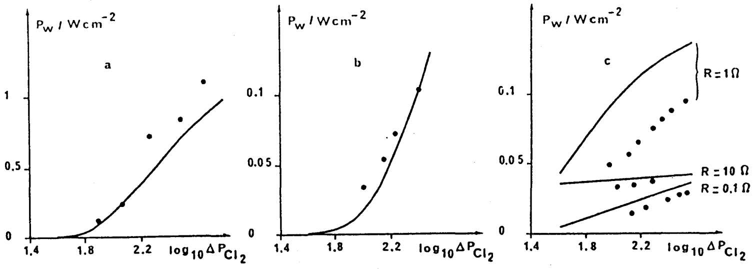

Fig. 5. Power density P_W of aluminum-chlorine batteries. Influence of the chlorine overpressure ΔP_{Cl2}; comparison with the theoretical model. Full line: theorical curves deduced from equation [4]. Circles: experimental points. *a*) chlorine electrode sample PG60 (Battery N°4 in Table III), *b)* chlorine electrode sample N°3780 (Battery N°1, R=0.1Ω, in Table III), *c*) chlorine electrode sample P2P (Battery N°5 in Table III), the curves correspond to three values of the external resistance R.

DOI: 10.1149/199017.0449PV

NUCLEATION OF DROPLETS AND METAL FOG DURING DEPOSITION OF LIQUID Mg FROM MOLTEN CHLORIDES

Geir M. Haarberg, Stein R. Johansen,
Jim Melaas, and Reidar Tunold

Institutt for teknisk elektrokjemi,
Norges Tekniske Høgskole,
Universitetet i Trondheim,
N-7034 Trondheim, Norway

ABSTRACT

Cathodic deposition of liquid magnesium from NaCl-KCl melts containing $MgCl_2$ was examined by electrochemical techniques and visual observations. Nucleation and growth of Mg droplets were studied during potentiostatic current transients, on electrodes of glassy carbon, graphite and pure iron. Metal fog was produced at the cathode during electrolysis. The mechanism of nucleation as well as visual observations of the appearance of the fog, are discussed. The influence of additions of hydroxide to the melt on the cathode process was studied.

INTRODUCTION

Socalled metal fog and metal streamers may form at the cathode during molten salt electrolysis. These phenomena have a negative influence on the metal deposition process and cause the current efficiency to reduce. Observations of fog formation have been made in several systems as reported in the literature (1,2,3). However the nature of the fog and the various factors affecting the fog formation are not fully understood.

Liquid Mg droplets are formed during electrolysis of molten chlorides containing $MgCl_2$. In the industrial process both products (Mg droplets and chlorine bubbles) are less dense than the electrolyte. It is of importance that large droplets are formed in order to maintain a high current efficiency.

A better understanding of the mechanism of nucleation and growth of Mg droplets on different substrates could lead to improvements of the process.

The presence of impurities in the electrolyte may influence nucleation and growth of droplets as well as fog formation.

EXPERIMENTAL

The experiments were carried out in a transparent gold film silica furnace. High quality NaCl and KCl were dried under vacuum and filtered through a silica frit. $MgCl_2$ was heated in HCl atmosphere and thereafter distilled under vacuum. Experiments were performed in pure salts, binary and ternary mixtures of NaCl-KCl-$MgCl_2$ at 670-750 °C, which is above the melting point of Mg. All handling of the chemicals was carried out in a dry-box with argon atmosphere. A transparent silica tube was used as the salt container during the experiments. Rods of pure iron, graphite and glassy carbon were used as the cathode (working electrode). Graphite or glassy carbon served as the counter electrode. A platinum wire placed in the molten salt served as the reference electrode. The potential for deposition of Mg was determined from cyclic voltammograms, and the measured potentials were corrected according to this potential.

Visual observations of the formation of metal fog and Mg droplets were made during constant current electrolysis (5-400 mA/cm^2). Linear sweep voltammetry and potential step chronoamperometry were employed to study deposition and nucleation of Mg.

In separate experiments a glassy carbon indicator electrode was placed above and near a larger graphite electrode. During electrolysis in NaCl-$MgCl_2$ (10 wt%) the larger electrode acted as a cathode producing Mg droplets and metal fog. The indicator electrode was polarized anodically in order to oxidize components of the fog.

The experimental cells used for visual observations and oxidation of metal fog are shown in Fig. 1 and 1b.

RESULTS AND DISCUSSION

Visual observations during electrolysis

Formation and growth of magnesium

Electrolysis was performed in the molten eutectic NaCl-KCl mixture with 5-10 wt% $MgCl_2$. The density of this melt is very close to the density of Mg. Thus the droplets did not detach from the cathode. Chlorine evolution caused some coloration of the melt; yellow at low concentrations and dark, brown at high contents of dissolved Cl_2. Magnesium droplets formed on iron became visible some time after the electrolysis started, with a time lapse varying from a few seconds at high cd (400 mA/cm^2) to several minutes at low cds (5-20 mA/cm^2). At the beginning of electrolysis small spherical droplets covered the entire cathode. The growth of Mg droplets, which also occurred by coalescence, led to a non-uniform size distribution of droplets. The wetting angle between Mg and Fe was found to be a little more than 90^o.

In some cases, during long time electrolysis, formation of small droplets on top of existing droplets was observed. This could be due to precipitation of a thin film of MgO on the larger droplets. The solubility of MgO is very low in this melt. Addition of $Mg(OH)_2$ (0.05 wt%) caused gas evolution (probably H_2) on the cathode before droplets were formed. In this case the droplets became smaller and more spherical due to deterioration of the wetting between Mg and Fe.

The metal fog

Socalled metal fog of lower density than the melt was formed cathodically from the very start of electrolysis. The fog was produced both when using carbon and iron electrodes. The amount of fog which was formed at the cathode decreased after an initial period, but fog was also observed after the electrode was covered with Mg droplets. The behaviour and appearance of the fog were dependent on the melt composition, and visual observations indicate that different kinds of fog could be produced.

Electrolysis of pure NaCl or KCl led to formation of a blue, transparent melt near the cathode which gradually spread in the electrolyte. This is probably due to dissolution of alkali metals. Similar observations have been reported in the literature (3).

In melts containing $MgCl_2$ both transparent and opaque fog were observed during electrolysis. In the ternary mixture $NaCl$-KCl-$MgCl_2$ (5-10 wt%) a grey-like transparent fog was often observed at the beginning of electrolysis. During potential step experiments (see later) fog was observed before the cathodic current started to increase due to nucleation of droplets. The fog gradually turned dark and opaque and filled the upper part of the electrolyte near the cathode. An abrupt change of the polarity of the current caused the fog to move away from the electrode and upwards at a high velocity (3 cm/s). In melts containing more than 50 wt% $MgCl_2$ a brown transparent fog was observed, the fog being less intense in pure $MgCl_2$. In KCl-$MgCl_2$ (10 wt%) two different fogs were observed; dark (grey or black) and brown fog. No movement of this fog could be detected when changing the polarity.

An anodic current was recorded on a separate glassy carbon indicator electrode during electrolysis in $NaCl$-$MgCl_2$ (10 wt%). Fig. 2 shows the current versus time relations obtained on the indicator electrode due to oxidation of species formed on the larger cathode during electrolysis at different cds. The increase of the current seems to occur in two steps. The anodic current was found to be much greater than the calculated current corresponding to oxidation of dissolved Mg, the solubility being 0.01 wt%.

The reported observations suggest that two different types of fog may be produced during deposition of Mg. In addition dissolved metals may form. It is likely that small Mg droplets are involved in both cases. Nucleation of droplets might occur from a supersaturated solution in the electrolyte. Adsorption of alkali metal cations (Na^+, K^+) on the surface of tiny Mg droplets, which has been reported (4), could explain the apparent positive charge of the grey/dark fog in the $NaCl$-KCl-$MgCl_2$ (10 wt%)melt. At higher $MgCl_2$ contents the tendency of adsorption decreases. The brown fog observed in $MgCl_2$-rich melts seemed to be uncharged.

Nucleation of magnesium droplets

Deposition of Mg from $NaCl$-KCl-$MgCl_2$ (1-10 wt%) was found to be diffusion controlled. A voltammogram recorded with an iron electrode is given in Fig.3, showing cathodic and anodic current peaks for reduction and oxidation of magnesium. Cathodic current at potentials more anodic than the deposition potential of Mg is due to underpotential deposition of alkali metals.

Typical current transients obtained on glassy carbon and iron during potential step experiments are shown in Fig. 4 and 5. The characteristic current increase after a few seconds indicates formation and growth of a new phase on the cathode. The current was found to be proportional to $t^{1/2}$ in the region where the current increases. This mechanism, which means that most of the nuclei are formed when Mg starts to deposit, was obtained for both glassy carbon, pyrolytic graphite and iron. Glassy carbon electrodes gave the better reproducibility. The number of nuclei was found to increase with increasing overvoltage. The current versus time relation at the very beginning of the experiment was different for glassy carbon and iron as shown in Fig. 4 and 5. This could be due to the difference in the codeposition of alkali metals, which is much more pronounced on glassy carbon. Metal fog was observed at the cathode surface also during the short period before the current increased.

REFERENCES

1. Qiu Zhuxian, Fan Liman, K. Grjotheim, and H. Kvande, J. Appl. Electrochem., 17, 707 (1987).

2. W. E. Haupin and W. C. McCrew, Aluminium, 51, 273 (1975).

3. W. E. Haupin, R. S. Danchik, and J. F. Luffy, Light Metals, 1, 159 (1976).

4. V. K. Shcherbakov and S. I. Kuznetsov, J. Appl. Chem. USSR, 42, 1492 (1962).

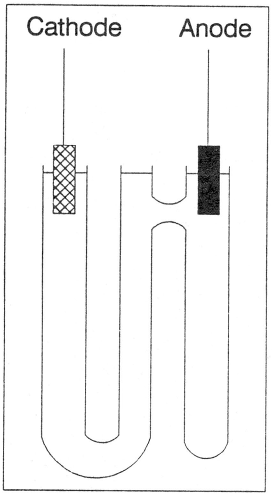

Fig.1a
Experimental cell used for observation of metal fog.

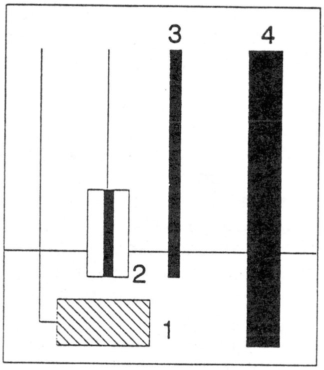

1: Working cathode
2: Indicator electrode
3: Counter electrode
4: Anode

Fig.1b
Experimental cell used for oxidation of metal fog.

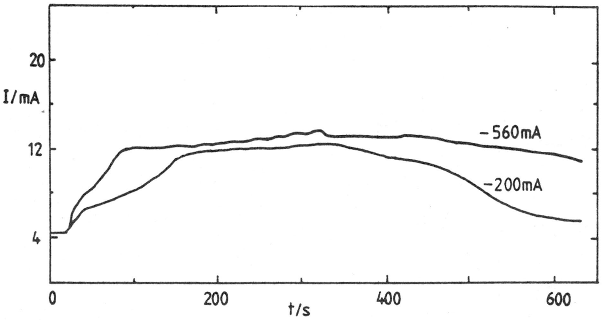

Fig.2
Current versus time during oxidation of metal fog on an indicator electrode. Potential applied on indicator electrode: 1740 mV referred to the Mg potential. Cathodic current on the fog producing cathode is indicated on the figure.

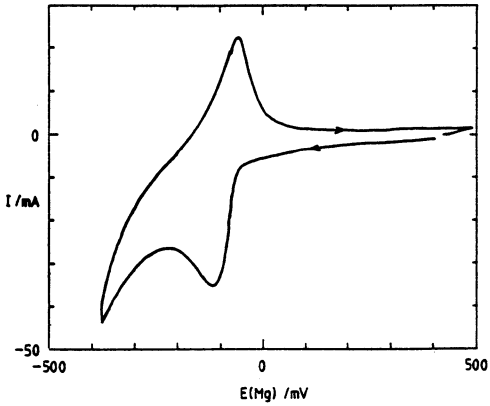

Fig.3
Voltammetry(10 mV/s) on iron in NaCl-KCl-$MgCl_2$(1.5 wt%) at 750°C.

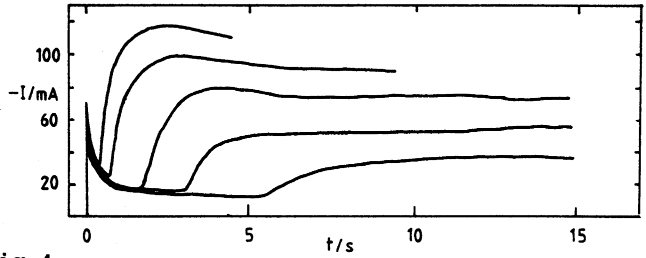

Fig.4
Current versus time during potential step chronoamperometry on glassy carbon at different overpotentials (from -150 to -190 mV/s in steps of 10 mV) in NaCl-KCl-$MgCl_2$(5wt%) at 700°C.

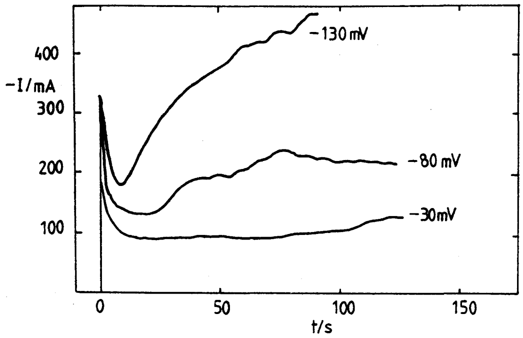

Fig.5
Current versus time during potential step chronoamperometry on iron at different overpotentials (in mV) in NaCl-KCl-$MgCl_2$ (5 wt%) at 700°C.

DOI: 10.1149/199017.0457PV

ELECTROCHEMICAL STUDY ON TITANIUM REDUCTION IN EUTECTIC LiCl-KCl MELT

M. Kawakami, K. Akaike, K. Ito and H. Kuma

Department of Production Systems Engineering
Toyohashi University of Technology
Tempaku-cho, Aza-Hibarigaoka, Toyohashi, 441 JAPAN
Tukuba Laboratory, Nippon Stainless Steel Co., LTD
Sengen 2-1-6, Tukuba, 305 JAPAN

ABSTRACT

Electrochemical reduction of Ti(III) and Ti(II) in eutectic LiCl-KCl melt has been investigated in three different modes of linear sweep voltammetry, cyclic voltammetry and potentiostatic voltammetry. Reduction of Ti(III) to Ti(II) took place from -0.6 V against the Ag/AgCl(10 mole%) reference electrode, whereas that of Ti(II) to metallic Ti, from -1.1V. Those reactions were reversible near the respective potential. The electrode deposit obtained at -1.2 V was metallic titanium of fine globular shape.

INTRODUCTION

Titanium has superior properties, such as high specific strength and high corrosion resistance. Its availability, however, is limited because of its relatively high production cost. One possible way to reduce the production cost might be the direct electrochemical reduction of titanium from a molten salt. Many papers have been published on the electrolysis of titanium from molten alkali or alkaline earth chlorides. Bockris et al.(1) and Dean et al.(2) reported that the alkaline earth cations were first electrochemically reduced and then the alkaline metal so formed reduced the titanium cations to produce metallic titanium. Nardins et al.(3) and Quemper et al.(4) reported the respective stepwise reduction potentials of Ti(IV) to Ti(III), Ti(III) to Ti(II) and Ti(II) to metallic Ti. From a practical view point, electroplating of titanium from molten salts has been investigated by several investigaters(5,6). Cobel et al.(7) recently reported that metallic Ti of high purity was obtained in their pilot plant scale experiment. The reduction potentials reported by many investigators, however, disaccorded with each other (3, 4, 8-11). Therefore, it can be said that the reduction mechanism is still not well understood.

It is the intent of the present work to clarify the reaction mechanism associated with the electrochemical reduction of Ti(III) to Ti(II) and Ti(II) to metallic Ti in the LiCl-KCl eutectic melt.

EXPERIMENTAL

Figure 1 shows the schematic diagram of experimental apparatus. The atmosphere in the apparatus was kept inert by the flow of highly purified Ar gas deoxidized by using a titanium trap at 1073 K. Chlorine or hydrochloric acid gas was used for purification of the melt. Figure 2 shows the schematic diagram of electrolytic cell and the reference electrode. Reagent grade powders of LiCl and KCl were mixed to the composition of 59 mole% LiCl and 41 mole% KCl in a glove box. These salts were preheated for 24 hours at about 473 K in a purified Ar flow and then were melted together in an alumina crucible. Chlorine or HCl gas was injected into the melt for three hours to purify the melt and then purified Ar was injected to remove dissolved chlorine or HCl gas for another three hours. A certain amount of $TiCl_3$, and Ti chips in the case of Ti(II) reduction, were added to the melt. Then, three electrodes were dipped into the melt. The working electrode was either a nickel rod of 5 mm in diameter or a 8 mm x 15 mm nickel plate of 0.5 mm thickness, which was polished with dry abrasive papers down to # 1000. The reference electrode was Ag/AgCl(10 mole%). The construction of the latter is shown in Fig. 2. The counter electrode was either a graphite rod of 11 mm in diameter or Ti rods that were 2 or 5 mm in diameter. The experimental temperature was mainly 773 K, but occasionally 873 and 973 K were used. The experiments were carried out in three different modes, namely linear sweep voltammetry, cyclic voltammetry and potentiostatic voltammetry. In the former two, the sweep rate was mainly 0.0017 V/s, and occasionally 0.005, 0.017 and 0.05 V/s. After the experiments in the last mode, the electrode deposit was examined with SEM and EPMA.

RESULTS

Figure 3 shows the result of linear sweep voltammetry before adding $TiCl_3$. The residual current density of the melt was effectively lowered by chlorine gas injection. It was especially lower at potentials higher than -1.5 V, which made the reduction wave of Ti(II) clearer, as will be shown later. The increase in current density at potentials higher than -2.5 V was attributable to the reduction of Li^+ to metallic lithium. So, most of the experiments were carried out after purification by chlorine gas injection.

Figure 4 shows the results of linear sweep voltammetry, after the addition of 1.2 mole% of $TiCl_3$ to the melt. Figure 5 is the magnification of Fig. 4 near -0.6 V. The rest potential was about -0.2 to -0.3 V. The reduction waves appeared at -0.6 and -1.1 V at 773 K. The broken line in this figure shows the residual current density. The increase in current density, and hence, the reduction wave due to the formation of titanium metal can be seen clearly following the addition of $TiCl_3$ to the melt. The same reduction waves were obtained at 873 K, although the current density was higher in magnitude. The reduction waves at -0.6 and -1.1 V were considered to correspond to the reduction of Ti(III) to Ti(II), and to the reduction of Ti(II) to metallic Ti, respectively, as follows:

$$Ti^{3+} + e = Ti^{2+} \tag{1}$$

$$Ti^{2+} + 2e = Ti \tag{2}$$

In order to reduce Ti(III) to Ti(II) in the melt prior to the experiment, metallic Ti chips were added to the melt simultaneously with the addition of $TiCl_3$. Thermodynamic calculations show that the equilibrium of equation (3) is shifted far to the right(12).

$$2TiCl_3 + Ti = 3TiCl_2 \tag{3}$$

Therefore, the melt must contain mostly Ti(II) when $TiCl_3$ and Ti chips are simultaneously added to the melt. Figure 6 shows the result of linear sweep voltammetry in the Ti(II) containing melt. The rest potential shifted to -0.8 or -0.9 V. The reduction wave corresponding to equation (1) disappeared and only the wave at -1.1 V can be seen. The current density increased with an increase in temperature, but the reduction potential did not change much regardless of the temperature. The increase in current density seen close to the rest potential has not been clarified yet. It might be attributable either to the reduction of impurities in the melt such as Al^{3+} or to the reduction of residual Ti(III). Figure 7 shows the effect of the Ti^{2+} content on the current density. The current density increased with an increase in the amount of $TiCl_3$ and Ti chips added. The current density at -1.2 V is plotted in Fig. 8. The current density increased linearly with the amount of added $TiCl_3$. Figure 9 shows the effect of sweep rate on the polarization curve. The current density increased with an increase in sweep rate. But the reduction potential was unchanged, regardless of the sweep rate. Figure 10 shows the result of cyclic voltammetry near -1.1 V. Both the reduction and oxidation current densities started to increase at -1.1 V, regardless of the sweep rate. The oxidation current is due to the oxidation of the metallic Ti electrode deposit which is formed in cathodic sweep. This shows that the reduction reaction of equation (2) is reversible.

In potentiostatic voltammetry, a Ti rod was used as the counter electrode. Figure 11 shows the change in current density with time in potentiostatic voltammetry at -1.2 V in which a nickel rod was used as the working electrode at 773 K. The amount of $TiCl_3$ and Ti chips added (mole%) were respectively, a)2.01 and 1.27, b)3.88 and 2.11, c)4.03 and 2.32, d)5.55 and 2.76. The current density increased in a), c) and d), but was almost constant in b). Except for a), the current increased with an increase in the amount of added $TiCl_3$ and Ti chips. Figure 12 shows the change in current density with time in similar potentiostatic voltammetry experiments in which a nickel plate was used as the working electrode. The amount of added $TiCl_3$ and Ti chips were 3.83 and 2.04 mole%, respectively, in all experiments. The current density was almost constant and of the same order of magnitude in all experiments. However, it was smaller than in the experiments with the nickel rod as the working electrode. Photogragh 1 shows the SEM image of the electrode deposit. Although at low magnifications the electrode surface was smooth, the photo shows that the surface was actually the agglomeration of small globular particles that were several microns in diameter. Table 1 shows the composition of electrode deposit. The electrode deposit was mainly composed of metallic Ti, which showed that the reduction wave at -1.1 V was attributable to the reduction reaction of equation (2). The deposit also contained a certain amount of aluminum. This is because the $TiCl_3$ powder originally contained 25 mole% of $AlCl_3$. Both Ti and Al were homogeneously distributed over the surface.

Table 1 Composition of the electrode deposit

	a	b	c	d	e	f	g
Ti (wt%)	86.4	93.5	91.5	73.7	71.7	70.6	72.2
Al (wt%)	13.6	6.5	8.5	26.3	28.3	29.4	27.8

The symbols correspond to those in Figs. 11 and 12.

DISCUSSION

As shown above, the reduction of Ti(II) to metallic Ti was reversible and the current density increased linearly with the concentration of Ti(II) cation. This suggests that the reduction is controlled by mass transfer in the melt. Generally, if the electrode reactions are controlled by mass transfer, the electrode potential can be represented in terms of the chemical potential difference of the anion-forming species between the reference and working electrodes, namely, the chemical potential difference of chlorine in the present case.

$$E = \frac{RT}{2F} \ln \frac{P_{Cl_2}(W.E.)}{P_{Cl_2}(R.E.)} \qquad (4)$$

where, P_{Cl_2} (R.E.) and P_{Cl_2} (W.E.) are the partial pressures of chlorine at the reference and working electrodes. At the reference electrode, the following equilibrium can be considered.

$$Ag + 1/2Cl_2 = AgCl \qquad (5)$$

$$\Delta G°(5) = - RT \ln \frac{a_{AgCl}}{a_{Ag}P_{Cl_2}^{1/2}} \qquad (6)$$

Therefore, P_{Cl_2} (R.E.) can be calculated, using the datum of ΔG°(5)(12) and taking $a_{Ag} = 1$ and $a_{AgCl} = 0.1$. Similarly at the working electrode, the following equilibrium must be considered in order to calculate the potential of the Ti(III) to Ti(II) reduction process.

$$TiCl_2 + 1/2Cl_2 = TiCl_3 \qquad (7)$$

$$\Delta G°(7) = -RT \ln \frac{a_{TiCl_3}}{a_{TiCl_2}P_{Cl_2}^{1/2}} \qquad (8)$$

Using the datum of ΔG° (7)(12), and assuming $a_{TiCl_3}/a_{TiCl_2} = 1$, P_{Cl_2} (W.E.) can be calculated. Putting these partial pressure of chlorine at the two electrodes into equation (4), the Ti(III) to Ti(II) reduction potential was calculated as -0.62 V at 773 K. This value is in good accord with the experimentalvalue of -0.6 V. In order to calculate the potential for the reduction of Ti(II) to metallic Ti, the following equilibrium must be considered.

$$Ti + Cl_2 = TiCl_2 \qquad (9)$$

$$\Delta G°(9) = -RT \ln \frac{a_{TiCl_2}}{a_{Ti}P_{Cl_2}} \qquad (10)$$

Using the datum of $\Delta G°(9)(12)$, and taking $a_{Ti} = 1$ and $a_{TiCl_2} = 0.1$, P_{Cl_2} for the reduction can be calculated. Putting this partial pressure of chlorine into equation (4), the reduction potential of Ti(II) to metallic Ti was calculated as -1.10 V. This value is also in good accord with the experimental value. In the same way, the reduction potential of Li^+ to metallic lithium was calculated to be as -2.5 V, which is in good accord with the experimental value.

Many investigators have reported the reduction potentials of the different Ti electrode reactions. They are listed in Table 2, together with the present results.

Table 2 Comparison of the reduction potentials resulting from the present work with those of other workers.

authors	melt	electrode	sweep rate	reduction potential
present	LiCl-KCl	WE: Ni	0.0017	
authors	($TiCl_3$)	CE: graphite		Ti(III) to Ti(II) -0.6 V
	($TiCl_2$)	RE: Ag/AgCl	0.05 V/s	Ti(II) to Ti -1.1 V
A	$BaCl_2$-	WE: Ni	0.0017	Ti(IV) to Ti(III) 0.0 V
ref.	LiCl-KCl	CE: graphite		Ti(III) to Ti(II) -0.5 V
(3)	($TiCl_4$)	RE: Ag/AgCl	0.0034 V/s	Ti(II) to Ti -1.2 V
B	LiCl-KCl	WE: graphite	0.001 V/s	Ti(IV) to Ti(III) +0.4 V
ref.	($TiCl_4$)	CE: graphite		Ti(III) to Ti(II) -0.6 V
(4)		RE: Ag/AgCl		Ti(II) to Ti -1.4 V
C	LiCl-KCl	WE: W		Ti(IV) to Ti(III) +0.6 V
ref.	($TiCl_3$)	CE: W	?	Ti(III) to Ti(II) -0.9 V
(8)		RE: Ag/AgCl		Ti(II) to Ti -1.1 V
D	LiCl-KCl	WE: Pt		Ti(IV) to Ti(III) -0.9 V
ref.	($TiCl_4$)	CE: graphite	?	Ti(III) to Ti(II) -1.0 V
(9)		RE: Ag/AgCl		Ti(II) to Ti -1.5 V

Table 2 (continued)

authors	melt	electrode	sweep rate	reduction potential
E ref. (10)	LiCl-KCl ($TiCl_3$)	WE: Pt CE: Pt RE: Ag/AgCl	0.001 V/s	Ti(III) to Ti(II) -1.2 V Ti(II) to Ti -1.5 V
F ref. (11)	KCl-NaCl (K_2TiF_6)	WE: Pt CE: Pt RE: Ag/AgCl	0.001 V/s	Ti(IV) to Ti(III) -0.4 V Ti(III) to Ti(II) -0.8 V Ti(II) to Ti -1.4 V

The potentials of the data in C (8) were originally given with respect to the Cl_2/Cl^- reference electrode. This data were converted to the Ag/ACl reference electrode by considering the potential difference of 1.0 V between the Ag/AgCl and Cl_2/Cl^- electrodes obtained in the present work. Further, Ti(IV)/Ti(III) potential given by the authors in C is the oxidation potential, rather than the reduction potential, because they used $TiCl_3$ as the starting species. The Ti(III)/Ti(II) reduction potential measured by the present authors is in good accord with those measured by authors A and B. The Ti(II)/Ti reduction potential measured by the present authors is in good accord with those measured by authors A and C. Many authors reported the latter reduction potential to be less positive than that found by the present authors. Presumably, they noticed that the wave positive to that for Li^+ reduction arises from the reduction of Ti(II) to metallic Ti. Actually, the wave appeared near -1.5 V in the present experiments also. But the electrode deposit composed mainly of Ti was obtained at -1.2 V, and the theoretical calculations showed that this reduction can take place at -1.1 V. Thus, it can be said conclusively that the Ti(II)/Ti reduction potential is -1.1 V with respect to the Ag/AgCl reference. The reduction process is reversible, although Ferry et al.(8) reported to be irreversible process based on impedance measurements.

The current efficiency in the potentiostatic voltammetry experiments with the nickel plate as the working electrode was calculated as follows. Since the electrode deposit was composed of Ti and Al, the efficiency was calculated for each metal and summed up to obtain the total efficiency,

$$\mathrm{Eff.}(i) = (W_i/W_{io})\times 100\ (\%) \qquad (11)$$

where Eff.(i) is the efficiency for metal i, W_i is the mass of the deposit of metal i obtained from the total amount of deposit and the composition of the deposit, W_{io} is the theoretical mass of the deposit of metal i calculated with the following equation.

$$W_{io} = \int \frac{M_i}{z_i F} I\, dt \tag{12}$$

where M_i and z_i are molar mass and balence of i, respectively, F is the Faraday constant, I is the total current, and t is time. Table 3 shows the calculated results.

Table 3 Current efficiency

specimen	Eff.(Ti) %	Eff.(Al) %	Eff. total %
e	6.9	7.3	14.2
f	5.5	6.0	11.5
g	6.4	6.6	13.0

The symbols for each specimen correspond to those shown in Fig. 12.

The current efficiency was very low. This is partly because some part of electrode deposit was lost during washing with water before weighing. But also, it is likely that some of the deposit was lost during the electrolysis, considering the fluctuation of current density with time. From careful observation of Photo. 1, the slow increase in current density seems attributable to an increase in the interfacial area and, the sudden drop in current density seems to result from the loss of the deposit.

CONCLUSION

The electrochemical reduction of Ti(III) to Ti(II) and the reduction of Ti(II) to metallic Ti was investigated in LiCl-KCl melt. The reduction wave of the former appeared at -0.6 V, whereas that of the latter appeared at -1.1 V against the Ag/AgCl(10 mole%) reference. These experimental potentials are in good accord with the calculated ones based on thermodynamic considerations. The latter reduction was shown to be reversible by cyclic voltammetry. An electrode deposit was obtained by potentiostatic voltammetry at -1.2 V. The deposit was composed of metallic Ti and Al with a globular shape. The current efficiency was as low as 15 %, because of the loss of material during washing before weighing and presumably due to the loss of material during the electrolysis.

ACKNOWLEDGEMENT

The present work is financially supported by Chubu Electric Power Co. LTD.

REFERENCES

1. J. OM. Bockris, G. J. Hills, I.A. Menzies and L. Young, Nature, 178, 654 (1956).

2. R. S. Dean, Metal. Ind., 90, 143 (1957).

3. M. Nardin, E. Chassing and G. Lorthioir, Instn. Min. Metal, 35 (1977).

4. F. Quemper, D. Deroo and M. Rigaud, J. Electrochem. Soc., 119, 1353 (1972).

5. M. E. Sibert and M. A. Steinberg, J. Electrochem. Soc., 102, 641 (1955).

6. B. J. Fortin, J. G. Wurm, L. Gravel and R. J. A. Potvin, J. Electrochem. Soc., 106, 428 (1959).

7. G. Cobel, J. Fisher and L. E. Snyder, Titanium' 80, proc. 4th Intl. Conf. on Titanium, Kyoto, 1969 (1980).

8. D. M. Ferry, G. S. Picard and B. L. Tremillon, Proc. Joint Intl. Symp. on Molten Salts, 517 (1987).

9. S. Mori, T. Koroda and K. Kawamura, Denki Kagaku, 42, 175 (1974).

10. H. Numata, I. Oono and S. Haruyama, Proc. Annual Meeting, Japan Inst. Met., 474 (1988).

11. T. Oki, M. Okido and G. Chen, Proc. Joint Intl. Symp. on Molten Salts, 507 (1987).

12. Denki-kagaku-binran, ed. by Denki-kagaku-kyoukai, Maruzen, 26 (1984).

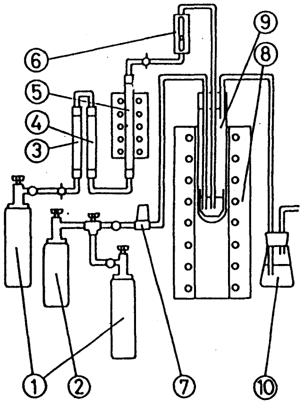

Fig. 1 Schematic diagram of the experimental apparatus; 1. Ar cylinder, 2. chlorine or HCl gas cylinder, 3. calcium chloride, 4. silica gel, 5 activated Ti tower, 6. gas lfow meter, 7. mass flow controller, 8. electric furnace, 9. electrolytic cell, 10. NaOH trap.

Fig. 2 Schematic diagram of the electrolytic cell and construction of the reference electrode.

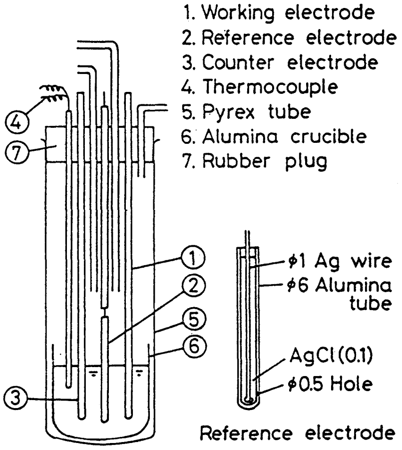

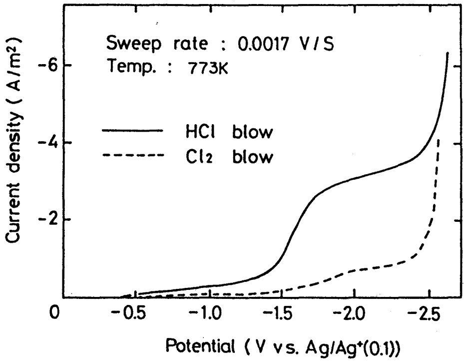

Fig. 3 Effect of purification on the residual current density.

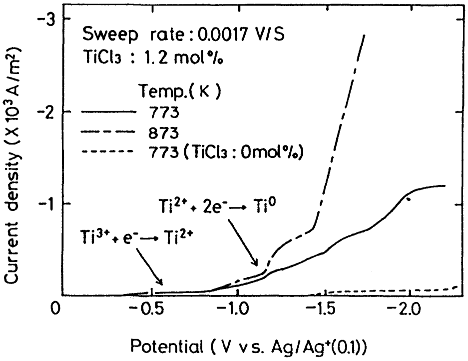

Fig. 4 Cathodic polarization curves in Ti^{3+} containing melt.

Fig. 5 Magnification of Fig. 4 near -0.6 V.

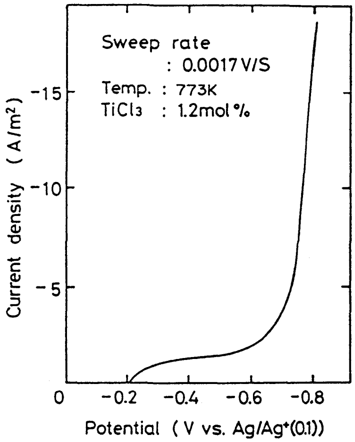

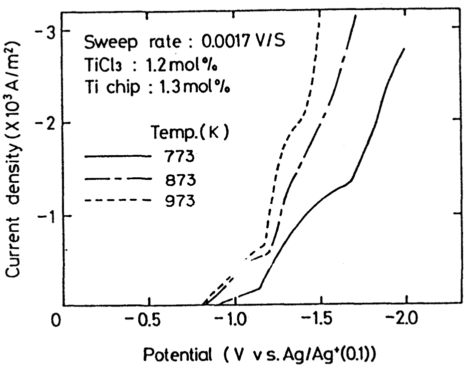

Fig. 6 Cathodic polarization curves in Ti^{2+} containing melt.

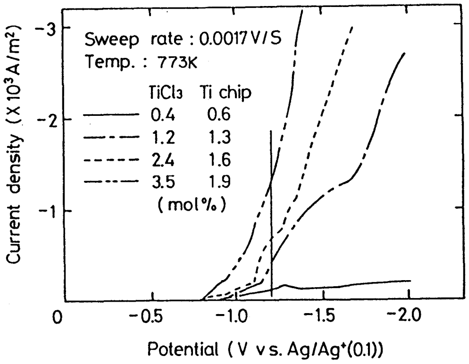

Fig. 7 Effect of the Ti^{2+} content on the cathodic polarization curve.

Fig. 8 Effect of the Ti^{2+} content on the current density at -1.2 V.

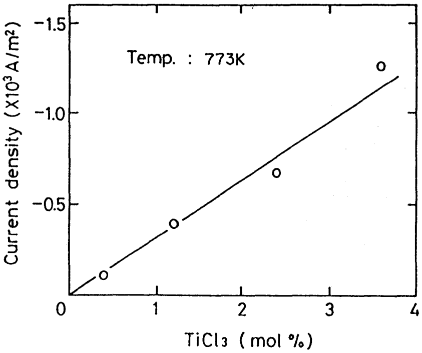

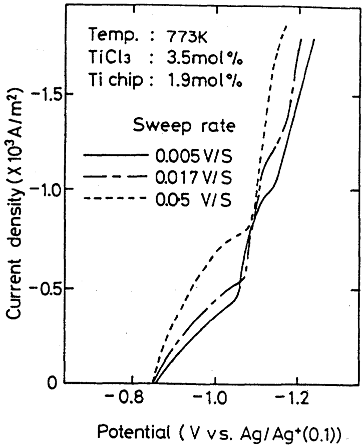

Fig. 9 Effect of sweep rate on the cathodic polarization curve in Ti^{2+} containing melt.

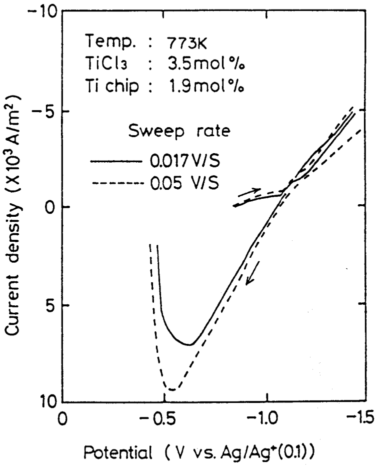

Fig. 10 Cyclic polarization curve in Ti^{2+} containing melt near -1.1 V.

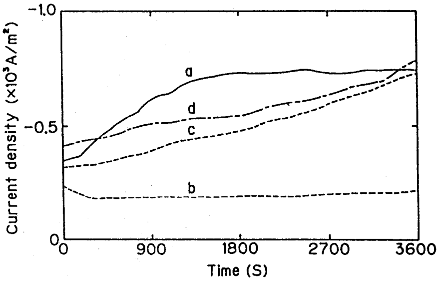

Fig. 11 Change in current density with time during the potentiostatic polarization at -1.2 V with a nickel rod electrode.

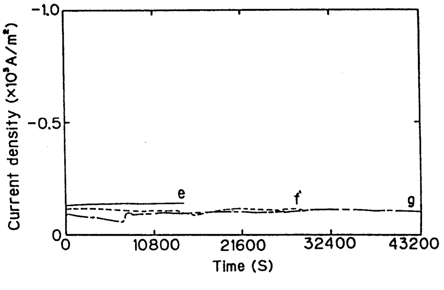

Fig. 12 Change in current density with time during the potentiostatic polarization of a nickel plate electrode at -1.2 V.

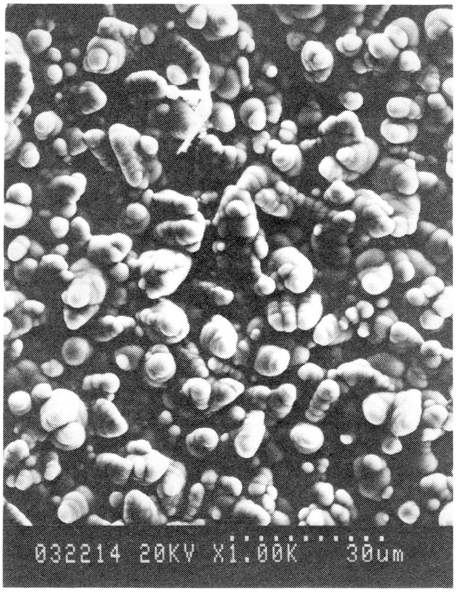

Photograph 1. Surface morphology of the deposit obtained at −1.2 V on a nickel plate electrode.

DOI: 10.1149/199017.0471PV

STUDY OF SOME RHENIUM ELECTROCHEMICAL PROPERTIES IN THE FUSED LiF-NaF-KF EUTECTIC.

A. Affoune, J.Bouteillon* and J.C. Poignet*
CREM GP/ ENSEEG UA CNRS 1212, BP 75
38402 St Martin d'Hères France

* Université Joseph FOURIER, Grenoble

ABSTRACT

The electrochemical properties of K_2ReCl_6 and $KReO_4$ dissolved in molten flinak at 700°C were studied. K_2ReCl_6 decomposed to a Re(II) species which could be reduced to Re in one reversible step, or it could be oxidized to a soluble Re(III) species. $KReO_4$ was reduced to Re via a two step mechanism.

INTRODUCTION

Few studies (1-5) have been published on the chemical or electrochemical properties of rhenium in fused salts. Some electrochemical properties of K_2ReCl_6 dissolved in the molten LiCl-KCl eutectic have been studied by Nobile and Bailey (3). These authors observed that Re(IV) was quite stable once in solution, although some decomposition reaction yielding the metal occurred during the dissolution process of K_2ReCl_6. From potentiometric experiments they gave some evidence for the reversibility of the Re(IV)/Re exchange and measured the corresponding standard potential. Using solid electrode polarography, they showed that the half-wave potential was very close to the standard potential, but they could not unambiguously demonstrate that the number of electrons exchanged was four. Rhenium metal was deposited by potentiostatic electrolysis in the vicinity of the reversible Re(IV)/Re equilibrium potential. Galvanostatic electrolysis ultimately yielded Li predeposition because of the formation of a Re-Li solid solution. The same authors obtained rather similar results in the case of $KReO_4$ solutions.

Russian authors (5) have obtained W-Re solid solutions from a NaCl-KCl melt containing 15 to 20 mol% WF_6, 1 to 3 mol% $ReCl_3$, and 20 mol% NaF.

To our knowledge, the electrochemistry of rhenium compounds has not been investigated in molten fluoride solvents, and this paper deals with the study of K_2ReCl_6 and $KReO_4$ solutions in the LiF-NaF-KF molten eutectic.

EXPERIMENTAL TECHNIQUES

The experimental setup has been described previously (6). The electrolyte was contained in a graphite crucible situated inside an air-tight stainless steel cell. In order to dehydrate the melt, 1.5 mol% KHF_2 were added to the salts. The mixture was heated to 200°C under vacuum then melted under argon flow. K_2ReCl_6 or $KReF_4$ were then added through a lock-chamber and proved to be quite soluble in the melt. Voltammetric and chronopotentiometric studies were performed using platinum, silver, tungsten or rhenium electrodes. Owing to the difficulties in obtaining good reference electrodes in molten fluorides, we used a platinum wire or the graphite crucible as a comparison electrode.

RESULTS AND DISCUSSION

A- PURE SOLVENT

Reference potential.- Our results were referred to the K^+/K limit of the solvent, which could be reached with the whole set of electrodes used, whereas oxidation of the electrode was the anodic limit. In order to compare our results to literature data, we have determined the standard equilibrium potential $E^\circ_{Ni(II)/Ni}$ versus our K^+/K reference, after having proved the reversibility of the Ni(II)/Ni exchange by making a convolutional analysis of nickel oxidation voltammograms. The result was :

$$E^\circ_{Ni(II)/Ni} = +\ 2.20 \text{ V vs } K^+/K \qquad [1]$$

Electrochemical window at a rhenium electrode.- On the voltammogram of Figure 1, rhenium oxidation occurs at + 2.8 V vs K^+/K (value taken for $i = 10$ mA/cm^2). The shape of the curves corresponding to various sweep rates (Figure 2) suggests that the oxidation product is soluble in the melt and shows the irreversible character of the reduction wave (peak A). Further anodic polarization resulted in gas evolution.

B- K_2ReCl_6 SOLUTIONS

Figure 3 shows a typical voltammogram on a silver electrode, with two well-characterized couples : in the 1.2 to 1.6 V potential range, the B/B' couple corresponds to reduction of the rhenium species yielding an insoluble product, followed by a stripping reoxidation peak of this product; in the 2.0 to 2.5 V potential range, the C/C' couple is related to the oxidation of the rhenium species yielding a soluble product, followed by reduction of this product.

Study of the B/B' couple.- Figure 4 presents several voltammograms obtained on a silver electrode in a 0.014 M K_2ReCl_6 solution. Due to the ohmic drop, the voltammograms were subsequently analysed by convolution procedures (8,9). The reversibility test was the comparison of the semi-integral curves obtained for different sweep rates (Figure 5). These curves were similar and for any given curve the direct and the reverse scans were identical within a large potential domain. These results indicate that the B'/B exchange may be considered as reversible in the sweep rate domain studied.

Figure 6 presents cathodic chronopotentiograms obtained on a silver electrode in a 0.014 molar K_2ReCl_6 solution. A single transition is observed, and the shape of the curves reveal a soluble-insoluble exchange. The transport of the rhenium species is governed by linear diffusion since Sand's law is obeyed (Figure 7). The potential measured at the quarter of the transition time is independant of the current density (Figure 6), which confirms the reversibility of the exchange. Figure 8 shows the logarithmic analysis of the chronopotentiograms in the case of an insoluble product (curve a) and of a soluble product (curve b). The best fit is obtained in the case of the insoluble product.. The insoluble character of the reaction product is confirmed by the equality of the reduction and reoxidation transition times on current reversal chronopotentiograms (Figure 9). We therefore postulated that the product was rhenium metal. From the slope of the straight part of curve a (Figure 8), we calculated the number of electrons exchanged as n = 2 . From the value of the potential at the quarter of the transition time, we calculated the value of the apparent standard potential :

$$E^{o}_{B/B'} = 1.97 \text{ V vs } K^{+}/K \qquad [2]$$

Study of the C/C' couple.- A few voltammograms restricted to the C/C' exchange are presented in Figure 10. In spite of a large residual current in this potential range, we could analyse the curves and concluded that the exchange was reversible. Firstly, the anodic and cathodic peaks potentials are independant of the sweep rate. Secondly, the i_{pa}/i_{pc} ratio remains close to one for all of the sweep rates studied. Moreover, the value of Epa-Epc is about 200 mV and not too far from the theoretical value corresponding to a one-electron exchange, which is 183 mV at 650°C. The semi-integral curves (Figure 11) do not yield a decisive reversibility criterion in this case, possibly because of the high residual current already mentioned. We can, however, observe that for a given sweep rate the direct and forward curves are identical.

Finally, assuming that the exchange is reversible, we can calculate the C/C'apparent standard potential from the half-peak potential by using the relation :

$$E_{p/2} = E_{1/2} + 1.09\ RT/F \qquad [3]$$

Assuming that the diffusion coefficients of both species are equal, we obtained $E°_{C/C'} = 2.14$ V vs K^+/K

<u>Interpretation of the results</u>.- The K_2ReCl_6 solutions appear to be cathodically reduced to rhenium(0) by a two-electron reversible exchange step and anodically oxidized to a soluble species by a one-electron reversible exchange process. This suggests that some divalent rhenium species could be present in the solution. Looking into the literature, we found that ReI_2 can be obtained by heating K_2ReI_6 to 350°C (10). In fact, two divalent rhenium halogenides seem to be known : ReF_2 and ReI_2. At the present state of our study, we assume that, in molten flinak at 650 °C, K_2ReCl_6 is, like the corresponding iodide, decomposed to a stable Re(II) species. The B/B' and C/C' exchange reactions may then be formulted as :

$$\text{Re(II)} + 2\,e \longrightarrow \text{Re} \qquad (B/B') \qquad [4]$$

$$\text{Re(II)} \longrightarrow \text{Re(III)} + e \qquad (C/C') \qquad [5]$$

C- $KReO_4$ SOLUTIONS

Figure 12 presents a typical voltammogram obtained on a platinum electrode. The characteristic features of the volmtammograms did not depend on the nature of the electrode (Pt, W or Re). The cathodic part of the voltammogram shows two steps : waves D and E. The heights of these waves increase with the $KReO_4$ concentration. When, during the direct scan, the potential reaches the domain of wave E, a shoulder F appears on the reverse scan in the vicinity of the generalized electrode oxidation domain. The potential domain of this shoulder is close to the potential at which rhenium was oxidized in the pure solvent

(Figure 1). Potentiostatic and galvanostatic electrolysis in the region of wave E yielded metallic rhenium, characterized by X ray analysis (Figure 13). We can therefore conclude that the ReO_4^- solutions undergo a two step reduction process according to the following reactions:

$$ReO_4^- + (7-x)\ e^- \longrightarrow Re(x) + 4\ O^{2-} \quad \text{(wave D)} \quad [6]$$

$$Re(x) + x\ e^- \longrightarrow Re(0) \quad \text{(wave E)} \quad [7]$$

The anodic oxidation of Re can be written as :

$$Re + 6\ F^- \longrightarrow ReF_6 + 6\ e^- \quad \text{(shoulder F, wave A/A')} \quad [8]$$

CONCLUSION

From electrochemical studies of K_2ReCl_6 solutions in the fused LiF-NaF-KF eutectic, it appears that the solute is first decomposed to give stable Re(II) solutions. This situation is different from the case of molten LiCl-KCl at lower temperatures, where Re(IV) is quite stable.

The Re(II) species is cathodically reduced to rhenium metal through a reversible two-electron step. This species can be anodically oxidized to a soluble Re(III) species in a reversible reaction.

The apparent standard potentials, referred to the standard Ni(II)/Ni couple are :

$E^\circ_{Re(III)/Re(II)} = -0.06$ V and $E^\circ_{Re(II)/Re} = -0.23$ V

The reduction of $KReO_4$ solutions to metallic rhenium proceeds through two electrochemical steps :

$$ReO_4^- + (7-x)\ e^- \longrightarrow Re(x)$$

$$Re(X) + x\ e^- \longrightarrow Re(0)$$

By comparison of the voltammograms resulting from ReO_4^- solutions and those resulting from Re in pure solvent, we can postulate that in both cases the metal is passivated and can only be oxidized to ReF_6 at very anodic potentials.

Acknowledgments
We are grateful to the General Electric CGR (France) Compagny for its financial support for this study.

REFERENCES

1. R. A. Bailey, J. A. MacIntyre, Inorg. Chem., 5, 964 (1966).

2. R. A. Bailey, J. A. MacIntyre, Inorg. Chem., 5, 1940 (1966).

3. R. A. Bailey, A. A. Nobile, Electrochim. Acta 17, 1139 (1972)

4. S. Senderoff, G. W. Mellors, J. Electrochem. Soc.,114, 586 (1966).

5. Z. M. Sominskaya, A. A. Nikitina, E. K. Artanomova, Electrokhim., 7 , 150 (1971).

6. R. Boen, J. Bouteillon, J. Applied Electrochem., 13, 109 (1983)

7 A. Robin, Thèse , INP Grenoble (1987).

8. K. B. Oldham, Anal. Chem., 44, 196 (1972).

9. J. C.Imbeaux, J. M. Saveant, J. Electroanal. Chem., 44, 169 (1973).

10. P. Pascal, Compléments au Nouveau Traité de Chimie Minérale, Vol. 10, Masson (1978)

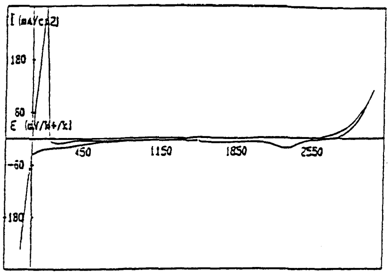

Figure 1:voltammetric study in the pure LiF-NaF-KF solvent at a rhenium electrode. Temperature:700C°;v=0.2 V/s.

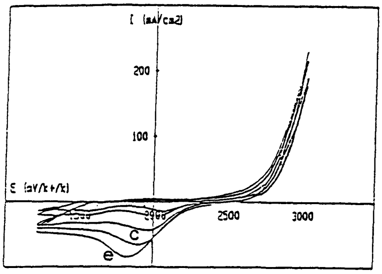

Figure 2:voltammetric study in the pure LiF-NaF-KF solvent at a rhenium electrode. Temperature:700C°;a)0.05V/s, b)0.1V/s,c)0.2V/s,d)0.5V/s e)1V/s.

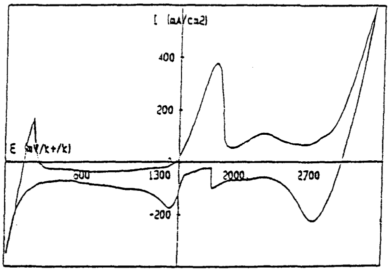

Figure 3:K2ReCl6 voltammetry. Temperature:650C°;Working electode:silver;v=0.2V/s.

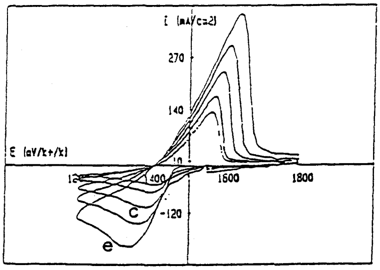

Figure 4:voltammetric transients related to K2ReCl6 reduction.Temperature:650C°; Working electrode:silver; C0=0.014 mol/l;a)0.1V/s; b)0.2V/s;c)0.5V/s;d)1V/s; e)2V/s.

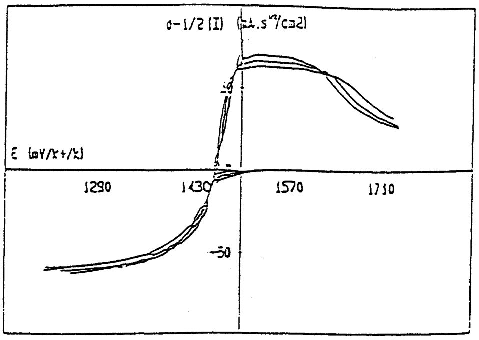

Figure 5:Semi-integral curves related to the voltammograms of figure 4.

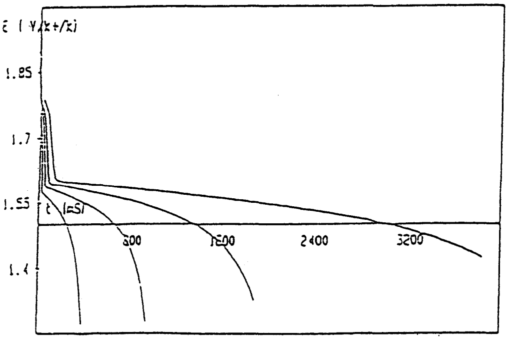

Figure 6:K2ReCl6 chronopotentiometry. Temperature:550C°;Working electrode:silver;C0=0.014mol/l; i (mA/cm2):a)60,b)38,c)26.6, d)19.

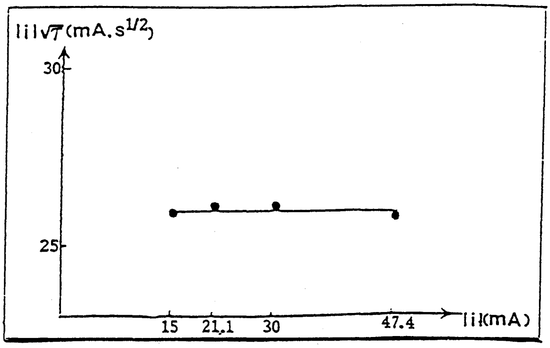

Figure 7:K2ReCl6 chronopotentiometry.Verification of the SAND's relation

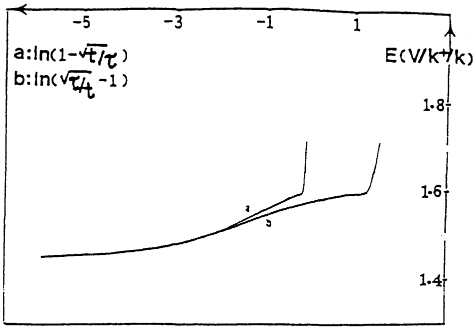

Figure 8:K2ReCl6 chronopotentiometry.Logarithmic analysis of chronopotentiograms.

Figure 9:current reversal chronopotentiograms obtained for K2ReCl6 at a silver electrode.

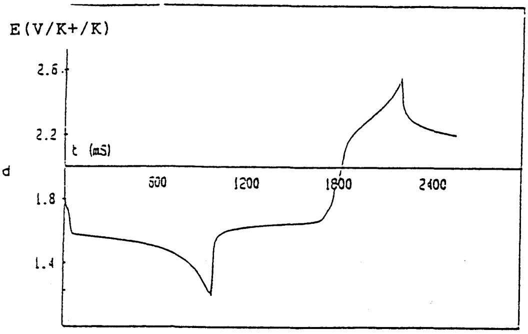

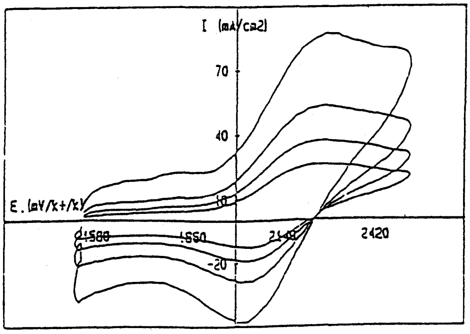

Figure 10:voltammetric transients related to K2ReCl6 oxidation.Temperature:650C°; Working electrode:silver; C0=0.014mol/l;a)0.2V/s,b)0.5V/s, c)1V/s,d)2V/s,e)5V/s.

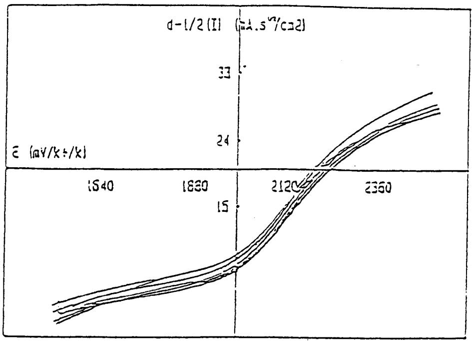

Figure 11:Semi-integral curves related to the voltammograms of the figure 10.

Figure 12:KReO4 voltammetry. Temperature:700C°;Working electrode:platinum; v=0.2V/s;C0=0.067mol/l.

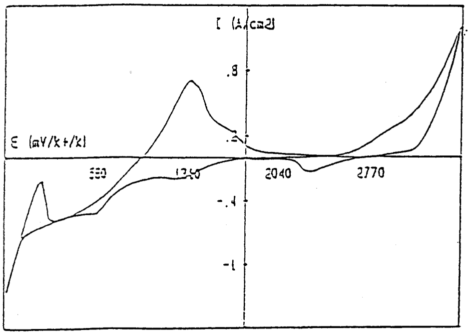

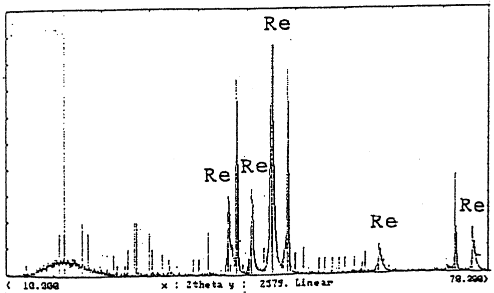

Figure 13:rhenium deposit X ray analysis.

DOI: 10.1149/199017.0481PV

ANODIC BEHAVIOR OF NICKEL IN A MOLTEN CsF-HF SYSTEM

Akimasa TASAKA, Yorihito OHANA, Nobuhiro SHINKA
and Hiroki NISHIMOTO

Doshisha University, Department of Applied Chemistry
Imadegawa, Karasuma, Kamigyo-ku, Kyoto 602 JAPAN

ABSTRACT

In order to seek after the metal anode for the electrolytic production of fluorine (F_2), the anodic behavior of nickel (Ni) in comparison with those of some metals such as copper (Cu), iron (Fe) and palladium (Pd) was investigated at 50 °C in a molten CsF-HF system by a few kinds of electrochemical methods. The platinum (Pt) wire was used as the reference electrode and the Ni-plate with a large surface area as the cathode.

In the cases of Cu and Fe electrodes, every anodic polarization curve in the 1st run obtained by the cyclic voltammetry had a current peak due to the anodic dissolution of metal at about 0 V vs. Pt and then a very small current flowed at the potentials over this peak because of the passivation of electrode. In the second run after, no current at 0 V was observed in the case of Fe electrode, but a current peak at 0 V was again observed in the case of Cu electrode. On the other hand, in the case of Ni electrode, an anodic current peak at 0 V was also observed on the cyclic voltammogram in the 1st run and it disappeared on them after the second run. At the potentials over 4 V, the anodic current flowed again and it increased with increasing both the potential and the number of cyclic scanning. The ratio of the amount of electricity of anodic dissolution on Ni to total amount of passing electricity during the potentiostatic electrolysis at 5.5 V was only 1.6 % or 3.2 % in the calculation from the electron number in the discharge of 2 or 4, respectively. Pd was also available as the anode in this system, but the ratio of its anodic dissolution of 9.7 % was larger than that of Ni. These results indicate that Ni is also the best material for the anode in this system. The ratio of anodic dissolution of Ni was dependent on the ratio of HF to CsF in the melt and the temperature of electrolyte. The mechanism on the anodic dissolution of Ni will be also discussed.

INTRODUCTION

Recently, gaseous fluoro-compounds such as nitrogen trifluoride (NF_3), sulphur hexafluoride (SF_6) and tungsten hexafluoride (WF_6) have been in quantities used in the japanese electronics industry. Highly pure (99.99 %) nitrogen trifluoride, especially free of CF_4, is at present produced by the electroytic process in the molten fluorides such as NH_4F-HF and NH_4F-KF-HF system (1∿6). Sulphur hexafluoride and tungsten hexafluoride are formed by the reactions of sulphur and tungsten with fluorine, respectively. However, fluorine is also produced by the electrolytic process in the molten KF·2HF. Hence, fluorine electrolysis and electrochemical fluorination are very useful processes for the production of the gaseous inorganic compounds containing fluorine.

Carbon is mainly used as the anode material in the molten fluorides due to no anodic dissolution, but it has a few disadvantages, especially the occurrence of anode effect and the breakdown of anode. Besides, the gaseous compounds obtained in electrolysis with the carbon anode may be always contaminated with CF_4.

The use of a metal anode enables to perform fluorine electrolysis and electrochemical fluorination at the higher current density, and to obtain the gaseous fluoro-compounds free of CF_4. Nickel (Ni) was the most favorable material for the anode from the viewpoint of both the production of NF_3 free of CF_4 and the anodic dissolution (6∿8). The ratio of the anodic dissolution of Ni to total amount of passing electricity was about 3 % at 120 °C in the molten $NH_4F\cdot 2HF$, and it increased with increasing the content of potassium fluoride (KF) in the molten $(NH_4F + KF)\cdot 2HF$ to reach the value of 14 % in the molten KF·2HF. For the purpose of decreasing the anodic dissolution of a metal electrode, a new electrolyte such as a CsF-HF system was used at 50 °C, and the anodic behaviors of some metals were investigated in this melt.

EXPERIMENTAL

The electrolyte was a molten CsF-HF system ans a diagram of this system was shown in Fig. 1 (9). On the basis of this figure, the ratio of HF to CsF in the range between 2 and 3 was selected as the composition of melt. An electrolytic cell of 0.45 cm^3 in capacity was made of polytetrafluoroethylen (PTFE) resin as shown in Fig. 2. The rods of some metals with the surface area od 0.07 cm^2 and their plates with the surface area of 1 cm^2 (W) were used as the anode for determination of polarization curves by the cyclic voltammetry and the anodic dissolution by the potentiostatic and galvanostatic methods, respectively. The platinum wire (R) was used as the reference electrode and the plate nickel with a large surface area (C) as the cathode. The cell was put in the glove box in order to eliminate the moisture as shown in Fig. 3 and the cell temperature was kept at 50 °C.

The electrolyte was pre-electrolyzed at a low current density for the duration of 7∿10 days, and then the anodic polarization curves and the anodic dissolution of some metals were determined by a few kinds of electrochemical methods.

RESULTS AND DISCUSSION

The cyclic voltammogram on copper in the molten CsF·2.7HF was shown in Fig. 4. An anodic polarization curve in the first run had a current peak due to the anodic dissolution of Cu at about 0 V vs. Pt and then a small current flowed at the potentials over this peak because of the passivation of electrode. Fig. 5 showed the cyclic voltammogram on iron in the first run in the same melt, and it seemed to be similar to that on Cu. After the second run, no current at about 0 V was observed in the case of Fe electrode, but a current peak at 0 V was again observed in the case of Cu electrode. So, these metals are unfavorable for the anode material in the electrolytic process in the molten fluoride.

Fig. 6 showed the cyclic voltammogram on nickel in the molten CsF·2.7HF. An anodic current peak at about -0.5 V in the first run was also observed and it disappeared on the cyclic voltammograms after the second run. At the potential range between 0 and 4 V, the current density was very small and this seemed to mean that the nickel anode would be coated with the oxide and/or fluoride films. At the potentials over 4 V, the anodic current flowed again, and it increased with increasing the potential. Furthermore, the anodic current at the potentials over 4 V increased with increasing the number of cyclic scanning and this seemed to mean that the roughness factor of anode surface would increase with the course of time. Therefore, it is concluded that a small amount of nickel and/or fluoride film on the anode would be also dissolved in this melt.

The weigh losses of metal anodes during the potentiostatic electrolysis at 5.5 V and 50 °C in the molten CsF·2.7HF were given in Table 1. In the cases of Cu and Fe electrodes, the current density was very small, and all amount of passing electricity was due to the anodic dissolution of metal electrode. In the case of palladium electrode, the current density was higher and the ratio of the anodic dissolution of Pd to total amount of passing electricity during electrolysis (Q_a/Q_t) was 9.7 %. In the case of Ni electrode, the current density was very high and the ratio of the anodic dissolution of Ni to total amount of passing electricity (Q_a/Q_t) was only 1.6 % or 3.2 % in the calculation from the electron number in the discharge of 2 or 4, respectively. Hence, it is concluded that Ni is also the most favorable material for the anode in the molten CsF-HF system.

Fig. 7 showed the effect of the current density on the ratio of the anodic dissolution of Ni to total amount of passing electricity during the galvanostatic electrolysis (Q_a/Q_t) at the current density range between 0.1 and 1 A·cm^{-2} in the molten CsF·2.5HF. The ratio of Q_a/Q_t was independent of the current density, and its value was about 1.3 %. Figs. 8 and 9 showed the effects of the composition of melt and the temperature on the ratio of Q_a/Q_t during the galvanostatic electrolysis at 500 mA·cm^{-2}. The ratio of Q_a/Q_t increased with increasing both the content of

HF in the melt and the temperature, and however, the value was under 2.5 % at 100 °C in the molten CsF·2.5HF.

Fig. 10 showed the chronopotentiograms on nickel at 50 °C in the molten CsF·2.5HF. At the current density of 2 $mA \cdot cm^{-2}$ (Curve 1), the anode potential stayed at about 0 V vs. H_2 and increased suddenly after 8.5 hours to reach the value of 6 V. And it decreased gradually through the maximum value of anode potential and then reached the value of about 5 V. At the current density of 5 $mA \cdot cm^{-2}$ (Curve 2), the anode potential change as a function of time was similar to that at 2 $mA \cdot cm^{-2}$, but the acute increase of anode potential occurred after electrolysis for the much shorter time. These chronopotentiograms could be analyzed as follows. At about 0 V vs. H_2, the nickel anode was dissolved and the concentration of dissolved nickel near the anode increased with the course of time. When the concentration of dissolved nickel reached the solubility, nickel oxide was at first deposited on the anode, and then nickel fluoride as well as nickel oxide was deposited on the anode, so that the anode potential increased suddenly. After electrolysis for 8.5 hours in the curve 1, the anode potential decreased gradually from 6 V to 5 V according to the exchange of nickel oxide for nickel fluoride, because of the lower resistivity of nickel fluoride than that of nickel oxide. At the potentials over 4 V, fluorine would also evolve on the nickel anode covered with nickel fluoride containing a small amount of nickel oxide and the anodic dissolution of Ni would occur through this film.

On the basis of our results, the mechanism on the anodic dissolution of Ni was proposed as follows:

$$Ni \longrightarrow Ni^{2+} + 2e^- \qquad [1]$$

$$Ni^{2+} + H_2O = NiO + 2H^+ \qquad [2]$$

$$Ni^{2+} + 2HF = NiF_2 + 2H^+ \qquad [3]$$

or

$$Ni^{2+} + 2F^- = NiF_2 \qquad [3']$$

$$HF = H^+ + F^- \qquad [4]$$

$$NiF_2 + nH_2O = [Ni(H_2O)_n]^{2+} + 2F^- \qquad [5]$$

$$Ni^{2+} + nH_2O \longrightarrow NiO_n + 2nH^+ + 2(n-1)e^- \qquad [6]$$

$$(1 < n \leqq 2)$$

$$NiO + 4F^- \longrightarrow NiF_4 + 1/2\ O_2 + 4e^- \qquad [7]$$

$$NiO_n + 4F^- \longrightarrow NiF_4 + n/2\ O_2 + 4e^- \qquad [8]$$

$$2F^- \longrightarrow F_2 + 2e^- \qquad [9]$$

$$NiF_2 + 2F^- \longrightarrow NiF_4 + 2e^- \qquad [10]$$

$$NiF_2 + 4F^- \longrightarrow NiF_6^{2-} + 2e^- \qquad [11]$$

$$NiF_4 + 2HF = NiF_6^{2-} + 2H^+ \qquad [12]$$

or $$NiF_4 + 2F^- = NiF_6^{2-} \qquad [12']$$

Fig. 11 showed the current efficiency of hydrogen evolved on the cathode. The current efficiency decreased with the course of time and reached the value of about 90 %. This fact indicated that any species except hydrogen ion (H^+), e.g., Ni^{2+} or NiF_6^{2-}, would be discharged on the cathode.

REFERENCES

1) N. Watanabe, A. Tasaka and K. Nakanishi, Denki Kagaku, 36, 685 (1968).
2) A. Tasaka and N. Watanabe, Z. anorg. allg. Chem., 386, 156 (1971).
3) O. Ruff, J. Fisher and F. Luft, Z. anorg. allg. Chem., 172, 417 (1928).
4) O. Glemser, J. Schröder and J. Knaak, Chem. Ber., 99, 371 (1966).
5) J. Massonne, Chemie Ing. Techn., 41, 695 (1969).
6) A. Tasaka, H. Kobayashi and M. Hori, Proceedings of the Joint International Symposium on Molten Salts, p. 949 (1987).
7) A. Tasaka and M. Hori, Proceedings of the Second Japan-China Bilateral Conference on Molten Salt Chemistry and Technology, p. 87 (1988).
8) M. Hori, Diploma Thesis, Doshisha University (1989).
9) R. V. Winsor and G. H. Cady, J. Amer. Chem. Soc., 70, 1500 (1948).

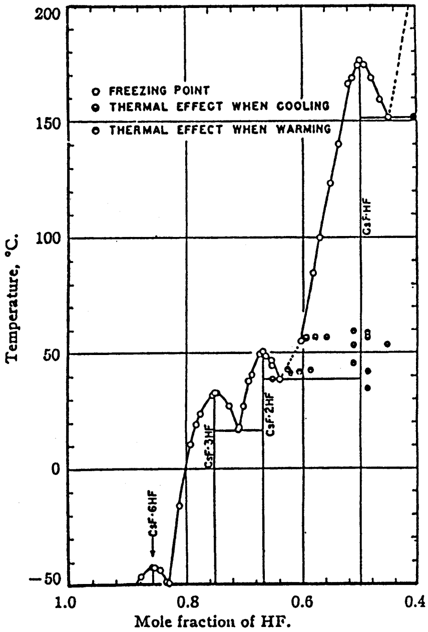

Fig. 1 The diagram of CsF-HF system[9].

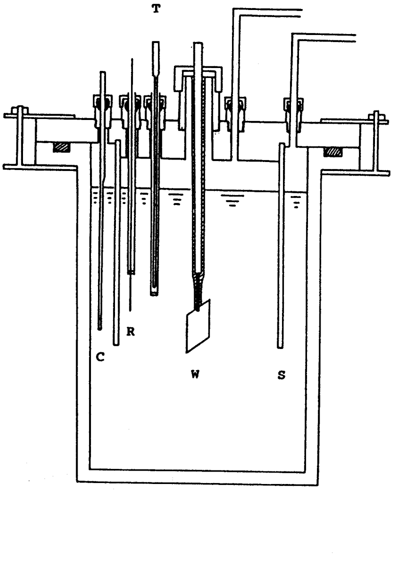

Fig. 2 Electrolytic cell for determination of polarization curve and anodic dissolution.

W: Working electrode,
C: Counter electrode,
R: Reference electrode,
S: Skirt,
T: Thermometer.

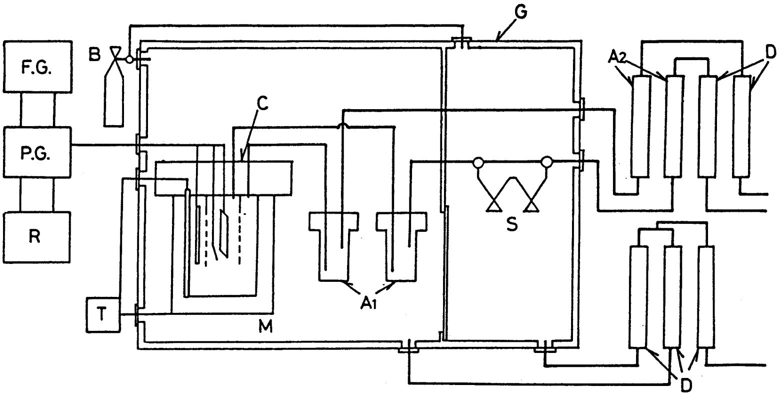

Fig. 3 Experimental apparatus

C: Cell
M: Mantle heater
G: Glove box
F.G.: Function generator
R: Recorder
D: desicator

T: Thermoregulator
B: N_2 bomb
S: Sampler
P.G.: Potentio-Galvanostat
A_1: HF absorber (NaF pellets)
A_2: HF absorber (NaF pellets and alumina)

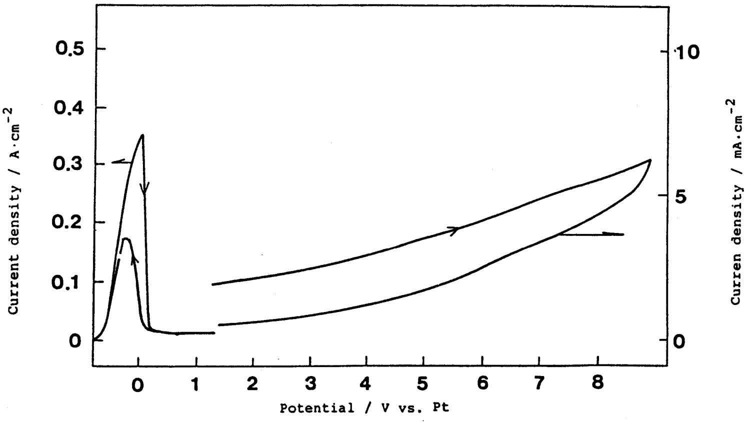

Fig. 4 Anodic polarization curve on copper electrode at 50 °C in the molten CsF·2.7HF by the cyclic voltammetry with sweep rate of 200 mV·s^{-1} (1st run).

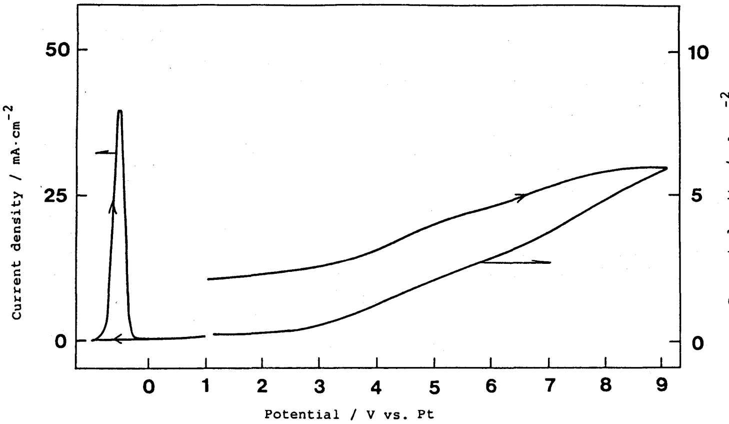

Fig. 5 Anodic polarization curve on iron electrode at 50 °C in the molten CsF·2.7HF by the cyclic voltammetry with sweep rate of 200 mV·s^{-1} (1st run).

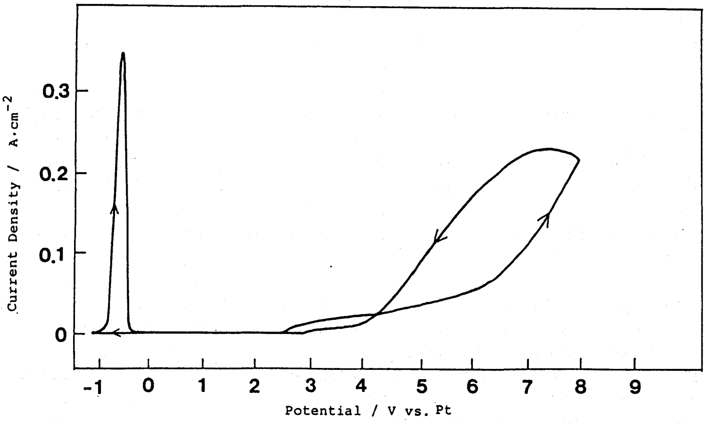

Fig. 6 Anodic polarization curve on nickel electrode at 50 °C in the molten CsF·2.7HF by the cyclic voltammetry with sweep rate of 200 mV·s^{-1} (1st run).

Table 1 Ratio of quantity of electricity dissipated by anodic dissolution of various metal electrodes to total quantity of electricity (Q_a/Q_t) in electrolysis at 5.5 V vs. Pt and 50 °C in the molten CsF·2.7HF.

Anode material	Current density ($mA \cdot cm^{-2}$)	Electron number of discharge / n	Total quantity of electricity / C	Q_a/Q_t (%)
Copper	2.5	2	108	97
Iron	2.7	2	37	110
Palladium	75.0	2	384	9.7
Nickel	1400.0	2	5420	1.6
Nickel	1400.0	4	5420	3.2

Heading; Q_a/Q_t: Ratio of quantity of electricity dissipated by anodic dissolution of electrodes to total quantity of electricity.

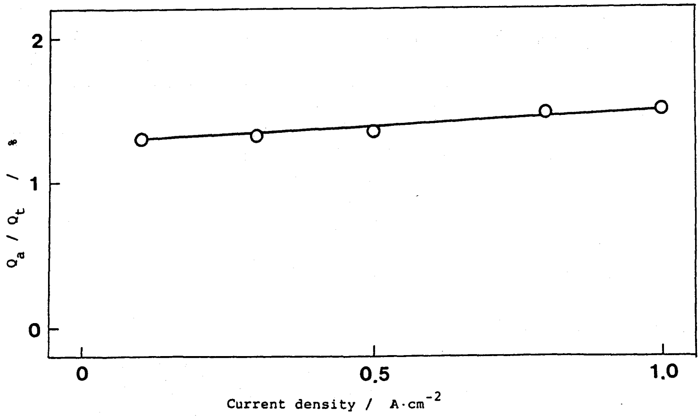

Fig. 7 Effect of current density on ratio of anodic dissolution of nickel to total quantity of electricity (Q_a/Q_t) in electrolysis at 50 °C in the molten CsF·2.5HF;

Total quantity of electricity = 5000 C·cm^{-2}

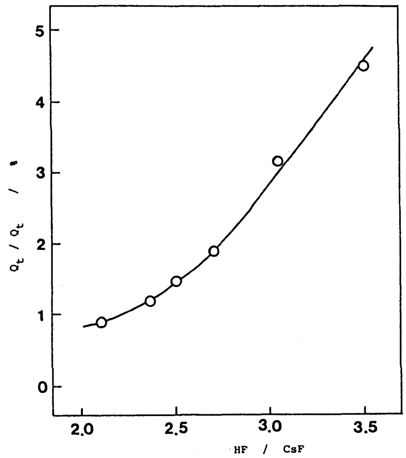

Fig. 8 Effect of composition of melt on ratio of anodic dissolution of nickel to total quantity of electricity (Q_a/Q_t) in electrolysis at 500 mA·cm^{-2} and 50 °C.

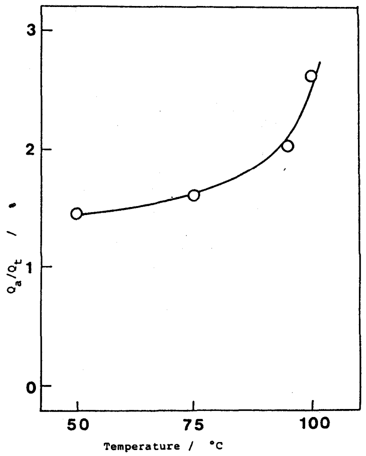

Fig. 9 Effect of temperature on ratio of anodic dissolution of nickel to total quantity of electricity (Q_a/Q_t) in electrolysis at 500 mA·cm^{-2} in the molten CsF·2.5HF;

Total quantity of electricity = 5000 C·cm^{-2}

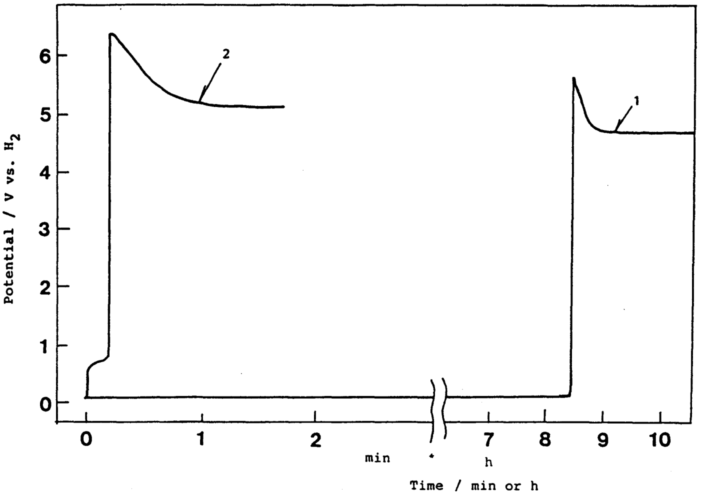

Fig. 10 Chronopotentiograms on nickel electrode during galvanostatic electrolysis at various current densities and 50 °C in the molten CsF·2.5HF;

1 ; 2 $mA \cdot cm^{-2}$, 2 ; 5 $mA \cdot cm^{-2}$

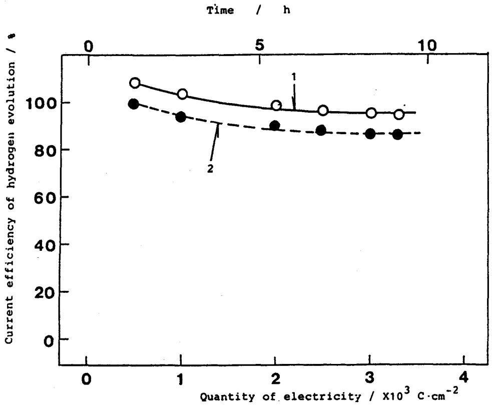

Fig.11 Change of current efficiency of hydrogen evolution on copper cathode during electrolysis at 100 $mA \cdot cm^{-2}$ and 50 °C in the molten CsF·2.6HF as a function of time;

1 ; Obtained line,
2 ; Corrected line for the maximum value as 100 %.

DOI: 10.1149/199017.0492PV

ELECTROCHEMICAL BEHAVIOR OF NICKEL IN THE 2HF-KF MIXTURE AT 80°C

Sylvie Rouquette-Sanchez, Daniel M. Ferry and Gérard S. Picard

Laboratoire d'Electrochimie Analytique et Appliquée
(Laboratoire associé au C.N.R.S., URA 0216)
E.N.S.C.P., 11 rue Pierre et Marie Curie
75231 Paris Cedex 05 - France

ABSTRACT

The electrochemical process of fluorine electrowinning may be improved in replacing the usual carbon anode which generally limits the cell life-time with a nickel anode. Therefore, we have investigated the electrochemical behavior of nickel in the 2HF-KF mixture at 80°C, using cyclic voltammetry and a.c.impedance measurements. A four step reaction pathway involving two adsorbed species has been proposed to account the experimental data, and its consistency was checked by a computerized simulation procedure taking into account the electrical properties of the corrosion layer formed.

INTRODUCTION

Industrial-scale fluorine electrowinning is nowadays performed from 2HF-KF mixture at 80°C. The current trends are to improve the electrochemical process in replacing the carbon anode which is responsible for an important anodic overpotential, and also, due to its fragility, to a severe limitation of the cell life-time. Knowing that before each electrolysis run with carbon anode, the electrolyte is electrochemically dehydrated using a nickel anode, it would be attractive to use also metallic nickel anode for the electrowinning of fluorine. In fact, nickel and platinum seem to be the only metals that can be used for this purpose[1-3].

Therefore, we have investigated the electrochemical behavior of nickel in a strictly fundamental point of view. A preliminary thermodynamic study[3] has shown that nickel oxide NiO can only be formed for very high and unrealistic water concentrations. So we have further only considered the nickel fluoride formation, because the water content of our mixture is about 50 ppm.

TECHNICAL

The lab-scale electrolysis cell and the experimental procedure have already been described in detail elsewhere[4]. The working and the counter electrodes were respectively a pure nickel wire supplied by Johnson Matthey (Ø=1mm) and a carbon rod (Ø=3mm) from Carbone Lorraine (carbon for spectrography 205). The reference electrode was constituted by a copper rod (Weber, Ø=3mm) electrochemically coated by CuF_2.

Voltammetric experiments were performed with a EG&G PAR Model 176 potentiostat-galvanostat connected to an Apple II microcomputer via a Model 273 interface. Chronoamperograms and impedance spectra were obtained using a Tacussel Z Computer System coupled to a Hewlett-Packard 9826A microcomputer. For a.c. impedance measurements, frequency ranged from 10^5 Hz to 10^{-2} Hz and the sinewave amplitude was 10 mV. The acquired experimental data were analysed (simulation curves) using a HP 9000 'series 300' microcomputer.

VOLTAMMETRIC STUDY :
REACTION STEPS OF THE OXIDATION OF NICKEL

Experimental results.

Steady-state voltammetry at a nickel electrode.

Fig.1b shows a typical sampled-current voltammogram obtained from chronoamperograms (Fig.1a) with a sample time of 20 mn. We observe that anodic current density increases from - 0.150 V to 0.057 V to reach a maximum value close to 0.26 $mA.cm^{-2}$, and then deeply decreases for reaching a constant value of 0.039 $mA.cm^{-2}$ from 0.4 V. The shape of this steady state voltammogram can be explained by considering that two main electrochemical reaction steps occur[3] as it was further confirmed by the Linear Sweep Voltammetry (L.S.V.) study. The limiting current density observed for potential values higher than 0.4 V is due to either a desorption or solubilization process of an adsorbed high oxidation state species of nickel. This is consistent whatever the nature (adsorbed or soluble) of the intermediate nickel species formed. In order to clarify the reaction mechanism, a L.S.V. study was undertaken.

Linear Sweep Voltammetry study at low sweep rates.

The shape of the cyclic voltammograms depends on the sweep rate (Fig. 2 and 3). For values lower than 0.1 V.s^{-1}, we can observe during the forward scans two oxidation current density peaks respectively at about 0 V and 0.2 V. They are followed by a fairly constant low curent density value. During the reverse scan, one oxidation peak of lower current density is only observed.

Forward scans. The two oxidation peaks observed in the forward scans can be attributed to two electrochemical subsequent reaction steps. This confirms the steady state voltammetry results. The sharp decrease of the current density after the first oxidation peak for 0.005 V.s^{-1} (Fig. 2a) clearly evidences the blockage of the nickel electroactive sites, which suggests the formation of an adsorbed species of nickel in the first electrochemical step. Moreover, this intermediate species has to be electrical conductive because a second oxidation peak is observed. Similarly, this latter corresponds to the formation of an adsorbed species of nickel of higher oxidation state, the desorption of which is responsible for the low limiting current observed at potential values higher than 0.4 V.

Reverse scans. The value of the oxidation current density relative to the oxidation peak observed in the reverse scans, decreases with an increase of the sweep rate (Fig. 2). This peak is observed in the potential range for which there is no oxidation of the intermediate species. In fact, this peak corresponds to the oxidation of metallic nickel, which requires regenerating of electroactive sites by desorption of the intermediate and the ultimate species. So, this peak can only be exist for low sweep rates in order to allow the electroactive sites to be regenerated. This peak does not appear for sweep rates higher than 0.1V.s^{-1} (Fig. 3). In fact for high sweep rate values, the reverse oxidation peak cannot be observed because the desorption of this species is impossible during the scan-time. Moreover, the desorption rate of the intermediate species of nickel must be higher than the one of the ultimate oxidized species of nickel. In fact, otherwise a decreasing current density would be expected for potential values for which the second electrochemical oxidation reaction does not occur[3].

Linear Sweep Voltammetry study at high sweep rates.

For very high values of the sweep rate, the shape of the voltammograms is quite different (Fig. 3). Only one oxidation peak is observed and there is no current flow during the reverse scan. This type of voltammogram was first studied by Calandra et al[5] which explained the shape observed by the formation of an insulating layer. They proposed a pure resistive model to analyze this type of curve. This model was further extensively used and improved especially by Devilliers et al[6] for accounting their experimental results relative to the oxidation of carbon in HF-KF melts, and by Lamirault[7] in her study on the electrochemical properties of copper in the 2HF-KF mixture. The obtention of this type of voltammogram proves the insulating character of the ultimate species of nickel electrochemically formed.

Discussion.

Proposal of a reaction pathway.

This electrochemical behavior of nickel can be explained by considering the following reaction mechanism :

- oxidation of metallic Ni into an adsorbed nickel species :

$$Ni - n_1 e^- = Ni(N_1)ads$$

- desorption (or solubilizing) of Ni(N1)ads :

$$Ni(N_1)ads = Ni(N_1)$$

- oxidation of adsorbed $Ni(N_1)$ into adsorbed $Ni(N_2)$:

$$Ni(N_1)ads - (n_2 - n_1)\, e^- = Ni(N_2)ads$$

- desorption (or solubilizing) of $Ni(N_2)ads$:

$$Ni(N_2)ads = Ni(N_2)$$

$Ni(N_1)ads$ beeing an electrical conductive species and $Ni(N_2)ads$ an insulated species .

In anhydrous HF and HF-NaF mixtures[2,8-11] oxidation of metallic nickel seems to lead to the formation of NiF_2, analysed by Hackerman et al[8]. This compound is an electrical conductor[12,13]. On contrast, in potassium fluoride containing media, the analysis of the compound formed during electrochemical oxidation of nickel is K_2NiF_6[14] which is an insulating compound. Based on these literature data, we can assume that $n_1 = n_2 = 2$, i.e. the formation of Ni(II) (probably NiF_2) and Ni(IV) (probably K_2NiF_6).

Kinetic constants (regression analysis of the steady state j-E curve).

The simplest mechanism corresponds to the oxidation of Ni into Ni(II) and subsequently into Ni(IV) coupled with the desorptions of this two species. The four kinetic steps may then be written as follows :

$$\begin{array}{lcl} \text{Ni, s} & \overset{k_{b1}}{\underset{k_{f1}}{\Leftrightarrow}} & \text{Ni(II), s} + 2e^- \\ \Gamma(1-\theta_1-\theta_2) & & \Gamma\theta_1 \end{array}$$

$$\begin{array}{lcl} \text{Ni(II), s} & \overset{k_{b2}}{\underset{k_{f2}}{\Leftrightarrow}} & \text{Ni(IV), s} + 2e^- \\ \Gamma\theta_1 & & \Gamma\theta_2 \end{array}$$

$$\begin{array}{lcll} \text{Ni(II), s} & \overset{K_1}{\rightarrow} & \text{Ni(II)} \; + & \text{s} \\ \Gamma\theta_1 & & C_1 & \Gamma(1-\theta_1-\theta_2) \end{array}$$

$$\begin{array}{lcll} \text{Ni(IV), s} & \overset{K_2}{\rightarrow} & \text{Ni(IV)} \; + & \text{s} \\ \Gamma\theta_2 & & C_2 & \Gamma(1-\theta_1-\theta_2) \end{array}$$

where C_1 and C_2 are respectively the electrode concentrations of Ni(II) and Ni(IV) ,k_{b1}, k_{b2}, k_{f1} and k_{f2} are the forward and reverse rate constants for the two electrochemical steps; they are connected to the intrinsic rate constants $k°_1$ and $k°_2$ by :

$$k_{b1} = k°_1 \exp\left(\frac{(1-\alpha_1)\,n\,F}{R\,T}\,(E - E°_1)\right) \qquad (1)$$

$$k_{f1} = k°_1 \exp\left(\frac{-\alpha_1\,n\,F}{R\,T}\,(E - E°_1)\right) \qquad (2)$$

$$k_{b2} = k^\circ{}_2 \exp\left(\frac{(1-\alpha_2)\,n\,F}{R\,T}\,(E - E^\circ{}_2)\right) \qquad (3)$$

$$k_{f2} = k^\circ{}_2 \exp\left(\frac{-\alpha_2\,n\,F}{R\,T}\,(E - E^\circ{}_2)\right) \qquad (4)$$

and $b_{b1} = \frac{(1-\alpha_1)\,n\,F}{R\,T}$: $b_{f1} = \frac{-\alpha_1\,n\,F}{R\,T}$: $b_{b2} = \frac{(1-\alpha_2)\,n\,F}{R\,T}$: $b_{f2} = \frac{-\alpha_2\,n\,F}{R\,T}$

where α_1 and α_2 are the charge transfer coefficients, $E^\circ{}_1$ and $E^\circ{}_2$ the standard potentials, respectively for the two electrochemical reactions, and E the applied potential.

Γ is the electroactive site number and θ_1, θ_2 are the fractional coverage of the electrode surface by Ni(II)ads and Ni(IV)ads respectively.

Because of the very large number of parameters involved (nine) to be determined, we have preferred instead of a direct simulation , to use a simplest and more systematic procedure for obtaining estimates of constants under consideration.

It was demonstrated elsewhere[3] that the steady state j-E curve may be approximated by the following expressions :

$$j = n\,F\,S\,\Gamma\,k_{b1} \qquad (5)$$
$$j = n\,F\,S\,\Gamma\,K_1\,K_2 / k_{b2} \qquad (6)$$
$$j = 2\,n\,F\,S\,K_2 \qquad (7)$$

applying respectively to the increasing-current part, the decreasing-current part and to the constant-current part of the curve, when neglecting the reverse electrochemical reactions.

Defining k^*_1 and k^*_2 as :

$$k^*_1 = k^\circ_1 \exp\left(\frac{(1-\alpha_1)\,n\,F}{R\,T}\;(-E^\circ_1)\right) \qquad (8)$$

$$k^*_2 = k^\circ_2 \exp\left(\frac{(1-\alpha_2)\,n\,F}{R\,T}\;(-E^\circ_2)\right) \qquad (9)$$

and from (1) we can write :

$$j = n\,F\,S\,\Gamma\,k^*_1 \exp\left(\frac{(1-\alpha_1)\,n\,F}{R\,T}\;E\right)$$

or

$$j = A \exp(BE)$$

By fitting the first part of the experimental curve, we have found for A and B the values $2.12.10^{-4}$ and 15.44 which led for Γk^*_1 and α_1 to the following values :

$$\Gamma k^*_1 = (1.10 \pm 0.05).10^{-9}\ s^{-1}.mol.cm^{-2}.$$

and

$$\alpha_1 = 0.765 \pm 0.001$$

In a similar manner, fitting the last part of the curve by applying (7) gives :

$$\Gamma K_2 = (10.0. \pm 0.2).10^{-11}\ s^{-1}.mol.cm^{-2}.$$

and, the second part of the curve by applying (6) allows us to obtain the ratio $K_1/k^*_2 = (77 \pm 2)$ and $\alpha_2 = 0.720 \pm 0.01$

Using these kinetic parameters, the steady state j-E curve was simulated (Fig. 4) . We can observe a good fitting of the experimental data with the calculated curve, confirming the consistency of both the mechanism and the method used for obtaining the various parameters.

A.C. IMPEDANCE SPECTROSCOPY

Experimental data.

Impedance spectra were then performed in the three potential areas previously defined. For potential values ranging from -0.150 to 0.057 V the j-E curve exponentially increases and the impedance spectra show one or several capacitive loops (Fig.5a). When potentials ranged from 0.057 to 0.2 V (decreasing part of the j-E curve) the impedance spectra show a negative polarisation resistance (Fig.5b), and for potentials higher than 0.2 V (constant current density part) the spectra are characterized by a capacitive loop followed by a vertical line which corresponds to an infinite value of the polarisation resistance (Fig.5c).

In order to make easier the interpretation of the impedance spectra, we have considered the equivalent electrical circuit given in Fig.6 which takes into account the electrical properties of the Ni-layer (capacitance C_c and resistance R_c) as usually considered[15-17], the faradaic impedance Z_f and the double layer capacitance C_d as well as the electrolyte resistance R_e.

Electrical properties of the Ni-layer formed.

Analysis of impedance spectra at high frequencies : Ni-layer capacitance Cc.

The overall impedance Z corresponding to the considered equivalent electrical circuit is given by :

$$Z = R_e + Z_1 + Z_2$$

$$Z = R_e + \frac{R_c}{1 + j\omega C_c R_c} + \frac{Z_f}{1 + j\omega C_d Z_f}$$

When the angular velocity $\omega \rightarrow \infty$, it is easy to demonstrate that the opposite of the imaginary part Z_i of the impedance is practically equal to $1/\omega.C_c$ when C_d is higher than C_c which has been verified a posteriori. In that case, the high frequency response has to be attributed only to the Ni-layer capacitance. A plot of $-Z_i$ vs. $1/\omega$ for the experimental data obtained at high frequencies leads to a straight line the slope of which (equal to $1/C_c$) giving the Ni-layer capacitance. Such plots obtained as a function of potential are given in Fig.7. The values so derived for the Ni-layer capacitance were the reported in Fig.8a vs. the applied potential. We can notice a sharp decrease of the capacitance value when potential becomes higher than 0.1 V. From the potential dependence of the fractional coverages θ_1 and θ_2 giving by the following expressions[3] :

$$\theta_1 = \frac{k_{b1} K_2}{K_2\left(K_1 + k_{b2} + k_{b1}\right) + k_{b1} k_{b2}}$$

$$\theta_2 = \frac{k_{b1} k_{b2}}{K_2\left(K_1 + k_{b2} + k_{b1}\right) + k_{b1} k_{b2}}$$

$$(1-\theta_1 - \theta_2) = \frac{K_2\left(K_1 + k_{b2}\right)}{K_2\left(K_1 + k_{b2} + k_{b1}\right) + k_{b1} k_{b2}}$$

we can notice (Fig.9b) that the nickel electrode is covered both by NiF_2 (θ_1) and K_2NiF_6 (θ_2) for potential values ranging from -0.30 V to 0.15 V. On the contrary, when the applied potential is higher than 0.15 V, the fractional coverage θ_2 of K_2NiF_6 tends to unity and the average value observed ($5.3.10^{-6}$ F.cm^{-2}) may be attributed to the K_2NiF_6 layer. The average capacitance value obtained for potentials lower than 0.15 V is higher ($2.4.10^{-5}$ F.cm^{-2}) and by comparing with the Fig.8b, we can deduce that the capacitance of the NiF_2 compound is likely higher than that of K_2NiF_6.

Simulation of the experimental overall impedance : Ni-layer resistance Rc and double layer capacitance.

The electrolyte resistance was determined by regression analysis of experimental data acquired at high frequencies. The value obtained is 3.85 Ω.cm^2. The calculated faradaic impedance is given by [3] :

$$Z_f = \frac{\begin{vmatrix} 1 & 1 & 1 & 0 & 0 \\ 0 & -1 & 0 & a & b \\ 0 & 0 & -1 & c & 0 \\ 0 & 1/nF\Gamma & -1/nF\Gamma & & e \\ 0 & 0 & 1/nF\Gamma & 0 & f \end{vmatrix}}{\begin{vmatrix} 0 & 1 & 1 & 0 & 0 \\ 1/R_{t1} & -1 & 0 & a & b \\ 1/R_{t2} & 0 & -1 & c & 0 \\ 0 & 1/nF\Gamma & -1/nF\Gamma & & e \\ 0 & 0 & 1/nF\Gamma & 0 & f \end{vmatrix}}$$

with :

$$R_{t1} = \frac{1}{nF\Gamma\left(b_{b1}k_{b1}\left(1-\theta_1-\theta_2\right)\right)}$$

$$R_{t2} = \frac{1}{nF\Gamma\left(b_{b2}k_{b2}\theta_1\right)}$$

$a = -nF\Gamma k_{b1}$
$b = -nF\Gamma k_{b1}$
$c = nF\Gamma k_{b2}$
$e = -(i\omega + K_1)$
$f = -(i\omega + K_2)$

The expression of Z_f is then function of Γ, k^*_1, k^*_2, K_1, K_2, α_1, α_2, and E. We have noticed that the faradaic impedance value depends on all the preceeding parameters itselves excepted for K_1 and k^*_2 which intervene only by their ratio K_1/k^*_2. Besides, as the quantities Γk^*_1, ΓK_2 , K_1/k^*_2, α_1

and α_2 are known (see above), only Γ remains to be varied for fitting the faradaic impedance.

For simulating the overall impedance we need also to know the values of the double layer capacitance C_d and the Ni-layer resistance R_c (the Ni-layer capacitance C_c and the electrolyte resistance R_e are known). Therefore, we have considered the three unknown parameters Γ, C_d and R_c as variables and determined their values leading to the best fitting of the experimental impedance spectra as a function of the applied potential E. This was obtained for the values reported in Table 1.

The resulting simulated spectra are represented Fig.9 to 11 and compared with the experimental data. Thus, we see that the simple mechanism we envisaged accounts pretty well for all our experiments performed at various potentials proving the consistency of the proposed model.

CONCLUSION

The electrochemical behaviour of nickel in the 2HF-KF mixture at 80°C may be described by a simple four step mechanism involving two adsorbed species and two desorption steps. Values of kinetic constants and electrical parameters have been determined by analysing both the steady state voltammogram and impedance spectra. Works are in progress to use these values for simulating the experimental cyclic voltammograms.

Acknowledgements.

The authors thank Comurhex (Pechiney Group) for financial support of this work. One author (S.R) thanks the French Research Ministry for providing a doctoral grant. Acknowledgements are also due to Pr.B.Tremillon (URA 0216) and Dr.F.Nicolas (Comurhex) for their interest in this work.

REFERENCES

[1].N.Hackermann,E.S.Snavely and L.D.Fiel, Corros.Sci.,7 (1967) 39.
[2].K.Ashok, Surf.Technol., 4 (1976) 401.
[3].S.Rouquette, Thesis, Paris 1989.

[4].S.Rouquette, D.Ferry and G.Picard, J.Electrochem.Soc.,**136** (1989) 3299.

[5] A. J. Calandra, N. R. De Tacconi, R. Pereiro, A. J. Arvia, Electrochim. Acta, **19** (1974) 901

[6] D. Devilliers, F. Lantelme, M. Chemla, Electrochim. Acta, **31** (1986) 1235

[7] S. Lamirault, Thèse de l'Université P. et M. Curie, 1987

[8] N. Hackerman, E. S. Snavely, Jr and L. D. Fiel, Electrochim. Acta, **12** (1967) 535

[9] I. L. Serushkin, G. A. Tedoradze, T. L. Razmerova, G. P. Il'inskaya, G. I. Kaurova, Electrokhimiya, **14** (1976) 58

[10] J. S. Clarke, A. T. Kuhn, J. Electroanal. Chem., **85** (1977) 299

[11] M. Novak, J. Boa, J. Electroanal. Chem., 109 (1980) 179

[12] J. Salardenne, M. Salagoity, J. Pichon, A. S. Barriere, Thin Solid Films, **88** (1982) 153

[13] Yu. A. Luk'yanychev, I. I. Astakhov, N. S. Nikolaev, Akad. Nauk SSSR, Ser. Khim., (1965) 577

[14] T. L. Court, M. F. A. Dove, J. Chem. Soc. Dalton trans., **19** (1973) 1995

[15] L. I. Maissel, R. Glang, "Handbook of thin film technology", p 16, 1970, McGraw-Hill ed.

[16] J. Ross Macdonald, "Impedance Spectroscopy", p 301, 1987, J. Wiley & sons ed.

[17] J. G. Thevenin, R. H. Muller, J. Electrochem. Soc., **134** (1987) 2650

Table 1 : Values of C_d and R_c derived from the simulation of experimental impedance spectra.

E (V)	C_d (F/ cm^2)	R_c (Ω. cm^2)
-0.25	2.9. 10^{-4}	1350
-0.15	2.6. 10^{-4}	1800
-0.1	1.3. 10^{-4}	720
0.1	3. 10^{-4}	160
0.12	1.25. 10^{-4}	250
0.14	7. 10^{-5}	700
0.5	4. 10^{-3}	3100
0.8	3.7. 10^{-3}	3600

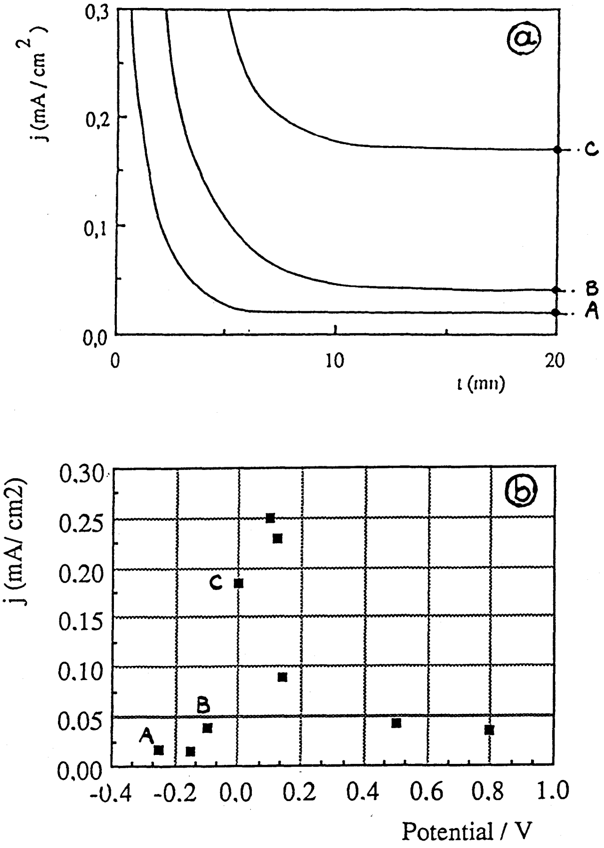

Fig.1 : a) Typical chronoamperograms obtained on a nickel electrode in the 2HF-KF mixture at 80°C. (curve A : E = -0.250 V; curve B : E = -0.100 V; curve C : E = 0.020 V)
b) Sampled-current voltammogram derived from chronoamperograms represented Fig.1a, with a sample time of 20 mn.

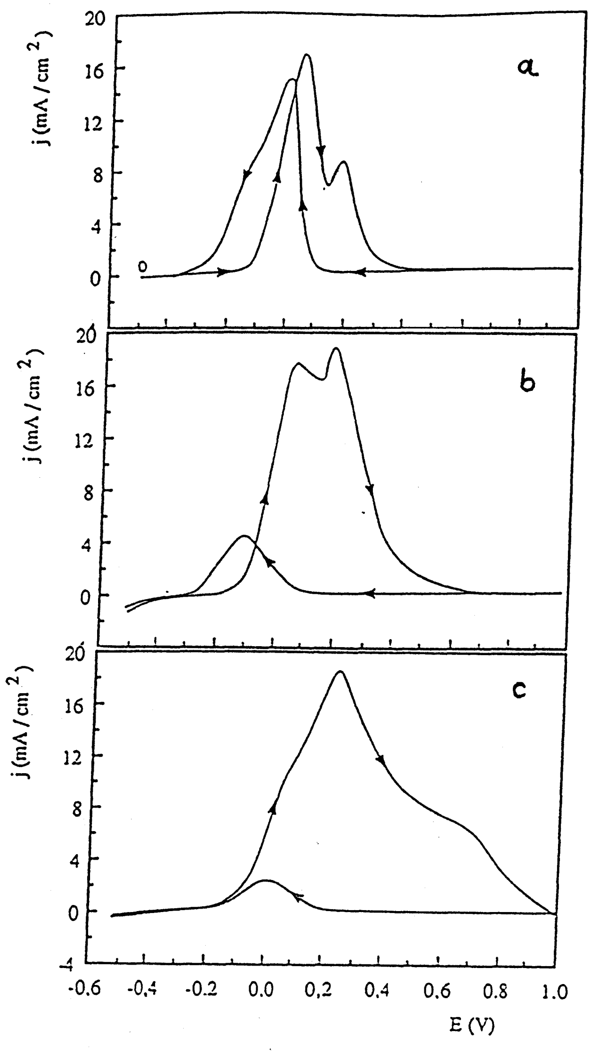

Fig.2 : Linear sweep voltammograms obtained on a nickel electrode in the 2HF-KF mixture at 80°C with various voltage sweep rates : a = 0.005 V.s^{-1}, b = 0.02 V.s^{-1}, c = 0.05 V.s^{-1} .

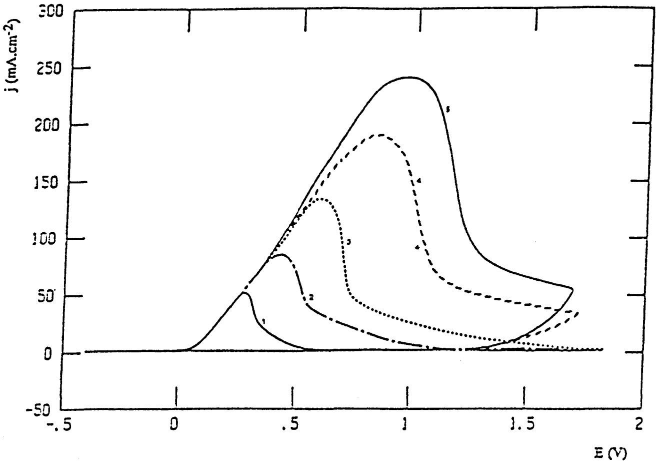

Fig.3 : Linear sweep voltammograms obtained on a nickel electrode in the 2HF-KF mixture at 80°C with various voltage sweep rates : 1 = 0.4 V.s^{-1}, 2 = 0.8 V.s^{-1}, 3 = 1 V.s^{-1} , 4 = 4 V.s^{-1} , 5 = 6.5 V.s^{-1}.

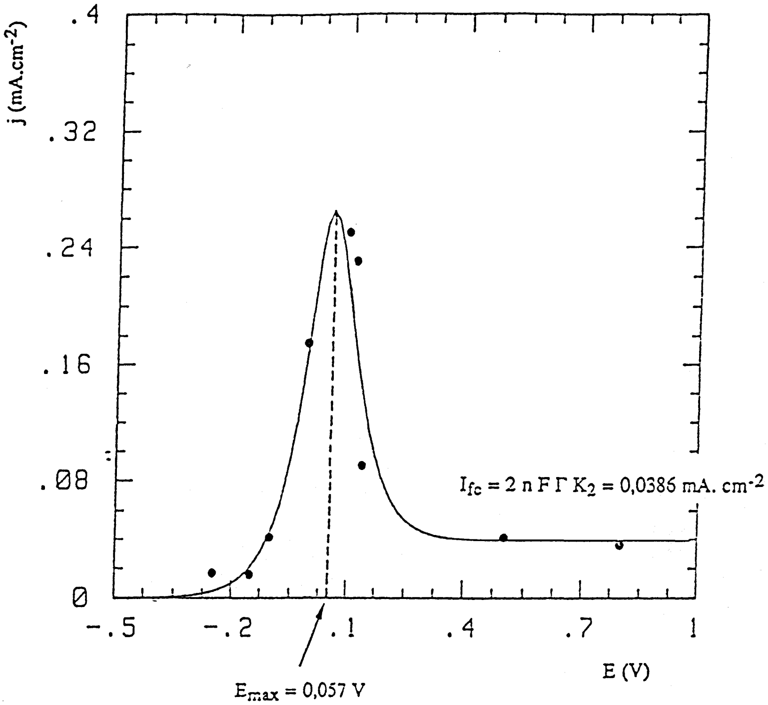

Fig.4 : Steady state j-E curve of Ni electrochemical oxidation in the 2HF-KF mixture at 80°C :

● : experimental data.

—— : simulated curve (see text).

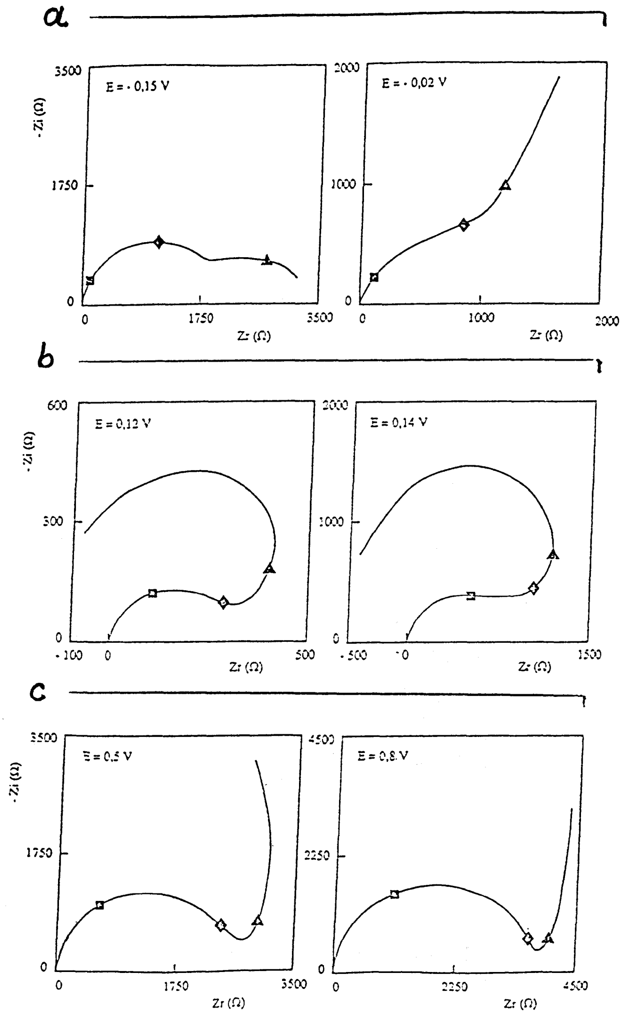

Fig.5 : A.C.Impedance spectroscopy in the 2HF-KF mixture at 80°C : Nyquist plots obtained with a working Ni electrode at various applied potentials.
1st frequency : 10^5 Hz , □ : 10Hz, ◇ : 1Hz,
Δ : 0.1Hz ; last frequency : 0.01Hz.

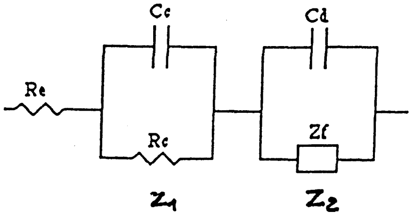

Fig.6 : Equivalent electrical circuit.

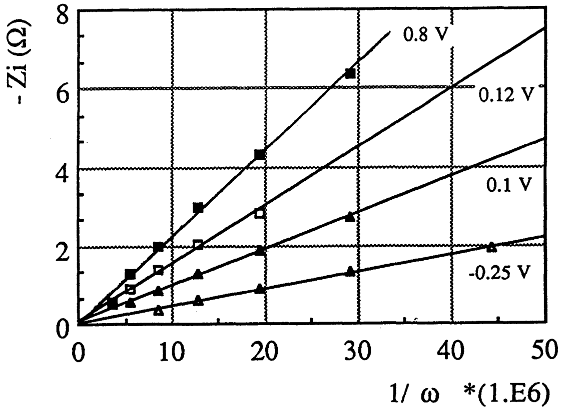

Fig.7 : Determination of the Ni-layer capacitance. Plots of $-Z_i$ vs. $1/\omega$ for high frequency data obtained at various applied potentials (S = 1 cm2).

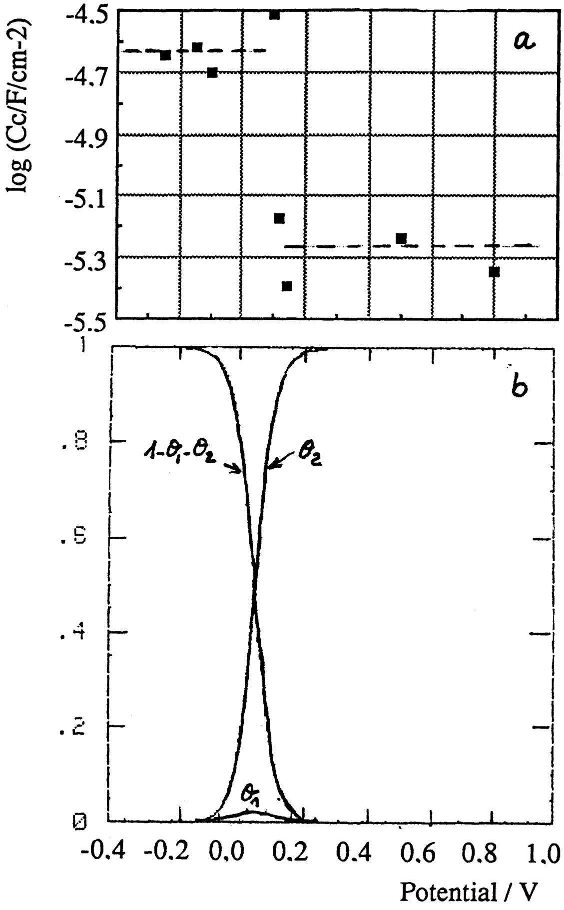

Fig.8 : a) Plot of the Ni-layer capacitance vs. applied potential.
b) Potential dependence of the fractional coverages θ_1 and θ_2.

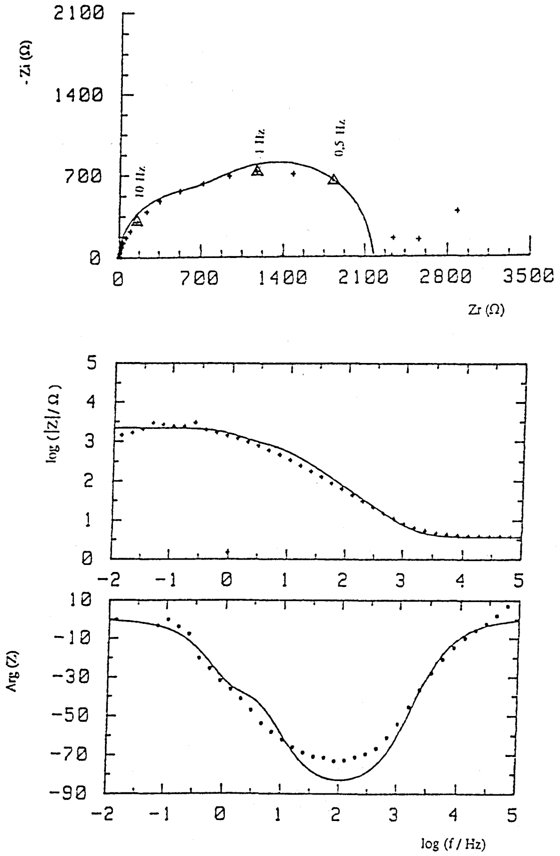

Fig.9 : Impedance spectrum obtained on a nickel electrode in the 2HF-KF mixture at 80°C (applied potential : -0.1 V)

- : experimental data.

— : simulated curve.

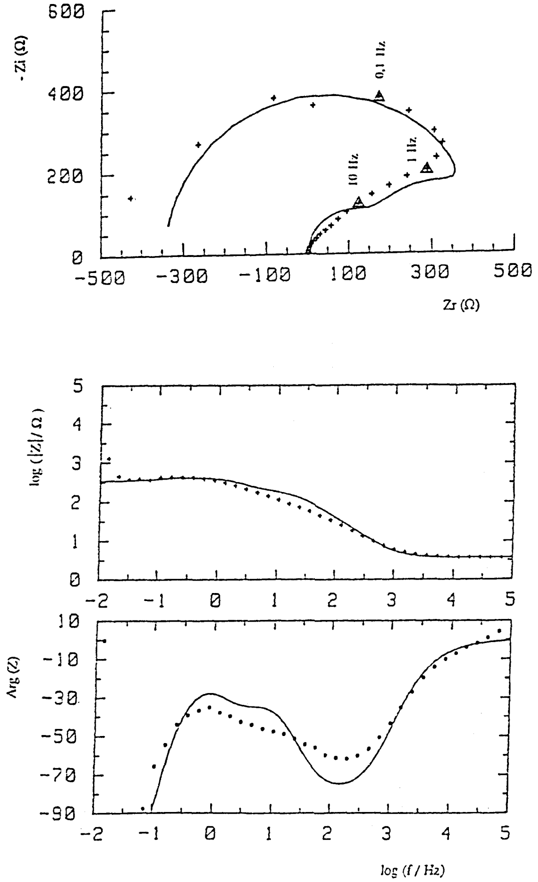

Fig.10 : Impedance spectrum obtained on a nickel electrode in the 2HF-KF mixture at 80°C (applied potential : 0.1 V)

- : experimental data.

— : simulated curve.

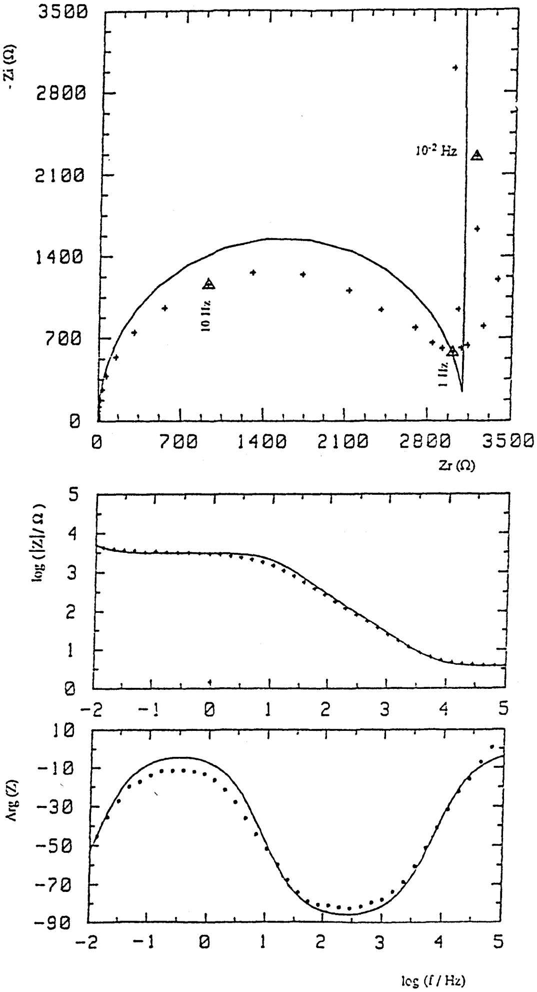

Fig.11 : Impedance spectrum obtained on a nickel electrode in the 2HF-KF mixture at 80°C (applied potential : 0.5 V)

• : experimental data.

— : simulated curve.

DOI: 10.1149/199017.0515PV

ELECTROCHEMICAL CORROSION OF IRON IN MOLTEN $Ca(NO_3)_2 \cdot 4\ H_2O$ AT 80°C

M. AZZI, J.J. RAMEAU, J.P. DIARD
Centre de Recherche en Electrochimie Minérale et en
Génie des Procédés, B.P. 75 Domaine Universitaire,
38402 Saint-Martin d'Hères (FRANCE)

S. BELCADI
Université Mohamed V, Faculté des Sciences, Avenue
Ibn Batouta, B.P. 1014 Rabat (MAROC)

ABSTRACT

The polarization curve of iron ($v = 1$ mV s^{-1}) in molten $Ca(NO_3)_2 \cdot 4\ H_2O$ at 80°C showed two peaks of activation on a motionless electrode and only one peak on a rotating electrode ; in the two cases, this behaviour is characteristic of multiple steady states. If on a rotating electrode that is due to ohmic drop, in the case of a motionless electrode, it is the simultaneous effect of ohmic drop and of an electrochemical reduction reaction which is responsible for this multivocal behavior.

From electrochemical impedance measurements associated to electrochemical tests, it is possible to propose a mechanism for iron passivation in molten tetrahydrate calcium nitrate at 80°C.

I INTRODUCTION

Multiple steady states behavior was observed for example with iron in nitric acid (1,2,3) and in sulphuric acid (2,4,5,6), with tin and zinc in basic solutions (7,8,9,10), with gold in KCl 1M, H_2SO_4 0,25 M (12), with cobalt in sulphuric acid (13) and with titanium in fluorhydric solutions (14).

In molten salt, this kind of behavior was observed in molten cryolite with graphite polarized anodically (15,16,17).

II EXPERIMENTAL APPARATUS AND TECHNIQUES

The glass electrochemical cell had a water-jacket for circulation of hot water to maintain the temperature at

80°C. The counter electrode was a gold plate (5 cm^2). Two types of iron working electrode (J.M.C. quality) were used : a rotating electrode (0,2 cm^2) and a motionless electrode (1 cm^2). All potentials are reported to Ag/Ag^+ reference electrode (18). The impedance measurements were carried out from 10^4 Hz to 10^{-2} Hz by a Solartron Schlumberger apparatus interface 1186 and analyzer 1250. The polarization curves were obtained by the interface 1186 and a signal generator (G.S.T.P. Tacussel).

III THE IRON BEHAVIOUR UNDER POLARIZATION

III.1 Motionless electrode

The polarization curve (fig. 1a) was plotted in quasi-stationary conditions ($v = 1$ mV s^{-1}) ; it showed two activation peaks. The transition between the first and the second peak occured suddenly at a potential $E = -0,40$ V. It was shown that a gas evoluted at the electrode. During the backward scanning, the polarization curve did not exhibit any reactivation phenomenon.

When the polarization curve (fig. 1b) of the same electrode in the same conditions was obtained with an internal negative resistance regulator, the transition between the two activation peaks occurred continuously exhibiting a multiple steady states behaviour.

After the polarization test, the observation of the electrode surface using a scanning electronic microscope (JEOL 540) showed the existence of oxidized grains and non-oxidized grains (fig. 2).

III.2 Rotating electrode

The polarization curve ($v = 1$ mV s^{-1} (fig. 3a) of a rotating electrode ($\omega = 2000$ rpm) showed only one activation peak. The transition from the activation to the passivation domain yet occurred suddenly. The polarization curve (fig. 3b) plotted with an internal negative resistance regulator showed that the transition between the two states occured continuously. Then, even in the case of a rotating electrode, the polarisation curve is under a multiple steady states control. During the backward scanning potential, the polarisation curve did not exhibit a reactivation phenomenon. This was probably due to a change in the structure of the oxide layer. After the polarization test, the electrode surface was black and bright.

III.3 Surface observation and analysis

The observation in the scanning electronic microscope of a passivated iron electrode did not indicate the presence of a passivation layer. So the thickness of this layer is lower than the microscope detection limit (about 1 µm.). The surface analysis of the same electrode by XPS (fig. 4) showed the presence of iron, oxygen and calcium even after a 300 Å thick by ionic bombardment erosion. So, the passivation layer was a mixed oxide of iron and calcium, its thickness was between 300 Å and 1 µm.

IV IMPEDANCE MEASUREMENTS

The electrochemical diagrams (fig. 5) plotted under linear conditions (alternative signal 10 mV) at different potentials on the polarization curve showed a high frequency capacitive loop, a medium frequency inductive loop and a low frequency capacitive loop. The size of the inductive loop decreased when the potential increased. In A and B domain of the polarization curve, the impedance diagrams were not reproductible because of the instability of experimental conditions.

V. DISCUSSION

The multiple steady state can be caused by (9,19) :
- the ohmic drop
- the diffusion in solution phenomenon
-an autocatalytic or a supplementary electrochemical reaction

The "Z" form of polarization curve was obtained both on a motionless or a rotating electrode. In the case of rotating electrode, the rotation speed did not involve a significant modification on the polarisation curve shape ; so the diffusion phenomenon is not responsible for the observed behavior.

V.1. Electrolyte resistance measurement

The iron current dissolution in molten calcium nitrate tetrahydrate was more important with a rotating than with a motionless electrode ; so the ohmic drop could be more important and it was necessary to measure this term to correct the polarization curve.

The resistance of the electrolyte between the reference electrode and the working electrode was determined by impedance measurements. The extrapolation to high frequencies of the impedance diagrams gave the value Re = 4 $\Omega.cm^2$ at 80°C.

V.2. Phenomenon responsible for the multiple steady states behavior

In the case of a rotating electrode, after ohmic drop correction ($E_{corr} = E_{exp} - R_e \times I$), the polarization curve did not show the multiple steady states behavior (fig. 6). The "Z" form was then assigned to ohmic drop.

In the case of a motionless electrode for which the ohmic drop is less important (lower current density), the corrected polarization curve remained multivocal (fig. 7). The gas evolution at the electrode indicated that multiple steady states must be attributed to the simultaneous effect of the ohmic drop and of an electrochemical reduction reaction which led to the gas evolution.

V.3. Identification of the gas formed

On a rotating platinum electrode, the addition of H^+ ions (as HCl or HNO_3) in the melt gave a reduction wave at - 0,35 V (fig. 8b) which did not exist in the pure melt (fig. 8a). The reduction limiting current was proportional to H^+ concentration. This reduction wave could not be attributed to H_2 evolution which appeared at a potential more cathodic (20). So the electrochemical reaction involves the intervention of NO_3^- species. The study by cyclic voltamperometry with convolutional analysis and by impedance measurement showed that the reduction wave corresponded to an electrochemical reaction with one exchanged electron according to :

$$NO_3^- + 2\ H^+ + 1e^- \Longrightarrow NO_2 + H_2O \qquad -1-$$

For this reaction to occur on iron in the pure melt, H^+ ions had to be in a sufficient quantity near the electrode ; they are produced by iron oxidation according to

$$Fe + xH_2O \Longrightarrow Fe(OH)_x + xH^+ + xe- \qquad -2-$$

As the molten salt at 80°C is viscous (16 cp), the H^+ ions formed remain near the electrode to react according to reaction -1-.

For impedance measurements, if the high frequencies capacitive loop is assimulated to a parallel R-C circuit, the deduced C_{HF} value was higher than the normal value of double layer capacitance in molten salts ; C_{HF} varied linearly and R_{HF} varied exponentially with electrode potential (fig. 9). The product $R_{HF} \star i = 50$ mV was independent from the set-on potential if $E < - 0{,}25$ V ; so R_{HF} can be simulated to a charge transfer resistance and the constant product $R_{H.F.} \star i = R \star T/(\alpha_{\star} n \star F)$ at 80°C gave an $\alpha_{\star}n$ value equal to 0.66.

In the case of a rotating electrode, the Tafel representation $E = f(\log i)$ of the polarization curve corrected for ohmic drop showed a linear portion in the activation domain with a slope equal to 47 mV (fig. 10).

The low frequencies capacitive phenomenon corresponds to the limiting step in the passivation process. The R_{BF} resistance associated to this loop and the product $R_{BF} \star i$ increased linearly with the potential. The slope of the straight line $R_{BF} \star i = f(E)$ was equal to 0.7, value near the unity. This phenomenon should be attributed to the conduction and the growth of semi-conducting passive layer (21).

The medium frequencies inductive loop and the lower frequencies capacitive loop was associated in literature to different phenomena; in particular they were attributed to the oxide layer properties of valve metals (22). It was also showed that it is necessery to have at least two different adsorbed species in a reaction mechanism for having an inductive loop with double point (23). We have then introduced the adsorbed species Fe(OH) and $Fe(OH)_2$ in the following mechanism :

$$Fe + H_2O \Longrightarrow Fe(OH)_{ads} + H^+ + 1e^-$$

$$Fe(OH)_{ads} + H_2O \Longleftrightarrow (Fe(OH)_2)_{ads} + H^+ + 1e^-$$

$$Fe(OH)_{ads} \Longrightarrow Fe(OH)^+ + 1e^-$$

The numerical simulation of this mechanism behavior allowed us to determine the characteristic kinetic constants which gave us a general description of experimental results (24).

SUMMARY

The polarization curve of iron showed a multiple steady

states behavior in molten $Ca(NO_3)_2 \cdot 4\ H_2O$ at 80°C. In the case of rotating electrode, ohmic drop is essentially responsible for this kind of behavior. On the other hand for a motionless electrode, the multivocal behavior was attributed to a simultaneous effect of ohmic drop and a supplementary reduction reaction which lead to NO_2 gas evolution.

The reduction reaction was :

$$H^+ + NO_3^- + 1e^- \Longrightarrow NO_2 + H_2O$$

H^+ ions were produced during iron oxidation as follows :

$$Fe + xH_2O \Longrightarrow Fe(OH)_x + xe^- + xH^+$$

The impedance measurements allowed us to propose the following dissolution passivation mechanism :

$$Fe + H_2O \Longrightarrow Fe(OH)_{ads} + H^+ + 1e^-$$

$$Fe(OH)_{ads} + H_2O \Longleftrightarrow (Fe(OH)_2)_{ads} + H^+ + 1e^-$$

$$Fe(OH)_{ads} + H_2O \Longrightarrow Fe(OH)^+ + 1e^-$$

The numerical simulation of the mechanism behavior allowed us to determine the caracteristic kinetic constants which gave a general description of experimental results.

REFERENCES

1. C. Gabrielli, M. Keddam, E. Stupnisek-Lisac and H. Takenouti, Electrochem. Acta, 21, 757 (1976).

2. I. Epelboin, C. Gabrielli and M. Keddam, Corros. Science, 15, 155 (1975).

3. C. Gabrielli, M. Keddam and H. Takenouti, J. Electroanal. Chem., 61, 367 (1975).

4. I. Epelboin and M. Keddam, Electrochem. Acta, 17, 177 (1972).

5. I. Epelboin, C. Gabrielli, M. Keddam and H. Takenouti, Electrochem. Acta, 20, 913 (1975).

6. I. Epelboin, C. Gabrielli, J. C. Lestrade M. Keddam and H. Takenouti, J. Electrochem. Soc., 119, 1632 (1972).

7. J. P. Diard, B. Le Gorrec, C. Montella and E. Saint-Aman, Electrchem. Acta, 27, 1055 (1982).

8. M. Keddam, O. R. Mattos and H. Takenouti, Electrochem. Acta, 24, 103 (1979).

9. J. P. Diard, Thesis, Grenoble ,France (1977).

10. D; Dorro, J. P. Diard, J. Guitton and B. Le Gorrec, J. Electroanal. Chem., 67, 269 (1976).

11. J. P. Diard and M. C. Gandon, Surf. Technol., 10, 349 (1980).

12. E. Saint-Aman, Thesis, Grenoble, France (1983).

13. I. Epelboin, C. Gabrielli and Ph. Morel, Electrochem. Acta, 18, 509 (1973).

14. A. Caprani, Thesis, Paris, France (1974).

15. A. Kerouanton and V. Plichon, C. R. A. Scien., Serie C, 280, 629 (1975).
16. A. Kerouanton, C. Gabrielli, M. Keddam and V. Plichon, J. Electoanal. Chem., 57, 273 (1974).

17. G. Charlot, J. Badoz-Lambling, P. Homsi, V. Plichon, J. P. Saget and A. Kerouanton, J. Electroanal. Chem., 75, 665 (1977).

18. D. Kurrikov Boris and Hurlen Tor, J. Electroanal. Chem., 91, 367 (1978).

19. C. Gabrielli, Thesis, Paris, France (1973).

20. M. Azzi, J. J. Rameau and S. Belcadi, to be published.

21. M. Keddam, J. F. Lizee, C. Pallotta and H.Takenouti, J. Electrochem. Soc., 131, 2016 (1984).

22. M. Dignam, Oxides and Oxides Films, Vol. 1, M. Dekker, N. Y. (1972).

23. Cecilia Montero-Ocampo, Thesis, Grenoble, France (1988).

24. M. Azzi, J. J. Rameau, J. P. Diard and S. Belcadi, to be published.

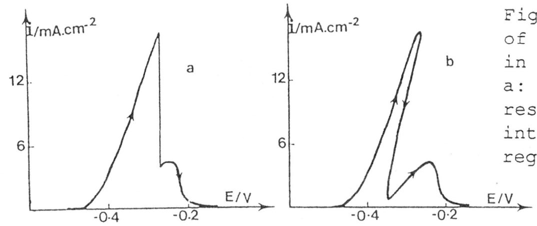

Figure 1. Polarization curve of motionless iron electrode in the melt (v = 1 mV s^{-1}). a: without internal negative resistance regulation. b: with internal negative resistance regulation.

Figure 2. Surface of motionless iron electrode observed by SEM after polarization test.

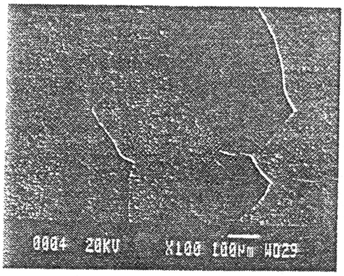

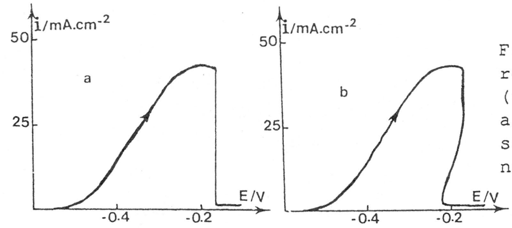

Figure 3. Polarization curve of rotating iron electrode (v = 1 mV s^{-1}, w = 2000 rpm). a: without internal negative resistance regulation. b: with internal negative resistance regulation.

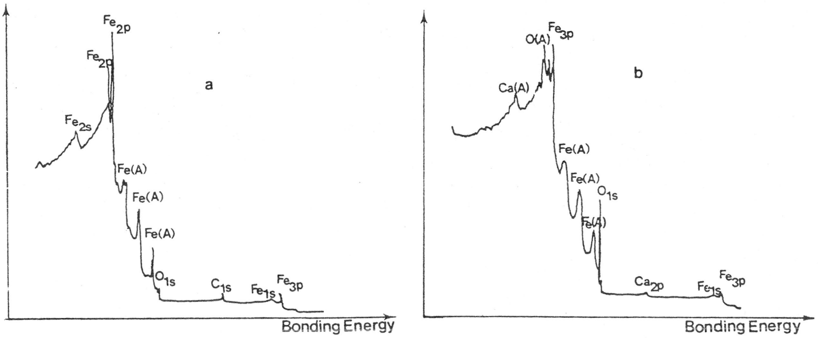

Figure 4. XPS analysis of oxide layer. a: not oxidized iron. b: oxidized iron in the melt.

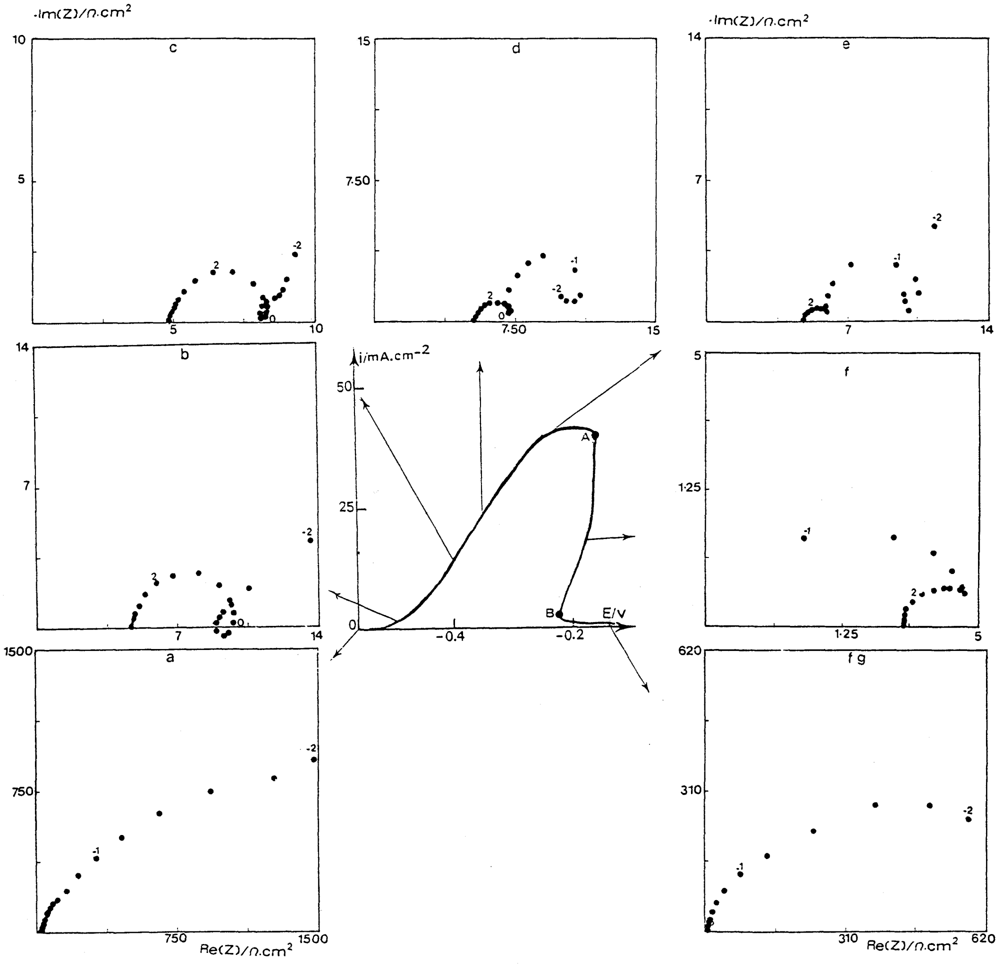

Figure 5. Impedance measurements at different potentials of iron rotating electrode (ω = 2000 rpm). a: E = -0.55 V. b: E = -0.5 V. c: E = -0.4 V. d: E = -0.35 V. e: E = -0.25 V. f: E = -0.15 V. g: E = 0.1 V. logarithmic parameter frequencies.

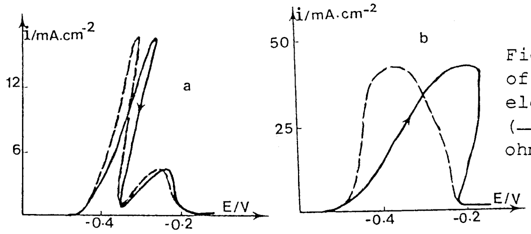

Figure 6. Polarization curve of iron in the melt. a: motionless electrode. b: rotating electrode. (———) as recorded. (---) with ohmic drop correction.

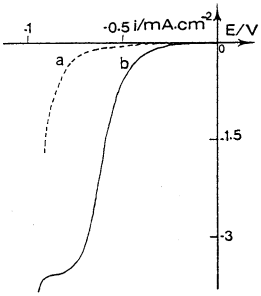

Figure 7. Polarization curve of platinum rotating electrode ($v = 100$ mV.s^{-1}, $w = 2000$ rpm) .
a: in pur2 melt. b: in melt with HNO_3,
$[HNO_3] = 1.06.10^{-2}$ M

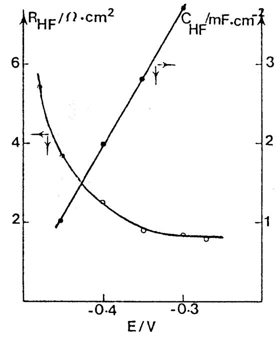

Figure 8. Evolution of R_{HF} and C_{HF} with potential.

Figure 9. Tafel plot of iron electrode polarization curve (ω = 2000 rpm).

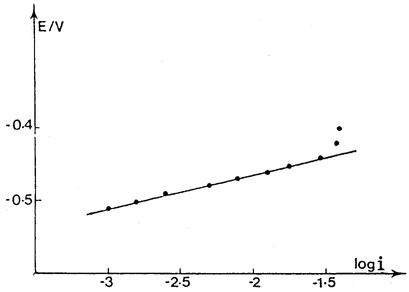

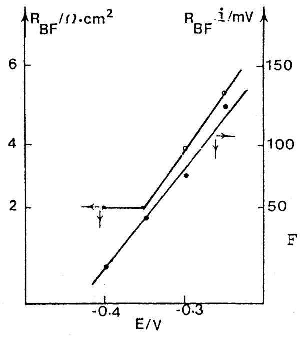

Figure 10. Evolution of R_{BF} and $R_{BF} \star i$ with potential.

DOI: 10.1149/199017.0525PV

ELECTRODEPOSITION OF YTTRIUM METAL IN MOLTEN CHLORIDES

Shuzhen Duan lizhong Zhao

Depatment of Physical Chemistry
University of Science and Technology Beijing
Beijing, 100083, China

ABSTRACT

In this paper, the electrochemical reduction of Y(III) on Mo electrode in LiCl–KCl eutectic in the temperature range of 723–803K has been studied by using cyclic voltammetry and chronoamperometry. The results show that the electroreduction of Y(III) on Mo electrode is a diffusion controlled and very close to reversible process. The reaction equation is Y(III)+3e = Y, and the initial stage of deposition involves instantaneous three dimensional nucleation, followed by the growth of nuclei controlled by diffusion of inos in the melt.

INTRODUCTION

The metal Yttrium as an alloy element is widely used in ferrous based alloy and also in non–ferrous alloy. Nowadays, the methods of producing metal Yttrium are mainly the calsium heat reduction and the combination of molten salt electrolysis of floride system and distillation(1). But the operating temperature for electrolysis is too high, many non–rare elements are carried into the substrate during electrolysising. However, fewer researchers have investigated the technology and the mechanism of how to produce metal Yttrium directly from raw materials by molten salt electrolysis under low temperature. This paper deals with the cathode processing of YCl_3 electrolysis in LiCl–KCl system under 730~ 803K temperature range, so as to provide needed data and parameters for the technological investigation of electrolysis.

EXPERIMENTAL

LiCl and KCl are all of analytical pure. Yttrium chloride is obtained from the reaction of pure Y_2O_3(99.9%) and HCl (of analytical pure). In order to prevent the hydrolysis of YCl_3 during concentration, a little bit of NH_4Cl is added. The dehydration of YCl_3 is obtained by heating it slowly when dry HCl existed(2).

Molybdenum wire of 1.5mm. in diameter is used as the working electrode. Ag / AgCl is used as the reference electrode. The graphite of spectroscopic pure is used as the counter electrode.

RESULTS AND DISCUSSION

The typical cyclic voltammogram (Figure 1.) shows that the Y(III) reduction is with one step to Y under −2.1V at 723K (corresponding to the Ag / AgCl lwt%) and the ratio of reduction current peak potential I_p^c to reoxidation current peak potential I_p^a is less than one. And the reoxidation curve is very sharp, which shows that the nature and shape of voltammogram is typical to that expected for the deposition and reoxidation of an insoluble product. Figure 2. shows the voltammogram is at 803K.

From the cyclic voltammogram at different scanning rates, (Figure 3.) we found the cathodic peak potential slightly moves toward negative potential direction. It means that the elctrochemical reduction reaction of Y(III) is a quasi reversible processing, but it is very close to a reversible processing. By using the following formula(3):

$$E_p^c - E_{p/2}^c = -0.77RT / nF$$

n = 3 can be calculated out, it further proves that Y(Ⅲ)+3e = Y, and Y(Ⅲ) reduction is a simple one step reaction.

Figure 4. shows that the plot of peak current of cathode I with the square root of scanning rate $v^{1/2}$ is linear relation, so the cathodic electrodeposition of Yttrium ion is a diffusion controlled process.

Chronoanperometry (I–t, transients at constant potential) was used to study the nucleation and growth phenomena per se. Figure 5 shows that the typical I–t transient curve obtained on Mo electrode indicates that the transient depends on the applied overpotential. At the beginning the current rises to very high values that is due to double layer charging and initial cluster formation. The current decays during the induction time and then increases again that is because the nucleation and subsequent growth of isolated stable nuclei which increases the area for deposition.

The rising parts of these I–t transient curves, the current I versus the square root of transient time t, (Figure 6.) $(I - t^{1/2})$ shows the expected linear dependency. The result indicates that the initial stage of Yttrium deposition on molybdenum cathode involves the instantaneous three–dimensional nucleation, followed the growth of the nuclei controlled by diffusion of ions in the melt.

CONCLUSIONS

In this paper, the electrochemical reduction of Y(III) on Mo cathode in LiCl–KCl eutectic in the temperature range of 723~803K has been studied by using cyclic voltammetry and chronoamperometry. The results show that the electroreduction of Y(III) on Mo electrode is a diffusion controlled and very close to reversible process. The reaction equation is Y(III)+3e = Y, and the initial stage of deposition involves instantaneous three dimensional nucleation, followed by the growth of nuclei controlled by diffusion of ions in the melt.

ACKNOWLEDGEMENT

The authors acknowledge the support of the work from Baotou Flint Factory and The National Natural Sciences Fundation.

REFERNCES

1.Sohen Singh et.al. J. Electrochem. Soc. India, 22–3 (1973) p.222–226;
2.M.Su and B.Qiu, Acta Metallurgica Sinica, 142 No.2 Vol. 9 1966;
3.S.Duan, P.dudley and D.Inman, J.Electroanal. Chem., 142 (1982) p.215–228;
4.G.J.Hills et al. Electrochem. Acta, 657,19(1974);
5.F.Lantelme et.al.,J.Electroanal. Chem., 121(1981), p.311–327;
6.G.Zao et. al. J. of Beijing University of Iron and Steel Technology, No.1 80(1987).

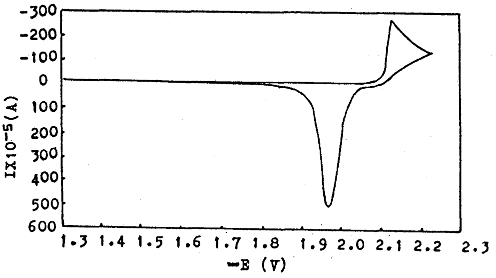

Fig.1. Cyclic voltammogram for the reduction of Y^{3+}ions in LiCl–KCl–YCl_3(3wt%) molten salt, T = 723°K, W.E:Mo, s = 0.018cm^2.

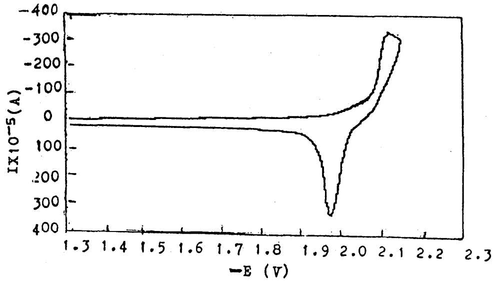

Fig.2. Cyclic voltammogram for the reduction of Y^{3+} ions in LiCl–KCl–YCl_3(3wt%) molten salt, T = 803K, W.E:Mo, s = 0.018cm^2.

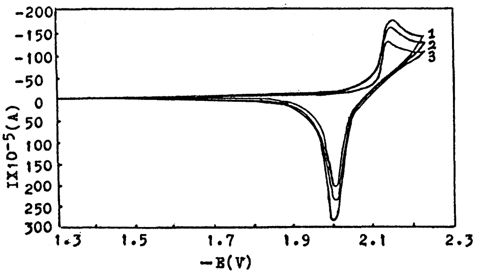

Fig.3. Different sweep rate voltammogram for the reduction of Y^{3+} ions in LiCl–KCl–YCl_3(3w%) molten salt, T = 723°K, W.E:Mo, s = 0.018cm^2. scan rate: $v_1 = 70V/s$, $v_2 = 50mV/s$, $v_3 = 30mV/s$.

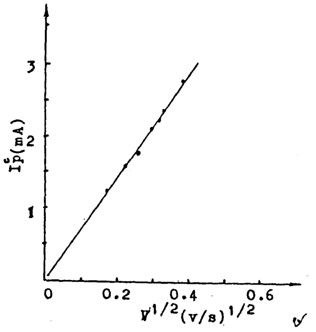

Fig.4. Relation between I_p^c and $V^{1/2}$ T=723°K, W.E.Mo. s=0.018cm^2

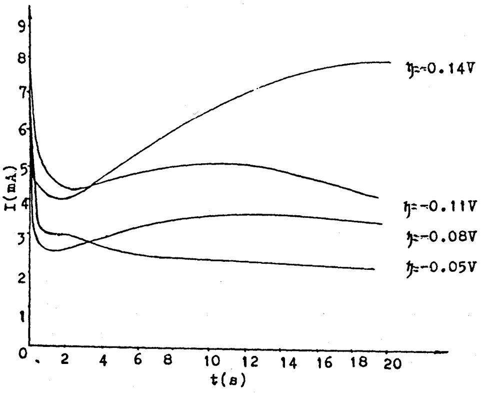

Fig.5. Chronoamperogram for reduction of Y^{3+} ions in LiCl−KCl−YCl_3 (3wt%) molten salt, T=803°K, W.E:Mo, s=0.018cm^2, R.E: Ag−AgCl(X = 0.01), C.E:Gruphite.

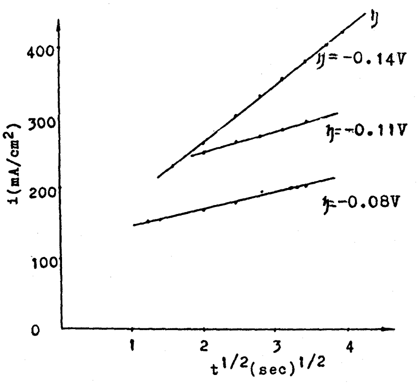

Fig.6. Relation between i and $t^{1/2}$ for the reduction of Y^{3+} ions T=803 K, in LiCl−KCl−YCl_3(3wt%) molten salt, W.E:Mo.

DOI: 10.1149/199017.0530PV

THE ELECTRODE PROCESS OF CHROMIUM IN LiCl–KCl FUSED SALTS

Shuzhen Duan Xingjiang Liu

Department of Physical Chemistry
University of Science and Technology Beijing
Beijing, 100083, China

ABSTRACT

The electrode process of Cr(Ⅱ) has been investigated by means of cyclic voltammetry, chronopotentiometry and ac impedance in molten LiCl–KCl eutectic system. The results show that, Cr(Ⅱ)+2e = Cr is a simple electrochemical reaction, close to reversible process. Under weak polarization conditions, the reaction is controlled by charge transfer and ion diffusion in the melt,but at stronger polarization conditions the reaction is controlled by ion diffusion completely. The diffusion coefficients of Cr(Ⅱ) have been calculated.

INTRODUCTION

The chromium electroplating in molten salt has its specific advantages(1,2), but there is also its prominent difficulty(3). One is needed to understand the Cr(Ⅱ) electrode processing before performing electroplating. Dr. Inman et.al(4). showed that the reaction of Cr(Ⅲ)+e→Cr(Ⅱ); Cr(Ⅱ)+2e→Cr(0) of which the first step is the diffusion control, while the second step is the absorption control which is an irreversible reaction. Duan et.al. have investigated it by means of voltammetry and chronoamperometry. They consider the reaction of Cr(Ⅱ)+2e→Cr(0) is a diffusion controlled processing and a reversible one. This paper further deals with the investigation of the reaction of Cr(Ⅱ)+2e→Cr(0) by using the method of cyclic voltammetry, chronopotentiometry and AC impedance techniques.

EXPERIMENTAL

The electrochemical bath is made of Pyrex, the working electrode is of platinum plate. The counter elctrode is a graphite rod of spectroscopic pure. The reference electrode is an 0.5M AgCl / Ag electrode. LiCl, KCl, $CrCl_2$ are all of analytical pure. LiCl–KCl eutectic salt is stricktly purified before using and is checked by the residue current of the cyclic voltammetry. The concentration for Cr(Ⅱ) is 0.057M—0.22M and the temperature range is 720～823K. The scanning rate is 0.04V—1V / s for the cyclic voltammetry. The density of the current is $25mA/cm^2 < i < 100mA/cm^2$, for the chronopotentiometry. The fluctuation of alternating current $E_{AC} = 5mV$ is for the AC impedance method.

RESULTS AND DISCUSSION

Figure 1. The typical cyclic voltammogram. Figure 2. The cyclic voltammogram in different scanning rate showed that there is no evident absorption and pre–reaction at the reduction peak. The peak current with the square root of scanning rates $I_p^c - - V^{1/2}$ (Figure 3.) shows a straight line passing through the origin, which satisfies the Randle–Sevick equation. It also indicates that the reduction process of Cr(Ⅱ) is diffusion controlled, and when increasing the scanning rate the reduction peak E_p^c slightly moves towards the negative direction. Therefore it is allowed to consider that the reduction reaction of Cr(Ⅱ) is close to a reversible processing.

Figure 4. The typical potential–time curve is obtained by using chronopotentiometry method(5) and Figure 5, the chronopatentiogramm, in increasing the applied current when plot the $I\tau^{1/2}$ with I, a straight line is obtained which parallel to the X–axis, as shown in Figure 6. Which shows the $I\tau^{1/2}$ is independent with I and is a constant. It also indicates that Cr(Ⅱ)+2e = Cr is a diffusion controlled simple electrochemical reaction and the plot of $E \sim \ln(\tau^{1/2} - t^{1/2}) / \tau^{1/2}$ is a straight line (Figure 7.). Means that the Cr(Ⅱ) reduction reaction should be a reversible electrochemical reaction and the product is insoluble.

By the Sand equation, the coeffients of diffusion of Cr(Ⅱ) can be calculated out as follow:

T = 743K	$D = 6.93 \times 10^{-6} cm^2 / s$
T = 778K	$D = 1.17 \times 10^{-5} cm^2 / s$
T = 798K	$D = 1.27 \times 10^{-5} cm^2 / s$
T = 813K	$D = 1.49 \times 10^{-5} cm^2 / s$

The diffusion activity energy can also be found out. E = 54 kJ / Mole.

When the ac impedance method(6) is used under near equilibrium potential position of the Cr(Ⅱ) reduction, the impedance curve (Figure 8.) shows that the Cr(Ⅱ) reduction is charge transfer and diffusion combined control, but under polarization conditions the impedance curve (Figure 9.) shows it is a diffusion controlled process. The exchange current density i_0 is calculated, $i_0 = 3.6 \times 10^{-3} / cm^2$, this value shows it approaches the high speed electrochemical reaction. Hence it is allowed to consider the Cr(Ⅱ) reduction reaction is a reversible or close to a reversible electrochemical reaction.

CONCLUSION

The electrode process of Cr(Ⅱ) has been investigated by means of voltammetry, chronopotentiometry and AC impedance in molten LiCl–KCl eutectic system. The results show that, Cr(Ⅱ)+2e→Cr is a simple electrochemical reaction, and is a non–absorption and prechemical reaction which approaches a reversible electrochemical reaction, the product is insoluble. Under polarization conditions, the reaction is controlled by ion diffusion completely. The diffusion coefficients and diffusion activity energy of Cr(Ⅱ) at different temperatures can be calculated out from the Sand equation.

REFERENCES

1.S.Duan, D.Inman and J.A.Sheward, U.K.Patent GB 2193508A 10 Feb. 1988;
2.S.Duan, Proc. of the Second Japan–China Bilateral conference on Molten Salt Chemistry and Technology, Japan 1988;
3.S.Duan ad G.Zhao Rare Metal Vol. 11 No.5 1987;
4.D.Inman, J.C.Legey and R.Spencer, J. Electroanal. Chem. Interfac. Electrochem., 61289 (1975);
5.T.Berzins and P.Delahay, J.Am. Chem. Soc. 75 4025 (1953);
6.S.Tian, Electrochemical Research Method, Press of Science, China 1984.

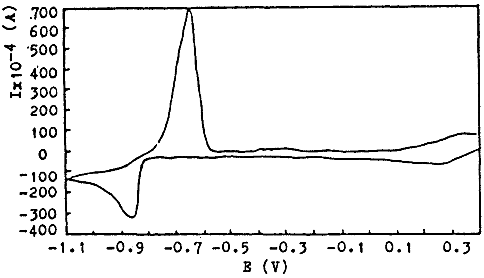

Fig.1. Cyclic voltammogram for the reduction of Cr(II) ions in LiCl–KCl–$CrCl_2$ (0.095M) molten salt, T=743°K, scan rate=500mV / s, W.E: Pt, S=$0.43cm^2$.

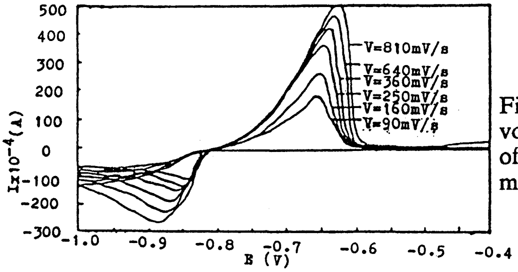

Fig.2. Different sweep rate cyclic voltammogram for the reduction of Cr(II) in LiCl–KCl–$CrCl_2$ molten salt

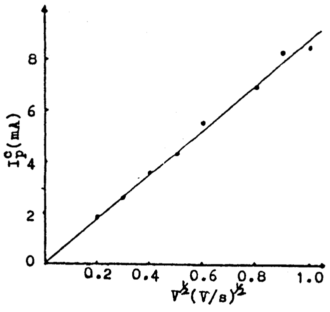

Fig.3. Relation between I_p^c and $V^{1/2}$.

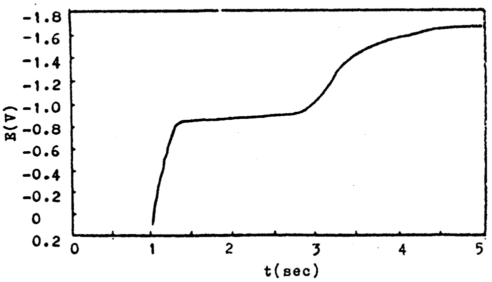

Fig.4. Chronopotentiogram for the rduction of Cr(II) ions, I=−4mA, (C)=0.089M, T=743°K, s=0.23cm^2, t=5s.

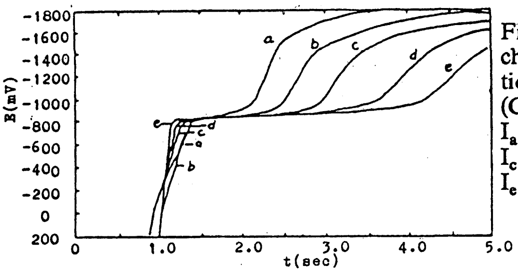

Fig.5. Different applied current chronopotentiogram for the reduction of Cr(II) ions, t=743°K, (C)=0.089M, s=0.23cm^2, I_a=−5.5mA, I_b=−4.5mA, I_c=−4.3mA, I_d=−3.5mA, I_e=−3.0mA

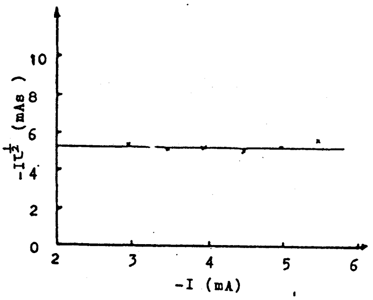

Fig.6. Relation between $I\tau^{1/2}$ and I.

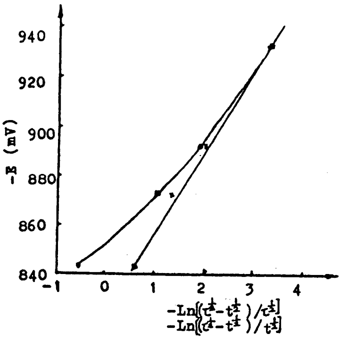

Fig.7. × Relation between E and $Ln((\tau^{1/2}-t^{1/2})/\tau^{1/2})$
• Relation between E and $Ln((\tau^{1/2}-t^{1/2})/t^{1/2})$

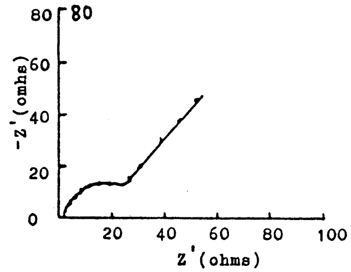

Fig.8. AC impedance studies of Cr(Ⅱ) ions under equilibrium potential conditions, T=813°K, W.E:Pt s=0.30cm^2, (c)=0.057M, f=0.01~ 1000KHz, Edc=−840mV.

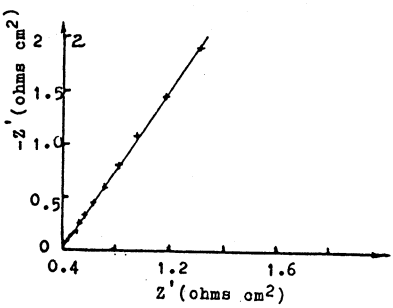

Fig.9. Ac impedance studies of Cr(Ⅱ) ions underpolarization conditions, T=723°K, (C)=0.11M, Edc=−850mV, W.E:Pt, R.E: Ag–AgCl(0.01M), f=5Hz~ 1000KHz.

DOI: 10.1149/199017.0536PV

THERMOCHEMISTRY AND MODELS OF IONIC AND NON-IONIC MELTS

Marcelle Gaune-Escard

SETT, UA 1168, Université de Provence,
Centre de St Jérôme, Av. Escadrille Normandie Niemen
13397 Marseille Cédex 13 (France).

ABSTRACT

Most molten salt industrial processes , for instance electrolytic elaboration of metals from melts, involve compromise between several parameters to be optimized.

Thermodynamic properties play an important role and the choice both of suitable electrolyte and molten salts to be electrolyzed is directely related to the operation temperature and to the "average valency" of the electrolytic bath.

Experimental thermochemical investigations conducted by high temperature calorimetry, differential enthalpic analysis, differential scanning calorimetry can provide information on phase equilibria in the melt. From a theoretical point of view, the molten salt mixtures considered in those investigations are not simple since they involve i) ions with different valency, ii) ionic and non-ionic components and iii) several components. Classical models used for the most simple molten salt mixtures cannot be used and suitable modelling involving complex species, should be developed.

INTRODUCTION

For years the chemical industry has recognized the importance of the thermodynamic and physical properties of solution in design calculations involving chemical separations, fluid flow and heat transfer. The development of techniques has enabled the experimental investigation of melts with convenience and accuracy. But even with modern instrumentation, experimental measurement of thermodynamic properties has become progressively more expensive and time-consuming with each additional component beyond binary mixtures. In the chemical literature, properties for binary systems are relatively abundant, properties for ternary systems are scarce and properties for higher order multicomponent systems are virtually nonexistent. Naturally, one of the primary goals of research in the area of solution thermodynamics has been the development of expressions for predicting the thermodynamic properties of multicomponent mixtures.

1. EXAMPLE OF APPLICATION

Most molten salt industrial processes , e.g. electrolytic elaboration of metals from melts, involve compromise between several parameters to be optimized. Electrolysis has many advantages over conventional pyrometallurgical processes employing metallic reducing agents (C, Si, ..) :

- it is selective since potential, electrode overvoltages and valency state (complexing) of the electrolyte can be adjusted.
- it allows elements either very electropositive or very electronegative to be obtained
- it is a quasi-continuous process and can be easily automated.

These advantages outweigh some drawbacks such as high capital and operation costs related to energy use (electricity), limitation of productivity by current density.

As a result, the design and engineering of an electrolytic process rises a number of technological challenges for the cell itself but also for the electrolyte and the salt to be electrolysed:

ELECTROLYTE	SALT
- Phase diagram	- solubility
- stability/hygroscopy	- stability/hygroscopy
- vapor pressure	- vapor pressure
- complexing ability	- etc...
- viscosity	
- conductivity	
- etc...	

Thermodynamic properties play an important role and the choice of a suitable molten salt solvent is directely related to the operation temperature and also to the "average valency" of the electrolytic bath. For the elaboration of niobium, for instance, from $NbCl_5$ (m.p. 478 K, b.p. 520 K) the choice of a chloride melt as a a solvent induces appreciable losses by evaporation (eutectic chloride mixtures generally melt at temperatures higher than 650 K). The problem is therefore to find a suitable solvent including anionic species, like F^-, corresponding to a higher stability of the niobium species in the melt.

Another example is the production of rare eath metals. Neodymium, for instance, is used for the fabrication of magnets ; alloys of neodymium can be obtained either by reduction with calcium or by electrolysis. In the electrolytic process a compromise had to be found between the following features :

- in molten chloride baths, a poor current efficiency is obtained because of the two coexisting valence states (II and III). Adding fluorides to the bath results in a stabilization of the III valence but also induces formation of neodymium oxychlorides and related operating problems.
- in molten fluoride melts, electrolysis of NdF_3 is easier but costs are higher ; electrolysis of oxides would not pose any problem of anodic reaction but is not promoted by the low solubility.

Nevertheless a compromise had been found and a process successfully developed [1] : a derivative of the industrial product, hydrated neodymium carbonate, is dissolved and electrolysed in a mixture of molten fluorides at 900°C.

Refining of elements is also an important application in the molten salt area, e.g. aluminium electrorefining by the "3-layer" Gadeau process which is a sequential refining employing more than one electrolyte [2] . This process uses chloride/fluoride melts, which involve lower energy consumption than required for fluoride-only melts and of adjustable complexing ability with respect to the impurities to be removed.

Experimental thermochemical investigations conducted by high temperature calorimetry, differential enthalpic analysis, differential scanning calorimetry can provide information on phase equilibria in the melt.
From a theoretical point of view, the molten salt mixtures considered in those investigations are not simple since they involve i) ions with different valency, ii) ionic and non-ionic components and iii) several components. Classical models used for the most simple molten salts mixtures cannot be used so far and a suitable modeling involving complex species, should be developed.

2. MODELING OF HIGH TEMPERATURE MELTS

The main problem when modeling is to account for the actual nature of the solution. In most actual cases, the melts involved are multicomponent systems; complete experimental studies are time-consuming and/or cannot be performed on the entire composition range .The strategy generally adopted to obtain the thermodynamics of such systems is :

- either purely estimative : *a priori* prediction from the properties of lower order systems (components and binary limiting systems).
- or "estimation-assisted" experimental : a restricted number of selected experiments is decided from the *a priori* estimations.

Suitable models should be used both for binary mixtures and multicomponent systems; of course, they have to take into account the nature of the species present in the melt and the magnitude of the interactions between these species.
A considerable amount of experimental thermodynamic investigations made evident that all melts do not behave identically and , therefore, also evident that specific thermodynamic models should be developed and used to describe their features[3] .

Though any classification usually is somewhat arbitrary, for the sake of clarity it will be distinguished between simple melts and complex melts in the following Simple mets are those molten salt mixtures in which no new species arise from the mixing of components. By opposition, complex melts include formation of new species (complexes) which did not exist in the constituting salts..

Two distinct types of molten salt solutions can be defined according to the nature and the number of involved components. These *additive* and *reciprocal* systems parallel two distinct types of metallic systems, *substitutional* alloys and *interstitial* alloys .Taking into account the nature of these different mixtures, appropriate relationships have been proposed for the ideal entropy of mixing. These are of primary importance to measure the deviation from ideality of the other functions of mixing.

Another distinction among ionic melts lies in the possibly different valencies of the ions involved.

Also those solutions obtained from at least one covalent salt have different features, generally characterized by the formation of complex species (e.g. $AlCl_4^-$, $Al_2Cl_7^{2-}$, ...in the aluminum chloride-based mixtures).

3. SIMPLE MELTS

3. 1.Binary mixtures

3. 1. 1. symmetrical mixtures

Common-ion molten salt symmetrical mixtures (AX+BX or AX_2+BX_2) are often described by quasi-lattice models, the main distinction lying in the interaction range of the species of the same nature, cations A^+ and B^+.

For an ideal solution, the energetic interactions of A^+ and B^+ with their environments are the same and these species mix randomly . Then the molar free energy of mixing is $-T\Delta S_{mix}$ and

$$\Delta S_{id}^{mix} = - R\,[x_A \ln x_A + x_B \ln x_B] \tag{1}$$

where n_A , n_B are the number of moles of atoms (or ions) in the mixture and the x's are the molar (or ionic) fractions defined as :

$$x_A = n_A/(n_A+n_B) \qquad \text{and} \qquad x_B = n_B\,/(\,n_A+n_B) \tag{2}$$

For molten salt mixtures, this relationship was proposed by Temkin [4] for the ideal entropy of mixing and the x_i's are the so-called (Temkin) ionic fractions.

Deviations from ideality ($\Delta G^{ex} \neq 0$, $\gamma_i \neq 1$) arise from a lack of balance in the interionic forces between the different species. If the components are similar in chemical nature (e.g., sodium chloride + potassium chloride), the mixture is nearly ideal. If they differ, the forces are usually greater between the cations .
For those melts exhibiting small deviations from ideality, e.g. weak interactions, in principle any simple model, based on a pair-wise interaction concept, can be used (regular or quasi-regular models).

The Surrounded Ion Model (SIM) [5] [6] [7] , which is a statistical model, gives a more realistic description of a melt since it takes into account all the possible energetic interactions of A^+ and B^+, depending on the local environment of each ion.The ideal entropy of mixing is given by a relationship identical to (1).The most interesting feature of this model lie in the fact that it is able to account for the asymmetry of the thermodynamic excess functions with only two energetic parameters having a physical meaning. The previous models based on a pair-wise interaction concept, generally failed in the description of such asymmetries which are observed experimentally.At this stage most authors arbitrarily assumed a linear dependance of the "interaction parameter" against composition (Hardy's [8] quasi-regular model) or used polynomial expansions whose parameters have no physical meaning. Also the more elaborated Guggenheim's "quasichemical model" [9] , though able to account for the temperature dependence of the thermodynamic excess functions, failed in describing experimental asymmetries.The SIM is generalization of the above binary models and has also been extended to other kinds of molten salt mixtures.

3. 1. 2. Asymmetrical mixtures

In asymmetrical molten salt mixtures of the type *AX_2 + BX,* the same lattice description of the melt implies that the substitution to the A^{++} divalent cation of the B^{+} monovalent cation creates one vacancy on the corresponding sublattice.Several relationships have been proposed for the ideal entropy[10] [11] ; they differ in the assumptions made on the vacancies.
The S.I.M.[12] [13] provides, from different theoretical grounds, a relationship for the ideal entropy which is identical to the one by Førland [10] :

$$\Delta S_{id}^{mix} = - R[\, 2x_A \ln x_A' + (1-x_A) \ln (1-x_A')] \tag{3}$$

where

$$x_A = n_A / (n_A + n_B) \quad \text{and} \quad x_A' = 2n_A / (2n_A + n_B) \tag{4}$$

The x_i's have been defined previously and the x_i''s are the so-called equivalent ionic fractions.
It should be stressed that many authors do not take into account this charge-dependent expression for the ideal entropy of mixing but arbitrarily use the *equivalent ionic fractions* defined by Førland [10] in the relationships expressing the other functions of mixing and Temkin's ideal entropy (1). It has been shown[14] that this may lead to some inconsistencies .

3. 2. Ternary mixtures

Models have been developed to permit the properties of common-ion and reciprocal ternary molten salt systems to be calculated from the binary coefficients. Empirical ternary coefficients may also be included in these equations.

3. 2. 1. Additive ternary mixtures

It is common to predict the properties of a ternary solution phase by a simple summation of the binary expressions, when they obey the regular solution model. Several "geometric" models have proposed which differ in the geometric weighting factors of the binary contributions. The binary models provide reasonable estimates for several systems of practical importance and they also address the problem of how to report experimental data.

This paragraph will be devoted to several of the empirical equations or models that have been suggested for parametrizing and predicting mixture data.
Redlich and Kister [15] proposed an expression for the excess Gibbs free energy of mixing of a ternary mixture

$$\Delta G^{ex} = x_1x_2 \sum (G_n^{ex})_{12} (x_1 - x_2)^n + x_1x_3 \sum (G_n^{ex})_{13} (x_1 - x_3)^n$$
$$+ x_2x_3 \sum (G_n^{ex})_{23} (x_2 - x_3)^n \tag{5}$$

which provisions for additional ternary parameters.

Kohler [16] proposed an equation for the excess Gibbs free energy of mixing of a ternary solution

$$\Delta G^{ex} = (x_1 + x_2)^2 \ \Delta G_{12}{}^{ex} + (x_1 + x_3)^2 \ \Delta G_{13}{}^{ex} + (x_2 + x_3)^2 \ \Delta G_{23}{}^{ex} \qquad (6)$$

in which $\Delta G_{ij}{}^{ex}$ refers to the excess Gibbs free energies of the binary mixtures at a composition (x^0_i , x^0_j) such that $x^0_i = 1 - x^0_j = x_i / (x_i + x_j)$.
Kohler's equation is symmetrical in that all three binary systems are treated identically. Its numerical predictions do not depend on the arbitrary designation of component numbering.

Colinet [17] established a slightly more complex relationship for expressing the thermodynamic excess properties of multicomponent systems

$$\Delta G^{ex} = \sum\sum x_i \,(1 - x_j)^{-1} \left[\Delta G_{ij}^{ex} \right]_{x_j} \qquad (7)$$

in which $\{\Delta G^{ex}_{ij}\}x_j$'s are calculated from the binary data at constant mole fraction x_j. This equation, although perfectly symmetrical, requires the addition of the thermodynamic properties at six different binary compositions for a ternary mixture.

Muggianu [18] also developed a geometric model with different weightings of the binary contributions :

$$\Delta G^{ex} = \sum\sum x_i \,(1 - x_j)^{-1} \left[\Delta G_{ij}^{ex} \right]_{x_1 ;\, x_2} \qquad (8)$$

So far all the three methods that have been discussed treat the components in the same way and may thus be characterized as symmetric methods.
Other asymmetric "geometric" numerical methods have been proposed by Toop[19] and Hillert[20] .
Very recently, Z.C. Wang et al.[21] reviewed nine regular-type ternary models models with different weight factors and proposed a new generalized model. The analytical expression of this general model may be given by :

$$W^E_{ABC}\,(x_A, x_B, x_C) = \sum_i \sum_j \sum_{l_{ij}} \beta_{ij}^{(l_{ij})} \frac{x_i\, x_j}{x_{i(ij)}^{(l_{ij})}\, x_{j(ij)}^{(l_{ij})}} \, W^E_{ij} \left(x_{i(ij)}^{(l_{ij})} , x_{j(ij)}^{(l_{ij})} \right) \qquad (9)$$

where $i = A$ $j = B$ $k = C$
$i = B$ $j = C$ $k = A$
or $i = C$ $j = A$ $k = B$

$l_{ij} = 1, 2, \ldots, l'_{ij}$; x_i and $W^E_{ABC}\,(x_A, x_B, x_C)$ are respectively the mole fractions of component *i* in the A-B-C ternary system and the ternary excess molar free energy or excess molar enthalpy ;
$x_{i(ij)}^{(l_{ij})}$ and $W^E_{ij}\left(x_{i(ij)}^{(l_{ij})}, x_{j(ij)}^{(l_{ij})}\right)$ are the corresponding binary properties at the l_{ij}th

point along the *i-j* binary comosition line . Here :

$$x_{i(ij)}^{(l_{ij})} = 1 - x_{j(ij)}^{(l_{ij})} = \frac{1 + x_i + x_j + \lambda_{ij}^{(l_{ij})} x_k}{2}$$

The weight factors of $\lambda_{ij}^{(l_{ij})}$ still depend on the regular solution assumption, while those of β_{ij} are independant from it and only follow the conditions $0 \leq \beta_{ij} \leq 1 \quad \sum \beta_{ij}^{l_{ij}} = 1$

This proliferation of similar expressions becomes confusing especially when the equations are encountered for the first time. There is no preferred way of knowing which method will provide the best predictions for a given system. The fact that so many empirical equations have been developed suggests that no single equation can describe all types of systems encountered.

Differing from the previous empirical equations in that they are based on a physical description of the melt and on statistical mechanics principles, some models also provide expressions able to predict multicomponent properties in terms of lower-order interactions.

The Surrounded Ion Model (SIM) [22] [23] yields an equation for the excess enthalpy of mixing of the symmetrical ternary mixture AX-BX-CX (or AX_2- BX_2-CX_2) :

$$\begin{aligned} \Delta H &= x_A x_B \{ x_A \Delta H_{B(A)} + (1 - x_A) \Delta H_{A(B)} \} \\ &+ x_A x_C \{ x_A \Delta H_{C(A)} + (1 - x_A) \Delta H_{A(C)} \} \\ &+ x_B x_C \{ x_C \Delta H_{B(C)} + (1 - x_C) \Delta H_{C(B)} \} \end{aligned} \tag{10}$$

where $\Delta H_{A(B)}$ is the limiting partial enthalpy of AX in the AX-BX binary mixture and the ideal Gibbs energy of mixing is always

$$\Delta G^{mix}_{id} = RT \{ x_A \ln x_A + x_B \ln x_B + x_C \ln x_C \}$$

For additive assymetrical ternary mixtures *(AX_2 + BX+ CX),* Equation (10) becomes :

$$\begin{aligned} \frac{\Delta H}{1 + x_A} = x'_A x'_B &\left\{ x'_B \frac{\Delta H}{2} A\,(B) + (1 - x'_B)\, \Delta H\, B(A) \right\} \\ x'_A x'_C &\left\{ x'_C \Delta H\, B\,(C) + (1 - x'_C)\, \Delta H\, C\,(B) \right\} \\ x'_C x'_A &\left\{ x_A \Delta H\, C\,(A) + (1 - x'_A)\, \Delta H\, A\,(C) \right\} \end{aligned} \tag{11}$$

with $x'_A = \frac{2x_A}{1 + x_A}$; $x'_B = \frac{x_B}{1 + x_A}$; $x'_C = \frac{x_C}{1 + x_A}$;

The Conformal Ionic Solution model [24] also gives a relationship for the excess enthalpy of mixing of a ternary solution :

$$\Delta H = \sum\sum a_{ij}\, x_i\, x_j + \sum\sum b_{ij}\, x_i^2\, x_j + \sum\sum c_{ij}\, x_i^2\, x_j^2 + P\, x_A\, x_B\, x_C + \sum\sum Q_i\, x_i^2\, x_j\, x_k \quad (12)$$

The coefficients a_{ij}, b_{ij} and c_{ij} are evaluated from data on the three binary subsystems. The coefficients P and Q_i of the "ternary" terms being calculated from the binary data .

Very recently, Hoch and Arpshofen developped a model which is applicable to binary, ternary and larger systems [25] [26] .It was derived originally by looking at the complexes in the solution, and the A-B bond strength (between species A and B) made dependent on the presence of other atoms in the complex.The model was applied to metal-salt [27] , metal-metal oxide[28] [29] , silicate[30] [31] , metallic systems[32] and ZrF_4-based fluoride mixtures[33] . For a binary system the basic equation for the enthalpy of mixing is :

$$\Delta H = W\, n\, (x - x^n) \quad (13)$$

The term n is an integer (2, 3, 4, etc..), W is the interaction parameter and x is the mole fraction of the component so that the maximum of ΔH (either positive or negative) is at $x > 0.5$. The quantity n is chosen such that W, determined from thermodynamic data, is independent of the composition.

The signs of the limiting partial enthalpies obtained from equation (13) are determined by W. In other words one interaction parameter describes one type of interaction or reaction in a system. If two reactions exist in the binary system such as the MgO-SiO_2 [34] , where a strong compound- forming tendancy exists on the magnesium-rich side (Mg_2-SiO_4) and a miscibility gap exists on the SiO_2-rich side, then two interaction parameters, an attractive W and repulsive M, are needed.Each has its major effect at different compositions with different dependency on composition (n and x in one case, m and y and the other) . Thus

$$\Delta H = W\, n\, (x - x^n) + M\, m\, (y - y^m) \quad (14)$$

W and M are determined by least square analysis; confidence limit and error in W and M are also calculated .
This model was extended to ternary or larger system by evaluating the effect of each limiting binary system in the multicomponent mixture.

3. 2. 2. Reciprocal mixtures

The A^+, $B^+ // X^-$, Y^- reciprocal mixture is also a ternary mixture ; there are four constituent salts, (AX, BX, AY, BY), but only three of them can be chosen as independent components.

The free energy of mixing of such systems was first deduced by Flood, Førland, and Grjotheim [35] .

$$
\begin{aligned}
\Delta G^{mix} \quad &= RT\,\{x_A \ln x_A + x_B \ln x_B + x_X \ln x_X + x_Y \ln x_Y\} \\
&\pm x_i x_j\, \Delta G^0 \qquad (15)
\end{aligned}
$$

where ΔG^0 is the standard free energy change for the metathetical reaction
$AX + BY <=> AY + BX$ (16)
and where *ij* is the salt which is not a component. This last term expresses the idea that the three components, in effect, "react" to form the last constituent. The + sign is for the case when ij is AY or BX and the - sign is for AX or BY. Everything beyond the last term given in Eq. (15) is the same no matter how the solution was made up.
Førland [36] improved the original FFG theory by including four binary interaction terms in (15)

$$
\begin{aligned}
\Delta G^{mix} \quad &= RT\,\{x_A \ln x_A + x_B \ln x_B + x_X \ln x_X + x_Y \ln x_Y\} \pm x_i x_j\, \Delta G^0 \\
&+ x_A x_B x_X \lambda_X + x_A x_B x_y \lambda_y + x_x x_y x_A \lambda_A + x_x x_y x_B \lambda_B \qquad (17)
\end{aligned}
$$

with λ_i the interaction parameter in the *i* common ion binary mixture.
Later, Blander and Yosim [26] generalized the Conformal Ionic Solution theory [37] [38] which has been applied to binary molten salt mixtures by Reiss, Katz and Kleppa [39] They found for the free energy of mixing a relationship identical to (17) and added a nonrandom term to this equation ; this correction term was only taken by analogy with the one obtained from the quasi-lattice theory[40] developped for binary mixtures.

$$
\begin{aligned}
\Delta G^{mix} \quad &= RT\,\{x_A \ln x_A + x_B \ln x_B + x_X \ln x_X + x_Y \ln x_Y\} \pm x_i x_j\, \Delta G^0 \\
&+ x_A x_B x_X\, \lambda_X + x_A x_B x_y\, \lambda_y + x_x x_y x_A\, \lambda_A + x_x x_y x_B\, \lambda_B \\
&+ x_A x_B x_X x_Y\, \Lambda \qquad (18)
\end{aligned}
$$

with $\Lambda = - (-\Delta G^0)^2 / zRT$ and z the cation-anion coordination number.

The Surrounded Ion Model (SIM) was also applied to ternary reciprocal mixtures [41] [42] .The equation found for the Gibbs free energy of mixing is :

$$
\begin{aligned}
\Delta G^{mix} \quad &= RT\,\{x_A \ln x_A + x_B \ln x_B + x_X \ln x_X + x_Y \ln x_Y\} \pm x_i x_j\, \Delta G^0 \\
&+ x_A\, \Delta G^{ex}{}_A + x_B\, \Delta G^{ex}{}_B + x_X\, \Delta G^{ex}{}_X + x_Y\, \Delta G^{ex}{}_Y \\
&+ x_A x_B x_X x_Y\, \Lambda \qquad (19)
\end{aligned}
$$

with $\Delta G^{ex}{}_i$ the excess free energy of mixing in the *i* common ion binary mixture, $\Lambda = - (-\Delta G^0)^2 / 2\,zRT$ and z the cation-anion coordination number.

It should be stressed that Eq.(19) is able to take into account experimental assymetries in binary systems and contains the non-random term Λ which has been calculated, and not estimated by formal analogy, as previously.

The Surrounded Ion Model has also been extended to quaternary reciprocal molten salt solutions [43] and to.asymmetrical ternary reciprocal mixtures (A^{2+},B^{+}//X^{-}, Y^{-})[44] .

4. COMPLEX MELTS

Under this category we have classified those mixtures in which the mixing process gives rise to species different from those in the pure components. For instance, the molten salt mixtures made from a ionic salt and of a covalent salt. Mixtures obtained from alkali halides AX (e.g. fully ionic salts) and transition, rare-earth, actinide, ..., metal halides M_iX_j (e.g. covalent salts), are examples of such melts, generally characterized by the formation of heterogeneous ionic complexes such as $AlCl_4^-$ and $Al_2Cl_7^{2-}$, etc..

Very few exists on the thermodynamics of such systems.The reason is two-fold : because of the very different physical and chemical properties of the components , experimental investigations of the mixture are not easy and, similarly, also the theoretical approaches are not simple.Some advances are being made for systems containing alkali halides and halides of aluminum, rare earth, niobium, tantalum, bismuth, zirconium and also for the very novel low melting systems containing aluminum chloride and organic chlorides. Most of these investigations are related to industrial interests and are parts of national research programs in France, China, Germany, India, Norway, Poland, USA .The applications fields are mainly the production of the metals from electrolysis of the melts, fabrication of halide glasses for optical fibers, elaboration of new materials...

A proper description of such melts can be given by models based on "associated solution" concepts. Very similar models have been developed, recently and independently, in Marseille [45] and in Trondheim [46] which are equally successful in describing the thermodynamics of $BiCl_3$- and $AlCl_3$-based mixtures.

The existence of complexes in molten salt mixtures has been the subject of lively discussions in the molten salt community [47] . The development of investigation methods of structure brought new arguments to the controversy and provided bases for the stuctural description of melts. The complexes contribute to the entropy of the mixture and should be taken into account when modeling the solution.

We recently have proposed an ideal associated model to describe the mixtures of alkali chlorides with bismuth chloride [45] or the mixtures of alkali fluorides with zirconium fluoride [48] . The excess thermodynamic quantities of the melt are assumed to only arise from the formation of complex ionic species. For the ZrF_4-based mixtures, for instance, the enthalpies and the constants of formation refer to the reactions :

$$(M)^+ (F)^- + ZrF_4 = (M)^+ (ZrF_5)^- \qquad : (h_1, K_1) \qquad (20)$$

$$3(M)^+ 3(F^-) + ZrF_4 = (3M)^{3+} (ZrF_7)^{3-} \qquad : (h_2. K_2) \qquad (21)$$

and the enthalpy of mixing is obtained as :

$$\Delta H = \frac{\overset{*}{n_4}}{(n_1 + n_3)} h_1 + \frac{\overset{*}{n_5}}{(n_1 + n_3)} h_2 \qquad (22)$$

$$\Delta H = x^*(1 - x^*) \frac{K_1 h_1 + K_2 h_2 x^{*2}}{1 + K_1 x^* (2 - x^*) + K_2 x^{*3} (4 - 3x^*)} \qquad (23)$$

with x = x(MF) :

$$x = x^* \frac{\left[1 + K_1 + K_2 x^{*2} (3 - 2x^*)\right]}{\left[1 + K_1 x^* (2 - \overset{*}{x_3}) + K_2 x^{*3} (4 - 3x^*)\right]} \qquad (24)$$

The four parameters K_1, K_2, h_1 and h_2 are obtained by numerical calculation. From the experimental enthalpy data it is possible to evaluate two approximative values for h_1 and h_2 ; they are used as the initial parameters h_{10} and h_{20} in the iterative procedure. Two arbitrary values are set for the initial parameters K_{10} and K_{20}.
For each experimental data set [x, ΔH(x)] , the programme solves equation (24) and calculates the solutions x^*.
A non-linear regression programme, applied to equation (23), yield optimized values of the parameters h_{11}, h_{21}, K_{11} and K_{21} . If these values differ from the initial values, the programme iterates with h_{11}, h_{21}, K_{11} and K_{21} as initial values. Convergence is attained after a few iterations.

CONCLUSION

Suitable modeling of high temperature melts has a crucial importance in the present context of thermochemical databanks and information systems. A few groups have developed such services which are currently used by scientists but also by industrial engineers. The service provided is firstthe access to all the data relative to a system but also the assessment of these data. Assessment is made through suitable modeling and numerical procedures, and results in thermodynamically consistent data and phase diagrams and in quantitative prediction of phase equilibria in multicomponent melts.
The **principle** of phase diagram calculation is the minimization of the Gibbs **free energy of the** mixture under investigation. Several numerical calculation

programs exist so far in Europe and North-America. These programs, developed by specialized research groups, differ in :

- the method of description of the system considered ; the thermodynamic functions of mixing are described either by empirical polynomial expansions or by equations deduced from theoretically based models
- the mathematical methods worked out in the search of a minimum.

For metallic systems, for instance, a very efficient program has been elaborated , and successively improved, by H.L. Lukas [49] (Max-Planck-Institute, Stuttgart). Least-square methods were developed, which enable all the thermodynamic and phase diagram data to be simultaneously optimized and thus to provide optimized coefficients in polynomial expansions of thermodynamic functions of mixing.

We have developped in Marseille THERMOSALT [50] [51] which is a thermodynamic data bank for molten salt mixtures.The previous optimization program has been satisfactorily used to calculate the phase diagrams of common-ion binary [52] or multicomponent [53] molten salt mixtures.
But modifications were necessary to deal with the less-simple melts.
For instance, the numerical procedure has been adapted to asymmetrical ionic systems [54] [55] This was made according to the theoretical developments quoted above [12-13,44].
Advances are also being made in the numerical procedures for complex systems.

REFERENCES

[1] Pechiney - French Patent FR 2 494 725.

[2] R. Sevin, J. four électrique & indus. chim., 1964, 8, 79

[3] M. Gaune-Escard, Pure & Aplied Chemistry, 1983, 55, 105

[4] M.Temkin, Acta Physicochim USSR, 1945, 20, 411.

[5] M. Gaune-Escard, J.C. Mathieu, P. Desré and Y. Doucet, J. Chim. Phys., 197 n°9, 1390.

[6] M. Gaune-Escard, J.C. Mathieu, P. Desré and Y. Doucet, J. Chim. Phys., 197 9, 1397.

[7] M. Gaune-Escard, J.C. Mathieu, P. Desré and Y. Doucet, J. Chim. Phys., 197 11-12, 1666.

[8] H.K. Hardy, Acta Metallurgica, 1, 202, 1953.

[9] E.A. Guggenheim, Mixtures, Clarendon Press, Oxford, 1952.

[10] T.Førland, in "Fused Salts", B.R. Sundheim. Ed., Mc Graw Hill , 1964.

[11] Flory, J.P., J. Chem. Phys., 49, 3919, 1971.

[12] G. Hatem and M. Gaune-Escard, J. Chim. Phys., 7-8, 754, 1977.

[13] G. Hatem and M. Gaune-Escard, J. Chim. Phys., 77, 925, 1980.

[14] G. Hatem and M. Gaune-Escard, Thermochimica Acta, 57, 351, 1982

[15] O. Redlich and A.T. Kister, Ind. Eng. Chem., 40, 341, 1948.

[16] F. Kohler, Monatsh. Chemie, 91, 738, (1960)

[17] C. Colinet, D.E.S. Univ. Grenoble, France (1967)

[18] Y.-M. Muggianu, M. Gambino and J.-P. Bros, J. Chim. Phys., 72, 83, 1975.

[19] G.W. Toop, Trans. TMS-AIME, 233, 850, 1965.

[20] M. Hillert, CALPHAD , 4, 1, 1980.

[21] Z.C. Wang, R. Lück and B. Predel, in Proc. CALPHAD XVIII, May 28-June 2 1989, Stockholm (Sweden)

[22] M. Gaune-Escard, J. Chim. Phys., 9, 1167,1974

[23] M. Gaune-Escard, J. Chim. Phys., 9, 1175,1974

[24] M. Blander and S.J. Yosim, J. Chem. Phys., 39, 2610, 1963.

[25] M. Hoch and I. Arpshofen, Z. Metallkde, 75, 23, 1984.

[26] M. Hoch, I. Arpshofen and B. Predel, Z. Metallkde, 75, 30, 1984.

[27] M. Hoch, CALPHAD, 9, 59, 1985.

[28] J. F. Babelot, R.W. Ohse and M. Hoch, J. Nucl. Mat., 137, 144, 1986.

[29] M. Hoch, CALPHAD, 11, ,1987.

[30] M. Hoch, CALPHAD, 11, ,1987.

[31] M. Hoch, in Proc. ASM Meeting, Orlando, 1986.

[32] M. Hoch, CALPHAD, 11, ,1987.

[33] M. Gaune-Escard,G. Hatem., P. Gaune and M. Hoch, in Proc.6th Int. Symp. o Halide Glasses, Clausthal, FRG, October 1-5, 1989,

[34] E. Huron and M Hoch, in Proc. 1984 Int. Symp. On Metallurgical Slags and Fl xes, D.F. Gaskell and H.A. Fine, Ed.;(pp. 305-318), AIME 1984 .

[35] H. Flood , T. Førland and K. Grjotheim, Z. Anorg. Allg. Chem., 276, 289, 1954.

[36] T. Førland, in "Fused Salts", B.R. Sundheim. Ed., Mc Graw Hill , 1964.

[37] H.C. Longuet-Higgins, Proc. Roy. Soc. (London), A 205, 247, 1951.

[38] W. Brown, Proc. Roy. Soc. (London), A 240, 561, 1957.

[39] H. Reiss, J.L. Katz and O.J. Kleppa, J. Chem. Phys., 36, 144, 1962.

[40] M. Blander and J. Braunstein, Ann. New York Acad. Sci., 79, 838, 1967 .

[41] M. Gaune-Escard, J.C. Mathieu, P. Desré and Y. Doucet, J. Chim. Phys., n°6 1003, 1973.

[42] M. Gaune-Escard, J.C. Mathieu, P. Desré and Y. Doucet, J. Chim. Phys., n°7-8 1033, 1973.

[43] M. Gaune-Escard, CALPHAD,

[44] G. Hatem, B. de Gasquet and M. Gaune-Escard, J. Chem. Thermodynamics 11, 927, 1979.

[45] M. Gaune-Escard., F. Tabariès and G. Hatem, Molten Salts Discussion Group London, December 1986.

[46] H.A. Øye, Molten Salts Discussion Group, London, December 1986.

[47] EUCHEM Conferences (Europe) and Gordon Conferences (USA) from 1966.

[48] G. Hatem, F. Tabariès and M. Gaune-Escard, Thermochimica Acta,149,15,1989

[49] P. Dorner, E. Th. Henig, K. Krieg, H.L. Lukas and G. Petzow, CALPHAD, 4, 241 1980.

[50] G. Hatem, Y. Fouque, J.P. Bros and M. Gaune-Escard, in Proc. 1st Int. Symp. o Molten Salt Chemistry and Technology,Kyoto, Japan, April 1983.

[51] M. Gaune-Escard, G. Hatem, Y. Fouque and J.P. Bros, CODATA Bulletin, 58 104, 1985

[52] M. Gaune-Escard, M. Gambino, G. Hatem, J.P. Bros, Y. Fouque and P. Juhem, in Proc.CALPHAD XVI, May 24-29, Irsee, FRG, 1987.

[53] P. Juhem, G. Hatem, J.P. Bros, Y. Fouque and M. Gaune-Escard, in Proc. XIV Journées d'équilibre entre phases, Montpellier, 1988,

[54] G. Hatem, M. Gaune-Escard and A.D. Pelton, J. Phys. Chem., 1982, 86, 3039.

[55] M. Gaune-Escard and G. Hatem, in Proc. High Temp. Mat. Conference, Apri 3-7, Gaiththersburg, USA, 1989.

DOI: 10.1149/199017.0550PV

CONCEIVING OF A NEW LOW-TEMPERATURE ALUMINUM ELECTROREFINING PROCESS AND TESTING OF ITS FEASIBILITY

Gérard S. Picard , Véronique A. Villard, Daniel M. Ferry
Jean-Marie H. Hicter** and Yves J. Bertaud**

Laboratoire d'Electrochimie Analytique et Appliquée
(Laboratoire associé au C.N.R.S., URA 0216)
E.N.S.C.P., 11 rue Pierre et Marie Curie
75231 Paris Cedex 05 - France
**Aluminium Pechiney, Centre de Recherche de Voreppe
BP.27 - 38340 Voreppe - France

ABSTRACT

The aim of this work was to study the possibility of an electrorefining process in alkaline chloride-fluoride melts, for obtaining high purity aluminum from raw material containing magnesium, zinc, copper and iron as major impurities.

In order to determine the optimizing conditions for refining aluminum, we have investigated the fundamental parameters related to the chemical and electrochemical reactions involved in such a process.

Based upon these fundamental data, an electrorefining process was proposed. Its originality comes from the use of (i) a two compartment cell, with a liquid alloyed metals bipolar electrode as the separator, and (ii) anolyte and catholyte compositions which differ eachother so that the efficiency of the electrorefining process is favoured. Some electrorefining tests were performed in order to demonstrate the consistency of the conceived process.

INTRODUCTION

Aluminum is produced throughout the world using the Hall-Heroult process[1,2]. The metal so obtained has a purity close to 99.9% which is better than the purity of metallurgical Al (99.7%), but not sufficient for some applications for which high purity, and sometimes ultra-high purity aluminum, are needed.

It is beyond the scope of this paper to give an historical overview of the aluminum refinement. Readers are invited to refer to the quoted references. We only give hereafter a very brief survey of the currently used techniques of Al refinement and applications of high purity aluminum.

MAIN INDUSTRIAL TECHNIQUES FOR PURIFYING ALUMINUM.

Three-layer process.

At the moment, industrial-scale electrorefining of aluminum is realized using the well known "three liquid layers" process[3-7], the principle of which was first given by Betts[4] in 1905. In 1925, Hoopes, Frary and Edwards[5] obtained in fluoride mixtures metal whose purity approaches 99.98%[4] and, in 1932 Pechiney process (mixed chloride-fluoride mixtures)[7] permitted to produce aluminum with a purity of 99.995%.

In this well-known electrorefining process, the anode is constituted by a dense layer of aluminum-copper alloy (the anode) upon which an aluminum(III)-containing electrolyte (fluorides or chlorides-fluorides mixtures) rests. This electrolyte (intermediate layer) has a density midway that of the dense alloy and that of the aluminum . So, the cathode constituted by the refined aluminum forms the upper layer. This process suffers from the disadvantage of a relatively high energy consumption (~15000 kWh/T) and of being not always effective for removing certain elements as especially magnesium, iron, copper and zinc (see Table 1).

Some improvements concerning the cell technology in order either to minimize the energy consumption or to increase the purity of aluminum were proposed.

Segregation or fractional crystallization .

Another important technique used for the purification of aluminum is segregation or fractional crystallization.

This process is based on liquid-solid equilibria and is described[8,9] as comprising effecting cooling to cause partial crystalization of a molten impure aluminum, then separating the solid phase (which is purified in respect of certain elements - the eutectic elements) from the liquid phase which is enriched in respect of the same elements.

Such a process has a low energy consumption compared with that of the three-layer process but requires an important manpower and does not remove Mn, Zn, Si, Ga, Mg and peritectic metals as Ti, V, Cr, Zr,..(i.e.

IVa,Va and VIa groups of the periodic table). Moreover, the yield reaches only 70% in the best cases.

APPLICATIONS OF HIGH PURITY ALUMINUM AND WORLD MARKET.

Standard purified aluminum (~4N).

The major application of standard purified aluminum is the manufacture of high voltage aluminum oxide capacitors. Other applications are the realization of substrates for computer disks and at a lesser extent those based on the reflecting power of pure aluminum (mirrors and decoration).

Fig.1 gives the distribution of the average production of refined aluminum in the world (~36 kT in 1988), the Eastern countries excepted. We can see in particular that Europe is the first producer of Al≥4N with a total of about 20 kT/year, followed by Japan with 13 kT/year. Refined aluminum is nearly produced at 90% by using the 3-layer process in Europe (only Pechiney has a production of Al by segregation way); in the USA, aluminum is purified by segregation, and the Japan production is ensured at 70% by fractional crystallization, the balance by electrorefining. The price of the Al 4N is about twice the one of the Hall-Heroult aluminum.

Ultra-high purity aluminum (≥5N).

For some special applications (aluminum magnets operating at cryogenic temperature, cryomagnetic devices, integrated circuit metallization), extremely high purity aluminum or ultra-high purity aluminum is required.

The world market is yet pretty low (~150 T/year), but partially compensated by the interest of its applications and by the price of this very purified metal (about ten or even hundred times the price of H-H aluminum, depending on the requirements of the trading customer).

Unfortunately, none of the previously described process individually remove all of the undesirable impurities. So, other processes were proposed[10,11] but ultra-high purity aluminum is nowadays prepared by improving the purity of the 3-layer or segregation aluminum either by combining the two main processes described above[12,13] or by using a subsequent purification step.

The technique generally used and very effective for improving the purity of Al 4N is ***zone melting refining*** [14]. This technique is very effective but it is not easy to realize it in a large scale. Other techniques have been proposed as alternatives (formation of a boron-containing compound[15], refining by gas purging and vacuum treatment or with reactive gases[16], and so on).

PROPOSED COMPLEMENTARY LOW-TEMPERATURE ELECTROCHEMICAL PROCESSES ($T<T_f(Al)$) FOR IMPROVING THE PURITY OF PREREFINED ALUMINUM.

Alkaline chloride-$AlCl_3$ mixtures.

More than one century after the early works of Deville[17] and Bunsen[18] a lot of papers deals with the electrodeposition of solid aluminum from the aluminum chloride-alkaline chloride (sodium, potassium and lithium) mixtures enriched in $AlCl_3$ (i.e. acidic media)[19-33]. The compositions are generally comprised between 50 and 66.7% of $AlCl_3$. The most investigated media are NaCl-$AlCl_3$ or NaCl-KCl-$AlCl_3$ mixtures. For the major part, these works concern the Al electroplating and few of them the purification of this metal[19,20,27,28,30,32]. In these studies, current densities is one of the major factors which governs the deposit quality. For avoiding the growth of dendrites one has to use a current density lower than a limiting current density which depends on the melt composition and the nature of the cathode used[20,30,32].

As early as 1955, Midorikawa[21,22] used these media with $AlCl_3>50\%$ to produce aluminum deposits. According to his works, the best results are obtained when a lead cathode is used. For improving the quality of the deposits, he studied the influence of a superimposition of pulsed currents and adding of ions as Pb^{2+}[21] .For avoiding the formation of dendrites , only very small currents were used (1-3 $mA.cm^{-2}$).

Before 1960, Aluminum Industry A.G.[23] tried to electrorefine Al from a NaCl(15-18%)-KCl(10-12%)-$AlCl_3$(70-75%) mixture with a current density of 5-15 $mA.cm^{-2}$ and a voltage of 0.15-0.30 V. This process was given up because of the formation of dendrites leading to short-circuits. Other experiments were performed[24-26] . Electrorefining of contaminated aluminum scrap from a NaCl-$AlCl_3$ electrolyte was examined by Pemsler et al[25,26]. Stable organic compounds were added to promote dense and adherent deposits.The higher current density used was 100 $mA.cm^{-2}$.

Pemsler and Dempsey[25] gave the purity of the metal obtained from the electrorefining of Al 83.81% in the NaCl-$AlCl_3$(64 mol%) melt with a current density of 70 mA.cm^{-2}. The resulting metal for three subsequent refining at 190°C with an electrolysis time of 2h30 reached a purity equal to 99.98%(see Table 1).

Organometallic electrolytic refining process.

Hein et al[34] have studied in 1926 the mixtures of sodium alkyls or tetraalkylammonium salts with trialkylaluminum, in which complex organoaluminum anions of the type AlR_4^- are present. They observed that these media exhibit a noticeable ionic conductivity. A sodium fluoride-triethylaluminum medium, NaF-$Al(C_2H_5)_3$, was the first envisaged. Ziegler and Lehmkuhl[35] expected that this method might be substitute the three-layer process because of its efficiency and its low energy consumption (3000 kWh/T). In fact these media seem to be more adapted either for producing high purity aluminum (see Table 1) in a small scale or for realizing electro-coatings. Yet, use of NaF-$Al(C_2H_5)_3$, alone or with an organic solvent, for purifying aluminum at a pilot-scale was described[38,39].

Obtention of ultra-high purity aluminum (99.9995%) with a yield close to 100% was reported[38].

OBJECTIVE OF THIS PAPER.

This paper concerns the investigation of a low-temperature electrorefining process to be used for converting standard purified aluminum into ultra-high purity aluminum, i.e. as an alternative to the alkaline halide-$AlCl_3$ or $AlEt_3$ electrolyte based-processes described above which suffer from high vapor pressure and chemical reactivity .

The aim of this work was to study the possibility of an electrorefining process in alkaline chloride-fluoride melts, for obtaining high purity aluminum from raw material containing magnesium, zinc, copper and iron as major impurities which are the remaining impurities of the three-layer process - see Table 1).

Numerous factors and phenomena are involved in an electrorefining process. In spite of the importance of melt chemistry on the efficiency of a process with respect to given impurities and also in the limitation due to its eventual corrosiveness (c.a. Mg content in the three-layer aluminum comes from the corrosion of the magnesia bricks of the cell walls), very few studies were undertaken on the influence of melt composition, and at our knowledge no study exist on the possibilities brought by reaction chemistry (complexation in particular) for improving the efficiency of a refining process.

So, we present in this paper a work in this topic in laying emphasis on complexation reactions in order to modify the melt properties with respect to impurities, and hence to demonstrate the possibilities offered by chemistry to conceive an electrorefining process.

Because in our study we considered only one factor, although one of the more important, we have been obliged to test the feasibility of the process we have conceived from our fundamental-type results by performing some refining tests.

CHEMISTRY OF THE ALUMINUM AND ITS MAJOR IMPURITIES IN THE (LiCl+KCl)EUTECTIC + LiF MIXTURES AT 470°C.

MELT GENERAL PROPERTIES AND TECHNICAL.

Melt density.

The melt density was investigated by Artsdalen and Yaffe[42,43] who found for the temperature dependence of the density the following expression :

$$d = 1.8851 - 5.275.10-4\ t(°C)$$

from which we can calculate : $d = 1.637$ at 470°C.

Aluminum chloride and lithium fluoride solubilities in pure LiCl+KCl eutectic melt.

The phase diagram of the $LiCl+KCl+AlCl_3$ system was widely studied[44-47]. In the LiCl+KCl eutectic melt, $AlCl_3$ can unmixt with the formation of a $KAlCl_4$-rich phase when $AlCl_3$ reaches a temperature dependent concentration which is pretty low. This was also observed by Lantelme et al[48] in a study realized in LiCl+KCl melt at 450°C. They determined the concentration of $AlCl_3$ from which unmixing occurs as being equal to 0.22 $mol.kg^{-1}$. From Schulze and Engel[46], this concentration can be estimated to 0.44 $mol.kg^{-1}$ at 525°C. Interpolation between these two values led to a $AlCl_3$ solubility equal to 0.28 $mol.kg^{-1}$ at 470°C.

The LiF solubility can be derived from the phase diagram of the LiCl+KCl+LiF+KF quaternary system studied by Berezina et al[49].The value so obtained is equal to 1.4 ± 0.2 $mol.kg^{-1}$ at 470°C.

The knowledge of the $AlCl_3$ and LiF solubility values allowed us to fix the concentration ranges inside which our experiments were performed.

Technical.

The electrochemical cell, electrodes and apparatus for potentiometric and voltammetric studies have already been described in detail elsewhere[19,43,50-52].

POTENTIOMETRIC STUDY.

Standard potentials of the metal/cation electrochemical systems relative to aluminum, copper, iron, zinc and magnesium in the pure LiCl+KCl eutectic melt.

The standard potentials of the electrochemical systems under consideration have been potentiometrically determined. The experimental concentration ranges are indicated in Fig.2 for each redox couple investigated. They are generally comprised between $1.6.10^{-3}$ and $1.6.10^{-1}$ $mol.kg^{-1}$. The standard potential value for the Al/Al^{3+} electrochemical system [(-2.095 ± 0.010)V] obtained in this study is in good agreement with the value previously determined by Picard et al[50] [(-2.089 ± 0.002)V]. Therefore we have considered in the following, the value (-2.090 ± 0.005)V.

Considering the impurities, the standard potentials of the Mg/Mg^{2+}, Zn/Zn^{2+} and Cu/Cu^{+} redox couples have been determined. Their values are respectively : (-2.863 ± 0.010)V, (-1.840 ± 0.015)V and (-1.210 ± 0.010)V at 470°C. The two latter values are respectively 0.032 and 0.026 V higher than the values obtained by Laitinen and Liu[53] at 450°C. The standard potential of the Fe/Fe^{2+} electrochemical system was previously determined by Picard et al[51] who gave the value : (-1.447± 0.010)V.

Fig.2 gives also the potential for which Li-Al alloys are electrochemically formed (~-3.32 V) when the cathodic current density is around 310 $mA.cm^{-2}$.

We can notice that in pure LiCl+KCl eutectic melt, zinc and especially iron and copper are more noble than aluminum. On the contrary, magnesium is a much more reducing species than aluminum.

The efficiency for a good removal of an impurity depends on the potential gap between aluminum and this said impurity. One mean for modifying this gap is using of complexation reactions. Possibilities concerning ligands in molten salts are yet limited because of the high working temperature. One of the widely used ligand in molten chlorides is fluoride anion. So we have studied the complexation of aluminum(III) and its impurities with this ligand.

Aluminum(III)-F(-I) compounds.

Formation constants of the soluble fluoro-complexes of aluminum(III). The formation of aluminum(III) fluoro-complexes was studied potentiometrically in LiCl+KCl eutectic melt at 470°C. Assuming several successive complexes AlF_i^{3-i} [i.e. $AlF_iCl_j^{(i+j-3)-}$], we can introduce the classical α function defined by the relation[54,55] :

$$\alpha_{Al(F)} = [Al(III)]_T/[Al^{3+}]$$

in which $[Al(III)]_T$ denotes the total concentration of aluminum(III) under all its forms (Al^{3+}, AlF^{2+}, ...AlF_i^{3-i}), and $[Al^{3+}]$ the concentration of aluminum(III) not complexed by fluoride ions. $\alpha_{Al(F)}$ is connected to the cumulative formation constants β_i of the different fluoro-complexes AlF_i^{3-i} ($\beta_i = [AlF_i^{3-i}].[Al^{3+}]^{-1}.[F^-]^{-i}$), by the expression :

$$\alpha_{Al(F)} = 1 + \Sigma_{i=1}{}^{n} \beta_i .[F^-]^{-i}$$

From the $\alpha_{Al(F)}$ values vs. the fluoride concentration, the constants can be obtained c.a. by means of a polynomial regression analysis[56] .

Experimentally, the function $\alpha_{Al(F)}$ vs. fluoride ion concentration was obtained by measuring the equilibrium potential of an aluminum electrode.

According to the Nernst relation, the expression is the following :

$$\log \alpha_{Al(F)} = 3F(E-E°)/(2.3RT)$$

where E° is the initial potential value when all the aluminum(III) is under the Al^{3+} form ($[F^-] = 0$) and E the potential value measured when $[F^-]$ is different from 0.

Typical experimental values of $\log \alpha_{Al(F)}$ obtained in function of $\log [F^-]_T$, for an aluminum(III) concentration of 9.10^{-3} $mol.kg^{-1}$, are represented on a logarithmic plot (Fig.3). As shown by the values of $\log \beta_i$ collected in Table 2, the fluoro-complexes appear very stable and thus would greatly decrease the apparent potential of the Al/Al^{3+} redox couple. The values we have determined are in very good agreement with those previously obtained by Séon[43] and Picard et al[50] in the same experimental conditions. So, we have used in the following the average values reported in Table 2.

We can redetermined the LiF solubility from the variation of logα as a function of $\log [F^-]_T$ for a given concentration of Al^{3+}. In fact, no more variation is observed when the LiF solubility is reached (Fig.3). This value is in good agreement with the one which was obtained from Berezina's work.

Fluoro-complexes of cations relative to aluminum impurities.

The fluoro-complexes of magnesium, zinc and copper were determined by performing experiments analogous to those carried out in the case of the study of the aluminum complexes stabilities.

Fig.3 and Fig.4 show that the complexing effect of fluoride anion is lesser on these cations than on aluminum(III). We found for the cumulative constants the following values :

$\log \beta_1 = 0.7 \pm 0.2$ and $\log \beta_2 = 1.5 \pm 0.1$

for the magnesium(II) fluoro-complexes,

$\log \beta_1 = -0.5 \pm 0.2$

for the zinc(II) fluoro-complexe, and

$\log \beta_1 = -1.0 \pm 0.2$

for the copper(I) fluoro-complexe. Because of the scattering of the experimental data (Fig.4), these values are not very accurate.

LINEAR SWEEP VOLTAMMETRIC STUDY.

Diffusion coefficient of Al^{3+}.

Fig.5a shows cyclic voltammograms obtained on a tungstene electrode in the pure (LiCl+KCl)eutectic melt. The Al/Al^{3+} electrochemical system is not reversible as indicated by applying the classical reversibility criteria[19]. In fact the charge transfer is quasi-reversible. Yet, the peak current density j_p varies linearly with the square root of the sweep rate (Fig.5b) indicating a diffusion-controlled process. An estimate of the Al^{3+} diffusion coefficient $D_{Al(Cl)}$ in the eutectic melt was obtained from the expression of j_p vs. $v^{1/2}$ corresponding to a reversible charge transfer[58] . The slope p of the straight line is then given by :

$p = 1.979.10^{-3} .[Al^{3+}].D_{Al(Cl)}{}^{1/2}$

when the cathodic current density j_p is expressed in $mA.cm^{-2}$, the [Al(III)] concentration in $mol.kg^{-1}$, the diffusion coefficient $D_{Al(Cl)}$ in $cm^2.s^{-1}$ and the voltage sweep rate v in $V.s^{-1}$. The value obtained is :

$D_{Al(Cl)} = (1.1 \pm 0.2).10^{-5}\ cm^2.s^{-1}$.

Diffusion coefficient of Al(III) and solubility product of Li_3AlF_6 in fluoride containing media.

During our investigations, the low solubility of Li_3AlF_6 was evidenced. In fact, it was observed, in particular in LiF-saturated melt, the formation of a precipitate when the concentration of aluminum(III) was sufficiently high. After decantation, most of the bath was eliminated by melting and the residue was rinsed with water and subsequently dryed. A RX-diffraction pattern of the recovered product is represented in Fig.6. Besides the lithium fluoride, we can so identified the presence of lithium cryolithe in the recovered product.

The solubility of Li_3AlF_6 corresponds to the equilibrium :

$$Li_3AlF_6\,(s) = Al^{3+} + 6\,F^- + 3\,Li^+$$

and the solubility product is defined as :

$$Ks = [Al^{3+}].[F^-]^6$$

and can be rewritten :

$$Ks = [Al(III)].[F^-]^6.\alpha_{Al(F)}{}^{-1}.$$

The solubility product Ks was experimentally determined by measuring the concentration of dissolved Al(III) from the peak current densities of cyclic voltammograms (c.a. Fig.5c) performed at various voltage sweep rates as a function of Al(III) added in a LiF-saturated melt (the amount of LiF in excess was ranged from 2.5 to 3 $mol.kg^{-1}$). After verifying that the cathodic peak current density j_p varies linearly with $v^{1/2}$ (Fig.5d), we have examined the experimental variation of $j_p/v^{1/2}$ vs. Al(III) concentration in a logarithmic plot (Fig.7). In fact, we have[58] :

$$\log\{j_p/v^{1/2}\} = 6.2964 + 0.5 \log D_{Al(F)} + \log [Al(III)]$$

when the cathodic current density j_p is expressed in $mA.cm^{-2}$, the voltage sweep rate v in $V.s^{-1}$, the diffusion coefficient $D_{Al(F)}$ in $cm^2.s^{-1}$, and the [Al(III)] concentration in $mol.kg^{-1}$. From the cumulative formation constants of the aluminum(III) fluoro-complexes that we have determined above, we can show that soluble Al(III) is essentially under the forms of $AlF_5{}^{2-}$ (<20%) and $AlF_6{}^{3-}$ (>80%) when the free fluoride ion concentration is equal to the LiF solubility. The apparent diffusion coefficient $D_{Al(F)}$ may then be assumed constant and a linear plot of slope unity has to be expected. Fig.7 shows this is practically the case in spite of a certain scattering of the experimental data. From the intercept, we can calculate for the diffusion coefficient $D_{Al(F)}$ the value : $(3.2 \pm 1.5).10^{-6}\ cm^2.s^{-1}$.

Moreover, when the solubility of the lithium cryolithe is reached, the Al(III) concentration becomes constant. Fig.7 shows that appears for a concentration equal to $(3.0 \pm 0.9).10^{-2}$ mol.kg^{-1}. Knowing the values of $[F^-]$ and $\alpha_{Al(F)}$ from the LiF solubility and the cumulative constants of the aluminum(III) fluoro-complexes, we can deduce an estimate of the solubility

product Ks of Li_3AlF_6. The value obtained is given by :

$\log\{Ks / mol^7.kg^{-7}\} = -10.6 \pm 0.8$.

DISCUSSION.

Distribution diagrams of the different complex species vs. fluoride anion concentration has been established for aluminum and impurities metallic cations (Fig.8) considering a total cation concentration of 0.1 mol.kg^{-1}. From them, we can deduce that whatever the fluoride concentration may be several fluorocomplexes are always coexisting.

However for aluminum, only AlF_2^+, AlF_4^- and Li_3AlF_6 can reach percentages higher than 50% as it is more visible in the predominance area diagram given in Fig.9, and for magnesium, only MgF_2 can also reach percentages higher than 50%. Zinc and copper are very few complexed by F^- (only 30% of zinc cation and 20% of copper cation are under the form of fluoro-complexes in LiF-saturated melt).

When the fluoride concentration is lower than 10^{-3} mol.kg^{-1}, none of the impurity cations is bonded by fluoride ion, and aluminum(III) cation is very weakly complexed. On contrast, for $[F^-]_T$ higher than 3.10^{-1} mol.kg^{-1} Al(III) is strongly complexed by F^- (and Li_3AlF_6 precipitates), magnesium becomes complexed by fluoride ion and zinc and copper are practically not complexed (less than 30%).

Application of these results allowed us to establish the principle of an aluminum electrorefining process.

ELECTROREFINING OF ALUMINUM

PRINCIPLE OF THE CONCEIVED ELECTROREFINING PROCESS.

What are the most favourable media for refining aluminum with respect to Mg, Zn, Fe and Cu ? We have shown that, contrary to the strong complexation observed for aluminum (in good agreement with previous results[50,57]) and the low stability of the magnesium(II)-fluoride complexes, zinc(II) and copper(I) cations are weakly bonded to the fluoride anion. Fe(II)-F(-I) complexes were not investigated because it was assumed, after the study of zinc(II) complexes that, if they exist, their stabilities are very low and, given the high standard potentials of the iron electrochemical systems[43,51], in any case not strong enough for making iron more reductant than aluminum.

From Fig.10 representing the conditional electrode potentials for the various redox couples considered, we can remark that the representative curves $E = f(\log[F^-]_T)$ are never crossing whatever the fluoride concentration. In particular, zinc never becomes more reductant than aluminum, nor aluminum more reductant than magnesium. Moreover, Fig.10 clearly evidences the differences of the potential of the element to be refined (aluminum) and the potentials of its impurities, on which depends the efficiency of an electrorefining process . The best efficiency with respect to magnesium may then be expected with a LiF-poor medium for which the highest difference for the two conditional potentials is observed (~800 mV). On the contrary, such a medium is not adequate for purifying aluminum with respect to zinc (ΔE~250 mV). The best removal should be obtained for the highest fluoride concentration which can be reached (LiF solubility).

Moreover another factor may influence the choice of the melt composition : If we wish to use sufficiently high current density, a noticeable Al(III) concentration is required; so we have to take care of avoiding the lithium cryolithe precipitation for fluoride-rich media.

From the solubility curves of Li_3AlF_6 (Fig.11) , we can notice that for Al(III) = 0.1 mol.kg^{-1}, Li_3AlF_6 precipitates when $[F^-]_T$ reaches 0.63 mol.kg^{-1}, this allows us to increase the ΔE's between (1) the zinc, copper and iron redox systems and (2) the aluminum redox system of about 270 mV compared with the value observed in pure chloride medium. So a good purification with respect to zinc, copper and iron may be expected.

This discussion above showed that optimizing conditions for aluminum electrorefining would be the use of two different media : a medium very poor in LiF for a good removal of magnesium, and a fluoride-concentrated medium for a good removal of zinc, copper and iron. It would be interesting to realize these two operations **with only one** cell, therefore we suggested the process whose a scheme is given in Fig.12 . The refining cell is constituted by two separated compartments, connected via a bottom Al-based liquid alloy acting as a bipolar electrode. The anodic compartment is filled with a melt containing very few or no LiF, the anode being the aluminum to be refined. In this compartment, magnesium and aluminum are oxidized. But only aluminum(III) is reducible at the melt-alloy interface, magnesium(II) concentrates in the melt, and the other metallic elements (not oxidized) coming from a possible breaking up of the anode, may reach the bottom alloy by gravity and penetrate into it. The second compartment is filled with a melt containing LiF the concentration of which corresponds to the beginning of the Li_3AlF_6 precipitation. At the second interface, only Al is oxidized (no magnesium exists in the alloy) and so only Al(III) are reduced at the cathode (refined metal).

We remark that with such a process, the impurities which are less noble than aluminum are removed in a first time in the anodic compartment in which they concentrate as cations, and the impurities which are more noble concentrate in the bottom alloy as alloying metals. Then, in the cathodic compartment, only aluminum is oxidized and this occurs with all the highest efficiency than the catholyte is richer in lithium fluoride.

ELECTROREFINING DEVICE AND PROCEDURE.

Laboratory aluminum refining cell.

Fig.13 gives the schematic cross-section of the laboratory aluminum refining cell realized in Pyrex. This cell is constituted in two parts forming a confined environment for controlling atmosphere. The first one is a Pyrex pot (ϕ~100 mm, h~230 mm) ended with a plane O-ring, inside which a Pyrex crucible (ϕ~80 mm) is introduced. The second part is a lid having 7 openings in order to allow the setting of the anode, the argon inlet and outlet, the material feed pipe and the chromel-alumel thermocouple (housed in a Pyrex tube).

The "double compartment" is realized by the setting up of a bell-shaped tube (ϕ~40 mm) through the central opening of the lid. This tube is immersed halfway down into the bottom liquid alloy.

The central compartment so realized is the cathodic compartment. A stopper allows us to hold the cathode. Some holes permit to balance the inside pressures of the two compartments. The bottom surface of the cathodic and anodic compartments are respectively 10.7 and 34 cm^2.

Temperature is maintained constant by means of a furnace Renat (3.3 kW) thermoregulated by a Gulton West 3200 device.

The design of this cell makes easier the refining procedure which is the following.

Procedure for electrorefining and operating conditions

The bottom alloy (prepared apart), is put in the crucible as well as 500g (LiCl+KCl)eutectic. The bell-shaped tube is then set in but not introduced into the alloy. The eutectic and alloy are melted under vacuum. An argon flow is then realized and the bell-shaped tube is immersed down through the alloy. The required amount of lithium fluoride and aluminum chloride are added in the central compartment so formed, and aluminum chloride is introduced in the ring anodic compartment. With the design of our cell, the anodic compartment contains 380g eutectic and the cathodic compartment 120g eutectic. The alloy height is 2.5 cm.

Three sets of experiments : A, B and C were performed. The first set was realized with a binary liquid alloy (Al 5wt%-Zn) melting at 382°C and the other two with a ternary liquid alloy (Al 15.5wt%-Zn 74wt%-Cu) melting at 396°C.

Electrolysis were realized in an unstirred melt. The duration of the two first sets were 15 days and the third one 21 days. The operating conditions are reported in Table 3. Fig.14 gives the distribution of the aluminum(III) species near the operating conditions as well as the aluminum anode potential which allows us to calculate the theoretical voltages of the refining experiments (Table 3). The changes from one test to the other one (liquid alloy, cathodic electrolyte composition, current density,...) were decided from analysis of the deposits resulting from each run.

The deposits were obtained sequentially (three times a run) during one run of Al electrorefining (three runs by each set). The recovered metal amounts (after several aqueous washings) ranged between 1 and 2 g, depending the case for each run. The deposits were analysed after their recovering.

Recovering and analysis of the samples.

The resulting materials were scraped off with an alumina knife, then weighed and washed to dissolve the dragged out salts. About 20 washings in 50ml of water for 20 mn under ultrasonic vibrations are necessary to eliminate the salts.

The lithium contents of the deposits were determined by Flame Atomic Absorption Spectroscopy (A.A) and the contents of the other elements under consideration by Inducted Coupled Plasma Absorption Electron Spectroscopy (I.C.P).

RESULTS AND DISCUSSION.

Current efficiency

The current efficiency was very high but difficult to determine with accuracy because of the metal loss due to the numerous washings necessary for extracting the high amount of dragged out salts. For all the sets of experiments, the metal yield was always higher than 90%.

Morphology of the deposits.

The resulting deposits relative to two runs belonging to the first and the third sets of experiments are shown in Fig.15a and 15b. respectively. Fig.15a shows a 38250 coulomb aluminum deposit obtained at 10 mA.cm^{-2} (set A). This sample shows that we obtained a mossy, non-adherent deposit, the size of which is given by the Al 5N cathode (ruler-shaped with side~1 cm) visible in this photograph. The sample resulting from the set C (57000 C) shown in Fig.15b is porous and friable.

Effect of the bottom liquid alloy composition on Zn amount of the refined aluminum.

Fig.16a gives the Zn amount of the samples recovered in typical runs for each set. The Zn impurity content of the cathodic deposits appears to decrease with time (or charge amount). The first 17000 coulombs serves to pre-electrolyse the melt. After the third one (i.e. after 50000 coulombs), no variation is observed . This is reproducible as shown in the case of the first set.

The limiting values obtained after each run is represented in Fig.16b for the three sets A, B,and C. We can observe that the Zn level is higher in samples resulting from the first set corresponding to the use of a Zn-rich liquid alloy than in the samples recovered from the sets B and C (ternary liquid alloy). Moreover, in the latter case, a decrease in the current leads to a decrease in the zinc amount. This was attributed to diffusion-controlled process in the alloy leading to a depletion of Al at the interface with the melt.

Results obtained with the ternary liquid alloy.

The efficiency of the Fe and Mg removals is not current dependent. Fig.17 shows that these impurities are well removed in runs of the second set (10 mA.cm^{-2}) . Iron content dropped from 1300ppm to 2ppm, and Mg from 36ppm to < 2ppm.

For refining runs realized at 10 mA.cm^{-2} (set B), the average value of the copper content was about 10ppm (Fig.18). But when the cathodic current density is decreased from 10 to 5 mA.cm^{-2}, the copper amount decreased rapidly to 2ppm. This result, as well as in the case of Zn, is attributed to the limitation due to the diffusion of Al in the ternary alloy.

At last, concerning the lithium content, we observe also a drastically decrease with the c.c.d.

CONCLUSION

From a pretty bad starting material containing 0.14 wt% of impurities (Al 99.86%), it was possible to obtain Al 99.995% thus demonstrating the possibilities of such an electrorefining process comparing with the three-layer process (Fig.19). Moreover, it appears from analysis of the results obtained with the organic electrolyte purification (Table 1) and ours that this new method may be an effective alternative process without the problem of handling high reactive material.

Yet, some improvements concerning the morphology of the deposits and the value of the current density are required. They can be acquired by increasing the working temperature (but remaining lower than the melting temperature of aluminum), modifying the nature of the melt[59], stirring the melt and the bottom alloy, using alternative or pulsed currents[31],...

Acknowledgements.

The authors thank Aluminium Pechiney for financial support of this work. One author (V.V) thanks the French Research Ministry for providing a doctoral grant and Aluminium Pechiney for allowed her to run electrorefining tests with financial facilities. Acknowledgements are also due to Pr.B.Tremillon (URA 216) for his interest in this work and to Mr.P.Mortreuil (Pechiney) for realizing the chemical analysis of the electropurified aluminum samples.

References.

[1].Fr.Patent, **759 588** (1934).

[2].K.Grjotheim, C.Krohn, M.Malinovsky, K.Matiasovsky, J.Thonstad, "Aluminium Electrolysis, the chemistry of the Hall-Heroult process", Aluminium-Verlag GmbH-Dusseldorf, 1977.

[3].G.Alan Wolstenholme, in "Molten Salt Technology", D.G.Lovering ed., Plenum Press - New York and London (1982), chap.2,p.50.
[4].Kirk-Othmer, "Encyclopedia of Chemical Technology", 2nd ed., Interscience Publishers, New York-London (1963),vol.1.p.946.
[5].US.Patent, **1 534 318** (1925).
[6].Fr.Patent, **364 521**.
[7].Fr.Patent, **759 588** (1932).
[8].J.Plateau, Fr.Patent, **2 524 490** (1982),US Patent, **4 444 585** (1984).
[9].M.G.Wintemberger, US Patent, **4 456 480** (1984).
[10].K.A.Bowman, US. Patent, **4 214 956** (1980).
[11].E.W.Dewing and A.J.Gesing, Eur. Patent, **0 049 600** (1982).
[12].R.K.Dawless and S.C.Jacobs,US Patent, **4 239 606** (1980).
[13].G.A.Kozarenko,A.V.Vakhobov,F.U.Obidov and M.K.Biktimirova, Dok.Akad.Nauk.Tadzh.SSR, **26** (1983) 370.
[14].G.A.Kozarenko,A.V.Vakhobov,S.K.Biktimirova and F.U.Obidov, Dok.Akad.Nauk.Tadzh.SSR , **28** (1985) 576.
[15].A.S.Russel, S.C.Jacobs,N.Jarrett andB.M.Starner, Trans.Metall.Soc.AIME, **239** (1967)1630.
[16].G.K.Sigworth and T.A.Engh,Scand.J.Metall., **11** (1982)143.
[17].S.C.Deville, Ann.Chim.Phys., **43** (1855) 5.
[18].Bunsen, Pogg.Ann., **92** (1854) 648.
[19].V.Villard, Thesis, Paris 1989.
[20].M.Paucirova and K.Matiasovski, Electrodeposition Surf.Treat., **3** (1975) 121.
[21].R.Midorikawa, Denki Kagagu, **24** (1956) 562.
[22].R.Midorikawa, J.Electrochem.Soc.Jap., **23** (1959) 127.
[23].P.Barrand and M.R.Gadeau, "L'aluminium. Production-Propriétés-Alliages-Fabrication des produits-Fabrications annexes", tome 1, Eyrolles ed., 1964.
[24].T.Yoshishige,T.Katsuburo and W.Shigonobu, Aruminyumu Kenyu Kaishi, **122** (1977) 60.
[25].J.P.Pemsler and M.Dempsey , Report n°NSF/CPE-81012, order n°PB **81 243 693** (1981), 25.
[26].J.P.Pemsler,V.R.Koch,D.D.Dempsey,J.K.Litchfield and S.E.Stone, Proc.Symp.Energy Reduct.Tech.Met.Electrochem.processes, Metall.Soc.Publish.(1985),p.457

[27].R.C.Howie and D.W.Macmillan, J.Applied Electrochem., **2** (1972) 217.

[28].B.Nayak and M.Misra, J.Applied Electrochem., **7** (1977) 45; **9** (1979) 699.

[29].P.Fellner,M.Chrenkova-Paucirova,A.Silny and K.Matiasovski, J.Applied Electrochem., **2** (1972) 217.

[30].K.Grjotheim and K.Matiasovsky, Acta Chem.Scand., **A 34** (1980) 666.

[31].L.Qingfeng,H.A.Hjuler,R.W.Berg and N.J.Bjerrum, J.Electrochem.Soc., **137** (1990) 593.

[32].M.Chrenkova-Paucirova,P.Fellner,A.Silny and K.Matiasovski, Surface Technology, **16** (1982) 15.

[33].Y.K.Delimarsky and N.K.Tumanova, Electrochim.Acta, **24** (1979) 19.

[34].F.Hein and F.A.Segitz, Z.anorg.allg.chem., **158** (1926) 153.

[35].K.Ziegler and H.Lehmkuhl, Z.anorg.allg.chem., **283** (1956) 414.

[36].R.Dotzer, Chemie Ing.Techn., **36** (1964) 616.

[37].Fr.Patent, **1 461 819** (1964).

[38].W.D.Hannibal, G.Ibe,H.Pfundt,W.Reuter and G.Winkhaus, Metall, **27** (1973) 203.

[39].R.Dotzer, Chemie Ing.Techn., **45** (1973) 653.

[40].K.Ziegler, Fr.Patent, **1 134 858** (1955).

[41].M.S.Su,J.S.Gentry,C.B.Boss,C.G.moreland and K.J.Bachmann, J.Electrochem.Soc., **132** (1985) 802.

[42].E.R.Van Artsdalen and I.S.Yaffe, J.Phys.Chem, **59** (1955) 118.

[43].F.Séon, Thesis, Doctorat d'Etat, Paris 1981.

[44].H.Grothe and C.A.Piel, Z.Elektrochem., **54** (1950) 210.

[45].H.Grothe, Z.Elektrochem., **54** (1950) 216.

[46].K.Schultze and H.J.Engell, Erzmetall, **2** (1969) 87.

[47].M.Pyatin, A.V.Stronkin and I.V.Vasilkova, Vest.Leningrad Univ.Fiz.Khim., **1** (1973) 165.

[48].F.Lantelme, H.Alexopoulos, M.Chemla and O.Haas, Electrochim.Acta, **33** (1988) 761.

[49].S.I.Berezina, A.G.Bergman and E.L.Bakumskaya, Russ.J.Inorg.chem., **8** (1963) 1118.

[50].G.Picard, F.Séon and B.Tremillon, Electrochim.Acta, **25** (1980)1453.

[51].G.Picard, F.Séon and B.Tremillon,J.Electrochem.Soc.,**129** (1982)1450.

[52].F.Séon, G.Picard and B.Tremillon, J.Electroanal.Chem., **138** (1982) 315.

[53].H.A.Laitinen and C.U.Liu, J.Electrochem.Soc.,**80** (1958)1015.
[54].I.Leden, Z.Physik.chem., **188A** (1941) 160.
[55].D.D.Deford and D.N.Hume, J.Am.Chem.Soc., **73** (1951) 532.
[56].D.Inman, I.Regan and B.Girling, J.Chem.Soc., **54** (1964) 348.

[57].D.Inman, J.C.Legey and R.Spencer, J.Appl.Electrochem., **8** (1978) 273.
[58].P.Delahay,"New Instrumental Methods in Electrochemistry", Interscience Publishers, New York, 1954.
[59].W.K.Rolland, Thesis, Trondheim (1987).

Table 1 .

	3-layer process T = 740°C			NaCl-AlCl$_3$ T = 190°C		NaF-2AlEt$_3$ T = 80-100°C				
	Anode/ppm	Cathode		Anode/ppm	Cathode	Anode/ppm	Cathode		Anode/ppm	Cathode
		1st ref./ppm	2st ref./ppm				1st ref./ppm	2st ref./ppm		
Li	1	1	0.5	-	-	-	-	-	-	-
Na	-	-	-	-	-	?	18	13	0.83	0.44
Mg	36	20	15	-	-	13	8.7	1.1	40	-
Ti	11	5	5	140	-	-	-	-	-	-
Cr	6	3	2	-	-	-	-	-	-	-
Mn	22	4	3	48000	48	-	-	-	-	-
Fe	1300	6-8	-	9000	25	125	<7	-	<7	-
Ni	-	-	-	54000	19	-	-	-	-	-
Cu	10	5	8	31700	40	10	<0.2	-	1.4	-
Zn	170	10	8	28000	24	230	4	1.2	5.5	0.17
Si	-	-	-	80800	-	500	43	-	25	-
Pb	-	-	-	-	-	60	0.31	0.07	0.73	0.04
c.c.d /mA.cm^{-2}		340			70		10			10
Ref					25		36			36

Table 2 : Stability of Al(III)-F(-I) complexes in the LiCl+KCl eutectic melt at 470°C (molality scale).

	logarithm of the cumulative constants log β_i		
i	This study	after [50]	average values
1	2.5 ± 0.5	2.5 ± 0.4	2.5 ± 0.5
2	5.2 ± 0.5	4.7 ± 0.6	5.0 ± 0.6
3	6.2 ± 0.5	5.7 ± 0.5	6.0 ± 0.5
4	8.0 ± 0.5	7.5 ± 0.4	7.7 ± 0.5
5	8.5 ± 0.5	8.0 ± 0.5	8.2 ± 0.5
6	9.0 ± 0.5	9.0 ± 0.6	9.0 ± 0.6

Table 3 : Operating conditions for electrorefining experiments (T = 470°C).

	1st set A	2nd set B	3rd set C
Anolyte composition ($mol.kg^{-1}$)			
$AlCl_3$	0.1	0.1	0.1
Catholyte composition ($mol.kg^{-1}$)			
$AlCl_3$	0.1	0.1	0.066
LiF	0.63	0.63	0.56
Liquid alloy composition(wt%)			
Al	5	15.5	15.5
Zn	95	74	74
Cu	0	10.5	10.5
Current intensity (mA)	107	107	50
Current density (mA/cm^{-2})	10	10	5
Average voltage (V)	0.30	0.23	0.17

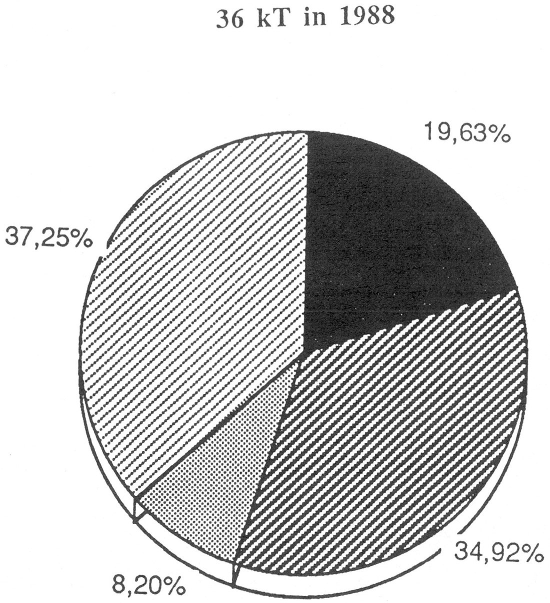

Fig.1 : Production of refined aluminum in the world (Eastern countries excepted).

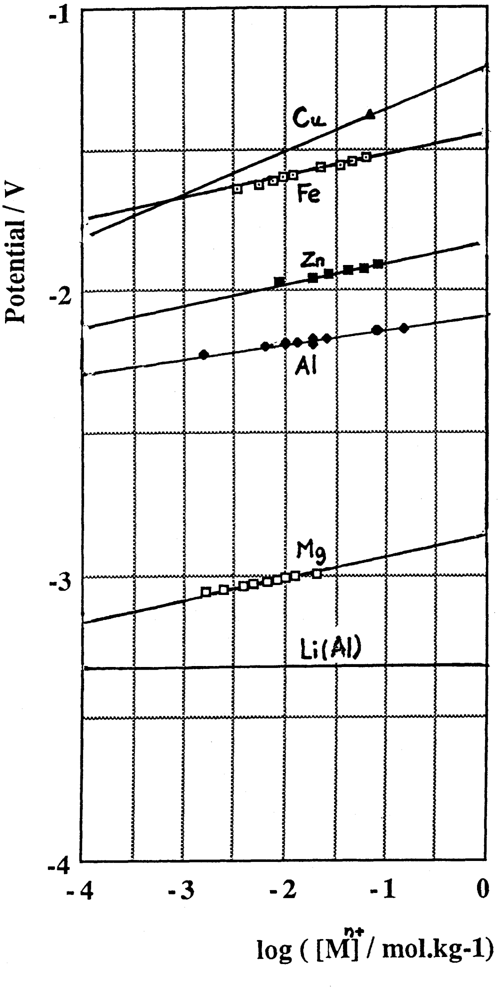

Fig.2 : Potentiometric determination of the standard potentials of some metallic cation / metal redox systems in the LiCl+KCl eutectic melt at 470°C (potentials are given vs. the Cl_2(1atm)/Cl^- electrochemical system).

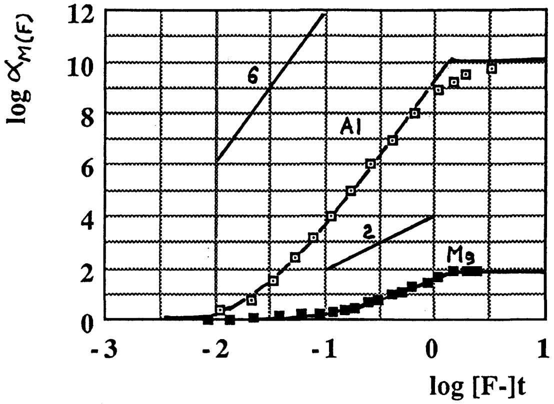

Fig.3 : Determination of the cumulative formation constants of Al(III) and Mg(II) fluoro-complexes in the LiCl+KCl eutectic melt at 470°C. Plot of log $\alpha_{Al(F)}$ and log $\alpha_{Mg(F)}$ vs.log $\{[F^-]_t$ / mol.kg$^{-1}\}$. ([Al(III)] = 9.10^{-3} mol.kg^{-1}; [Mg(II)] = 2.10^{-2} mol.kg^{-1}).

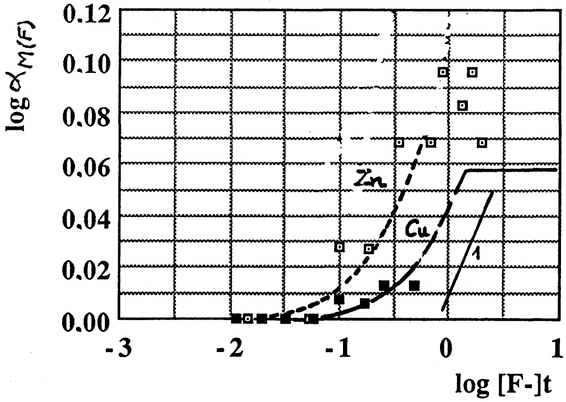

Fig.4 : Determination of the cumulative formation constants of Zn(II) and Cu(I) fluoro-complexes in the LiCl+KCl eutectic melt at 470°C. Plot of log $\alpha_{Zn(F)}$ and log $\alpha_{Cu(F)}$ vs.log $\{[F^-]_t$ / mol.kg$^{-1}\}$. ([Zn(II)] = 8.7.10^{-2} mol.kg^{-1}; [Cu(I)] = 7.10^{-2} mol.kg^{-1}).

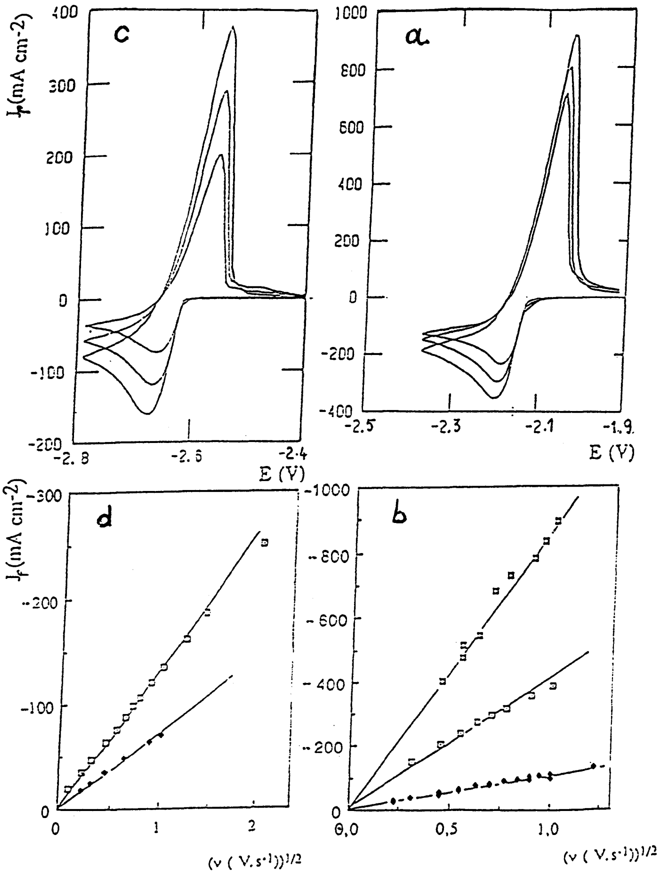

Fig.5 : Linear sweep voltammetric study of the Al/Al(III) electrochemical system. Typical voltammograms obtained on a tungstene electrode (Surface area : 0.17 cm^2) : a) in the pure LiCl+KCl eutectic melt ([Al(III)] = 6.10^{-2} mol.kg^{-1}; v = 0.3, 0.5 and 0.8 V.s^{-1}); c) in LiF and Li_3AlF_6 saturated melt (v = 0.3, 0.8 and 1.5 V.s^{-1}); plots of cathodic peak current density vs. v$^{1/2}$:b) [Al(III)] = 1.84.10^{-2} , 6.10^{-2} and 0.13 mol.kg^{-1}; d) [Al(III)] = 1.84.10^{-2} mol.kg^{-1} and equal to the solubility of Li_3AlF_6.

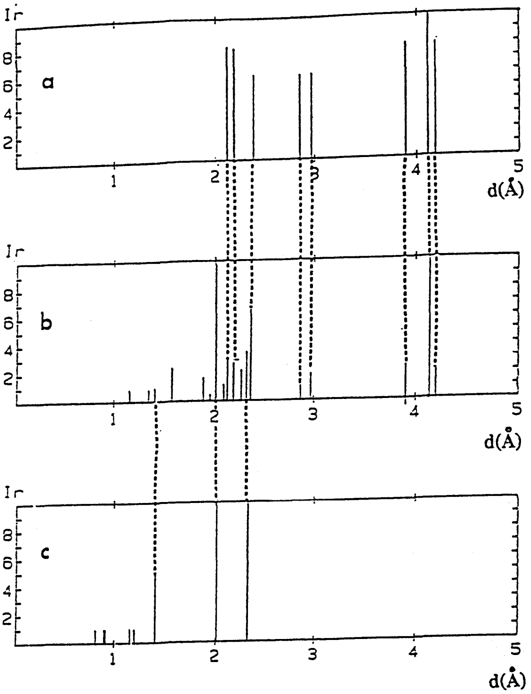

Fig.6 : RX-diffraction patterns :

a : Li_3AlF_6.

b : recovered product (see text).

c : LiF.

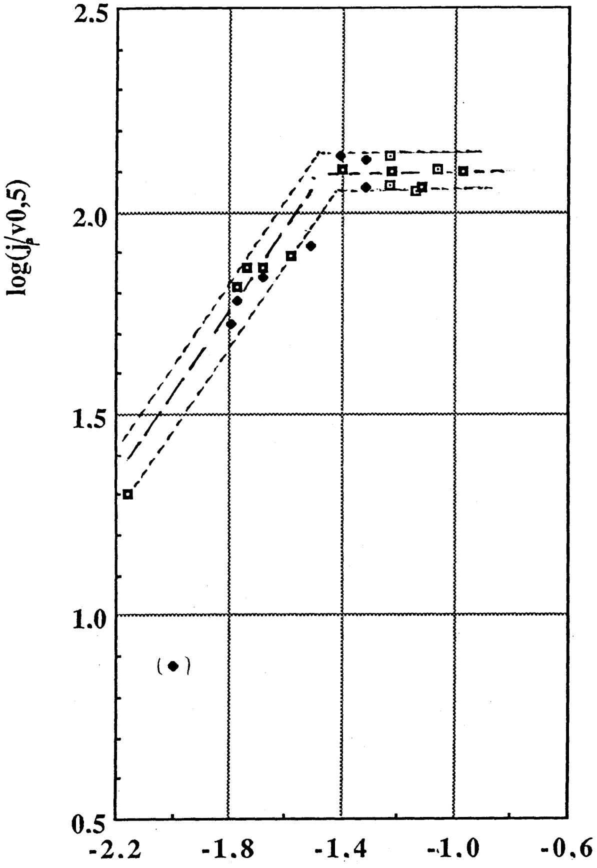

log [Al(III)]T

Fig.7 : Determination of the diffusion coefficient of Al(III) in LiF-saturated melt and of the solubility of Li_3AlF_6. Logarithmic plot of j_p / $v^{1/2}$ vs. $[Al(III)]_t$ (molality scale, j_p in $mA.cm^{-2}$, v in $V.s^{-1}$)

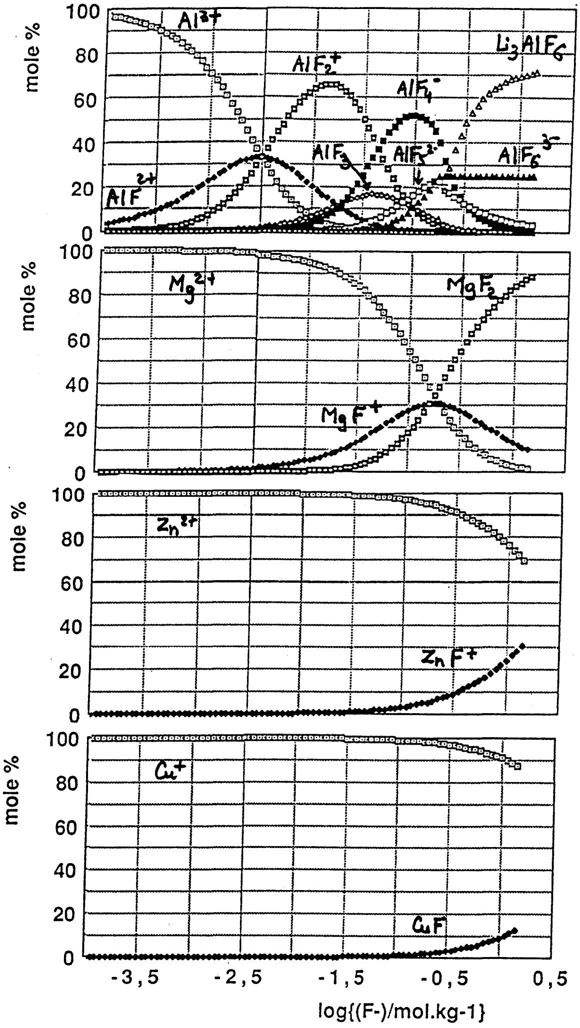

Fig.8 : Distribution diagrams of the metallic cations fluoro-complexes in the LiCl+KCl eutectic melt at 470°C

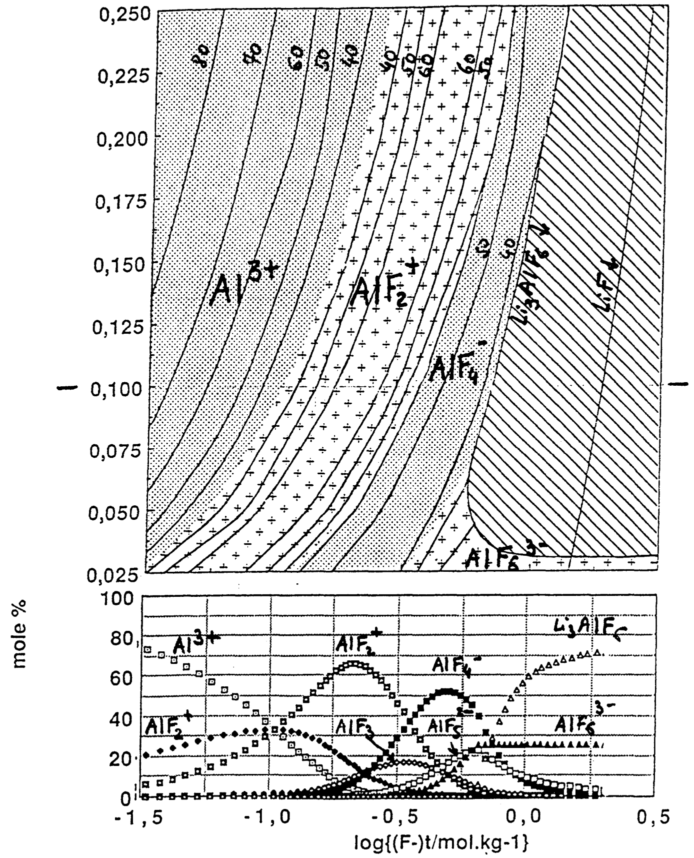

Fig.9 : Predominance area diagram for aluminum(III) species in the LiCl+KCl eutectic melt at 470°C as a function of total fluoride ion concentration.

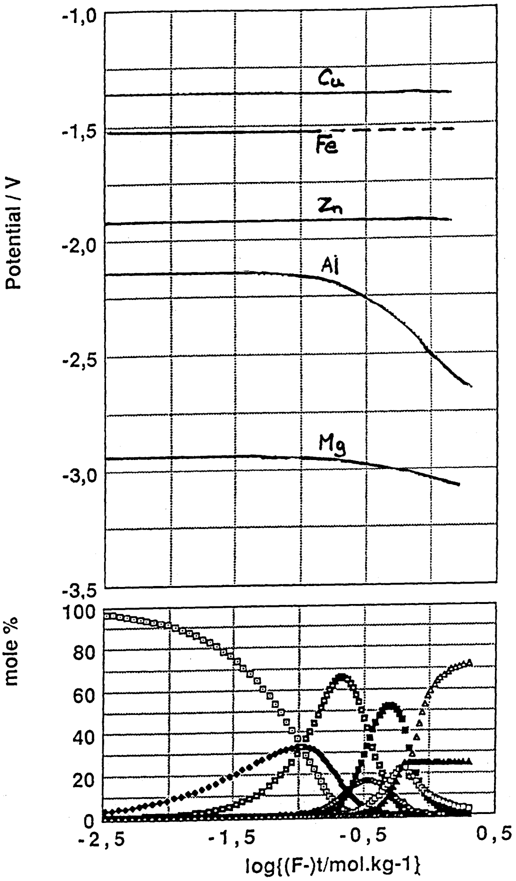

Fig.10 : Conditional potential-log$[F^-]_t$ equilibrium diagram for aluminum, magnesium, iron, zinc and copper in (LiCl+KCl)eutectic+LiF mixtures at 470°C.

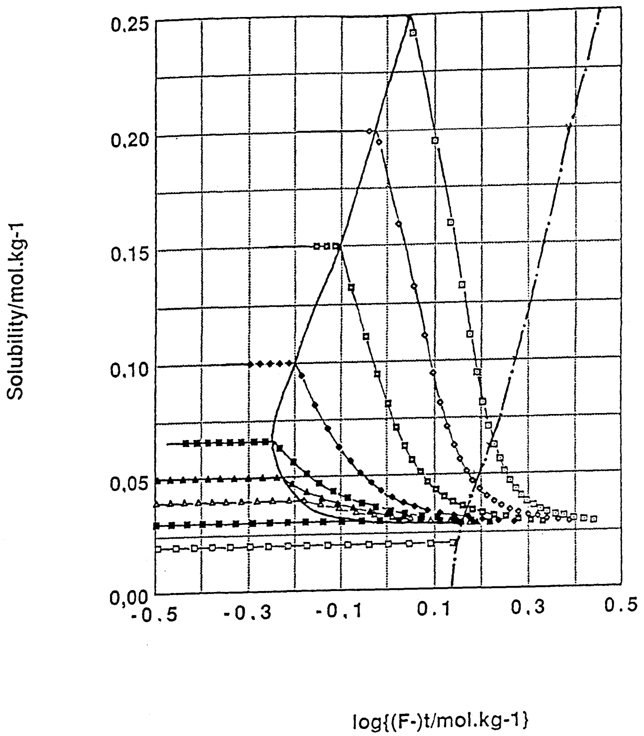

Fig.11 : Li_3AlF_6 solubility curves in (LiCl+KCl)eutectic+LiF mixtures at 470°C.

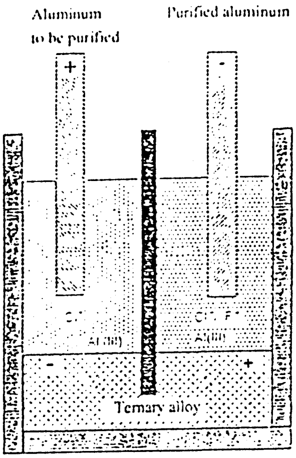

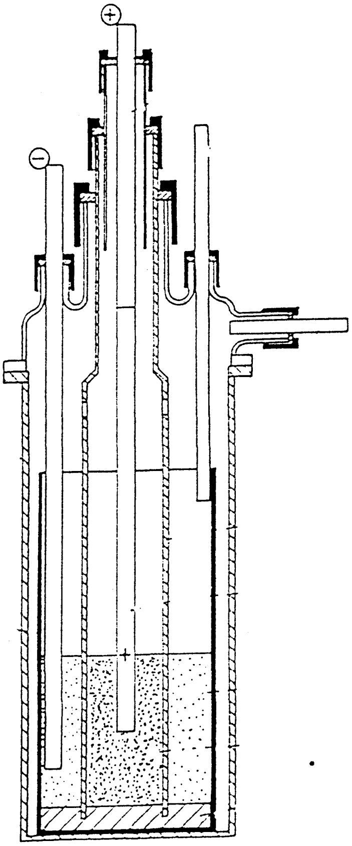

Fig.12 : Principle of the electrorefining cell.

Fig.13: Laboratory aluminum refining cell (see text for explanation).

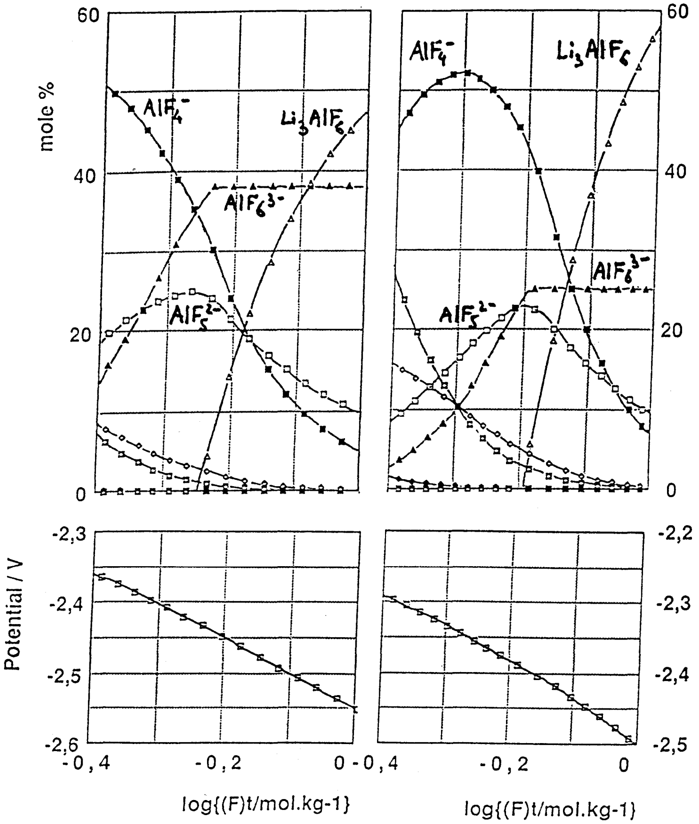

Fig.14: Theoretical potentials of the cathode and Al(III) species distributions around the fluoride ion concentration relative to the Li_3AlF_6 precipitation, for total Al(III) concentrations of 0.1 and 0.066 $mol.kg^{-1}$.

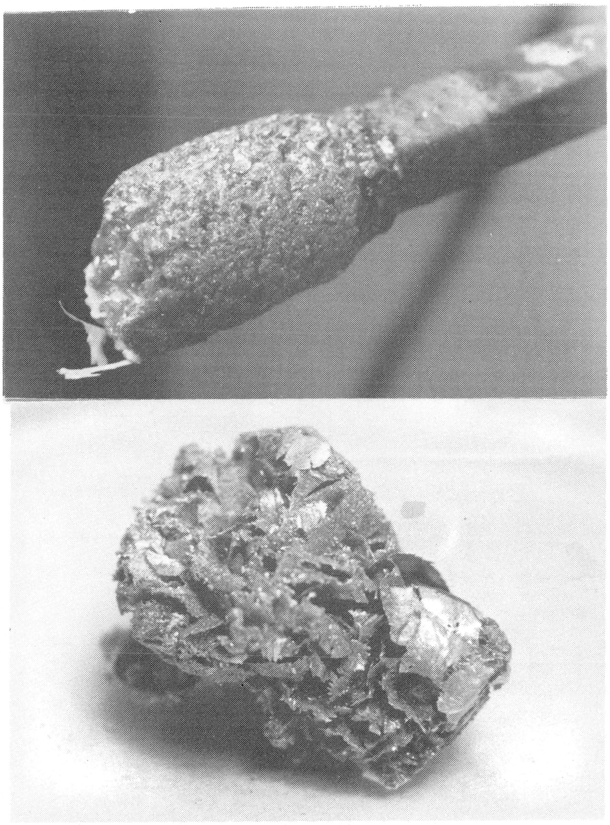

Fig.15: Photographs of aluminum deposits.

a (upper) : a 38250 Coulomb deposit obtained at 10 mA.cm^{-2} (set A).

b (lower) : a 57000 Coulomb deposit obtained at 5 mA.cm^{-2} (set C).

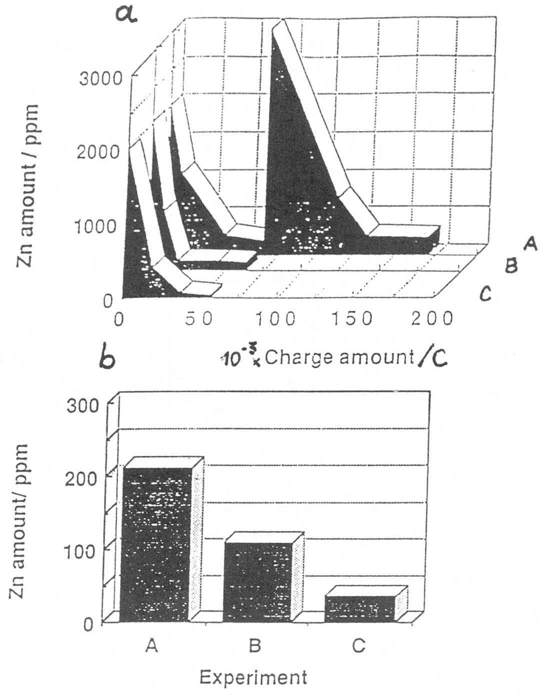

Fig.16: Comparison of metallic impurity levels.

a) zinc content of electrorefining samples as a function of charge amount or (time) for the three sets of experiments.

b) typical values for zinc content in samples recovered after each electrolysis run for the three sets of experiments.

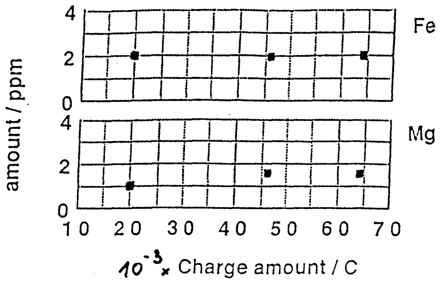

Fig.17: Average maximum values observed for Fe and Mg impurities in Al deposits obtained with the ternary liquid alloy (set B).

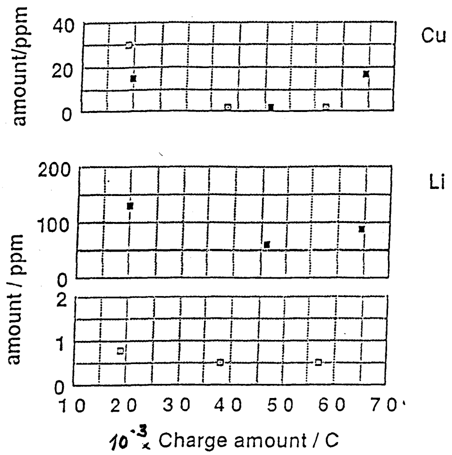

Fig.18: Current density dependence of copper and lithium amounts in Al deposits obtained with the ternary liquid alloy.

■ : set B ; □ : set C.

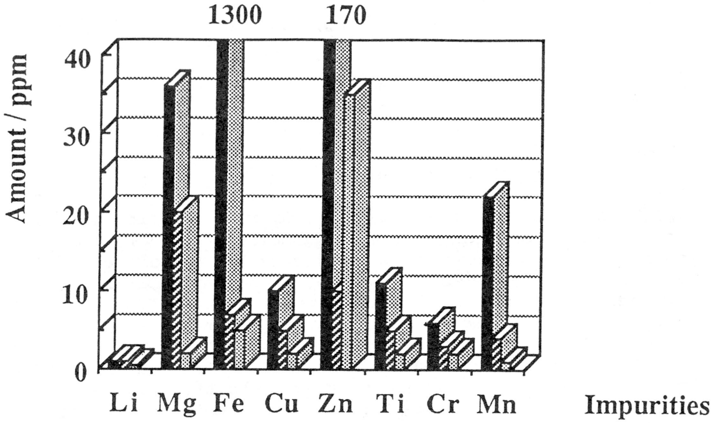

Fig.19: Comparison of metallic impurity levels found for Hall-Heroult aluminum (■) and purified aluminum (▧ : three-layer, ▩ new process).

DOI: 10.1149/199017.0588PV

ELECTROLYTIC PRODUCTION OF CALCIUM METAL

J. J. Lukasko and J. E. Murphy

Reno Research Center
U.S. Bureau of Mines
1605 Evans Avenue, Reno, Nevada 89512-2295

ABSTRACT

The Bureau of Mines developed an alternative electrochemical process for the production of calcium metal. The current industrial practice is costly, complex, and inefficient. The Bureau method involves electrowinning of a calcium-tin alloy followed by electrorefining to produce calcium metal. In the electrowinning cell, calcium chloride was fed to a potassium chloride-calcium chloride electrolyte. The calcium was electrowon at 650° C into the pure molten tin cathode until the cathode contained 7.5 wt pct Ca. Current efficiency for electrowinning averaged over 90 pct. The resulting tin-calcium alloy served as the anode for the electrorefining cell which employed a calcium chloride-calcium fluoride fused salt as the electrolyte. Calcium metal was electrorefined at 850° C with a current efficiency of 85 pct based on calcium metal recovered. The calcium metal analyzed 99.2 pct, which is purer than commercially produced calcium.

INTRODUCTION

The Bureau of Mines has investigated the electrolytic production of calcium metal. The procedure has low energy requirements and may lower the cost of producing calcium. Lower cost calcium metal would promote wider use.

Before adoption of the present commercial process, calcium metal was manufactured by the direct electrolysis of calcium chloride (1). In this batch process, a "carrot" of solid calcium was electrowon which contained a large amount of occluded salt. The process was difficult to control and operated at only 60-pct current efficiency (2). Aluminothermic reduction of lime to produce calcium metal, which was commercialized in the 1940's, is the only process currently used for calcium production in the United States (3). Calcium oxide and aluminum powder are briquetted and then retorted at 1,200° C under vacuum. Purity of the calcium metal is 98.8 pct, and the purity can be improved to 99.5 pct by redistillation (4-7). The major impurity of the redistilled calcium is magnesium at 0.5 wt pct. High-energy consumption and a labor intensive, batch operation are disadvantages of the process. Moreover, powdered aluminum metal is an expensive reductant, and aluminum utilization is only about 60 pct.

The proposed electrochemical process depicted in Figure 1 is simple, energy efficient, and could be made continuous. Calcium chloride was fed to the electrowinning cell which had a molten tin cathode. The electrowinning cell produced Ca-Sn alloy and byproduct Cl_2. After electrowinning calcium into the tin cathode, the Ca-Sn alloy became the anode for the electrorefining cell. Calcium metal analyzing 99.2 pct pure was recovered from the electrorefining cell. The calcium electrowinning cell was modified to produce Pb-Ca alloys by electrowinning calcium into a molten-lead cathode.

EQUIPMENT AND MATERIALS

Analyses of the reagent grade chemicals employed in the electrowinning-electrorefining tests are shown in Table 1. The salts were dried in an oven and stored in a desiccator prior to use. Before electrolysis, the tin cathodes and electrolytes were melted in graphite crucibles with induction heating.

A proportioning controller and wire wound resistance furnace maintained the electrolytic cell at the desired temperature for all experiments. Type K inconel-clad thermocouples encased in alumina sheaths were used to monitor temperature. A Hewlett Packard 6264B rectifier provided electric current for electrolysis. A Curtis Model 1002 integrator was used to measure electrolysis current, and a Fluke Model 8026B multimeter was used to monitor electrolysis voltage.

Figure 2 depicts the electrowinning cell. A 250-mL alumina crucible served as the cell container. One-hundred-twenty grams of pure tin was placed on the bottom of the crucible to serve as the cathode. The salt charge containing 170 g of well mixed chlorides (75 mol pct KCl-25 mol pct $CaCl_2$) was added to the crucible. The thermocouple assembly was placed into the powdered salt. When the salt became molten, the cathode current feeder and anode assemblies were positioned. The cathode current feeder was a 0.6-cm-diam by 30.5-cm-long tungsten rod which was encompassed by a 1.8-cm-diam ID open-ended alumina tube. The anode assembly consisted of a 0.6-cm-diam by 30.5-cm-long graphite rod which was inserted into the middle of a 1.8-cm-ID alumina tube and submerged 2.5 cm into the molten-salt electrolyte. The open-ended alumina tube served as an anode sheath which vented chlorine gas and prevented both oxidation of the graphite rod and backreaction of the calcium in the cell. Upon completion of electrowinning, all the components were removed and the metal cathode and electrolyte were poured into a graphite mold. After cooling, the tin alloy button was separated from the electrolyte.

The electrorefining cell is shown in Figure 3. The apparatus was housed in a glove box to prevent oxidation of the calcium metal at the cathode. The glove box was evacuated to approximately 100 microns and backfilled with 99.995 pct pure argon that had been passed through a Drierite desiccant column and an oxygen getter assembly. The getter assembly consisted of a 2-cm-ID by 33-cm-long Vycor[1] tube filled with minus 4 plus 40 mesh titanium sponge which was heated to 850° C in a tube furnace. The Ca-Sn cathode alloy from the electrowinning step was placed

---

[1] Reference to specific products does not imply endorsement by the Bureau of Mines.

Table 1. Analysis of Reagent-Grade Chemicals, parts per million

	$CaCl_2$	KCl	Sn	CaF_2
Al..	<500	<200	<600	[1]0.43
Ca..	[1]34.45	<200	<600	[1]49.5
K...	<150	[1]44.8	<100	<1,000
Mg..	740	<50	<200	[1]0.20
Na..	[1]0.29	<200	<600	[1]1.1
Sn..	170	<10	[1]99.9	<20
Sr..	150	<0.5	<2	400

[1] Percent.

at the bottom of a 250-mL alumina crucible. An alumina sheathed 1.5-mm-diam thermocouple and an alumina sheathed 3-mm-diam stainless steel rod were placed between a 4-cm-diam by 5-cm-tall molybdenum foil liner and the crucible wall. The stainless steel rod served as the anode bus and was positioned to ensure electrical contact with the Ca-Sn alloy anode. The bottom of the thermocouple sheath was positioned 2 cm below the electrolyte surface. The bottom of the foil liner was approximately 1 to 2 cm above the salt-alloy interface. The molybdenum foil liner contained the calcium metal that floated during production and prevented attack on the alumina. One-hundred-seventy grams of electrolyte (52 mol pct $CaCl_2$-48 mol pct CaF_2) was placed on the alloy. Once the electrolyte was molten, a 6-mm-diam tungsten rod, which served as the cathode, was immersed 1 cm into the molten-salt bath.

EXPERIMENTAL PROCEDURE AND RESULTS

The results of preliminary tests dictated the parameters of the electrowinning operation. Several pure metals, including cadmium, lead, tin, and zinc, were tried as liquid cathodes. Tin accepted the highest calcium loading. Several runs were performed to identify acceptable ranges for temperature, voltage, and current density. Different molten-salt baths composed of $CaCl_2$, and one or more of KCl, LiCl, $BaCl_2$, and $SrCl_2$ were tested as electrolytes. Lithium, barium, and strontium were electrowon with calcium into the cathode. As a result, only the KCl-$CaCl_2$ bath was suitable. Feeding calcium chloride at approximately the same rate that decomposition occurred provided for steady operation and prevented freezing of the molten-salt bath.

Electrolysis was initiated after the temperature reached 650° C. The applied current was adjusted to 8 A (0.4 A/cm^2 cathode current density) and the voltage monitored to determine if the cell was shorted or if the circuit was open. The rectifier was controlled in a constant current mode. Electrowinning started at approximately 2.7 V. Ammonia gas was passed over the anode vent to verify electrolysis by forming white ammonium chloride. Once steady operation was obtained, the stoichiometrically required amount of calcium chloride was fed to the cell to replace electrolyte depleted during electrowinning. This semicontinuous feeding provided for very smooth operation with little

Table 2. Calcium Metal Production Operating Data

	Electro-winning	Electro-refining
Feed	$CaCl_2$	$CaSn_3$
Electrolyte, pct:		
KCl	67	NAp
$CaCl_2$	33	60
CaF_2	NAp	40
Cell:		
Material	Alumina	([1])
Atmosphere	Air	Argon
Operating temp.......°C..	650	850
Applied current.......A..	8	4
Voltage..............V..	4.5	1.6
Current efficiency..pct..	91	85
Anode:		
Material	Graphite	$CaSn_3$
Size, cm:		
Height	30	1.0
Diameter	0.6	5.4
Active area.........cm^2..	4.8	21
Current density...A/cm^2..	1.7	0.2
Cathode:		
Material	Tin	Tungsten
Size, cm:		
Height	0.7	30
Diameter	5.4	0.6
Active area.........cm^2..	21	2.2
Current density...A/cm^2..	0.4	1.8

NAp Not applicable.
[1] Alumina, molybdenum liner.

voltage fluctuation. Each test was continuously monitored and operating data were recorded. Immediately after terminating a test, the apparatus was disassembled and the contents of the crucible were poured into a conical graphite mold. After cooling, the tin alloy button could be easily separated from the salt phase. Examination of the apparatus showed there was no corrosion or chemical attack. Table 2 shows typical electrowinning data.

An investigation of operating parameters was undertaken to determine optimum conditions and to model cell characteristics. Temperature, current density, calcium loading, and cathode additives were examined to evaluate their effect on current efficiency.

Figure 4 depicts the relationship between anode current density and cell voltage for a 0.6-cm-diam graphite rod anode. The voltage was measured from the top of the anode to the top of the cathode. The cell was operated at 650° C with standard conditions. The graphite anode was immersed 2.5 cm into the molten-salt bath. When the data are projected to zero amperes, the decomposition voltage is approximately 2.7 V. This voltage is lower than the theoretical decomposition voltage for $CaCl_2$ at 650° C which is 3.45 V (8) because of the exothermic reaction in forming the compound, $CaSn_3$.

The effect of cell temperature on current efficiency is shown in Figure 5. The electrowinning tests which were run for 16 A·h (approximately 5.6 pct Ca loading) show that current efficiency decreases linearly with increasing temperature. The lowest possible operating temperature was 635° C. Below 635° C, additions of $CaCl_2$ would initiate localized freezing and upset operation of the cell.

Current efficiency decreased with calcium loading of the cathode. Table 3 relates current efficiency and calcium loading in percent calcium. Current efficiency was decreased because the calcium activity in the cathode was increased, and the melting point of the alloy was increased causing viscosity and surface tension of the cathode to increase. The increased viscosity and surface tension impeded the transfer of the calcium metal into the tin cathode.

Current efficiency decreased linearly with increasing cathode current density as shown in Figure 6. The cell was operated at 655° C for 9 A·h (approximately 5.1 pct Ca) for these experiments. Increasing cathodic current density caused calcium to build up at the cathode surface.

The data in Table 4 show that the addition of copper, lead, zinc, and silver metals to the tin cathode decreased the current efficiency. The conditions for these experiments were the same as for the experiments with the tin cathode. The purpose of adding metals was to increase calcium solubility, to reduce tin content by partial substitution of a cheaper metal, and to improve loading and current efficiency. The predicted efficiency is the average efficiency that was obtained with a pure tin cathode. The addition of another metal to the tin cathode decreased the current efficiency.

A scanning electron microscope picture of the tin-calcium alloy showed that $CaSn_3$ was the predominant species with trace amounts of CaSn. The $CaSn_3$ grains could easily be seen in the tin matrix. An X-ray diffraction analysis of the cathode indicated major $CaSn_3$ and minor tin. The electrolyte was determined to be KCl and $KCaCl_3$ by X-ray diffraction. Table 5 shows an analysis of the electrolyte and the tin-calcium cathode.

Table 3. Current Efficiency Versus Percent Calcium Loading of the Cathode for the Electrowinning Cell

Run	Efficiency, pct	Calcium, pct	Run	Efficiency, pct	Calcium, pct
20..	93.0	8.5	39..	95.9	5.1
27..	82.0	11.9	40..	91.2	8.4
29..	93.0	6.9	41..	91.5	8.4
37..	94.5	5.1	47..	92.5	8.5
38..	96.9	5.2	49..	91.0	8.3

Table 4. Effects of Metallic Additions to the Cathode in the Electrowinning Cell upon Current Efficiency

Alloy	Weight percent	Ampere hour	Current efficiency pct	Predicted efficiency, pct	Percent change
Sn-Cu	80-20	9.0	75.0	96.4	-22.2
Sn-Cu	90-10	9.0	88.0	96.4	-8.7
Sn-Cu	95- 5	9.0	91.5	96.4	-5.1
Sn-Pb	50-50	12.0	86.0	94.1	-8.6
Sn-Zn	50-50	14.0	19.0	92.6	-79.5
Sn-Ag	90-10	4.5	90.0	99.8	-9.8

Table 5. Analysis of Electrowon Alloy and Electrolyte, parts per million

	Cathode	Electrolyte
Al...	<400	<500
Ca...	[1]7.3	[1]11.8
K....	50	[1]37.6
Mg...	<200	<200
Na...	<400	[1]0.23
Sn...	[1]93	<20
Sr...	400	1,000

[1] Percent.

Electrorefining

The electrorefining cell was initially used in air with an argon gas blanket, but excessive oxidation of calcium at the melt surface resulted. Subsequent electrorefining was done in a glove box with an argon atmosphere which permited visual examination and adjustments during cell operation.

Table 2 summarizes typical electrorefining data. A calcium chloride-calcium fluoride (52-48 mol pct) electrolyte was determined to be satisfactory. Other electrolytes tested included mixtures of LiF, BaF_2, $CaCl_2$, CaF_2, and $BaCl_2$. Because calcium reduced these salts in the cell, significant metallic contamination of the product occurred. The $CaCl_2$-CaF_2 electrolyte melted at 800° C, was fluid, exhibited 2 pct Ca solubility, and had no detectable tin solubility.

The cell was operated at 850° C to ensure that the calcium product was molten. Higher temperatures would have increased calcium volatilization and calcium solubility in the electrolyte. Cell voltage was adjusted to a maximum of 2 V to prevent electrolysis of the calcium chloride. The anode current density at 0.2 A/cm^2 was near the operating level in aluminum and magnesium molten-salt electrorefining cells which ranges from 0.3 to 0.8 A/cm^2 (9-10).

Periodic inspection of the cell during electrorefining revealed that calcium was oxidizing at the electrolyte surface. A major oxygen source was probably outgassing of the furnace refractories. After the initial adjustment of the rectifier, fluctuations of output voltage and applied current were small. Fuming of the electrolyte was not visible. After the desired ampere hour was reached, heating was terminated and the cell contents froze within 5 min. The voltage was maintained to provide cathodic protection which prevented dissolution of calcium metal at the cathode. Once the electrolyte was frozen, it could be easily separated from the calcium deposit which was free of occluded salt. The electrolyte remained clean and white and exhibited a sharp interface with the tin-calcium anode. The calcium product was analyzed as soon as possible to limit oxidation. The apparatus showed no signs of chemical attack or corrosion upon disassembly.

A plot of anode current density versus cell voltage is depicted in Figure 7. A potential of 0.6 V was required before electrorefining would proceed.

Several tests were performed to examine the influence of cell parameters on current efficiency and product purity. Electrorefining experiments ranged between 30 and 190 min. Current densities were varied from 0.07 to 0.29 and from 0.58 to 2.52 A/cm^2 for the anode and cathode, respectively. Calcium loading of the anode feed ranged between 4.9 and 9.2 wt pct with an average of 7.36. Removal of calcium from the anode varied from 40 to 70 pct in these experiments. Within the above tested ranges, varying the parameters had no discernible effect on purity or current efficiency.

The measured current efficiencies which were based on calcium recovery ranged from 75 to 88 and averaged only 85 pct. Normally, electrorefining operates at very high current efficiencies. However, when the calcium metal floats on the electrolyte, there is significant oxidation and some evaporation. Also, calcium is 2 wt pct soluble in the electrolyte, and the solubility limit must be reached before the solubility loss is zero. In short duration tests, the solubility loss is significant, but it was not taken into account.

Typical analyses of the calcium metal product and spent electrolyte are found in Table 6. Examination of the calcium metal by scanning electron microscopy (SEM) showed one continuous phase of calcium. Thus, impurities in the calcium did not form separate phases and could not be seen by SEM. According to inductively coupled plasma and atomic absorption analysis, approximately 0.15 wt pct tin transferred during electrorefining. SEM inspection of the calcium found tin contamination to be uniform. The tin analyzed less than 20 ppm (detection limit) throughout the electrolyte. The calcium could be distilled to remove the tin if desired. Other impurities found in the calcium metal were aluminum, sodium, and magnesium. The impurities were present in the electrolyte reagents and reported to the calcium product. Thus, eventually a purer product would be obtained because the electrorefining operation removed the impurity metals from the electrolyte. After sustained operation with clean feed, the recovery of a high-purity calcium metal product should be possible.

Table 6. Analysis of Calcium Product and Electrolyte from the Electrorefining Cell, percent

	Calcium	Electrolyte
Al...	0.48	0.16
Ca...	99.2	44.4
K....	[1]<1,000	[1]1,000
Mg...	0.16	[1]690
Na...	0.15	0.47
Sn...	0.15	[1]<20
Sr...	[1]200	0.11

[1] Parts-per-million.

Proposed Electrorefining Cell

Figure 8 is a schematic of a proposed electrorefining cell for the large-scale, continuous production of calcium. The cell would have an alumina or other refractory liner to contain the Ca-Sn alloy feed and electrolyte. Steel proved to be suitable for electrodes and lining where calcium metal may be contacted. The levels of $CaSn_3$, electrolyte, and calcium metal would be controlled by monitoring feed and tapping flows. An inert atmosphere above the molten calcium would be required. Cell voltage, temperature, and anode current density should be similar to those of the electrorefining cell in present work.

Lead-Calcium Alloys

Lead-calcium alloys were produced by electrowinning calcium into a molten lead cathode. Table 7 contains lead-calcium alloy cell data. Calcium chloride was fed to a $KCl-CaCl_2$ molten-salt electrowinning cell to make Pb-Ca alloys containing up to 6.1 pct Ca with 94 pct current efficiency. Also, Pb-Sn-Ca and Pb-Sn-Ca-Al alloys were made in the electrowinning cell with current efficiencies above 90 pct. These alloys could be blended with lead to produce other desired alloys. Pb-Ca alloys have application as electrowinning anodes and battery grids.

Table 7. Lead-Calcium Alloy Cell Data

Feed	$CaCl_2$
Electrolyte, pct:	
KCl	66.9
$CaCl_2$	33.1
Cell:	
Temperature, °C	650
Amperage, A	8
Voltage, V	3.7
Anode current density, A/cm^2	1.7
Cathode current density, A/cm^2	0.4
Current efficiency, pct	98
kW·h/kg, 2 pct Ca	0.24

SUMMARY AND CONCLUSIONS

The two-step electrochemical process for the production of calcium metal is simple and efficient. The electrowinning step entails controlled feeding of $CaCl_2$ to a $KCl-CaCl_2$ molten-salt at 650° C. The molten tin cathode is loaded to 7.5 wt pct (18.7 mol pct) calcium. The Ca-Sn alloy cathode from electrowinning serves as the anode for the electrorefining cell. Electrorefining is performed at 850° C in a $CaCl_2-CaF_2$ electrolyte. Calcium metal collects at the cathode on the surface of the electrolyte. The recovered product analyzed 99.2 wt pct calcium. The electrowinning cell should be easily scaled up. On the other hand, the electrorefining cell needs further development to determine what current efficiency can be expected and what recovery problems will be encountered in handling molten calcium metal, in scale-up, and in longer term cell operation.

REFERENCES

1. Kirk-Othmer (ed.). Calcium and Calcium Alloys. Ch. in Encyclopedia of Chemical Technology. Wiley, 3d ed., v. 4, 1978, pp. 412-421.

2. S. A. Tucker and J. B. Whitney. Some Observations on the Preparation of Metallic Calcium by Electrolysis. J. Amer. Chem. Soc., v. 28, 1906, pp. 84-87.

3. C. C. Loomis. The Production of Metallic Calcium by Thermal Reductions. Trans. Electrochem. Soc., v. 89, 1946, pp. 207-216.

4. L. Pelham. Calcium and Calcium Compounds. Ch. in Bureau of Mines Minerals Yearbook 1987, v. 1, pp. 181-185 pp.

5. H. A. Wilhelm and O. N. Carlson. Methods for Producing High-Purity Calcium. J. Met., v. 16, 1964, pp. 170-174.

6. W. J. McCreary. High-Purity Calcium. J. Met., v. 10, 1958, pp. 615-617.

7. I. I. Betcherman and L. M. Pidgeon. The Distillation of Calcium and Magnesium. Can. Min. and Metall. Bull., v. 44, 1964, pp. 253-262.

8. C. L. Mantell. Electrochemical Engineering. McGraw-Hill, 1960, 680 pp.

9. T. G. Pearson. The Chemical Background of the Aluminum Industry. Royal Inst. Chem., 1955, 102 pp.

10. J. Schmorak. Electrolytic Production of Magnesium. English Transl., NTIS PB-271 946T, 1977, 325 pp.

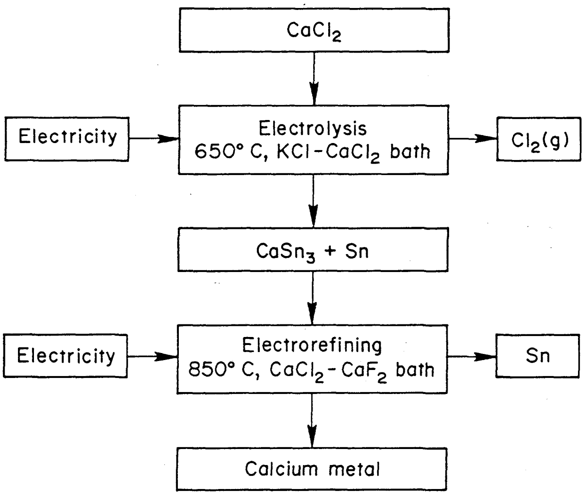

Figure 1. Flowsheet.

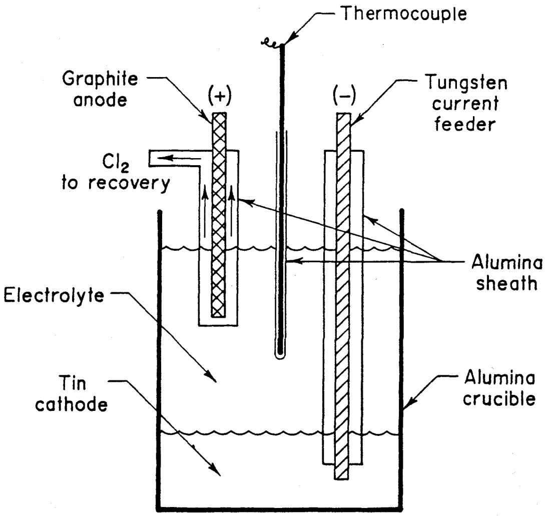

Figure 2. Electrowinning Cell.

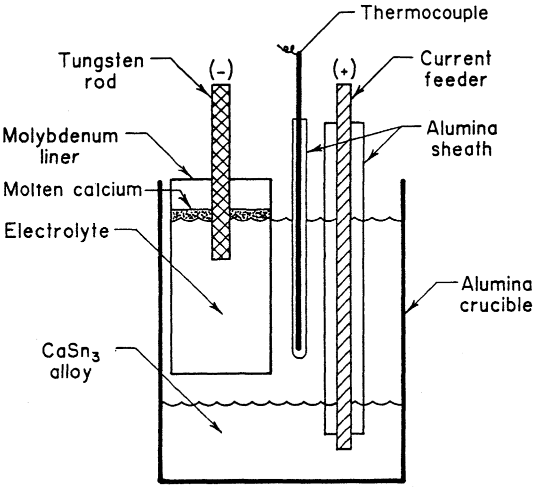

Figure 3. Electrorefining Cell.

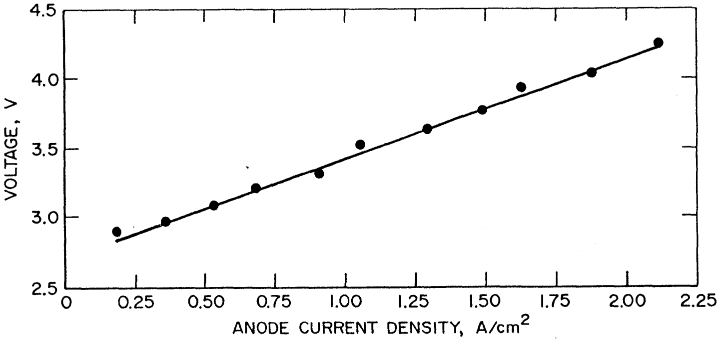

Figure 4. Voltage Versus Anode Current Density for Electrowinning Cell.

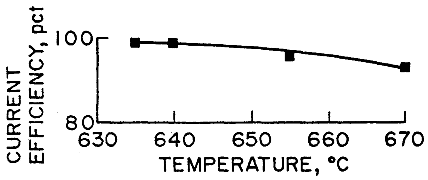

Figure 5. Temperature Versus Current Efficiency.

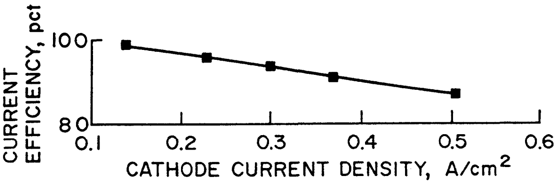

Figure 6. Cathode Current Density Versus Current Efficiency.

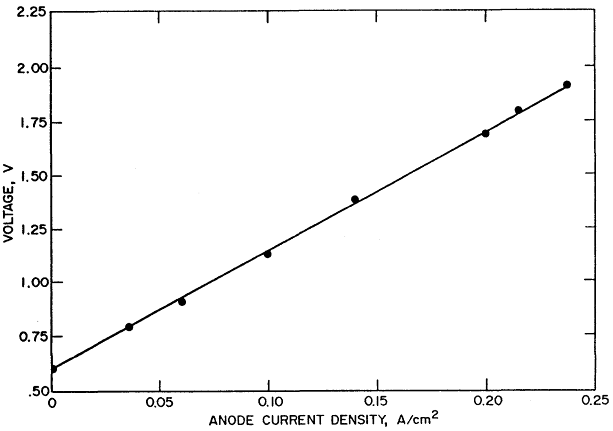

Figure 7. Anode Current Density Versus Voltage for the Calcium Electrorefining Cell.

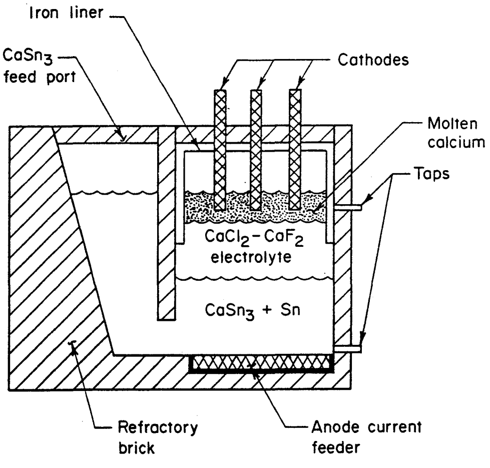

Figure 8. Proposed Electrorefining Cell.

DOI: 10.1149/199017.0600PV

ELECTROWINNING OF LIQUID MAGNESIUM BY USING A STACKED-TYPE BIPOLAR ELECTRODE CELL

Tatsuo Ishikawa, Toshio Narita, and Shoichi Konda

Department of Metallurgical Engineering
Faculty of Engineering, Hokkaido University
Kita-13, Nishi-8, Kita-ku, Sapporo 060, Japan

ABSTRACT

This paper describes the design and construction of a stacked-type bipolar electrode cell for electrowinning liquid magnesium from chloride melts. The laboratory-scale electrolysis was carried out with a bipolar electrode-type cell operated at 50 A current at about 750° C. During electrolysis the metallic particles of magnesium move to the melt surface together with gas bubbles of chlorine. The experimental results are discussed considering the collection of magnesium particles from chlorine gas and the circulation of chloride melt.

INTRODUCTION

Nearly half of the metallic magnesium produced in Japan today is being used as a reducing agent in a Kroll process for the titanium production. Magnesium dichloride as a reaction product in the titanium manufacturing process is used again as a raw material for electrowinning metallic magnesium. It is worth noting that the electric energy consumed in the magnesium process accounts for a large part of the total energy consumption in the titanium manufacturing process.

In order to achieve energy-saving during the electrowinning of aluminum we have developed over a period of ten years a stacked-type bipolar electrode cell and carried out laboratory-scale experiments in NaCl-$MgCl_2$ fused salts containing aluminum chloride.(1) In the course of the investigation we proposed a principle for the design of such stacked-type bipolar electrode cells in order to attain homogeneous melt circulation.(2)

In the present paper, the progress in design and construction of the stacked-type bipolar electrode cells for electrowinning liquid magnesium from mixtures of chloride melts is described. The results of laboratory-scale electrolysis using cells composed of four anode-cathode units are also presented. In the electrowinning process described above, metallic magnesium particles deposited on cathode surfaces move upward in the melts with chlorine gas bubbles evolved on anode surfaces. The experimental results are discussed taking into account the separation of metal particles from the chlorine gas and the circulation of melts in the cells, and an optimum cell construction for high current efficiency is proposed.

EXPERIMENTAL MATERIALS AND PROCEDURES

Electrolytic cell and bipolar electrodes

A transparent quartz tube with an inner diameter of 95 mm and a length of 700 mm was used as the electrolysis cell. It was placed in an electric furnace which had a window for the observation of the inside of the cell during electrolysis. The electric furnace wound with nicrome wire was composed of two parts. The frozen salts at the bottom of the container was melted at the lower part and the fused salts were discharged after an experiment. An end cathode, an end anode, and three bipolar electrodes made of graphite were cylinders with thick walls and with a hole each in the center. The upper and lower surfaces of the columns function as a cathode and an anode, respectively, and they have an inclination of 30° to the horizontal. The thickness of the bipolar electrodes is 30 mm. Each electrode has six projections made of graphite on the side to fit in the center of the container. The five electrodes were separated by three alumina rods (3 mm in outer diameter) each placed between electrodes to construct the four anode-cathode units. The distance between electrodes was kept at 15 mm. Two graphite rods,18 mm in diameter, were attached to the end anode and the end cathode each and one was used for measurements of bath voltage and the other was used for applying current. The rods to the cathode were covered with alumina tubes. All electrodes were supported at the bottom of the end anode by three alumina rods with a diameter of 15 mm and a length of 100 mm.

Determination of electrode sizes

Some preliminary experiments of magnesium electrowinning by using an anode-cathode pair cell showed that the sizes of chlorine gas bubbles were larger than that in aluminum electrowinning. It appears that it would be difficult to circulate the chloride melts in the cell, if the cell was designed according to the same design principle as for aluminum electrowinning. Accordingly for magnesium electrowinning, the cross-sectional area of the clearances between electrode peripheries and the container wall and the cross-sectional area of the center holes of electrodes were determined so as to enlarge such cross-sectional areas from the bottom to the top, keeping the ratio of both cross-sectional areas constant. The values of those sizes are presented in Table 1.

Preparation of melts and supplement of raw materials

A mixture of NaCl 90 m/o-$BaCl_2$ 10 m/o was employed as a supporting electrolyte; the specific gravity of the melt is enough large to float metallic magnesium produced by electrolysis. Magnesium chloride as a raw material was supplied into the cell during electrolysis continuously in a solid state and intermittently in a liquid state and its concentration was kept between 20 and 25 m/o. The cross section of the electrolytic cell with the feeder of solid magnesium chloride is presented schematically in Fig.1.

A liquid mixture of $MgCl_2$ 25m/o-NaCl 75 m/o was added to the electrolysis cell, pre-heated at 700° C and pre-electrolysis was carried out at 30 A for 30 minutes, to remove impurities such as moisture. The $BaCl_2$ predried was added to make up the concentration of 10 m/o to NaCl. In order to supply magnesium chloride in a solid state anhydrous magnesium chloride was melted and solidified as small particles. These were added to the melt by using a rotary valve (see Fig. 1) at a fixed rate from the top of the cell under nitrogen carrier gas.

Discharge of chlorine gas and sampling method of melts for chemical analysis

As shown in Fig.1, the chlorine gas evolved during electrolysis was trapped into the 10 % sodium hydroxide solution by driven by the pumping action of an aspirator. The container of sodium hydroxide was replaced every 30 minutes and the amount of chlorine gas absorbed in it was determined by iodometry. From this the current efficiency for magnesium electrowinning was calculated.

In order to determine the concentration of $MgCl_2$ in the course of an experiment a small amount of the melt was taken at fixed time intervals, carefully, so as not to contain metallic magnesium. The samples were dissolved into twice-distilled water and the concentration of $MgCl_2$ was measured by ICP spectroscopy.

Electrolysis procedures

After addition of $BaCl_2$ to the melts electrolysis was carried out at a current of 50 A for seven hours. During the experiment applied current, bath voltage, and temperature were recorded by a computer system. In the course of electrolysis, the relation between current and voltage was determined at every 30 minutes by lowering current stepwise for short time. The replacement of the sodium hydroxide container and sampling of the melts were also carried out simultaneously. If necessary, liquid magnesium chloride prepared in other vessels was poured in 100 or 200 gram portions to the melts. After electrolysis for a given time, the frozen salts in the bottom of the container were melted to discharge the electrolyte.

RESULTS AND DISCUSSION

Calculation of net current efficiency from the relationship between current and voltage

As reported elsewhere (2), the current efficiency(gross current efficiency) in operation of a bipolar electrode cell is represented as a product of a cell efficiency, η_{cl}, and a net current efficiency, η_{net}. The former is determined in terms of dimensional factors of the bipolar electrode cell and the latter is concerned with electrochemical reactions and/or chemical reactions.

The cell efficiency is estimated by using the decomposition voltage, V_d, and the relation between applied current, I_T, and the bath voltage, V_B under the multi-working state of the cell; the slope, c', and the intercept on the ordinate, d', of the V_B-I_T relations are used for the calculations. In Fig.2, the procedure obtaining η_{cl} from the V_B-I_T relations is described. n is the number of the inter-spacing reaction zone between electrodes. $\beta'$is a constant corresponding to the resistance ratio and I_T^{SM} is the minimum applied current for electrodes to work in bipolar manner. Thus η_{cl} is given as a function of applied current.

Fig.3 shows an example of the V_B-I_T relations obtained during electrolysis and η_{cl} is calculated as 0.818 from c', d', and V_d given as 2.65 V. The values of η_{net} shown in the following figures were obtained by dividing the gross current efficiency by η_{cl}; the gross current efficiency was determined from chemical analysis of evolved chlorine gas.

Results in a stacked funnel-type electrode cell

In the present experiments two kinds of bipolar electrode cells were investigated, one is a cell where funnel-type electrodes are stacked and the other, conical-type electrodes are stacked.

A vertical section of the funnel-type cell is schematically described in Fig.4. In this figure the arrows indicate the flow of the melts in the cell, and magnesium particles deposited on cathode surfaces also move upward through the periphery clearances with chlorine gas evolved on anode surfaces.

As shown in Fig.5, the net current efficiency remains in the range between 40 and 60 %, though it increases a little with time. During the experiments, it was observed that a lot of magnesium particles were caught in the descending flow of the melts through the center holes of the electrodes and were circulating in the system. Therefore the low current efficiency is attributed to the recombination of magnesium with chlorine and/or the electrochemical dissolution on anode surfaces. In order to reduce the descending flow rate of the melts, the diameters of the center holes were enlarged. Also, by supplying liquid $MgCl_2$ to the melts the sizes of chlorine gas bubbles became smaller probably due to impurities like moisture, and it resulted in the increase in the circulation rate of the melts. The net current efficiency obtained in such experiments, as shown in Fig.6, has very small values.

Results in a stacked conical-type electrode cell

As indicated in the previous paragraph, in order to achieve high current efficiency, it is required to lower the descending flow rate of the melt. For this purpose, a cell composed of conical-type electrodes (funnel-type electrodes stacked upside down) was constructed in which the descending flow passed though the periphery clearances.

The vertical section of the upper part of the cell is presented in Fig.7. As shown in the figure, magnesium particles and chlorine gas come together in the center holes. An alumina tube attached to the top of the end cathode works as a guide for magnesium particles so as not to be caught by the descending flow at the periphery clearances. The magnesium particles floating on the melt surface settle as a ring around the inner wall of the container, as shown in the figure.

Fig.8 shows the time variation in net current efficiency and the $MgCl_2$ concentration in the course of the electrolysis experiments at 700° C, using the cell shown in Fig.7. During the experiments solid $MgCl_2$ was added continuously. For the first five hours of the electrolysis the level of the melts was kept at 5 cm above the top of the guiding alumina tube and for the next two hours it was kept at nearly same height as the top. As seen from the figure, the net current efficiency stays in the range from 40 to 50 % for high level of melts, but by keeping the melt level low it reaches nearly 70 %.

Taking into account the above results, electrolysis experiments at low melt levels were carried out at 750° C. The results are presented in Fig.9. The arrows in the figure indicate that a liquid $MgCl_2$ of 200 g was added at that points. From this figure it is shown that a net current efficiency over 70 % is attained by keeping the melt levels nearly same as the top of the guiding tube, though it decreases a little just after the addition of liquid $MgCl_2$ which causes the acceleration of the melt circulation. In order to improve the net current efficiency further, it is preferable not to add $MgCl_2$ to the melts frequently.

CONCLUSIONS

A stacked-type bipolar electrode cell was developed for energy-saving electrowinning of liquid magnesium from magnesium chloride. The cell was composed of three bipolar electrodes, an end cathode, and an end anode; those electrodes were stacked at equal intervals of 15mm from the end anode at the bottom to the end cathode in the top. The active surfaces of the bipolar electrodes have an inclination of 30° to the horizontal.

A cell efficiency was calculated from analysis of the linear relation between applied current and bath voltage under the multi-working state of the cell, and a gross current efficiency was determined by the amount of evolved chlorine gas. A net current efficiency at the electrode surfaces was calculated from both current efficiencies. The performance of the constructed cells was evaluated from the time variation of the net current efficiency.

The constructed cells are classified into two groups by the type of stacking of the bipolar electrodes; the first is the stacked funnel-type electrode design and the second is a stacked conical-type cell. Judging from the net current efficiency obtained from both these cells, the conical-type cells are superior to the funnel-type cells. In order to improve the current efficiency further, it is essential to separate effectively magnesium particles from chlorine gas bubbles and prepare a gentle circulation of melts.

REFERENCES

1. Ishikawa,T. and Konda,S., Proc. of 1st International Symposium on Molten Salts Chemistry and Technology (Kyoto), p.5 (1983).
2. Ishikawa,T., Konda,S., and Narita, T., Proc. of 6th International Symposium on Molten Salts, p.734 (1987). The Electrochem. Soc.

Table 1 Dimension of Graphite Electrode Stacked

Electrode	Outer- diameter (mm)	Center Hole- diameter (mm)
E. Cathode	83.4	23 → (30)
Bipolar 3	86.5	20 → (26)
Bipolar 2	89.4	16 → (21)
Bipolar 1	92.2	11 → (15)
E. Anode	89.4	16 → (21)

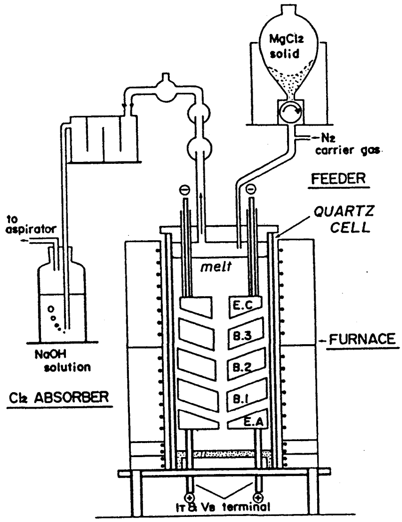

Fig.1 Schematic Diagram of Experimental Apparatus.

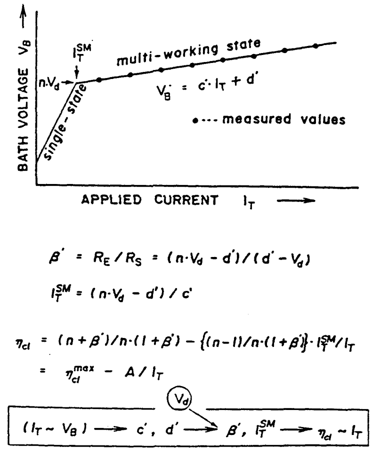

Fig.2 Calculation of Cell Efficiency from Linear Relation between Applied Current and Bath Voltage.

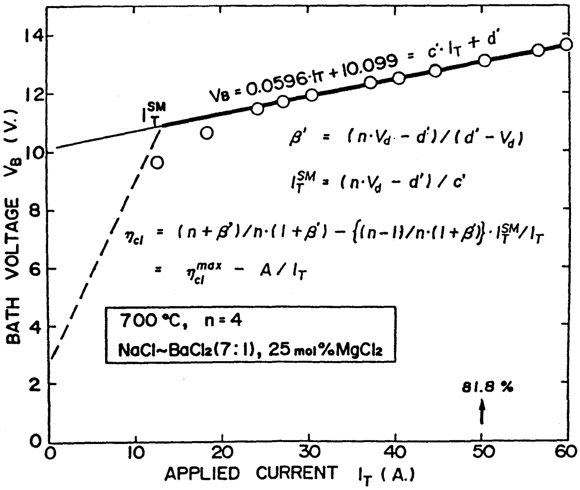

Fig.3 An Example of Linear Relation between Applied Current and Bath Voltage.

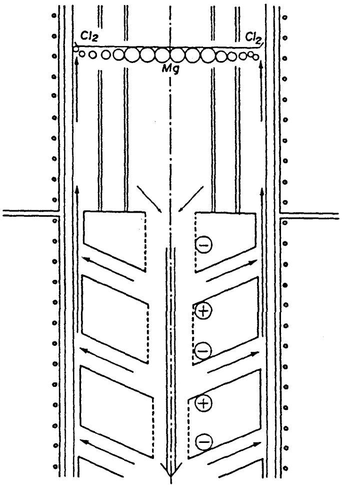

Fig.4 Circulating Path of Chloride Melt in the Funnel-type Bipolar Cell.

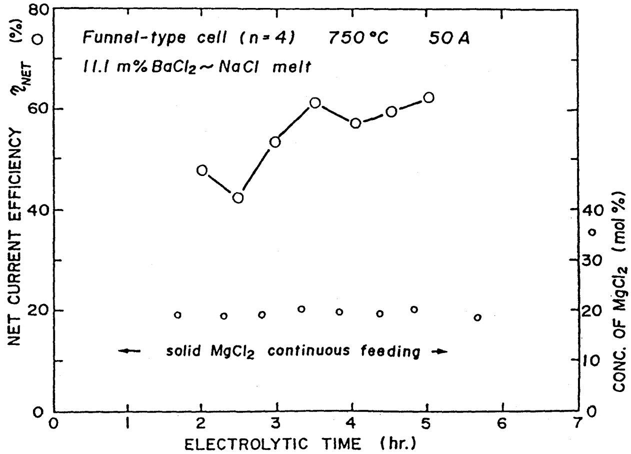

Fig.5 Time Variation of the Net Current Efficiency Calculated and Magnesium Chloride Content in the Melt. Smaller Center-hole and Solid Continuous Feeding.

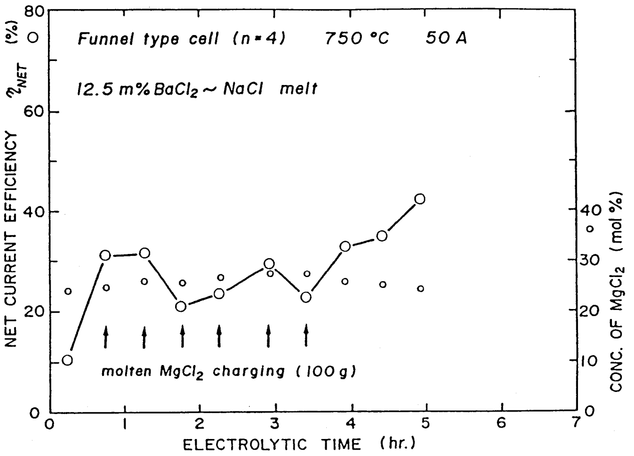

Fig.6 Time Variation of the Net Current Efficiency Calculated and Magnesium Chloride Content in the Melt. Larger Center-hole and Molten Intermittent Charging.

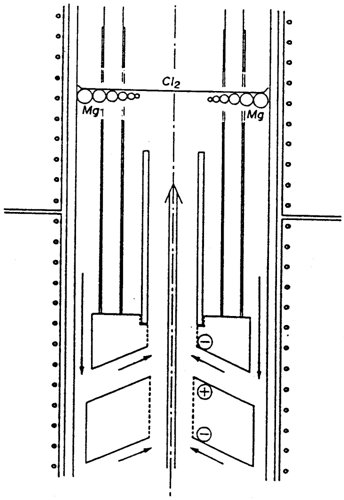

Fig.7 Circulating Path of Chloride Melt in the Conical-type Bipolar Cell.

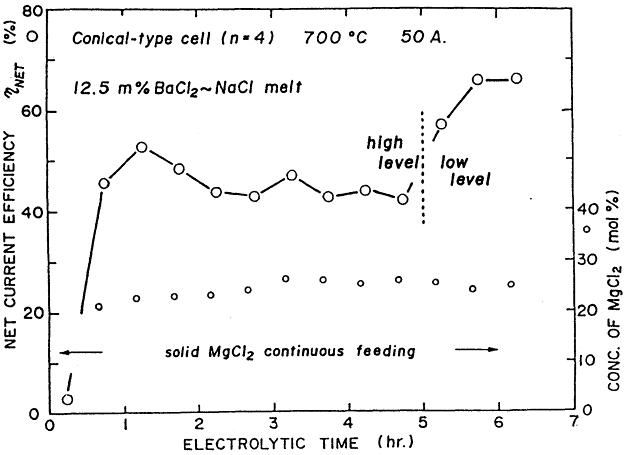

Fig.8 Time Variation of the Net Current Efficiency Calculated and Magnesium Chloride Content in the Melt. Melt Level Changing and Solid Continuous Feeding.

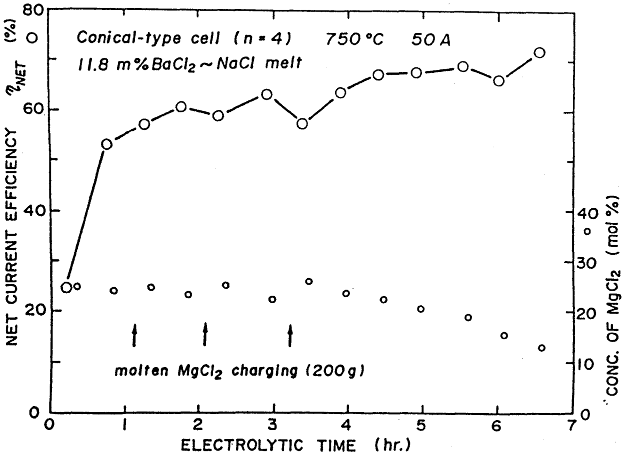

Fig.9 Time Variation of the Net Current Efficiency Calculated and Magnesium Chloride content in the Melt. Melt Level Controlling and Molten Intermittent Charging.

DOI: 10.1149/199017.0611PV

NEW INDUSTRIAL PROCESS FOR ELECTROWINNING OF ND-FE ALLOY

Hideo Tamamura, Tadayoshi Shimo-oka, and Masahide Utsunomiya

Chichibu Research Laboratory
Showa Denko K.K.
1505, Shimokagemori, Chichibu-shi, Saitama-ken, 369-18 Japan

ABSTRACT

The process presented in this paper was developed to commercially produce neodymium-iron alloy by molten salt electrolysis for the first time in the world; the alloy is used principally for manufacture of magnets.

Since rare earth metals combine readily with oxygen, it has been a conventionally common practice both in molten salt electrolysis and metal reduction to reduce them in vacuum or inert atmosphere. On the contrary, however, this process features electrolysis performed intentionally in oxidizing atmosphere.

With this process, concentrations of carbon and oxygen, each of which adversely affects the quality of magnet, decrease so markedly compared with other manufacturing processes that the purity of the alloy reaches 99.9% minimum as RE-Fe.

The process enables the continuous production at high current density and efficiency, and more than twelve months of the stable operation was confirmed.

INTRODUCTION

First of all, neodymium is compared with samarium as raw material for permanent magnets in this paper. Figure 1 (1) gives a history of development of permanent magnets.

As seen in the figure, samarium-containing magnets, which represent the rare earth magnets, replaced ferrite magnets and the excellent advantages of samarium-containing magnets such as smallness and strong magnetic force have helped expand their applications to such areas as OA equipment, camera, camcorder and small-sized audio equipment. The magnets, however, have a drawback as well, that is, insufficient samarium resources, hence its high price.

Under the circumstances, therefore, development of a strong magnet from raw material that is more easily available was hoped for and a neodymium-iron-boron magnet was developed to satisfy such hope.

Not only the neodymium-iron-boron magnet is stronger than samarium-containing magnets but also neodymium resources are about nine times as much, hence the price is about one quarter. Demand for the magnet, therefore, is expected to soar in the foreseeable future.

Figure 2 (2) gives forecast of magnet production until 1997. Production of neodymium-containing magnets is expected to rapidly increase to boost requirement of neodymium as much as 1,500 tons a year in 1992 and 3,000 tons a year in 1997.

The purpose of the study presented in this paper was development of a process by which neodymium of high quality can be commercially manufactured as is or in the form of neodymium-iron for application to neodymium-iron-boron magnets.

Table 1 (3) shows two representative physical properties, melting and boiling points, of transitional and rare-earth metals. As seen in the table, the melting and boiling points of one transitional metal are similar to those of another whereas those of one rare-earth metal are quite different from those of another.

In the case of rare-earth metals, therefore, the manufacturing process is different from one metal to another. The following briefly explains the manufacturing processes of samarium and those of neodymium, in each case of which the metal is manufactured as is or in the form of an alloy.

Samarium is manufactured either by the reduction and diffusion process or by the reduction and vaporization process.

In the reduction and diffusion process, a samarium oxide is reduced by calcium and diffused in cobalt to obtain samarium in the form of an alloy.

$$Sm_2O_3 + 3Ca + 10Co \dashrightarrow 2SmCo_5 + 3CaO$$

A drawback of this process is incapability of recovering high-purity samarium from the alloy.

In the reduction and vaporization process, which takes advantage of a low boiling point of samarium, samarium is reduced by a misch metal and vaporized under high temperature and reduced pressure to deposit and cool on a condenser.

$$Sm_2O_3 + 2R \xrightarrow[10^{-3}-10^{-5}\text{mmHg}]{1,300°C \sim 1,400°C} 2Sm\uparrow + R_2O_3$$

In general, $SmCo_5$ is manufactured by the reduction and diffusion process and Sm_2Co_{17}, from samarium manufactured by the reduction and vaporization process.

Unlike samarium, however, the reduction and vaporization process cannot be applied to manufacture of neodymium because of its high boiling point.

Neodymium can be manufactured by the following three processes.

One is the reduction and diffusion process, in which a neodymium compound is reduced by calcium and diffused in iron.

$$Nd_2O_3 + Ca + Fe\text{-}B + CaCl_2 \dashrightarrow Nd\text{-}Fe\text{-}B + CaO + CaCl_2$$

Note that stoichiometry is disregarded in this chemical formula.

Another is the one in which a neodymium compound is reduced by a metal such as calcium or sodium.

$$NdF_3 + 3Ca + mFe + nCaCl_2 \dashrightarrow 2Nd\text{-}mFe + 3CaF_2 + nCaCl_2$$

Last but not least is the manufacturing process by molten salt electrolysis that is the subject of this paper.

The first and second processes are generally adopted to commercially produce neodymium. No success, however, has so far been reported in commercial production of neodymium or its alloy by molten salt electrolysis except the case presented in this paper, though there are some cases where the metal was produced by molten salt electrolysis on a laboratory scale. Furthermore, no success has ever been reported even on a laboratory scale in obtaining by that method neodymium of such a high purity as required of magnetic material.

Molten salt electrolysis, however, is expected to be the most economical method of all for mass production of neodymium in the future for the following two reasons.

1. It enables continuous operation, hence suitability to mass production.

2. It does not require any expensive metals as reducing agent.

Table 2 (4, 5) compares three typical cases of electrolysis of neodymium or its alloy, thereby enabling the differences to be easily recognized. As seen in the table, the raw material is different in each case and so are the electrolytic conditions, indicating that the three electrolytic processes are basically different from one another.

In the electrolysis conducted by Dr. Shiokawa and Dr. Morrice, the electric current was small and the electrolytic time, short, which fact proves that the electrolysis was of a laboratory scale in their cases.

Figure 3 (4) shows Dr. Morrice's experimental apparatus.

In his experiment, an electrolytic cell is placed in a chamber at first and an inert atmosphere is generated around the cell. Then, direct current is applied to the cell for electrolysis and alternating current, for maintenance of the molten salt temperature. The molten salt is held in a graphite crucible and neodymium is solidified by means of a heat exchanger to precipitate and deposit on the bottom of the crucible.

Although his process is marvelous in that it enables electrowinning of neodymium, the following problems are yet to be solved for continuous commercial production.

One of the problems is discharge of the metal from the crucible, the second, replacement of the electrodes by new ones, the third, continuous feeding of raw material, last but not least, considerable amount of investment on plant and equipment.

From the viewpoint of commercial production, therefore, the processes developed on a laboratory scale by Dr. Shiokawa and Dr. Morrice independently cannot be considered more economical than what is called a metal reduction process. It should also be noted that even if neodymium production by molten salt electrolysis is successful on a laboratory scale, it cannot be always possible on a commercial scale.

In production of a metal, there is always a side reaction to some extent.

In the case of the reduction and diffusion process or metal reduction process, any side reaction product can readily be removed from the reactor because it is basically a batch-by-batch production process, thereby posing no significant problem to commercial production.

Production by molten salt electrolysis, however, is different in that the side reaction product cannot be readily removed from the electrolytic cell because it is basically a continuous operation. If the side reaction product is produced in the amount of 2% of total production every day, the electrolytic cell will be filled up with it within 50 days of operation.

The following are prerequisite for commercial production of neodymium by molten salt electrolysis.

1. Development of the basic technology to produce the metal or its alloy

2. Continuous operation over a long period of time

3. Stable and economical production of high-purity neodymium

Researches were conducted on molten salt electrolysis, aiming at the prerequisite and a proprietary process that enables economically feasible commercial production was finally developed.

Figure 4 shows the experimental apparatus used in the researches. As seen in the figure, an external heating furnace was installed to melt salt as well as to maintain the temperature of the molten salt at a given degree. A graphite anode and an iron cathode, both shaped like a plate, were placed in the electrolytic cell and moved to a given position by means of an electrode lift and carrier. Electrolysis was performed in an oxidizing atmosphere like in the air and not in an atmosphere of inert gas as generally accepted. With this apparatus in use, it has been confirmed that stable and highly efficient electrolysis is possible for production of neodymium.

As for the raw material, an attempt was made to electrolyze a molten salt of lithium fluoride and neodymium fluoride, as Dr. Morrice did, by adding neodymium oxide as raw material.

Since the theoretical voltage for electrolysis of neodymium oxide at 1,000 degrees in Celsius is 2.64 volts and that of neodymium fluoride, 4.84 volts, neodymium oxide was believed to be the electrolytic raw material.

During the experiment, however, something strange was noticed.

Firstly, neodymium was produced in larger quantities than theoretically expected to be derived from neodymium oxide, which fact indicates that the raw material is not neodymium oxide but neodymium fluoride.

Secondly, the graphite anode was consumed, which fact indicates that the raw material is an oxide. It was presumed that such consumption cannot take place if the raw material is a fluoride.

In electrolysis of magnesium chloride, for example, it does not react on the graphite anode and only generates chlorine gas. It was supposed, therefore, that the same must be true of neodymium fluoride because it is a halogenous compound as is magnesium chloride.

Recognition of neodymium fluoride as the raw material, however, contradicts consumption of the graphite anode.

Then, it was judged that the anode gas had a clue to the solution of the contradiction and the gas was analyzed to prove that it is fluorocarbon.

In other words, it was made known that the neodymium fluoride of the molten salt reacts on the graphite anode to generate fluorocarbon, which means that although neodymium fluoride and magnesium chloride are halogenous compounds, their respective reactions on graphite are different from each other. That is, although they are both halogenous compounds, chloride does not react on graphite but fluoride does.

The third phenomenon that seemed strange to us was formation of a strange layer in the bottom of the molten salt. That layer was different in color from the rest of the molten salt.

The layer was checked to find neodymium oxyfluoride in large quantities in it. That explains the neodymium oxide added to the primary molten salt reacted on neodymium fluoride of the molten salt to produce neodymium oxyfluoride that cannot be electrolyzed.

$$Nd_2O_3 + NdF_3 \dashrightarrow 3NdOF$$

As a matter of course, the iron cathode was consumed because of its reaction on the neodymium in the molten salt.

From all those facts mentioned above, it was presumed that it is the neodymium fluoride of the molten salt that was electrolyzed and not the neodymium oxide.

On that presumption, an oxide-free molten salt of lithium fluoride and neodymium fluoride was prepared and combined with additional neodymium fluoride that was to be consumed as raw material and then the oxide-free solution was electrolyzed. The electrolysis was smoothly conducted and neodymium-iron alloy was obtained without formation of the layer of a different color in the molten salt.

The electrolysis conducted presumptively proved the presumption to be right. In other words, it was misunderstood that the raw material of the alloy was neodymium oxide despite the fact that it was one component of the electrolytic solution, that is, neodymium fluoride.

As for the electrolytic atmosphere produced for the process introduced in this paper, it is unique and completely different from the one produced for any other processes of refining rare-earth metals.

In general, rare-earth metals are refined in a vacuum or inert atmosphere. The reasons are as follows.

1. Metals in the molten state burst into flame when exposed to the air.

2. Graphite, molybdenum or tungsten, which is commonly used as raw material of electrodes, is consumed by oxidation in process of refining by electrolysis when exposed to the air.

There are, however, some problems with electrolysis of rare-earth metals in an inert atmosphere, as follows.

1. A closed apparatus is required to maintain an inert atmosphere, hence more investment.

2. The closed apparatus makes it difficult to feed raw material into the electrolytic cell, to take out the product metal and to replace the electrodes with new ones.

3. Part of the graphite anode changes into powdery carbon during the electrolysis, which then gets into the electrolytic solution.

It was then presumed that the powdery carbon causes unstable electrolysis as well as increase of carbon concentration in the product alloy.

It was intended, therefore, to eliminate the powdery carbon by oxidation by positively creating an oxidizing atmosphere instead of an inert atmosphere. Positive creation of an oxidizing atmosphere, however, raised other problems already referred to above in connection with refining of rare-earth metals in a vacuum or inert atmosphere, that is, intense combustion of molten metals and electrode consumption by oxidation in the case of electrolysis.

The following measures were taken, therefore, to solve those problems.

1. Use of the electrolytic solution to protect the alloy from exposure to the air

2. Faster consumption of the graphite anode by electrolysis than that by oxidation, which means an increase of the density of electric current through the anode.

As for elimination of the powdery carbon by positively creating an oxidizing atmosphere, it depends on oxygen concentration in the oxidizing atmosphere. Therefore, a test was conducted by changing the concentration, the result of which is as follows.

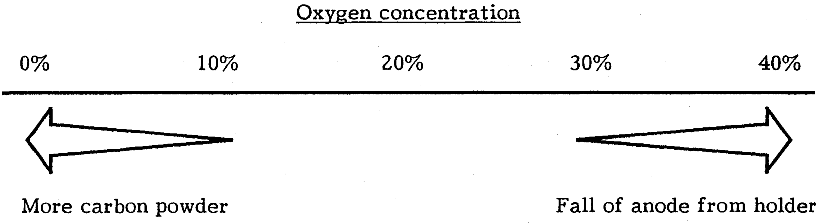

The test revealed that the lower the concentration, the more the powdery carbon and the higher the concentration, the more the consumption to such an extent that the anode will come off from the holder.

The density of the electric current applied to the anode was so satisfactory that stable electrolysis could be conducted in the natural atmosphere, proving that the biggest problem in development of this new process was solved.

Carbon concentration markedly decreased in the alloy, as expected, that is, from several thousands of ppm to about 100 ppm.

One of the features of the process is that although the alloy is produced by electrolysis in an oxidizing atmosphere, oxygen concentration in it is about 100 ppm, which is extremely low compared with that in the alloys produced by other processes.

It is certain, however, that the alloy produced by this process is partially oxidized because there is a partial pressure of oxygen in the electrolytic solution.

The following are prerequisite, therefore, to implement the process in which growth of the alloy by electrolysis is overwhelmingly faster than its oxidation.

1. The current density must be sufficiently high.
2. The growth of the alloy per surface of the electrolytic solution must be high.
3. The efficiency of the electric current must also be high.

The best shape and placement of the electrodes were also studied to produce the largest possible quantity of the alloy in one electrolytic cell.

It is a generally accepted practice to place tubular electrodes in an electrolytic cell as seen in Figure 5 (A). In this case, however, electric current takes the shortest way to the anode to minimize resistance, thereby developing uneven current density over the entire reactive surface of the anode.

As shown in Figure 5 (B), therefore, the electrodes were formed like a plate in such a manner that the same size of the reactive surface of the anode will be maintained as in the case of a tubular electrode and they were so placed in the electrolytic cell as to make the density even over the entire reactive surface. As a result, current efficiency and quantity increased as given in the figure.

Another improvement was made, which can be seen in comparison of Figure 5 (B) and (C). The electrodes were enlarged, making the best use of room available in the case of (B). The striped ends in (C) shows enlargement, which doubled the total reactive surface as well as the alloy production.

The process was further improved by installing another anode on the other side of the cathode as seen in Figure 5 (D), thereby increasing the alloy production more than twofold once again.

It is noteworthy that the alloy production was increased to as much as 7.5 times in the same electrolytic cell.

After a series of improvements like those given above, a commercial electrolytic cell was constructed, which has been in stable operation for more than twelve months now.

Table 3 compares electrolysis of the alloy with that of aluminum which is most advanced of all as commercial molten salt electrolysis.

Although the current capacity is 3 kA for the alloy production electrolysis as against 100 kA for aluminum production, an excellent result is obtained as seen in the table. The current efficiency is 85%, which is larger than the value given in literatures and similar to that for aluminum production. The anode current density is about two times that for aluminum production, which fact proves a high efficiency of the process described in this paper.

This process also has some other advantages over electrolysis for aluminum production. That is, capability of production adjustment and operation without operator at night.

SUMMARY

A new commercial process for production of neodymium-iron alloy by molten salt electrolysis has been described. The production has been continuously under way for more than twelve months with a high productivity as proved by current efficiency of 85% as well as anode current density of 1 A/cm^2.

The process enables production of the alloy, the main component neodymium of which is more than 99.9% in purity. Although carbon and oxygen adversely affect the alloy as magnetic material, the concentration of each element in it is 100 ppm, which is markedly low compared with the alloys produced by other processes.

It should be noted that the raw material to produce neodymium from a molten salt of lithium fluoride and neodymium fluoride plus neodymium oxide is not the neodymium oxide but the neodymium fluoride.

This new process enables electrolysis in an oxidizing atmosphere, which in turn produces a variety of excellent effects. Change in the shape of the electrode combined with installation of an additional electrode has markedly improved the productivity.

REFERENCES

1. Nikkei New Material, April 28, 1988

2. Mr. Hideo Kaneko's Forecast, Rare Metal News, 1432 (1988)

3. The Rare Earth, New Metals Association (1989)

4. E. Morrice and T. A. Henrie, Electrowinning High-Purity Neodymium, Praseodymium, and Didymium Metals from Their Oxides, BuMines Rept., 11, 6957 (1967)

5. Jiro Shiokawa, Takao Kurita, and Toshio Ishino, Production of Neodymium Metal by Molten Salt Electrolysis in Electrochemistry, 496~501, Vol. 35 (1967)

Table 1. Melting and Boiling Points of Transitional and Rare-Earth Metals

	Transitional metal			Rare-earth metal				
	Fe	Co	Ni	Ce	Pr	Nd	Sm	Eu
M.P.	1535	1493	1452	797	935	1024	1072	826
B.P.	3000	3100	2900	3468	3017	3210	1670	1430

Table 2. Three Cases of Molten Salt Electrolysis

	Shiokawa[1)]	**E. Morrice**[1)]	**Showa Denko**[2)]
Raw material	NdCl3	Nd_2O_3	NdF_3
Product	Nd	Nd	Nd-Fe
Electrolytic bath	$KCl\text{-}NdCl_3$	$LiF\text{-}NdF_3\text{-}Nd_2O_3$	$LiF\text{-}NdF_3$
Anode	C (crucible)	C (tubular)	C (plate-shaped)
Cathode	W (tubular)	W (tubular)	Fe (plate-shaped)
Electrode placement	Anode/Cathode	Anode/Cathode	Anode/Cathode/Anode
Atmosphere	Ar	He	Air
Cell material	Graphite	Graphite	Stainless steel
Current, A	5~10	55	3,000
Electrolytic time	1~3 hr	2 hr	>200 days
Heat source	-	Internal heating by alternating current	Internal and external heating

1) Laboratory scale
2) Commercial scale

Figure 1. History of Permanent Magnet

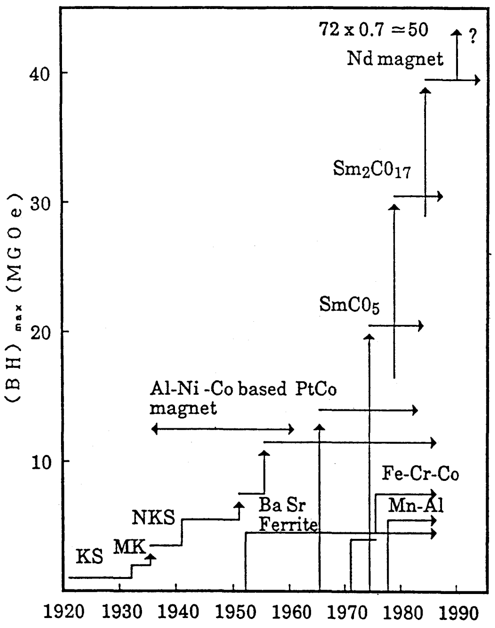

Figure 2. Worldwide Magnet Production Forecast

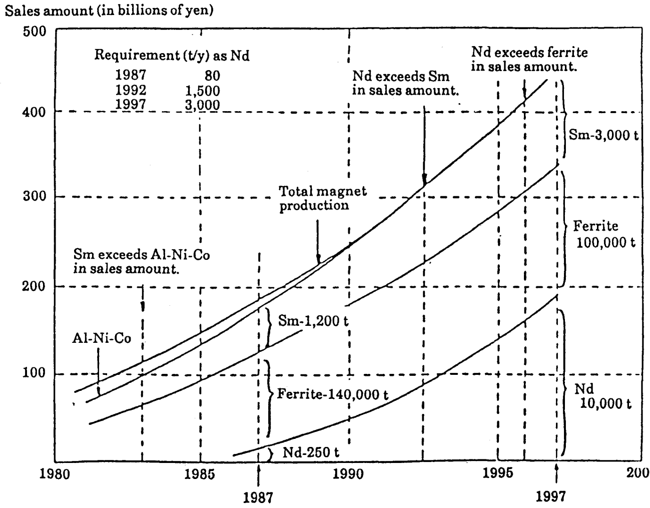

Figure 3 Dr. Morrice's experimental apparatus

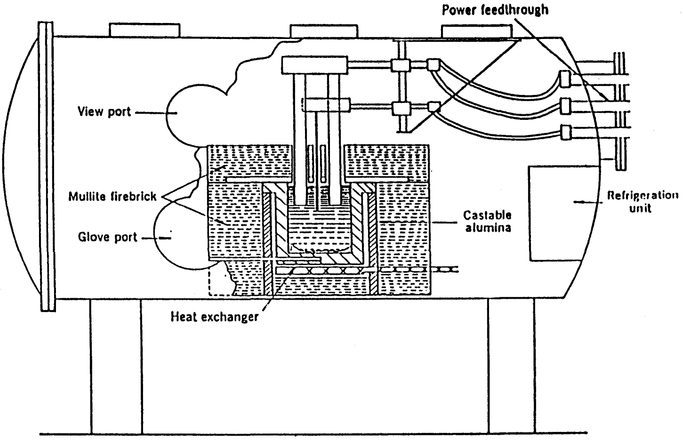

FIGURE 1. - Protective Atmosphere Chamber.

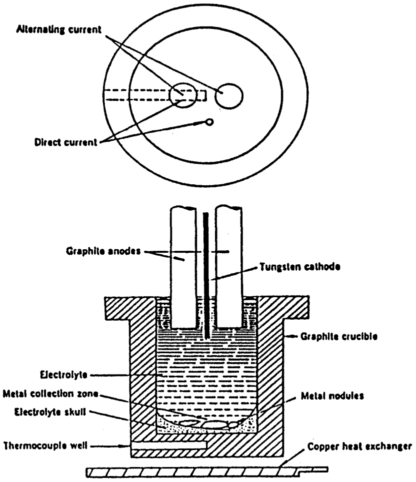

FIGURE 2. - Electrowinning Cell With Alternating Current Applied to Two Anodes.

Figure 4 Showa Denko's Experimental Apparatus

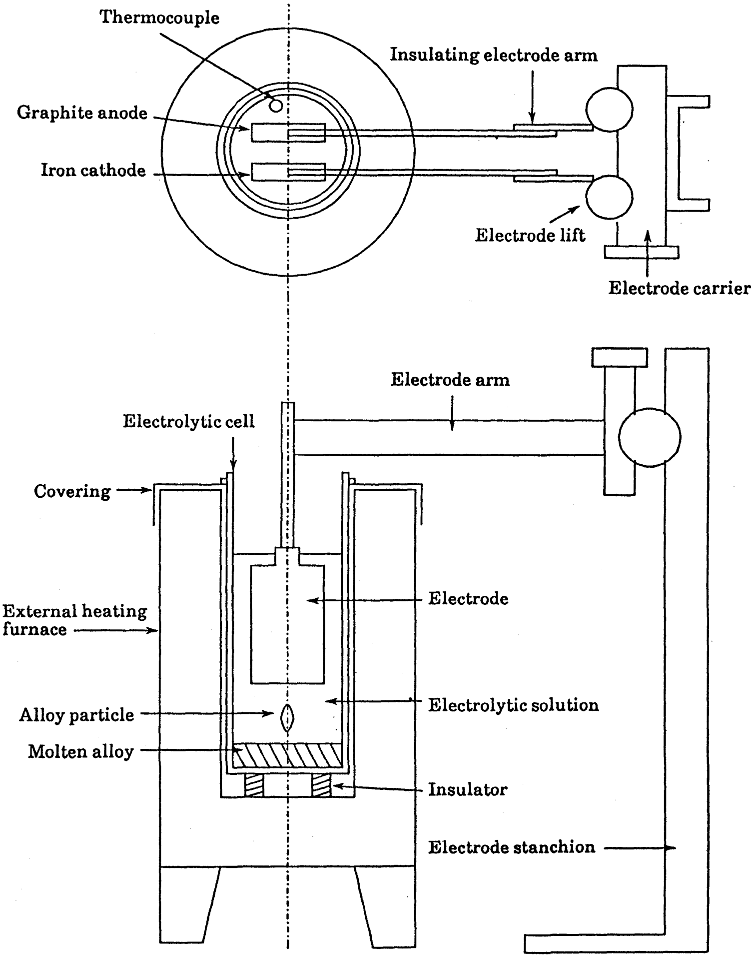

Figure 5 Shape and Placement of Electrodes and Alloy Production

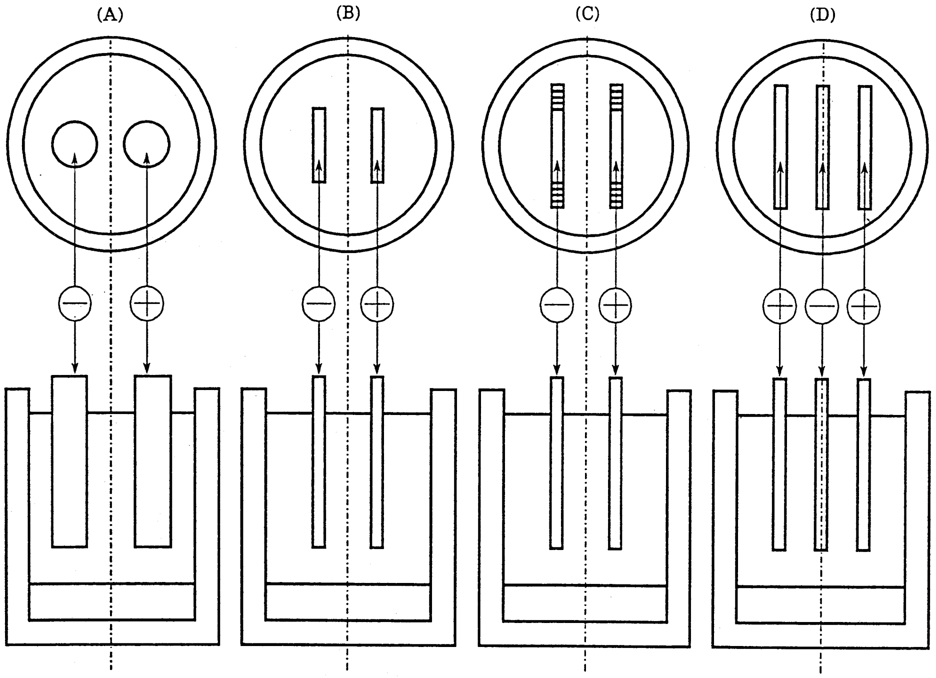

Current efficiency (%)	65	80	83	85
Current quantity (A)	70	100	200	400
Production (ratio)	1	1.8	3.6	7.5

Table 3. Electrolysis for Nd-Fe and Al

	Nd-Fe (as Nd)	Al
Current capacity, kA	3	100
Current efficiency, %	85	80~90
Anode current density, A/cm^2	1.0	0.6
Production adjustment	Possible	Impossible
Overnight operation	Unmanned	Manned

DOI: 10.1149/199017.0626PV

ON THE MECHANISM OF THE PRODUCTION OF ZIRCONIUM AND HAFNIUM METALS BY FUSED SALT ELECTROLYSIS

G.J. Kipouros* and S.N. Flengas

Department of Metallurgy and Materials Science,
University of Toronto, Toronto, Ontario, Canada
M5S 1A4

Abstract

The electrochemical and thermodynamic behaviour of the molten solutions of $ZrCl_4$ and $HfCl_4$ with alkali metal chlorides or fluorides, has been investigated. These solutions should be considered as potential electrolytes for the recovery of the reactive metals Zr and Hf by fused salt electrolysis. Solubilities of Zr in melts containing, the higher valence chloride $ZrCl_4$, have also been investigated. The measurements included the determination of parts of the corresponding phase diagrams, equilibrium vapour pressures and of the solubility of Zr metal in various electrolytes. With respect to the recovery of metals by fused salt electrolysis it is shown that the thermodynamic behaviour of the solutions has a pronounced effect on the mechanism of the electrode reactions.

Introduction

Because of their ability to withstand high temperatures, corrosive environments and of their characteristic mechanical and physical properties, metals like Zr and Hf and their alloys with other metals, are becoming increasingly important in nuclear metallurgy. Nuclear-grade, hafnium-free zirconium metal is used in atomic reactors for structural purposes and for containing the nuclear fuel. Zirconium is irreplaceable because of its very low neutron-capture-cross section. Nb-Zr alloys are also used in the nuclear industry, whilst Hf, which is impermeable to fission neutrons, could be used to suppress ongoing fission reactions.

Compounds of these elements exist over several oxidation states and their chloride or fluoride salts hydrolyze in water. Chlorides like $ZrCl_4$ and $HfCl_4$ are predominantly covalently bonded, sublime at low temperatures and have very low electrical conductivities. Fluoride salts are more ionic but very corrosive towards ceramic containers. Metal-metal

---

* Present address: Department of Mining and Metallurgical Engineering, Technical University of Nova Scotia, Halifax, N.S., Canada.

salt reactions leading to compounds at lower oxidation states are known to be taking place. Zirconium metal at high temperatures reacts with oxygen, nitrogen, hydrogen and carbon. Because of their complex chemical behaviour Zr and Hf are still produced by the batch type Kroll process which involves, respectively, the reduction of $ZrCl_4$ or $HfCl_4$ by Mg metal in a closed reactor (1,2,3). The oxygen content for nuclear grade zirconium is critical as 0.7 wt % oxygen make the metal unworkable and more than 500 p.p.m. oxygen reduces the efficiency of the neutron flux in the reactor. In this respect the closed "airtight" reactor used in the Kroll process ensures that oxygen carried into the zirconium sponge product depends on the oxygen impurity levels present in the $ZrCl_4$ and Mg reagents. Recent advancements in the extraction of Zr have been reviewed elsewhere (3).

For any high temperature electrolytic process to be truly competitive with Kroll, it should be continuous, contamination with oxygen should be avoided at all costs and the metal produced should be in the form of dense coherent ductile deposits, without salt occlusions and to be free of impurities. With regard to Zr and Hf, high temperature electrolysis from molten salt baths appears to be an attractive alternative to Kroll, or to other thermite type processes, all of which are expensive batch operations.

For reasons of thermodynamic stability the choice of electrolytes seems to be restricted to solutions of metal chlorides like $ZrCl_4$ and $HfCl_4$ in alkali metal chlorides, alkali metal fluorides, or their mixtures. The world's production of zirconium metal is based almost entirely on the treatment of two minerals; zircon a zirconium silicate, accounts for the bulk of production, although baddeleyite, an impure zirconium oxide is also treated. Zircon is also available in Canada as a by-product of the Athabasca tar sands. These ore minerals, like all zirconium minerals, contain between 0.5 to 3 percent by weight hafnium which substitutes for zirconium in the mineral's lattice. So great is the chemical similarity between zirconium and hafnium that unless special and costly techniques, like low temperature solvent extraction are followed to remove the hafnium impurity, the zirconium metal will contain hafnium. It is therefore necessary to develop new separation techniques which will be compatible with the high temperature electrolytic process in which Hf-free $ZrCl_4$ will be used as the feed material. Separation of $ZrCl_4$ from $HfCl_4$ in the $Zr(Hf)Cl_4$ mixture by anhydrous processes should be considered as part of any successful high temperature electrolytic process (4,6,7).

The current successful efforts (8) on the direct electrolytic reduction of titianium metal, have sparked renewed efforts to replace the conventional Kroll process for the production of zirconium and hafnium metals or their alloys (30). Some properties of Zr and Hf metals and of compounds of metallurgical interest are shown in Table 1.

Table 1. Metals of Group 4-B and Their Compounds of Metallurgical Interest

Metals and Compounds	Melting Temp. °C	Boiling Temp. °C	ΔH°_f KJ. mole^{-1} at 298 K	Oxidation States	Complex Compounds	Melting Temp. of Complex Compounds (°C)
Zr	1857	(4300)	0	1,2,3,4	-	-
$ZrCl_4$	(437)	335(s)	-980			
ZrF_4	(932)	904(s)	-1910		Li_2ZrCl_6	535
					Na_2ZrCl_6	646
					K_2ZrCl_6	799
					Rb_2ZrCl_6	812
					Cs_2ZrCl_6	817
					A_2ZrF_6	
Hf	2230	(4600)	0	2,3,4	-	-
$HfCl_4$		316(s)	-990			
HfF_4			-1930		Li_2HfCl_6	557
					Na_2HfCl_6	680
					K_2HfCl_6	800
					Rb_2HfCl_6	
					Cs_2HfCl_6	825
					A_2HfF_6	

The work reported in this paper is the culmination of a series of experiments conducted in our laboratory for the purpose of understanding the mechanism of reactive metal recovery and of the thermodynamic and electrochemical behaviour of the appropriate electrolytic solutions.

Thermodynamic Stability of Potential Electrolytes

It has been shown that the volatile vapours $ZrCl_4$ (s.t. 607 K) and $HfCl_4$ (s.t. 589 K) react with alkali metal chlorides, or alkali earth metal chlorides and form stable complex compounds which are stoichiometric and congruently melting. The corresponding reactions may be written as:

$$2ACl_{(solid,\ T)} + MCl_{4\,(vapour\ lat.,\ T)} = A_2MCl_{6\,(solid,\ T)} \qquad (1)$$

where ACl, is an alkali metal chloride like LiCl, NaCl, KCl, RbCl and CsCl.

$$BCl_{2\,(\mathrm{solid,\,T})} + MCl_{4\,(\mathrm{vapour\ lat.,\,T})} = BMCl_{6\,(\mathrm{solid,\,T})} \qquad (2)$$

where BCl_2, represents the alkaline earth chlorides $SrCl_2$ and $BaCl_2$.
M for both reactions 1 and 2 was Zr or Hf.

The methods for the preparation of these compounds have been given in previous publications (9-12).

The $ZrCl_4$-ACl and $HfCl_4$-ACl binary systems have been investigated in several laboratories, including ours, by the cooling curve technique. Congruently melting compounds have been identified by X-ray diffraction and by chemical analysis. The $ZrCl_4$-ACl and $HfCl_4$-ACl binary systems indicate two eutectics and congruently melting compounds such as, A_2ZrCl_6 and A_2HfCl_6, respectively. For the pseudobinary systems A_2ZrCl_6-A_2HfCl_6 a continuous series of solid-liquid solutions of nearly ideal behaviour is indicated. The formation of stable hexachloro-complex compounds was also verified by Raman spectroscopy (13).

Vapour pressures of the reactive MCl_4 vapours in equilibrium with the various complex compounds were measured using high temperature quartz Bourdon type gauges, including a hollow spiral quartz gauge. The latter was able to sustain sudden decompression without breakage and to be inert towards the reactive metal vapours at high temperatures.

The results for the pure compounds Li_2ZrCl_6, Na_2ZrCl_6, K_2ZrCl_6 and Cs_2ZrCl_6 are plotted in Figures 1 and 2. Log P_{HfCl_4} versus $\frac{1}{T}$ for the corresponding hafnium compound are also included in these figures.

The ln P_{MCl_4} versus 1/T curves for the pure compounds inflect at the corresponding eutectic and melting temperatures, as predicted from theory (9,11,14). ln P_{MCl_4} versus 1/T curves are linear only below the eutectic temperatures of the corresponding binary solutions.

$T_{dec.}$ is defined as the temperature at which the equilibrium MCl_4 vapour pressure over a given compound becomes 1 at. Plots of $T_{dec.}$ versus the ionic radius of the alkali metal cation are given in Fig. 3. The decomposition temperature is a measure of the thermal stability of a compound. The higher its decomposition temperature, the more stable is the compound. It is evident that the hafnium complex compounds are more stable thermodynamically than the corresponding zirconium compounds. Between reactive metals the order of thermodynamic stability for the alkali chloride series increases as in the order of Li to Cs. The difference in thermodynamic stability between the Zr and Hf complex compounds has been used as the basis for separating $ZrCl_4$ from $HfCl_4$ (5,6).

Considering the overall MCl_4-ACl binary which is characterized by the formation of the congruently melting compound A_2MCl_6 at 66.6 mole % ACl, there are two important composition ranges to be considered.

1 -The ACl-rich solutions which are in the concentration range representing the pseudobinary ACl-A_2MCl_6, for which $0.67 \leq X_{ACl} \leq 1$.

2 -The MCl_4 rich melts which are in the concentration range representing the A_2MCl_6-MCl_4 pseudobinary, for which $0.67 > X_{ACl} > 0$.

For MCl_4 rich melts the decomposition pressures are expected to be very high. The solutions in this composition range may be considered as molecular mixtures of A_2MCl_6 and MCl_4 and as such are of no consideration for electrolysis purposes.

For ACl rich melts the decomposition pressures of MCl_4 are defined by the equilibrium,

$$2ACl_{(\text{in soln})} + MCl_{4(v)} \rightleftharpoons A_2MCl_{6\,(\text{in soln})} \qquad (3)$$

and by the magnitude of the equilibrium constant K, where

$$P_{MCl_4} = \frac{a_{A_2MCl_6}}{a^2_{ACl}K} \qquad (4)$$

a_{ACl} and $a_{A_2MCl_6}$, are respectively, the activities in the molten solutions. It should be noted that the activity of ACl is not zero at the composition representing the pure A_2MCl_6 compound, because ACl is also part of the overall ACl-MCl_4 system. The activity of ACl is zero only at $X_{ACl} = 0$. For compounds having large K values the solutions are expected to be thermodynamically stable and to exhibit low decomposition pressures of MCl_4.

Pressures of $ZrCl_4$ vapour in equilibrium with molten solutions of ACl-A_2ZrCl_6, at various compositions are given in Fig. 4.

Pressures decrease dramatically as the alkali chloride changes from LiCl to CsCl. These results are in agreement with the theoretical expectations. The addition of an alkali metal fluoride into a solution containing Cs_2ZrCl_6 and CsCl will further enhance the thermodynamic stability of the system due to an exchange reaction which results in the formation of fluoro-complex compounds, as required by,

$$6F^- + ZrCl_6^{2-} = 6Cl^- + ZrF_6^{2-} \qquad (5)$$

Thus, dilute solutions of A_2ZrCl_6 in ACl represent stable potential electrolytes for the recovery of zirconium metal. Similar trends are expected for the $HfCl_4$ solutions.

TABLE 2

Electrolytic solutions for electrorefining at 750°C.*

1. Chloride Rich Melts (in wt %)

	(a)	(b)	(c)	Current densities
X_{CsCl}	0.890	0.839	0.795	0.5 - 6 A/dm^2
X_{KF}	0.062	0.061	0.063	Current efficiency
$X_{Cs_2ZrCl_6}$	0.048	0.100	0.142	about 30 %.
	1.00	1.00	1.00	

2. Fluoride Rich Melts (Binary) (in wt %)

	(a)	(b)	(c)	
X_{ZrF_4}	0.05	-	-	
$X_{K_2ZrCl_6}$	-	-	0.10	Current densities 2 - 20 A/dm^2
$X_{Cs_2ZrCl_6}$	-	0.05	-	Current efficiency 0 - 95 % (Conditioning was an important factor)
$X_{\left(\begin{smallmatrix}\text{NaF-LiF}\\ .6\ \ 1\ \ .4\end{smallmatrix}\right)_{\text{eut.}}}$	0.95	0.95	0.90	
	1.00	1.00	1.00	

3. Fluoride Rich Melts (Multicomponent) (Mole fraction composition)

	a	b	c	d	
$X_{\left(\begin{smallmatrix}\text{KF-NaF-LiF}\\ 0.45\ \ 0.10\ \ 0.45\end{smallmatrix}\right)_{\text{eutectic}}}$	0.975	-	-	-	Potassium metal evaluation
$X_{\left(\begin{smallmatrix}\text{KF-NaF-LiF}\\ 1\ :\ 1\ :\ 1\end{smallmatrix}\right)}$	-	0.943	0.95	0.925	otherwise excellent Zr deposits
K_2ZrCl_6	0.025	0.057	0.05	0.025	
	1.00	1.00	1.00	1.00	

* A total of 51 electrowinning and electrorefining deposition experiments have been conducted. (20,21)

Zirconium metal was recovered by fused salt electrolysis in our laboratory, in both electrowinning (20) and electrorefining (21) experiments. The experimental cells were operated under purified inert gas atmospheres of argon or helium. A system of vacuum sliding gates allowed the withdrawal of a cathode and its isolation after deposition, into a cooling compartment, for subsequent removal without contaminating the melt. This allowed the continuation of electrolysis, using a different zirconium electrode each time, without changing the molten electrolyte in the crucible in the lower hot section of the cell. Electrolytes were made using high purity chemicals and were contained in zirconium or nickel crucibles. Alumina containers or silica were found to be highly reactive towards reduced zirconium species which were always formed during electrolysis. The electrolytic solutions were chosen following the guidelines provided by our previous work on thermodynamic stability, and on metal solubility. Against expectations the electrolysis from all chloride electrolytes yielded disappointing results (20,21). Metal was produced from melts containing various mixtures of $ZrCl_4$ and alkali metal chlorides, but it was dendritic, contained large amounts of salt occlusions and there was evidence of excessive zirconium metal solubility. Best deposits were been obtained with melts containing alkali fluorides. A summary of the most successful melt compositions investigated are given in Table 2.

In all experiments involving all chloride electrolytes the presence of a black material was observed, the nature of which could not be identified. From literature reports (3) it resembles the black pyrophoric material observed in the Kroll reduction. It also appears as "mud" which has been attributed to the production of zirconium powders in a size range of 10 to 20 μm.

Solubility of Zr metal in melts containing Zr^{4+} specie

Reduced zirconium species may form either electrochemically or by the direct chemical reaction between a zirconium metal electrode and an electrolyte containing tetravalent zirconium. The chemical reduction reaction may be written as,

$$\left(\frac{4}{n}-1\right)Zr^{o}_{(s)} \quad + \quad (ZrCl_4)_{(\text{in soln})} \quad = \quad \frac{4}{n}(ZrCl_n)_{(\text{in soln})} \qquad (6)$$

where n could have values like 1,2,3 or 4. Anodic current efficiencies greater than 100% during electrolysis should be an indication of such metal solubility reactions. In addition, the formation of ions in lower oxidations states should create redox couples like Zr^{4+} / Zr^{n+} where, $n < 4$ and the mechanism of the overall reduction process could be altered.

Reaction (6) describes the formation of subhalides and it has been used by various investigators for the preparation and characterization of zirconium and hafnium subchlorides. Recently, non-stoichiometric and cluster-type compounds have been prepared in the solid state. There is generally disagreement regarding the stability of the various subchlorides of the products of the disproportionation reactions. Unknown also remain the solubility of the zirconium subchlorides in molten salts. It has been reported that ZrCl is insoluble and behaves like an electronic conductor. $ZrCl_2$ has been reported as a semiconductor.

It is difficult to determine the nature of the reduced Zr species in solution due to the limitations of analytical techniques and the impossibility of isolating the various reduction reactions. The reducibility of tetravalent zirconium by zirconium metal and the appearance of zirconium species lower than tetravalent were confirmed in separate experiments (20,21) and the results are summarized in Figure 5.

The results are given as number of moles of dissolved Zr metal versus the initial number of moles of $ZrCl_4$ present in the solution. Dashed lines in Figure 5 represent theoretical solubilities in accordance with various possible reduction mechanisms. The results indicate that the solubility of zirconium metal is related to the degree of reduction of tetravalent zirconium in solution. The latter is affected by the size of the alkali metal cation of the alkali chloride present. For example, solutions of $ZrCl_4$ in mixtures of NaCl-KCl, or in molten KCl, appear to have been reduced to monovalent zirconium with a corresponding high solubility of zirconium metal. Solutions of $ZrCl_4$ in molten CsCl are reduced approximately to a mixture of di- and tri-valent zirconium species. The addition of KF or CsF further reduces the solubility of zirconium metal and the zirconium in solution appears to be a mixture of tri- and tetravalent species.

The effect of metal solubility on the potential of a zirconium electrode immersed in a solution of $ZrCl_4$ in the equimolar melt of NaCl-KCl, was also investigated (22). The initial mole per cent of $ZrCl_4$ was 0.85. A second platinum redox electrode was inserted in the same melt and the potentials of these two electrodes were recorded as functions of time. The results are given in Figure 6.

The potential of the zirconium electrode appears to be changing very slowly with time. The shape of the potential versus time curve for the platinum electrode resembles a potentiometric titration curve. Pt acts as a redox electrode and responds to the presence of the reduced zirconium specie which appear during the chemical reduction of Zr^{4+} by the zirconium metal electrode. When equilibrium is reached, the various possible redox potentials and the metal-metal ion potentials representing the equilibrium composition of the melt, are expected to reach a common value. Unfortunately a further thermodynamic analysis with the zirconium system was not possible because of the existence of several simultaneous reduction reactions and of the unknown position of equilibrium.

The effect of metal electrode solubility on the electrode potential was also observed on the $Cr/CrCl_3$ system (23) for which at high temperatures only the Cr^{2+} and Cr^{3+} specie are known to exist. The cell consisted of the Cr metal indicator electrode and a Pt redox electrode both immersed in the same solution of $CrCl_3$ in molten KCl.

The metal solubility reaction may be written as

$$(CrCl_3)_{soln.} \quad + \quad \frac{1}{2}Cr_s \quad = \quad \frac{3}{2}(CrCl_2)_{soln.} \qquad (7)$$

Potential versus time curves for the reacting Cr-electrode, and the Pt-redox electrode were similar to those in Figure 6 and showed that the cell reached equilibrium after several days. At equilibrium both the Cr and the Pt electrodes indicated the same potential.

At this point the Cr/Cr^{2+}, Cr/Cr^{3+} and Pt, Cr^{2+}/Cr^{3+} potentials converged to the same value indicating that reaction 7 had reached equilibrium.

<u>Electrode Potential Measurements in Reacting Cells</u>

Considering the cells,

$$\underset{(-)}{Zr} \quad / \quad \underset{CsCl}{ZrCl_4(x_2)} \quad \underset{\text{Asbestos Fibre Diaphragm}}{//} \quad \underset{CsCl}{AgCl(x_1)} \quad / \quad \underset{(+)}{Ag}$$

Cell A

and,

$$\underset{(-)}{Zr} \quad / \quad \underset{CsCl}{ZrCl_4(x_2)} \quad \underset{\text{Asbestos Fibre Diaphragm}}{//} \quad \underset{CsCl}{ZrCl_4(x_2)} \quad / \quad \underset{(+)}{C, Cl_{2(1\ at)}}$$

Cell B

the corresponding cell reactions are given respectively as,

$$Zr_{(s)} \quad + \quad 4(AgCl)_{soln.} \quad = \quad (ZrCl_4)_{soln.} \quad + \quad 4Ag_{(s)} \qquad \text{Cell A}$$

$$Zr_{(s)} \quad + \quad 2Cl_{2\,(1\ at,g)} \quad = \quad (ZrCl_4)_{soln.} \qquad \text{Cell B}$$

In Cell A, the Ag/AgCl was the reference electrode with silver chloride having the mole fraction of $x_{AgCl} = 7 \times 10^{-3}$.

The cell construction is given in Figure 7.

The Zr indicator electrode was of reactor grade metal, having a 4 mm diameter, connected to a steel rod which served as the electrode lead connection. The electrode could be raised or lowered into the melt through an Edwards vacuum sliding seal.

The reference electrodes were Ag/AgCl, or the standard chlorine electrode, shown in Cells A and B, respectively. These electrodes have been extensively used in previous investigations (24-26). The diaphragm separating the two half-cell compartments was the fused in quartz asbestos strands also described earlier. Because of the reactivity of quartz glass towards the reduced zirconium species, the container was a crucible of Inconel alloy. The cells were operated in the temperature range 700 to 850°C, and all measurements were taken under an inert atmosphere of purified, oxygen free, Helium gas. $ZrCl_4$ in its stable form as Cs_2ZrCl_6 was compressed into pellets in an argon filled dry box and was introduced in the cell through a closed end side feeding tube. Pellets were preweighed and were pushed into the cell by a steel rod magnetically operated. If the dilute solutions are taken as Henrian, the Nernst equation for cell A may be written as

$$E_{cell} \;=\; \left(E^{o}_{f,ZrCl_4} - E^{o}_{f,AgCl}\right) \;-\; \frac{RT}{4F}\ln\frac{(X_{ZrCl_4})_E}{X^4_{AgCl}} \qquad (8)$$

where, $(X_{ZrCl_4})_E$, represent the mole fraction of $ZrCl_4$ in a solution in which reaction 6 is at equilibrium.

$E^{o}_{f(ZrCl_4)}$ and $E^{o}_{f(AgCl)}$ in equation 8 are, respectively, "formal", formation potentials with reference to the infinitely diluted solution "standard state", of unit mole fraction. $(X_{ZrCl_4})_E$ could be significantly different from the initial mole fraction of $ZrCl_4$ in solution due to the metal solubility reactions. However, from Figure 6 it is evident that such metal solubility reactions have very slow rates and (X_{ZrCl_4}) could be taken to be almost identical to the initially X_{ZrCl_4}, if the immersion time for the Zr electrode could be kept to a minimum. Such "instantaneous" potentials were obtained by the following procedure. With the Zr-electrode raised, a pellet of Cs_2ZrCl_6 was fed into the CsCl melt. The zirconium electrode was then immersed into the melt and the emf's were measured for about 15 minutes until they appeared to have stabilized. Then the Zr electrode was withdrawn and the same procedure was repeated. The Nernst plot, at 700°C, of $\log\frac{(X_{ZrCl_4})}{X^4_{AgCl}}$ is given in Figure 8.

The slope of the linear curve is 0.051 as compared with 0.0487 for a 4-electron reduction process at 700°C.

The results indicate that under the chosen experimental conditions no appreciable reduction of Zr^{4+} had taken during the time of a measurement. Furthermore, Henrian behaviour is confirmed from the linearity of the curve. The "formal" formation potential for $ZrCl_4$ in CsCl was calculated against the "standard" chlorine electrode from the "formal" formation potential of AgCl in CsCl, reported elsewhere (26) as 0.972 Volt at 700°C. Thus, the formal potential of $ZrCl_4$ in CsCl, with respect to the chlorine reference electrode, is calculated from equation 8 as $E^{o}_{f(ZrCl_4 \text{in } CsCl)} \;=\; 2.218$ V.

Plots of E_{cell} versus temperature, for various "initial" $ZrCl_4$ compositions are also given in Fig. 9 and 10 and were found to be reproducible during cooling and heating. Such potentials should not be described as "reversible" and their values cannot be used for constructing proper Nernst plots. However, they are useful as representing "threshold" potentials for Zr metal recovery at the indicated compositions and temperatures. Similar plots are also given for the $HfCl_4$-CsCl melts.

TABLE 3

Summary of Formal Potentials For $ZrCl_3$ and $ZrCl_4$ Alkali Chloride Melts (in Volts)

Cell Reaction	Solvent Melt	Temperature (°C)					Reference
		670	700	750	800	900	
$(ZrCl_3) + \frac{1}{2}Cl_{2(g,1at)} = (ZrCl_4)$	KCl - NaCl 1:1	1.266	1.240	1.205	-	-	17
or							
$(ZrCl_3) + 2(ACl) + \frac{1}{2}Cl_{2(g,1at)} = (A_2ZrCl_6)$		-	1.319	1.292	1.271	1.228	28
$Zr_{(s)} + 2Cl_{2(g,1at)} = ZrCl_4$	KCl	-	-	-	1.994	1.917	29
or							
$Zr_{(s)} + 2Cl_{2(g,1at)} + 2(ACl) = (A_2ZrCl_6)$	KCl - NaCl 1:1	1.888	1.863	1.830	-	-	17
	KCl - NaCl 1:1	-	1.843	1.809	1.777	1.714	28
	CsCl	-	2.218	-	-	-	This work.
$Hf_{(s)} + 2Cl_{2(g,1at)} = (HfCl_4)$							
or $Hf_{(s)} + 2Cl_{2(g,1at)} + 2(ACl) = (A_2HfCl_6)$	CsCl	-	(2.2)	-	-	-	This work.

where ACl is KCl, KCl - NaCl (1:1 mole) or CsCl.

Deviations from Nernst behaviour for a 4-electron reduction process are evident in Figure 11 which represents a Nernst plot at 700°C obtained from all the emf measurements given in Figures 8,9 and 10.

The "formal" potential of $ZrCl_4$ in the $CsCl$-$ZrCl_4$ system is located at $X_{ZrCl_4} = 1$, and the straight line representing the 4 -electron slope is constructed using 2.218 V as the starting point.

It may be seen that the dilute solutions of $ZrCl_4$ or $HfCl_4$ are in better agreement with a 4-electron slope than the more concentrated solutions. This behaviour indicates that the tetravalent states are more stable in dilute solutions in which the activities of $ZrCl_4$ or $HfCl_4$, respectively, are also lower, as expected.

There are very small differences between the "threshold" potentials for $ZrCl_4$ and $HfCl_4$ in CsCl melts, as expected from the chemical similarity between Zr and Hf compounds. It follows that the separation of Zr from Hf, by electrolysis of dilute solutions of $ZrCl_4$-$HfCl_4$-$CsCl$ in which $HfCl_4$ content is only 1 to 3 wt% may be possible.

Table 3, presents a summary of measured formal potentials for $ZrCl_4$ in alkali chloride melts and for the redox $ZrCl_3$ - $ZrCl_4$ potential. The data obtained by various authors appear to be in substantial agreement. In the KCl - NaCl melts they indicate that trivalent zirconium may be produced electrochemically at a potential of about 1.2 to 1.3 Volts, which is much lower than the potential of about 1.8 to 1.9 Volts which is required for zirconium metal recovery. The formal formation potential of $ZrCl_4$ in a CsCl solvent melt is much higher, and has the value of 2.218 V., because of the increased stability of tetravalent zirconium in CsCl.

Conclusions

The process for the successful recovery of Zr and Hf metals by fused salt electrolysis should be described as being overwhelmingly controlled by thermodynamic considerations. The solubility of $ZrCl_4$ or $HfCl_4$ in alkali chloride melts and the thermodynamic stability of the resulting solutions are determined by equilibria involving the formation of complex species in solution according to reactions like:

$$2(ACl) + MCl_4 = (A_2MCl_6) \tag{9}$$

where, A, is an alkali metal, and M is Zr or Hf.

The thermal stability of the pure A_2ZrCl_6 compounds and of the solutions of A_2ZrCl_6 and ACl at comparable concentrations increases with the size of the alkali-metal cation. In this sense, the solutions of $ZrCl_4$ in LiCl are the least stable, and solutions of $ZrCl_4$ in CsCl are the most stable in this series. It should also be noted that the solutions of $ZrCl_4$ in alkaline-earth chlorides are even less stable than those in LiCl.

It is evident that in high temperature electrolytic cells in which the parts outside the furnace are at room temperature and act as a condenser, equilibrium conditions cannot be maintained, and industrially useful electrolytic solutions should have escaping pressures of $ZrCl_4$ of no more than 1-2 mm Hg. This requirement restricts the optimum bath compositions to those that contain about less than 10 mole percent A_2ZrCl_6 and to solvent melts that contain alkali-metal cations such as K^+ and Cs^+ and anions like Cl^- and F^-.

The thermodynamic stability of the A_2ZrCl_6 complex compounds in solution also affects the solubility of zirconium metal. In consideration of the possible equilibria between Zr metal and Zr^{4+} species in solution, such as those given in reaction (6), it is reasonable to expect that the position of equilibrium for each reaction will be determined primarily by the state of the zirconium species having the highest valency. Melts that contain $ZrCl_4$ at low activity levels should also be expected to contain the least amounts of zirconium of lower valency. This is in agreement with the trends indicated by the reducibility results where solutions containing cesium chloride, in which the activity of $ZrCl_4$ is very low, were reduced to a lesser extent that those containing NaCl or KCl.

With regard to melts containing fluoride salts, the latter introduce an additional element of stability. Again, within the alkali fluoride salt series, the thermodynamic stability of the compounds A_2ZrF_6 where A is an alkali metal cation should increase as in the order $Li^+ \rightarrow Cs^+$. From such considerations, the expected sequence of thermodynamic stability of Zr^{4+} ions in solution in alkali halide melts should be as follows

$2\,ACl_{(s,l)} + ZrCl_{4(v)} =$ $A_2ZrCl_{6(s,l)}$

Li_2ZrCl_6
Na_2ZrCl_6 ALL CHLORIDE SYSTEMS
K_2ZrCl_6
Cs_2ZrCl_6 $ACl - A_2ZrCl_6$

MIXED CHLORIDE-FLUORIDE SYSTEMS

$2\,AF_{(s,l)} + ZrF_{4(s,l)} =$ $A_2ZrF_{6(s,l)}$ $A_2ZrCl_6 - A_2ZrF_6 -$ ACl or AF

Li_2ZrF_6
Na_2ZrF_6 ALL-FLUORIDE SYSTEMS
K_2ZrF_6
Cs_2ZrF_6 $AF - A_2ZrF_6$

The probable anodic and cathodic reactions in an electrorefining cell may be written as follows.

1. For a chloride type electrolyte, the cathodic reaction is

$$ZrCl_6^{2-} + 4e^- \rightarrow Zr^o_{(s)} + 6Cl^- \tag{10}$$

and side reactions which could lower current efficiencies may be written schematically as

$$Zr^o_{(s)} + Zr^{4+} \rightarrow \begin{matrix} Zr^{+} \\ Zr^{2+} \\ Zr^{3+} \end{matrix} \qquad (11)$$

Redox electrode reaction also causing lower current efficiencies could also be considered, such as

$$Zr^{4+} + e^- \rightarrow Zr^{3+} \qquad (12)$$

and so on. Disproportionation reactions of the type

$$2(ZrCl_2) \rightarrow (ZrCl_4) + Zr^o \qquad (13)$$

which are thought to be responsible for producing metal powders, could also be part of the overall equilibrium process.

The anodic reactions are the opposite of the cathodic processes. In the absence of diaphragms, mass transfer of reduced zirconium species should be taking place and could result in their oxidation to tetravalent zirconium at the anode. In this manner, electrons are consumed without gaining any useful metallic deposit, creating a "redox loop".

2. For a fluoride-type electrolyte, the main cathodic reaction may be written as

$$ZrF_6^{2-} + 4e^- \rightarrow Zr^o_{(s)} + 6F^- \qquad (14)$$

and the side reaction, in addition to possible Zr metal solubility and other redox schemes, may include the potassium evolution reaction

$$Zr + 6KF \rightarrow ZrF_6^{2} + 2K \qquad (15)$$

All these equilibria depend upon the activity levels of the zirconium species in solution and could be controlled through choice of a solvent electrolyte having the appropriate salt components.

The potassium metal producing reaction was found to be predominant in the all-fluoride electrolytes, containing potassium ions, because in such electrolytes Zr^{4+} ions are present at a very low activity state in the form of ZrF^{2-}_6 and reaction 15 is driven to the right.

To avoid potassium metal evolution, it is necessary to add an alkali chloride, which, in effect, increases the activity of Zr^+ ions, probably by an exchange reaction like,

$$ZrF_6^{2-} + 6Cl^- \qquad ZrCl_6^{2-} + 6F^- \qquad (16)$$

which, however, could introduce some zirconium metal reducibility side reactions. Thus, the conditioning of the electrolytes prior to electrodeposition which was observed experimentally is necessary for obtaining good zirconium metal deposits.

It appears that conditioning contributes to the purification of the melt and allows the formation of zirconium species having a high mean valence, from which successful electrodeposition becomes possible.

A promising electrolytic process for Zr-deposition has been reported earlier by Mellors and Senderoff.(27) Their solutions contained ZrF_4 in a ternary solvent melt of NaF - KF - LiF at 750°C. The results confirm the need for a high mean valence state for zirconium and for the absence of reduced zirconium species.

The present results and, particularly, the chemical and electrochemical behavior of the molten salt electrolytes investigated in our laboratory appear to be consistent with these general comments.

The measured "formal" potential of $ZrCl_4$ in CsCl indicates that zirconium metal deposition should be taking place at much lower potentials than the breakdown of the alkali metal chloride electrolyte. Furthermore, in a mixed chloride-fluoride electrolyte the anodic product should be gaseous chlorine.

References

1. R.J.H. Clark, D.C. Bradley and P. Thornton, "The Chemistry of Titanium, Zirconium and Hafnium", Pergamon Press, Volume 19, Toronto, 2nd edition (1975).
2. W.J. Kroll, J. Less Common Metals, 8, 361 (1965).
3. W.W. Stephens, in "Zirconium in the Nuclear Industry" ed. D.G. Franklin and R.B. Adamson, ASTM special publication 824, 5 (1984).
4. J.E. Dutrizac and S.N. Flengas, Canadian Patent No. 863 258, Feb. 1971.
5. S.N. Flengas and J.E. Dutrizac, Metallurgical Trans. B, 88, 377-85, 1977.
6. R.L. Skaggs, D.T. Rogers, and D. B. Hunter, "Review of Anhydrous Zr-Hf Separation Techniques", U.S. Bureau of Mines I.C. 8963, Circular 1984.
7. R. Mallikavjunan and J.C. Sehra, Bull. Mat. Science, 12, 3, 407-34, 1989.
8. M.W. Ginatta and G. Orsello, European Patent No. 210 961, Feb. 4, 1987.
9. R.L. Lister and S.N. Flengas, Can. J. Chem., 43, 2947 (1965).
10. R.L. Lister and S.N. Flengas, Can. J. Chem., 41, 1548, (1963).
11. J.E. Dutrizac and S.N. Flengas, "Adv. in Extractive Metallurgy", Symposium April 17-20 (1967), Inst. Mining and Metallurgy.
12. R.L. Lister and S.N. Flengas, Can. J. Chem.,42, 1102 (1964).
13. G.J. Kipouros, J.H. Flint and D.R. Sadoway, Inorg. Chem., 24, 3881 (1985).
14. S.N. Flengas and P. Pint, Can. Metall. Quarterly, 8, 3, 151-166 (1968).
15. G.J. Kipouros and S.N. Flengas, Can. J. Chem.,56, 11, 1549 (1978).
16. G.J. Kipouros and S.N. Flengas, Ibid.,59, 6, 990 (1981).
17. G.J. Kipouros and S.N. Flengas, Ibid.,61, 9, 2183 (1983).
18. D.A. Asbestas, P. Pint and S.N. Flengas, Can. J. Chem.,5, 1154 (1977).
19. I.S. Morozov and Sun In Chzhu, Russ. J. Inorg. Chem. (English Translation),4, 11, 1179 (1959).
20. P. Pint and S.N. Flengas, Trans I.M.M.,C 29, 87 (1978).
21. G.J. Kipouros and S.N. Flengas, J. Electroch. Soc.,132, 5, 1087 (1985).
22. B. Swaroop and S.N. Flengas, Can. J. Chem., 44, 199, (1966).
23. P. Tumidajski and S.N. Flengas, unpublished results.
24. S.N. Flengas and T.R. Ingraham, J. Electroch. Soc.,106, 8, 714 (1959).
25. A.D. Pelton and S.N. Flengas, J. Electroch. Soc.,117, 1130 (1970).
26. P. Tumidajski and S.N. Flengas, Proc. of the 7th International Symposium of Molten Salts, Montreal, Canada, May 6-11, 1990.

27. G.W. Mellors and S. Senderoff, J. Electroch. Soc., 113, 60, (1966).

28. T. Sakakura and T. Kirihava, Denki Kagaku, 36, 306, (1968).

29. V. Ya. Kydyakov and M.V. Smivnov, Electroch. of Molten and Solid Electrolyt., Russian Transl., 3, 15, (1966).

30. C.F. Warren, European Patent 219157, April 22, 1987. Also E.P. 286176, 286175, and 286230.

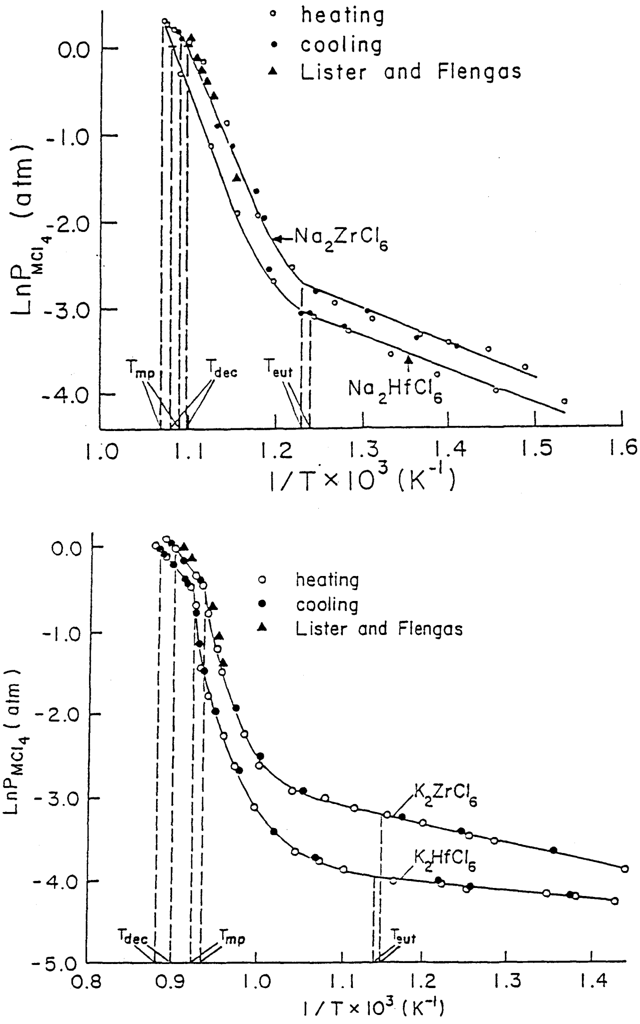

Figure 1. Equilibrium vapour pressures for the pure compounds Na_2ZrCl_6, Na_2HfCl_6, K_2ZrCl_6 and K_2HfCl_6 (15,16), representing the reactions,

$$A_2MCl_{6(s,1,\text{or soln})} = 2ACl_{(s,\text{or soln})} + MCl_{4(v)}$$

Figure 2.

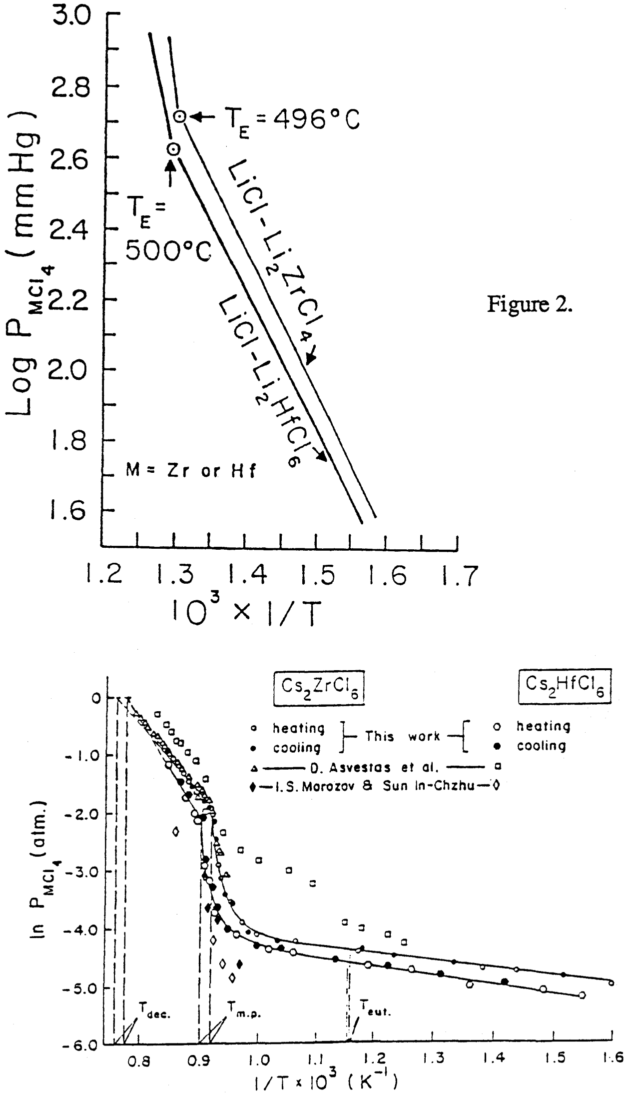

Equilibrium vapour pressures for the pure compounds Li_2ZrCl_6, Li_2HfCl_6, Cs_2ZrCl_6 and Cs_2HfCl_6, representing the reactions, $A_2MCl_{6(\text{pure solid, liq. or soln.})} = 2ACl_{(\text{in soln.})} + MCl_{4(\text{vapour})}$, (11,17,18,19), where, A is an alkali metal and M is Zr or Hf.

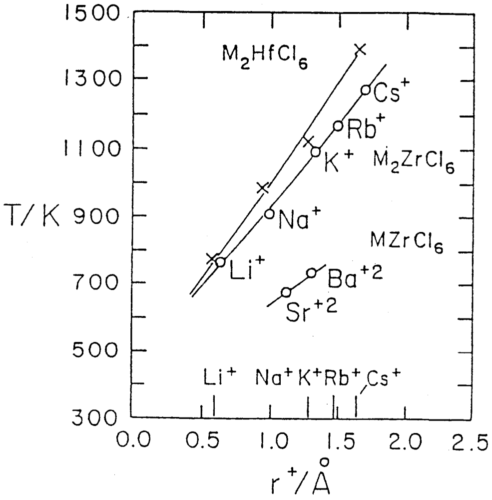

Figure 3.

Decomposition temperatures plotted versus the alkali metal cation radii (Pauling radii) for all the complex compounds investigated. Decomposition temperatures for the alkaline earth compounds $SrZrCl_6$ and $BaZrCl_6$ are also included. (14)

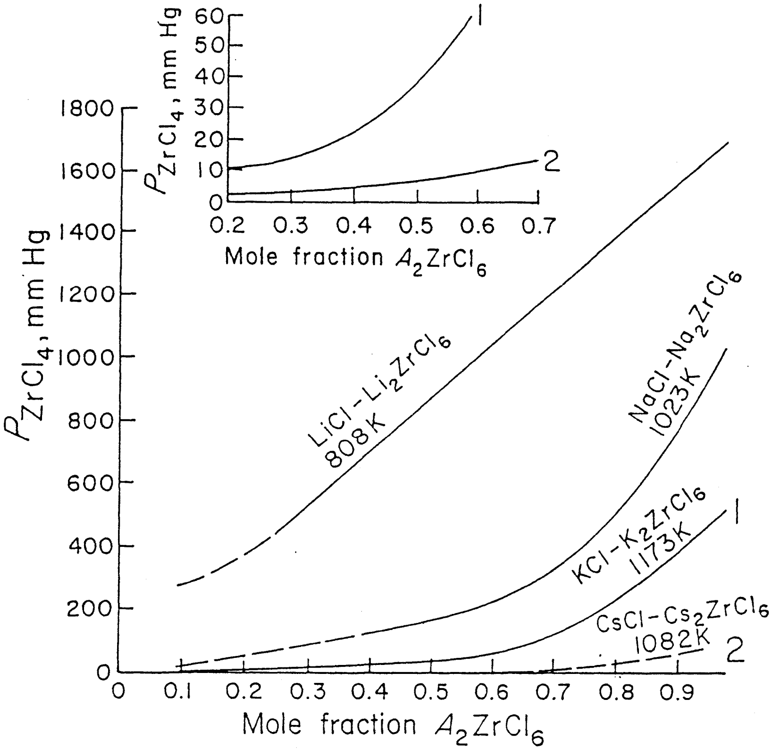

Figure 4. Pressures of $ZrCl_4$ vapour in equilibrium with molten solutions of ACl-A_2ZrCl_6 at various compositions. Pressures have been calculated at the melting temperatures of the pure complex compounds. A is an alkali metal, like Li, Na, K and Cs. (14,21)

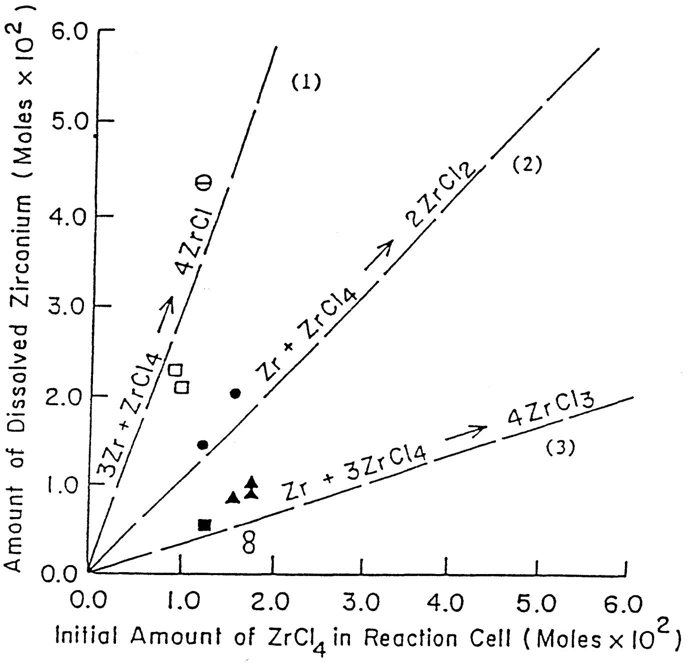

Figure 5. Solubility of Zr metal in various molten salt solutions containing Zr^{4+} specie. (20,21)

Curve 1- KCl-$ZrCl_4$ molten solution at 827°C. Boron nitride container. KCl-$NaCl$-$CsCl$-$ZrCl_4$ molten solution at 700°C. Al_2O_3 container.

Curve 2- $CsCl$-$ZrCl_4$ molten solution at 700°C Boron nitride container.

Curve 3- $CsCl$-$ZrCl_4$ molten solution at 700°C in Al_2O_3 container. $CsCl$-KF-$ZrCl_4$ molten solution at 675°C, in an inconel alloy container. $CsCl$-CsF-KF-$ZrCl_4$ molten solution at 675°C, in an inconel alloy container.

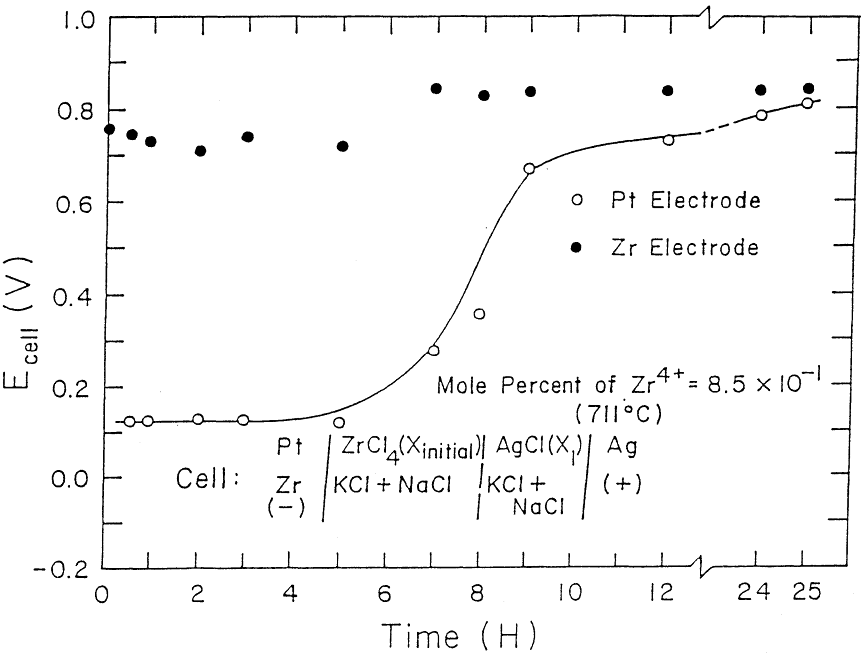

Figure 6. Potential measurements of Zr and Pt electrodes which are immersed in the same solution of $ZrCl_4$ in KCl-NaCl at 711°C. The appearance of a redox potential due to the reduction of Zr^{4+} by the Zr metal is indicated by the rapid potential changes of the Pt electrode. Potential curve is typical of a potentiometric titration. (22)

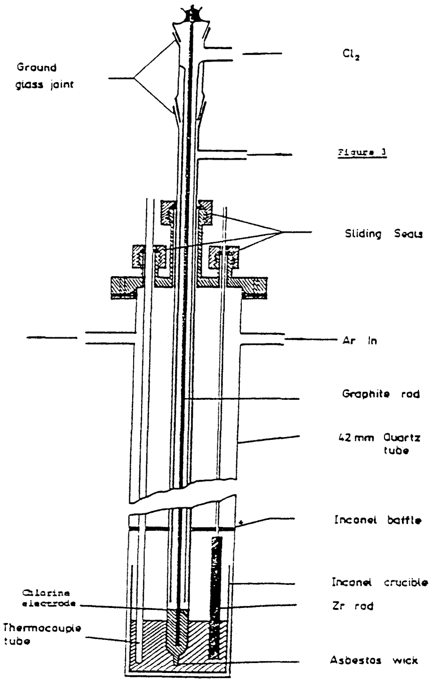

Figure 7.

EMF cell for measuring Zr electrode potentials.

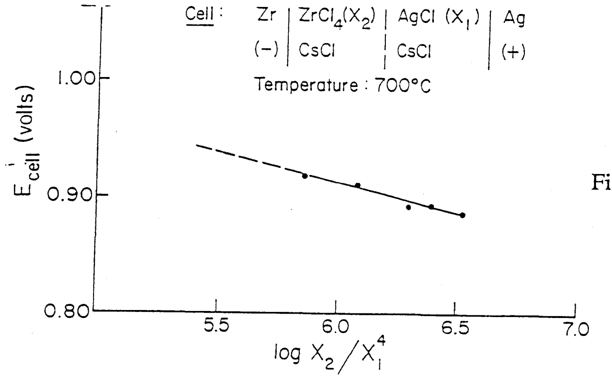

Figure 8.

Nernst plot for "Instantaneous emf" measurements at 700°C, of a Zr electrode immersed in solutions of Cs_2ZrCl_6 in CsCl.

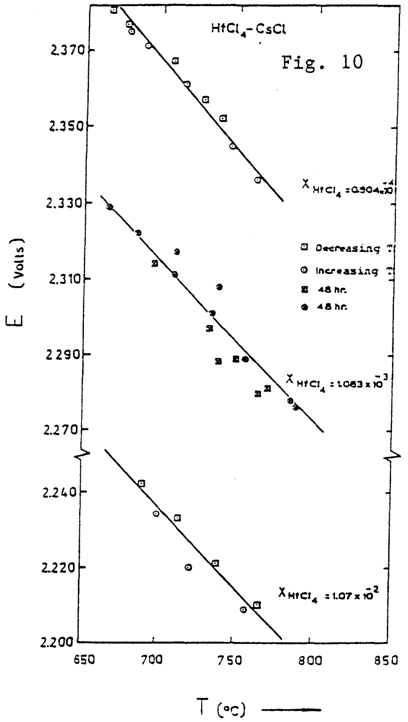

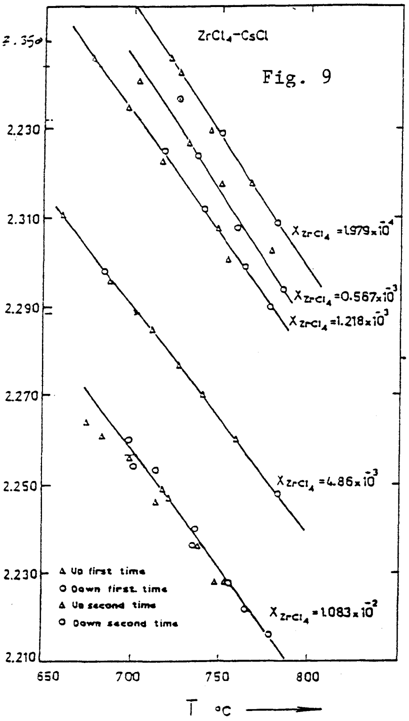

Figure 9. EMF versus temperature for the cell

$$\underset{-}{Zr} \; / \; \underset{CsCl}{Cs_2ZrCl_6(x)} \; \underset{\text{asbestos fibre}}{//} \; \underset{CsCl}{Cs_2ZrCl_6(x)} \; / \; \underset{+}{\underset{1\,at}{C, Cl_2}}$$

Figure 10. EM versus temperature for the cell

$$Hf \; / \; \underset{CsCl}{Cs_2HfCl_6(x)} \; \underset{\text{asbestos fibre}}{//} \; \underset{CsCl}{Cs_2HfCl_6(x)} \; / \; \underset{1\,at}{C, Cl_2}$$

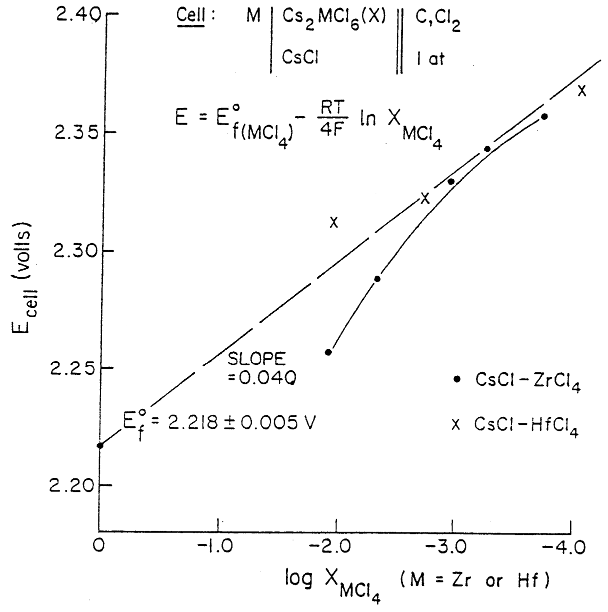

Figure 11. Plot of E_{cell} (V) versus log X_{MCl_4} for systems CsCl-Cs_2ZrCl_6 and CsCl-Cs_2HfCl_6. Dotted line starting from 2.218 V has a slope close to a 4-electron electrode reaction. (s = 0.040 instead of 0.049)

DOI: 10.1149/199017.0652PV

ELECTROPLATING AT HIGH TEMPERATURE. METAL INTERDIFFUSION AT THE SOLID STATE. FAST TRANSPORT IN THE FIRST LAYERS.

Marius CHEMLA and Frédéric LANTELME

Laboratoire d'Electrochimie, UPMC, 4 Place Jussieu,
F 75252 PARIS CEDEX 05 FRANCE.

ABSTRACT

The interdiffusion of metals in the solid state was studied by transient electrochemical techniques at high temperature using molten salts. The method was applied to several binary metal systems and proved to be efficient to determine the diffusion coefficient D as a function of temperature and composition of the generated alloys. The electrochemical response at short time showed a net departure from usual diffusion laws and could be interpreted as revealing a very fast transport in the first layer of the metal interface.

INTRODUCTION

Electrodeposition from fused electrolytes has been used to form protective metallic coatings with good anti-corrosion properties. Three electrolytic deposition processes were developed :-(i) electroplating which produces a constant composition layer of metal coating on the substrate,-(ii) metalliding which involves deposition and solid state intermetallic diffusion,-(iii) alloy deposition by simultaneous electroreduction of two or more cations. When deposition is carried out at high temperature the kinetics of formation of a diffusion layer is fast and it results in the growing of an intermediate alloy and in a good adhesion of the deposited coating to the substrate metal [1].

These technical applications of electrocoating from molten salts involve the study of electrochemical reactions which are under the control of diffusion of electroactive species : diffusion of ions in the liquid electrolyte and of metallided atoms into the solid substrate. These two kinds of diffusion in the electrolyte and in the solid state intervene also when coating is built up by codeposition of several elements; the composition of the coating depends on the diffusion fluxes in the electrolyte and on the interdiffusion in the coating [2].

These mechanisms can be studied quantitatively by use of transient electrochemical techniques. The response is dependent on the time scale under consideration. Most generally, as a consequence of the elementary electrochemical reaction and the high temperature, the electron transfer is fast enough to give a reversible response, and then the surface activity of deposited metal is controlled by the electrode potential.

On the other hand, at very short time the response contains additional terms such as double layer capacity charging or electroreduction of adsorbed species. Moreover, we could find, in most cases, that the current density shows an excess with respect to the computed values at very short time. This result could be assigned to a rapid motion of the deposited atoms in the very first layers of the interface.

EXPERIMENTAL

The method involves the use of polarization cell which have the general configuration

Alloy electrode / Liquid or solid electrolyte / Pure M
M-M' containing M^{n+} (1)

The electrochemical cell for molten salt study was built to be sufficiently tight to sustain a residual pressure of 0.1 torr at 500 °C. In most of our experiments the electrolyte was a eutectic LiCl-KCl mixture whose component salts were of analytical reagent grade Merck. Before each experiment, the mixture was heated in the cell at 130°C under vacuum for 4h, and then heated at the experiment temperature (400 - 540°C) under HCl atmosphere for 6h. Finally, argon gas was kept flowing for a few hours to eliminate HCl.

A special electronic device built in the laboratory was used to deliver potentiostatic or galvanostatic pulses. The pulse and the electrode responses were recorded on double-trace digital oscilloscope Nicolet 310.

The purity of the bath is examined by cyclic voltammetry. The residual current density measured on a platinum electrode was less than 0.1 mA cm^{-2}. In these experiments the metal ions M^{n+} are generated by anodic dissolution of a rod of pure M, the counter electrode being a chlorine electrode [3] set in a separated compartment adapted with a porous connecting tube. The chlorine electrode is also used as reference electrode. For the measurements using cell (1) secondary reference electrode and counter electrode were made of a rod of pure M.

BASIC PRINCIPLE OF THE METHOD

When diffusion is the rate determining step, the concentration changes of electroactive species j (M^{n+} ions or metal atoms M) in the bulk of the two phases (electrolyte and metal) obey the equation

$$\frac{dC_j(x,t)}{dt} = \frac{d}{dx}\left(D_j \frac{dC_j(x,t)}{dx}\right) \qquad (2)$$

where D_j and C_j are the diffusion coefficient and the concentration of electroactive species; x is the distance normal to the electrode. The initial boundary condition is

$$C_j(x,0) = C_j^* \qquad (3)$$

C_j^* is the concentration of electroactive species at equilibrium. The thickness of the diffusing medium is considered to be large compared with the diffusion penetration depth; the condition of semi-infinite diffusion is fulfilled

$$C_j(\infty,t) = C_j^* \qquad (4)$$

The flow of metal away from the cathode surface into the interior of this electrode by diffusion is limited by the flow of metal, J_M, by electrodeposition and equal to it. Therefore the current density, i, associated with the perturbation is (i being positive for an oxidation process)

$$i=-nFJ_M=-\beta nFD_j\left(\frac{dC_j(x,t)}{dx}\right)_{x=0} \qquad (5)$$

with $\beta=+1$ for $j=M^{n+}$ and $\beta=-1$ for $j=M$. The concentration profile $C_j(x,t)$ is calculated by integrating the rate equation (2) for boundary conditions expressing the electrochemical constraints arising from the experimental conditions.

For example, using the potentiostatic method, the variation of current versus time should obey the Cottrell law following the expression:

$$i = nF\ (C_j - C_j^*)\ (D_j/\pi t)^{1/2} \qquad (6)$$

This expression is available as well for the determination of D in the liquid phase as in the solid metal. However the concentration changes in the metal and the electrolyte are interrelated at any time by:

$$\frac{C_M^* - C_M}{C_{M^{n+}} - C^*_{M^{n+}}} = \left(\frac{D_{M^{n+}}}{D_M}\right)^{1/2} \qquad (7)$$

The diffusion coefficient in the solid metal being smaller by a factor 10^5 than in the melt, the potential step is easily adjusted to values such as the current is only dependent on the solid state interdiffusion.

The values of C_j^* and C_j are determined by the values of imposed potentials provided that the activity coefficients of the components are known. In most cases, thermodynamic data are obtained in the literature and then expressed in a polynomial expansion such as:

$$\log \gamma = a + b(1-x) + c(1-x)^2 + \ldots. \qquad (8)$$

x being the molar fraction of the species j.

The linear relationship of i versus $t^{-1/2}$ remains available even if D is c-dependent and whatever the variation of D as a function of c is (Figure 1). This property of the potentiostatic method could be demonstrated by using the Boltzmann transformation, since the limiting conditions of the method can be expressed with the adimensional variable $x.t^{-1/2}$. The calculation shows that the slope of the linear variation of i versus the reciprocal of square root of t leads to the a value of D nearly equal to that corresponding to the concentration near the metal surface [4].

The potential step can be chosen either positive or negative with respect to the equilibrium value, in order to measure D when diffusion phenomenon takes place "in" or "out" the sample material. Most generally for a given composition, the experimental D value does not depend on whether the diffusion take place "in" or "out" the substrate. Moreover the variation of the amplitude of the potential perturbation permits to generate superficial alloys with different compositions. The method then provides an efficient tool for the determination of D values as a function of concentration.

Other electrochemical pulse techniques are used in this investigation. Chronopotentiometry and cyclic voltammetry are useful for obtention of the same informations in the form of signals which are often more readily interpreted [5].

Three mathematical difficulties appear in the resolution of the diffusion equation corresponding to a given technique. 1) The diffusion constant of deposited metal may be quite different from that of the substrate. This property induces a Kirkendall effect and leads to a movement of the internal reference frame. Then only an interdiffusion coefficient D is observed. 2) The interdiffusion coefficient of metal is strongly dependent on the composition of alloy, thus a variable D should be introduced along the concentration gradient. 3) The deposition of metal by itself makes the volume of the substrate to grow. It results in a shift of the interface which must be accounted for as a translation of the abscissae origin.

For these results the equations of chronoamperometry and chronopotentiometry often used by electrochemists are not available in these conditions. We have to develop new mathematical expressions to account mainly for condition 3). Moreover experimental results were checked by numerical simulation of the elementary transport processes using a computer. Figure 2 shows the adjustment of computed values of the potential against time in a typical chronopotentiogram showing the best values of the parameters for adjustment of experimental data.

RESULTS

Several systems forming a solid solution were investigated: copper-gold, lithium-aluminium, lithium-magnesium, aluminium-iron, aluminium-nickel, aluminium-silver and iron-nickel. The first metal is the deposited metal, the second one forms the substrate. Experimental values show that for most of these solid solutions the interdiffusion coefficient D depends on the alloy concentration according to the expansion :

$$\log D = \log D^{\circ} + Ax + Bx^2. \qquad (9)$$

It is also pointed out that the transient electrochemical techniques are convenient and probably a unique means to investigate the transport processes at very short time. Experimental results exhibit a large departure from classical laws and indicate that the rate of the electrochemical reaction becomes faster at short time, i.e. at very short distances from the metal surface (Figure 3). For example, the predicted value of concentration near the interface, as computed from diffusion equations, often leads to molar fraction x larger than unity. In fact, this erroneous conclusion can be excluded by considering the real concentration profile near the interface which is a direct consequence of the Relevant Rapid Diffusion Thickness [2] (Figure 4). Various mechanisms can be invoked to account for this observation : double-layer charging, adsorption of electroactive species, surface roughness.

However careful examination of the results leads to another interpretation, based on a net increase of the diffusion coefficient in the region close to the surface, which takes into consideration the mechanism of diffusion itself. The theories of solid state physics indicate that the atom diffusion is controlled by the concentration N_d of lattice defects. According to the Schottky theory,

$$N_d = A \exp(-\Delta G_d/RT) \qquad (10)$$

where A is the frequency factor depending on the crystal structure. In the theory developed by Schottky the energy of defect formation ΔG_d is the sum of several terms containing mainly the coulombic interaction, the repulsion term, Van der Waals and polarization interactions, and the residual energy at zero point. In the classical lattice defect theory, ΔG_d is deduced from the summation of the potential terms carried out on the whole space (4π solid angle). The important consequence of our results is that, in the very first atomic layers, the number of lattice defects should be different of that in the bulk of the solid, since the integration of potential terms is performed on a smaller solid angle. In the extreme case of the first layer, the summation is made on a 2π solid angle and thus $\Delta G_d(s) = 1/2\ \Delta G_d(b)$. Then the molar fraction of defects at the surface could reach the value $N_d(s)=N_d(b)^{1/2}$, and could be responsible for a steep increase of the diffusion coefficient.

REFERENCES

1. N. C. Cook, Sci. Am., 221, 38 (1969)

2. F. Lantelme, A. Derja and N. Kumagai, J. Electroanal. Chem., 248,369 (1988).

3. M. Chemla and J. Périé, French Patent, N° 1332 518 (1963).

4. F. Lantelme and M. Chemla, Z. Naturforsch., 38a, 106 (1983).

5. F. Lantelme, A. Derja, N. Kumagai and M. Chemla, Electrochem. Acta, 34, 1371 (1989).

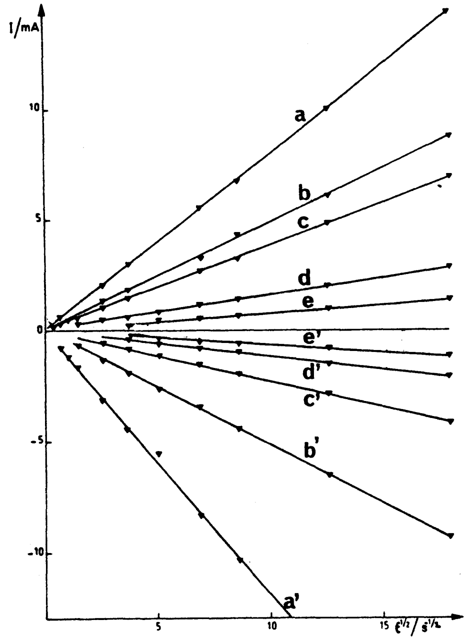

Figure. 1. Analysis of chronoamperograms after potential steps on a copper-gold alloy. Temperature: 402°C. $C^*_{Cu^+}$= 91 10^{-3} M in LiCl-KCl. Alloy composition: C^*_{Cu}= 13.7 mmol cm^{-3}. Electrode area: 1.11 cm^2. Values of the potential step : a, a' ±200 mV; b, b' ±100 mV; c, c' ±50 mV; d, d' ±20 mV; e, e' ±10 mV.

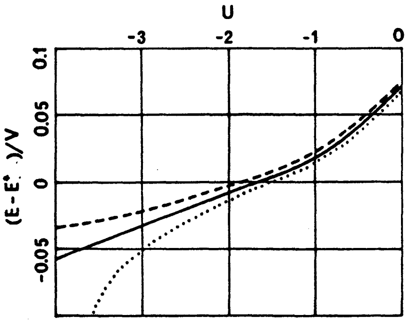

Figure 2. Analysis of a chronopotentiogram for the reduction of Al^{III} in LiCl-KCl at 500°C on a nickel electrode; I=-18 mA, $C^*_{Al^{III}}$= 10^{-4} mol cm^{-3}. S= 0.44 cm^2. η vs. $U=\log[(\tau/t)^{1/2}-1]$; $\eta=E-E^*$, E^* is the equilibrium potential. Influence of the computed value of the transition time τ : Continuous line, τ=6.22 s. Dashed line, τ=5.91 s. Dotted line, τ=6.53 s.

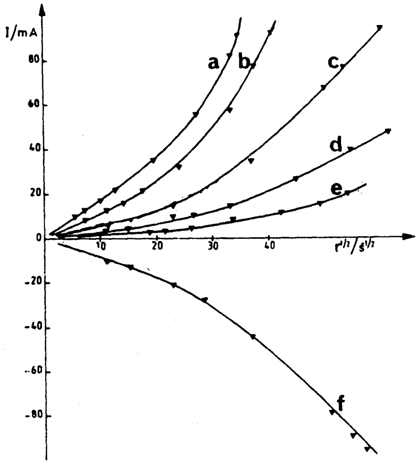

Figure 3. Analysis of a chronoamperogram at short time after potential steps on a copper-gold alloy. Temperature: 554°C . C^*_{Cu+}= 64 10^{-3} M in LiCl-KCl. Alloy composition: C^*_{Cu}= 10.5 mmol cm^{-3}. Electrode area : 0.372 cm^2. Values of the potential step : a, 500 mV; b, 200 mV; c, 80 mV; d, 40 mV; e, 20 mV; f, -80 mV.

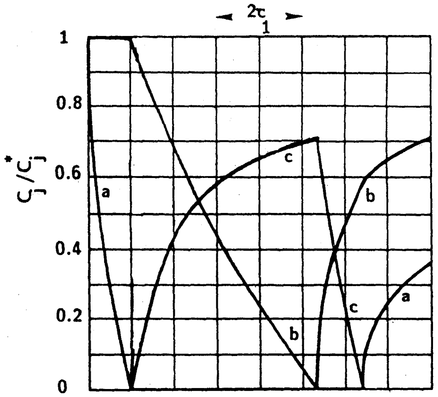

Figure 4. Computed relative concentrations at the surface of a nickel electrode during the reduction of Ni^{2+} and Fe^{2+} in LiCl-KCl at 503°C. Relevant Rapid Diffusion Thickness : 7.2 10^{-8} cm [2]. τ_1 = 0.93 s. Constant current I=-3.4 mA, C^*_{Ni2+} = C^*_{Fe2+} = 7.5 10^{-3} M. S=0.78 cm^2. At the end of the pulse (when C_{Fe2+}= 0) the current was switched off. a= Ni^{2+}; b=Fe^{2+}; c=Fe.

DOI: 10.1149/199017.0661PV

Electroplating of Aluminum from Room Temperature Molten Salts Baths

Setsuko Takahashi
New Materials Research Laboratories
Nisshin Steel Co., Ltd.
7-1, Koyashinmachi, Ichikawa, Chiba 272, Japan

Kazuhiko Ida and Shoichiro Mori
Tsukuba Research Center
Mitsubishi Petrochemical Co., Ltd.
8-3-1, Chuo, Ami, Inashiki 300-03, Japan

ABSTRACT

Room temperature molten salts baths of $AlCl_3$-BPC (1-butylpyridinium chloride) and $AlCl_3$-EMIC (1-ethyl-3-methylimidazorium chloride) were found as an electrolyte to obtain an excellent and high purity Al plating. These are inflamable and are easily operated at room temperature.

The properties of the molten salts and the plated Al film were investigated. The most suitable electrolyte composition was 67mol%$AlCl_3$-33mol%BPC or EMIC. The EMIC bath was better than the BPC bath as an Al plating electrolyte.

The Al plated carbon steel showed high corrosion resistivity.

A continuous Al plating process was developed.

INTRODUCTION

Electroplating of aluminum has been hoped as a surface treatment to improve a corrosion resistance of metals. Because the electroplating of aluminum from an aqueous solution is impossible, non aqueous solution must be used to carry out it. However, organic solvent systems are flamable(1-4), and molten salt systems should be operated at high temperature(5) Therefore, an ambient temperature molten salt electrolyte has been examined to enable a low temperature and safe operation to plate aluminum(6,7).

EXPERIMENTAL

Molten salts baths were prepared by mixing of $AlCl_3$ and BPC or EMIC. Experimentals were done in the dry box under N_2 atmosphere. A polarization curve was mesured by using the Al, Cu, Pt electrodes. Counter electrode was 99.99% Al, and a reference electrode was an aluminum wire in a 67mol%$AlCl_3$-33mol% BPC bath. Sweep rate was 50mV/sec.

The salt spray test was done to evaluate a corrosion resistance of the Al plated sample. The solution was 5%NaCl and the temperature was 35 ^oC. Surface and cross section of the sample was investigated by SEM.

RESULTS AND DISCUSSION

As an ambient temperature molten salt, a mixture of aluminum chloride and onium halide was investigated. The conductivity of the mixture is shown in Table 1. When imidazorium salts are used, high conductivity is obtained. However, when an alkyl group becomes large, the conductivity is close to that of pyridinium salt. In the case of ammonium salt that does not have a double bond, the conductivity is low. Then, a 1-butylpyridinium chloride (BPC) system and a 1-ethyl-3-methylimidazorium chloride (EMIC) system were selected for an Al plating bath.

Some characteristics for these $AlCl_3$-BPC systems are investigated. The results are shown in Fig.1. Specific gravity became large with the $AlCl_3$ concentration. It was 1.34 for the 67mol% $AlCl_3$ bath. Viscosity and conductivity became low with the $AlCl_3$ concentration. When the viscosity decrease, the conductivity usually increases. However, in this case the conductivity decreased, although the viscosity decreased. This was considered to depend on a change of ionic species in the bath. Similarly, a change of some characteristics of EMIC system was also studied (Fig.2). The specific gravity was larger than that of BPC system. The viscosity was smaller and the conductivity was larger than those for the BPC. Furthermore, melting point of EMIC system was lower than that of BPC system.

Cathodic polarization curves for various BPC baths are shown in Fig.3. The potential, where a flow of a cathodic current begins, became noble when the $AlCl_3$ concentration goes up. The curves showed 2 peaks. A peak current of b increased with increasing the $AlCl_3$ concentration. Then, ionic species in the bath was investigated. Fig.4 was obtained by the computer simulation from the equilibrium potential data and the equilibrium constants. In the acidic melt, a major Al ion is $Al_2Cl_7^-$ and in the basic melt, a major Al ion is $AlCl_4^-$. The $AlCl_4^-$ ion decreases gradually with increasing the $AlCl_3$ concentration, while $Al_2Cl_7^-$ ion increases suddenly from 50mol% $AlCl_3$. In Fig.3, curve (1) has no peak b. Moreover, the peak current of b is going up with $AlCl_3$ concentration. Therefore, it was considered that $Al_2Cl_7^-$ is reduced at the potential range of b. Moreover, the reaction of $AlCl_4^-$ and 1-butylpyridinium cation may occur simultaneously at the range of a.

Next, anodic polarization curves were measured(Fig.5). When the $AlCl_3$ concentration increased, a peak current of an anodic reaction decreased. A dissolution reaction of aluminum is an opposite reaction of the deposition. It was conceivable that the peak current became small with $AlCl_3$ concentration as an activity of $AlCl_4^-$ becomes small with $AlCl_3$ concentration. Same tendency was obtained for the EMIC bath. Then, the reactions of aluminum dissolusion and deposition were considered as follows.

(Cathodic reaction) $4Al_2Cl_7^- + 3e \quad Al + 7AlCl_4^-$ (1)
(Anodic reaction) $Al + 7AlCl_4^- \quad 4Al_2Cl_7^- + 3e$ (2)

From above facts, the Al plating bath composition was decided on 67mol% $AlCl_3$ baths.

First, maximum current densities of the plating and the dissolving were actually studied at various temperature as shown in Fig.6. The current densities go up together with temperature for both EMIC and BPC baths. The value for the EMIC was double of the BPC. It was consequently known that the EMIC bath is better than the BPC bath for the Al plating electrolyte. On the other hand, the dissolving current density is about 1/3 of the plating current density. Therefore, the positive electrode area needs 3 times of the negative electrode. SEM photographs of a surface and a cross section of the Al plating were observed. Very smooth coating was obtained.

The corrosion resistance of the Al plated sample was investigated by SST(Table 2). The substrate was a carbon steel precoated with Ni of 0.3um thickness. The chromate processing was not carried out. In the case of 5um plating thickness, 700 hours was required to rust occurrence. It was 1800h and 3000h at 10um and 30um, respectively. It was known that the aluminum plated material gives high corrosion resistance.

Next, a manufacturing process of the Al plating was examined. The flow chart is shown in Fig.7. The degreasing and also washing with acid were carried out. Both of the BPC melt and the EMIC melt strongly react with moisture. As the susbstrate is generally covered with oxides after drying, an adhesive Al plating can not be obtained. Then, the "activation" process was devised as follows. First, an anodic dissolution of the oxides in the BPC bath was attempted. In the case of Pt anode, a current was not observed up to 2.1V(Fig.8). In the case of stainless steel(SUS430), an anodic current flowed. Namely, a possibility of the dissolution of oxides was shown. The "activation" was studied at various electricities at anodic current of 0.4A/dm^2 in the BPC bath(Fig.9). It was expected that the activation of surface completes over 1.3 coulomb/cm^2. Relationship betwen the activation and the adheasion were studied(Fig.10). It was known that a sufficient adhesion for the Al plating is obtained, when the substrate is dissolved in 2 coulombs and then Al is plated on it. As a results, the industrialized Al plating line was completed. The Al plated coil and wire were made by the contineous plating line. The Al plated bolts were made by the barrel type line.

CONCLUSION

Room temperature molten salts of $AlCl_3$-BPC and $AlCl_3$-EMIC were investigated as an Al plating electrolyte. The results are as follows.

1) The most suitable electrolyte composition was 67mol%$AlCl_3$-33mol%BPC

or EMIC.

2) In the case of the EMIC bath, the highest plating current density was 4 and 17 A/dm^2 at 25 and 100^{o}C, respectively.
3) The anode surface area must need 3 times of the cathode.
4) The morphology of the Al plating was dense and smooth.
5) The high corrosion resistivity of the Al plated sample was proved.
6) A continuous Al plating process was developed.

Consequently, many applications of the Al plating are expected.

REFERENCE

1) Richard Suchentrunk, Z. Werkstofftech, 12(1981), 190
2) K.Sekimoto, K.katayama, E.Takeshima, S.Takano, Nisshin Gihou, 28(1973), 53
3) J.F.M. van de Berg, G.A.R. van Dijk and R.E. van de Leest, Metal Finishing, (1985),15
4) G.A.Capuano and W.G. Davenport, J. Electrochem. Soc., 118(1971), 1688
5) Fannin Armand A., J. Electro chem. Soc., 119(1972), 801
6) S.Takahashi, K.Akimoto, I.Saeki, Hyoumen Gijutsu, 4(1989),42
7) S.Takahashi, I.Saeki, K.Tanaka, H.kanezashi, Nisshin Gihou , 60(1989), 36

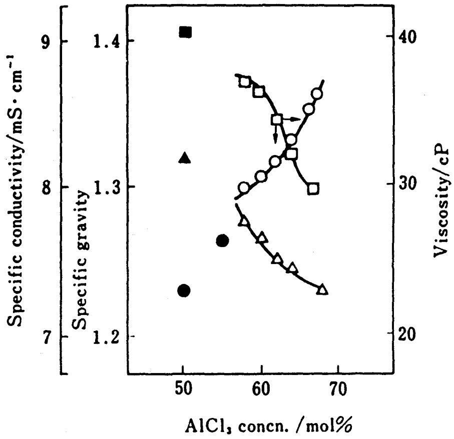

Fig.1 Some characteristics for $AlCl_3$-BPC baths.

○ : Specific gravity, 25°C, ● : 30°C
△ : Specific conductivity, 25°C, ▲ : 30°C
□ : Viscosity, 20°C, ■ : 30°C

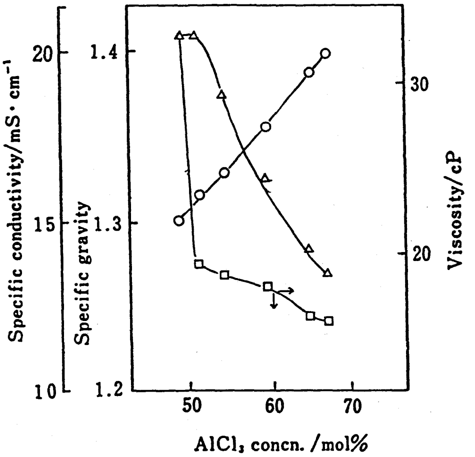

Fig.2 Some characteristics for $AlCl_3$-EMIC baths.

○ : Specific gravity, 25°C
△ : Specific conductivity, 25°C
□ : Viscosity, 20°C

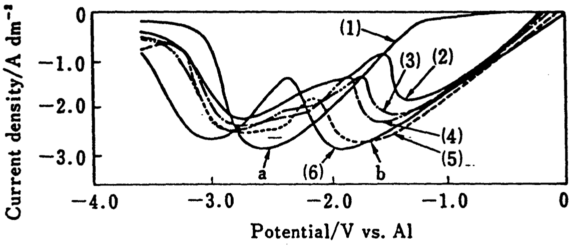

Fig.3 Polarization curves for $AlCl_3$-BPC baths.

Sweep rate : 50 mV/s
(1) 50 mol% $AlCl_3$ - 50 mol% BPC
(2) 58 mol% $AlCl_3$ - 42 mol% BPC
(3) 60 mol% $AlCl_3$ - 40 mol% BPC
(4) 62 mol% $AlCl_3$ - 38 mol% BPC
(5) 64 mol% $AlCl_3$ - 36 mol% BPC
(6) 67 mol% $AlCl_3$ - 33 mol% BPC

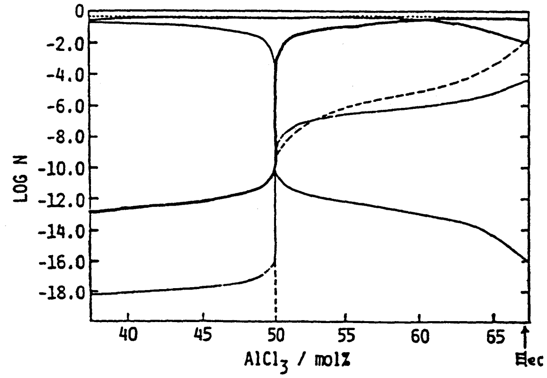

Fig.4 Mole fraction N of the species in the melt at 60 C as afunction of $AlCl_3$ content.

——: Cl^-, ——: $Al_2Cl_7^-$, ——: $AlCl_4^-$,
----: Al_2Cl_6, ——: $AlCl_3$, ·······: BP^+

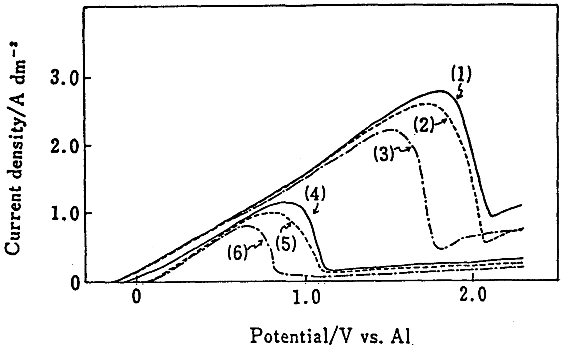

Fig.5 Polarization curves for $AlCl_3$-BPC baths.

Sweep rate: 50 mV/s
(1) 58 mol% $AlCl_3$ - 42 mol% BPC
(2) 60 mol% $AlCl_3$ - 40 mol% BPC
(3) 62 mol% $AlCl_3$ - 38 mol% BPC
(4) 64 mol% $AlCl_3$ - 36 mol% BPC
(5) 66 mol% $AlCl_3$ - 34 mol% BPC
(6) 67 mol% $AlCl_3$ - 33 mol% BPC

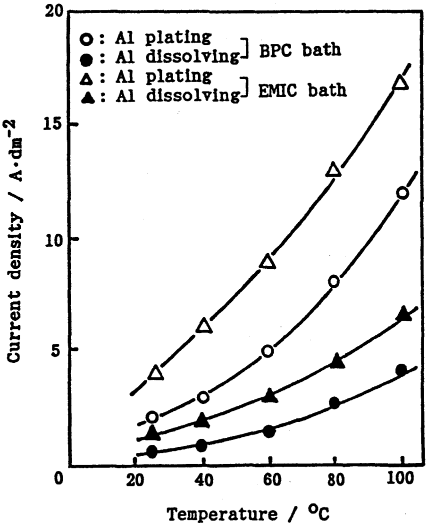

Fig.6 Maximum Al plating and Al dissolving current densities vs. temperatures.

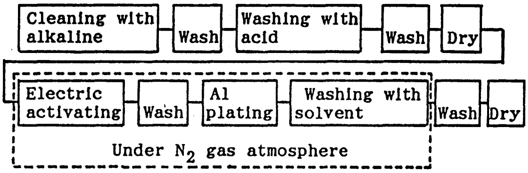

Fig.7 Flow chart of Al plating.

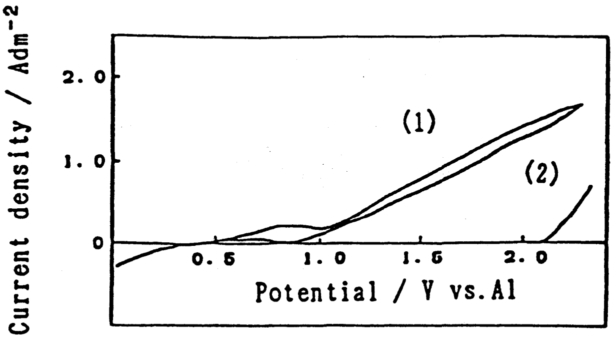

Fig.8 Anodic polarization curves for 67mol%$AlCl_3$-33mol%BPC bath.

(25°C)

(1) SUS 430

(2) Pt

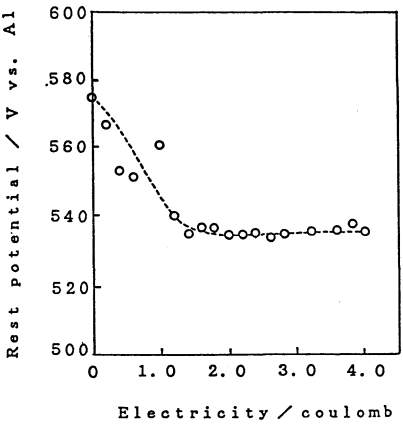

Fig.9 Rest potential after anodic polarization of various electricities at 0.4Adm^{-2} in the BPC bath.

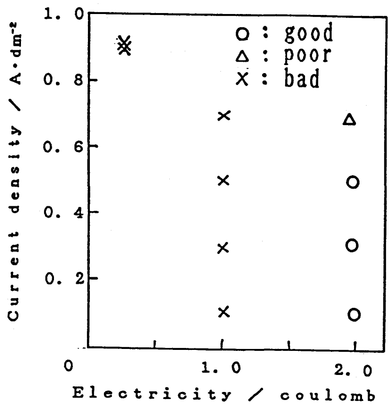

Fig.10 Adhesion of Al plating for various activation conditions.

Table 1 Conductivity of $MCl/2AlCl_3$.

(25℃)

Structure of M⁺	Conductivity (mS/cm)
	7.2
	13.5
	10.3
	8.7
	8.8
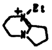	2.9
Et_3MeN^+	2.1

Table 2 Results of salt spray test.

Time (hour)	Coating thickness (no chromate)		
	5µm	10µm	30µm
100	◎	◎	◎
200	◎	◎	◎
300	◎	◎	◎
400	○	◎	◎
500	○	◎	◎
600	○	◎	◎
700	○	◎	◎
800	×	◎	◎
900		◎	◎
1000		○	◎
1100		○	◎
1200		○	◎
1300		○	◎
1400		○	◎
1500		○	◎
1600		○	◎
1700		○	◎
1800		△	◎
1900		×	◎
2000			◎
2100			◎
2200			◎
2300			◎
2400			◎
2500			◎
2600			◎
2700			◎
2800			◎
2900			◎
3000			◎

<Sample>

Substrate:Steel

Precoating:Ni 0.3µm

<Test condition>

Temperature:35℃

Spray: 5% NaCl

DOI: 10.1149/199017.0671PV

DESIGN AND PERFORMANCE OF SIMPLIFIED TEST LOOP FOR MOLTEN-SALT FLOW

H.Hashimoto, K.Amagai, H.Hiyama* and K.Yamamoto*

Institute of Fluid Science, Tohoku University,
Katahira 2-1, Sendai, Japan
*Ebara Research Co., Ltd.,
Honfujisawa 4-2-1, Fujisawa, Japan

ABSTRACT

Thermal-fluid dynamic data are essential for establishing the practical application of molten-salt. A simplified test loop was designed for obtaining highly accurate fundamental data on molten-salt flow. Flow rate calibration, pressure loss measuring and temperature control methods were also examined. Furthermore, assessments were made on flow rate fluctuation, temperature fluctuation and velocity distribution.

INTRODUCTION

Molten-salts have several important industrial applications. Molten-salt loops have been designed for developing molten-salt nuclear reactors (1,2,3). Molten-salts are also used as a substitute for other high temperature molten materials (molten slags, molten rock = lava, and other such high temperature flowing molten systems) in simulation tests. However, very few basic fluid dynamic research data on molten-salt flow are available.

The simplified test loop for molten-salt (hereinafter termed as 'test loop'), designed and developed by the authors, has made it possible to carry out experiments on fluid dynamic properties of molten-salt and to accumulate the much sought basic data on molten-salt flow. To confirm the operational performance of the test loop, studies were made on fluctuations in the flow rate and temperature of the molten-salt. The simple calibration systems of the flow meter and the pressure gauge were also studied. In the following design factors and operational performances of the test loop are presented. Data on the treatment of molten-salt, based on actual flow data, are also introduced.

FEATURES OF SIMPLIFIED TEST LOOP

The design of the test loop includes the following: [1] A test section for carrying out various thermal-fluid dynamic experiments, [2] A compact design, enabling manually controlled operation and easy maintenance, for using the test loop in a relatively small laboratory, [3] Ability to use the molten-salt (KNO_3-$NaNO_3$-$NaNO_2$; 7-44-49 mol%) as the test medium, [4] Ability to calibrate the flow rate measurement devices, and [5] Guarantee of a safe operation up to 400 °C maximum.

Figure 1 and 2 show cross sections and a schematic diagram of the test loop, respectively. The total volume of molten-salt was $0.14m^3$. The 304 stainless steel was used for all part of the test loop as the corrosion rate of SUS304, exposed to molten $NaNO_3$-KNO_3 and under a temperature of 600 °C(5), is approximately $2.5x10^{-2}$mm/year. In an attempt to avoid the thermal stress, a pump, tanks and pipes were mounted in such a way so that they could slide on their fixed support tables. The safety of the operation was confirmed by preliminary tests in which water was used as the medium for checking the cover gas pressure control and the valve behavior for the test loop operation under various pump speed ranges. Water was also used as the medium for investigating the pump and flow meter performances. Some details on the components of the test loop are discussed in the following.

Figure 3 shows a cross-sectional view of the test loop storage tank. The storage tank had an inner diameter of 600mm and a height of 600mm, and could hold $0.14m^3$ of molten-salt. A 6kW power electric resistance heater coils was applied around the tank for melting solid salt. Lagging materials, 150mm in thickness, were wrapped around the exterior tank as well. To enable visual observation of the molten-salt, the tank was equipped with some heat resistance glass windows (60mm diameter and 8mm thickness). Nitrogen was made to flow into the tank as the cover gas for preventing the molten-salt from absorbing impurities from the air. Molten-salt was transported from the storage tank, shown as ① in Figure 1, into a pressure control tank, shown as ② in the same figure, by the pressure force of the cover gas. Figure 4 shows a cross-sectional view of the pressure control tank. It was the same in size as the storage tank and had the function of preventing pressure surges due to temperature and velocity changes in the main loop. The fluctuation of the molten-salt flow rate was realized to be less than 1%. A stainless steel wire mesh was installed in the tank for degassing. Nitrogen gas was used here as a cover gas. The bulk pressure in the main loop molten-salt flow could be adjusted by simply adjusting the cover gas pressure.

A magnetic coupling centrifugal pump, shown as ③ in Figure 1, was installed for molten-salt circulation in the main loop. Figure 5 shows a cross-sectional view of this pump. For cooling the motor and sealing off the molten-salt, the motor torque was indirectly transmitted to the impeller shaft by a magnetic force. The pump performance was set at 10^5Pa and $1.67 \times 10^{-3} m^3/s$ at 1460rpm (see Figure 6). A good correlation between water and molten-salt, over a wide temperature range, was confirmed experimentally with regard to pump performance. The relation between the pump delivered pressure and the flow rate, at various temperature settings, was established as the physical properties of the molten-salt strongly depended on temperature. The total length of a main loop was 5 meters. The piping was covered with electric resistance heating coils and 70mm thick lagging materials. The main loop was also equipped with a 1.5m test section, shown as ④ in Figure 1. All pipes, with the exception of the test section, were set at an angle of approximately 2 degrees in an effort to prevent any residual molten-salt from remaining in the test loop after drainage. Asbestos sealing materials were used at the pipe flange. Results of a chemical compatibility test between asbestos packings and molten KNO_3-$NaNO_3$ confirmed its applicability at temperature ranges below 400 °C (6). The test loop was equipped with several manually controlled ball-type valves for controlling the flow rate. Inconel type metal sealings were applied on the moving parts of the valves. The maximum heat resisting temperature of the valve was up to 500 °C. The pipes and tanks were wrapped with electric resistance heating coils for controlling the temperature. Figure 7 shows the temperature control system. Thermal cement was applied around each heater to enable fast heat conductivity into the wall. Figure 8 shows a cross-sectional view of the insulation materials. Chromel-alumel thermocouples were installed on the pipe and tank walls. A mixing chamber (see Figure 9) was installed in the test section for checking the mean temperature of the flow. Figure 10 shows an example of temperature fluctuation and of input power supply by the heater. It was found that molten-salt temperature can be controlled within an error of 1%.

TEST SECTION

Two contraction nozzles, shown as ⑤ in Figure 1 were installed upstream the test section to enable a uniform flow. Figure 11 shows geometrical data of the nozzles. Nozzle-1 had an exit dia. 37.6mm while Nozzle-2 had that of 21.7mm. A high temperature pressure gauge was used to measure the pressure, while a turbine flow meter was used to measure the mean flow rate. Accurate measurement on the velocity profile of high temperature molten-salt is considered to be very difficult. However, using the convenient analytical method, developed by one of the authors, in which the analytical results agree well with actual water velocity profiles(7), it was possible to estimate the velocity profile at the test section of the loop. Thus, highly accurate velocity distribution data at the inlet of the test section can be obtained through this convenient method with no need to measure the velocity. This analytical estimate, based on the potential flow, can be used for each specific nozzle geometric configuration. Cross-sectional velocity profiles at the nozzle inlet and outlet are assumed to be expressed in simple mathematical curves. If $\hat{u}$ represents the maximum velocity and U represents the cross sectional mean velocity, and the subscripts i and o indicate the nozzle inlet and outlet, respectively (see Figure 12), the relation between the outlet uniformity, defined by $\Delta u_o/U_o = \hat{u}_o/U_o-1$, and the inlet uniformity, defined by $\Delta u_i/U_i = \hat{u}_i/U_i-1$, where Δu means the deviation from the mean velocity U, can be expressed as in the following equation:

$$\Delta u_o/U_o = (D_i/D_o)^{-4} \Delta u_i/U_i + b. \qquad (1)$$

The constant b is determined from Figure 13. The parameter X^* is x_p/L, wherein x_p is the distance from the nozzle inlet to the inflection point of the nozzle and L is the length of the nozzle. For the 36.7mm exit dia. nozzle, $D_i/D_o=4$ and $X^*=0.5$. b is then determined as b=-0.001. Whereby a relatively great non-uniformity $\Delta u_i/U_i = 1$ leads to $\Delta u_o/U_o = 0.003$. This analysis finally reveals that the velocity profile at the nozzle outlet was approximately uniform, except in the area just adjacent to the pipe wall. It was confirmed through many examples of inlet velocity profiles that the use of the nozzles enables uniform and stable flow at the entrance of the test section.

The test section is used for carrying out various thermal-fluid experiments systematically and for measuring systems which require careful operational procedures. It can also be used in the research for developing high temperature pumps, for investigating high temperature gas-liquid multi-phase flow, for investigating the forced convection flow which accompanies local solidification for developing solidification valves, and so on.

SYSTEMATIC MEASUREMENT OF MOLTEN-SALT FLOW

Calibration System by Volumetric Flow Meter; For engineering applications of molten-salt, accurate measurements of flow rates are essential. Such accurate measurements were made possible by a volumetric flow meter shown in Figure 14. The mean flow rate in the test loop was measured by this flow meter through the following procedure. The molten-salt was first introduced to the volumetric flow meter tank by controlling a valve. The ascending time of the molten-salt surface in the tank was then measured by two electric probes set at different levels. The volume corresponding to the distance between the edges of the two probes was then measured taking into consideration the thermal expansion of the tank. One problem that had to be solved was an error by the volumetric flow meter which is caused by the liquid surface disturbances. Introducing a baffle plate solved this problem and the ascending surface of the molten-salt in the tank was stable and completely smooth. The flow rate was adjusted by a valve and by controlling the pump rotational speed for the purpose of minimizing fluctuations in the flow due to shift in the liquid level in the pressure control tank. Such fluctuations were caused by the changes in pump suction head. A 12V, 60Hz alternate current was applied on the electric probes to prevent electrolysis. The maximum error in the flow rate measurement was estimated to be less than 1%. The molten-salt was transported back into the main loop utilizing the nitrogen gas pressure. The experimental results indicated that the calibration system by the volumetric flow meter should be installed in the test loop for the high accuracy measurements.

The turbine flow meter was calibrated by the volumetric flow meter using both molten-salt and water. The rotating speed of the magnetized impeller of the turbine flow meter was measured by a frequency counter. Data on molten-salts in various temperature were in agreement with water within 3%. As can be seen in Figure 15, measurement error in the large flow rate ($6x10^{-4} \sim 3x10^{-3}$ m^3s^{-1}) was +/-2%. If the turbine flow meter is correctly calibrated using water, it can also be used for measuring the molten-salt flow, i.e. calibration using molten-salt becomes unnecessary.

Differential Pressure Measuring System; Two molten-salt manometers were designed and developed for measuring pressure losses between two points in the flow (see Figure 16). The differential pressure was determined by molten-salt levels in these manometers. Heat resisting glass was used for the tubes in the manometers and fluoridate rubber O-rings were used for sealing off the molten-salt and the gas. Nitrogen gas was added into the manometers as a pressure force. This measuring system is also useful when applied with an orifice, or a ventuli flow meter, or a solidification valve, and the like. Figure 17 shows an example of the measurement data of orifice flow meter obtained through this measurement system(4). Measurements on molten-salt using this pressure difference system, show good agreement with those in water. It is suggested that data on water obtained through this system can be used directly for making estimates on the flow rate of molten-salts.

SUMMARY

Various experiments using the simplified molten-salt test loop, which was designed and developed for carrying out thermal-fluid experiments, showed relatively satisfactory results due to simplicity of operation and accuracy in measurement. The test section was found to be adequate for enabling stable flow and temperature. The volumetric flow meter was also found to be effective for use with calibration devices for other molten-salt flow meters. All in all, the molten-salt test loop, including its measurement and control systems discussed in this paper, is useful for obtaining basic data in regard to high temperature molten systems.

REFERENCES

1. W.R.Huntley, Oak Ridge National Labs. Report, ORNL/TM-5540 (1976).

2. W.H.Hoffman and S.I.Cohen, Oak Ridge National Labs. Report, ORNL-2433 (1960).

3. Y.Kato, Molten-Salt, 24, 100 (1981), (in Japanese).

4. H.Hashimoto, K.Amagai, Y.Hosono, M.Takahashi and H.Hiyama, Modern Techniques and Measurements in Fluid Flows, S.Xjong and S.Xijiu, eds., International Academic Publishers, 418 (1989).

5. R.W.Bradshaw, Sandia National Labs. Report, SAND80-8856 (1980).

6. R.W.Bradshaw, Proceeding of 21st IECEC, 828 (1986).

7. T.Suzuki, T.Arai, H.Hashimoto and H.Nasuno, Mem. Inst. High Speed Mech., Tohoku Univ., 58 (1987), (in Japanese).

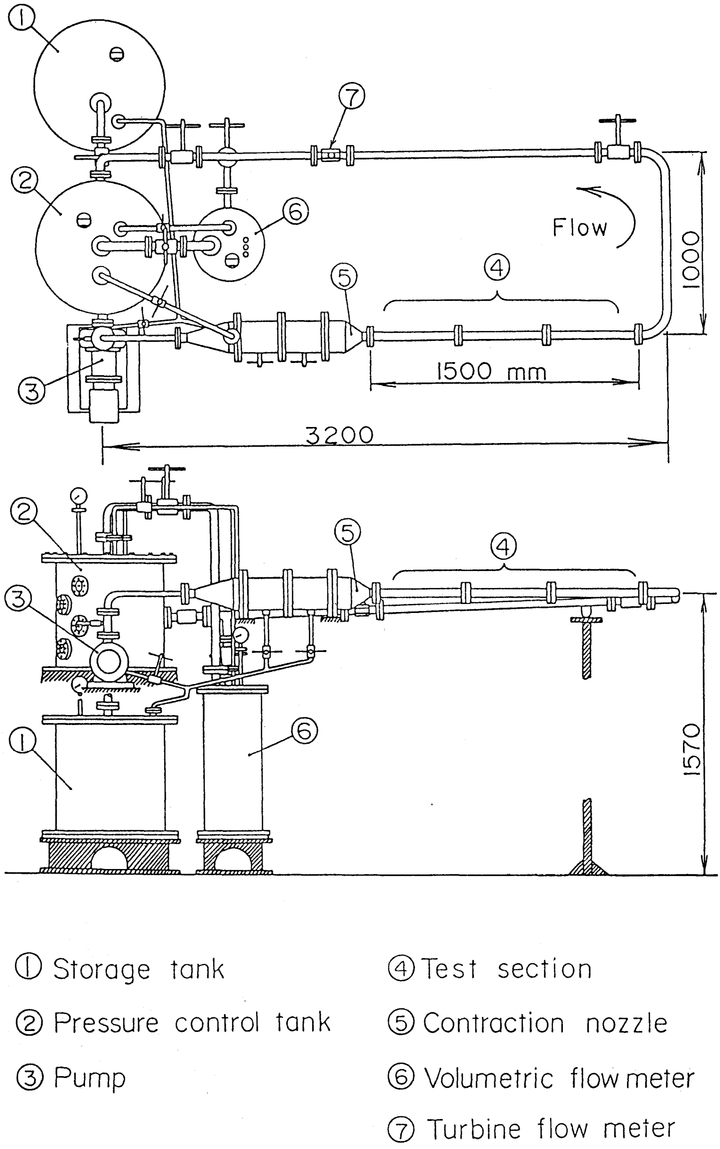

Figure 1. Molten-Salt Test Loop

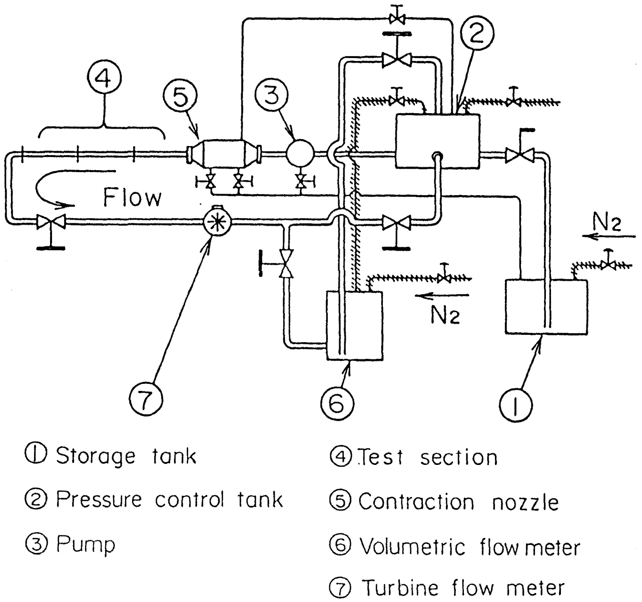

Figure 2. Schematic Diagram of Test Loop

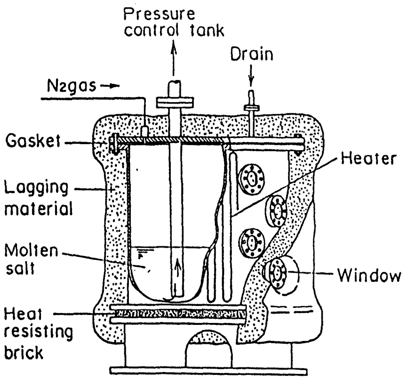

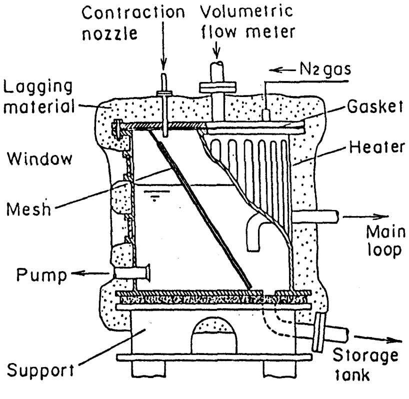

Figure 3. Storage Tank

Figure 4. Pressure Control Tank

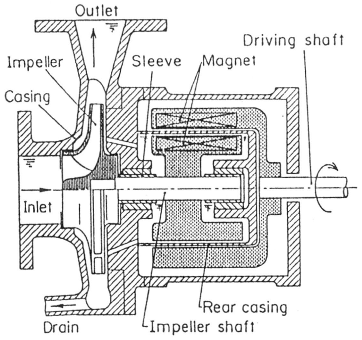

Figure 5. Magnetic Coupling Pump

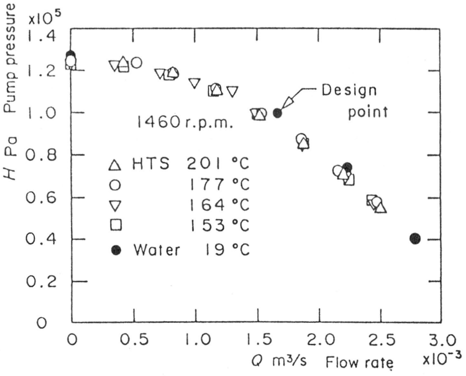

Figure 6. Pump Performance

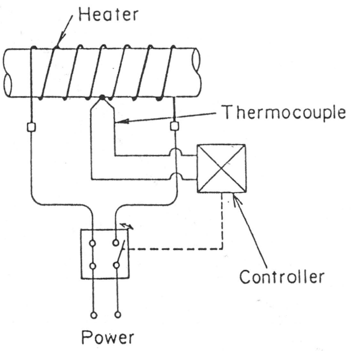

Figure 7. Temperature Control System

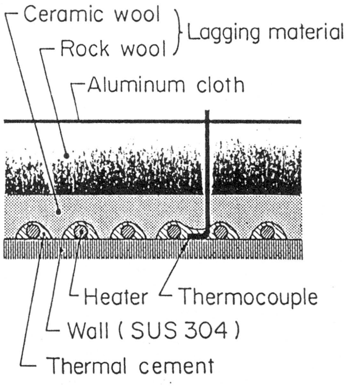

Figure 8. Cross Section of Insulation

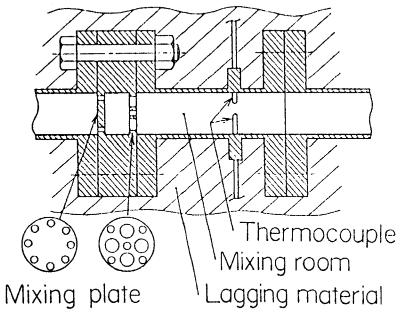

Figure 9. Mixing Chamber

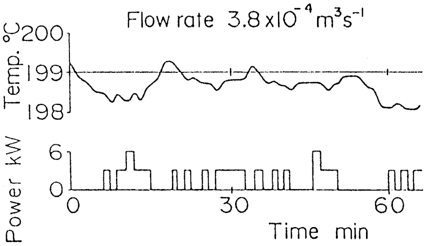

Figure 10. Temperature Fluctuation

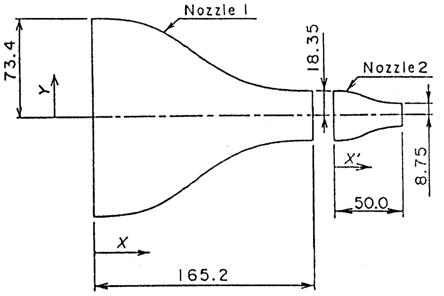

X	0	3.7	7.3	11.0	14.7	18.0	22.0	25.7
Y	73.4	73.3	73.3	73.0	72.9	72.5	72.2	71.7
X	29.4	33.0	36.7	40.4	44.0	47.7	51.4	55.0
Y	71.1	70.3	69.4	68.3	66.9	65.3	63.5	61.5
X	58.7	62.4	66.1	69.7	73.4	77.1	80.7	84.4
Y	59.3	57.0	54.6	52.1	49.5	46.9	44.4	41.8
X	88.1	91.8	95.4	99.1	102.8	106.4	110.1	113.8
Y	39.5	37.2	35.1	33.0	31.1	29.4	27.6	26.2
X	117.4	121.1	124.8	128.5	132.1	135.8	139.5	143.1
Y	24.7	23.5	22.4	21.4	20.6	19.8	19.3	19.0
X	146.8	150.5	154.1	157.8	161.5	165.2	Nozzle 1	
Y	18.7	18.5	18.5	18.4	18.4	18.35		

X'	0	2.2	4.5	6.7	8.9	11.1	13.3	15.6
Y	18.35	18.3	18.2	18.1	18.0	17.6	17.2	16.6
X'	17.8	20.0	22.2	24.4	26.7	28.9	31.1	33.3
Y	15.9	15.1	14.2	13.3	12.4	11.7	11.0	10.4
X'	35.5	37.8	40.0	42.2	46.6	50.0	Nozzle 2	
Y	9.9	9.5	9.1	8.9	8.8	8.75		

Figure 11. Data on Contraction Nozzle

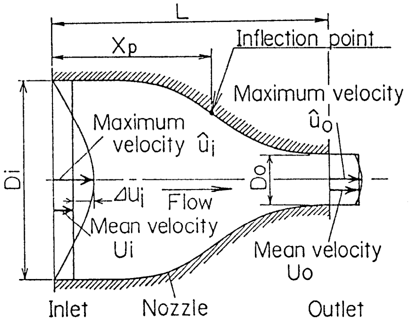

Figure 12. Flow Model

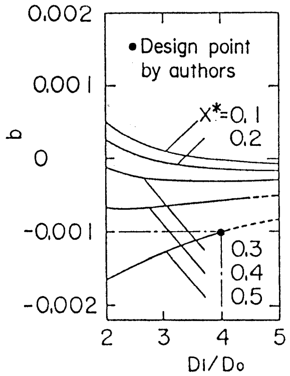

Figure 13. Relation between b and Di/Do

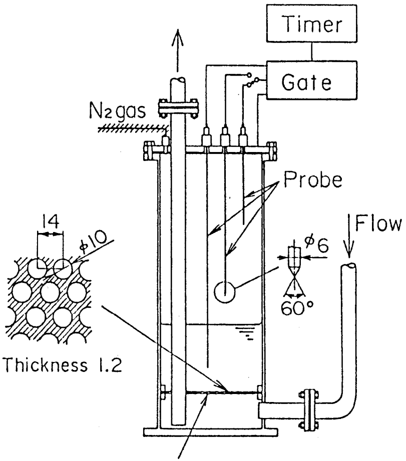

Figure 14. Volumetric Flow Meter

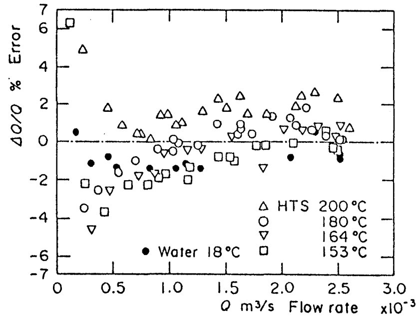

Figure 15. Measurement Error of Turbine Flow Meter

$\Delta Q/Q$; relative error of actual and measurement flow rate.

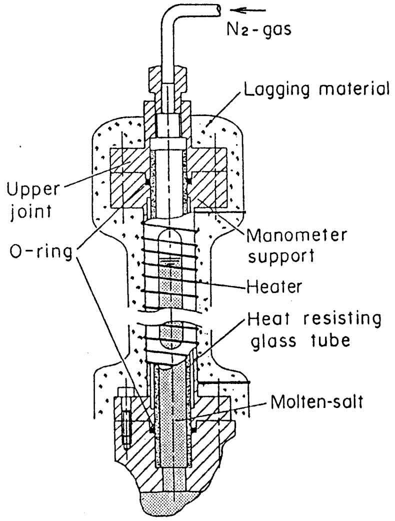

Figure 16 Molten-Salt Manometer

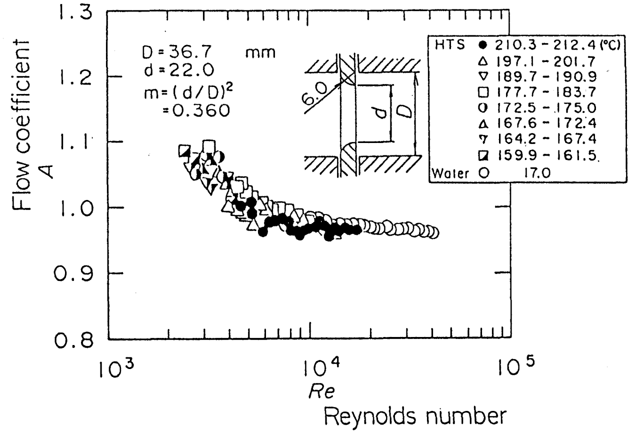

Figure 17. Data on Orifice Flow Meter

A and Re were defined by $Q(\pi d^2/4)^{-1}(2\Delta p/\rho)^{-1/2}$ and $4\rho Q/(\pi\mu D)$, respectively, where, Q=flow rate, Δp=differential pressure, ρ=density and μ=viscosity.

DOI: 10.1149/199017.0683PV

PYROCHEMICAL PARTITIONING OF ACTINIDES AND FISSION PRODUCTS IN A MOLTEN CHLORIDE/LIQUID CADMIUM SYSTEM

Hirotake Moriyama, Kensuke Kinoshita, Yoshiyuki Asaoka,
Kimikazu Moritani and Yasuhiko Ito

Department of Nuclear Engineering
Kyoto University
Sakyo-ku, Kyoto 606, Japan

ABSTRACT

The distribution behaviours of actinides and fission products in a molten chloride/liquid cadmium system have been investigated in support of the development of a pyrochemical group partitioning process. The different distribution behaviours due to different group elements were clearly observed, indicating that the group partitioning is essentially feasible. However, the actinide and lanthanide elements were found to be less soluble in the cadmium phase and to form their solid intermetallics on reduction. A reductive exraction process combined with filtration of such intermetallics is proposed on the basis of the observations.

INTRODUCTION

Molten salts and liquid metals are highly radiation resistant and serve as high-density fluids at elevated temperatures. The use of these fluids makes it possible to develop the more compact processes and to decrease the amount of low-level radioactive wastes. The pyrochemical separation systems of these fluids are thus considered to be much useful for future nuclear engineering. A number of applications have been proposed and some of them are now being developed for the reprocessing of nuclear reactor fuels (1,2) and for the group partitioning of radioactive wastes (3,4).

In the present study, the distribution behaviours of actinides and fission products in a molten chloride/liquid cadimium system have been investigated in support of the development of a pyrochemical partitioning process. The results are analyzed by comparing with a theoretical prediction (5) and the feasibility of group partitioning of radioactive wastes is discussed on the basis of the distribution behaviours observed. The results obtained in the present study will also be important for the reprocessing of fast breeder metallic fuels (1,2).

EXPERIMENTAL

All the reagents were of reagent grade obtained from Nacalai Tesque, Co. The LiCl-KCl mixture of 50 mole% LiCl was prepared by melting the known amounts of LiCl and KCl. The reductant Li was prepared in the form of a Li-Cd alloy(25 mole% Li) to make the addition into the Cd phase easy. The radioactive tracers of Np-239, Pa-233, La-140, Ce-143, Eu-152m, Pd-109 and Zr-97 were produced by thermal neutron irradiation of U, Th, La, Ce, Eu, Pd and Zr metals, respectively, in Kyoto University Research Reactor. Non-irradiated metals were also used as solutes in some runs.

The experimental apparatus and general procedures employed in this study are much the same as in the previous ones for the salt/Bi systems (6-8). In a typical experiment, 1 mol of the LiCl-KCl, 2 mol of Cd metal and small amounts (less than 100 mg each) of the solute elements were loaded in a graphite crucible and dried by vacuum at 450 K in the extraction vessel of stainless steel. The system was then heated under an inert-atmosphere. In order to ensure the purification of the system, a H_2-10 vol% HCl gas was bubbled for about 10 hours in some runs.

The distribution of the solutes was controlled by the incremental addition of the Li-Cd alloy to the system. After some equilibrations, the samples were taken out from each phase with a stainless steel sampling tube under a reduced pressure. The concentrations of the radioactive solutes were measured by direct γ-spectroscopy, and those of the reductant Li in the Cd phase and of non-radioactive solutes were determined by atomic absorption spectrophotometry.

RESULTS AND DISCUSSION

1. Mechanism of equilibrium distributions

Fig. 1 shows a typical result of the measurement of distribution coefficients. The distribution coefficients are defined as

$$D_M = A_{M(Cd)} / A_{M(salt)} \tag{1}$$

$$D_{Li} = X_{Li(Cd)} / X_{LiCl(salt)} \tag{2}$$

where A_M is the molar radioactivity of the element M, X_{Li} and X_{LiCl} are the mole fractions of Li and LiCl, respectively, and the subscripts (Cd) and (salt) denote the Cd phase and the salt phase, respectively. Fig. 1 also shows the distribution coefficients which are predicted with a thermodynamic model (5) by taking the reaction mechanism:

$$Li_{m-n}MCl_m + n\ Li + x\ Cd = MCd_x + m\ LiCl \qquad (3)$$

where $Li_{m-n}MCl_m$ and MCd_x represent the complex compound formed in the salt phase and the intermetallic compounds in the Cd phase, respectively. The similar mechanisms have well been established in the salt/Bi systems by observing the effects of salt and metal compositions on the equilibrium distributions (6-8). According to the model, the extractability $D_M/D_{Li}{}^n$ of each element is represented by

$$\begin{aligned}\log(D_M/D_{Li}{}^n) = {} & -(2.3RT)^{-1}[\ \Delta G_f^o(MA_x) + m\ \Delta G_f^o(LiX) - \Delta G_f^o(Li_{m-n}MX_m)] \\ & + x \log X_A - (m-n) \log X_{LiX} - \log \gamma_{MAx} - m \log \gamma_{LiX} \\ & + \log \gamma_{Lim-nMXm} + n \log \gamma_{Li} + x \log \gamma_A \qquad (4)\end{aligned}$$

The terms in the right hand side in Eq. (4) are constant at a given temperature and composition and then the logarithm of D_M is proportional to that of D_{Li} with a slope of n. The thermodynamic data in Eq. (4) are taken from the literatures and estimated theoretically (5). Fairly good agreements between the experimental and predicted values are observed for lanthanide elements. The above mechanism is thus supported. However significant disagreements are found for actinides.

2. Effect of intermetallic compounds on equilibrium distributions

In order to know the behaviour of actinides, a careful measurement was made with uranium as a solute. The changes of uranium concentration in both phases with time are shown in Fig. 2 and the distribution coefficient is plotted in Fig. 3. Fig. 2 indicates that the uranium concentration in the salt phase rapidly decreases with the addition of reductant but that the concentration in the Cd phase does not increase so rapid. This suggests that most of the reduced uranium forms another phase in the system.

After the melt was frozen, the interface layer between both phases was inspected and the presence of a solid intermetallic compound, possibly UCd_2, was inferred by a chemical analysis. The reduced uranium seems to remain at the interface as the solid intermetallics rather than to be dissolved into the Cd phase. Since a much higher solubility has been reported of uranium in liquid cadmium (9), this may be due to a very slow kinetics of dissolution of the compound or to an entrainment effect in the salt phase. A similar phenomenon has been observed in the salt/Bi system although the formation of solid intermetallics for a few hours is only temporary in that case (8). The distribution coefficient of uranium in Fig. 3 seems to be lowered by the entrainment of the solid intermetallics in the salt phase. The disagreements observed for the actinide elements in Fig. 1 can similarly be explained.

3. Systematics of equilibrium distributions

For applications, it is important to know some regularities in the equilibrium distributions. Fig. 4 shows the temperature dependences of the $D_M/D_{Li}{}^n$ value for each element. The values have been evaluated in several measurements for the species homogeneously dissolved into both phases. The datum of Nd is taken from the literature (10). All the $D_M/D_{Li}{}^n$ values decrease with the increasing temperature.

Fig. 5 shows the atomic number dependence of the normalized extractability, $(D_M/D_{Li}{}^n)^{1/n}$, which are calculated from the experimental data in a $LiF\text{-}BeF_2/Bi$ system (6,8,11). The analysis of this type is very useful not only to discuss the systematics of extractability but also to estimate the unknown $(D_M/D_{Li}{}^n)^{1/n}$ values. Some regularities, possibly due to the f-electrons, can be seen for the actinide and lanthanide elements; it is interesting to note that such a tetrad effect(12) is observed for the actinide elements in Fig. 5. The data for the present system of LiCl-KCl/Cd are plotted in Fig. 6 and the similar regularities can be expected. As seen in Figs. 5 and 6, the extractabilities of the actinide elements are systematically different from and higher than those of the lanthanide. This supports the partitioning of both group elements in liquid-liquid extraction systems.

4. Group partitioning process

Fig. 7 shows the fractional distributions of typical solute elements in the molten LiCl-KCl, liquid Cd, and intermetallic compound phases. Palladium is always found in the Cd phase and cesium and strontium are in the salt phase. In the studied range, on the other hand, the distributions of actinide and lanthanide elements are much sensitive to the lithium concentration in the Cd phase, which is a measure of the redox potential of the system. In the case of the lower lithium concentration of 5×10^{-4}, most of uranium was reduced to form the intermetallic compound phase while only a part of lanthanum was reduced. At the higher lithium concentration of 9×10^{-3}, on the other hand, almost all of the lanthanide elements were reduced into the intermetallic compound phase. The actinide elements are reduced more easily than the lanthanide and most of both group elements seems to form thier solid intermetallics on reduction.

In the present system, the actinide and lanthanide elements seem to be less soluble into the Cd phase and to form their solid intermetallics on reduction. The intermetallics would be dispersed into the salt phase, or sometimes into the metal phase, and then the recovery yields and separation/decontamination factors might be affected. This might be a problem for the development of the liquid-liquid extraction systems. In order to improve the situation, for example, it is suggested to combine the reductive extraction process with the filtration of solid intermetallics as shown in Fig. 8. Sufficiently high separation factors may be achieved in such a combined process although those factors are much dependent on the efficiency of filtration.

CONCLUSIONS

The following conclusions can be drawn on the feasibility of the present pyrochemical separation system:

(1) Different distribution behaviours due to different group elements were clearly shown. The reduction of metal chlorides occurs in the order of platinum group elements, actinides, lanthanides, and strontium and cesium. The group partitioning in the system is thus essentially feasible.

(2) The actinide and lanthanide elements were less soluble in the Cd phase and remained at the interface as solid intermetallics on reduction. When the system is used for a liquid-liquid extraction, the recovery yields and separation/decontamination factors will be affected by the intermetallics.

(3) The performance might be improved significantly by combining the extraction process with the filtration of the solid intermetallics. Sufficiently high separation factors are expected in this case from the present distribution data.

ACKNOWLEDGEMENTS

A part of this work was performed under the Visiting Researchers' Program of the Kyoto University Research Reactor Institute. The authors wish to thank Prof. T. Tamai and Mr. S. Nishikawa for their encouragement. This work was partly supported by a Grant-in-Aid Scientific Research from the Ministry of Education, Science and Culture and by Central Research Institute of Electric Power Industry.

REFERENCES

1. D. C. Wade and Y. I. Chang, Nucl. Sci. Eng., 100, 507(1988).

2. L. Burris, Chem. Eng. Prog., 82, 35(1986).

3. G. A. Jensen, A. M. Platt, G. B. Mellinger and W. J. Bjorklund, Nucl. Technol, 65, 305(1984).

4. K. Naito, T. Matsui and Y. Tanaka, J. Nucl. Sci. Technol., 23, 540(1986).

5. H. Moriyama, K. Kinoshita, Y. Asaoka and Y. Ito, Extended Abstracts of 40th International Society of Electrochemistry Meeting, Vol. 1, p. 55(1989).

6. H. Moriyama, K. Yajima, N. Nunogane, T. Ohmura, K. Moritani and J. Oishi, J. Nucl. Sci. Technol., 21, 949(1984).

7. H. Moriyama, N. Nunogane and J. Oishi, ibid., 24, 120(1987).

8. J. Oishi, H. Moriyama, K. Moritani, S. Maeda, M. Miyazaki and Y. Asaoka, J. Nucl. Mater., 154, 163(1988).

9. A. E. Martin, I. Johnson and H. M. Feder, Trans. Metall. Soc. AIME, 221, 789(1961).

10. M. Sakata, T. Kusakabe, M. Kurata and T. Inoue, Report of Central Research Institute of Electric Power Industry, T89027(1990), (in Japanese).

11. L. M. Ferris, J. C. Mailen and F. J. Smith, J. Inorg. Nucl. Chem., 33, 1325(1971).

12. D. F. Peppard, C. A. A. Bloomquist, E. P. Horwitz, S. Lewey and G. W. Mason, J. Inorg. Nucl. Chem., 32, 339(1970).

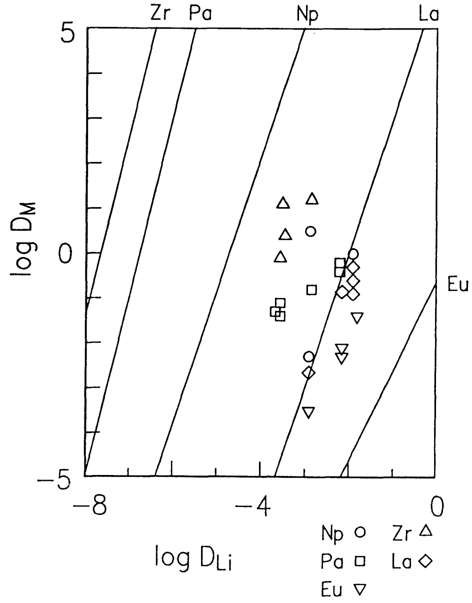

Fig. 1.
Distribution coefficient of some typical elements in the LiCl-KCl/Cd system at 873K. Marks are experimental and curves are predicted (5).

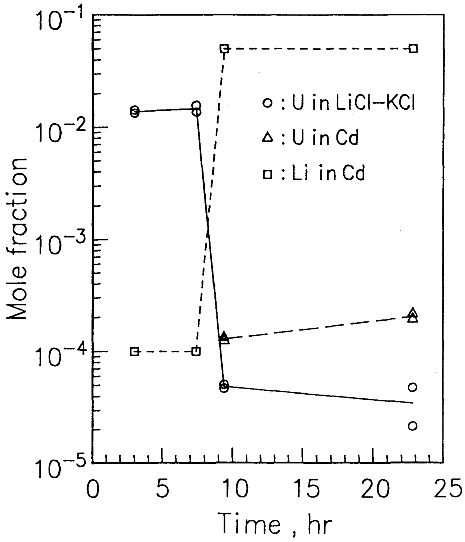

Fig. 2.
Changes of uranium concentration in molten LiCl-KCl and liquid Cd phases at 840K.

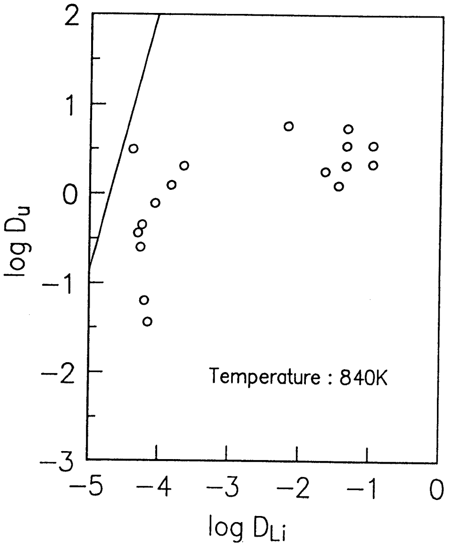

Fig. 3.
Distribution coefficient of uranium in the LiCl-KCl/Cd system at 840K. Marks are experimental and curve is predicted (5).

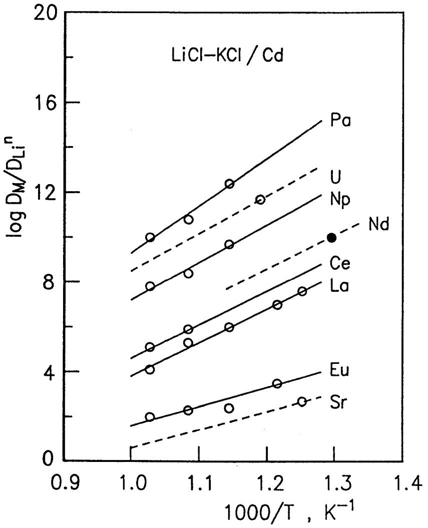

Fig. 4.
Temperature dependence of equilibrium distributions in LiCl-KCl/Cd system. Open marks are of the present study and closed is from the literature (10).

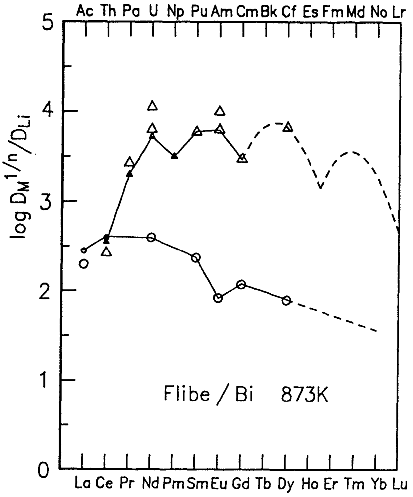

Fig. 5.
Atomic number dependence of equilibrium distributions in LiF-BeF_2/Bi system at 873K. Marks are taken from the literatures (6,8,11).

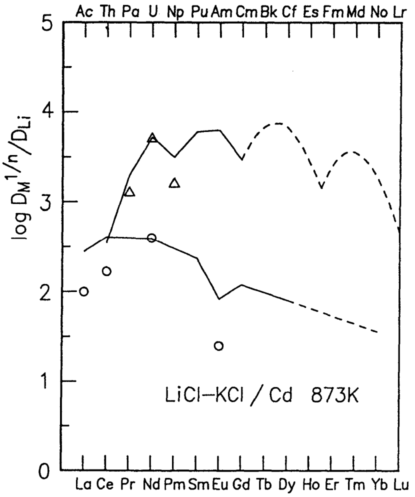

Fig. 6.
Atomic number dependence of equilibrium distributions in LiCl-KCl/Cd system at 873K. Marks are taken from Fig. 4 and curves are for LiF-BeF_2/Bi system.

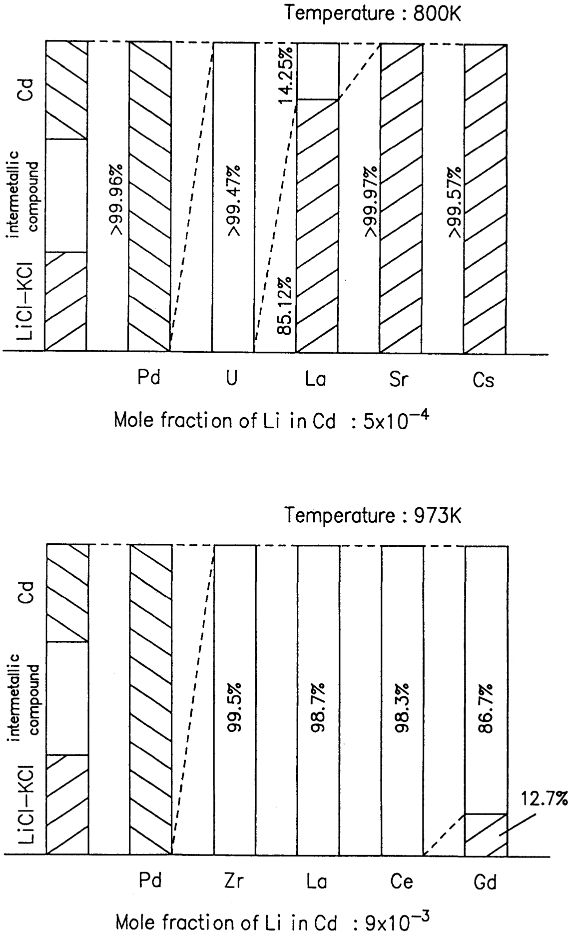

Fig. 7. Fractional distributions of typical solute elements among LiCl-KCl, Cd and intermetallic compound phases.

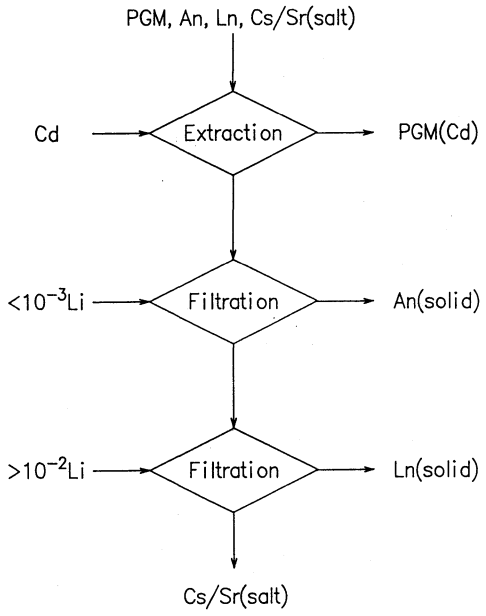

Fig. 8. A reductive extraction process combined with filtration of solid intermetallic compounds. PGM: platinum group elements; An: actinides; Ln: lanthanides.

DOI: 10.1149/199017.0694PV

SURFACE MODIFICATION OF NICKEL ELECTRODES BY MOLTEN SALT ELECTROLYTIC PROCESSES

Yasuhiko Ito*, Hideki Yabe, and Keiko Ema

Department of Nuclear Engineering
Faculty of Engineering
Kyoto University
Sakyo-ku, Kyoto 606, Japan

ABSTRACT

The surface of a porous nickel electrode has been modified by electrodeposition of either tungsten or tungsten carbide from molten halides. The electrode thus obtained shows high performance as an MCFC anode. The bare nickel electrode also operates well when a small amount of K_2WO_4 is added to the carbonate electrolyte, which is due to the result of in situ modification. High-performance hydrogen evolution cathode is also obtained by a similar modification process.

1. INTRODUCTION

It is well known that tungsten or tungsten carbide can be electrodeposited from molten halides [1 - 6]. In particular, electrodeposition of tungsten or tungsten carbide from halide melts containing WO_4^{2-} ion or the mixture of WO_4^{2-} ion and CO_3^{2-} ion seems so promising that several experimental studies of this reaction have been reported [7 - 9]. One of the applications of this electrodeposition reaction has been the surface modification of electrode materials, e.g., MCFC anode and hydrogen evolution cathode.

2. POROUS NICKEL ELECTRODE FOR MOLTEN CARBONATE FUEL CELLS

The molten carbonate fuel cell (MCFC) constitutes the second-generation of fuel cell technology and has many advantages in terms of fuel flexibility and system design[10-13]. The technology is directed towards large scale power generation that can utilize a wide variety of fossil fuels (including gasified coal, natural gas and alcohol) with high efficiency and low pollution.

In order to develop MCFC systems, many technological problems have to be solved through conducting strategic research programs. The development of suitable electrode materials is vital: present materials severely limit both the lifetime and the performance of the cell. As a consequence, many investigations have been devoted to this area of endeavor. In order to develop an appropriate anode material for MCFCs, it is necessary to consider many factors, e.g., electrocatalytic activity, corrosion resistance, sintering resistance, creep resistance, etc. To date, Ni-Cr, Ni-Co, or Ni-Cu alloys have been considered as possible anode materials. A different approach, described here, is to modify the surface of the nickel anode by the electrodepositon of tungsten or tungsten carbide from molten halides [14].

2-1.EXPERIMENTAL

The experimental apparatus used to effect the electrodeposition is shown in Fig. 1. A gastight vessel, made of stainless steel, contained a high purity alumina or nickel crucible that could be raised or lowered. By this arrangement, electrodes that were fixed on the upper flange could be immersed in the molten electrolyte contained in the crucible. The electrolyte consisted of a LiCl-KCl eutectic melt(59 mol% LiCl, 41 mol% KCl)that was prepared under an argon atmosphere. All chemicals were of reagent grade (Wako Chemicals Co., Ltd.) and were dried under vacuum for several days at a temperature just below the melting point of the mixture. An Ag/Ag^+ electrode or a platinum wire was used as the reference electrode. The former electrode comprised a silver wire and chloride that were both contained in a pyrex glass tube, which had a very fine tip. The potential of the electrode was calibrated against an alkali metal electrode, Li/Li^+, that was electrodeposited on a nickel wire [15]. The electrode thus prepared exhibited good reproducibility. Unless otherwise stated,all potentials are reported with respect to the Li/Li^+ reference electrode. The anode was made from glassy carbon. Sintered nickel-powder or nickel-fiber (porosity: 60-80%, mean pore size: 8 μm), placed inside an alumina tube, was employed as the cathode.

After melting the salt, vacuum-dried potassium tungstate or a mixture of potassium tungstate and potassium carbonate was added to a concentration of 0.02-0.1 mol%. The electrodeposition was conducted on the cathode at a temperature of 973 K and at a potential of 0.1-0.5 V or a current density of 100-300 mA cm^{-2}. After the electrolysis, 2-100 mg cm^{-2} of tungsten or tungsten carbide was deposited on the electrode surface. The electrodeposited samples were removed from the vessel after several hours, washed with distilled water, dried, and kept in a desiccator. The samples were subjected to analysis using SEM, EPMA, EDX, ESCA, RBS and X-ray diffraction techniques.

The experimental apparatus used for polarization studies is shown in Fig. 2. The electrolyte comprised an Li_2CO_3-K_2CO_3 eutectic melt (62 mol% Li_2CO_3, 38 mol% K_2CO_3) contained in a high-purity alumina crucible. The electrolyte was dried under vacuum at just under its melting point for a few days. It was then melted under an argon atmosphere and maintained at the temperature of the experiment. An "oxygen electrode" [16] (O_2:CO_2=1:2) or platinum wire was employed as a reference electrode. The counter electrode was also an oxygen electrode. The working electrode (anode) was made from nickel (see above) and was housed in an alumina tube. Fuel gas (H_2:CO_2=4:1, after passing through water at 323 K) was introduced through the alumina tube. In order to effect in situ surface modification of the working electrode, K_2WO_4 was added to the molten carbonate electrolyte.

2-2.RESULTS AND DISCUSSION

Figure 3 shows an electron micrograph of a typical tungsten-coated electrode obtained at 0.1 V in a LiCl-KCl melt containing 0.1 mol% of K_2WO_4 at 973 K. Analysis showed that 13.2 mg cm^{-2} of tungsten was deposited on the surface. An EPMA investigation revealed that small amounts of tungsten were uniformly deposited on the nickel substrate (Fig. 4). The deposit was identified as tungsten by X-ray diffraction analysis.

Figure 5 presents an electron micrograph of a typical tungsten carbide sample obtained at 0.2 V in a LiCl-KCl melt containing 0.1 mol% of K_2WO_4 and 0.1 mol% of K_2CO_3 at 973 K. A coating of 2.6 mg cm^{-2} was found on the surface. EPMA studies showed (Fig. 6) small amounts of tungsten and carbon to be uniformly dispersed across the surface. Using X-ray diffraction, it was found that the deposit was composed of W_2C, WC and W. The results from EDX and RBS further confirmed that both tungsten and tungsten carbide were electrodeposited from the chloride melt onto the porous nickel substrate.

The results of polarization measurements conducted on an MCFC anode, modified by tungsten and tungsten carbide and immersed in molten carbonate, are presented in Fig. 7. In this figure, the apparent current density is plotted along the abscissa and the potential of the MCFC anode (vs. the oxygen electrode) on the ordinate. Curve (a) was obtained on a bare, sintered nickel-powder substrate (porosity: 60%), curve (b) on a sintered nickel-powder substrate (porosity: 60%) coated with tungsten, and curve (c) on a sintered nickel-fiber substrate (porosity: 80%) coated with tungsten. It can be seen that when modified by tungsten the MCFC exhibits good performance.

The polarization characteristics of a bare, sintered nickel-powder substrate (porosity: 60%) in molten carbonate containing 0.1 mol% tungstate ion are given by curve (d) in Fig. 7. This system was examined in order to study the effects of in situ surface modification in the MCFC electrolyte. The data show that this very simple treatment enhances the performance of the electrode.

After this in situ surface modification, a small amount of tungsten is deposited on the nickel powder substrate as shown in Fig 8, which might explain the high performance of the electrode.

Curve (e) represents the polarization characteristics of the MCFC anode when modified by tungsten and tungsten carbide by adding 1.0 mol% of tungstate ion to the molten carbonate. This anode was obtained at 0.2 V in a LiCl-KCl melt containing 0.1 mol% K_2WO_4 and 0.02 mol% K_2CO_3 at 973 K. After the electrolysis, about 10 mg cm^{-2} of tungsten plus tungsten carbide were deposited on the surface. This anode shows good electrical performance, greater durability, and enhanced resistance to corrosion. Other studies demonstrated that the electrodeposition of tungsten carbide alone increased the electrode durability, but did not improve the polarization characteristics.

2-3.COUNCLUSIONS

The principal results obtained from the above experiments are summarized as follows.

(i) The electrodeposition of tungsten and tungsten carbide from molten chloride on porous nickel substrates has been achieved.

(ii) Polarization measurements show that the performance in molten carbonate electrolyte of an MCFC anode modified by tungsten is superior to that of its bare, porous nickel counterpart. However, similar improvement was not observed when the anode was modified by tungsten carbide.

(iii) The porous nickel electrode itself gives excellent performance as an MCFC anode when K_2WO_4 is added to the electrolyte. This may be due to the exertion of a catalytic effect by tungsten

The above electrodes showed similar improvements in polarization and durability when tested with tile electrolyte over a period of more than several hundred hours.

3.HYDROGEN EVOLUTION CATHODE

The development of a low overvoltage hydrogen evolution cathode is still an important research subject in the field of hydrogen energy systems, as well as the soda electrolysis industry. Namely, the development of a hydrogen cathode which shows low overvoltage and high corrosion resistance at high temperatures in high concentrations of caustic soda is still desired. In order to obtain new-type low overvoltage hydrogen evolution cathode, we have tried to apply our molten salt electrodeposition method to the surface modification of a cathode to be used for the hydrogen evolution reaction.

3-1.EXPERIMENTAL

The experimental apparatus used to effect surface modification is almost the same as that described before. Nickel and mild steel were used as electrode substrates onto which tungsten or tungsten carbide were electrodeposited. LiF-KF eutectic melt was used as the electrolyte. For an electrodeposition experiment, 0.1 mol% K_2WO_4 or a mixture of 0.1mol% K_2WO_4 and 0.1 mol % K_2CO_3 were added to the electrolyte. Furtheremore, for some experiments, 0.001 - 0.01 mol % of K_2PtCl_6 was added in an attempt to lower the hydrogen overvoltage. The experimental temperature was 973K.

The electrolytic cell used for overvoltage measurements is shown in Fig. 9. Aqueous 9N-NaOH was used as the electrolyte and the experimental temperature was kept at 60 - 80 ^{o}C. To minimize the concentration change or the effect of contamination, 50 % of the electrolyte was changed every few days.

3-2.RESULTS AND DISCUSSION

Figure 10 shows the overvoltages measured with bare nickel and mild steel electrodes. The results are in fair agreement with the results reported by other researchers. In this figure, large overvoltages of about 300 or 400 mV are observed in the high current density range.

Figure 11 shows the scanning electron micrograph of tungsten electrodeposited on the mild steel substrate. With this electrode, hydrogen overvoltage was measured. The result is shown in Fig. 12.

Compared with the results shown in Fig. 10, a drastic decrease of overvoltage is realized. Figure 13 shows the result obtained with the use of nickel electrode modified by tungsten carbide. This modification was conducted by electrodepositing tungsten carbide from LiF-KF eutectic melt containing 0.1 mol% K_2WO_4 and 0.1 mol% K_2CO_3 at 200 mA/cm^2. The polarization characteristics are better than those obtained with the use of bare nickel substrates but worse than those obtained with mild steel substrates. From these results, although some improvement can be effected by surface modification with tungsten or tungsten carbide, much more improvement is still required. So, in anticipation of some significant improvement in overpotential, a small amount of K_2PtCl_6 was added to the electrolyte. As shown in Fig. 14, a drastic change in morphology is observed. Hydrogen overvoltage was measured by using this electrode. The result is shown in Fig. 15.

Much improvement in performance is observed in this figure. From a duration test, the high performance of the tungsten-platinum modified electrode was confirmed for a longer-term electrolysis. Figure 16 summarizes the polarization characteristics obtained by using electrodes prepared by several methods.

The practical effect of platinum addition (1/100 of tungsten) is significant even though the mechanism leading to this improved performance is not so clear yet.

3-3.CONCLUSIONS

The principal results obtained from the above experiments are summarized as follows.

(i) The polarization characteristics of nickel and mild steel cathodes were improved by electrodepositing tungsten film on the surfaces of the materials from LiF-KF eutectic melt containing WO_4^{2-}.

(ii) A drastic morphology change was observed when very small amounts of platinum are codeposited during the electrodeposition of tungsten.

(iii)The tungsten-platinum modified electrode thus obtained showed significantly improved performance as a low overvoltage hydrogen evolution cathode.

4.CONCLUSIONS

As described above, the surface modification of electrodes by molten salt electrolytic processes (including in-situ surface modification in a molten salt system) is promising, though there remains further problems for the implementation of this process on an industrial scale.

REFERENCES

1. S. Senderoff and G. W. Mellors, J. Electrochem. Soc., 114, 586 (1967)

2. S. Senderoff and G. W. Mellors, Science, 153,1475(1966)

3. K. E. Johnson and J. R. Mackenzie, Anal. Chem., 41, 1483 (1969)

4. J. M. Gomes and M. M. Wong, U.S. Bur. Mines Rep. Invest., 7247 (1972)

5. K. H. Stern and I. L. Singer, "Thin Solid Films", 108,9 (1983)

6. K. H. Stern and M. L. Deanhardt, J. Electrochem. Soc., 132, 1891 (1985)

7. H. Yabe, K. Ema and Y. Ito, J. Electrochem. Soc., 137, 1739 (1990)

8. H. Yabe, K. Ema and Y. Ito, Electorchim. Acta., 35, 187 (1990)

9. H. Yabe, S. Hikino, K. Ema and Y. Ito, Electrochim. Acta, in press.

10. J. R. Selman and L. G. Marianowski, in D. G. Lovering(ed.), "Molten Salt Technology", New York, 1982.

11. J. R. Selman and H. C. Maru, in G. Mamantov and J. Braunstein (eds.), "Advances in Molten Salt Chemistry", Vol.4, Plenum, New York, 1981.

12. Molten Salt Committee of The Electrochemical Society of Japan (ed.), "Proc. 1st Symp. on Molten Carbonate Fuel Cells", Kyoto, Japan, 23-24 April, 1985.

13. Molten Salt Committee of The Electrochemical Society of Japan (ed.), "Proc. 2nd Symp. on Molten Carbonate Fuel Cells", Kyoto Japan, February, 1988.

14. H. Yabe, Y. Ito, K. Ema and J. Oishi,J. Power Sources, 24, 297, (1988)

15. T. Takenaka, Y. Ito and J. Oishi, Denki Kagaku, 53, 476, (1985)

16. A. Borucka and C. M. Sugiyama, Electrochim. Acta, 13 1887 (1963)

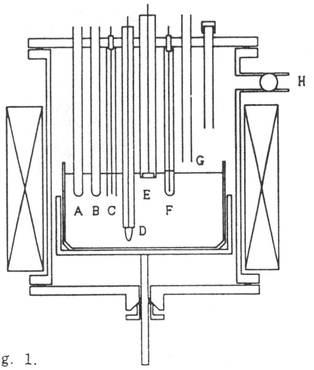

Fig. 1.

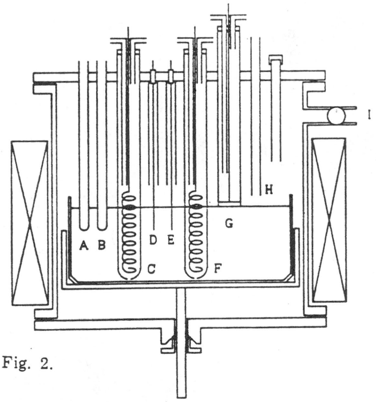

Fig. 2.

Fig. 1. Experimental apparatus for electrodeposition studies. A: thermocouple; B: zirconia electrode; C: Li/Li$^+$ electrode; D: counter electrode(anode); E: working electrode(cathode); F: reference electrode; G: gas inlet; H: gas outlet.

Fig. 2. Experimental apparatus for polarization studies in molten carbonate. A: thermocouple; B: zirconia electrode; C: counter electrode("oxygen electrode"); D: platinum wire; E: nickel wire; F: reference electrode("oxygen electrode"); G: working electrode(MCFC anode); H: gas inlet; I: gas outlet

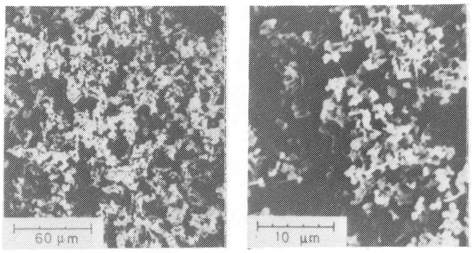

Fig. 3. Electron micrograph of electrodeposited tungsten on sintered nickel powder substrate.

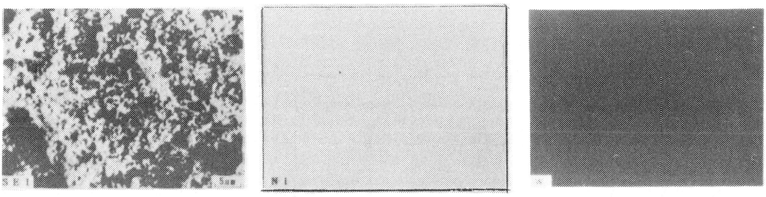

Fig. 4. EPMA of the electrodeposited tungsten sample shown in Fig. 3.

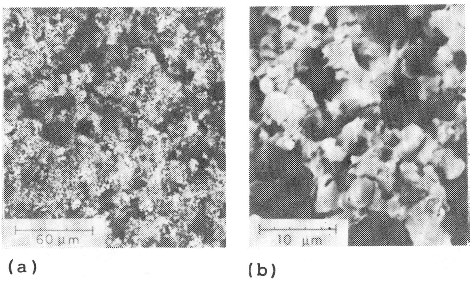

(a) (b)

Fig. 5. Electron micrograph of electrodeposited tungsten carbide on sintered nickel powder substrate.

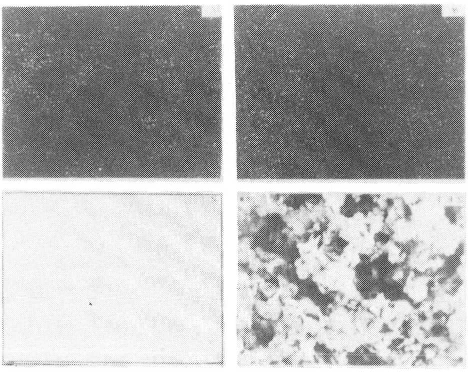

Fig. 6. EPMA of the tungsten carbide sample shown in Fig. 5.

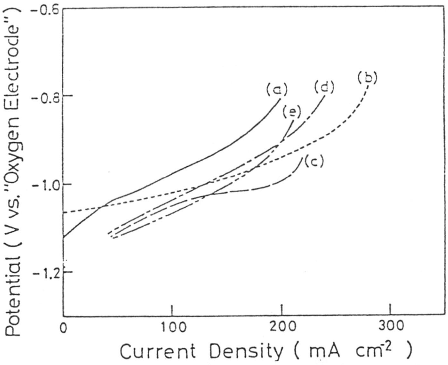

Fig. 7 Polarization curves for electrodes in the Li_2CO_3-K_2CO_3 eutectic, 923K.

(a) Sintered nickel powder;
(b) Sintered nickel powder modified by tungsten(Fig.3);
(c) Sintered nickel fiber modified by tungsten;
(d) Sintered nickel powder;
(e) Sintered nickel powder modified by tungsten and tungsten carbide.

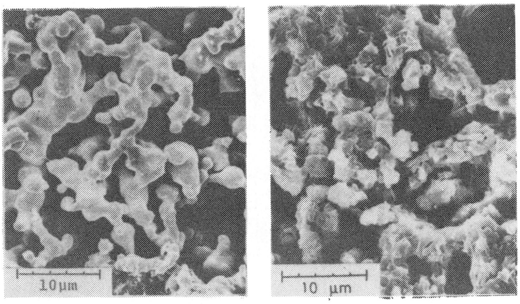

(a) Sintered nickel powder substrate (porosity 60%, mean pore size: 8μm).

(b) After in situ surface modification

Fig. 8. Electron micrograph of the electrode

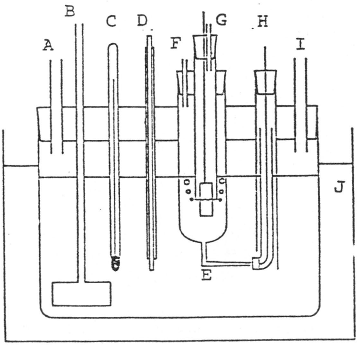

A: Ar Outlet
B: Stirrer
C: Thermometer
D: Counter Electrode
E: Reference Electrode
F: H_2 Outlet
G: H_2 Inlet
H: Working Electrode
I: Ar Inlet
J: Water Bath

Fig. 9. Schematic diagram of the cell used for hydrogen overvoltage measurements.

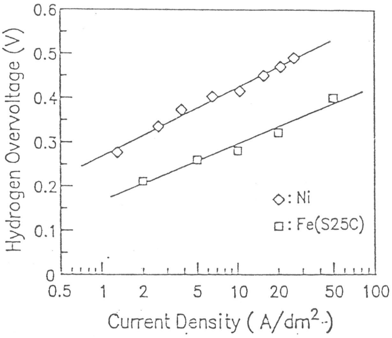

Fig. 10. Hydrogen overvoltage at several electrodes (9N NaOH,80°C).

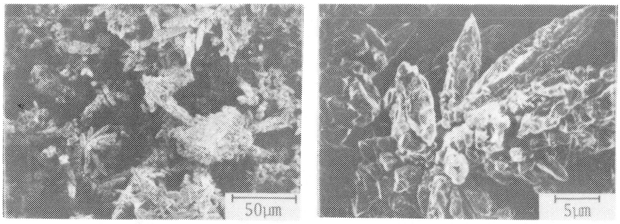

Fig. 11. Electron micrograph of tungsten

(LiF-KF, K_2WO_4: 0.1mol%,deposition potential:

0.2V vs. Li, K/Li$^+$,K$^+$, 973K).

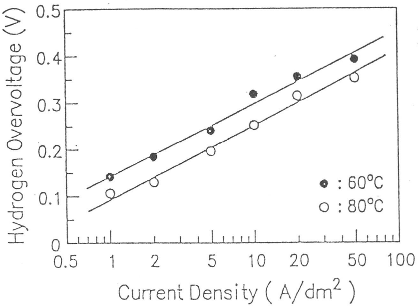

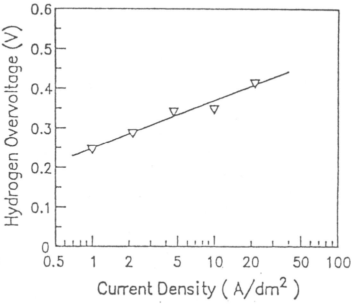

Fig. 12. Hydrogen overvoltage of the nickel electrode modified by tungsten under various conditions.

Fig. 13. Hydrogen overvoltage of the nickel electrode modified by tungsten carbide(9N NaOH, 80°C).

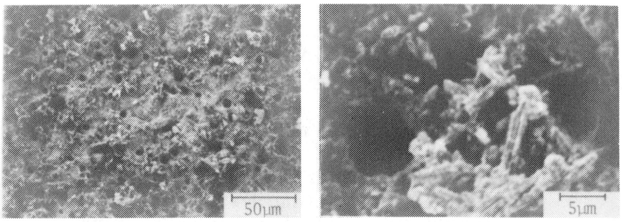

Fig. 14. Electron micrograph of tungsten-platinum (LiF-KF, K_2WO_4:0.1mol%, K_2PtCl_6:0.001mol%, deposition potential:0.2V vs. $Li,K/Li^+,K^+$ 973K).

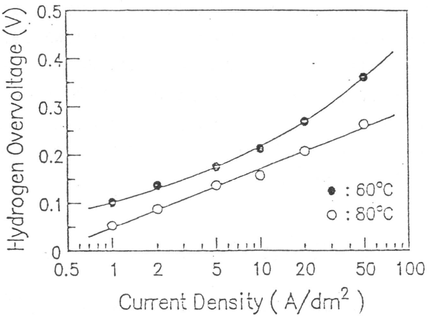

Fig. 15. Hydrogen overvoltage of the nickel electrode modified by tungsten-platinum under various conditions (9N NaOH, Fig. 13. sample).

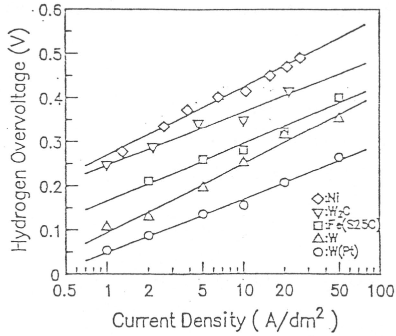

Fig. 16. Hydrogen overvoltage at several electrodes (9N NaOH, 80°C).

DOI: 10.1149/199017.0706PV

EFFECT OF O_2/CO_2 GAS PARTIAL PRESSURES ON OXYGEN REDUCTION KINETICS IN MOLTEN CARBONATE

Tatsuo Nishina and Isamu Uchida

Department of Molecular Chemistry and Engineering
Faculty of Engineering, Tohoku University
Aramaki-Aoba, Aoba-Ku, Sendai 980, Japan

ABSTRACT

The effect of O_2 and CO_2 gas partial pressures on oxygen reduction path at Au flag electrode has been investigated in a (62+38)mol% $(Li+K)CO_3$ melt at 600-800°C. We carried out precise measurements of the Warburg coefficient of the ac impedance at the rest potential, using a Randles'-Ershler equivalent circuit. Taking into account three possible diffusing species, i.e., O_2^-, O_2^{2-} and CO_2, a graphical reaction order analysis was made, using the Warburg coefficients. Only the case of mixed diffusion of O_2^- and CO_2 was found to result in a satisfactory linear relationship. Therefore, we conclude that simultaneous diffusion of O_2^- and CO_2 is the dominant feature of the oxygen reduction process in bulk $(Li+K)CO_3$ melt.

INTRODUCTION

Recent work has shown that the exchange current density, i_o, of oxygen reduction in molten carbonate at 650°C is of the order of 10 mA/cm^2. However, the reaction mechanism is still not well understood. According to Appleby and Nicholson (1-3), the oxygen reduction follows the superoxide path(SOP) or the peroxide path(POP), where these oxygen species are chemically formed in the carbonate melts as follows.

(A) Superoxide Path(SOP)

$$3O_2 + 2CO_3^{2-} = 4O_2^- + 2CO_2 \qquad [1]$$

$$[O_2^-] = K_1 P_{O_2}^{0.75} P_{CO_2}^{-0.5} \qquad [2]$$

$$O_2^- + 2CO_2 + 3e = 2CO_3^{2-} \qquad [3]$$

(B) Peroxide Path(POP)

$$O_2 + 2CO_3^{2-} = 2O_2^{2-} + 2CO_2 \qquad [4]$$

$$[O_2^{2-}] = K_2 P_{O_2}^{0.5} P_{CO_2}^{-1.0} \quad [5]$$

$$O_2^{2-} + 2CO_2 + 2e = 2CO_3^{2-} \quad [6]$$

It has been pointed out that experimental O_2 and CO_2 reaction orders in $(Li+K)CO_3$ melt do not agree with the predictions according to the SOP and POP mechanisms (4). Also, it has been demonstrated that the rate at which oxide ion, which is an intermediate reduction product of peroxide or superoxide according to Equations [3] and [6], is neutralized by CO_2 may be limiting the overall reduction process (5). This neutralization rate in turn may be limited by CO_2 diffusion.

In this work, a reaction order analysis is applied to ac impedance results obtained for moderate partial pressures(0.1-0.9 atm) at temperatures of 600-800°C. The objective is to elucidate the reaction mechanism by identifying the species which dominate the mixed diffusion process, i.e., any or all of the following: O_2^-, O_2^{2-} and dissolved CO_2.

EXPERIMENTAL

(62+38)mol% $(Li+K)CO_3$ melt was used as solvent. Electrochemical cell assembly, melt purification and gas handling have been described previously (4). The working electrode was a fully-immersed Au flag electrode(0.4 cm^2). In the present study, we concentrated precise measurements of the Warburg coefficient at the rest potential, using an ac impedance analysis based on the Randles'-Ershler equivalent circuit, and we present a reaction order analysis based on these coefficients. Impedance measurements were carried out using a Solartron 1250 frequency response analyzer (FRA) coupled with the Solartron 1186 (or 1286) electrochemical interface. Frequencies were varied from 1 Hz to 60 kHz and the signal amplitude was 5 mV rms. Data were transferred to microcomputers (Hewlett Packard 85 and NEC PC-9800) for faradaic impedance analysis.

ANALYSIS ON WARBURG COEFFICIENT

In the present study, the precise measurements of $CD^{1/2}$ is the most important things to be done. This may be done using standard electrochemical methods such as cyclic voltammetry, potential step, chronopotentiometry and chronocoulometry. However, these methods require relatively higher overvoltage than ac impedance method, and this may changes the local basicity of carbonate melt at the electrode surface (5). On the other hand, ac impedance method uses small perturbation amplitude (5 mV rms) at the rest potential in the measurement, the local basicity change may be negligiblly small. Furthermore, it is possible to obtain quite reliable impedance data over a wide frequency range (1 Hz to 60 kHz), because well-designed electronic apparatus, e.g., a recent FRA, are available and this can lead to a detailed view of the electrode process together with interfacial parameters such as the double layer capacitance, using well-established impedance theory. Thus, the ac impedance method seems to be most promising method for our purpose and applied to this study. Detailes of the analysis on impedance data were described in the previous paper (4).

According to the theory of ac impedance in the presence of semi-infinite diffusion, the Warburg coefficient, σ, is

$$\sigma = \frac{RT}{n^2F^2\sqrt{2}}\left(\frac{1}{C_O\sqrt{D_O}} + \frac{1}{C_R\sqrt{D_R}}\right) \qquad [7]$$

In the case of reactions [3] and [6], $1/C_RD_R^{1/2}$ is negligible compared with $1/C_OD_O^{1/2}$, because the product is CO_3^{2-}, i.e., the melt itself, and $C_O << C_R$. When the electrode processes take place at the electrode surface simultaneously, we have to take into account three diffusing species, i.e., O_2^-, O_2^{2-} and CO_2, in the interpretation of the reaction order. In the Randles-Ershler circuit adopted in this study, the diffusion impedance is simply represented by a single element, W, as shown in Figure 1.

$$W = (1 + j)\frac{\sigma_{app}}{\sqrt{\omega}} \qquad [8]$$

However, in the case of multiple (parallel) reaction pathes the observed σ values are to be regarded as effective values, not necessarily reflecting the reaction orders deduced from either the SOP and POP mechanism. Considering that the O_2^- and O_2^{2-} reactions both involve CO_2, the apparent diffusion impedance can be divided into three components as illustrated in Figure 2. According to this scheme, the apparent σ value may be expressed as follows.

$$\sigma_{app} = \frac{1}{A[O_2^-] + B[O_2^{2-}] + C[CO_4^{2-}]} + \frac{1}{D[CO_2]} \qquad [9]$$

where A, B, C and D are constants, and [ ] means the bulk concentration of a species in the melt.

Using equations [2] and [5] for $[O_2^-]$ and $[O_2^{2-}]$ respectively, and Henry's law for $[CO_2]$,

$$[CO_2] = K_h P_{CO_2} \qquad [10]$$

the apparent value of σ may be expressed as a function of P_{O_2} and P_{CO_2}. To simplify the analysis, three limiting cases are considered as follows.

(I). $A[O_2^-] > B[O_2^{2-}], C[CO_4^{2-}]$; O_2^-/CO_2 mixed diffusion case.

$$\sigma_{app}P_{CO_2} = aP_{CO_2}^{1.5}P_{O_2}^{-0.75} + b \qquad [11]$$

$$\sigma_{app}P_{O_2}^{0.75}P_{CO_2}^{-0.5} = a + bP_{O_2}^{0.75}P_{CO_2}^{-1.5} \qquad [12]$$

(II). $B[O_2^{2-}] > A[O_2^-], C[CO_4^{2-}]$; O_2^{2-}/CO_2 mixed diffusion case.

$$\sigma_{app}P_{CO_2} = aP_{CO_2}^{2}P_{O_2}^{-0.5} + b \qquad [13]$$

$$\sigma_{app}P_{O_2}^{0.5}P_{CO_2}^{-1} = a + bP_{O_2}^{0.5}P_{CO_2}^{-2} \qquad [14]$$

(III). $D[CO_2] > A[O_2^-], B[O_2^{2-}] > C[CO_4^{2-}]$; O_2^-/O_2^{2-} mixed diffusion case.

$$\sigma_{app}^{-1}P_{CO_2}P_{O_2}^{-0.5} = aP_{O_2}^{0.25}P_{CO_2}^{0.5} + b \qquad [15]$$

If any of these three limiting cases applies, it will show up as linear relationship of the Warburg coefficient in combination with the appropriate powers of P_{O_2} and P_{CO_2}.

REACTION ORDER PLOTS OF WARBURG COEFFICIENTS

Based on the above analysis, we have made reaction order plots for the Warburg coefficients, obtained at 650°C, according to equations [11]-[15]. The results are shown in Figures 3-5.

(I). $A[O_2^-] > B[O_2^{2-}], C[CO_4^{2-}]$; O_2^-/CO_2 mixed diffusion case.

Figure 3 shows the reaction order plot using equation [11]. The linearity was fairly good. This suggests that the oxygen reduction in $(Li+K)CO_3$ melt is dominated by the mixed diffusion of O_2^- and CO_2.

(II). $B[O_2^{2-}] > A[O_2^-], C[CO_4^{2-}]$; O_2^{2-}/CO_2 mixed diffusion case.

Figure 4 shows the reaction order plot using equation [13]. The plot did not show a linear relationship. This suggests that the oxygen reduction in (Li+K)CO_3 melt is unlikely to involve mixed diffusion of O_2^{2-} and CO_2.

(III). $D[CO_2] > A[O_2^-], B[O_2^{2-}] > C[CO_4^{2-}]$; O_2^-/O_2^{2-} mixed diffusion case.

Figure 5 shows the reaction order plot using equation [15]. Again, the plot did not show a linear relationship. This suggests that the oxygen reduction in (Li+K)CO_3 melt is unlikely to involve mixed diffusion of O_2^- and O_2^{2-}.

Consequently, we find that only one case, i.e., mixed O_2^-/CO_2 diffusion, results in a satisfactory linearity, and the other two cases do not produce a consistently linear dependence for bulk melt at 650°C. These results suggest that the simultaneous diffusion of O_2^- and CO_2 in the melt is the dominant feature of the oxygen reduction process at the fully-immersed Au flag electrode.

EFFECT OF TEMPERATURE

The above results apply only at the temperature of 650°C. The concentrations of O_2^-, O_2^{2-} and CO_2 are strong functions of temperature. Therefore, the reaction path of oxygen reduction may change with temperature. Thus, we have studied the reaction order correlation of the Warburg coefficients as a function of temperature, and the results are shown in Figure 6.

In this figure, only case (I), i.e., the mixed diffusion of O_2^- and CO_2, is shown. The other two cases did not produce a consistently linear dependence over the temperature range used in this study. Therefore, we conclude that simultaneous diffusion of O_2^- and CO_2 is the dominant feature of the oxygen reduction process in bulk (Li+K)CO_3 melt over the temperature range of 610-800°C.

CONCLUSIONS

The effect of O_2 and CO_2 partial pressures on O_2 reduction at a Au flag electrode in (62+38)mol% (Li+K)CO_3 melt has been analyzed in the temperature rage of 600-800°C. We carried out precise measurements of the Warburg coefficient of ac impedance at the rest potential, using a Randles'-Ershler equivalent circuit. Taking into account three possible diffusing species, i.e., O_2^-, O_2^{2-} and CO_2, a graphical analysis of reaction order was made, using the Warburg coefficients. We found that only the case of mixed diffusion of O_2^- and CO_2 results in a satisfactory linear relationship over the entire temperature rage of 600-800°C. Therefore, we concluded that the simultaneous diffusion of O_2^- and CO_2 is the dominant feature of oxygen reduction in (62+38)mol% $(Li+K)CO_3$ melt used in this study.

ACKNOWLEDGEMENT

This work was supported by a Grant-in-Aid for Scientific Research from the Ministry of Education, Science and Culture.

REFERENCES

1. A.J. Appleby and S.B. Nicholson, J. Electroanal. Chem., 53, 10 (1970).
2. A.J. Appleby and S.B. Nicholson, J. Electroanal. Chem., 83, 309 (1977).
3. A.J. Appleby and S.B. Nicholson, J. Electroanal. Chem., 112, 71 (1980).
4. I. Uchida, T. Nishina, Y. Mugikura and K. Itaya, J. Electroanal. Chem.,. 206, 229 (1986).
5. S.H. Lu and J.R. Selman, J. Electrochem. Soc., 137, 1125-1130 (1990).

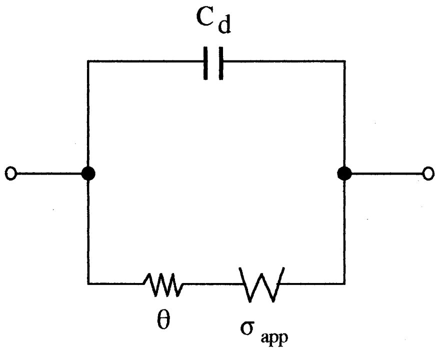

Figure 1. Randles'-Ershler Equivalent Circuit for AC Impedance of Oxygen Electrode in Molten Carbonate.

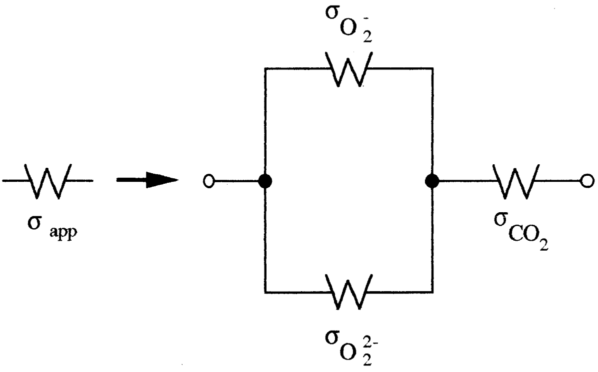

Figure 2. Equivalent Circuit for Diffusion Impedance, Taking into Account Mixed Diffusion of O_2^-, O_2^{2-} and CO_2.

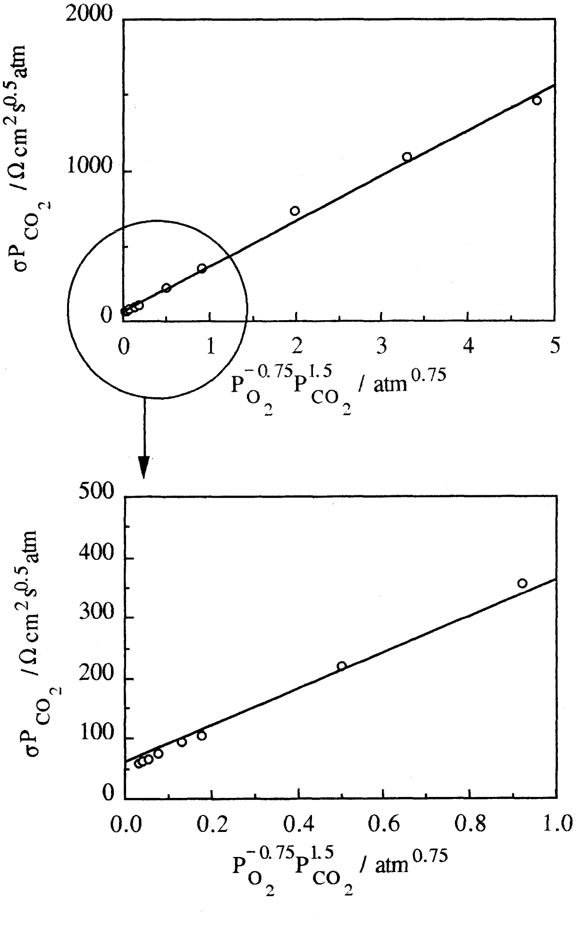

Figure 3. Reaction Order Analysis of Warburg Coefficients Assuming Mixed Diffusion of O_2^- and CO_2 in (62+38)mol% (Li+K)CO_3 Melt at 650°C.

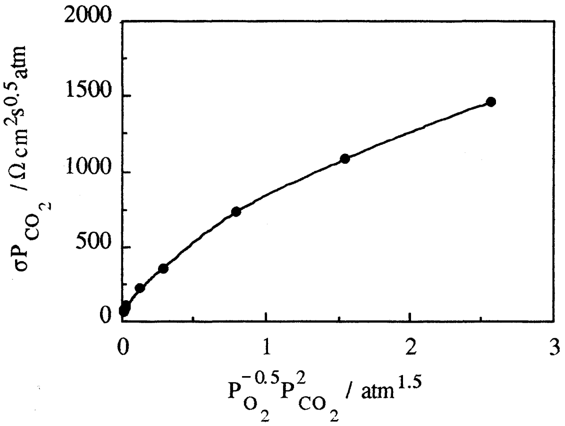

Figure 4. Reaction Order Analysis of Warburg Coefficients Assuming Mixed Diffusion of O_2^{2-} and CO_2 in (62+38)mol% (Li+K)CO_3 Melt at 650°C.

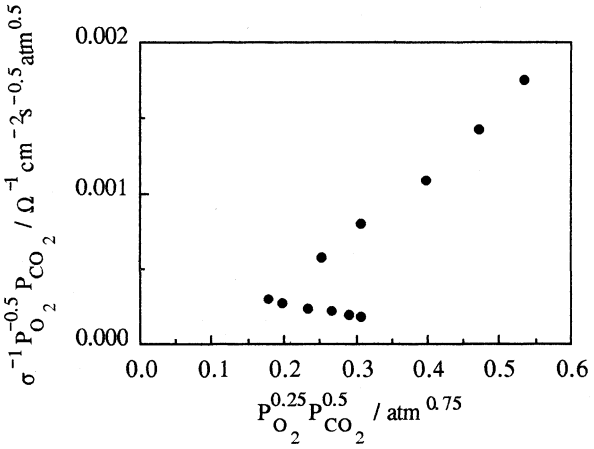

Figure 5. Reaction Order Analysis of Warburg Coefficients Assuming Mixed Diffusion of O_2^- and O_2^{2-} in (62+38)mol% (Li+K)CO_3 Melt at 650°C.

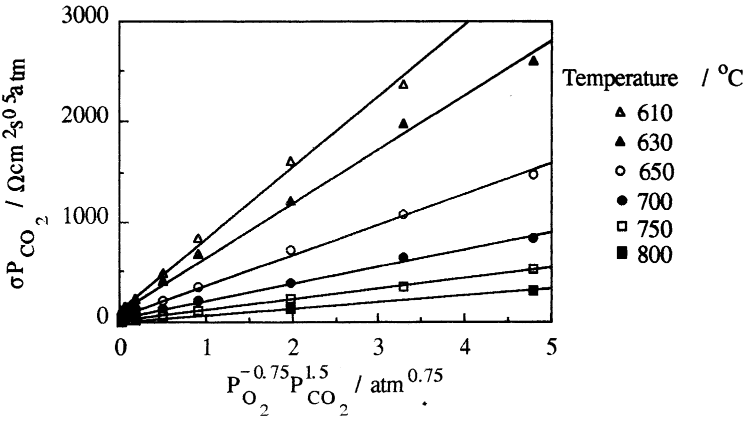

Figure 6. Reaction Order Analysis of Warburg Coefficients Assuming Mixed Diffusion of O_2^- and CO_2 in (62+38)mol% (Li+K)CO_3 Melt for Various Temperature.

DOI: 10.1149/199017.0716PV

CO_2 PRESSURE DEPENDENCE OF OXYGEN REDUCTION IN MOLTEN CARBONATE

Ken-ichiro OTA, Kenichi KURODA and Masao TAKAHASHI

Dep. of Energy Engineering, Yokohama National Univ.
Tokiwadai, Hodogaya-ku, Yokohama 240, Japan

ABSTRACT

Cyclic voltammetry on gold electrode has been used to study the dissolved oxygen species in alkaline molten carbonate.It has been found that the peak current per square root of the potential aweep rate, $I_p/v^{1/2}$ is the function of square root of the concentration of the dissolved oxygen species.The slopes of CO_2 dependence were explained neither by peroxide formation or superoxide formation high CO_2 pressure region. Since the slopes of CO_2 and O_2 dependence, in high CO_2 pressure region, were nealy 0 and 0.5, respectively, percarbonate ion, $CO_4{}^{2-}$ might coexist with another ion.

The cathodic oxygen reduction on Au has been studied by the potential sweep method in several alkaline carbonate melts. The first reduction current peak that was near the reversible oxygen potential was proportional to the square root of the sweep rate. The ratio $I_p/v^{1/2}$ corresponds to $P_{O2}{}^{0.5}$. The dependence of the ratio on P_{CO2} was different by the melt compositions. Generally, the factor of the dependence of the ratio on P_{CO2} was larger at lower CO_2 pressure. At high CO_2 pressure region, the ratio did not depend on P_{CO2} so much. The percarbonate ion may exist in the melt.

INTRODUCTION

On the cathode of a molten carbonate fuel cell(MCFC), oxygen is reduced to carbonate ion($CO_3{}^{2-}$).

$$O_2 + 2CO_2 + 4e = 2CO_3{}^{2-}$$

In the study of the reaction mechanisms of oxygen reduction, the pressure dependence of the reduction current gives an important information. Although several reports[1-13] have been published on this matter, the reaction mechanism of the oxygen reduction has not been clearly understood especially on the oxygen species in the carbonate melt. In this study the CO_2 and the O_2 pressure dependences of the reduction current of O_2 have been studied in Li_2CO_3, $(Li\text{-}K)CO_3$ and $(Na\text{-}K)CO_3$ melts.

Appleby[3-5] measured the oxygen reduction current on a gold electrode in alkaline carbonate melts by the potential sweep method. The following two reactions on the oxygen reduction have been proposed in the reports.

i) Peroxide formation

$$2CO_3^{2-} + O_2 = O_2^{2-} + 2CO_2$$

$$[O_2^{2-}] = K_1 \ P_{O_2}^{0.5} \ P_{CO_2}^{-1}$$

ii) Superoxide formation

$$2CO_3^{2-} + 3O_2 = 4O_2^{-} + 2CO_2$$

$$[O_2^{-}] = K_2 \ P_{O_2}^{0.75} \ P_{CO_2}^{-0.5}$$

The peroxide ion has been reported to dominate in Li-rich melt and the superoxide ion is dominant in K-rich melt. Vogel et al[7] measured the limiting current of oxygen reduction on gold and claimed that the superoxide ion was dominant at low CO_2 pressures region in 62 mol% Li_2CO_3-38 mol% K_2CO_3 melt.

If the formation of the peroxide ion and the superoxide ion follow the above reactions, the concentration of the peroxide ion should be proportional to $P_{CO_2}^{-1}$ and also to $P_{O_2}^{0.5}$ and the concentration of the superoxide ion should be proportional to $P_{CO_2}^{-0.5}$ and to $P_{O_2}^{0.75}$.

Although the factor of the oxygen pressure dependence is usually 0.5, the factor of CO_2 pressure dependence varies with CO_2 pressure. At low CO_2 pressure region, the concentration of oxygen species in the carbonate melt has been reported to be proportional to $P_{CO_2}^{-1}$, and at high CO_2 pressure region, the concentration was less dependent on P_{CO_2} and sometimes independent of the CO_2 pressure. There might be another reaction present at high CO_2 pressure region,i.e, percarbonate formation.

iii) Percarbonate formation

$$O_2 + 2CO_3^{2-} = 2CO_4^{2-}$$

$$[CO_4^{2-}] = K_3 \ P_{O_2}^{0.5} \ P_{CO_2}^{0}$$

Figure 1 shows the relation between P_{CO_2} and the concentration of the oxygen species in a carbonate melt. At low CO_2 pressure region, peroxide ions might be dominant and the concentration should be inversely proportional to P_{CO_2}. At high CO_2 pressure region the percarbonate ion might be dominant and the concentration should be independent of CO_2 pressure. In the intermediate pressure region the factor of the CO_2 pressure dependence changes from 1 to 0.

In this study the oxygen reduction current was measured on Au electrode in order to detect the dissolved oxygen species in the alkaline carbonate melt.

EXPERIMENTAL

Figure 2 shows the schematic drawing of the cell. The reagent grade alkaline carbonates(Li_2CO_3, Na_2CO_3, K_2CO_3) were used. The carbonate powder was placed in a pure alumina crucible. The cell was evacuated and dried at 623K for 12 hours. After that, the cell was heated up to 923K and CO_2 gas was bubbled for 24 hours.

An Au disk (10mmφ x1mm) was utilized for the cathode. The surface area was $2cm^2$. The counter electrode and the reference electrode were Au wires (2mmφ) in the same melt. This reference electrode should show the potential of the reversible oxygen electrode (ROE) and the difference from the potential corresponds directly to the oxygen overpotential of the electrode.

In order to obtain the oxygen reduction current the potential sweep method(cyclic or single sweep) was utilized. The sweep rate was varied from 0.1 to 1V/s. The temperature range was from 923 to 1123K. The O_2 pressure was from 0.1 to 0.9atm and the CO_2 pressure range was from 10^{-5} to 0.9 atm.

RESULTS AND DISCUSSION

A typical potential sweep voltammogram in (Li-K)melt is shown in Fig.3. The O_2 reduction peaks appear near the theoretical potential(~ 30mV vs ROE) and show the reversible characteristic. The peak currents were plotted against the square root of the sweep rate, as shown in Fig.4. The linear relations were observed. This means that the oxygen reduction was controlled by the diffusion process. The slopes of these lines correspond the $CD^{1/2}$, where C is the concentration of the reactant and D is the diffusion coefficient.

The value, $I_p/v^{1/2}$ was proportional to $P_{O_2}^{0.5}$ in 62 mol% Li_2CO_3-38 mol% K_2CO_3 at the fixed CO_2 pressure. This tendency was also observed in any carbonate melt of this study. Figure 5 shows the dependence of the value, $I_p/v^{1/2}$ on CO_2 pressure. The relation is complicated. At low CO_2 pressure region, the slope of this line is 0.3~ 0.4. At high CO_2 pressure region, the slopes are 0.1~ 0.2. If the diffusion coefficient, D does not depend on the CO_2 pressure at a fixed temperature, the slope of the line might show the relation between the oxygen species (reductant) in the melt and the CO_2 pressure. If the peroxide ion or the superoxide ion is dominant, the slope should be -1 or -0.5, respectively. Our result can be explained neither by the presence of peroxide nor superoxide since the slope is small especially at high CO_2 pressures region. Taking into account of the O_2 pressure dependence, the percarbonate ion might be present in the melt. If the percarbonate ion is dominant in the melt, the concentration should not depend on CO_2 pressure. Our results can be explained by the transition region from percarbonate to peroxide.

Figure 6 shows the cyclic voltammograms on Au at low CO_2 pressure region (0.009 atm CO_2, 0.1 atm O_2) in (Li-K)melt. Although the CO_2 pressure is very low, the first reduction peak was clearly observed near 0V vs ROE. The result of this first peak is given in Fig.5. Figure 6(a) shows the result of the potential sweep at the same conditions. The potential was sweeped cathodically from the oxygen potential. The second reduction peak appeared at -0.6V vs ROE. This second peak was clearly observed at the slow sweep rate. The second peak in (Li-K)melt has been reported before by Uchida et al[10].

Figure 7 shows the potential sweep voltammograms for oxygen reduction in 43 mol% Na_2CO_3-57 mol% K_2CO_3 at 1073K. There is not much difference in the shape from (Li-K)melt. The second reduction peaks were not observed. The value, $I_p/v^{1/2}$ was only 1.4 time larger when the CO_2 pressure was decreased from 0.9 to 0.1atm. This difference is very small.

Figure 8 shows the result in low CO_2 pressure and high O_2 pressure in the same melt. The shape is quite different from those at Fig.7. The first reduction peak is no more clear. The second peak becomes very large. The second peak decreased with decrease of O_2 pressure.

Generally the counter diffusion of O^{2-} ion formed on the cathode is considered to be very fast, since the solubility of CO_2 in alkaline carbonate is ten times larger than that of O_2. However, when the ratio of the partial pressures, P_{O_2}/P_{CO_2} is high, the neutralization and the diffusion of O^{2-} is not fast and the large potential shift might be observed.

The reason why the second reduction peak appeared easily in (Na-K)melt is not due to the low solubility of

CO_2, but the high solubility of Na_2O or K_2O. Since the solubilities of Na_2O and K_2O are high and the concentration of O^{2-} on cathode becomes high, the cathode can easiliy polarize up to -0.6V. After the O^{2-} concentration becomes saturated, the diffusion controlled current peak appears at -0.6V.

ACKNOWLEDGEMENT

The support of the Ministry of Education, Science and Culture Japan under the Grant-in-Aid on Priority-Area Research is gratefully acknowledged.

REFERENCES

1) J. R. Selman and H. C. Maru, Advances in Molten Salt Chemistry, vol.**4**, 300(1981).

2) A. Borucka and C. M. Sugiyama, Electrochimica Acta, **14**, 871(1969).

3) A. J. Appeleby and S. B. Nicholson, J. Electroanal. Chem., **53**, 105(1974).

4) A. J. Appeleby and S. B. Nicholson, J. Electroanal. Chem., **83**, 309(1977).

5) A. J. Appeleby and S. B. Nicholson, J. Electroanal. Chem., **112**, 71(1980).

6) S. H. White and U. M. Twardoch, Electrochimica Acta, **27**, 1599(1982).

7) W. M. Vogel , S. W. Smith and L. J. Bregoil, J. Electrochem. Soc., **130**, 574(1983).

8) I. Uchida, T. Nishina, Y. Mugikura and K. Itaya, J. Electroanal. Chem., **206**, 229(1986).

9) I. Uchida, Y. Mugikura, T. Nishina and K. Itaya, J. Electroanal. Chem., **206**, 241(1986).

10) I. Uchida, T. Nishina, Y. Mugikura and K. Itaya, J. Electroanal. Chem., **209**, 125(1986).

11) S. H. White and U. M. Twardoch, J. Electrochem. Soc., **135**, 892(1988).

12) S. H. White and U. M. Twardoch, J. Appl. Electrochem., **19**, 901(1989).

13) B. B. Dave, R. E. White, S. Srinivasan and A. J. Appleby, Proceeding of the symposium on fuel cells, 168(1989).

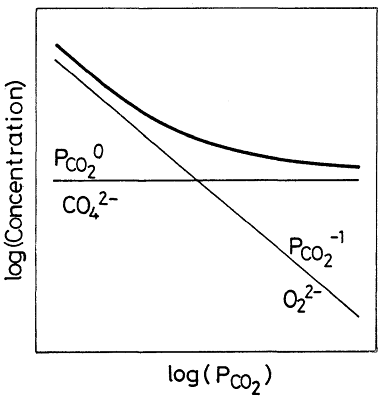

Fig.1 Relation between the total concentration of the dissolved oxygen species and CO_2 pressure in the coexistance of peroxide and percarbonate ions (arbitrary scale).

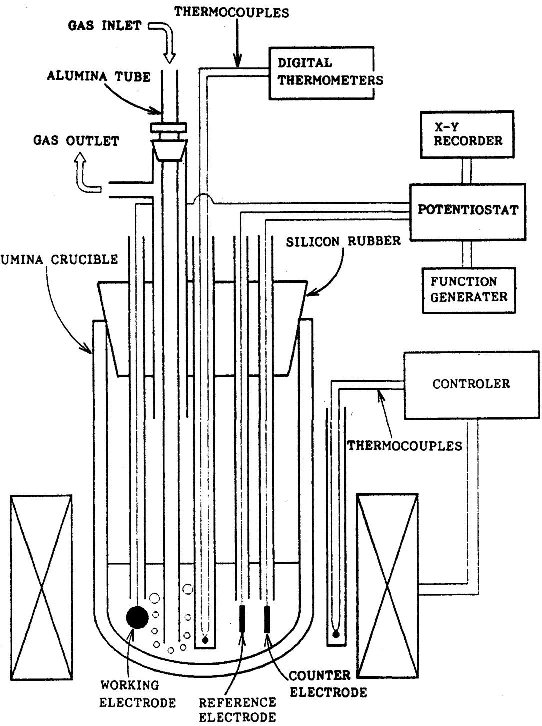

Fig.2 Experimental apparatus.

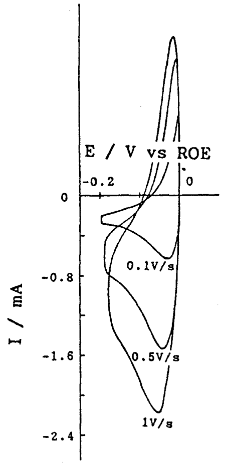

Fig.3 Potential sweep voltammogram for oxygen reduction. Li/K=62/38 melt, 923K, 0.9atm CO_2, 0.1atm O_2.

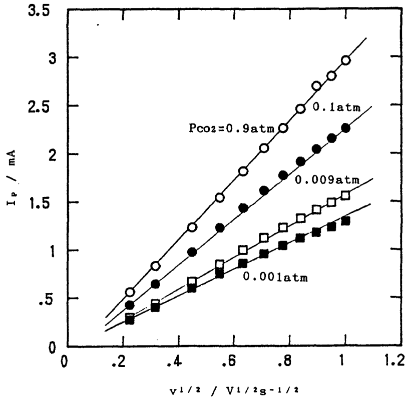

Fig.4 Relation between peak current and sweep rate. Li/K=62/38 melt, 873K, 0.1atm O_2.

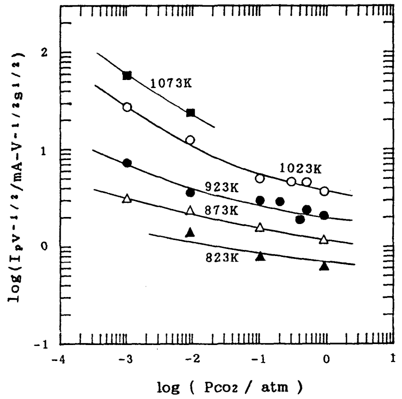

Fig.5 Relation between peak current per square root of potential sweep rate and CO_2 pressure. Li/K=62/38 melt, 0.1atm O_2.

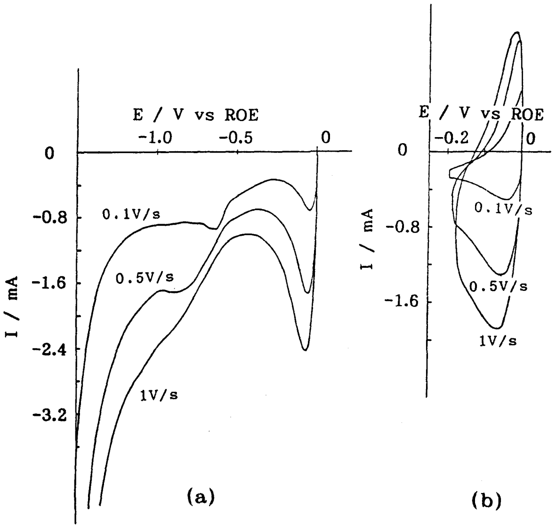

Fig.6 Potential sweep voltammogram for oxygen reduction. Li/K=62/38 melt, 823K, 0.009atm CO_2, 0.1atm O_2.

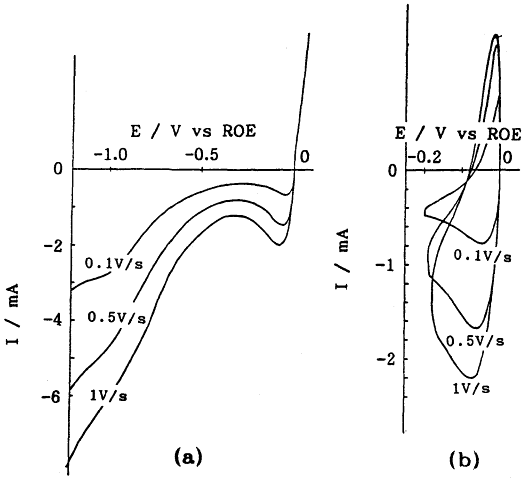

Fig.7 Potential sweep voltammogram for oxygen reduction. Na/K=43/57 melt, 1073K, 0.9atm CO_2, 0.1atm O_2.

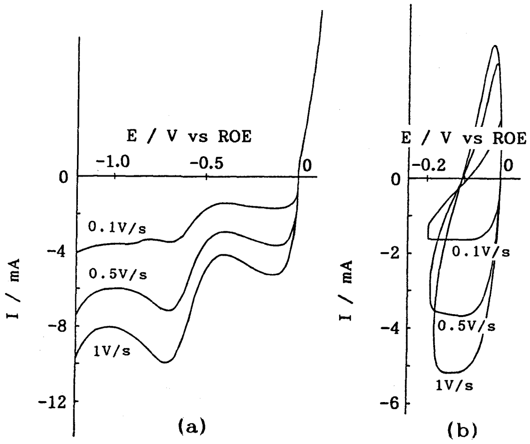

Fig.8 Potential sweep voltammogram for oxygen reduction. Na/K=43/57 melt, 1073K, 0.1atm CO_2, 0.9atm O_2.

DOI: 10.1149/199017.0726PV

IMPEDANCE ANALYSIS OF OXYGEN REDUCTION IN LITHIUM CARBONATE MELT: EFFECT OF PARTIAL PRESSURE OF CARBON DIOXIDE

Bhasker B. Davé*, Ralph E. White*, Supramaniam Srinivasan
and A. John Appleby
Center for Electrochemical Systems and Hydrogen Research
Texas Engineering Experiment Station
and
*Department of Chemical Engineering
Texas A&M University
College Station, Texas 77843

Abstract

Effects of partial pressure of carbon dioxide and temperature on oxygen reduction kinetics in lithium carbonate melt were examined using a electrochemical impedance spectroscopy (EIS) and cyclic voltammetry. The impedance spectra were analyzed by a Complex Nonlinear Least Square (CNLS) method, using the Randles-Ershler equivalent circuit model, to estimate the electrode kinetic and mass transfer parameters such as the charge transfer resistance and Warburg coefficient. The cyclic voltammetric measurements indicated that the oxygen reduction process in lithium carbonate melt is "reversible" up to 200 mV/s. Values of the diffusion parameter, $D_O^{1/2}C_O$, determined by cyclic voltammetry concurred with those estimated by the EIS method. The reaction order with respect to carbon dioxide and the activation energy for the exchange current density were determined to be −0.52 and 132 kJ/mol respectively. Also, the reaction order with respect to carbon dioxide and the activation energy for $D_O^{1/2}C_O$ were calculated to be −0.8 and 185 kJ/mol respectively.

Introduction

The oxygen reduction reaction in molten alkali carbonate electrolytes has been studied for the past 25 years because of its vital role in the molten carbonate fuel cell. Appleby and Nicholson (1-4) examined this reaction on a submerged gold electrode using steady state and potential sweep techniques. They observed that oxygen reacts with carbonate ions and forms peroxide and/or superoxide ions and the concentrations of these species depend on the cations present in the melt. In a pure Li_2CO_3 or a Li-rich melt the peroxide species is dominant, whereas in a K-rich melt the superoxide species is dominant. Hence, the mechanism of oxygen reduction strongly depends on the cations present in the melt. Further, they also concluded that the molecular oxygen does not participate in the electrochemical reduction process, directly. They proposed the following reaction mechanism for oxygen reduction in pure lithium carbonate melt:

$$1/2O_2 + CO_3^{2-} \rightleftharpoons O_2^{2-} + CO_2 \qquad [1]$$

$$O_2^{2-} + e^- \rightleftharpoons (O^-) + O^{2-} \qquad [2]$$

$$(O^-) + CO_2 + e^- \rightleftharpoons CO_3^{2-} \qquad [3]$$

$$\underline{O^{2-} + CO_2 \rightleftharpoons CO_3^{2-}} \qquad [4]$$

$$1/2O_2 + CO_2 + 2e^- \rightleftharpoons CO_3^{2-} \qquad [5]$$

where (O^-) is a transient species. According to this reaction mechanism, the first charge transfer reaction is the rate determining step for an immersed electrode. Andersen (5) carried out a thermodynamic study on the chemical equilibria in molten alkali carbonate electrolytes and demonstrated the presence of peroxide ions in quenching experiments followed by chemical analyses. Appleby and Van Drunen (6) determined the total solubility of oxygen (mainly in the form of peroxide and superoxide ions) in molten carbonate electrolytes as a function of temperature using quenching method. Vogel et al. (7) studied the $(Li\text{-}K)CO_3$ eutectic melt at 650 °C, using a rotating gold wire and concluded that superoxide is dominant in this melt and the concentration of molecular oxygen in the melt is negligible. Smith et al. (8) determined the total solubility of oxygen in $(Li\text{-}Na\text{-}K)CO_3$ eutectic melt as a function of gas composition at 650 °C, using a chemical method. They concluded that oxygen reacts with $(Li\text{-}Na\text{-}K)CO_3$ melt at 650 °C to form superoxide ions and the concentration of physically dissolved, molecular, oxygen is negligible. Lu (9) investigated the oxygen reduction process in pure Li_2CO_3 and a Li-K (62 mol%:38 mol%) carbonate eutectic mixture using a potential step method. The exchange current density, determined by Lu, is two orders of magnitude higher than that reported by Appleby and Nicholson who used the potential scan tèchnique. But the dependence of oxygen reduction kinetics on partial pressures of oxygen and carbon dioxide observed by Lu could not be explained by any of the mechanism proposed in the literature. Uchida et al. (10) determined the electrode kinetic parameters for oxygen reduction in a $(Li\text{-}K)CO_3$ (42.7 mol%:57.3 mol%) eutectic melt on a gold electrode using impedance analysis, potential step, and coulostatic relaxation techniques. They found that the exchange current density was about the same order of magnitude as that of Lu. In addition, they concluded that of the three methods for the determination of the electrode kinetic parameters for oxygen reduction in molten carbonates the impedance analysis is the most reliable. They (11) also determined the temperature dependence of the electrode kinetic parameters for oxygen reduction on gold in (Li-K)CO_3.

The previous studies show that the presence of physically dissolved molecular oxygen in molten carbonate electrolyte is insignificant. Oxygen reacts with the molten alkali carbonates to form peroxide and/or superoxide ions; the concentrations of these species depend on the cations present in the melt. The mechanism of oxygen reduction in molten carbonate is not well understood and the results reported in the literature are not consistent. Consequently, in the present work, we used pure lithium carbonate melt to avoid the complexity of simultaneous formation of peroxide and superoxide ions. The influence of partial pressure of oxygen on the oxygen reduction kinetics was investigated by electrochemical impedance spectroscopy (EIS) and cyclic voltammetry. Also, the temperature dependence of oxygen reduction kinetic was determined.

Experimental

The experimental setup for high temperature electrode kinetic study and methodology are as described in a previous publication (12). The working electrode was made of a submerged gold flag (0.025 mm thick), with a geometrical area of one square centimeter, connected to the gold current collector (0.5 mm diameter) by a thin gold wire to minimize the meniscus effect (2, 13). The counter electrode was a large gold foil circumscribing the working electrode to ensure uniform current distribution. The reference electrode was also made of a gold foil, but encased in an alumina tube which was pressed against the bottom of the electrochemical cell. The Puratronic grade (4 N) gold foils and wires were obtained from Johnson Matthey/ÆSAR Group.

Digital mass flow controllers/meters manufactured by Teledyne-Hastings Raydist were used to provide the gas mixtures of the desired compositions (O_2, CO_2 and Ar) with high precision (± 1% Full Scale). The high purity gases were obtained from Matheson Gas Products and the traces of water were removed by passing the blended gas through a column of 5 Å molecular sieves and Drierite (Fisher Scientific). The gas mixture was bubbled into the melt in the vicinity of the working electrode at a flow rate of 50 $cm^3\ min^{-1}$ through a long alumina tube with four holes. The composition of the gas mixture supplied to the reference electrode compartment was the same as the one used for the working electrode, but at a lower flow rate (5 $cm^3\ min^{-1}$). In this study, P_{CO_2} was varied from 0.02 to 0.4 atm., while P_{O_2} was maintained constant at 0.6 atm. The total pressure was 1 atm., by varying the partial pressure of argon. The high purity (5 N) lithium carbonate (Alfa Products) was carefully weighed in an alumina crucible

(90 ml capacity)and the electrochemical cell was slowly heated (50 °C/hr) to 350 °C in an inert environment. The electrochemical cell assembly was dried at 350 °C in a carbon dioxide environment for 24 hours before heating to 800 °C.

The data acquisition set-up consisting of a potentiostat/galvanostat (Model 273), lock-in-amplifier (Model 5301A), personal computer (IBM PS/2), and software (Model 378) supplied by EG&G Princeton Applied Research was used for the cyclic voltammetric and electrochemical impedance spectroscopic experiments. For the EIS, measurements were made over a wide range of frequencies (0.05 Hz to 10 kHz) for the sinusoidal excitation signal, because the capacitive effect, attributed to the double layer, is significant at high frequency, and the diffusional (Warburg) impedance is dominant at low frequency. The impedance measurements for frequencies higher than 5 Hz were carried out by the Phase Sensitive Detection (PSD) technique using the lock-in-amplifier and the potentiostat. For frequencies below 5 Hz, the cell impedance was measured by the Fast Fourier Transform (FFT) technique using, the personal computer and potentiostat. The results of low frequency measurements (below 5 Hz) represent the average values of 15 data cycles, which was done to improve the accuracy of the data by averaging out the noise interference. The amplitude of the excitation signal was kept at 5 mV to ensure a linear electrochemical response.

Results and Discussion

Impedance Measurements and Analyses

The impedance spectra were obtained for oxygen reduction on the submerged gold electrode in lithium carbonate melt at the equilibrium potential as a function of P_{CO_2} and temperature. As described in the previous work (12), the absence of a semicircle in the complex plane impedance plot indicated fast oxygen reduction kinetics (14). In the region of low frequency, the complex plane plot showed a linear behavior with a slope of 45° due to the Warburg impedance (15). The effect of partial pressure of carbon dioxide on the Bode plot, phase angle vs. log ω, at 800 °C is shown in Fig. 1. In a high frequency region, the phase angle approached 0° for all plots, indicating a purely resistive behavior of the cell impedance. The impedance at 0° phase angle is a measure of the uncompensated electrolyte resistance, R_s, between the working and reference electrodes. At frequencies below 30 Hz, the phase angle approached −45°, indicating that the diffusional impedance is significant. The influence of partial pressure of carbon dioxide on oxygen reduction kinetics was evident at the intermediate frequencies, showing the increased charge transfer resistance with an increase in P_{CO_2}. The sharp deviations in the Bode plots at about 120 Hz (second harmonic frequency of the line) are due to the measurement system.

The impedance spectra were resolved by using the Randles-Ershler equivalent circuit (16, 17) model shown in Fig. 2. The Randles-Ershler equivalent circuit reflects two parallel process occurring at the electrode-electrolyte interface, namely, the double layer charging and the faradaic reaction. The faradaic impedance consists of the charge transfer resistance which is in series with the Warburg (diffusional) impedance. The uncompensated electrolyte resistance between the working and reference electrodes, R_s, is connected in series with the interfacial impedance. A Complex Nonlinear Least Square (CNLS) parameter estimation program (18-20), based on Levenberg-Marquardt algorithm, was used to resolve the impedance spectra. In our analysis, we found that the weighting factor (inverse of the error variance) considerably influenced the accuracy of the parameters estimated from the impedance data (21). Here, we have used the proportional and functional proportional weighting factors (22) to determine the electrode kinetic and mass transfer parameters This analysis yields parameters such as the charge transfer resistance, double layer capacity, Warburg coefficient, and uncompensated electrolyte resistance.

The influence of partial pressure of carbon dioxide on real part of impedance (Z') vs. inverse square root of angular frequency ($\omega^{-1/2}$) for 800 °C temperature is shown in Fig. 3. In a low frequency region, Z' vs. $\omega^{-1/2}$ plots showed a linear behavior with a slope proportional to the Warburg Coefficient (σ). As demonstrated in Fig. 3, the Warburg coefficient increased with an increase in P_{CO_2}, which is mainly due to the decrease in the peroxide ion concentration (Eqn. [1]). As shown in Fig. 3, the model impedance data, calculated using the estimated parameters and the Randles-Ershler equivalent circuit model, agreed with the experimental data. The electrode kinetic and mass transfer parameters as function of P_{CO_2} for temperatures 750, 800 and 850 °C are presented in Tables 1-3 respectively. These tables show that a decrease in P_{CO_2} from 0.4 to 0.02 atm., causes a ten fold decrease in the magnitude of the Warburg coefficient. A similar effect was observed when temperature was increased from 750 to 850 °C. The charge transfer resistance also decreased with an increase in temperature and a decrease in partial pressure of carbon dioxide. The double layer capacity increased with the decrease P_{CO_2}. The change in the uncompensated electrolyte resistance with temperature and P_{CO_2} was negligible. The effect of partial pressure of carbon dioxide on log $|Z|$ vs. log ω plot is shown in Fig. 4. The log $|Z|$ vs. log ω plot converged to the value of uncompensated electrolyte resistance at high frequencies. In the low frequency region, complete relaxation due to the charge transfer process was not observed due to the diffusional impedance. Also, it is evident from Fig. 4 that the experimental data concurred with the model data for the entire frequency range of the experiment. Since impedance measurements were obtained at the rest potential, the following expressions can be used for the charge transfer resistance and the Warburg coefficient (23):

$$R_{ct} = \frac{RT}{nFi_o} \qquad [7]$$

$$\sigma = \frac{RT}{n^2F^2A\sqrt{2}}\left(\frac{1}{D_O^{1/2}C_O} + \frac{1}{D_R^{1/2}C_R}\right) \qquad [8]$$

For peroxide reduction in Li_2CO_3 melt, C_O is much smaller than C_R because the final product is carbonate ion. Therefore $1/D_R^{1/2}C_R$ is negligible compared with $1/D_O^{1/2}C_O$. Thus Eqn. [8] can be approximated by the following expression:

$$\sigma = \frac{RT}{n^2F^2A\sqrt{2}}\left(\frac{1}{D_O^{1/2}C_O}\right) \qquad [9]$$

The calculated values of the exchange current density and product, $D_O^{1/2}C_O$, as a function of P_{CO_2} and temperature are given in Tables 1-3. The dependence of the exchange current density on P_{CO_2} was determined to be -0.5 from the slope of $\log i_0$ vs. $\log P_{CO_2}$ shown in Fig. 5. The Arrhenius plots for the exchange current density are shown in Fig. 6, for various partial pressures of carbon dioxide, and the activation energy was calculated to be 131.8 kJ/mol; this value is consistent with the value obtained in the previous work (12). The plots of $\log D_O^{1/2}C_O$ vs. $\log P_{CO_2}$, for three temperatures, are shown in Fig. 7, and the value of the reaction order with respect to carbon dioxide calculated from these plots is -0.8. The Arrhenius plots for $D_O^{1/2}C_O$ for four partial pressures of carbon dioxide are shown in Fig. 8; the average value of the apparent activation energy was 185 kJ/mol.

Cyclic Voltammetry

Cyclic voltammetry measurements were made for oxygen reduction on gold electrode in quiescent Li_2CO_3 melt as a function of scan rate, temperature, and P_{CO_2}. The working electrode potential was scanned between the rest potential and -0.5 V vs. the potential of the reference electrode; the scan rate was varied from 10 to 200 mV/s. The effect of P_{CO_2} on the cyclic voltammogram, recorded at the scan rate of 100 mV/s at 800 °C temperature is shown in Fig. 9. During the forward scan, a diffusion-limited peak followed by a limiting plateau was observed. The peak potential (E_p) was found to be independent of the scan rate (up to 200 mV/s) and the position of this peak was 40-45 mV negative to the rest potential. As shown in Fig. 9, an increase in partial pressure of carbon dioxide, decreased the cathodic peak current density. The current densities in the reverse scan were less cathodic than those obtained in the forward sweep. At the end of the sweep, a large anodic current was observed which subsided slowly and reached zero in a few minutes. This phenomenon is attributed to the local accumulation of the unneutralized oxide ions which shifts the reversible electrode potential in negative direction (24). The effects of P_{CO_2} on the peak current density (i_p) vs. square root of the scan rate ($v^{1/2}$) plot at 800 °C are shown in Fig. 10. A linear behavior of i_p vs. $v^{1/2}$ and invariance of E_p with respect to the scan rate indicate that oxygen reduction in Li_2CO_3 melt is "reversible" up to 200 mV/s (25). An increase in partial pressure of carbon dioxide decreased the slope of i_p vs. $v^{1/2}$ plot, which is directly proportional to $D_O^{1/2}C_O$, where D_O is the diffusion coefficient and C_O is the bulk concentration of the diffusion limiting reactant species. As suggested by Appleby et al. (2), the diffusion-limited peak for O_2 reduction in Li_2CO_3 can be described by the theory developed by Berzins and Delahay (26) for the reversible diffusion controlled peak where the product activity is considered to be invariant and equal to unity (e.g. metal deposition). According to Berzins et al., the peak current density is given by the following expression:

$$i_p = 0.61(nF/RT)^{1/2} nF D_O^{1/2} C_O^* v^{1/2} \qquad [9]$$

The transport parameter, $D_O^{1/2}C_O$, was calculated from the slope of i_p vs. $v^{1/2}$ plot using equation [9]. The calculated values of the transport parameter for various P_{CO_2} and temperatures are compared with those estimated by the electrochemical impedance spectroscopy. An increase in partial pressure of carbon dioxide decreased the product, $D_O^{1/2}C_O$, which is mainly due to the decrease in peroxide ion concentration. Temperature has a significant effect on the product, $D_O^{1/2}C_O$, e.g for 0.02 atm. partial pressure of carbon dioxide, more than an eight fold increase in $D_O^{1/2}C_O$ was observed when temperature was increased from 750 to 850 °C. However, the influence of temperature on $D_O^{1/2}C_O$ was less significant at higher P_{CO_2}. The reaction order and apparent activation energy for $D_O^{1/2}C_O$, estimated by cyclic voltammetry technique concurred with those obtained by impedance analysis.

Conclusions

The kinetic and mass transfer related parameters for the oxygen reduction in pure Li_2CO_3 were determined as a function of P_{CO_2} and temperature by electrochemical impedance spectroscopy and cyclic voltammetry. The impedance spectra were analyzed by the complex nonlinear least square method. The diffusion parameter $D_O^{1/2}C_O$ obtained by impedance analysis and by cyclic voltammetry showed excellent agreement. The reaction order with respect to carbon dioxide and the activation energy for the exchange current density were determined to be −0.52 and 132 kJ/mol respectively. Also, the reaction order with respect to carbon dioxide and the activation energy for $D_O^{1/2}C_O$ were calculated to be −0.8 and 185 kJ/mol respectively.

Acknowledgement

Financial support for this project from the U. S. Department of Energy (Contract No. DE-FG22-87PC79931) and Electric Power Research Institute (Contract No. RP8002-7) is gratefully acknowledged.

References

1. A. J. Appleby and S. B. Nicholson, *J. Electroanal. Chem.*, **38**, App. 14, (1972).
2. A. J. Appleby and S. B. Nicholson, *J. Electroanal. Chem.*, **53**, 105, (1974).
3. A. J. Appleby and S. B. Nicholson, *ibid.*, **83**, 309, (1977).
4. A. J. Appleby and S. B. Nicholson, *ibid.*, **112**, 71, (1980).
5. B. Kr. Andersen, Ph. D. Dissertation, The Technical University of Denmark, Lyngby, Denmark, (1975).
6. A. J. Appleby and C. Van Drunen, *J. Electrochem. Soc.*, **127**, 1655, (1980).
7. W. M. Vogel, S. W. Smith, and L. J. Bregoli, *ibid.*, **130**, 575, (1983).
8. S. W. Smith, W. M. Vogel and S. Kapelner, *ibid.*, **129**, 1668, (1982).
9. S. H. Lu, Ph. D. Dissertation, Illinois Institute of Technology, Chicago, Il., (1985).
10. I. Uchida, T. Nishina, Y. Mugikura and K. Itaya, *J. Electroanal. Chem.*, **206**, 229, (1986).
11. I. Uchida, T. Nishina, Y. Mugikura and K. Itaya, *ibid.*, **209**, 125, (1986).
12. B. B. Dave, R. E. White, S. Srinivasan and A. J. Appleby, "Impedance Analysis for Oxygen Reduction Process in Molten Carbonate Electrolyte," to be submitted to *J. Electrochem. Soc.*, (1989).
13. T. Nishina, M. Takahashi, and I. Uchida, *J. Electrochem. Soc.*, **137**, 1112, (1990).
14. R. De Levie and L. Pospísil, *J. Electroanal. Chem.*, **22**, 277, (1969).
15. E. Warburg, *Ann. Phys. Chem.*, **67**, 493, (1899).
16. J. E. B. Randles, *Discuss. Faraday Soc.*, **1**, 11, (1947).
17. B. Ershler, *ibid.*, **1**, 269, (1947).
18. J. R. Macdonald, *J. Electroanal. Chem.*, **223**, 25, (1987).

19. J. R. Macdonald, in "Impedance Spectroscopy -Emphasizing Solid Materials and Systems," J. R. Macdonald, Editor, p. 1, John Wiley & Sons, New York, (1987).

20. J. R. Macdonald, "Impedance Spectroscopy: Old Problems and New Developments," submitted to *Electrochim. Acta*, (August 1990).

21. B. B. Dave, R. E. White, S. Srinivasan and A. J. Appleby, "Impedance Analysis for Randles-Ershler Equivalent Circuit: Effect of Weighting Factor," to be submitted to *J. Electrochem. Soc.*, (1990).

22. J. R. Macdonald and L. D. Potter, Jr., *Solid State Ionics*, **23**, 61, (1987).

23. M. Sluyters-Rehbach and J. H. Sluyters, in "Electroanalytical Chemistry," Vol. 4, A. J. Bard, Editor, p. 1, Marcel Dekker, New York, (1970).

24. S. H. Lu and J. R. Selman, *ibid.*, **137**, 1125, (1990).

25. R. S. Nicholson and I. Shain, *Anal. Chem.*, **36**, 706, (1964).

26. T. Berzins and P. Delahay, *J. Amer. Chem. Soc.*, **75**, 555, (1953).

Table 1. Parameters Estimated by Impedance Analysis Using CNLS Program: Temperature 750 °C and 0.6 atm. P_{O_2}.

CO_2:O_2:Ar	σ $\Omega s^{1/2}$	R_{ct} Ω	i_0 mA/cm^2	C_{dl} μF	R_s Ω
2 : 60 : 38	27.3	0.53	84.0	558.0	0.51
4 : 60 : 36	47.2	0.62	71.7	388.6	0.50
8 : 60 : 32	82.9	1.05	41.9	312.5	0.38
20 : 60 : 20	158.6	1.55	28.5	255.9	0.36

Table 2. Parameters Estimated by Impedance Analysis Using CNLS Program: Temperature 800 °C and 0.6 atm. P_{O_2}.

CO_2:O_2:Ar	σ $\Omega s^{1/2}$	R_{ct} Ω	i_0 mA/cm^2	C_{dl} μF	R_s Ω
2 : 60 : 38	10.4	0.23	205.7	1209.2	0.50
4 : 60 : 36	18.4	0.40	115.9	715.0	0.53
8 : 60 : 32	31.7	0.58	79.4	508.6	0.37
20 : 60 : 20	63.2	0.83	55.7	329.5	0.37
40 : 60 : 00	103.3	1.28	36.2	277.8	0.40

Table 3. Parameters Estimated by Impedance Analysis Using CNLS Program: Temperature 850 °C and 0.6 atm. P_{O_2}.

CO_2:O_2:Ar	σ $\Omega s^{1/2}$	R_{ct} Ω	i_0 mA/cm^2	C_{dl} μF	R_s Ω
2 : 60 : 38	4.3	0.14	358.5	3161.8	0.51
4 : 60 : 36	6.9	0.18	273.4	1874.2	0.59
8 : 60 : 32	13.3	0.27	179.3	883.7	0.39
20 : 60 : 20	27.0	0.47	102.8	510.8	0.37
40 : 60 : 00	47.7	0.59	81.6	376.6	0.40

Table 4. Comparison of Values of Product $D_O^{1/2}C_O$ Estimated by Cyclic Voltammetry and Impedance Analysis at 0.6 atm. P_{O_2}.

	$10^9 X D_O^{1/2} C_O$ mol/cm^{2}sec$^{1/2}$					
Temperature °C	750		800		850	
P_{CO_2} atm	Cyclic Voltammetry	Impedance Analysis	Cyclic Voltammetry	Impedance Analysis	Cyclic Voltammetry	Impedance Analysis
0.02	5.67	5.92	15.62	16.25	38.76	40.95
0.04	3.32	3.42	9.24	9.23	24.93	25.72
0.08	1.92	1.95	5.07	5.35	12.61	13.38
0.20	1.06	1.02	2.53	2.68	6.12	6.57
0.40	0.68		1.55	1.64	3.61	3.80

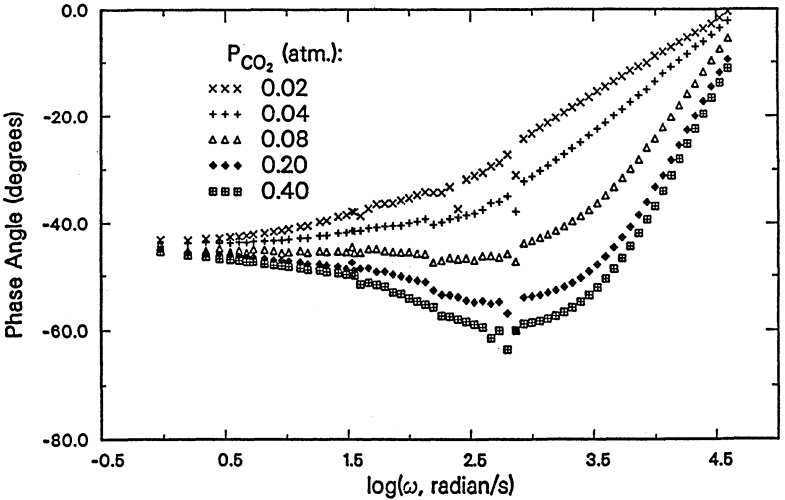

Fig. 1 Phase Angle vs. log ω Plot as a Function of P_{CO_2} for O_2 Reduction on Gold Electrode in Li_2CO_3 Melt at 0.6 atm. P_{O_2} and 800 °C.

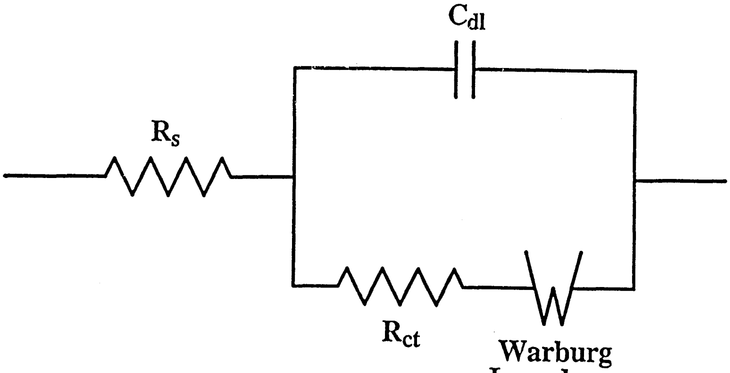

R_S = Solution Resistance

R_{ct} = Charge Transfer Resistance

C_{dl} = Double Layer Capacitance

Fig. 2. Randles–Ershler Equivalent Circuit

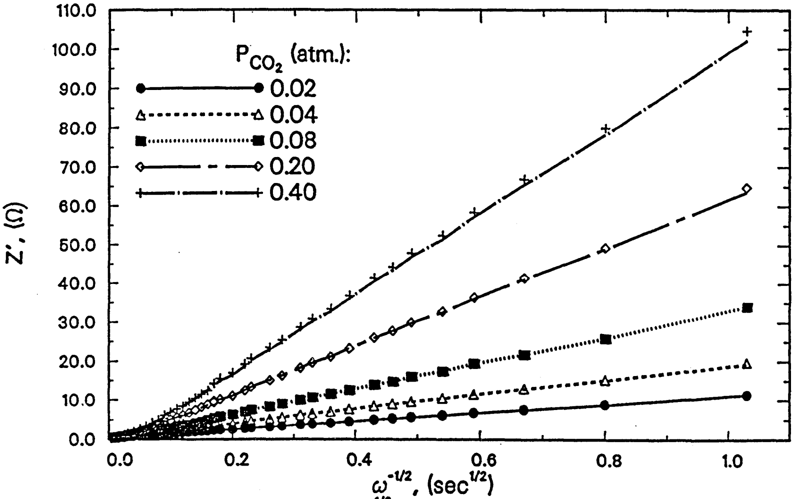

Fig. 3. Effect of P_{CO_2} on Z' vs. $\omega^{-1/2}$ Plot for O_2 Reduction on Gold Electrode in Li_2CO_3 Melt at 0.6 atm P_{O_2} and 800 °C; Symbols: Experimental Data; Lines: Model Data.

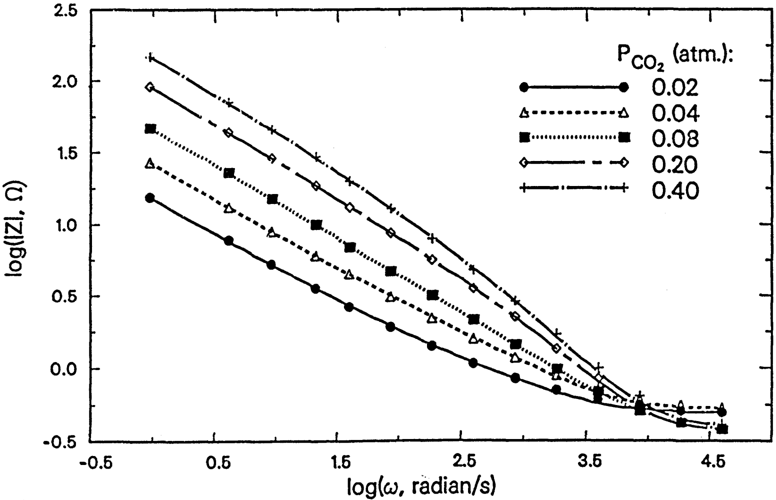

Fig. 4. Effect of P_{CO_2} on log |Z| vs. log ω Plot for O_2 Reduction on Gold Electrode in Li_2CO_3 Melt at 0.6 atm P_{O_2} and 800 °C; Symbols: Experimental data; Lines: Model Data.

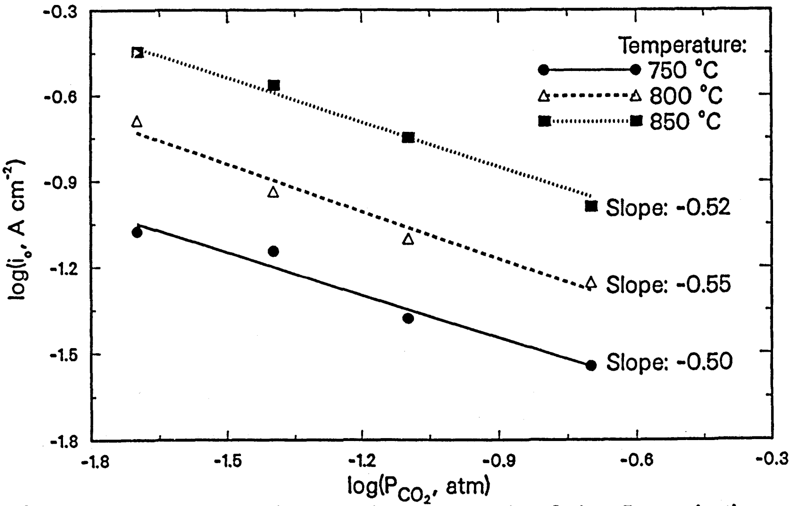

Fig. 5. Plots of log i_o vs. log P_{CO_2} for CO_2 Reaction Orders Determination at 0.6 atm P_{O_2}; Symbols: Experimental Data; Lines: Regression Data.

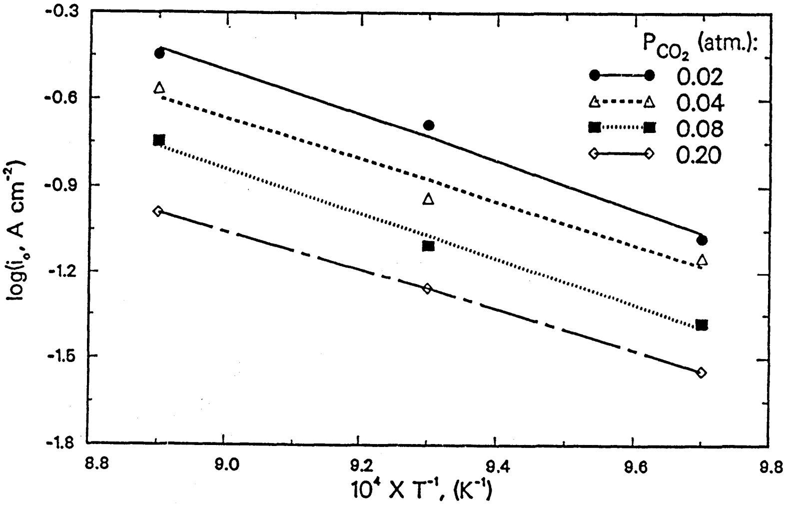

Fig. 6. Plots of log i_o vs. T^{-1} for Activation Energies Determination at 0.6 atm. P_{O_2}; Symbols: Experimental Data; Lines: Regression Data.

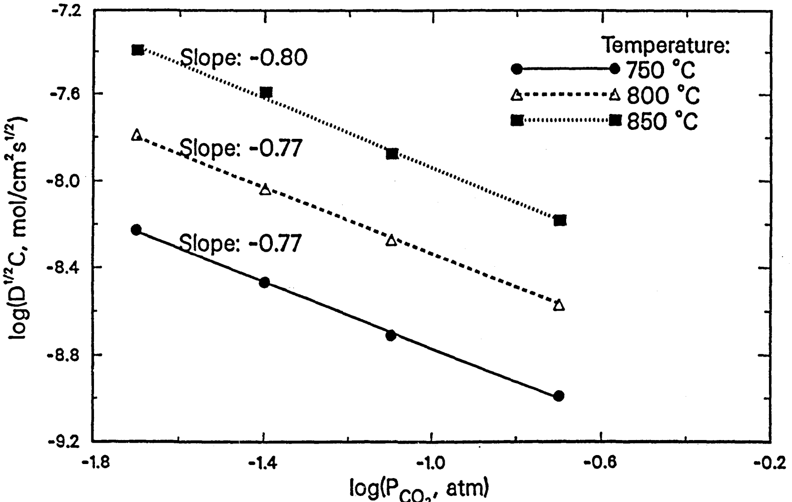

Fig. 7. Plots of $\log(D^{1/2}C)$ vs. $\log(P_{CO_2})$ for CO_2 Reaction Orders Determination at 0.6 atm P_{O_2}; $D^{1/2}C$ Obtained by Impedance Analysis.

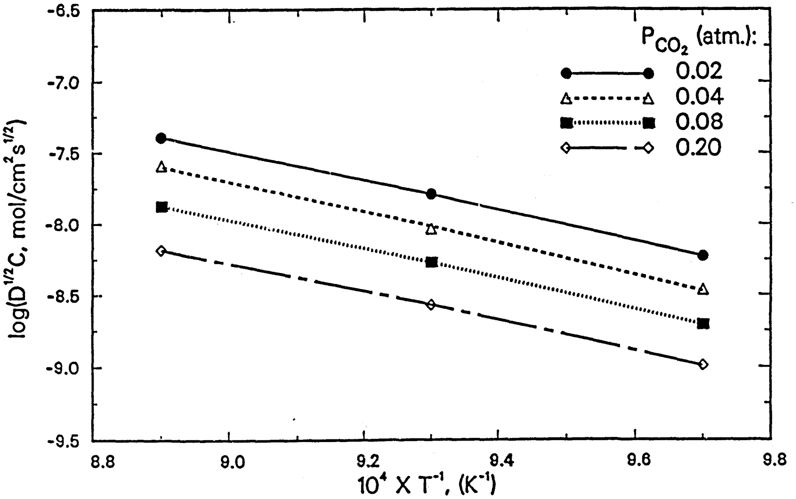

Fig. 8. Plots of $\log(D^{1/2}C)$ vs. T^{-1} for Activation Energies Determination at 0.6 atm P_{O_2}; $D^{1/2}C$ Obtained by Impedance Analysis.

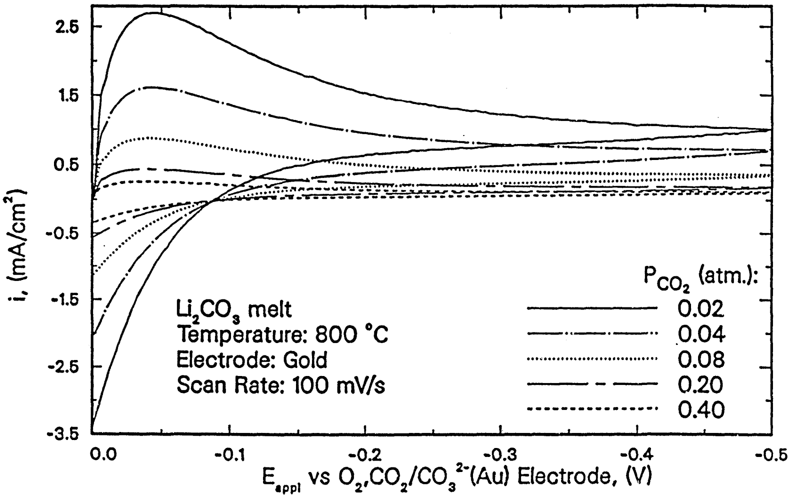

Fig. 9. Effect of P_{CO_2} on Cyclic Voltammogram for O_2 Reduction at 0.6 atm. P_{CO_2}; Reference and Working Gases Have Same Composition.

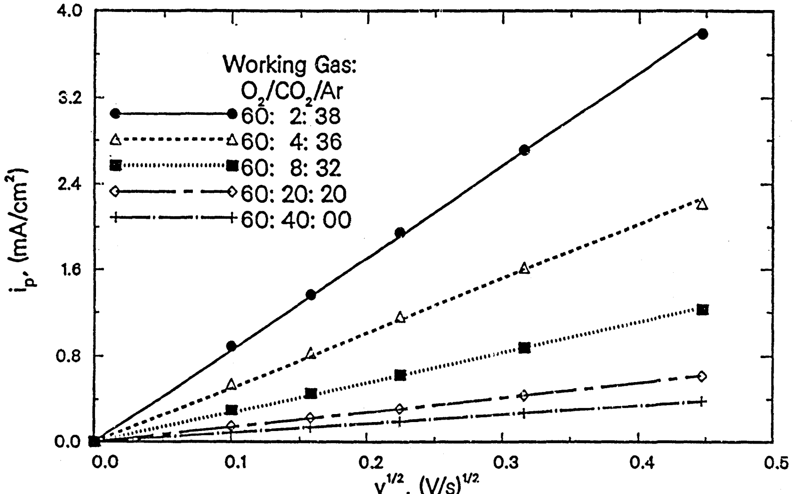

Fig. 10. Effect of P_{CO_2} on i_p vs. $v^{1/2}$ Plot for O_2 Reduction on Gold Electrode in Li_2CO_3 Melt at 0.6 atm. P_{O_2} and 800 °C.

DOI: 10.1149/199017.0743PV

A CHLORIDE ION CONDUCTING MEMBRANE FOR USE IN AMBIENT TEMPERATURE MOLTEN SALT BATTERIES

David S. Newman and Chomin Lee

Department of Chemistry
Bowling Green State University
Bowling Green, OH 43403

ABSTRACT

Nafion 901 was modified by first substituting a Cl atom for the OH groups of the carboxyllic and sulfonic acid pendents. The acetyl and sulfonyl chloride groups then reacted with dibenzo-18-crown-6-ether in molten pyridinium heptachloroaluminate which added the ether to the pendents. The etherated membrane was then complexed with LiCl which converted the essentially cationic conductor to an anionic conductor with the Cl^- as the mobile species.

INTRODUCTION

A major deterrent to the development of a practical imidazolium chloroaluminate molten salt battery is that gaseous Cl_2 from the cathode attacks the imidazolium ring of the electrolyte:(1)

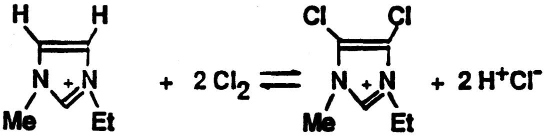

[1]

The chlorinated melts are poorer conductors, have a higher molecular weight and a narrower electrochemical window than the original melts. A way to prevent this attack is to isolate the electrolyte from the Cl_2 gas by means of a Cl^- ion conducting membrane. The difficulty with this approach is that both the gaseous chlorine and the molten salt electrolyte are chemically very harsh environments and the membrane itself must be a good ionic conductor so that the number of materials that may be used for this purpose is severely limited. One material that has many of the required properties is Nafion,(2) but Nafion in its usual state is a cation conductor. We therefore decided to modify Nafion by converting it to an anion conductor.

For this preliminary investigation we used Nafion 901 which is a carboxyllic acid - sulfonic acid perfluorinated membrane shown schematically below:

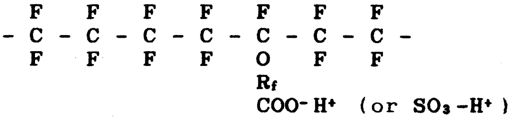

$$\begin{array}{ccccccccccccccc} & F & & F & & F & & F & & F & & F & & F & \\ - & C & - & C & - & C & - & C & - & C & - & C & - & C & - \\ & F & & F & & F & & F & & O & & F & & F & \\ &&&&&&&&& R_f &&&&& \\ &&&&&&&&& COO^-H^+ \text{ (or } SO_3\text{-}H^+\text{)} &&&&& \end{array}$$

In an earlier study, we produced a solid electrolyte with a mobile Cl^- ion by reacting LiCl with the crown ether dibenzo-18-Cr-6 to form the compound shown in Fig. 1.(3,4)

Our objective in the present investigation was to attach this compound to the Nafion backbone in place of the OH groups on the carboxyllic acid or sulfonic acid pendents. If this could be done successfully, and the anionic conducting properties of the solid electrolyte maintained in the Nafion membrane, an anionic conductor would be produced. The technique we used was to turn the carboxyllic acid or sulfonic acid into acetyl or sulfonyl chlorides and then do a Friedel - Crafts (F-C) acylation of the crown ether by the acyl chloride pendent of the Nafion in molten pyridinium heptachloroaluminate. This chemistry should be somewhat similar to the acylation of benzene in methylethylimidazolium chloride reported by Boon and coworkers (5) or the acylation of coal and model coal compounds done by Newman and coworkers (6,7). In order to demonstrate that F-C chemistry works on Nafion 901, benzene was used as the model compound.

EXPERIMENTAL DETAILS

A 1 cm^2 piece of Nafion 901 sheet was refluxed in thionyl chloride for several hours forming the acyl or sulfonyl chloride compound:

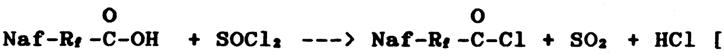

$$\text{Naf-}R_f\text{-}\overset{O}{C}\text{-OH} + SOCl_2 \longrightarrow \text{Naf-}R_f\text{-}\overset{O}{C}\text{-Cl} + SO_2 + HCl \quad [2]$$

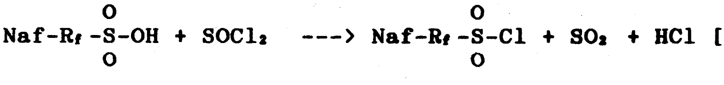

$$\text{Naf-}R_f\text{-}\overset{O}{\underset{O}{S}}\text{-OH} + SOCl_2 \longrightarrow \text{Naf-}R_f\text{-}\overset{O}{\underset{O}{S}}\text{-Cl} + SO_2 + HCl \quad [3]$$

The chlorinated Nafion was then immersed in 50 ml of molten pyridinium heptachloroaluminate melt saturated with dibenzo-18-Cr-6-ether and allowed to react for 24 hours at 25°C under nitrogen gas in a glove box. A second series of experiments were performed in which the temperature was raised to 80°C, the other variables being kept constant. A control experiment was performed in which the Nafion was immersed in a $C_5H_6N^+Al_2Cl_7^-$ solution for 24 hours with no benzene or crown ether present. The crown ether containing Nafion was then soaked for 24 hours in 5 wt% LiCl-methanol solution at 65 °C after which most of the methanol was allowed to evaporate. The LiCl containing Nafion was rinced in water for several minutes to ensure removal of any adhering LiCl or methanol and dried under vacuum at 80°C.

The results of these experiments were monitored by measuring the Nafion coupon's FTIR spectrum using a Nicolet 20 FTIR machine. In addition, the weight increase or decrease of each coupon was measured.

Modified and unmodified Nafion coupons were immersed for four days in Cl_2 gas that was maintained at one atmosphere pressure and ambient temperature.

The pyridinium heptachloroaluminate was prepared by mixing $AlCl_3$ (Cerac 99,999%) with pyridinum chloride (Aldrich 98% that had been distilled at 219°C and whose purity was 99.9%) in a two to one molar ratio. The dibenzo-18-Cr-6-ether was supplied by Aldrich Chemical Co. All transfer operation were carried on in a nitrogen filled dry box. Nafion 901 sheet was supplied by E.I. du Pont & Co. And was approximately 0.5 mm thick.

The ac conductivity of the Nafion membrane was measured with a Jones Bridge. The direct current and dc conductivity were measured using the cell shown in Fig. 2.

RESULTS AND DISCUSSION

The sulfonic acid group did not chlorinate as readily as the carboxyllic acid group did so that in the subsequent discussion only the acylation reaction will be considered in detail. However, the reaction between Naf-SO_2Cl and an aryl site is expected to be somewhat similar to the reaction between Naf-COCl and an aryl site.

In order to demonstrate the feasibility of the technique, a coupon of chlorinated Nafion was immersed in pyridinium heptachloroaluminate and phenolated at room temperature. The FTIR spectra of the chlorinated Nafion and of the phenolated Nafion are shown in Fig. 3 and 4 respectively. Two new peaks appeared at 1489 and 1539 cm^{-1}

in the spectrum of the phenolated Nafion which are indicative of the aromatic carbon-carbon bond in benzene. These peaks persisted after thorough washing in water and in methanol indicating that benzene did indeed add to the Nafion.

The reaction mechanism for the acylation of benzene is most likely:

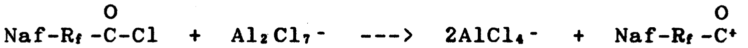

$$\text{Naf-R}_f\text{-}\overset{O}{\text{C}}\text{-Cl} + Al_2Cl_7^- \text{--->} 2AlCl_4^- + \text{Naf-R}_f\text{-}\overset{O}{\text{C}}{}^+ \quad [4]$$

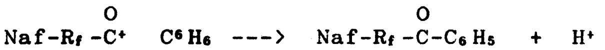

$$\text{Naf-R}_f\text{-}\overset{O}{\text{C}}{}^+ \quad C^6H_6 \text{--->} \text{Naf-R}_f\text{-}\overset{O}{\text{C}}\text{-}C_6H_5 + H^+ \quad [5]$$

$$H^+ + AlCl_4^- \text{--->} HCl + AlCl_3 \quad [6]$$

$$AlCl_3 + AlCl_4^- \text{--->} Al_2Cl_7^- \quad [7]$$

The chlorinated Nafion reacted with dibenzo-18-Cr-6-ether According to the equation:

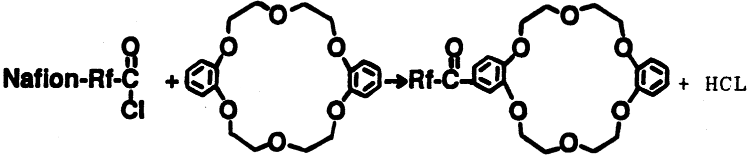

[8]

The average weight gained by the Nafion coupons as a function of temperature are summarized in Table I. It is obvious from these data that the reaction goes more readily at 80°C than at 25°C, which is consistent with the results of F-C acylations generally,i.e., they go more readily at higher temperatures than at lower temperatures. Fig. 5 shows the FTIR spectrum of the crown ether-Nafion membrane formed at 80oC. The peaks at 1456, 1503, and 1596 cm^{-1} represent the aryl groups in dibenzo-18-Cr-6-ether bonded to the membrane. Neat Nafion 901 did not react at all with the crown ether dissolved in $C_5H_6N^+Al_2Cl_7^-$.

The complexation of LiCl with the Nafion-crown ether resulted in an average weight gain of 0.0032g which is equivalent to 0.0067 g LiCl/g Nafion-complex or 0.0016 molLiCl/g Nafion-complex. This means that, within experimental error, all of the crowns are complexed and the reaction is quantitative. The FTIR spectrum of the dibenzo-18-Cr-6-ether-LiCl olid electrolyte is shown in Fig.6. All but two of the peaks are the same as those of the pure crown ether and are in agreement with Pederson's classical results.(8) The peak at 1635 cm^{-1} represents the LiCl "bond" and is virtually at the same energy reported in the literature (9) and obtained by us for pure LiCl. The second peak at 759 cm^{-1} shifted from 746 cm^{-1} where it was before the crown was complexed. This increase in energy is due to the Cl^- or Li^+ restricting the motion of the C-H groups in the crown and is consistent with Pederson's observation that the complexation of dibenzo-18-Cr-6-ether with KCNS restricts the motion of the C-H groups and moves their spectrum to higher energies. Since the unique peaks of the complex appearing at 1635 cm^{-1} and 759 - 746 cm^{-1} are masked by the Nafion's spectrum itself, the LiCl-crown-ether-Nafion's spectrum cannot be used to prove complexation, but the weight increase, the reaction of the neat crown ether with LiCl, and the subsequent increase in electrical conductivity, make it a virtual certainty that the membrane formed a complex.

The ac resistances of the dried Nafion membranes, which were treated in different ways, are summarized in Table II. It is clear from these data that the LiCl-crown ether complex is a much better conducting solid electrolyte than the other membranes. The reason for producing the NaCl-Cr-ether-Nafion complex was to compare its conductivity to that of the LiCl containing membrane. The NaCl-crown ether solid electrolyte is not as good a conductor of electricity as the LiCl-crown ether solid electrolyte.(3) From the data in Table II, it can be seen that the same behavior occurs in the membranes.

In order to confirm that the LiCl-Naf-Cr-ether complex is a Cl- ion conductor, a dc was applied across the membrane using the cell shown in Fig. 3. Green copper chloride formed at the anode and Li (and probably H_2) formed at the cathode. The Li was detected by wetting the cathode and measuring the pH. Since Li reacted with water to form LiOH, the pH was always basic. When 3 volts were applied for several hours, only a small amount of green formed at the anode and no Li was detected at the cathode. The cathodic reaction was probably $1/2\ O_2 + 2e \longrightarrow O^=$ or $2H^+ + 2e \longrightarrow H_2$. When 10 volts were applied, the copper turned green immediately and Li was deposited at the platinum electrode. In all likelihood, 10 volts is enough to cause the Li^+ to break loose from the crown ether and deposit. In any case, an essentially Cl^- ion conducting membrane was produced.

Nafion 901 membrane did not gain weight or change color after reacting with Cl_2 gas for four days. The crown-ether containing Nafion did react with Cl_2 gas and increased its weight approximately 0.2%. The color turned from white to a light orange and then back to nearly white after several days contact with air. On the other hand, the Nafion-crown-ether-LiCl increased its weight, on the average, 0.25%, changed color almost immediately, and did not turn back to the original white color after several days. The interpretation of these results is somewhat ambiguous because the FTIR spectra of the coupons before and after reacting with Cl_2 gas did not differ significantly, but it is reasonably certain some sort of reaction did occur with each membrane. Plausible reactions of Nafion-crown ether with Cl_2 are:

$$[\text{-O-}(CH_2)_2\text{-O-}] + Cl_2 \text{ ---> } \{[\text{-O-CHCl-CH}_2\text{-O-}]/H^+Cl^-\} \qquad [9]$$

$$\{[\text{-O-CHCl-CH}_2\text{-O-}]/H^+Cl^-\} + Cl_2 \text{ --> } \{[\text{-O-}(CHCl\text{-}CH_2)\text{-O-}]/H^+Cl_3^-\} \qquad [10]$$

$$\{[\text{-O-CHCl-CH}_2\text{-O-}]/H^+Cl_3^- \text{ --> } Cl_2(g) + HCl(g) + [\text{-O-}(CHClCH_2)\text{-O}] \qquad [11]$$

Reaction [11] proceeds slowly and is largely responsible for the Nafion returning to its original color. The chlorinated crown ether is probably colorless like the original crown ether. Plausible reactions of LiCl-Naf-Crown ether with Cl_2 are:

$$[\text{-O-}(CH_2)_2\text{-O-}Li^+Cl^-] + Cl_2 \text{ --> } [\text{-O-}(CH_2)_2\text{-O-}Li^+Cl_3^-] \qquad [12]$$

$$[\text{-O-}(CH_2)_2\text{-O-}Li^+Cl_3^-] + Cl_2 \text{ ---> } [\text{-O-CH}_2\text{-CHCl-}Li^+Cl_3^-/H^+Cl^-] \qquad [13]$$

Reaction [12] is probably responsible for producing Cl_3^- which causes the Nafion coupon to turn orange and for the 20% greater weight increase of the final coupon. Reaction [13] forms the species that are responsible for the increased conductivity of the membrane (Table II) because the Cl_3^- and H^+ are also capable of carrying current. The likelihood of Eq.[13] actually occurring is further increased by the fact that the pH of water in which the reacted coupon was soaked was always lower (usually between 2 and 3) than the pH of an equivalent amount of water in which the original LiCl-Naf-Cr-ether complex had been immersed. This observation implies that some of the HCl formed by Eq.[13] had dissolved in the water. It may even be the case that if the number of moles of chlorine gas entering the membrane can be kept equal to or less than the number of moles of Cl^- ion in the membrane, the membrane can be made to last indefinitely. This idea will be explored in more detail in a future study, but it should be recalled that when Br_2 combined with Cl^- to form Br_2Cl^-, it did not react with Methylethylimidazolium ions.(10)

CONCLUSION

Complexes of LiCl with Nafion-crown ether seem to be Cl- ion conductors that may eventually be developed into useful Cl- ion selective separators in the $Al/MeEtImCl\text{-}AlCl_3/Cl_2$ batteries. A schematic diagram of how the membrane might be used is shown in Fig. 7. Since carboxyllic acid reacts more readily than does sulfonic acid, an all carboxyllic acid membrane might be more useful than a membrane with both carboxyllic acid and sulfonic acid pendents and this idea is also being investigated and will be reported on in the future.

ACKNOWLEDGMENT

The authors wish to thank E.I. du Pont for donating the Nafion 901 membrane.

LIST OF REFERENCES

1. F.M. Donahue, J.A. Levisky, G.F. Reynolds, J.S. Wilkes; Proceedings of the Fifth International Symposium on Molten Salts; M-L Saboungi, K. Johnson, D.S. Newman, D. Inman, Eds. *The Electrochemical Society*, p 332 - 337 (1986)

2. Nafion is a registered trademark of E.I. du Pont de Nemours & Company.

3. D.S. Newman, D. Hazlett, K.F. Mucker; Solid State Ionics, *3/4* 389, (1981)

4. M. Fujimoto, T. Nogami, H. Mikawa, Chem. Lett. 547-550, (1982)

5. J.A. Boon, J.A. Levisky, J.S. Wilkes; J.Org.Chem., *51*, 480 (1986)

6. D.S. Newman, T.H. Kinstle, G. Thambo; Proceedings of the Joint International Symposium on Molten Salts, G. Mamantov et.al., Editors, The Electrochemical Society Softbound Series, Pennington, N.J.,pp 991 - 1001, (1987)

7. D.S. Newman, E.M. Kurt, D. Chen; Preprints of Papers Presented at the 196th ACS National Meeting, Los Angeles, CA, *33* 113 -119 (1988)

8. C.J. Pederson, J.Am. Chem. Soc. *89* 7017 (1967)

9. R.A. Nyquist, R.O. Kagle; Infrared Spectra of Inorganic Compounds, 1971

10. C.J. Dymek, G.F. Reynolds, J.S. Wilkes; J. Electrochem Soc, *134* 1658 (1987)

Table I : Quantitative results of Nafion-Crown ether experiment

Reaction Temperature	Weight Nafion	Weight Nafion-CE	Weight Gained	$\frac{\text{Crown ether}}{\text{Nafion}}$
25°C	.4904g	.5095g	.0191g	.0389(g/g)=.00010(mole/g)
80°C	.4798g	.5084g	.0286g	.0596(g/g)=.00016(mole/g)

Table II : The ac resistances of various membranes

Membranes	ac resistances
(1). Unmodified Nafion membrane:	~40,000 Ohms
(2). Complex of NaCl with crown ether modified Nafion membrane:	36,000 Ohms
(3). Complex of LiCl with crown ether modified Nafion membrane:	7,300 Ohms
(4). Complex of LiCl with crown ether modified Nafion membrane after chlorine test:	1,900 Ohms

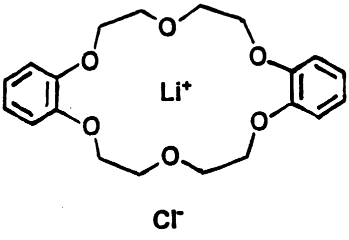

Figure I Complex of LiCl with dibenzo-18-crown-6-ether

Figure 2

dc circuit for Cl- ion conducting test

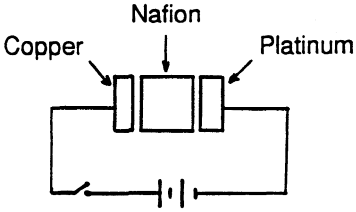

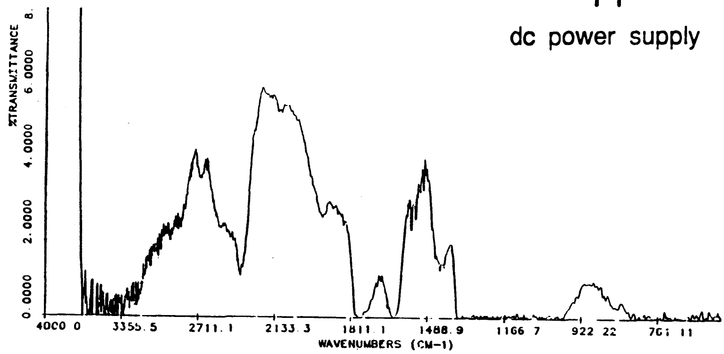

Fig. 3. FTIR spectrum of Nafion-Rf-COCl

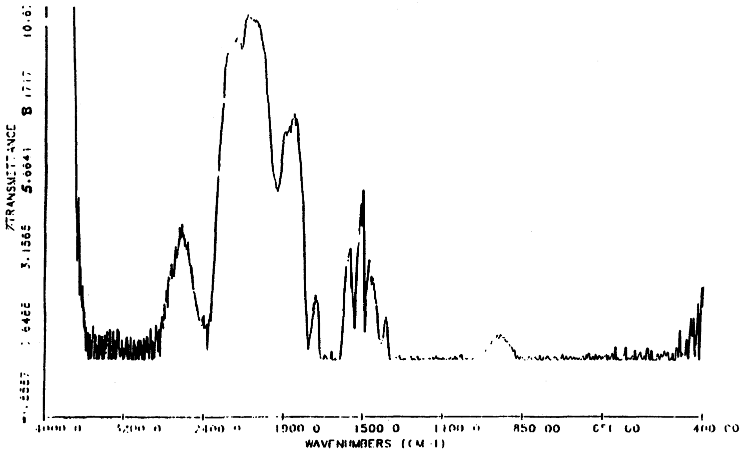

Fig. 4. FTIR spectrum of Naf-Rf-COC_6H_6

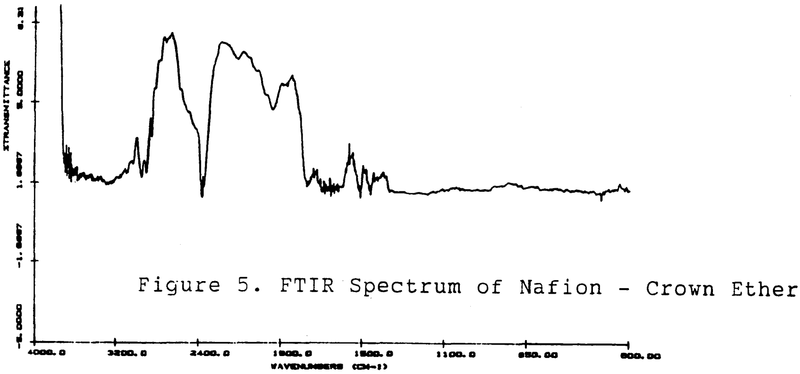

Figure 5. FTIR Spectrum of Nafion - Crown Ether

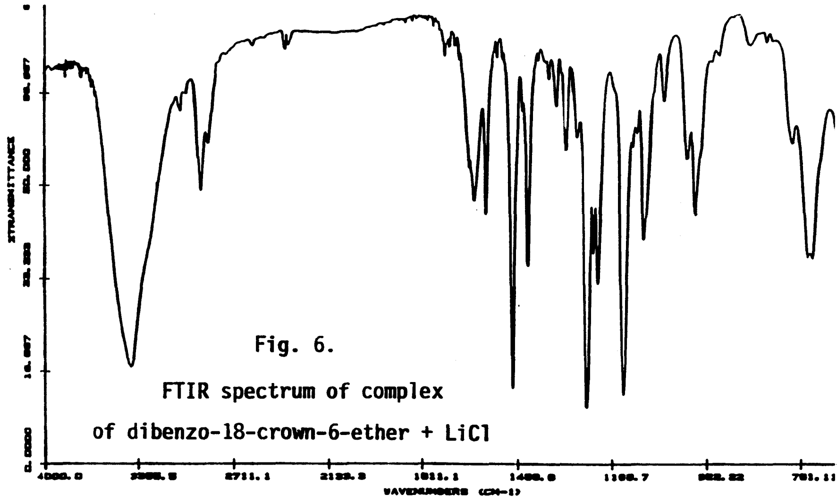

Fig. 6.

FTIR spectrum of complex of dibenzo-18-crown-6-ether + LiCl

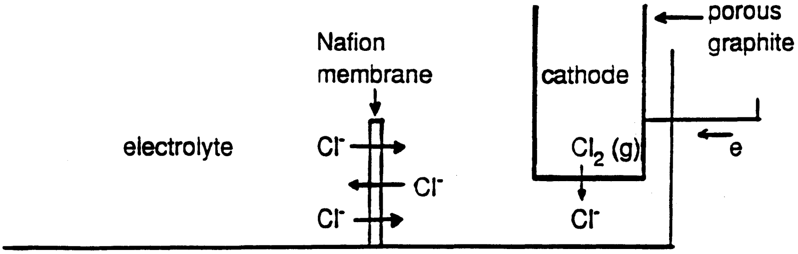

Figure 7 : Application of modified Nafion membrane as a chloride ion-selective separator in the cell.

DOI: 10.1149/199017.0753PV

SODIUM-SELENIUM(IV) MOLTEN CHLOROALUMINATE CELLS WITH POROUS NICKEL AND VITREOUS CARBON CURRENT COLLECTORS

Morio Matsunaga, Masatsugu Morimitsu, and Kunisuke Hosokawa

Department of Applied Chemistry, Faculty of Engineering,
Kyushu Institute of Technology,
Tobata, Kitakyushu 804, Japan

ABSTRACT

The charge-discharge behaviors of sodium/β"-alumina/tetravalent selenium in a basic chloroaluminate melt have been investigated with porous vitreous carbon and nickel as the positive current collector. The discharging capacity of the cells with the vitreous carbon current collector was limited by the deposition of solid sodium chloride, which often caused the breakage of reticulated vitreous carbon. The redox reaction of Se(IV)/Se(0) could occur on the nickel current collector covered with nickel chloride film. Thick nickel chloride film, however, made the polarization higher at discharging, whereas the voltage at charging unchanged.

INTRODUCTION

A rechargeable cell, sodium/β"-alumina/tetravalent selenium in chloroaluminate melt, is one of the most attractive batteries for the load leveling and electric vehicle applications, since this cell has high voltage such as 3.8V at 150-250°C, and high energy density higher than 400Wh/kg (1-3). The composition of $AlCl_3$-NaCl melt changes with charging and discharging in this cell, which indicates the cell operates within wider range of melt composition to obtain high energy density (2,4). When the melt is basic, it is necessary to use porous materials as the positive current collector, since sodium chloride deposits and covers the electrode at discharging (2,3). The degradation of the percent utilization and energy efficiency was, however, usually observed after several decades cycles in the cells with the carbon felt current collector (2,3). In this study porous nickel and vitreous carbon have been utilized for the positive current collector to improve the cell performance , especially life time.

EXPERIMENTAL

Commercial reagents of $AlCl_3$ and NaCl were purified as follows. $AlCl_3$ was sublimed through a glass filter after reaction with aluminum metal (m5N) for one day. NaCl was dried under vacuum for a few days at 400°C. Commercial grade of selenium(m6N) was used without pretreatment. Salt mixtures were prepared with purified chemicals in a glove box filled with high-purity nitrogen. Sodium metal was purified by double filtration.

A schematic representation of an experimental cell is shown in Fig.1. The cell consisted of a Pyrex glass compartment filled with positive mixture, which was separated from sodium electrode by mean of a β''-alumina tube (NGK Spark Plug Co.). Open pore "foam" nickel (Sumitomo Denko Co.) or reticulated vitreous carbon (Fluoro-carbon Ltd.) was used as a positive current collector, which was bound with tungsten spiral lead. An experimental cell was kept under vacuum at 400-450°C for a few weeks before the loading of sodium and positive mixture in order to remove moisture adsorbed on the β''-alumina tube.

RESULTS AND DISCUSSION

Typical charge-discharge curves of a cell, No.RS-807, are shown in Fig.2, which utilized reticulated vitreous carbon (RVC) as a positive current collector, of which specific surface area was $6700m^2/m^3$. In this cell the molar ratios of $AlCl_3/NaCl$ in the melt were prepared to be 50/50 and 30/70 at fully charging and discharging, respectively. The voltage during charging and discharging in this cell was quite stable, comparing to those with a carbon felt current collector (2,3). The RVC electrode has uniform open pore structure, and better electronic contact to tungsten lead because of its hardness. Therefore, the current distribution might be uniform on the current collector, which would make the charging and discharging voltages stable. In the cells with a RVC current collector the second voltage plateau was usually observed at the end of the discharging. This second plateau corresponds to the reduction of lower oxidized selenium (5,6), whereas the first long plateau is the discharging of tetravalent selenium. The oxidation number of this low oxidized species might be less than unity, since the coulombs passed for the second plateau was much less than those for the first step.

Three kinds of RVC were utilized in this study to investigate the effects of the surface area on discharging capacity. Typical charge-discharge curves observed in the cells, No.RS-901 and RS-808, are shown in Fig.3 and Fig.4. The specific surface areas of RVC were 4000 and $1100m^2/m^3$, respectively. In these cells the specifications were the same of the cell No.RS-807, such as the volume of RVC current collectors, the weight of melt and the melt compositions at fully charging and discharging. These results suggested the discharging capacity depended on the surface area of the RVC current collector. It has become apparent that the discharging capacities in these three cells were almost identical with same current densities for the unit surface area of the RVC current collector as shown in Fig.5. These results suggest the discharging limit in these cells relates to the coverage of the RVC with solid sodium chloride, like that in the carbon felt current collector (2). The values of polarization in these three cells were quite different as shown in Figs.2, 3 and 4, which mainly depended on the resisitivity of the RVC current collector.

Although Na/Se(IV) cells with the RVC current collector showed high energy density and high energy efficiency at early cycles, the abrupt change of performance was often observed especially for the cells with high capacity as shown in Fig.6. It has become apparent that the RVC electrodes were partially or wholly fractured after the degradation of performances. The observation of segments by SEM indicated the mechanical stress caused the breakage of vitreous carbon. In high capacity cells larger amounts of sodium chloride deposited during the discharging in a basic chloroaluminate melt. This deposit occupied the open pores in the RVC, and the compressive stress by the deposit might cause the cracking. These troubles suggest the elastic materials are preferred for the positive current collector of a sodium/tetravalent selenium cell which utilizes the basic chloroaluminate melts.

It is well known that nickel chloride is insoluble in basic chloroaluminate melts, which is utilized as the positive of a Na/$NiCl_2$ battery (7,8). It will be possible to use nickel for the positive current collector of a sodium/tetravalent selenium cell, since no higher oxidation state than divalent is stable in $AlCl_3$-NaCl melts. Fig.7 shows the first charge-discharge curve of an experimental cell with a porous nickel current collector of which specific surface area is $2500m^2/m^3$. The cell voltage at discharging was clearly divided into two region. One corresponded to the reduction of tetravalent selenium above 3.5V, the other to the reduction of nickel chloride at 2.5V. This result suggests that redox reaction between Se(IV) and Se(0) can reversibly occur on the nickel electrode covered with nickel chloride film.

The discharging capacity above 3.5V, however, decreased with charge-discharge cycles as shown in Fig.8. In 73rd cycle new plateau at 3.2-3.3V appeared, although the charging curve changed little. This second plateau was different from those observed in the cells with the RVC current collector, since the cell voltage was not the same and the discharging period of this plateau increased with the number of cycles. To explain the cause of this low voltage at discharging, selenium was loaded into the cell which had operated more than one hundred cycles as a Na/$NiCl_2$ cell. The typical charge-discharge curves of this cell No.NS-905 are shown in Fig.9. In this type of experimental cells the discharging period of the high voltage region, first plateau, was quite short even at the early cycles. The charge-discharge curves observed in this cell have changed little at cycles more than one hundred. The discharging capacity at the first plateau decreased with an increase of current density and with lowering the temperature, whereas the voltage drop was less than the cells with carbon current collectors.

The ohmic drop and polarization at discharging were measured with current pulses to elucidate the change of the discharging curve. Fig.10 depicts typical results measured with 1A pulses, of which on-time and off-time were 10ms. The ohmic drop measured from the abrupt voltage change at switching off was constant during the discharging. The polarization increased with the change of cell voltage, which was determined as the difference of the cell voltage at the ends of on-time and off-time. The dashed line in the discharge curve indicates the cell voltage compensated by the ohmic drop, which could not explain the polarization at the second plateau. The values of polarization measured with longer pulses were quite different from those shown in Fig.10. The variation of cell voltage with 1min pulses are shown in Fig.11. The voltage drastically changed except the early stage of discharging. The cell voltage observed at the ends of on-time and off-time are depicted in Fig.12. These results suggest the open circuit voltage measured at the end of off-time gradually changed, which corresponds to the reduction of tetravalent selenium for both plateaus. The difference between the voltages at on-time and off-time in Fig.12 is the polarization at discharging, which has never been observed in the cells with carbon current collectors. The reason of this large polarization would depend on the nickel chloride film which covered the nickel current collector. The diffusion of tetravalent selenium ions in this solid film must be the rate determining step at the discharging of the cell, which induced the large polarization.

The variations of turnaround energy efficiency and percent utilization of tetravalent selenium with the number of cycles are shown in Fig.13. In spite of the larger polarization at discharging, the performance of Na/Se(IV) cells changed little with the number of cycles in the cells prepared with the same manner as No.NS-905. These results suggest the porous nickel will have longer life as the current collector of Na/Se(IV) cells, although the polarization due to the nickel chloride film should be reduced.

SUMMARY

Charge-discharge behaviors of sodium/tetravalent selenium cells with reticulated vitreous carbon or nickel as the current collector have been described. The discharging capacity of the cells with vitreous carbon depends on the surface area of the current collector, and is limited by the deposition of sodium chloride on the current collector in basic $AlCl_3$-NaCl melts. The vitreous carbon has, however, often broken by deposited sodium chloride especially in the cells with high capacity. The redox reaction of Se(IV)/Se(0) can occur on nickel electrode covered with nickel chloride film. Thick nickel chloride film induces higher polarization at discharging, since the diffusion of tetravalent selenium species in the film is the rate determining step. The performance of the cells with a porous nickel current collector changes little with the number of cycles, when the nickel chloride film becomes relatively thick.

ACKNOWLEDGMENT

This work has been done under Cooperative Research between Kyushu Electric Power Co. and Kyushu Institute of Technology supported by Ministry of Education, Science and Culture.

REFERENCES

1. M. Matsunaga, K. Kitagawa, and K. Hosokawa, Denki Kagaku, 51, 847 (1983)
2. M. Matsunaga and K. Hosokawa, Proc. Joint Internat. Symp. on Molten Salts, p.669 (1987)
3. M. Matsunaga, T. Gohda, R. Otogawa, and K. Hosokawa, Nippon Kagaku Kaishi, 1988, 1416 (1988)
4. M. Matsunaga and K. Hosokawa, Yoyuen (Molten Salts), 30, 83 (1987)
5. R. Fehrmann, N. J. Bjerrum, and H. A. Andreasen, Inorg. Chem., 14, 2259 (1975)
6. R. Fehrmann and N. J. Bjerrum, Inorg. Chem., 16, 2089 (1977)
7. J. Coetzer, R.C. Galloway, J. Bones, D.A. Teagel, and P.T. Mosely, U.S. Pat., 4,546,055 (1985)
8. R. C. Galloway, J. Electrochem. Soc., 134, 256 (1987)

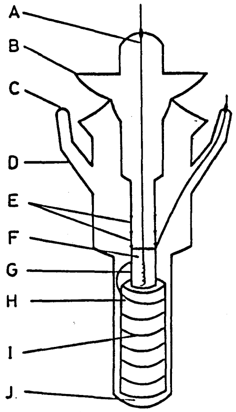

Fig.1 Schematic Diagram of an Experimental Na/Se(IV) Cell
(A) Tungsten Wire (B) Sodium Inlet
(C) Positive Mixture Inlet
(D) Pyrex Glass (E) Sealing Glass
(F) Sodium (G) β''-Alumina Tube
(H) Reticulated Nickel or RVC
(I) Tungsten Spiral
(J) Molten Salt MIxture

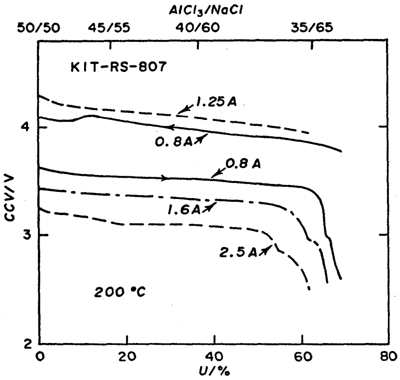

Fig.2 Chaege-Discharge Curves of a Cell No.RS-807 with a RVC Current Collector at 200°C

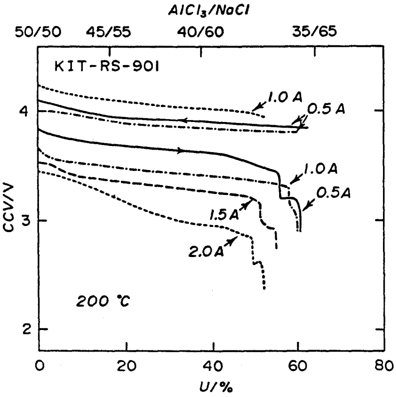

Fig.3 Charge-Discharge Curves of a Cell No.RS-901 with a RVC Current Collector at 200°C

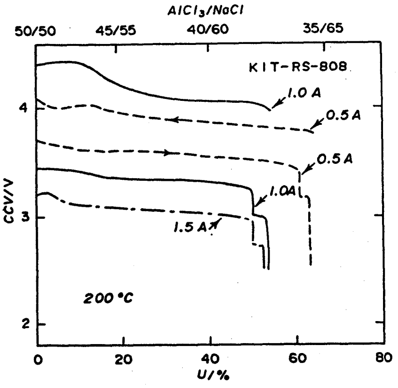

Fig.4 Charge-Discharge Curves of a Ceil No.RS-808 with a RVC Current Collector at 200°C

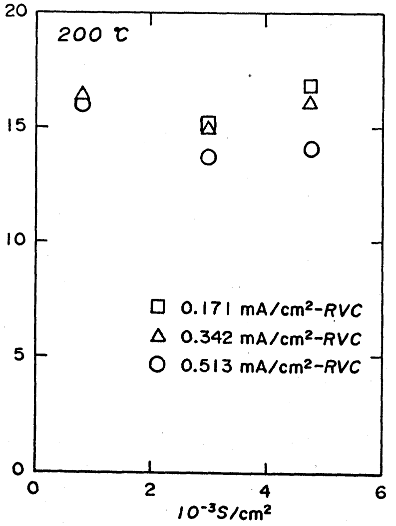

Fig.5 Relations between Surface Area of RVC and Discharginag Capacity of Na/Se(IV) Cells

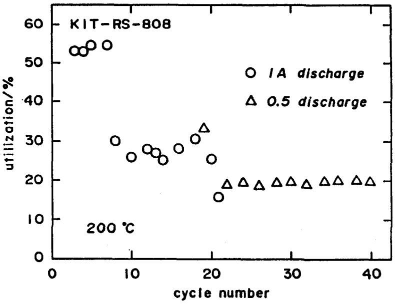

Fig.6 Effect of the Number of Cycles on Discharging Capacity of a Na/Se(IV) cell with a RVC Current Collector at 200°C

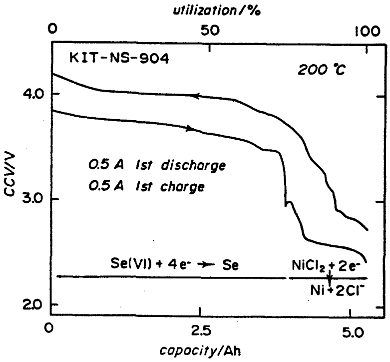

Fig.7 First Charge and Discharge Curves of a Cell No.NS-904 with a Nickel Current Collector

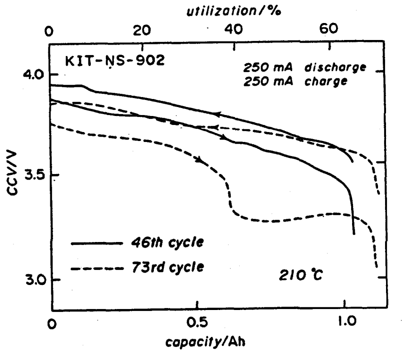

Fig.8 Change of Charge-Discharge Curves of a Cell No.NS-902 with Cycles

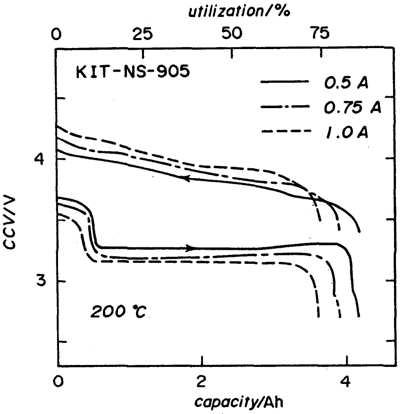

Fig.9 Charge-Discharge Curves of a Na/Se(IV) Cell with a Nickel Current Collector, Which Has Operated as a Na/NiCl$_2$ Cell for More Than 100cycles

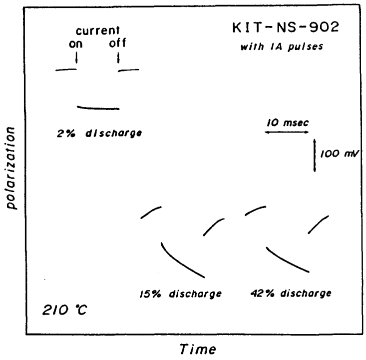

Fig.10 Voltage Transient at Dischargign Observed with Current Pulses

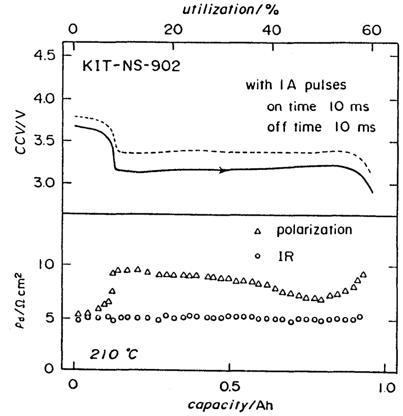

Fig.11 Polarization and Ohmic Drop of a Cell with a Nickel Current Collector at Dischargign Measured with Current Pulses

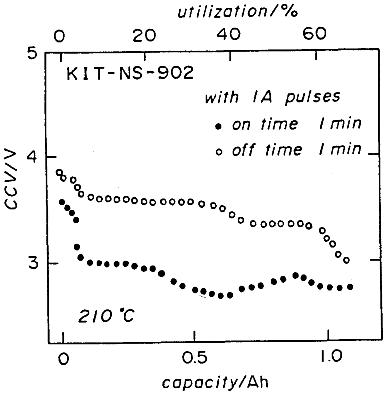

Fig.12 Cell Voltages at the Ends of On-Time and Off-Time with 1A Pulses at Various Discharging States

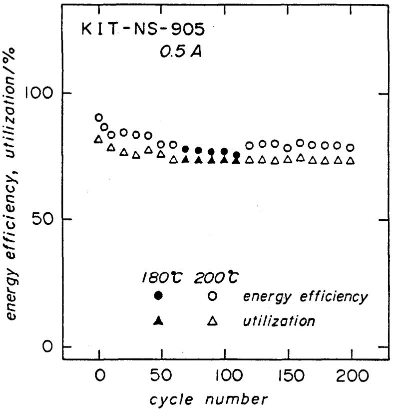

Fig.13 Effect of the Number of Cycles on Performance of a Cell with a Nickel Current Collector

DOI: 10.1149/199017.0761PV

NCA FOR ALUMINA ELECTROLYSIS

Vittorio de Nora
Moltech S.A. - Geneva - Switzerland

Abstract

Attempts to replace carbon anodes in aluminum production have failed mainly because oxides are the only materials which resist to the attack of oxygen at high temperature and all oxides are more or less soluble in cryolite.

Stable non-carbon anodes (NCA), developed by Moltech, consist of a metal structure protected by an oxygen barrier and a conductive ceramic substrate which in turn is protected form the attack of the cryolite by a dense cerium oxyfluoride coating (Cerox) stable in cryolite baths containing small constant given amounts of cerium ions.

Aluminum was first produced in 1886 by the electrolysis of alumina dissolved in molten cryolite. The first commercially successful cell, which came to be known as the Hall-Heroult cell, used anodes fabricated from petroleum coke and pitch and a cathode of carbon covered with a pool of aluminum.

Although significant technological refinements in the cell design and construction have been made, the process remains basically the same as it was one hundred years ago.

Carbon is still the only material used today as an anode, in spite of the fact that the carbon is consumed during electrolysis and anode blocks must be replaced after about four weeks of operation.

The oxygen which is formed at the anode surface as the electrochemical product of the decomposition of alumina, burns the carbon at a rate of approximately one-half ton per ton of aluminum produced and this results in the emission of carbon oxides, sulfur oxides and other undesirable gases or vapors and fumes.

DISADVANTAGES OF CARBON ANODES

The use of carbon anodes in the Hall-Heroult process presents a number of disadvantages which provide incentives for the development of a non-carbon, Non-Consumable Anode referred to as NCA™.
Some of these are :

Table I - Disadvantages of Carbon Anodes

1. High investment in plants for the manufacture of carbon anodes.

2. Consumption of carbon anodes represents a major operating cost.

3. Disturbing polluting gases escape from furnaces during the fabrication of prebaked anodes or from cells during operation, particularly from the old fashioned cells with Søderberg anodes.

4. Extensive bubble effect. The shape and size of the present anodes prevent the free escape of gas bubbles from the surface facing the cathode. This causes shielding of a good part of the active anode surface area with a consequent increase of the overvoltage and of the gap required between the anode and cathode.

5. Irregular gas release. The thick layer of the aluminum cathode fluctuates due to the irregular gas release.

6. Uneven magnetic field resulting from non-uniform current distribution.

7. Frequent replacement is a difficult and unpleasant operation for the workmen with consequent high operating costs and plant investments.

NEED FOR AN NCA

For many years, the aluminum industry has searched for possible substitutes which would eliminate the disadvantages of carbon anodes. However, all attempts made so far by both the aluminum industry and outside investigators have been unsuccessful in identifying new anode materials meeting all the requirements. These efforts sometimes involved sporadic interest and only small investments in research and development. Perhaps more sustained efforts and perseverance were required to find a solution to this difficult problem. Without an acceptable new solution, carbon has continued to be the only anode material in use, and this has limited the improvements in basic cell design.

To find a substitute for carbon for aluminum electrolysis is certainly an unique and difficult problem. The hurdles to arrive at a solution are many, and often appear unsurmountable. However, a sustained major research effort by dedicated and enthusiastic experts should give hope that a technically and economically acceptable solution will be found.

NCA DEVELOPMENT
REQUIREMENTS FOR A SUCCESSFUL NCA

The requirements for a stable anode can be readily defined.
However, to specify the requirements is a necessary step but only the first of many more towards the goal of solving the problem which remains insurmountable

Table II - Requirements for a Successful NCA

1. Stable to the cryolite electrolyte.
2. Stable to oxygen.
3. High electronic conductivity.
4. Negligible ionic conductivity
5. Low oxygen overvoltage.
6. Good mechanical strength.
7. Resistance to thermal shock.
8. Easy electrical connections.
9. Readily fabricated into the right shapes and sizes.
10. Non-polluting in manufacture, use and disposal.
11. Acceptable contamination of the aluminum produced.
12. Economically attractive.

Anodes in aluminum cells must resist the corrosive action of the cryolite at the operating temperature of almost 1000°C. There is no known material insoluble in cryolite which, at the same time, resists the attack of the oxygen generated during electrolysis on the surface of the anode. Only oxides would be expected to resist the oxygen attack but all oxides are more or less soluble in cryolite.

Even those oxides which are less soluble and might be considered as possible candidates for NCA, contaminate the electrolysis bath and the aluminum produced to such an extent that the purification of the metal is difficult or costly or both.

Another important required characteristic of the anode is the electronic conductivity which unfortunately is very low in most oxides, some of which may also have an undesirable ionic conductivity. To increase the electronic conductivity of oxides, doping agents can be added which, when well chosen, may improve considerably their electronic conductivity. These doping agents must also be oxides because oxygen would rapidly oxidize any metal added to increase conductivity.

It is important to mention also that the surface of the anode must be a good electrocatalyst for oxygen evolution to be able to operate with a low overvoltage at the high current densities utilized.

The mechanical characteristics, which include resistance to mechanical stress and to thermal shock and the possibility of producing anodes having the right shapes and sizes will additionally limit the choice of the materials the economically attractive for the fabrication and operation of NCA.

A large number of materials have been evaluated by the various investigators, but none has yet met, in a satisfactory manner, all the difficult requirements for a stable anode.

PREVIOUS DEVELOPMENT WORK

The Oronzio de Nora Company was probably one of the first companies from outside the aluminum industry to be active in the search for a substitute for carbon. Intensive work started in 1972, and a strong incentive was provided by the successful experience in the development and application of Dimensionally Stable Anodes as a substitute for graphite in the electrolysis of brine for the production of chlorine and caustic, hypochlorite and chlorates.

More recently a new company, Moltech Systems Limited, has been established with the specific object to develop new molten salt technology with non-carbon, Non-Consumable Anodes (NCA) and non-carbon, Non-Consumable Cathodes (NCC).

In this difficult and challenging endeavor, Moltech has obtained the valuable co-operation of the de Nora Permelec Group, Permascand AB, Heraeus Elektroden and Eltech Systems Corporation in addition to the indispensable co-operation of certain aluminum producers (Alcan of Canada and Aluminia of Italy).

This important international group of companies is proceeding successfully toward the development and production of NCA and to the design and engineering of cells with Non-Carbon Cathodes (NCC) to utilize efficiently NCA of new geometry which will permit improved operating conditions and cells performance.

MOLTECH'S DEVELOPMENT WORK

Over the years, Moltech and its predecessors had tested many materials, including anodes made of ferrites of various compositions, as well as of tin oxide doped with different agents including oxides of copper, antimony and others.

Different ferrites, particularly doped nickel ferrites, were tried and their solubility in cryolite was among the lowest. However, the high electrical resistance (more than $5x10^{-2}$ ohm cm at 1000°C) of this material did not permit its utilization even when metallic additions were introduced because metals were rapidly oxidized during electrolysis and the anode had an unacceptably short life.

The resistivity of doped tin oxide was reduced to less than $2x10^{-3}$ ohm cm at 1000°C. However, the solubility of tin oxide in cryolite, even if very low, contaminates the aluminum to an extent too high to be acceptable and tin cannot be eliminated.

More recently, Moltech has tried successfully these and other materials in combination with a special coating.

In fact, the first indication of success arose when Moltech discovered that by adding cerium to the melt, a cerium oxide containing some cerium fluoride formed on an oxygen-evolving anode which seemed to protect the substrate on which it formed.

This proprietary coating system, which was named Cerox™, opened up a number of new possibilities. With a coating that was sufficiently conductive and resistant to cryolite, many substrates which did not meet all the requirements as an anode material could now be reconsidered in combination with a Cerox Coating.

A NEW CONCEPT
THE COMPOSITE ANODE SYSTEM

Based on past experience with ceramic materials and coatings, Moltech has developed a new type of non-carbon Non-Consumable Anode based on a new concept. Recognizing that it was unlikely that any single material could meet all the difficult requirements for a successful non-carbon anode, the new NCA developed is based on combining several materials for the best combination of required properties. The composite anode system is formed by a Structure, a Substrate and a Coating.

Table III - The NCA System

1. The Metal Structure for more convenient geometries of anodes, for mechanical resistance, better conduction of current and easy electrical connections,

2. The Ceramic Substrate for protection of the Metal Structure and

3. The Cerox Coating, for protection of the Ceramic Substrate from the cryolite attack.

THE METAL STRUCTURE

It has been determined that, due to the relatively high electrical resistance of the oxides, it is necessary to have a core of metal in the NCA system for current feeding and distribution.
The Metal Structure must have good electrical contact with the Substrate without subjecting it to stresses due to the differences in coefficients of thermal expansion.
Anodes have been prepared having a metal core protected by the oxide Substrate, or an oxide Substrate in which a metallic core has been provided.

Table IV - NCA Metal Structure

When metals are used as structures, their composition is important because the oxygen formed at the anode surface will diffuse through the Cerox and the substrate which are not impervious barriers to oxygen.
The presence of chromium in the metal structure is important, because chromium oxide, which is readily formed at the surface of the metal, is an excellent barrier to oxygen penetration.

Steels containing high percentage of chromium or alloys containing high percentage of nickel and chromium seem to be among the best alloys to be utilized as Structures.
Nickel copper alloys are also possible candidates for the Metal Structure.

The search for the best metal to form the Structure or the core of the Ceramic Substrate continues, and the results so far obtained are very encouraging.

THE CERAMIC SUBSTRATE

Cerox alone is not sufficient to protect the metal and an intermediate Ceramic Substrate is required.

The choice of the Substrate has been guided mainly by the electric conductivity and the corrosion resistance of the material.

Table V -NCA Ceramic Substrates

Different oxides have been produced and tested with dopants added in various concentrations, in order to increase the conductivity and resistance to corrosion by the cryolite. Optimization of the sintering process has provided dense samples with a low residual porosity.

Doped ceramic oxides remain the major anode Substrate candidates. Therefore, it is important that their quality standards and performance be controlled and tested.

In addition to the chemical composition and the thermal cycle of the sintering process, the ceramic oxides must be adherent to the Metal Structures and have special surface characteristics for obtaining adherent dense and impervious Cerox Coatings.

Some of the doped ceramic oxides had previously been tried as anode materials without success, but surprisingly, when combined with the Cerox Coating, they performed well.

CEROX
THE CRYOLITE-RESISTANT COATING

In the NCA developed by Moltech, the Cerox Coating is the most important material, because under proper conditions, provides an impervious protective coating for the Ceramic Substrate.

Table VI - NCA Coating

Dense, impervious Cerox coatings have been deposited electrochemically. Other coating techniques such as plasma spray, flame spray, dip coating, co-sintering, have also been used to produce Cerox top coats or intermediate ceramic layers.

The first layer of Cerox coating, however formed, must be of good quality as a first requisite for any additional formation and the maintenance of a protective layer during the subsequent electrolysis for the production of aluminum. The chemical composition and physical characteristics of the Substrate surface are important factors influencing the quality of the first Cerox layer

Coarse-grained coatings may contain cracks and may not be completely impervious to cryolite.

It is advisable to keep the Cerox thickness at a value sufficient to protect the underlining structure without creating a too high resistance to the passage of current.

ELECTROCHEMICAL FORMATION AND MAINTENANCE OF CEROX COATINGS

The mechanism of formation and maintenance of Cerox during electrolysis is not clearly known. The Cerox is probably deposited on the anode because Ce^{3+} ions in the molten cryolite are oxidized by either elimination of electrons to form Ce^{4+} ions or by the atomic oxygen formed. This will depend upon the concentration at the anode surface of Ce^{3+} ions and of O^{2-} ions and upon the anodic potential.

Some of the factors influencing the physico-chemical characteristics of Cerox obtained by electrochemical deposition have been identified and include the following :

Table VII -Factors Influencing the Characteristics of Cerox

1. Chemical composition of the Substrate surface.
2. Physical characteristics of the Substrate surface.
3. Bath composition, in particular Al_2O_3 concentration and NaF/AlF_3 ratio as well as the presence of other ions.
4. Cerium concentration in the bath, particularly the concentration of Ce^{4+} and Ce^{3+} ions in the vicinity of the anode surface.
5. Doping agents such as tantalum and niobium which improve the density and the conductivity of Cerox.
6. Current density and current density distribution over the active surface of the anode.
7. Overpotential of oxygen evolution.

During electrolysis, bath composition, and particularly a constant concentration of cerium, is critical to maintain a permanent dense, impervious coating of the desired thickness. A high concentration of cerium will increase the thickness of Cerox .
On the other side, the change in current density has probably no major effect on the solubility and stability of Cerox in cryolite. However, it is to be expected that when the current density and overvoltage increase, the Cerox solubility may be reduced.

Cerox, which during stable conditions is in equilibrium with the electrolyte containing cerium, during electrolysis may undergo modifications and go into solution at one site and crystallize at another site. Recrystallization may also take place with formation of crystals of larger size or different structure, if there is sufficient difference in free energy to drive the change.

The diffusion phenomena of oxygen, metals and metal oxides complicate the equilibrium among the different layers of the NCA System and influence its stability.

The high resistivity of Cerox, (2 to 5 ohm cm at 1000°C) lower however than that of cerium oxide due to the co-deposition of cerium fluoride, is one of the factors influencing the thickness of the deposit. It will in fact facilitate the concentration of current at thin spots in the coating with a consequent increase of the oxygen overvoltage and a local decrease of the alumina concentration thus providing a favorable stabilizing effect in the maintenance of the Cerox Coating.

Regardless of the initial method of formation of Cerox Coatings, their maintenance and their quality during the electrowinning of aluminum is influenced by the operating conditions . Some of these, such as temperature and current density, cannot be modified at will unless the basic conditions of the commercial electrolysis process are changed. Other factors, such as alumina concentration and NaF/AlF3 ratio can be slightly modified while others, like the presence of other elements which do not influence the efficiency of the process or the purity of the aluminum produced, may be modified to a large extent if required to maintain a good Cerox Coating.

Of course, with the use of a non-carbon anode, the electrochemical reactions take place at an anode surface which has different characteristics such as anode potential, overpotential, and may permit drastic changes in the electrolyte composition and in the operating conditions.

The requirements for the maintenance of an initially good Cerox Coating are still being optimized and most of the important factors which influence the stability and maintain the thickness and imperviousness of the Cerox Coating have been identified.

The cerium in the electrolyte is also in equilibrium with the cerium in the aluminum produced from which it can be removed to acceptable levels. It is recovered as cerium fluoride which can be returned to the bath to keep its cerium concentration constant.

ELECTROLYSIS TESTING OF NCA

Ceramic Substrates with Cerox coatings have been operating at current densities up to more than 100 amps/dm^2. The problems which have been encountered are being resolved in order to have NCA with a geometry and size suited to the operation of commercial cells and having a life of sufficient duration.
Some of the operating problems include:

Table VIII - Operating Problems

1. Resistance of metal structures to the attack of oxygen.
2. Resistance to thermal shock of the Substrate and of the Cerox coatings.
3. Adherence of the Ceramic Substrate to the Metal Structure and adherence of the Cerox Coating to the Substrate.
4. Conductivity of the Ceramic Substrate for more uniform current distribution.
5. Chemical stability of Cerox coatings during electrolysis and maintenance of its imperviousness.

Progress has been made to overcome the hurdles.

The key to the current approach to the development of an NCA is the ability of Cerox to provide complete protection to a Ceramic Substrate and to be self-healing in the spots where thickness decreases or cracks are formed. To establish the feasibility of this, the availability of good quality cryolite-tight Cerox coatings is indispensable.

Hopefully, current efforts will soon give a reliable and reproducible process to provide near-perfect Cerox coatings on Ceramic Substrates of various sizes and shapes.

It is well recognized that, if a Cerox Coating rearranges its structure during electrolysis, it might lose its protective properties. In order to assess and attack the problem, good quality initial coatings are needed in order to have Cerox stable under conditions of electrolysis so that long-term tests can be carried out.

The current rod-shaped anodes, while useful in much of the initial test work, are not satisfactory for scale up. It is likely that some of the problems we are now facing may be unique to the rod anode. Therefore, anodes of improved geometry are being developed.

The discovery of Cerox formation has been a great contribution to the development of non-carbon, Non-Consumable Anodes, particularly if one thinks that all oxides are more or less soluble in cryolite and only a continuous self-forming process would permit the realization of what has been considered a dream.

CURRENT STATUS OF THE NCA DEVELOPMENT

The work of Moltech and its Partners has advanced beyond the identification of promising candidate materials for NCA.
Testing is now being carried out in pilot scale cells.

The composite anode concept has been developed and several promising materials have been identified for the Metal Structure and the Ceramic Substrate. Various methods of applying the Ceramic Substrate have been demonstrated.

The cryolite protection offered by Cerox is a key element. Procedures have been developed to deposit near-impervious Cerox coatings on Substrates. Anode design, scale-up and fabrication are progressing to a model more closely related to commercial practice.

Combining all these elements in some long term testing at the pilot scale, will lead to further tests in commercial cells in the near future.

OUTLOOK

Considerable progress have been made, however, the very difficult operating conditions and requirements of the Hall-Heroult cell present a still formidable challenge. Cerox, which is unique in its ability to resist cryolite, is the key to success where so many other materials have failed.

To attack the problem, Moltech has brought together a group of companies, which include knowledgeable individuals and outside consultants, representing expertise in all phases of material science, electrochemistry, ceramics, coatings technology, and aluminum production. This team, with its enthusiasm, determination, necessary experience and resources is well positioned to develop the first successful NCA.

Hopefully, NCA will soon revolutionize the aluminum industry and lead to innovations that will permit the construction of more efficient electrolytic cells of new designs, with savings in capital investment and manufacturing costs, but above all with non-polluting and long-lasting anodes.

DOI: 10.1149/199017.0771PV

RECHARGEABLE SODIUM/NASICON BATTERIES WITH CHLOROALUMINATE ELECTROLYTE AND TRANSITION METAL SULFIDE CATHODES.

H.A. Hjuler[a], B.C. Knutz[a], B. Vestergaard[a],
N.J. Bjerrum[a], N. Dalsgaard[b], J.W. Høj[b],
J. Engell[b] and S. von Winbush[c]

[a]Molten Salts Group, Chemistry Department A,
Building 207, The Technical University of Denmark,
DK-2800 Lyngby, Denmark

[b]Institute for Mineral Industry, Building 204,
The Technical University of Denmark,
DK-2800 Lyngby, Denmark

[c]State University of New York at Old Westbury,
New York, USA

ABSTRACT.

The rechargeable molten salt battery system $Na/Nasicon/NaAlCl_4/Ni_3S_2$ (or FeS_2) has been investigated at 175°C. Nasicon is a ceramic Na-ionic conductor.

The charge/discharge performance of experimental cells are presented. Further, the corrosion of Nasicon in $NaCl-AlCl_3$ melts (49.8 (saturated with NaCl) or 66 mol % $AlCl_3$) is examined.

INTRODUCTION.

At the Technical University of Denmark we have performed an intensive investigation on rechargeable molten salt batteries during the last nine years.

Molten chloroaluminates have been used as electrolytes and aluminium as anode material, while the preferred cathodes have been transition metal sulfides (1).

Further, during the last few years sodium batteries utilizing the same electrolyte and cathodes as the aluminum batteries but with Nasicon ceramic as separator to the anode have been studied. These sodium batteries are in principle a competitor to the sodium metal chloride (Zebra) batteries (2). Their advantages compared with the sodium-sulfur batteries are higher voltage (2.6 versus 2.0 Volts) and a much lower operating temperature (175-250°C contra 300-350°C) resulting in less corrosion of the sodium ionic conductor.

EXPERIMENTAL.

The preparation of the molten salt electrolyte has been described previously (1). The cathodes are prepared from ca. 90% Ni_3S_2 or FeS_2 (both from Cerac, USA), 5% teflon (as a dispersion from Dupont) and 5% active carbon (Darco G60 from Fluka). This cathode material was pressed onto a nickel mesh current collector.

The experimental cells, Fig. 1, 2, and 3, were filled with freshly cut sodium (analytical grade from Merck except cells Na/Ni-6 and 8 where Na from Fluka, pract. were used) in a Vacuum Atmosphere Co. model HE-553 glove box with argon atmosphere with a measured oxygen content of ca. < 5-10 ppm (Dansensor model TIA-2 oxygen monitor). The preparation and properties of Nasicon has been described in ref. 3-4. The wall thickness of the tubes was approx. 1 mm, while that of the Nasicon discs were ca. 0.2 mm. The composition of the Nasicon is shown in Table I.

The beta-alumina tube was obtained from Asea Brown Bovery, Heidelberg, West Germany.

The filled cells were transferred to temperature controlled ovens and tested with a battery cycling equipment as described earlier (1).

Corrosion of Nasicon in the NaCl-$AlCl_3$ Electrolyte.

Static corrosion of the Nasicon ceramic has been examined in slightly basic or strongly acidic NaCl-$AlCl_3$ melts at 175°C. The actual melts were either saturated with NaCl (49.8 mol % $AlCl_3$) or contained 66 mol % $AlCl_3$, respectively. After exposure to the melts in sealed Pyrex ampoules, the ceramic Nasicon discs were rinsed in distilled water, dried and the weight loss was determined as a function of the period of time the discs were immersed in the melt.

The surface/melt ratio (i.e. cm^2 disc-surface area divided by cm^3 of melt-volume) was 0.20 for the acidic experiment, while two basic series of experiments were performed with surface/melts ratios of 0.10 and 0.20, respectively.

Reaction between ceramic and melt can ideally appear either as bulk dissolution or as diffusion controlled processes. Accordingly, the weight loss depicted as a function of immersion time in a log-log plot is expected to follow straight lines with slope 1 or 0.5, respectively (5).

In basic melts - with a surface/melt ratio of 0.20 - the corrosion slows down after 200-250 hours, see Fig. 4. The weight loss in this case is approx. 3 mg/cm^2. The maximum weight loss after the following 1800 hours was ca. 6 mg/cm^2, after which the experiments were terminated.

In the first 250 hours the slope of the corrosion curve in a log-log plot is 0.77 ± 0.08 (correlation coefficient 0.97) indicating that the corrosion rate is controlled partly by bulk dissolution and partly by diffusion processes.

With a surface/melt ratio of 0.10 the corrosion also slows down after 200-250 hours, see Fig. 5. Here the weight losses are ca. 4 and 8.5 mg/cm^2, respectively. In this case, however, the slope is 0.50 ± 0.10 (corr. coefficient 0.95) indicating a more clear diffusion controlled process (perhaps due to restrictions to melt movements).

For acidic melts - with surface/melt ratios of 0.20 - the corrosion also seems to slow down after approx. 200-250 hours, see Fig. 6. We have, however, not sufficient measurements with more than 1000 hours of testing time to determine this with certainty. The weight loss after 200-250 hours is ca. 4 mg/cm^2, and the slope is 0.73 ± 0.10 (corr. coefficient 0.96).

All the above mentioned experiments were performed by rocking the ampoules during immersion of the Nasicon ceramics (the rocking period was 4 sec and the rocking angle ca. 30°). Rocking causes stirring of the $NaCl-AlCl_3$ melt, which may have impact on the rate and mechanism of corrosion. In order to investigate this possibility another series of experiments (in basic melts with a surface/melt ratio of 0.20) were performed without rocking the ampoules. In this case the slope of the corrosion curve for times less than 200 hours was 0.47 (based on three data points) - indicating a diffusion controlled corrosion process. Therefore, rocking seems as expected to increase corrosion by a bulk dissolution process.

Finally, a number of experiments were performed in order to find a way to avoid or control the corrosion. The most likely corrosion products are $AlPO_4$, $SiCl_4$ and $ZrCl_4$ which were added individually to the melts before immersing the Nasicon discs. Great care was taken to weigh out the correct amount of NaCl and $AlCl_3$ giving the same acidity/-basicity as before (additives affects the acid-base equilibria of the electrolyte).

It was, however, not possible to find any positive influence on the rate of corrosion with either $AlPO_4$, $SiCl_4$ or $ZrCl_4$.

At present, the only known way to reduce the corrosion of Nasicon in NaCl-$AlCl_3$ melts is to saturate the electrolyte with Nasicon powder before assembling the battery.

Contact Angle Measurements.
It is of interest to know how well Nasicon is wetted by the liquid anode and liquid electrolyte. The wetting properties were studied by measuring contact angles between Nasicon and droplets of the liquid materials by a photographic technique. The Na-Nasicon contact angle was measured in a pyrex glass ampoule at 175°C to be 129±4° (average of the right and left angles for 4 experiments) indicating that sodium only slightly wets Nasicon. This value can be compared with a value of 128° found at 265°C by Viswanathan and Virkar (6). The contact angle between $NaAlCl_4$ and Nasicon was measured in the same way giving a value of 0° indicating that Nasicon is completely wetted by $NaAlCl_4$. Further, the contact angle between Na-K (50:50 atom %) alloy and Nasicon ceramic was measured due to the interest for batteries that can be operated close to room temperature. The alloy is liquid down to 3.6°C and the contact angle was measured at room temperature to be 119±1°C, see Fig. 7, thus indicating a slightly better wetting ability than for pure sodium. It was, however, later discovered that Nasicon can not be used in direct

contact with molten Na-K. Probably, due to solid-state ion exchange the ceramic expands and in this way causes fractures in the material.

Sodium batteries.

Many sodium batteries with Nasicon ceramic, $NaAlCl_4$ electrolyte and FeS_2 or Ni_3S_2 cathodes have been constructed and tested at 175°C with constant charge/discharge currents. Some results are presented in Table II and in Fig. 8-11.

The general trend is that high cathode utilizations can be obtained, that high performance cells can be cycled 1500 times or more, and that the charge/discharge voltages usually are 2.8/2.0 Volts - slightly higher for the nickel containing cells than for iron containing cells.

It should be noted that since the anode is chemically separated from the electrolyte, the relatively high solubility of FeS_2 in $NaAlCl_4$ melts do not cause any problems.

As seen from the Figures no obvious differences were found between cells containing Nasicon or containing beta-alumina.

Flat cells of the $Na/Nasicon/NaAlCl_4/Ni_3S_2$ system have also been constructed. After many practical difficulties it has now been shown that these cells can be cycled (at least) 750 times with voltages as above, see Fig. 11.

The charge/discharge curves of all cells with Ni_3S_2 reveal up to three voltage plateaus, indicating that three different cathode reactions are taking place during charging and discharging.

The overall cell reaction during the lowest plateau (2.0-2.1 V) involves formation/decomposition of essentially Ni_3S_2 (7,8). The electrode reactions are accordingly:

Anode: $$\mathrm{Na} \underset{\text{charge}}{\overset{\text{discharge}}{\rightleftharpoons}} \mathrm{Na}^+ + e^- \qquad (1)$$

Cathode: $$Ni_3S_2 + 4e^- \underset{charge}{\overset{discharge}{\rightleftarrows}} 3Ni + 2S^{2-} \qquad (2)$$

Since the sulphide ions are complexed in the electrolyte (9) the cathode reaction becomes:

$$Ni_3S_2 + 2AlCl_4^- + 4e^- \underset{charge}{\overset{discharge}{\rightleftarrows}} 3Ni + 2AlSCl_2^- + 4Cl^- \qquad (3)$$

Thus the total reaction is

$$4Na + Ni_3S_2 + 2NaAlCl_4 \underset{charge}{\overset{discharge}{\rightleftarrows}} 3Ni + 2NaAlSCl_2 + 4NaCl \qquad (4)$$

According to (7) the second plateau is associated with a compound containing both sodium and sulfide, presumably a $Na_xNi_yS_zCl_{2y-2z+x}$-type compound. Most probably x=z. The reaction taking place during the third plateau has not been identified yet.

CONCLUSION.

The cycling performance and the voltages of $Na/NaAlCl_4/-Ni_3S_2$ batteries are high. They seem to be very promising candidates for future high energy density rechargeable battery systems.

ACKNOWLEDGEMENTS.

We will like to thank Dr. R. Knödler, ABB, Heidelberg, FRG for the beta-alumina tubes and K.S. Birdi, Physical-Chemistry Institute, The Technical University of Denmark, for valuable discussions concerning the contact angle measurements. Further, the Danish Ministry of Energy, "Direktør Ib Henriksens Fond" and "Fabrikejer Louis Dreyer Myhrwold og hustru Janne Myhrwolds Fond" are thanked for financial support.

REFERENCES.

1. H.A. Hjuler, R.W. Berg and N.J. Bjerrum, Power Sources, 14, 1 (1985). (Proceedings from the 14th International Power Sources Symposium, Brighton, England, 1984).

2 R.J. Bones, D.A. Teagle, S.D. Brooker and F.L. Cullen, J. Electrochem. Soc., 136, 1274 (1989).

3. S. Yde Andersen, S. Lundsgaard, L. Møller and J. Engell, Solid State Ionics, 14, 73 (1984).

4. J. Engell, S. Mortensen and L. Møller, Solid State Ionics, 9 & 10, 877 (1984).

5. L.L. Hench, J. Non-Cryst. Solids, 25, 344 (1977).

6. L. Viswanathan and A.V. Virkar, J. Mat. Sci. 17, 753 (1982).

7. H.A. Hjuler, B.C. Knutz, R.W. Berg and N.J. Bjerrum, J. Electrochem. Soc., submitted.

8. K.M. Abraham, and J.E. Elliot, J. Electrochem. Soc. 131, 2211 (1984).

9. R.W. Berg, S. von Winbush and N.J. Bjerrum, Inorg. Chem., 19, 2688 (1984).

Table I. Composition of the used Nasicon Ceramic (NZPS-82-1BC) and the Observed Phases, Sintered for 10 h at 1200°C. The Nasicon Phase is Determined by XRD and the Glass Phase is Examined by Electron Microprobe.

	- wt% -				atoms in formula unit				
	P_2O_5	SiO_2	ZrO_2	Na_2O	Na	Zr	Si	P	O
NZPS-82-1BC	12.25	28.51	39.60	19.64	2.94	1.49	2.20	0.80	10.85
Nasicon- x = 2.14*	10.73	24.30	46.58	18.39	3.14	2.00	2.14	0.86	12.00
Glass phase	16.67	38.50	19.37	25.46					

*$Na_{1+x}Zr_2Si_xP_{3-x}O_{12}$.

Table II. Testing Results of Sodium Batteries.

Cell no.	Type	Cathode	Open circuit voltage Volts	Cycle no.	Current density (a) mA/cm^2	Test time h	Current efficiency %	Energy efficiency (b) %
Na/Ni-6	Beta-alumina tube	Ni_3S_2	2.65	5	1	5	100	87
				50	1	5	100	88
				100	1	5	100	89
				200	1	5	100	83
				500	1	5	100	83
				1000	1	5	100	80
				1500	1	5	100	79
				2000	1	5	100	86
Na/Ni-8	Nasicon tube	FeS_2	2.7 (c)	5	3	5	100	78
				50	3	5	100	80
				100	3	5	100	92
				200	3	5	100	79
Na/Ni-26	Nasicon tube	Ni_3S_2	2.63	5	4	5	100	87
				50	4	5	100	86
				100	4	5	100	87
				200	4	5	98	70
				500	4	5	96	76
				1000	4	5	92	75
Na/Ni-48	Nasicon disc	Ni_3S_2	2.72	5	5	3	100	85
				50	5	3	100	70
				100	5	3	100	71
				200	5	3	100	72
				500	5	3	100	81

(a) Actual test currents for the four cells are 25, 20, 25, and 5 mA, respectively.

(b) Cathode material utilization in each cycle was ca. 21%, 31%, 23% and 18%, respectively.

(c) Measured after cycle no. 1.

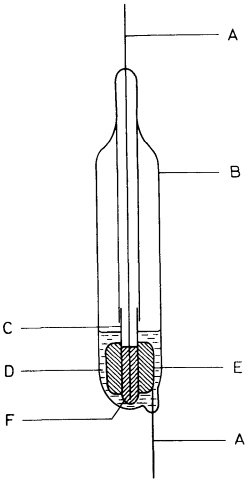

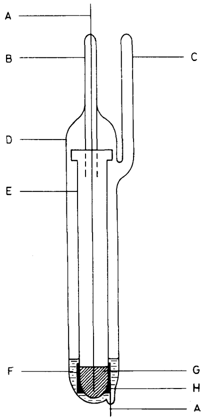

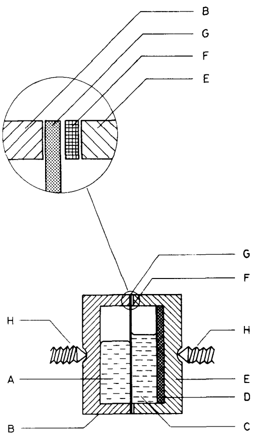

Figure 1. (Left) Nasicon tube test cell. A) Terminal (tungsten wire); B) Pyrex glass; C) Nasicon tube; D) $NaAlCl_4$ electrolyte; E) Cathode; F) Sodium anode.

Figure 2. (Center) Beta-alumina tube test cell. A) Terminal (tungsten wire); B) Glass tube for addition of Na; C) Glass tube for addition af $NaAlCl_4$ electrolyte; D) Pyrex glass body; E) Beta-alumina tube; F) $NaAlCl_4$ electrolyte; G) Sodium anode; H) Cathode.

Figure 3. (Right) Nasicon disc test cell. A) Sodium Anode; B) Aluminum housing; C) $NaAlCl_4$ elektrolyte; D) Cathode; E) Stainless steel housing; F) Teflon O-ring; G) Nasicon disc; H) Mounting screw.

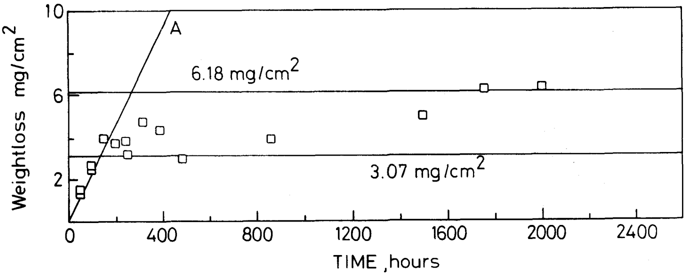

Figure 4. Corrosion of Nasicon as a function of time in basic NaCl-$AlCl_3$ at 175°C with a surface/melt ratio of 0.20.

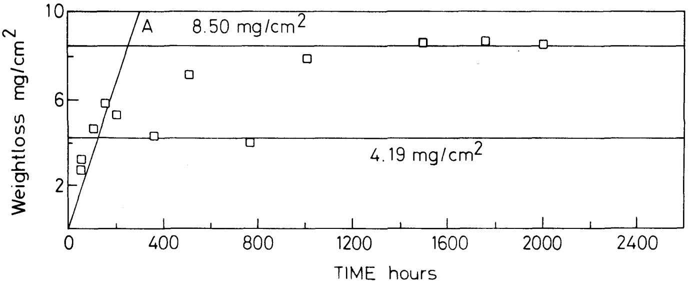

Figure 5. Corrosion of Nasicon as a function of time in basic NaCl-$AlCl_3$ at 175°C with a surface/melt ratio of 0.10.

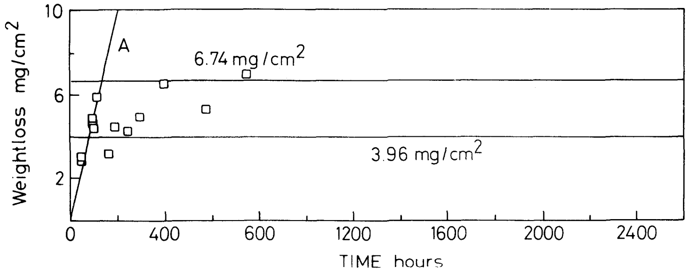

Figure 6. Corrosion of Nasicon as a function of time in acidic NaCl-$AlCl_3$ at 175°C with a surface/melt ratio of 0.20.

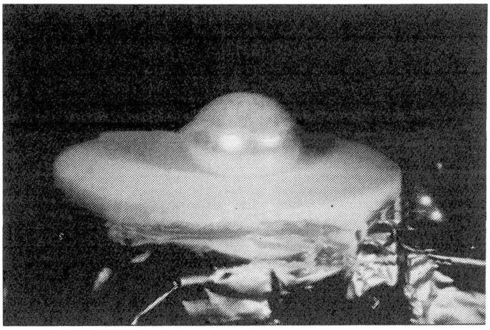

Figure 7. Sodium-potassium (50:50 atom %) drop photographed on a Nasicon disc at room temperature. The diameter of the disc is ca. 19 mm.

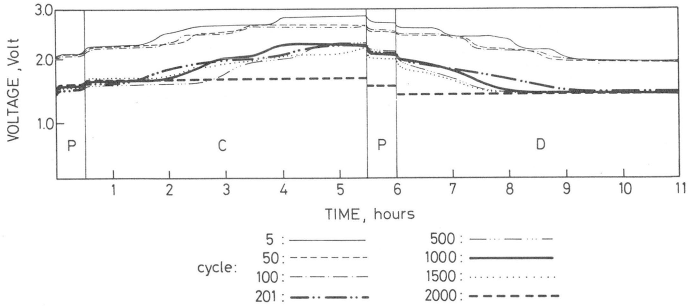

Figure 8. Charge/discharge curves for the testing of cell Na/Ni-6 with β-alumina separator and Ni_3S_2 cathode. Other experimental details are given in Table II.
C = Charge; D = Discharge and P = Pause.

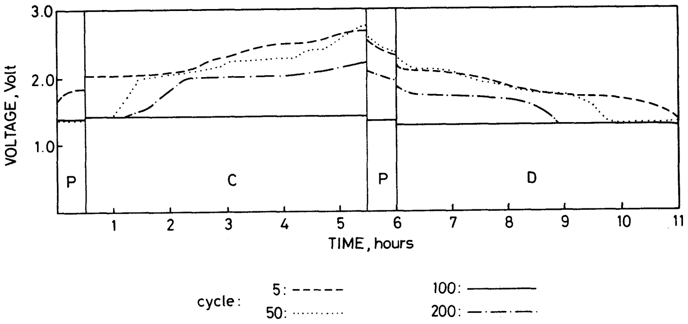

Figure 9. Charge/discharge curves for the testing of cell Na/Ni-8 with a Nasicon tube and FeS_2 as cathode material. The experimental details are given in Table II. C = Charge; D = Discharge and P = Pause.

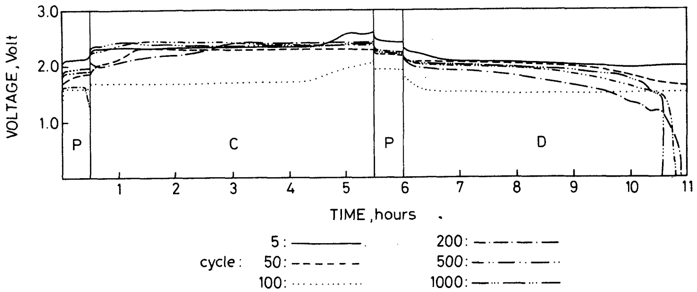

Figure 10. Charge/discharge curves for the testing of cell Na/Ni-26 with a Nasicon tube and Ni_3S_2 as cathode material. The experimental details are given in Table II. C = Charge; D = Discharge and P = Pause.

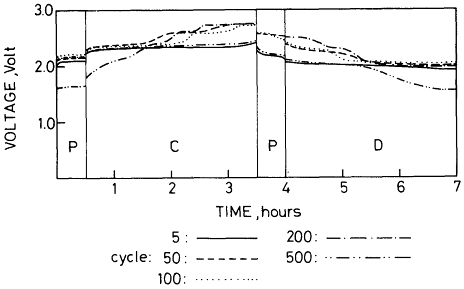

Figure 11. Charge/discharge curves for the testing of cell Na/Ni-48 with a Nasicon disc and Ni_3S_2 as cathode material. The experimental details are given in Table II. C = Charge; D = Discharge and P = Pause.

DOI: 10.1149/199017.0785PV

ALUMINUM/POLYANILINE BATTERIES WITH AMBIENT TEMPERATURE MOLTEN SALT ELECTROLYTES

Nobuyuki Koura and Hirokazu Ejiri

Department of Industrial Chemistry
Tokyo University of Science
Yamazaki, Noda, Chiba 278, Japan

ABSTRACT

Polyaniline electrodes and ambient temperature molten salts electrolytes have been studied to develop a new type Al/polyaniline secondary cell. The $AlCl_3$-EMIC melt was much better than the $AlCl_3$-BPC melt as the cell electrolyte. The reason was attributed to that the former conductivity is large and the viscosity is small. The polyaniline was synthesized in a non-aqueous electrolyte to reduce bad effect of a small amount of H_2O in the polyaniline synthesized in an aqueous solution. An electroactive and stable polyaniline was obtained from a BPC bath at about 2.0V vs.Al. The polyaniline was porous. In the case of the cell used polyaniline synthesized at 2.2V vs.Al in the BPC bath, the open circuit voltage, the discharge capacity, and the charge/discharge efficiency was 1.6V, 68Ah/kg, and 99%, respectively.

INTRODUCTION

An application of conductive polymers to positive electrode materials for the secondary cells has been investigated(1). Among these polymers, a polyaniline (PAn) is most strongly expected and commercialized in part(2), because it has a relatively high doping level per polymer unit and a large discharge capacity(3,4).

Moreover, from the ambient temperature molten salts electrolytes, i.e., an $AlCl_3$-1-butylpyridinium chloride (BPC) system and an $AlCl_3$-1-ethyl-3-methylimidazolium chloride (EMIC) system, a dense and smooth Al plating can be obtained(5,6,7). Therefore, the rechargeability of Al electrode in these electrolytes is very good. Then, we have investigated a new type Al/PAn secondary cell(8) with the above electrolytes, where a PAn powder(9) is used as the positive electrode material.

An electroactive PAn is usually synthesized by the electrochemical polymerization method in an acidic aqueous solution. A small amount of H_2O in the PAn should attack the ambient temperature molten salt which is very active against water. It was attempted that a PAn is synthesized in a non-aqueous electrolyte, because the

PAn must show good charge/discharge characteristics in the molten salt electrolyte.

EXPERIMENTAL

Synthesis of PAn --- In the case of the polymerization from an aqueous electrolyte, the PAn was electrolytically synthesized from a 0.5M aniline + 1.0N HCl aqueous solution as a powder. On the other hand, in the case of the polymerization from non-aqueous electrolyte, the PAn was prepared from an $AlCl_3$-BPC (mole ratio: 2/1) + benzene (50vol.%) + aniline (0.5M) bath.

Electrolyte --- Anhydrous $AlCl_3$ and BPC or EMIC (mole ratio: 2/1) were mixed, then purified by the substitution method with Al wire(10).

Batteries --- A PAn powder and film were used as the positive electrode(9). An Al rod (99.99%) was used as the negative electrode. Batteries were operated in N_2 atmosphere at room temperature.

RESULTS AND DISCUSSION

1) Cell with ambient temperature molten salts electrolytes.

The characteristics of the $AlCl_3$-BPC and $AlCl_3$-EMIC melts as the cell electrolyte was studied. The charge and discharge curves for the PAn powder electrode at $0.4mA/cm^2$ in the melts are shown in Fig. 1. Obviously, the EMIC bath is better than the BPC bath. The reason may be attributed to high conductivity and low viscosity of the EMIC bath. These data as shown in Table 1 prove the reason. Moreover, it was known that these data for the EMIC bath are near to those of aqueous solution.

Figure 2 shows the discharge capacity and coulombic efficiency versus charge capacity. The discharge capacity increased linearly up to 50Ah/kg of charge capacity. An oxidation decomposition of PAn due to the overcharging may occur from 60Ah/kg. The reason may be attributed to that the electric contact of PAn powder and the electric conductivity of electrolyte are not so good. It was also known that a performance for the EMIC bath is much better than that for the BPC bath.

2) Synthesis of PAn from non-aqueous electrolyte

A small amount of H_2O in the PAn synthesized in an aqueous electrolyte should be poisonous, because H_2O reacts strongly with the ambient temperature molten salts. Then, a synthesis of PAn from a non-aqueous electrolyte, i.e., aniline-$AlCl_3$-BPC-benzene bath, was attempted. Under 1.7V, no reaction occurred as shown from 1st to 10th cycle in Fig.3. When the sweep range was widened, some reaction occurred. The reaction current increased with increasing cycle number. We considered that this peak current is of both a Cl_2 evolution and a polymerization of aniline. The first peak of anodic current may be a doping current for PAn, and that of cathodic current may be the undoping current. On the other hand, when the return potential of anodic side is lowered to 1.7V, the curve was constant as shown from 31st to 40th cycle. This means that the polymerization of aniline dose not occur in the potential range of 0.6 to 1.7V.

Figure 4 shows cyclic voltammograms for the PAn synthesized from the non-aqueous BPC bath and from the aqueous bath. In the case of the BPC bath, the reaction current is large. Moreover, after 10th cycle, the current is still same level. Namely, the PAn is very stable. In the case of the aqueous bath, the current is very small. Even at the 2nd cycle, the current becomes very small. These tendencies were strongly cleared when the sweep range was widened up to the Cl_2 evolution potential. The PAn from the BPC bath was still stable, however, that from the aqueous bath was broken.

The PAn film surface deposited on a Pt plate from the BPC bath at $1.0mA/cm^2$ was observed by the SEM. The grain size of PAn was about 1 to 2μm. On the other hand, in the case of the polymerization at constant potential at 1.9V is fairly smooth. The PAn at 2.0 or 2.2V have about 2 to 3μm grain. In particular, at 2.2V the surface is very porous. These differences among the morphologies are considered to influence to the cell performance. Then, the in-cell cycling test was done.

3) In-cell test of PAn

The cells with the PAns synthesized at $1.0mA/cm^2$, at 1.9V, and at 2.2V were operated at a constant current density of $0.1mA/cm^2$ as shown in Fig.6. All of them showed larger capacity than that from an aqueous bath. In particular, by using the PAn synthesized at 2.2V, the largest capacity was obtained. Figure 7 shows the relationships between the charge capacities and the charge/discharge efficiencies. In the case of the PAn at 2.2V, when it was charged under 70Ah/kg, the coulombic efficiency showed about 100%.

The charge and discharge curves are shown in Fig.8. For the PAn cell at 2.2V, the open circuit voltage, the discharge capacity, and the charge/discharge efficiency were 1.6V, 68Ah/kg, and 99%, respectively.

In conclusion, it was known that the Al/PAn cell with the PAn synthesized from the non-aqueous BPC bath has an excellent performance.

REFERENCES

1. M.Hishinuma and T.Yamamoto, Kagakukogyo, 40, 241(1989)
2. H.Daifuku, T.Kawagoe, and T.Matsunaga, Denkikagaku, 57,

557(1989)

3. A.F.Diaz and J.A.Logan, J.Electroanal.Chem., 111, 111(1989)
4. A.G.MacDiarmid, J.C.Chiang, M.Halpern, W.S.Huang, J.R.Krawczyk, R.J.Mammone, S.L.Mu, N.L.Somasiri, and W.Wu, Poly.Prepr., 25, 248(1984)
5. Y.Kato, S.Takahashi, and N.Koura, Jpn.Kokai Tokkyo Koho JP 60,208,144; 60,208,145(1985)
6. A.Morita and S.Takahashi, Hyomengijutsu, 40, 56(1989)
7. S.Takahashi, K.Akimoto, and J.Saeki, ibid., 40, 134(1989)
8. N.Koura, T.Kijima, and H.Ejiri, Denkikagaku, 56, 1024(1988)
9. N.Koura and T.Kijima, ibid., 55, 386(1987)
10. S.Takahashi and N.Koura, J.Electroanal.Chem., 188, 245(1985)

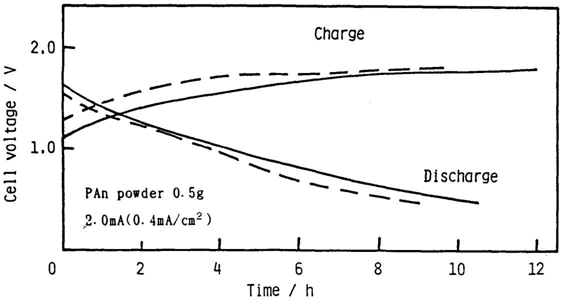

Fig. 1 Charge and discharge curves for the Al/PAn powder secondary cell.

——— : 66.7mol%AlCl$_3$-33.3mol%EMIC electrolyte

— — —: 66.7mol%AlCl$_3$-33.3mol%BPC electrolyte

PAn : Synthsized in the aqueous bath.

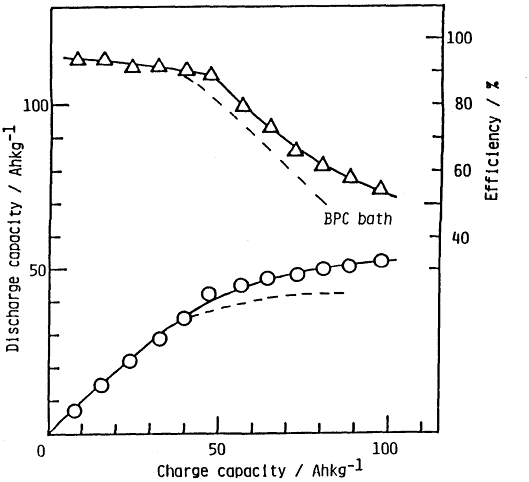

Fig. 2 Change of the discharge capacity and the charge/discharge efficiency with the charge capacity for the Al/PAn secondary cell.

Electrolyte : 66.7mol%AlCl$_3$-33.3mol%EMIC.

PAn : Synthesized in the aqueous bath.

Table 1 Specific conductivity and viscosity of the electrolyte (25°C).

Electrolyte	Conductivity ($mScm^{-1}$)	Viscosity (cP)
66.7mol%$AlCl_3$-33.3mol%BPC	6.99	22.5
66.7mol%$AlCl_3$-33.3mol%EMIC	15.0	6.0

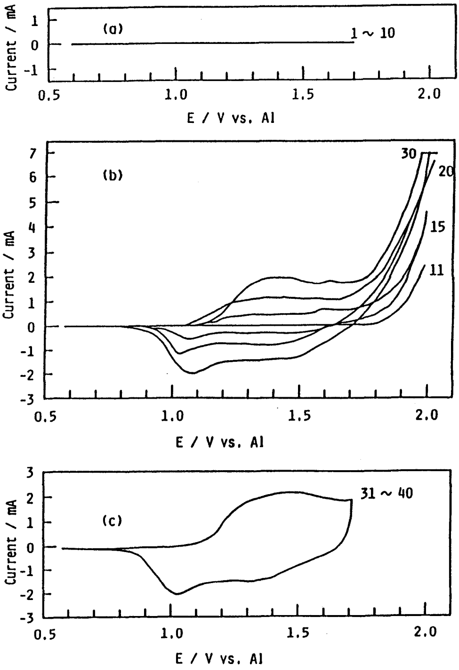

Fig. 3 Cyclic voltammograms for the polymerization of aniline in a 66.7mol%$AlCl_3$-33.3mol%BPC-benzene(50vol.%) bath.

(a) Sweep range : 0.6~1.7V vs. Al

(b) Sweep range : 0.6~2.0V vs. Al

(c) Sweep range : 0.6~1.7V vs. Al

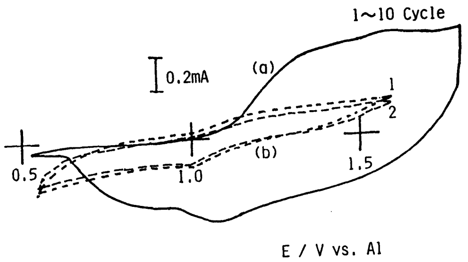

Fig. 4 Cyclic voltammograms for PAn in an $AlCl_3$-BPC(2:1) melt at 25℃.
(a)PAn film synthesized in an $AlCl_3$-BPC bath.
(b)PAn film synthesized in an aqueous bath.
W. E. : PAn film (Pt substrate, $5C/cm^2$, $1cm^2$)
C. E. : Al(99.99%)
R. E. : Al(99.99%)
v : 10mV/s

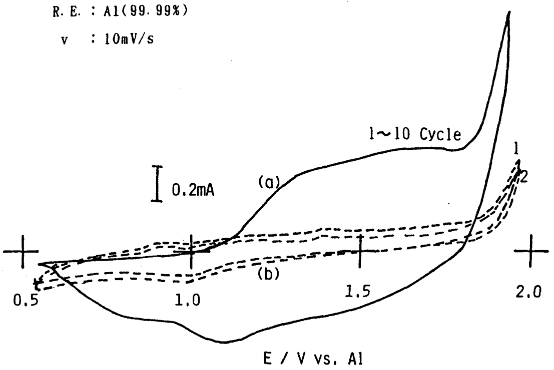

Fig. 5 Cyclic voltammograms for PAn in an $AlCl_3$-BPC(2:1) melt at 25℃.
(Polarized up to a Cl_2 evolution potential.)
(a)PAn film synthesized in an $AlCl_3$-BPC bath.
(b)PAn film synthesized in an aqueous bath.
W. E. : PAn film(Pt substrate, $5C/cm^2$, $1cm^2$)
C. E. : Al(99.99%)
R. E. : Al(99.99%)
v : 10mV/s

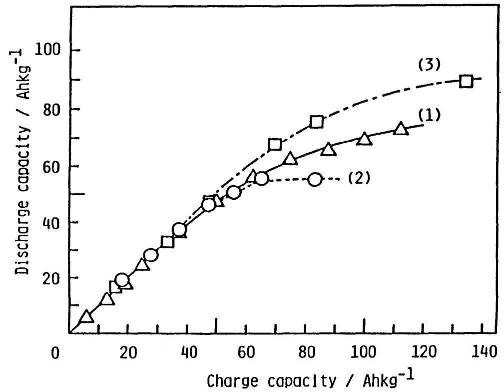

Fig. 6 Change of the discharge capacity with the charge capacity for the Al/PAn secondary cell.
C.D. : 0.1mAcm^{-2}, PAn was synthesized at (1) 1.0mAcm^{-2}, (2) 1.9, and (3) 2.2V vs. Al

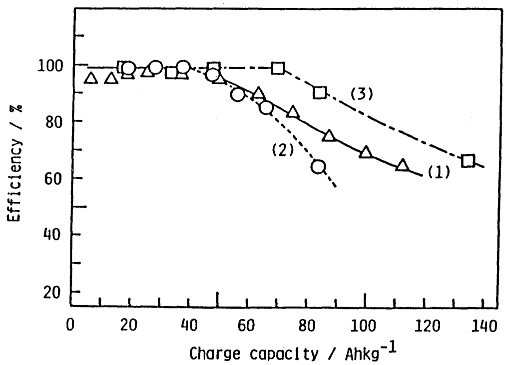

Fig. 7 Change of the charge/discharge efficiency with the charge capacity for the Al/PAn secondary cell.
C.D. : 0.1mAcm^{-2}, PAn was synthesized at (1) 1.0mAcm^{-2}, (2) 1.9, and (3) 2.2V vs. Al

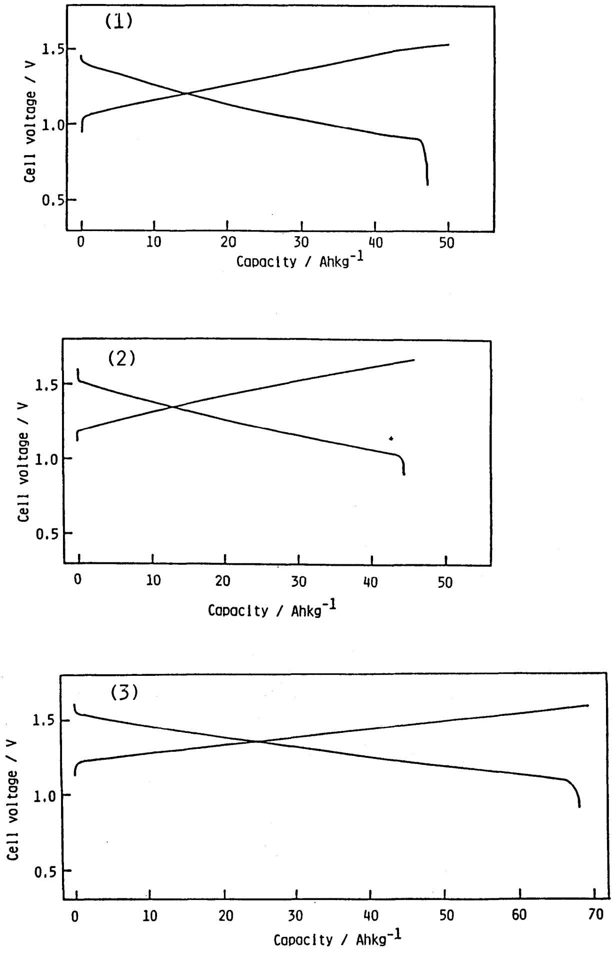

Fig. 8 Charge and discharge curves for the Al/PAn film secondary cell. The PAn film was synthesized at (1)1.0mA/cm^2,(2)1.9, and (3)2.2 V vs. Al

DOI: 10.1149/199017.0794PV

INVESTIGATIONS OF SOME ASPECTS OF CHEMISTRY IN ALKALI CHLOROALUMINATE MELTS

G. Mamantov, L. J. Tortorelli, P. A. Flowers
B. L. Harward, D. S. Trimble, E. M. Hondrogiannis
J. E. Coffield, A. G. Edwards

Department of Chemistry
University of Tennessee
Knoxville, TN 37996-1600

L. N. Klatt

Analytical Chemistry Division
Oak Ridge National Laboratory
P. O. Box 2008
Oak Ridge, TN 37831-6142

ABSTRACT

Two aspects of chemistry in alkali chloroaluminate melts are discussed. The first topic involves in situ spectroscopic studies of $IrCl(CO)_3$ and $Ir_4(CO)_{12}$ during the catalytic hydrogenation of CO in an $AlCl_3$-NaCl (63-37 mole %) melt. Infrared, UV-visible, Raman, and ^1H NMR data indicate that similar monomeric species are generated from both precursors during catalysis. Infrared investigation of the introduction of $IrCl(CO)_3$ into molten $AlCl_3$-NaCl under $CO:H_2$ (1:3) and the reaction between $IrCl(CO)_3$ and CO in the melt suggest the initial formation of an iridium-carbonyl species followed by the generation of a hydridocarbonyl complex. The second topic involves infrared, Raman and UV-visible spectroelectrochemical studies of the reduction of chloranil in $AlCl_3$-NaCl melts.

INTRODUCTION

This paper describes two studies in $AlCl_3$-NaCl melts. The first (A) involves in situ spectroscopic studies of catalyst precursors $IrCl(CO)_3$ and $Ir_4(CO)_{12}$ in the $AlCl_3$-NaCl (63-37 mole% ≡ 63/37) melt under different conditions. The second part (B) deals with spectroelectrochemical (SE) studies of the reduction of a model compound, chloranil, using UV-visible, infrared and Raman spectroscopies. The two parts are only indirectly related and will be discussed separately.

Part A. Catalytic activity of $Ir_4(CO)_{12}$ under $CO:H_2$ (1-2 atm) at 160-180°C in an acidic ($AlCl_3$-rich) Na chloroaluminate melt was first studied by Demitras and Muetterties(1) who observed the formation of saturated hydrocarbons. The ethane to methane ratio varied significantly with reaction time, from a 10:1 after 3 hr to 1:2 after several days. Evidence for homogeneous Fischer-Tropsch synthesis was presented. This reaction was studied further by Muetterties and coworkers(2) who obtained as the major products isobutane and propane, and by Collman et al. (3) who obtained methane, ethane and methyl chloride as the major carbon-containing products. Collman and coworkers found that a mononuclear "precatalyst", $IrCl(CO)_3$, shows similar chemistry, indicating that the presence of a metal cluster was not essential as implied initially (1). The results of Collman et al. (3) were sufficiently different from those of Muetterties and coworkers (1,2) that Collman et al. (3) concluded that a different active catalyst was involved in their work.

The major difference between the procedures employed by the two groups was the method of introduction of $Ir_4(CO)_{12}$ into the melt. Muetterties and coworkers premixed the iridium complex with the frozen melt before heating (pre-melt addition), whereas Collman et al. added the iridium complex to the melt at 175°C (post-melt addition).

In this paper the results of in situ spectroscopic studies of $AlCl_3$-NaCl(63/37) melts containing $IrCl(CO)_3$ or $Ir_4(CO)_{12}$ under various atmospheres are summarized in an effort to obtain additional information on the catalytically active species in this complex chemical system.

Part B. Spectroelectrochemistry involves the study of the redox chemistry of solute species through the simultaneous use of electrochemical and spectroscopic techniques. This approach can be utilized to obtain spectra and redox potentials of electrogenerated species and to study chemical reactions involving the products (4).

In this study spectroelectrochemical techniques involving UV-visible transmission, infrared transmission, and Raman spectroscopy were used to examine a model compound, tetrachloro-p-benzoquinone (chloranil), dissolved in both acidic and basic alkali chloroaluminates. In this way a comparison among three spectroelectrochemical approaches applied to a solute dissolved in an ionic melt, became available.

EXPERIMENTAL

Part A. $Ir_4(CO)_{12}$ and $IrCl(CO)_3$ were obtained from Strem Chemicals. High purity nitrogen (99.998%), carbon monoxide (99.8%), hydrogen (99.9%), and deuterium (99%) were used as received. Anhydrous $AlCl_3$(Fluka) was purified as described previously (5). Reagent grade NaCl was vacuum dried at 400°C before use. The sodium chloroaluminate melts were prepared as previously described (5). Infrared instrumentation and the cell used to obtain spectra of melts have been described previously (6). Proton NMR spectra were obtained with a JEOL FX90Q spectrometer using tetramethylammonium bromide (TMAB) as the internal reference. All manipulations involving melts were performed in a Vacuum Atmospheres dry box (moisture level < 2ppm). Iridium carbonyls were introduced to the melts either prior to melting by mixing the two solids or afterwards by means of a FLICKET valve (Ace Glass).

Part B. Spectroelectrochemical techniques used to study molten salt solutions have been previously described (4). The infrared spectroelectrochemical results for chloranil have been published recently (6). Raman spectroelectrochemical instrumentation included a SPEX Triplemate spectrograph, a Tracor Northern (TN) intensified array detector coupled to a TN Model 6500 computer data station, and UV excitation (333.6-363.8 nm) from a Coherent Innova Model 1-100-15 argon ion laser. Backscattering geometry was used; the details are described elsewhere (7). UV-visible transmission experiments involved a reticulated vitreous carbon (RVC) optically transparent electrode (OTE). Most of the experiments were performed in a dry box equipped with quartz fiber optics (8) using a TN diode array spectrometer.

RESULTS AND DISCUSSION

Part A. Infrared spectrum of $IrCl(CO)_3$ in $AlCl_3$-NaCl(63/37) under CO at 150°C exhibits a single intense band at 2125 cm^{-1}; the intensity of this band remained constant over a 24 hr period. The spectrum of this solution in the carbonyl stretching region (2250-1600 cm^{-1}) becomes more complex either under N_2 or under $CO:H_2$(1:3 mole ratio) (see Table 1 for a summary of infrared results for $IrCl(CO)_3$). It should be noted that some spectral differences were observed with time when the solute was added to the melt (as was done by Collman et al. (3)) compared to the "pre-melt" addition (the technique used by Muetterties and coworkers (1,2)). The infrared results for $Ir_4(CO)_{12}$ are summarized in Table 2. The spectra varied with time and were dependent on the atmosphere (either CO or $CO:H_2$; under N_2 the cluster decomposes to Ir metal) and the method of addition of the solute. The time dependence of several infrared bands of $Ir_4(CO)_{12}$ solutions is shown in Fig. 1. Infrared spectra of $IrCl(CO)_3$ and $Ir_4(CO)_{12}$ in the 63/37 melt under $CO:D_2$ (1:3 mole ratio) exhibited some frequency shifts relative to the hydrogen systems suggesting that the species produced are hydrido (or deuterido-) carbonyls (see Tables 1 and 2).

Solutions of $IrCl(CO)_3$ and $Ir_4(CO)_{12}$ in a 63/37 melt under 1 atm of CO at 150°C yielded similar UV-visible spectra with maxima at 278, 326, and 430 nm. The intensity of these bands increased with time. After 10 hr the ratio of the molar absorptivities of the cluster to the monomer was 4:1, indicating that the iridium cluster reacted to form a mononuclear complex. The rate of this conversion was shown to follow first-order kinetics. A rate constant of $1.32 \pm 0.26 \times 10^{-4}$ s^{-1} was obtained.

Raman spectra of $Ir_4(CO)_{12}$ in a 63/37 melt (post-melt addition) under 1 atm CO at 150°C exhibited a weak band at 202 cm^{-1}, which disappeared within one hour after introduction of the cluster to the melt. This band is within the region expected for a metal-metal stretch, and its dependence upon the polarization state of the exciting radiation suggests that it is a symmetric vibration. Under identical conditions, this band was not observed with $IrCl(CO)_3$.

^1H NMR spectra of $IrCl(CO)_3$ (pre-melt addition) in a 63/37 melt under 1 atm of $CO:H_2$ (1:3 mole ratio) at 130°C exhibited one major peak at -10.7 ppm vs. TMAB (internal reference, 3.21 ppm vs. tetramethyl silane) over the 36 h time period examined; this feature was observed immediately after melting. Two much weaker proton resonances at -19.5 (0.9% the intensity of the peak at -10.7 ppm) and +5.4 ppm (1.3% the intensity of the peak at -10.7 ppm) appeared about 2 h after melting. No significant change in the intensity of these resonances was observed throughout the experiment.

^1H NMR spectra of $Ir_4(CO)_{12}$ in a 63/37 melt (pre-melt addition) under 1 atm of $CO:H_2$ at 130°C exhibited a major resonance at -10.7 ppm, which appeared roughly 1.5 h after melting and remained throughout the 24 h period the reaction was monitored. Weaker proton resonances were observed at -19.5 and +1.4 ppm. The peak at +1.4 ppm, first observed about 3 h after melting, was initially flanked by two other resonances at +0.9 and +0.3 ppm which disappeared after 4 h. The relative intensities of the two weaker features at -19.5 and +1.4 ppm increased roughly twofold during the 24 h reaction period. Toward the end of the experiment a proton resonance appeared at +5.3 ppm (28% the intensity of the peak at -10.7 ppm). When the ^1H NMR spectra of $Ir_4(CO)_{12}$ were acquired with TMAB as an external reference, an additional peak at +3.6 ppm was observed about 5 h after melting. Spectral interference from the TMAB prevented the observation of this resonance when TMAB was used as an internal reference. During the course of the experiment, the intensity of the resonance at +3.6 ppm increased while the intensity of the major resonance at -10.7 ppm decreased.

A ^1H NMR spectrum of a 63/37 melt under hydrogen chloride atmosphere at 130°C exhibited a proton resonance at +1.6 ppm.

The following tentative conclusions have been drawn from the spectroscopic results described above (a more detailed description of the results and of the reasoning leading to the conclusions will appear elsewhere (9)).

1. A Lewis acid adduct between the iridium species and $AlCl_3$ in which aluminum is joined to the iridium atom, is formed in the melt.

2. The likely iridium carbonyl complex in the 63/37 melt formed from $IrCl(CO)_3$ under a CO atmosphere is trans-$(AlCl_3)_2Ir(CO)_4$.

3. Under a $CO:H_2$ atmosphere a similar monomeric hydridocarbonyl iridium complex is generated from $IrCl(CO)_3$ and $Ir_4(CO)_{12}$ precursors. Other unstable complexes may also be formed, particularly in the case of $Ir_4(CO)_{12}$.

We speculate that the active homogeneous Fischer-Tropsch catalyst in the experiments of Muetterties, Collman and coworkers (1-3) is a monomeric hydridocarbonyl iridium adduct with $AlCl_3$ formed under a CO-H_2 atmosphere. This complex is converted to either $(AlCl_3)_2Ir(CO)_4$ under excess CO or irreversibly to iridium metal under excess hydrogen.

4. The acidic chloroaluminate melt serves as the oxide sink (arising from the reaction between CO and H_2) to form AlOCl and related species in the melt.

<u>Part B</u>. The redox behavior of chloranil in molten $AlCl_3$-NaCl has been examined by Bartak and Osteryoung (10). They concluded that the reduction of chloranil proceeds via the ECEC mechanism in which the radical anion formed initially reacts with a Lewis acid (presumably $AlCl_3$ from $Al_2Cl_7^-$). The complexed radical anion is reduced at the same potential as the chloranil. At very fast scan rates (in cyclic voltammetry) or for short pulses (normal pulse voltammetry) the uncomplexed radical anion is reduced further to the dianion which is complexed by the Lewis acid.

The chloranil reduction was studied in our group by infrared SE (6). Evidence for closely spaced stepwise one electron reductions in acidic melts was obtained by both infrared SE and differential pulse voltammetry. In basic melts no evidence for the formation of a radical anion was obtained. We decided, therefore, to examine chloranil by UV-visible SE since the molar absorptivities are frequently much higher in this spectral region compared to the infrared region. A weak band at 512 nm was found to reach a maximum at intermediate potentials; this band was not present at potentials corresponding to either chloranil or the dianion of chloranil. The Nernstian plot constructed from the variation of absorbance with potential results in an n-value of 1.2. The uncomplexed radical anion of chloranil exhibits absorption bands at 422 and 448 nm (11). The shift of these bands to a broad band at 512 nm, upon the complexation of the radical anion by $AlCl_3$, is probably not unreasonable.

To obtain additional information on the existence of the radical anion in chloroaluminate melts, Raman SE [illegible] performed. Using UV (363.8 nm) excitation (in order to minimize problems with fluorescence) the controlled potential electrolysis using Pt foil electrode at potentials corresponding to the formation of the radical anion in acidic melts, resulted in the decrease of Raman bands of chloranil observed at 1576 and 593 cm^{-1} (7) and the growth of Raman bands at 1338 and 1076 cm^{-1}. After further electrolysis at potentials corresponding to the formation of the dianion of chloranil, only solvent bands were visible. Upon reoxidation, the bands at 1338 and 1076 cm^{-1} appeared at intermediate potentials followed by the reappearance of chloranil bands at very positive potentials. The Raman bands at 1338 and 1076 cm^{-1} are in the same spectral range as the infrared bands previously attributed to the chloranil radical anion (980-1486 cm^{-1}) (6). Further work is needed to determine whether the above Raman and infrared bands are due to the radical anion complexed by $AlCl_3$.

Very recent work in our group using NaCl-saturated $AlCl_3$-NaCl melts has resulted in the observation of weak Raman bands at 1071 and 1350 cm^{-1} which are observed only at potentials corresponding to the radical anion. Further work in this area is in progress.

In summary, this study illustrates the usefulness of a combined SE approach for the characterization of electrochemical intermediates in molten salt solutions. UV-visible absorption SE is frequently a more sensitive technique than vibrational (infrared and Raman) SE methods. On the other hand, the latter techniques, if applicable, can result in an unambiguous characterization, particularly if independent standards are available.

ACKNOWLEDGEMENT

This work was supported in part by Grants 85-08321 and 88-0307 from the Air Force Office of Scientific Research and in part by the U.S. Department of Energy, Office of Energy Research, under contract DE-AC05-84OR21400 with Martin Marietta Energy Systems, Inc. B. L. Harward acknowledges support from the Laboratory Graduate Participation Program administered by the Oak Ridge Associated Universities for the U. S. Department of Energy.

REFERENCES

1. G. C. Demitras and E. L. Muetterties, J. Am. Chem. Soc., 99, 2796 (1977).

2. H. K. Wang, H. W. Choi, and E. L. Muetterties, Inorg. Chem., 20, 2661 (1981).

3. J. P. Collman, J. I. Brauman, G. Tustin, and G. S. Wann III, J. Am. Chem. Soc., 105, 3913 (1983).

4. V. E. Norvell and G. Mamantov, "Spectroelectrochemistry," in Molten Salt Techniques, Vol. 1, D. G. Lovering and R. J. Gale, eds., Plenum Press, 1983, pp. 151-176.

5. R. Marassi, J. Q. Chambers and G. Mamantov, J. Electroanal. Chem., 69, 345 (1976).

6. P. A. Flowers and G. Mamantov, J. Electrochem. Soc., 136, 2944 (1989).

7. D. S. Trimble, Ph.D. Dissertation, University of Tennessee, 1989.

8. J. E. Coffield, Ph.D. Dissertation, University of Tennessee, 1989.

9. L. J. Tortorelli, P. A. Flowers, B. L. Harward, G. Mamantov, and L. N. Klatt, submitted to Inorg. Chem.

10. D. E. Bartak and R. A. Osteryoung, J. Electroanal. Chem., 74, 69 (1976).

11. J. J. Andre and G. Weill, Molec. Physics, 15, 97 (1968).

TABLE I

CO STRETCHING FREQUENCIES OBTAINED FROM THE IR SPECTRA OF $IrCl(CO)_3$

$IrCl(CO)_3$	ν_{CO}, cm^{-1}
KBr	2141(m), 2078(s), 2053(s)
$AlCl_3$-NaCl (63-37)-N_2	2178(m), 2168(w), 2143(m), 2125(s), 2107(m), 2085(w)
$AlCl_3$-NaCl (49-51)-N_2	2170(w), 2153(w), 2126(w), 2087(s) 1985(s)
$AlCl_3$-NaCl (63-37)-CO	2125(s)
$AlCl_3$-NaCl (63-37)-CO:H_2 (pre-melt addition)	2230(w), 2187(m), 2157(s), 2125(m)
$AlCl_3$-NaCl (63-37)-CO:D_2 (pre-melt addition)	2187(m), 2176(sh), 2157(s), 2125(m)
$AlCl_3$-NaCl (63-37)-CO:H_2 (post-melt addition) t=0 h	2187(vw), 2178(vw), 2157(vw), 2168(vw), 2125(s), 2085(vw)
$AlCl_3$-NaCl (63-37)-H_2	2125, 2107 (decay) 2178, 2168, 2157, 2143 (growth-decay) 2075(w), 2041(w) (growth)

s=strong, m=medium, w=weak, sh=shoulder

TABLE II

CO STRETCHING FREQUENCIES OBTAINED FROM THE IR SPECTRA OF $IR_4(CO)_{12}$

$Ir_4(CO)_{12}$	ν_{CO}, cm^{-1}		
KBr	2112(w), 2090(wsh), 2056(s), 2023(m), 2006(wsh)		
$AlCl_3$-NaCl (63-37)-CO, t=0 h	2157(w), 2143(s), 2125(m), 2107(sh) 2083(w)		
$AlCl_3$-NaCl (63-37)-CO, t=4 h	2156(w), 2125(s), 2110(sh), 2083(w)		
$AlCl_3$-NaCl (63-37)-CO:H_2 (Pre-melt addition)	<u>t=1 h</u>	<u>t=10 h</u>	<u>t=24 h</u>
	2187(m)	2187(m)	2187(w)
			2178(s)
			2168(sh)
	2157(s)	2157(s)	2157(m)
			2143(s)
			2132(m)
	2125(m)	2125(m)	
		2114(m)	
	2107(m)	2107(sh)	2107(w)
	2085(w)		
		1656(w)	1656(m)
$AlCl_3$-NaCl-CO:D_2 (63-37) (Pre-melt addition)	<u>t=1 h</u>	<u>t=10 h</u>	<u>t=24 h</u>
			2182(s)
	2176(w)	2178(m)	
		2168(vw)	2168(w)
	2157(m)	2157(s)	
			2143(s)
	2125(s)	2131(s)	2125(m)
	2107(s)	2107(m)	2107(m)
	2085(m)		
		1639(w)	1639(m)
$AlCl_3$-NaCl-(63-37) CO:H_2, t=0 h (Post-melt addition)	2164(sh), 2157(w), 2140(s), 2134(s), 2125(s), 2105(m), 2085(sh), 2043(vw)		

TABLE II (CONTINUED)

$AlCl_3$-NaCl-(63-37) $CO:H_2$, t=4 h (Post-melt addition)	2187(sh), 2180(m), 2170(sh), 2154(m) 2143(m), 2125(s), 2107(s), 2085(m), 2043(w)
$AlCl_3$-NaCl-(63-37) $CO:H_2$, t=9 h (Post-melt addition)	2230(w), 2187(m), 2157(s), 2125(m)

s=strong, m=medium, w=weak, vw=very weak, sh=shoulder

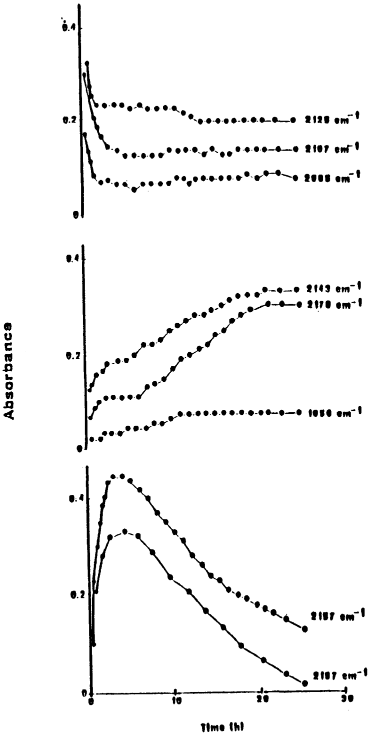

Figure 1. Plots of absorbance versus time after melting for several prominent features from the infrared spectra of $Ir_4(CO)_{12}$ in $AlCl_3$-NaCl(63/37) melts (pre-melt addition) under 1 atm of $CO:H_2$ obtained ca. 1 h (upper), 10 h (middle), and 24 h (lower) after melting; $[Ir_4(CO)_{12}]$~2 mM, 175°C.

DOI: 10.1149/199017.0805PV

FRIEDEL-CRAFTS ALKYLATION REACTIONS IN A ROOM TEMPERATURE MOLTEN SALT

Bernard J. Piersma and Melinda Merchant

Houghton College, Houghton, NY 14744

ABSTRACT

Room temperature molten salts have found usefulness as solvents for electro-organic studies because of their aprotic properties, wide electrochemical windows and reasonable conductivities as ionic liquids. The 1-methyl-3-ethylimidazolium chloride - aluminum chloride system was chosen for this study for its ease of preparation, its wide range of Lewis acidities and its carbocation stabilizing properties. We have studied the alkylation of benzene using the seven stable chloropentane isotopes. Cyclic voltammetry at a glassy carbon rotating disk electrode indicates carbocation formation from the chloropentanes only in acidic melts and no oxidation peaks are observed without prior reduction. Multiple reduction peaks and product analyses indicate that significant rearrangement occurs in the carbocations. Stabilization of carbocations probably results from compexation with the $Al_2Cl_7^-$ ion and this is strongly indicated by the delay of Al deposition in the presence of carbocations.

INTRODUCTION

The Friedel-Crafts reaction using anhydrous aluminum chloride as catalyst has been the most important method for attaching alkyl side chains to aromatic rings. The role of aluminum chloride is to abstract the halogen from the alkyl halide generating a carbocation which then acts as an electrophile attacking the aromatic ring. Friedel-Crafts systems are best considered as generalized acid-base systems with the electron deficient catalyst as the acid and the electron donor ability of the reagent as the base. Chloroaluminate room temperature molten salts provide a unique solvent system for Friedel-Crafts alkylations since the melts function as both solvent and catalyst. In the 1-methyl-3-ethylimidazolium chloride - aluminum chloride system, the catalyst has been identified as the heptachloro-aluminate ion (4), the Lewis acid in the equilibrium:

$$2AlCl_4^- \rightleftharpoons Al_2Cl_7^- + Cl^-$$

Thus carbocation formation and alkylation reactions have not been observed in basic or neutral melts but only for acidic melts (mole fraction of $AlCl_3$ is greater than 0.500).

In alkylation reactions with a series of alkyl halides the long established sequence of reactivity is: tertiary halide > secondary halide > primary halide, which follows carbocation stability (2). Olah has also noted that Friedel-Crafts reactions are notoriously irreproducible, being traced to the presence of impurities which serve as co-catalysts without which Friedel-Crafts halides are often inactive (3). Following Olah, the carbocation generated as the alkylating species is most likely the classical trivalent carbenium ion rather than the penta- or tetracoordinated carbonium ion. Alkylation of benzene may proceed through a tetracoordinated aronium ion or π - complex or the trivalent arenium ion or σ - complex (4):

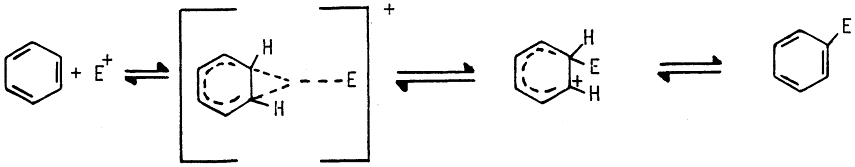

π - complex σ - complex

Olah has suggested that most Friedel-Crafts reactions probably do not involve formation of a free carbenium type reagent that reacts with the substrate. The alkylation of benzene with 1-chloropropane has shown an absence of isomerization of the alkylating agent indicating an S_N2 type displacement reaction (5):

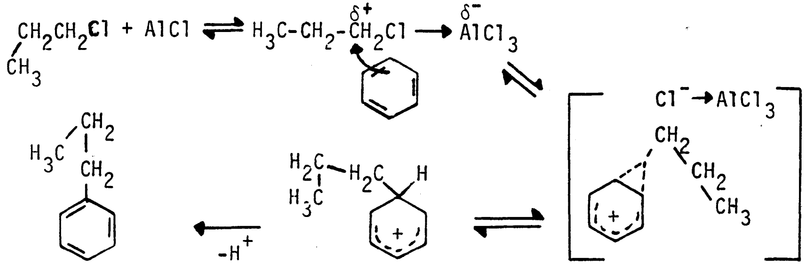

Wilkes, et.al. have recently shown that in the MEIC-$AlCl_3$ melt system, 1-chloropropane does isomerize with 57% of the alkylation product being isopropyl benzene and 24% n-propylbenzene with the remainder of product being di - and tri substituted benzenes (1). This is a strong indicator that these melt systems stabilize carbocations and that Friedel-Crafts alkylations may proceed somewhat differently than in conventional organic solvent systems.

EXPERIMENTAL

Procedures for melt preparation and general experimental conditions were those described by Wilkes, et.al. (1) All experiments were carried out in a helium environment in a Vacuum Atmosphere glove box system. Cyclic voltammetric measurements were made with a glassy carbon rotating disk electrode (normally with a rotation rate of 100 rpm), a tungsten counter electrode and an aluminum wire in 0.60 melt as reference. The chloropentane isomers were either Pfaltz-Bauer or Kodak and used as received.

Alkylation reactions for product analyses were generally run with 10 g melt / 1 g chloropentane / 10 g benzene, with the excess benzene to limit multiple substituted benzene products. After 48 hours in closed containers with magnetic stirring inside the glove box, each reaction sample was removed, reacted with 25 g crushed ice and then made basic with 6N NaOH. The liquid was added to a separatory funnel and extracted with 25 ml of diethyl ether. The ether samples were dried with anhydrous Na_2SO_4, then concentrated by evaporation of ether to final volumes of 10 ml which were then retained for analyses. Separation of various components was accomplished with GC on a fused glass capillary column with a stationary phase of SupelcoWax-10 and identified with MS using a HP model 5992 GC/MS instrument. (The GC/MS analyses were performed under contract with an independent analytical laboratory.)

RESULTS AND DISCUSSION

Cyclic voltammetry in acidic melts with the seven chloropentanes (1-Cl-, 2-Cl-, and 3-Cl-pentane, 1-Cl-2-methyl-, 1-Cl-3-methyl-, 2-Cl-2-methylbutane and neopentyl chloride) show two characteristic and consistent reduction peaks which are slightly dependent on melt acidity as follows:

melt composition	redn. peak #1	redn. peak #2
0.505	-0.16V	-0.38V
0.515	-0.26V	-0.53V
0.550	-0.37V	-0.57V

No significant differences were observed for reductions with any of the seven isomers. With anodic sweeps, no oxidation was observed without prior reduction. Fig. 1 illustrates typical CV behavior in the MEIC-$AlCl_3$ melts with Al deposition occurring at about -0.37V in 0.515 melt and at -0.26V in 0.55 melt. In following diagrams with added chloropentanes, we observe that Al deposition is either significantly delayed or prevented altogether. Formation of the carbenium ion results in a buffering action in the melt shifting it toward the neutral composition:

$$Al_2Cl_7^- + Cl^- \rightleftharpoons 2AlCl_4^-$$

For a typical CV experiment with 1 g of Cl-pentane in 20 g of 0.55 melt, there should be approximately twice as many heptachloroaluminate ions as Cl^- ions resulting from carbenium ion formation, assuming complete reaction. Thus we should still observe Al deposition based on melt acidity. That no deposition is observed is indicative of complex formation between the carbenium ion and $Al_2Cl_7^-$.

Figures 2-8 present representative CV behavior for the chloropentanes with varying melt acidity. Compounds were selected to demonstrate the range of carbocations that should be formed, thus 1-chloro-pentane and neopentyl chloride should form primary carbenium ions, 3-chloropentane a secondary ion and 2-Cl-2-methylbutane a tertiary ion. Essentially identical CV behavior was observed, not only for these four isomers, but in fact, for all seven of the chloropentane isomers studied. Figures 9-11 give qualitative comparisons of reaction rates of the alkylation reactions as a function of alkylating agent and melt acidity. These results show that the alkylation rate is strongly dependent on melt acidity (compare Figures 9 and 10). In addition, alkylation by a tertiary carbenium ion (assuming 2-Cl-2-methylbutane forms a tertiary ion as the most stable species) occurs much faster and to a greater extent than by a primary carbenium ion (which would be the initial species formed from neopentyl chloride).

Product analyses were performed for products from alkylation reactions of benzene in 0.515 and 0.55 melts with 1-Cl- and 3-Cl-pentane, 2-Cl-2-methylbutane and neopentyl chloride. Very little product could be isolated from reactions in the 0.515 melt and no reliable information can be reported. Results for 0.55 melt were as follows:

alkylating agent	products identified
neopentyl chloride	isopentylbenzene
2-Cl-2-methylbutane	n-pentyl- and 2-pentylbenzene
3-Cl-pentane	n-pentyl-, 2-pentyl- and 3-pentylbenzene
1-Cl-pentane	5 products as follows:

Benzene alkylation products with 1-Cl-pentane

product	percent
1,2-dimethyl-propylbenzene	78.5%
3-pentylbenzene	13.5
2-pentylbenzene	4.5
isopentylbenzene	2.5
n-pentylbenzene	1.0

Using a 10/1 benzene / chloropentane ratio effectively limited multiple alkylation products. Neopentyl chloride resulted in only a relatively small amount of alkylated benzene product. 1-Cl-pentane which should form the least stable carbocation and hence lead to the greatest degree of rearrangement resulted in the greatest variety of products as expected. The major product from 1-Cl-pentane alkylation of benzene (compound 1)

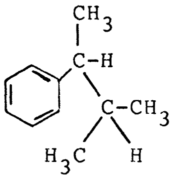

(1)

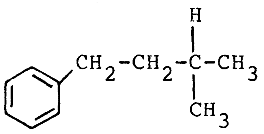

(2)

is not one we would have predicted. The isopentylbenzene (compound 2) is likewise an unexpected product. While $-CH_3$ group migration is not as common as -H migration in carbocation rearrangements to form more stable ions, it is not unusual.

The products observed are not easily correlated with the electrochemical observations. The presence of two reduction peaks at essentially the same reduction potentials for each of the chloropentane isomers strongly suggests that the same two carbocation species are present in each case. The variety of products observed may be the result of rearrangements after alkylation has occurred. At present we cannot answer this question.

SUMMARY

Cyclic voltammetric studies of chloropentane isomers in MEIC-$AlCl_3$ acidic melts indicate the presence of two reducible species formed with each of the seven isomers studied. Similarity of the reduction potentials in every case suggests that significant rearrangements of the carbocations occur to produce similar carbenium ions from each of the isomers. Retardation and in some cases prevention of aluminum deposition indicate complex formation between the carbenium ions formed and the heptochloroaluminate ions of the acidic melt. Identification of several alkylation products suggest that rearrangements occur after the carbocation has attacked the benzene ring.

ACKNOWLEDGEMENT

The authors are pleased to acknowledge helpful discussions with Dr. John Wilkes who suggested this project.

This work was supported by a Cottrell College Science Grant of the Research Corporation.

REFERENCES

1. J.A. Boon, J.A. Levisky, J.L. Pflug and J.S. Wilkes, J. Org. Chem., 51, 480 (1986)
2. G.A. Olah, Friedel Crafts Chemistry, Wiley-Interscience Publishers, 1973, p. 409
3. Ibid, p. 414
4. Ibid, p. 516
5. Ibid, p. 533

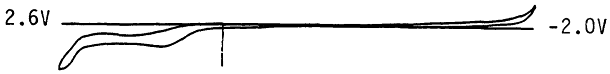

0.500 melt

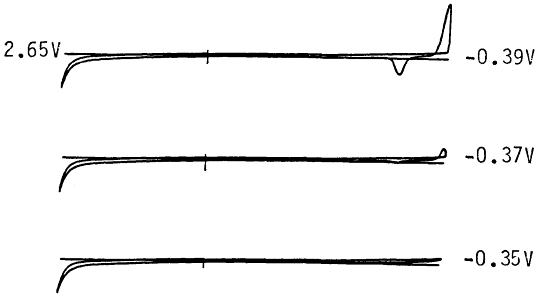

0.515 melt

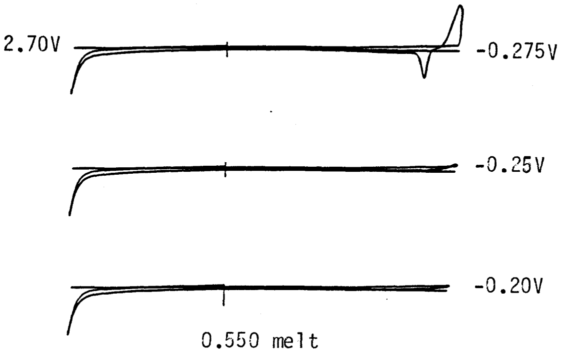

0.550 melt

Figure 1. Electrochemical windows of MEIC/$AlCl_3$ melts. ν = 100 mV/sec.

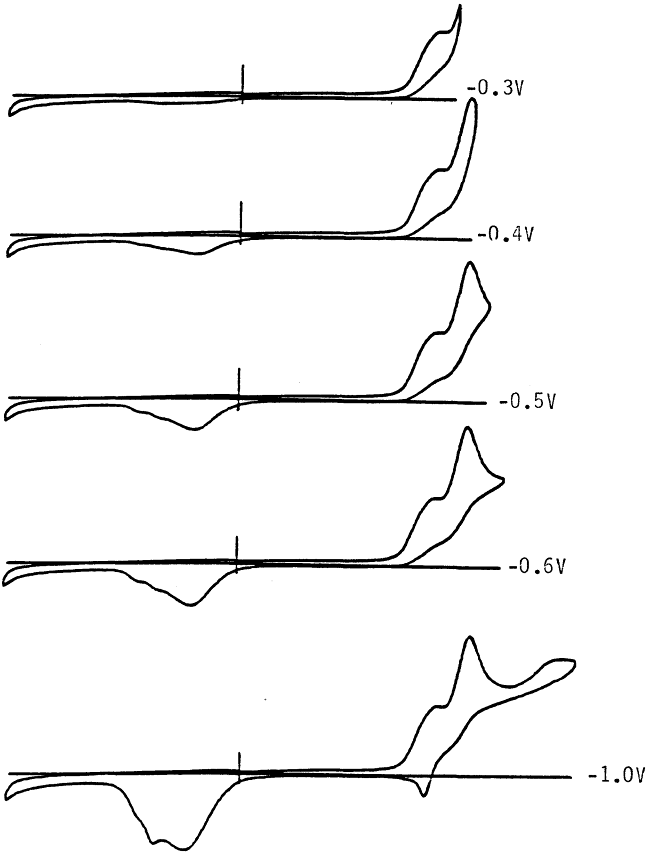

Figure 2. Cyclicvoltammetry of neopentyl chloride in 0.5067 melt. Anodic sweep limit: 2.4V.

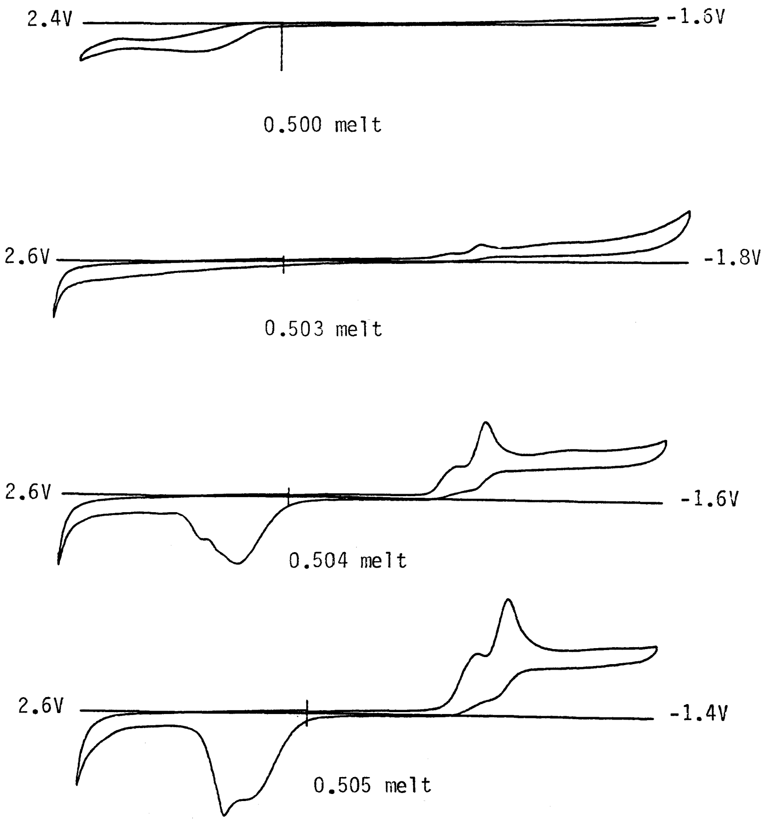

Figure 3. Cyclicvoltammetry of neopentyl chloride as a function of melt acidity.

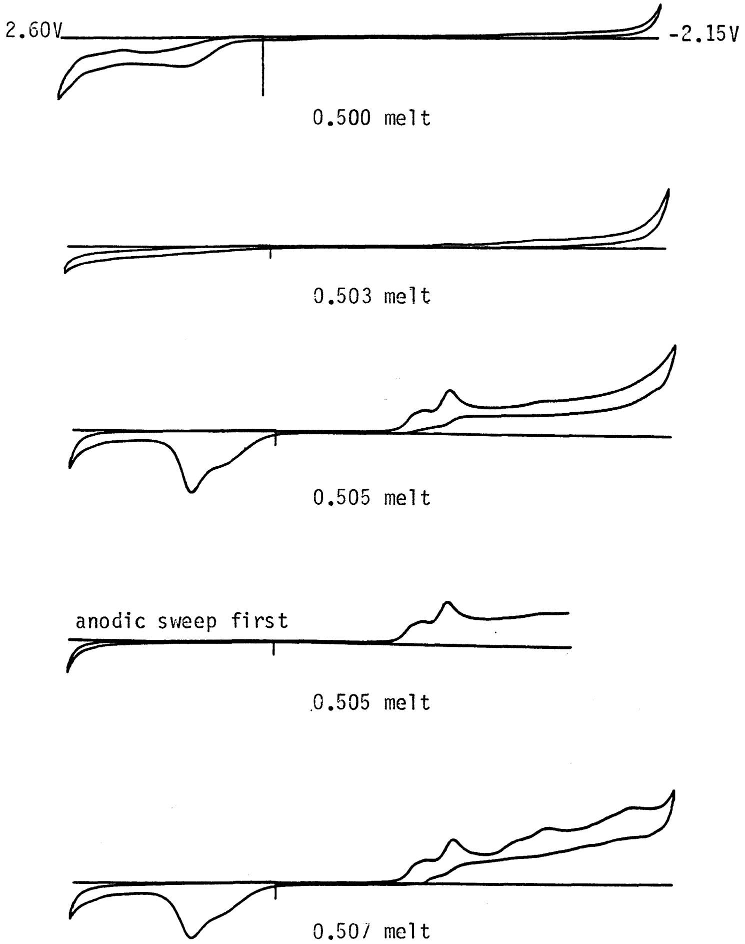

Figure 4. Cyclicvoltammetry of 3-Cl-pentane as a function of melt acidity.

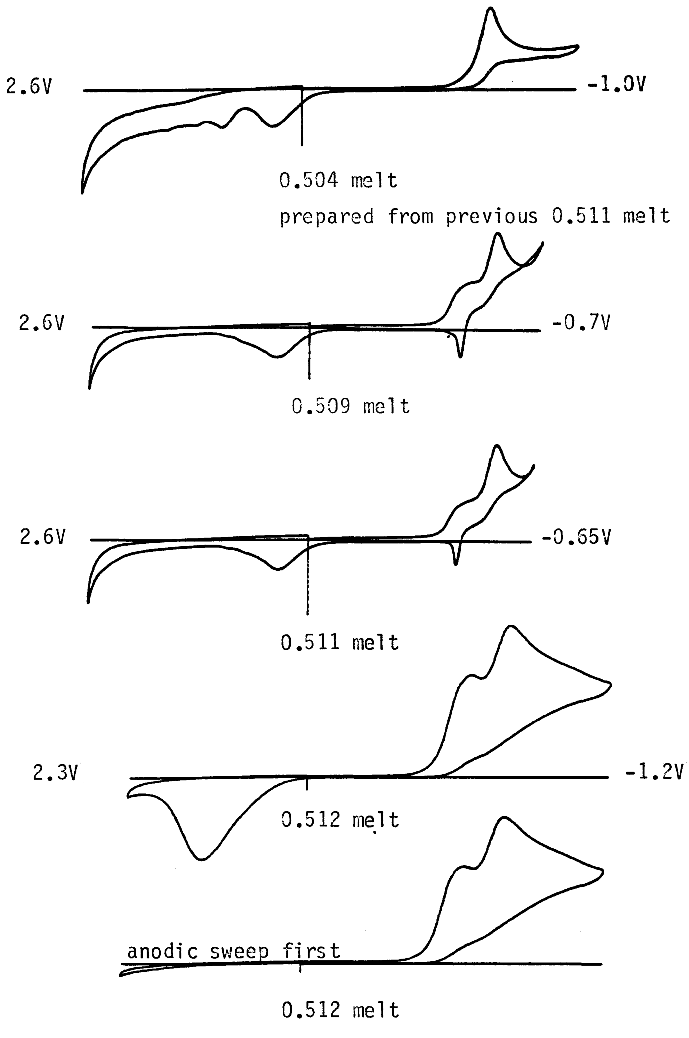

Figure 5. Cyclicvoltammetry of 3-Cl-pentane as a function of melt acidity.

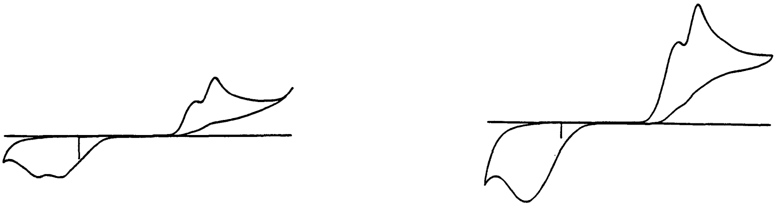

a. 3-Cl-pentane

b. 1-Cl-pentane

c. 2-Cl-2-me-butane

d. neopentyl chloride

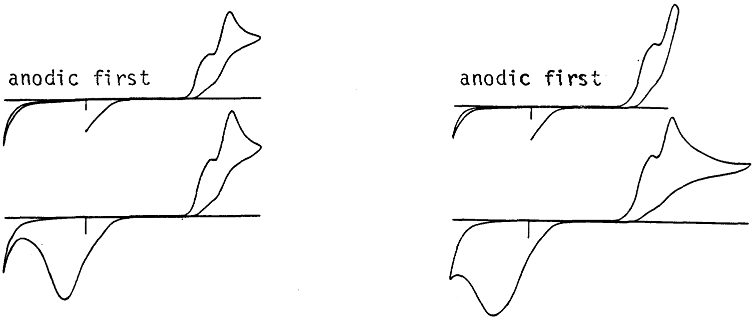

Figure 6. Comparisons of cyclicvoltammetric behavior in 0.515 melt. Voltage ranges: +2.6 to -1.6V; except (c) with +2.65V to -1.3V.

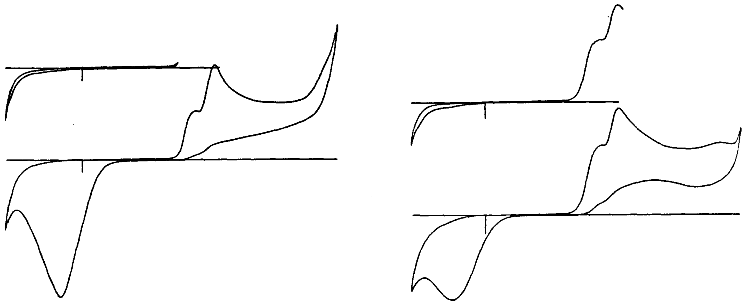

a. 3-Cl-pentane

b. 1-Cl-pentane

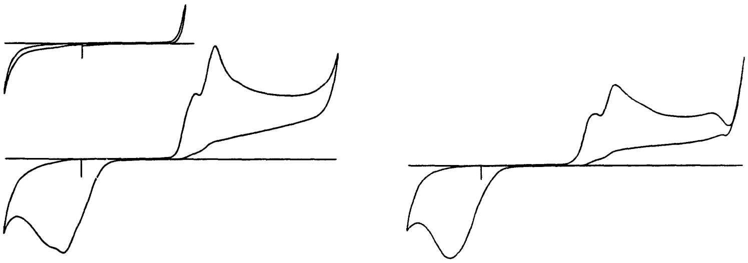

c. 2-Cl-2-me-butane

d. neopentyl chloride

Figure 7. Comparisons of cyclicvoltammetric behavior in 0.515 melt with extended cathodic sweep. Voltage ranges: 2.65V to -2.3V; except (d) to -2.4V.

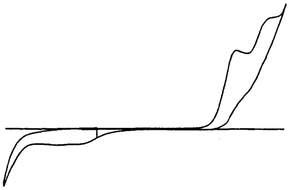

a. 3-Cl-pentane

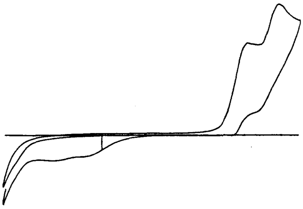

b. 1-Cl-pentane

d. neopentyl chloride

c. 2-Cl-2-me-butane

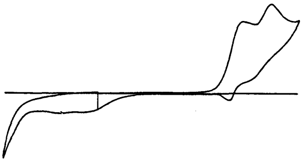

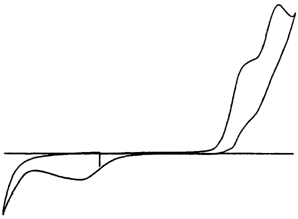

Figure 8. Comparisons of cyclicvoltammetric behavior in 0.55 melt. Voltage ranges: 2.6V to -0.75V.

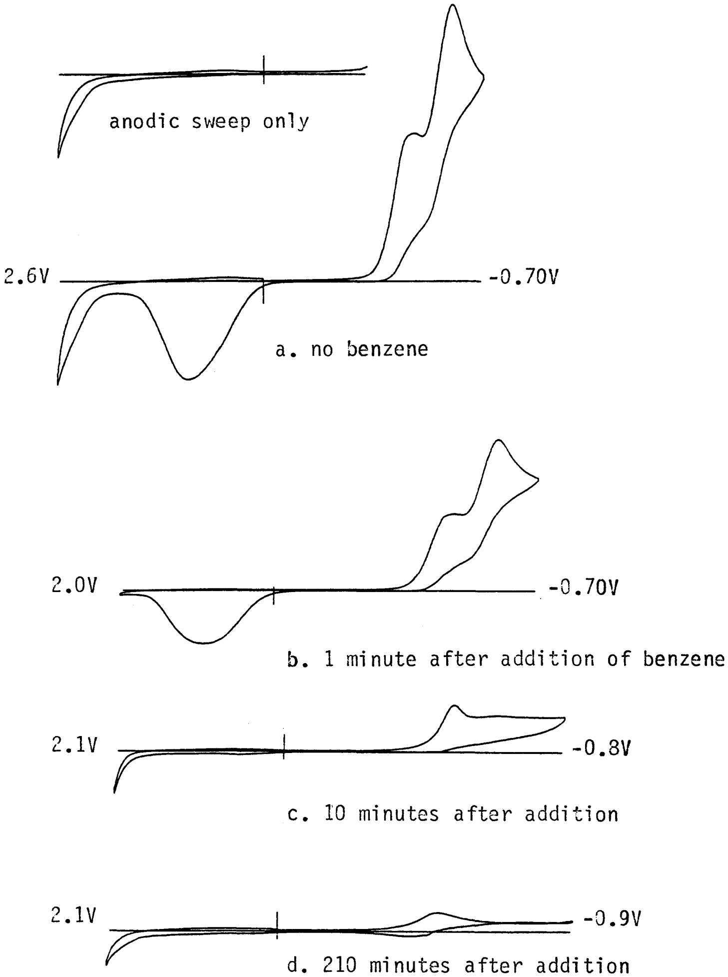

Figure 9. Time dependence of cyclicvoltammograms for reaction of benzene with 2-Cl-2-me-butane in 0.55 melt.

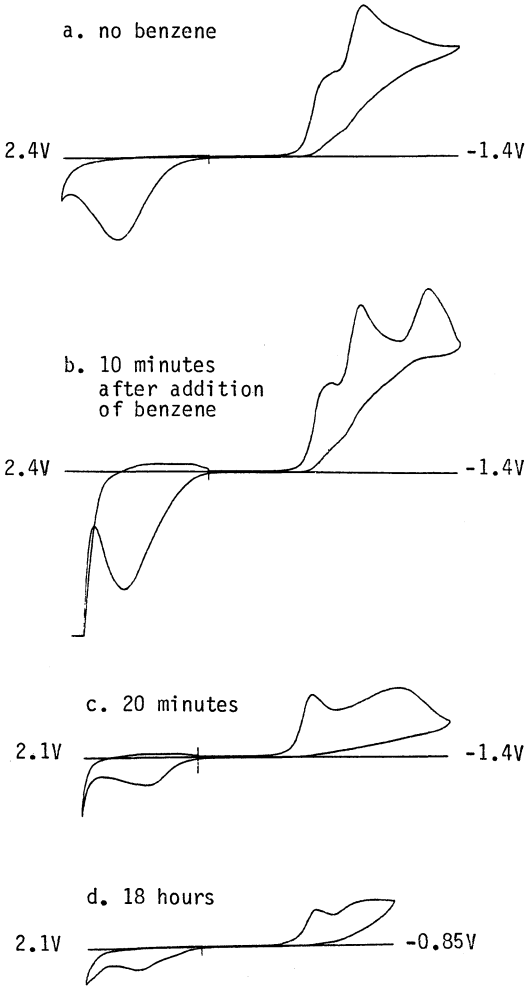

Figure 10. Time dependence of cyclicvoltammograms for reaction of benzene with 2-Cl-2-me-butane in 0.52 melt.

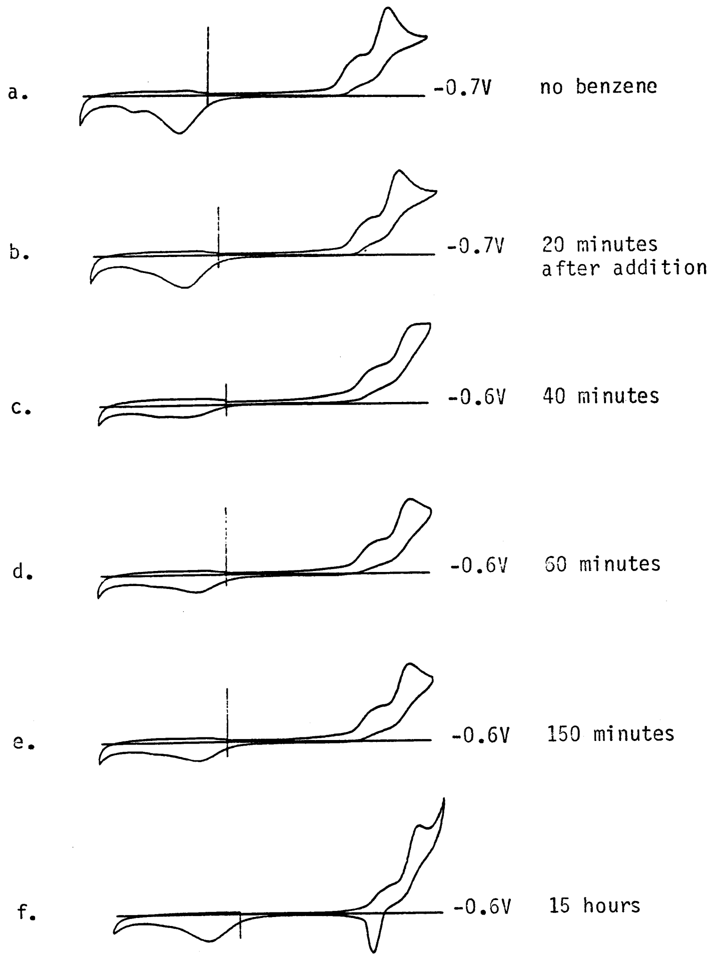

Figure 11. Time dependence for reaction of benzene with neopentyl chloride in 0.52 melt. Anodic limit: 2.0V.

DOI: 10.1149/199017.0822PV

CATALYTIC DIMERIZATION OF OLEFINS BY NICKEL COMPLEXES IN ORGANOCHLOROALUMINATE MOLTEN SALTS

Yves Chauvin,*[a] Bernard Gilbert[b] and Isabelle Guibard[a]

[a]Institut Français du Pétrole, BP 311, 92506 Rueil-Malmaison, France
[b]Laboratoire de Chimie Analytique, Université de Liège, 4000 Liège, Belgium

ABSTRACT

Organochloroaluminate molten salts based on aluminum trichloride or aluminum ethyl dichloride and 1-methyl 3-butylimidazolium chloride, 1-butylpyridinium chloride or tetrabutylphosphonium chloride can be used as solvents for the catalytic dimerization of propylene to isohexenes by nickel complexes; the structure of the new molten salts has been determined by Raman and ^1H *n.m.r. spectroscopies.*

INTRODUCTION

Molten salts have already been used in organic synthesis either as solvents or acidic catalysts (1,2). However it seems that no attempt has been made to take advantage of the solubility of an organometallic catalyst and of the insolubility of the reaction products of the catalytic reaction in these solvents. That is what we have tried to do by dissolving, in organochloroaluminates (3), nickel complexes already known to catalyze the dimerization of olefins when used in aromatic or chlorinated hydrocarbons (4). From this point of view chloroaluminate molten salts are all the more interesting in that it is possible to make their Lewis acidity vary within a wide range, while still remaining liquid below ambient temperature. If the mole fraction of AlX_3 in the melt is higher than 0.5, the medium is acidic; if lower, the medium is basic. Complexes such as η^3-allylnickel bromide are soluble (and stable) in, e.g., 1-methyl 3-butylimidazolium chloride (MBIC)/$AlCl_3$, whereas olefins are not.

Figure 1 illustrates the mechanism generally assumed for e.g. the dimerization of propylene by nickel complexes. The formation of dimers results from a series of insertions into the Ni-H and Ni-C bonds, thus affording various structures: n-hexenes, methyl pentenes, dimethylbutenes. The presence of basic trialkylphosphines can modify the repartition of dimers by increasing the dimethylbutene content.

EXPERIMENTAL PART

All experiments were performed under nitrogen or argon atmosphere by standard Schlenk techniques or in drybox. MIBC/$AlCl_3$ molten salt was prepared as described previously (5). *$AlEtCl_2$ based molten salts:* the calculated volume of freshly distilled $AlEtCl_2$ was transfered to the solid quaternary salt at room temperature.

Dimerization of propylene. In a typical experiment $NiCl_2$. $2PiPr_3$ (0.009g; 0.02 mmol) was placed in a 60 ml double-walled glass reactor with a magnetic bar. The reactor was purged from air and moisture, connected to a propylene supply and cooled at -15°C. Then 3ml heptane and 2 ml 0.7 M $AlEtCl_2$/MBIC molten salt were successively added and stirred. When the reactor was nearly full of liquid, the hydrocarbon phase was decanted and withdrawn by syringe through a septum without releasing the pressure. The product was weighted and analyzed by conventional VPC techniques. The yellow molten salt, containing the catalyst, can be used several times.

RESULTS

Selected results obtained for the oligomerization of propylene are given in Table 1. As commonly observed in two-phase systems, the reaction rate (hence the yield) strongly depends on the stirring efficiency, so the figures herein in no way represent a chemical limitation. In the absence of any nickel complex acidic melts catalyze the formation of oligomers, the molecular weight of which is characteristic of a cationic reaction (entry 1). This can be probably ascribed to the presence of traces of protons. In 0.45 M melts, η^3- methallyl nickel bromide is not active (entry 3), whereas in the 0.60 M melt, nickel complexes catalyse the formation of dimers and trimers in mixture with cationic oligomers (entry 2).

To overcome the drawback of cationic side reactions, we have developed new salts based on aluminum ethyl dichloride ($AlEtCl_2$ was already known as a proton scavenger in organochloroaluminates (6)) and conventional quaternary salts such as pyridinium and imidazolium chloride. These mixtures proved to be liquid at low temperature. Their eutectic points are lower than these of the corresponding $AlCl_3$ based melts, permitting to obtain liquid compositions for several other quaternary salts, e.g. tetrabutylphosphonium chloride. Not only cationic side reactions were suppressed (entry 4), but catalytic activity could also be extended to nickel complexes not containing a metal-carbon bond, such as $Ni(acac)_2$ (entry 5) or $NiCl_2.2PiPr_3$ (entries 6,7,8,9,). In these latter experiments the 2,3-dimethylbutene content in the dimer fraction is high, thus demonstrating the effectiveness of the "phosphine effect" (4) in molten salts (there is no displacement of trialkylphosphine bonded to nickel by any anionic species present in the medium).

Although we were, up to now, unable to characterize the active species during the reaction, it is likely to be cationic nickel complexes as in chlorinated solvents (4).

The structure of $AlEtCl_2$ based molten salts was elucidated by Raman spectroscopy. Raman spectra of the pure compounds, MBIC and $AlEtCl_2$ are given Figure 2. No strong vibration appears in the frequencies range 100-800 cm^{-1}.Thus,the strong band at 367 cm^{-1} observed in basic and neutral melts (Figure 3.) can be assigned to an aluminum ionic species. When the acidity of the melt increases ($N>0.5$) the intensity of the 367 cm^{-1} band decreases with parallel appearance of two new strong bands at 349 and 420 cm^{-1} (Figure 4.), the intensity ratio of which is nearly constant ($I_{349}/I_{421} = 1.20$) (Table 2.), thus proving that these two bands are characteristic of a single species. These band positions may be compared to the assignements which have been made for $AlCl_4^-$ (351 cm^{-1}) and for $Al_2Cl_7^-$ (315 and 434 cm^{-1}) in $AlCl_3$ based molten salts (7). Assuming that the mole fractions of the ionic species are proportional, approximately, to the intensity of the strongest bands for each species we have compared the intensity ratio for the peaks at 349 and 367 cm^{-1} for different compositions with the ratio of the concentrations of the species calculated by supposing the existence of the quantitative reaction:

$$AlEtCl_3^- + AlEtCl_2 \longrightarrow Al_2Et_2Cl_5^-$$

The straight-line confirms this assumption (Figure 5)
Table 3 summarizes the Raman vibrational frequencies (cm^{-1}) of $AlEtCl_3^-$ and $Al_2Et_2Cl_5^-$. In Figure 6 are given spectra obtained for a very acidic melt (0.7 N) before and after removal of contributions of other species. Three characteristic bands at 272, 337 and 404 cm^{-1} may be assigned to a third species that we tentatively formulate as $Al_3Et_3Cl_7^-$ and which compares with $Al_3Cl_{10}^-$ (8).

Up to now, there has not been any accurate method for the determination of the charge on the metal atom in chloroaluminate molten salts. Due to the presence of an aluminum-carbon bond in MBIC/$AlMeCl_2$ we were able to determine the ^1H n.m.r. shift of the Al-Me protons. The downfield shift is all the greater as the molar fraction of aluminum is high (less negatively charged): 0.45 M (-0.240); 0.55 M (-0.145); 0.65 M (+0.034). The use of ethyl aluminum dichloride based melt would allow to calculate the electronegativity of the aluminum atom by the Dailey-Shoolery equation:

$$\chi = 0.62\ \Delta + 2.07$$

This relationship between the electronegativity of a central metal atom of a compound CH_3-CH_2M and its internal chemical shift $\Delta_{CH_2-CH_3}$, a difference in proton chemical shifts of CH_2 and CH_3, has been previously applied to ethylaluminum halides and their complexes (9,10). This opens up a way to the quantitative determination of the charge on the aluminum atom in such liquids.

CONCLUSION

Chloroaluminate molten salts seem to be useful solvents for coordination catalysts, mainly for the dimerization of olefins. With such a solvent the separation between the reaction products and the catalyst becomes easy.

The new molten salts containing $AlEtCl_2$ prove to be all the more interesting as:

- they are liquid within a wide range of composition and temperature;
- they can remove protons impureties and thus suppress the cationic side reactions;
- they allow to use nickel complexes not containing metal carbon-bonds.

From a fundamental point of view, the main feature of these new molten salts is the possible determination of the charge of the aluminum atom by ^1H NMR.

REFERENCES

1. R.M.Pagni, in Advances in Molten Salt Chemistry, G.Mamantov, C.B. Mamantov, and J.Braunstein, eds., Elsevier, 1987.

2. J.K.Knifton, in Aspect of Homogeneous Catalysis, R.Ugo, ed.,D.Reidel Publishing Company, 1988.

3. R.A.Osteryoung, in Molten Salt Chemistry, G.Mamantov and R.Marassi, eds., D.Reidel Publishing Company, 1987.

4. P.W.Jolly and G.Wilke, in The Organic Chemistry of Nickel, F.G.A.Stone and

R.West, eds., Academic Press, 1975.

5. J.S. Wilkes, J.A.Levisky, R.A.Wilson, and C.L. Hussey, Inorg.Chem., 21, 1263 (1982).

6. T.A.Zawodzinski,R.T.Carlin, and R.A.Osteryoung, Anal.Chem. , 59, 2639 (1987).

7. R.J. Gale, B.Gilbert, and R.A. Osteryoung, Inorg.Chem. , 17, 2728 (1978).

8. B.Gilbert, unpublished results.

9. B.P.Dailey, and J.N.Shoolery, J.Am.Chem.Soc., 77, 3977 (1955).

10. T.Takeshita, and W.E.Frankle, Tetrahedron Letters, 56, 5913 (1968)

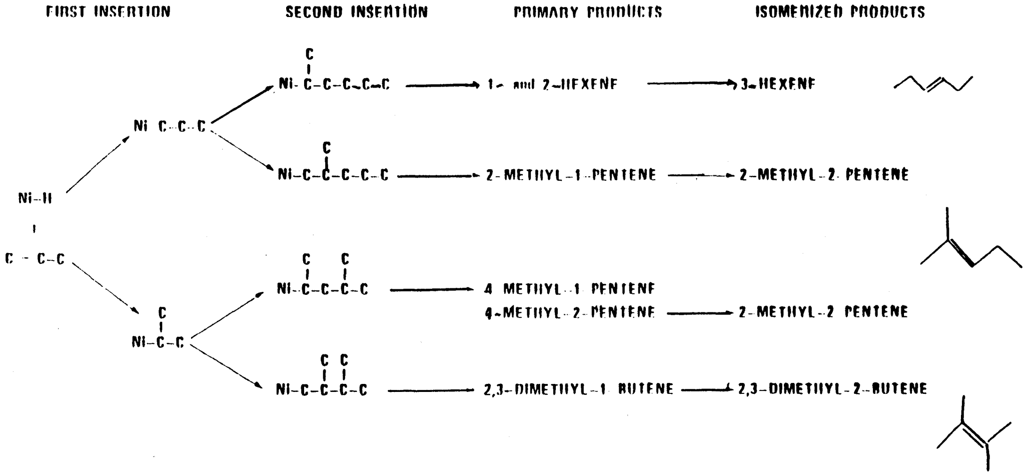

Figure 1. Mechanism of the Dimerization of Propylene by Nickel Complexes.

Entry	Molten salts		Ni complexes		Temp.	Pressure	Dimers			
	Composition	Al molar fraction	Type	mol dm^{-3} x10	^{0}C	MPa	yield g/g Ni	Composition % DMB	M2P	nH[b]
1	AlCl$_3$/MBIC	0.60	none		-15	atm.	0[d]			
2	AlCl$_3$/MBIC	0.60	$\prec$NiBr/$_2$	6.7	-15	atm.	1500	1	67	32
3	AlCl$_3$/MBIC	0.45	$\prec$NiBr/$_2$	4.2	-15	atm	0			
4	AlEtCl$_2$/MBCI	0.70	$\prec$NiBr/$_2$	3.4	-15	atm	6600	6	76	18
5	AlEtCl$_2$/MBIC	0.70	Ni(acac)$_2$	6.1	-15	atm.	1400	16	46	38
6	AlEtCl$_2$/MBIC	0.70	NiCl$_2$.2P(iPr)$_3$	1.2	-15	atm.	3300	76	21	3
7	AlEtCl$_2$/BPC	0.70	NiCl$_2$.2P(iPr)$_3$	1.0	0	atm	5300	69	28	3
8	AlEtCl$_2$/MBIC	0.70	NiCl$_2$.2P(iPr)$_3$	0.7	-10	0.2	4900	40	48	12
9	AlEtCl$_2$/TBPC	0.65	NiCl$_2$.2P(iPr)$_3$	8.2	50	0.5	900	44	48	8

[a] Preparation of molten salts: to a suspension of quaternary chloride in heptane maintained below 0^{0}C was added the calculated amount of aluminum coumpound; the upper phase was then eliminated. Propylene dimerization: in a well dried double-walled reactor were added: the nickel derivative, 3ml heptane, 2ml molten salt; a propylene pressure was kept constant with good stirring for two h.

[b] DMB: 2,3-dimethylbutenes; M2P: 2-methylpentenes; nH: n-hexenes.

[c] MBIC: 1-methyl 3-butylimidazolium chloride.

[d] 6.55 g of viscous oligomers were obtained.

[e] BPC: 1-butylpyridinium chloride.

[f] TBPC: tetrabutylphosphonium chloride.

Table 1. Dimerization[a] of Propylene by Nickel Complexes in Molten Salts

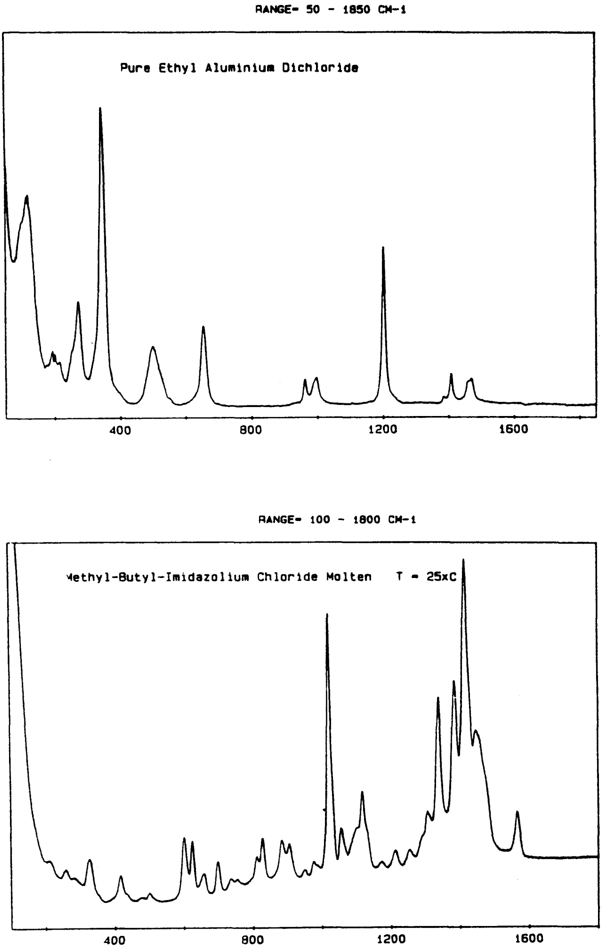

Figure 2. Raman Spectra of Pure Compounds:
-upper: Ethyl Aluminum Dichloride
-lower: 1-Methyl 3-Butyl Imidazolium Chloride Molten

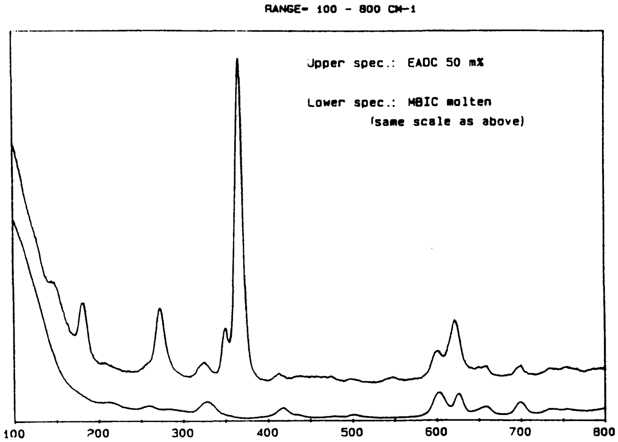

Figure 3. Raman Spectra: - upper: AlEtCl$_2$-MBIC 0.50 N
- lower: MBIC Molten

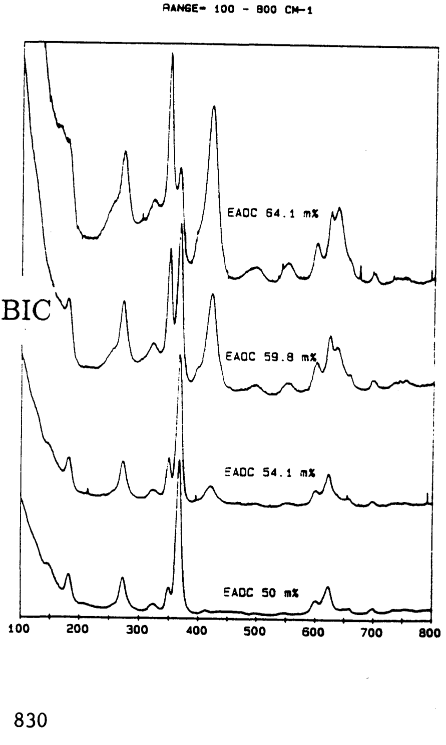

Figure 4.

Raman Spectra of AlEtCl$_2$-MBIC
Composition:a)0.50 N
b)0.54 N
c)0.60 N
d)0.64 N

N	I_{349}	I_{421}	I_{349}/I_{421}
0.541	184	150	1.23
0.556	226	181	1.25
0.574	587	490	1.20
0.598	854	709	1.20
0.625	1057	919	1.15
0.641	1535	1246	1.23

Table 2. Intensity Ratio of the Vibrations at 349 and 421 cm^{-1}

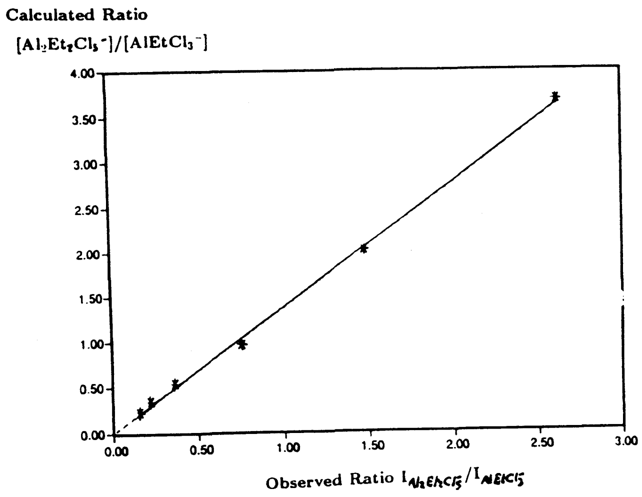

Figure 5. Variation of the Intensities Ratio of Vibrations of $AlEtCl_3^-$ (367 cm^{-1}) and of $Al_2Et_2Cl_5^-$ (349 cm^{-1})

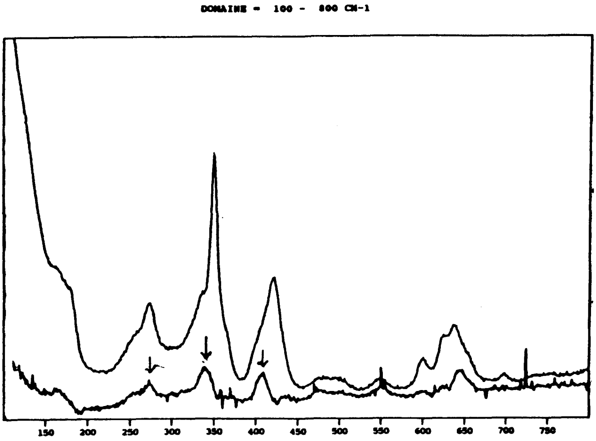

Figure 6. Raman Spectra: - upper $AlEtCl_2$-MBIC 0.70 N
- lower $AlEtCl_2$-MBIC 0.70 N
after removal of contributions of $Al_2Et_2Cl_5^-$

$AlEtCl_3^-$	$Al_2Et_2Cl_5^-$		
150 (m, dp)	166 (m, dp)	349 (s, p)	621 (m, p)
182 (m, dp)	178 (m, dp)	398 (m, p)	635 (m,dp)
273 (m, dp)	253 (m, p)	420 (st,p)	696 (w,dp)
349 (sh, p)	271 (m, p)	494 (s, p)	
367 (st, p)	305 (br, p)	550 (s, p)	
450 (w, dp)	321 (m, p)	600 (m,dp)	
621 (m, p)			

st = strong, br = broad, m = medium, sh = shoulder, s = small, w = weak

dp = depolarized, p = polarized

Table 3. Raman Frequencies (cm^{-1}) of $AlEtCl_3^-$
and of $Al_2Et_2Cl_5^-$

DOI: 10.1149/199017.0833PV

CHLORINATION OF CaO IN $CaCl_2$ BASED MELTS

Ram A. Sharma and Randall N. Seefurth

General Motors Research Laboratories
Physical Chemistry Department
Warren, Michigan 48090

ABSTRACT

The CaO in synthetic mixtures of $CaCl_2$ and KCl was successfully converted into chloride by chlorination at temperatures between 750 and 850°C. The chlorinations were carried out with chlorine, or mixtures of chlorine and argon containing up to 50 volume percent (v/o) argon, at flow rates ranging between 100 and 350 milliliters per minute (ml/min). Conversion rates of 0.23, 0.57 and 0.80 g CaO/min were successfully obtained. The stoichiometric amount of chlorine was sufficient to reduce the CaO content of the salt to ~1 weight percent (w/o) at 800°C.

INTRODUCTION

New processes for the production of the Actinide and Rare Earth metals are being developed (1-11). In these processes, metal oxide, fluoride or chloride is reduced by calcium in the presence of a salt medium such as molten calcium chloride. The metal produced is then trapped in a molten alloy pool consisting of the metal and another suitable metal such as zinc. General Motors has also developed such a process for the production of neodymium metal (6-11). In this process, fine Nd_2O_3 particles are suspended in a $CaCl_2$-based salt media by mechanical stirring at temperatures between 725 and 850°C. The suspended Nd_2O_3 reacts with $CaCl_2$ to form CaO and NdOCl which in turn is reduced by calcium to produce fine neodymium powder and additional CaO. The calcium reductant can either be added directly, or generated in situ by the reaction of less costly sodium with $CaCl_2$. The neodymium is extracted from the salt phase by dissolving it in a Nd-Zn or Nd-Fe pool at the bottom of the reactor.

The flow diagram for the neodymium production process is given in Figure 1. As shown in this diagram, the salt is presently being discarded, but may be regenerated for recycling. The amount of salt discarded is approximately four times the weight of neodymium theoretically produced.

In all the above processes, regeneration of the spent salt can further reduce the metal production cost and high temperature chlorination of the CaO by-product appears to be a promising method. Therefore, feasibility studies on this high-temperature chlorination process to regenerate the spent salt were conducted and the results of preliminary tests are communicated in this report.

THEORETICAL CONSIDERATIONS

Chlorination of CaO in the spent salt is proposed to be carried out by the following reaction

$$CaO + Cl_2 \rightarrow CaCl_2 + \frac{1}{2} O_2 \quad (1)$$

The standard free energy change of this reaction, ΔG°, as shown in Figure 2, is negative at all temperatures of interest indicating it should proceed spontaneously in the forward direction. In addition, the magnitudes of this negative standard free energy change (-26.5 kcal at 1000 K) should be sufficient to overcome the effect of lower CaO activity in the final stages of chlorination.

The standard free energy change of the reaction

$$MgO + Cl_2 \rightarrow MgCl_2 + \frac{1}{2} O_2 \quad (2)$$

is positive at chlorination temperatures (Figure 2). In addition, MgO does not form any solid solution or compound with CaO and is practically insoluble in the salt phase. Likewise, the standard free energy change of the reaction

$$\frac{1}{3} Al_2O_3 + Cl_2 \rightarrow \frac{2}{3} AlCl_3 + \frac{1}{2} O_2 \quad (3)$$

is positive at the temperatures of interest (Figure 2), and Al_2O_3 is also practically insoluble in the salt. Therefore, containers of either MgO or Al_2O_3 (if CaO does not appreciably react with Al_2O_3) can be used for the chlorination process.

EXPERIMENTAL

Materials

Potassium chloride of 99.7% purity, anhydrous calcium chloride of 99.9+% purity and calcium oxide of 98% purity were used to make the synthetic spent salt mixtures. Prior to use, the chlorides were oven baked for 2 h at 500°C and the oxide for 2 h at 1000°C to remove moisture and other volatiles.

High purity chlorine (99.9%) and argon (99.999%) were used for the chlorination reactions and to purge the reactor, respectively.

Apparatus

The synthetic salt mixtures were prepared inside a helium-atmosphere drybox furnace well (9). The chlorination reactions were carried out in alumina crucibles (5.5 cm OD by 18 cm deep by 0.3 cm wall thickness) inside closed quartz containers (7 cm OD by 65 cm deep by 0.2 cm wall thickness) fitted with gas and outlet ports (Figure 3). A tubular clam-shell heating element furnace (7.5 cm ID by 46 cm long) regulated by means of a programmable temperature controller was used to heat the test reactor. The temperature was monitored by a calibrated thermocouple positioned adjacent to the furnace wall at mid-melt level. Alumina sparge tubes (0.6 cm OD by 76 cm long by 0.15 cm wall thickness) were used to bubble the gases through the salt mixtures, while a mass flow controller and a dual tube mixing rotameter were used to regulate the chlorine and argon flow rates, respectively.

Procedures

The preweighed chloride salt mixture was melted at 850°C in an alumina crucible. The calcium oxide was slowly stirred into the molten salt, and then the mixture was slowly cooled (<3°/min) overnight.

The alumina crucible was positioned inside the closed quartz container. Quartz felt thermal insulation was wrapped around the crucible to protect the quartz from splashing of the salts. The alumina sparge tube was positioned above the solid salt surface and sealed into the inlet port with a rubber stopper. This assembly was positioned in the furnace and hooked up to the facilities gas lines. The unit was purged with argon (~50 ml/m) as it was slowly heated (~3°C/min) to the reaction temperature.

Upon reaching thermal equilibrium, the sparge tube was lowered to within 1 cm of the crucible bottom. The chlorine was turned on at the required flow rate and allowed to pass through the melt for a predetermined time interval. At the completion of the chlorination reaction, the melt was purged with argon at 200 ml/m for ~15 min, the sparge tube was lifted out of the melt and the reactor was slowly cooled (~2.5°C/min) under a reduced argon purge rate (~25 ml/min) overnight.

The reactor was disassembled and the alumina crucible was transferred into a drybox where a 1 cm diameter core sample (~20 g) was taken for chemical analysis. The remaining salt was dissolved in ~3.5 liters of deionized water and the residual solids were filtered out, calcined weighed and reported as gravimetric CaO. In all cases, the alumina crucibles were not noticeably attacked by CaO during these experiments.

RESULTS AND DISCUSSION

The results of initial chlorination experiments are given in Table I. Synthetic salt mixtures consisting of 270 g of $CaCl_2$, 30 g of KCl and 50 g of CaO (14.3 w/o CaO) were used in these experiments. The effects of chlorine flow rate, temperature, excess chlorine (over the stoichiometric amount) and dilution of chlorine were studied. As can be seen from the first five experiments in Table I, the results appear to be fairly reproducible.

Effect of Chlorine Flow Rate

As shown in Table I, the CaO content of the synthetic salts was reduced to ~1 w/o at 800°C using the stoichiometric amount of chlorine at flow rates ranging between 100 and 350 ml/min. On the average, the amount of CaO remaining in the salt was ~4 g, which agrees with the solubility of CaO in $CaCl_2$ at 800°C (13). Apparently the soluble CaO was not easily chlorinated under these experimental conditions. However, the suspended particles of CaO were converted into $CaCl_2$ at conversion rates of 0.23, 0.57 and 0.80 g/min. As shown in Figure 4, the rate of CaO conversion is proportional to the chlorine flow rate. This means the rate of chlorination, within the flow rates studied, is controlled by the availability of chlorine gas.

Effect of Temperature

Chlorination with the stoichiometric amount of chlorine at a flow rate of 100 ml/min reduced the gravimetric CaO content of the synthetic salt mixtures to 0.57, 0.98 and 1.09 w/o as indicated by the gravimetric analysis at 750, 800 and 850°C, respectively. At the corresponding temperatures, the amount of residual CaO remaining in the salt increased from 2.29 to 3.89 to 4.13 g. Since the solubility of CaO in $CaCl_2$ also increases with temperature, it appears that the soluble CaO is comparatively more difficult to chlorinate than the CaO particles suspended in the salt.

Effect of Excess Chlorine

The effect of the amount of chlorine on CaO conversion was studied at 800°C at a chlorine flow rate of 100 ml/min. The CaO in the salt as indicated by gravimetric analysis decreased from 0.98 to 0.58 w/o when the amount of chlorine was increased from the stoichiometric amount to 10% excess, while the CaO was 1.23 and 1.98 w/o when the amount of chlorine was 10 and 20% less than stoichiometric, respectively. This trend is as expected, however, the average rate of CaO conversion increased slightly with a decrease in the amount of chlorine from the stoichiometric amount (Figure 5). This indicates when the amount of chlorine supplied is less than the stoichiometric amount, it is more efficient in converting CaO into chloride.

Effect of Diluting Chlorine

The effect of diluting chlorine with argon on CaO conversion was studied at 800°C using the stoichiometric amount of chlorine at a total flow rate of 250 ml/min. The CaO content of the salts was reduced from 14.3 to ~1 w/o (Table I), while the rate of CaO conversion was found proportional to the volume percent of chlorine in the gas phase (Figure 6). This again indicates the rate of CaO conversion is controlled by the availability of chlorine in the gas phase.

Further Interpretation of Results

The chlorination reaction can be basically represented as

$$O^{=} + Cl_2 \rightarrow 2Cl^{-} + \frac{1}{2} O_2 \qquad (4)$$

However, in the chlorination process, three phases exist; gaseous chlorine with oxygen, solid CaO (during most of the process), and a liquid solution of CaO in the $CaCl_2$ based salt. As the chlorine gas is bubbled through the melt, reaction (4) most likely takes place at the interface between the gas bubble and the melt. Oxide ions react with chlorine at this interface; the chloride ions formed pass into the melt, while the oxygen formed passes into the bubble. Due to high interfacial surface energy and agitation provided by gas bubbling, CaO particles will probably collect at the gas bubble-melt interface. In this way, the melt at the interface will be saturated with oxide ions and they will be available to react with chlorine until all the solid CaO particles are consumed. On the other hand, after a certain period, the oxide ions dissolved in the melt will have to migrate to the bubble surface to react with chlorine. The rate of oxide ion migration may be slow and could be the reason that it is comparatively more difficult to chlorinate the CaO in solution than CaO particles in suspension. To facilitate the chlorination of the dissolved CaO, it may be necessary to agitate the melt.

Since the melt at the bubble interface remains saturated with oxide ions when CaO particles are present, it may then be concluded that the rate of chlorination is not limited by the transport of oxide ions. In other words, the rate of reaction is controlled by the rate at which chlorine is available. Under such conditions, the amount of chlorine passed can be totally consumed due to sufficient residence time (determined by the chlorine flow rate and melt height) in the molten salt. Therefore, with proper design of experiments, all the chlorine can be used to convert CaO to $CaCl_2$, and chlorine corrosion problems can be avoided. This will require a reactor having the proper aspect ratio and chlorine flow patterns. However, oxygen corrosion problems must still be faced.

ACKNOWLEDGMENTS

The authors wish to acknowledge the assistance of Bud Verrier in carrying out the experiments, Noel Potter and his associates in the Analytical Chemistry Department for analyses of the salt samples, and Drs. Kathleen C. Taylor and John S. Dunning for helpful suggestions in preparing this manuscript.

REFERENCES

1. J. B. Knighton, I. Johnson, and R. K. Steunenberg, "Uranium Purification by the Process of Salt Transport," Argonne National Laboratory, Chemical Engineering Division Report, ANL-7524, March 1969.

2. R. C. Vogel, et al., "Chemical Engineering Division Research Highlights," Argonne National Laboratory, Chemical Engineering Division Report, ANL-7850, January-December 1971.

3. M. S. Coops, J. B. Knighton and L. J. Mullins, Pyrochemical Processing of Plutinium in ACS Symposium Series No. 216, Plutonium Chemistry, eds. W. T. Carnall and G. R. Choppin, pp. 381-408, 1983.

4. G. S. Perry and L. G. MacDonald, "Role of $CaCl_2$ in the Reduction of PuO_2," J. Nucl. Mat., 130, 234-241 (1985).

5. D. C. Christensen, et al., "Plutonium Metal Preparation and Purification at Los Alamos-1984," Los Alamos National Laboratory, Los Alamos, New Mexico.

6. R. A. Sharma, "Processes for Neodymium Production," Journal of Metals, 39, 33 (1987).

7. R. A. Sharma, "Metallothermic Reduction of Rare Earth Oxides," U.S. Patent No. 4,578,242, March 25, 1986.

8. R. A. Sharma, "Metallothermic Reduction of Rare Earth Chlorides," U.S. Patent No. 4,680,055, July 14, 1987.

9. R. A. Sharma and R. N. Seefurth, "Metallothermic Reduction of Nd_2O_3 with Ca in $CaCl_2$-NaCl Melts," J. Electrochem. Soc., 135-1, 66 (1988).

10. R. A. Sharma and R. N. Seefurth, "A Molten Salt Process for Producing Neodymium Metal," Light Metals 1988, L. G. Boxall, editor, The Metallurgical Society, Inc., Warrendale, PA (1987).

11. R. A. Sharma and R. N. Seefurth, "A Molten Salt Process for Producing Neodymium-Iron Alloys," Rare Earths, Extraction, Preparation and Applications, Edited by R. G. Boutista and M. M. Wong, The Minerals, Metals & Materials Society (1988).

12. JANAF Thermochemical Tables, 2nd Edition, NSRDS-NBS, June 1971-1978.

13. D. A. Wenz, I. Johnson and R. O. Wolson, Journal of Chemical and Engineering Data, 14-2, 250 (1969).

TABLE I

Results of Preliminary Chlorination Tests

	Reaction Parameters							Chlorinated Salts*			
		Gas Flow Rates									
Exp't	Temp (°C)	Total (ml/m)	Ar (ml/m)	Cl_2 (ml/m)	Total Time (min)	Cl_2 Vol. (l)	Excess Cl_2 (%)	Core-S CaO (w/o)	Grav. CaO (w/o)	Residual CaO (g)	CaO Conversion Rate (g/min)
Experimental Reproducibility and Effect of Chlorine Flow Rate											
1	800	100	-	100	200	20.0	0	1.09	0.99	3.93	0.23
2	800	100	-	100	201	20.1	<1	1.10	0.98	3.89	0.23
3	800	250	-	250	80	20.0	0	0.61	1.23	4.72	0.57
4	800	350	-	350	57	20.0	0	0.82	1.21	4.68	0.80
5	800	350	-	350	57	20.0	0	1.29	1.11	4.43	0.80
Effect of Temperature											
2	800	100	-	100	201	20.1	<1	1.10	0.98	3.89	0.23
6	750	100	-	100	200	20.0	0	0.70	0.57	2.29	0.24
7	850	100	-	100	200	20.0	0	0.19	1.09	4.13	0.23
Effect of Excess Chlorine											
2	800	100	-	100	201	20.1	<1	1.10	0.98	3.89	0.23
8	800	100	-	100	220	22.0	10	0.44	0.58	2.28	0.22
9	800	100	-	100	180	18.0	(-10)	1.22	1.23	4.83	0.25
10	800	100	-	100	160	16.0	(-20)	2.25	1.98	7.80	0.26
Effect of Diluting Chlorine											
3	800	250	-	250	80	20.0	0	0.61	1.23	4.72	0.57
11	800	250	125	125	160	20.0	0	0.56	1.03	3.96	0.29
12	800	250	50	200	100	20.0	0	0.30	1.13	4.30	0.46

* See appendix.

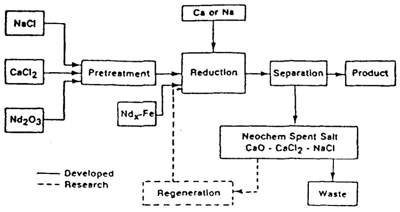

Fig. 1 Flow diagram of the Nd_2O_3 reduction process.

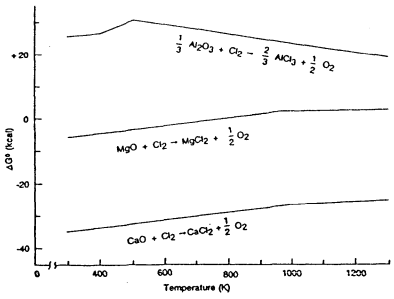

Fig. 2 Standard free energy change of reactions, ΔG°, versus temperature (12).

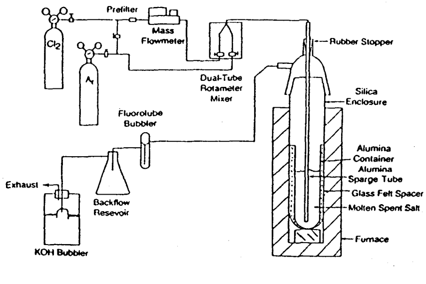

Fig. 3 Schematic diagram of the chlorination apparatus.

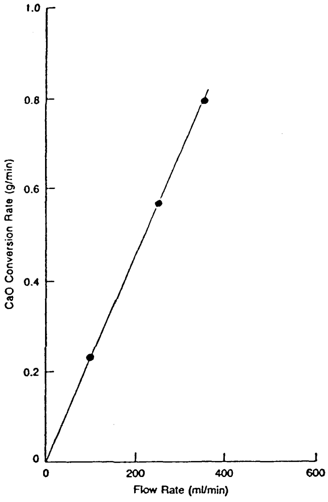

Fig. 4 Rate of CaO conversion versus chlorine flow rate.

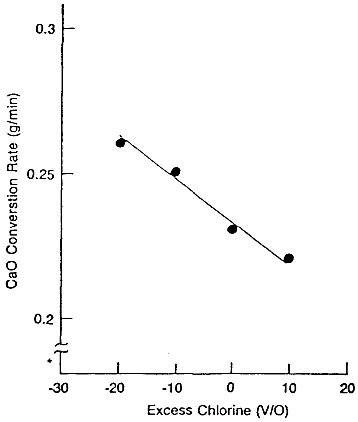

Fig. 5 Rate of CaO conversion versus chlorine in excess of stoichiometry.

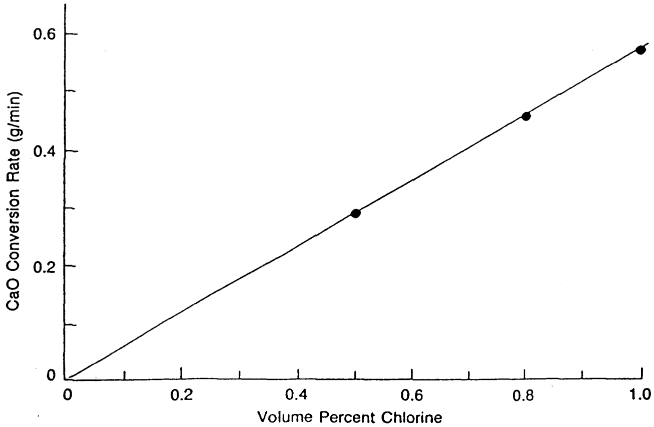

Fig. 6 Rate of CaO conversion versus volume percent chlorine in the gas phase.

APPENDIX

Determination of the CaO Content in the Chlorinated Salt

The synthetic salt mixtures contained 270 g of $CaCl_2$, 30 g of KCl and 50 g of CaO before chlorination.

After chlorination, a 20 g core sample of the salt was taken for chemical analysis of CaO. The results of these analyses on the core samples are reported in Table I as Core-S CaO (w/o).

The remainder of the chlorinated salt sample was dissolved in water and the precipitate calcined and weighed. The calcined precipitate is reported in Table I as Gravimetric CaO (w/o). These values were calculated as follows:

$$\text{Grav. CaO (w/o)} = \frac{100\,(x)}{300\text{ g} + \dfrac{(50\text{ g} - x)\,(110.99)}{56.08} - 20\text{ g} + x}$$

where x = the amount (g) of calcined CaO precipitate, and 20 g is the portion of the salt mixture used for chemical analysis.

The residual CaO reported in Table I is the sum of the CaO obtained from the gravimetric analysis (calcined precipitate) and the chemical analysis, or

$$\text{Residual CaO (g)} = x + \frac{20\text{ g (Core-S CaO)}}{100} \quad .$$

DOI: 10.1149/199017.0843PV

CHARACTERIZATION OF OXYGEN SYSTEMS IN MOLTEN BARIUM HYDROXIDE. APPLICATION TO OXIDATIVE CONVERSION OF METHANE

J. Devynck, M. Cassir, C. Moneuse and B. Trémillon

Laboratoire d' Electrochimie (URA 216 du CNRS)
Ecole Nationale Supérieure de Chimie de Paris
11 rue Pierre-et-Marie-Curie
F 75231 Paris Cedex 05 (France)

ABSTRACT

Molten barium hydroxide at 800°C is investigated for oxidative coupling of methane by oxygen to form ethane and ethylene.
The characterization of oxygen species by voltammetry in basic (BaO saturated) and acidic (under $P(H_2O) = 1$ atm.) media shows that peroxide ion, involved in the catalytic effect, is stable in the whole acidity range.
Catalytic activity of $Ba(OH)_2$ is tested by bubbling mixtures of CH_4 and oxygen in molten phase at various acidity levels. Methane conversion of 20% and C2 yield of 7% are obtained. Results are compared with those of solid oxide catalysts.

INTRODUCTION

The conversion of methane into more easily transportable fuels (ethane and ethylene) is a potentially important process [1]. The oxidative coupling of methane by molecular oxygen involves active species as peroxide ions in a diatomic (O_2^{2-}) [2].or a monoatomic form (O^-)[3] and peroxide ions O_2^- [3]. These species, characterized on solid catalysts at high temperatures (800°C to 900°C), can also be stabilized in homogeneous phases (molten salts) at the same temperature. The most common molten salts in which peroxide ion have been characterized are molten carbonates [5] and molten hydroxides [6].

The aim of this study was to describe the thermodynamic behaviour of oxygen species in molten $Ba(OH)_2$, comparing it to experimental data based on a voltammetric study at Pt and Ni electrodes and to test the catalytic properties for the methane oxidation by oxygen in this medium.

THERMOCHEMICAL DATA

Theoretical studies based on thermochemical data allow to predict the redox properties of oxygen species and their evolution with the acidity of the medium. Thermochemical data of the different species in molten barium hydroxide are given in the Kubashewski and Alcock tables [6], or in the case of $Ba(OH)_2$ in Janaf thermochemical tables [7].

The autodissociation equilibrium of molten barium hydroxide is :

$$Ba(OH)_2\ (l) \Leftrightarrow BaO(s) + H_2O\ (g)$$

(where (l), (s) and (g) refer to the liquid, solid and gas phases respectively). This equilibrium can be expressed in term of ionic species :

$$2\ OH^- \Leftrightarrow O^{2-} + H_2O$$

the expression of the autodissociation constant is :

$$K^* = a(O2^-)\ P(H_2O) = ([O^{2-}] / SBaO).P(H_2O)$$

where $a(O2-)$ is the activity of oxide ions, $P(H_2O)$ the water vapour pressure and $[O^{2-}]$ the concentration of oxide ions. This constant characterizes the limits of the acidity range which are fixed by the saturation of the molten salt by BaO (the most basic medium) and by a water vapour pressure of 1 atmosphere (the most acidic medium).
The oxidation of $Ba(OH)_2$ (oxygen in the oxide form) yield oxygen or peroxide (BaO_2) . The oxidation reactions are as follows :

$$2\ Ba(OH)_2\ - 4\ e^- \Leftrightarrow O_2 + 2H_2O + 2Ba^{2+}$$
$$2\ Ba\ (OH)_2\ - 2\ e^- \Leftrightarrow BaO_2 + 2H_2O + Ba^{2+}$$

the acidity range in which peroxide species are stabilized can be predicted from the variations of equilibrium potentials of both systems versus acidity, characterized by - log $P(H_2O)$. The oxidation potentials of these systems have been calculated for various water vapour pressure at different temperatures.

Figure 1 shows the evolution of these potentials under the following conditions $P(O_2) = 10^{-2}$ atm and $[BaO_2] = 10^{-1}S$ (where S is the solubility of BaO_2 in $mol.Kg^{-1}$). The broken lines part (a) and (b) fix the limit between hydroxide ion (lower domain) and its oxidized form (upper domain). The vertical line part (c) indicates the limit of the acidity range, fixed by the solubility of BaO. The corresponding acidity level (- log P (H_2O) is reported on the X axis. At temperatures lower than 550°C, the stable form of oxidized $Ba(OH)_2$ is oxygen in acidic media (low $p(H_2O)$ values). Oxygen is not stable in neutral and basic media and reacts with oxide ion to form peroxide ion.
When temperature increases BaO_2 is stabilized over the whole acidity range. The increase in the autodissociation constant with temperature ($pK^* = 0{,}19$ at 800°C) shows that the acidity shift between the most acidic and the most basic medium is rather small : molten $Ba(OH)_2$ appears to be quite buffered at this temperature.

These calculations allow to predict that the peroxide ion is stable in the molten salt and that its stability increases with basicity and temperature.

ELECTROCHEMICAL STUDY OF OXYGEN SYSTEMS

Electrochemical measurements were carried out with Tacussel Instruments PRGS and GSTP connected to a Sefram recorder. The cell was a compact alumina crucible with an alumina cap. The working electrodes were platinum and nickel wires sealed into an alumina jacket.. At 500°C, the reference electrode was a nickel wire dipped into molten $Ba(OH)_2$ saturated with NiO in a pyrex tube (its potential is attributed to O^{2-}/O_2^{2-} system ; O_2 in the molten salt, due to a permanent contact with atmosphere reacted with O^{2-} ions producing O_2^{2-}). At higher temperatures a platinum pseudo reference electrode was used ; potentials were adjusted in relation to the pyrex reference electrode.

Voltammetric studies showed that the extent of the electrochemical stability range of the molten salt was independent of the acidity level. Figure 2 shows that a rise of temperature provoked a decrease in the electrochemical stability range according to theoretical predictions and an increase of the oxidation current located at a potential close to OV/ref.

Voltammograms obtained at a Pt electrode under the conditions described in Figure 3 show a first oxidation wave at a potential of -0,2 V/ref due to the following oxidation reactions of Pt :

$$Pt + 2\,O^{2-} - 2\,e^- \Leftrightarrow Pt\,O_2^{2-}$$

$$\text{and } Pt + PtO_2^{2-} - 2\,e^- \Leftrightarrow 2\,PtO\downarrow$$

and a second wave at a potential of + 0,03 V/ref. probably due to the oxidation of O^{2-} into O_2^{2-}(in agreement with the results previously obtained in NaOH and NaOH-KOH [5])*.This oxidation step was not followed, as in molten NaOH, by a second oxidation step of peroxide ions into superoxide ions, which are thermodynamically unstable in this medium. Reduction waves overlap and are probably due to the reduction of PtO and PtO_2^{2-} and to the species formed when oxidizing O^{2-} and OH^-.

Voltammograms obtained at a Ni electrode (fig. 4) show a system due to the following redox reaction of Ni : $Ni + O^{2-} - 2\,e^- \Leftrightarrow NiO\downarrow$ (Ep anodic = -0,60 V/ref. and Ep cathodic = -0,95 V/ref) and an oxidation current due to $O^{2-} - 2\,e^- \Leftrightarrow O_2^{2-}$ at a potential of -0,01 V/ref ; confirming the results obtained at Pt electrode. The reduction current at a potential of -0,2 V/ref

---

* As it was mentioned, a rise in temperature provoked an increase in the diffusion current of O^{2-} ions due to a decrease in the viscosity of the molten salt.

corresponds to O_2^{2-} formed by the oxidation of O^{2-} and OH^-, or by the reaction of molecular oxygen with O^{2-}. This current can overlap with a reduction current due to molecular oxygen.

The calibration of the voltammetric wave corresponding to the oxidation of O^{2-} allowed to obtain the solubility of BaO: SBaO = 3.10^{-3} mol/kg.

CATALYTIC APPLICATION

Oxidative conversion of methane was performed by bubbling a mixture of methane and oxygen (with argon as diluent) in liquid barium hydroxide at 800°C. The reactor was a sintered alumina cell closed by a stainless steel cap equiped with an air-cooled Viton O-ring (the temperature of the cap did not exceed 150°C). Water produced by the reaction or introduced to fix the acidity level was collected in a cold trap (0°C) before the gases were introduced into a chromatograph equipped with TCD and F/D, coupled to a recorder integration used for product analysis. The column was a carbosphere (3 m, 80-100 Mesh).

The C_2 selectivity and the yield of methane conversion have been determined as a function of the acidity of the medium and temperature.
The results reported in table 1 show that the empty reactor exhibits a catalytic activity (assay 1) which is significantly increased by the presence of the molten phase (assays 2, 3, 4, 5 and 6).

Table 1 - General conditions : 90 g catalyst., initial pressures of 125.0 Torr CH_4, 41.5 Torr O_2, 593.5 Torr He, total flow rate of 128 ml/min, gas bubbling, dry gas. (a) $P(H_2O)$ = 17.5 Torr; (b) empty reactor; (§) present in gas outlet.
t (hours) is the reaction time (reactant gas in contact with the catalytic phase); h (hours) is the time spent from the beginning of the fusion of the melt; (h - t) is the time during which the melt is maintained under an inert gas (helium) at atmospheric pressure.

ASSAY	t	h	Selectivity %				conv.% O_2	Yield,% C_2	Conv.,% CH_4
			CO	CO_2	C_2H_4	C_2H_6			
1[a,b]	0	0	51.5	20.4 (§)	21.0	6.9	21.6	3.1	11.0
2[a,c]	1	1	8.0	64.2	20.8	6.9	73.2	4.6	16.8
3[a]	3	4.75	0	70.3	24.3	5.4	95.9	6.1	20.7
4[a]	3.75	23	0	66.9	26.8	6.2	97.3	7.2	21.7
5	5.75	25	0	65.2	30.1	4.6	95.9	7.5	21.7
6	9.50	95	0	61.8	29.9	8.2	73.2	6.6	17.3

In an acidic medium (under a water vapour pressure of 17,5 Torr, the methane conversion was about 21% and the C_2 selectively was 31% (assays 3 and 4). When the acidity level was shifted towards basic level by dehydration (and precipitation of BaO), the conversion was not changed but the selectivity increased up to 35% - 38%. Thus, despite a small acidity variation, a higher selectivity can be correlated with an increase in the stability of peroxide ions.

CONCLUSION

A catalytic effect on the oxidative coupling of methane is observed in molten barium hydroxide, at 800°C, as previously mentioned in other molten salts (8). Even though the selectivity (formation of ethane and ethylene) was not very high, the reproducibility of the results was good enough to establish that a significant increase in selectivity can be obtained by a shift in the acidity level from acidic media (under a fixed water vapour pressure) where the ethane + ethylene selectivity was about 31%, to a strongly basic medium (BaO saturated solution), where the corresponding value was about 38%. This effect can be correlated with the stabilization of the peroxide form of oxygen, in agreement with thermodynamic studies which have shown that peroxide is the stable form of reduced oxygen in basic medium. However, at 800°C, the narrow acidity range of $Ba(OH)_2$ (less than 0,2 pO^{2-} unit) limits the possible variation of acidity.

ACKNOWLEDGMENTS

This work was financially supported by Gaz de France (G.D.F.) and benefited from the advice of A. Ben Hadid.

REFERENCES

1. G.E. Keller and M.M. Bhasin, J. Catal., 43 (1982) 9.

2. K. Otsuka, S. Yokoyama, and A. Morikawa, Chem. Lett., (1985) 319 ; K. Otsuka, K. Jinno, and A. Morikawa, J. Catal., 100 (1986) 353 ; K. Otsuka, Q. Liu, M. Hatano, and A. Morikawa, Chem. Lett., 467 (1986) 903 ; K. Osuka, Q. Liu, M. Hatano, and A. Morikawa, Inorg. Chim. Acta, 118 (1986) L23 ; K. Otsuka and T. Komatsu, Chem. Lett., (1987) 483 ; J. Chem. Soc. Chem. Commun., (1987) 388; K. Otsuka and K. Jinno, Inorg. Chim. Acta, 121 (1986) 237 ; K. Otsuka, A.A.Said, K. Jinnoo and T. Komatsu, Chem. Lett. (1987) 77.

3. I. Ito and J.H. Lunsford, Nature, 314 (1985) 721 ; I. Ito, J.X. Wang, C.H. Lin and J.H. Lunsford, J. Am. Chem. Soc., 107 (1985) 5062 ; C.H. Lin, K.D. Campbell, J.X. Wang, and J.H. Lunsford. J. Phys. Chem., 90 (1986) 534.

4. A.J. Appleby and Nicholson, J. Electroanal. Chem., 38 (1972) App. 13 ; ibid, 53 (1974) 105 ; ibid, 83 (1977) 309 ; ibid, 112 (1980) 71.

5. B. Trémillon and R. Doisneau, J. Chim. Phys.,71 (1974) 1379 ; M. Cassir, C. Piolet, C. Moneuse and Jacques Devynck, Electrochim. Acta.,34, 11 (1989) 1563.

6).O. Kubashewski and C.B. Alcock, Metallurgical thermochemistry, Pergamon Press, Oxofrd (1979).

7. Janaf, Thermochemical tables (2nd edn), U.S. Dept of Commerce (1970)

8. H. Mazurek and B. Cynwyd US Pat. 4,678,862 (1986) ; H. Mimoun, S. Bonnaudet and A. Robine, B.F., 2 607 804 (1988) ; J.H. Lunsford and J. Szanyi, ACS Division of Colloid Chem., Preprints, n° 233, Los Angeles, 25-30 Sept, 1988 ; S.J. Conway, J. Szanyi and J.H. Lundsford, Appl. Catal., 56 (1989) 149.

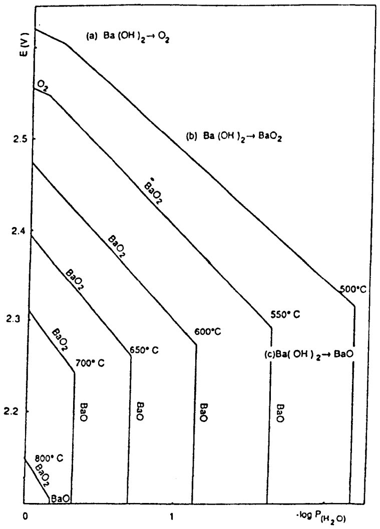

Figure 1 - Oxidizing properties of oxygen in molten barium hydroxide at various temperatures : evolution of the oxidation limit of the molten salt with acidity for $P(O_2) = 10^{-2}$ atm and $BaO_2 = 10^{-1}$ S (S : solubility, mol/kg). Redox potential of (a) : system O_2/O^{2-} ; (b) : system O_2^{2-}/O^{2-} ; (c) : precipitation of BaO.

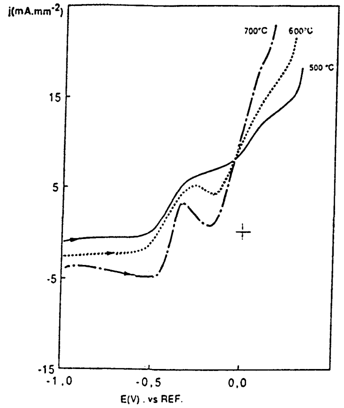

Figure 2 - Evolution of voltammograms of molten $Ba(OH)_2$ (under argon) with temperature, Pt electrode ; Pt pseudo ref. electrode ; V = 30 $mV.S^{-1}$.

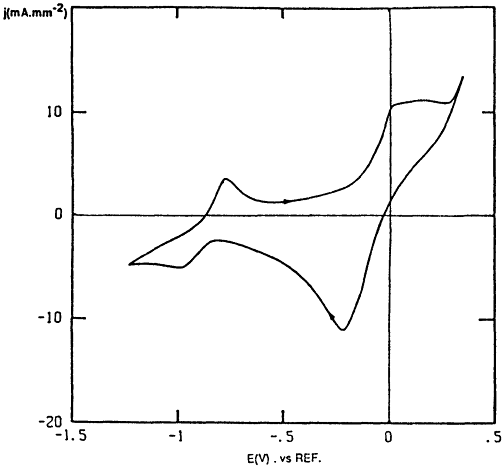

Figure 3 - Voltammogram of Ba(OH)2 at 500°C under argon Pt electrode, Ref. electrode Ni in Ba(OH)2 saturated with NiO ; V = 30 mV.S^{-1}.

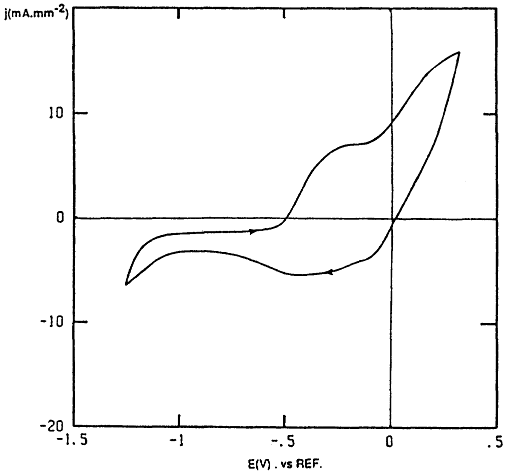

Figure 4 - Voltammogram of Ba(OH)2 at 500°C under argon Ni electrode, Ref. electrode Ni in Ba(OH)2 saturated with NiO ; V = 30 mV.S^{-1}.

DOI: 10.1149/199017.0851PV

EQUILIBRIUM CONSTANTS OF THE NITRATE/NITRITE/OXYGEN REACTION IN MOLTEN TERNARY NITRATE SALT MIXTURES

R. W. Bradshaw and D. E. Meeker
Sandia National Laboratories
Livermore, CA 94551-0969

ABSTRACT

We have evaluated the chemical equilibria of the decomposition reactions of ternary mixtures of molten nitrate salts consisting of sodium and potassium nitrate with additions of either calcium, barium or lithium nitrate. The equilibrium constant of the initial reaction, nitrate = nitrite + oxygen, was relatively insensitive to the composition of the mixtures. The extent to which subsequent decomposition reactions proceeded was dependent on the type and amount of the additions to the binary alkali nitrate mixture and was related to the charge and size of the added cationic species.

Introduction

Ternary mixtures of $NaNO_3$ and KNO_3 with other alkali and alkaline earth nitrates have much lower melting points than the binary alkali salt mixture (equimolar, m.p. 238°C). For example, the eutectic of $LiNO_3$, $NaNO_3$ and KNO_3 (30:18:53, wt.%) melts at 120°C, while the mixture 30 $Ca(NO_3)_2$-24 $NaNO_3$-46 KNO_3 (wt.%) melts at approximately 160°C [1]. Salt mixtures with lower melting points have potential applications as energy collection and storage fluids in advanced solar thermal energy systems [2].

The chemical equilibrium of the binary alkali mixture has been studied at high temperature and the mixture is quite stable, in the presence of oxygen, up to 600°C [4]. The stability of ternary mixtures containing calcium or lithium nitrate additions is expected to be less than that of the binary mixture because pure $Ca(NO_3)_2$ and $LiNO_3$ are less stable at high temperature than $NaNO_3$ and KNO_3 [5]. No quantitative measurements of the equilibria of mixtures containing calcium or lithium nitrate appear to have been made, although some incidental observations of decomposition of mixtures of $Ca(NO_3)_2$ and KNO_3 [6,7,8] and a mixture of $Li/Na/K/NO_3$ [9] have been reported.

The purpose of this study was to evaluate the chemical stability of ternary mixtures of alkali and alkaline earth nitrates. The approach taken was to determine the extent of decomposition, with respect to the formation of nitrite and oxide ions, of oxygen-saturated, ternary salt mixtures at equilibrium. Experiments were conducted with mixtures of Li/Na/K/NO_3, Ca/Na/K/NO_3 and Ba/Na/K/NO_3.

EXPERIMENTAL

The ternary nitrate mixtures were prepared from reagent grade salts without further purification. Melts were allowed to equilibrate for at least 48 hours after establishing the temperature of each experiment. Several samples of salt were withdrawn, using a quartz pipet, at various times during the next 24 hours or more, which was sufficient to attain constant composition. The temperature of a given mixture was raised in increments until insoluble decomposition products were observed or a temperature of 600°C was reached. The details of the experimental procedure can be found in Ref. [3].

Melts containing lithium nitrate were studied using the apparatus described by Nissen and Meeker [4]. Salt mixtures were prepared in a glove box to avoid water absorption by $LiNO_3$. The melts were contained in platinum crucibles, enclosed within a hermetically-sealed vessel, and were sparged with oxygen at one atmosphere total pressure. This apparatus had a provision for removing traces of carbon dioxide from the inlet gas stream, which eliminated the possibility of reactions between CO_2 and oxide ions formed in the melt.

Experiments with melts containing alkaline earth nitrates were conducted in a furnace open to the atmosphere. Mixtures totaling 300 to 400 grams were melted in aluminum oxide crucibles. Water was readily evolved from the salts upon melting, with visual indications ceasing after a few hours. The melts were sparged with air from the laboratory compressed air supply at a rate of 100-200 sccm. Air was passed through a Drierite (calcium sulfate) column to dry and filter it before bubbling through the melt. CO_2 was not removed from the inlet gas stream. A small amount (<0.03 wt.%) of a reddish-brown precipitate, apparently derived from calcium nitrate, formed upon heating to about 300°C. The insoluble material was filtered out by passing the melt through Pyrex-glass wool, after which the melts became water-clear. The residue was analyzed by X-ray diffraction and infrared spectroscopy and found to consist of CaO and a silicate.

RESULTS AND DISCUSSION

The equilibrium chemistry of molten nitrate salts has been reviewed elsewhere [10,11]. Metal nitrates decompose to yield the corresponding nitrite in equilibrium with the ambient oxygen activity, according to Eq. 1.

$$(1) \qquad NO_3^- = NO_2^- + 1/2\ O_2$$

The equilibrium constant for the above reaction, K_1, is given by

(2) $K_1 = [NO_2^-](P_{O_2})^{1/2} / [NO_3^-]$

where the molal concentrations of the anions and the partial pressure of oxygen are substituted for the activities of the compounds.

Nitrite, formed by Eq. 1, and nitrate may subsequently decompose to yield various oxide ion species (oxide, peroxide and superoxide). The equilibrium chemistry of oxide ions in nitrate/nitrite melts is rather complicated and somewhat controversial [10,11]. Common impurities, such as water vapor and carbon dioxide, which behave as Lux-Flood acids in these melts, have marked effects on the concentrations of oxide ion species in nitrate melts [10,11]. For example, the carbon dioxide in air may convert oxide ion species to carbonate,

(3) $CO_2 + O^{--} = CO_3^{--}$

In this study, the decomposition behavior of ternary nitrate melts was characterized by the amount of nitrite ion formed and by the concentrations of oxide ions or derivative species, such as carbonate.

Lithium-Sodium-Potassium Nitrate Mixtures

A number of ternary mixtures of $LiNO_3$ with $NaNO_3$ and KNO_3 were studied at temperatures between 500°C and 600°C. These values of K_1 were comparable to those of the binary mixture of $NaNO_3$ and KNO_3 over the temperature range studied, as shown in Figure 1. A small but systematic increase in K_1 was observed as the mole fraction of $LiNO_3$ increased (neglecting variations in the amounts of $NaNO_3$ and KNO_3). The enthalpy change of reaction 1, obtained from the slope of the Arrhenius plot, was essentially independent of composition. The average slope of the five $LiNO_3$-containing mixtures was 22.9 kcal/mol, essentially equal to that of the binary mixture, 23.0 kcal/mol [4].

Ternary mixtures containing $LiNO_3$ formed much larger concentrations of oxide ions at high temperature than the binary mixture, which was reported to have less than 10 micromolal total oxide under these conditions [4]. The formation of oxides was very sensitive to the amount of $LiNO_3$ in the mixtures, as shown in the semi-log plot in Figure 2. Below about 40 mol.% $LiNO_3$, the concentration of oxide ions increased sharply as the $LiNO_3$ content increased. A further increase in $LiNO_3$ content resulted in a much smaller increase in oxide concentration. Solubility may have been limiting the amount of oxide in the melt.

The equivalent concentration of oxide ions attained a maximum value at 550°C, regardless of the initial composition. Increasing the temperature from 550°C to 600°C caused a small decrease in the total oxide concentration of all the ternary mixtures analyzed. This behavior may be due to conversion of oxide or peroxide ions to superoxide at high temperature [14], thereby reducing the equivalent amount of hydroxide measured during titrations by half.

Calcium-Sodium-Potassium Nitrate Mixtures

Molten salt mixtures containing calcium nitrate behaved quite similarly to the binary alkali mixture with respect to nitrite formation. The Arrhenius plot in Figure 3 shows values of K_1 for several mixtures of $Ca(NO_3)_2$, $NaNO_3$ and KNO_3 and compares them to the data in the literature for the binary mixture [4], $NaNO_3$ [12] and KNO_3 [13]. Although calcium-containing mixtures displayed slightly lower values of K_1 than the binary salt, the effect of $Ca(NO_3)_2$ concentration on K_1 was negligible over the range studied. The data for all ternary mixtures were fitted to a single Arrhenius equation and a slope corresponding to an enthalpy change of 16.4 kcal/mol for Eq. 1 was obtained, somewhat less than that reported for the binary mixture, 20.3 kcal/mol [4].

The most obvious indication of decomposition at high temperature was the formation of a solid phase. Typically, the melts were maintained at each successively higher temperature for several days, without discoloration or other visible deterioration, over a cumulative period of several weeks. At the highest temperature of each experiment, solid formation was observed. In one experiment, a mixture containing 30 mol% $Ca(NO_3)_2$ was kept at 462°C for more than two weeks without a significant change in the chemical analysis or any visible changes in the melt.

The solid phase that formed in the melts was identified as calcium carbonate by X-ray diffraction analysis. The amount of each precipitate was not measured but was less than a few percent of the total mass of the melts in all experiments. The temperature at which the precipitate appeared decreased as the concentration of $Ca(NO_3)_2$ increased. The temperatures attained show that although $Ca(NO_3)_2$ reduces the stability of the mixture, the reduction is not as drastic as might be expected from the behavior of the pure salt [5].

Carbonates are formed by the reaction of carbon dioxide, in the air passed through the melts, with oxide ions produced by decomposition of nitrite and nitrate. No free oxide ions were detected in these mixtures, which indicates that the equilibrium constant for Eq. 3 is large, just as it appears to be in the binary alkali salt [15].

Barium-Sodium-Potassium Nitrate Mixtures

Equilibrium experiments were conducted with two ternary mixtures comprised of barium nitrate in sodium/potassium nitrate. Barium-containing mixtures were more stable than calcium-containing mixtures at the same concentration of alkaline earth nitrate. With respect to the nitrate-nitrite-oxygen reaction, barium-containing mixtures behaved similarly to the binary alkali mixture, as shown by the values of K_1 plotted in Figure 4. The differences between mixtures in which the mole fractions of $Ba(NO_3)_2$ were 0.2 or 0.3 were quite small. The enthalpy changes for Eq. 1 for these two mixtures were 27.4 and 25.6 kcal/mol respectively, somewhat larger than the values for the binary mixture or calcium-containing ternary salts.

Decomposition of barium-containing ternary salts at high temperature produced a solid phase. This phase was not analyzed but it was assumed to be barium carbonate, since the titrimetric analysis showed carbonate but no free oxides. The temperature required to produce visible quantities of decomposition products decreased as the concentration of $Ba(NO_3)_2$ increased analogous to ternary mixtures containing $Ca(NO_3)_2$. However, the temperature required to cause decomposition was higher than for mixtures with added $Ca(NO_3)_2$ at the same mole fraction of the alkaline earth nitrate.

Effect of Composition on Stability of Mixtures

The trend of stability of ternary salt mixtures, as indicated by the maximum temperature at which decomposition products became appreciable, is approximately Ca < Li < Ba. This order is somewhat arbitrary for Li and Ba since the cover gases were not the same. Regardless of this distinction, the stability of ternary salts followed the correlation for single salts established by Stern [5]. This correlation is based upon a parameter of the cationic specie consisting of the square root of the covalent metallic radius, r, divided by the effective nuclear charge, Z. Stability increases as the cation parameter increases, which implies that electrostatic effects between the cations and the polyatomic anions are important. The values of this parameter for the alkali and alkaline earth metals of interest are given below [5].

Cation	$r^{0.5}/Z$
Ca	0.38
Li	0.45
Ba	0.46
Na	0.53
K	0.62

The stability of ternary mixtures appears to be determined primarily by the least stable constituent since the nitrates of sodium and potassium are much more stable than the other nitrates. However, molten mixtures of nitrates appeared to be more stable than the least stable individual salts. Lithium nitrate has been reported to decompose to nitrite and oxide just above its melting point of 258°C [5], but ternary mixtures of $Li/Na/K/NO_3$ were relatively stable in the presence of oxygen. Similarly, barium nitrate reportedly decomposes upon melting [5], but its mixtures were fairly stable.

The types of cations in the salt mixtures had relatively little effect on the nitrate/nitrite reaction (Eq. 1) over the range of compositions investigated. The equilibrium constants for this reaction were quite similar for all the ternary mixtures, although a systematic increase in the enthalpy change of Eq. 1 was observed in the order Ca < Li < Ba. This order follows Stern's correlation for the pure salts [5], although the relative differences in enthalpies were less for mixtures. This observation suggests that nitrate ions are surrounded by a group of cations corresponding to the composition of a given ternary mixture and that clustering of one type of cation does not occur. It is also possible that the larger sodium and potassium ions may shield nitrate anions somewhat from the smaller, more polarizable cations (Ca^{+2}, Li^{+}, Ba^{+2}) and thereby stabilize the ternary mixtures.

In contrast, decomposition of the ternary mixtures beyond the nitrate/nitrite/oxygen reaction was strongly influenced by the types of cations present. This suggests that cations may interact with nitrite or oxide ions, which are smaller than nitrate, by clustering, rather than randomly. Clustering is a possible explanation for the marked dependence of oxide ion formation on the concentration of $LiNO_3$ in ternary salts discussed above.

CONCLUSIONS

The high temperature chemical stability of molten mixtures of sodium and potassium nitrates were reduced somewhat by the addition of either calcium (or barium) nitrate or lithium nitrate. The ternary mixtures behaved quite similarly to binary (sodium and potassium nitrate) mixtures with regard to the nitrate/nitrite/oxygen reaction. The equilibrium constant of this reaction was relatively insensitive to the composition of the ternary salt mixtures over the range studied. Oxide ion equilibria in ternary nitrate melts appear to exert a strong influence on the formation of insoluble material, which is a limiting factor with regard to the maximum useable temperature in applications.

Acknowledgements

This work was supported by U.S. Dept. of Energy Contract DE-AC04-76DP00789. Helpful discussions with D. A. Nissen of Sandia National Laboratories were much appreciated.

References

1. Phase Diagrams for Ceramists, E. M. Levin, C. R. Robbins and H. F. McMordie, eds., Vols. I and II, Amer. Ceram. Soc., 1964.
2. R. W. Bradshaw and C. E. Tyner, "Chemical and Engineering Factors Affecting Solar Central Receiver Applications of Ternary Molten Salts", A.I.Ch.E., Summer National Meeting, Denver, CO, Reprint 90b, Aug. 1988;

3. R. W. Bradshaw and D. E. Meeker, "Chemical Equilibria of Molten Ternary Nitrate Salt Mixtures," Sandia National Laboratories, SAND88-8845, May 1989.
4. D. A. Nissen and D. E. Meeker, *Inorg. Chem.*, *22*, 716 (1983).
5. K. H. Stern, *J. Phys. Chem. Ref. Data*, *1* (3), 747 (1972).
6. E. Rhodes, W. E. Smith and A. R. Ubbelohde, *Proc. Roy. Soc.*, *A285*, 263 (1965).
7. M. D. Ingram and G. G. Lewis, *J. Electroanal. Chem.*, *5*, 399 (1974)
8. A. A. K. Al-Mahdi, *J. Appl. Chem.*, *14*, 269 (1964).
9. R. A. Archer and B. R. Dunbobbin, "Pilot Plant Development of a Chemical Air Separation Process", Air Products and Chemicals, Inc., U.S.D.O.E. report DOE/CS/40544-T1, May 1985.
10. B. W. Hatt, in *Molten Salt Technology*, D. G. Lovering, ed., Plenum Press, p. 483ff, 1982.
11. J. Jordan, W. B. McCarthy and P. G. Zambonin, in *Molten Salts*, G. Mamantov, ed., Academic Press, p. 575ff (1969).
12. G. D. Sirotkin, Russ. *J. Inorg. Chem.*, *4*, 1180 (1959).
13. R. F. Bartholomew, *J. Phys. Chem.*, *70*, 3442 (1960).
14. D. R. Flinn and K. H. Stern, *J. Electroanal. Chem.*, *63*, 39 (1975).
15. R. N. Kust, *Inorg. Chem.*, *3* (7), 1035 (1964).

Registry No. NO_3^-, 14797-55-0; NO_2^-, 14797-65-0. $NaNO_3$, 7631-99-4; KNO_3, 7757-79-1; $Ca(NO_3)_2$, 10124-37-5; $Ba(NO_3)_2$, 10022-31-8; $LiNO_3$, 790-69-4;

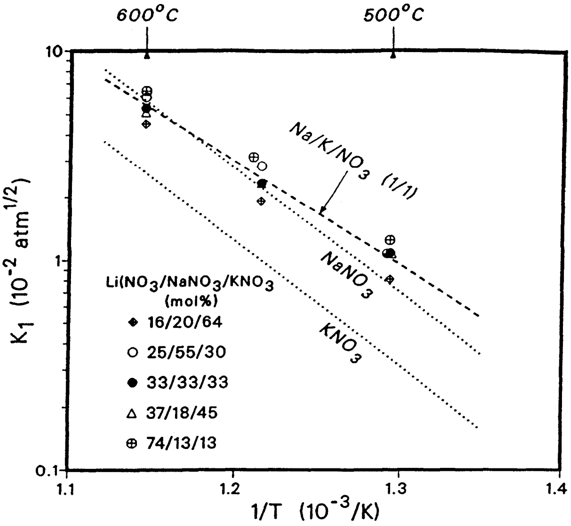

Figure 1
Arrhenius plot of the equilibrium constants of the reaction, nitrate = nitrite + oxygen, for Li/Na/K/NO$_3$ mixtures. The dashed line represents data from the literature for the equimolar mixture of NaNO$_3$ and KNO$_3$.

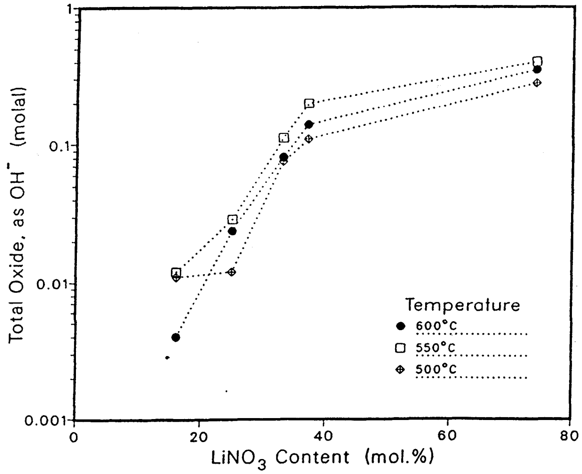

Figure 2
Semi-log plot of the equivalent oxide ion concentration of various molten Li/Na/K/NO$_3$ mixtures at 1 atm. O$_2$ pressure.

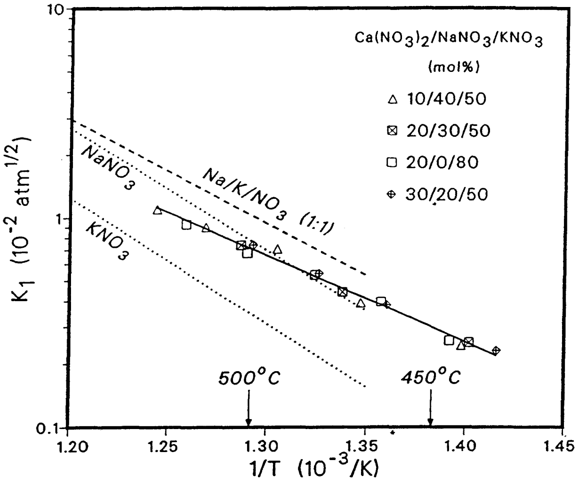

Figure 3
Arrhenius plot of the equilibrium constants of the reaction, nitrate = nitrite + oxygen, for Ca/Na/K/NO_3 mixtures (solid line). The broken lines represent data from the literature for the salts designated.

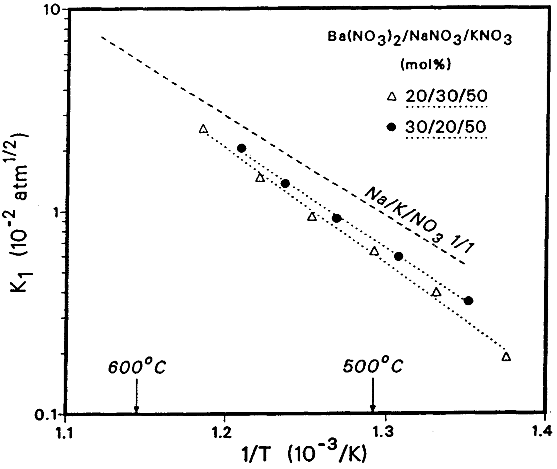

Figure 4
Arrhenius plot of the equilibrium constants of the reaction, nitrate = nitrite + oxygen, for Ba/Na/K/NO_3 mixtures.

AUTHOR INDEX

SUBJECT INDEX